

NASA CONTRACTOR
REPORT

NASA CR-183837

RESEARCH REPORTS - 1989 NASA/ASEE SUMMER FACULTY
FELLOWSHIP PROGRAM

The University of Alabama in Huntsville
Huntsville, Alabama
and
The University of Alabama
Tuscaloosa, Alabama

December 1989

Final Report

Prepared for
NASA, George C. Marshall Space Flight Center
Marshall Space Flight Center, Alabama 35812

(NASA-CR-183837) RESEARCH REPORTS: 1989
NASA/ASEE SUMMER FACULTY FELLOWSHIP PROGRAM
Final Report (Alabama Univ.) 888 COSOL 130

N90-19090
--THRU--
N90-19424
Unclass
G253150

05/31

RESEARCH REPORTS

1989 NASA/ASEE SUMMER FACULTY FELLOWSHIP PROGRAM

George C. Marshall Space Flight Center
The University of Alabama in Huntsville

and

The University of Alabama

EDITORS:

Dr. Gerald R. Karr
Chairman of Mechanical Engineering
The University of Alabama in Huntsville

Dr. Frank Six
NASA/ASEE Program Co-Director
Assistant for University Affairs
Marshall Space Flight Center

Dr. L. Michael Freeman
Assistant Professor of Aerospace Engineering
The University of Alabama

NASA CR-183837



Report Documentation Page

1. Report No. NASA CR- 183837	2. Government Accession No.	3. Recipient's Catalog No.	
4. Title and Subtitle Research Reports - 1989 NASA/ASEE Summer Faculty Fellowship Program		5. Report Date December 1989	
		6. Performing Organization Code	
7. Author(s) Editors: Dr. Gerald R. Karr Dr. Frank Six Dr. L. Michael Freeman		8. Performing Organization Report No.	
		10. Work Unit No.	
9. Performing Organization Name and Address The University of Alabama in Huntsville, and The University of Alabama, Tuscaloosa, Alabama		11. Contract or Grant No. NGT-01-008-021	
		13. Type of Report and Period Covered Contractor Report	
12. Sponsoring Agency Name and Address National Aeronautics and Space Administration Washington, D.C. 20546		14. Sponsoring Agency Code	
15. Supplementary Notes			
16. Abstract: For the twenty-fifth consecutive year, a NASA/ASEE Summer Faculty Fellowship Program was conducted at the Marshall Space Flight Center (MSFC). The program was conducted by the University of Alabama in Huntsville and MSFC during the period June 5 through August 11, 1989. Operated under the auspices of the American Society for Engineering Education, the MSFC program, as well as those at other NASA Centers, was sponsored by the Office of University Affairs, NASA Headquarters, Washington, D.C. The basic objectives of the programs are (1) to further the professional knowledge of qualified engineering and science faculty members; (2) to stimulate an exchange of ideas between participants and NASA; (3) to enrich and refresh the research and teaching activities of the participants' institutions; and (4) to contribute to the research objectives of the NASA Centers. The Faculty Fellows spent ten weeks at MSFC engaged in a research project compatible with their interests and background and worked in collaboration with a NASA/MSFC colleague. This document is a compilation of Fellows' reports on their research during the summer of 1989. The University of Alabama in Huntsville Report No. 817 presents the Co-Directors' report on the administrative operations of the program. Further information can be obtained by contacting any of the editors.			
17. Key Words (Suggested by Author(s)) Middle atmosphere spacelink, SEDS, PBL-radiation, trend analysis, SSME-HPOTP, LOX compatibility, X-ray detectors, lift-off seal, rotordynamics, alternating gradient magnetometer, gamma- ray burst, artificial intelligence.		18. Distribution Statement Unclassified - Unlimited	
19. Security Classif. (of this report) Unclassified	20. Security Classif. (of this page) Unclassified	21. No. of pages 912	22. Price NTIS

PREFACE

This document is a collection of technical reports on research conducted by the participants in the 1989 NASA/ASEE Center (MSFC). This was the twenty-fifth consecutive year the program has been conducted at MSFC. The 1989 program was administered by the University of Alabama in Huntsville (UAH) in cooperation with MSFC and the University of Alabama (UA). The program was operated under the auspices of the American Society for Engineering Education (ASEE) with sponsorship and funding from the Office of External Relations, NASA Headquarters, Washington, D.C. The MSFC program was one of the eight such Aeronautics and Space Research Programs funded by NASA Headquarters in 1989. Similar programs were conducted at seven other NASA centers. The basic common objectives of the NASA/ASEE Summer Faculty Fellowship Program are:

- a. To further the professional knowledge of qualified engineering and science faculty members;
- b. To stimulate an exchange of ideas between participants and NASA;
- c. To enrich and refresh the research and teaching activities of participants' institutions; and,
- d. To contribute to the research objectives of the NASA centers.

The MSFC Faculty Fellows spent 10 weeks (June 5 through August 11, 1989) working with NASA scientists and engineers on research of mutual interest to the University faculty member and the NASA colleague. The editors of this document were responsible for selecting appropriately qualified faculty to address some of the many problems of current interest to NASA/MSFC. A separate document (UAH Report No. 817, September 1989) reports on the administrative aspects of the 1989 program. This document contains the technical reports on research performed by the individual 1989 participants. The NASA/ASEE program is basically a two-year program to allow in-depth research by the University faculty member. The reports are arranged in alphabetical order.

TABLE OF CONTENTS

I.	Baginski, Michael E.:	"Characterization of Thunderstorm Induced Maxwell Current Densities in the Middle Atmosphere"
II.	Blake, Jean A.:	"NASA Spacelink Electronic Information System"
III.	Carrington, Connie K.:	"Kalman Estimation for SEDS Measurements"
IV.	Chang, Chia-Bo:	"A PBL-Radiation Model for Application to Regional Numerical Weather Prediction"
V.	Chiu, Huei-Huang:	"Potential Theory of Radiation"
VI.	Church, Curtis K.:	"Methods for Trend Analysis: Examples With Problem/Failure Data"
VII.	Chyu, Mingking K.:	"A Parametric Heat Transfer Study for Cryogenic Ball Bearings in SSME HPOTP"
VIII.	Diwan, Ravinder M.:	"Liquid Oxygen LOX Compatibility Evaluations of Aluminum Lithium (Al-Li) Alloys: Investigation of the Alcoa 2090 and MMC Weldalite 049 Alloys"
IX.	Eldridge, Hudson B.:	"Background Studies in Gas Ionizing X-Ray Detectors"
X.	Elrod, David A.:	"Investigation of SSME Alternate High Pressure Fuel Turbopump Lift-Off Seal Fluid and Structural Dynamic Interaction"
XI.	Flowers, George T.:	"A Study of the Effects of Disk Flexibility on the Rotordynamics of the Space Shuttle Main Engine Turbo-Pumps"

- XII. Garland, Michael M.: "A Computer Control System for the Alternating Gradient Magnetometer"
- XIII. Hakkila, Jon: "Monte Carlo Models and Analysis of Galactic Disk Gamma-Ray Burst Distributions"
- XIV. Hornfeck, William A.: "Artificial Intelligence Issues Related to Automated Data Processing Operations"
- XV. Hui, David: "Low-Energy Impact Resistance of Graphite-Epoxy Plates and ALS Honeycomb Panels"
- XVI. Irwin, R. Dennis: "Investigations Into a New Algorithm for Calculating H Optimal Controllers"
- XVII. Keyhani, Majid: "Evaluation of the Heat Transfer Module (FAHT) of Failure Analysis Nonlinear Thermal and Structural Integrated Code (FANTASTIC)"
- XVIII. Lestrade, John P.: "Radial Response of the Burst and Transient Source Experiment"
- XIX. Magana, Mario E.: "Determination of the Implementation of the 3-Axis Attitude Motion Simulator Digital Position Controller"
- XX. Mehrabadi, M. M.: "Mechanics of Aeolian Processes - Soil Erosion and Dust Production"
- XXI. Moorhead II, Robert J.: "Evaluation and Analysis of the Orbital Maneuvering Vehicle Video System"
- XXII. Peterson, Lennart R.: "Transmission and Reflection Studies of Thin Films in the Vacuum Ultraviolet"
- XXIII. Phanord, Dieudonne D.: "Analytical Optical Scattering in Clouds"

- XXIV. Radcliff, Roger: "Radar Transponder Antenna Pattern Analysis for the Space Shuttle"
- XXV. Rule, William K.: "ROCOPT - A User Friendly Interactive Code to Optimize Rocket Structural Components"
- XXVI. Santi, L. Michael: "Iterative Procedures for Space Shuttle Main Engine Performance Models"
- XXVII. Smith, Wayne D.: "Marshall Avionics System Testbed (MAST)"
- XXVIII. Steranka, Jr., Paul O.: "Heat Sink Effects on Weld Bead - VPPA Process"
- XXIX. Thomas, Daniel L.: "Frequency Response of Porous Battery Electrodes"
- XXX. Walcott, Bruce L.: "YAW Rate Control of an Air Bearing Vehicle"
- XXXI. Whitaker, Kevin W.: "The Influence of a Wall Function on Turbine Blade Heat Transfer Prediction"
- XXXII. Wiens, Gloria J.: "Multibody Modeling and Verification"
- XXXIII. Wilson, Howard B.: "A Vectorized Algorithm for 3D Dynamics of a Tethered Satellite"
- XXXIV. Young, Ronald B.: "Techniques for Studying the Effects of Microgravity on Model Particle/Cell Systems"

1989

N90-19391

NASA/ASEE SUMMER FACULTY FELLOWSHIP PROGRAM

MARSHALL SPACE FLIGHT CENTER
THE UNIVERSITY OF ALABAMA HUNTSVILLE

CHARACTURIZATION OF THUNDERSTORM INDUCED MAXWELL
CURRENT DENSTIES IN THE MIDDLE ATMOSPHERE

PREPARED BY: MICHAEL EDWARD BAGINSKI

ACADEMIC RANK: ASSISTANT PROFESSOR

UNIVERSITY AND
DEPARTMENT: AUBURN UNIVERSITY
DEPARTMENT OF ELECTRICAL ENGINEERING

NASA/MSFC:
LABORATORY: SPACE SCIENCE
DIVISION: EARTH SCIENCE AND APPLICATION
BRANCH: REMOTE SENSING

MSFC COLLEAGUE: DR. HUGH CHRISTIAN
DR. RICHARD BLAKESLEE

DATE: SEPTEMBER 1, 1989

CONTRACT NO: NGT-01-008-021
THE UNIVERSITY OF ALABAMA HUNTSVILLE

CHARACTERIZATION OF THUNDERSTORM INDUCED MAXWELL CURRENT DENSITIES IN THE MIDDLE ATMOSPHERE

by

Michael Edward Baginski
Assistant Professor of Electrical Engineering
Auburn University
Auburn, Alabama

ABSTRACT

Middle atmospheric transient Maxwell current densities generated by lightning induced charge perturbations are investigated via a simulation of Maxwell's equations. A time domain finite element analysis is employed for the simulations. The atmosphere is modeled as a region contained within a right circular cylinder with a height of 110 km and radius of 80 km. A composite conductivity profile based on measured data is used with charge perturbations are centered about the vertical axis at altitudes of 6 and 10 km. The simulations indicate that the temporal structure of the Maxwell current density is relatively insensitive to altitude variation within the region considered. It is also shown that the electric field and Maxwell current density are not generally aligned.

ACKNOWLEDGEMENTS

I would like to thank NASA/ASEE for allowing me to participate in the Summer Faculty Program at Marshall Space Flight Center. The Program was well coordinated by Mr. Frank Six of NASA and Dr. Gerald F. Karr of UAH. Dr. Hugh Christian, Dr. Richard Blakeslee and Dr. James Arnold were especially helpful in obtaining the necessary computer software and technical materials required for the research.

This summer's research endeavors have lead to the submittal of a manuscript to The Journal of Geophysical Research. This would not have been possible without the assistance of Dr. Hugh Christian and Dr. Richard Blakeslee. My appreciation for the personal interest both of these scientists have taken in the research can not be stated strongly enough. I am looking forward to future research in the area of Atmospheric Electricity with Dr. Christian and Dr. Blakeslee

INTRODUCTION

The use of Maxwell currents and current densities to describe the electromagnetic response of the atmosphere is a fairly recent development. Krider and Musser and Nisbet have suggested that the thunderstorm is fundamentally a current source and should therefore be investigated in terms of current densities rather than electric fields. The current densities generated by charge perturbations associated with lightning consist of either conduction (resulting from charge movement) or displacement ($\epsilon \partial E / \partial t$) terms. The sum of these current densities are referred to as the Maxwell current density (J_m).

$$J_m = \nabla \times H = J_p + \epsilon \partial E / \partial t \quad (1)$$

J_m = Maxwell current density

J_p = the sum of all conduction current densities including source terms

$\epsilon \partial E / \partial t$ = displacement current density

The Maxwell current density has several properties that may be exploited to more accurately describe both the local and global effects of lightning on the atmosphere. Probably the most important of these is that the divergence of the Maxwell current density is zero ($\nabla \cdot J_m = 0$) making it a solenoidal quantity. As a consequence of this, the lines of the Maxwell current density form closed loops. Along these Maxwell current density streamlines the displacement term is usually dominant at low altitudes with the conduction current density dominating the high altitude Maxwell current density.

This solenoidal character of the Maxwell current density implies that the electrical parameters of the entire path of circulation strongly affect its response and conversely; if the Maxwell current density along the streamline is mathematically describable, the corresponding streamline's electric field may be formulated by a simple

time domain integration. An analogy exemplifying this phenomenon can be made to a source driving a series ladder network with each element consisting of a parallel RC. The relative analogies in the circuit are as follows: $J_m \sim I_s$, voltage $\sim E$, $C\partial V/\partial t \sim \epsilon\partial E/\partial t$, $V/R \sim \sigma E$. It is obvious that the total impedance of the circuit limits the current response, analogous to the peak surge impedance along the streamline's path governing the behavior of the Maxwell current density. Therefore, if the limiting factors (peak surge impedance) could be identified and incorporated in an atmospheric electrodynamic model, the electric fields along the entire streamline could be easily derived.

Modeling of the Thunderstorm

The simulated thunderstorm's electrical activity is sustained by a constant current generator that exists between the upper and lower charge centers (6 and 10 km respectively, upper center positive). Intra-cloud lightning, resulting from the accumulation of the generator charge, occurs at time intervals determined primarily by the charging current and amount of charge exchanged per flash. For the purposes of modeling, the effects of the constant current generator will be analyzed separately from that of the charge perturbation associated with intra-cloud lightning. The resulting steady state and transient solutions will then be superimposed to determine the total electrical response of interest [Baginski, 1987].

Several implicit assumptions used in the modeling should be noted. The net amount of charge accumulation at either of the charge centers due to the thundercloud generator current and the neutralization of charge by lightning was assumed to be zero. This required that the time average amount of charge neutralized by lightning equaled the amount deposited by the thundercloud current generator. In the modeling a one ampere charging current was used. Charge accumulation at the charge centers occurred until a breakdown field strength was obtained [pg 72, Uman, 1987]. The resulting steady state field mapping at the time breakdown was reached was used as the steady state component of the simulated field signatures. Specific details of the spatial and temporal distribution of the thundercloud's charge used in the modeling

The computer model used in the study was based on an adaptation of an earlier computer code that was used to simulate lightning induced field signatures in the middle atmosphere and ionosphere [Baginski et al., 1988]. The major changes necessary were to the inclusion of the thundercloud's current generator as an additional electrical source and use of a conductivity profile based on measurements. Since the earlier code simulated transient behavior that was observed at greater distances from the source and had much shorter durations, no changes were required in time step or spatial discretization used.

Charging Mechanisms

In thunderstorm research, the most difficult phenomena to explain have been the processes involved in cloud electrification. The difficulty is twofold: on the one hand, there are a large number of possible mechanisms responsible for charge separation and current generation; on the other hand, it is usually impossible to isolate such mechanisms and test each for its relative effect. Regardless of the mechanisms, what is known is that a thunderstorm is sustained by charge separation which can be approximated by net positive and negative charge centers. The height of the charge centers is somewhat affected by seasonal changes and the geographic location. Typical heights of 10 km for the upper charge center and 6 km for the lower charge center are widely found in the literature and were selected for this research [pp 50-61, Uman, 1987].

According to measurements, the amount of charge neutralized by lightning, and the thunderstorm's current generator will vary over a considerably larger range than the charge center's heights. For instance, Kasimer (1959) has measured values of cloud electrification currents from less than 0.1 ampere to 10 amperes. Lightning return stroke currents are reported to have an even larger range of values [pp 161-162 Uman, 1987]. It was therefore necessary to carefully consider the affects the temporal signature and magnitude of these sources would have on the simulations of interest prior to their specification in the model.

Since the research presented here focused on field recovery behavior at times ~ 100 ms after the cessation of the lightning current, the temporal variation of the lightning current was assumed to have little effect on the simulations of interest. In fact, after the modeling and comparative studies were completed, a simulation was done where the time variation of the charge neutralized (source of transient) by lightning was described mathematically by a simple impulse ($\delta(t)$) and resulted in field recovery curves that were identical.

Sunde's (1968) lightning current model was used in the study in the form shown below:

$$I_{ic}(t) = IO(\exp(-at) - \exp(-bt)) \quad (2)$$

where $I_{ic}(t)$ = return stroke current (Sunde's model)

$a = 10^4$ seconds $^{-1}$

$b = 0.5 \times 10^6$

IO = proportional to amount of charge
displaced during return stroke

Sunde's model consists of two exponential terms and is relatively simple compared to some of the more recent models [pp 330-334 Uman, 1987]. For the time frames of interest in this study ($t > 100$ msec), it included the necessary temporal information required for late time transient electromagnetic analysis.

The charge neutralized by the lightning current (charge perturbation) was described in terms of the temporal behavior of this current as follows ($I_{ic} = dQ_f/dt$):

$$Q_f(t) = \int_0^t I_{ic}(\tau) d\tau \quad (3)$$

where $I_{ic}(\tau)$ = lightning current

$Q_f(t)$ = total amount of charge neutralized
by lightning

The neutralization of charge by lightning occurs over the entire charge center and the possible effects of its spatial distribution must be considered in any thunderstorm electrical modeling. Its spatial profile will obviously strongly influence field behavior within the cloud, but at distances much larger than the charge centers extent (maximum feature size), its distribution will have little effect on the transient signatures [Baum, 1980]. Since the electric fields of interest were at least 20 km from the charge center (charge center's maximum feature size ~ 2 km) there was a certain degree of freedom in the specification of the distribution of neutralized charge. Also, since there is virtually no published data describing the charge neutralization within the cloud the selection was even more arbitrary. A modified Gaussian spatial profile was chosen for the modeling and has been used in the modeling of many man-made and naturally occurring forced charge events [Baum, 1980].

The Gaussian profile used to describe the charge neutralized by lightning was also assumed for the charging caused by the thundercloud generator current. Here too, many possible profiles could have been used and for simplicity the Gaussian profile was selected. The mathematical description used in the modeling is shown below:

$$\pm \partial \rho_f(r,z,t) / \partial t = \pm (\partial Q_f(t) / \partial t \pm \alpha) (f(r,z)) \quad (4)$$

$$f(r,z) = (\exp(-R^2/(2\lambda))) / (2\pi\lambda)^{1.5}$$

where λ = variance ($\lambda = 4000 \text{ m}^2$ for simulations)

$$R^2 = r^2 + (z - z')^2$$

z' = altitude of charge center (6 or 10 km)

α = term arising from steady state charging current
($\pm 1 \text{ A}$ used in the modeling)

A cylindrical coordinate system was used in the model with symmetry assumed about the vertical (z) axis (Figure 1). The effect of the magnitudes of the charge sources on the solutions will be discussed in a later section.

It is well known that the electric field recovery following lightning is a result of the neutralization of charge by the return stroke [pp 171-172 Uman, 1987]. The field's behavior is dictated primarily by the atmosphere's conductivity, the amount of charge neutralized by lightning and the magnitude of the thunderstorm's current generator.

Geometry of the Region

Before describing the geometry, consider again the phenomenon of interest: charge sources, located at altitudes no greater than approximately 10 km, induce electric fields throughout the atmosphere, but only those fields induced within the middle atmosphere were of interest in this study. Therefore, the model constructed must meet two criteria:

- 1) If not obviously constrained, the geometrical limits of the model will approximate the entire atmosphere's electrical effect on the regions where the simulations take place.
- 2) The boundary conditions of the region will be electrically equivalent to those of the atmosphere.

The region selected (Figure 1) is contained within a right circular cylinder with a radius of 80 km and height of 110 km. A discussion of how each of the boundaries was arrived at follows:

- Lower Plate - The earth's surface was electrically modeled as a perfect conductor. This assumption was based on the very large difference that exists between the earth's conductivity and adjacent atmosphere's conductivity. Typically, values of 10^{-3} to 10^{-2} mhos/meter are used for the earth's conductivity, while 10^{-14} to 10^{-13} mhos/meter is the usual range of the adjacent atmosphere's conductivity [pg 225, Voiland, 1984]. This difference of more than 11 orders of magnitude makes the earth appear (electrically) as a perfect conductor. This assumption is commonly used in practical antenna engineering for frequencies whose range would correspond to time scales of 10^{-9} to 10^0 seconds [Baum, 1980], ranges well beyond the maximum and minimum time scales of this research (minimum time step used in the research is 5×10^{-5} seconds with a total duration 20 seconds.).

- Upper Plate - The selection of 110 km for the height of the upper boundary was a necessary consequence of the atmospheric conductivity structure being complicated by the Hall and Pederson components above an altitude of approximately 70 km [Volland, 1984]. The tensor conductivity components result when the mean free path and velocities of the charged carriers are sufficient to allow their trajectories to be altered by the effect of the earth's magnetic field [Stratton, 1941]. The finite element routine employed in the solution is not capable of modeling tensor conductivities, therefore an altitude limit must be set in the vicinity of 70 km.

The 110-km altitude was selected based on the following considerations:

- 1) The relative magnitude of the two tensor conductivity components is approximately proportional to the additional distance in altitude (beyond 70 km) considered. The maximum value of either of these components with respect to the parallel conductivity's magnitude (for the range of altitudes considered) is less than 20 percent [Volland, 1984].

- 2) The middle and upper atmospheric electric fields resulting from lightning (with the exception of the $\sim 10^{-4}$ propagating component) are approximately vertically oriented [Volland, 1984], i.e., the horizontal component is negligible.

- 3) The off-diagonal tensor components of the conductivity will only interact with electric fields that are not aligned with the earth's magnetic field [Volland, 1984]. Since the earth's magnetic field with the exception of the equatorial regions, is primarily vertically aligned [Chalmers, 1967], the influence of both the Pederson and Hall components on the lightning induced vertical electric fields will be, to first order, negligible.

An obvious concern is the influence this 110-km altitude limit may have on the simulations. To investigate the maximum possible error (assuming an electrically passive ionosphere) that this would introduce in the solutions, two sets of simulations were done with the 110-km upper plate electrically described by :

- 1) The vertical electric field and charge density are set to a value of zero.
- 2) The divergence of the electric field is set to the value of the charge density divided by the

and charge density are set to a value of zero. 2) The divergence of the electric field is set to the value of the charge density divided by the permittivity of free space ($\nabla \cdot \mathbf{E} = \rho/\epsilon$). When the results were compared, little, if any, difference could be seen for the time frames of interest in any of the cases (all cases were subject to this test).

The probable reason for this behavior is that, in general, for lightning-induced transients, the electrical properties of the atmosphere below the point of observation of the field, rather than above, govern the transient response [Hale and Baginski, 1987]. This may be explained by simply considering the fact the conductivity rapidly increases with altitude (i.e., resistivity decreasing), and therefore its influence (restrictive effect) on total global charge movement decreases. Hence, it seems reasonable to assume the middle atmosphere's simulated response to low-altitude charge perturbations is governed by the adjacent and lower altitude conductivity values.

The conductivity used in the previously referenced high altitude simulations [Baginski *et al.* 1988] was slightly modified to depict the observed conductivity [Blakeslee *et al.*, 1988] and used for the study in the form shown below (Figure 2):

$$\sigma(z) = 1.3875 \times 10^{-14} / (F1 + F2 + F3 + F4)$$

$$\begin{aligned} \text{where} \quad F1 &= 2.94 / (\exp(4.5 \times 10^{-3} \times z)) \\ F2 &= 1.39 / (\exp(0.375 \times 10^{-3} \times z)) \\ F3 &= 0.369 / (\exp(0.12987 \times 10^{-3} \times z)) \\ F4 &= 9.0 / (\exp(2.777 \times 10^{-3} \times z)) \end{aligned}$$

- Outer Cylindrical Surface - The lateral boundary had no distance constraint and could have been extended indefinitely. However, there exists a trade-off between accuracy and resolution: the smaller the model dimensions, the greater the accuracy in solving the differential equations. Therefore, the errors resulting from the adoption of finite boundaries for the model must be weighed against those resulting from degrading the numerical resolution of the simulation by involving too large a volume.

The simulations were found to be insensitive to increases in the radial limit beyond 70 km for all cases. No visible difference could be detected in the responses using either 70-km or 80-km radial boundaries when plotted together. Therefore, selecting a 80-km radial limit is a measure taken to provide additional confidence in the simulations.

- Axis of Symmetry (z-axis) - Since $r = 0$ defines an axis of symmetry and since there are no discontinuities in the charge distribution, the derivative of the vertical electric field ($\partial E_z / \partial r$) with respect to radial distance reduces to zero on the axis.

The differential forms of the four boundaries are summarized as follows:

- 1) At ARC = +1 (z-axis), $\partial E_z / \partial r = 0$
- 2) At ARC = +2 (lower boundary), $E_r = 0$, equal potential surface
- 3) At ARC = -3 (outer radial boundary), $\rho = E_z = 0$
- 4) At ARC = +4 (upper boundary) $\nabla \cdot E = \rho / \epsilon_0$

Maxwell's Equations

From Maxwell's Equations a single equation is developed in which the electric field is dependent on the source charge and current densities as follows [Holzworth and Chiu, 1982]:

$$\nabla \times \nabla \times E = -\mu_0 (\sigma \partial E / \partial t + \partial J_s / \partial t + \epsilon_0 \partial^2 E / \partial t^2) \quad (5)$$

$$\nabla \rho / \epsilon_0 = \nabla^2 E - \mu_0 (\sigma \partial E / \partial t + \partial J_s / \partial t + \epsilon_0 \partial^2 E / \partial t^2) \quad (6)$$

where J_s = source current density associated with high intensity lightning current, was neglected in the simulations
 ρ = charge density

The continuity equation is derived by taking the divergence of the Maxwell current density:

$$0 = \nabla \cdot \nabla \times H = \nabla \cdot (\sigma E + \epsilon_0 \partial E / \partial t + J_s) \quad (7)$$

$$0 = \rho\sigma/\epsilon_0 + \nabla\sigma \cdot E + \partial\rho/\partial t + G_s \quad (8)$$

where $\nabla \cdot J_s = G_s$ = source of charge perturbation
 (deposition of charge by the lightning current and
 thunderstorm current generator)

The above equations were derived from Maxwell's equations and were used to describe the electrodynamic response of the atmosphere to the thunderstorm.. It is important to note the primary difference in the forcing function G_s (charge related) used here relative to forcing functions used for most spheric analysis (typically current-related forcing functions). A current related transient (e.g., current loop) is allowable in a charge neutral region, but charge movement through space does not necessarily imply a zero volume charge density. Furthermore, a charge perturbation may be considered separately from the currents which cause it (charge perturbation implies charge generation at a point in space). In the latter case charge motion is required (conservation of charge), but the relative contribution of each (charge versus current) mechanism to the resulting total electric field may be analyzed separately. Initially (prior to the first iterative time step of the transient analysis), no charge is displaced and the transient electric field everywhere is assumed zero.

Equations 6 and 8 used in the modeling are linear partial differential equations. This fact greatly reduced the degree of complexity in the thunderstorm electrical modeling. Linearity allows the use of superposition to construct the total solution desired based on each source's individual response. The amplitude of the solution is also directly proportional to the source's magnitude. This was especially important in the comparative analysis when the specific thunderstorm's current generator and amount of charge neutralized by lightning were derived.

SIMULATIONS

The vertical component of the simulated Maxwell current density signatures are shown in Figure 3 for altitudes of 46, 53, and 60 km at a radial distance of 15 km from the vertical axis of symmetry. The waveforms show only slight differences in both magnitude and temporal character. Vertical electric field signatures at the same positions show relatively large variations in both magnitude and temporal character (Figure 4).

Figure 5 and 6 identify the normalized Maxwell current density and electric field for altitudes of 40-60 km and radial distances of 15-30 km at $t = 200$ milliseconds. The interesting feature is that the Maxwell current density and electric field are not aligned. This observation is of importance to experimentalists who typically infer field characteristics from a single measured quantity (E and J_m).

The simulated vertical electric field signatures (Figure 4) are based on conductivity measurements obtained concurrently with with transient electric field data. There are two traits common to both measurements and simulations that are not explainable in terms of simple relaxation time solutions: the significant time delay prior to the onset of the maximum field strength, and the relatively long duration of the transient. This fact indicates that the use of relaxation time solutions would not be valid for the study conducted.

CONCLUSIONS

The major contribution of the study is to emphasize the general importance modeling has in identifying the allowable atmospheric transient behavior. This reduces the researchers need to rely on assumptions that are in many cases not rigorously justifiable. It is probable that the next major advances in atmospheric electricity will involve numerical simulation predictions of otherwise unexpected behavior.

Lightning researchers may benefit from the relative spatial and

temporal invariance of the Maxwell current density with respect to the corresponding electric field signature. It is likely that this type of characterization would provide an alternative fundamental description of the lightning event that would greatly reduce the complexity of much current thunderstorm electrical research.

REFERENCES

- Anderson, F.J. and G.D. Freier, "Interaction of the Thunderstorm with a Conducting Atmosphere," J. Geophys. Res., 74, 5390, 1969.
- Baginski, M.E., "Finite element simulation of the atmosphere's electromagnetic response to charge perturbations associated with lightning," Ph.D. thesis, Pennsylvania State University, 1987.
- Baginski, M.E., L.C. Hale, and J.J. Olivero, "Lightning-Related Fields in the Ionosphere," Geophys. Res. Let., August, 1988
- Baum, C.E., "Simulation of Electromagnetic Aspects of Lightning," Proc. of Lightning Tech., NASA Conf. Pub. 2128, April 1980.
- Blakeslee, R.J., H.J. Christian, and B. Vonnegut, "Electrical Measurements Over Active Thunderstorms," submitted to J. Geophys. Res., September 1988.
- Browning, G. L., I. Tzur, and R.G. Roble, "A Global Time-dependent Model of Thunderstorm Electricity. Part I: Mathematical Properties of the Physical and Numerical Models," JAS., 49, 2166, 1987
- Chalmers, J.A., Atmospheric Electricity, 2nd ed., Pergamon, New York, 1967.
- Gish, O.H., and R.G. Wait, "Thunderstorms and the earth's general electrification," J. Geophys. Res., 55, 473, 1950.
- Golde, R.H., Lightning, Volume I., Academic Press, 1977.

- Greifinger, C., and P. Greifinger, "Transient ULF Electric and Magnetic Fields Following a Lightning Discharge," J. Geophys. Res., 81, 2237, 1976.
- Hale, L.C., and M.E. Baginski, "Current to the ionosphere following a lightning stroke," Nature, 329, 814, 1987
- Holzer, R.E. and D.S. Saxon, "Distribution of electrical conduction currents in the vicinity of Thunderstorms," J. Geophys. Res., 57, 207, 1952.
- Holzworth, R.H. and Y.T. Chiu, "Spherics in the Stratosphere," in CRC Handbook of Atmospherics, volume one, H. Volland, CRC Press, Boca Raton, Florida, 65, 1982.
- Illingworth, A.J., "Electric Field Recovery After Lightning as the Response of a Conducting Atmosphere to a Field Change," Quart. J. Roy. Meteorol. Soc., 98, 604, 1972.
- Israel, H., Atmospheric Electricity, Israel Program for Scientific Translations, vol. 2, Jerusalem, 1973.
- Kasemir, H.W., "The Thunderstorm as a Generator in the Global Electric Circuit (in German)," Z. Geophys., 25, 33, 1959.
- Krider, E.P., and J.A. Musser, "Maxwell currents under a thunderstorm," J. Geophys. Res., 87, 171-176, 1982.
- Nisbet, J.S., "A dynamic model of thundercloud electric fields," J. Atmos Sci., 40, 2855, 1983.

- Park, C.G., and M. Dejnakarindra, "Penetration of Thundercloud Electric Fields into the Ionosphere and Magnetosphere 1. Middle and Subauroral Latitudes," J. Geophys. Res., 78, 6623-6633, 1973.
- Stratton, J.A., Electromagnetic Theory, McGraw-Hill, New York, 1941.
- Stremier, F.G., Introduction to Communication Systems, Addison-Wesley, California, 1977.
- Sunde, E.D., Earth Conduction Effects in Transmission Systems, Dover, New York, 1968.
- Tamura, Y., "An Analysis of the Electric Field After Lightning Discharges," Geophys. Res. Pap., 42, 190-200, 1955.
- Tzur, I. and R.G. Roble, "The Interaction of a Dipolar Thunderstorm with its Global Electric Environment," J. Geophys. Res., 90, 5989, 1985.
- Uman, M.A., Lightning, McGraw-Hill, New York, 1987.
- Volland, H., Atmospheric Electrodynamics, Chemistry in Space, vol. II, Springer-Verlag, Berlin, Germany, 1984.
- Willett, J.C., "Maxwell Currents and the Thunderstorm Generator," presented at 1984 AGU Fall Meeting, San Francisco, California
- Wilson, C.T.R., "Some Thundercloud Problems," J. Franklin Inst., 208, 1916.

ORIGINAL PAGE IS
OF POOR QUALITY

ELECTRICAL MODEL OF ATMOSPHERE

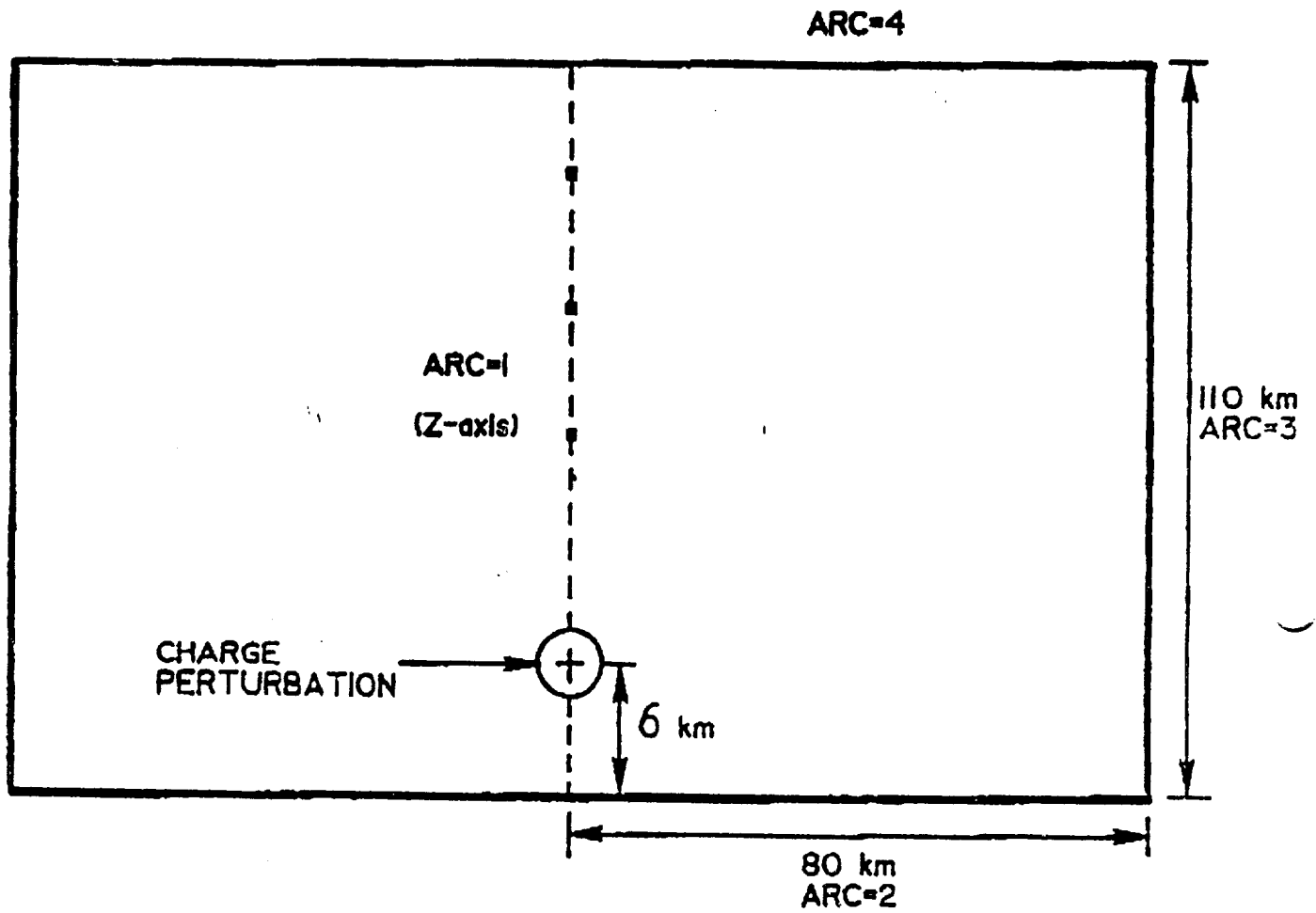


Figure 1 Electrical Model of the Atmosphere.

COMPOSITE CONDUCTIVITY

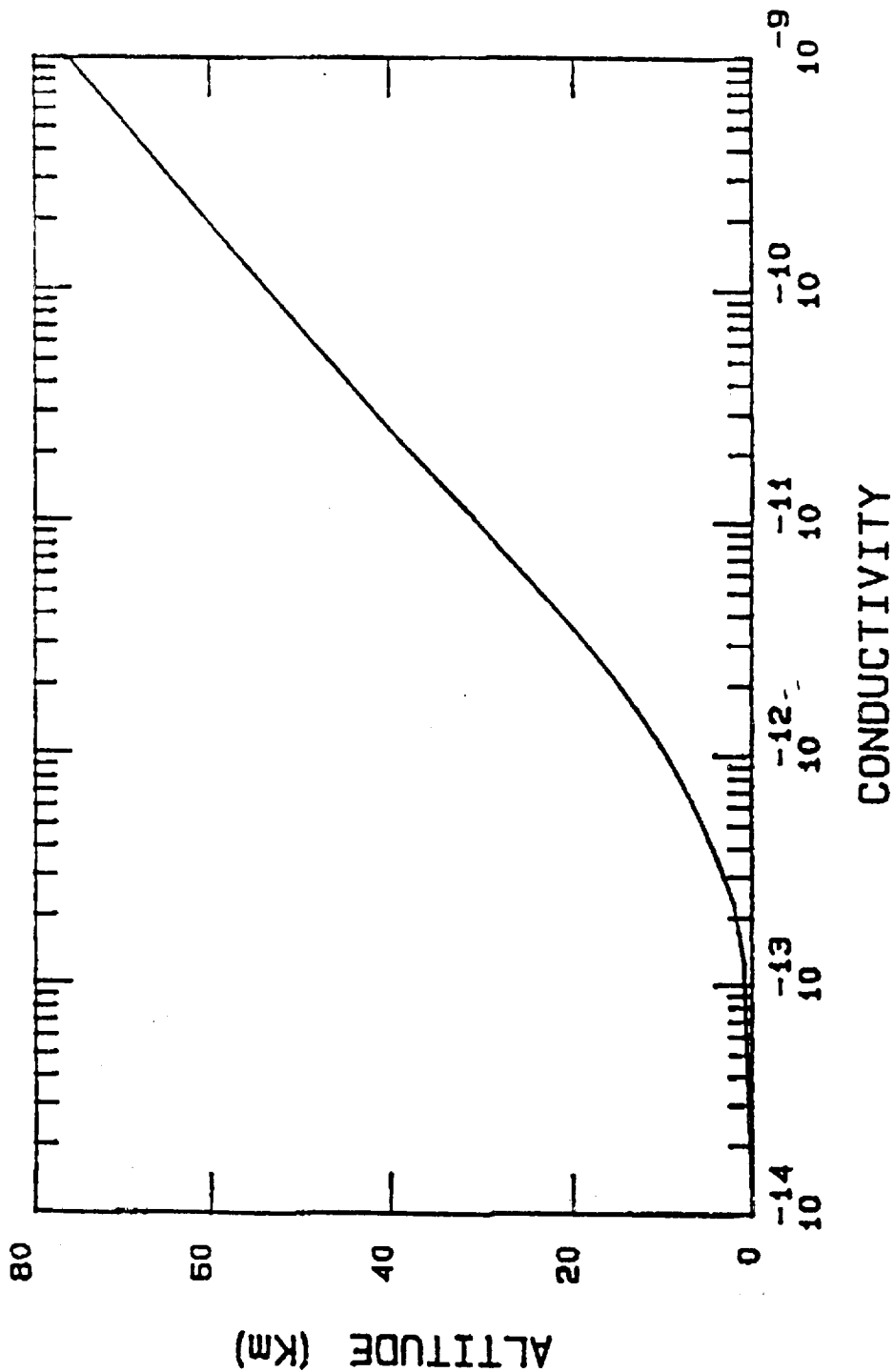


Figure 2 Composite Conductivity Profile Based on Measured Data
Obtained August 8, 1981 at Wallops Island, Virginia.

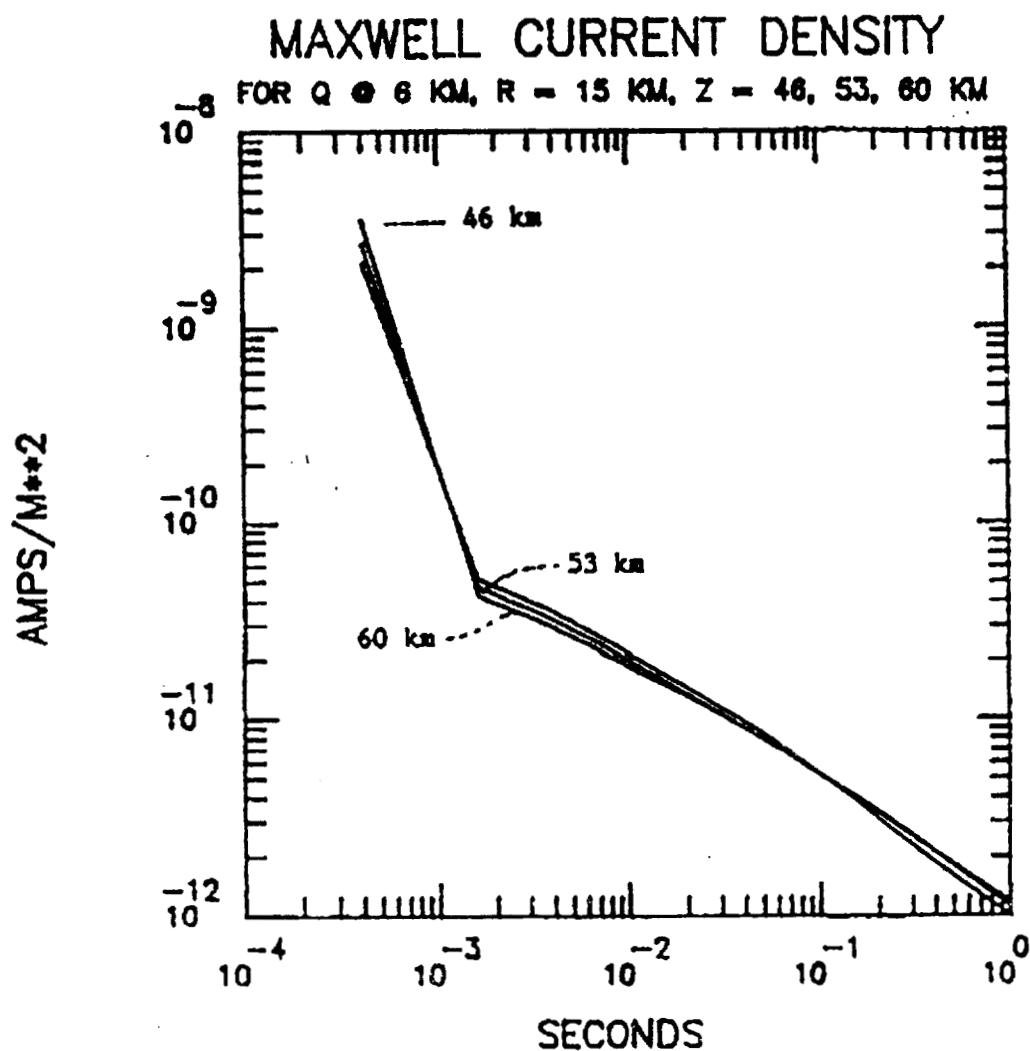


Figure 3 Maxwell Current Density Simulations at a Radial Distance of 15 km for Altitudes of 46, 53, and 60 km.

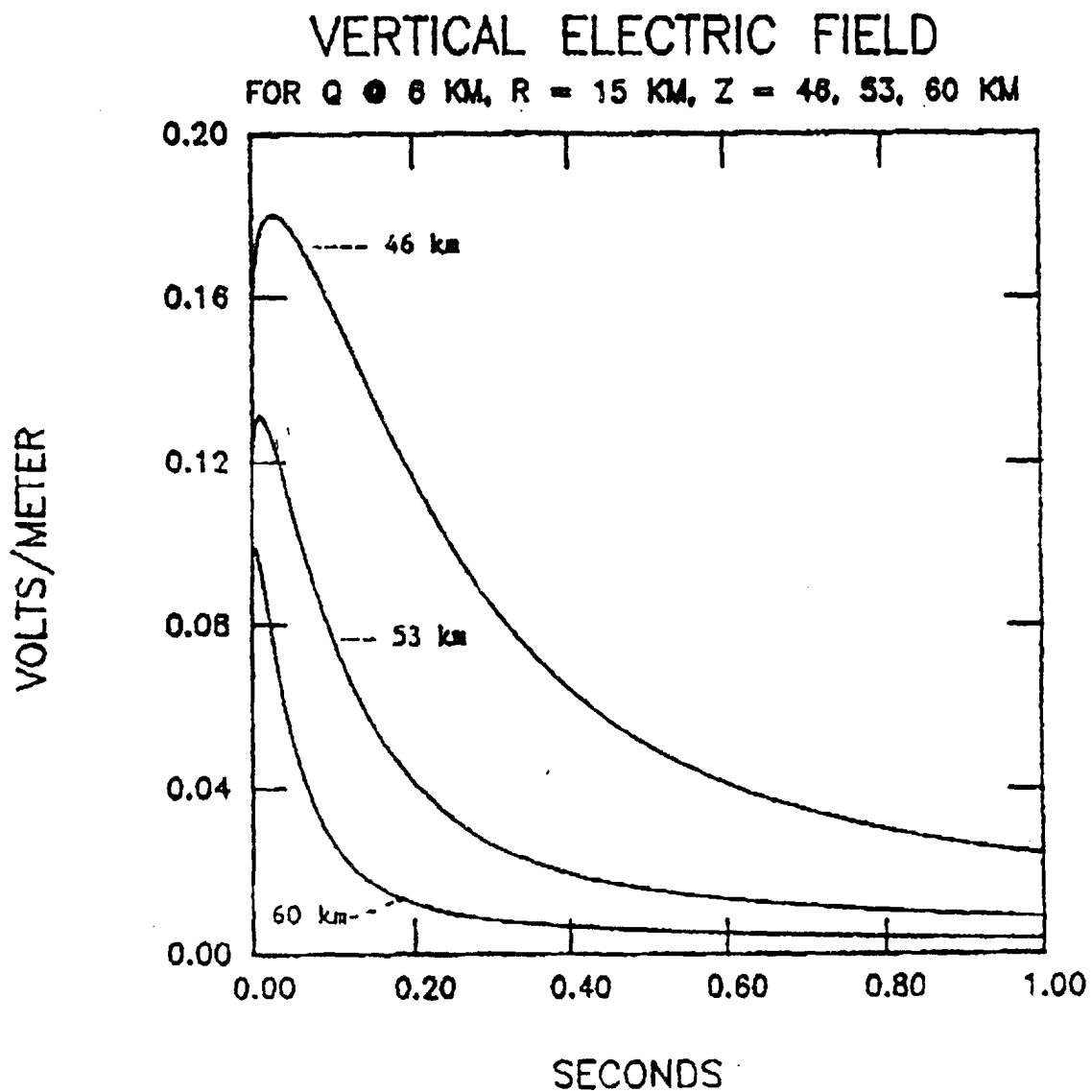


Figure 4 Electric Field Simulations at a Radial Distance of 15 km for Altitudes of 46, 53, and 60 km.

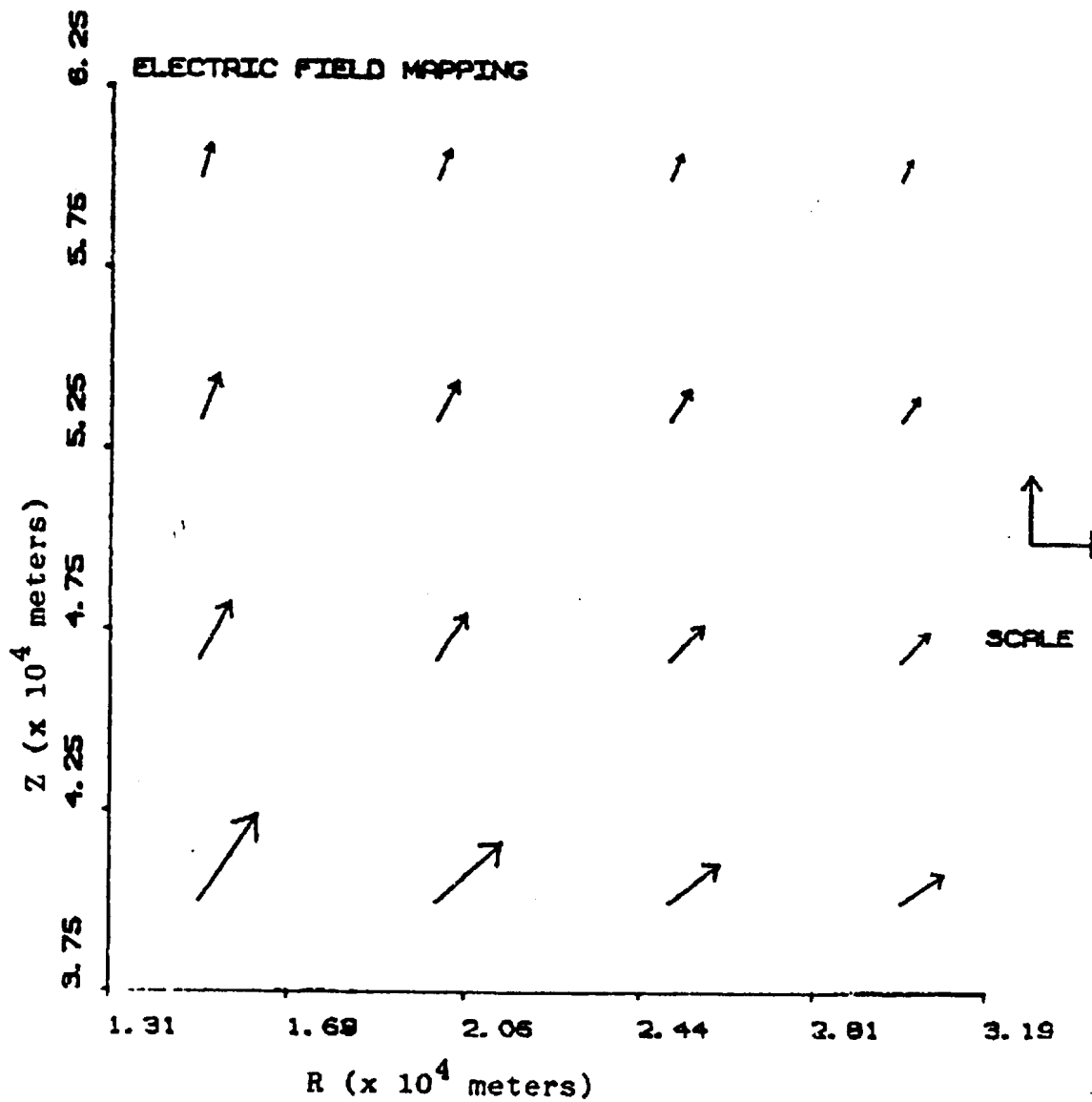


Figure 5 Normalized Simulated Electric Field Mapping for
 $t = 200$ milliseconds.

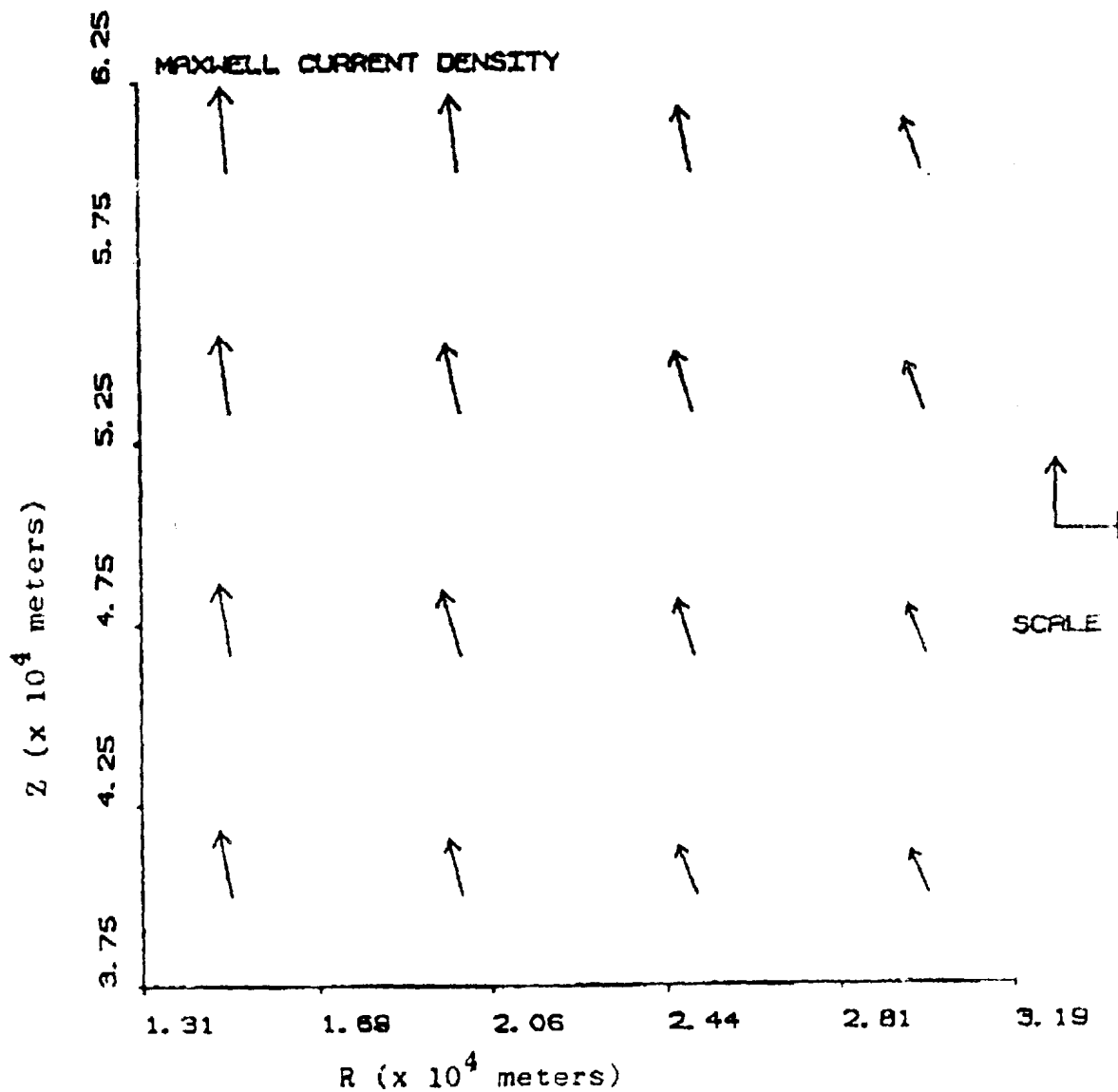


Figure 6 Normalized Simulated Maxwell Current Density Mapping for $t = 200$ milliseconds.

ORIGINAL PAGE IS
OF POOR QUALITY

1989

NASA/ASEE SUMMER FACULTY FELLOWSHIP PROGRAM

MARSHALL SPACE FLIGHT CENTER
THE UNIVERSITY OF ALABAMA IN HUNTSVILLE

AUGMENTING AND UPDATING
NASA SPACELINK ELECTRONIC INFORMATION SYSTEM

Prepared By:	Jean A. Blake
Academic Rank:	Professor
University and Department	Alabama A&M University Mathematics
NASA/MSFC	
Division:	Public Affairs Office
Branch:	Public Services & Education
NASA Colleague:	William E. Anderson
Date:	August 4, 1989
Contract No:	The University of Alabama in Huntsville NGT-01-008-021

ACKNOWLEDGEMENT

Thank you:

John Dumoulin, Charlene McGlothin, and Chris Scantland for your help with the Macintosh;

Barbara Cady and Ernie Shannon for sharing your Macintosh;

All unmentioned members of the Public Affairs Staff for your support; and

Rick Chappell, Jerry Karr, Frank Six, and all other members of the NASA/ASEE staff for affording me the opportunity to make this summer's experience possible.

Most of all, thank you Bill Anderson for your patience, wisdom, guidance and understanding as we worked together on Spacelink these past three summers. Be assured that I have had enriching and rewarding experiences, the memory of which I will always treasure. Good luck to you, Bill, in your new position.

ABSTRACT

I was privileged to participate in the development of Spacelink during the periods of its gestation, birth, infancy, and childhood. In addition to compiling and developing more material for implementation in Spacelink, Summer 1989 was spent scanning the insignias of the various manned missions into Spacelink.

Material for the above was extracted from existing NASA publications, documents and photographs.

1. Introduction

The National Aeronautics and Space Administration offers educators a wide range of educational services including speakers, publications, audiovisual materials, software, advanced educational technology, curriculum assistance, electronic communications, in-school satellite programs, student programs and training opportunities. One of its relatively new offerings is Spacelink, an Electronic Information System for Educators, operated by the Marshall Space Flight Center. (See Appendix A.)

I was privileged to participate in the development of Spacelink during the periods of its gestation, birth, infancy, and childhood. In addition to compiling and developing more material for implementation in Spacelink, Summer 1989 was spent scanning the insignias of the various manned missions into Spacelink.

Material for the above was extracted from existing NASA publications, documents and photographs.

2. The Process

The material entered into Spacelink consisted of photographs and text documents. The photographs were scanned through the Abaton scanner into the Macintosh using the software C Scan 1.5. Each photograph was then sent to Spacelink via an Xmodem transfer (See Appendix B).

Most of the text was on Macintosh disks. It was necessary to convert each document set up in a Macintosh format to a form that would conform to the Data General format. Each document was then sent to Spacelink via an Xmodem transfer from whence it was imported into the Data General where the editing process took place. The rest of the text was first edited and/or compiled on the Data General. Each edited document was then exported to a simulated version of the Spacelink program where it was tested and refined. Thereafter, it was sent to Spacelink ready to be used by its users.

The following is a list of some of the material included:

1. Astronaut Biographical Data
2. Gemini Program Summary
3. NASA 1989 Long Range Program Plans
4. Software for Aerospace Education
5. Macintosh Graphics of Manned Mission Logos

CONCLUSIONS and RECOMMENDATIONS

Now that the computer has become the basic underpinning of the space program and society, it is important that this vital resource be maximized in keeping classroom instruction relevant and current. The material prepared for Spacelink has found widespread use by teachers and others across the nation, and is being used to stimulate students in their quest for excellence. A review of the summary of Spacelink's use, testifies to the fact that NASA is making a very worthwhile investment in this endeavor, an investment which should be continued.

REFERENCES

1. Biographical Data, Lyndon B. Johnson Space Center, Houston, Texas 77058, NASA 1989
2. Crew Insignias, Lyndon B. Johnson Space Center, Houston, Texas 77058
3. Gemini Program Summary, A NASA Publication
4. 1989 Long-Range Program Plan, NASA, National Aeronautics and Space Administration, Washington, D.C. 20546
5. Mission Facts Summary, NASA, U.S. Government Printing Office
6. NASA Spacelink, Marshall Space Flight Center, Huntsville, Alabama 35812
7. Software for Aerospace Education, NASA, National Aeronautics and Space Administration, Washington, D.C. 20546

APPENDIX A

"NASA Spacelink is a collection of NASA information and educational materials stored on a computer at the Marshall Space Flight Center in Huntsville, Alabama. It is designed to communicate with a wide variety of computers and modems, especially those most commonly found in classrooms and homes. The system may be accessed over regular telephone lines. NASA Spacelink is free" except for the cost of long distance calls.

It provides information on:

- Current NASA News
- Aeronautics
- Space Exploration Before the Shuttle
- Space Exploration Beyond the Shuttle
- Nasa and Its Centers
- NASA Educational Services
- Classroom Materials
- Space Program Spinoffs

"NASA Spacelink runs on a Data General ECLIPSE MV-7800 minicomputer located at the George C. Marshall Space Flight Center in Huntsville, Alabama. NASA Spacelink software was developed and donated to NASA by the Data General Corporation of Westboro, Massachusetts. The system has a main memory of 14 megabytes (14 million characters), disk storage space for 708 megabytes, and can communicate with eight callers simultaneously at 300, 1200, or 2400 baud. The data word format is 8 data bits, no parity, and 1 stop bit. NASA Spacelink is a dynamic system that changes and expands daily. It was made available to the public in February, 1988.

Initial funding for NASA Spacelink was provided by the Educational Affairs Division at NASA Headquarters. The NASA Spacelink data base is maintained by the Public Services and Education Branch of the Marshall Space Flight Center Public Affairs Office. Operational support is provided by the Information Systems Office at the Marshall Center. Information on NASA scientific projects and educational programs is provided to NASA Spacelink by education specialists at NASA Headquarters and the NASA field centers.

While NASA understands that people from a wide variety of backgrounds will use NASA Spacelink, the system is specifically designed for teachers. The data base is arranged to provide easy access to current and historical information on NASA aeronautics and space research. Also included are suggested classroom activities that

incorporate information on NASA projects to teach a number of scientific principles. Unlike bulletin board systems, NASA Spacelink does not provide for interaction between callers. However, it does allow teachers and other callers to leave questions and comments for NASA."

APPENDIX B

"An Explanation of XMODEM

A public domain file transfer protocol created by Ward Christensen in 1977, XMODEM allows information to be transferred rapidly from one computer to another with 99% accuracy. Also known as the Christensen Protocol, XMODEM is found in many communications packages and may be run on a wide range of computers. The XMODEM option was installed on NASA Spacelink in May 1988.

The XMODEM protocol sends files in 128-byte sequentially numbered blocks of information with a checksum appended to each block. The receiving computer, which must have XMODEM capable software, receives a block of data, calculates a checksum, and then compares it to the checksum contained in the data received. If the checksums match, the receiving computer acknowledges the data and the next block is sent and checked. If an error occurs in transmission, the checksums will not match, and the receiving computer will ask for the block to be sent again. If more than a predetermined number of consecutive errors occur, the transfer will be aborted. Most communications programs do not display actual information as it is received during an XMODEM transfer. Instead, a count of the blocks will be displayed.

Just before an XMODEM transfer begins, NASA Spacelink displays the number of 128-byte blocks in the file to be transferred. With this information a caller can calculate the approximate transfer time for a file. At 300 baud, each block is transferred in about 4.5 seconds. At 1200 baud, each block is transferred in about 1.1 seconds, and at 2400 baud, each block is transferred in about 0.5 seconds."

1989

NASA/ASEE SUMMER FACULTY FELLOWSHIP PROGRAM

MARSHALL SPACE FLIGHT CENTER
THE UNIVERSITY OF ALABAMA IN HUNTSVILLE

KALMAN ESTIMATION FOR SEDS MEASUREMENTS

Prepared by: Connie K. Carrington

Academic Rank: Assistant Professor

University and Department: University of South
Carolina Mechanical
Engineering Dept.

NASA/MSFC:
Laboratory: Program Development
Division: Orbital Systems

MSFC Colleague: Charles C. Rupp

Date: August 23, 1989

Contract No.: The University of
Alabama in Huntsville
NGT-01-008-021

KALMAN ESTIMATION FOR SEDS MEASUREMENTS

Connie K. Carrington
Assistant Professor of Mechanical Engineering
University of South Carolina
Columbia, South Carolina

ABSTRACT

The first on-orbit experiment of the Small Expendable Deployer System (SEDS) for tethered satellites will collect telemetry data for tether length, rate of deployment, and tether tension. The post-flight analysis will use this data to reconstruct the deployment history and determine payload position and tether shape.

Two Kalman estimator algorithms were written, and output using simulated measurement data was compared. Both estimators exhibited the same estimated state histories, indicating that numerical instability in the traditional algorithm was not the cause of filter divergence. Estimation of acceleration biases was added, which reduced the error but did not correct the divergence. An "add-a-bead" estimator that adds lumped masses as the tether is deployed was written, which provides a state model that matches the BEADSIM simulation providing the "true" measurements and states. This twenty-one bead estimator produced state histories similar to those of the two-bead estimator, indicating that the filter divergence was not caused by a reduced-order model.

The noise models used to date are relatively simple and may be the source of estimator divergence. The investigation of colored noise models, cross-correlated measurement and process covariances, and noise-adaptive filter techniques is recommended.

ACKNOWLEDGEMENTS

The summer program participant would like to thank Program Development at Marshall Space Flight Center for a most enjoyable summer of research. The SEDS analysis provided a "real-life" problem that has demonstrated the importance of statistical characteristics in Kalman filter design.

INTRODUCTION

A Kalman estimator post-flight data reduction program has been written to process measurement data from the Small Expendable-tether Deployment System (SEDS) experiment to be flown in 1991. The tether will be deployed from an expendable launch vehicle to a length of 20 km; it will swing to vertical and then be cut. Measurement data will be collected and relayed to the ground to be processed after flight.

The estimator processes length, length rate, and deployer position and velocity measurements, and estimates velocities and positions of tether endpoints and points between. Two algorithms has been developed for both two and twenty-one bead models, and simulated measurements have been processed.

OBJECTIVES

The objective of the summer faculty research was to continue development of the post-flight data reduction algorithms started the previous summer.

STATE MODEL

Several computer simulations of tether deployment dynamics are available, ranging from planar simple-pendulum representations to three-dimensional partial-differential-equation models. Last summer the investigator had chosen Energy Science Laboratories (ESL) BEADSIM model to provide the tether dynamics state equations, since it is relatively simple and yet still produces results that are comparable to more complex models. BEADSIM is a lumped mass model, in which masses or "beads" are added as the tether becomes longer (Fig. 1). No out-of-orbit-plane motion is modelled, and the external forces on each bead are the gravity gradient, aerodynamic drag, and Coriolis and centripetal accelerations. The equations are written using a Cartesian coordinate frame with an origin at the center of mass and moving at orbit speed.

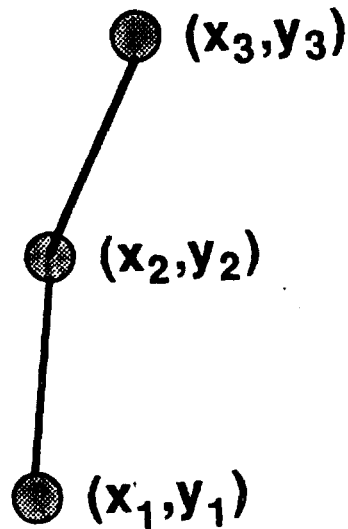


Fig. 1. BEADSIM lumped mass model.

Each bead's motion is governed by a second-order nonlinear differential equation, with a uniform tether tension providing the coupling between beads. Four states represent the motion of each bead: the x and y positions, and the x and y velocities. If we define z as a vector containing positions and velocities for each bead, then the state equations may be written as

$$\dot{z} = F(z,t) + \rho \quad (1)$$

where $F(z,t)$ contain the gravity gradient, aerodynamic drag, and tension forces on each bead, and ρ is a vector of process noise. The process noise has been modelled as white random noise with zero mean and covariance matrix

$$Q = E(\rho \rho^T) = \begin{bmatrix} \sigma_1^2 & 0 & 0 & \dots & 0 \\ 0 & \sigma_2^2 & 0 & \dots & 0 \\ 0 & 0 & 0 & \dots & \sigma_N^2 \end{bmatrix} \quad (2)$$

where E is the expected value.

The SEDS measurements consist of tether length l , length rate \dot{l} , and the deployer position and velocity. These measurements are nonlinear functions of the states, represented by the following measurement equations

$$l = G(z) + v \quad (3)$$

where l represents the vector of measurements at a given time, z the corresponding states, and v a vector of measurement noise. The measurement noise has been modelled as white with zero mean and covariance matrix

$$R = E(v v^T) = \begin{bmatrix} \gamma_1^2 & 0 & 0 & \dots & 0 \\ 0 & \gamma_2^2 & 0 & \dots & 0 \\ 0 & 0 & 0 & \dots & \gamma_m^2 \end{bmatrix} \quad (4)$$

STATE ESTIMATORS

The measurements are not the same variables as the states, so that payload position and tether shape cannot be directly determined from the measurements. A state estimator uses the measurements as input, filter the measurement noise, and then output the values of the states. Two estimator algorithms have been developed:

the traditional Kalman estimator algorithm, and the U-D square-root factorization technique. Both estimators process simulated measurements generated by BEADSIM to which white noise is added.

Estimators for dynamic systems were developed primarily for linear systems; for nonlinear systems represented by equations (1) and (3), an extended Kalman estimator is used. The nonlinear equations are used for state and measurement prediction at the next time step, and the state correction is calculated using a local linearization of these equations. The linearization of equations (1) and (3) are

$$\dot{z} = Az + \rho \quad (5)$$

and

$$l = Hz + v \quad (6)$$

where

$$H = \left. \frac{\partial G}{\partial z} \right|_{z_{\text{current}}} \quad (7)$$

$$A = \left. \frac{\partial F}{\partial z} \right|_{z_{\text{current}}} \quad (8)$$

The estimators correct the predicted states at each time step by multiplying the error between the actual measurement and the predicted measurement by a gain matrix. This gain matrix is calculated using the measurement covariance matrix and an extrapolated state estimate covariance, which is based on the linearized system's state transition matrix. The state transition matrix $\Phi(t_2, t_1)$ for equation (5) is the transformation that takes the state z_1 at time t_1 into the later state z_2

$$z_2 = \Phi(t_2, t_1)z_1 \quad (9)$$

For linear systems, the state transition matrix obeys the same differential equation as the states themselves

$$\dot{\Phi}(t) = A\Phi(t) \quad (10)$$

and can be integrated forward in time along with the state equations. For nonlinear systems, however, equation (10) is a linearized approximation valid only

in a neighborhood of the current state value. A comparison of the linearized and nonlinear state and measurement values indicates that a time-step size of one second produces four decimal digit agreement during deployment, and hence measurements will be processed at one-second intervals.

SIMULATION RESULTS

Traditional Kalman algorithm

The traditional Kalman algorithm using a two-bead model was developed in the summer of 1988. Payload position and velocity estimates are shown in Figs. 2 and 3, in which the solid line is the BEADSIM deployment and the dashed line is the estimator output. Fig. 4 contains the tether length and length rate during deployment, and Fig. 5 shows the rms position and velocity errors for the payload. This algorithm uses the identity matrix for the initial state covariance estimate, and propagates the covariance estimates with no checks on element values. Note that the payload position error reaches a maximum of 1500 m using this algorithm.

Filter divergence in many cases is due to overly optimistic covariance estimates, in which the algorithm depends heavily on the state prediction, and tends to reject the measurement data corrections. One way to treat filter divergence is to monitor the covariance estimates and reinitialize this matrix if the diagonal elements fall below a set threshold. Figs. 6 and 7 show the deployer and payload position and velocity errors using reinitialization of the state covariance matrix. The payload position error now has a maximum of 300 m. Similar results can be attained by increasing the estimates of the process noise.

Criticism of the traditional Kalman algorithm includes numerical instability, which can produce filter divergence such as that shown in Figs. 2 through 5, and that process-noise adjustments or reinitialization of the covariance matrix may tune the filter to produce any output desired, whether it is reasonable or not. The U-D square-root factorization algorithm provides an alternative method for Kalman estimation, and is considered a more numerically-stable method.

U-D Factorization Algorithm

The U-D factorization algorithm is computationally slower than the traditional Kalman algorithm, but in many cases produces more reliable results. The same two-bead model was used for state and covariance

propagation, and the U-D algorithm produced estimates similar to those of the untuned traditional algorithm (Figs. 2 through 5). The estimation of acceleration biases due to aerodynamic drag on the deployer and payload improved these results. This algorithm produced the tether length and length rate history shown in Fig. 8, and payload position and deployer position rms errors shown in Fig. 9.

To determine the magnitude of errors associated with the two-bead model, a twenty-one bead model and estimator was developed. This estimator starts with two beads, and adds beads for every 1000 m of tether deployed, similar to the BEADSIM simulation. Figs. 10 and 11 show the length, length rate, payload position and deployer position rms errors for the twenty-one bead estimator. Comparison between Figs. 9 and 11 indicates that little improvement was obtained by using the twenty-one bead estimator, and that the filter errors do not occur due to the reduced-order model.

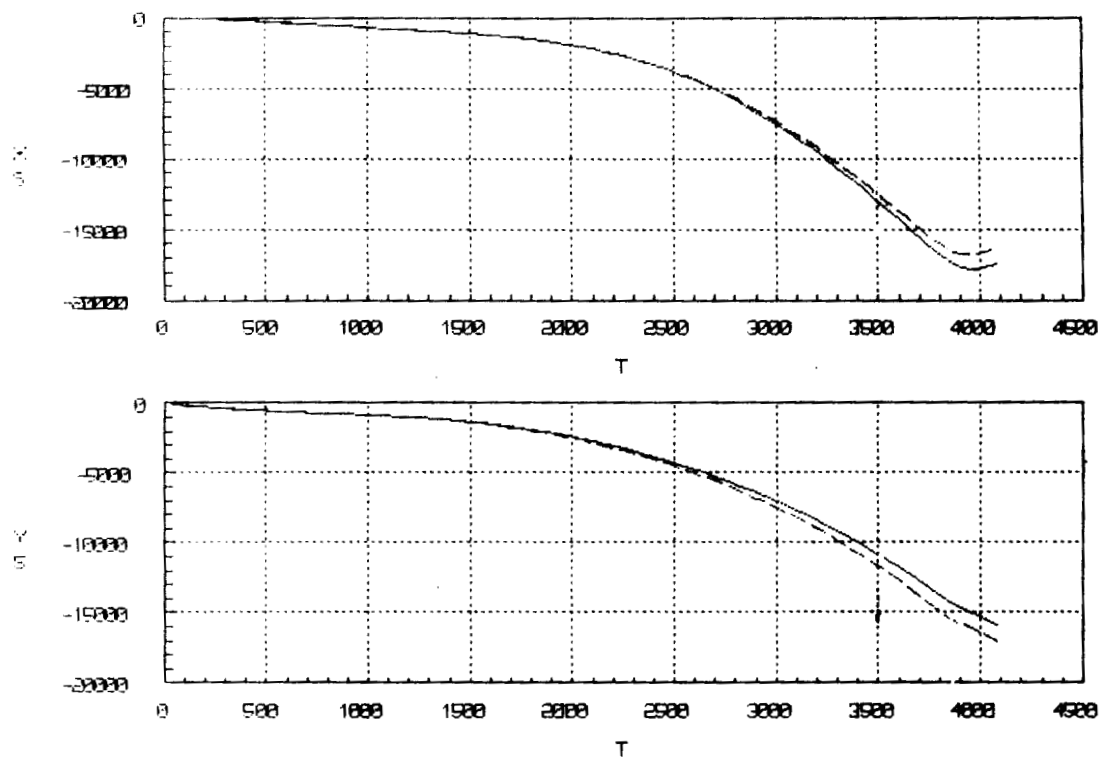


Fig. 2. Estimated payload position using untuned traditional Kalman algorithm.

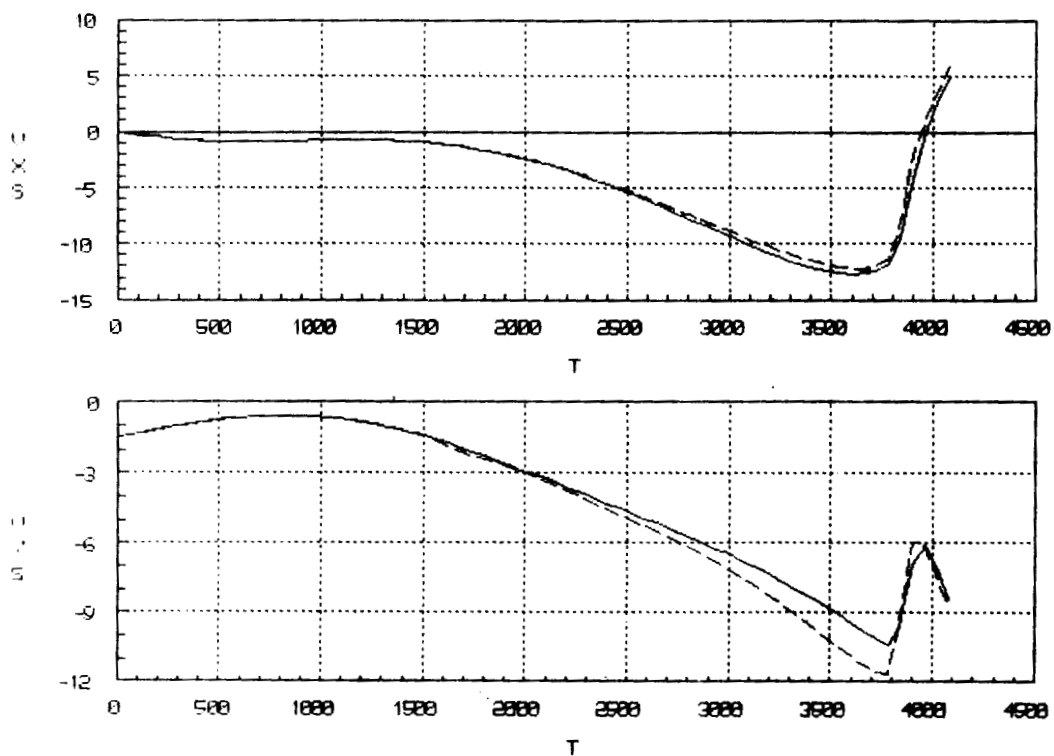


Fig. 3. Estimated payload velocity using untuned traditional Kalman algorithm.

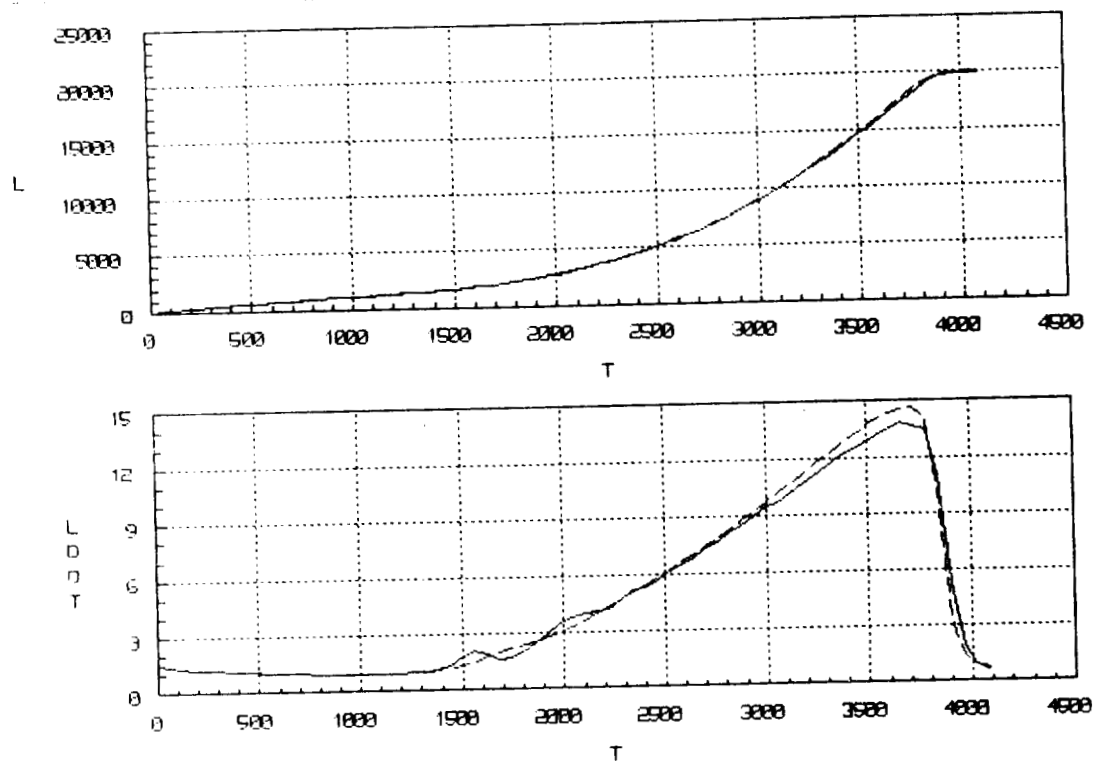


Fig. 4. Tether length, length rate using untuned traditional Kalman algorithm.

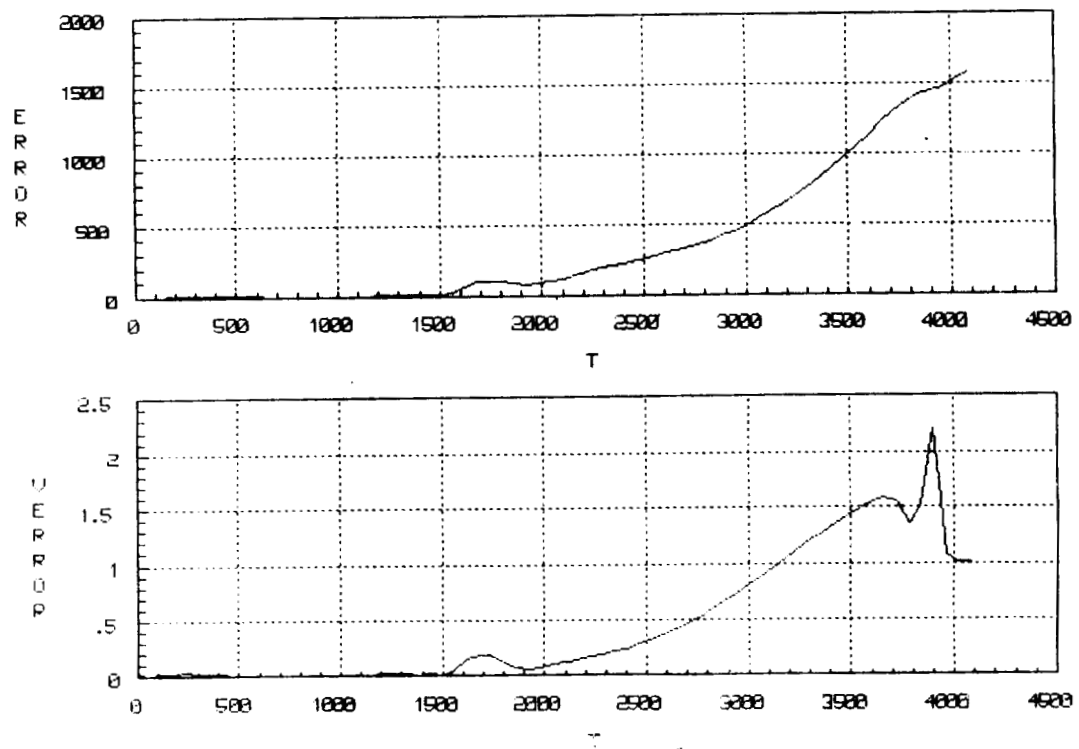


Fig. 5. Payload position and velocity rms errors using untuned traditional Kalman algorithm.

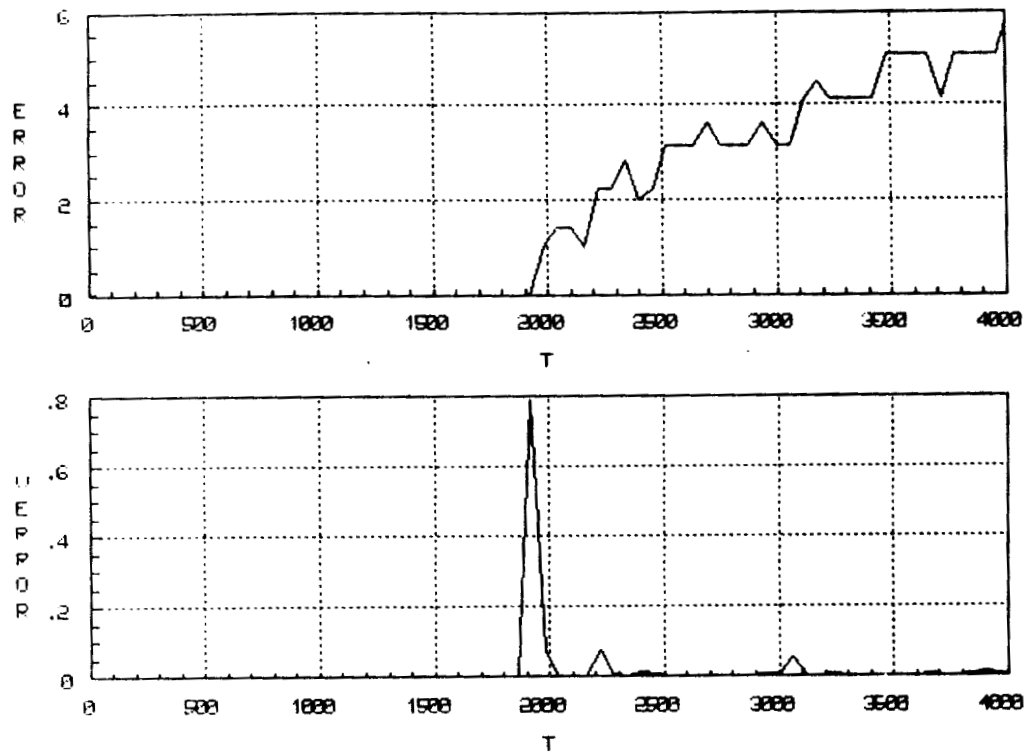


Fig. 6. Deployer position and velocity rms errors using tuned traditional Kalman algorithm.

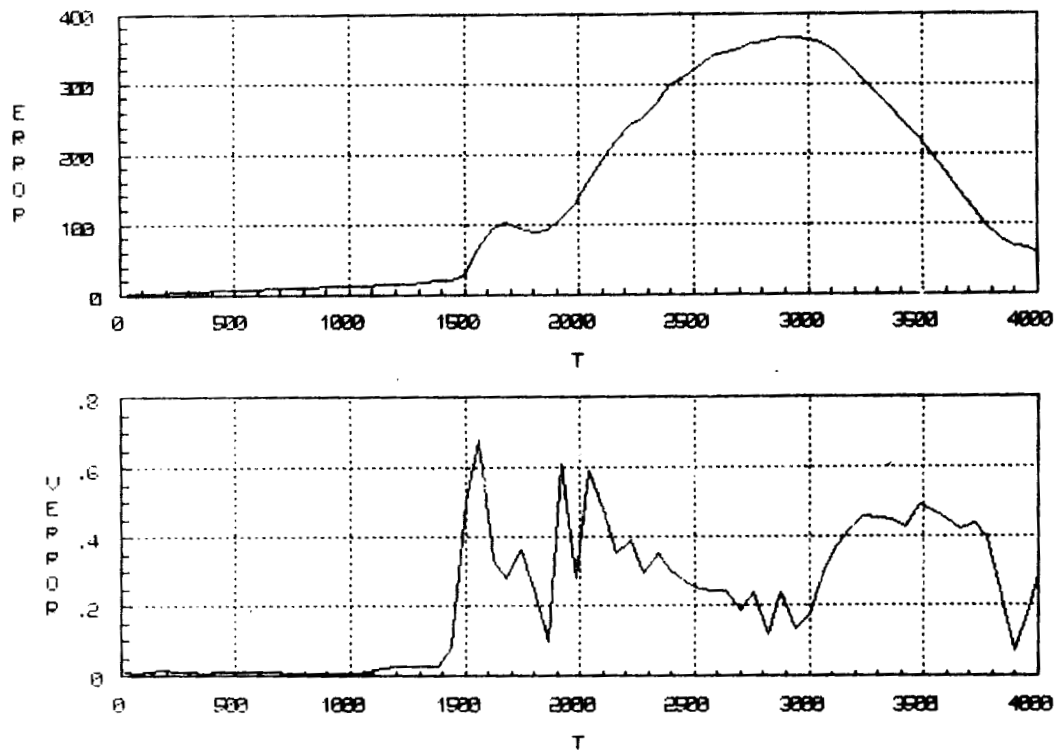


Fig. 7. Payload position and velocity rms errors using tuned traditional Kalman algorithm.

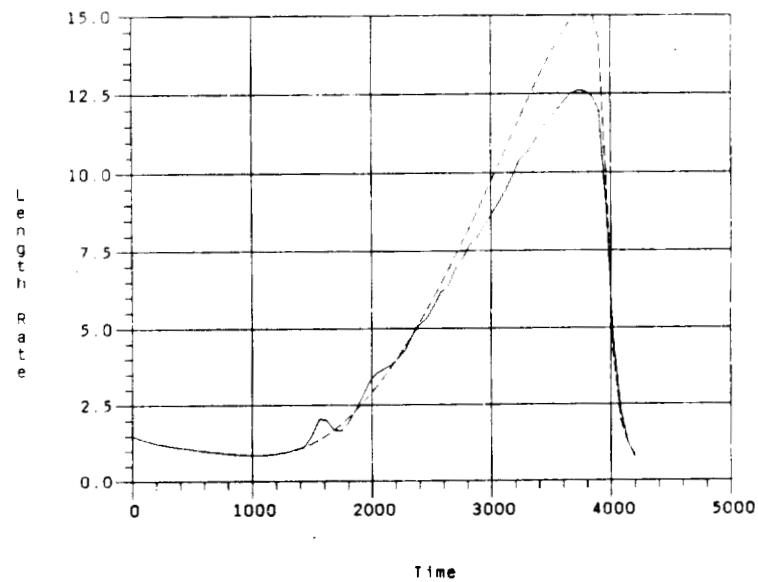
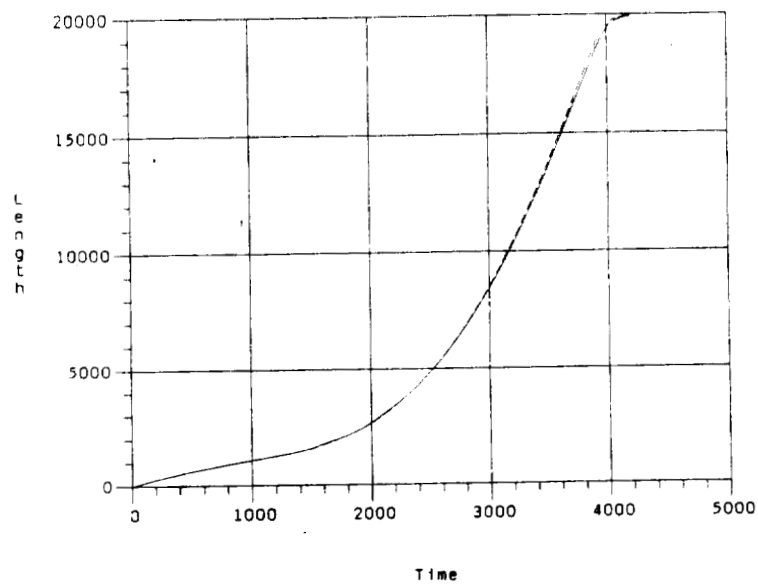


Fig. 8. Length and length rate using U-D factorization with two-beads and estimation of acceleration biases.

III-11

ORIGINAL PAGE IS
OF POOR QUALITY

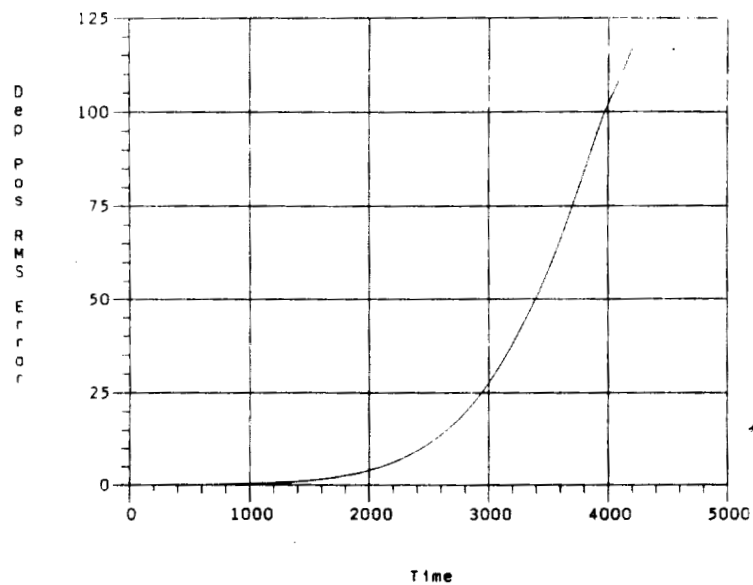
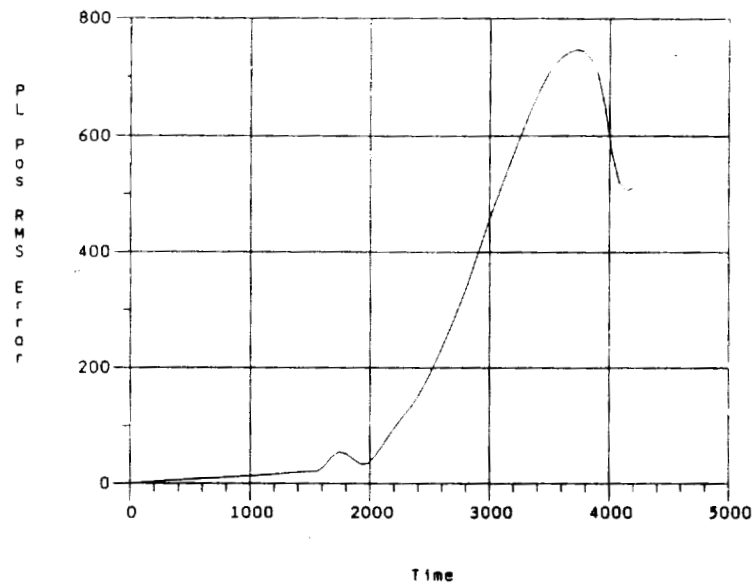


Fig. 9. Payload and deployer position rms errors using U-D factorization with two-beads and estimation of acceleration biases.

III-12

ORIGINAL PAGE IS
OF POOR QUALITY

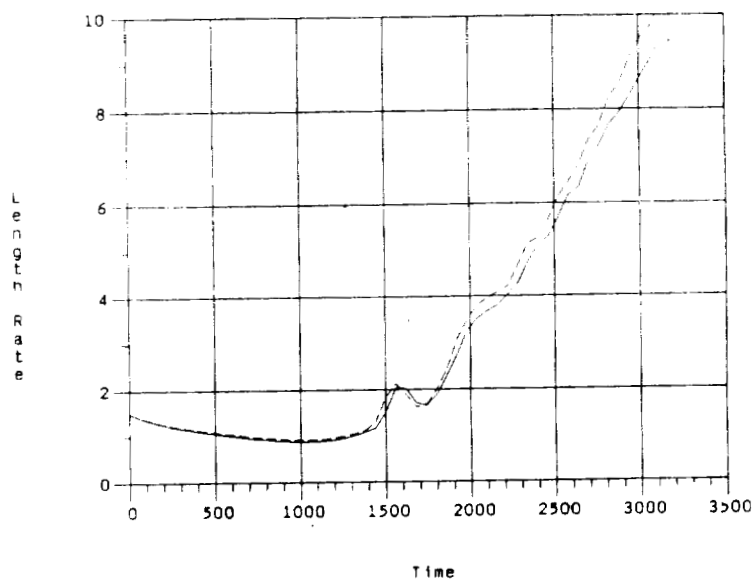
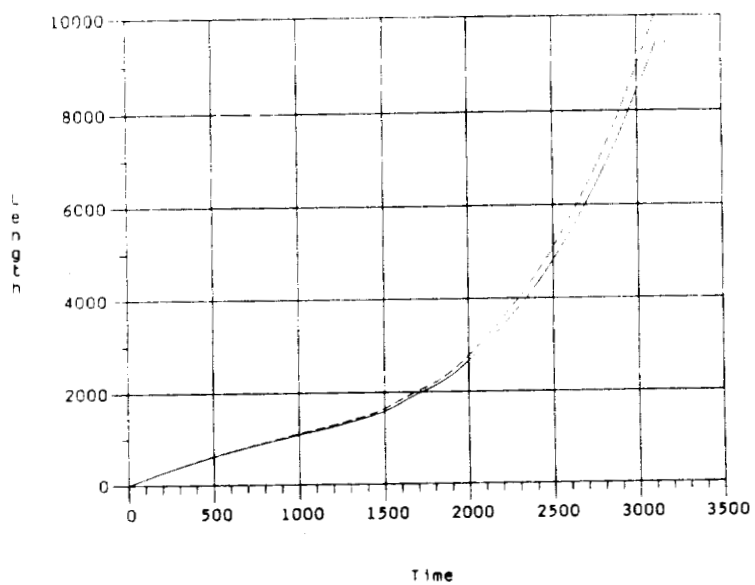


Fig. 10. Length and length rate using U-D factorization with "add-a-bead": up to twenty-one beads.

III-13

ORIGINAL PAGE IS
OF POOR QUALITY

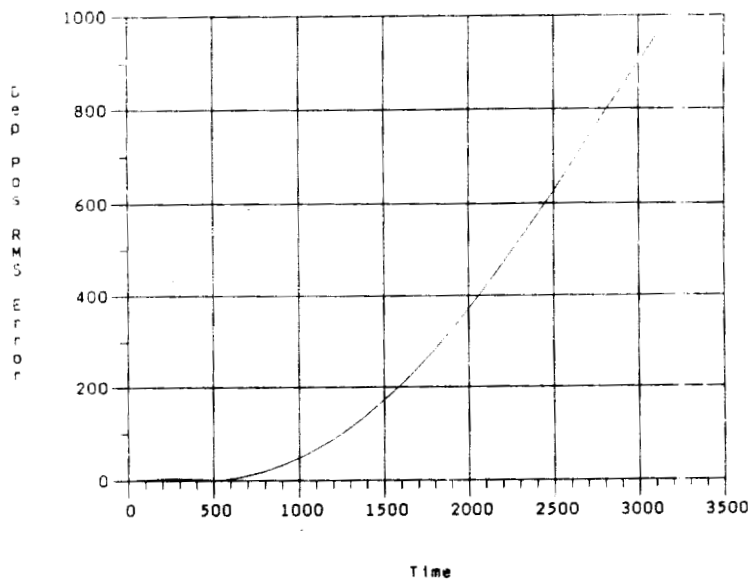
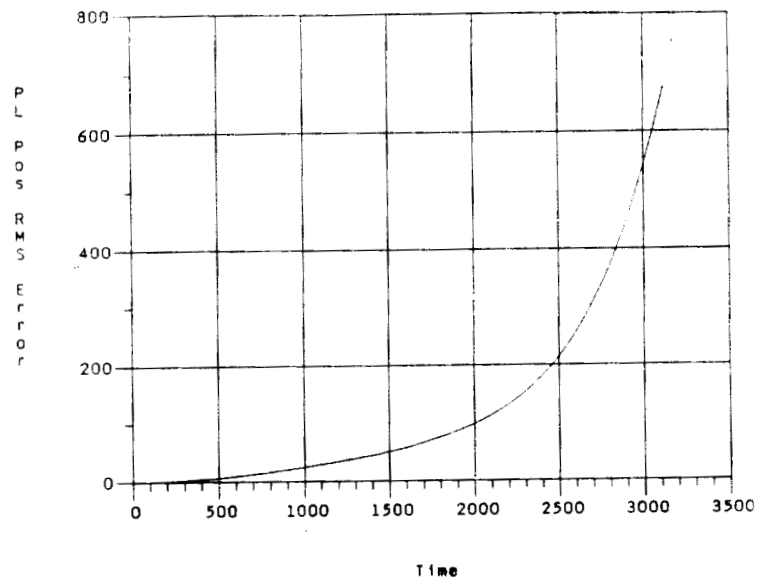


Fig. 11. Payload and deployer position rms errors using U-D factorization with "add-a-bead": up to twenty-one beads.

CONCLUSIONS AND RECOMMENDATIONS

The untuned traditional Kalman estimator using two-beads produced state estimates that diverged from the "true" state values during deployment. By monitoring the state covariance matrix, we found that the estimated variances became unacceptably small, so that measurement information was being ignored by the algorithm, and the estimates from the state equations were favored. Tuning this algorithm by adjustment of the process noise levels or by reinitialization of the covariance matrix during deployment reduced this divergence, but these techniques may be unreliable for flight-data use. The estimator divergence may come from a variety of sources: numerical instability in the traditional algorithm, errors from ignoring acceleration biases, modelling errors from using a two-bead model, linearization errors, measurement and process noise models that are not accurate, or incorrect apriori covariance estimates.

To determine if numerical instability was a primary cause of filter divergence, the U-D factorization algorithm was programmed. Similar estimates were obtained from both methods using the two-bead model, indicating that errors in the traditional algorithm are not due to numerical instability. Estimation of acceleration biases, which occur primarily due to aerodynamic drag, reduced the estimator errors. The "add-a-bead" estimator that reproduces the BEADSIM state model produced estimates that were very similar to those of the two-bead model, indicating that filter divergence is not due to a reduced-order model.

Linearization errors in the A and H matrices of equations (7) and (8) have been monitored by comparison with the actual states and their derivatives, and calculations have agreed to four decimal digits. This linearization directly impacts the gain calculation and the propagation of the state covariance matrix, and could be the source of filter divergence. The measurement and process noise models used in these calculations have been white, Gaussian, with zero mean; the linearization errors are by definition colored, since they are the product of a dynamic process. A correlation calculation of both the measurements and states produced by the estimator indicates that they are both correlated, and yet these algorithms have not used off-diagonal elements in the covariance matrices. Both estimators are sensitive to changes in the apriori covariance estimates; in some cases, the U-D

factorization algorithm overflows early in deployment when large initial covariance estimates are used.

Recommendations include the use of cross-correlation terms in the covariance matrices, which is easily accommodated by the traditional Kalman algorithm. Since the linearization of the state and measurement equations most likely pollute the white noise models for the process and measurement noise, a Gauss-Markov model should be developed for these processes. The time-sequence of linearization errors for both the measurements and state derivatives could be saved, and the correlation matrices calculated for both. The time-varying correlation matrix for the process noise would provide the transition matrix A_{k-1} for a shaping filter of the form

$$\rho_k = A_{k-1}\rho_{k-1} + \xi_{k-1} \quad (11)$$

where ρ_k is the colored process noise sequence and ξ_k is white-noise. The same calculations could be done to provide a colored noise model for the measurement linearization errors. (see Stengel).

Noise-adaptive filtering techniques may be necessary when apriori covariance estimates are not accurate. These techniques sample the measurement residuals and calculate measurement biases and covariances; similar techniques can be used to give better estimates of an initial state covariance matrix. (see Myers and Tapley).

REFERENCES

Bierman, Gerald J., Factorization Methods for Discrete Sequential Estimation, Academic Press, New York, 1977.

Bierman, Gerald J., "Measurement Updating Using the U-D Factorization," Proceedings of the 1975 IEEE Conference on Decision and Control, pp. 337-346.

Bierman, Gerald J. and Thornton, Catherine L., "Numerical Comparison of Kalman Filter Algorithms: Orbit Determination Case Study," Automatica, Vol. 13, 1977, pp. 23-35.

Jazwinski, A.H., Stochastic Processes and Filtering Theory, Academic Press, New York, 1970.

Junkins, John L., An Introduction to Optimal Estimation of Dynamical Systems, Sijthoff & Noordhoff International Publishers, Alphen aan den Rijn, The Netherlands, 1978.

Myers, K.A. and Tapley, B.D., "Adaptive Sequential Estimation with Unknown Noise Statistics," IEEE Transactions on Automatic Control, AC-21(4), Aug. 1976, pp. 520-523.

Press, William H., Flannery, Brian P., Teukolsky, Saul A., and Vetterling, William T., Numerical Recipes: The Art of Scientific Computing, Cambridge University Press, 1986.

Sage, A.P., and Melsa, J.L., Estimation Theory with Applications to Communications and Control, McGraw-Hill, New York, 1971.

Stengel, Robert F., Stochastic Optimal Control, Theory and Application, John Wiley & Sons, New York, 1986.

1989

NASA/ASEE SUMMER FACULTY RESEARCH FELLOWSHIP PROGRAM

**MARSHALL SPACE FLIGHT CENTER
THE UNIVERSITY OF ALABAMA IN HUNTSVILLE**

**A PBL-Radiation Model for Application to Regional Numerical
Weather Prediction**

Prepared by: Chia-Bo Chang
Academic Rank: Associate Professor
University and Department: Texas Tech University
Atmospheric Science Group

NASA/MSFC:

Laboratory: Space Sciences
Division: Earth Science and Applications
Branch: Fluid Dynamics

MSFC Colleague: Franklin R. Robertson
and
Mike Kalb

Date: August 11, 1989

Contract No.: The University of Alabama
in Huntsville
NGT-01-008-021

A PBL-Radiation Model for Application to
Regional Numerical Weather Prediction

Chia-Bo Chang

Atmospheric Science Group
Texas Tech University
Lubbock, Texas

ABSTRACT

Often in the short-range limited-area numerical weather prediction (NWP) of extratropical weather systems the effects of planetary boundary layer (PBL) processes are considered secondarily important. However, it may not be the case for the regional NWP of mesoscale convective systems over the arid and semi-arid highlands of the southwestern and south-central United States in late spring and summer. Over these dry regions, the PBL can grow quite high up into the lower middle troposphere (600 mb) due to very effective solar heating and hence a vigorous air-land thermal interaction can occur. The interaction representing a major heat source for regional dynamical systems can not be ignored.

The present study focuses on the development of an one-dimensional PBL-radiation model. The model PBL consists of a constant-flux surface layer superposed with a well-mixed (Ekman) layer. The vertical eddy mixing coefficients for heat and momentum in the surface layer are determined according to the surface similarity theory, while their vertical profiles in the Ekman layer are specified with a cubic polynomial. Prognostic equations are used for predicting the height of the nonneutral PBL. The atmospheric radiation is parameterized to define the surface heat source/sink for the growth and decay of the PBL. A series of real-data numerical experiments has been carried out to obtain a physical understanding how the model performs under various atmospheric and surface conditions.

This one-dimensional model will eventually be incorporated into a mesoscale prediction system. The ultimate goal of this research is to improve the NWP of mesoscale convective storms over land.

ACKNOWLEDGEMENTS

I am grateful for the opportunity to participate in the Summer Faculty Fellowship Program at NASA/MSFC. I would like to express my appreciation to Co-directors Dr. Gerald R. Karr of UAH and Dr. Frank Six of NASA/MSFC and their staffs for arranging a very enjoyable program.

The PBL program used in this air-land interaction research is a modified version of the marine PBL code written by Dr. S. Yoh of Drexel University. I appreciate valuable discussion and comments on this work by my colleagues Dr. F. Robertson of NASA/MSFC and Dr. M. Kolb of USRA and their interest in this research. Also, I wish to thank Ms. J. Srikishen for technical help in carrying out numerical experiments, and friends at USRA for a delightful summer.

1. INTRODUCTION

Often in the short-range limited-area numerical weather prediction (NWP) of extratropical weather systems the effects of planetary boundary layer (PBL) processes are considered secondarily important. This is probably true over land in winter or over the oceans in summer when the PBL is generally very shallow. However, it may not be the case for the regional NWP of mesoscale convective systems over the arid and semi-arid highlands of the southwestern and south-central United States. Over these arid regions, in late spring and summer the PBL can grow quite high up into the lower middle troposphere (600 mb) due to very effective solar heating. This can cause vigorous air-land thermal interaction. The interaction representing a very significant heat source/sink for regional dynamical systems can not be ignored.

The present study will focus on the development of an one-dimensional model coupling the PBL processes and atmospheric radiative transfer. The model PBL consists of a constant-flux surface layer superposed with a well-mixed (Ekman) layer. The vertical eddy (turbulence) mixing coefficients for heat and momentum in the surface layer will be determined according to the surface similarity theory, while their vertical profiles in the Ekman layer are specified with a cubic polynomial. Prognostic equations are formulated for predicting the height of nonneutral PBL. The atmospheric radiation including solar and infrared components is parameterized to define the surface heat source/sink for the growth and decay of the PBL. This one-dimensional model will eventually be incorporated into the limited-area mesoscale prediction system (LAMPS) (Perkey, 1976; Chang *et al.*, 1981) for regional NWP over land.

The model levels range from 0 to 16 km with relatively higher resolution in the PBL. A discussion of PBL physics and techniques for solving the atmospheric radiative transfer in this study is included in Sections 3 and 4, respectively. The results of three numerical experiments conducted on the PBL-radiation model are described in Section 5.

2. OBJECTIVES

The ultimate goal of this research is to improve the NWP of mesoscale

convective storms over arid land. Before incorporating the PBL-radiation model into LAMPS, we like to carry out a series of real-data numerical experiments to have a physical understanding how the one-dimensional model performs under various atmospheric conditions. The specific objectives include:

- 1) To assess the impact of clouds on the surface heat sources and on the PBL development.
- 2) To determine the sensitivity of the PBL height to its initial value.
- 3) To understand the impact of surface conditions such as roughness length, albedo, the Bowen ratio on the structure of the PBL.
- 4) To understand the role of the static stability in the growth and decay of the PBL.

3. PLANETARY BOUNDARY LAYER

The PBL is a layer of atmosphere on the order of 1 km in depth above the earth's surface. This thin layer of air is characterized by small-scale turbulence of spatial dimension no greater than 1 km. In the free atmosphere above the PBL, the turbulent motions are considerably weaker. The PBL processes represent a consequence of interaction between the lowest layer of air and the underlying surface. The interaction can significant impact on the dynamics of the upper air flows.

The influences of the small-scale eddies on large-scale (model resolvable scale) atmospheric circulations may be included in the model equations as described below. These equations are formulated on the (x,y,z,t) coordinate system, in which x is along the latitudinal (west to east), y is along the longitudinal (south to north) circles on the earth's surface, while z is perpendicular to the x-y plane.

3.1 The basic equations

Equations of horizontal motion:

$$du/dt = fv - \rho^{-1} \partial p / \partial x - \rho^{-1} [\partial \rho \langle u'u' \rangle / \partial x + \partial \rho \langle u'v' \rangle / \partial y + \partial \rho \langle u'w' \rangle / \partial z] \quad (1)$$

$$dv/dt = -fu - \rho^{-1} \partial p / \partial y - \rho^{-1} [\partial \rho \langle u'v' \rangle / \partial x + \partial \rho \langle v'v' \rangle / \partial y + \partial \rho \langle v'w' \rangle / \partial z] \quad (2)$$

Hydrostatic equation:

$$\partial p / \partial z = -\rho g \quad (3)$$

Equation of state for air:

$$p = \rho R \theta (p/1000)^{0.28571} \quad (4)$$

Mass conservation:

$$dp/dt = -\rho(\partial u/\partial x + \partial v/\partial y + \partial w/\partial z) \quad (5)$$

Energy conservation:

$$d\theta/dt = H + \rho^{-1}[\partial(-\rho u'\theta')/\partial x + \partial\rho(-v'\theta')/\partial y + \partial\rho(-w'\theta')/\partial z] \quad (6)$$

Moisture conservation:

$$dq/dt = Q + \rho^{-1}[\partial(-\rho u'q')/\partial x + \partial\rho(-v'q')/\partial y + \partial\rho(-w'q')/\partial z] \quad (7)$$

where $d/dt = \partial/\partial t + u\partial/\partial x + v\partial/\partial y + w\partial/\partial z$. There are seven basic large-scale variables in the above system: three velocity components in the x, y, and z directions, respectively, u, v, and w; pressure p; air density ρ ; potential temperature θ ; and specific humidity q. Other symbols include the Coriolis parameter f, heat source H, moisture source Q, and the gas constant for dry air R.

The prime ' denotes the small-scale turbulent fluctuations, while the bracket < > denotes a time average over a period much longer than the time scale of the turbulent fluctuations. In the u- and v-equations, the first term represents the Coriolis force due to the earth's rotation, and the second term represents the pressure gradient force. The six covariances (e.g., $-\rho\langle u'u' \rangle$) are referred to as eddy stresses representing eddy or turbulent fluxes of momentum. Similarly, there are eddy flux of heat in the θ equation and eddy flux of moisture in the q equation.

3.2 Closure problem

Considering the basic variables only, we note that the above set of equations forms a closed system. Given initial conditions, the future states of the seven basic unknowns can be determined in principle by numerical integration. However, with the eddy flux terms representing additional dependent variables additional equations are required to close the system. This is so-called closure problem in dealing with atmospheric turbulence.

In the free atmosphere, for the atmospheric circulations of horizontal scale larger than 100 km and time scale on the order of one day or longer the contribution to the local change ($\partial/\partial t$) due to the eddy stresses as well as the eddy fluxes of heat and moisture is insignificant in comparison with those due to large-scale processes (e.g., pressure gradient force, advection, etc.). In NWP models, we may neglect the eddy flux terms in the above set of equations. This is known as the zero-order closure.

In the PBL, however, the eddy flux terms may have the same order of magnitude as the other terms and can not be neglected under most situations. To close the system without neglecting PBL processes in a NWP model, we may consider the following two closure approaches.

a) First-order closure

A well-known and commonly used technique in PBL meteorology for the first-order closure is the so-called K-theory. The theory simply states that the turbulent flux of any physical quantities such as momentum and heat may be treated analogously to molecular diffusion. For example, for the vertical eddy flux of heat, we may write

$$\langle \theta'w' \rangle = K \partial \theta / \partial z$$

which indicates the vertical mixing of heat as a result of turbulence is parameterized in terms of the large-scale variables. Similar expressions can be formulated for the eddy mixing of momentum. A more detailed discussion of the K-theory and the procedures to implement the theory to PBL modeling in this research is presented in Section 3.3.

b) Higher-order closure

The concept consists of deriving prognostic equations for the eddy flux

terms from the basic equations. The derived equations contain higher-order correlations. For example, in the case of second-order closure triple correlations such as $\langle u'u'v' \rangle$ will appear in the prediction equation for $\langle u'u' \rangle$. Thus, the closure problem remains and closure assumptions have to be made at a higher level to complete the system. Moreover, the introduction of the equations for the eddy components in NWP models will drastically increase the demand for computer time. Also, the current observations are insufficient to provide an accurate initial condition for the eddy fluxes. To date, higher-order closure approaches are not yet desirable for NWP models.

3.3 First-order closure PBL model

As shown in the basic equations, the eddy mixing of momentum, heat, and moisture includes both horizontal and vertical components. Due to the horizontally stratified nature of the atmosphere, the gradient of u , v , θ , and q is much greater in the vertical than in the horizontal direction. The eddy mixing in the horizontal is negligible comparing to its counterpart in the vertical. Hence, with the use of the K-theory the central issues in PBL research involve the determination of the vertical profiles of K for momentum, heat, and moisture as well as the depth of the PBL within which the profiles are applied.

In formulating equations for the K profiles, a two-layer model is developed. The PBL is divided into a constant-flux surface layer superposed with a well-mixed Ekman layer.

a) Surface layer

This is a very thin turbulent layer within a depth less than 50 m above the surface. In this layer, the turbulent fluxes are nearly constant with height and the vertical wind profile depends on the static stability and surface roughness. There are mechanical turbulence driven by the vertical wind shear as well as thermal turbulence driven by buoyancy (dry convection). The former decreases rapidly with height, while the latter varies slowly with height.

For a surface layer of neutral or near-neutral stability ($\langle \theta'w' \rangle \approx 0$ or mechanical turbulence only, the vertical wind profile is very close to the well-known logarithmic form

$$u = (u_* / k) \ln (z / z_0) \quad (8)$$

and the corresponding K , eddy viscosity for both u and v , is

$$K = kz u_* \quad (9)$$

where $k = 0.35$ the von Karmon constant, u_* the friction velocity, and z_0 the roughness length. Over a given surface, z_0 is a known constant, while u_* can be evaluated from the observed wind profile. Thus, K is determined. Note that K increases upward suggesting the eddy size is proportional to the height above the surface.

For a nonneutral surface layer, there will be vertical heat exchanges between air and the underlying surface. We will have predominant mechanical turbulence if the layer is stable ($\partial\theta/\partial z > 0$), or both mechanical and thermal turbulence if the layer is unstable ($\partial\theta/\partial z < 0$). According to the similarity theory summarized in the book by Haltiner and Williams (1980), the vertical gradients of the wind and potential temperature can be expressed as follows, respectively.

$$\partial u / \partial z = [(u_* / k) / z] \phi_m(z/L) \quad (10)$$

$$\partial \theta / \partial z = [(\theta_* / k) / z] \phi_h(z/L) \quad (11)$$

$$L = \theta_0 u_*^2 / (kg \theta_*) \quad (12)$$

where θ_* analogous to u_* representing a temperature scale related to the vertical eddy heat flux, and θ_0 the potential temperature at the surface.

The length scale L , called the Monin-Obukhov length derived based upon dimension analysis, measures the relative role between mechanical and thermal forcing in generating the turbulence. L is negative in unstable air with upward heat flux, while positive in stable air with downward heat flux. Also, physically the absolute value of L may be interpreted as the height above which the mechanical turbulence becomes insignificant compared to the thermal turbulence. Thus, as air becomes more unstable, the absolute

value of L becomes smaller. ϕ_m and ϕ_h are two nondimensional universal functions determined empirically from observations. The corresponding eddy viscosity K_m and eddy conductivity K_h are

$$K_m = k u_* z / \phi_m \quad (13)$$

$$K_h = k u_* z / \phi_h \quad (14)$$

For unstable air

$$\phi_m = [1 - 15z/L]^{-1/4} \quad \text{and} \quad \phi_h = 0.74[1 - 9z/L]^{-1/2} \quad (15)$$

For stable air

$$\phi_m = [1 + 4.7z/L] \quad \text{and} \quad \phi_h = 0.74 + 4.7z/L \quad (16)$$

For moisture flux, K_q known as eddy diffusivity is assumed to be the same as K_h .

b) The Ekman layer

The vertical extent of the PBL is variable. Its depth may range from 100 m (e.g., the nocturnal PBL) in stable air to over 1 km (e.g., the daytime PBL over arid land) in unstable air. Out of the total depth the surface layer occupies less than 10% of the lowest part, and the rest is the well-mixed Ekman layer. Because of its elevation, it is much more difficult to conduct observational study in the Ekman layer than in the surface layer. As a result, there is lack of a simple and elegant theory, such as the surface similar theory, which may be used to define the K profiles in this upper part of the PBL. Here, a cubic polynomial similar to the O'Brien's formulation (1970) except for the constraint of zero slope at the top of the PBL is adopted for the the K profiles in the Ekaman layer.

The cubic polynomial has the following form:

$$K(z) = K(z_s) [1 - 9.75z + 8.75z^3] + \partial K(z_s)/\partial z [z_e - z_s] [z - 3.5z^2 + 2.5z^3] + K(z_m) [125z^2 (1-z)/12] + K(z_e) [z^2(5z-2)/3] \quad (17)$$

where $K(z_s)$, $K(z_e)$, and $K(z_m)$ are K evaluated at the top of the surface layer (z_s), at the top of the Ekman layer (z_e), and at the middle of the PBL (z_m), separately. $K(z_s)$ and $\partial K(z_s)/\partial z$ are obtained from the surface layer physics discussed earlier, and $K(z_e)$ has to be specified. Also, K has the maximum value at z_m . In the current PBL model z_s is set at 25 m and $K(z_e)$ is set equal to $1 \text{ m}^2\text{s}^{-1}$.

c) Height of the PBL

To apply the K profiles, we must know the depth of the PBL. Based on theoretical and observational studies, for the neutral PBL, Panofsky and Dutton (1984) suggested

$$z_e = 0.2u_* / f \quad (18)$$

For the unstable PBL, the Deardorff's (1974) prognostic equation is used.

$$dz_e/dt = 1.8(w_*^3 + 1.1u_*^3 - 3.3u_*^2 f z_e) / (z_e^2 \sigma + 9w_*^2 + 7.2u_*^2) \quad (19)$$

where $w_* = [g\theta_* z_e / \theta_0]^{1/2}$, the vertical velocity scale; $\sigma = (g/\theta_0) \partial \theta / \partial z$, the static stability at the surface. For the stable PBL, the following equation suggested by Nieuwstadt and Tennekes (1981) is used.

$$\partial z_e / \partial t = -u \partial z_e / \partial x - v \partial z_e / \partial y + (z' - z_e) / t_s \quad (20)$$

where $z' = 0.4(u_* L / f)^{1/2}$, the equilibrium height; $t_s = 0.75[\theta(z_e) - \theta_0](d\theta_0/dt)^{-1}$, the time scale.

d) Extremely unstable PBL

Recently, Yoh (1989) suggested that under extremely unstable conditions

some modifications of the surface similarity theory were necessary. In very unstable air, $-L$ approaches the order of meters and free convection responsible for generating large local eddies plays a key role in the vertical eddy mixing. It is inappropriate to use u_* , which is strongly influenced by the mean wind, as a velocity scale to determine the eddy fluxes. Also, because $\phi_m(z/L)$ and $\phi_h(z/L)$ are accurate for a relatively small $|z/L| (< 5)$, both functions may only be applied at the level of a few meters in height.

Yoh subdivided the surface layer into two layers: the lowest layer of 1.22 m upward from the surface, in which the modified similarity theory will be applied, and 1.22-25 m layer, in which the mixed layer scaling will be applied. The major difference between the modified and the original similarity theory discussed earlier is the incorporation of w_* , a free convection scaling velocity, in computing the modified friction velocity, u_+ and Monin-Obuhkov length L_+ . The mixing length scaling technique is designed to relate u , v , θ , and q at 1.22 m to those at 25 m. This information provides an input for the modified surface similarity. The relationship between u_+ and L_+ is identical to that between u_* and L (see Equ. 12). After L_+ is determined, Equations (13)-(16), with L replaced by L_+ , are used to obtain K_s at 25 m. Finally, the K profiles in the Ekman layer under very unstable conditions can be determined from (17).

e) Surface heat source

From the above discussion, it is clear that under the nonneutral conditions surface heat fluxes exert great influences on the K profiles in the PBL. The intensity of these heat fluxes depends on to a large extent the temperature difference between air and the surface. To solve numerically the PBL equations, we often need the surface temperature as one of lower boundary conditions.

Over the oceans, water responds slowly to atmospheric radiation and the temporal variation of water temperature is small. A constant sea surface temperature (SST) field at its initial observed values is adequate for model PBL in a short-range (< 48 h) NWP. Over land, due to its quick response to solar heating the temporal variation of surface temperature is rather large.

A diurnal character is expected in the PBL height as well as the K profiles. Thus, a mechanism for determining the surface temperature and the associated heat flux is needed for properly resolving the essential features of the PBL over land. This is particularly true over arid land.

In this study, the land surface temperature will be calculated based on a heat budget consideration. The surface heat budget involves infrared and solar irradiance, and sensible and latent heat flux. Also, the surface heat budget is well known to be a strong function of cloud cover and moisture content in air. In the next section, a brief description of the treatment of radiation processes as well as the procedures to obtain the surface temperature is presented.

4. RADIATIVE ENERGY AND HEAT BUDGET AT THE SURFACE

In modeling radiative transfers the usual constraints of a numerical model, i.e., not to be too time-consuming, must be considered. In this study only water vapor, which is one of the prognostic variables in the model equations, is regarded as a radiatively active gas in the model atmosphere. Ozone and carbon dioxide are not considered in radiation computation because the model top is set at the lower stratosphere. In the troposphere, for a short-range NWP carbon dioxide contribution to the atmospheric radiation processes is negligible comparing with that due to water vapor.

To solve the transfer equations for infrared radiation a simplified method based on the broad-band emissivity technique (Staley and Jurica, 1970) is used. The technique has been successfully applied in many NWP studies (Danard, 1969; Chang, 1980). With respect to infrared radiation, clouds and the earth's surface are treated as a blackbody radiator. For modeling solar radiation, an empirical technique designed for the UCLA general circulation model (Haltiner and Williams, 1980) is used. Some modifications have been made to accommodate multi-layer clouds in the current model atmosphere. The reflection of insolation at the cloud top and the earth's surface, and the absorption of insolation by clouds are considered. The intensity of solar radiation varies with the zenith angle which is computed as a function of location and time.

The sum of the insolation and the net infrared (downward minus

upward) radiation at the surface is taken as the total available surface heat source in the day or sink at night. The heat source/sink is partitioned into sensible heat flux, H_s , and latent heat flux, H_l , according to the Bowen ratio (Sellers, 1967). The surface temperature is then related to sensible heat flux by a bulk aerodynamic formula of the form

$$H_s = \rho c_p C_d [\sqrt{(u^2 + v^2)}] (\theta_s - \theta_a)$$

where c_p specific heat capacity of air at constant pressure, θ_s the surface potential temperatures, and θ_a the potential temperature at 25 m. The drag coefficient, C_d , is defined as

$$C_d = k^2 [\ln(z/z_t) - \phi_h(z/L)]^{-1} [\ln(z/z_0) - \phi_m(z/L)]^{-1}$$

where z_t the roughness length for temperature.

5. RESULTS

Disregarding the large-scale processes in the basic equations shown earlier and with the use of K-theory for the small-scale eddies, we reduce the u , v , θ , and q equations to the following forms.

$$\partial u / \partial t = - \rho^{-1} \partial (\rho K_m \partial u / \partial z) / \partial z$$

$$\partial v / \partial t = - \rho^{-1} \partial (\rho K_m \partial v / \partial z) / \partial z$$

$$\partial \theta / \partial t = - \rho^{-1} \partial (\rho K_h \partial \theta / \partial z) / \partial z$$

$$\partial q / \partial t = - \rho^{-1} \partial (\rho K_h \partial q / \partial z) / \partial z$$

These equations in conjunction with the hydrostatic equation and the equation of state for air constitute a closed system for the one-dimensional PBL-radiation model

The model has 15 levels in the vertical (z in Table 1). The PBL structure is resolved in terms of the lowest 6 levels. The time step used for the model integration was 1 minute and the radiation computation was updated every 30 minutes. The input sounding (Table 1) for the experiments was taken in Kansas at 1200 GMT on 11 June 1985 during the PRE-STORM. Other PBL parameters required for integrating the equations include the roughness length = 20 cm, the Bowen ratio = 0.65, and the surface albedo = 0.9. Major findings of three model experiments are presented below.

Figure 1 summarizes the results of experiment under a clear sky. The model simulated PBL height, θ at the surface and 25-m level, heat and momentum fluxes in the surface layer, and the eddy conductivity at the 25-m level are shown as a function of local time for a 24-h period starting at 6 am (0 h on the figure). The initial PBL height was set at 375 m. During the first 12-h, solar heating resulted in a large amount of upward heat flux. The unstable PBL grew to about 800 m at the noon and reached a maximum of about 1050 m near 6 pm. The maximum air temperature lagged behind the largest temperature difference between the surface and air as well as the maximum upward heat flux by about 6 h. The diurnal range for the surface temperature was close to 25°C and for the air temperature was about 4°C.

In the period after sunset and before sunrise the stable environment prevailed. Air was warmer than the surface and slightly downward heat flux was observed. The stable PBL was much shallower than the unstable one. There was a sharp drop in the height and the eddy conductivity during the transition period from the unstable to stable PBL but a relatively minor decrease in the momentum flux took place. This simulated the collapse of unstable PBL after the cut-off of the surface heat source and the slow re-development of stable PBL at night.

Figure 2 is similar to Fig. 1 except for the experiment under a cloudy sky. A layer of low cloud was placed between the 1.25 km and 2 km model levels. Comparisons between Figs. 1 and 2 reveal that

- 1) The model cloud decreased the unstable PBL height in the daytime, while increased the stable PBL height slightly at night. The vertical mixing in the unstable PBL was suppressed as indicated by the lower K value.

- 2) The model cloud had modulated the surface temperature considerably

resulting in much smaller diurnal range. Also, it caused few degree cooling of air in late afternoon and slightly warming of air in the early morning.

3) The model cloud reduced the temperature differences between the surface and air and consequently the heat fluxes, but had relatively minor impact on the momentum fluxes.

Figure 3 shows the results from the third experiment. In this experiment, the model integration started at the local noon instead of 6 am and the initial PBL height was set at 750 m. The main purpose of this experiment is to see how the model behaves during the transition periods from unstable to stable then back to unstable air. Also, it will reveal how sensitive the model is to the initial PBL height. Comparing Figs. 3 with 1, we find that except for the first few hours the model behaved very similarly between the two experiments. For examples, in both cases the PBL grew to slightly over 1 km at 6 pm, and the diurnal ranges in the surface and air temperatures in the two experiments were very close.

6. CONCLUSIONS AND RECOMMENDATIONS

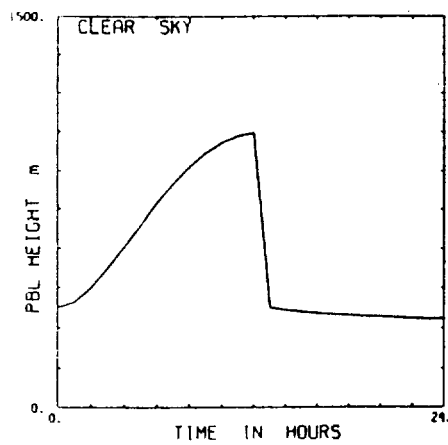
An one-dimensional model coupling the PBL processes and atmospheric radiation has been developed. The simulated results indicate that the model is capable of producing physically realistic solutions. A few more sensitivity tests with different soundings and surface parameters will be desirable for further understanding. For example, we may alter the roughness length or the Bowen ratio and see how the one-dimensional system responds to the changes. We hope to obtain some PBL observations for detailed model verifications in the near future. Comparisons with other approaches in modeling the PBL processes will also be very interesting. After carefully assessment of its performance under various conditions, the PBL-radiation scheme will then be incorporated into the LAMPS.

Table 1 Observed data used in the numerical experiments

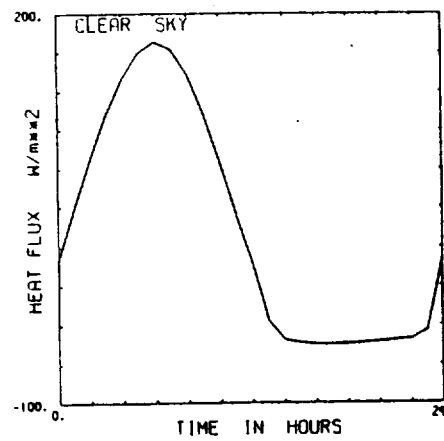
z (km)	u (m/s)	v (m/s)	θ (K)	q (g/kg)
16.0	10.	-5.8	403	0.01
14.0	32.2	3.0	359	0.05
12.0	15.2	20.9	341	0.1
10.5	15.9	16.3	337	0.2
9.0	21.7	8.0	332	0.3
7.5	18.3	12.0	327	0.3
6.0	18.9	14.4	322	2.0
4.5	7.8	-10.0	316	2.8
3.0	-3.4	-5.9	310	3.3
2.0	-5.6	-7.3	304	6
1.25	-6.0	-8.5	299	9
0.75	-4.7	-9.4	297	10
0.375	-1.1	-6.0	296	11
0.25	2.5	-3.0	295	12
0.0	2.5	-3.0	295	12

7. REFERENCES

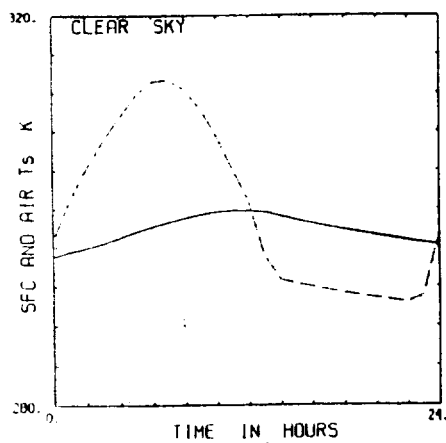
- Chang, C.-B., D. J. Perkey, and C. W. Kreitzberg, 1981: A numerical case study of the squall line of 6 May 1975. *J. Atmos. Sci.*, **38**, 1601-1615.
- Chang, C.-B., 1980: On the influences of solar radiation and diurnal variation of surface temperature on African disturbances. Ph.D dissertation, The Florida State University, 157 pp.
- Danard, M., 1969: A simple method of including long-wave radiation in a tropospheric numerical prediction model. *Mon. Wea. Rev.*, **97**, 77-85.
- Deardorff, J. W., 1974: Three dimensional numerical study of the height and mean structure of a heated planetary boundary layer. *Bound.-Layer Meteor.*, **7**, 81-106.
- Haltiner, G.J., and R. T. Williams, 1980: *Numerical Prediction and Dynamic Meteorology*. Wiley, New York, 477 pp.
- Nieuwstadt, F. T., and H. Tennekes, 1981: A rate equation for the nocturnal boundary layer height. *J. Atmos. Sci.*, **27**, 1418-1428.
- O'Brien, J. J., 1970: A note on the vertical structure of the eddy exchange coefficient in the planetary boundary layer. *J. Atmos. Sci.*, **27**, 1213-1215.
- Perkey, D. J., 1976: A description and preliminary results from a fine-mesh model for forecasting quantitative precipitation. *Mon. Wea. Rev.*, **104**, 1513-1526.
- Panofsky, H. A., and J. A. Dutton, 1984: *Atmospheric Turbulence*. John & Wiley, New York, 397 pp.
- Sellers, W. D., 1967: *Physical Climatology*. The University of Chicago Press, 272 pp.
- Staley, D. O., and G. M. Jurica, 1970: Flux emissivity tables for water vapor, carbon dioxide and ozone. *J. Appl. Meteor.*, **9**, 365-372.
- Yoh, S., 1989: Impact of marine boundary layer parameterization on a numerical simulation of cyclogenesis during a cold air outbreak event. Ph.D dissertation, Drexel University, 130 pp.



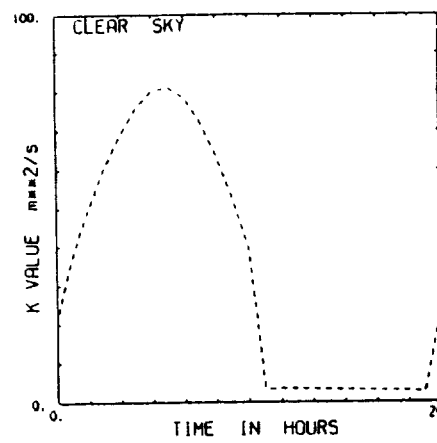
(a)



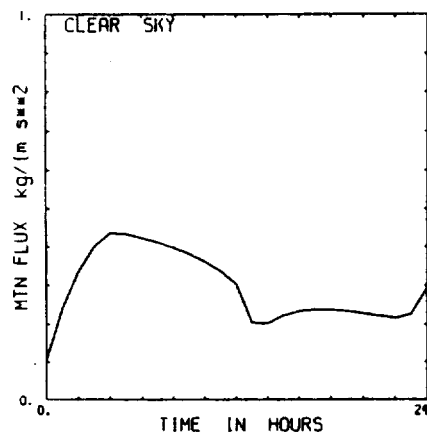
(b)



(c)

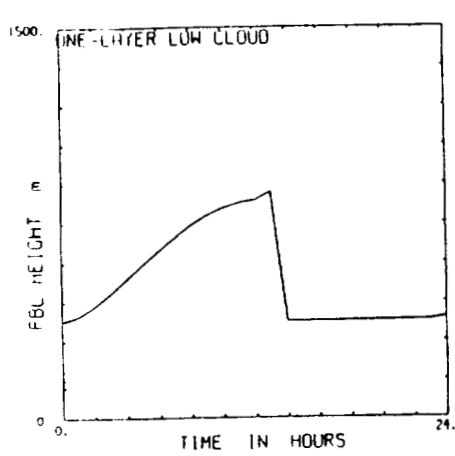


(d)

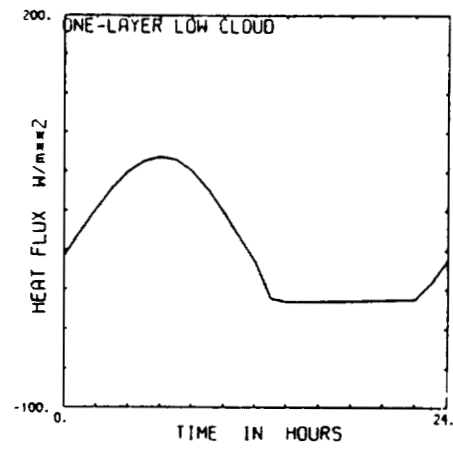


(e)

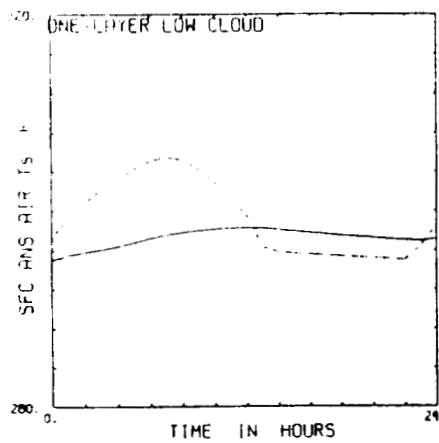
Fig. 1 Model simulated (a) the PBL height, (b) heat flux, (c) ground (dashed line) and 25-m air temperatures, (d) eddy conductivity, and (e) momentum flux as a function of local time starting at 6 am for the case of clear sky.



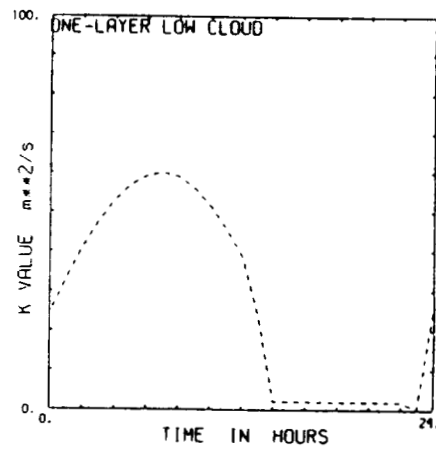
(a)



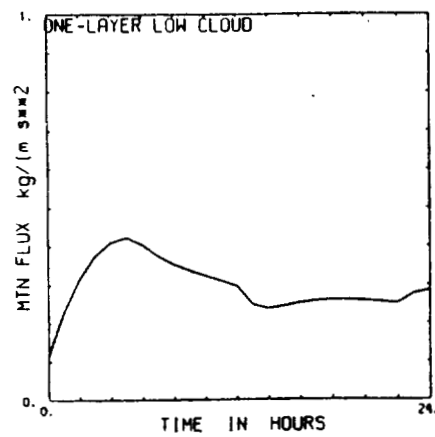
(b)



(c)



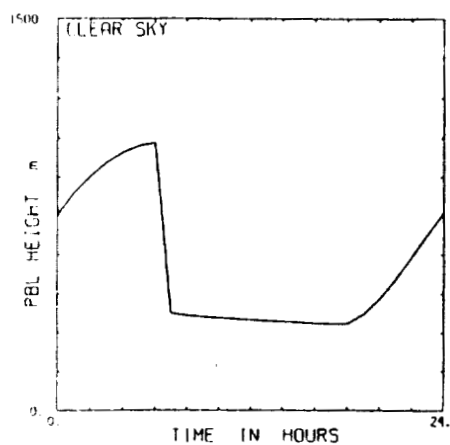
(d)



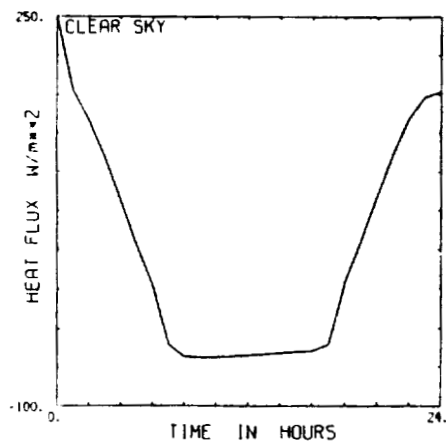
(e)

ORIGINAL PAGE IS
OF POOR QUALITY

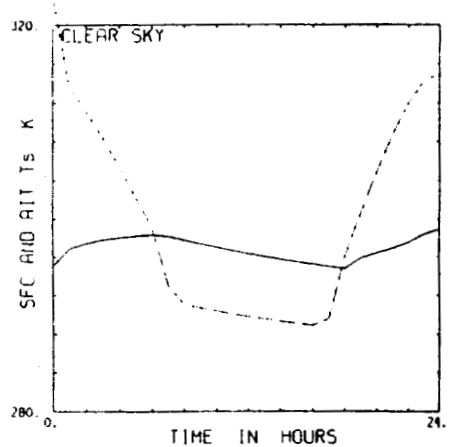
Fig. 2 Similar to Fig. 1 except for the case of cloudy sky.



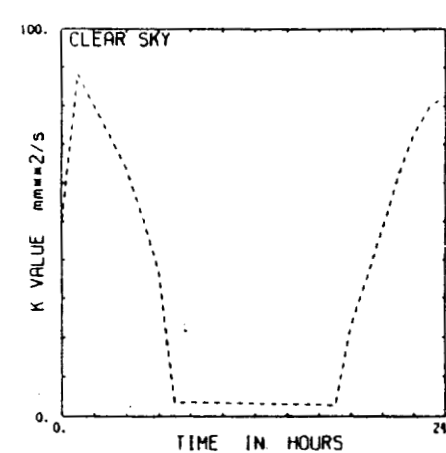
(a)



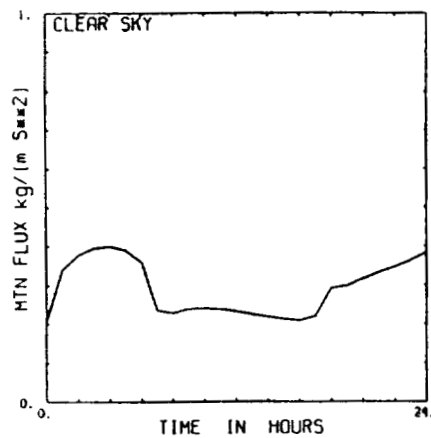
(b)



(c)



(d)



(e)

Fig. 3 Similar to Fig. 1 except for starting at noon. The initial PBL height is set at 750 m.

1989

NASA/ASEE SUMMER FACULTY FELLOWSHIP PROGRAM

MARSHALL SPACE FLIGHT CENTER

THE UNIVERSITY OF ALABAMA IN HUNTSVILLE

POTENTIAL THEORY OF RADIATION

Prepared by:	Huei-huang Chiu
Academic Rank:	Professor
University and Department:	University of Illinois at Chicago Mechanical Engineering Department
NASA/MSFC:	
Laboratory:	Propulsion
Division:	Propulsion Systems
Branch:	Performance Analysis
MSFC Colleague:	Klaus W. Gross
Date:	September 5, 1989
Contract No.:	The University of Alabama in Huntsville NGT-01-008-021

ACKNOWLEDGMENTS

I would like to express my sincere appreciation to Mr. Klaus W. Gross, MSFC, for his continuing interest and encouragement in the study of radiation processes and the development of CFD methodology for high temperature flows. His strong personal commitment and dedication to the science of liquid propulsion technology have been an extraordinary inspiration to many who have worked with him.

I wish to extend my appreciation to Mr. R. Bachtel, Dr. C. Schafer, and all the members of the Performance Analysis Branch for their hospitality and generous support. The opportunity and stimulating research environment provided by NASA, MSFC and ASEE during my second year summer program under the skillful management of Dr. Frank Six and Professor Gerald R. Karr is greatly appreciated.

POTENTIAL THEORY OF RADIATION

BY

Huei-Huang Chiu

Professor of Mechanical Engineering

University of Illinois at Chicago

Chicago, Illinois

ABSTRACT

This study aims to develop a new theoretical method by which the structure of a radiation field can be predicted by a radiation potential theory, similar to a classical potential theory. The introduction of a scalar potential is justified on the grounds that the spectral intensity vector is irrotational. The vector is also solenoidal in the limits of a radiation field in complete radiative equilibrium or in a vacuum. This method provides an exact, elliptic type equation that will upgrade the accuracy and the efficiency of the current CFD programs required for the prediction of radiation and flow fields.

A number of interesting results emerge from the present study. First, a steady state radiation field exhibits an "optically modulated inverse square law" distribution character. Secondly, the unsteady radiation field is structured with two conjugate scalar potentials. Each is governed by a Klein-Gordon equation with a frictional force and a restoring force. This steady potential field structure and the propagation of radiation potentials are consistent with the well known results of classical electromagnetic theory. The study also recommends the extension of the radiation potential theory for spray combustion and hypersonic flow.

1. INTRODUCTION

Thermal radiation plays an important role in the broad area of engineering and scientific applications involving high temperature flow processes. In high performance rocket engines¹, industrial boilers and furnaces, as well as in many astrophysical flow fields², the radiative transfer frequently makes a dominant contribution to the energy redistribution, mass, and the momentum transfer in the participating media.

Recently, an assessment of the impact of radiation in rocket engine performance was conducted by this writer³. It was concluded that the radiative heat loss and the enhancement of the burning rate of droplets by radiation can significantly affect the overall performance of low-intermediate enthalpy engines. The results of this preliminary study were brought to the attention of the research community of liquid propulsion technology. Subsequently, the JANNAF workshop⁴ on "Radiation effect on flow characteristic in combustion chambers" was conducted to indentify the problem areas that could have potential impacts on rocket engine hardware design, performance, life cycles thermal material fatigue, and reliability as well as the radiative modulation on spray flow field behavior and combustion instability.

The present study is the continuation of the radiation research which aims to promote a state-of-the-art understanding of the phenomena and to upgrade the predictive capability as well as the accuracy of Computational Fluid Dynamics (CFD) codes with radiative heat transfer.

The specific goals of this study are (1) to establish a theoretical link between two principal theories of radiation, electromagnetic (EM) theory vs. radiative transfer (RT) theory, and (2) to develop a unified theoretical methodology that can be incorporated in a computational algorithm and a grid structure similar to those of the participating fluid.

The first problem treated is a fundamental issue of establishing a unified view of radiation by examining the structures of the radiation field predicted by two rival theories; the EM and RT models.

The most remarkable findings that emerged from this study are (1) the radiation field intensity vector is irrotational and therefore the field vector is derivable from a scalar potential, (2) a steady state field structure predicted by RT theory obeys an elliptic type equation in much the same manner as an electro-magnetic static field and (3) a non-steady radiative field is governed by a wave equation which has the same general features of an electro-magnetic field characterized by the Maxwell equation.

The second problem in this study is the establishment of an exact radiation potential equation for a radiation modulated Computational Fluid Dynamics program. This study is further motivated by the fact that the radiation equations currently adopted in the majority of the Computational Fluid Dynamics (CFD) approaches are approximate equations⁵; e.g., Two-Flux model, Six-Flux model, discrete-ordinate or zonal method. The accuracy of these equations in general is not compatible with that of the conservation laws and associated submodels which are more sophisticated in the process description and mathematical characterization; e.g., $k - \epsilon$ model, combustion-turbulence interaction and spray-droplet models⁶.

Since the equation governing the radiation potential in the present theory is of an elliptic type, a numerical algorithm and grid net work similar to those of the Navier-Stokes equations, or turbulent flow conservation laws can be adopted for the simultaneous prediction of the radiation and flow field. These advantages facilitate computational efficiency and accuracy.

The potential theory serves to provide a new physical perception and an useful

methodology toward the understanding of radiation processes in high temperature flow phenomena. It also provides a gauge for the comparative assessment of the validity and limitation of the classical electromagnetic theory and the phenomenological radiative transfer approach.

This writer recommends that the steady state potential theory be implemented for the prediction of the combustion flow field in a selected liquid rocket combustion chamber, such as TRW's variable thrust engine, to test the viability of the present method. It is also suggested that this theory be extended to treat the interaction of radiation with droplets and particles in a spray combustion environment.

Additionally, spontaneous or non-steady radiation processes in combustion environments may be examined to assess the radiation induced ignition, vaporization and combustion in advanced propulsion systems.

2. BASIC PROPERTIES OF SPECTRAL INTENSITY VECTOR AND RADIATION POTENTIAL

The radiative transfer equation⁷ (RTE) which governs the spectral intensity is given by

$$\frac{1}{c} \frac{\partial I_\nu}{\partial t} + \nabla \cdot \bar{s} I_\nu = \beta_\nu (S_\nu - I_\nu) \quad (1)$$

where c is the speed of light in a vacuum, I_ν is the spectral intensity of radiation in the frequency interval ν and $\nu + d\nu$, β is the volumetric extinction, which is the sum of the absorption coefficient K_ν and scattering coefficient σ_ν , \bar{s} is the unit propagation vector and S_ν is the sum of emitted and in-scattered radiation given by

$$S_\nu = (\eta_\nu / \beta_\nu) + (\sigma_\nu / 4\pi\beta_\nu) \times \int \int \chi_\nu(\bar{s}' \rightarrow \bar{s}, \nu' \rightarrow \nu) I_{\nu'}(\bar{s}') d\Omega' d\nu' \quad (2)$$

in which η_ν is the emission coefficient, χ_ν is the scattering function and Ω is a solid angle.

2.1 Irrotationality of Spectral Intensity Vector at Steady State

The spectral intensity vector is defined as the vector which has the magnitude equal to the spectral intensity I_ν and the direction coincides with that of the propagation of a ray of light. The spectral intensity vector at a steady state can be shown to be "irrotational" by the following mathematical procedure.

By a simple quadrature the solution of Eq.(1). is given by

$$I_\nu = I_o \exp\left(-\int_{\vec{r}_o}^{\vec{r}} \beta_\nu \vec{s}' \cdot d\vec{r}'\right) + \int \beta_\nu S_\nu \exp\left(-\int_{\vec{r}'}^{\vec{r}} \beta_\nu \vec{s}'' \cdot d\vec{r}''\right) d\vec{s}' \cdot d\vec{r}' \quad (3)$$

Note that Eqn (3) is an integral equation if S_ν contains the scattering term which is represented by the third term on the right hand side of Eq.(2). In order to show the irrotationality of the spectral intensity vector, the curl of $I_\nu \vec{s}$ must vanish.

$$\begin{aligned} \nabla \times (I_\nu \vec{s}) &= \left\{ I_{\nu o} (-\beta_\nu \vec{s}) \exp\left(-\int_{\vec{r}_o}^{\vec{r}} \beta_\nu \vec{s}' \cdot d\vec{r}'\right) \right. \\ &\quad \left. - \beta_\nu \vec{s} \int_{\vec{r}_o}^{\vec{r}} \beta_\nu S_\nu \exp\left(-\int_{\vec{r}'}^{\vec{r}} \beta_\nu \vec{s}'' \cdot d\vec{r}''\right) \vec{s}' \cdot d\vec{r}' \right. \\ &\quad \left. + \beta_\nu S_\nu \vec{s} \right\} \times \vec{s} = -(\beta_\nu I_\nu - \beta_\nu S_\nu) \vec{s} \times \vec{s} = 0 \end{aligned} \quad (4)$$

The irrotationality of a spectral intensity vector allows one to introduce a "radiation potential ϕ_ν " from which the spectral intensity vector can be calculated as follows

$$\nabla \phi_\nu = I_\nu \vec{s} \quad (5)$$

Additionally, a ray of light propagates in the direction normal to an equipotential surface, as shown in the following.

Since \bar{s} is a unit vector, the magnitude of the spectral density vector I_ν is given by

$$\sqrt{\nabla \phi_\nu \cdot \nabla \phi_\nu} = I_\nu \quad (6)$$

Thus from Eq.(5), the unit propagation vector \bar{s} is

$$\bar{s} = \frac{\nabla \phi_\nu}{I_\nu} = \frac{\nabla \phi_\nu}{\sqrt{\nabla \phi_\nu \cdot \nabla \phi_\nu}} = \bar{n} \quad (7)$$

Hence the propagation vector coincides with the unit vector, \bar{n} , normal to an equipotential surface.

By substituting (5) into (1) one finds that the radiation potential ϕ_ν obeys the following "Radiation Potential Equation" (RPE)

$$\nabla^2 \phi_\nu + \beta_\nu \bar{s} \cdot \nabla \phi_\nu = \beta_\nu S_\nu \quad (8)$$

The structure of a radiation field and spectral intensity vector can be predicted by the solution of Eq.(8). A general solution of Eq.(8) will be discussed in section 3.

2.2 Solenoidal Characteristics of Spectral Intensity Vector for Two Limiting Cases

An observation of Eq.(1) suggests that when the right hand side of the equation vanishes, the spectral intensity vector is solenoidal or divergent free, providing that the radiation is independent of time. This special case corresponds to (1) a complete radiative equilibrium, and (2) non-participating media i.e. $\beta_\nu = 0$ including a vacuum space.

In the special cases listed above, the radiation potential ϕ_ν satisfies the Laplace equation

$$\nabla^2 \phi_\nu = 0$$

Thus the determination of the distribution of the spectral intensity vector for these limited cases is equivalent to the boundary value problem of a "Laplace" potential field. Principle tools and the results of classical potential theories (such as the method of image, conformal mapping, as well as Green functions for Dirichlet and Neumann boundary value problems) can be used with or without modification for the prediction of the flow coupled or decoupled radiation field problems.

3. POTENTIAL THEORY OF STEADY STATE RADIATION

The determination of a radiation intensity in a domain bounded internally or externally by a physical surface is reduced to an appropriate boundary value problem of RPE, Eq.(8).

A general solution of Eq.(8), "optically modulated inverse square law", is discussed in the following section.

3.1 Optically Modulated Inverse Square Law

In order to determine the radiation field one has to predict I_ν simultaneously with the conservation laws of a flow field because the source term S_ν appearing on the right hand side of Eq.(8) depends, in general, on the properties of a gas flow field and radiation.

In the following analysis, however, the S_ν will be treated as a source term so that the formal solution of Eq.(8) can be expressed in an integral form which contains S_ν in an integrand.

The general solution is first expressed by the method of potential splitting as follows

$$\nabla \phi_\nu = \exp \left\{ - \int_{r_0}^{\bar{r}} \beta_\nu \bar{s}' \cdot d\bar{r}' \right\} \nabla \psi_\nu \quad (9)$$

Subsequently by substituting (9) into (8) one obtains

$$\nabla^2 \psi_\nu = \exp \left\{ \int_{\bar{r}_o}^{\bar{r}} \beta_\nu \bar{s}' \cdot d\bar{r}' \right\} \beta_\nu S_\nu \quad (10)$$

Thus a particular solution of Eq.(10) is what may be termed as an "optically retarded inverse square law potential" given by

$$\psi_\nu = \iiint \frac{\beta_\nu S_\nu(\bar{r}') \exp(\int_{\bar{r}_o}^{\bar{r}'} \beta_\nu \bar{s}'' \cdot d\bar{r}'')}{|\bar{r} - \bar{r}'|} dV' \quad (11)$$

The spectral intensity vector is obtained by substituting Eq.(11) into (9) as follows

$$I_\nu \bar{s} = \nabla \psi_\nu = - \iiint \frac{\beta_\nu S_\nu(\bar{r}')}{|\bar{r} - \bar{r}'|^2} \exp \left\{ - \int_{\bar{r}'}^{\bar{r}} \beta_\nu \bar{s}'' \cdot d\bar{r}'' \right\} dV' \quad (12)$$

Observation of Eq.(2) suggests that the intensity decay pattern has two primary characteristics; inverse square and exponential decay in source strength due to an opacity factor. This decay pattern is one of the basic characteristics of the radiation heat transfer and will be referred to as "optically modulated inverse square law".

3.2 Steady State Radiation Potential Solution

A general solution satisfying a prescribed potential and its normal derivative at a physical boundary shown in Fig.1 can be constructed from the solution of an associated potential ψ_ν . Since ψ_ν satisfies the Poisson equation, the general solution is given by the following classical expression

$$\begin{aligned} \psi_\nu(\bar{r}) = & \iiint \frac{\beta_\nu S_\nu(\bar{r}') \exp(\int_{\bar{r}_o}^{\bar{r}'} \beta_\nu \bar{s}'' \cdot d\bar{r}'')}{|\bar{r} - \bar{r}'|} dV' \\ & + \iint \psi_\nu(\bar{r}_o) \frac{\partial}{\partial n} \frac{1}{|\bar{r} - \bar{r}_\gamma|} d\Sigma_o - \iint \frac{\partial \psi(\bar{r}_o)}{\partial n} \frac{1}{|\bar{r} - \bar{r}_o|} d\Sigma_o \end{aligned} \quad (13)$$

where $\psi_\nu(\bar{r}_0)$ and $\frac{\partial \psi_\nu(\bar{r}_0)}{\partial n}$ is the value of the potential and its normal derivative at \bar{r}_0 , located on the boundary. The numerical values of $\frac{\partial \psi_\nu}{\partial n}$ are related with those of $\frac{\partial \phi_\nu}{\partial n}$ as follows

$$\frac{\partial \psi_\nu}{\partial n}(\bar{r}_0) = \lim_{\bar{r} \rightarrow \bar{r}_0} \bar{n} \cdot \nabla \psi_\nu = \lim_{\bar{r} \rightarrow \bar{r}_0} \bar{n} \cdot \exp\left(\int_{\bar{r}_0}^{\bar{r}} \beta_\nu \bar{s}' \cdot d\bar{r}'\right) \nabla \phi_\nu$$

Thus the numerical value of $\frac{\partial \psi_\nu}{\partial n}$ at $r = r_0$ is equal to that of $\frac{\partial \phi_\nu}{\partial n}$; i.e.

$$\frac{\partial \psi_\nu(\bar{r}_0)}{\partial n} = \frac{\partial \phi_\nu(\bar{r}_0)}{\partial n}$$

The numerical values of $\psi_\nu(\bar{r}_0)$ must be calculated from the prescribed value of $\phi_\nu(\bar{r}_0)$ by integrating Eq.(9) as follows

$$\psi_\nu(\bar{r}) = \psi_\nu(\bar{r}_{0,0}) + \int_{\bar{r}_{0,0}}^{\bar{r}} \exp\left(\int \beta_\nu \bar{s}' \cdot d\bar{r}'\right) d\psi_\nu \quad (14)$$

where $\bar{r}_{0,0}$ is a reference point on the wall.

An additional step is required to determine the value of $\psi_\nu(\bar{r}_0)$ in terms of $\phi_\nu(\bar{r}_0)$. Firstly, Eq.(14) will be specialized to the boundary by replacing \bar{r} by \bar{r}_0 , i.e.

$$\psi_\nu(\bar{r}_0) = \psi_\nu(\bar{r}_{0,0}) + \int_{\bar{r}_{0,0}}^{\bar{r}_0} \exp(\lambda) d\phi_\nu \quad (15)$$

where

$$\lambda = \int_{\bar{r}_{0,0}}^{\bar{r}_0} \beta_\nu \bar{s}' \cdot d\bar{r}'_0 \quad (16)$$

Since the distribution of a potential is prescribed as function ϕ_ν i.e.

$$\phi_\nu = \phi_\nu(\lambda)$$

Finally, by substituting (17) into (16) one obtains

$$\psi_\nu(\bar{r}_0) = \psi_\nu(\bar{r}_{0,0}) + \int_{\bar{r}_{0,0}}^{\bar{r}_0} e^\lambda f(\lambda) d\lambda \quad (18)$$

where

$$f(\lambda) = \frac{d\phi_\nu}{d\lambda} \Big|_{r=r_0}$$

The spectral intensity vector is derived from Eqs.(9) and (13) as follows

$$\begin{aligned} I_\nu \bar{s} = \nabla \psi_\nu = & - \iiint \frac{\beta_\nu s_\nu(\bar{r}')}{|\bar{r} - \bar{r}'|^2} \exp\left(\int_{\bar{r}_0}^{\bar{r}'} \beta_\nu \bar{s}'' \cdot d\bar{r}''\right) \bar{s}' dV' \\ & + \iint \frac{\partial \psi_\nu / \partial n}{|\bar{r} - \bar{r}_0|^2} \exp\left(\int_{\bar{r}_0}^{\bar{r}} \beta_\nu \bar{s}'' \cdot d\bar{r}''\right) \bar{s}_0 d\sum_0 \\ & - \iint \psi_\nu(\bar{r}_0) \frac{\partial}{\partial n} \left\{ \frac{\bar{s}_0}{|\bar{r} - \bar{r}_0|^2} \right\} d\sum_0 \end{aligned} \quad (19)$$

where

$$S'_i = \frac{x_i - x'_i}{\sqrt{\sum (x_j - x'_j)^2}} \quad (20)$$

$$S_{ai} = \frac{x_i - x_{oi}}{\sqrt{\sum (x_j - x'_j)^2}} \quad (21)$$

and $\psi_\nu(\bar{r}_0)$ is given by Eq.(18).

In general, the method of Green functions can be used to predict the solution corresponding to the boundary value problem with a prescribed normal derivative of the radiation potential. For instance, the solution with a prescribed inhomogeneous Neumann boundary condition is given by

$$\begin{aligned} I_\nu \bar{s} = \nabla \phi_\nu = & \iiint \nabla G(\bar{r}/\bar{r}') \beta_\nu S_\nu(\bar{r}') \exp\left(-\int_{\bar{r}_0}^{\bar{r}} \beta_\nu \bar{s}'' \cdot d\bar{r}''\right) dV \\ & + \iint \nabla G_\nu(\bar{r}/\bar{r}_0) \frac{\partial \psi_\nu^*(\bar{r}_0)}{\partial n} \exp\left(-\int_{\bar{r}_0}^{\bar{r}} \beta_\nu \bar{s}'' \cdot d\bar{r}''\right) d\sum_0 \end{aligned} \quad (22)$$

where

$$\frac{\partial \psi_\nu^*(\bar{r}_0)}{\partial n} = \frac{\partial \psi_\nu(\bar{r}_0)}{\partial n} - \iiint \nabla G(\bar{r}_0/\bar{r}') \beta_\nu S_\nu(\bar{r}') dV \quad (23)$$

The Green function G satisfies the following equation

$$\nabla^2 G(\bar{r}/\bar{r}') = -4\pi \delta(\bar{r} - \bar{r}') \quad (24)$$

and homogeneous Dirichlet condition i.e. $G(\bar{r}_0/\bar{r}') = 0$

3.3 Structural Equivalence Between the Radiation Potential Theory and the Electro-magneto Static Theory

The fact that the radiative potential equation Eq.(8a) and (8b) is an elliptic type suggests the structural similarity between the radiation field predicted by the Radiation Potential Theory, and the electro-magnetic static field which is governed by the Laplace or the Poisson equation in electromagnetic theory. However, it must be pointed out that the radiation potential ϕ_r and spectral intensity vector $I_r \bar{s}$ are not the same physical quantities as the electro-magnetic static potential and electro-magnetic intensity. Hence, complete equivalence between the two theories will require the knowledge of the functional relationship between those of the electromagnetic properties and those of the radiation field. This issue will be discussed further in section 4.

4. POTENTIAL THEORY OF NON-STEADY RADIATION

Unsteady radiation phenomena involve the propagation and interaction of light with matter in a participating fluid. The objective of this section is to develop a hyperbolic type equation that governs what may be termed a "conjugate spectral intensity". The proposed formulation of a "Radiation Wave Equation" exhibits another interesting insight into the structural equivalence between the radiative transfer and electromagnetic theories.

4.1 Conjugate Spectral Intensities

The radiative transfer equation Eq.(1) does not remain invariant under the inverse transformation of the propagation vector \vec{s} . Thus, it is appropriate to define two independent spectral intensities; I_ν^+ and I_ν^- which satisfy the following pair of equations.

$$\frac{1}{c} \frac{\partial I_\nu^\pm}{\partial t} \pm \vec{s} \cdot \nabla I_\nu^\pm = \beta_\nu (S_\nu - I_\nu^\pm) \quad (25)$$

The equation governing I_ν^+ is the radiative transfer equation with the propagation vector being equal to \vec{s} , whereas the conjugate equation governing I_ν^- has a propagation vector of $-\vec{s}$.

Following a mathematical proof similar to that which was presented in section 2.1, one can show that the conjugate spectral intensity vectors are irrotational and therefore derivable from two conjugate radiation potentials i.e.

$$I_\nu^\pm \vec{s} = \nabla \phi_\nu^\pm \quad (26)$$

Substitution of Eq.(26) into (25) gives

$$\nabla \cdot \vec{L}^\pm \phi_\nu^\pm = \beta_\nu S_\nu \quad (27)$$

where \vec{L}^\pm are first order vectorial operators

$$\vec{L}^\pm = \frac{\vec{s}}{c} \frac{\partial}{\partial t} \pm \nabla + \beta_\nu \vec{s} \quad (28)$$

Two vectors $\vec{L}^\pm \phi_\nu^\pm$ can be decomposed into two components as follows

$$\vec{L}^\pm \phi_\nu^\pm = \nabla \psi^\pm + \nabla \times \vec{W}^\pm \quad (29)$$

Where ψ^\pm and \vec{W}^\pm are scalar and vector potentials respectively. Two conjugate scalar potentials ψ_ν^\pm are governed by the following Poisson equation

$$\nabla^2 \psi_\nu^\pm = \beta_\nu S_\nu \quad (30)$$

whereas the vectorial potential functions obey the following homogeneous vectorial equation with repeated curl operators.

$$\nabla \times \nabla \times \bar{W}^{\pm} = 0 \quad (31)$$

The absence of the source term in Eq.(31) is demonstrated, initially, by applying a curl operator in Eq.(29). The result is

$$\nabla \times \bar{L}^{\pm} \phi_{\nu}^{\pm} = \nabla \times \nabla \times \bar{W}^{\pm} = \nabla \times \left(\frac{\bar{s}}{c} \frac{\partial}{\partial t} \pm \nabla - \beta_n u \bar{s} \right) \phi_{\nu}^{\pm} \quad (32)$$

Secondly, the irrotationality of $\bar{L}^{\pm} \phi_{\nu}^{\pm}$ is proved by showing that the first and third terms appearing on the right hand side of Eq.(32) vanish. The proof is shown in the following

$$\nabla \times (\bar{s} \phi_{\nu}^{\pm}) = \nabla \times \left(\bar{s} \int I_{\nu}^{\pm} \bar{s}' \cdot d\mathbf{r}' \right) = \bar{s} \times I_{\nu}^{\pm} \bar{s} \equiv 0 \quad (33)$$

In order to establish the structural equivalence between the radiative transfer and electromagnetic theory, one has to demonstrate the similarity in the type of the partial differential operations for the conjugate radiation potentials and the electromagnetic potentials. This is discussed in the next subsection.

4.2 Conjugate Radiative Wave Equations: Klein-Gorden Equations

According to the irrotational characteristics of $\bar{L}^{\pm} \phi_{\nu}^{\pm}$, one expresses

$$\bar{L}^{\pm} \phi_{\nu}^{\pm} = \nabla \psi_{\nu}^{\pm} \quad (34)$$

By applying the vectorial conjugate operator to Eq.(34), one obtains

$$\bar{L}^{\mp} \cdot \bar{L}^{\pm} \phi_{\nu}^{\pm} = \bar{L}^{\mp} \cdot \nabla \psi_{\nu}^{\pm} \quad (35)$$

The above equations, (35), are rewritten into two components explicitly as follows

$$\frac{1}{c^2} \frac{\partial^2 \phi_\nu^+}{\partial t^2} - \nabla^2 \phi_\nu^+ + 2 \frac{\beta_\nu}{c} \frac{\partial \phi_\nu^+}{\partial t} + (\beta_\nu^2 - \vec{s} \cdot \nabla \beta_\nu) \phi_\nu^+ = \left(\frac{\vec{s}}{c} \frac{\partial}{\partial t} + \beta_\nu \vec{s} \right) \cdot \nabla \psi_\nu^+ - \beta_\nu S_\nu \quad (36)$$

$$\frac{1}{c^2} \frac{\partial^2 \phi_\nu^-}{\partial t^2} - \nabla^2 \phi_\nu^- + 2 \frac{\beta_\nu}{c} \frac{\partial \phi_\nu^-}{\partial t} + (\beta_\nu^2 + \vec{s} \cdot \nabla \beta_\nu) \phi_\nu^- = \left(\frac{\vec{s}}{c} \frac{\partial}{\partial t} + \beta_\nu \vec{s} \right) \cdot \nabla \psi_\nu^- + \beta_\nu S_\nu \quad (37)$$

where ψ_ν^\pm are given by

$$\begin{aligned} \psi_\nu^\pm = & \int \int \int \frac{\beta_\nu S_\nu(\vec{r}')}{|\vec{r} - \vec{r}'|} dV' + \int \int \psi_\nu^\pm(\vec{r}_0) \frac{\partial}{\partial n} \frac{1}{|\vec{r} - \vec{r}_0|} d\vec{Z}_0 \\ & - \int \int \frac{\partial \psi_\nu^\pm(\vec{r}_0)}{\partial n} \frac{1}{|\vec{r} - \vec{r}_0|} d\vec{Z}_0 \end{aligned} \quad (38)$$

in which $\psi_\nu^\pm(\vec{r}_0)$ and $\frac{\partial \psi_\nu^\pm(\vec{r}_0)}{\partial n}$ are the potentials and their normal derivatives on the boundary surface respectively.

The pair of the wave equations (36) and (37) are Klein-Gordon Equations with a friction force represented by the term involving the first order derivative with respect to time. The difference between two conjugate wave equations (36) and (37) is the sign of the second restoring term $\beta_\nu^2 \mp \vec{s} \cdot \nabla \beta_\nu$ and the source terms appear on the, $\pm \beta_\nu S_\nu$, present on the right hand side of Eqs.(36) and (37). The structural similarity between the two theories; RT and EM is the key feature of the present theory. Presently, however, the functional interrelation between the properties of the two fields has not being indentified. Thus the complete similarity between two fields can not be fully established. It may be mentioned, nevertheless, that there is an indirect method for the interrelation of the energy-stress tensors of an electromagnetic field and that of a photon gas field. Such photon gas-electromagnetic equivalence⁸ has been established in the frame work of the relativistically covariant theory of photon gas conservation laws derived from the conservation of

proper photon density. This latter equation corresponds to the covariant radiative transfer equation in a four-dimensional space.

Observation of Eqs.(36) and (37) reveals the following basic features. First, two equations are reduced to a conventional wave equation when β_ν vanishes. This is consistent with the well known result of the propagation of an electromagnetic wave in a vacuum. Secondly, in an optically thin medium, i.e., $\beta_\nu \ll 1$ restoring forces for two conjugate waves are different from each other depending on the sign of the gradient of β_ν in the direction of the propagation. For example, the coefficient of a restoring force is positive in the direction of the increasing β_ν . However in an optically thick media $\beta_\nu \gg 1$, the restoring force coefficient is positive for two conjugate waves. Thirdly, an opacity retards the wave propagation. Finally, the radiation potential ϕ_ν^+ is degenerated by the sink $\beta_\nu S_\nu$ whereas it is generated by a source term $\beta_\nu S_\nu$ for the ϕ_ν^- wave. Furthermore both ϕ_ν^\pm waves are partially generated by the source term proportional to the temporal variation of the gradient of an associated potential ϕ_ν^\pm and the product of the opacity with the latter quantity.

5. CONCLUSION

The potential theory of radiation presented in this paper provides a new physical perception of the structure of a radiation field through the identification of the basic characteristics of the irrotationality of a spectral intensity vector. Scalar potential representation of a radiation field allows a unique interpretation of the laws of radiative decay, effects of the boundary values on the field variables for the case of steady state, propagation, retardation, as well as the generation of a radiation wave for unsteady radiation. This preliminary theoretical development is focused ,by design, upon a narrowly scoped mathematical problem, and on the identification of the basic commonality between radia-

tive transfer and electromagnetic theories. The comparative study yields a confirmation of a structural similarity between two fields: radiation and electromagnetic . It is projected, without proof, that the ultimate equivalence theory will serve to determine the validity limit of the existing phenomenological theory of radiative transfer. The results of such a comparative study will serve to guide the formulation of a new radiative transfer theory.

In the mean time, the steady state potential equation seems to be a viable equation for the prediction of radiation coupled problems because of its accuracy and elliptic type of equation. This formulation has not presently been applied in modern CFD calculations. However, in view of an increasing interest in radiation phenomena in high performance liquid rocket engines and hypersonic flows, the present method is recommended for further advancement toward the numerical prediction of the radiation effects on a gas phase flow as well as for spray combustion processes. This potential method is also expected to provide a unique mathematical tool for the prediction of the radiation fields of various geometrical objects. Such options should be explored to enhance the radiation modelling activity.

Finally, the unsteady radiation phenomena is a largely unexplored area. The effects of highly pulsed radiation on propellant heating, vaporization and ignition have a practical significance on the engine start-up and instability of liquid rocket engines.

REFERENCES

1. R. Viskanta, R. and M.P. Mengüç, Prog. Energy Combust Sci., vol. 13, pp. 97-160 (1987).
2. Karl-Heinz A. Winkler and M.L. Norman, Astrophysical Radiation Hydrodynamics NATO ASI Series C: Mathematical and Physical Sciences, vol. 88 (1986).
3. H.H. Chiu, Radiation Effects on Rocket Engine Performance: NASA/MSFC CR 183533 (1989).
4. M.Q. Brewster and K.W. Gross: Radiation Effects on Flow Characteristics in Combustion Chambers, JANNAF WORKSHOP, Monterey Calif. (1989).
5. R. Viskanta: Advances in Heat Transfer, T.F. Irvine and J.P. Hartnett (ds), vol. 7, pp. 175-248, Academic Press, N.Y. (1974).
6. T.L. Jiang and H.H. Chiu: Theory of Bipropellant Combustion II, Conjugate, Normal and Composite Combustion in a Liquid Propellant Combustion Chamber, AIAA paper No. AIAA-86-0221, 24th Aerospace Sciences Meeting, Reno, Nevada (1985).
7. R. Siegel and J.R. Howell: Thermal Radiation Heat Transfer 2nd Ed. Hemisphere Washington, D.C. (1981).
8. H.H. Chiu: Class of Exact Solution of Relativistic Gas, Physics of Fluid, vol. 13, no. 8, pp. 1978-1983 (1970).

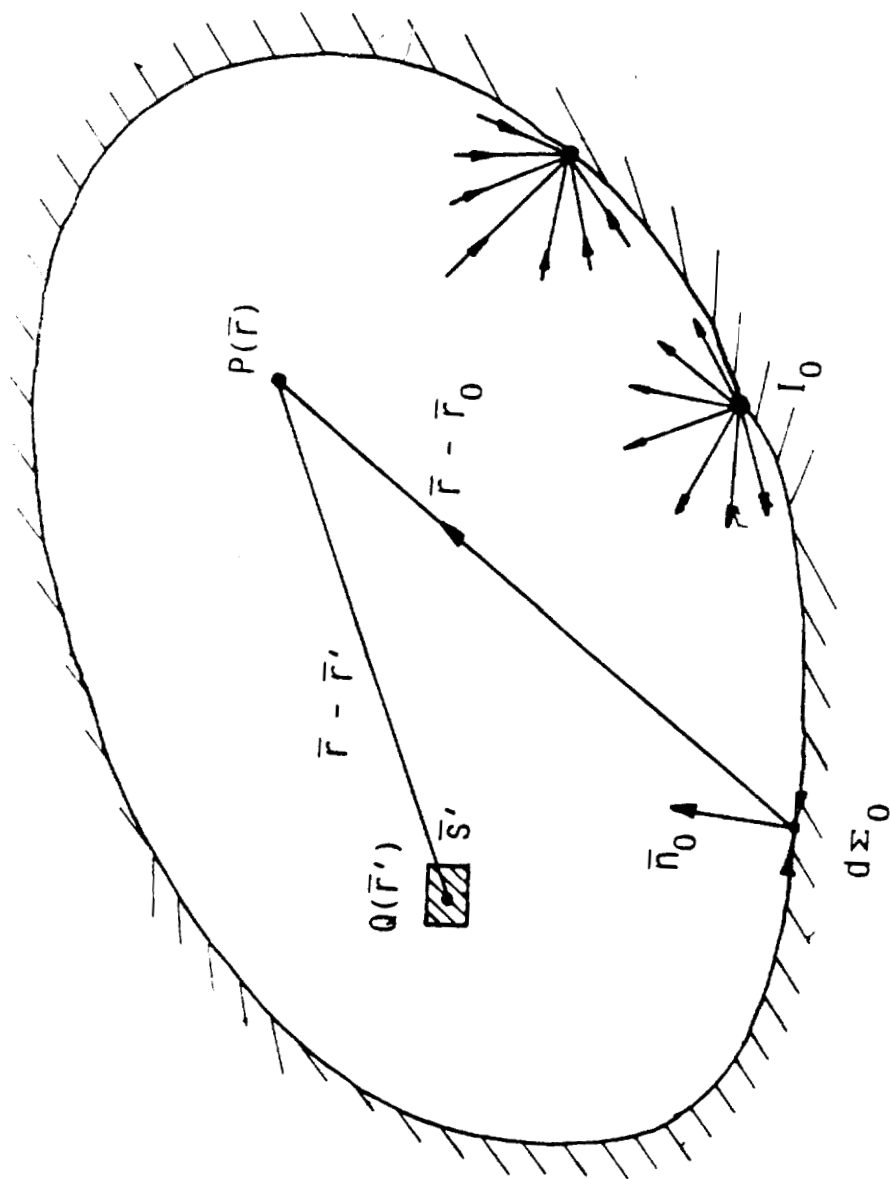


Fig. 1 Schematic of the radiation field bounded by a boundary surface

1989

NASA/ASEE SUMMER FACULTY FELLOWSHIP PROGRAM

MARSHALL SPACE FLIGHT CENTER
THE UNIVERSITY OF ALABAMA IN HUNTSVILLE

METHODS FOR TREND ANALYSIS: EXAMPLES WITH
PROBLEM/FAILURE DATA

Prepared by: Curtis K. Church, Ph.D.
Academic Rank: Associate Professor
University and Department: Middle Tennessee State
University, Department of
Mathematics and Statistics

NASA/MSFC:

Directorate: Safety, Reliability, Main-
tainability & Quality
Assurance
Office: Systems Safety & Reliability
Division: Reliability & Maintainability
Engineering
Branch: Problem Assessment

MSFC Colleagues: Raymond Dodd, Ph.D.
Frank Pizzano

Date: July 20, 1989

Contract No: The University of Alabama
in Huntsville
NGT-01-008-021

ABSTRACT

NASA Headquarters is emphasizing that statistics has an important role in quality control and reliability. Consequently, 'Trend Analysis Techniques' (NASA-STD-8070.5) recommended a variety of statistical methodologies that could be applied to time series data. The major goal of this report or 'working handbook', using data from the MSFC Problem Assessment System, is to illustrate some of the techniques in the NASA standard, some different techniques, and to notice patterns of data. Techniques for trend estimation used are: regression (exponential, power, reciprocal, straight line) and Kendall's rank correlation coefficient. The important details of a statistical strategy for estimating a trend component are covered in the examples. However, careful analysis and interpretation is necessary because of small samples and frequent zero problem reports in a given time period. Further investigations to deal with these issues are being conducted.

CONTENTS

Introduction	1
Methods and Examples	
Exponential Model	2
Power Model	11
Reciprocal Model	14
Straight Line Model	17
Kendall's τ	22
Remarks	25
References	25
Appendix	26

INTRODUCTION

The purpose of this report or 'working handbook' is to discuss strategies and methods for statistical evaluation of trend for problem/failure data. Statistical analysis provides a tool to add insight and complement engineering judgement. Much of this work elaborates and clarifies the application of approaches contained in 'Trend Analysis Techniques' (NASA-STD-8070.5). Problem trend analysis tracks and categorizes problems over time. The problems may be for an entire system, subsystem, or any other appropriate level of aggregation. Techniques useful for statistically measuring a trend component will be illustrated in the next section. All examples contained in this report use data supplied by the MSFC Problem Assessment System.

There are two basic techniques for trend analysis in this report. One is regression and the second is a distribution free rank correlation method. Regression analysis is a statistical tool that utilizes the relation between two or more quantitative variables so that one variable can be predicted from the other, or others. A regression model is a formal means of expressing the two essential ingredients of a statistical relation:

1. A tendency of the dependent variable Y to vary with the independent variable or variables in a systematic way.
2. A scattering of the observations around the curve of statistical relationship.

We are interested in using a regression model to perform a test of hypothesis for trend. This requires that the experimenter postulate a probability model, commonly the normal distribution, to be used in the development of the hypothesis testing procedure. On the other hand, the distribution free approach eliminates specification of an underlying probability distribution. The rank correlation coefficient, known as Kendall's tau (τ), is used in the examples below as the distribution free basis for determining the existence of trend. For this method there are no assumptions about the form of the probability distribution involved and there are minimal calculations.

METHODS AND EXAMPLES

The mechanics of applying the regression and rank correlation methods for problem/failure data will be covered through examples given below. The strategy for the regression

approach will be as follows: examine a scatter plot of the data, fit an appropriate model to the observed data, perform a test of hypothesis for trend, and, if appropriate, generate a prediction interval for a future observation. In situations where there appears to be a positive (downward) trend the most advisable regression models are: exponential model, power (or multiplicative) model, or a reciprocal model. These models possess the desirable feature that the predicted values for the number of (normalized) problems will never be less than zero. The examples using the reciprocal model also illustrate the influence of extreme (or outlying) observations. In the case of an increasing trend a straight line model is also considered. Finally, Kendall's rank correlation coefficient will be adapted and discussed as an alternative means to perform a test of hypothesis for trend.

Fifteen sets of data on the SSME were selected from the problem assessment system. Each data set was normalized to give the rate of problem reports per 10,000 seconds of engine test firing time. Some data was at the system level, some at the subsystem level, and some at the failure mode level. These data sets are used to illustrate the issues and details of applying the above mentioned approaches. You will notice a common pattern in many of the data sets. There is an apparent adverse (increasing) trend from 1979 through 1982 plus or minus one year and then a positive trend from that point through 1988. This pattern appears in roughly 2/3 of the example data sets. In instances of an adverse trend followed by a positive trend, a model for the regression approach will be fit to the portion of the series exhibiting the positive trend, that is, the most recent six to seven years. In applying and interpreting the statistics one needs to rely on good judgement and sound engineering considerations. As you look through the examples notice similarities and dissimilarities in the data patterns. Statistical procedures cannot be applied in a vacuum.

Exponential Model

The exponential model is intrinsically linear. It is made linear by using a logarithmic transformation. Thus, applying an exponential model means that we will be regressing the natural logarithm of Y on time. The deterministic part of the model is:

$$Y = \beta_0 e^{\beta_1 t}$$

where: Y is the number of normalized problem reports,

β_0 and β_1 are parameters, and

t is a constant denoting the time period.

A positive (downward) trend is indicated if $\beta_1 < 0$. Thus, if an exponential model is fit to the data, the statistical justification for claiming a positive trend will be to perform a test of hypothesis of $H_0: \beta_1 \geq 0$ against $H_1: \beta_1 < 0$. This presumes a flat or increasing trend in the null hypothesis in hopes that we have evidence to reject it in favor of the alternative hypothesis, which is a positive (downward) trend.

An important note is that the exponential model, through the logarithmic transformation, cannot be applied when there is a zero value in the normalized data. In instances where there are no problem reports in a time period and you wish to use the exponential model the logarithmic transformation needs to be modified. Under general conditions it is reasonable to approximate the number of normalized problem reports in the transformed data by using .5 as the number of problems before normalizing and transforming. So, if there are zero problem reports in a time period it will be replaced with .5 for the purpose of fitting the exponential model. This adjustment is relevant only for the logarithmic transformation. A justification for this modification is given in the appendix.

On the next several pages appear scatter plots and analysis summaries. The scatter plots display the number of normalized problems as asterisks (vertical axis) to the year (horizontal axis). For these five sets of data we observe the pattern of an apparent adverse trend for the first three to four years and then an apparent positive trend. These scatter plots were generated with the PC software package NWA Quality Analyst.

For each of these sets of data an exponential model provided a good fit to the data. The beginning time period for the fitted model varied from 1981 to 1983 and ended with the 1988 data. The regression analysis summaries below the scatter plots indicate the beginning time period. All of the computational work is performed with the transformed data. The PC software package Statgraphics generated the given regression analysis summaries.

Inspection of the coefficient of determination, r^2 , value for each data set indicates a strong association between the normalized problems and year. Further evaluation of the appropriateness of the fitted model by inspecting a

graph of the fitted curve together with the observed data or other means may be easily carried out using Statgraphics or other software package. The statistical justification for claiming a positive trend, however, lies in the hypothesis testing procedure. Fortunately, the Statgraphics regression summary contains results of all necessary calculations. To conclude acceptance of $\beta_1 < 0$ focus attention on what the regression summary labels "prob. value". For regression with two coefficients, the value of interest appears twice, once on the row identified by the slope and once in the analysis of variance table. For our purpose divide this number by two. This value is the observed significance level of the test, often called the p-value. It represents the likelihood, based on the observed data, of claiming a positive trend when there is actually not a positive trend. Thus, we want the p-value to be small, say less than .025 or possibly less than .01. Note that this value is less than .01 for each of the five data sets. The r^2 value and (twice) the p-value are circled on the following summaries.

Following the hypothesis test for trend, we may wish to forecast (or predict) a new value. We can then compare the predicted value with the new value when it becomes available to assess a continuing trend. For example, we may predict the rate of problems (i.e. the normalized data) for 1989 and compare with the first quarter rate when it becomes available. The predicted value comes from the fitted equation and then prediction limits are constructed. The 95% prediction limits will roughly be the fitted value plus or minus two standard deviations of the predicted value. The standard deviation is given by:

$$\sqrt{MSE \left\{ 1 + \frac{1}{n} + \frac{(89 - \bar{t})^2}{\sum (t - \bar{t})^2} \right\}}$$

The value n is the number of data points used in the model fit, and MSE is the mean square error that appears in the analysis of variance portion of the printout. Note that the sample size is incorporated in the prediction limits through the standard deviation.

For example, the data for the SSME main combustion system is:

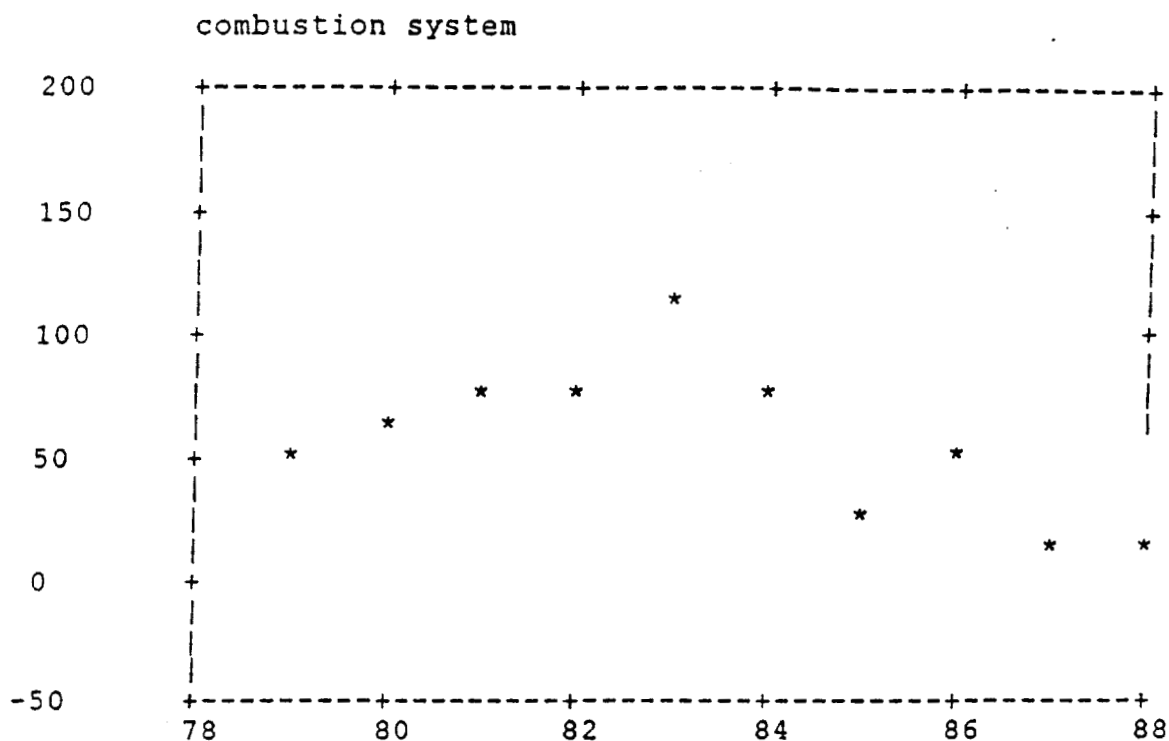
year	:	83	84	85	86	87	88
normalized							
problems:		112.21	78.64	29.98	47.83	16.44	14.48

The predicted value for $t=89$ is 8.95. Through March 1989 the normalized value of problem reports is 11.88. The upper 95%

prediction limit is 25.82 and the upper 68% prediction limit (roughly one standard deviation) is 15.96. The calculations were done with the transformed data but expressed in terms of the original units.

Regardless of the regression model chosen, the strategy is the same. Consequently, the other regression models that have been useful, the power model, the reciprocal model, and the straight line model, will only be briefly discussed and examples presented. The key statistical element is the test of hypothesis for the 'slope' parameter. This is the justification for the claim of a measurable association between problems and year.

The five sets of data that were used as examples of fitting an exponential model follow on the next several pages.



Regression Analysis - Exponential model: $Y = \exp(a+bX)$

Dependent variable: 112.2068 78.64413 29 Independent variable: 83 84 85 86 87 88

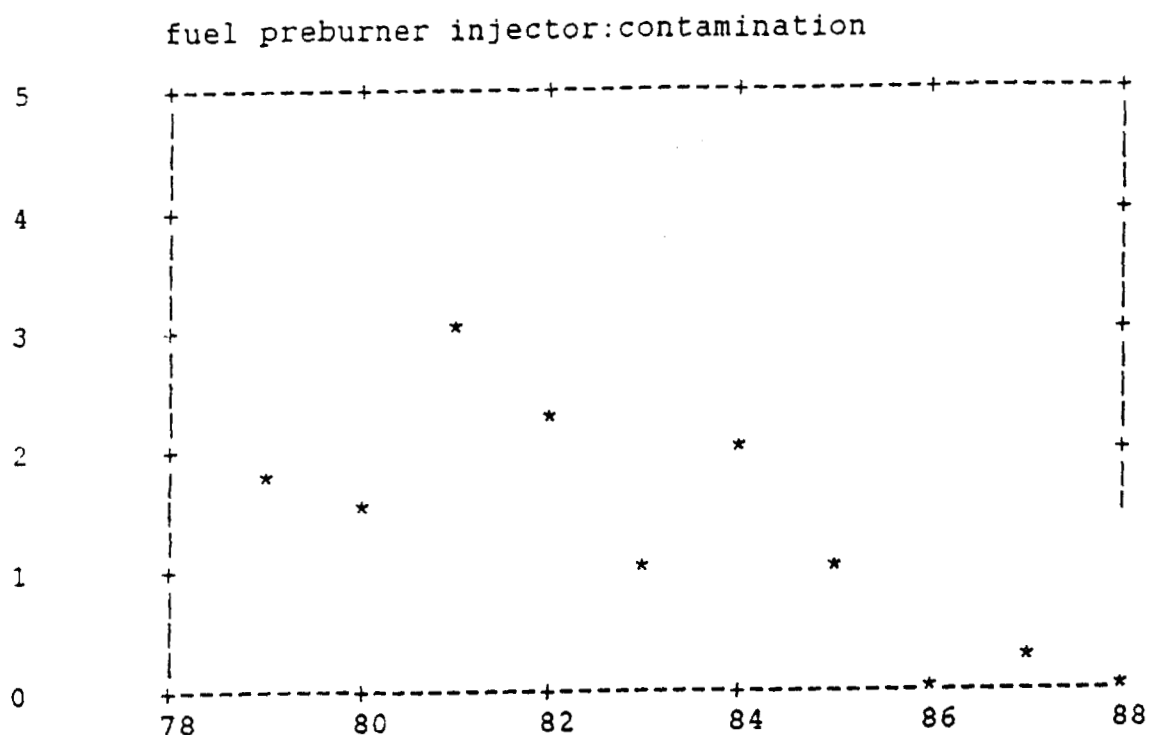
Parameter	Estimate	Standard Error	T Value	Prob. Level
Intercept	38.9737	6.88526	5.66046	.00480
Slope	-0.413287	0.0805133	-5.13315	.00682

Analysis of Variance

Source	Sum of Squares	Df	Mean Square	F-Ratio	Prob. Level
Model	2.989101	1	2.989101	26.34922	.00682
Error	.4537670	4	.1134418		
Total (Corr.)	3.4428682	5			

Correlation Coefficient = -0.931773
 Stnd. Error of Est. = 0.336811

R-squared = 86.82 percent



Regression Analysis - Exponential model: $Y = \exp(a+bX)$

Dependent variable: 3.114 2.2049 1.0454 Independent variable: 81 82 83 84 85 86

Parameter	Estimate	Standard Error	T Value	Prob. Level
Intercept	37.4537	5.74436	6.52008	.00062
Slope	-0.44566	0.0679556	-6.5581	.00060

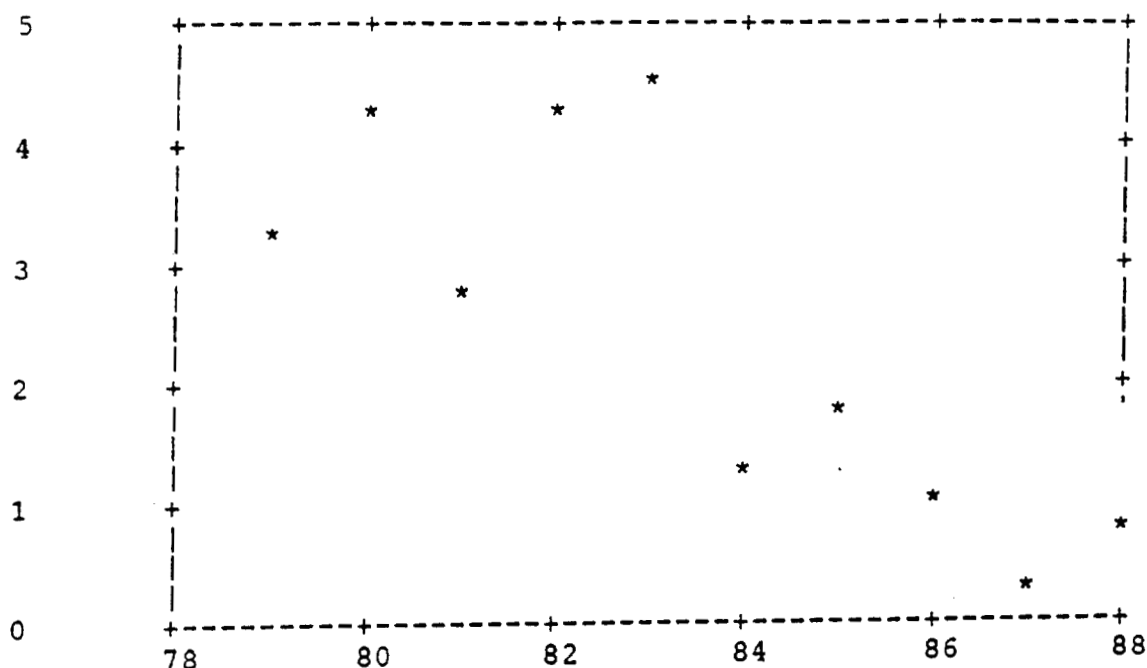
Analysis of Variance

Source	Sum of Squares	Df	Mean Square	F-Ratio	Prob. Level
Model	8.341733	1	8.341733	43.00874	.00060
Error	1.1637263	6	.1939544		
Total (Corr.)	9.5054592	7			

Correlation Coefficient = -0.936789
Std. Error of Est. = 0.440403

R-squared = 87.76 percent

fuel preburner injector:dent/crack



Regression Analysis - Exponential model: $Y = \exp(a+bX)$

Dependent variable: 4.134282 4.53009 1.2 Independent variable: 82 83 84 85 86 87

Parameter	Estimate	Standard Error	T Value	Prob. Level
Intercept	35.4645	9.73999	3.64112	.01489
Slope	-0.41411	0.114556	-3.6149	.01530

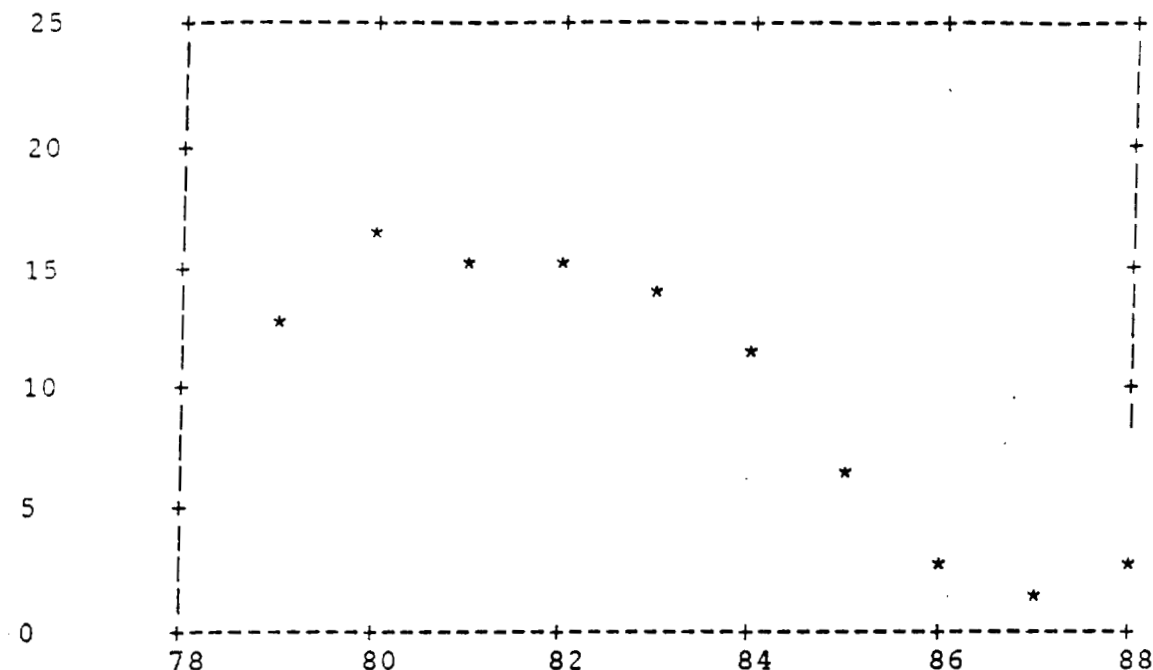
Analysis of Variance

Source	Sum of Squares	Df	Mean Square	F-Ratio	Prob. Level
Model	4.801630	1	4.801630	13.06749	.01530
Error	1.8372425	5	.3674485		
Total (Corr.)	6.6388723	6			

Correlation Coefficient = -0.850447
Std. Error of Est. = 0.606175

R-squared = 72.33 percent

fuel preburner subsystem



Regression Analysis - Exponential model: $Y = \exp(a+bX)$

Dependent variable: 15.43465 13.2418 11. Independent variable: 82 83 84 85 86 87

Parameter	Estimate	Standard Error	T Value	Prob. Level
Intercept	42.9973	9.20094	4.67314	.00547
Slope	-0.487541	0.108216	-4.50524	.00637

Analysis of Variance

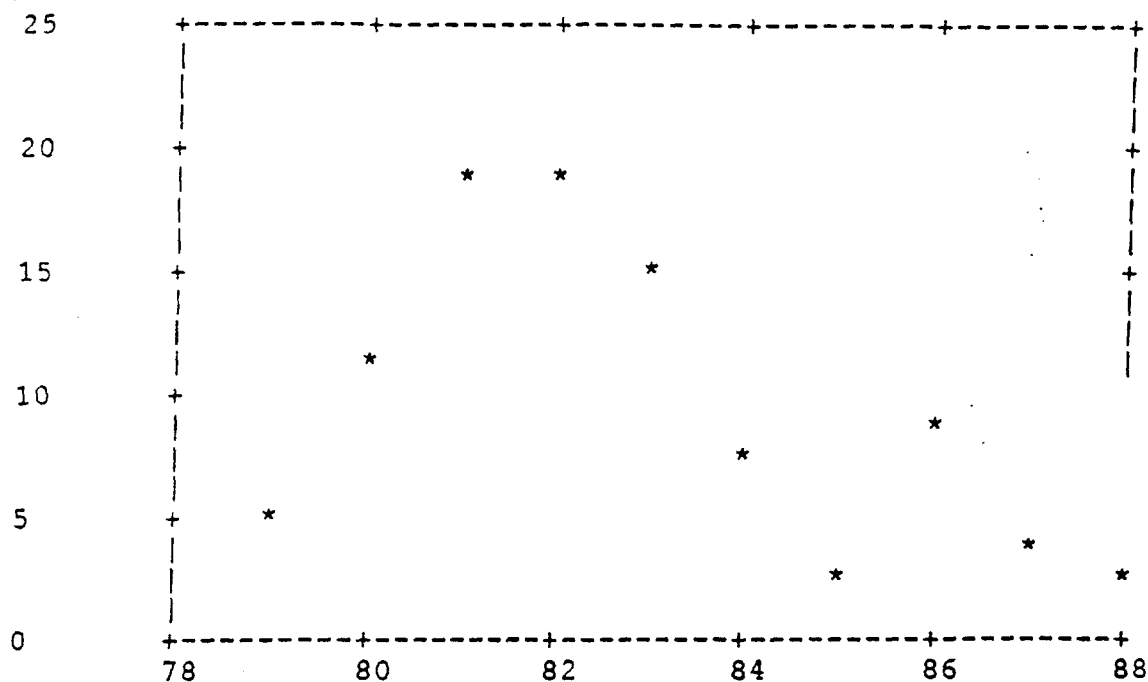
Source	Sum of Squares	Df	Mean Square	F-Ratio	Prob. Level
Model	6.655493	1	6.655493	20.29720	.00637
Error	1.6395101	5	.3279020		
Total (Corr.)	8.2950031	6			

Correlation Coefficient = -0.89574
Std. Error of Est. = 0.572627

R-squared = 80.23 percent

ORIGINAL PAGE IS
OF POOR QUALITY

main injector subsystem



Regression Analysis - Exponential model: $Y = \exp(a+bX)$

Dependent variable: 18.74208 15.33261 7. Independent variable: 82 83 84 85 86 87

Parameter	Estimate	Standard Error	T Value	Prob. Level
Intercept	30.6808	8.45004	3.63085	.01505
Slope	-0.33945	0.0993847	-3.41551	.01893

Analysis of Variance

Source	Sum of Squares	Df	Mean Square	F-Ratio	Prob. Level
Model	3.226328	1	3.226328	11.66572	.01893
Error	1.3828243	5	.2765649		
Total (Corr.)	4.6091525	6			

Correlation Coefficient = -0.83665
Std. Error of Est. = 0.525894

R-squared = 70.00 percent

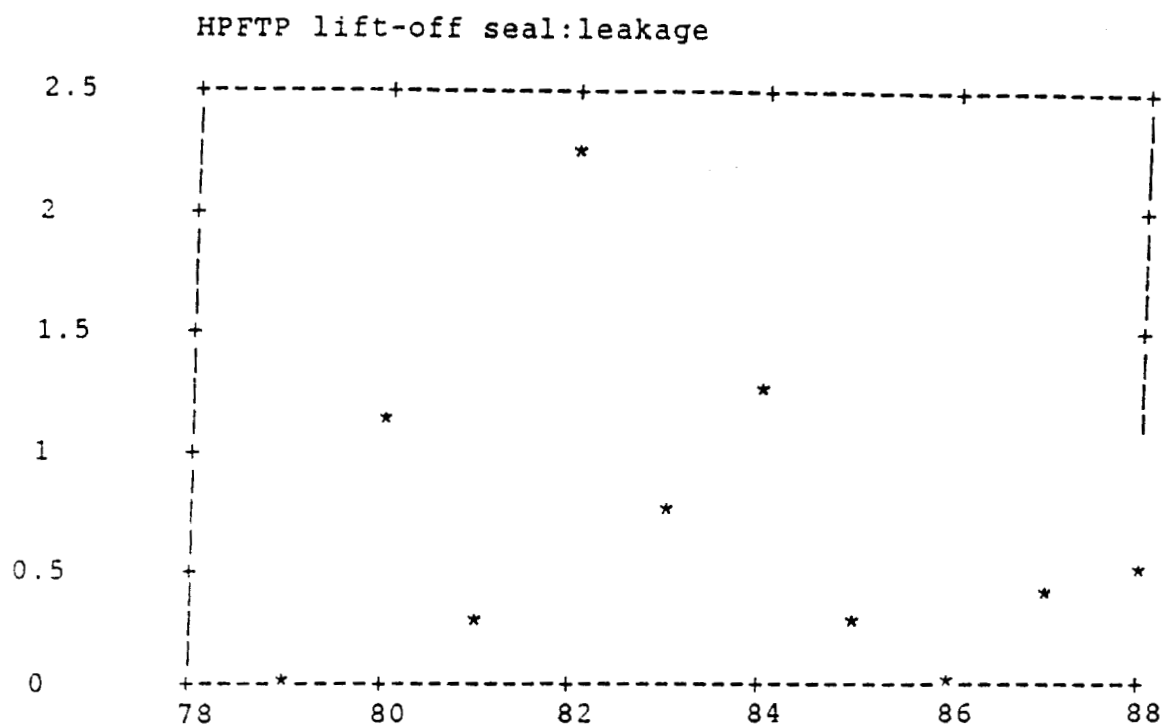
Power Model

This model is also intrinsically linear and uses the logarithmic transformation just as the exponential model. It differs in that this model uses the logarithm of both the independent and dependent variables. The regression will be for the natural logarithm of Y on the natural logarithm of time. The deterministic portion of the model is:

$$Y = \beta_0 t^{\beta_1}.$$

As with the exponential model, a positive (downward) trend is claimed if $\beta_1 < 0$. Since the logarithmic transformation is used, the same modification in the presence of no problem reports in a time period as that used with the exponential is appropriate.

The mechanics of application are the same as with the exponential model. In the two examples below, there is some evidence of an increasing pattern followed by a decreasing trend. For the example of leakage of the HPFTP lift-off seal an adverse pattern exists from 1979 to 1983. A power (or multiplicative) model is then fit from 1982 to 1988. The coefficient of determination is .48 and, consequently, the test of hypothesis does not conclude a positive trend. Visual inspection of the scatter plot causes some concern by noticing the increase from 1986 to 1988. However, the normalized values are quite small, so there would be a good deal of (engineering) judgement in the interpretation. The second example, the main oxidizer valve subsystem, shows an erratic pattern from 1979 to 1983 and then a decreasing pattern through 1988. There is an excellent fit for the decreasing portion of the data with strong indication of a significant downward trend (p-value less than .01).



Regression Analysis - Multiplicative model: $Y = aX^b$

Dependent variable: 2.2049 .6969 1.2617 Independent variable: 82 83 84 85 86 87

Parameter	Estimate	Standard Error	T Value	Prob. Level
Intercept*	87.6083	40.941	2.13986	.08533
Slope	-19.8174	9.2159	-2.15035	.08421

* NOTE: The Intercept is equal to Log a.

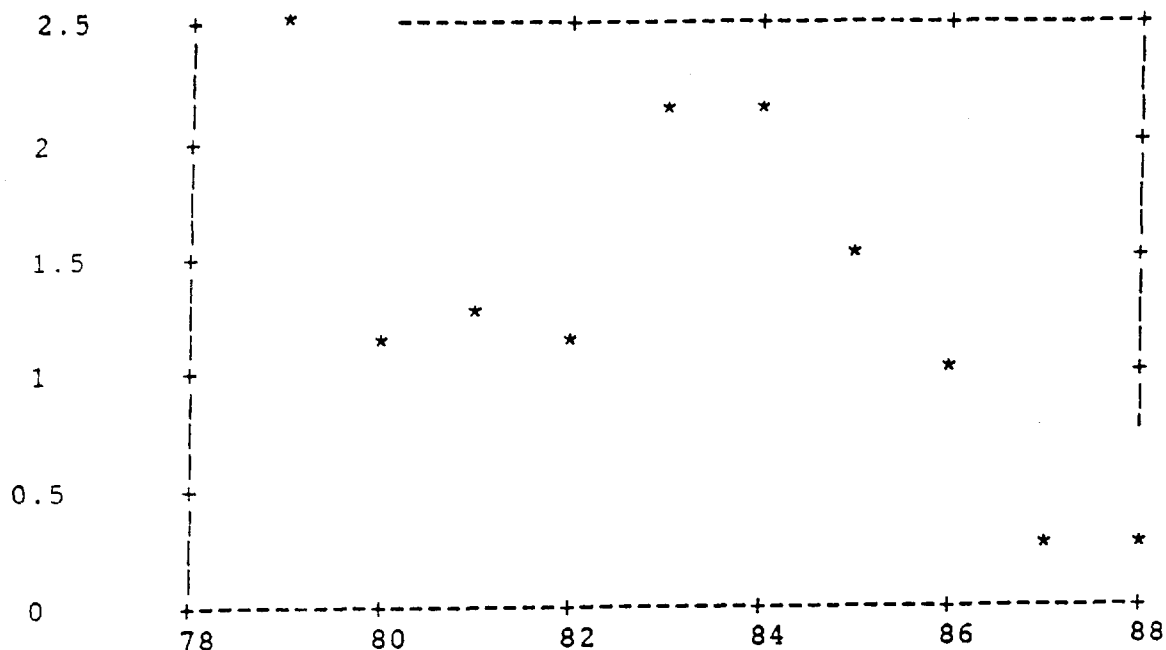
Analysis of Variance

Source	Sum of Squares	Df	Mean Square	F-Ratio	Prob. Level
Model	1.5231355	1	1.5231355	4.623994	.08421
Error	1.6469911	5	.3293982		
Total (Corr.)	3.1701266	6			

Correlation Coefficient = -0.693156
 Std. Error of Est. = 0.573932

R-squared = 48.05 percent

main oxidizer valve subsystem



Regression Analysis - Multiplicative model: $Y = aX^b$

Dependent variable: 2.0908 2.1028 1.5114 Independent variable: 83 84 85 86 87 88

Parameter	Estimate	Standard Error	T Value	Prob. Level
Intercept*	196.247	40.9927	4.78737	.00873
Slope	-44.1576	9.21523	-4.79181	.00870

* NOTE: The Intercept is equal to Log a.

Analysis of Variance

Source	Sum of Squares	Df	Mean Square	F-Ratio	Prob. Level
Model	4.670341	1	4.670341	22.96140	.00870
Error	.8135986	4	.2033996		
Total (Corr.)	5.4839396	5			

Correlation Coefficient = -0.922843
Std. Error of Est. = 0.450999

R-squared = 85.16 percent

Reciprocal Model

The reciprocal model is another model with the feature that will not generate a fitted value below zero since the problem data is non-negative. It can be made linear with a simple reciprocal transformation. The deterministic portion of the model is:

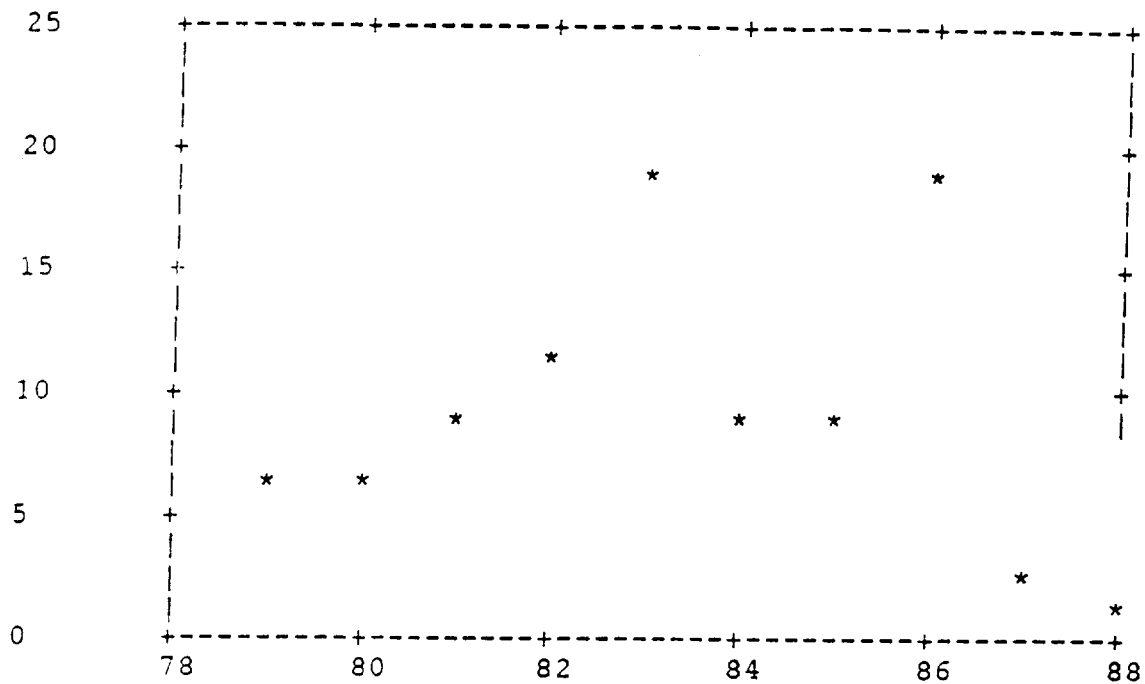
$$Y = \frac{1}{\beta_0 + \beta_1 t}$$

The application if this model regresses $1/Y$ on t . In contrast to the above two models, a positive (downward) trend is indicated if $\beta_1 > 0$. This model is not applicable if there are zero problem reports in a given time period.

The two examples below employ a reciprocal model. The data for the SSME combustion chamber subsystem shows again an adverse pattern followed by a positive one. There is an increasing trend from 1979 to 1983. A reciprocal model fit to the data beginning in 1983 gives marginal statistical evidence of a positive trend. The extreme value in 1986 has substantial influence on the goodness of the fit. Removing this observation and fitting again a reciprocal model beginning in 1983 the coefficient of determination, r^2 , increases from .68 to .87. An extreme observation (or outlier) can dramatically effect the quality of the fitted model.

The second example, the nozzle assembly subsystem, has a pattern that appears decreasing from 1979 to 1988 with two outlying observations. There is no adverse trend in the early years. Fitting a reciprocal model beginning in 1979 yields statistical evidence of a positive (downward) trend. The p-value is less than .01. Deleting the 1983 and 1984 observations, the coefficient of determination, r^2 , goes from .71 to .84 for the reciprocal model. Also given below is a regression summary of an exponential model fit to the data beginning in 1983.

main combustion chamber subsystem



Regression Analysis - Reciprocal model: $1/Y = a + bX$

Dependent variable: 13.46883 8.831693 8. Independent variable: 83 84 85 86 87 88

Parameter	Estimate	Standard Error	T Value	Prob. Level
Intercept	-9.51288	3.35553	-2.83499	.04711
Slope	0.114038	0.0392381	2.90631	.04384

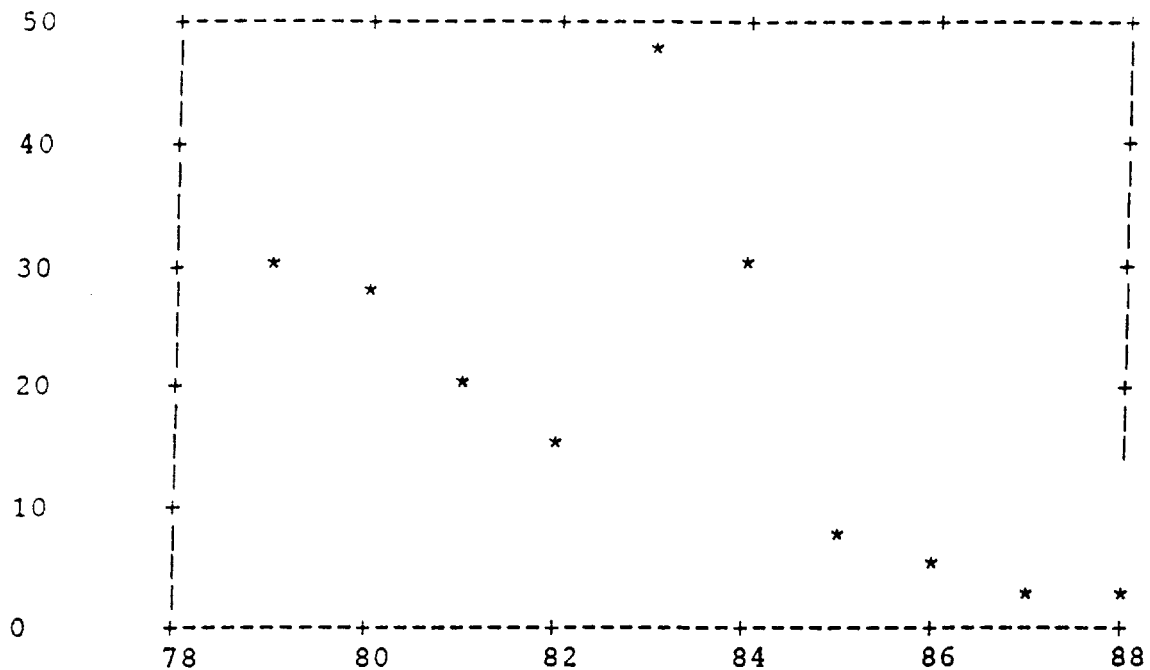
Analysis of Variance

Source	Sum of Squares	Df	Mean Square	F-Ratio	Prob. Level
Model	.2275812	1	.2275812	8.446613	.04384
Error	.1077739	4	.0269435		
Total (Corr.)	.3353551	5			

Correlation Coefficient = 0.823788
Std. Error of Est. = 0.164145

R-squared = 67.86 percent

Comment: nozzle assembly subsystem



Regression Analysis - Reciprocal model: $1/Y = a + bX$

Dependent variable: 28.98 28.35 19.62 15 Independent variable: 79 80 81 82 83 84

Parameter	Estimate	Standard Error	T Value	Prob. Level
Intercept	-2.92075	0.692515	-4.2176	.00293
Slope	0.0364916	8.28869E-3	4.40258	.00228

Analysis of Variance

Source	Sum of Squares	Df	Mean Square	F-Ratio	Prob. Level
Model	.109860	1	.109860	19.38268	.00228
Error	.0453435	8	.0056679		
Total (Corr.)	.1552035	9			

Correlation Coefficient = 0.841335
Std. Error of Est. = 0.0752857

R-squared = 70.78 percent

Regression Analysis - Exponential model: $Y = \exp(a + bX)$

Dependent variable: 46.69478 30.70065 7. Independent variable: 83 84 85 86 87 88

Parameter	Estimate	Standard Error	T Value	Prob. Level
Intercept	54.7792	7.47381	7.32949	.00184
Slope	-0.615199	0.0873955	-7.03925	.00215

Analysis of Variance

Source	Sum of Squares	Df	Mean Square	F-Ratio	Prob. Level
Model	6.623225	1	6.623225	49.55105	.00215
Error	.5346587	4	.1336647		
Total (Corr.)	7.1578840	5			

Correlation Coefficient = -0.961928
Std. Error of Est. = 0.365602

R-squared = 92.53 percent

Straight Line Model

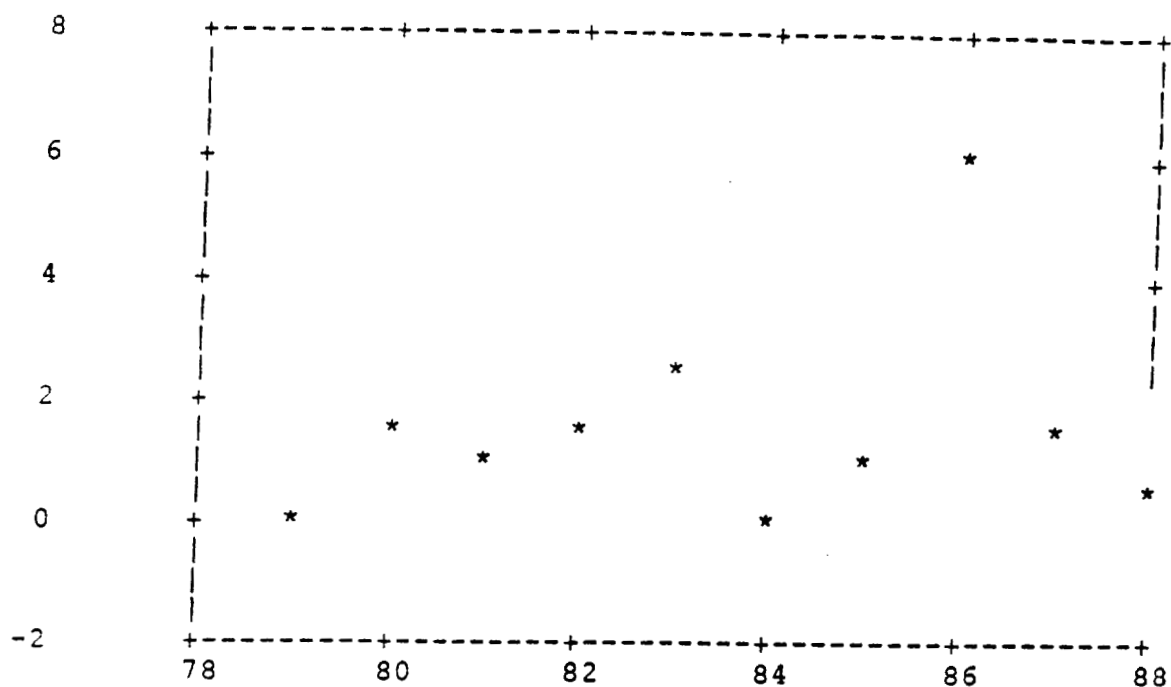
The straight line model, even though simple, can be useful and informative in a couple of situations. In instances of an increasing trend the straight line model is effective in providing statistical support. For example, a straight line model applied to the early years data (1979-1983) of the heat exchanger subsystem indicates a significant increasing trend. The scatter plot for intermittent sparking in the igniters subsystem also shows a hint of an adverse pattern for 1979 to 1982. Refer to the scatter plots and regression summaries below to observe this. Again we see that curious pattern of increasing measurements through the first few years.

A second situation arises when the data appear to be random, but, the level of the data is close to zero. A straight line fit with both slope and intercept zero could then be viewed as desirable. The regression summary contains calculations for the test of hypothesis that the intercept is zero, as well as doing so for the slope. So, when the data are close to zero, a random scattering might indicate a positive situation. A great deal of engineering assessment and judgement is required.

Referring back to the intermittent sparking in the igniters subsystem, the regression summary is for a straight line fit from 1983 to 1988. Note that the r^2 value is very low, .035, indicating a random pattern. The test of hypotheses that both the slope and intercept are zero would be accepted. This is seen with a large p-value for both tests. The two scatter plots following the igniters subsystem data summary have the appearance of a random scattering of the data. The regression summaries for a straight line fit beginning in 1979 for both the oxidizer preburner erosion data and the combustion subsystem leakage data had a slope and intercept that were not measurably different from zero.

A data summary for a broken main fuel valve is also given. This data set indicates a possible decreasing trend or at least, if the first one or two observations are deleted, a flat line through the remaining data. Note again that the straight line model for the data from 1981 to 1988 would conclude no measurable deviation from zero for both the slope and intercept. An exponential model fit to the full range of the data points to marginal acceptance of a positive trend, as seen in the corresponding regression summary.

heat exchanger subsystem



Regression Analysis - Linear model: $Y = a + bX$

Dependent variable: .21 1.405811 .934201 Independent variable: 79 80 81 82 83

Parameter	Estimate	Standard Error	T Value	Prob. Level
Intercept	-36.7937	10.8388	-3.39463	.04263
Slope	0.470646	0.133792	3.51775	.03898

Analysis of Variance

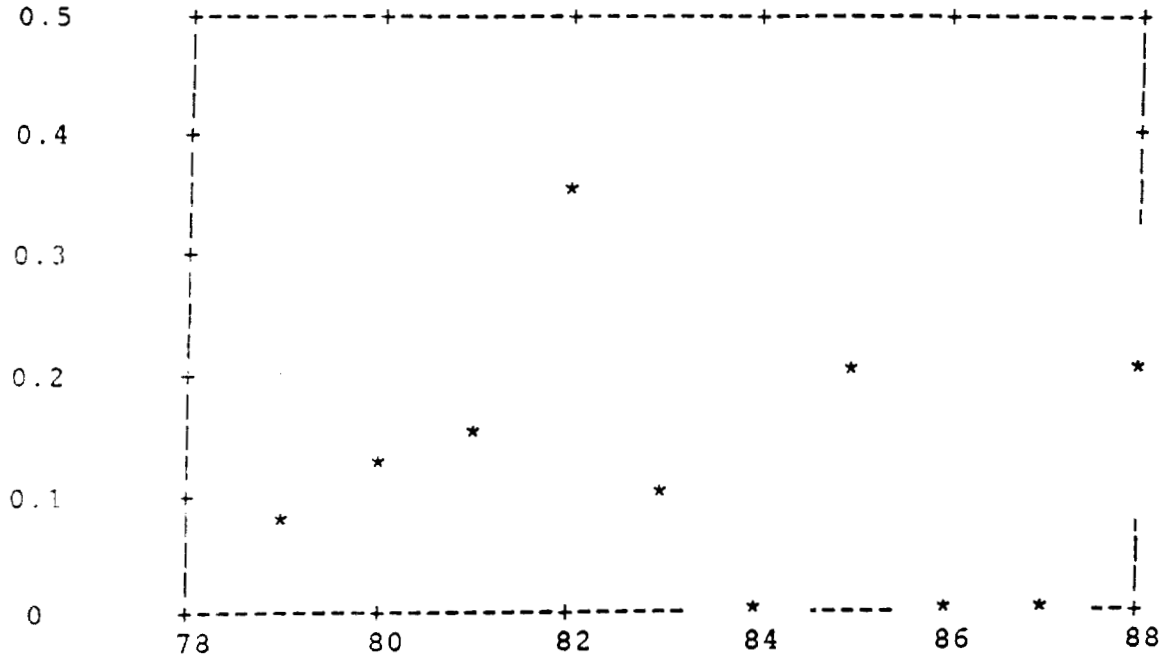
Source	Sum of Squares	Df	Mean Square	F-Ratio	Prob. Level
Model	2.215077	1	2.215077	12.37455	.03898
Error	.5370077	3	.1790026		
Total (Corr.)	2.7520843	4			

Correlation Coefficient = 0.897147

R-squared = 80.49 percent

Std. Error of Est. = 0.423087

igniters subsystem:intermittent sparking RTV voids



Regression Analysis - Linear model: $Y = a + bX$

Dependent variable: .09 0 .189 0 0 .194 Independent variable: 83 84 85 86 87 88

Parameter	Estimate	Standard Error	T Value	Prob. Level
Intercept	-0.729752	2.10973	-0.345898	.74685
Slope	9.45714E-3	0.0246703	0.383341	.72097

Analysis of Variance

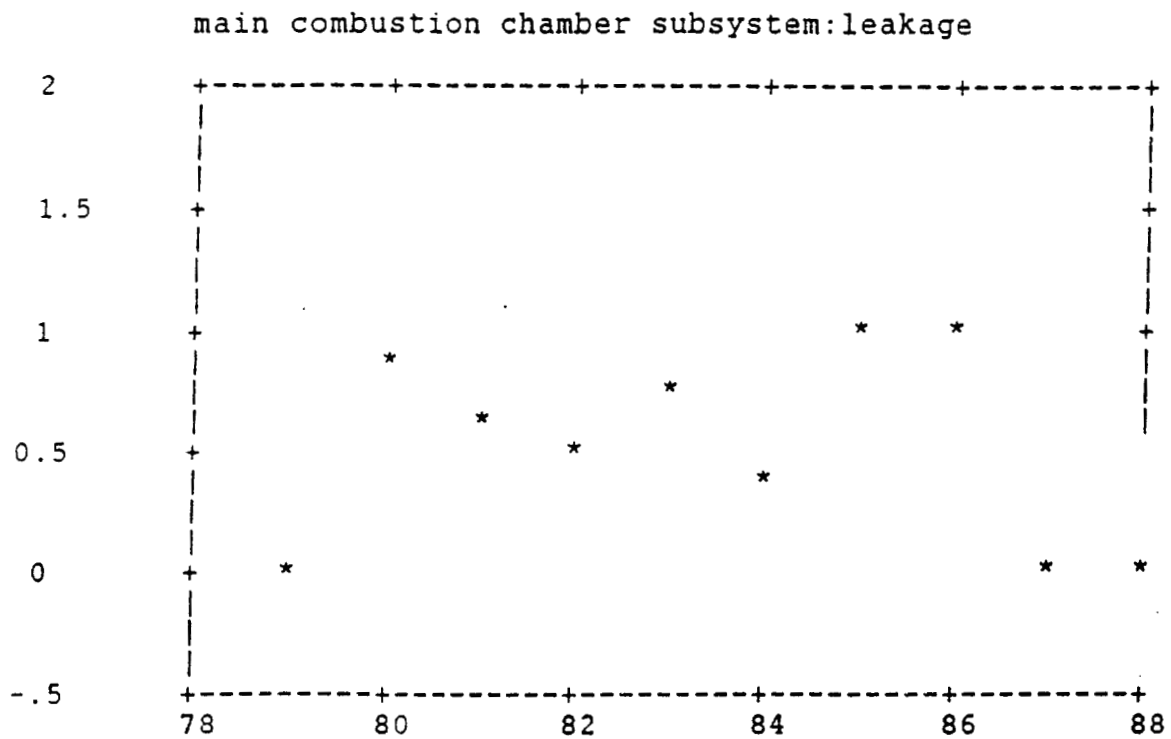
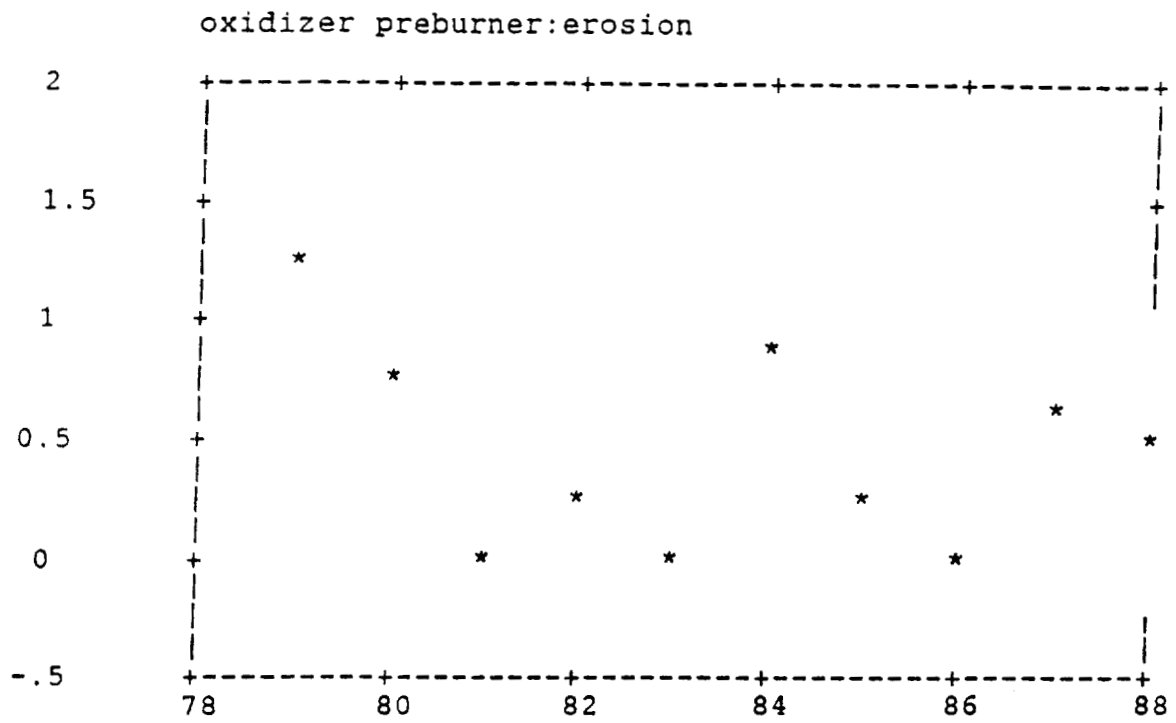
Source	Sum of Squares	Df	Mean Square	F-Ratio	Prob. Level
Model	.0015652	1	.0015652	.146950	.72097
Error	.0426037	4	.0106509		

Total (Corr.) .0441688 5

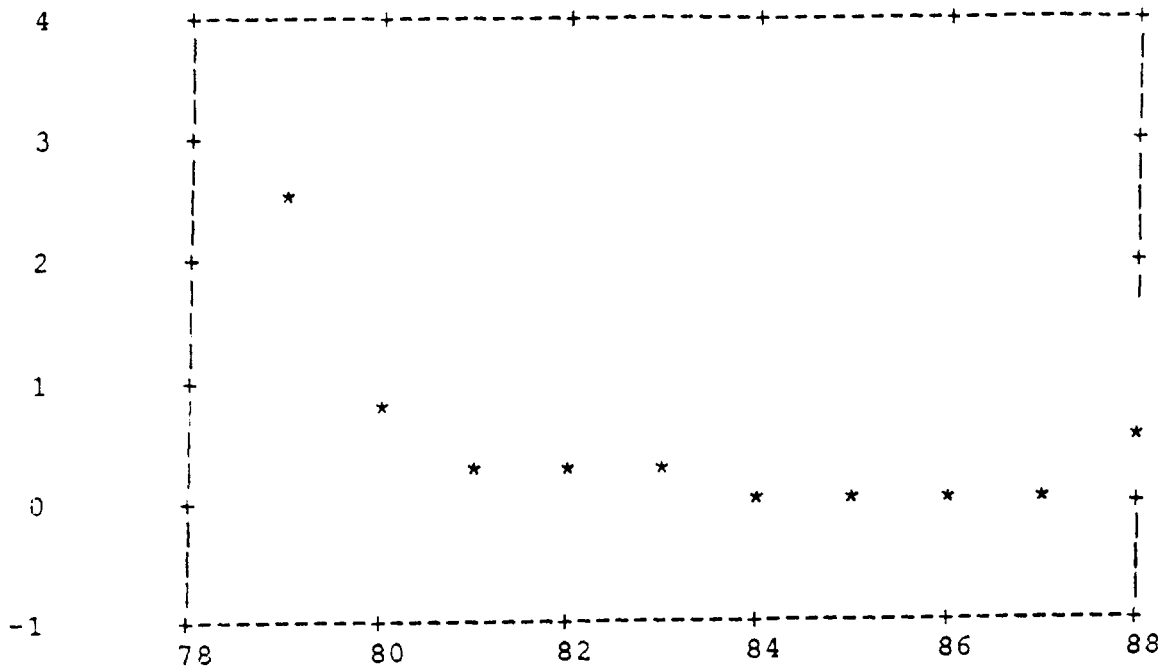
Correlation Coefficient = 0.188244
Std. Error of Est. = 0.103203

R-squared = 3.54 percent

ORIGINAL PAGE IS
OF POOR QUALITY



main fuel valve subsystem:broken



Regression Analysis - Linear model: $Y = a + bX$

Dependent variable: .3114 .2756 .3485 0 Independent variable: 81 82 83 84 85 86

Parameter	Estimate	Standard Error	T Value	Prob. Level
Intercept	1.4636	2.72275	0.537547	.61023
Slope	-0.0152345	0.03221	-0.472974	.65295

Analysis of Variance

Source	Sum of Squares	Df	Mean Square	F-Ratio	Prob. Level
Model	.0097478	1	.0097478	.223705	.65295
Error	.2614465	6	.0435744		
Total (Corr.)	.2711943	7			

Correlation Coefficient = -0.189589
Std. Error of Est. = 0.208745

R-squared = 3.59 percent

Regression Analysis - Exponential model: $Y = \exp(a + bX)$

Dependent variable: 2.52 .7 .31 .28 .35 Independent variable: 79 80 81 82 83 84

Parameter	Estimate	Standard Error	T Value	Prob. Level
Intercept	13.3621	7.11328	1.87847	.09713
Slope	-0.172212	0.0851386	-2.02272	.07773

Analysis of Variance

Source	Sum of Squares	Df	Mean Square	F-Ratio	Prob. Level
Model	2.4466945	1	2.4466945	4.091409	.07773
Error	4.7840627	8	.5980078		
Total (Corr.)	7.2307572	9			

Correlation Coefficient = -0.581699
Std. Error of Est. = 0.77331

R-squared = 33.84 percent

Kendall's τ

Kendall's rank correlation coefficient is a most efficient distribution free or nonparametric measure to test for linear trend. In applying Kendall's τ we will be testing a series of data for randomness, the null hypothesis, against a decreasing trend, the alternative hypothesis. Application of this procedure involves comparing the values of the time series in terms of larger or smaller. Whereas a parametric procedure, like regression, uses the recorded values in computations, the nonparametric approach only notes greater than or less than from the observed values and, hence, is not influenced by extreme values.

Given a series y_1, y_2, \dots, y_n , let us count the number of cases in which $y_j > y_i$ for $j > i$. Call this number P . There are $n(n-1)/2$ pairs for comparison. The expected number in a random series is $n(n-1)/4$. The excess of P over this number, if significant, suggests a rising trend; a deficiency suggests a falling trend. The rank correlation coefficient, known as Kendall's τ , is then:

$$\tau = \frac{4P}{n(n-1)} - 1.$$

This coefficient may vary from -1 to $+1$. Its expected value in a random series is zero, and its variance is given by:

$$\text{var } \tau = \frac{2(2n+5)}{9n(n-1)}.$$

In working with the normalized problem data there can be one or more values in the series that equal zero. The only possible occurrence of equal values are at zero. The above results for the calculation of τ and for the variance are based on no tied values in the data. However, it is appropriate to use these computations if we regard successive zero values as a continuing positive trend. There are adjustments to the variance computation for tied values; but, with our only possible tied values at zero, we will count successive zero values in favor of a positive (downward) trend. So, the value for P will be tabulated as described in the above paragraph where n is the number of values in the series. We will not disregard multiple values of zero, but regard them as desirable.

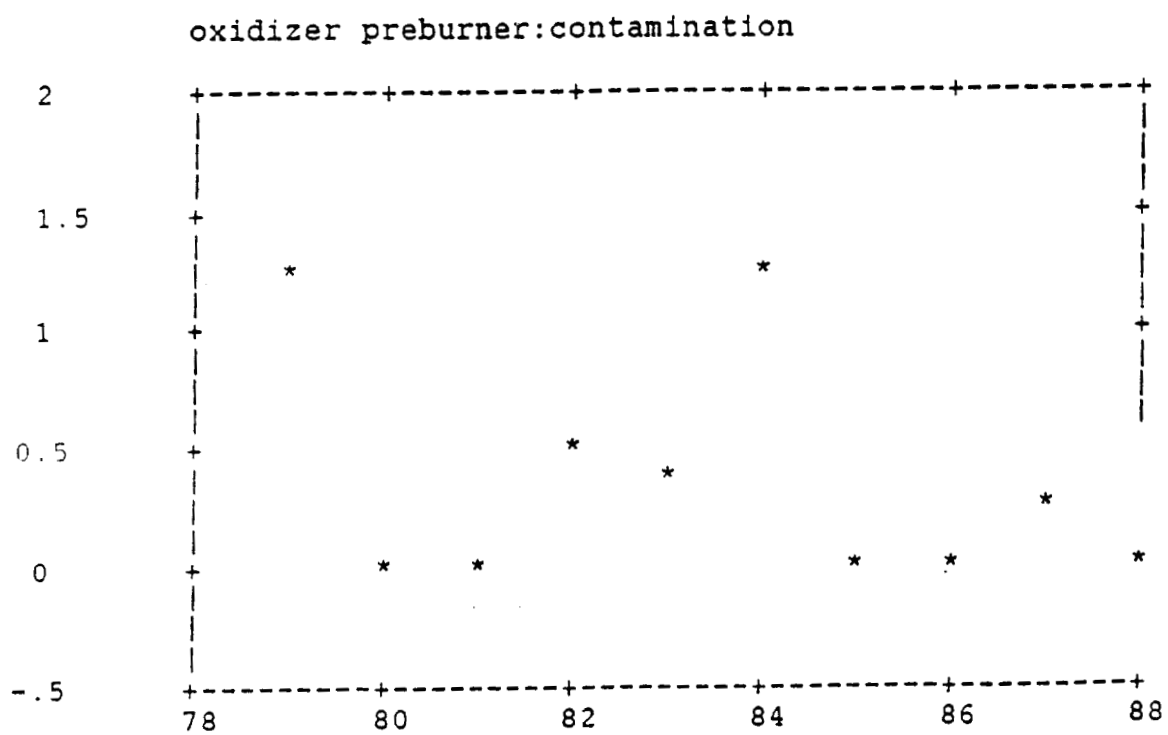
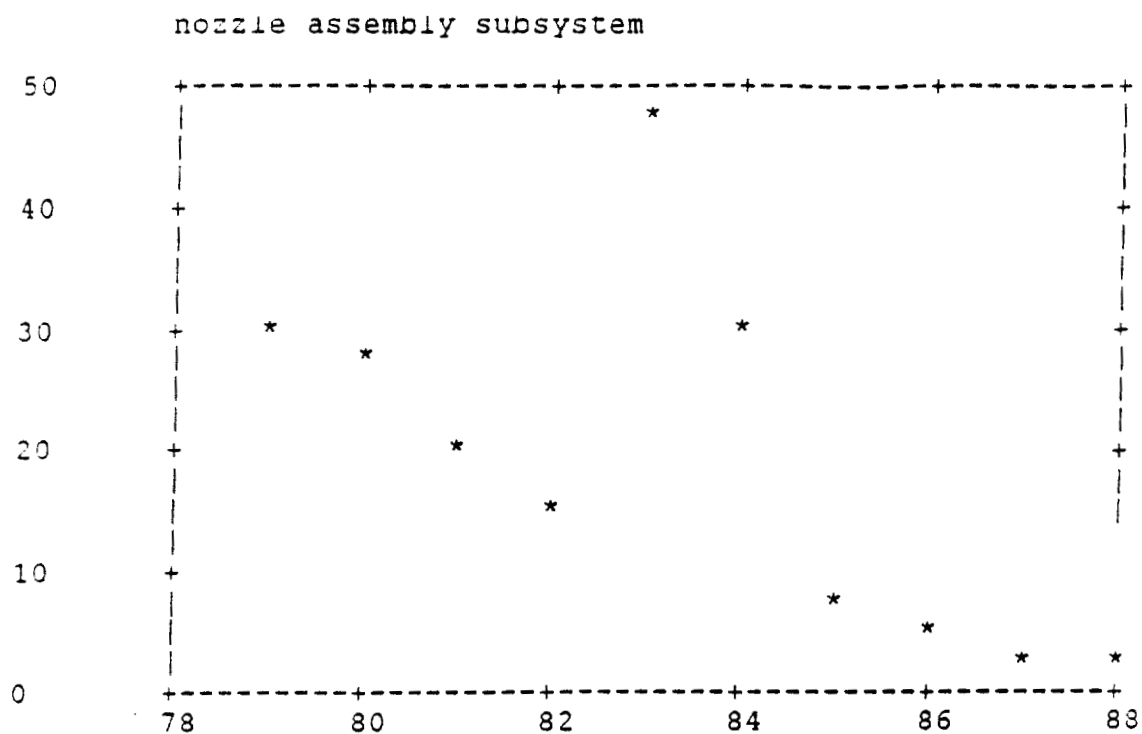
The distribution of τ tends rapidly to normality. Hence, the test statistic under the hypothesis of randomness will be a standard normal variable. If n is less than 10, the calculation of τ will use $4(P+1)$ instead of $4P$. This is a

continuity correction factor used when testing randomness versus decreasing trend. The calculated statistic will then be:

$$Z = \frac{\tau}{\sqrt{\text{var } \tau}}$$

where Z represents a standard normal variable. If this value is less than -2.33 that will be evidence of a decreasing trend. This is a significance level of .01.

Let's apply this procedure to the nozzle subsystem data and to the oxidizer preburner contamination data. The scatter plots are seen below. For the nozzle subsystem, which was previously modeled with a reciprocal model, the calculated value for τ is -.644, and the calculated value for the Z statistic is -2.59. This corresponds to our previous analysis which concluded a significant downward trend. The p-value for this test is less than .01. The scatter plot for the oxidizer preburner contamination reveals more of a random scattering than decreasing pattern. Note that there are five zero values. Successive zero values are regarded as positive (downward) in our application of Kendall's τ . The calculated value of τ is -.422 and the calculated Z is -1.70, not evidence enough of a positive trend. If you cover up the 1984 observation, there is some hint of a trend. Kendall's τ is one of the, if not the, most efficient distribution free approaches for detecting trend.



REMARKS

The foregoing examples are enough to show that trend fitting and trend estimation are very far from being a purely mechanical process which can be handed over regardless to an electronic computer. There is great scope, even a necessity, for personal judgement. To a scientist it is felt as a departure from correctness to incorporate subjective elements into his work. The student of time series cannot be a purist in that sense. What he can do, of course, is to make available the data on which he worked and explain unambiguously how he has treated them.

There are other approaches and considerations, such as increasing the sample sizes with semiannual or quarterly problem reports and time to failure patterns, that could be investigated. It is possible that some experimental design ideas could be used to identify significant factors in problem reporting. Further exploration of the data bases for problem reporting to address these and other issues seems to be the next step in developing trending approaches.

REFERENCES

1. Kendall, M. G., Rank Correlation Methods, 4th Edition, Charles Griffin & Company Ltd. (1975) London
2. Neter, J., Wasserman, W., Kutner, M. H., Applied Linear Statistical Models, Second Edition, Richard D. Irwin Inc. (1985) Homewood, Ill.
3. NSTS Problem Trending Special Study C43a-3, Calspan Corp., June 30, 1989

APPENDIX

The logarithmic transformation used with the exponential and power models needs modification because it is undefined at zero. If R denotes the number of problem reports in a given time period and m denotes the number of seconds of engine firing, one plausible way of modifying the transformation is to define a transform as

$$\ln\left(\frac{R+a}{m} \times 10^4\right)$$

We would then choose the constant a so that the expected value of the above quantity is as nearly as possible $\ln(\theta \times 10^4)$ where θ denotes the true fraction of problems per second.

Write $R = m\theta + Z\sqrt{m}$, where

$$E(Z) = 0, \quad E(Z^2) = \theta(1-\theta),$$

E is the expected value operator and Z is of order one in probability as $m \rightarrow \infty$. Then

$$\begin{aligned} E\left\{\ln\left(\frac{R+a}{m} \times 10^4\right)\right\} - \ln(\theta \times 10^4) &= \ln\left\{1 + \frac{(Z\sqrt{m} + a)^2}{2m^2\theta^2}\right\} \\ &\doteq \frac{a - \frac{1}{2}(1-\theta)}{m\theta} \end{aligned}$$

where we have neglected terms of smaller order than $1/m$ in probability. As $\theta \rightarrow 0$ and $m \rightarrow \infty$ in such a way that $m\theta$ remains constant the above quantity is zero as a approaches $1/2$.

1989

NASA/ASEE SUMMER FACULTY RESEARCH FELLOWSHIP PROGRAM

**MARSHALL SPACE FLIGHT CENTER
UNIVERSITY OF ALABAMA IN HUNTSVILLE**

**A PARAMETRIC HEAT TRANSFER STUDY FOR
CROGENIC BALL BEARINGS IN SSME HPOTP**

Prepared by

Mingking K. Chyu

Academic Rank:

Assistant Professor

University and Department

Carnegie Mellon University
Department of
Mechanical Engineering

NASA/MSFC:

Laboratory:

Division:

Branch:

Propulsion
Component Development
Turbomachinery and
Combustion Devices, EP62

MSFC Colleague:

James L. Cannon
George M. Young, III

Date:

August 1989

Contract No.:

The University of Alabama
in Huntsville
NGT-01-008-021

A PARAMETRIC HEAT TRANSFER STUDY FOR CROGENIC BALL BEARINGS IN SSME HPOTP

Mingking.K. Chyu
Department of Mechanical Engineering
Carnegie Mellon University
Pittsburgh, PA 15213

James L. Cannon and George M. Young III
Propulsion Laboratory
NASA Marshall Space Flight Center
Huntsville, AL 35812

ABSTRACT

A numerical modeling is to examine the effects of coolant convective heat transfer coefficient and frictional heating on the local temperature characteristics of a ball element in SSME HPOTP bearing. The present modeling uses a control-volume based, finite-difference method to solve the non-dimensionalized heat conduction equation in spherical coordinate system. The dimensionless temperature is found as a function of Biot number, heat flux ratio between the two race contacts, and location in the ball. The current results show that, for a given cooling capability, the ball temperature generally increases almost linearly with the heat input from the race-contacts. This increase is always very high at one of the two contacts. An increase in heat transfer coefficient generally reduces the ball temperature and alleviates the temperature gradient, except for the regions very close to the race contacts. For a 10-fold increase of heat transfer coefficient, temperature decrease is 35% for the average over entire ball, and 10% at the inner-race contact. The corresponding change of temperature gradient displays opposing trends between the regions immediately adjacent to the contacts and the remaining portion of the ball. The average temperature gradient over the entire ball decreases about 50%. On the contrary, the temperature gradient in the vicinity of both contacts increases approximately 70% to 100%. A higher temperature gradient produces excessive thermal stress locally which may be detrimental to the material integrity. This, however, is the only unfavorable issue for an increase of heat transfer coefficient.

ACKNOWLEDGEMENTS

The first author (MKC) of this report is grateful to NASA-Marshall Space Flight Center and ASEE for the appointment of Summer Faculty Research Fellowship. In addition, he expresses special appreciation to Messrs. James L. Cannon and George M. Young III for their collaboration in this project.

Thanks to Ms. Joan G. Trolinger for her help in collecting references, Mr. Craig Gilden for his assistance in preparing presentation material and Mr. Loren A. Gross for his enthusiastic interest in this project.

For Professor Gerald R. Karr and Dr. Frank Six, their excellent management of the entire program is highly appreciated.

LIST OF FIGURES

- Figure 1. Heat Transfer Coefficient of Pool Boiling Oxygen
- Figure 2. Rolling Ball Schematic
- Figure 3. Spherical Coordinate System
- Figure 4. Ball Temperature Distribution, $Bi = 1$, $Q_{ir} = 1.2$
- Figure 5. Ball Temperature Distribution, $Bi = 1$, $Q_{ir} = 2.0$
- Figure 6. Ball Temperature Distribution, $Bi = 1$, $Q_{ir} = 7.5$
- Figure 7. Ball Temperature Distribution, $Bi = 10$, $Q_{ir} = 1.2$
- Figure 8. Ball Temperature Distribution, $Bi = 10$, $Q_{ir} = 2.0$
- Figure 9. Ball Temperature Distribution, $Bi = 10$, $Q_{ir} = 7.5$
- Figure 10. Effect of q_{or} on Ball Temperature Variation, $Bi = 10$, $Q_{ir} = 1.2$
- Figure 11. Effect of q_{or} on Ball Temperature Variation, $Bi = 1$, $Q_{ir} = 7.5$
- Figure 12. Thermal Coupling of Bearing Elements

NOMENCLATURE

Bi	Biot number
h	heat transfer coefficient
k	thermal conductivity of bearing ball
Q_{ir} , Q_{IR}	ratio of heat flux at inner-race contact to that at outer-race contact
q_{or} , Q_{OR}	heat flux at outer-race contact
q	heat flux
R	dimensionless radial coordinate, see Equation (5)
r	radial coordinate
T	temperature
T.05	temperature corresponding to dimensionless temperature equal to 0.05
T.AVG	mean temperature averaged over entire ball
T.CENTER	temperature at ball center
T.INLET	temperature of LOx bulk temperature, -240 F in present study
T.IR	temperature at inner-race contact
T.OR	temperature at out-race contact
θ	azimuthal angle in spherical coordinate system, see Figure 3
ϕ	yaw angle in spherical coordinate system, see Figure 3
Θ	dimensionless temperature, see Equation (7)

Subscript

ir	contact of inner race
o	sphere outer surface
or	contact outer race
f	coolant fluid

INTRODUCTION AND RESEARCH OBJECTIVES

The reliability and service life of the ball bearings in the High-Pressure Oxidizer Turbo Pump (HPOTP) has become one of the most, if not the most, critical issues concerning the safety and future development of the Space Shuttle Main Engine (SSME). These bearings are operated under severe loading conditions with very high rotational speeds. Liquid Oxygen (LOx), the primary fluid media in HPOTP, is directed to flow through the bearings to provide cooling and lubrication. LOx with its cryogenic feature is an effective coolant but has poor lubrication capability. The present data has indicated that the actual bearing life is about one order of magnitude lower than that as designed for seven and one-half hours. This service-life is directly limited by fatigue and wear on the bearing components. Bearing removed from the pump has often shown discoloration which is evidently caused by intense surface oxidation and over-heating. The excessive heating is largely frictional and implies the current level of cooling and lubrication is apparently insufficient.

Significant endeavor on improving bearing service life and reliability has been pursued by NASA since early 1980's [1]. These include both testing and numerical modeling of the problem. At NASA Marshall Space Flight Center (MSFC), Bearing and Seal Material Tester (BSMT) was installed, with which near-engine, actual scale bearing testings can be performed. Data collected from BSMT provides basis for experimental investigation and modeling verification [2]. The modeling effort is primarily focused on the development of analytical tools for prediction of bearing behavior, in both mechanical and thermal aspects. There are two different approaches in present-day shuttle bearing modeling. One, using the SHABERTH/CINDA computer code, performs a lumped analysis with mechanical and thermal coupling [3]. The other employs computational fluid dynamics (CFD) which solves the transport equations numerically [4]. The CFD approach generally does not include mechanical modeling. Both approaches, to date, have shown success and continuing progress in certain areas; however, their potency to evolve as the ultimate design tool is still impervious. This is largely attributable to the lack of knowledge on coolant flow, bearing dynamics, ball-to-race interfacial friction and wear mechanism.

Despite these efforts, uncertainty still remains concerning the primary cause or causes for the bearing deterioration. It has been generally recognized for several years that the problem to the damage is primarily thermal. Under this notion, an improvement of the convective cooling can at least partially alleviate the problem. Thermodynamically, cryogenics are operated near the critical state, and the peculiarly-behaving properties under this condition often result in a higher heat transfer coefficient than those of subcritical states. The heat transfer coefficient can increase to an even higher value as a supercritical state is reached. Hydrodynamically, the nature of bearing flow is very complex as the axial through flow interacts with the rotational motions of balls and inner-race. Moreover, the combination of intense frictional heating and inadequate cooling may cause LOx vaporized in the vicinity of the ball surface. This boiling phenomenon further complicates the flow pattern and heat transfer to a great extent. The essential aspects of momentum and energy transport in the HPOTP bearings thus involve cryogenic, forced convection boiling in a rotating environment. A review of the literature reveals that virtually no study of this nature has been explored. The only relevant study has been done by Cuan et al. [5] who investigated

the effects of pressure and subcooling on the average heat transfer from a sphere with and without spinning in a pool of liquid-nitrogen. However, their data are still considered inadequate for actual bearing application.

Since the heat transfer information under the actual bearing environment is lacking, the pool boiling curve with a stationary sphere becomes the primary source of heat transfer data. Such a pool boiling curve for Oxygen is shown in Fig. 1. Note that the value of boiling heat transfer coefficient can differ by a factor of 10 or even 100 depending on the stage of boiling. Although it is a fact recognized widely that the ball surface is under the film boiling regime with low values of heat transfer coefficient, literally the entire spectrum of boiling can occur in different time, locations and loading conditions. Hence the choice of heat transfer coefficient of film boiling in a stationary pool as a valid representative for the bearing forced-flow is conservative and fundamentally incorrect.

The variation of heat transfer coefficient affects the temperature distribution in a bearing ball, which, in turn, influences the thermo-mechanical and wear properties of the material. To evaluate the nature of thermal expansion, thermal stress, and subsurface crack, the temperature distribution must be known as a priori. Thus it is necessary to gain detailed response of ball temperature to a change in the external heat transfer coefficient. The present study is primarily directed to fill this need. It uses a numerical method for a parametric analysis which covers a wide range of different cases. This includes the effect of different heating levels occurred at the contacts between the ball and two races.

Figure 2 shows the schematic sketch of a rolling ball and its adjacent races. Frictional heat is generated at the locations in contact with inner and outer races. For simplicity but without loss of generality, the ball is assumed rolling smoothly and with a very high speed; thus the two heated spots can be considered to be two heated "strips." The original three-dimensional problem can thus be reduced to a two-dimensional. Also shown in Fig. 2 are the locations and sizes of contact area. Measure of a contact area is given by the angle of opening, and it is assumed 8 degree for the outer-race and 5 degree for the inner race. The choice of these sizes are based on the corresponding magnitudes used in a recent CFD modeling by Owens [4]. In addition, any influence due to the presence of cage is assumed to be negligible. The following discusses the numerical computation which gives the details of the present analysis.

NUMERICAL COMPUTATION

The heat transfer in a ball element is governed by the following equation in spherical coordinate system as shown in Fig. 3.

$$\nabla \cdot (k \nabla T) = 0 \quad (1)$$

where k is the thermal conductivity of the ball and $T = T(r, \theta, \phi)$ represents the temperature field. In the present analysis, k is assumed constant and Eq. (1) becomes a Laplace equation; i.e.,

$$\nabla^2 T = 0 \quad (2)$$

Furthermore, with the assumption of "strip heating" as mentioned earlier, the temperature dependency on ϕ can be eliminated. Thus T is a function of r and θ .

The boundary conditions on the ball surface ($r = r_o$) are specified as

(i) At contacting area:

$$-k (\partial T / \partial r) = q \quad (3)$$

where q is the frictional heat flux generated on the contact area. Note that the value of q is different between contact with the inner-race (q_{ir}) and that with the outer-race (q_{or}).

(ii) At non-contacting area:

$$-k (\partial T / \partial r) = h (T - T_f) \quad (4)$$

where h is the convective heat transfer coefficient and T_f is the bulk temperature of the coolant flow.

To further extend the generality of the present analysis, the aforementioned governing equation and boundary conditions, eqs. (2) to (4), are transformed to their dimensionless counterparts. This is accomplished by introducing the following dimensionless variables; i.e.,

$$R = r/r_o \quad (5)$$

$$Q_{ir} = q_{ir}/q_{or} \quad (6)$$

$$\Theta = (T - T_f)/(q_{or}r_o/k) \quad (7)$$

and

$$Bi = hr_o/k \quad (8)$$

where Bi is the Biot number representing the ratio of thermal resistance inside the sphere to that outside the sphere. The governing equation in dimensionless form is

$$\nabla^2 \Theta = 0 \quad (9)$$

and the boundary condition becomes

$$\begin{aligned} \nabla \Theta &= 1 && \text{at outer-race contact} \\ &= Q_{ir} && \text{at inner-race contact} \end{aligned}$$

$$= - Bi \Theta \quad \text{at non-contacting area} \quad (10)$$

Thus the solution Θ , a dimensionless temperature, is a function of R , θ , Q_{ir} and Bi . It represents a generalized solution for any variation of ball size, operating temperature, and heat transfer coefficient. The value of Q_{ir} ranges from 1.2, 2, to 7.5, and Bi varies between two cases, 1 and 10. These values are calculated based on the practical information and material properties of actual HPOTP bearings.

Equations (9) and (10) are solved numerically using a control-volume based finite-difference method described in detail by Patankar [6]. Although the present study requires only two-dimensional and steady-state calculation, the computer program developed herein is capable of solving three-dimensional, transient heat conduction problems in generalized, body-fitted coordinate systems. Of particular feature in this computer code is the implementation of the so-called periodic boundary condition in the azimuthal, θ , direction. At the boundary, say $\theta = 0$ and 2π , the dependent variable, Θ , and its associated quantities are not explicitly specified at these two grids, but they must be correspondingly equal, since the two grids are, in fact, the same point. In other words, for a given radial coordinate, all variables repeat themselves with a period of 2π . One effective solution strategy in dealing with problems with such a periodic nature is given by Patankar et al. [7], and it is adopted for the present computation. Here, the so-called Cyclic Tri-Diagonal Matrix Algorithm (CTDMA), facilitates a direct solution along the θ -coordinate. Correspondingly, in the radial direction where periodicity is non-existent, the non-cyclic version of such a direct solver, TDMA, is used. During a computation, the two direct solutions are swept across the entire domain in an alternate fashion using the so-called "line-by-line iteration." The iteration as well as the entire calculation procedure terminates at an attainment of a converged solution.

All the computations are performed with a grid of 40 and 100 points in R and θ direction, respectively. The choice of this grid size which gives sufficiently accurate data and reasonable computing time is a result of an extensive grid-independence study. The grid is nonuniform and denser near the outer surface and contact regions where steeper gradients of dependent variables exist. The convergence criterion is that the percentage change of a variable at any grid should be within 0.1%. A typical run on a Micro VAX II computer takes approximately 500 iterative steps with a CPU time about 1 minute. Note that the present numerical scheme, particularly for computing time, may not be the most efficient for solving heat conduction or diffusion dominant problems. However, the framework of the present program is designed to be completely compatible with one of the most effective, pressure-based computational fluid dynamics (CFD) code. Future extension in simultaneous modeling the heat convection in coolant flow and heat conduction in solid ball - a conjugate problem - is possible.

RESULTS AND DISCUSSION

The computed results are shown in figures 4 to 9, each of which includes a contour plot of the dimensionless temperature, Θ , and a table listing values of actual temperature and heat flux at locations of interest. The temperature and heat flux

shown in the table use the units of degree F and BTU per square foot per second, respectively. The actual temperature at any location, according to Eq. (7), can be inferred from the calculated Θ with given q_{or} and T_f . The value of T_f (denoted as T.INLET in tables) is taken at -240 degree F for all cases, which is the critical temperature of Oxygen. To facilitate the sample calculation, it uses five levels of q_{or} ranging from 100 to 1500 BTU/ft² sec as listed in the first column. The nomenclature stated in second row of the table, T.OR, T.IR, T.AVG and T.CENTER represent the temperature at outer-race contact, at inner-race contact, average over entire ball and at center, respectively. Note that T.05 stands for the actual temperature for $\Theta = 0.05$, and its values tabulated in the last column are correspondingly equal for all figures. This is rather obvious, since the relation between Θ and T is governed by Eq. (7) alone and independent of Bi and Q_{ir} , the primary variables between any two figures. The third row in these tables displays the numerical data of Θ for the corresponding temperature indicated in the second row.

For given values of Bi and Q_{ir} temperature in a sphere increases nearly linearly with the amount of frictional heating at the outer-race contact, q_{or} . This is clearly shown in the listed temperature of Figs. 4 to 9. Moreover, Figs. 10 and 11 respectively exhibit additional graphic view of this effect for the case Bi = 10, $Q_{ir} = 1.2$ and Bi = 1, $Q_{ir} = 7.5$. The overall thermal scale for the former is the lowest (coolest) and the highest (hottest) for the latter. An examination of these two figures reveals that the rate of temperature increase vs. q_{or} varies with differences in location, external cooling (Bi), and level of frictional heating (Q_{ir}). It is clear that the temperature at one of the race-contact areas has the highest rate of increase, and temperature averaged over the entire volume or at the center has the lowest increasing rate. For $Q_{ir} = 1.2$, representing an almost equivalent heat generation between the two race-contacts, the highest temperature as well as the increasing rate exists at the outer-race contact. However, for $Q_{ir} = 7.5$, such an extreme instead occurs at the inner-race contact. The value of Q_{ir} greater than unity implies that the heat flux at the inner-race contact is higher than that at the outer-race contact. Accordingly, the total heat generated and local temperature near the inner-race contact should be higher provided that both contact areas are of the same size. This is not the case for $Q_{ir} = 1.2$, because the area of outer-race contact is about 1.6 times higher than the inner-race contact. Thus the inner-race contact has a smaller amount of total heat generation and lower local temperature than its outer-race counterpart. For $Q_{ir} = 2.0$ or 7.5, the effect of area differential becomes secondary as the highly elevated heat flux dominates the local heating at the inner-race contact. As a result, the local temperature at the inner-race contact is higher than that of the outer race. For intense frictional heating, say $q_{or} \geq 500$ BTU/ft² sec, the temperature difference between the two contacts is nearly an order of magnitude for Bi = 1, $Q_{ir} = 7.5$, as Fig. 6 shows.

Of particular interest is to investigate the effects of external heat transfer coefficient on the ball temperature distribution. In the present dimensionless approach, this can be done by examining the variation of Θ as a function of Bi for a given Q_{ir} . According to the Θ definition (Eq. 7), such an effect is independent of the actual values of q_{or} and coolant temperature. Comparing the data shown in the third row of each table, as Bi increases from 1 to 10, the resulting decrease is approximately 35%, 8% and 10% for the temperature of average, outer-race contact and inner-race contact, respectively. To be noted is that these values are virtually independent of the relative

amount of heat generation between the two race-contacts (i.e., Q_{ir}), less than 1% within the present studying range. Apparently the temperatures at or near the contact areas is quite insensitive to the change of heat transfer coefficient. The rest of sphere reacts effectively and accordingly to the increase of heat transfer coefficient. Note that the temperature at the center core (fifth column in tables) is very close to the average temperature over the entire ball. This implies there are regions, mainly near the surface but away from the two contacts, the temperature reduction is more than 35%.

One general concern in cooling enhancement is the excessive temperature gradient accompanying with an overall temperature temperment. This is undesirable as additional thermal stress could result. An effective cooling scheme is capable of removing heat from the system by reducing its temperature uniformly throughout the entire domain. As observed in the contour plots for all cases, temperature gradients near a race contact is much greater than that of the remaining region, by nearly an order of magnitude. As expected, the lowest gradient typically occurs near the central portion of the sphere. The influence of Bi on the temperature gradient varies strongly with difference in location and level of contact heating.

An increase in Q_{ir} raises both temperature and temperature gradient in the vicinity of the inner-race contact. For a given Bi , the same effect, in fact, occurs in the remaining portion of the sphere, but to a much less extent. A comparison between Figs. 5 and 6 shows that, for $Bi = 1$ and Q_{ir} increasing from 2 to 7.5, the temperature gradient increases approximately 9 and 2.5 times at the inner-race contact and near the core region, respectively. This is understood as a stronger temperature gradient is established to facilitate the greater heat transfer for the case with a higher magnitude of Q_{ir} . Due to the absence of convective cooling at contacts, frictional heat in the present modeling must be transferred by conduction inside the ball first and then rejected from the surface by convection. However, the heat path is considered to be far more complex in actual bearing conditions. Heat transfer takes place in various mode among all the bearing constituents. Figure 12 displays a thermal coupling diagram to illustrate this phenomenon. In reality, the heat generation at a contact must be transferred with partitions among the ball, the race and the lubrication (coolant) film immediately adjacent to the contact. The last represents the only convection related effect and is little understood currently. The other two partitions are predominant by conduction, but the details of heat sharing can not be determined without considering the overall heat balance in the bearing system, as shown in Fig. 12.

For a given heating level at race contacts, one may expect that an increase in Bi or heat transfer coefficient will result in decreases of both temperature and temperature gradient. The former is true as discussed earlier; but the latter is not always the case. The fact is that, as Bi increases from 1 to 10, the temperature gradient decreases about 50% away from the contact zones, and, on the contrary, increases 70 to 100% in the close vicinity of both contacts. This is mainly caused by a much less temperature reduction at the contacts than in the remaining portion of the sphere, as the external cooling effectiveness increases. Such an elevation of temperature gradient near contact may be detrimental to the material integrity as the local thermal stress is expected to rise. However, this is the only unfavorable result due to the increase of heat transfer coefficient.

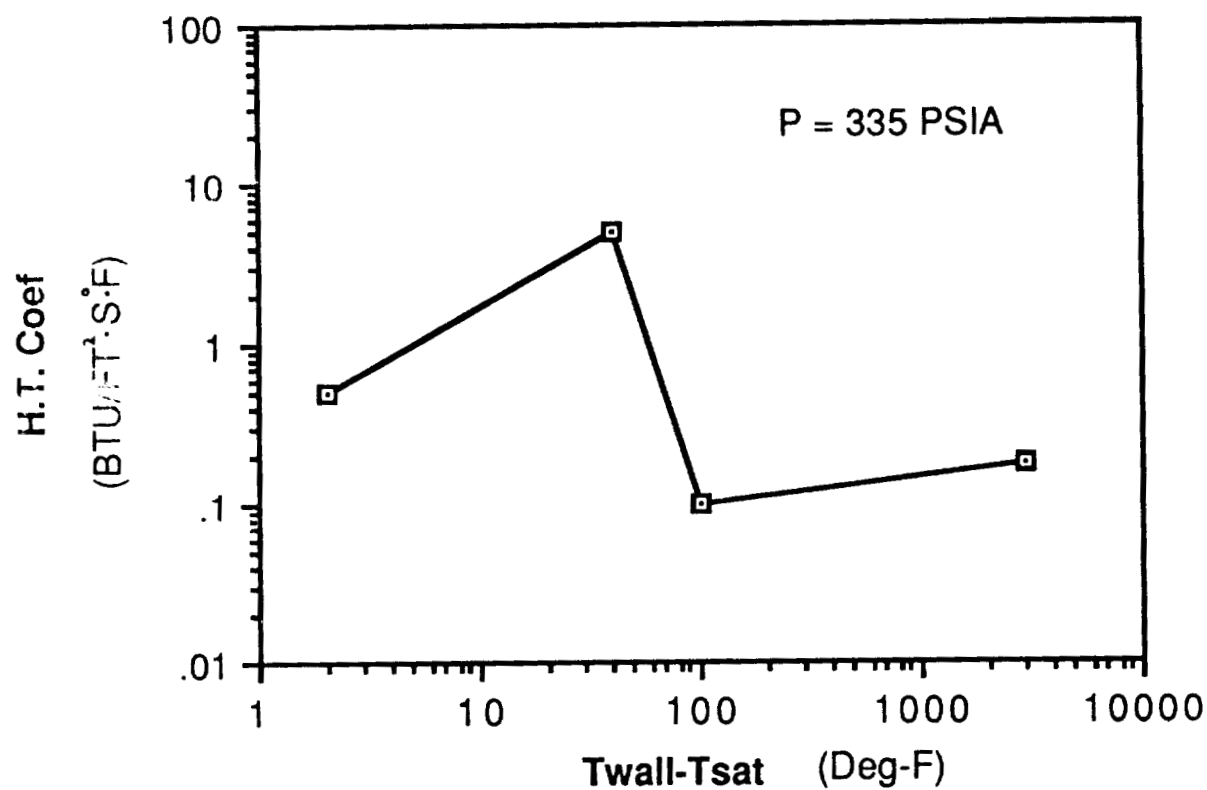
CONCLUSIONS

The effects of contact heating and heat transfer coefficient on the temperature in a HPOTP bearing ball is studied numerically. The present analysis solves the non-dimensionalized equation for heat conduction in a spherical domain. The boundary condition is comprised of two heated stripes, each representing the frictional heat generation at contact with one of the two races, and boiling convection of LOx on the remaining surface. For a given value of heat transfer coefficient, the ball temperature, in general, increases linearly with the heat input from the race-contacts. However, the actual trend of increase varies with location. The greatest increase occurs at one of the two contacts, the one that has the higher total heat generation.

An increase of heat transfer coefficient significantly decreases the ball temperature and alters its distribution. The present computation shows that, the average ball temperature decreases about 35% (with coolant bulk temperature as datum) for a 10-fold increment of the heat transfer coefficient. At the contacts, temperature decrease is much less, in the order of 10%, due mainly to the intense local heating. The corresponding change of temperature gradient is strongly dependent on the location, and opposite effects exist. For the major portion of the ball and away from the contact zones, the temperature gradient decreases about 50%. On the contrary, it increases 70 to 100% in the vicinity of both contacts. This increase of temperature gradient may cause the subsurface material become vulnerable and susceptible to wear. However, this is the only adverse effect induced by an increase in the heat transfer coefficient.

REFERENCES

1. Scibbe, H. and Dolan, F.J., "Bearing Technology - Overview," NASA CP 2372, *Advanced High Pressure O₂/H₂ Technology*, June, 1984, pp. 201-204.
2. Dolan, F.J., Gibson, H.G., Cannon, J.L. and Cody, J.C., "Cryogenic, High Speed, Turbopump Bearing Cooling Requirements," NASA CP 3012, *Advanced Earth-to-Orbit Propulsion Technology 1988*, pp. 110-132.
3. Cody, J.C., Marty, D.E. and Moore, J.D., "Evolution and Use of Combined Mechanical and Thermal Codes for Cryogenic Turbopump Bearings," NASA CP 3012, *Advanced Earth-to-Orbit Technology 1988*, pp. 88-101.
4. Owens, S.F., "Flow and Heat Transfer in the SSME HPOTP 4th Ball Bearing Assembly," CHAM 2005/5, February, 1989
5. Cuan, W.M. and Schwartz, S.H., "Pool Boiling From a Rotating and Stationary Spheres in Liquid Nitrogen," NASA CP 3012, *Advanced Earth-to-Orbit Propulsion Technology 1988*, pp. 142-158.
6. Patankar, S.V., *Numerical Heat Transfer and Fluid Flows*, McGraw-Hill, 1980
7. Patankar, S.V., Liu, C.H. and Sparrow, E.M., "The Periodic Thermally Developed Regime in Ducts with Streamwise Periodic Wall Temperature or Heat Flux," *J. Heat Transfer*, Vol. 99, 1977, pp. 180-186.



ORIGINAL PAGE IS
OF POOR QUALITY

Figure 1. Heat Transfer Coefficient of Pool Boiling Oxygen

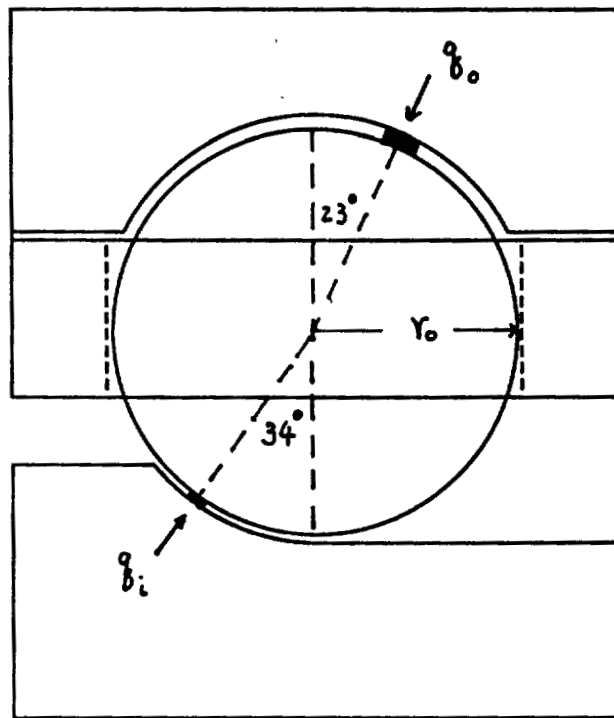


Figure 2. Rolling Ball Schematic

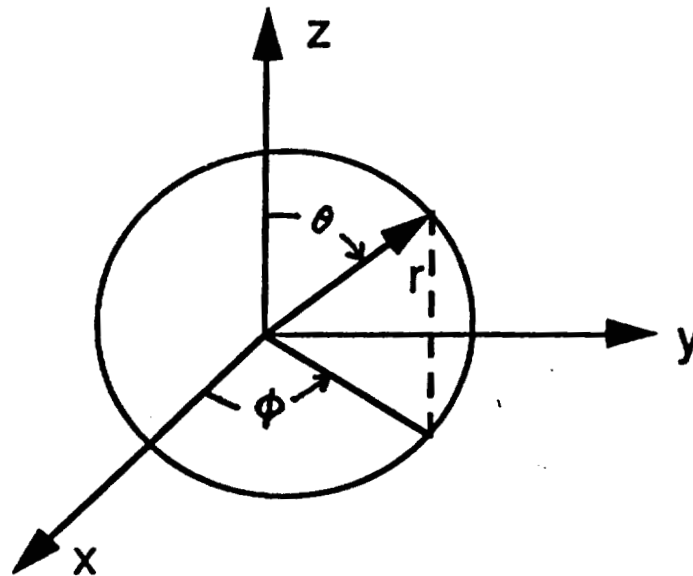


Figure 3. Spherical Coordinate System

Bi=1	Q _{IR} =1.2	DEG-F	T.INLET=-240		
QOR	T.OR	T.IR	T.AVG	T.CENTER	T.O5
	0.114	0.109	0.026	0.025	0.05
100	-113	-119	-211	-212	-184
250	76.7	61.4	-168	-171	-101
500	393	363	-95.6	-102	37.8
1000	1027	966	48.8	36.7	316
1500	1660	1568	193	175	593

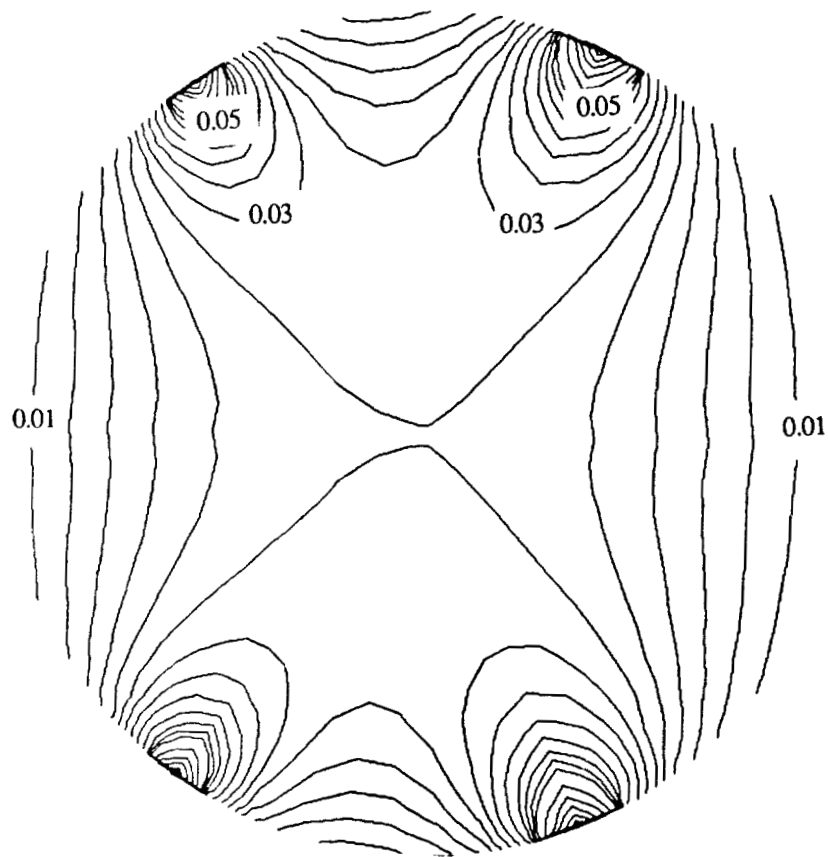


Figure 4. Ball Temperature Distribution, $Bi = 1$, $Q_{ir} = 1.2$

Bi=1	Q _{IR} =2	DEG-F	T.INLET=-240		
Q _{OR}	T _{OR}	T _{IR}	T _{AVG}	T _{CENTER}	T ₀₅
	0.115	0.18	0.033	0.032	0.05
100	-112	-40	-203	-204	-184
250	79.5	260	-147	-151	-101
500	399	760	-51.4	-64.7	37.8
1000	1038	1760	131	117	316
1500	1677	2760	317	295	593

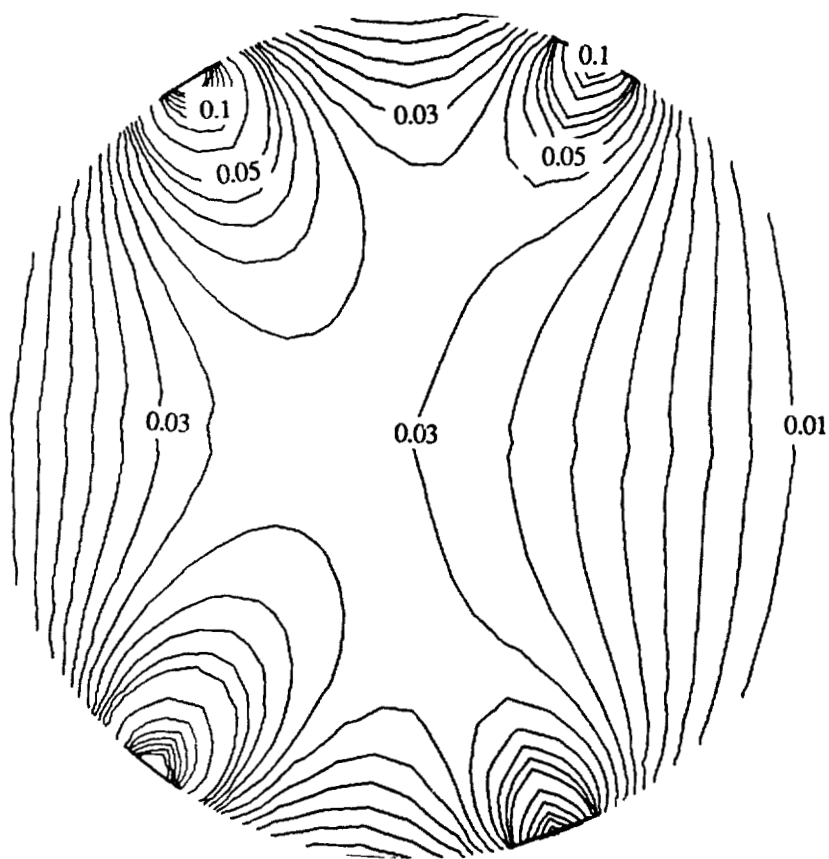


Figure 5. Ball Temperature Distribution, $Bi = 1$, $Q_{ir} = 2.0$

Bi=1	Q.IR=7.5	DEG-F	T.INLET=-240			
QOR	T.OR	T.IR	T.AVG	T.CENTER	T.05	
	0.121	0.669	0.084	0.082	0.05	
100	-105	504	-146	-149	-184	
250	96.3	1619	-5.56	-13.6	-101	
500	433	3478	229	213	37.8	
1000	1106	7195	698	666	316	
1500	1778	10913	1167	1118	593	

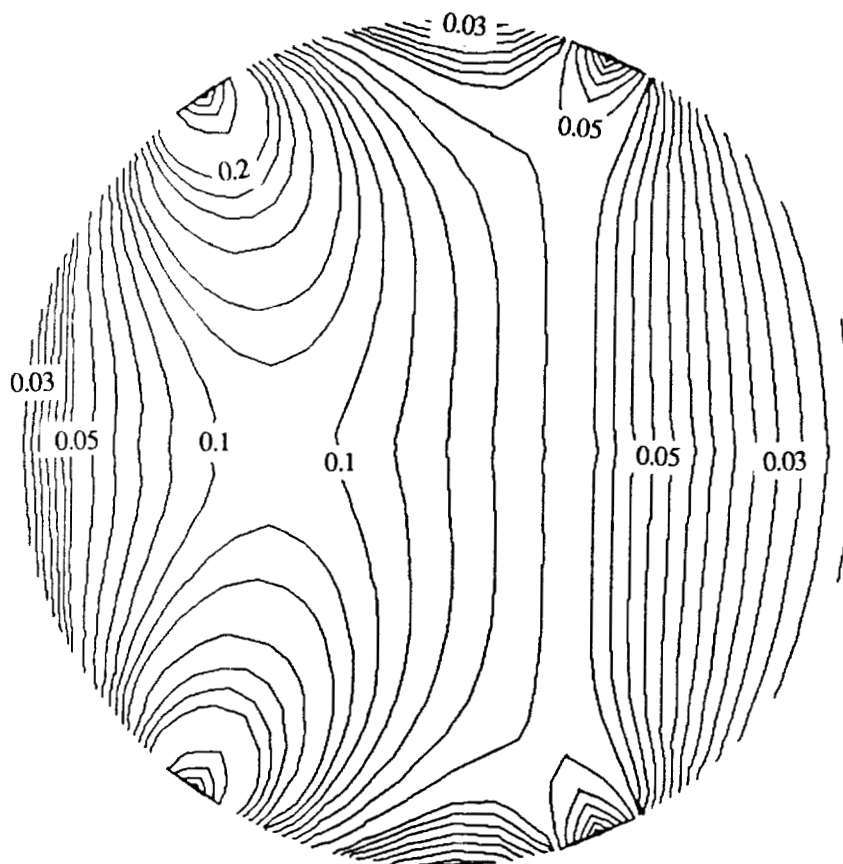


Figure 6. Ball Temperature Distribution, Bi = 1, $Q_{ir} = 7.5$

Bi=10	Q _{IR} =1.2	DEG-F	T.INLET=-240		
QOR	T.OR	T.IR	T.AVG	T.CENTER	T.05
	0.106	0.098	0.017	0.016	0.05
100	-122	-131	-221	-222	-184
250	54.5	31.7	-193	-194	-101
500	349	303	-146	-149	37.8
1000	938	847	-52.5	-58	316
1500	1527	1390	41.2	33	593

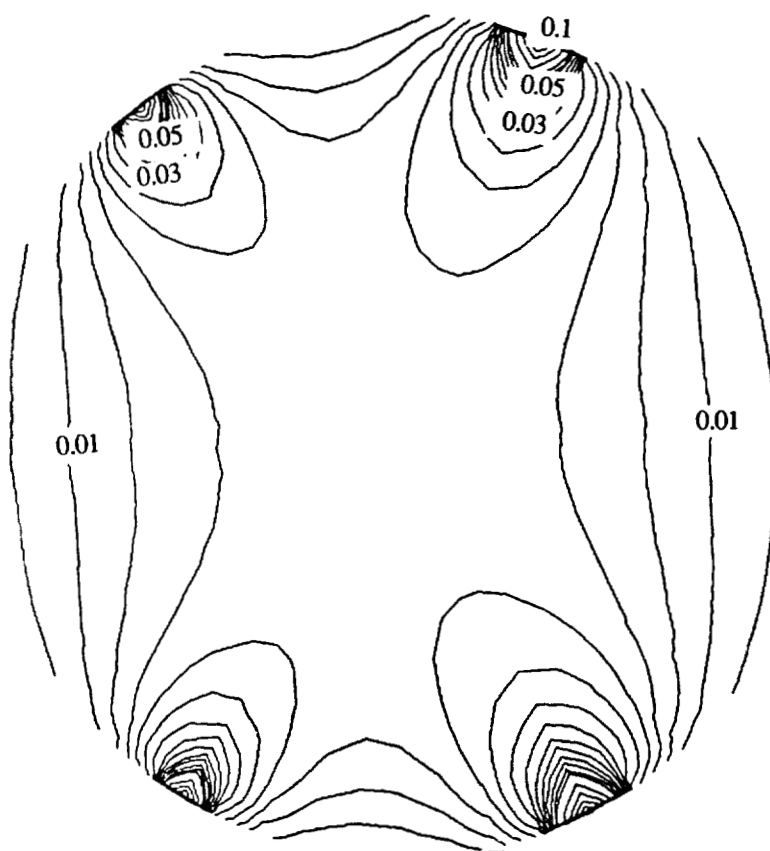


Figure 7. Ball Temperature Distribution, Bi = 10, $Q_{ir} = 1.2$

Bi=10	Q _{IR} =2	DEG-F	T.INLET=-240		
Q _{OR}	T _{OR}	T _{IR}	T _{AVG}	T _{CENTER}	T ₀₅
	0.107	0.162	0.021	0.021	0.05
100	-122	-59.7	-216	-217	-184
250	56.1	211	-180	-182	-101
500	352	662	-121	-124	37.8
1000	945	1563	-1.76	-7.98	316
1500	1537	2465	117	108	593

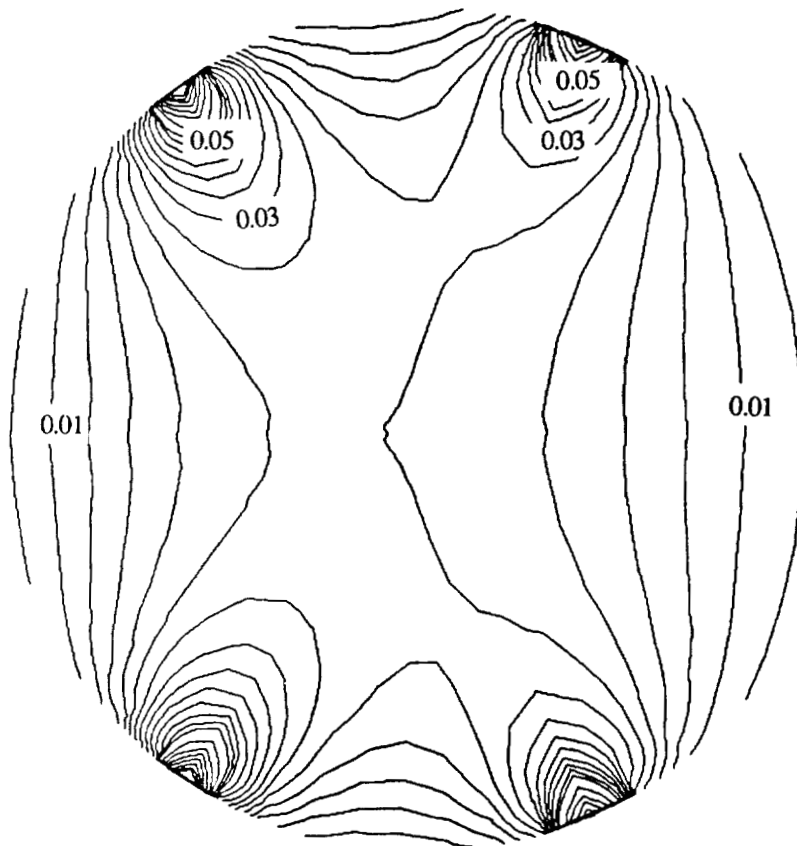


Figure 8. Ball Temperature Distribution, Bi = 10, Q_{ir} = 2.0

Bi=10	Q _{ir} =7.5	DEG-F	T.INLET=-240		
Q.OR	T.OR	T.IR	T.AVG	T.CENTER	T.05
	0.11	0.606	0.053	0.05	0.05
100	-117	433	-181	-182	-184
250	65.7	1443	-93.2	-96.1	-101
500	371	3126	53.6	47.9	37.8
1000	983	6492	347	336	316
1500	1594	9858	641	624	593

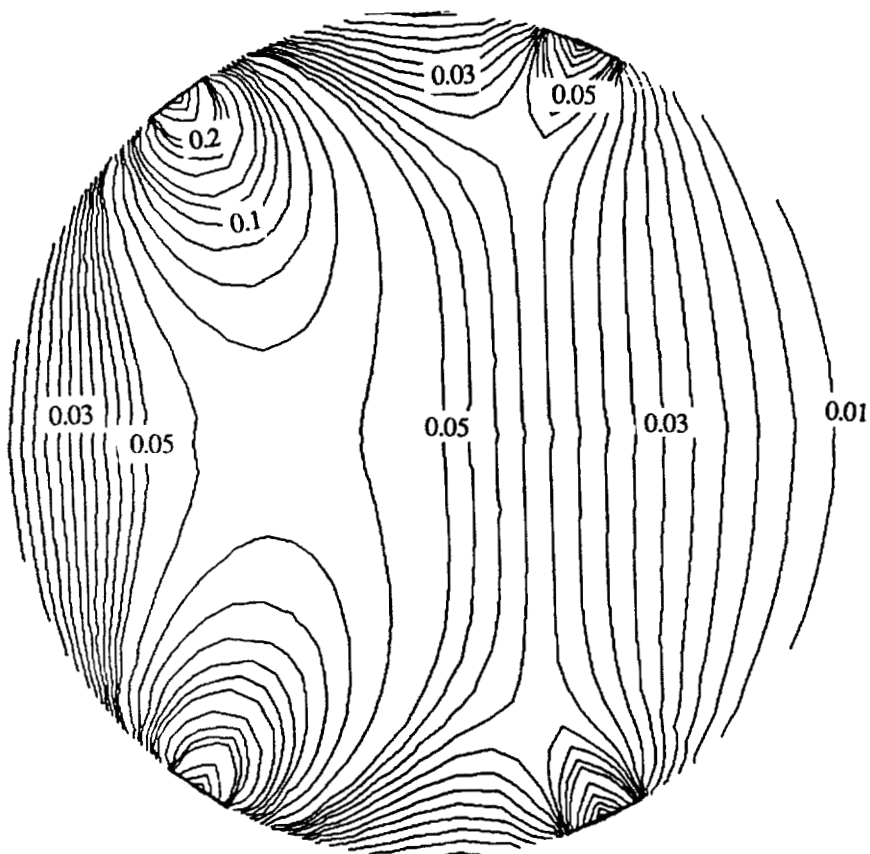


Figure 9. Ball Temperature Distribution, Bi = 10, Q_{ir} = 7.5

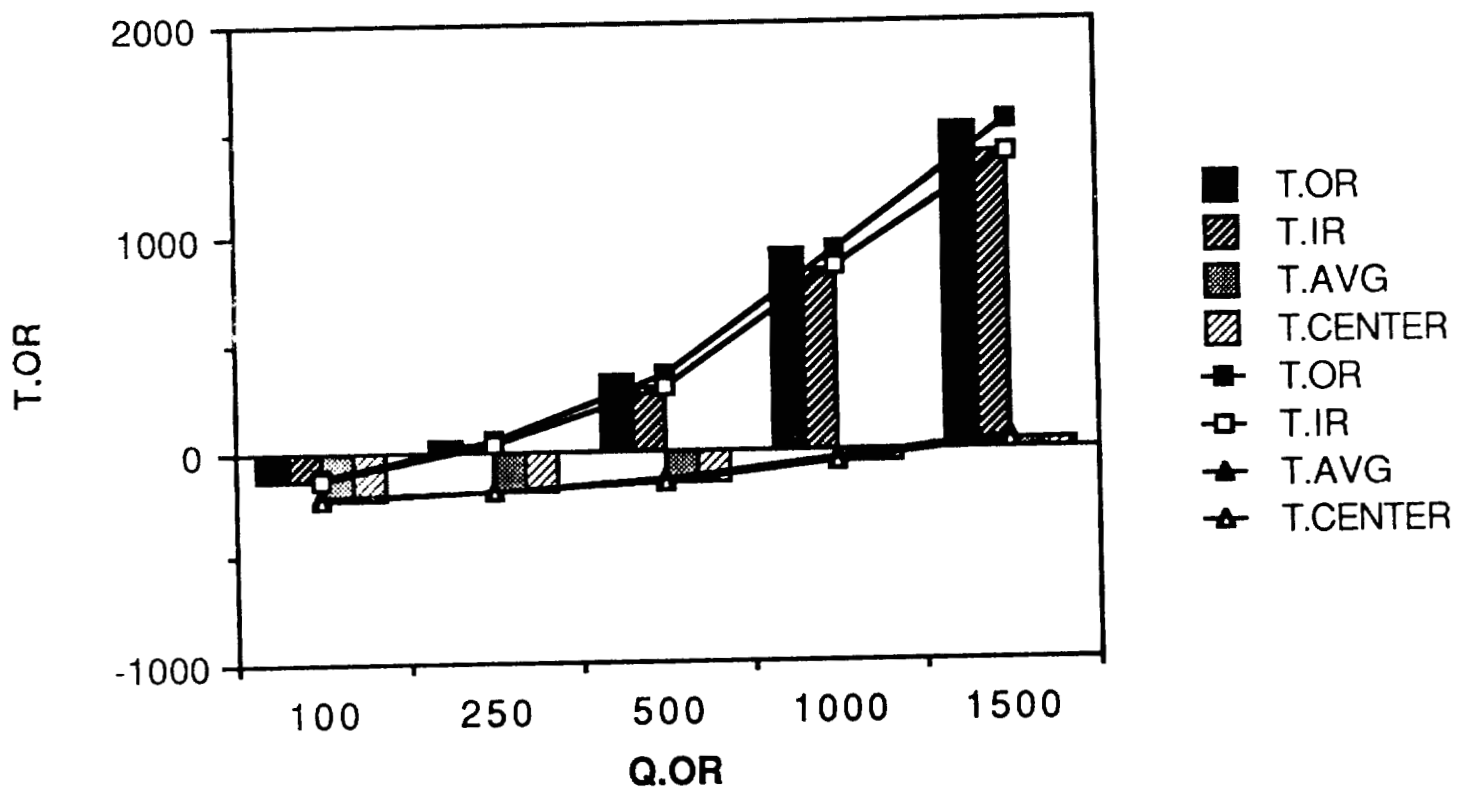


Figure 10 Effect of q_{or} on Ball Temperature Variation, $Bi = 10$, $Q_{ir} = 1.2$

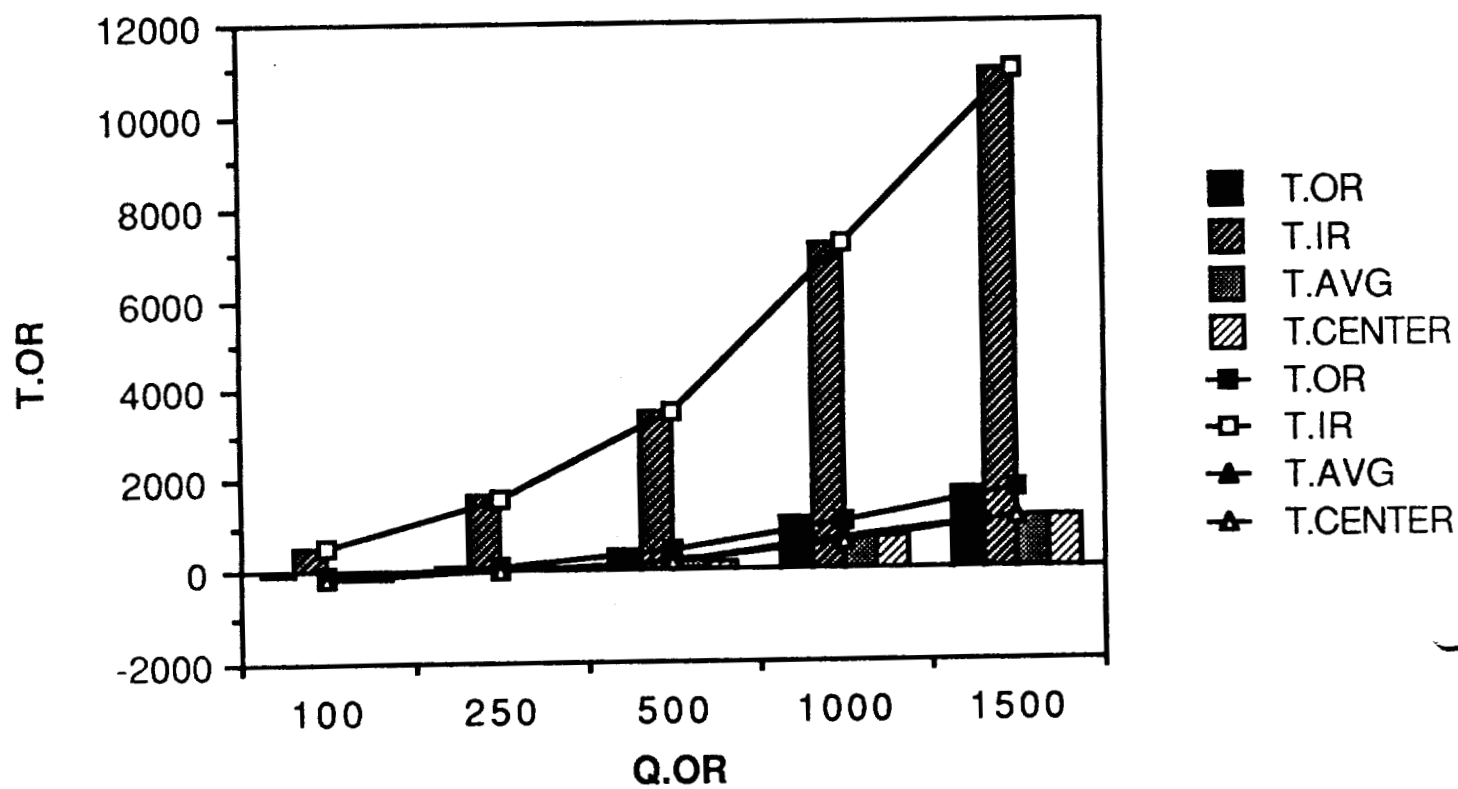


Figure 11 Effect of q_{or} on Ball Temperature Variation, $Bi = 1$, $Q_{ir} = 7.5$

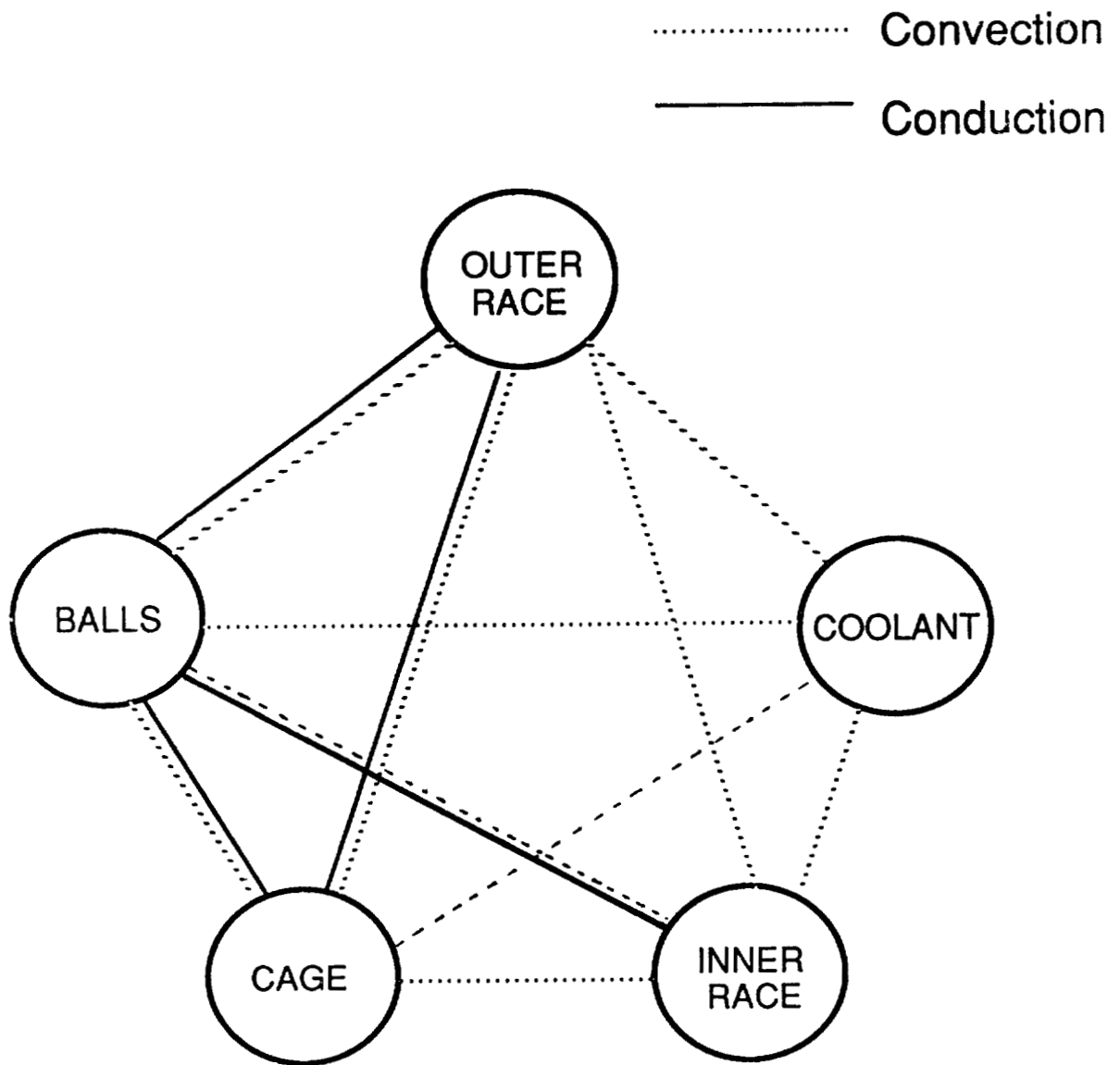


Figure 12. Thermal Coupling of Bearing Elements

1989

NASA/ASEE SUMMER FACULTY RESEARCH FELLOWSHIP PROGRAM

MARSHALL SPACE FLIGHT CENTER
THE UNIVERSITY OF ALABAMA IN HUNTSVILLE

LIQUID OXYGEN LOX COMPATIBILITY EVALUATIONS OF ALUMINUM
LITHIUM (Al-Li) ALLOYS : INVESTIGATION OF THE ALCOA 2090
AND MMC WELDALITE 049 ALLOYS

Prepared By:	Ravinder M. Diwan
Academic Rank:	Professor
University and Department:	Southern University Mechanical Engineering Department Baton Rouge, Louisiana
NASA/MSFC:	
Laboratory:	Materials and Processing Laboratory
Division:	Metallic Materials Division
Branch:	Metallurgy Research Branch
NASA Colleagues:	T.P. Vaughn and B.N. Bhat
Date:	August 11, 1989
Contract No:	The University of Alabama in Huntsville NGT-01-008-021

LIQUID OXYGEN LOX COMPATIBILITY EVALUATIONS OF ALUMINUM
LITHIUM (Al-Li) ALLOYS : INVESTIGATION OF THE ALCOA 2090
AND MMC WELDALITE 049 ALLOYS

by

Ravinder M. Diwan
Professor
Mechanical Engineering Department
Southern University
Baton Rouge, Louisiana 70813

ABSTRACT

The present research work is an investigation into the behavior of liquid oxygen LOX compatibility of aluminum lithium (Al-Li) alloys. Alloy systems of Alcoa 2090, vintages 1-3, and of Martin Marietta Corporation MMC Weldalite 049 were evaluated for their behavior related to the LOX compatibility employing liquid oxygen impact test conditions under ambient pressures and upto 1000 psi. The developments of these aluminum lithium alloys are of critical and significant interest because of their lower densities and higher specific strengths and improved mechanical properties at cryogenic temperatures. Of the different LOX impact tests carried out at the Marshall Space Flight Center (MSFC) , it is seen that in certain test conditions at higher pressures , not all Al-Li alloys are LOX compatible. In case of any reactivity, it appears that lithium makes the material more sensitive at grain boundaries due to microstructural inhomogeneities and associated precipitate free zones (PFZ). The objectives of this research were to identify and rationalize the microstructural mechanisms that could be related to LOX compatibility behavior of the alloy system in consideration.

The LOX compatibility behavior of Al-Li 2090 and Weldalite 049 is analyzed in detail using microstructural characterization techniques with light optical metallography, Scanning Electron Microscopy (SEM) , electron microprobe analysis , and surface studies using Secondary Ion Mass Spectrometry (SIMS), Electron Spectroscopy in Chemical Analysis (ESCA) and Auger Electron spectroscopy (AES). Differences in the behavior of these aluminum lithium alloys are assessed and related to their chemistry , heat treatment conditions and microstructural effects.

ACKNOWLEDGEMENTS

The author is grateful for the opportunity and financial support to carry out this research work at the Materials and Processing Laboratory, at the Marshall Space Flight Center. He would like to express gratitude to his NASA colleagues Mr. T.P. Vaughn and Dr. B.N. Bhat for their excellent support and cooperation in conducting the activities related to this research. Thanks are also expressed to Mr. R.R. Rowe, Chief, Metallurgy Research Branch and several technical personnel for their providing the facilities and support in different areas to carry out this work. Special thanks are expressed to Messers W. DeWeese and S. Cato for metallography work, J. Coston for SEM and microprobe work, and to Dr. I. Dalins for surface studies with ESCA, SIMS and Auger spectroscopy. Finally, he is grateful to the NASA/ASEE Summer Faculty Fellowship Program for his selection in this program and for sponsoring of this research work. Thanks are expressed to Dr. G. Karr, UAH Program Codirector and to Dr. F. Six, University Affairs Officer, MSFC Program Codirector for their enthusiasm and support of this program.

I. INTRODUCTION

The developments of the new aluminum lithium Al-Li alloys have been driven due to high performance demands of aerospace applications and for use of materials in Space Transportation Systems and as cryotankage materials. Lithium is the lightest element and the only metal, with the exception of beryllium that is toxic, expensive and difficult to use, which alloyed with aluminum is known to improve both the modulus and the density of these Al-Li alloys in place of current conventional alloys. This can reduce the weight by 7-15 % and increase the elastic modulus by 10-20 %. For these and several other special advantages, the aluminum lithium alloys are now gaining considerable importance as the future advanced aerospace materials. (1,2). Understanding the behavior of these materials is of special interest to MSFC and of particular interest is the cryogenic behavior and the LOX compatibility behavior of these materials as this could advance and affect the applications of these aluminum lithium alloys as the future advanced cryogenic materials.

Design and developmental aspects of certain Al-Li based alloys (3-11), their fundamental characteristics, special advantages at cryogenic temperatures, superior fracture toughness at ambient and cryogenic temperatures, and the corrosion and weldability of these high strength Al-Li alloys (12-16) have all shown immense potentials of these developing aluminum lithium based alloys. For these potentials to be realized, further in-depth scientific and technological, commercial evaluations of these alloy systems are essential and vital to the future development of these alloy systems.

The cryogenic behavior of the Al-Li 2090 has exhibited improved fracture toughness between room temperature 298K and liquid helium 4K temperatures (12-14). This improved strength toughness relationship is similar to the earlier data of J. Glazer et. al. (12) on standard aerospace and 2219 aluminum alloys. However, the origin of this behavior is not clear and further such behavior has not been shown in the short transverse orientations and has not been found for all alloys and aging conditions. There is clearly need to evaluate the cryogenic mechanical behavior of the developing Al-Li alloys and to understand the mechanisms responsible for such behavior and relationships between the microstructures and

potential cryogenic properties. A good description and understanding of the microstructures and development of microconstituents is essential to the understanding of such structure property relationships.

Of the many potential applications for the Al-Li alloys, the most prominent are as cryotankage materials and for LOX environments. In recent LOX impact compatibility tests at MSFC, it is seen that not all Al-Li alloys of different chemistry and specifications are compatible under some test conditions at higher pressures. The reasons for these LOX sensitivity and the mechanisms related to the LOX compatibility are not currently understood and this research has been undertaken to identify the causes of such reduced LOX compatibility and sensitivity of certain specimens of Al-Li alloys and their related microstructural mechanisms. This investigation has centered on the evaluations of material supplied by Alcoa of Al-Li 2090, T8E41, vintages 1-3, and of Weldalite 049 alloys T4 and T8 tempers supplied by the Martin Marietta Corporation.

Of the LOX impact tests, as per NHB 8060.1B (17), using the Army Ballistic Missile Agency ABMA type tester, in the tests carried out it has been observed that Weldalite 049 is mostly seen as compatible but more tests are required. The Alcoa 2090 exhibited improvements from vintage 1 to vintage 3. No reaction was observed in the vintage 3 materials. The mechanisms of the LOX compatibility and sensitivity were analyzed using metallographic techniques, x-ray diffraction, SEM and microprobe studies, and surface studies using ESCA, SIMS and Auger spectroscopy and related to microstructural characterizations, chemistry and processing conditions of the specific Al-Li alloys.

II. OBJECTIVES

The objectives of this research that has been pursued are:

- 0 Evaluation of LOX Compatibility Impact Test procedures , testing , and data analysis
- 0 Characterization of the microstructures of the aged and unaged 2090 and Weldalite 049 in suitable tempers in sheet and / or plate form of the typical "as received", "reacted" and "unreacted" LOX tested material specimens
- 0 Analyses of LOX test results, their predicted behavior, relationships with material chemistry and tempers, and microstructural characterization
- 0 Correlation of material properties with microstructure and test results
- 0 Development of rationale for LOX Compatibility criteria and material behavior

III. EXPERIMENTAL PROCEDURES

The starting materials comprised of aluminum lithium alloys 2090-T8E41, in vintages 1-3, supplied by Alcoa and from Weldalite 049 alloys of T4 and T8 tempers supplied by Martin Marietta Corporation and also of conventional aluminum copper Alcoa 2219 materials. These several formulations and tempers were produced by appropriate solution heat treatment, quenching, cold work and aging for suitable time and temperature conditions. Details of the tested 2090, Weldalite 049 and 2219 alloy chemistry, heat treatment and temper conditions are provided in Table 1. All test materials were produced as 11/16-in. diameter discs, .063-in. / or .125 in. thick, and tested as per NHB 8060.1B using the Army Ballistic Missile Agency ABMA type impact tester. The test method is similar to standard ASTM D 2512.82 for compatibility of materials with liquid oxygen (18). All of the necessary and special precautions as in the test specifications are strictly adhered to in carrying out the LOX impact compatibility tests. This includes special degreasing, cleaning, drying and packing of the test specimens before carrying out of the actual LOX impact tests.

In accordance with NHB 8060.1B, a material is considered to have material sensitivity if it shows any reaction in 20 successive impact tests at 10 kg-m (72 ft.-lbs) . A material is said to show sensitivity or reaction if the test results in any of the conditions such as : audible explosion, flash, evidence of burning or charring, or major discoloration. These test criteria are used to evaluate the performance of all test materials. In order to assess the behavior of the 2090 and Weldalite 049 , selected test specimens of the typical as received , reacted and unreacted specimens of these alloy systems were evaluated using standard metallographic procedures, x-ray diffraction, SEM, electron microprobe analysis, ESCA, SIMS and Auger spectroscopy in an effort to analyze the microconstituents and their behavior related to LOX impact compatibility of these particular Al-Li alloys.

Metallographic analyses for microconstituent characteristics , inhomogeneities, any precipitate free zones PFZ , deformation and heat treatment effects etc. were carried out using standard procedures and suitable etching techniques. The grain boundaries seem to have shown enhanced

effects with use of the differential interference contrast DIC microscopy. Where possible, microhardness measurements were taken of certain Cu/Fe rich precipitates . In conjunction with metallographic analyses , some SEM and electron probe microanalysis work was performed. This revealed presence of Al in base material and some Cu/Fe rich particles as evidenced by SEM and microprobe analyses. These analyses ,however, were not capable to characterize and identify the presence of Li. The SEM scanning electron microscopy with energy dispersive analysis was carried out on Cambridge Stereoscan Model 250 Mark II, and microprobe work was carried on CAMICA SX model. The analyses of the presence of lithium and lithium related phases by the ESCA, SIMS and Auger spectroscopy techniques of reaction products of some of the test specimens were carried out. These , however, were useful to detect Li and to understand the behavior of these materials and nature of some of the reaction products.

The x-ray photo electron spectroscopy (XPS) or the electron spectroscopy in chemical analysis (ESCA) was performed on Surface Science Instrument the SSX - 100 ESCA spectrometer, and the Auger electron spectroscopy (AES) was performed using Modified Physical Electronics 545 Auger System. The secondary ion mass spectrometry (SIMS) was performed on a Modified UTI 100C 3M model. The results of these several analyses and related microstructural mechanisms that could be affecting the LOX compatibility behavior of the Al-Li alloys under investigation are presented in the next section.

Table 1A Compositions of AA 2090 and
Weldalite 049

AA 2090

Li	Cu	Si	Fe	Mn	Mg	Cr	Zn
1.9-2.6	2.4-3.0	.10	.12	.05	<.25	.05	<.10

Zr	Ti	other (each)	other (tot.)	Al
.08-.15	<.15	<.05	<.15	bal.

Weldalite 049

Li	Cu	Ag	Mg	Zr	Al
1.3	6.0	0.4	0.4	0.14	bal.

AA 2219

Cu	Mn	Ti	Al
6.3	0.30	0.06	bal.

Table 1B Tempers and heat treatments

AA 2090	SHT 1000 - 1020 F , 2 - 6 % CW , aging 300 - 350 F for different times. (TBE41)
Weldalite 049	SHT 940 F , natural age > 600 hrs. (T4) SHT 940 F , 3 % CW , art. age 20 hrs. 160C(T8)
AA 2219	SHT 995 F ; art. age 350 F , 18 hrs. (T81)

IV. RESULTS AND DISCUSSION

The LOX impact compatibility test data are shown in Table 2A-C. These LOX impact compatibility evaluations were carried out by conducting tests under liquid oxygen under fixed pressure at ambient pressure and upto 1000 psi.

For assessment of the LOX cryogenic behavior of the Al-Li alloys, it is first essential to understand the precipitation mechanisms in these alloy systems, their phase equilibria information as related to strengthening mechanisms, and then evaluate and rationalize the several metallographic characterizations and results of the surface studies.

A. Precipitation Strengthening and Phase Equilibria in Al-Li based alloy systems

The phase equilibria diagrams of interest related to the Al-Li based alloy systems under study are presented in figures 1 and 2. As is well known, for an alloy system to be amenable to age hardening, there must be a decrease in solid solubility of one or more of the alloying elements with decreasing temperature. Major alloying elements of interest in the systems under investigation include Cu, Mg and Li. Some of the information on the phase transformations in this section is based on references 19-23.

Lithium produces order strengthening superlattice L1 2 type precipitates of metastable δ' (Al_3Li). Additionally, phases such as T_1 (Al_2CuLi) or T_2 (Al_5CuLi) are potential strengthening phases alongwith θ' (Al_2Cu). It is further seen that with additions of transition metals such as of chromium, manganese and zirconium with solubilities less than 1 atomic %, potential improvements in alloy properties are possible. With Zr additions, grain refining microconstituent precipitates of β' (Al_3Zr) are known to be present that control the grain structure and inhibit recrystallization in the alloy system.

The nature and formation of coherent particles of δ' by order strengthening mechanism, variations in distributions of this and associated particle phases, interactions of these with dislocations, subgrains, and grain boundaries and localized plastic strain, and presence of precipitate free zones PFZ will affect the microstructural developments and

thereby affect the strengthening behavior of these Al-Li based alloys. With higher copper content and presence of Mg, δ' (Al_2CuMg) precipitates can be formed. In analyzing the Al-Li 2090 and Weldalite 049 alloys, it is seen that only limited phase equilibria information is available related to these systems. These include investigations of Sigli and Sanchez (20) and of Flower and Gregson (21), (23). The additions of Ag and Mg give unique properties to these Al-Cu-Li alloys. For alloy design considerations, minor additions ($\sim 0.4\text{wt.}\%$) of Ag and Mg are seen to stimulate precipitation and promote the refinement of strengthening phases. Pickens et. al. (8) and Langan and Pickens (9) have identified $\alpha_{ss} + T_1 + T_B$ phases for Al-Cu-Li alloy with 1.3 wt.% Li. The δ' (Al_3Li) phase is not considered to be present if T_B ($\text{Al}_{7.5}\text{Cu}_4\text{Li}$) phase is included on precipitation. These studies and identification of the multiple phases expected in Weldalite 049, particularly with variations in lithium, still need to be carried out in detail to confirm their nature and effects on the properties of these alloys.

The δ' particles are spherical and in some cases coprecipitate with β' (Al_3Zr), and with T_1 phase precipitating as laths or platelets. Polmear and coworkers (24) have attributed the strengthening to increase in an Al-6.7Cu-0.5Mn alloy with 0.5 % Ag and 0.5 % Mg due to a Ω phase. This Ω phase precipitates with a plate like morphology and could be another potential strengthening phase in Weldalite 049. Studies related to this and T_1 phase are required to establish this and the morphology and composition of this Ω phase.

B. LOX Compatibility Evaluations and Metallographic Characterizations

The LOX impact compatibility test results of 2090, vintage 1, 100796 exhibited a rather violent reaction under 500 psi. LOX impact test conditions. This tested material was sectioned and examined for reaction products. This same vintage material had also shown at 100 psi. some holes in a reaction in which the impactor had melted together with bottom of the cup of inconel 718 material. This was also sectioned and examined for reaction products, figures 3A-c.

The Al-Li 2090 LOX tested specimens, in other cases, on reaction had only shown discoloration such as seen in figure 4. These reacted specimens were sectioned and examined for microstructural characteristics and potential causes for the LOX sensitivity and or reactivity of such materials.

The Weldalite 049, with 1.3 wt. % lithium , ~ 6 wt. % Cu and 0.4 % Ag, 0.4 % Mg additions, as received material shows on metallographic analysis effects of deformation , and presence of multiple phases as seen in figure 5. Plastic strain localization and unrecrystallized grain structure is clearly seen . This material of Weldalite T4 temper on LOX impact test conditions had shown no reaction. These alloys and also the Al-Li 2090 materials of several specimens , on etching with Graff / Sargent chemical etchant revealed presence of coarse particle precipitates , figure 6 and 7. These particles on detailed examination are identified as Cu/Fe rich precipitate particles. Wherever possible, these particles were tested for their microhardness. Hardness data of several Al-Li 2090 and Weldalite 049 specimens tested clearly exhibited that these particles had distinctly higher hardness than the matrix aluminum rich material , about 120 - 145 HV for matrix and 190-370 HV for the precipitate particles.

In case of Al-Li 2090 , vintage 1 , 100589, the as received material on microstructural examination shows typical pancake type microstructure with characteristic bead like or a necklace structure , with few precipitates only inside the interior of the grains. The localized precipitation at the grain boundaries , figure 8 , appears to produce the precipitate free zones PFZ areas. This causes lithium depletion and possibly is responsible for weakness and LOX impact sensitivity of these Al-Li materials. The localized behavior , and enhanced effect of the PFZ's can be better observed using differential interference contrast DIC microscopy. Effects of this and possible localized behavior at the grain boundaries are shown in figure 9. It is to be noted that the extent of the PFZ and the extent of the precipitate formation seems reduced from vintage 1 to vintage 3 material, as also is seen less LOX impact sensitivity in these materials. These effects could also be related to processing conditions, less inclusions, and trace elements such as Na,K,Ca,B etc. (25). The presence of possible PFZ's is very sparse and highly isolated when detected in case of Weldalite 049 alloys . It thus is indicative that the localized precipitation behavior , the PFZ, and ofcourse , the nature of the precipitating phases , all are contributing to the LOX impact compatibility of these Al-Li materials. With x-ray diffraction in some analyses, the aluminum rich matrix was indexed but other phases due to their small amounts could not be identified. As earlier discussed, the SEM analyses could not detect lithium and its related phases with any microprobe analyses, but identified the Cu/Fe rich precipitates in the materials that were examined.

TABLE 2A. ALUMINUM ALLOY IMPACT RESULTS - 2090 LOX IMPACT TEST

<u>MATERIAL</u>	<u>14.7 psi</u>	<u>50 psi</u>	<u>100 psi</u>	<u>200 psi</u>	<u>500 psi</u>	<u>600 psi</u>	<u>1,000 psi</u>
2090 - T8E41 0.063" thick 100496 Vintage 1	No Reactions 20 Impacts	2 Reactions 37 Impacts	5 Reactions 20 Impacts		1 Reaction 1 Impact Extremely Violent		1 Reaction 1 Impact Extremely Violent Reaction
2090 - T8E41 0.063" thick 100525 Vintage 1	No Reactions 20 Impacts	7 Reactions 20 Impacts					1 Reaction 3 Impacts Extremely Violent Reaction
2090 - T8E41 0.125" thick 100589 Vintage 1	No Reactions 20 Impacts	1 Reaction 60 Impacts	1 Reaction 33 Impacts	2 Reactions 45 Impacts	2 Reactions 12 Impacts		
2090 - T8E4 0.25 mach. to 0.125" 100797 Vintage 2		0 Reaction 100 Impacts			0 Reaction 25 Impacts		1 Reaction 20 Impacts
2090 - T83 0.125" thick 100796 Vintage 1			3 Reactions 20 Impacts 2 Reactions 20 Impacts		1 Reaction 1 Impact Very Violent		1 Reaction 1 Impact Very Violent
2090 - T8E41 0.125" thick 100796 Vintage 3		0 Reactions 100 Impacts					0 Reactions 20 Impacts

VIII-10

VIII-11

TABLE 2B. ALUMINUM ALLOY IMPACT RESULTS - WELDALITE LOX IMPACT TEST

<u>MATERIAL</u>	<u>14.7 psi</u>	<u>50 psi</u>	<u>100 psi</u>	<u>200 psi</u>	<u>500 psi</u>	<u>600 psi</u>	<u>1,000 psi</u>
Weldalite T4 0.125" thick 100524	No Reactions 20 Impacts	No Reactions 20 Impacts				No Reactions 20 Impacts	No Reactions 20 Impacts
Weldalite T8 0.125" thick 100781							0 Reactions 20 Impacts
Weldalite T8 0.125" thick 100781 Rerun 100910		No Reactions 100 Impacts					2 Reactions 18 Impacts Violent Reaction

TABLE 2C. ALUMINUM ALLOY IMPACT RESULTS - 2219 LOX IMPACT TEST

<u>MATERIAL</u>	<u>14.7 psi</u>	<u>50 psi</u>	<u>100 psi</u>	<u>200 psi</u>	<u>500 psi</u>	<u>600 psi</u>	<u>1,000 psi</u>
2219-T81	No Reactions	No Reactions				No Reactions	No Reactions
0.129" thick	20 Impacts	20 Impacts				20 Impacts	20 Impacts
100526							
2219-T81	No Reactions	No Reactions	No Reactions	No Reactions	No Reactions	No Reactions	No Reactions
0.063" thick	20 Impacts	20 Impacts	20 Impacts	20 Impacts	20 Impacts	20 Impacts	20 Impacts

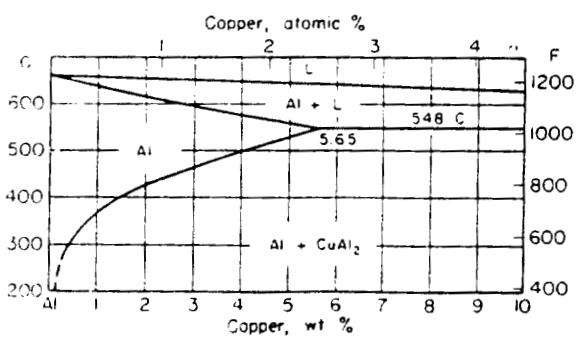
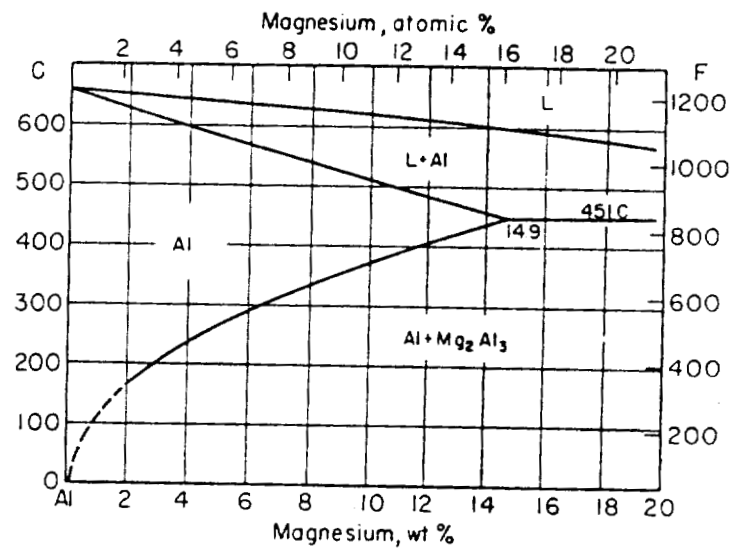
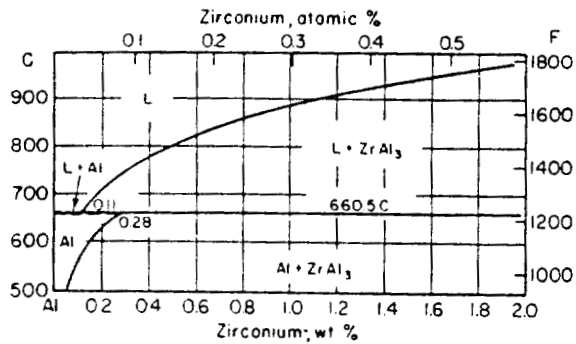


Fig.1 Section of Al-Zr, Al-Mg and Al-Cu phase diagrams showing limits of solid solubility (19).

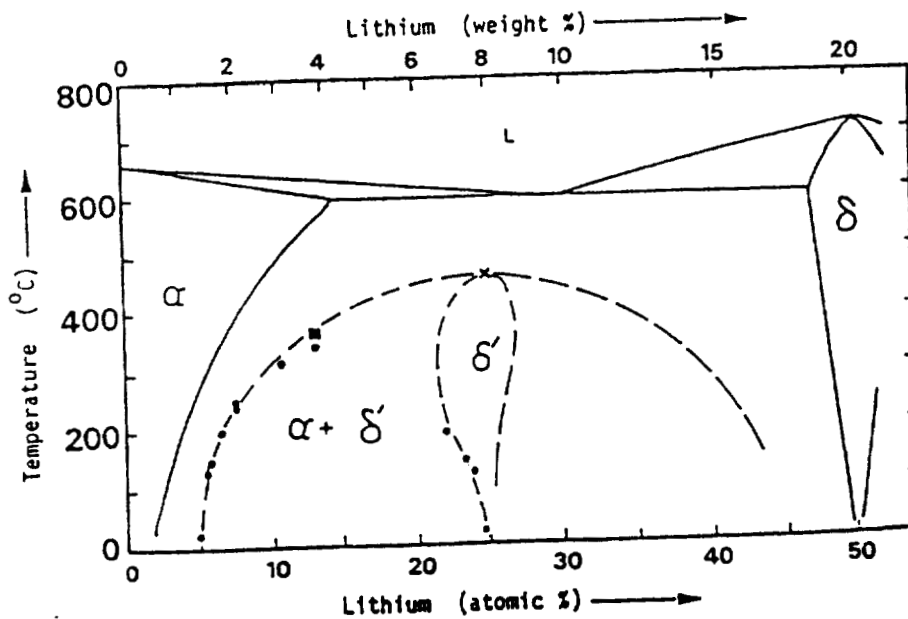
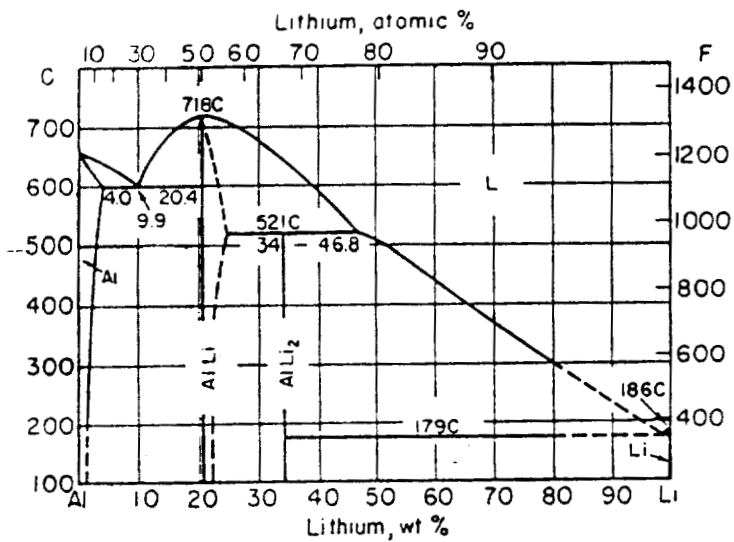
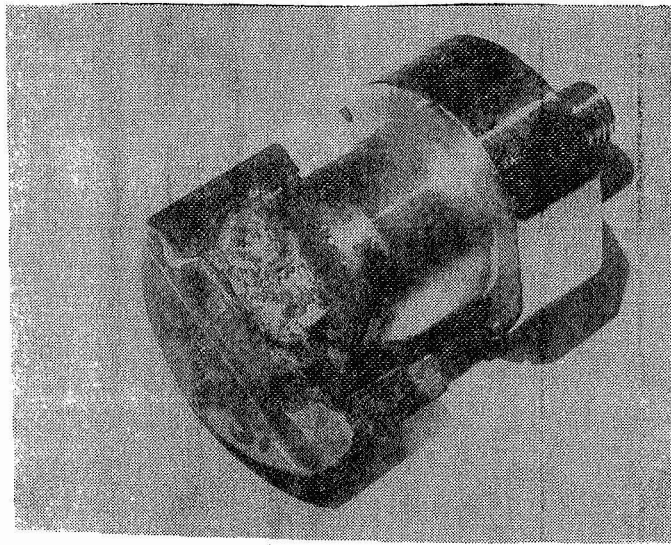


Fig.2 Al-Li phase diagram and section of the system showing presence of δ' (Al_3Li). (22).

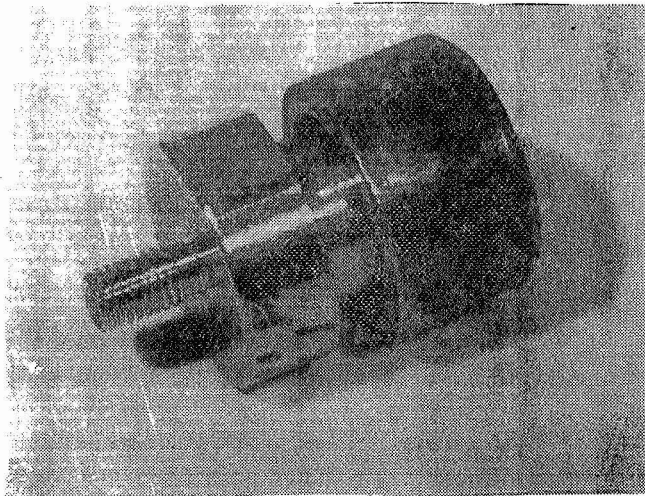
ORIGINAL PAGE
BLACK AND WHITE PHOTOGRAPH



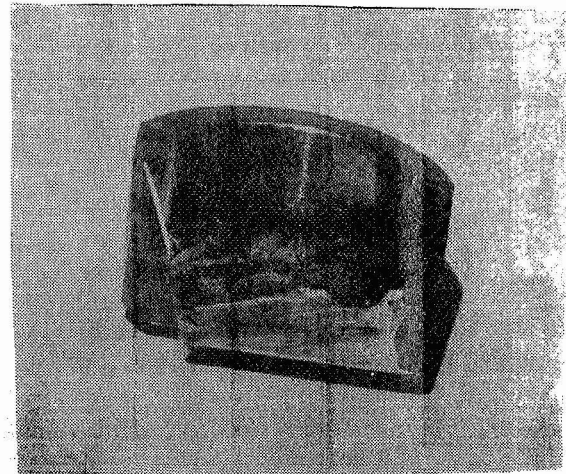
ORIGINAL PAGE IS
OF POOR QUALITY

(a)

Fig. 3a Al-Li 2090-100796, vintage 1, LOX tested , 500 psi.,
cut-away section of the reacted specimen



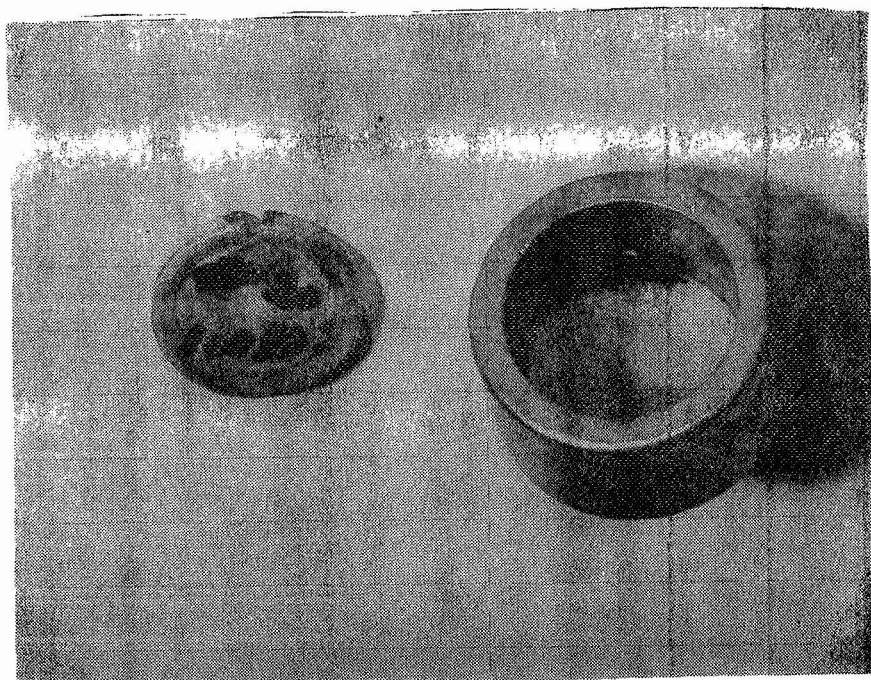
(b)



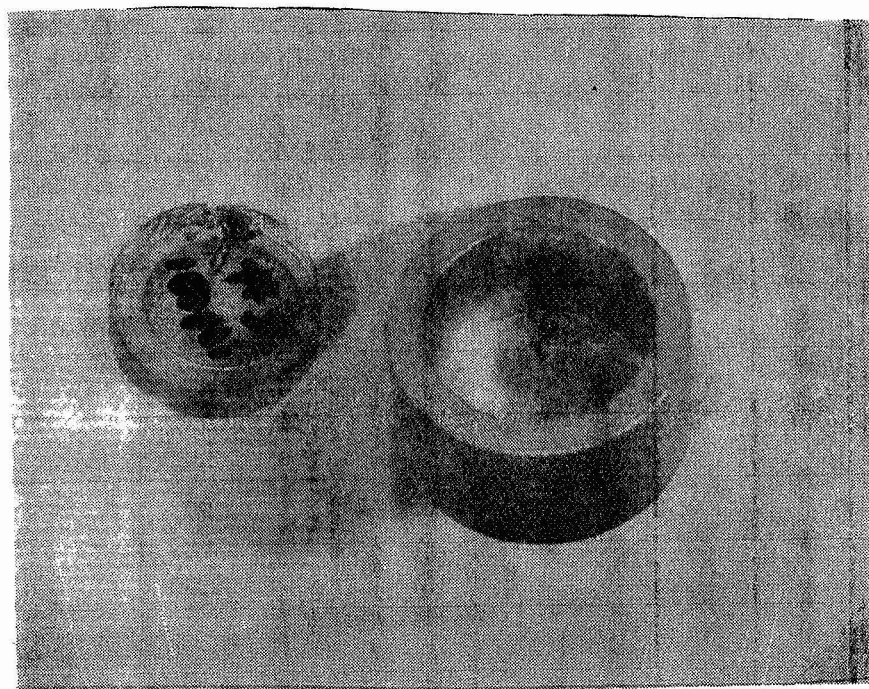
(c)

Fig. 3b and 3c Al-Li 2090-100796, vintage 1, LOX tested
100 psi., As reacted (b), and cut-away of the same (c).

ORIGINAL PAGE
BLACK AND WHITE PHOTOGRAPH



(a)



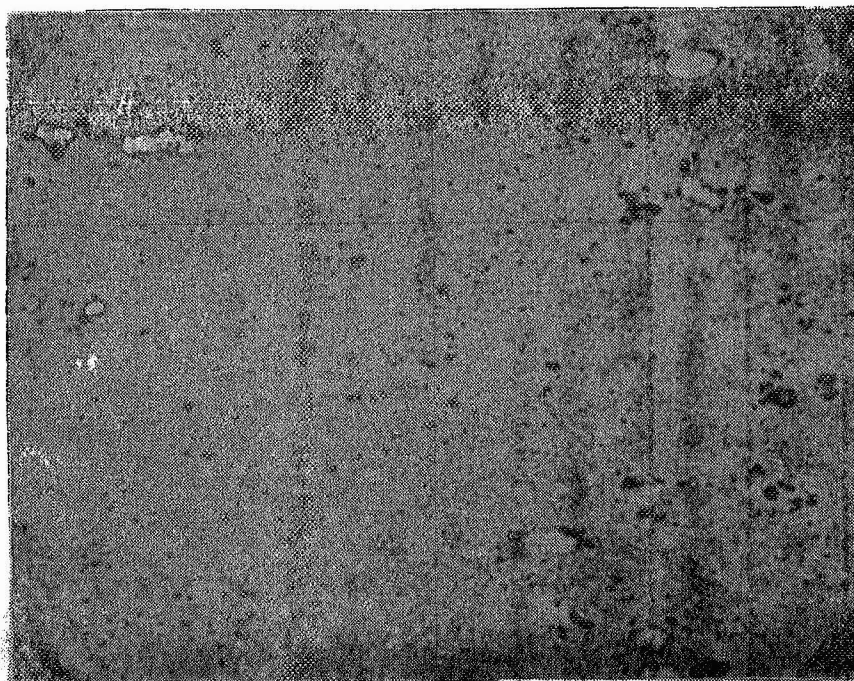
(b)

Fig.4 Al-Li 2090 LDX tested , at 100 psi. As reacted
impact test specimen and test cup, (a)3/20 (b)2/20

VIII-16

ORIGINAL PAGE IS
OF POOR QUALITY

ORIGINAL PAGE
BLACK AND WHITE PHOTOGRAPH



(a)



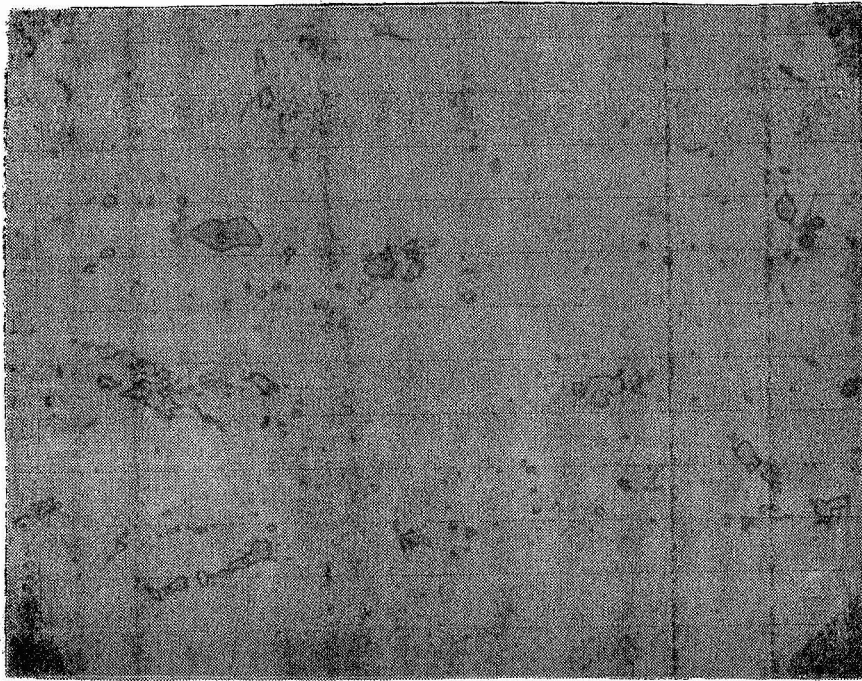
(b)

Fig.5 Al-Li Weldalite 049 As received (a) transverse section , 1000x (b) longitudinal section, 200x. This material shows no reaction on LOX testing.

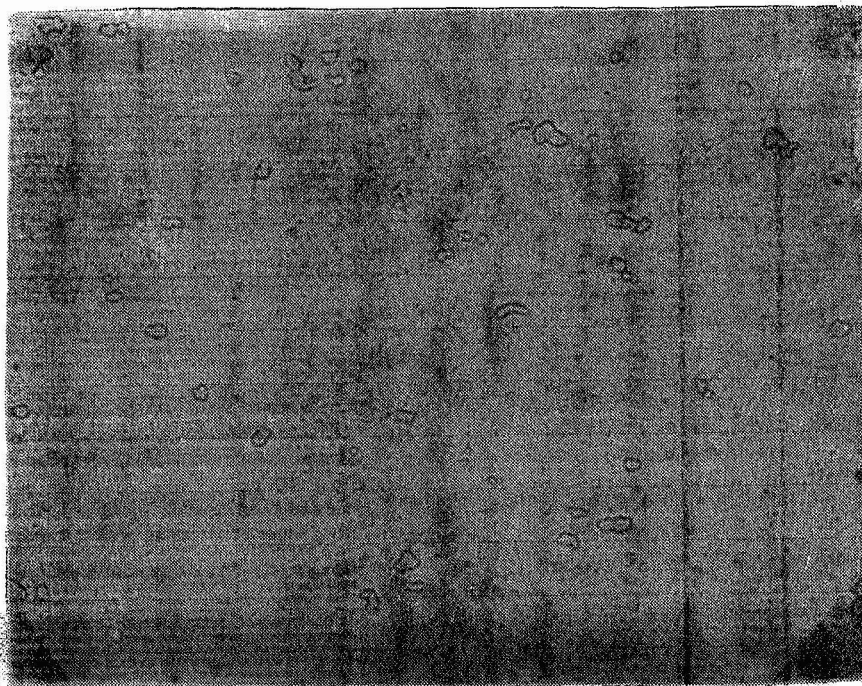
VIII-17

ORIGINAL PAGE IS
OF POOR QUALITY

ORIGINAL PAGE
BLACK AND WHITE PHOTOGRAPH



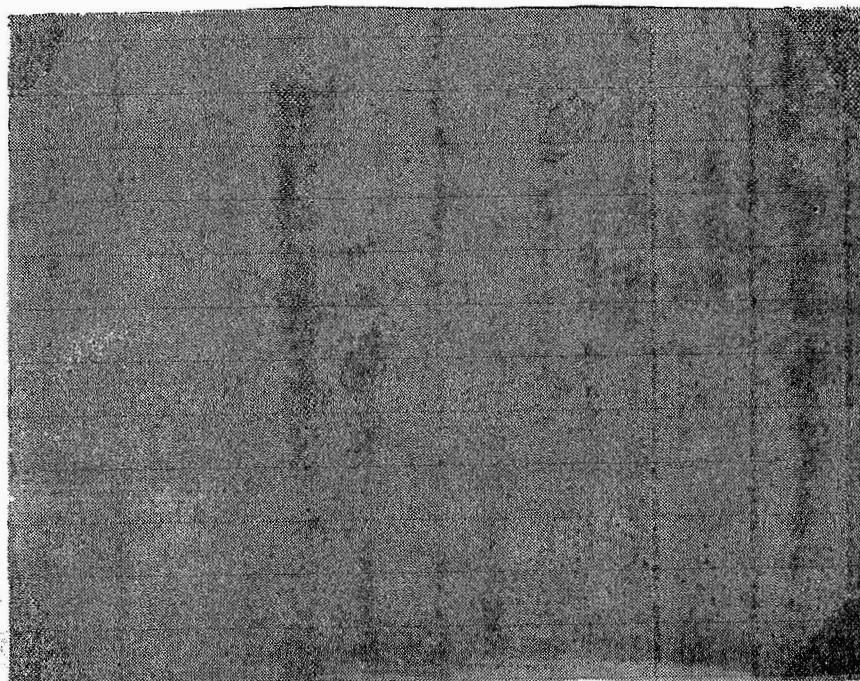
(a)



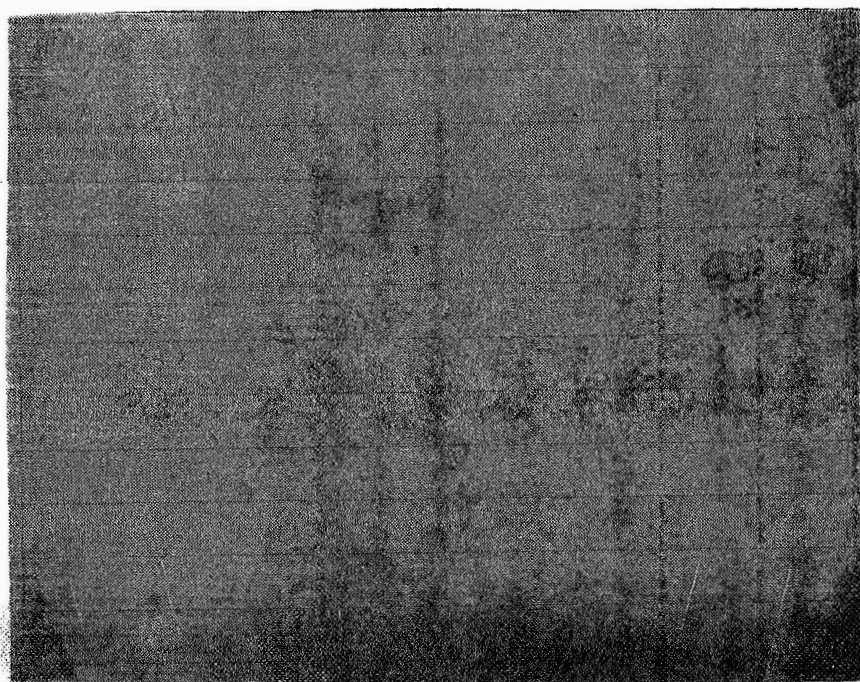
(b)

Fig.6 Al-Li Weldalite 049 (T4) As received
(a) longitudinal section Graff/Sargent 1000x
(b) transverse section Graff/Sargent 400x.

ORIGINAL PAGE
BLACK AND WHITE PHOTOGRAPH



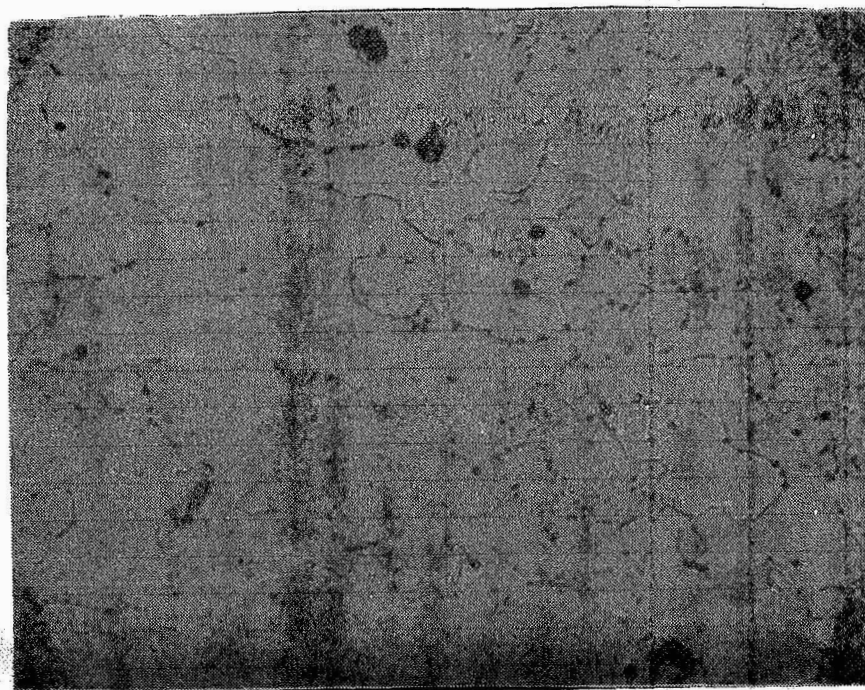
(a)



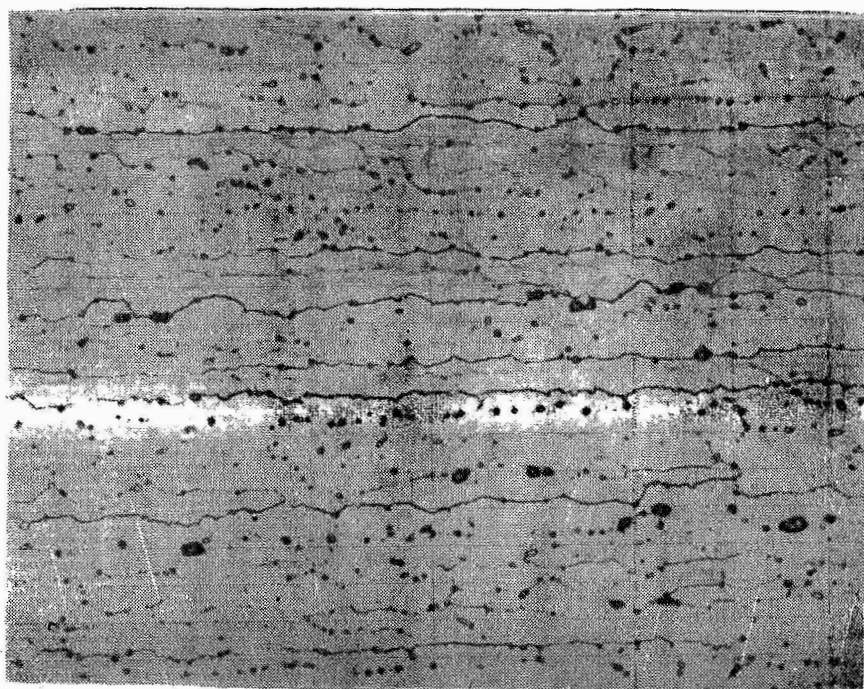
(b)

Fig.7 Al-Li 2090 - 100797 (a) LOX tested, 50 psi.
(b) LOX tested , 500 psi. ; Unreacted
Graff/Sargent, 1000x .

ORIGINAL PAGE
BLACK AND WHITE PHOTOGRAPH



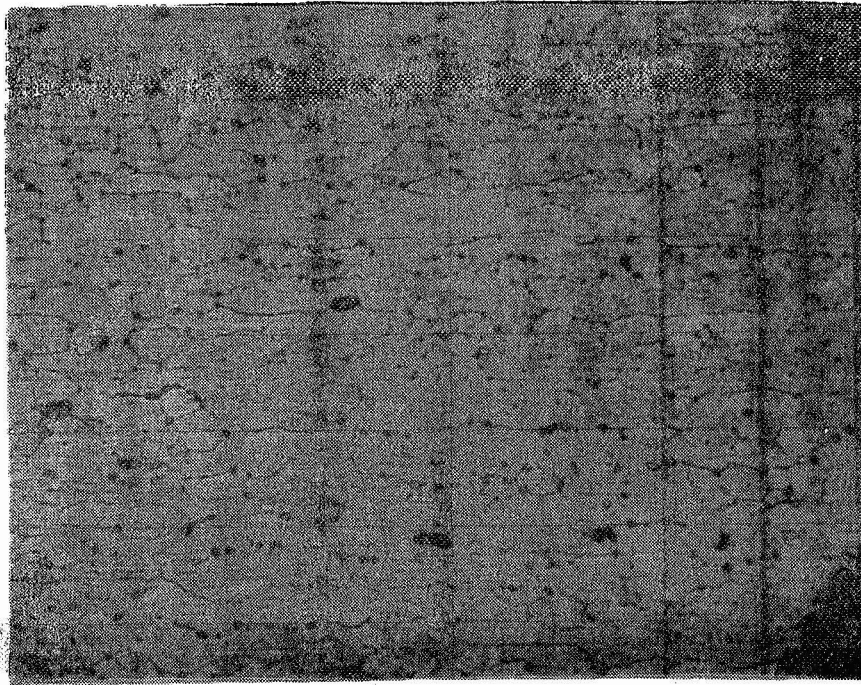
(a)



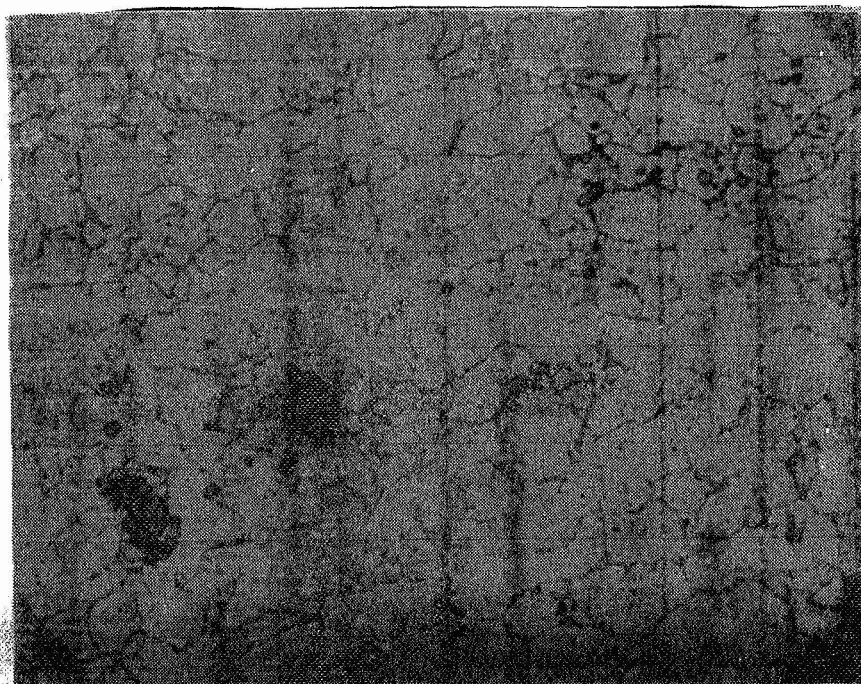
(b)

Fig.8 Al-Li 2090-100589 As Received (a) longitudinal section and (b) transverse section, 1000x .

ORIGINAL PAGE
BLACK AND WHITE PHOTOGRAPH



(a)



(b)

Fig.9 Al-Li 2090 LOX tested micrographs showing possible
PFZ's and localized behavior at the grain
boundaries (a) 2090-100796 , 100 psi. and
(b) 2090-1000797 , 500 psi; unreacted .

VIII-21

ORIGINAL PAGE IS
OF POOR QUALITY

C. Surface Studies and Analyses of the Reaction Products

XPS (ESCA), SIMS and Auger Spectroscopy (AES) techniques were used in analyses of reaction products after LOX impact testing in cases where severe reaction had caused the melting of not only of the test material but also of the test cup and the striker pin in the test assembly. In these , the test specimen , the inconel test cup and the test pin in examination of the section of the reacted specimen exhibited severe oxidation and gouging of inconel 718. In analyses of the grayish material of the reaction product, the characteristic peaks of these in ESCA related to mostly Al and O and small amounts of Cr. Al to O ratio in reaction product is found to be 0.64, close to that of Al/O ratio in Al_2O_3 . These analyses , also, could clearly detect the presence of Li, at 55 ev , and also appear close to peaks for LiO . In SIMS and Auger Spectroscopy, the dark gray material of the reaction product was analyzed . In these AES analyses, the surface charging was quite severe making useful signal analyses impossible. However, this in turn confirmed the material to be Al_2O_3 which is highly insulating in nature. SIMS and ESCA analyses confirm the presence of lithium and that the reaction product is Cr contaminated aluminum oxide. The identification of lithium and lithium related phases, for microanalyses and imaging of phases effectively causing the sensitivity could not be analyzed with SIMS equipment available at MSFC. A survey of related studies in the literature (26-29) for microanalysis of precipitates in aluminum lithium alloys indicates difficulties related to these analyses , and that these quantitative analyses possibly can be carried out with Scanning Ion Microprobe or with SIMS equipment with direct imaging capabilities for surface analyses of the bulk specimens or with Electron Loss Spectroscopy studies.

V. CONCLUSIONS AND RECOMMENDATIONS

Based on the LOX compatibility evaluations of the Al-Li 2090 and Weldalite 049 alloys and their relationships with the microstructural characterizations and the surface studies carried out in this study, the following conclusions can be made. Recommendations for further work are also made .

1. While Weldalite 049 is mostly seen as compatible in LOX impact tests, in Al-Li 2090 lithium makes this material more sensitive at grain boundaries in some cases due to PFZ's.
2. The Al-Li 2090 in LOX impact tests has shown improved behavior in vintage 2 material and has no reaction in vintage 3 ; the several factors related to this could be due to processing conditions and less inclusions, cleanliness , lower Na, K, etc.
3. The reactivity or the LOX compatibility behavior as related to microconstituents in case of Al-Li 2090 appears to be due to the strengthening phases such as δ' (Al_3Li) , θ' , and T_1 .
4. The strengthening behavior in these Al-Li alloys is mainly due to order hardening , and involves different particle sizes, shapes and distributions. In addition, there can be gross inhomogeneities such as PFZ's. The additional mechanisms of modulus strengthening and coherency strengthening to some extent also affect the strengthening behavior of these materials. The presence of Zr inhibits recrystallization in these materials and precipitates the β' phase.
5. The δ' phase is L_{12} ordered strengthening phase ; the coherency strengthening is not a very valid factor in strengthening as the misfit between the matrix and the δ' phase is very low about 0.1 %. In addition to the very fine strengthening phase as small δ' nearly spherical precipitates, T_1 (Al_2CuLi) and T_2 (Al_5CuLi) can precipitate in plate like morphology. The sizes and amounts of these phases are small and their characterization requires selected area diffraction pattern (SADP) and transmission electron microscopy (TEM) analyses. The localized precipitates in the metallographic analyses carried out are seen as

coarse Cu/Fe rich precipitates in a certain necklace type configuration in case of some Al-Li 2090 alloys. In addition, some of these precipitates could also be present in some case on secondary grain boundaries.

6. In Weldalite 049 type Al-Li-Cu-Mg-Ag alloys, other multiple phases such as T_1 and S' (Al_2CuMg) can coprecipitate with the δ' . The additions of Ag and Mg are also considered to be giving another phase Λ . Additionally, T_2 and T_B ($Al_{7.5}Cu_4Li$) phases can precipitate. The several dislocation interactions with these multiple phases further affect the properties of these materials.

RECOMMENDATIONS FOR FURTHER WORK :

1. The SEM microprobe phase analyses should be carried out as far as possible to identify any phases without Li that possibly could be detected with these analyses .
2. The LOX impact compatibility would be related to the amount of Li and Cu and a critical ratio in these commercial alloys. These variants in chemistry should be analyzed to identify and understand these effects.
3. The LOX impact compatibility and the sensitivity at grain boundaries needs to be analyzed in more detail and in sufficient detail. For this DIC differential interference contrast microscopy can be further utilized.
4. The grain boundary effects and any sensitivity in these Al-Li alloys has been searched by some authors for effects of Na, K, and P. Ca and B could also be affecting the sensitivity behavior. This needs to be analyzed for any effects on LOX compatibility .
5. The effects and analyses of the several microconstituents in these commercial Al-Li alloys deserve further detailed study with microanalytical phase studies using TEM as necessary , and possibly with differential scanning calorimetry DSC techniques.
6. These above studies should be used to coorelate and completely understand the LOX impact compatibility of these newer and significant low density, high specific strength Al-Li alloys.

REFERENCES

1. W.E. Frazier, E.W. Lee, M.E. Donnellan and J.J. Thompson, " Advanced Lightweight Alloys for Aerospace Applications ," J. Met. 41 (5), 1989, pp. 22-26.
2. J. Wadsworth and F.H. Froes, " Developments in Metallic Materials for Aerospace Applications " , J. Met. 41 (5) , 1989, pp. 12-19.
3. " Alcoa Alithalite Alloy 2090 Technical Information," Proceedings of 17th Intl. SAMPE Technical Conference 1985, Oct. 22-24, Kiamesha Lake, New York.
4. R.J. Rioja, B.A. Cheney, R.S. James, J.T. Staley and J.A. Bowers, " Structure Property Relationships in Al-Li Alloys : Plate and sheet Products," WESTEC 1989 conference presentation. To be published.
5. A.P. Divecha, S.D. Karmarkar, " The Search for Al-Li Alloys, " Advanced Materials and Processes Inc. , Metal Progress, 10/86, pp. 74-79.
6. P.E. Bretz and R.R. Sawtell, " Alithalite Alloys: Progress, Products and Properties," In Al-Li Alloys III, The Institute of Metals, 1986, pp. 47-56.
7. R.F. Ashton, D.S. Thompson, E.A. Starke Jr. and F.S. Lin, " Processing of Al-Li-Cu(Mg) Alloys," In Al-Li III, The Institute of Metals, 1986, pp. 66-77.
8. J.R. Pickens, F.H. Heubbaum, T.J. Langan and L.S. Kramer, " Al-4.5-6Cu-1.3Li-.4Mg-.4 Ag-.14Zr Alloy Weldalite 049," To be published Proceedings of the Fifth Intl. Al-Li Conf., March 1989.
9. T.J. Langan and J.R. Pickens, " Identification of Strengthening Phases in Al-Cu-Li Alloy," To be published Proceedings of the Fifth Intl. Al-Li Conf., March 1989.
10. I.J. Polmear, " Design and Development of a New High Strength Aluminum Alloy, " Materials Australasia, July/August 1986, pp. 22.
11. E.W. Lee and W.E. Frazier, " The Effect of strength on the Microstructure and Mechanical Properties of 2090 Al-Li," Scripta Metallurgica, Vol. 22, 1988, pp. 53-57.

12. J. Glazer, S.L. Verzasconi, R.R. Sawtell and J.W. Morris, Jr., " Mechanical Behavior of Aluminum-Lithium Alloys at Cryogenic Temperatures," Metall. Trans. A, 1987, Vol.18 A, pp. 1695-1701.
13. K.T. Venkateswara Rao, W. Yu and R.O. Ritchie, " Cryogenic Toughness of Commercial Aluminum-Lithium Alloys: Role of Delamination Toughening, " Metall. Trans. A, Vol. 20 A, March 1989, pp. 485-497.
14. K.T. Venkateswara Rao, H.F. Hayashigatani, W. Yu and R.O. Ritchie , " On the Fracture Toughness of Aluminum-Lithium 2090-T8E41 At Ambient and Cryogenic Temperatures, " Scripta Met., vol.22 , 1988, pp. 93-98.
15. R.C. Dorward, "On the Mechanical Properties and Stress Corrosion Resistance of Ternary and Quarternary Al-Li-Cu-Mg Alloys, " Mat. Sci.and Eng., Vol. 84, 1986, pp. 89-95.
16. R.P. Martukanitz, C.A. Natalie and J.O. Knoefel, " The Weldability of an Al-Li-Cu Alloy, " J. Met. , Nov. 1987 pp. 38-42.
17. NASA Office of Space Transportation Systems, NHB 8060.1B , In " Ambient Liquid Oxygen and Pressurized Liquid and Gaseous Oxygen Mechanical Impact Test, " Test 13 of - Flammability, Odor, and Offgassing Requirements and Test Procedures for Materials in Environments that Support Combustion, NASA 1981.
18. ASTM D 2512-82, " Standard Test Method for Compatibility of Materials with Liquid Oxygen Impact Sensitivity Threshold and Pass-Fail Techniques, " Am. Soc. for Testing and Materials, 1982.
19. K.R. VanHorn Ed. , " Aluminum, Properties, Physical Metallurgy and Phase Diagrams, " Vol. I , ASM, 1967.
20. C. Sigli and J.M. Sanchez, " Calculation of Phase Equilibrium in Al-Li Alloys, " Acta Metall., V.34, No. 6, 1986, pp. 1021-1028.
21. H.M. Flower and P.J. Gregson, " Solid State Phase Transformations in Aluminum Alloys Containing Lithium," Mat. Sci. and Tech., Feb. 1987, Vol.3, pp. 81-90.

22. F.W. Gayle and J.B. Vandersande, " Al (Li,Zr) or α' phase in Al-Li-Zr System, " In Al-Li Alloys III, The Institute of Metals, 1986, pp. 376-385.
23. P.J. Gregson and H.M. Flower, " Phase Transformations in Al-Li-Cu-Mg-Zr Alloys, " Aluminum Technology, 1986, PP. 423-428.
24. I.J. Polmear and M.J. Couper, " Design and Development of an Experimental Wrought Aluminum Alloy for Use at Elevated Temperatures, " Metall. Trans. , Vol. 19A, 1988, pp. 1027-1035.
25. D. Webster, " The Effect of Low Melting Point Impurities on the Properties of Aluminum-Lithium Alloys, " Metall. Trans. , Vol. 18A, 1987, pp. 2181-2193.
26. C. Jardin and R. Robert, " AES and ELS Characterizations of Surface Oxides on Al-Li Alloys," Applied Surface Science 35, 1988-89, pp. 495-506.
27. D.B. Williams, R. Levi-Setti, J.M. Chambala, Y.C. Wang and D.E. Newbury, " Microanalysis of Precipitates in Aluminum-Lithium Alloys with a Scanning Ion Microprobe ," Applied Surface Science 37, 1989, pp. 78-94.
28. B. Dubost, J.M. Lang and F. Degreve, " Metallography and Microanalysis of Aluminum-lithium Alloys by Secondary Ion Mass Spectrometry SIMS, " In Al-Li Alloys III , The Institute of Metals, 1986, pp. 355-359.
29. L.A. Larson, M. Avalos-Borja and P.P. Pizzo, " A Surface Analytical Examination of Stringer Particles, " In Al-Li II , Eds E.A. Starke, Jr. and T.H. Sanders, AIME, Warrendale, 1984, pp. 303-312.

1989

NASA/ASEE SUMMER FACULTY FELLOWSHIP PROGRAM

MARSHALL SPACE FLIGHT CENTER
THE UNIVERSITY OF ALABAMA

BACKGROUND STUDIES IN GAS IONIZING
X-RAY DETECTORS

Prepared by:	Hudson B. Eldridge
Academic Rank:	Associate Professor
University and Department:	University of Central Arkansas Physics Department
NASA/MSFC:	
Laboratory:	Space Sciences
Division:	Astrophysics
Branch:	X-Ray Astronomy
MSFC Colleague:	Martin C. Weisskopf
Date:	July 28, 1989
Contract No.:	The University of Alabama in Huntsville NGT-01-008-021

ABSTRACT

The background response of a gas ionizing proportional X-Ray detector is estimated by solving the one dimensional photon transport equation for two regions using Monte Carlo techniques. The solution was effected using the SSL VAX 780 and the CRAY XMP computers at Marshall Space Flight Center. The isotropic photon energy spectrum encompassing the range from 1 to 1000 KeV incident onto the first region, the shield, is taken so as to represent the measured spectrum at an altitude of 3 mb over Palastine, Texas. The differential energy spectrum deposited in the gas region, xenon, over the range of 0 to 100 KeV is written to an output file. In addition, the photon flux emerging from the shield region, tin, over the range of 1 to 1000 KeV is also tabulated and written to a separate file. Published tabular cross sections for photoelectric, elastic and inelastic Compton scattering as well as the total absorption coefficient are used. Histories of each incident photon as well as secondary photons from Compton and photoelectric interactions are followed until the photon either is absorbed or exits from the regions under consideration. A study is made of the effect of shielding thickness upon the energy spectrum deposited in the xenon region for this background spectrum incident upon the tin shield.

ACKNOWLEDGMENTS

I am grateful for the opportunity that I have had to participate in the Summer Faculty Fellowship Program in the Space Sciences Laboratory, Astrophysics Division, X-Ray Astronomy Branch under the direction of Dr. Martin C. Weisskopf. My appointed task for the summer could not have been completed without the competent advice and kind assistance of Dr. Brian Ramsey from the same laboratory.

During the course of my summer, many helpful discussions were provided by Drs. Marshall Joy, Ron Elsner, and Steve O'Dell. The computations required during my summer visit were possible only because the expertise of Tom Schlenker, Tom Brister, Debbie Bowerman, and Debbie Hager of Grumman Aircraft Corporation was made so readily available.

I would like to thank Dr. Gerald R. Karr, whose attention to all details of the program's administration prior to, during, and after, made my visit to Marshall Space Flight Center an enjoyable, intellectually stimulating, and professionally rewarding experience. I am grateful to the National Aeronautics and Space Administration and the American Society for Engineering Education for their support of the Summer Faculty Fellowship Program.

INTRODUCTION

X-ray sources that are of interest to astrophysical research appear very faint when observed from the vicinity of earth. This quite low signal intensity puts severe constraints onto the detectors, especially imaging types, to be used in planned orbiting observatories. In the interest of increasing the signal to noise in future detector design by reducing the background, a study was undertaken of the background sensitivity of a possible type of detector being considered for the AXAF project scheduled for the near future. There are advantages to using a position sensitive proportional detector and considerable development of this type of counter has transpired. As a first step in the study of the background to be expected in such a detector from the ambient photon flux, a one dimensional geometry calculation of the transport through two regions was made.

The mathematical description of the transport of so called "Hard X-rays" through matter yields integral equations that become unwieldy in even the simplest of geometrical arrangements. Instead of an analytic solution, it is frequently adequate to perform a stochastic or Monte Carlo type calculation. In the Monte Carlo calculation, individual photon histories are catalogued as they transit the various media characterized by its cross sections. The result of such a calculation could be either the energy spectrum of photons at a surface in the medium or the energy deposited due to the transport of photons into a volume of the medium.

Central to a Monte Carlo calculation is a sequence of random (or at least pseudo-random) numbers. The sequence used in this calculation was generated by the FORTRAN routine RAN(J) on the SSL VAX 780 or RANF() on the CRAY. In order to test just how random this sequence was, 10 million random numbers were generated and sorted into 100 intervals evenly distributed from 0 to 1. The number in each bin, divided by the 10 million, could be interpreted as the probability of occurrence of a number within each interval. Such a distribution is shown in Figure 1 and it does indeed appear quite uniform. Figure 2, however, shows the deviation from the average of each bin which is a more severe test of randomness and, while the deviations are quite small, some of the "Pseudo" of the randomness of the sequence may be seen.

THE INCIDENT X-RAY SPECTRUM

The incident photon spectrum was taken as:

$$dI/dE = 26(p/3)^{0.2}E^{-1.97} \text{ photons cm}^{-2}\text{s}^{-1}\text{KeV}^{-1}. \quad (1)$$

An expression which reasonably describes the energy spectrum measured at balloon altitudes over Palastine, Texas (Dean and Dipper 1981). The zenith angle of the photons incident upon the horizontal plane (the tin sheet) was considered isotropic. At a given pressure, the above expression may be considered, when properly normalized over the interval $[0,1]$, the probability density in the variable E . The prescription for selecting the energies at random so that as the number of selections approach infinity the energies will be distributed as the above expression yields:

$$1-r = (E_0/E)^{0.97} \quad (2)$$

Where r is a member of a random sequence over the interval $[0,1]$ which, in practice, is a pseudo-random sequence generated by a computer. E_0 is a cutoff energy which is required for normalization because the expression does not remain finite as E approaches zero. Also since $1-r$ is itself just a random sequence it can be replaced by r . The expression may be solved for E in terms of r and then the energies (E) calculated from the resulting formula will be distributed according to Equation (1). Inverting Equation (2) yields:

$$E = (1.0/r)^{1.031} \quad (3)$$

To verify the validity of the Monte Carlo scheme a program was written to pick one million energies over the interval 1 to 1000 KeV using Equation (3) and the RAN(J) random number generator on the SSL VAX 780 computer. These energies were sorted into 10 KeV intervals to simulate the original spectrum, Equation (1).

Since the same distribution can be calculated analytically by just integrating Equation (1) over each of the 10 KeV intervals, this was done and TABLE 2 shows the comparison of the one million history Monte Carlo simulation with the analytic calculation.

TABLE 1 - COMPARISON OF MONTE CARLO (A MILLION HISTORIES)
WITH THE ANALYTIC CALCULATION OF
THE INCIDENT ENERGY SPECTRUM

Interval	Monte Carlo	Analytic
00.00 -> 10.99	23.4613	24.1833
10.99 -> 20.98	1.8475	1.2211
20.98 -> 30.97	0.4256	0.4404
30.97 -> 40.96	0.2210	0.2278
40.96 -> 50.95	0.1344	0.1396
50.95 -> 60.94	0.0912	0.0944
60.94 -> 70.93	0.0668	0.0681
.....
.....
.....
930.07->940.06	0.0003068	0.0003648
940.06->950.05	0.0003536	0.0003572
950.05->960.04	0.0002990	0.0003499
960.04->970.03	0.0003510	0.0003428
970.03->980.02	0.0003198	0.0003359
980.02->990.01	0.0003276	0.0003292
990.01->1000.0	0.0002782	0.0003227

In the interest of brevity, the entire spectrum from 1 to 1000 KeV is not presented, only the beginning and the end. As may be noted by examining TABLE 2, 1 million histories are not adequate to represent the desired energy spectrum where the derivative of the curve is large (low energies) and where the magnitude of the flux is very small (high energies). Figure 3 shows a plot of the Monte Carlo simulation of the incident spectrum at the higher energies which is to be compared with Figure 4, the analytic calculation of the incident spectrum, integration of Equation (1) over each interval. Here again the inadequacy of a million histories is evident. Consequently, all subsequent Monte Carlo calculations made using this representation of the incident spectrum were made by compiling 10 million or more photon histories.

THE MEAN FREE PATH

A photon of given energy while traversing a medium, in contrast to a charged particle, does not have a well defined range or distance it travels before undergoing any one of a number of possible interactions with the medium. The number of photons, dN , that have an interaction within an infinitesimal distance dx is given by (Jenkins, Gould, and Gedcke, 1981):

$$dN = s N dx \quad (4)$$

Where s is the total cross section in inverse centimeters, x being in centimeters, and is a function of the photon's energy. N is the number of photons present at the position x . s is the sum of the cross sections for the photoelectric, Compton elastic, and Compton inelastic interactions. The energies being considered in this work are below the threshold for pair production.

Equation (4) may be rearranged as:

$$dN/N = s dx \quad (5)$$

This differential equation has the following solution:

$$N/N_0 = e^{-sx} \quad (6)$$

N_0 is the flux at $x = 0$ and the ratio N/N_0 is the probability that a photon travels the distance x before it undergoes an interaction and it is properly normalized for all positive x . This probability function may be solved for x using a random sequence r as has been done before:

$$x = -(1.0/s) \log_{10}(r) \quad (7)$$

Where the natural logarithms are to be used.

A FORTRAN program was written which computed a million values of x using Equation (7), with s taken as 1, using the function $RAN(J)$ to generate a random sequence. These values were

sorted into 10 equal intervals over the range of 0 to 1 and normalized for comparison with the analytic evaluation of Equation (6) over the same intervals. This comparison is shown in TABLE 2.

TABLE 2 - EVALUATION OF THE FREE PATH DISTRIBUTION
ONE MILLION HISTORIES

Interval	Monte Carlo	Analytic
0 -> .1	.094876	.0951626
.1 -> .2	.086219	.0861066
.2 -> .3	.077935	.0779126
.3 -> .4	.070229	.0704982
.4 -> .5	.063695	.0637894
.5 -> .6	.057681	.0577191
.6 -> .7	.052426	.0522263
.7 -> .8	.047123	.0472643
.8 -> .9	.042736	.0427513
.9 -> 1.	.038735	.0386902

It may be noted that the Monte Carlo calculation, compiling 1 million histories, differs from the analytic calculation by less than one percent over the entire range of the table.

THE CROSS SECTIONS

Values of the photoelectric, Compton elastic, Compton inelastic, and total cross sections as functions of the photon energy, were taken from the literature (Veigele 1973), multiplied by the density (Weast 1987), and entered into sequential data files for the SSL VAX 780 and the CRAY computers. There is a separate file for each element. The file structure, not all records, is shown below in TABLE 3. The fields in the first record are number of records in the table, and then the energies of the first four absorption edges. Each subsequent record contains five fields also: energy, total, photoelectric, Compton elastic, and Compton inelastic. The cross section values are in inverse centimeters. Logarithmic interpolation in both energy and cross section is made for energies between the tabulated values and, if the energy at which the cross section is desired falls exactly on an absorption edge, the greater value of the cross section is used. A separate program was written to check the accuracy of the cross section tables' transcription to the files from the journals.

TABLE 3 - STRUCTURE OF XENON CROSS SECTION FILE

```
37,4.782,5.104,5.453,34.56
1.0,60.593,60.593,.04607,.00002431
1.145,43.317,43.317,.04531,.00003054
1.145,47.573,47.573,.64531,.00003054
1.5,24.262,24.262,.04356,.00004682
2.0,11.843,11.816,.04056,.00007035
3.0,4.332,4.306,.03530,.0001162
4.0,2.128,2.098,.03054,.0001560
4.782,1.372,1.344,.02754,.0001848
4.782,40.312,40.06,.02754,.0001848
5.0,3.555,3.530,.02679,.0001923
5.104,3.380,3.355,.02654,.0001955
5.104,4.707,4.682,.02654,.0001955
5.453,3.931,3.906,.02529,.0002065
5.453,4.732,4.707,.02529,.0002065
6.0,3.656,3.630,.02371,.0002228
8.0,1.680,1.660,.01878,.0002754
```


DETECTOR SIMULATION

The straightforward calculation of the energy deposited in the xenon by the incident photon spectrum discussed above after it had passed through a layer of tin involves the solution of an integral equation wherein the integrand is not a simple function (Jenkins, Gould, and Gedcke, 1981). What is frequently done, instead of analytically solving the equation representing the response of the device, which of course would be generally preferred, is to compromise by performing a "Monte Carlo" or stochastic simulation of the process (Kalos and Whitlock, 1986), (Rubinstein, 1981), and (Hammersley and Handscomb, 1967). The first step in the simulation consists of dividing the physical process into a number of sequential events whose outcomes are governed by known probability distribution functions. The outcomes of these events are then determined by properly choosing from these probability distribution functions. The individual histories of the objects under study, in this case x-ray photons, are then compiled. These historical compilations are the desired solution which, in this case is, the differential energy spectrum deposited in the xenon layer by a photon spectrum after it first passes through a layer of tin.

For the particular case under study, the sequence of events in the history of a photon starts by having its energy selected according to Equation (3). Next the direction of the photon, polar angle only, is selected so as to reflect the isotropic flux onto a horizontal plane. This distribution, after considering the solid angle and the projection onto the horizontal plane factors, one has:

$$p(x) = 2x, \quad (8)$$

where x is the cosine of the polar angle. Equation (8) may be integrated to give:

$$r = x^2 \quad (9)$$

Where r is again a member of a random sequence. Equation (9) may be easily solved for the cosine of the polar angle, x , and that is what will be required in the program.

Once an energy and a polar angle for the photon is selected, it starts its migration through the tin region by having the tin

cross sections written into the active array. The photon history in the tin will be discussed first because, although, the historical sequence is the same in tin as it is in xenon, different historical facts are compiled in the two cases. The free path of this photon, the distance to where it interacts with the medium, is then computed from Equation (7) using the total cross section, s , in this case for tin, and its z coordinate is updated. The z coordinate, serves as a tag to determine which medium the photon is in at any time, is checked against the cumulative thicknesses of the media and, depending upon which medium it is in, the type of interaction is selected. The selection consists of picking a random number and comparing its magnitude with the cumulative fraction of the total cross section that the various types of reactions cross sections are at that energy. To consider a particular example, let's suppose that the total cross section is 100 while, at that same energy, the photoelectric, Compton elastic, and Compton inelastic are 80, 15, and 5 respectively. Now, if the random number selected is .54321, the interaction would be photoelectric; while, if the random number selected was .96752, the type of interaction would be Compton inelastic.

If the type of interaction turns out to be Compton elastic, a photon with the same energy is started again from this z and the polar angle is chosen uniformly over the interval 0 to π . If, however, the interaction was a Compton inelastic interaction, a new photon of reduced energy E_1 is started at that z . The energy of the emergent photon from this reaction site is given by (Jenkins, Gould, and Gedcke, 1981):

$$E_1 = E / (1.0 + (E/511) * (1.0 - \cos(x))) \quad (10)$$

Its polar angle is also chosen uniformly over the interval 0 to π . By choosing the polar angle uniformly here one deviates from reality somewhat for the higher energy photons. The Klein-Nashina formula (Jenkins, Gould, and Gedcke, 1981) should be used for the higher energy photons, which is not uniform in scattering angle but peaks in the forward direction.

Photoelectric interactions give a much wider choice of possibilities. If the photon energy is below the L-edge, it is considered absorbed in the xenon and the history ends in the tin. For energies above the L-edge but below the K-edge, only an L-vacancy could be excited in an atom when the photon was absorbed photoelectrically. The probability that an L-vacancy was formed was calculated from the "jump factors" (Jenkins, Gould,

and Gedcke, 1981) (Conde and dos Santos 1985) (McMaster, Kerr, Mallet, and Hubbell 1969) at the photon energy by comparing its magnitude with a member of the random sequence. This excited ion could then either decay radiatively, the emission of a fluorescent L photon, or it could decay non-radiatively, i.e. Auger processes. Which happened was determined by comparison of a random number and the fluorescent yield w_{KL} (Bambynek, Crasemann, Fink, Frund, Swift, Price, and Rao 1972). A photon whose energy was above the K-edge could create either a K- or L-vacancy in the atom that absorbed it. Which it created was determined by comparing the magnitude of a member of a random sequence and the jump factors for the K and L edges in the same fashion that was done in selecting the type of interaction from the cross sections as was described above. If the random number's magnitude was greater than the combined probability of creating a K- added to the probability of creating an L-vacancy, the photon was considered absorbed (it really excited a higher level but we are not considering them). If a K-vacancy was formed, the probability that it decayed by radiative emission, a fluorescent K photon, or non-radiative (Auger process) was taken as the fluorescent yield w_K (Bambynek, Crasemann, Fink, Frund, Swift, Price, and Rao 1972). It was then decided if the K photon emitted was a K-alpha or a K-beta using the yield ratios as the relative probability (Johnson and White 1985). In case it was a K-alpha, an excited ion was left at that position with an L-vacancy which would have to be dealt with after the K-alpha's history terminated.

In the tin region, a photon's history terminated when it was absorbed or escaped from the surface of the tin opposite the xenon i.e. was reflected back in the incident direction so as to make z less than zero. The energy spectrum of the photons that leave the tin into the xenon is compiled and serves as one of the output files.

The history of the photons that enter the xenon are continued in the same fashion as they were in the tin except they are restarted at the surface of the xenon with the same energy and direction they had when they left the tin. Their paths and interactions are now governed by the xenon cross sections and the absorbed energy spectrum is compiled for them.

RESULTS AND CONCLUSION

The present version of the program provides two output files: ENGDEPXE.DAT and ENGEXTIN.DAT. ENGDEPXE.DAT is the energy deposited in the xenon region over the range of 0 to 100 KeV in 1 KeV intervals. ENGEXTIN.DAT is the photon energy spectrum that penetrates through the tin shield and enters the xenon region. This spectrum covers the energy range of 1 to 1000 KeV in 100 10 KeV intervals. Figure 5 is a plot of the incident spectrum, Equation (3), superimposed over the spectrum exiting a 3/32 inch tin shield. It may be seen that, while the tin shield is very effective in attenuating the background flux at the lower energies, the shield is effectively transparent to the higher energy photons.

Figure 6 is a plot of the spectrum emerging from the tin shield and entering the xenon region except the vertical scale is expanded to emphasise the lower energy part. It may be noted that, except for the fluorescent tin peaks, there are no photons below 60 KeV which penetrate the shield. There is only one fluorescent K peak shown on the plot because the "resolution" of 10 KeV per channel does not permit separation of the K-alpha and K-beta peaks. There appears, on close inspection, even a very small L fluorescent peak in the first channel.

Figure 7 is a plot of the spectrum of the energy deposited in the xenon region (30.0 cm @ 1 atmosphere) for the same shielding as was present in Figure 3. Here both the K-alpha and K-beta fluorescent peaks of tin are resolved and a slight background is present due to higher energy photons that Compton scatter in either the shield or the xenon itself.

Figure 8 is a plot of the background spectrum deposited in the xenon with the tin fluorescence "turned off" for several thicknesses of the tin shield. It may be noted that for 0.1 cm of tin that there is a considerable background. Increasing the thickness of tin to 0.238125 (=3/32 inch) reduces this background considerably but that additional shielding does not appear to reduce the background significantly.

REFERENCES

- Dean, A.J and Dipper, N.A., "An evaluation of the background effects in actively shielded hard X-ray telescopes at balloon altitudes", Mon. Not. R. astr. Soc., 194, 219-227, (1981).
- Conde, C.A.N and dos Santos, J.M.F., "The Recessed Source Geometry For Source Excited X-Ray Fluorescence Analysis", Advances in X-Ray Analysis, 29, 545-550, (1985).
- Jenkins, R., Gould, R.W., and Gedcke, D., Quantitative X-Ray Spectrometry, Marcel Dekker, Inc., New York, (1981)
- McMaster, W.H., Kerr Del Grande, N., Mallett, J.H., and Hubbell, J. H. "Compilation of X-Ray Cross Sections", UCRL - 50174, TID-4500, UC - 34 Physics, Lawrence Radiation Laboratory, University of California, Livermore, California (1969).
- Bambynek, W., Crasemann, B., Fink, R.W., Freund, H.U., Mark, H., Swift, C.D., Price, R.E., Rao, P.V., "X-Ray Fluorescence Yields, Auger, and Coster-Kronig Transition Probabilities" Reviews of Modern Physics Vol. 44 Number 4., 716-814, (1972).
- Johnson, G.G and White, E.W., X-Ray Emission Wavelengths and KeV Tables for Nondiffractive Analysis, ASTM Data Series DS 46, American Society For Testing and Materials, (1985)
- Weast, R.C., Editor, Handbook of Chemistry and Physics, E136, CRC Press, Boca Raton, Florida, (1987).
- Kalos, M.H. and Whitlock, P.A., Monte Carlo Methods, John Wiley & Sons, New York, (1986).
- Rubinstein, R.Y., Simulation and the Monte Carlo Method, John Wiley & Sons, New York, (1981).
- Hammersley, J.M. and Handscomb, D.C., Les Methodes de Monte Carlo, Dunod, Paris, (1967).
- Veigele, W.J., Atomic Data, Vol. 5, No. 1, (1973)

APPENDIX I

FORTRAN PROGRAM TO SIMULATE AN X-RAY DETECTOR
ON SSL-VAX FILE: [ELDRIDGE]PHOTRAN2.FOR
ON CRAY FILE: EADS::HHBE219.PROGRAMS.FORTRAN(TRAN2)

PROGRAM PHOTRAN2

```
*COMPUTES THE ENERGY DISTRIBUTION DEPOSITED IN XENON AFTER
* TRANSPORT THROUGH A TIN PLATE SHIELD.
* USES SUBROUTINES; INCPHO, XSEC, MFP, XENON
* INPUT FROM KEYBOARD; TINTH, XENONTH, PRESSURE, N(number of histories)
  REAL*4 EP(50), SIGTOT(50), SIGPHO(50), SIGCCO(50), SIGCIN(50),
  2      EB(101), E, SIGT, SIGP, SIGC, SICI, X, INTENSITY(101),
  2      XSECT(2,5,50), EA(101), PHO(101)
  INTEGER*4 J
  COMMON J, EP, SIGTOT, SIGPHO, SIGCCO, SIGCIN, NXC, EB, INTENSITY,
  2      XSECT, TINTH, XENONTH, PRESSURE
  J=987654321      ! SEED THE RANDOM NUMBER GENERATOR
* READ IN FROM THE CONSOLE THE NUMBER OF PHOTONS THAT ARE TO BE DONE
  PRINT *, 'TYPE IN THICKNESS OF THE TIN IN CENTIMETERS(X.XXX)'
  READ (*,2) TINTH
  PRINT *, 'TYPE IN THICKNESS OF THE XENON IN CENTIMETERS(X.XXX)'
  READ (*,2) XENONTH
  PRINT *, 'TYPE IN THE XENON PRESSURE IN ATMOSPHERES(X.XXX)'
  READ(*,2) PRESSURE
  PRINT *, 'TYPE IN THE NUMBER OF PHOTON HISTORIES TO BE DONE(XXX)'
  READ (*,1) N
  1  FORMAT (I8)
  2  FORMAT (F12.6)
* READ IN THE CROSS SECTION DATA FROM FILES: TIXXSECT.DAT, XENXSECT.DAT
  OPEN (UNIT=1, FILE='[ELDRIDGE]TIXXSECT.DAT', STATUS='OLD')
  OPEN (UNIT=2, FILE='[ELDRIDGE]XENXSECT.DAT', STATUS='OLD')
  DO 50 L=1,2 !XSECT(L,M,N) L=THE ELEMENT; M=TYPE XSECT; N=ENERGY
  READ (L,1000) XSECT(L,1,1), XSECT(L,2,1), XSECT(L,3,1),
  XSECT(L,4,1),
  2      XSECT(L,5,1)
  NXC = INT(XSECT(L,1,1))
  DO 10 I=2,NXC !READ IN THIS ELEMENT'S CROSS SECTIONS
    READ (L,1000) (XSECT(L,M,I), M=1,5)
  10  CONTINUE
  50  CONTINUE
  1000 FORMAT(5F13.6)
  CLOSE (UNIT=1, STATUS='KEEP')
  CLOSE (UNIT=2, STATUS='KEEP')
* SET UP THE ENERGY BINS FOR THE OUTPUT SPECTRUM
```



```

        EB(1) = 0.0
        DO 20 I = 2, 101
            EB(I) = EB(I-1) + 1.0
20      CONTINUE
        EA(1) = 0.0
        DO I = 2, 101
            EA(I) = EA(I-1) + 10.0
        ENDDO
        DO 300 I = 1, N
            CALL INCPHO(E)
            IF (E) 100, 100, 400
*      IF(E .LT. 100.0) GOTO 100
400      CTHETA = SQRT(RAN(J))
*      SET CROSS SECTION TABLES FOR TIN
        NXC = INT(XSECT(1,1,1))
        DO IN=2,NXC
            EP(IN-1)=XSECT(1,1,IN)
            SIGTOT(IN-1)=XSECT(1,2,IN)
            SIGPHO(IN-1)=XSECT(1,3,IN)
            SIGCCO(IN-1)=XSECT(1,4,IN)
            SIGCIN(IN-1)=XSECT(1,5,IN)
        END DO
        NXC=NXC-1
500      CALL XSEC(E, SIGT, SIGP, SIGC, SIGI)
        CALL MFP(SIGT, PATHLEN)
        Z = Z + PATHLEN*CTHETA
        IF(Z .GT. TINTH .AND. Z .LE. (TINTH+XENONTH)) THEN
            DO III = 2, 101
                IF(E.GE.EA(III-1).AND.E.LT.EA(III)) PHO(III-1)=PHO(III-1)+1.0
            ENDDO
            CALL XENON(E, Z, CTHETA)
            GOTO 1100
        ELSE IF (Z .LE. 0.0 .OR. Z .GT. (TINTH+XENONTH)) THEN
            GOTO 1100
        ELSE
            CONTINUE
        END IF
*      PHOTON IS STILL INSIDE THE PLATE; SELECT THE TYPE OF INTERACTION
*      SET CROSS SECTION TABLES FOR TIN
        NXC = INT(XSECT(1,1,1))
        DO IN=2,NXC
            EP(IN-1)=XSECT(1,1,IN)
            SIGTOT(IN-1)=XSECT(1,2,IN)
            SIGPHO(IN-1)=XSECT(1,3,IN)
            SIGCCO(IN-1)=XSECT(1,4,IN)
            SIGCIN(IN-1)=XSECT(1,5,IN)

```



```

      END DO
      NXC=NXC-1
200      X = RAN(J)
          Y = SIGP/SIGT
          W = SIGC/SIGT
          V = SIGI/SIGT
          IF (0.0 .LE. X .AND. X .LT. Y) GOTO 600
          IF (Y .LE. X .AND. X .LT. (Y+W)) GOTO 700
* PICK ANGLE (NOT -- KLEIN-NASHINA)!COMPTON INELASTIC
800      THETA = 3.1415927*RAN(J)
          CTHETA= COS(THETA)
* COMPUTE NEW ENERGY DEPENDS ON ANGLE
          E = E/(1.0+(E/511)*(1.0-CTHETA))
          GOTO 500
* PHOTOELECTRIC INTERACTION
600      IF(E .LT. 3.929) GOTO 1100
          IF(E .LT. 29.2) GOTO 704
* BOTH K AND L VACANCIES ARE ENERGETICALLY POSSIBLE
          X = RAN(J)
          IF(X .LT. 0.84556) GOTO 701
703 IF(X .LT. 0.949529) GOTO 702
* GOT NEITHER K NOR L VACANCY THIS TIME; START NEW PHOTON
          GOTO 1100
* GOT AN L VACANCY; DID IT DECAY BY RADIATIVE TRANSITION?
702 X = RAN(J)
          IF(X .GT. 0.064) GOTO 1100
* YES IT WAS A RADIATIVE TRANSITION; ENERGY OF 3.44 KEV
          E = 3.44
          GOTO 700
* GOT A K VACANCY; DID IT DECAY BY RADIATIVE TRANSITION?
701 X = RAN(J)
          IF(X .GT. 0.859) GOTO 1100
* YES, IT WAS A RADIATIVE TRANSITION; K-ALPHA OR K-BETA??
          X=RAN(J)
          IF(X .LE. 0.78) THEN
              E = 25.2      ! IT WAS A K-ALPHA
              KL = KL + 1  ! CREATES AN L VACANCY
          ELSE
              E = 28.5
          END IF
          GOTO 700
* ONLY AN L VACANCY WAS ENERGETICALLY POSSIBLE
704 X = RAN(J)
          IF(X .GT. 0.6732) GOTO 1100
* GOT AN L VACANCY; DID IT DECAY BY RADIATIVE TRANSITION?
          GOTO 702

```



```

* ALSO COME TO HERE FOR ELASTIC COMPTON EVENTS
700 THETA = 3.1415927*RAN(J)
    CTHETA = COS(THETA)
    GOTO 500
* PHOTON TRAVERSED THE PLATE; START NEXT PHOTON AT THE SURFACE
* FIRST, HOWEVER; ARE THERE ANY L VACANCIES LEFT??
1100      IF(KL .NE. 0) THEN
        KL = KL - 1      ! FINISH OFF THE L-VACANCIES CREATED EARLIER
        GOTO 702
    END IF
* GO BACK AND START ANOTHER PHOTON
100 Z = 0.0
300 CONTINUE
* UNLESS; OF COURSE, FNINISHED; WRITE THE SPECTRUM TO A FILE
    OPEN (UNIT=1, FILE='[ELDRIDGE]ENGDEPXE.DAT', STATUS= 'OLD')
    OPEN (UNIT=2, FILE='[ELDRIDGE]ENGEXTIN.DAT', STATUS= 'OLD')
    DO 40 L = 1, 100
*   NORMALIZE INTENSITY; FACTOR OF 26.0 FROM ENERGY DISTRIBUTION
        INTENSITY(L) = 26.0*INTENSITY(L)/FLOAT(N)
        PHO(L) = 26.0*PHO(L)/FLOAT(N)
        WRITE (1,900) EB(L), INTENSITY(L)
        WRITE (2,900) EA(L), PHO(L)
900      FORMAT (F8.2, F20.10)
    40  CONTINUE
        CLOSE (UNIT=1, STATUS='KEEP')
        CLOSE (UNIT=2, STATUS='KEEP')
* THEN, AT LAST, STOP!!!!
    STOP
    END
*
*
    SUBROUTINE INCPHO(E)
*   SELECTS ENERGY OF PHOTON FROM BACKGROUND DIST.
*   RETURNS A VALID ENERGY FOR A PHOTON IF SUCCESSFUL; HISTORY BEGINS
*   RETURNS 0 FOR PHOTON ENERGY IF NOT SUCCESSFUL; END OF HISTORY
    REAL*4 EP(50), SIGTOT(50), SIGPHO(50), SIGCCO(50), SIGCIN(50),
    2      E, SIGT, SIGP, SIGC, SICI, X
    INTEGER*4 J
    COMMON J, EP, SIGTOT, SIGPHO, SIGCCO, SIGCIN, NXC
*   RANDOM ENERGY UNIFORM 0 TO 1000 KEV
    X=RAN(J)
    IF(X .EQ. 0.0) X=RAN(J)
    E=1.0/X**1.031
*   DISREGARD PHOTONS WITH: 1 KEV > ENERGY > 1000 KEV
    IF(E .LT. 1.0 .OR. E .GT. 1000.0) THEN
        E = 0.0

```



```

        RETURN
* SUCCESS; SO ACCEPT THIS ENERGY; DO PHOTON HISTORY
    ELSE
        RETURN
    END IF
END

*
*
*
SUBROUTINE MFP(SIGT, PATHLEN)
* PICKS THE PHOTON PATH LENGTH FROM THE PROPER DISTRIBUTION
* WHEN FURNISHED THE TOTAL CROSS SECTION
    REAL*4 EP(50), SIGTOT(50), SIGPHO(50), SIGCCO(50), SIGCIN(50),
    2      E, SIGT, SIGP, SIGC, SICI, X
    INTEGER*4 J
    COMMON J, EP, SIGTOT, SIGPHO, SIGCCO, SIGCIN, NXC
    X = RAN(J)
    PATHLEN = -(1.0/SIGT)*ALOG(X)
    RETURN
END

*
*
*
SUBROUTINE XSEC(E, SIGT, SIGP, SIGC, SIGI)
* INTERPOLATES TABLES OF CROSS SECTIONS VERSUS ENERGY
* WHEN FURNISHED WITH AN ENERGY FROM 1 TO 1000 KeV
* TOTAL, PHOTOELECTRIC, COMPTON ELASTIC, COMPTON INELASTIC ALL RETURNED
    REAL*4 EP(50), SIGTOT(50), SIGPHO(50), SIGCCO(50), SIGCIN(50),
    2      E, SIGT, SIGP, SIGC, SICI, X
    INTEGER*4 J
    COMMON J, EP, SIGTOT, SIGPHO, SIGCCO, SIGCIN, NXC
    IF (E .LT. EP(1) .OR. E .GT. EP(NXC)) THEN
* IS ENERGY OUT OF RANGE ?
        GOTO 500
* RETURN TO CALLING ROUTINE
    ELSE
* INTERPOLATE TABLES TO GET X-SECTIONS FOR THAT ENERGY
* CASE THE ENERGY IS EXACTLY THE FIRST POINT IN THE TABLE
        IF (E .EQ. EP(1)) THEN
            SIGT=SIGTOT(1)
            SIGP=SIGPHO(1)
            SIGC=SIGCCO(1)
            SIGI=SIGCIN(1)
            GOTO 500
        END IF
* CASE IF THE ENERGY FALLS EXACTLY ON ANY POINT IN THE TABLE

```



```

DO 10 K=2,NXC
  IF (E .EQ. EP(K) .AND. EP(K) .EQ. EP(K+1)) THEN
    SIGT=SIGTOT(K+1) !AT A POINT; AN EDGE
    SIGP=SIGPHO(K+1)
    SIGC=SIGCCO(K+1)
    SIGI=SIGCIN(K+1)
    GOTO 500
  ELSE IF (E .EQ. EP(K)) THEN !AT A POINT IN TABLE
    SIGT=SIGTOT(K)
    SIGP=SIGPHO(K)
    SIGC=SIGCCO(K)
    SIGI=SIGCIN(K)
    GOTO 500
  ELSE
* OTHERWISE INTERPOLATE TO GET CROSS-SECTIONS AT THAT ENERGY
    IF (E .GT. EP(K-1) .AND. E .LT. EP(K)) THEN
      X=LOG(E/EP(K-1))/LOG(EP(K)/EP(K-1))
      SIGT=EXP(LOG(SIGTOT(K)/SIGTOT(K-1))*X+LOG(SIGTOT(K-1)))
      SIGP=EXP(LOG(SIGPHO(K)/SIGPHO(K-1))*X+LOG(SIGPHO(K-1)))
      SIGC=EXP(LOG(SIGCCO(K)/SIGCCO(K-1))*X+LOG(SIGCCO(K-1)))
      SIGI=EXP(LOG(SIGCIN(K)/SIGCIN(K-1))*X+LOG(SIGCIN(K-1)))
    END IF
  END IF
10 CONTINUE
END IF
500 RETURN
END
*
*
*
SUBROUTINE XENON(E, Z, CTHETA)
REAL*4 EP(50), SIGTOT(50), SIGPHO(50), SIGCCO(50), SIGCIN(50),
2      EB(101), E, SIGT, SIGP, SIGC, SIGI, X, INTENSITY(101),
2      XSECT(2,5,50), ETOT
INTEGER*4 J
COMMON J, EP, SIGTOT, SIGPHO, SIGCCO, SIGCIN, NXC, EB, INTENSITY,
2      XSECT, TINTH, XENONTH, PRESSURE
* SET CROSS SECTION TABLES FOR XENON
NXC = INT(XSECT(2,1,1))
DO IN=2,NXC
  EP(IN-1)=XSECT(2,1,IN)
  SIGTOT(IN-1)=XSECT(2,2,IN)*PRESSURE
  SIGPHO(IN-1)=XSECT(2,3,IN)*PRESSURE
  SIGCCO(IN-1)=XSECT(2,4,IN)*PRESSURE
  SIGCIN(IN-1)=XSECT(2,5,IN)*PRESSURE
END DO

```



```

NXC=NXC-1
Z = TINTH
ETOT = 0.0
500 CALL XSEC(E, SIGT, SIGP, SIGC, SIGI)
CALL MFP(SIGT, PATHLEN)
Z = Z + PATHLEN*CTHETA
200 IF (Z .LE. TINTH .OR. Z .GT. (TINTH+XENONTH)) GOTO 1100
X = RAN(J) ! IN XENON; PICK TYPE INTERACTION
Y = SIGP/SIGT
W = SIGC/SIGT
V = SIGI/SIGT
IF (0.0 .LE. X .AND. X .LT. Y) GOTO 600 !PHOTOELECTRIC
IF (Y .LE. X .AND. X .LT. (Y+W)) GOTO 700 !COMPTON ELASTIC
800 THETA = 3.1415927*RAN(J) !COMPTON INELASTIC
CTHETA= COS(THETA) !ISOTROPIC (NOT VERY GOOD)
EG = E/(1.0+(E/511)*(1.0-CTHETA)) ! NEW ENERGY DEPENDS ON ANGLE
EE = E-EG ! THE ELECTRON ENERGY (ABSORBED)
ETOT = ETOT + EE ! TALLY THE DEPOSITED ENERGY
E = EG ! THE NEW ENERGY OF THE PHOTON
GOTO 500 ! START A PHOTON FROM THIS POSITION AT NEW ENERGY

* PHOTOELECTRIC INTERACTION
600 IF(E .LT. 4.781) THEN !ENERGY TOO LOW TO EXCITE L-VACANCY
ETOT = ETOT + E ! THIS PHOTON ABSORBED; HIGHER LEVEL EXCITATION
GOTO 1100 ! ANY MORE EXCITED ATOMS ???
END IF
IF(E .LT. 34.582) GOTO 704 !L-VACANCY ENERGETICALLY POSSIBLE

* BOTH K AND L VACANCIES ARE ENERGETICALLY POSSIBLE
X = RAN(J)
IF(X .LT. 0.8355) GOTO 701 ! GOT A K-VACANCY
703 IF(X .LT. 0.949529) GOTO 702 ! GOT AN L-VACANCY
* GOT NEITHER K NOR L VACANCY THIS TIME; START NEW PHOTON
* THE PHOTON WAS COMPLETELY ABSORBED
ETOT = ETOT + E
GOTO 1100
702 X = RAN(J) ! GOT AN L-VACANCY; DID IT DECAY BY RADIATIVE TRANSITIO
IF(X .GT. 0.1) THEN
ETOT = ETOT + E ! NO; COMPLETELY ABSORBED
GOTO 1100
END IF
ETOT = ETOT + E - 4.781 ! YES; RADIATIVE
E = 4.781 ! ENERGY EMITTED PHOTON
GOTO 700 ! START 4.781 KEV PHOTON OUT FROM HERE
* GOT A K VACANCY; DID IT DECAY BY RADIATIVE TRANSITION?
701 X = RAN(J)
IF(X .GT. 0.88) THEN

```



```

      ETOT = ETOT + E      ! NOT RADIATIVE; COMPLETELY ABSORBED HERE
      GOTO 1100           ! ANY MORE EXCITED IONS???
    ELSE
* YES, IT WAS A RADIATIVE TRANSITION; WAS IT A K-ALPHA OR K-BETA??
      X = RAN(J)
      IF(X .LE. 0.7667) THEN
        ETOT = ETOT + E - 34.582    ! THIS MUCH ENERGY WAS DEPOSITED
        E = 29.801                  ! WHEN A K-ALPHA PHOTON WAS EMITTED
        KL = KL + 1                  ! ALSO AN L-VACANCY PRODUCED
      ELSE
        ETOT = ETOT + E - 33.644    ! THIS MUCH ENERGY WAS DEPOSITED
        E = 33.644                  ! WHEN A K-BETA PHOTON WAS EMITTED
      END IF
    END IF
    GOTO 700
704 X = RAN(J)      ! ONLY AN L-VACANCY WAS ENERGETICALLY POSSIBLE
    IF(X .GT. 0.6527) THEN
      ETOT = ETOT + E !NO L-VACANCY, HIGHER LEVELS??
      GOTO 1100      ! ANY MORE EXCITED IONS??
    END IF
    GOTO 702 ! L-VACANCY WAS PRODUCED; BUT WAS IT RADIATIVE??
* ALSO COME TO HERE FOR ELASTIC COMPTON EVENTS
700 THETA = 3.1415927*RAN(J)
    CTHETA = COS(THETA)
    GOTO 500
* PHOTON TRAVERSED THE XENON REGION; START NEXT PHOTON
* BUT FIRST; ARE THERE ANY L VACANCIES LEFT IN THE XENON??
1100      IF(KL .NE. 0) THEN
          E = 4.781
          KL = KL - 1
          GOTO 702
        END IF
      CALL BINIT(ETOT)
      RETURN
    END
*
*
*
      SUBROUTINE BINIT(E)
      REAL*4 EP(50), SIGTOT(50), SIGPHO(50), SIGCCO(50), SIGCIN(50),
2          EB(101), E, SIGT, SIGP, SIGC, SICI, X, INTENSITY(101),
2          XSECT(2,5,50), ZL(500)
      INTEGER*4 J
      COMMON J, EP, SIGTOT, SIGPHO, SIGCCO, SIGCIN, NXC, EB, INTENSITY
* SELECT THE PROPER BIN FOR THIS PHOTON
      DO 30 K = 2, 101

```



```
IF (E .GT. EB(K-1) .AND. E .LE. EB(K)) THEN
    INTENSITY(K-1)=INTENSITY(K-1)+1.0
ELSE
    CONTINUE
END IF
30 CONTINUE
RETURN
END
```

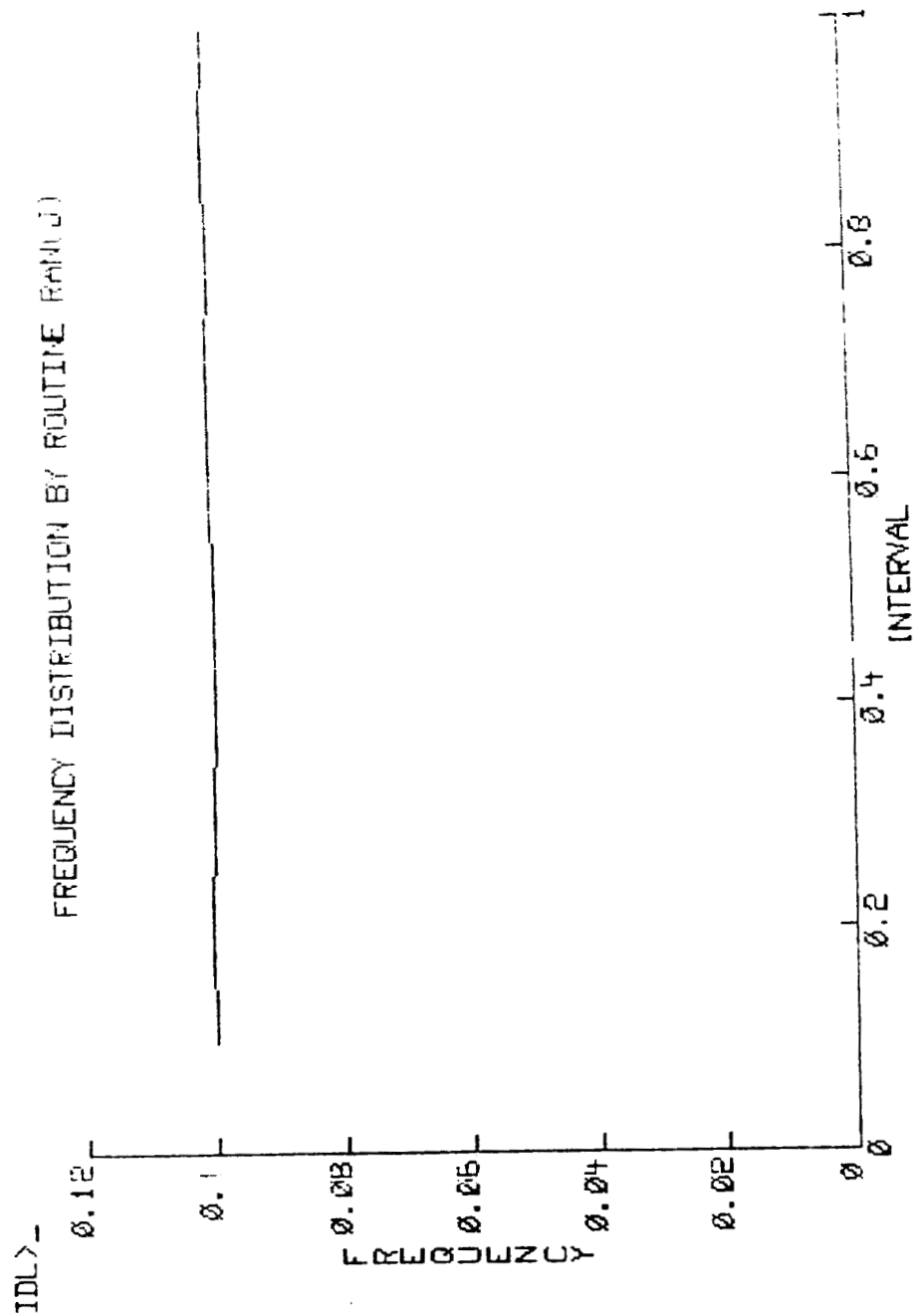



Figure 1

ORIGINAL PAGE IS
OF POOR QUALITY

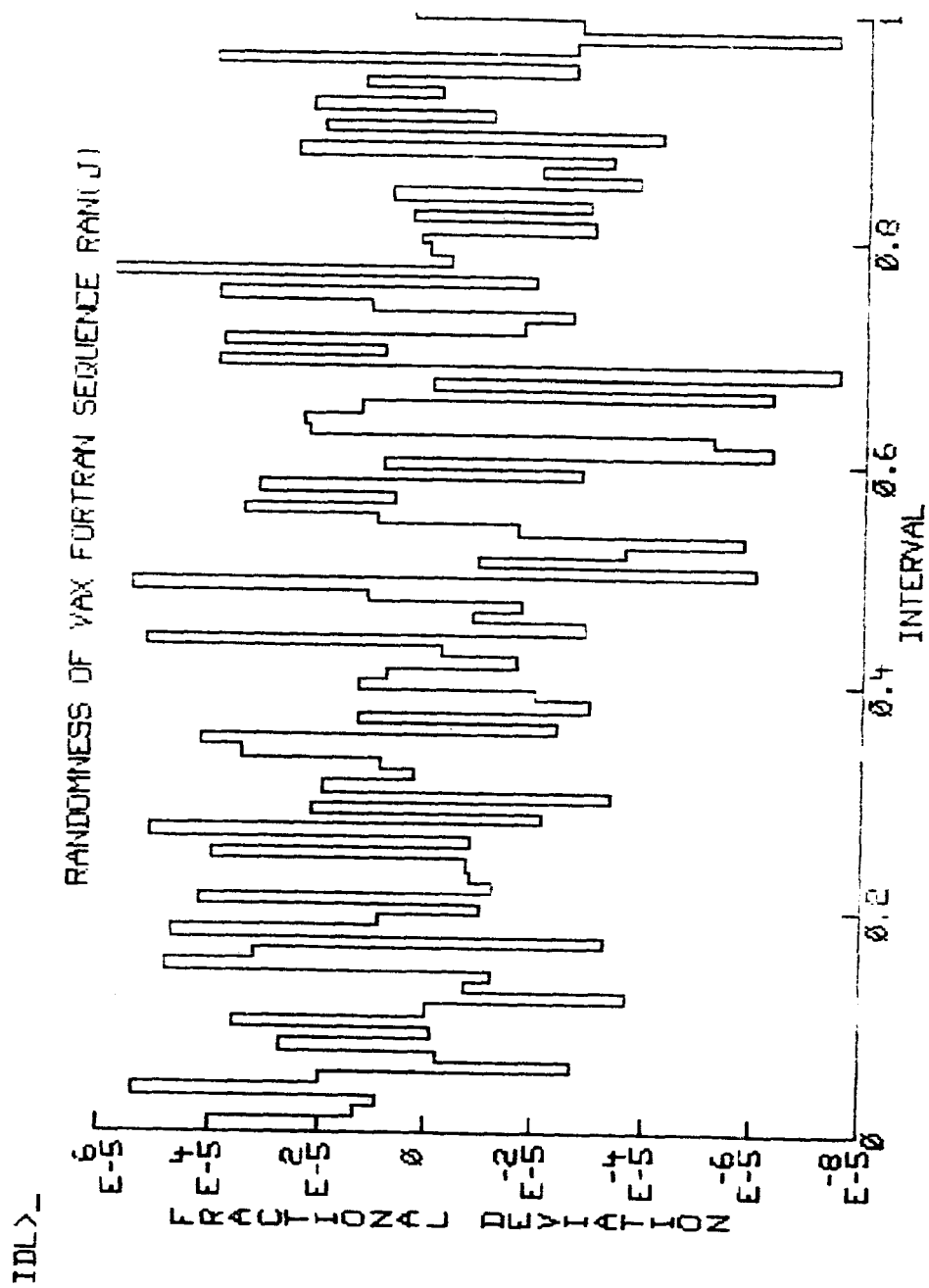


Figure 2

IDL>IMTILE='MONTE CARLO CALCULATION OF INCIDENT FLUX'

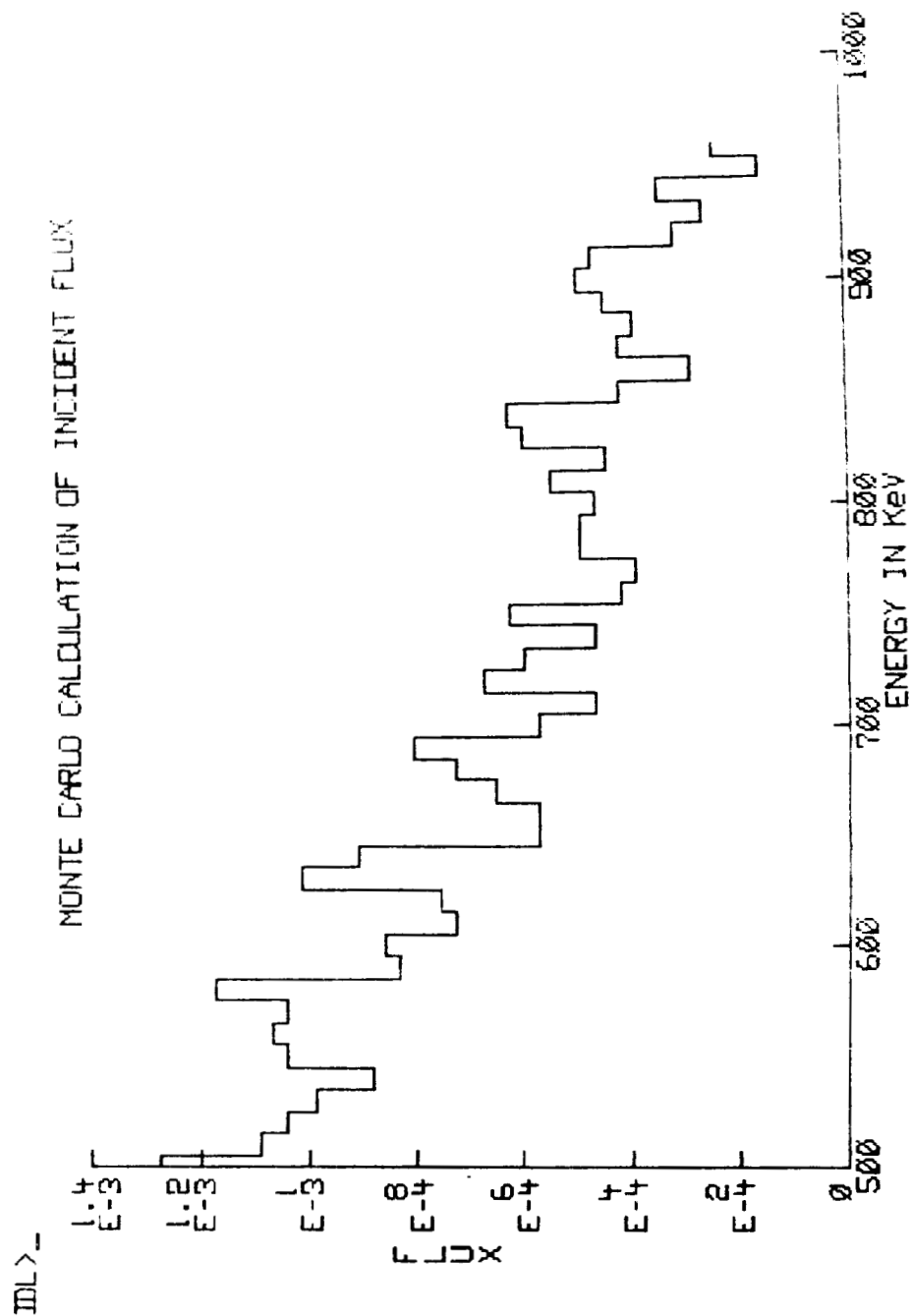


Figure 3

ANALYTIC CALCULATION OF INCIDENT FLUX

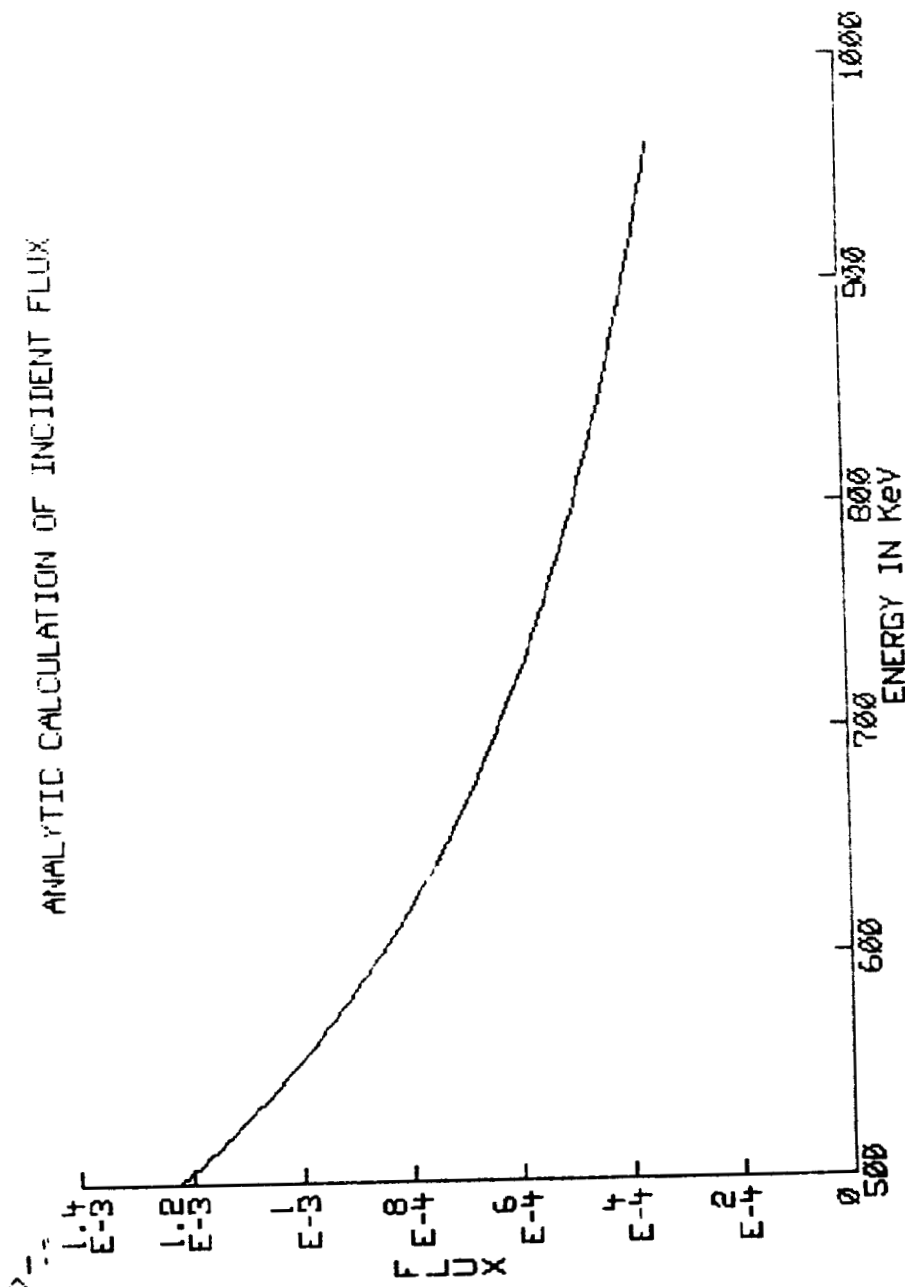


Figure 4

ORIGINAL PAGE IS
OF POOR QUALITY

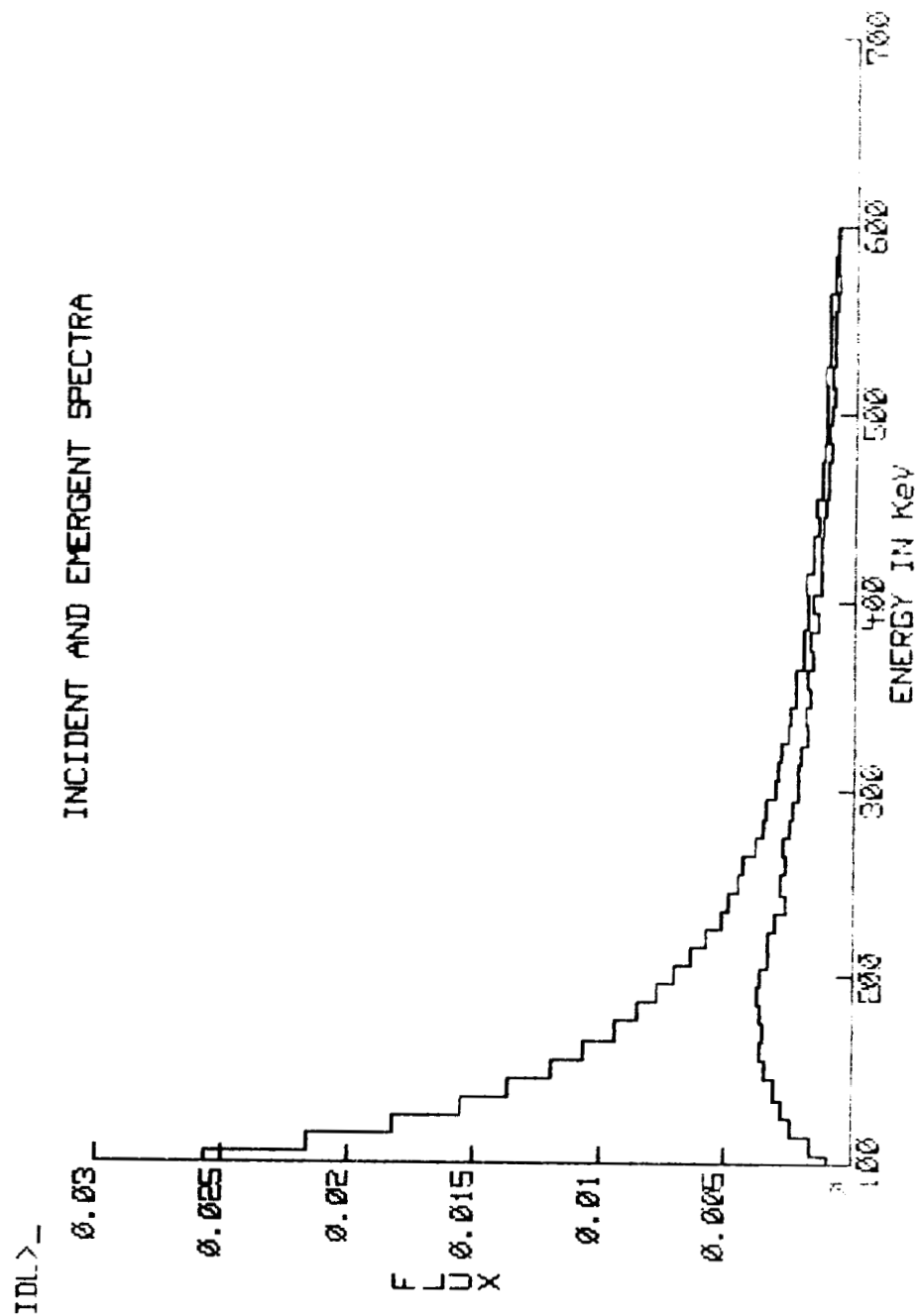


Figure 5

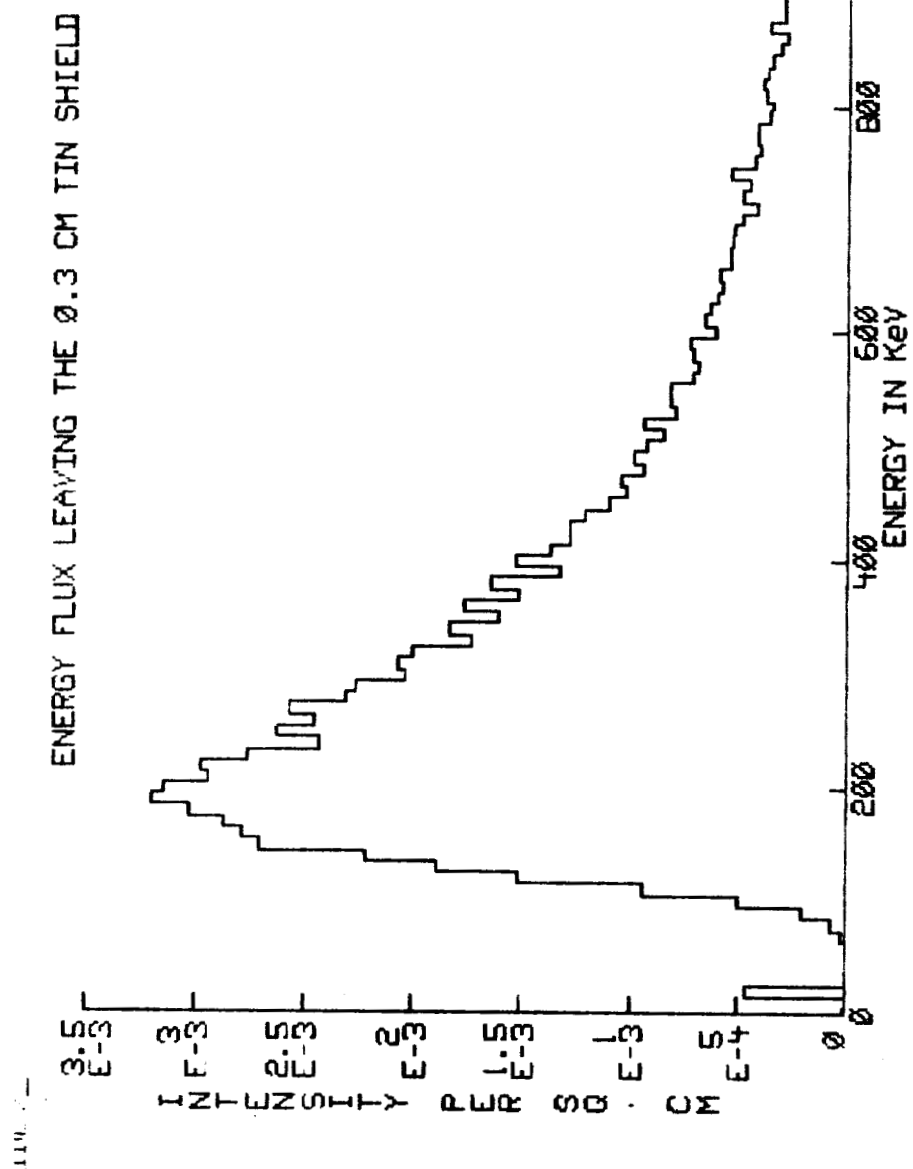


Figure 6

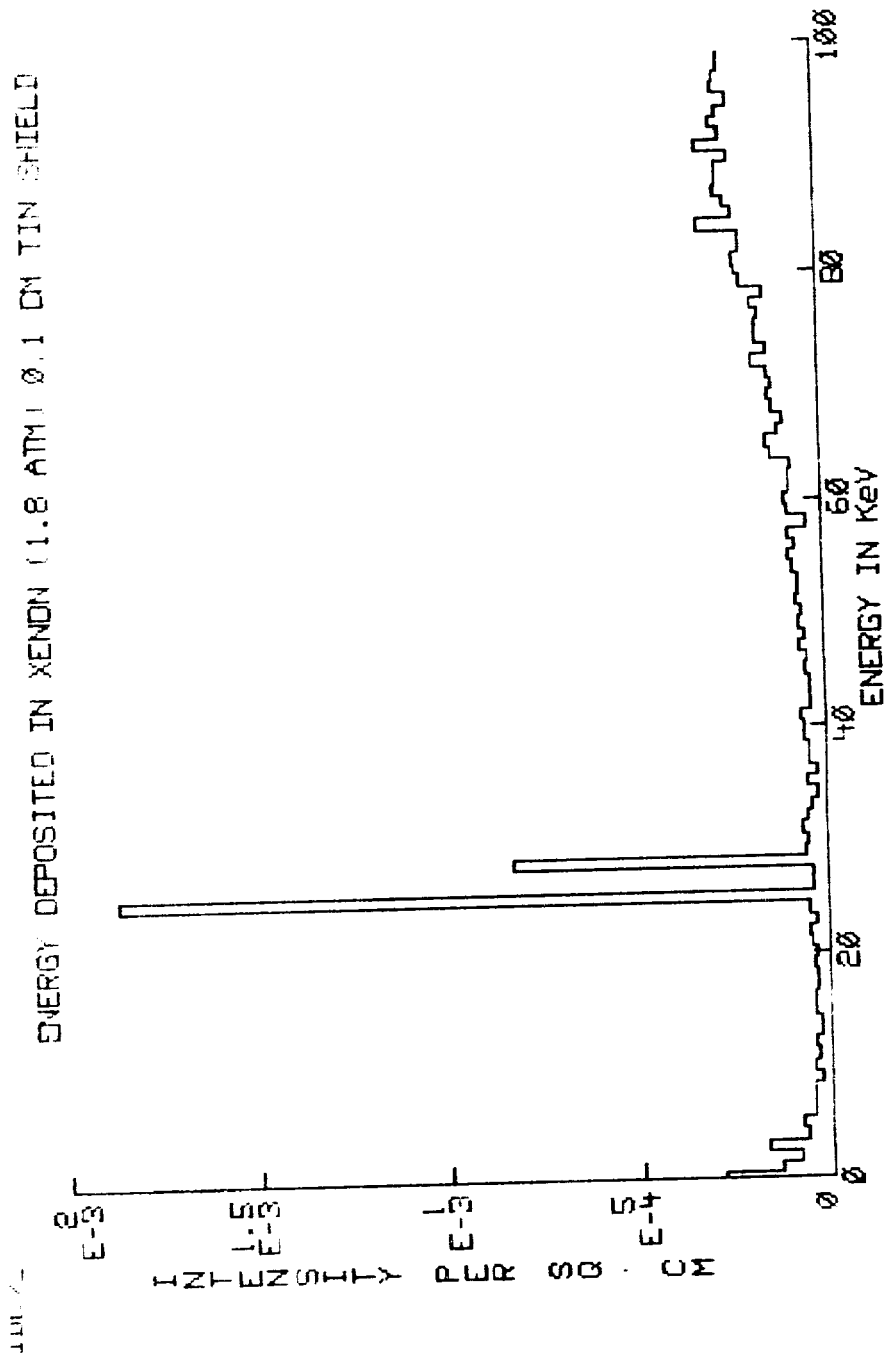


Figure 7

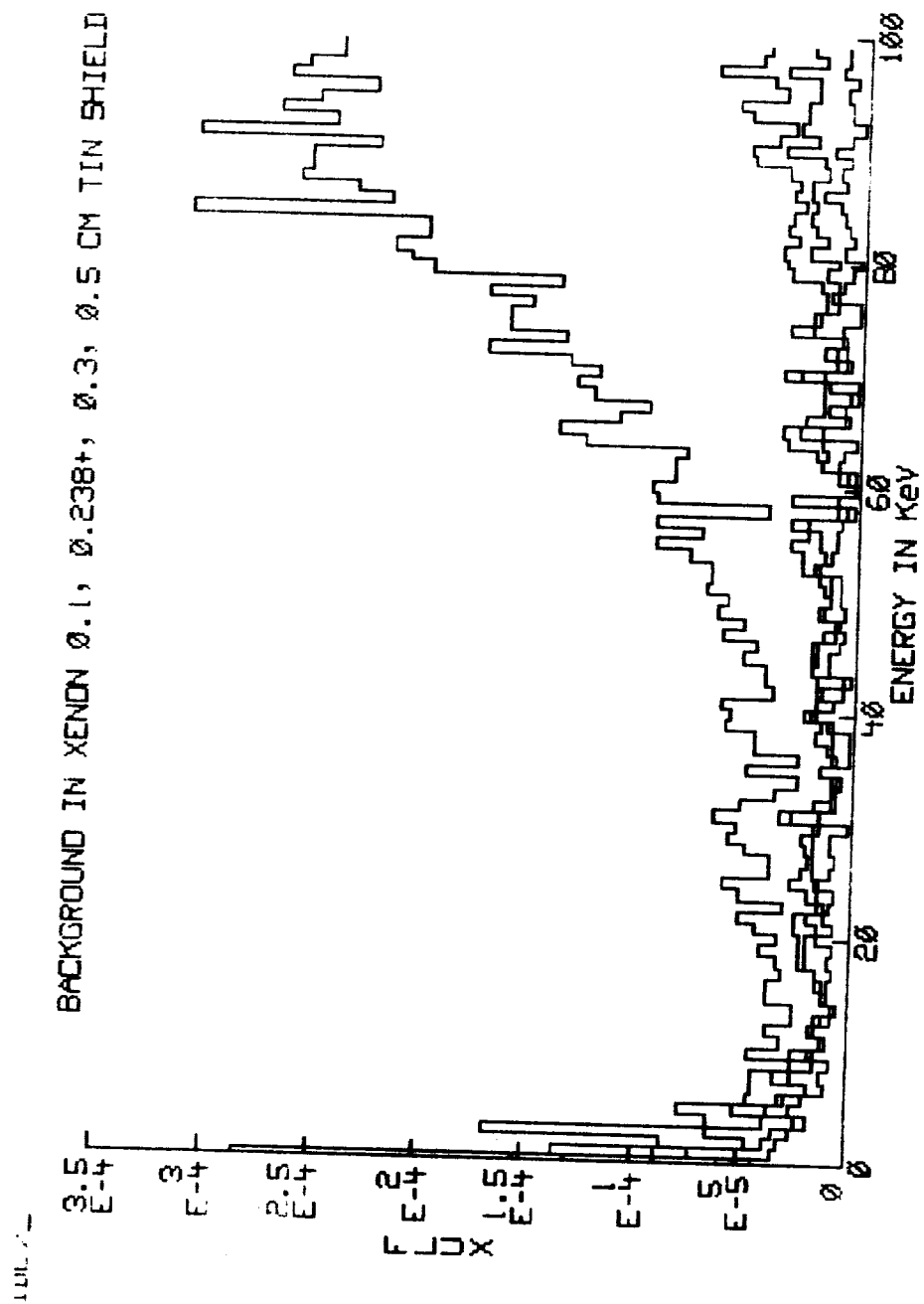


Figure 8

1989

NASA/ASEE SUMMER FACULTY FELLOWSHIP PROGRAM

MARSHALL SPACE FLIGHT CENTER
THE UNIVERSITY OF ALABAMA IN HUNTSVILLE

INVESTIGATION OF SSME ALTERNATE HIGH PRESSURE FUEL
TURBOPUMP LIFT-OFF SEAL FLUID AND STRUCTURAL
DYNAMIC INTERACTION

Prepared by:	David A. Elrod
Academic Rank:	Assistant Professor
University and Department:	Virginia Polytechnic Institute and State University Mechanical Engineering
NASA/MSFC:	
Laboratory:	Propulsion
Division:	Component Development
Branch:	Turbomachinery and Combustion Devices
MSFC Colleague:	Henry P. Stinson
Date:	July 28, 1989
Contract No.:	The University of Alabama in Huntsville NGT -01-008-021

INVESTIGATION OF SSME ALTERNATE HIGH PRESSURE FUEL
TURBOPUMP LIFT-OFF SEAL FLUID AND STRUCTURAL
DYNAMIC INTERACTION

by

David A. Elrod
Assistant Professor
Mechanical Engineering Department
Virginia Polytechnic Institute and State University
Blacksburg, Virginia

ABSTRACT

The Space Shuttle Main Engine (SSME) alternate turbopump development program (ATD) high pressure fuel turbopump (HPFTP) design utilizes an innovative lift-off seal design that is located in close proximity to the turbine end bearing. Cooling flow exiting the bearing passes through the lift-off seal during steady state operation. The potential for fluid excitation of lift-off seal structural resonances is investigated. No fluid excitation of LOS resonances is predicted. However, if predicted LOS natural frequencies are significantly lowered by the presence of the coolant, pressure oscillations caused by synchronous whirl of the HPFTP rotor may excite a resonance.

ACKNOWLEDGEMENTS

I would like to thank my NASA colleague, Henry Stinson, for his insight, cooperation, and encouragement during my work at the Marshall Space Flight Center this summer. Thanks also to George Young for his patience in helping me find a task which was a diversion from my previous research efforts. I appreciate the hospitality of the whole Turbomachinery and Combustion Devices Branch. I was made to feel a part of the daily problem-solving efforts of the team, and I appreciate the efforts made to include me.

Thanks to Frank Six, Gerald Karr, Billie Swinford, and the others in their offices who helped make the Summer Program pleasant and enlightening with the frequent activities and weekly seminars. Thanks also to those who presented their work at the seminars.

I would also like to thank: Mr. Carl Ring of Pratt & Whitney for his quick and thorough response to my questions about lift-off seal dimensions; Mr. Andy Brown for providing the results of his analysis of lift-off seal dynamics; and Mr. David Herda for information concerning the seal structure.

Finally, thanks to NASA and ASEE for selecting me to participate in the Summer Faculty Fellowship Program.

NOMENCLATURE

A	cross-sectional area (L^2)
a	diaphragm radius (L)
d_o	jet diameter (L)
F	force (F)
f_r	frequency ratio
h	diaphragm thickness (L)
L	jet developing flow region length (L)
\dot{m}	mass flow rate (M/T)
P	fluid pressure (F/L^2)
R	radius (L)
V	fluid velocity (L/T)
ρ	fluid density (M/L ³)
ρ_d	diaphragm density (M/L ³)
ϕ	jet direction to surface normal angle

Subscripts

j	jet
r	radial
z	axial
0,1	zeroth- and first-order

INTRODUCTION

In the high pressure fuel turbopump (HPFTP) design of the Space Shuttle Main Engine (SSME) alternate turbopump development program (ATD), hydrogen from the discharge of the third stage pump impeller is used to cool the turbine-end roller bearing and turbine. Figure 1 is a cross-section of the ATD-HPFTP. Between the roller bearing and turbine, a lift-off seal (LOS) controls the coolant flow from the bearing discharge region to the turbine parts. Figure 2 shows details of the lift-off seal in the "closed" position. Before start-up, the corrugated LOS diaphragm holds the LOS seal element against a polished seal plate, preventing flow to the turbine. The chamber upstream of the LOS is fed by two sources: the roller bearing discharge flow and eight 3.5 mm (0.138 in.) diameter axial nozzles (see figure 2). When the turbopump is started, the increasing hydrogen pressure on the pump side of the LOS deflects the diaphragm axially until it seats on the LOS retainer. Coolant flows through radial holes in the seal element and diaphragm to cool the outer turbine elements, and past the seal element knife edge to cool the liners and rear face of the turbine disk.

A one dimensional analysis of the ATD-HPFTP coolant flow has been performed for 65% to 115% power levels (see Gregory, 1989). The structural dynamic characteristics of the LOS have been investigated by Brown (1989). In the present study, LOS fluid/structural interactions are investigated.

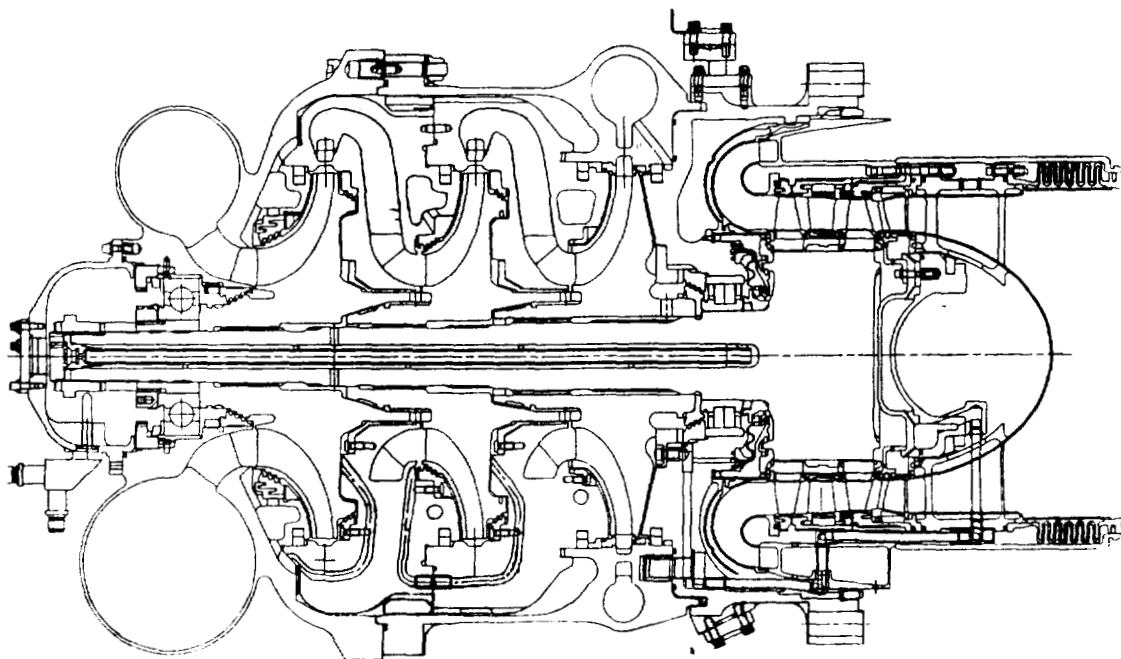


Figure 1. ATD-HPFTP cross-section.

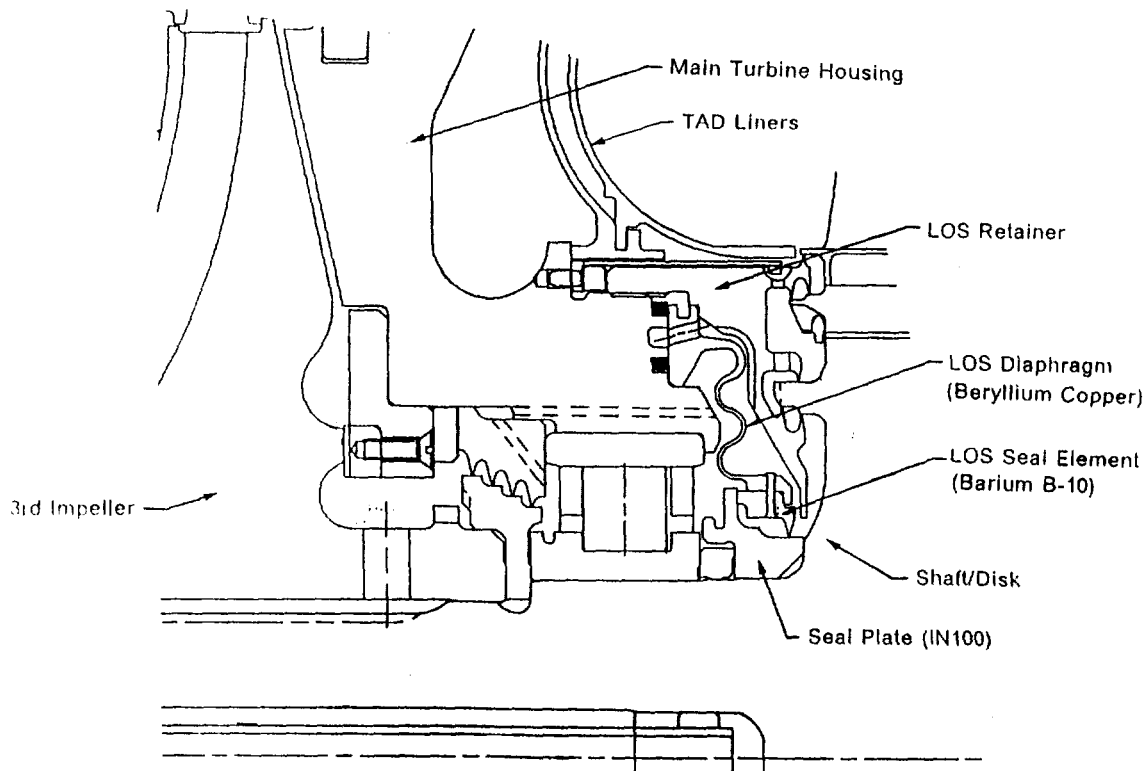


Figure 2. ATD-HPFTP lift-off seal.

OBJECTIVES

The objective of the present work is to investigate the potential for fluid excitation of LOS structural resonances. Two questions which must be answered at the outset are:

- (1) What are the predicted eigenvalues (natural frequencies) and mode shapes of the LOS structure?
- (2) What are the coolant pressures and flow rates in the LOS region?

Question (1) is answered by Brown's analysis. His predictions are summarized in the next section. The flow rates and flow geometry provided by Pratt & Whitney (P&W), the ATD contractor, are then used to identify the most likely sources of excitation of LOS resonances. These sources are then analyzed individually.

LOS STRUCTURAL DYNAMICS

In a structural analysis of the LOS, the part of interest is the diaphragm/seal element assembly (see figure 2). The assembly has been modelled using NASTRAN, EAL (Engineering Analysis Language), and the P&W "Shell Deck" code. There are three mode "families" for this assembly: a ring family and two disk families. For a ring mode,

motion is radial, nodes are diametral, and waves are present along a circumferential line. For both disk mode families, motion is axial. A "diametral" disk mode has nodes along diametral lines, and waves along circumferential lines. A "circular" disk mode has concentric, circular nodes, and waves along radial lines.

Predicted natural frequencies of the diaphragm/seal element assembly are shown in figure 3. No circular disk modes are predicted below 20,000 Hz. The lowest predicted natural frequency is a diametral disk mode at 782 Hz, which is 29% higher than the ATD HPFTP 109% power level design speed of 606 Hz (36,353 rpm). Synchronous excitation of the diaphragm by the coolant will not excite a resonance. However, it should be noted that the natural frequency of a diaphragm depends on the fluid in which it is submerged. For a flat diaphragm, the ratio f_r of the natural frequency in a fluid of density ρ to the natural frequency in a vacuum is

$$f_r = \frac{1}{\sqrt{1 + \frac{0.669 \rho a}{\rho_d h}}}$$

(Di Giovanni, 1982) where a is the diaphragm radius, h is the diaphragm thickness, and ρ_d is the density of the diaphragm material. The radius and thickness of the LOS corrugated diaphragm are approximately 86 mm (3.4 in.) and 0.8 mm (0.03 in.), respectively. The density of the diaphragm material is 8230 kg/m³ (514 lbm/ft³), and the coolant density is approximately 76 kg/m³ (4.7 lbm/ft³). A flat diaphragm with these dimensions in the LOS operating environment would have a frequency ratio of 0.78. For the corrugated diaphragm of the LOS, a frequency ratio of 0.78 would lower a 782 Hz natural frequency to 610 Hz - too near the 109% power level design speed.

ONE-DIMENSIONAL FLOW ANALYSIS

In this section, results of a P&W one-dimensional flow analysis are used to identify potential sources of seal-resonance excitation. In figure 4, the flow paths in the LOS region of the ATD-HPFTP are numbered. In the following discussion, they are referred to as resistances 1 through 6. The 115% power level flow predictions of P&W are listed in Table 1. Discussion of the fluid forces on the LOS are restricted to the 115% power level, for which pressure drops, fluid velocities, and, therefore, fluid forces, are highest.

Table 1. LOS Coolant Flow - 115% Power Level

Resis. #	ΔP (bars)	\dot{m} (kg/s)	ρ (kg/m ³)	A (mm ²)	V_z (m/s)	V_r (m/s)
1	29.8	1.207	76.4	77.	205.2	0.0
2	2.7	1.102	76.4	283.	50.1	0.0
3	5.4	2.309	76.2	366.	0.0	82.6
4	8.5	1.009	75.7	127.	0.0	105.0
5	71.5	1.300	76.2	52.	328.1	0.0
6	62.9	0.016	75.7	3.	0.0	70.5

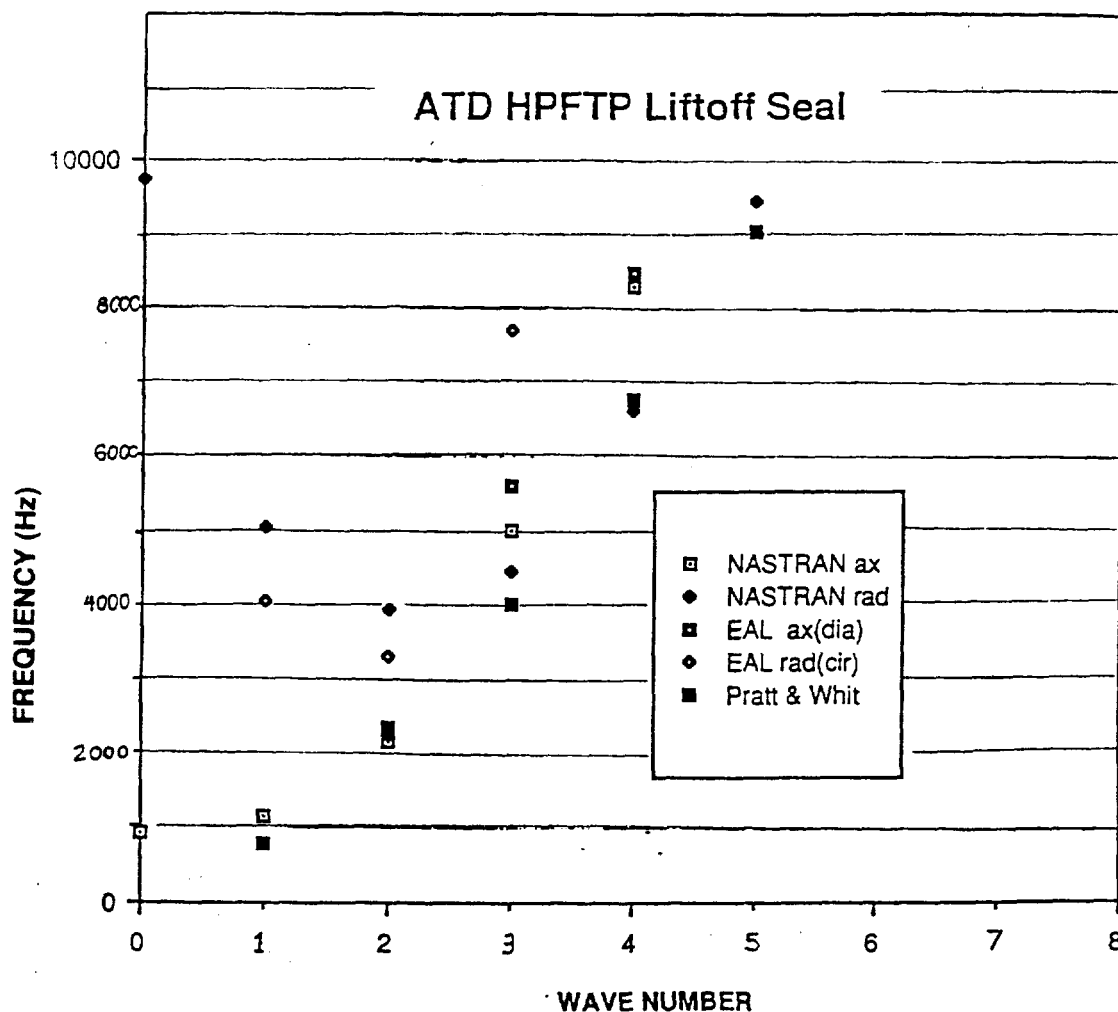


Figure 3. LOS diaphragm/seal element natural frequencies.

For each restriction listed in Table 1, \dot{m} is the mass flow rate, ρ is the density of the coolant at the restriction discharge, A is the cross-sectional area perpendicular to the assumed one-dimensional flow through the restriction, and $V (= \dot{m}/\rho A)$ is the one-dimensional velocity. For restriction 1, A is the total cross-sectional area of eight 3.5 mm (0.138 in.) diameter nozzles. For restriction 2, A is the total cross-sectional area of fourteen passages through the roller bearing. Each of the fourteen passages is bounded by the inner diameter of the bearing cage, the inner race rail diameter, and two adjacent rollers (see figure 5). For restriction 4, A is the total cross-sectional area of sixteen 3.2 mm (0.125 in.) radial holes through the seal element and diaphragm. Though a one-dimensional analysis was used to model the coolant flow network, figure 4 and Table 1 indicate that flow through the LOS is highly three-dimensional.

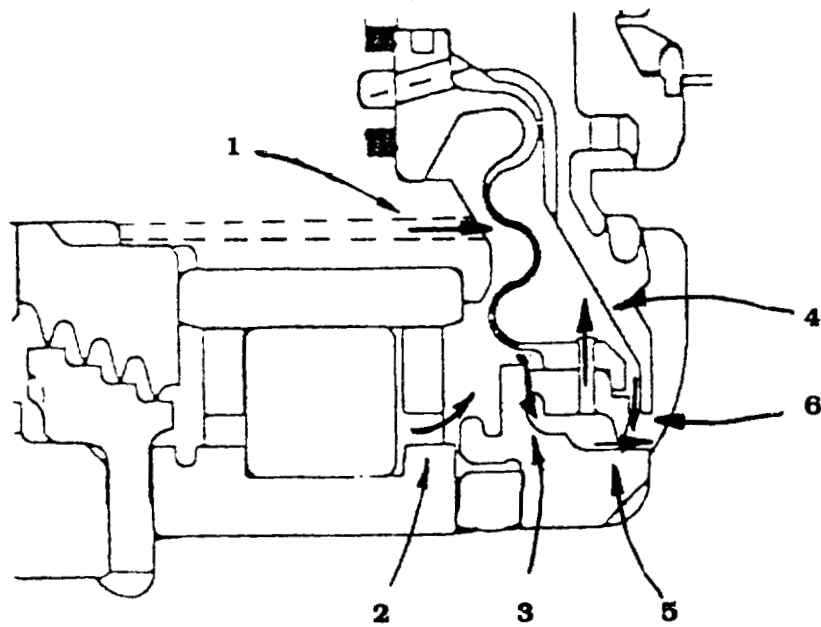


Figure 4. LOS coolant flow paths.

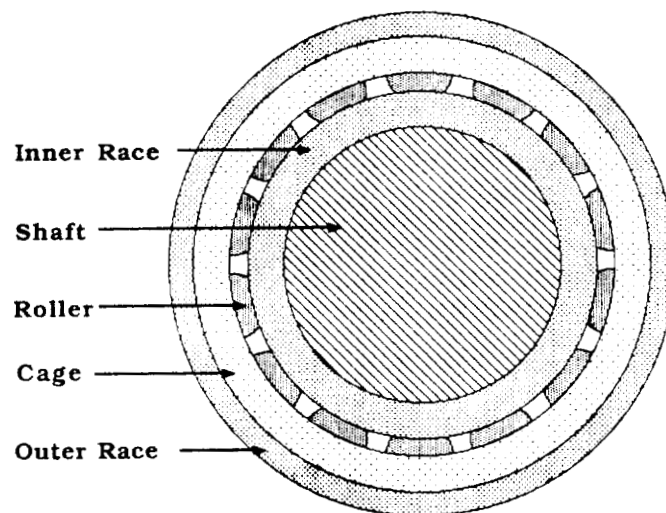


Figure 5. ATD-HPFTP roller bearing cross-section.

The predicted pressure drop across the corrugated diaphragm is the sum of the pressure drops across resistances 3 and 4. For the 115% power level, the diaphragm pressure drop is 13.9 bars (202 psi). The static axial force on the diaphragm/seal element assembly due to the diaphragm and restriction 5 pressure drops is greater than 20 kN (4500 lbf). Synchronous whirling of the HPFTP rotor (due to rotor unbalance) will cause flow oscillations at the rotor speed frequency in restrictions 3 through 6. The oscillations will produce dynamic forces, but at a frequency (606 Hz at the 109% power level) well below the predicted LOS resonances. The roller bearing coolant flow (restriction 2 in figure 4) may be roughly analyzed as 14 oblique jets discharging into a cross-flow, upstream of the LOS. However, the jets rotate at the bearing cage speed, which is less than half of the HPFTP rotor speed. Therefore, no excitation of LOS resonances by the bearing coolant flow is predicted.

Five of the six LOS flow paths shown in figure 4 have been eliminated as likely causes of LOS resonance excitation. The remainder of this study is an analysis of the fluid/structural interaction at the discharge of restriction 1 of figure 4. The factors which collectively point to a need for further analysis of this flow are:

- (1) the high flow velocity through restriction 1,
- (2) the distance from the nozzle exits to the LOS diaphragm (from 1.3 to 2.8 mm, according to P&W predictions); and
- (3) the shape of the diaphragm corrugation at the point of jet impingement.

JET/DIAPHRAGM INTERACTION

In 1924, Wilfred Campbell explained a thin-turbine-disk, fluid excitation mechanism which he called "feathering". Campbell demonstrated experimentally that an axial flow of steam through the blades of a thin turbine disk could sustain a vibratory wave travelling opposite the direction of normal disk rotation. The wave was excited by striking the disk with a stick, and the amplitude of the sustained wave was a function of the flow rate of the steam. Campbell explained that, as turbine blades vibrate, the angles between the fluid flow and blade surfaces change, causing oscillating forces which support a "backward" traveling wave (see Campbell, 1924). In the ATD-HPFTP lift-off seal, the force of a jet impinging on the corrugated diaphragm surface depends on the angle between the surface and the jet flow direction. The angles between the axial jets exiting restriction 1 of figure 4 and the corrugated surface depend on the radial positions of the jets relative to the diaphragm. The question which must be answered is:

If a LOS resonance is momentarily excited (e.g., by start-up of the HPFTP), could flow from restriction 1 (figure 4) sustain the resonance vibration in a manner similar to the feathering action described by Campbell?

In the following paragraphs, the dissipation of the jet flow upstream of the LOS diaphragm is analyzed, and an equation is derived for the force on the diaphragm caused by a jet. Then, a perturbation analysis is applied to determine the force due to radial motion of the diaphragm.

Jet Flow - Upstream of the LOS diaphragm, circular jets emerge from eight 3.5 mm (0.138 inch) diameter nozzles. Figure 6 (from Rajaratnam, 1976) shows the characteristics of a circular jet flowing into a reservoir. A shear layer originates at the jet boundary as the jet comes out of the nozzle, penetrating into the jet and into the surrounding fluid as the jet flows away from the nozzle. Up to section 1-1 in figure 6,

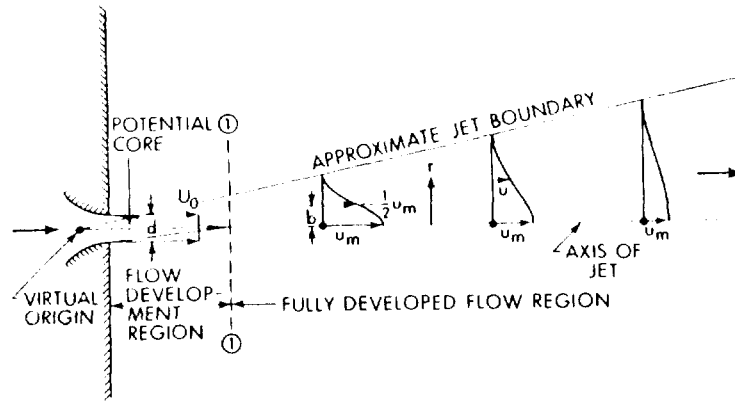


Figure 6. Definition sketch of circular turbulent jets.

there is a core of undiminished jet velocity. This region is called the "flow development region". Beyond section 1-1 in figure 6, in the "fully developed flow region", the centerline jet velocity decreases. The length of the flow development region is

$$L = 4.895 d_0 ,$$

where d_0 is the nozzle diameter. For the jets upstream of the LOS, $L = 17.2$ mm (0.676 in.). Since the clearance between the nozzles and the diaphragm is between 1.3 and 2.8 mm (0.051 and 0.110 in.), the full jet velocity impinges on the diaphragm.

Jet Force - The force on the diaphragm by each jet depends on the shape of the corrugation at the point of impingement. In figure 7, for a jet impinging on the surface shown at an angle ϕ from the surface normal, the force on the surface is approximately

$$F_j = \frac{1}{2} \rho (V_j \cos \phi)^2 \frac{A_j}{\cos \phi} \quad (1)$$

where V_j is the jet velocity, and $A_j (= \pi d_0^2/4)$ is the cross-sectional area of the jet. Figure 8 is a computer-generated detail drawing of the jet/diaphragm region. The figure was provided by P&W. The shaded region is a jet nozzle. The corrugation profile at the jet impingement location is approximately circular. In this analysis, ϕ is the angle shown in figure 8, at the location where the jet centerline intersects the corrugation profile. Dimensions of the diaphragm provided by P&W have been used to develop an equation for the angle ϕ as a function of the radial distance R from the diaphragm centerline to a point on the diaphragm in the jet region. When R is expressed in mm,

$$\phi = \tan^{-1} \left[\frac{74.6 - R}{\sqrt{3.6^2 - (R - 74.6)^2}} \right] \quad (2)$$

From figure 8 and equation (1), the radial component F_{jr} of a jet force F_j is

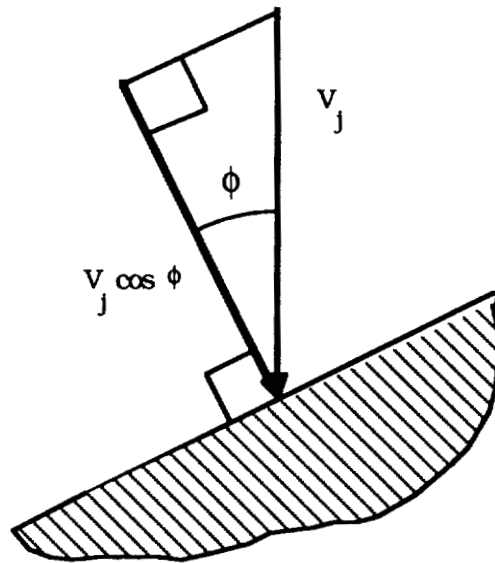


Figure 7. Jet impinging on a surface at an angle ϕ .

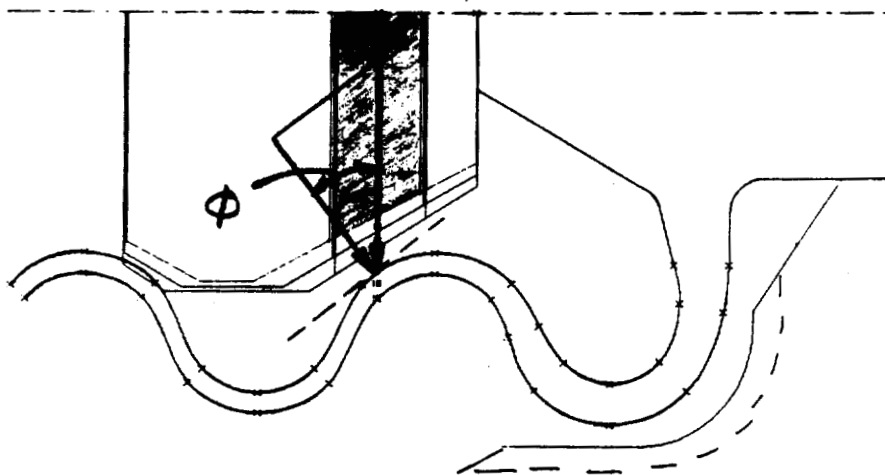


Figure 8. Jet/diaphragm detail.

$$F_{jr} = \frac{1}{2} \rho V_j^2 A_j \cos \phi \sin \phi \quad (3)$$

It is assumed that the eight jets strike the diaphragm concentrically, at a radius R . Relative motion between the diaphragm and jet nozzle locations causes a force perturbation if the angle ϕ changes with the motion. Motion of the diaphragm in the axial direction would cause no change in the angles between the jets and the diaphragm surface, and therefore no change in the jet forces on the diaphragm. If the diaphragm moves radially (and, therefore, the jets move radially relative to the diaphragm) the angle ϕ changes. The following perturbation analysis is used to approximate the change in radial force on the diaphragm caused by a small radial deflection of the diaphragm relative to the jet radial positions.

Jet Force Perturbation - To find the perturbation in the radial force F_{jr} on the diaphragm by jet j , due to small radial motion of the LOS diaphragm, equation (3) is expanded in terms of the perturbation variable

$$\phi_j = \phi_{j0} + \epsilon \phi_{j1}$$

yielding

$$F_{jr1} = \frac{1}{2} \rho V_j^2 A_j [-\sin^2 \phi_{j0} + \cos^2 \phi_{j0}] \phi_{j1} \quad (4)$$

where ϕ_{j1} is the perturbation of ϕ_j caused by radial motion R_{j1} of jet nozzle j relative to the diaphragm. Expansion of equation (2) in terms of the perturbation

$$R_j = R_{j0} + \epsilon R_{j1}$$

yields the following equation for ϕ_{j1} :

$$\phi_{j1} = \cos^2 \phi_{j0} \left\{ -[3.6^2 - (R_{j0} - 74.6)^2]^{-1/2} - \frac{(R_{j0} - 74.6)^2 [3.6^2 - (74.6 - R_{j0})^2]^{3/2}}{R_{j1}} \right\} \quad (5)$$

To evaluate the perturbation F_{jr1} (equation (4)) caused by radial motion of the diaphragm, the nominal value ϕ_{j0} is calculated using equation (2) and the nominal radial position of jet impingement R_{j0} , and ϕ_{j1} is evaluated in terms of R_{j1} . Values of ρ and V_j are given in Table 1 for the 115% power level, and A_j is calculated using the known nozzle diameter, d_o . The following section provides the numerical results of this analysis.

NUMERICAL RESULTS

For each of the eight jets upstream of the LOS, $A_j = 9.6 \text{ mm}^2$ (0.015 in²). According to P&W drawings, the radius of the jet centerlines is 72.4 mm (2.85 in). Setting $R_{j0} = 72.4 \text{ mm}$ and using the density and velocity values in Table 1 for ρ and V_j , the following values are obtained from equations (2), (5), and (4):

$$\phi_0 = 0.66 \text{ rad } (37.7^\circ)$$

$$\phi_1 = -0.35 R_{j1}$$

$$F_{jr1} = (-1.37 \text{ N/mm}) R_{j1}$$

The coefficient -1.37 N/mm in the expression for F_{jr1} may be interpreted as a radial stiffness introduced by a jet. The schematic in figure 9 provides a basis for explaining the effect of this radial stiffness.

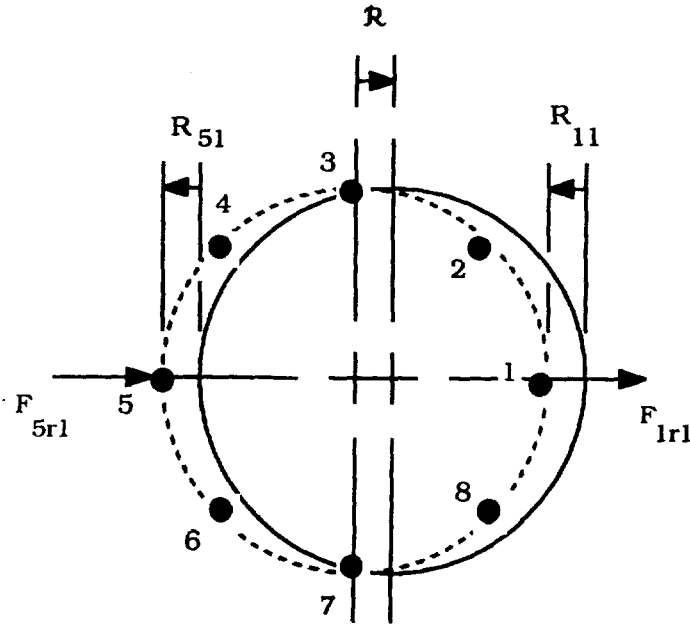


Figure 9. Relative motion of diaphragm and jet ring.

In figure 9, the black spots numbered 1 through 8 represent the eight jets upstream of the ATD-HPFTP lift-off seal. The circles represent a circle on the LOS diaphragm with the same diameter as the jet ring. If the diaphragm moves radially a distance R relative to the jet ring, in the direction of jet number 1, the radial motion of jets 1 and 5 relative to the ring (R_{11} and R_{51} , respectively) are as shown. In this case, R_{11} is negative (towards the center of the diaphragm), and R_{51} is positive. The perturbation force on the diaphragm at jet 1 is F_{1r1} in the direction shown (positive radial direction). The perturbation force on the diaphragm at jet 5 is in the negative radial direction, as shown. Thus, the effect of the radial stiffness of the jets is to support radial motion of the diaphragm, or to reduce the radial stiffness, and therefore the ring mode natural frequencies. However, the magnitude of the jet radial stiffness has been calculated as 1.37 N/mm (8.8 lbf/in). The effect of this low radial stiffness on the LOS dynamic response is negligible.

CONCLUSIONS

The fluid/structural interactions of the ATD-HPFTP lift-off seal have been investigated for the possibility of fluid excitation of LOS resonances. The results of this study are summarized as follows:

- Synchronous pressure oscillations in the LOS region will not excite the resonances predicted by Brown and Pratt & Whitney, the ATD contractor. At the 109% power level, the synchronous force frequency is 77% of the lowest predicted natural frequency (782 Hz).
- Though the fourteen rotating jets exiting the roller bearing upstream of the LOS may produce oscillating loads on the LOS, the jets rotate at the bearing cage speed, less than half of the HPFTP operating speed, and a frequency well below the LOS natural frequencies.
- The eight axial jets upstream of the LOS affect the seal diaphragm as negative radial stiffnesses. However, the stiffness magnitudes are negligible compared to the material stiffness of the diaphragm/seal element assembly.
- For flat diaphragms, natural frequencies decrease as the density of the fluid in which the diaphragm is immersed is increased. If the natural frequencies of the corrugated diaphragm in the LOS are lowered significantly by the presence of the hydrogen coolant during operation of the ATD-HPFTP, synchronous pressure oscillations may excite LOS resonances.

REFERENCES

- Brown, Andrew M., 1989, "Dynamic Modeling of Alternate Turbopump Liftoff Seal," internal NASA memorandum, June 22.
- Campbell, Wilfred, 1924, "The Protection of Steam-Turbine Disk Wheels from Axial Vibration," *ASME Transactions*, No. 1920, pp. 31-160.
- Di Giovanni, Mario, 1982, *Flat and Corrugated Diaphragm Design Handbook*, Marcel Decker, Inc., New York, NY, pp.196-197.
- Gregory, H. K., 1989, V169 Flow and Bearing Load, computer printout, April 15.
- Rajaratnam, N., 1976, *Turbulent Jets*, Elsevier Scientific Publishing Company, Amsterdam, The Netherlands, pg. 27.

1989

NASA/ASEE SUMMER FACULTY FELLOWSHIP PROGRAM

**MARSHALL SPACE FLIGHT CENTER
THE UNIVERSITY OF ALABAMA IN HUNTSVILLE**

**A STUDY OF THE EFFECTS OF DISK FLEXIBILITY
ON THE ROTORDYNAMICS OF THE SPACE SHUTTLE
MAIN ENGINE TURBO-PUMPS**

Prepared by:	George T. Flowers
Academic Rank:	Assistant Professor
University and Department:	University of South Florida Department of Mechanical Engineering

NASA/MSFC:	
Laboratory:	Structures and Dynamics
Division:	Control Systems
Branch:	Mechanical Systems Control

MSFC Colleague:	Donald P. Valley
Date:	August 2, 1989
Contract No.	The University of Alabama in Huntsville NGT-01-008-021

TABLE OF CONTENTS

ABSTRACT	XI-ii
ACKNOWLEDGEMENTS	XI-iii
LIST OF FIGURES	XI-iv
LIST OF TABLES	XI-v
NOMENCLATURE	XI-vi
INTRODUCTION	XI-1
OBJECTIVES	XI-2
PREVIOUS RESEARCH	XI-3
FINITE ELEMENT ANALYSES	XI-4
ANALYTICAL STUDY	XI-6
CONCLUSIONS AND RECOMMENDATIONS	XI-11
REFERENCES	XI-12

ABSTRACT

Rotordynamical analyses are typically performed using rigid disk models. Studies of rotor models in which the effects of disk flexibility have been included indicate that it may be an important effect for many systems. This work addresses this issue with respect to the Space Shuttle Main Engine high pressure turbo-pumps. Finite element analyses have been performed for a simplified free-free flexible disk rotor model and the modes and frequencies compared to those of a rigid disk model. The simple model was then extended to a more sophisticated HPTOP rotor model and similar results were observed. Equations have been developed that are suitable for modifying the current rotordynamical analysis program to account for disk flexibility. Some conclusions are drawn from the results of this work as to the importance of disk flexibility on the HPTOP rotordynamics and some recommendations are given for follow-up research in this area.

ACKNOWLEDGEMENTS

I am indebted to the NASA Marshall Space Flight Center and the NASA/ASEE Summer Faculty Fellowship Program which provided support for this research effort. I would like to thank my NASA colleague, D.P. Vallely, for his support for my participation in the *summer faculty* program. I would also like to thank S.G. Ryan, G. L. Von Pragenau, W.A. Adams, and A.M. Brown for their assistance and guidance in this project.

LIST OF FIGURES

Figure (1) : Simple Rotor Models – First Bending Modes	XI-14
Figure (2) : Simple Rotor Models – Second Bending Modes	XI-15
Figure (3) : Simple Rotor Models – Third Bending Modes	XI-16
Figure (4) : HTOTP Rotor Models – First Bending Modes	XI-17
Figure (5) : HTOTP Rotor Models – Second Bending Modes	XI-18
Figure (6) : HTOTP Rotor Models – Third Bending Modes	XI-19
Figure (7) : HTOTP Flexible Disk Rotor Model – Disk Mode	XI-20
Figure (8) : Coordinate System Rotation Sequence	XI-21

LIST OF TABLES

Table (1) : Free -- Free Natural Frequencies for Simple Rotor Models . . . XI-4

Table (2) : Free -- Free Natural Frequencies for HTOP Rotor Models . . . XI-5

NOMENCLATURE

h = disk thickness coordinate
 $I_{a,i}$ = axial moment of inertia
 $I_{t,i}$ = transverse moment of inertia
 $I_{k,i} = \int \int \int (h^2 r \rho) dr d\nu dh$
 M = mass of rotor
 m = mass matrix of rotor
 q_i = i^{th} generalized coordinate
 r = disk radial coordinate
 x_i, y_i, z_i = Translational coordinates of rotor disk hub
 X = Lateral translational coordinate of rotor disk hubs
 ξ_i = i^{th} generalized coordinate for non - rotating system
 Φ = mode shape
 Ψ = mode shape
 Δ = mode shape
 ν = disk angular coordinate
 ρ = material density
 $\Gamma = \{\Psi\}^T \{I_b\} \{\Psi\}$
 $\Lambda = \{\Psi\}^T \{I_h\} \{\Psi\}$
 Ω = Rotor speed
 $\theta_y, \theta_x, \theta_z$ = Euler angles

INTRODUCTION

In the modeling of any physical device or process, certain assumptions and restrictions must be made. It is important to carefully assess their validity in order to determine the accuracy and range of applicability of the mathematical model. The current procedure for analyzing the rotordynamics of the Space Shuttle Main Engine Turbo-pumps consists of coupling the free-free rotor and housing modes with constraints to produce a model for the complete turbo-pump. This model is then used in stability analyses and for time response simulations.

The standard practice in obtaining the free-free rotor modes is to neglect the effects of rotor disk flexibility. Research into this area has indicated that disk flexibility may play an important role in the rotordynamical behavior of turbo-machinery. If rotor disk flexibility has a significant effect on the rotordynamics of the SSME turbo-pumps, significant errors could be introduced into analyses. So, it is important to assess such effects and develop means of accounting for it in analysis procedures. This work attempts to address this issue by examining some simplified finite element rotor motors and developing analytical methods of dealing with disk flexibility effects.

OBJECTIVES

- (1.) Develop finite element rotor models to evaluate the influence of disk flexibility on the rotor free-free modes.
- (2.) If justified by (1.), develop methods of modifying the current rotordynamical analysis program to account for rotor disk flexibility.
- 3.) Develop recommendations for follow-up research.

PREVIOUS RESEARCH

There is a large body of research that is available on the dynamical behavior of rotating flexible bodies. A classic work by Lamb and Southwell presented a discussion of the vibrational behavior of a spinning disk.¹ This work served as the basis for much further work in this area. Likins performed a study of mathematical modeling of spinning elastic bodies for use in modal analyses.² Wilgens and Schlack investigated the dynamical behavior of a flexible beam attached to a rotating shaft.³ Brown and Schlack extended this work to a study of the stability of a spinning body.⁴ Pringle presented a method for examining the dynamical behavior of a system with connected moving parts.⁵ Laurenson discussed methods for performing modal analysis on rotating flexible structures.⁶ Meirovitch presented an analytical study of discretization methods for flexible gyroscopic systems and drew conclusions concerning the appropriateness of various techniques.⁷

There is also a fairly large body of work documented in the literature concerning studies of disk flexibility on rotors and turbomachinery. Vance studied several rotor systems, performing a combined experimental - analytical investigation.⁸ His analytical model was configured so that the effects of disk flexibility could be accounted for in an approximate fashion. These studies indicated that, for most cases, the inclusion of rotor disk flexibility could significantly improve the correlation between experimentally measured rotor free-free natural frequencies and calculated values. Klompas developed a technique for studying shaft whirling which included the effects of flexible disks and blades.⁹ Klompas extended his study further by including the effects of disk flexibility in a study of the unbalance response of a turbo-machine.¹⁰ This work was primarily aimed at a study of the effects of blade loss. Palladine and Rosettos developed a finite element method for examining the effects of flexibility on the behavior of a rotor.¹¹ Wilgen and Schlack investigated the effects of disk flexibility on shaft whirl stability using Liapunov techniques.¹² The resulting procedure is analytically very nice, but for complicated disk shapes and multi-disk systems the method could quickly become intractable. Dopkin and Shoup performed a study of the effects of disk flexibility on the resonant frequencies of an axisymmetric rotating shaft. They found that the effects of disk flexibility may significantly reduce the rotor resonant speeds and that this effect was particularly pronounced at low rotor speeds.¹³ Shahab and Thomas studied finite element models of single and multi-disk rotor systems and compared the results to experimental models.¹⁴ This study indicated that coupling effects between the shaft and disk modes can have a significant effect on the dynamical behavior of a rotor. Sakata, Aiba, and Ohnabe studied the transient vibration behavior of a rotor subjected to a blade loss and included the effects of disk flexibility.¹⁵

FINITE ELEMENT ANALYSES

The first objective of this research effort is aimed at evaluating the influence of disk flexibility on the rotor free-free modes. The most straight-forward way of studying this effect is by developing finite element rigid and flexible disk rotor models and comparing the rotor free-free modes.

Examination of schematics of the HTOTP and HTFTP rotor disk configurations reveals that the second turbine stage of the HTOTP has the thinnest disk configuration and is probably most likely to exhibit flexibility effects. In order to establish what types of behavior might be expected for a rotor with a flexible disk, a simple model was first examined. A configuration was selected that is approximately that of the HTOTP rotor shaft with a disk attached to represent the second turbine stage. This model consists of a 0.051 m. diameter, 0.59 m. steel shaft. A 0.239 m. diameter, 0.0161 m. thick disk was attached to the shaft with its center point 0.528 m. from the end of the shaft. For the flexible disk study, the properties of steel were used for the disk. For the rigid disk study, the density and poisson's ratio of steel and a modulus of rigidity and modulus of elasticity three orders of magnitude above those of steel were used as the material properties. The free-natural frequencies for the two models are compared in Table 1 and the mode shapes are illustrated in Figure 1.

Table 1 : Free-Free Natural Frequencies
For Simple Rotor Models

Natural Frequencies (Hz)		
Mode	Flexible Disk	Rigid Disk
First Bending	487	502
Second Bending	1003.0, 1997.0	1225.0
Third Bending	3393.0	2453.0

Note that the first rotor bending mode is not significantly affected by the disk flexibility. However, the second and third bending modes are strongly influenced.

In order to better evaluate the influence of disk flexibility, it was decided to develop a second, more sophisticated rotor model of the HPTOP. A finite element code was developed based on work by Muller¹⁰. The model was developed using

ANSYS, a finite element analysis package. The types of beams and rigid masses used are the same as those used by Muller except the second turbine has been replaced by a 0.239 m. diameter, 0.0161 m. thick disk, and rigid inertias $I_{xx} = 5.28 \times 10^{-3} \text{ kg} - \text{m}^2$, $I_{yy} = 2.96 \times 10^{-3} \text{ kg} - \text{m}^2$, and $I_{zz} = 2.96 \times 10^{-3} \text{ kg} - \text{m}^2$. As in the previous study, the material properties of steel are used for the flexible disk case. For the rigid disk, the density and poisson's ratio of steel are used with a modulus of elasticity and modulus of rigidity increased by three orders of magnitude. The resulting model was examined using an eigenanalysis to determine the free-free rotor modes.

**Table 2 : Free-Free Natural Frequencies
For HPOTP Rotor Models**

Natural Frequencies (Hz)		
Mode	Flexible Disk	Rigid Disk
First Bending	462.2	467.6
First Torsional	913.8	944.3
Second Bending	926.7, 1652.0	1072.0
Second Torsional	1255.2	1274.0
Third Bending	1773.6	1983.0
Third Torsional	2636.7	2486.0

For the first bending modes, the mode shapes and frequencies for the two cases match closely. Similar behavior is observed for the first torsional modes. For the second bending modes, the rigid disk system has a single mode shape. The flexible disk model exhibits two second bending modes. The first is characterized by motion of the disk in-phase with the hub. The second is characterized by motion of the disk out-of-phase with the hub. The in-phase motion serves to effectively reduce the second bending mode natural frequency and the out-of-phase motion serves to effectively increase it.

ANALYTICAL STUDY

The results of the finite element studies indicate that rotor disk flexibility can significantly alter the free-free rotor modes and frequencies. As a result, it is appropriate to develop techniques for accounting for such effects in the current rotordynamical analysis program so that the significance of disk flexibility can be evaluated for the complete turbo-pump model.

The equations of motion for two formulations of a flexible rotor - flexible disk model are presented. Each of the approaches presented in this study assume that the deflection of the rotor disk is primarily in the lateral direction. The beam is assumed to be axially and torsionally rigid, which implies that the disk hubs move together as a rigid body in the lateral direction. In addition, it is assumed that the beam is axially stiff so that the axial hub position of i^{th} disk is $x_i \equiv X$, for all i . For each of the following developments, the rotor is considered to consist of a series of flexible disks. The equations are formulated using a Lagrangian formulation.

Rotation Sequence

$\theta_{y,i}$ about y
 $\theta_{x,i}$ about z'
 $\theta_{x,i}$ about \bar{x}
 ν about \bar{i} (disk angular coordinate)

Formulation Using Flexible Rotor - Flexible Disk Modes

Position of Arbitrary Point In Inertial Coordinate System

First, obtain the position vector \vec{P}_i for an arbitrary point on the i^{th} rotor disk.

$$\vec{P}_i = P_{x,i} \hat{x} + P_{y,i} \hat{y} + P_{z,i} \hat{z}$$

where

$$P_{x,i} = u_i$$

$$P_{y,i} = Y_i + h \sin(\theta_{x,i}) + r \cos(\nu + \theta_{x,i}) \cos(\theta_{x,i})$$

$$P_{z,i} = Z_i + r \sin(\nu + \theta_{x,i}) \cos(\theta_{y,i}) - h \cos(\theta_{x,i}) \sin(\theta_{y,i}) \\ + r \cos(\nu + \theta_{x,i}) \sin(\theta_{y,i}) \sin(\theta_{x,i})$$

Velocity of Arbitrary Point

Differentiation of the position vector with respect to time yields a velocity vector for the arbitrary point.

$$\vec{V}_i = V_{x,i} \hat{x} + V_{y,i} \hat{y} + V_{z,i} \hat{z}$$

where

$$V_{x,i} = \dot{u}_i$$

$$V_{y,i} = \dot{Y} - \dot{\theta}_{x,i} h \cos(\theta_{x,i}) - r \Omega \sin(\nu + \theta_{x,i}) \cos(\theta_{x,i}) - r \dot{\theta}_{x,i} \cos(\nu + \theta_{x,i}) \sin(\theta_{x,i})$$

$$V_{z,i} = \dot{Z}_i + r \Omega \cos(\nu + \theta_{x,i}) \cos(\theta_{y,i}) - r \dot{\theta}_{y,i} \sin(\nu + \theta_{x,i}) \sin(\theta_{y,i}) \\ + h \dot{\theta}_{x,i} \sin(\theta_{x,i}) \sin(\theta_{y,i}) - h \dot{\theta}_{y,i} \cos(\theta_{x,i}) \cos(\theta_{y,i}) \\ - r \Omega \sin(\nu + \theta_{x,i}) \sin(\theta_{y,i}) \sin(\theta_{x,i}) + r \dot{\theta}_{y,i} \cos(\nu + \theta_{x,i}) \cos(\theta_{y,i}) \sin(\theta_{x,i}) \\ + r \dot{\theta}_{x,i} \cos(\nu + \theta_{x,i}) \sin(\theta_{y,i}) \cos(\theta_{x,i})$$

Kinetic Energy

Express the kinetic energy of each disk as

$$T_i = \frac{1}{2} \int \int \int (V_{x,i}^2 + V_{y,i}^2 + V_{z,i}^2) \rho r dr d\nu dh$$

The total kinetic energy of the rotor is then

$$T = \sum_i T_i$$

$$T = \frac{1}{2} \int \int \int (\{\dot{u}\}^T \{\dot{u}\}) r dr d\nu dh$$

$$\begin{aligned}
& + \frac{1}{2} \{\dot{\theta}_z\}^T [I_h] \{\dot{\theta}_z\} + \frac{1}{2} \{\dot{\theta}_y\}^T [I_h] \{\dot{\theta}_y\} + \frac{1}{2} \Omega \{\dot{\theta}_y\}^T [I_a] \{\theta_z\} + \frac{1}{2} \Omega \{\dot{\theta}_z\}^T [I_a] \{\theta_y\} \\
& + \frac{1}{2} \Omega^2 [I_a] + \frac{1}{2} \{\dot{Y}\}^T [m] \{\dot{Y}\}^2 + \frac{1}{2} \{\dot{Z}\}^T [m] \{\dot{Z}\}^2 - \frac{1}{4} \Omega^2 \{\theta_z\}^T [I_a] \{\theta_z\} \\
& - \frac{1}{4} \Omega^2 \{\theta_y\}^T [I_a] \{\theta_y\}
\end{aligned}$$

where $I_{h,i} = \int \int (h^2 \rho r) dr d\nu dh$

$$\{I_h\} = \begin{pmatrix} I_{h,1} & 0 & 0 & \cdot & \cdot & 0 \\ 0 & I_{h,2} & 0 & \cdot & \cdot & 0 \\ \cdot & \cdot & \cdot & \cdot & \cdot & \cdot \\ 0 & 0 & 0 & \cdot & \cdot & I_{h,n} \end{pmatrix}$$

$$\{u\} \equiv \begin{pmatrix} u_1 \\ u_2 \\ \cdot \\ \cdot \\ \cdot \\ u_n \end{pmatrix}$$

For a non-spinning rotor, the position of a point on the disk can be expressed in terms of the free-free rotor disk modes.

$$\{u\} = \{h\} + \{X\} + \begin{pmatrix} \Delta_x & 0 \\ 0 & \Delta_y \end{pmatrix} \begin{pmatrix} \xi_y \\ \xi_x \end{pmatrix}$$

where X is the hub axial position.

For a spinning rotor, it is necessary to transform this relation to account for the rotor spin. Notice that u_i is defined in terms of the inertial reference frame. In order to express u_i in terms of the free-free disk modes, one can make the following coordinate transformation.

$$\{\xi_y\} = \cos(\Omega t) \{q_y\} + \sin(\Omega t) \{q_x\}$$

$$\{\xi_z\} = \cos(\Omega t)\{q_z\} - \sin(\Omega t)\{q_y\}$$

$$\{u\} = \{h\} + \{X\} + \begin{pmatrix} \Delta_z & 0 \\ 0 & \Delta_y \end{pmatrix} \begin{pmatrix} \cos(\Omega t) & \sin(\Omega t) \\ -\sin(\Omega t) & \cos(\Omega t) \end{pmatrix} \begin{pmatrix} q_y \\ q_z \end{pmatrix}$$

Notice that since the rotor is axisymmetric,

$$\int \int \int ([\Delta_y]^T [\Delta_y] r \rho) dr d\nu dh = \int \int \int ([\Delta_z]^T [\Delta_z] r \rho) dr d\nu dh$$

$$\text{Let } [A] = \int \int \int ([\Delta_y]^T [\Delta_y] r \rho) dr d\nu dh$$

and

$$\begin{aligned} T = & \frac{1}{2} \{\dot{q}_y\}^T [\Lambda] \{\dot{q}_y\} + \frac{1}{2} \{\dot{q}_z\}^T [\Lambda] \{\dot{q}_z\} - \frac{1}{2} \Omega \{\dot{q}_z\}^T [\Gamma] \{q_y\} - \frac{1}{2} \Omega \{\dot{q}_y\}^T [\Gamma] \{q_z\} \\ & + \frac{1}{2} [\Omega] [I_a] [\Omega] + \frac{1}{2} M \dot{X}^2 + \frac{1}{2} \{\dot{q}_y\}^T \{\Phi\}^T \{m\} \{\Phi\} \{\dot{q}_y\} \\ & + \frac{1}{2} \{\dot{q}_z\}^T \{\Phi\}^T \{m\} \{\Phi\} \{\dot{q}_z\} - \frac{1}{4} \Omega^2 \{q_z\}^T [\Gamma] \{q_z\} - \frac{1}{4} \Omega^2 \{q_y\}^T [\Gamma] \{q_y\} \\ & + \frac{1}{2} \Omega \{\dot{q}_y\}^T [A] \{q_z\} - \frac{1}{2} \Omega \{\dot{q}_z\}^T [A] \{q_y\} + \frac{1}{2} \Omega \{q_z\}^T [A] \{\dot{q}_y\} \\ & - \frac{1}{2} \Omega \{q_y\}^T [A] \{\dot{q}_z\} + \frac{1}{2} \Omega^2 \{q_y\}^T [A] \{q_y\} + \frac{1}{2} \Omega^2 \{q_z\}^T [A] \{q_z\} \\ & + \frac{1}{2} \{\dot{q}_y\}^T [A] \{\dot{q}_y\} + \frac{1}{2} \{\dot{q}_z\}^T [A] \{\dot{q}_z\} \end{aligned}$$

$$\Gamma = \{\Psi\}^T [I_a] \{\Psi\}$$

$$\Lambda = \{\Psi\}^T [I_h] \{\Psi\}$$

Potential Energy

$$[\omega_n^2] \equiv \begin{pmatrix} \omega_{n1}^2 & 0 & \cdot & \cdot & \cdot & 0 \\ 0 & \omega_{n2}^2 & \cdot & \cdot & \cdot & 0 \\ \cdot & \cdot & \cdot & \cdot & \cdot & \cdot \\ \cdot & \cdot & \cdot & \cdot & \cdot & \cdot \\ 0 & 0 & \cdot & \cdot & \cdot & \omega_{n2}^2 \end{pmatrix}$$

$$\begin{aligned} [V] &\equiv (\xi_y \quad \xi_x) \begin{pmatrix} [\omega_n^2] & 0 \\ 0 & [\omega_n^2] \end{pmatrix} \begin{pmatrix} \xi_y \\ \xi_x \end{pmatrix} \\ &\equiv (q_y \quad q_x) \begin{pmatrix} \cos(\Omega t) & -\sin(\Omega t) \\ \sin(\Omega t) & \cos(\Omega t) \end{pmatrix} \begin{pmatrix} [\omega_n^2] & 0 \\ 0 & [\omega_n^2] \end{pmatrix} \begin{pmatrix} \cos(\Omega t) & \sin(\Omega t) \\ -\sin(\Omega t) & \cos(\Omega t) \end{pmatrix} \begin{pmatrix} q_y \\ q_x \end{pmatrix} \\ &\equiv (q_y \quad q_x) \begin{pmatrix} [\omega_n^2] & 0 \\ 0 & [\omega_n^2] \end{pmatrix} \begin{pmatrix} q_y \\ q_x \end{pmatrix} \end{aligned}$$

where $[\omega_n^2]$ represents the squared natural frequencies of the flexible rotor - flexible disk.

Equations of Motion

$$\{\Phi\}^T \{m\} \{\Phi\} \ddot{q}_y + [A] \{\ddot{q}_y\} + [\Lambda] \{\ddot{q}_y\} + 2\Omega[A] \{\dot{q}_x\} + \frac{1}{2}\Omega^2[\Gamma] \{q_y\} - \Omega^2[A] \{q_y\} + [\omega_n^2] \{q_y\} = \{0\}$$

$$\{\Phi\}^T \{m\} \{\Phi\} \ddot{q}_x + [A] \{\ddot{q}_x\} + [\Lambda] \{\ddot{q}_x\} - 2\Omega[A] \{\dot{q}_y\} + \frac{1}{2}\Omega^2[\Gamma] \{q_x\} + \Omega^2[A] \{q_x\} + [\omega_n^2] \{q_x\} = \{0\}$$

$$\{\ddot{X}\} = \{0\}$$

CONCLUSIONS AND RECOMMENDATIONS

From the results of the finite element analyses, it is clear that rotor disk flexibility can significantly alter the rotor free-free modes and frequencies. While the first rotor bending mode is not strongly affected by disk flexibility, the second and third bending modes are significantly altered. In fact, two second bending modes are identified. The first is associated with in-phase motion of the disk with the rotor and the second is associated with out-of-phase motion of the disk with the rotor.

Equations have been developed for accounting for disk flexibility in a rotor model. Particular emphasis has been placed on obtaining equations that are suitable for incorporation into the current used rotordynamical analysis program.

From these results, the following conclusions and recommendations have been drawn.

- 1.) The rotordynamical analysis program should be modified to account for disk flexibility.
- 2.) The revised program should be tested with modal data from a simplified rotor finite element model.
- 3.) If results warrant, develop full-scale finite element models of the SSME turbo-pump rotors and use the resulting modal data in the revised rotordynamical analysis program.
- 4.) Compare these results to the responses predicted for a rigid disk rotor and evaluate the influence of rotor disk flexibility on the SSME turbo-pumps.
- 5.) In order to develop further physical insight into the effect of rotor disk flexibility, construct appropriately scaled rotor models and study their responses using a rotor test kit.
- 6.) Relate the results of these studies to actual observed behavior of the SSME turbo-pumps in order to gain physical insight and understanding of their rotordynamical behavior. Such understanding could enhance failure analysis .

REFERENCES

1. Lamb, H., and Southwell R.V., "The Vibrations of a Spinning Disk," *Proceedings of the Royal Society, Series A*, Vol. 99, July, 1921, pp. 272-280.
2. Likins, Peter W., Barbera, Frank J., and Braddeley, Victor, "Mathematical Modeling of Spinning Elastic Bodies for Modal Analysis," *AIAA Journal*, Vol. 11, No. 9, September, 1973, pp. 1251-1258.
3. Wilgen, F.J., Schlack, A.L., "Effects of Radial Appendage Flexibility on Shaft Whirl Stability," Vol. 15, No. 10, October, 1977, pp. 1531-1533.
4. Brown, D.P., and Schlack, A.L., Jr., "Stability of a Spinning Body Containing an Elastic Membrane via Liapunov's Direct Method," *AIAA Journal*, October, 1972, pp. 1286-1290.
5. Pringle, Ralph, Jr., "On the Stability of a Body with Connected Moving Parts," *AIAA Journal*, Vol. 7, No. 6, June, 1969, pp. 1054-1063.
6. Laurenson, R.M., "Modal Analysis of Rotating Flexible Structures," *AIAA Journal*, Vol. 14, No. 10, October, 1976, pp. 1444-1450.
7. Meirovitch, Leonard, "A Stationarity Principle for the Eigenvalue Problem for Rotating Structures," *AIAA Journal*, Vol. 14, No. 10, October, 1976, pp. 1387-1394.
8. Vance, John M., Rotordynamics of Turbomachinery, John Wiley and Sons, 1988.
9. Klompas, Nicholas, "Theory of Rotor Dynamics with Coupling of Disk and Blade Flexibility and Support Structure Assymmetry," presented at *ASME Gas Turbine Conference and Products Show*, Zurich, Switzerland, March 30-April 4, 1974, paper no. 74-GT-159.
10. Klompas, N. "Unbalance Response Analysis of a Complete Turbomachine," *ASME Journal of Engineering for Power*, Vol. 105, January, 1983, pp. 184-191.
11. Palladine, J.A., and Rosettes, J.N., "Finite Element Analysis of the Dynamics of Flexible Disk Rotor Systems," presented at *ASME International Gas Turbine Conference and Exhibit, 27th*, London, England, April 18-22, 1982, paper no. 82-GT-240.
12. Wilgen, F.J., and Schlack, A.L., 1957, "Effects of Disk Flexibility on Shaft Whirl Stability," *AIAA Journal*, Vol. 15, No. 10, Oct., 1977, pp. 1531-1533.

13. Dopkin, J.A., Shoup, T.E., "Rotor Resonant Speed Reduction Caused by Flexibility of Disks," *ASME Journal of Engineering for Industry*, November, 1974, pp. 1328-1333.
14. Shahab, A.A.S., and Thomas, J., "Coupling Effects of Disc Flexibility on the Dynamic Behaviour of Multi Disc-Shaft Systems," *Journal of Sound and Vibration*, Vol. 114, No. 3, 1987, pp. 435-452.
15. Sakata, M., Aiba, T., and Ohnabe, H., "Transient Vibration of High Speed Lightweight Rotor Due to Sudden Imbalance," presented at *ASME International Gas Turbine Conference and Exhibit, 27th*, London, England, April 18-22, 1982, paper no. 82-GT-231.
16. Muller, G.R., "Finite Element Models of the Space Shuttle Main Engine," NASA TM-782660, January, 1980.
17. Ryan, Stephen G., "Turbomachinery Rotordynamics Analysis Package," NASA Internal Document, August 20, 1980.
18. Kulla, P., "Comment of 'Effects of Radial Appendage Flexibility on Shaft Whirl Stability'," and Wilgen, F.J., and Schlack, A.L., Jr., "Reply by Authors to P. Kulla," Vol. 16, No. 10, October, 1978, pp. 1117-1119.
19. Childs, Dara W., "Two Jeffcott-Based Simulation Models for Flexible Rotating Equipment," *ASME Journal of Engineering for Industry*, August 1975, pp. 1000-1014.

ORIGINAL PAGE IS
OF POOR QUALITY

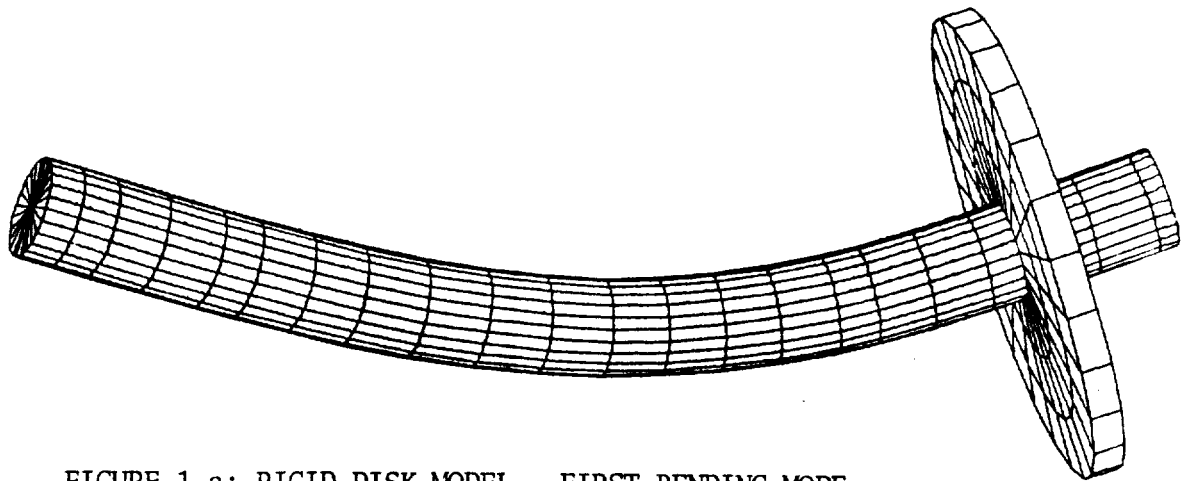


FIGURE 1.a: RIGID DISK MODEL - FIRST BENDING MODE
FREQUENCY = 502 Hz

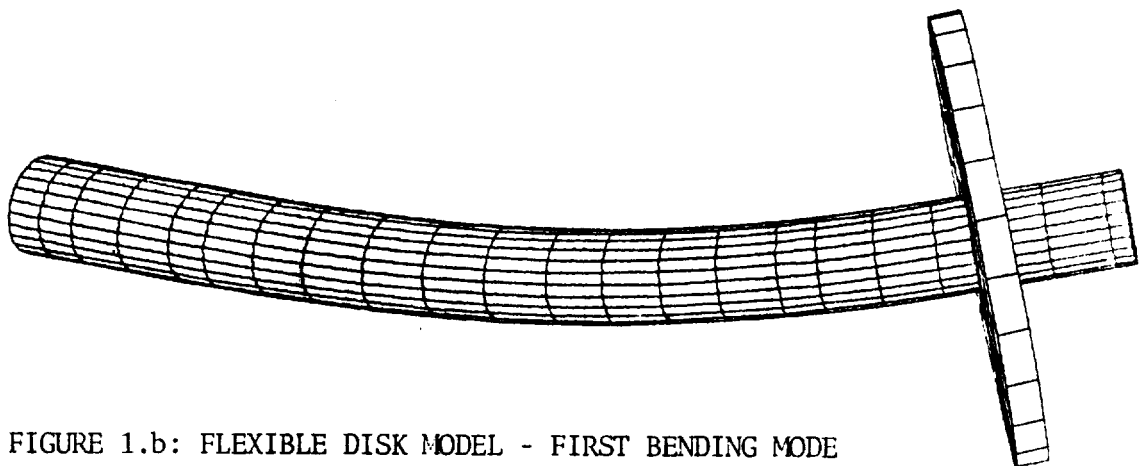


FIGURE 1.b: FLEXIBLE DISK MODEL - FIRST BENDING MODE
FREQUENCY = 487 Hz

FIGURE 1: SIMPLE ROTOR MODELS - FIRST BENDING MODES

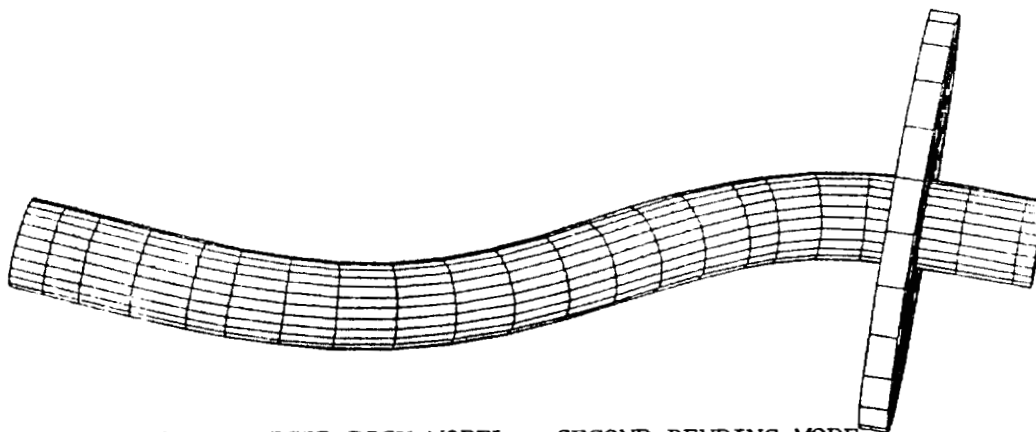


FIGURE 2.a: RIGID DISK MODEL - SECOND BENDING MODE
FREQUENCY = 1225 Hz

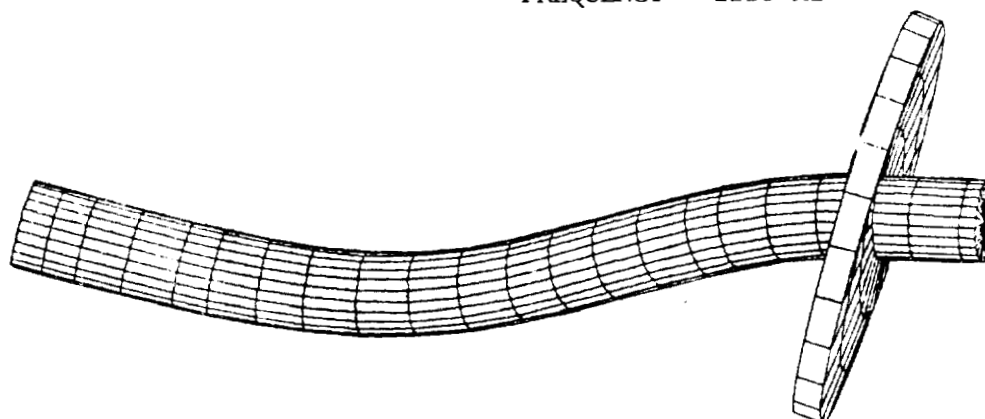


FIGURE 2.b: FLEXIBLE DISK MODEL - SECOND BENDING MODE, DISK IN-PHASE
FREQUENCY = 1003 Hz

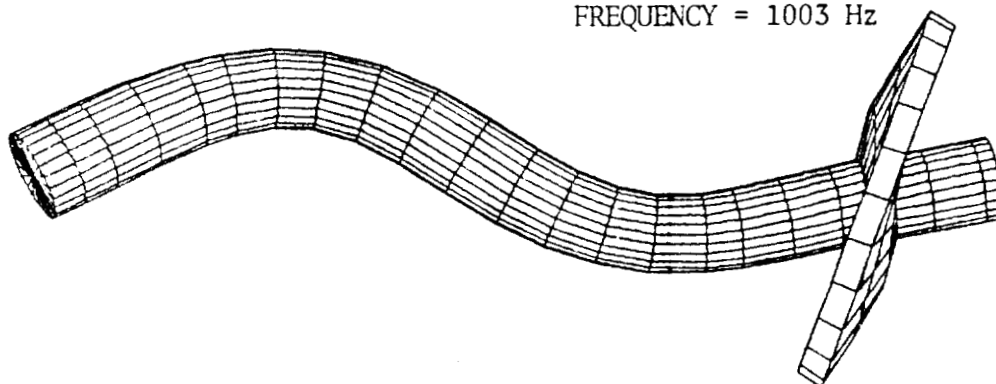


FIGURE 2.c: FLEXIBLE DISK MODEL - SECOND BENDING MODE, DISK OUT-OF-PHASE
FREQUENCY = 1997 Hz

FIGURE 2: SIMPLE ROTOR MODELS - SECOND BEARING MODES

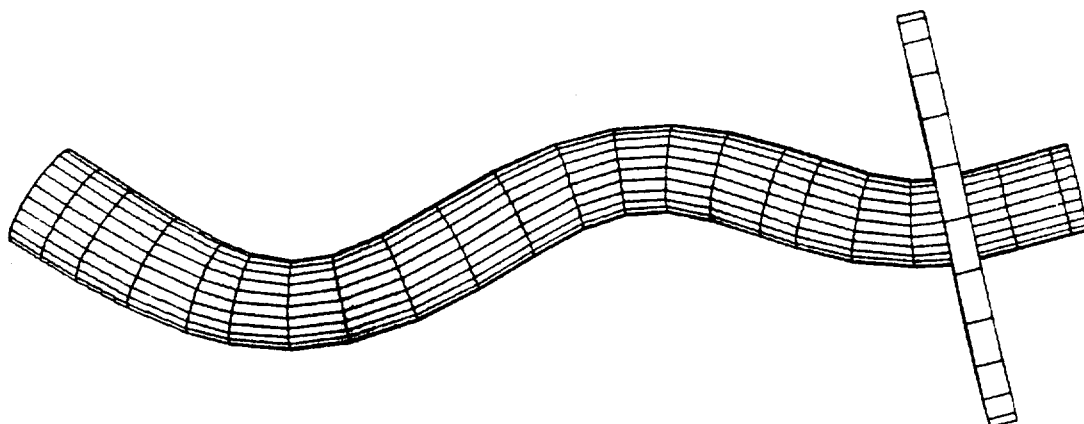


FIGURE 3.a: RIGID DISK MODEL - THIRD BENDING MODE
FREQUENCY = 2453 Hz

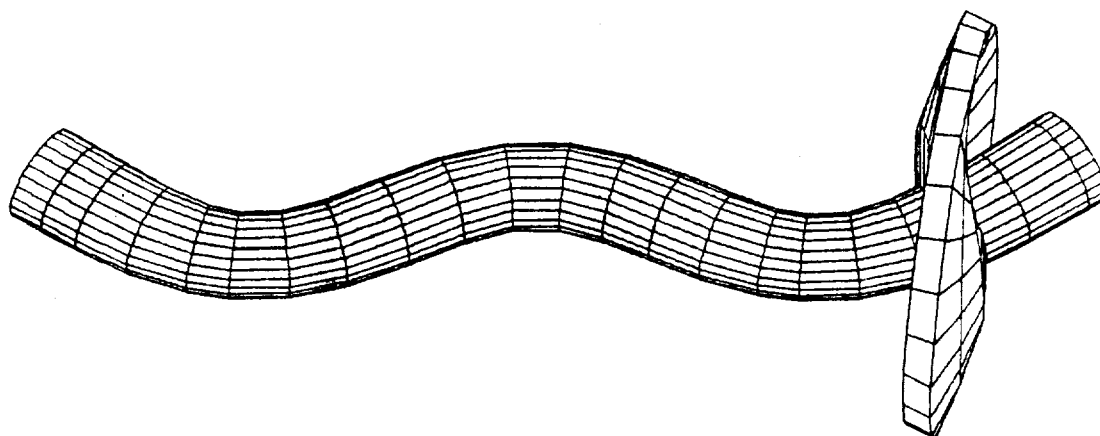


FIGURE 3.b: FLEXIBLE DISK MODEL - THIRD BENDING MODE, DISK OUT-OF-PHASE
FREQUENCY = 3393 Hz

FIGURE 3: SIMPLE ROTOR MODELS - THIRD BENDING MODES

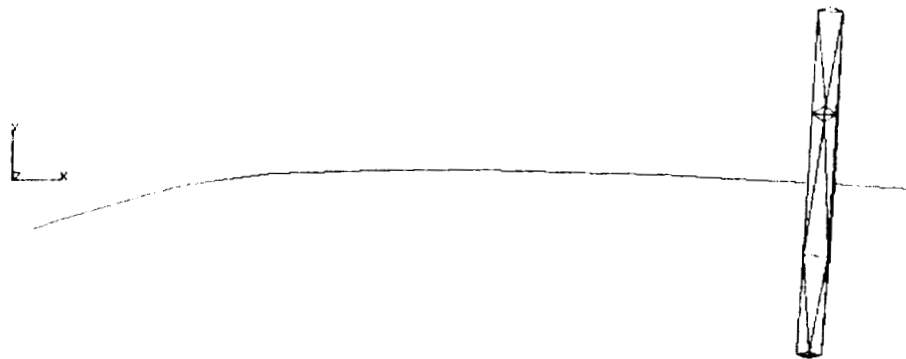


FIGURE 4.a: RIGID DISK MODEL - FIRST BENDING MODE
FREQUENCY = 467.6 Hz

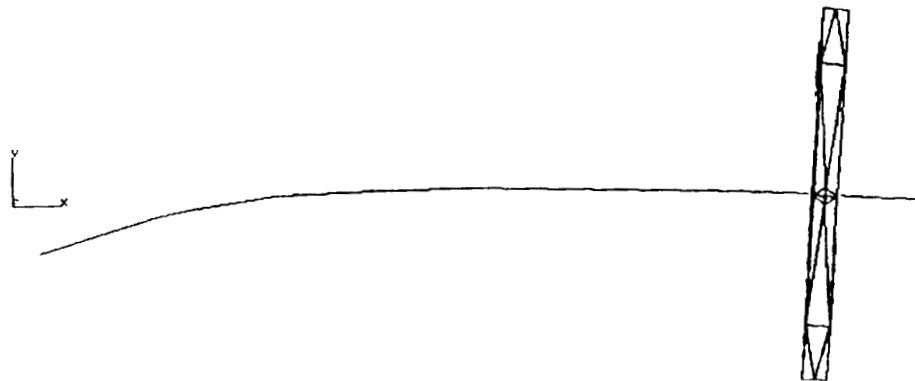


FIGURE 4.b: FLEXIBLE DISK MODEL - FIRST BENDING MODE
FREQUENCY = 462.2 Hz

FIGURE 4: HPOTP ROTOR MODELS - FIRST BENDING MODES

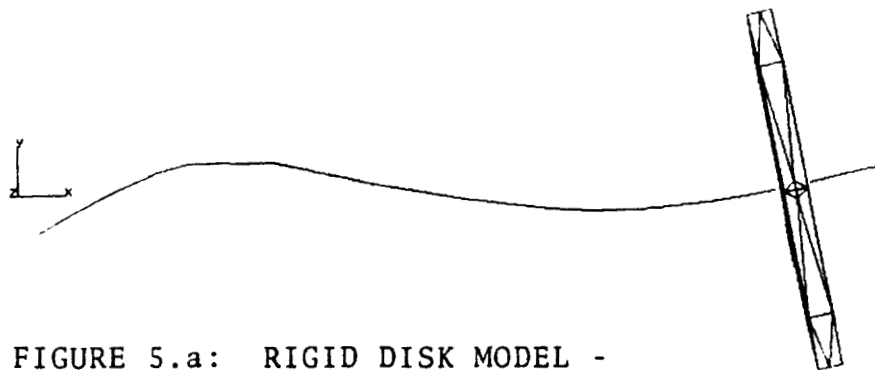


FIGURE 5.a: RIGID DISK MODEL -
SECOND BENDING MODE
FREQUENCY = 1072 Hz

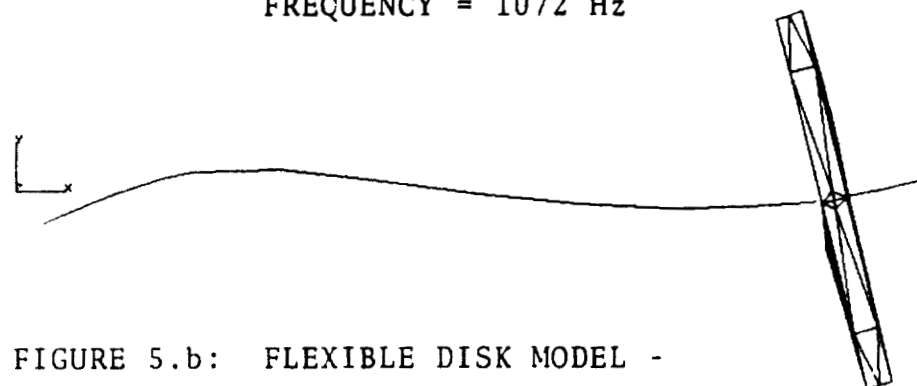


FIGURE 5.b: FLEXIBLE DISK MODEL -
SECOND BENDING MODE, DISK
IN-PHASE
FREQUENCY = 926.7 Hz

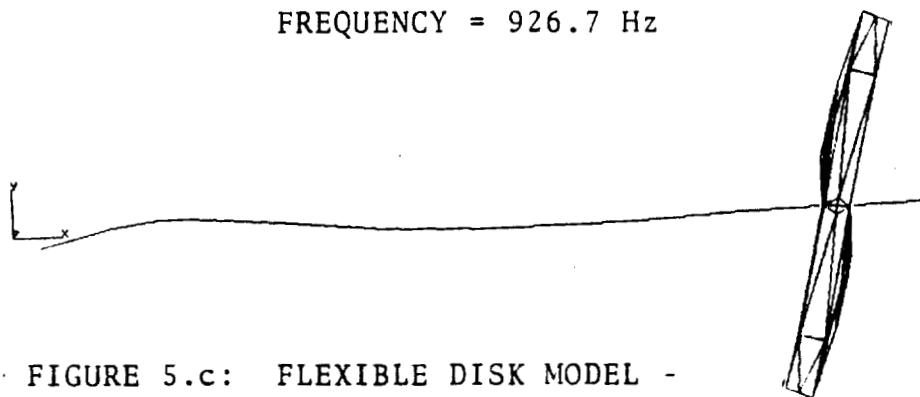


FIGURE 5.c: FLEXIBLE DISK MODEL -
SECOND BENDING MODE, DISK OUT-OF-PHASE
FREQUENCY = 1652.0 Hz

FIGURE 5: HPOTP ROTOR MODELS - SECOND BENDING MODES

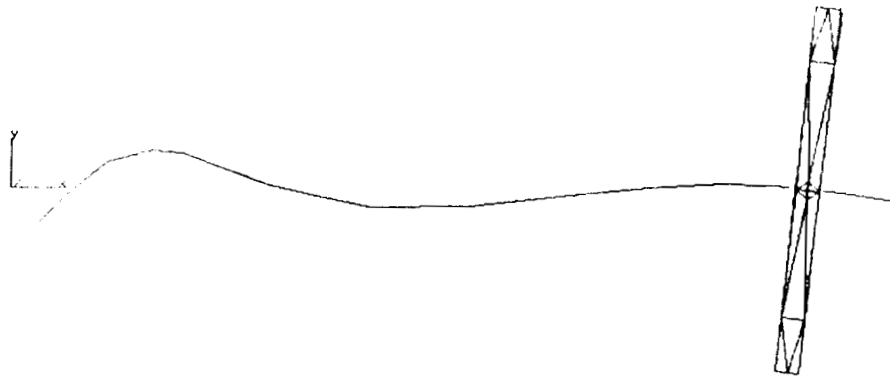


FIGURE 6.a: RIGID DISK MODEL - THIRD BENDING MODE
FREQUENCY = 1983 Hz

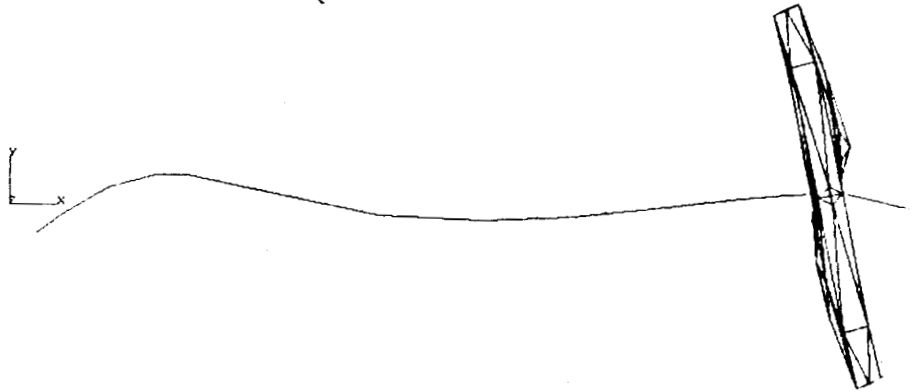


FIGURE 6.b: FLEXIBLE DISK MODEL - THIRD BENDING MODE
FREQUENCY = 1773 Hz

FIGURE 6: HPOTP ROTOR MODELS - THIRD BENDING MODES'

ORIGINAL PAGE IS
OF POOR QUALITY

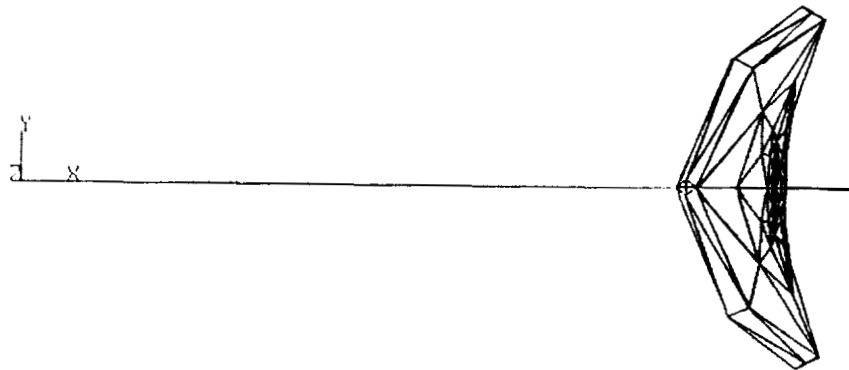


FIGURE 7: HPOTP FLEXIBLE DISK ROTOR MODEL - DISK MODE

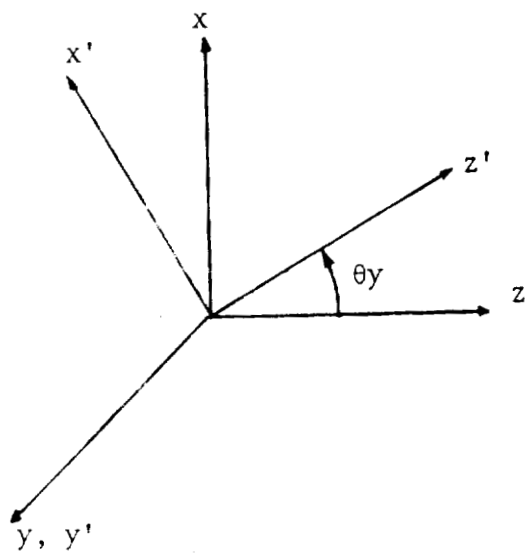


FIGURE 8.a

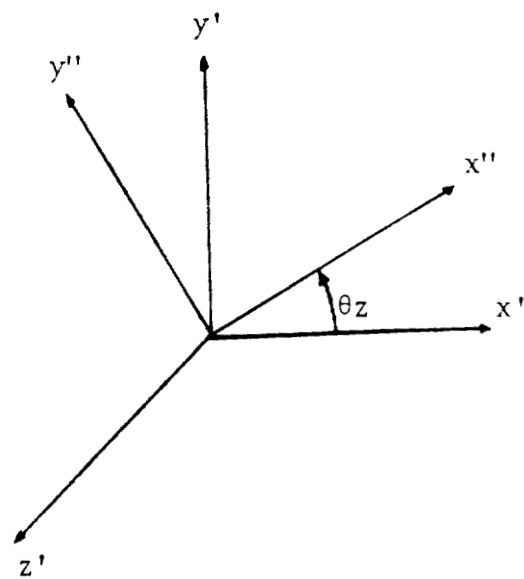


FIGURE 8.b

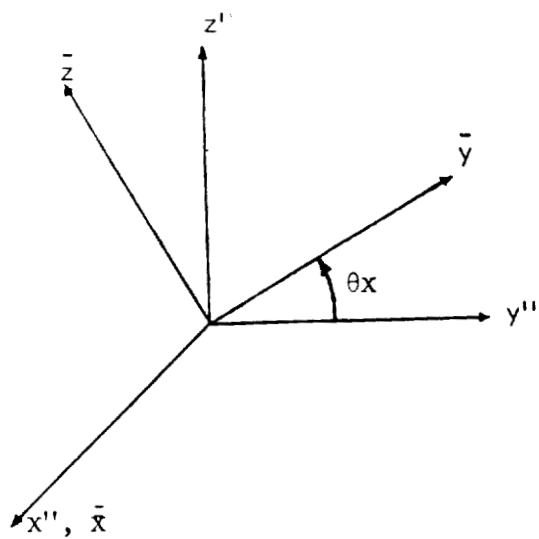


FIGURE 8.c

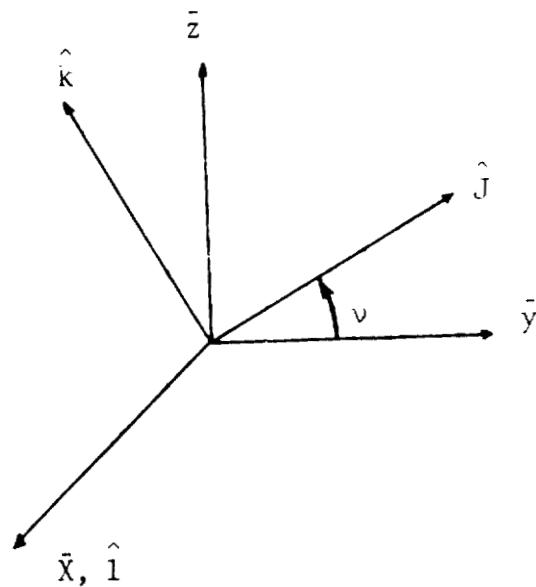


FIGURE 8.d

FIGURE 8: COORDINATE SYSTEM ROTATION SEQUENCE

1989

NASA/ASEE SUMMER FACULTY FELLOWSHIP PROGRAM

MARSHALL SPACE FLIGHT CENTER
THE UNIVERSITY OF ALABAMA

A COMPUTER CONTROL SYSTEM FOR THE ALTERNATING GRADIENT
MAGNETOMETER

Prepared by:	Michael M. Garland
Academic Rank:	Professor
University and Department:	Memphis State University Department of Physics
NASA/MSFC:	
Laboratory:	Space Science
Division:	Astrophysics
Branch:	Cryogenic Physics
MSFC Colleague:	Eugene W. Urban
Date:	July 28, 1989
Contract No.:	The University of Alabama in Huntsville NGT-01-008-021

**A COMPUTER CONTROL SYSTEM FOR THE ALTERNATING GRADIENT
MAGNETOMETER**

by

Michael M. Garland
Professor of Physics
Memphis State University
Memphis, Tennessee

ABSTRACT

An alternating gradient magnetometer has been interfaced to a computer for the automation of data taking. Using a fast Fourier transform analysis system data can be acquired and processed in real time. Data is stored on disk and can be recalled for plotting and further analysis. With the addition of a simple liquid nitrogen cryostat, magnetization measurements can be carried out in the range from 300 K to 77K. Results are reported on three different types of piezoelectric transducers.

Acknowledgements

I would like to thank Dr. Palmer Peters for his assistance and encouragement and Dr. Eugene Urban for giving me this opportunity. I would especially like to thank Mr. Charles Sisk for his help in writing the programs and for sharing his equipment.

I also wish to thank the ASEE and NASA for providing the opportunity for me to work at MSFC this Summer.

LIST OF FIGURES

1. Magnetometer	5
2. Program Flow Chart	7
3. Frequency Response of PZT Reed	9
4. Frequency Response of Kynar Reed	10
5. Magnetization Curve for Superconducting Er123.....	11
6. Magnetization Curve for Normal Er123.....	12
7. Susceptibility Curves for Er123	13
8. Magnetization Curve for Field Cooled Y123.....	14
9. Magnetization Curve for Field Cooled Y123+Ag.....	16
10. Hysteresis Loop for Eu123+Ag.....	17
11. Hysteresis Loop for Field-Cooled Eu123+Ag.....	18

Introduction

The discovery of the ceramic superconductor Y-Ba-Cu-O¹ and its related compounds has led to a renewed interest in the general field of superconductivity. The ceramic superconductors, which have transition temperatures ranging from 90K to 120K and perhaps higher²⁻⁴ have given rise to expectations of great technological utility. Unfortunately, most of these materials have low critical currents, which limits their current carrying abilities. This is a serious drawback for applications involving superconducting magnets and power transmission and storage.

In order to understand the limitations to the critical current it is important to be able to characterize the magnetic properties of a superconductor, as the two are intimately related⁵. Measurements of magnetization and magnetic hysteresis allow one to determine the extent of magnetic flux pinning, which is related to the microscopic critical current.

In the current research an alternating gradient magnetometer, which was constructed in the Summer of 1988, was interfaced with a computer in order to automate the taking of magnetization data.

Objectives

The objectives of this experiment were to interface the alternating gradient magnetometer to a computer and to write the program which would automate data taking. The program must be capable of reading the magnetization, temperature, and applied magnetic field, in real time, and storing them on a disk for later analysis.

Theory

The internal magnetic field in a non-ferromagnetic material is described by the equation

$$B = H + 4\pi M \quad (\text{cgs units})$$

where B is the magnetic induction, H is the external applied field and M is the magnetization. For homogeneous paramagnetic and diamagnetic materials M is a linear function of H . Thus, in a homogeneous material $M = XH$, where X is the magnetic susceptibility. In a paramagnetic material X is positive and in a diamagnetic material it is negative. Superconductors are diamagnetic when in the superconducting state and (usually) paramagnetic or non-magnetic ($X=0$) in the normal state. So a graph of M as a function of H should yield a straight line of slope X . In a superconductor, this will be true as long as the applied field does not approach the lower critical field H_{c1} . Once H_{c1} is exceeded, magnetic flux begins to penetrate the sample, in the form of quantized flux lines. These flux lines become pinned in the sample, reducing the diamagnetic magnetization. The presence of pinned flux, therefore, produces a hysteresis in the magnetization vs field curve. The extent of the hysteresis is an indication of the extent of flux pinning. If an electric current is introduced in the sample, once it exceeds some critical value the flux lines will begin to move, giving rise to an electrical resistance. So, the extent of the hysteresis is also related to the critical current, at which electrical resistance begins to appear.

If a paramagnetic or diamagnetic material is placed in an external, non-uniform, magnetic field, it experiences a force in the direction of the field gradient dH/dx . This force is directly proportional to the field gradient, and to M , the magnetization. If one can measure this force then, knowing the field gradient, the magnetization can be computed.

The theory and construction of an alternating gradient magnetometer has been described by Flanders⁶ and by the author⁷. In the original design, the gradient field was swept sinusoidally and the force on the sample was measured using a piezoelectric transducer connected to a lock-in amplifier. In its present form the piezoelectric output is detected by a fast Fourier transform analyzer.

Apparatus

Magnetometer

A block diagram of the magnetometer and associated circuitry is shown in figure 1. The major components will be discussed separately in the following paragraphs. A complete description of the field coils and vane can be found in reference 7.

Wave Analyzer

The output of the piezoelectric transducer is processed by an Ono Sokki Mini FFT Analysis System. The FFT system is a small dedicated computer which performs a fast Fourier transform on the input signal and displays the wave spectrum in near real time. The amplitude of the peak corresponding to the driving frequency can be selected thereby eliminating other peaks caused by noise and overtones. The amplitude of the selected peak is read by the computer and stored in an array.

Function Generator

The driving current for the sweep coils is obtained from a Wavetek model 270 Function Generator. The drive voltage and frequency are input at the start of the program and written to the Wavetek by the computer. The frequency is set at the resonant frequency of the reed, or one of its overtones. The drive voltage is set to produce an rms current of 100 mA through the sweep coils.

Current Source

The current for the D.C. magnet is obtained from a Hewlett-Packard model 228A Current Source. The magnet current is ramped in steps of 0.10 Amp preceding each measurement of the signal amplitude. It was necessary to add a time delay of 2 to 4 seconds in order to allow the system to settle down between measurements. A further provision was added to allow the sample to be cooled initially in a preset magnetic field, in order to analyze the extent of flux pinning.

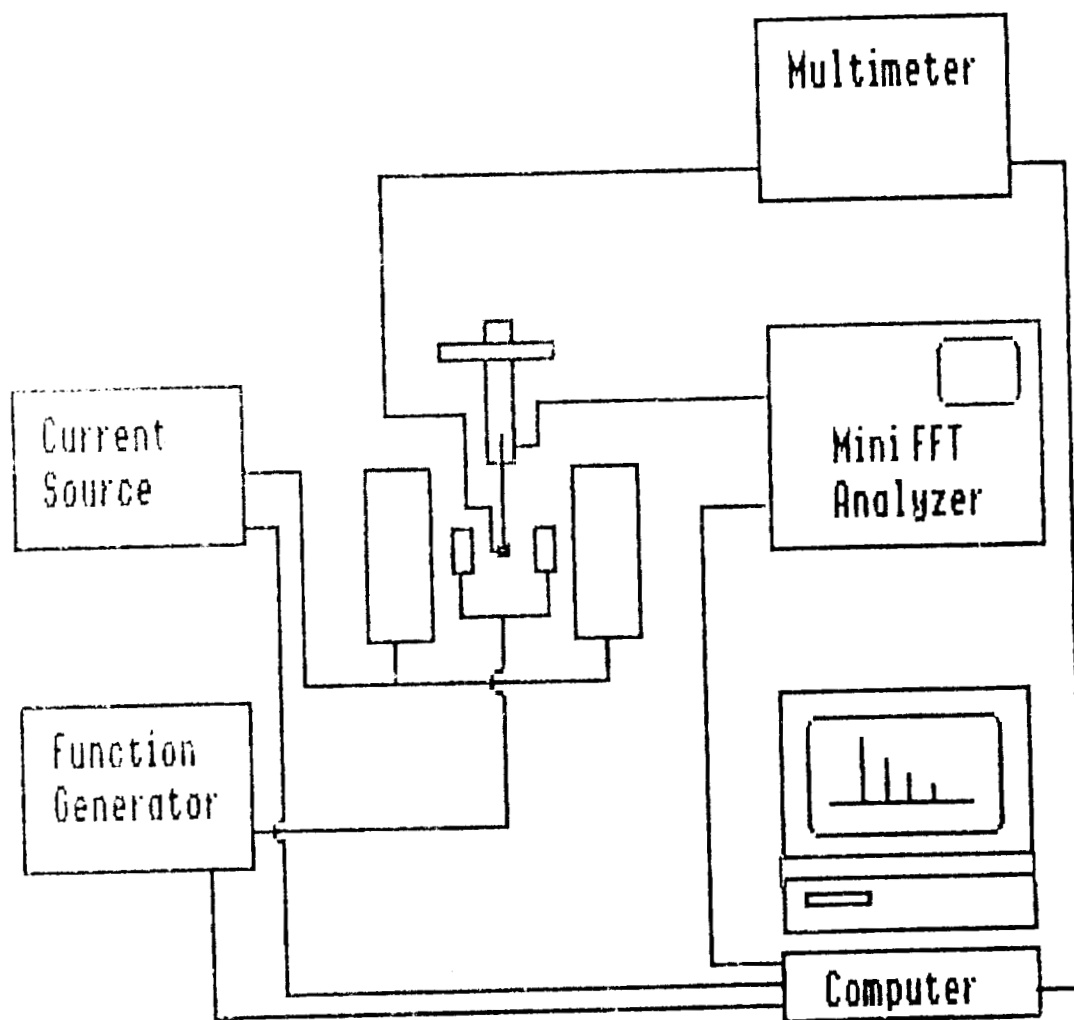


Figure 1. Magnetometer Block Diagram.

Computer

The HP 9133 computer was programmed in Basic to control the magnetometer and collect data on the magnetization, magnetic field, and temperature, through the GPIB bus. Data could be saved to disk and printed out or plotted. An HP 631 printer and an HP 7470A plotter were connected to the computer for these purposes.

Temperature Measurements

The temperature sensor is a Copper-Constantan thermocouple which is glued to the end of the vane, next to the sample, with GE 7031 varnish. The thermocouple output goes to an HP Model 3451A programmable multimeter. The thermocouple voltage is read by the computer and recorded as part of the data each time a measurement is made.

Programs

Four different variations of the Basic program were developed. (1) Magnitude, which measures the magnitude of the peak, at the sweep coil frequency, as a function of magnet current, from 0 to 1 A. (2) Cross Spectrum, which measures the real part of $A \times B$, where A is the sweep coil drive signal and B is the transducer output signal. The field current is swept from 1 A to -1 A. (3) Quick, which measures the magnitude at five values of magnet current, from 0 to 0.5 A and calculates the average slope and (4) TC, which records the magnetization and temperature as a sample is warmed through the superconducting transition. The flow chart in figure 2 applies to all three programs. The programs are menu driven. The first section initializes the four instruments and sets the operating parameters. The operator selects the frequency and voltage for the sweep coils, the input voltage range for the analyzer, and the gain for the display Y-axis. In program 1 the option of field cooling is provided as well. Following the initialization the subroutine "Acquire" is called which manages the actual acquisition of data. Once the data is taken, the subroutine "Store" is called and the data is stored on disk. The operator is prompted for a filename and may elect to not store the data at this point by doing a reset, in which case the data is lost. Once the data is stored on disk the menu provides options of plotting on the screen, printing on the screen, plotting on the plotter, or printing on the printer. Program listings are given in the Appendix.

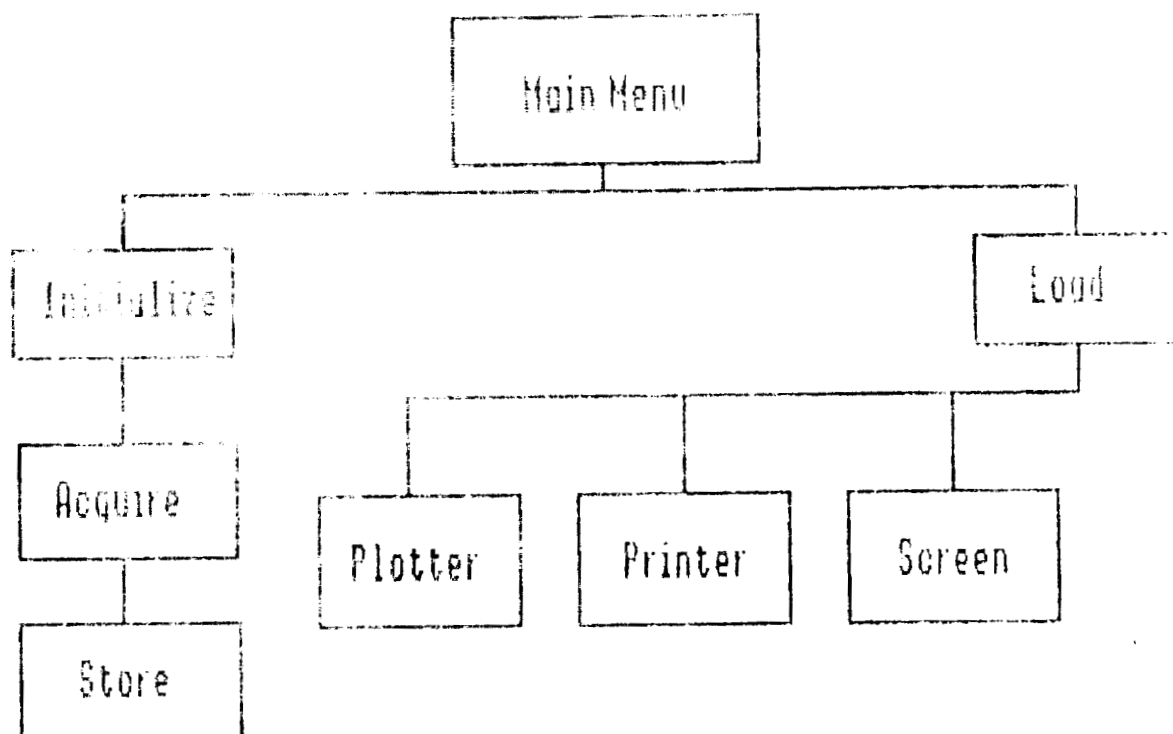


Figure 2. Program Flow Chart.

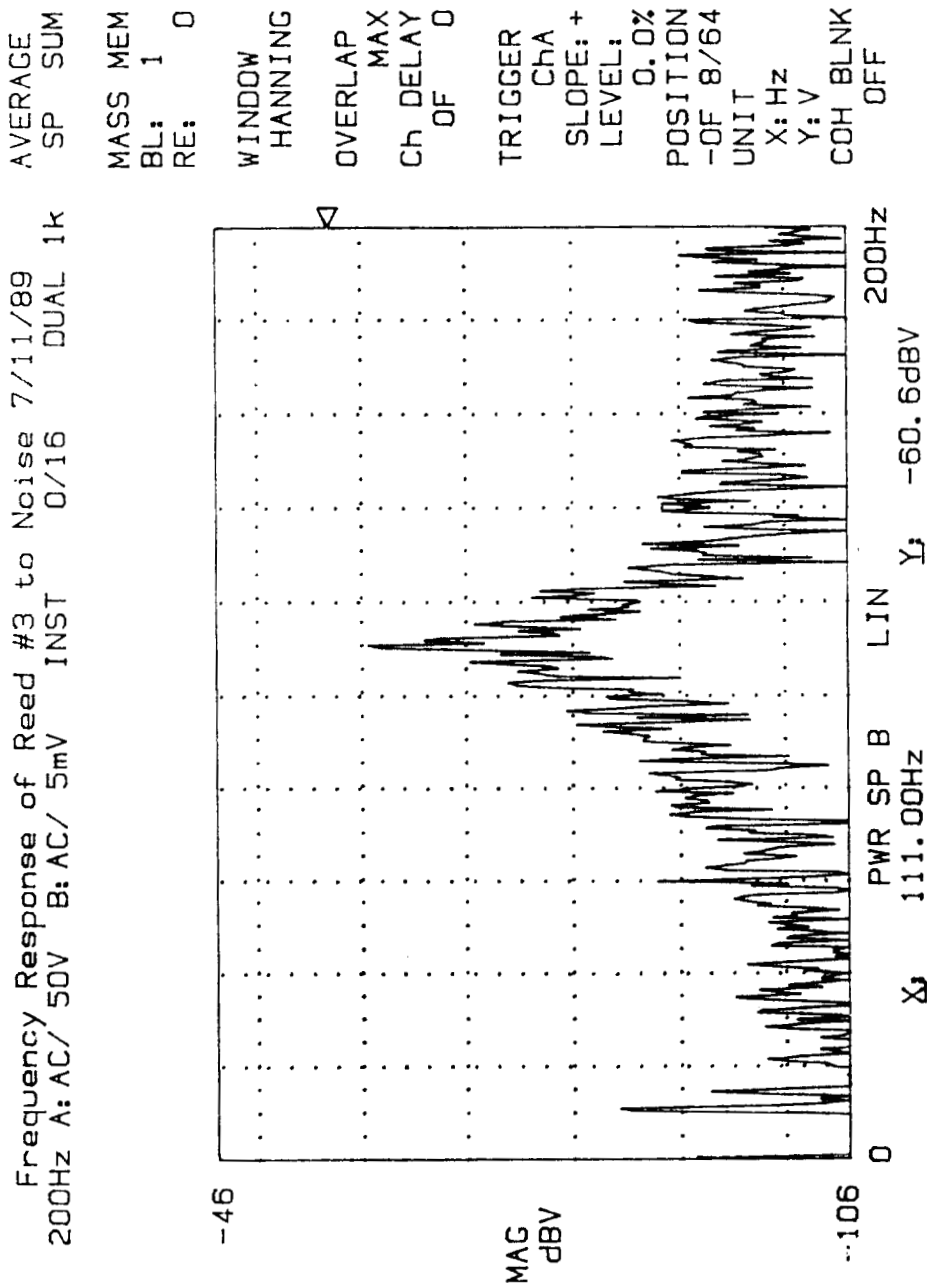
Results

Of the three types of piezoelectric transducers used, the PZT ceramic was found to give the most stable and reproducible results. This was largely due to the failure of the silver paint to properly bond the Kynar films to their copper supports. The response of the PZT reed to a white noise signal applied to the sweep coils is shown in Figure 3. This particular reed has a resonant frequency of 111 Hz. The peak at 10 Hz is due to vibrations of the isolation table on which the magnetometer was mounted. Figure 4 shows the response curve for an unsupported Kynar film. No resonance is seen, the 10 Hz noise peak is particularly large, followed by peaks at 60 and 180 Hz due to line noise. The response of this reed was nearly independent of frequency but was not nearly as good as that of the PZT reed near resonance. All of the following data were taken with the PZT reed.

Initially, two types of curves were generated. The curves of magnetization vs magnetic field, and curves of susceptibility vs temperature, which were generated by taking average slopes of the magnetization curves, fitted to straight lines. Figures 5 and 6 show a set of magnetization curves for $\text{Er}_1\text{Ba}_2\text{Cu}_3\text{O}_x$, the material which is referred to as Er123. The value of x is between 6.5 and 7 in the superconducting phase of this compound. In figure 5 the material is superconducting and diamagnetic while in figure 6 it is normal and paramagnetic, due to the Er ion in the lattice. The average slope of each curve was taken to determine the change in magnetic susceptibility with temperature, the result is shown in figure 7.

The degree of magnetic flux pinning can be determined by comparing magnetization curves for samples which have been field-cooled (Meissner effect) and zero-field cooled (shielding). If a sample is cooled below its superconducting critical temperature while in an applied magnetic field, the internal field is expelled, this is the Meissner effect. For type II materials, however, some magnetic flux can be pinned in the material and, for small fields, will not be expelled. This results in a positive contribution to the magnetization. Thus a difference in slope between field-cooled and zero-field cooled data on the same sample will give an indication of the extent of the flux pinning.

Figure 8 shows the magnetization vs magnetic field curves for a sample of Y123. The curves represent field-cooled ($H=27$ Oe) and zero-field cooled ($H=0$) conditions. The difference in slope between the two curves indicates the



DISPLAY 00:15

FORMAT	LIST	3-ARRAY	COH	BLK	XFER	P.OV	INHIBIT	EXIT
--------	------	---------	-----	-----	------	------	---------	------

Figure 3. Frequency Response of the PZT Reed.

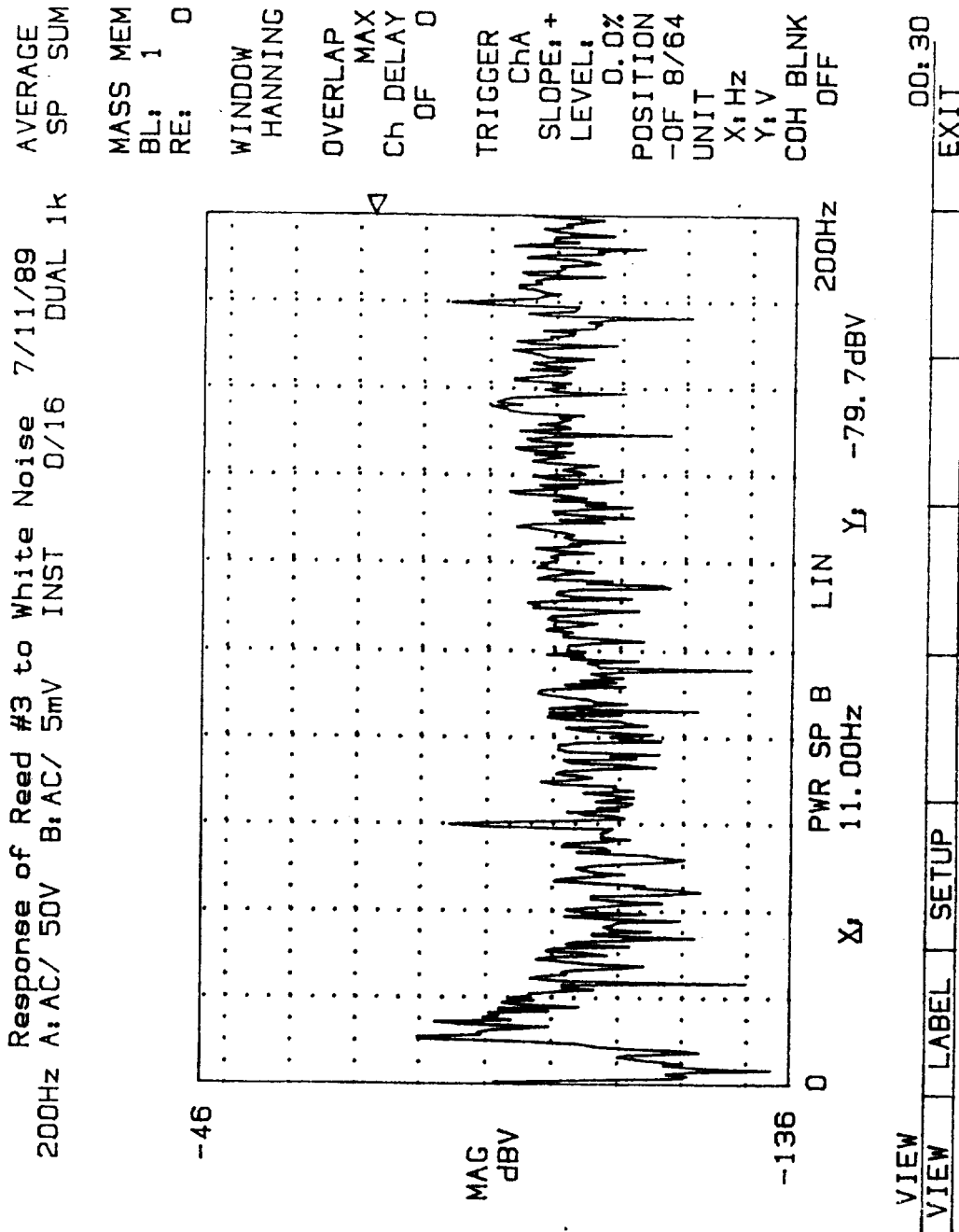


Figure 4. Frequency Response of Kynar Reed.

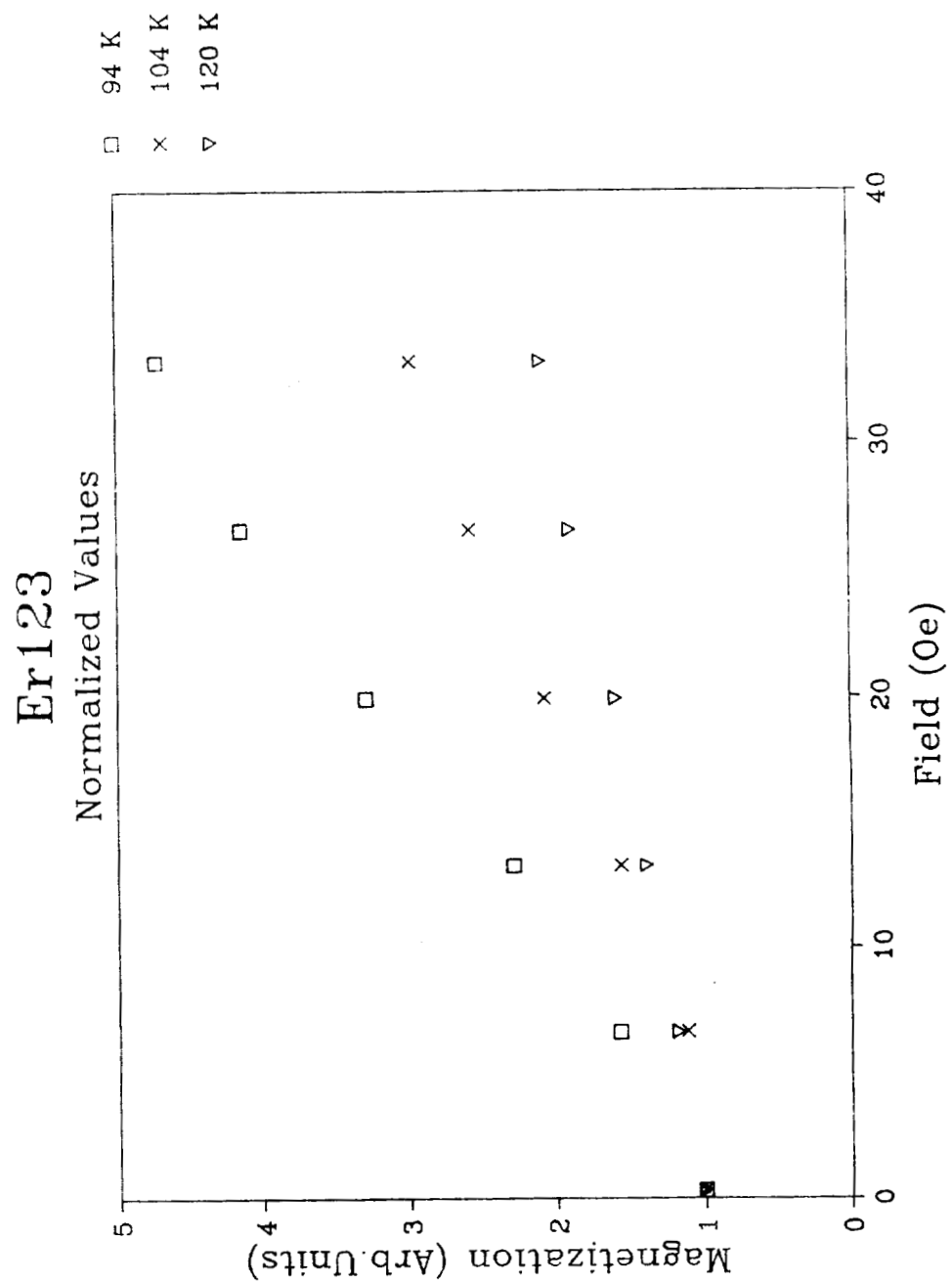


Figure 5. Magnetization Curve for Superconducting Er123.

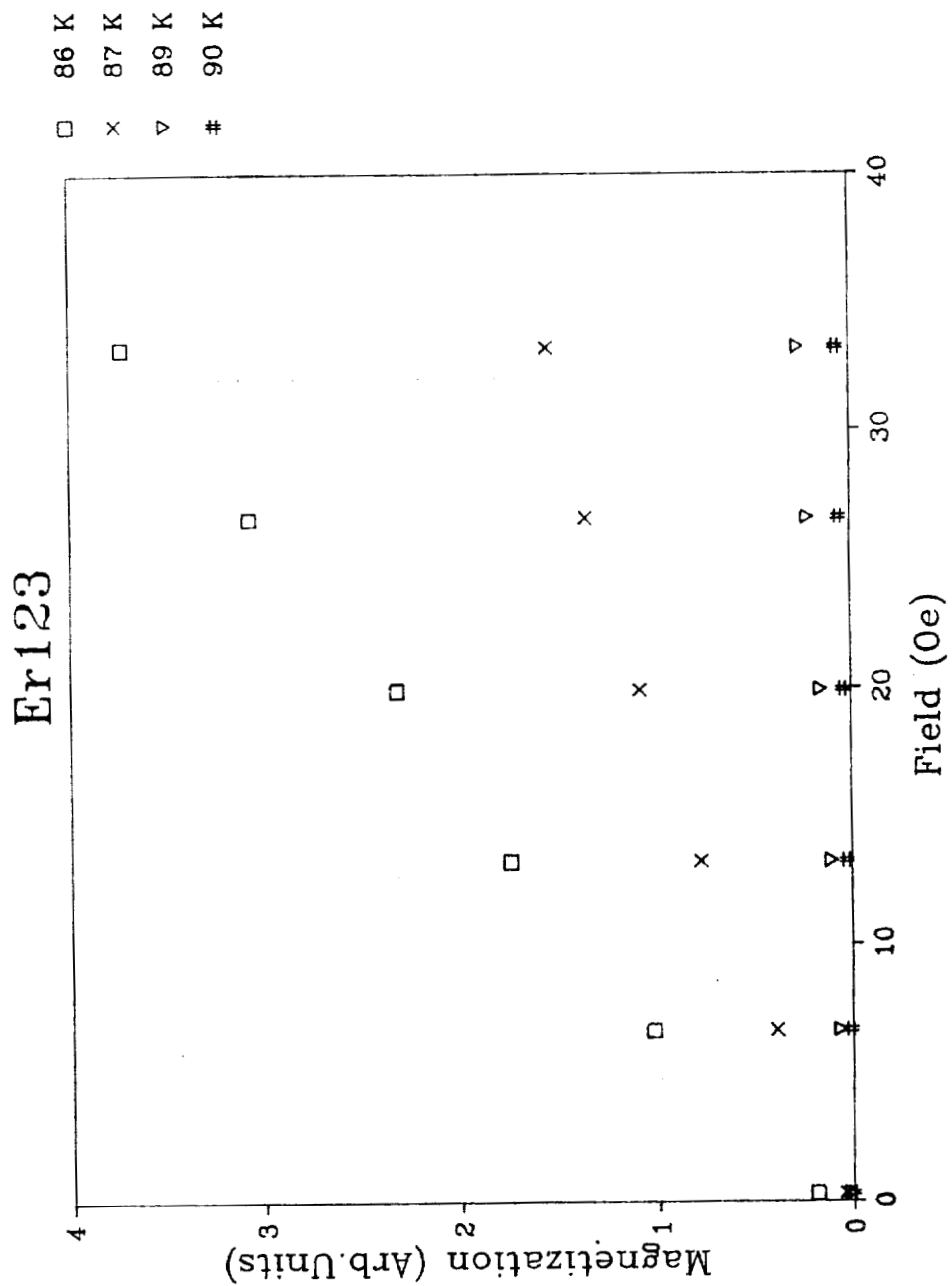


Figure 6. Magnetization Curve for Normal Er123.

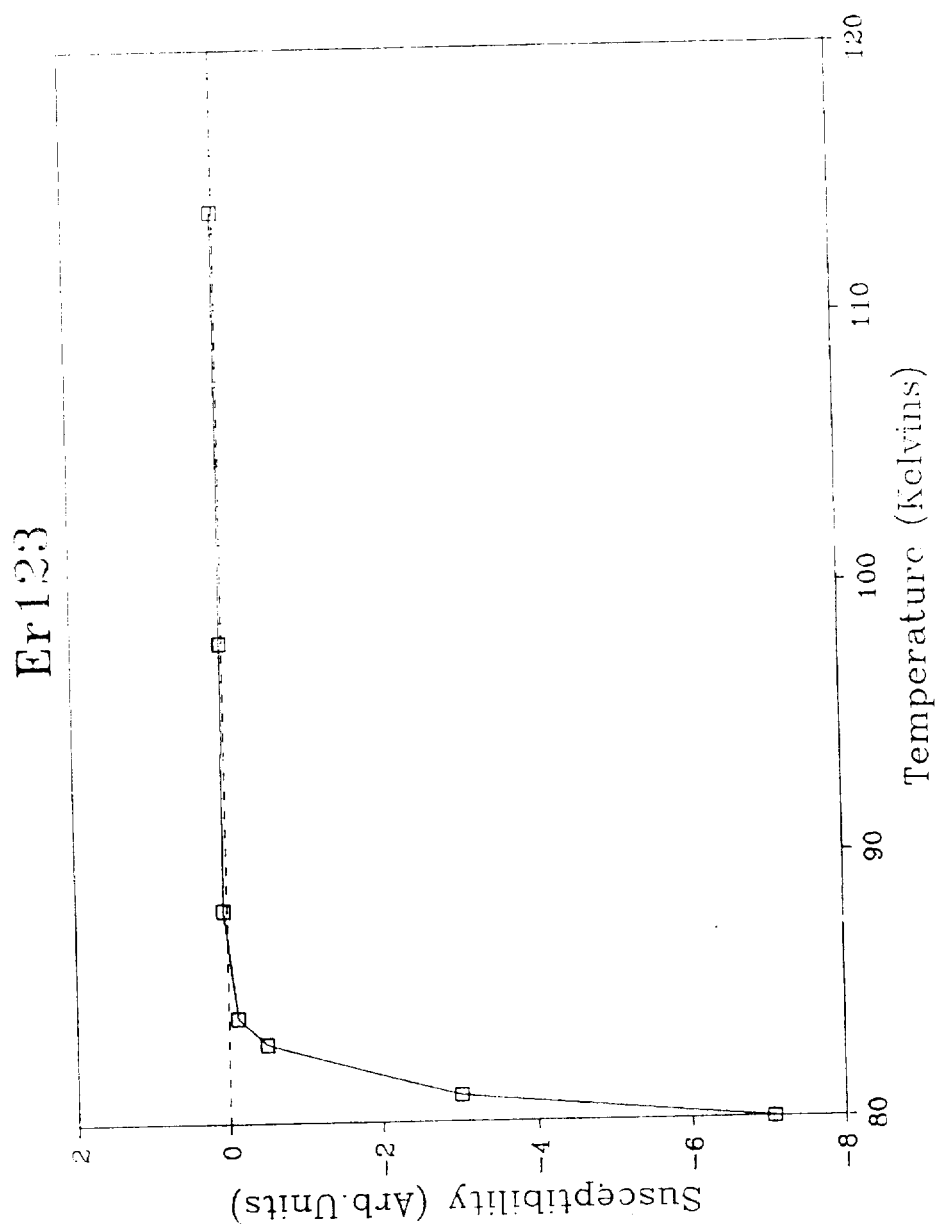


Figure 7. Susceptibility Curve for Er123.

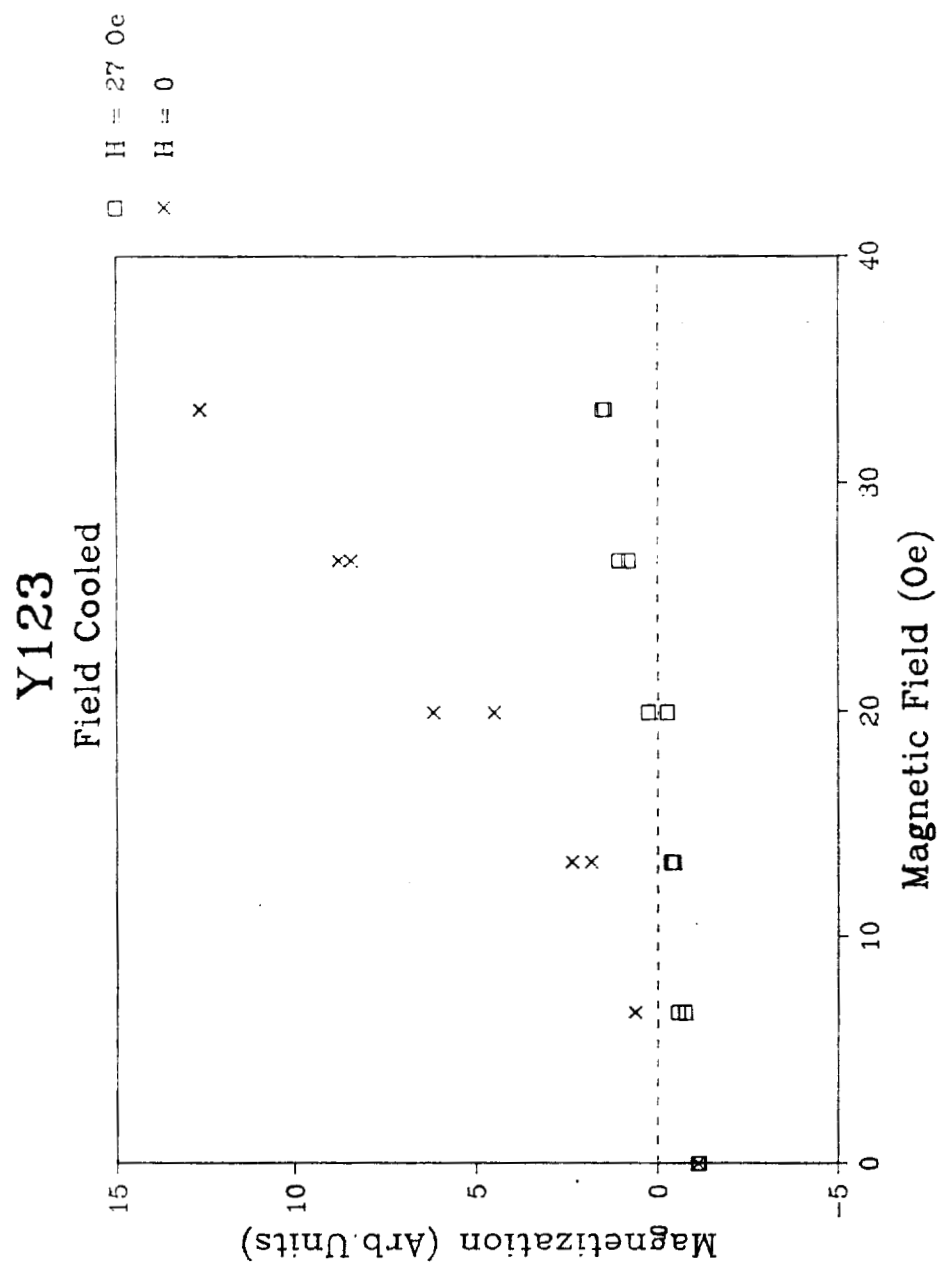


Figure 8. Magnetization Curve for Field-Cooled Y123.

extent of the flux pinning. Figure 9 shows the same experiment for Y123 which has been doped with Ag. Here the slopes of the two curves are practically identical, indicating little flux pinning in the doped material.

The program "Cross Spectrum" has the capability of distinguishing between positive and negative magnetization and can be used to generate hysteresis curves for magnetic materials. Figure 10 shows a hysteresis curve for a sample of Eu123+Ag which was zero-field cooled. The increase in (negative) magnetization on going once around the loop is a measure of the amount of trapped flux. The same sample is shown in figure 11 after field-cooling in a 66.4 Oe magnetic field. The curve is now closed, indicating that flux was trapped upon cooling.

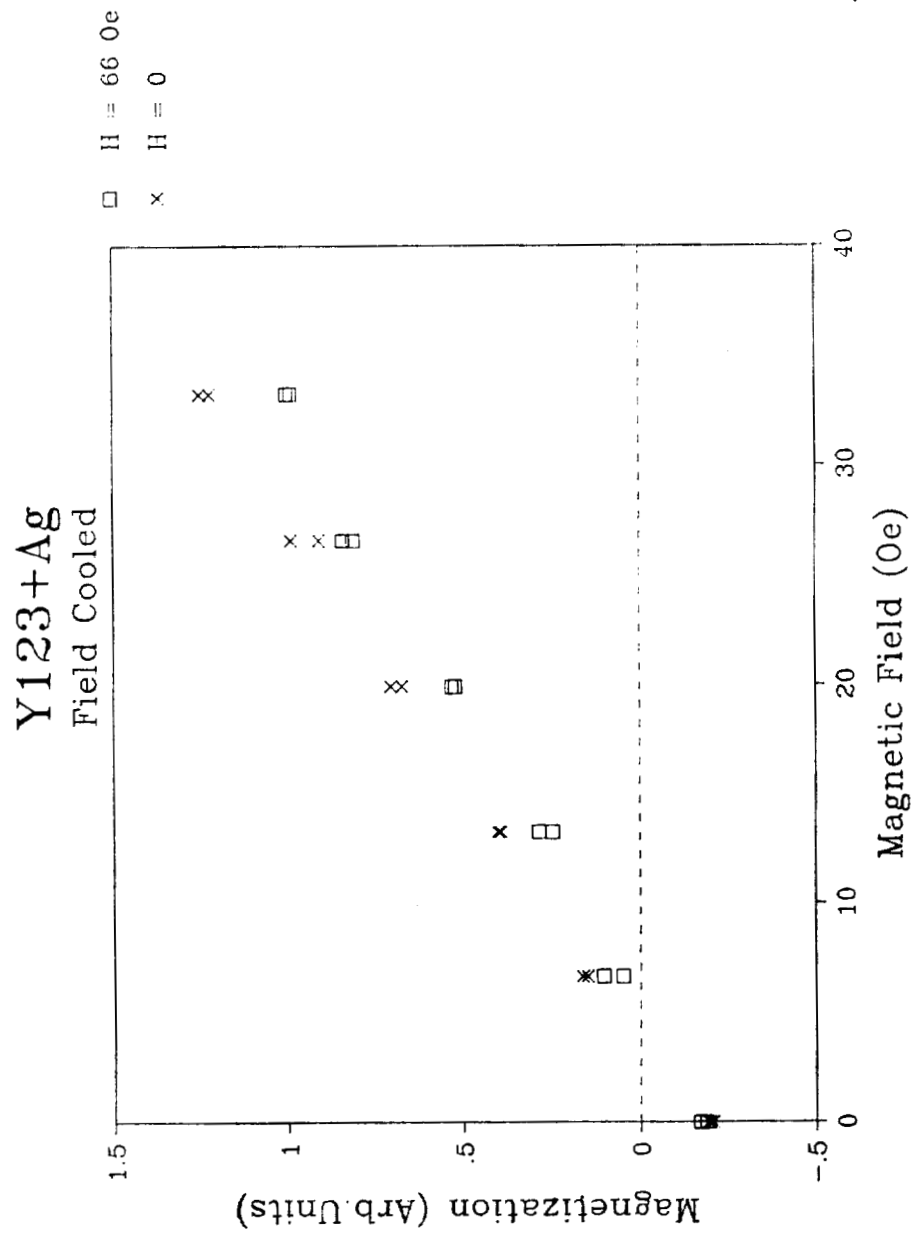


Figure 9. Magnetization Curve for Field-Cooled Y123+Ag.

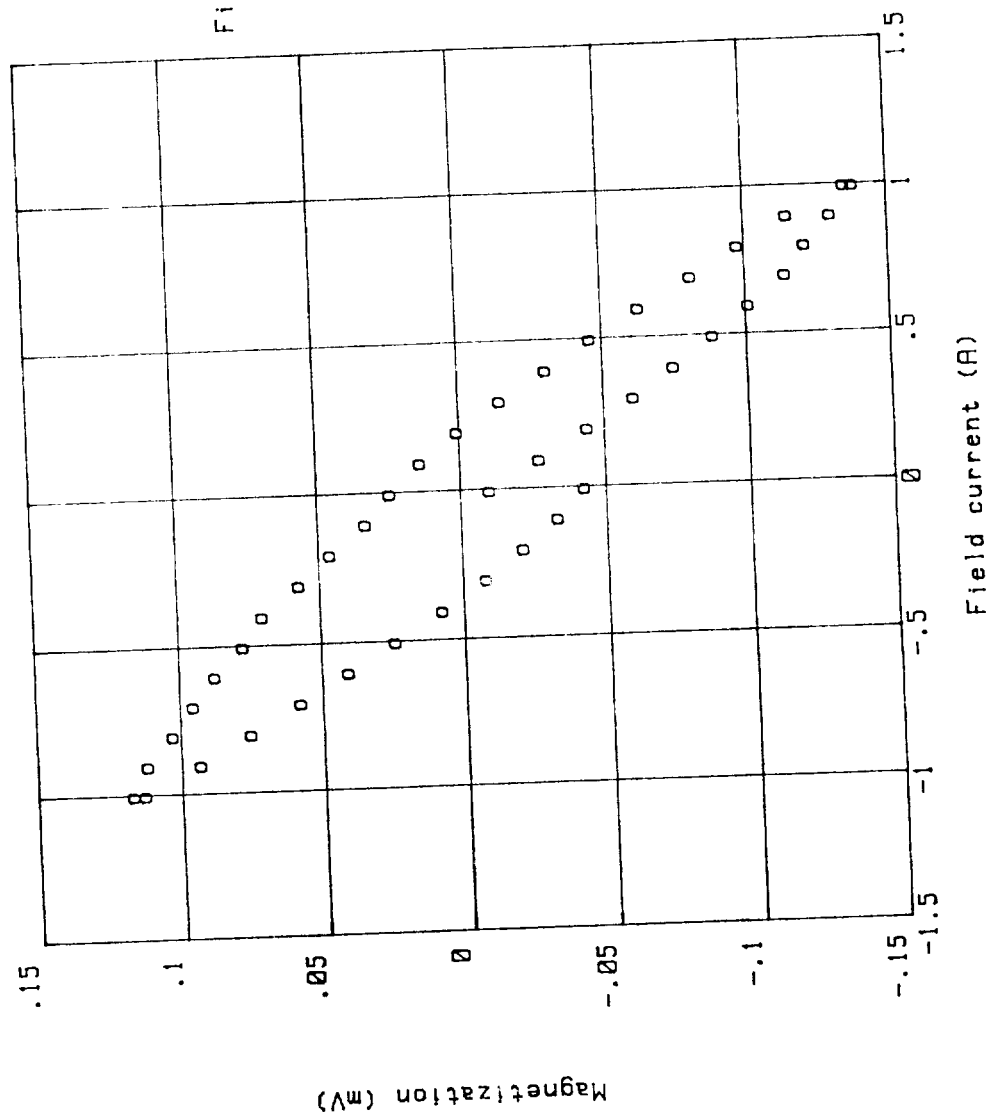


Figure 10. Hysteresis Loop for Eu123+AG.

Eu123+Ag
Filename = JUL25F
09:46:32
27 Jul 1989

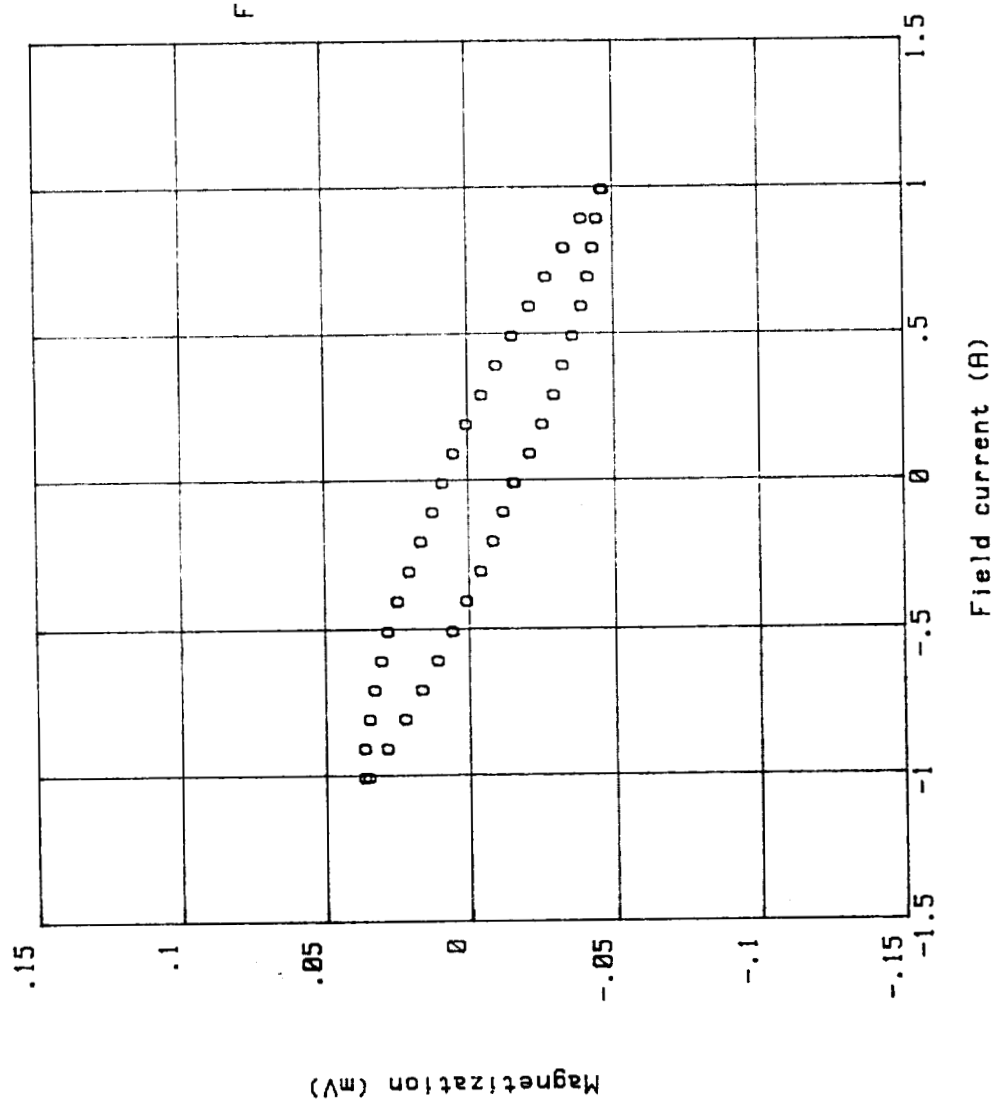


Figure 11. Hysteresis Loop for Field-Cooled Eu123+Ag.

Conclusions and Recommendations

The alternating gradient magnetometer can be a valuable tool for the characterization of the magnetic properties of materials. It should be particularly usefull in superconductivity research because of its sensitivity and ease of use. With the current data acquisition system, data may be taken more quickly than before and the data analysis is greatly simplified. The data which is acquired will become even more useful if the instrument is calibrated to measure magnetization in absolute units. This should not be difficult to do using a standard material, such as one of the rare-earth salts.

The chief difficulty in using this instrument is the lack of precise temperature control. The temperature of the sample changes with the liquid nitrogen level in the dewar. As the liquid evaporates the sample slowly warms. It would be convenient to be able to take a series of magnetization measurements at a fixed temperature. This is not possible with the current instrument although the rate of temperature change can be kept quite low, so that the temperature does not change more than about 0.1 K during the course of a measurement.

The computer program can be improved in several places. The program called Magnitude could be rewritten so that it would take a series of measurements, say one magnetization curve each degree of temperature change, and save them to disk automatically. The program called Cross Spectrum needs to have the temperature measuring routine added to it as well. Finally, some way needs to be devised to keep track of any variation in the resonant frequency of the reed and adjust the function generator accordingly.

References

1. M. K. Wu, J. R. Ashburn, C. J. Torng, P. H. Hor, R. L. Meng, L. Gao, Z. J. Huang, Y. Q. Wang and C. W. Chu, Phys. Rev.Lett., 58, 908 (1987).
2. M. M. Garland, Appl.Phys.Lett., 52, 1913 (1988).
3. Z. Z. Sheng, A. M. Hermann, A. Elali, J. Estracalu, T. Datta, and R. J. Matson, Phys.Rev.Lett., 60, 937 (1988).
4. S. R. Ovshinsky, R. J. Young, D. D. Allred, G. Demaggio and G. A. Vander Leeden, Phys.Rev.Lett., 58, 2578 (1987).
5. C. P. Bean, Rev.Mod.Phys., 36, 31 (1964).
6. P. J. Flanders, J.Appl.Phys., 63, 3940 (1988).
7. M. M. Garland, MSFC NASA Summer Faculty Research Report

Appendix


```

10 ! *****
20 ! PROGRAM: MAGNITUDE
21 !
30 ! PLOTS THE MAGNITUDE OF THE SIGNAL ON CHANNEL B
40 ! FROM ZERO TO 1/2 AMP MAGNET CURRENT
50 ! USING THE CF-920 FFT ANALYSIS SYSTEM
60 ! JUNE 8, 1989
70 !
80 ! MODIFIED JULY 7, 1989 TO USE THE PZT TRANSDUCER
81 ! MODIFIED JULY 17, 1989 TO MONITOR TEMPERATURE
82 !
90 ! *****
100 !
110 ! Number of Averages is in Line 580
120 !
130 OPTION BASE 1
140 CONTROL 1,12;1
150 DIM Magnitude(250),Fieldcurrent(250),Temperature(250)
160 PLOTTER IS 3,"INTERNAL"
170 GCLEAR
180 !
190 ! ***** MENU *****
200 !
210 PRINT CHR$(12)
220 PRINT " (1) Acquire magnetization data"
230 PRINT
240 PRINT " (2) Load magnetization data from disc"
250 PRINT
260 PRINT " (3) Plot magnetization data on screen"
270 PRINT
280 PRINT " (4) Print magnetization data on screen"
290 PRINT
300 PRINT " (5) Plot magnetization data on plotter"
310 PRINT
320 PRINT " (6) Print magnetization data on printer"
330 INPUT Selection$
340 IF Selection$="1" THEN GOSUB Initialize
350 IF Selection$="2" THEN GOSUB Load
360 IF Selection$="3" THEN GOSUB Screenplot
370 IF Selection$="4" THEN GOSUB Screenprint
380 IF Selection$="5" THEN GOSUB Plotterplot
390 IF Selection$="6" THEN GOSUB Printerprint
400 GOTO 210 ! Clear Screen and Show Menu
410 Initialize: ! Setup Display Window
420 PLOTTER IS 3,"INTERNAL"
430 GINIT
440 GCLEAR
450 VIEWPORT 0,100,0,100
460 WINDOW 0,1,0,3
470 GRID .25,1
480 GRAPHICS ON
490 FRAME
500
510
520
530 ! ***** SET UP FOR CF920 *****
540
550 INPUT "Channel B Range (1-15)",Br$
560 IF Br$="" THEN Br$="10"
570 OUTPUT 710;"AMS3" ! Spectrum peak averaging

```



```

580 OUTPUT 710;"ANS5"           ! Take 5 squared averages
590 OUTPUT 710;"TRE"           ! Repeated trigger
600 OUTPUT 710;"TIA"           ! Channel a trigger
610 OUTPUT 710;"AAS2"          ! Channel A input voltage range
620 OUTPUT 710;"BAS"&Br$      ! Channel b input voltage range
630 OUTPUT 710;"FRS9"          ! Channel A&B input frequency range
640 OUTPUT 710;"BSP"           ! Display B spectrum
650 OUTPUT 710;"YLI"           ! Selects linear scaling
660 ! OUTPUT 710;"SDN"          ! Search function on
670 ! OUTPUT 710;"SPS401"       ! Sets search marker for peak point
680
690 !***** CF920 SETUP COMPLETE *****
700
710
720
730 !*****SETUP FOR THE 228 CURRENT SOURCE*****
740
750 CLEAR 711
760 OUTPUT 711;"V25"           ! Voltage limits to 25 volts
770 INPUT "Initial Current (0-1)",Current ! Used for Field Cooling
780 IF Current=0 THEN GOTO 810
790 OUTPUT 711;"I"&VAL$(Current)
800 GOTO 820
810 OUTPUT 711;"I0"           ! Initializes current to 0 amperes
820 OUTPUT 711;"F1X"          ! Execute
830 INPUT "Press a Key to Continue",K$
840 !***** SETUP FOR THE 228 CURRENT SOURCE COMPLETE *****
850
860 !***** SETUP FOR HP3457A TO READ TEMPERATURE *****
870 ! USING A COPPER-CONSTANTAN THERMOCOUPLE
880 !
890 ! INTEGER I
900 ASSIGN @Temp TO 724
910 OUTPUT @Temp;"TRIG SYN"
920 OUTPUT @Temp;"NDIG 4"      ! Four Digit Accuracy
930 OUTPUT @Temp;"FIXEDZ OFF"
940 OUTPUT @Temp;"DCV"         ! Read DC Volts
950 OUTPUT @Temp;"AZERO 1"     ! Automatic Zero
960 OUTPUT @Temp;"NPLC 10"     ! Ten Power Line Cycle Delay
970 !
980 !***** TEMPERATURE SETUP COMPLETE *****
990 !
1000 !***** SETUP FOR THE 270 *****
1010 !
1020 Rf$="100"                 ! Resonant frequency of PZT
1030 Swv$="4.40"              ! Sweep voltage of little coils
1040 PRINT CHR$(12)           ! Clears screen
1050 CLEAR 709
1060 INPUT "Resonant frequency",Trf$
1070 IF Trf$="" THEN
1080     Rf$=Rf$               ! Default value is 74.4 Hz
1090 ELSE
1100     Rf$=Trf$
1110 END IF
1120 INPUT "Sweep voltage",Tswv$
1130 IF Tswv$="" THEN
1140     Swv$=Swv$             ! Default value is 4.4 volts
1150 ELSE
1160     Swv$=Tswv$
1170 END IF

```



```

1180 Freq=VAL(Rf$)
1190 Rf$="F"&Rf$ ! Adds a F for frequency to variable
1200 OUTPUT 709;Rf$ ! Sets frequency of Wavetek
1210 OUTPUT 709;"I" ! Execute
1220 Swv$="A"&Swv$ ! Adds an A for amplitude to variable
1230 OUTPUT 709;Swv$ ! Sets voltage for Wavetek
1240 OUTPUT 709;"I" ! Execute
1250 OUTPUT 709;"P1" ! Output on
1260 OUTPUT 709;"I" ! Execute
1270 OUTPUT 709;"TSI" ! Displays frequency on front of 270
1280 OUTPUT 709;"F"
1290 !
1300 !***** ENABLE CF920 DELTA SEARCH FUNCTION *****!
1310 !
1320 OUTPUT 710;"SON" ! SEARCH ON
1330 Hf=(Freq)*2+5 ! UPPER LIMIT OF SEARCH
1340 Lf=(Freq)*2-5 ! LOWER LIMIT OF SEARCH
1350 Lf$=VAL$(Lf)
1360 Hf$=VAL$(Hf)
1370 OUTPUT 710;"SPS"&Lf$ ! SET LOWER LIMIT
1380 OUTPUT 710;"DON" ! DELTA FUNCTION ON
1390 OUTPUT 710;"DCS" ! SET THE DELTA CURSOR
1400 OUTPUT 710;"SPS"&Hf$ ! SET UPPER LIMIT
1410 INPUT "Y-AXIS GAIN (1-5)",Yag
1420 FOR G=1 TO Yag
1430 OUTPUT 710;"YGU"
1440 NEXT G
1450 OUTPUT 710;"PA0" ! PARTIAL OVERALL ON
1460
1470 !***** SETUP FOR THE 270 WAVETEK COMPLETE *****!
1480 !
1490 !
1500 !
1510 GOSUB Acquire ! Take data
1520 !*****
1530 GOSUB Store ! Write the data to disc
1540 RETURN ! Back to the Menu
1550 STOP
1560 Acquire: ! Take data *****
1570 I=0
1580 FOR Fieldi=0 TO .5 STEP .1 ! 0 to 0.5 Amps in 5 steps
1590 IF Fieldi<1.E-9 AND Fieldi>-1.E-9 THEN Fieldi=0
1600 I=I+1
1610 Fieldi$="I"&VAL$(Fieldi) ! Adds an I to the field current vairable
1620 OUTPUT 711;Fieldi$ ! Sends value of current to current source
1630 OUTPUT 711;"FIX" ! Execute
1640 WAIT 3 ! Wait for system to settle
1650 OUTPUT 710;"LYS" ! Selects Display Y search value
1660 ENTER 710;Volts ! Reads display Y search value ; volts
1670 Magnitude(I)=Volts
1680 Fieldcurrent(I)=Fieldi
1690 GOSUB Plot ! Plot data on the screen
1700 NEXT Fieldi
1710 FOR Fieldi=.5 TO 0 STEP -.1 ! .5 to 0 amps
1720 IF Fieldi<1.E-9 AND Fieldi>-1.E-9 THEN Fieldi=0
1730 I=I+1
1740 Fieldi$="I"&VAL$(Fieldi) ! Adds an I to the field current vairable
1750 OUTPUT 711;Fieldi$ ! Sends value of current to current source
1760 OUTPUT 711;"FIX" ! Execute
1770 WAIT 3 ! Wait for system to settle

```



```

1780     OUTPUT 710;"LYS"      ! Selects display Y search value
1790     ENTER 710;Volts      ! Reads display Y search value
1800     Magnitude(I)=Volts
1810     Fieldcurrent(I)=FieldI
1820     GOSUB Plot           ! Show data point on screen
1830     NEXT FieldI
1840     ENTER @Temp;Voltage   ! Read the Temperature
1850     Volts=Voltage*1000    ! Convert to Millivolts
1860     GOSUB Temperature    ! Calculate the Temperature
1870     OUTPUT 711;"FOX"     ! Put Current Source on Standby
1880     CLEAR 709
1890     OUTPUT 710;"PAF"     ! DISABLE PARTIAL OVERALL
1900     OUTPUT 710;"DOF"    ! DISABLE DELTA SEARCH
1910     OUTPUT 710;"SOF"    ! DISABLE SEARCH FUNCTION
1920     CLEAR 710
1930     RETURN               ! From ACQUIRE
1940 Plot:                   ! Plot data points on the screen *****
1950     LOG 5                ! Label origin at center
1960     MOVE Fieldcurrent(I),Magnitude(I)
1970     LABEL "*"            ! Plot using asterisks
1980     PRINT I,Fieldcurrent(I),Magnitude(I)
1990     RETURN
2000 Store:                 ! Store the data in a disc file *****
2010     N=I
2020     REDIM Magnitude(N),Fieldcurrent(N)
2030     GRAPHICS OFF
2040     ALPHA ON
2050     PRINT CHR$(12)       ! Clear screen
2060     INPUT "File name ?";File$
2070     CREATE $DAT File$,INT(N*8/256)+2
2080     ASSIGN @Path TO File$
2090     OUTPUT @Path;N,Temp,Magnitude(*),Fieldcurrent(*)
2100     ASSIGN @Path TO *
2110     RETURN               ! From STORE
2120 Load:                 !
2130     PRINT CHR$(12)       ! Clear screen
2140     Controller=1
2150     CAT;NAMES             ! Display catalog filenames
2160     INPUT "Enter file name to be loaded from above list.";File$
2170     IF File$="" THEN 2240 ! Return if no entry
2180     ASSIGN @Track TO File$
2190     ENTER @Track;N        ! Number of data points
2200     ENTER @Track;Temp
2210     REDIM Magnitude(N),Fieldcurrent(N)
2220     ENTER @Track;Magnitude(*),Fieldcurrent(*)
2230     ASSIGN @Track TO *   ! Close the file
2240     RETURN               ! From LOAD
2250 Screenprint:          ! Print the data on the screen
2260     IF Controller=0 THEN
2270         DISP "LOAD A FILE FIRST!!!"
2280         GOTO 2480
2290     END IF
2300     PRINT "Filename = ";File$
2310     PRINT "Temperature = ";Temp
2320     FOR I=1 TO N
2330         PRINT I,Magnitude(I),Fieldcurrent(I)
2340     NEXT I
2350     FOR K=1 TO 4
2360         Mag(K)=Magnitude(K+1)-Magnitude(1) ! Calculate slope
2370     NEXT K

```



```

2380 Sum=0
2390 FOR K=1 TO 4
2400 Sum=Sum+Mag(K)
2410 NEXT K
2420 Slope=Sum/.5 ! Average slope of first 5 points
2430 PRINT
2440 PRINT "Initial Slope = ";Slope
2450 DISP "Hit CONTINUE to continue program."
2460 PAUSE
2470 Controller=0
2480 RETURN ! From SCREENPRINT
2490 !
2500 Printerprint: ! Send data to the printer
2510 PRINTER IS 701
2520 GOSUB Screenprint
2530 PRINTER IS 1
2540 RETURN ! From PRINTERPRINT
2550 !
2560 Screenplot: ! Plot the full graph on the screen
2570 PRINT CHR$(12) ! Clear screen
2580 GCLEAR ! Clear graphic screen
2590 GRAPHICS OFF
2600 ALPHA ON
2610 GOSUB Sort ! Find min and max values
2620 GRAPHICS ON
2630 ALPHA OFF
2640 Yinta=Yint-(Maxy-Miny)/75
2650 Xinta=Xint-(Maxx-Minx)/75
2660 VIEWPORT 20,100,12,92
2670 FRAME
2680 WINDOW Minx,Maxx,Miny,Maxy
2690 AXES Xtic,Ytic,Minx,Miny,1,1,2
2700 PEN 1
2710 LORG 6 ! Label origin above character
2720 GRID Xtic,Ytic ! Draw a grid
2730 CLIP OFF
2740 CSIZE 3,.5 ! Character size/aspect ratio
2750 FOR I=Minx TO Maxx+Xtic/100 STEP Xtic
2760 MOVE I,Miny ! X-axis numbers
2770 IF ABS(I)<1.E-15 THEN
2780 J=0
2790 LABEL J
2800 GOTO 2830
2810 END IF
2820 LABEL I
2830 NEXT I
2840 LORG 7 ! Label origin lower right
2850 FOR I=Miny TO Maxy+Ytic/100 STEP Ytic
2860 MOVE Minx,I ! Y-axis numbers
2870 IF ABS(I)<1.E-15 THEN
2880 J=0
2890 LABEL J
2900 GOTO 2930
2910 END IF
2920 LABEL I
2930 NEXT I
2940 LORG 5 ! Label origin to center
2950 PEN 2 ! Pen for data points
2960 FOR I=1 TO N
2970 MOVE Fieldcurrent(I),Magnitude(I)

```



```

2980 LABEL "o" ! Character for points
2990 NEXT I
3000 PEN 1
3010 VIEWPORT 20,100,15,95
3020 WINDOW 20,100,15,95
3030 CLIP OFF
3040 MOVE 60,5 ! Position of X-axis label
3050 LORG 5
3060 LDIR 0 ! Horizontal
3070 LABEL "Field current (A)" ! X-axis label
3080 MOVE 5,55 ! Position of Y-axis label
3090 DEG ! Use degrees
3100 LDIR 90 ! Orient vertically
3110 LORG 5 ! Center
3120 LABEL "Magnetization (mV) " ! Y-axis label
3130 LDIR 0 ! Horizontal
3140 MOVE 115,75 ! Position for sidebar
3150 LABEL Title$ ! Sidebar header
3160 LABEL "Temp. = ";Temp
3170 LABEL "Filename = ";File$
3180 LABEL TIME$(TIMEDATE) ! Time
3190 LABEL DATE$(TIMEDATE) ! Date
3200 RETURN ! from SCREENPLOT
3210 !
3220 Sort: ! Get max and min
3230 Minx=MIN(Fieldcurrent(*))
3240 Maxx=MAX(Fieldcurrent(*))
3250 Miny=MIN(Magnitude(*))
3260 Maxy=MAX(Magnitude(*))
3270 PRINT "Fieldcurrent ranges from";Minx;"to";Maxx
3280 PRINT
3290 PRINT "Magnetization ranges from";Miny;"to";Maxy
3300 PRINT
3310 INPUT "Input (Minx,Maxx,Miny,Maxy) to be plotted",Minx,Maxx,Miny,Maxy
3320 PRINT
3330 PRINT "Fieldcurrent plot ranges from";Minx;"to";Maxx
3340 PRINT
3350 PRINT "Magnetization ranges plot from";Miny;"to";Maxy
3360 PRINT
3370 INPUT "Input tick mark spacing and axes intercepts (Xtic,Ytic,Xint,Yint)",Xtic,Ytic,Xint,Yint
3380 PRINT
3390 INPUT "Title for graph",Title$ ! Sidebar title
3400 RETURN ! From SORT
3410 !
3420 Plotterplot: ! Send plot data to plotter
3430 PLOTTER IS 705,"HPGL"
3440 GOSUB Screenplot
3450 RETURN ! From PLOTTERPLOT
3460 Temperature: ! Calculate the Temperature from Thermocouple Voltage
3470 LET V=Volts
3480 IF V>=-5.602 AND V<=-5.439 THEN
3490 Temp=73+61.109*(V+5.603)
3500 END IF
3510 IF V>=-5.439 AND V<=-5.261 THEN
3520 Temp=83+58.602*(V+5.439)
3530 END IF
3540 IF V>=-5.261 AND V<=-5.069 THEN
3550 Temp=93+54.159*(V+5.261)
3560 END IF

```



```

3570 IF V>-5.069 AND V<-4.865 THEN
3580 Temp=103+50.596*(V+5.069)
3590 END IF
3600 IF V>-4.865 AND V<-4.468 THEN
3610 Temp=113+47.587*(V+4.865)
3620 END IF
3630 IF V>=-4.468 THEN ! Just report the voltage
3640 Temp=V
3650 END IF
3652 PRINT Temp
3660 RETURN ! From Temperature
3670 END

```


1989

NASA/ASEE SUMMER FACULTY FELLOWSHIP PROGRAM

MARSHALL SPACE FLIGHT CENTER
THE UNIVERSITY OF ALABAMA IN HUNTSVILLE

MONTE CARLO MODELS AND ANALYSIS OF
GALACTIC DISK GAMMA-RAY BURST DISTRIBUTIONS

Prepared by: Jon Hakkila
Academic Rank: Assistant Professor
University and Department: Mankato State University
Department of Mathematics,
Astronomy, and Statistics

NASA/MSFC:
Laboratory: Space Science
Division: Astrophysics
Branch: High Energy Astrophysics

MSFC Colleague: Charles A. Meegan

Date: August 24, 1989

Contract No.: The University of
Alabama in Huntsville
NGT-01-008-021

Abstract

MONTE CARLO MODELS AND ANALYSIS OF GALACTIC DISK GAMMA-RAY BURST DISTRIBUTIONS

Jon Hakkila
Assistant Professor of Astronomy
Department of Mathematics, Astronomy, and Statistics
Mankato State University
Mankato, MN

Gamma-ray bursts are transient astronomical phenomena which have no quiescent counterparts in any region of the electromagnetic spectrum. Although temporal and spectral properties indicate that these events are likely energetic, their unknown spatial distribution complicates astrophysical interpretation.

Monte carlo samples of gamma-ray burst sources are created which belong to Galactic disk populations. Spatial analysis techniques are used to compare these samples to the observed distribution. From this, both quantitative and qualitative conclusions are drawn concerning allowed luminosity and spatial distributions of the actual sample.

Although the BATSE experiment on GRO will significantly improve knowledge of the gamma-ray burst source spatial characteristics within only a few months of launch, the analysis techniques described herein will not be superceded. Rather, they may be used with BATSE results to obtain detailed information about both the luminosity and spatial distributions of the sources.

Acknowledgements

I would particularly like to thank Charles Meegan for his guidance, assistance, and helpfulness on this enjoyable project, Jerry Fishman for inviting me here and for extending such warm hospitality, and Geoffrey Pendleton for introducing me to the wiles of monte carlo analysis. I would like to thank Gerald Karr, Frank Six, Billie Swinford, and the entire NASA/ASEE staff for coordinating such a fine and valuable program. I would also like to thank a few of the many people who made this summer more fun than a vacation could have been: Pat Lestrade, Tom Parnell, Ron Elsner, Bob Austin, Bob Wilson, Bill Pacesias, Scott Storey, Martin Brock, Charles Telesco, Roger Knacke, Stayce Harris, Philip Moore III, Jim Derrickson, John Watts, Ellen Roberts, Fred Berry Jr., and Peggy Champion. The FORTRAN function GAUSSD was written by Tom Jenkins of Case Western Reserve. Finally, I would like to thank my wife, Fahn, for sharing with me this wonderful summer in Huntsville.

Introduction

A. General Properties of Gamma-Ray Burst Sources

Since their discovery via examination of Vela satellite data records (Klebesadel, Strong, and Olson 1973), gamma-ray burst sources have remained one of the most enigmatic classes of objects in modern astronomy. The strong bursts of observed gamma-radiation that these objects emit have no quiescent counterparts at any other wavelength of the electromagnetic spectrum, and are at present of unknown origin. Multi-wavelength observations of the transient events are also unverified, although sporadic visible flashes have been reported (e.g. Schaefer 1981).

The burst durations range from $\tau < 0.1$ sec to $\tau > 100$ sec, although the majority apparently lie between 3 and 20 seconds (Hurley, unpublished). The events span a wide range of relative rise and decay times (Barat et al. 1984), although their general rapidity, as well as variations on timescales as short as milliseconds, suggest that at least some of the events must be associated with compact objects ($r < 10^3$ km). Since the events are time-integrated, the registered output is generally measured in fluence (erg cm^{-2}) instead of more conventional flux units ($\text{erg cm}^{-2} \text{ sec}^{-1}$).

Although the peak burst power output lies between 150 and 500 keV for most bursts, the distribution (as observed from the KONUS catalogue) is sharply peaked around 200 keV (Higdon and Lingenfelter 1986). SMM observed hard high-energy tails, showing that burst power decreases at high energies (Nolan et al. 1984a). Burst power is also observed to turn over at low energies (e.g. Katoh et al. 1984). There are indications of cyclotron absorption features in the spectra from KONUS (Mazets et al. 1981), HEAO-A4 (Hueter et al. 1984), and GINGA (Murakami et al. 1988, Fenimore et al. 1989). Additionally, controversial observations of features thought to be positron-electron annihilation lines in emission have been made by KONUS (Mazets et al. 1981) and by SMM (Nolan et al. 1984b).

B. Spatial Analyses of Burst Sources

The location of the burst sources in space is difficult to determine. Without prior knowledge of their luminosities, their observed fluxes cannot accurately be converted into spatial positions. Astrophysical models for the bursts must therefore remain vague until this controversy is resolved, as the burst sources might be local, disk-population Galactic, halo-population Galactic, or extragalactic in origin. There are two approaches by which this spatial distribution can be studied; (1) by examining the angular distribution of sources, (2) by examining the radial distribution of sources (such as is attempted using the $\log(N)$ - $\log(S)$ method or the V/V_{\max} test).

1. The Angular Distribution of Sources

Angular spatial methods attempt to determine if the observed distribution prefers a position in space (such as the Galactic Center) or a symmetry plane (such as the ecliptic plane, the Galactic plane, or the plane containing the Local Supercluster of galaxies). Down to a minimum fluence of roughly 3×10^{-6} erg/cm², the spatial distribution of burst sources appears to be extremely isotropic (Mazets et al. 1981, Atteia et al. 1987). It also shows a negligible dipole moment, minimal quadrupole moments, and no propensity for clustering (Hartmann and Blumenthal 1988, Hartmann and Epstein 1989), in agreement with a random spatial distribution.

2. The Radial Distribution of Sources

a. $\log(N)$ - $\log(S)$ Curves

The number of sources N brighter than some fluence S provides one method by which the radial (distance) distribution of the sample can be measured. The luminosity distribution of a sample of sources with spatial density n in the luminosity interval $(L, L+dL)$ is described by the luminosity function $\Phi(L) dL$. Functionally, $N(\geq S) = \int n V \Phi(L) dL$, and, since the fluence of a source decreases as r^2 (where r is the

distance to the source), $S = L/(4\pi r^2)$. For a uniform spatial distribution of sources (where the volume $V = [4\pi/3] r^3$), integration yields $N \propto S^{-3/2}$, or $\log(N) \propto -3/2 \log(S)$. Similarly, a distance-limited sample will start off as $\log(N) \propto -3/2 \log(S)$, but will turn over at faint fluence such that $\log(N) \propto 0$. A sample confined to the volume of a disk initially yields $\log(N) \propto -3/2 \log(S)$; tilts over to become $\log(N) \propto -\log(S)$ at fainter fluence, and finally reaches $\log(N) \propto 0$ at faint fluence (when the disk has been completely sampled). A general description of $\log(N)$ - $\log(S)$ plots for disk models may be found in Fishman (1979).

Analysis of the $\log(N)$ - $\log(S)$ distribution of burst sources from early satellite catalogs (e.g. from KONUS, Mazets et al. 1981) indicates that the sample is in some way radially bounded, although this interpretation is quite controversial.

Higdon and Lingenfelter (1986) have noted that KONUS looks for bursts on low-energy (soft) channels, whereas some bursts apparently have stronger high-energy (hard) emissions. They suggest that the observed sample is biased to brighter (nearer) sources (as both hard and soft sources are detected at high fluence, whereas hard sources are more difficult for the equipment to trigger on if they are farther away), and argue that the corrected KONUS data is consistent with a $\log(N)$ - $\log(S)$ slope of $-3/2$. However, since the exact peak energy distribution (the relative number of soft to hard sources) is unknown, the amount of correction applied to obtain these results is quite model-dependent.

Since the detectors used trigger on minimum flux rather than on minimum fluence, they are more likely to sense short bursts than long ones. Although many observers suggest that the raw peak photon rate C should be used instead of fluence to bypass detector response, the overall problem of interpretation still remains unresolved. Paczynskii and Long (1986) infer that the faint-end $\log(N)$ - $\log(C)$ slope is -1.07 (indicating a radial limit in agreement with a Galactic disk model), while Jennings (1982, 1984) corrects the data to a slope of $-3/2$.

Meegan et al. (1985) have placed an upper limit on the $\log(N)$ - $\log(S)$ curve from balloon data. Their analysis incorporates (1) calculation of a detector count-rate triggering threshold, (2) conversion of this rate threshold to a fluence threshold, (3) simulations of the fraction of incident photons that will trigger each detector, (4) corrections for temporal triggering effects, and (5) analysis of the distribution based upon assumed spectral shapes of bursts. Their results indicate an upper limit of 2300 bursts/year at a fluence of 6×10^{-7} erg cm^{-2} . In order to fall below this limit, the $\log(N)$ - $\log(S)$ curve must turn over below 10^{-4} erg cm^{-2} .

b. The Radial/Angular Distribution of Sources

Schmidt (1968) developed another statistical test which analyzes the radial distributions of an astronomical sample, known as the V/V_{\max} test. This test is based upon the instrumental parameters C_{Lim} (the limiting count rate for a detector) and C_S (the source's observed count rate). For a uniformly-distributed sample, the count rate of a source depends upon its distance R_S . Since the limiting count rate corresponds to the distance R_{\max} that the source would have with count rate C_{Lim} , $R_{\max} = R (C_S/C_{\text{Lim}})^{1/2}$, and $V/V_{\max} = (C_S/C_{\text{Lim}})^{-3/2}$. For a sample of sources, the average value $\langle V/V_{\max} \rangle = \int_1^\infty (C_S/C_{\text{Lim}})^{-3/2} d(C_S/C_{\text{Lim}}) = 1/2$. Thus, a sample with $\langle V/V_{\max} \rangle < 1/2$ is distributed preferentially nearby, whereas one with $\langle V/V_{\max} \rangle > 1/2$ is located preferentially far away. Schmidt, Higdon, and Hueter (1988) have used the V/V_{\max} test on 13 HEAO-A4 gamma-ray bursts (with varying values of C_{Lim}) to indicate that $\langle V/V_{\max} \rangle = 0.40 \pm 0.08$, which they point out is consistent with uniformity. However, this value is also consistent with the beginnings of a $\log(N)$ - $\log(C)$ turnover.

C. Astrophysical Models of Burst Sources

Many astrophysical models exist for gamma-ray burst production, and are summarized in reviews by Liang (1989) and Hurley (1989). Possible models include compact sources in the cores of active galactic nuclei, massive galaxies, and globular clusters. However, the short timescale variability, cyclotron absorption features, and possible redshifted positron-electron annihilation lines in burst spectra lead to a favored model; that of a neutron star emitting by (1) accreting material and flashing, (2) vibration, (3) undergoing a crustquake, (4) being resurrected as a pulsar, or (5) via a magnetic flare. The limited power outputs of neutron star models suggest that a turnover in the $\log(N)$ - $\log(S)$ curve should be visible at some point.

Objectives

Accurate models of the gamma-ray burst distribution are not obtained simply. Direct integrations of $\log(N)$ - $\log(S)$ and angular functions describing the distribution are generally quite difficult to perform. Also, the functional forms of these distributions are quite model-dependent, so direct integration of a great number of possible distributions is needed. This makes the problem even more unwieldy.

Monte carlo techniques eliminate the difficulties of direct integration while simultaneously allowing great freedom in examining model parameters. By creating a variety of discrete sources randomly, radial and angular distributions may be examined and compared to those of the actual data set. New models are easily created by merely adjusting model parameters. Models which are obviously incompatible with the observed data can be eliminated, while statistical tests performed on compatible models place restrictions on allowed parameter values.

For this project, a Galactic disk spatial distribution is chosen for the sources (halo models can be easily incorporated in the future, although the $\log(N)$ - $\log(S)$ distributions of these models do not apparently turn over fast enough at low fluence). A variety of source luminosity functions are tested within this framework, so that models with unreasonable luminosity functions might be eliminated.

A Monte Carlo Model of Galactic Disk Sources

The procedure used to test the validity of a model is to (1) choose model parameters from which a monte carlo data set is generated, (2) select only those generated sources which have fluences bright enough to be measured, and (3) statistically compare the radial and angular properties of the artificial data set with the real one. A number of these models can be eliminated from consideration. Finally, general luminosity and spatial properties of the real data may be inferred from the monte carlo models. Creation of the monte carlo data set is carried out via program GAMMA.FOR (figure 1), and the data analysis is performed by program GAMMA.PRO.

A. General Model Parameters

The general model parameters are allowed to be changed within the program, and it is in fact not difficult to change the functional forms of any parameters. The gamma ray bursts are assumed to originate on Galactic neutron stars, so the spatial distribution is that of the Galactic disk. Model parameters describing the Galactic disk are taken from the book *Galactic Astronomy*, by Mihalas and Binney (1981), and are meant to mimic general properties of the Milky Way (as presently understood). These values may, however, be varied easily within the program. A variety of luminosity functions are also allowed in the model, and parameters describing these functions may be easily changed.

1. The Three-Dimensional Galactic Disk

This disk model is intended to represent a variety of stellar ages and populations, but the youngest disk (spiral arm) population has been purposefully overlooked because the spatial distribution of bursts is apparently too isotropic to be associated with (1) spiral arms, and (2) a tendency to cluster as is observed for the youngest objects.

The Galactic disk is therefore characterized

- (1) in the Θ -direction by an isotropic distribution (i.e. there are

- no angular structures such as spiral arms).
- (2) in the z -direction (perpendicular to the Galactic plane) by a Gaussian distribution. There are physical reasons for choosing this model over either a linearly- or an exponentially-decreasing one (although both of these are often used in Galactic astronomy): Primarily, these models exhibit discontinuities at $z = 0$, whereas a Gaussian model does not. Furthermore, these models are not as easy to explain in terms of maintenance via a Galactic gravitational potential. The width of the Gaussian distribution is represented by the variance σ_z^2 , where σ_z differs from the exponential scale height by $\sqrt{2}$. Choosing a value for σ_z is difficult. Scale heights of stellar populations are estimated from Mihalas and Binney (1981) p. 278, to be as follows: Spiral Arm population (age $\leq 10^8$ years) = 120 parsecs, Young disk population (age $\approx 10^9$ years) = 200 parsecs, Intermediate disk population (age $\approx 5 \times 10^9$ years) = 400 parsecs, and Old Disk population (age $\leq 10^{10}$ years) = 700 parsecs. A disk sample with a constant birthrate function would have an average age of around 5×10^9 years (if the disk is 10^{10} years old), and a scale height of roughly 400 parsecs. This might be an underestimate, as the suspected scale height of white dwarf stars is 500 parsecs. A best guess value for σ_z is therefore 350 parsecs, corresponding to a scale height of 500 parsecs.
 - (3) in the r -direction (radially outward from the Galactic center) by an exponentially-decreasing density function. This is both observed locally and from brightness distributions of other spiral galaxies of similar Hubble types. This exponential decrease is convolved with the infinitesimal radial increase ($r \times dr$) needed to keep a constant disk density for cylindrical geometry. The exponential scaling factor R_g of the distribution $\exp(-r/R_g)$ is obtained from scaling the size of the Milky Way Galaxy to that of the Andromeda Galaxy (M31), and is therefore $R_g = 3.9$ kpc.

The sun is assumed to lie at a distance of 8.5 kpc from the Galactic center, in the Galactic plane.

2. The Luminosity Function of Burst Sources

Several "standard" luminosity functions of burst sources are allowed:

- (1) All sources have the same luminosity, $\langle L \rangle$.
- (2) The sources are chosen from a Gaussian luminosity function characterized by $\langle L \rangle$ and σ_L .

- (3) The sources are chosen from a topheavy luminosity function linearly increasing in number between L_{\min} and L_{\max} .
- (4) The sources are chosen from a bottomheavy luminosity function linearly decreasing in number between L_{\min} and L_{\max} .
- (5) The sources are selected from a bottomheavy power law luminosity function where $N(L) \propto (L/L_{\min})^{-\alpha}$.

A sample of the modeled disk distribution (for sources of a single luminosity $\langle L \rangle$) is shown in figure 3.

B. Selection of Data for Analysis

Once each "burst" has been given a Galactic position and a luminosity, fluences and observed positions for it (in Galactic coordinates l and b) are calculated. Only those sources with fluences greater than S_{\min} are selected (S_{\min} is chosen to be 2×10^{-7} erg cm^{-2} , as this represents a minimum value of $\log(S)$ for which reliable $\log(N)$ data exists). From these data, a $\log(N)$ - $\log(S)$ array is built and angular characteristics are examined. An estimate must be made of the total number of sources, since this in part determines the "goodness of fit" of the $\log(N)$ - $\log(S)$ plot. At present this fit is estimated by inspection; future work may introduce a subroutine which optimizes the number of sources used.

It should be noted that Galactic disk samples of low-luminosity sources take much more CPU time to create than those of high-luminosity sources. This is due to the sample's (disk height/limiting distance) ratio, which is larger for low-luminosity sources than it is for high-luminosity ones. In other words, the luminous sources are confined to an almost two-dimensional flat disk (which the computer rapidly fills), whereas the low-luminosity ones are confined within a three-dimensional sphere (which fills in more CPU time).

Samples with a range of luminosities (such as the power law luminosity distribution described above) also use larger amounts of CPU time, which sometimes can be prohibitively large on a small computer such as a VAX.

C. Method of Data Analysis

The $\log(N)$ - $\log(S)$ curve is produced from the data, and is chosen to (1) match the $\log(N)$ - $\log(S)$ plot observed from satellite data at high fluence, and (2) stay below the balloon limit (Meegan et al. 1985) of 2300 bursts/year at a fluence of 6×10^{-7} erg cm $^{-2}$. The slope $d[\log(N)/\log(S)]/d[\log(S)]$ is also compared to that of the actual data set.

The spatial distribution can be plotted for any minimum fluence in Galactic coordinates l and b . A quick-and-dirty analysis checks the distribution of events brighter than this minimum fluence as a function of Galactic latitude region by considering three latitude regions of equal area. The Galactic latitude regions $0^\circ \leq |b| \leq 19.5^\circ$ (low-latitude), $19.5^\circ < |b| \leq 41.8^\circ$ (mid-latitude), and $41.8^\circ < |b| \leq 90^\circ$ (high-latitude), should contain equal numbers of stars n , with errors $n/\sqrt{n-1}$. A more accurate method of analysis is also presented, as the system's dipole and quadrupole moments are calculated. A large dipole moment indicates that the distribution is biased towards one direction. The quadrupole moments yield two useful parameters: η (the difference between the two closest eigenvalues of the quadrupole tensor) and ζ (the most different eigenvalue). When $\eta = \zeta = 0$, the distribution is isotropic. An oblate (disk) distribution is indicated by $\zeta \geq 0$, whereas a prolate distribution (one which is strongly bipolar) is indicated by $\zeta \leq 0$.

D. Results of Preliminary Data Analysis

Samples of program output and data analysis are shown in figures 4, 5, and 6. Once a number of models have been run, a comparison can be made between them and the actual data.

The constraints imposed by both an isotropic angular distribution for high minimum fluence ($S_{\min} \geq 3 \times 10^{-6}$ erg cm $^{-2}$) and an apparent turnover in the $\log(N)$ - $\log(S)$ curve turn out to be quite strict. For $\sigma_z = 400$ parsecs and a single luminosity function $L = \langle L \rangle$, a lower luminosity limit of $\langle L \rangle \approx 4 \times 10^5$ solar luminosities or 1.5×10^{39} erg is necessary to turn the $\log(N)$ - $\log(S)$ curve over by $S = 2 \times 10^{-5}$ erg cm $^{-2}$ (the "elbow", or the lowest fluence where the $\log(N)$ - $\log(S)$ curve can turn over in order to stay below the balloon data limit with a physically meaningful slope). Models with lower average luminosities do not stay below the balloon data $\log(N)$ upper limit. Those with

higher average luminosities effectively stay below the balloon limit, but do not match the $\log(N)$ - $\log(S)$ curve at high fluence, do not show spatial isotropy for minimum fluences below that of the "elbow", and predict a Galactic radius exceeding 15 kpc (compared to the apparent radius of 13.5 kpc). Thus only a small range of average luminosities between these extremes satisfies the observations, and the model is strongly constrained.

Many implications arise from these limits:

- (1) The spatial density of sources is somewhere around $3 \times 10^{-8} \text{ pc}^{-3} \text{ yr}^{-1}$. If there are roughly 3×10^7 neutron stars in the Galaxy (Hartmann, Epstein, and Woosley 1989), then the bursts sources must repeat on an average of around 10^5 years to explain the burst rate.
- (2) The range of acceptable luminosities is too high for existing astrophysical models of neutron star crustquakes or resurrected pulsars (see Liang 1989), suggesting that these models are unlikely.
- (3) The effects of other luminosity functions on the results are not very pronounced. A Gaussian function broadens the "elbow" from a well-defined point to a curve and strengthens any spatial anisotropies that are present, due to an oversampling of the luminous sources (see also Hakkila 1989). The topheavy and bottomheavy functions, being linear, exhibit slight effects that are very similar to the Gaussian distribution, although the bottomheavy function tends to show more spatial isotropy at high fluence. The power law function is the most promising luminosity function, but at present consumes an inordinate amount of CPU time.

Conclusions and Recommendations

A. Conclusions

This approach appears to provide a useful method for analyzing the properties of gamma-ray burst sources, as well as for analyzing properties of other astronomical objects. Detailed analysis which include interstellar absorption could lead to a better understanding of Galactic structure, stellar populations, and stellar evolution.

Observations of gamma-ray bursts (angular isotropy at high fluence coupled with a $\log(N)$ - $\log(S)$ turnover) strongly constrain the number and types of allowed monte carlo simulations. The allowed models suggest that, for a distribution characterized by a single source luminosity $\langle L \rangle$, only a small range of luminosities (10^{39} erg $\leq \langle L \rangle \leq 6 \times 10^{39}$ erg) result in acceptable fits to the actual data. Other luminosity functions do not significantly alter these general conclusions, although the effects of bottomheavy power law functions are still unknown (due to prohibitive use of CPU time).

The implications of these results are worrisome, as they indicate that (1) some of the observational data is in error, (2) selection effects are still present in the existing data, (3) the Galactic disk model used in this monte carlo analysis is significantly in error, (4) a Galactic disk model is not the proper representation for the distribution of gamma-ray burst sources, or (5) the bursts really all have only a small luminosity range.

B. Recommendations

This approach is still only in the preliminary stages. More work still needs to be done in order to

- (1) quantify the comparison between models and observations,
- (2) vary disk parameters in order to see what effects different stellar populations have upon the resultant distributions,
- (3) examine the effects of a Galactic halo component,
- (4) integrate models over larger data samples to get better statistics,
- (5) include a method for optimizing the number of generated

sources,

- (6) study the effects of a bottomheavy power-law luminosity function,
- (7) refine the Galactic model to incorporate new understanding about Galactic structure,
- (8) prepare for the possibility the BATSE will identify burst subpopulations, as these will then have to be examined separately,
- (9) etc.

Of course, the new data obtained from the BATSE experiment on GRO should resolve the bulk of the burst distribution problem within only a few months of launch, and the data set that it generates can help isolate the locations of and mechanisms responsible for the gamma-ray burst sources. With the BATSE data, methods such as this will prove useful in isolating (1) the luminosity function of the burst sources, and (2) the stellar population of the burst sources (should they prove to have Galactic origins).

References

- Atteia, J.-L. et al. 1987, *Ap. J. Supp. Ser.* **64**, 305.
 Barat, C. et al. 1984, *Ap. J.* **285**, 791.
 Fenimore, E. et al. 1989, *Ap. J.* submitted.
 Fishman, G. J. 1979, *Ap. J.* **233**, 851.
 Hakkila, J. 1989, *Ap. J.* in press.
 Hartmann, D., and Epstein, R. I. 1988, *Ap. J.* in press.
 Hartmann, D., Epstein, R. I., and Woosley, S.E. 1989, *Nucl. Phys. B.* in press.
 Hartmann, D., and Blumenthal, G. 1989, *Ap. J.* submitted.
 Higdon, J., and Lingenfelter, R. 1986, *Ap. J.* **307**, 197.
 Hueter, J. 1987, Ph. D. Dissertation, U. C. San Diego.
 Hurley, K. 1989, *Proc. NATO ASI Erice School on Cosmic Rays*, ed. Shapiro, M. M. (Dordrecht: Reidel).
 Jennings, M. C. 1982, *Ap. J.* **258**, 110.
 Jennings, M. C. 1984, *AIP Conf. Proc. No. 115*, ed. Woosley, S. E. (New York: AIP Press), p. 412.
 Katoh et al. 1984, *AIP Conf. Proc. No. 115*, ed. Woosley, S. E. (New York: AIP Press), p. 390.
 Klebesadel, R. W., Strong, I., and Olson, R. 1973, *Ap. J. (Letters)* **182**, L85.
 Liang, E. P. 1989, preprint.
 Mazets, E. P., et al. 1981, *Ap. Sp. Sci.* **80**, 3.
 Meegan, C. A., Fishman, G. J., and Wilson, R. B. 1985, *Ap. J.* **291**, 479.
 Mihalas, D., and Binney, J. 1981, *Galactic Astronomy: Structure and Kinematics* (San Francisco: W. H. Freeman).
 Murakami, T. et al. 1988, *Nature* **335**, 234.
 Nolan, P. L. et al. 1984a, *AIP Conf. Proc. No. 115*, ed. Woosley, S. E. (New York: AIP Press), p. 399.
 Nolan, P. L. et al. 1984b, *Nature* **311**, 360.
 Paczynskii, B., and Long, K. 1988, *Ap. J.* **301**, 213.
 Schaefer, B. 1981, *Nature* **294**, 722.
 Schmidt, M. 1968, *Ap. J.* **151**, 393.
 Schmidt, M., Higdon, J. C., and Hueter, G. 1988, *Ap. J. (Letters)* **329**, L85.

XIII- 14


```

10. Program GAMMA.PRO written by Jon Halliday

Program GAMMA.PRO analyzes output from GAMMA.FOR1 producing
four (4) plots and one (1) output file (GAMMA.OUT).
Parameters which need to be set in this program are the input
file's name, the total number of sources created (JTOT) identical
to JTOT in GAMMA.FOR1, JN (the number of logN entries, which can
be obtained from the input file's total number of lines NUP as
JN=JTOT-JN1-B1, STET is minimum (flux), and INTITLE (the desired
main title for the plots).

The program plots a logN-logS curve for the Monte Carlo data and
converts it to observations. It also plots the slope of this line
a logN/d logS as a function of logS. The total distribution is then
spatially sampled for four minimum fluxes: 1E-6, 1E-5, 1E-4,
and 1E-3. For each of these a latitude distribution of the data
is obtained into three equal areas on the sky in Galactic coordinates.
I and B1 is obtained, and is compared to that of a random distribution.
Also calculated are the dipole and quadrupole moments of the
distributions, which should be zero for a randomly distributed
sample.

Additional variables which can be easily set in this program are JN1
the smallest value of N to be used in calculating a logN/d logS
and INTB (the number of equal-sized logN divisions that will be used
in this calculation. A "division-by-zero" error is generally corrected
either by slightly raising JN1 or lowering INTB.

OPENR(1,"AL756.DAT")
OPENW(2,"GAMMA.OUT")
INTITLE="Avg Log Dist Level? SED Level"
JN1=497
JTOT=7500
JN1B1
JN1B2
JN1B3
JN1B4
JN1B5
JN1B6
JN1B7
JN1B8
JN1B9
JN1B10
JN1B11
JN1B12
JN1B13
JN1B14
JN1B15
JN1B16
JN1B17
JN1B18
JN1B19
JN1B20
JN1B21
JN1B22
JN1B23
JN1B24
JN1B25
JN1B26
JN1B27
JN1B28
JN1B29
JN1B30
JN1B31
JN1B32
JN1B33
JN1B34
JN1B35
JN1B36
JN1B37
JN1B38
JN1B39
JN1B40
JN1B41
JN1B42
JN1B43
JN1B44
JN1B45
JN1B46
JN1B47
JN1B48
JN1B49
JN1B50
JN1B51
JN1B52
JN1B53
JN1B54
JN1B55
JN1B56
JN1B57
JN1B58
JN1B59
JN1B60
JN1B61
JN1B62
JN1B63
JN1B64
JN1B65
JN1B66
JN1B67
JN1B68
JN1B69
JN1B70
JN1B71
JN1B72
JN1B73
JN1B74
JN1B75
JN1B76
JN1B77
JN1B78
JN1B79
JN1B80
JN1B81
JN1B82
JN1B83
JN1B84
JN1B85
JN1B86
JN1B87
JN1B88
JN1B89
JN1B90
JN1B91
JN1B92
JN1B93
JN1B94
JN1B95
JN1B96
JN1B97
JN1B98
JN1B99
JN1B100
JN1B101
JN1B102
JN1B103
JN1B104
JN1B105
JN1B106
JN1B107
JN1B108
JN1B109
JN1B110
JN1B111
JN1B112
JN1B113
JN1B114
JN1B115
JN1B116
JN1B117
JN1B118
JN1B119
JN1B120
JN1B121
JN1B122
JN1B123
JN1B124
JN1B125
JN1B126
JN1B127
JN1B128
JN1B129
JN1B130
JN1B131
JN1B132
JN1B133
JN1B134
JN1B135
JN1B136
JN1B137
JN1B138
JN1B139
JN1B140
JN1B141
JN1B142
JN1B143
JN1B144
JN1B145
JN1B146
JN1B147
JN1B148
JN1B149
JN1B150
JN1B151
JN1B152
JN1B153
JN1B154
JN1B155
JN1B156
JN1B157
JN1B158
JN1B159
JN1B160
JN1B161
JN1B162
JN1B163
JN1B164
JN1B165
JN1B166
JN1B167
JN1B168
JN1B169
JN1B170
JN1B171
JN1B172
JN1B173
JN1B174
JN1B175
JN1B176
JN1B177
JN1B178
JN1B179
JN1B180
JN1B181
JN1B182
JN1B183
JN1B184
JN1B185
JN1B186
JN1B187
JN1B188
JN1B189
JN1B190
JN1B191
JN1B192
JN1B193
JN1B194
JN1B195
JN1B196
JN1B197
JN1B198
JN1B199
JN1B200
JN1B201
JN1B202
JN1B203
JN1B204
JN1B205
JN1B206
JN1B207
JN1B208
JN1B209
JN1B210
JN1B211
JN1B212
JN1B213
JN1B214
JN1B215
JN1B216
JN1B217
JN1B218
JN1B219
JN1B220
JN1B221
JN1B222
JN1B223
JN1B224
JN1B225
JN1B226
JN1B227
JN1B228
JN1B229
JN1B230
JN1B231
JN1B232
JN1B233
JN1B234
JN1B235
JN1B236
JN1B237
JN1B238
JN1B239
JN1B240
JN1B241
JN1B242
JN1B243
JN1B244
JN1B245
JN1B246
JN1B247
JN1B248
JN1B249
JN1B250
JN1B251
JN1B252
JN1B253
JN1B254
JN1B255
JN1B256
JN1B257
JN1B258
JN1B259
JN1B260
JN1B261
JN1B262
JN1B263
JN1B264
JN1B265
JN1B266
JN1B267
JN1B268
JN1B269
JN1B270
JN1B271
JN1B272
JN1B273
JN1B274
JN1B275
JN1B276
JN1B277
JN1B278
JN1B279
JN1B280
JN1B281
JN1B282
JN1B283
JN1B284
JN1B285
JN1B286
JN1B287
JN1B288
JN1B289
JN1B290
JN1B291
JN1B292
JN1B293
JN1B294
JN1B295
JN1B296
JN1B297
JN1B298
JN1B299
JN1B300
JN1B301
JN1B302
JN1B303
JN1B304
JN1B305
JN1B306
JN1B307
JN1B308
JN1B309
JN1B310
JN1B311
JN1B312
JN1B313
JN1B314
JN1B315
JN1B316
JN1B317
JN1B318
JN1B319
JN1B320
JN1B321
JN1B322
JN1B323
JN1B324
JN1B325
JN1B326
JN1B327
JN1B328
JN1B329
JN1B330
JN1B331
JN1B332
JN1B333
JN1B334
JN1B335
JN1B336
JN1B337
JN1B338
JN1B339
JN1B340
JN1B341
JN1B342
JN1B343
JN1B344
JN1B345
JN1B346
JN1B347
JN1B348
JN1B349
JN1B350
JN1B351
JN1B352
JN1B353
JN1B354
JN1B355
JN1B356
JN1B357
JN1B358
JN1B359
JN1B360
JN1B361
JN1B362
JN1B363
JN1B364
JN1B365
JN1B366
JN1B367
JN1B368
JN1B369
JN1B370
JN1B371
JN1B372
JN1B373
JN1B374
JN1B375
JN1B376
JN1B377
JN1B378
JN1B379
JN1B380
JN1B381
JN1B382
JN1B383
JN1B384
JN1B385
JN1B386
JN1B387
JN1B388
JN1B389
JN1B390
JN1B391
JN1B392
JN1B393
JN1B394
JN1B395
JN1B396
JN1B397
JN1B398
JN1B399
JN1B400
JN1B401
JN1B402
JN1B403
JN1B404
JN1B405
JN1B406
JN1B407
JN1B408
JN1B409
JN1B410
JN1B411
JN1B412
JN1B413
JN1B414
JN1B415
JN1B416
JN1B417
JN1B418
JN1B419
JN1B420
JN1B421
JN1B422
JN1B423
JN1B424
JN1B425
JN1B426
JN1B427
JN1B428
JN1B429
JN1B430
JN1B431
JN1B432
JN1B433
JN1B434
JN1B435
JN1B436
JN1B437
JN1B438
JN1B439
JN1B440
JN1B441
JN1B442
JN1B443
JN1B444
JN1B445
JN1B446
JN1B447
JN1B448
JN1B449
JN1B450
JN1B451
JN1B452
JN1B453
JN1B454
JN1B455
JN1B456
JN1B457
JN1B458
JN1B459
JN1B460
JN1B461
JN1B462
JN1B463
JN1B464
JN1B465
JN1B466
JN1B467
JN1B468
JN1B469
JN1B470
JN1B471
JN1B472
JN1B473
JN1B474
JN1B475
JN1B476
JN1B477
JN1B478
JN1B479
JN1B480
JN1B481
JN1B482
JN1B483
JN1B484
JN1B485
JN1B486
JN1B487
JN1B488
JN1B489
JN1B490
JN1B491
JN1B492
JN1B493
JN1B494
JN1B495
JN1B496
JN1B497
JN1B498
JN1B499
JN1B500
JN1B501
JN1B502
JN1B503
JN1B504
JN1B505
JN1B506
JN1B507
JN1B508
JN1B509
JN1B510
JN1B511
JN1B512
JN1B513
JN1B514
JN1B515
JN1B516
JN1B517
JN1B518
JN1B519
JN1B520
JN1B521
JN1B522
JN1B523
JN1B524
JN1B525
JN1B526
JN1B527
JN1B528
JN1B529
JN1B530
JN1B531
JN1B532
JN1B533
JN1B534
JN1B535
JN1B536
JN1B537
JN1B538
JN1B539
JN1B540
JN1B541
JN1B542
JN1B543
JN1B544
JN1B545
JN1B546
JN1B547
JN1B548
JN1B549
JN1B550
JN1B551
JN1B552
JN1B553
JN1B554
JN1B555
JN1B556
JN1B557
JN1B558
JN1B559
JN1B560
JN1B561
JN1B562
JN1B563
JN1B564
JN1B565
JN1B566
JN1B567
JN1B568
JN1B569
JN1B570
JN1B571
JN1B572
JN1B573
JN1B574
JN1B575
JN1B576
JN1B577
JN1B578
JN1B579
JN1B580
JN1B581
JN1B582
JN1B583
JN1B584
JN1B585
JN1B586
JN1B587
JN1B588
JN1B589
JN1B590
JN1B591
JN1B592
JN1B593
JN1B594
JN1B595
JN1B596
JN1B597
JN1B598
JN1B599
JN1B600
JN1B601
JN1B602
JN1B603
JN1B604
JN1B605
JN1B606
JN1B607
JN1B608
JN1B609
JN1B610
JN1B611
JN1B612
JN1B613
JN1B614
JN1B615
JN1B616
JN1B617
JN1B618
JN1B619
JN1B620
JN1B621
JN1B622
JN1B623
JN1B624
JN1B625
JN1B626
JN1B627
JN1B628
JN1B629
JN1B630
JN1B631
JN1B632
JN1B633
JN1B634
JN1B635
JN1B636
JN1B637
JN1B638
JN1B639
JN1B640
JN1B641
JN1B642
JN1B643
JN1B644
JN1B645
JN1B646
JN1B647
JN1B648
JN1B649
JN1B650
JN1B651
JN1B652
JN1B653
JN1B654
JN1B655
JN1B656
JN1B657
JN1B658
JN1B659
JN1B660
JN1B661
JN1B662
JN1B663
JN1B664
JN1B665
JN1B666
JN1B667
JN1B668
JN1B669
JN1B670
JN1B671
JN1B672
JN1B673
JN1B674
JN1B675
JN1B676
JN1B677
JN1B678
JN1B679
JN1B680
JN1B681
JN1B682
JN1B683
JN1B684
JN1B685
JN1B686
JN1B687
JN1B688
JN1B689
JN1B690
JN1B691
JN1B692
JN1B693
JN1B694
JN1B695
JN1B696
JN1B697
JN1B698
JN1B699
JN1B700
JN1B701
JN1B702
JN1B703
JN1B704
JN1B705
JN1B706
JN1B707
JN1B708
JN1B709
JN1B710
JN1B711
JN1B712
JN1B713
JN1B714
JN1B715
JN1B716
JN1B717
JN1B718
JN1B719
JN1B720
JN1B721
JN1B722
JN1B723
JN1B724
JN1B725
JN1B726
JN1B727
JN1B728
JN1B729
JN1B730
JN1B731
JN1B732
JN1B733
JN1B734
JN1B735
JN1B736
JN1B737
JN1B738
JN1B739
JN1B740
JN1B741
JN1B742
JN1B743
JN1B744
JN1B745
JN1B746
JN1B747
JN1B748
JN1B749
JN1B750
JN1B751
JN1B752
JN1B753
JN1B754
JN1B755
JN1B756
JN1B757
JN1B758
JN1B759
JN1B760
JN1B761
JN1B762
JN1B763
JN1B764
JN1B765
JN1B766
JN1B767
JN1B768
JN1B769
JN1B770
JN1B771
JN1B772
JN1B773
JN1B774
JN1B775
JN1B776
JN1B777
JN1B778
JN1B779
JN1B780
JN1B781
JN1B782
JN1B783
JN1B784
JN1B785
JN1B786
JN1B787
JN1B788
JN1B789
JN1B790
JN1B791
JN1B792
JN1B793
JN1B794
JN1B795
JN1B796
JN1B797
JN1B798
JN1B799
JN1B800
JN1B801
JN1B802
JN1B803
JN1B804
JN1B805
JN1B806
JN1B807
JN1B808
JN1B809
JN1B810
JN1B811
JN1B812
JN1B813
JN1B814
JN1B815
JN1B816
JN1B817
JN1B818
JN1B819
JN1B820
JN1B821
JN1B822
JN1B823
JN1B824
JN1B825
JN1B826
JN1B827
JN1B828
JN1B829
JN1B830
JN1B831
JN1B832
JN1B833
JN1B834
JN1B835
JN1B836
JN1B837
JN1B838
JN1B839
JN1B840
JN1B841
JN1B842
JN1B843
JN1B844
JN1B845
JN1B846
JN1B847
JN1B848
JN1B849
JN1B850
JN1B851
JN1B852
JN1B853
JN1B854
JN1B855
JN1B856
JN1B857
JN1B858
JN1B859
JN1B860
JN1B861
JN1B862
JN1B863
JN1B864
JN1B865
JN1B866
JN1B867
JN1B868
JN1B869
JN1B870
JN1B871
JN1B872
JN1B873
JN1B874
JN1B875
JN1B876
JN1B877
JN1B878
JN1B879
JN1B880
JN1B881
JN1B882
JN1B883
JN1B884
JN1B885
JN1B886
JN1B887
JN1B888
JN1B889
JN1B890
JN1B891
JN1B892
JN1B893
JN1B894
JN1B895
JN1B896
JN1B897
JN1B898
JN1B899
JN1B900
JN1B901
JN1B902
JN1B903
JN1B904
JN1B905
JN1B906
JN1B907
JN1B908
JN1B909
JN1B910
JN1B911
JN1B912
JN1B913
JN1B914
JN1B915
JN1B916
JN1B917
JN1B918
JN1B919
JN1B920
JN1B921
JN1B922
JN1B923
JN1B924
JN1B925
JN1B926
JN1B927
JN1B928
JN1B929
JN1B930
JN1B931
JN1B932
JN1B933
JN1B934
JN1B935
JN1B936
JN1B937
JN1B938
JN1B939
JN1B940
JN1B941
JN1B942
JN1B943
JN1B944
JN1B945
JN1B946
JN1B947
JN1B948
JN1B949
JN1B950
JN1B951
JN1B952
JN1B953
JN1B954
JN1B955
JN1B956
JN1B957
JN1B958
JN1B959
JN1B960
JN1B961
JN1B962
JN1B963
JN1B964
JN1B965
JN1B966
JN1B967
JN1B968
JN1B969
JN1B970
JN1B971
JN1B972
JN1B973
JN1B974
JN1B975
JN1B976
JN1B977
JN1B978
JN1B979
JN1B980
JN1B981
JN1B982
JN1B983
JN1B984
JN1B985
JN1B986
JN1B987
JN1B988
JN1B989
JN1B990
JN1B991
JN1B992
JN1B993
JN1B994
JN1B995
JN1B996
JN1B997
JN1B998
JN1B999
JN1B1000
JN1B1001
JN1B1002
JN1B1003
JN1B1004
JN1B1005
JN1B1006
JN1B1007
JN1B1008
JN1B1009
JN1B1010
JN1B1011
JN1B1012
JN1B1013
JN1B1014
JN1B1015
JN1B1016
JN1B1017
JN1B1018
JN1B1019
JN1B1020
JN1B1021
JN1B1022
JN1B1023
JN1B1024
JN1B1025
JN1B1026
JN1B1027
JN1B1028
JN1B1029
JN1B1030
JN1B1031
JN1B1032
JN1B1033
JN1B1034
JN1B1035
JN1B1036
JN1B1037
JN1B1038
JN1B1039
JN1B1040
JN1B1041
JN1B1042
JN1B1043
JN1B1044
JN1B1045
JN1B1046
JN1B1047
JN1B1048
JN1B1049
JN1B1050
JN1B1051
JN1B1052
JN1B1053
JN1B1054
JN1B1055
JN1B1056
JN1B1057
JN1B1058
JN1B1059
JN1B1060
JN1B1061
JN1B1062
JN1B1063
JN1B1064
JN1B1065
JN1B1066
JN1B1067
JN1B1068
JN1B1069
JN1B1070
JN1B1071
JN1B1072
JN1B1073
JN1B1074
JN1B1075
JN1B1076
JN1B1077
JN1B1078
JN1B1079
JN1B1080
JN1B1081
JN1B1082
JN1B1083
JN1B1084
JN1B1085
JN1B1086
JN1B1087
JN1B1088
JN1B1089
JN1B1090
JN1B1091
JN1B1092
JN1B1093
JN1B1094
JN1B1095
JN1B1096
JN1B1097
JN1B1098
JN1B1099
JN1B1100
JN1B1101
JN1B1102
JN1B1103
JN1B1104
JN1B1105
JN1B1106
JN1B1107
JN1B1108
JN1B1109
JN1B1110
JN1B1111
JN1B1112
JN1B1113
JN1B1114
JN1B1115
JN1B1116
JN1B1117
JN1B1118
JN1B1119
JN1B1120
JN1B1121
JN1B1122
JN1B1123
JN1B1124
JN1B1125
JN1B1126
JN1B1127
JN1B1128
JN1B1129
JN1B1130
JN1B1131
JN1B1132
JN1B1133
JN1B1134
JN1B1135
JN1B1136
JN1B1137
JN1B1138
JN1B1139
JN1B1140
JN1B1141
JN1B1142
JN1B1143
JN1B1144
JN1B1145
JN1B1146
JN1B1147
JN1B1148
JN1B1149
JN1B1150
JN1B1151
JN1B1152
JN1B1153
JN1B1154
JN1B1155
JN1B1156
JN1B1157
JN1B1158
JN1B1159
JN1B1160
JN1B1161
JN1B1162
JN1B1163
JN1B1164
JN1B1165
JN1B1166
JN1B1167
JN1B1168
JN1B1169
JN1B1170
JN1B1171
JN1B1172
JN1B1173
JN1B1174
JN1B1175
JN1B1176
JN1B1177
JN1B1178
JN1B1179
JN1B1180
JN1B1181
JN1B1182
JN1B1183
JN1B1184
JN1B1185
JN1B1186
JN1B1187
JN1B1188
JN1B1189
JN1B1190
JN1B1191
JN1B1192
JN1B1193
JN1B1194
JN1B1195
JN1B1196
JN1B1197
JN1B1198
JN1B1199
JN1B1200
JN1B1201
JN1B1202
JN1B1203
JN1B1204
JN1B1205
JN1B1206
JN1B1207
JN1B1208
JN1B1209
JN1B1210
JN1B1211
JN1B1212
JN1B1213
JN1B1214
JN1B1215
JN1B1216
JN1B1217
JN1B1218
JN1B1219
JN1B1220
JN1B1221
JN1B1222
JN1B1223
JN1B1224
JN1B1225
JN1B1226
JN1B1227
JN1B1228
JN1B1229
JN1B1230
JN1B1231
JN1B1232
JN1B1233
JN1B1234
JN1B1235
JN1B1236
JN1B1237
JN1B1238
JN1B1239
JN1B1240
JN1B1241
JN1B1242
JN1B1243
JN1B1244
JN1B1245
JN1B1246
JN1B1247
JN1B1248
JN1B1249
JN1B1250
JN1B1251
JN1B1252
JN1B1253
JN1B1254
JN1B1255
JN1B1256
JN1B1257
JN1B1258
JN1B1259
JN1B1260
JN1B1261
JN1B1262
JN1B1263
JN1B1264
JN1B1265
JN1B1266
JN1B1267
JN1B1268
JN1B1269
JN1B1270
JN1B1271
JN1B1272
JN1B1273
JN1B1274
JN1B1275
JN1B1276
JN1B1277
JN1B1278
JN1B1279
JN1B1280
JN1B1281
JN1B1282
JN1B1283
JN1B1284
JN1B1285
JN1B1286
JN1B1287
JN1B1288
JN1B1289
JN1B1290
JN1B1291
JN1B1292
JN1B1293
JN1B1294
JN1B1295
JN1B1296
JN1B1297
JN1B1298
JN1B1299
JN1B1300
JN1B1301
JN1B1302
JN1B1303
JN1B1304
JN1B1305
JN1B1306
JN1B1307
JN1B1308
JN1B1309
JN1B1310
JN1B1311
JN1B1312
JN1B1313
JN1B1314
JN1B1315
JN1B1316
JN1B1317
JN1B1318
JN1B1319
JN1B1320
JN1B1321
JN1B1322
JN1B1323
JN1B1324
JN1B1325
JN1B1326
JN1B1327
JN1B1328
JN1B1329
JN1B1330
JN1B1331
JN1B1332
JN1B1333
JN1B1334
JN1B1335
JN1B1336
JN1B1337
JN1B1338
JN1B1339
JN1B1340
JN1B1341
JN1B1342
JN1B1343
JN1B1344
JN1B1345
JN1B1346
JN1B1347
JN1B1348
JN1B1349
JN1B1350
JN1B1351
JN1B1352
JN1B1353
JN1B1354
JN1B1355
JN1B1356
JN1B1357
JN1B1358
JN1B1359
JN1B1360
JN1B1361
JN1B1362
JN1B1363
JN1B1364
JN1B1365
JN1B1366
JN1B1367
JN1B1368
JN1B1369
JN1B1370
JN1B1371
JN1B1372
JN1B1373
JN1B1374
JN1B1375
JN1B1376
JN1B1377
JN1B1378
JN1B1379
JN1B1380
JN1B1381
JN1B1382
JN1B1383
JN1B1384
JN1B1385
JN1B1386
JN1B1387
JN1B1388
JN1B1389
JN1B1390
JN1B1391
JN1B1392
JN1B1393
JN1B1394
JN1B1395
JN1B1396
JN1B1397
JN1B1398
JN1B1399
JN1B1400
JN1B1401
JN1B1402
JN1B1403
JN1B1404
JN1B1405
JN1B1406
JN1B1407
JN1B1408
JN1B1409
JN1B1410
JN1B1411
JN1B1412
JN1B1413
JN1B1414
JN1B1415
JN1B1416
JN1B1417
JN1B1418
JN1B1419
JN1B1420
JN1B1421
JN1B1422
JN1B1423
JN1B1424
JN1B1425
JN1B1426
JN1B1427
JN1B1428
JN1B1429
JN1B1430
JN1B1431
JN1B1432
JN1B1433
JN1B1434
JN1B1435
JN1B1436
JN1B1437
JN1B1438
JN1B1439
JN1B1440
JN1B1441
JN1B1442
JN1B14
```

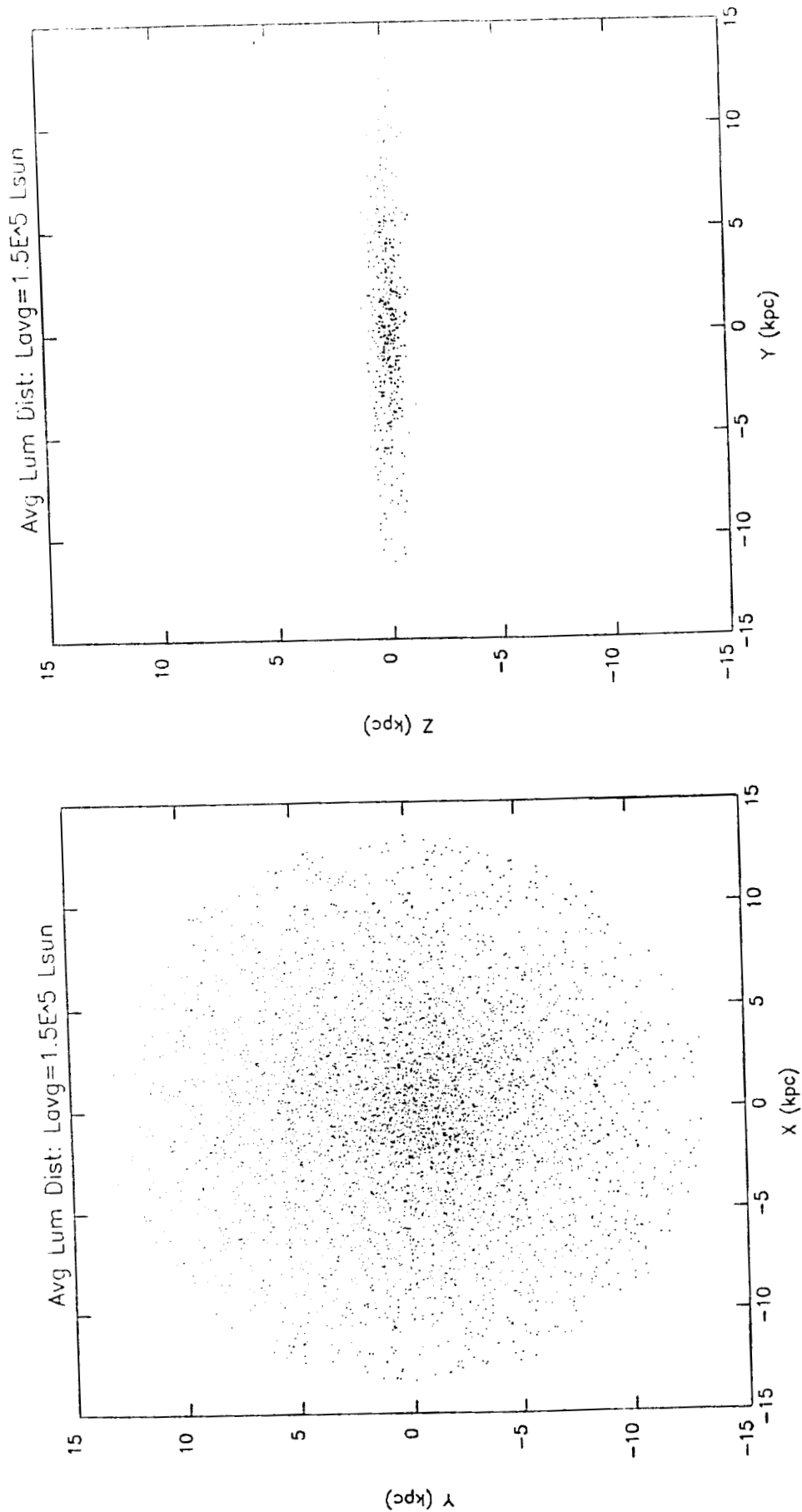
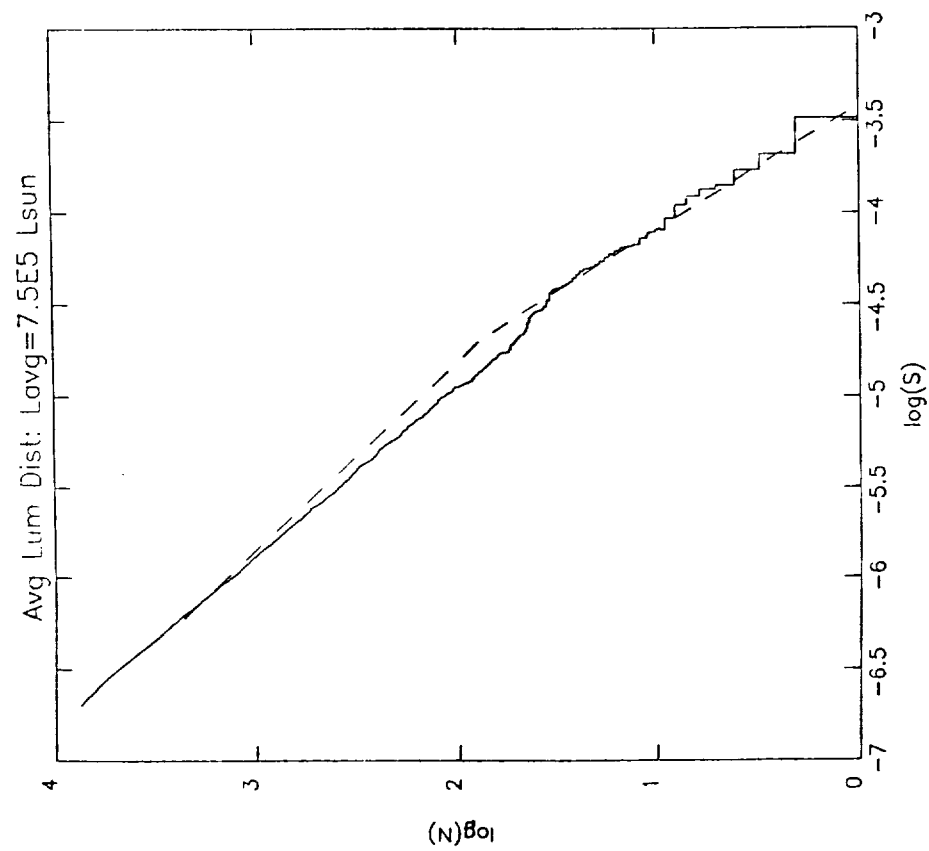
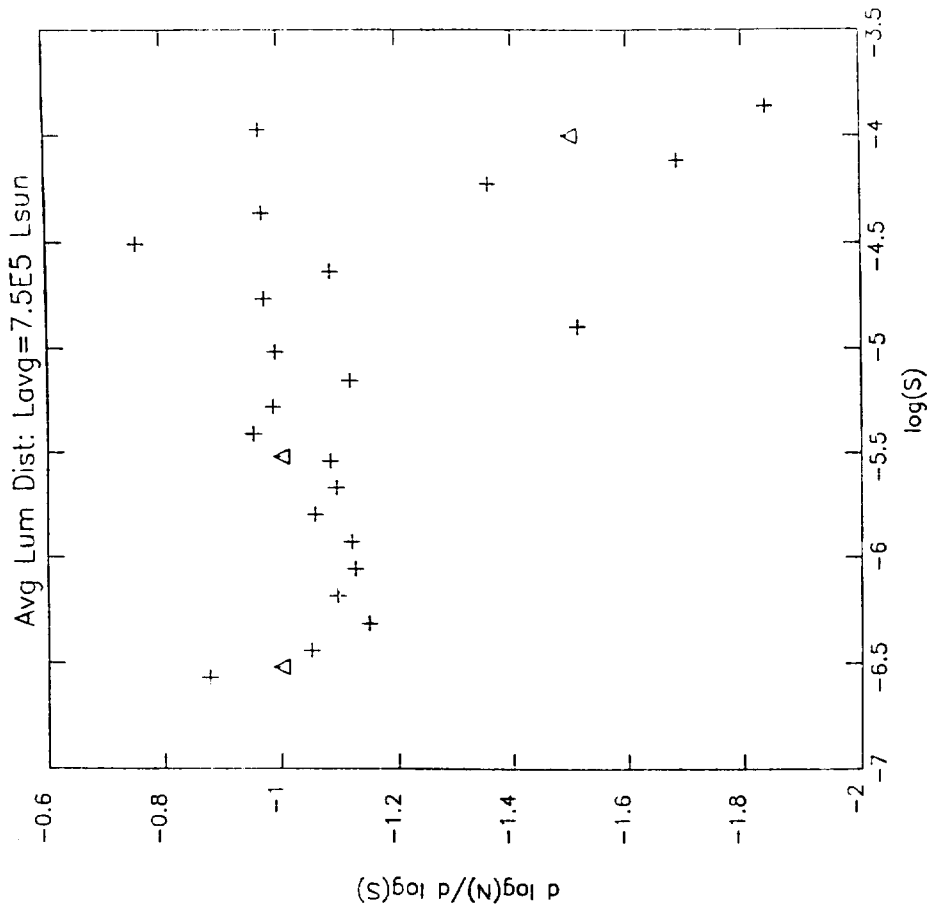



Figure 3. An example of the disk distribution produced by monte carlo analysis. This disk, with a radius of 13.5 kpc and a width of 400 pc, is shown (a) from above, and (b) looking at a band 1 kpc wide running across its diameter.



(a)



(b)

Figure 4. $\log(N) - \log(S)$ results for a sample of 7500 observed sources with luminosity $\langle L \rangle = 7.5 \times 10^5 L_{\text{sun}} = 3 \times 10^{39} \text{ erg cm}^{-2}$. The $\log(N) - \log(S)$ plot (which fits the observed data) is shown in (a). The high-fluence end of the dotted line depicts satellite data, while the low-fluence end is an upper limit based upon the balloon observations of Meegan et al. (1985). $\log(N) - \log(S)$ slopes from balloon and satellite data (triangles), are compared to those of the monte carlo analysis (crosses) in (b).

MODEL PARAMETERS

Number of iterations needed to get 7500 data points was 13340
Space density of sources to 0.2 kpc is $2.230E-01$ sources/pc³
Disk ht = 0.4 kpc; max & min radii are 0.0 and 20.1 kpc; scale = 3.9 kpc
Avglum = $7.500E+05$ siglum = $0.000E+00$

LOGN-LOGS SUMMARY

Index	#	LogN	LogS
0	1	0.699	-3.862
1	2	0.903	-3.972
2	3	1.041	-4.116
3	4	1.230	-4.228
4	5	1.415	-4.367
5	6	1.556	-4.500
6	7	1.653	-4.630
7	8	1.792	-4.766
8	9	1.919	-4.896
9	10	2.104	-5.010
10	11	2.241	-5.156
11	12	2.384	-5.281
12	13	2.511	-5.413
13	14	2.633	-5.542
14	15	2.772	-5.670
15	16	2.914	-5.799
16	17	3.050	-5.920
17	18	3.194	-6.036
18	19	3.339	-6.162
19	20	3.479	-6.313
20	21	3.627	-6.442
21	22	3.762	-6.570
22	23	3.875	-6.692

SPACE DISTRIBUTION PROPERTIES

Min. Fluor: $1.00E-06$ Total = 1331, Avg = 443.7 +/- 21.1
1264 (94.97) 56 (4.21) 11 (0.83)

DIPOLE: 0.065 at l = 0.98 and b = 0.12
QUADRUPOLE: eta = 0.053 zeta = 0.162

Min. Fluor: $1.00E-05$ Total = 119, Avg = 39.7 +/- 6.3
72 (60.50) 36 (30.25) 11 (9.24)

DIPOLE: 0.001 at l = 142.03 and b = -22.85
QUADRUPOLE: eta = 0.004 zeta = 0.008

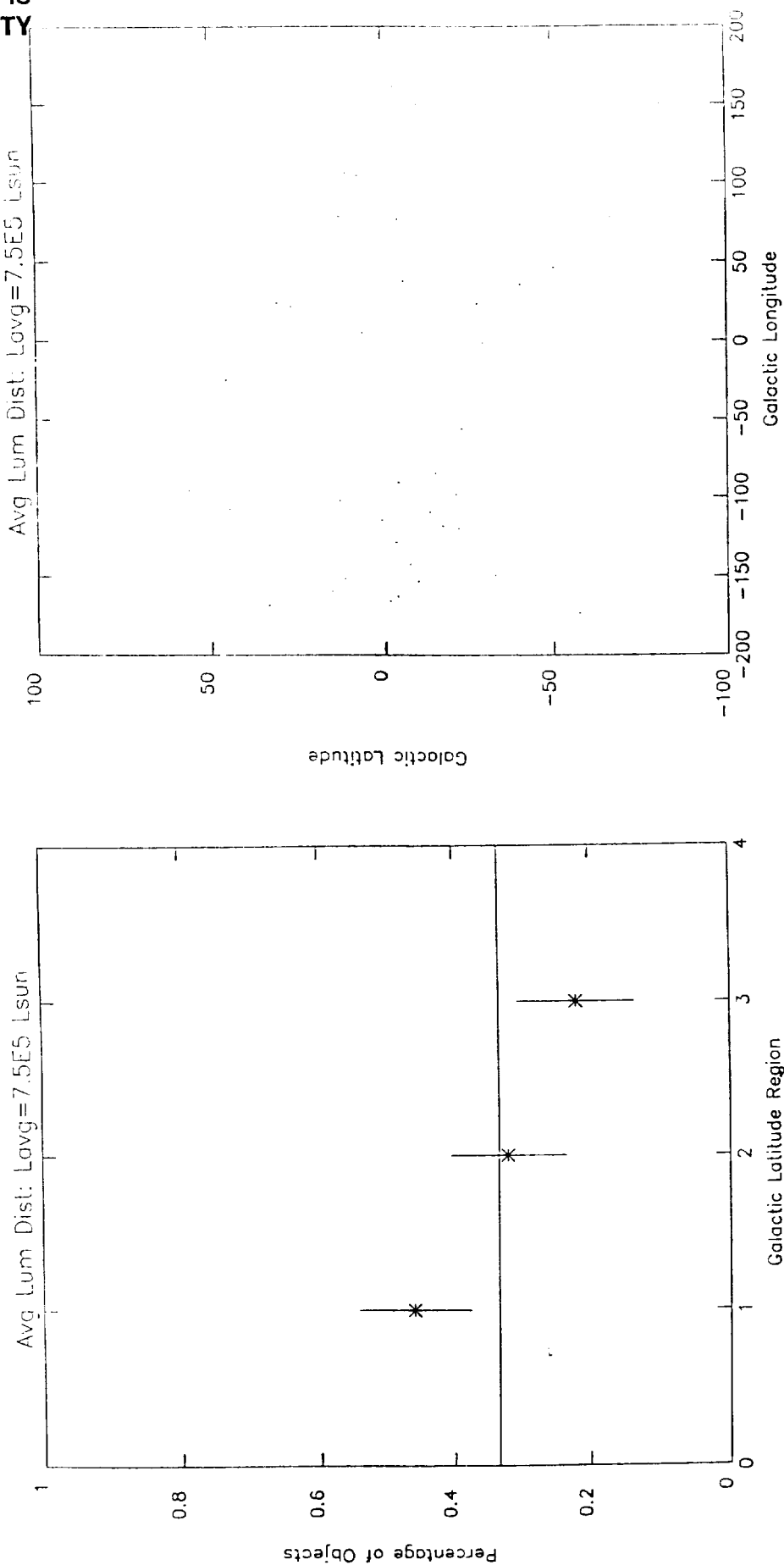
Min. Fluor: $1.00E-04$ Total = 8, Avg = 2.7 +/- 1.7
2 (25.00) 3 (37.50) 3 (37.50)

DIPOLE: 0.000 at l = -16.53 and b = -38.85
QUADRUPOLE: eta = 0.000 zeta = 0.001

Min. Fluor: $1.00E-03$ Total = 30, Avg = 18.7 +/- 4.1
23 (46.00) 16 (32.00) 11 (22.00)

DIPOLE: 0.002 at l = 173.18 and b = -16.47
QUADRUPOLE: eta = 0.001 zeta = 0.002

Figure 5. Sample output of monte carlo data analysis for the data set plotted in the previous figure. In addition to summarizing the parameters used to generate the model, the output lists the latitude distribution of the sample, the dipole moment, and parameters η and ζ of the quadrupole moment for a variety of minimum fluences. The angular anisotropies present at low minimum fluence disappear when considering only bright sources.



(b)

Figure 6. Angular distribution plots for the sample described in the previous figures. The latitude distribution (a) and the local spatial distribution (b) are plotted for a minimum fluence of $2 \times 10^{-5} \text{ erg cm}^{-2}$. Above this fluence, the sample is fairly isotropic.

(a)

1989

NASA/ASEE SUMMER FACULTY FELLOWSHIP PROGRAM

MARSHALL SPACE FLIGHT CENTER
THE UNIVERSITY OF ALABAMA IN HUNTSVILLE

ARTIFICIAL INTELLIGENCE ISSUES RELATED TO AUTOMATED COMPUTING
OPERATIONS

Prepared by:	Dr. William A. Hornfeck
Academic Rank:	Professor
University and Department:	Lafayette College Electrical Engineering Department
NASA/MSFC Office: Division:	Information Systems Systems Development and Implementation
MSFC Colleague:	Mr. Charles E. Houston
Date:	August 10, 1989
Contract No.:	NGT 01-008-021 The University of Alabama in Huntsville

ARTIFICIAL INTELLIGENCE ISSUES
RELATED
TO
AUTOMATED DATA PROCESSING OPERATIONS

by

William A. Hornfeck
Professor of Electrical Engineering
Lafayette College

ABSTRACT

Large data processing installations represent target systems for effective applications of artificial intelligence (AI) constructs. The system organization of a large data processing facility at the NASA Marshall Space Flight Center is presented. This paper describes the methodology and the issues which are related to AI application to automated operations within a large-scale computing facility. Problems to be addressed and initial goals are outlined.

ACKNOWLEDGEMENTS

I would like to thank the American Society for Engineering Education, ASEE, and NASA for making this summer's faculty fellowship program possible. I am grateful to my research colleagues at Marshall, Charles Houston and Gene Leckie, for their sponsorship; and to Sue Newberry for preparation of this report.

Dr. Frank Six of the MSFC Director's staff and Dr. Gerald Karr of the University of Alabama in Huntsville performed an outstanding service in administering and coordinating the various functions of the Summer Faculty Program.

OBJECTIVES

The objectives of the research reported herein are to investigate the notion of applying artificial intelligence (AI) techniques for the automated operation of a very large computer system; to focus on the conceptual aspects of this automated system; and to report on the more important issues surrounding such an effort.

The objectives of the research were achieved by first observing the nature of the computing system involved, reviewing the more important references which set the stage for eventual applications of AI, reviewing the more relevant applications articles, and reporting on the topics which are germane to the study.

INTRODUCTION

It has recently become very obvious that Artificial Intelligence (AI) techniques can be useful in a broad spectrum of programming domains. AI research was once regarded as somewhat "borderline". There was serious doubt concerning the usefulness of AI techniques for the solution of real production problems. Many areas of Computer Science currently exploit AI concepts: areas such as database management, computer-aided instruction, and human-machine interaction. These are certainly areas which are of great importance to computer operations conducted by NASA at MSFC. Further research and development would invite applications of existing AI algorithms as well as extensions which promote the maximum level of automation for the computing/data processing function.

A consideration of operational aspects of the data processing function and their automation would require the modeling of expertise and the construction of programs called expert systems. The core elements of the AI discipline which would be exploited in arriving at an expert system goal are: knowledge representation, knowledge utilization, and knowledge acquisition.

THE EXISTING ENVIRONMENT

The Engineering Analysis and Data System (EADS) provides Cray computer users at Marshall Space Flight Center with a front-end processor to the super computer mainframe. Jobs submitted to the Cray are submitted through EADS. Figure 1 shows the system configuration for EADS.

An inspection of Figure 1 reveals the computer communication links between principle elements of the system and the control consoles which are used to monitor and control major elements in the system. These include:

- Front-End Processor (FEP-1);
- Front-End Processor (FEP-2);
- Support Processor (SP-1);
- Support Processor (SP-2);
- Cray X-MP/4 Processor; and
- Bus Service Center

These are pointed out to gain some perspective on the magnitude of the automation problem, as it regards an artificial intelligence application.

EADS SYSTEM CONFIGURATION

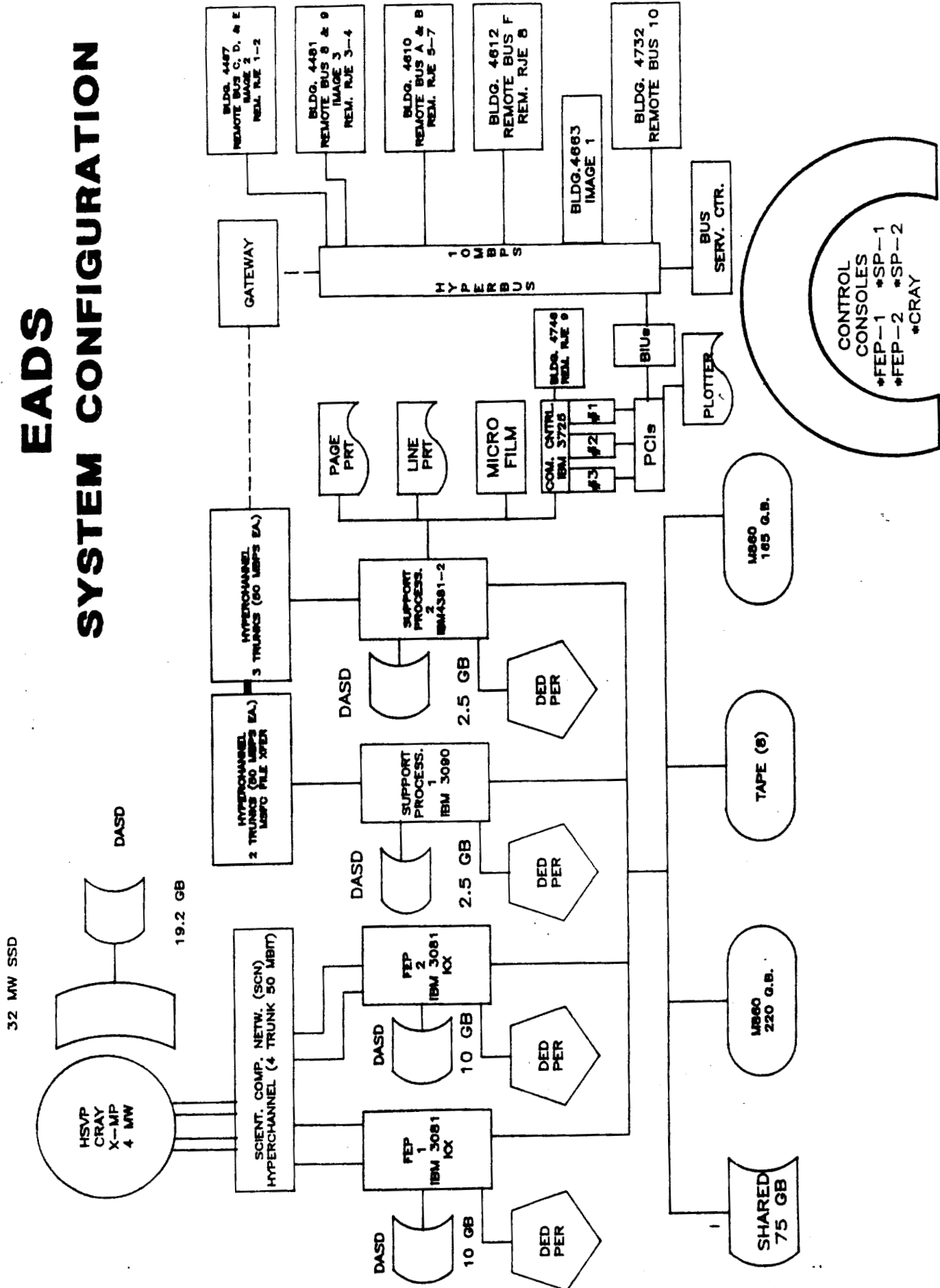


FIGURE 1. EADS SYSTEM

BACKGROUND

There is currently a tremendous optimism concerning artificial intelligence, expert systems, and knowledge-based programming and the potential applications of these technologies. There is very little agreement, however, regarding when AI systems should be applied, how AI systems should be developed, and the fundamental limitations of AI system capabilities.

Artificial Intelligence uses computing machines to process facts by using complex reasoning based on rules in order to produce "intelligent conclusions." It is generally agreed upon by experts in the field of AI that the discipline does not allow its practitioners to capture common sense abilities or the sense to distinguish relevant from irrelevant information.

An Expert System can be defined as a system that draws conclusions from facts, beliefs, and rules, some of which are heuristic, using complex reasoning based on inference rules. This definition of an expert system and the definition of Artificial Intelligence from the preceding paragraph should be contrasted with a definition of intuition. That is, S. Dreyfus in [18] defines intuition as the ability, effortlessly and rapidly, to associate with one's own present situation an action or decision which experience has shown to be appropriate.

Intuition is what people have and complex reasoning systems do not have and, probably, will never have. The development of any AI or Expert System should be mindful of the limitations of these definitions.

ORIGINAL PAGE IS
OF POOR QUALITY

FUNDAMENTAL STRATEGIES

There are two important aspects to any AI program or algorithm:

1. A knowledge-representation framework
2. Problem-solving and inference methods.

Once an AI application is identified, these two aspects interact closely with each other. The choice of the knowledge-representation framework determines the kind of problem-solving strategies which are appropriate.

Computer systems at MSFC represent two areas where AI applications exist:

1. Equipment
 - a. Design
 - b. Diagnosis
 - c. Instruction
 - d. Maintenance
 - e. Configuration
 - f. Monitoring
 - g. Sales
2. Data Processing
 - a. Instructions
 - b. Natural-language Interface
 - c. Intelligent Data Access
 - d. Intelligent Data Analysis
 - e. Planning and Scheduling

Each of these categories presents an array of possibilities where AI solutions could be investigated. AI systems should be developed which provide their economic leverage by performing the types of tasks that occupy a high percentage of highly-paid people's time, rather than "far-out" or science-fiction notions.

The selection of an AI application area and the evolution toward automated computing systems should be done with considerable forethought. It is also important to think differently from the classical programming approach. That

is, the usual software engineering cycle -- define problem, specify requirements, design software, code program, test program, and deliver software system -- is no longer appropriate. Instead, incremental development of the expert system is possible where program structures and mechanisms that contain knowledge, infer information, and control program inferences are independent and separate. Figure 2 below shows the component parts of an "exploratory" programming system.

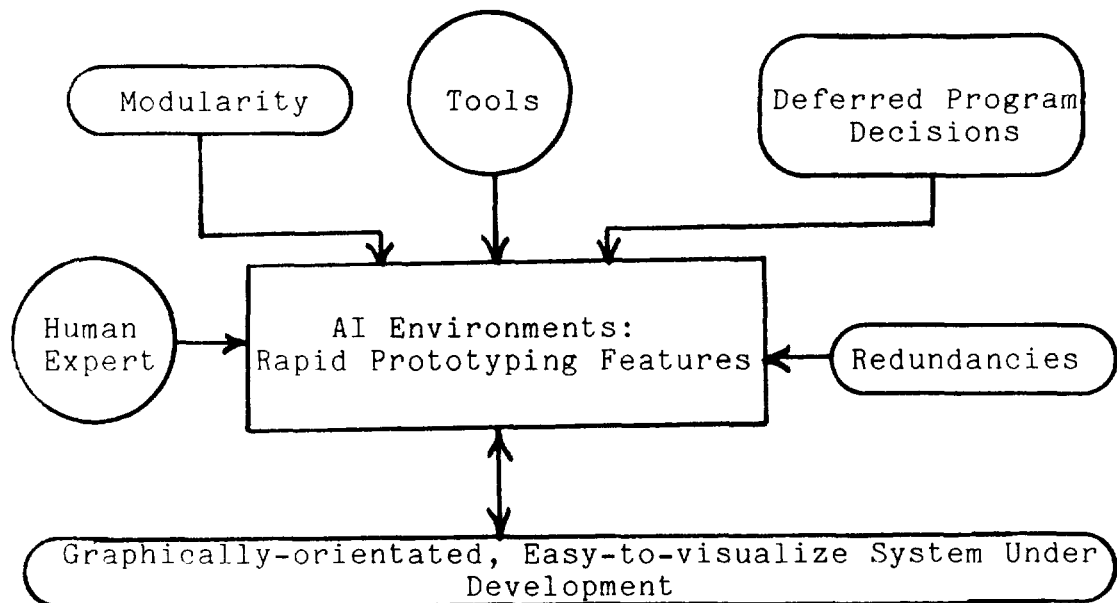


Figure 2. Exploratory Programming Features

EXPERT SYSTEM BUILDING CYCLE

There are four major steps to follow in building a knowledge system using standard AI tools. [8] The itemized list shown below provides an outline of the usual methodology:

1. ANALYZE THE PROBLEM;
 - a. Choose the problem,
 - b. Determine the value of applying AI,
 - c. Decide on the expert, and
 - d. Gather knowledge.
2. DESIGN THE SYSTEM;
 - a. Organize the knowledge,
 - b. Gather additional knowledge, and
 - c. Create basic structure.
3. CONSTRUCT A PROTOTYPE;
 - a. Identify and enter goal,
 - b. Code judgmental rules,
 - c. Code control rules,
 - d. Write user questions & allowable answers,
 - e. Add more questions and answers,
 - f. Expand the basic structure, and
 - g. Add still more knowledge.
4. TEST THE PROTOTYPE;
 - a. Identify real test cases, and test,
 - b. Consult expert about erroneous results,
 - c. Revise expert system,
 - d. Test, consult, revise again, as appropriate, and
 - e. Submit to field testing.

Some further explanation regarding the second step in the outline shown above. It should be pointed out that the typical expert system has four major components:

- o The Knowledge Base
- o The Inference Engine
- o The Acquisition Module
- o The Explanatory Interface

The knowledge base consists of the information structures that encode the system's expertise. This is usually elicited from a human expert and reformulated in the computer's format as a collection of rules, a network of facts, or a frame-based structure. A knowledge base would differ from a database most importantly in the fact that it contains rules for deducing facts not explicitly stored.

The inference engine uses the knowledge base and facts of the case to derive new conclusions. Often it can cope with missing or unreliable data by means of some form of approximate reasoning.

The acquisition module eases the knowledge gathering process by testing proposed rules for inconsistency and redundancy, with advanced systems actually using some induction to create rules from examples. The explanatory interface allows the user to interrogate the system by posing HOW or WHY queries.

SOME POINTS OF CAUTION

Most of this brief report deals optimistically with the current state of AI technology and the possibility of AI applications in the MSFC computing and data processing environment. A number of issues surrounding such an endeavor give rise to some degree of caution and are listed here.

- o One of the most critical problems with today's means for building expert systems is that virtually each new system must be custom crafted.
- o Significant changes will likely arise in expert systems as AI research uncovers newer aspects of areas such as parallel processing, non-Von-Neumann machines, connectionism, neural networks, and so on.
- o As the amount of knowledge in an expert system grows larger and more comprehensive, the problem of control of reasoning becomes ever-greater.
- o The central problem in AI research is "common-sense reasoning", and is not about to be solved.
- o An expert system project fails unless experts cooperate. There is not other source of expertise, and without knowledge the program will not work.

CONCLUSIONS AND RECOMMENDATIONS

A computer program which has the ability of making intelligent decisions in the world must have a general representation of "world", which it is able to use in interpreting inputs. The development of such a program requires that knowledge be defined and its acquisition be accomplished. [19] In general, a computer program is needed which decides what to do by inference using a formal language. The outcome being that a certain strategy will achieve its assigned goal. The notion of an intelligent machine being devised which is programmed to make intelligent decisions regarding its own operation is reasonable. The idea presents an interesting and recursive relation; however, the solution methodology should be no different than any other AI application.

AI is solving more and more real-world problems, but application to government systems and administration has been minimal. [2] The effective development of AI software for automated computer operations presents some difficult problems. These include:

- (i) the machine-compatible knowledge must be synthesized which reflects expertise about a large number of facts, rules, or decision factors;
- (ii) software must account for the probability of outcomes as opposed to procedural certainty, based on changing conditions;
- (iii) heuristic solutions must emerge based on expert experience and knowledge gained over long periods of time in an often unstructured manner.

Not only does AI Technology have the potential to enhance the automation process, but it is quite reasonable to expect that traditional automation applications could be easier and less costly using an expert system approach. The most likely projects which would begin an AI-based automation effort in a computer system installation are the following:

- o Document and Archival Retrieval;
- o Computer-Aided Engineering Techniques;
- o Computer-Aided Instructions;
- o Procurement Management Processes;

- o On-line Operations Manuals;
- o Natural-language Querying of Database;
- o Network and Computer Communication Management.

We will likely see AI techniques embedded within commercial mainframe applications on a routine basis in the not-too-distant future. Expert system tools are also likely to be available as modular packages so that application-specific architectures can be derived using standard modules.

REFERENCES

1. AI Magazine, Expert Systems: How Far Can They Go?, R. Davis, ed., Vol. 10, No. 1, Spring 1989.
2. AI Magazine, Expert Systems in Government Administration, J. Weintraub, Vol. 10, No. 1, Spring 1989.
3. IEEE Expert, Planning by Transformational Synthesis, T. Linden, Vol. 4, No. 2, Summer 1989.
4. Third IEEE Computer Society Conference on Artificial Intelligence Applications (CAIA), IEEE Computer Society Press, 1987.
5. Fourth IEEE Computer Society Conference on Artificial Intelligence Applications (CAIA), IEEE Computer Society Press, 1988.
6. Proceedings of the International Workshop on Artificial Intelligence for Industrial Applications, IEEE Computer Society Press, 1988.
7. Artificial Intelligence III: Methodology, Systems, Applications, O'Shea and Squirev, eds., North-Holland, 1988.
8. Artificial Intelligence in Business, Science, and Industry, Volumes I and II, W. B. Rauch-Hindin, Prentice-Hall, 1986.
9. Progress in Artificial Intelligence, Steels and Campbell, eds., Ellis Horwood Ltd., 1985.
10. AI in the 1980's and Beyond, Grimson and Patil, eds., MIT Press, 1987.
11. Artificial Intelligence: Principles and Applications, Masoud Yazdani, ed., Chapman and Hall, 1986.
12. Artificial Intelligence: Concepts, Techniques, and Applications, Shirai and Tsujii, John Wiley & Sons, 1984.
13. Intelligent Systems: the Unprecedented Opportunity, Hayes and Michie, eds., Ellis Horwood Ltd., 1984.

14. Putting Artificial Intelligence to Work: Evaluating and Implementing Business Applications, Schoen and Sykes, Stephen Kippur Pub., 1987.
15. What Every Engineer Should Know about AI, William A. Taylor, MIT Press, 1988.
16. Artificial Intelligence, Elaine Rich, McGraw-Hill, 1983.
17. Computational Intelligence, an International Journal, Learning to Control a Dynamic Physical System, Connell and Utgoff, Vol. 3, No. 4, November 1987.
18. Mind over Machine, Dreyfus and Dreyfus, New York: The Free Press, 1986.
19. Readings in Artificial Intelligence, "Some Philosophical Problems from the Standpoint of AI", McCarthy and Hayes, Tioga Pub., 1981.
20. The Society of Mind, M. Minsky, Simon and Schuster, 1986.

1989

NASA/ASEE Summer Faculty Fellowship Program

Marshall Space Flight Center
The University of Alabama in Huntsville

LOW-ENERGY IMPACT RESISTANCE OF GRAPHITE-EPOXY PLATES AND
ALS HONEYCOMB SANDWICH PANELS

Prepared by:	David Hui
Academic Rank	Associate Professor
University and Dept.	University of New Orleans Dept. of Mechanical Engineering New Orleans, LA 70148

NASA/MSFC:

Laboratory:	Materials and Process Laboratory
Division:	Non-Metallic Materials Division
Branch:	Polymers and Composites Branch

MSFC Colleague: Alan Nettles

Date: August 11, 1989

Contract Number: The University of Alabama in Huntsville
NGT-01-008-021

Table of Contents:

- . Abstract
- 1. Introduction
- 2. Impact Analysis of Graphite-Epoxy Plates
- 3. Impact Analysis of ALS Honeycomb Sandwich Plates
- 4. Discussions and Comparisions between Theory and Experiments
- 5. Conclusions

Acknowledgements

- Appendix A Constitutive Equations for Laminated Plates
- Appendix B Coefficients of Hertz Law
- Appendix C Design Guideline for Stacking Sequence of Quasi-Isotropic
 Laminated Plates
- Appendix D Equilibrium and Compatibility Equations for Circular Plates
 and Rectangular Plates

ABSTRACT

Low energy impact may be potentially dangerous for many highly optimized "stiff" structures. Impact by foreign objects such as birds, ice and runways stones or dropping of tools occur frequently and the resulting damage and stress concentrations may be unacceptable from a designer's standpoint. The present work is concerned with the barely visible, yet potentially dangerous dents due to impact of foreign objects on the Advanced Launch System (ALS) structure. Of particular interest is the computation of the maximum peak impact force for a given impactor mass and initial velocity. The theoretical impact forces will be compared with the experimental dropweight results for the ALS face sheets alone as well as the ALS honeycomb sandwich panels.

1. INTRODUCTION.

One of the earliest work on the low velocity impact on composite sandwich structures was performed by Rhodes (1974, 1978) and Rhodes et al (1979). They showed that the honeycomb core considerably reduced the area of delamination damage as compared with the unsupported graphite-epoxy laminates. and the crippling of the core allows high bending stresses in the face sheets. Oplinger and Slepetz (1975) found from the dropweight experiments that the graphite sandwich panels exhibit marked damage due to nominal impact energy levels as low as 2 ft-lb. due to low strain to fracture of graphite material and low compressive crushing strength of the honeycomb core. They analysed the sandwich panel as a plate resting on an elastic foundation. Sharma (1981) measured the preload and impact energy combination necessary to cause catastrophic failure of graphite/epoxy sandwich structures and examined the residual

strength of the specimens. Further, 't Hart (1981) examined the effect of impact damage on the tension-compression fatigue properties of Carbon/Epoxy Sandwich Panels and found that significant damage may occur at low impact energy. Labor and Bhatia (1980) examined the impact resistance of hybrid and graphite layups and investigated the effects of core densities of the sandwich structure. Gottesman et al. (1987) and Bass (1986) presented experimental and analytical results on the strength of sandwich structures due to low velocity impact. Further studies on the impact resistance and damage tolerance of sandwich plates were reported by Bernard (1987) and Bernard and Lagace (1987). They found that damage in the impacted facesheets was primarily delaminations with the largest delamination occurring between the bottom two plies (5th and 6th plies) in the top facesheet; and debonding of the top facesheet from the adhesive layers was more pronounced in stiffer core. Recent work on the instrumented impact testing of composite sandwich panels was performed by Shih and Jang (1979). They found that the impact resistance was mainly controlled by the facesheets and relatively independent of the density of the poly-vinyl-chloride (PVC) foam core, provided the facesheet material is tough enough; however, for less tough facesheets, the impact failure becomes foam core dominated rather than facesheet dominated. In particular, the macroscopic and microscopic failure modes and energy absorbing characteristics of these sandwich panels were examined by Shih and Jang (1979).

The NASA Langley researchers have done extensive experimental and analytical studies on the low energy impact resistance of graphite/epoxy plates. Bostaph and Elber (1982) presented static indentation tests on graphite epoxy plates and the results are compared with the theoretically predicted plate stiffness and maximum strain energy at failure. Bostaph (1984) from the US Army showed that toughened materials were able to delay insipient delamination, but not significantly, in quasi-static indentation tests. Many other experiments on impact resistance of composite plates have been performed by numerous investigators (see for example Ciarns and Lagace 1988, Sjoblom et al. 1988). For brevity, the remaining part of this introduction will focus on the "theoretical" studies on impact of composite plates.

One of the earliest theoretical investigations on the impact of isotropic-homogeneous plates was presented by Eringen (1953) and Timoshenko in 1913 as reported in Timoshenko and Goodier (1970). An excellent survey of the historical contributions of various authors was presented by Greszczuk in 1982. Based on the Hertzian contact parameters for transversely isotropic laminates (Conway 1956), Greszczuk presented theoretical and experimental "peak" maximum impact force for quasi-isotropic circular plates under a spherical impactor at the plate center. Further investigations on the theoretical prediction of low velocity impact force and the delamination growth analysis in quasi-isotropic laminates were reported by Shivakumar and Elber (1984) and Shivakumar et al. (1985a,b). The present work follows closely the method presented by Shivakumar (1985b) which includes the finite deflection effects.

2. Impact Analysis of Graphite-Epoxy Plates

The energy-balance method is used to obtain the peak impact force for circular or square graphite-epoxy plates under a concentrated load at the plate center. This method was used by Greszczuk(1975, 1981,1982), Greszczuk and Chao (1977) and Shivakumar et al. (1985b) and the theoretical peak impact force was computed based on the equation,

$$(1/2)(M_I)(V_I)^2 = (1/2)(K_b)W^2 + (1/4)K_m W^4 + (2/5) P^{5/3}/n^{2/3} \quad (1)$$

In the above expression, M_I and V_I are the mass and velocity of the impactor, K_b and K_m are the bending and membrane stiffness of the plate, W is the deflection at the center of the plate and the impact force P is proportional to the relative displacement α raised $3/2$ power according to Hertz law (Conway 1956, Willis 1966 and Timoshenko and Goodier 1970) such that,

$$P = n \alpha^{3/2} \quad (2)$$

The various coefficients of Hertz law are computed for the present graphite-epoxy plate and they can be found in Appendix B. From finite deflection plate theory, the impact force can also be written as (Shivakumar et al. 1985b, Vol'mir 1967 and Timoshenko and Woinowsky-Krieger 1959),

$$P = K_b W + K_m W^3 \quad (3)$$

Although the above formulae are intended for isotropic-homogeneous plates, they can also be applied to transversely isotropic material

(see Dahan and Zarka 1977) and quasi-isotropic materials (Agarwal and Broutman 1980 and Greszczuk 1982), provided one can obtain the average Young's modulus and average Poisson's ratio as described in Appendix A. The energy-balance can be written in a non-dimensional form by dividing through by $E_{av}h^3$ (the total thickness of the composite plate is h),

$$e_o = (1/2) k_b (W/h)^2 + (1/4) k_m (W/h)^4 + (2/5) p^{5/3} / (n^*)^{2/3} \quad (4)$$

where,

$$e_o = (1/2) M_I V_I^2 / (E_{av} h^3)$$

$$k_b = K_b / (E_{av} h) \quad (5)$$

$$k_m = K_m h / E_{av}$$

$$p = P / (E_{av} h^2) = k_b (W/h) + k_m (W/h)^3$$

$$n^* = n / (E_{av} h^{1/2})$$

The value of n^* for the contact between a steel punch and a graphite-epoxy plate is given by eqn. B10 in Appendix B, using the average value of the composite plate,

$$E_{av} = 7.0 \times 10^6 \text{ psi}, \quad \nu_{av} = 0.30, \quad n^* = 0.567400142 \quad (6)$$

so that the energy balance equation becomes,

$$e_o = (1/2) k_b (W/h)^2 + (1/4) k_m (W/h)^4 + 0.583624746 p^{5/3} \quad (7)$$

From Shivakumar et al. 1985b, there are four possible boundary conditions for the axisymmetric deflection of a circular plate under a concentrated load at the plate center. They are, using $h = 0.081$ in. , $a = 1.50$ in. , based on the governing equilibrium and compatibility eqns described in Appendix D.

(i) Clamped, In-Plane Immovable, $P = (616.588 \text{ lb})(W/h) + (274.273 \text{ lb})(W/h)^3$

$$k_b = K_b / (E_{av} h) = 4.603066 (h/a)^2 = 0.01342254$$

$$k_m = K_m h / E_{av} = 2.0479915 (h/a)^2 = 0.005971943$$

(ii) Clamped, In-Plane Movable, $P = (616.588 \text{ lb})(W/h) + (124.012 \text{ lb})(W/h)^3$

$$k_b = K_b / (E_{av} h) = 0.01342254$$

(8a, b, c, d)

$$k_m = K_m h / E_{av} = 0.92599413 (h/a)^2 = 0.002700199$$

(iii) Simply Supported, In-plane Immovable,

$$P = (242.846 \text{ lb})(W/h) + (347.017 \text{ lb})(W/h)^3$$

$$k_b = K_b / (E_{av} h) = 1.813329093 (h/a)^2 = 0.005287668$$

$$k_m = K_m h / E_{av} = 2.59117215 (h/a)^2 = 0.007555858$$

(iv) Simply Supported, In-plane Movable,

$$P = (242.846 \text{ lb})(W/h) + (66.09859 \text{ lb})(W/h)^3$$

$$k_b = 0.005287668$$

$$k_m = K_m h / E_{av} = 0.493558614 (h/a)^2 = 0.001439217$$

The above k_b and k_m values for all four types of boundary conditions for a circular plate agree with those reported by Vol'mir (1967 section 43).

The bending stiffness K_b should be replaced by $K_b c_s$ using thick plate theory which takes into account transverse shear effect (Lukasiewicz 1976, 1979 and Shivakumar et al. 1985b) where,

$$c_s = [1 + (K_b/K_s)]^{-1} \quad (9)$$

$$K_b/K_s = [3/(4\pi)] [K_b/(G_{zr}h)] [1 - 4\nu_{rz}(G_{zr}/E_{av})] [(4/3) + \ln(a/a_{\text{contact}})]$$

Using

$$\nu_{rz} = 0.28,$$

$$G_{zr} = 0.5959 \times 10^6 \text{ psi}$$

$$E_{av} = 7.0 \times 10^6 \text{ psi}$$

$$\ln(a/a_{\text{contact}}) = \ln(2a/h) = 3.6119184$$

one obtains,

$$K_b/K_s = 1.0680294 k_b (E_{av}/G_{zr}) = 12.54607 k_b \quad (11)$$

Thus, we have, for each of the four boundary conditions,

$$\begin{aligned} \text{(i) Clamped Immovable, or Movable, } c_s &= 0.855871, \quad k_b c_s = 0.01148796 \\ \text{(ii)} & \end{aligned} \quad (12)$$

$$\text{(iii) or (iv) Simply Supported, Immovable or Movable, } c_s = 0.9377876$$

$$k_b c_s = 0.0049587 \quad (13)$$

For a simply supported square plate under a concentrated load P at the plate center, the load deflection relation is (see Timoshenko and Woinowsky-Krieger 1959, section 34 and Ugural 1981 section 3.3),

$$W = 0.01160 Pb^2/D \quad (14)$$

where b is the length of the side of the square plate and D is the flexural rigidity and W is the deflection at the plate center. This equation can be re-arranged as, letting $\nu_{av}=0.30$,

$$P = 86.20689(hD/b^2) (W/h) = 7.894403(E_{av}h^4/b^2) (W/h) \quad (15)$$

or (letting b =diameter of the circular plate = 3.00 in.),

$$k_b = K_b/(E_{av}h) = 7.894403 (h/b)^2 = 0.00575502 \quad (16)$$

$$P = (264.3107 \text{ pounds}) (W/h)$$

Finally, for a clamped square plate under a concentrated load at the center of the plate, one obtains (see Ugural 1981, section 3.12),

$$W = 0.005592 Pb^2/D, \quad \text{let } b=2a = 3.00 \text{ in.},$$

$$P = 184.327 (hD/b^2)(W/h) = 16.87984 (E_{av}h^4/b^2) (W/h) \quad (17)$$

$$k_b = K_b/(E_{av}h) = 16.87984 (h/b)^2 = 0.012305$$

$$P = (565.150 \text{ pounds}) (W/h)$$

Comparing the impact force on a simply supported circular plate with radius a and a simply supported square plate with side $b=2a$ such that the circular plate is just inscribed inside the square plate, the impact force on the circular plate is smaller than that of the square plate. That is, the deflection of the circular plate is larger than that of the square plate for the same impact concentrated force.

$$\begin{aligned}
 P &= (242.846 \text{ lb})(W/h) + \dots && \text{s.s.: circular plate, radius } a \\
 P &= (264.310 \text{ lb})(W/h) + \dots && \text{s.s. square plate, side } =2a \\
 &&& (264.31/242.846 = 1.08838)
 \end{aligned}
 \tag{18}$$

This somewhat unusual result arises from the fact that the deflection mode shape for a square plate is quite different from that of the circular plate. Further, the reaction forces at the four corners of the plate tend to produce a convex upward deflections under the applied downward concentrated force P . On the other hand, for clamped plates,

$$\begin{aligned}
 P &= (616.588 \text{ lb})(W/h) + \dots && \text{clamped circular plate, radius } a \\
 P &= (565.150 \text{ lb})(W/h) + \dots && \text{clamped square plate, side } =2a \\
 &&& (616.588/565.15 = 1.09101)
 \end{aligned}
 \tag{19}$$

the effects of the reaction forces at the four corners are much less apparent due to the reaction moments along the four edges of the square plate. Since the area of the circular plate is πa^2 and the area of the square plate with side $=2a$ is $4a^2$, the ratio of the area is 1.27323. The impact force of the circular plate is larger than that of the square plate. Since the experimental data lies somewhere between simply supported and clamped conditions, it is expected that the impact forces for the circular plates are approximately the same as the square plate.

3. Impact Analysis of ALS Honeycomb Sandwich Plates

The ALS honeycomb sandwich structure is composed of a top and bottom graphite/epoxy facesheets and a honeycomb core. The core is made of HFT-3/16-2.0 glass-phenolic material and the core material was manufactured by Hexcel Inc. The facesheets are identical to those examined in section two and each sheet is composed of 16-layer quasi-isotropic laminate. The material property of the honeycomb core is,

$$E_{\text{core}} = 17000 \text{ psi},$$

$$G_{xz}(\text{L-straight direction}) = 15000 \text{ psi} \quad (20)$$

$$G_{yz}(\text{W-non-straight direction}) = 5000 \text{ psi}$$

The above core material properties are higher than those for the Nomex honeycomb core reported by Bernard and Lagace (1987). The sandwich structure is being analysed as a plate resting on an elastic foundation. The flexural rigidity of the top sheet is,

$$D = E_{av} h^3 / [12(1 - \nu_{av}^2)] = 340.6673 \text{ lb-in} \quad (21)$$

The elastic foundation is assumed to be linear elastic so that the force is proportional to the displacement and the core stiffness is,

$$k = E_{\text{core}} / h_{\text{core}} = 1700 \text{ psi} / 1.370 \text{ in} = 12408 \text{ lb/in}^3 \quad (22)$$

where the core thickness is 1.370 and the total thickness is

$$h_{\text{total}} = h_{\text{core}} + 2h = 1.370 + (2)(0.081 \text{ in}) = 1.532 \text{ in} \quad (23)$$

The characteristic length is

$$\ell = (D/k)^{1/4} = 0.40705 \text{ in} \quad (24)$$

Thus, from Timoshenko and Woinowsky-Krieger (1959) and Hui (1986), the concentrated force is related to the deflection (directly at the location of the application of the force)

$$P = (8Dh/\ell^2) (W/h) = (1332.324 \text{ lb}) (W/h) \quad (25)$$

In the above, the top facesheet is assumed to be infinitely large and this assumption is reasonable since the deflection is highly localized near the concentrated load location (within about 1/2 inch radius as seen from experiments). Recall that $P = K_b W$ so that,

$$K_b = 16448. \text{ lb/in} \quad (26)$$

$$k_b = K_b/(E_{av}h) = 0.029009 \quad (27)$$

4. Discussions of Results

The graphite-epoxy plates and the ALS honeycomb sandwich panels were subjected to a dropweight impactor loading with a mass of either 2.66 lb or 3.9 lb. By varying the initial height of the impactor, the velocity of the impactor just before hitting the plate was recorded by the machine. The "Dynatup" IBM/PC Impact Testing System was manufactured by General Research Corporation, 5383 Hollister Ave., Santa Barbara, Calif. 93111 Tel (805)-964-7724., dated Sept. 12, 1985.

Table 1 shows the maximum peak impact force for graphite/epoxy circular plates and the initial kinetic energy, assuming no energy loss. Both the clamped in-plane immovable boundary condition and the simply supported in-plane movable condition are considered and the results are tabulated in this table. It appears that the experimental results show that the plates are closer to being clamped rather than simply supported at the edge.. The majority of the energy was loss due to the vibration of the impactor system and it ranges from 70 to 75% energy loss. Assuming a 75% energy loss, the predicted maximum peak impact forces are plotted in Figure 1 along with the experimental data. Three different boundary conditions are used in the experiments (i) the circular plates are glued to the circular blocks to avoid in-plane slipping (ii) no glue is applied and in-plane slipping may not be fully prevented (iii) the circular plate is resting on a three inches diameter hole with no supporting system on top of the plate. The peak impact forces for the circular plates with these three boundary conditions differ from 5 to 12% and the theoretical values agree with the experiments.

Figure 2 shows the peak impact force versus the initial kinetic energy for graphite/epoxy square plate with side being 3 inches. It can be seen that the measured impact forces for square plates are almost identical to the circular plates. This experimental observation is consistent with the theoretical predictions described in section 2 for square plates. Again, the theoretical impact forces (shown by the solid curves) agree with the experimental values.

Finally, the maximum peak impact force versus the initial kinetic energy for honeycomb sandwich panels are shown in Figure 3. In order to test the validity of the theoretical model of a plate resting on an elastic foundation, the "loose" honeycomb sandwich panels are used for comparison purposes. The "loose" honeycomb sandwich panel consists of top and bottom face sheets and a honeycomb core but the face sheets are not glued to the core. Experimental data show that the "loose" and "bonded" honeycomb sandwich panels have approximately the same impact force. The theoretical impact force are tabulated in Table 2. Based on a 70% energy loss, the theoretical impact forces are plotted in solid line in Figure 3 and they agree with the the experimental data. The theoretical impact forces are higher than the experimental data since the effects of "buckling" or "crushing" of the core is neglected in the plate on elastic foundation model.

In all these three figures, it can be seen that the peak impact force is proportional to the initial kinetic energy, at least for low initial kinetic energy.

W/h	P Clamped Immovable (pounds)	$(1/2)M_I V_I^2$ (ft-lb)	P SS Movable (pounds)	$(1/2)M_I V_I^2$ (ft-lb)
0.10	53.0350	0.2418323	22.8399	0.099145
0.20	107.7156	0.9534993	46.07643	0.392906
0.30	165.6876	2.1523598	70.01061	0.8848849
0.40	228.59651	3.876113	95.32561	1.5833349
0.50	298.08794	6.179474	122.1314	2.500326
0.60	375.80758	9.133731	150.92029	3.651588
0.70	463.40106	12.826800	182.0886	5.056470
0.80	562.51402	17.363477	216.0332	6.737934
0.90	674.79211	22.865793	253.1505	8.72257
1.00	801.88096	29.473412	293.8371	11.04062
1.10			338.4896	13.72602
1.20			387.50479	16.81643
1.30			441.27900	20.35326
1.40			500.2089	24.38172
1.50			564.69117	28.95090
1.60			635.12231	34.11373
1.70			711.89895	39.927134
1.80			795.4176	46.45196
1.90			886.0750	53.753146
2.00			984.2677	61.89964

Table 1 Maximum peak impact forces and the initial kinetic Energy

Impact Support Comparison (Circle)

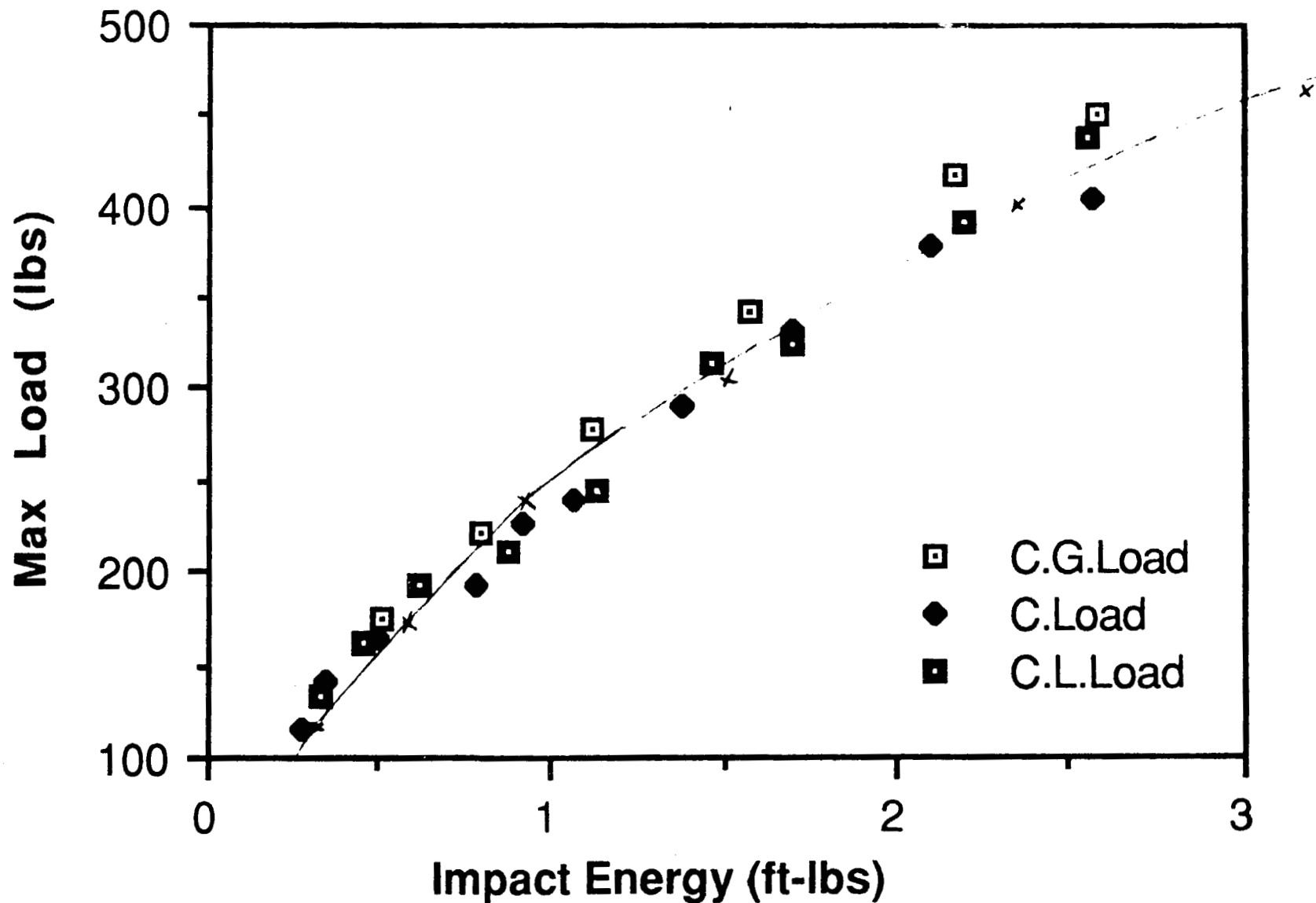


Figure 1 Maximum Peak Impact Force versus the Initial Kinetic Energy
for circular graphite-epoxy plates (diameter = 3 inches)

Impact Support Comparison (Square)

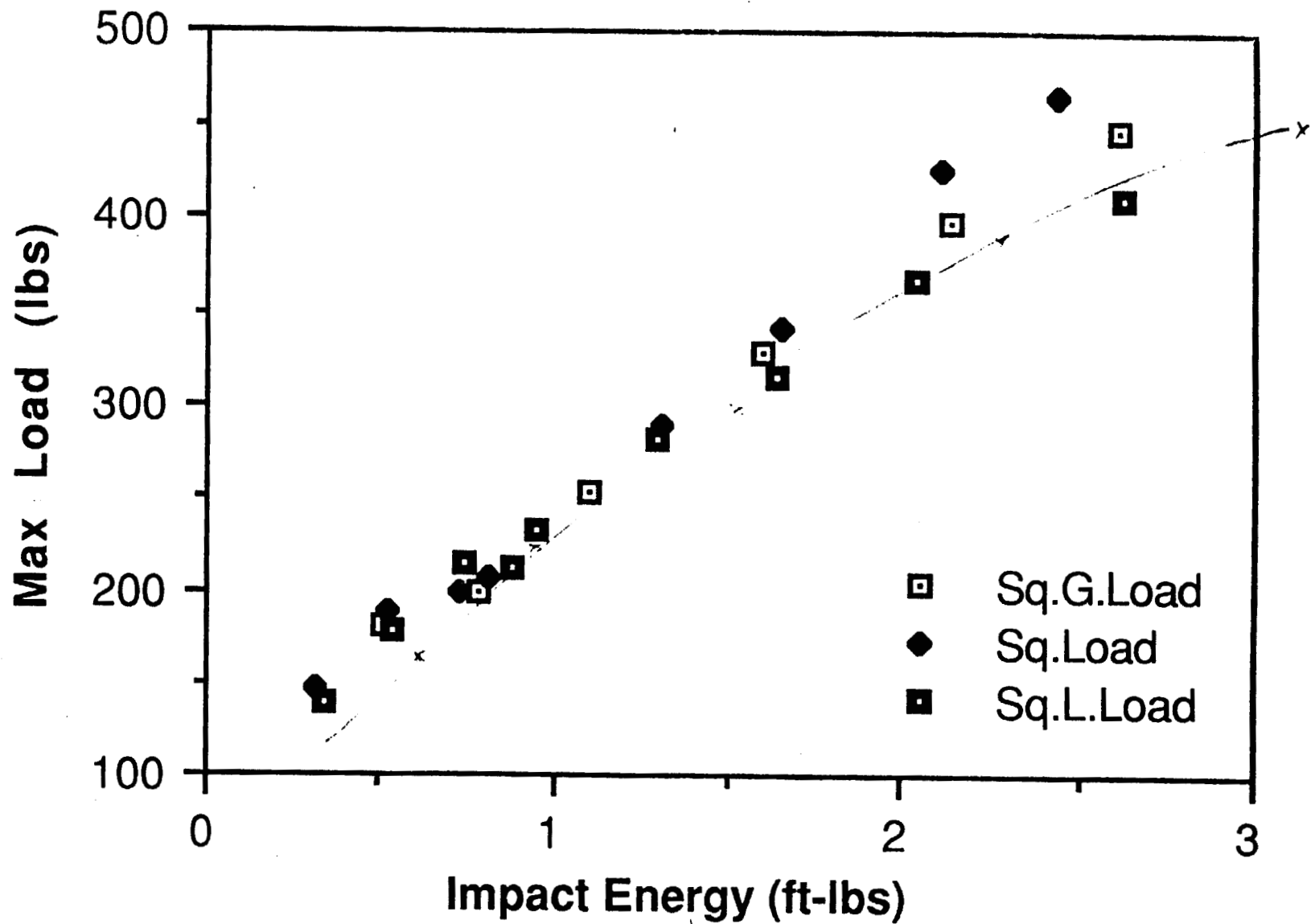


Figure 2 Maximum Peak Impact Force versus Initial Kinetic Energy for Graphite Epoxy Square Plates with Side being 3 inches

ORIGINAL PAGE IS
OF POOR QUALITY

ALS Honeycomb Sandwich Panel

W/h	P (lbs)	$(1/2)M_I V_I^2$ (ft-lbs)
0.10	133.2323	0.667702
0.20	266.464	2.56509
0.30	399.6970	5.65577
0.40	532.929	9.924744
0.50	666.1618	15.3627
0.60	799.3941	21.96337
0.70	932.626	29.7215
0.80	1065.85	38.6334

Table 2 Predicted Peak Impact Forces using a Plate
on a Linear Elastic Foundation Model

Honeycomb vs "Loose comb"

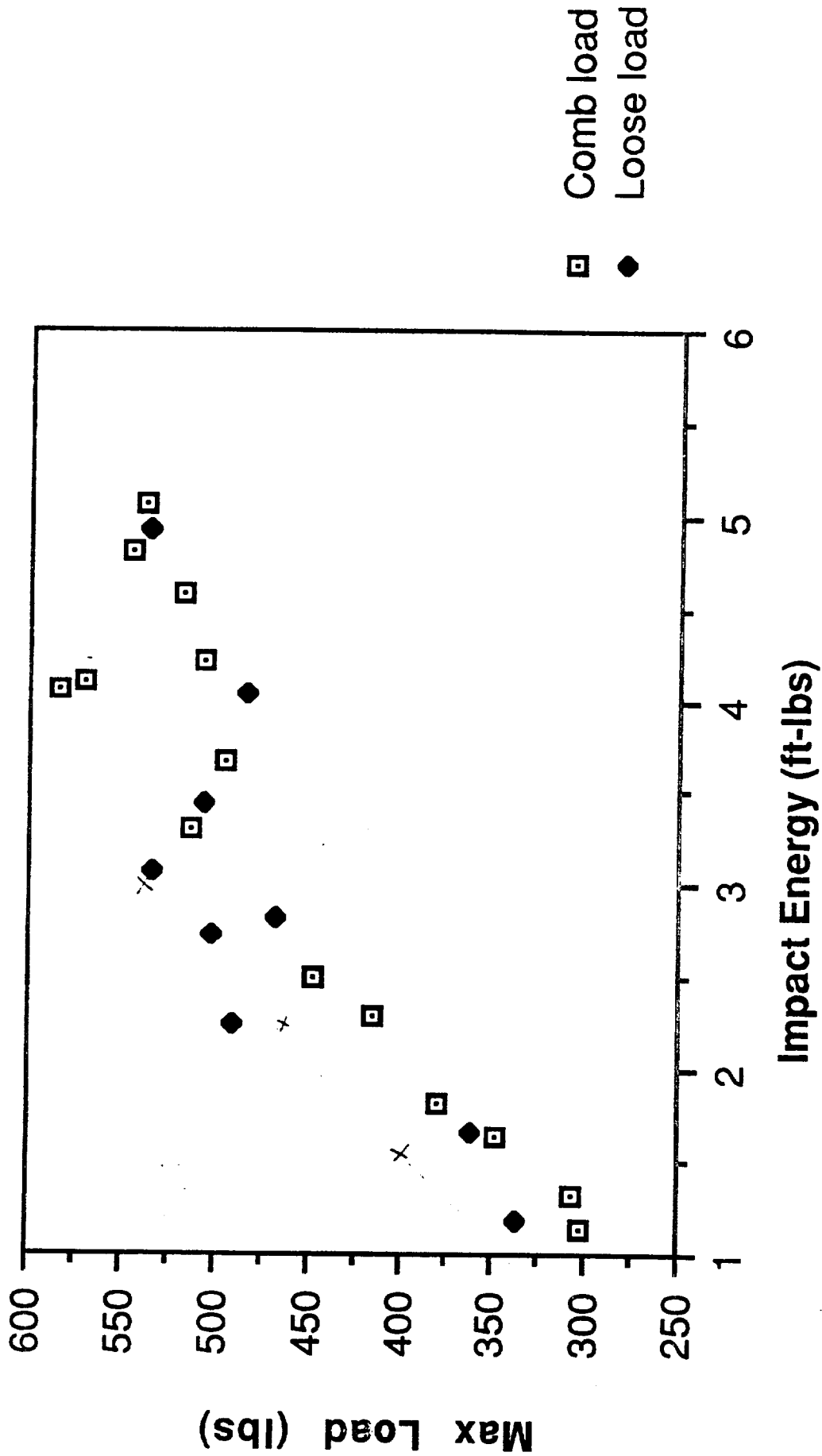


Figure 3 Maximum Peak Impact Forces versus the Initial Kinetic Energy for "loose" or "bonded" honeycomb Sandwich Panels

5. Conclusions

The theoretical energy balance model is used to predict the maximum impact forces based on a given initial kinetic energy of the impactor. The low energy impact resistance of graphite/epoxy circular and square plates subjected to concentrated forces at the plate center is examined. A theoretical model of a plate resting on a linear elastic foundation is proposed for the ALS honeycomb sandwich structure and the theoretical impact forces agree with the experimental data.

Further work is being planned for the four point bending of the ALS sandwich panel. The sandwich panels were previously damaged and it is important to study the residual strength of the structure due to various loads including the shear loads.

ACKNOWLEDGEMENTS

The author would like to thank Alan Nettles for his many helpful advices, especially for his guidance in the experimental portion of the work. Sincere thanks are due to David Lance (a summer student from Georgia Institute of Technology) for his experimental skill in obtaining the data. Finally, Dr. Jerry Patterson provided an excellent opportunity to conduct research in a well-equipped laboratory. It was my pleasure to work for the Composite Branch in a friendly environment.

APPENDIX A Constitutive Equations for Laminated Plates

For a symmetrically laminated plate, there is no bending-stretching coupling and the membrane stress resultants (N_x, N_y, N_{xy}) are related to the in-plane strains of the middle surface ($\epsilon_x, \epsilon_y, \gamma_{xy}$) by

$$\begin{bmatrix} N_x \\ N_y \\ N_{xy} \end{bmatrix} = \begin{bmatrix} A_{11} & A_{12} & A_{16} \\ A_{12} & A_{22} & A_{26} \\ A_{16} & A_{26} & A_{66} \end{bmatrix} \begin{bmatrix} \epsilon_x \\ \epsilon_y \\ \gamma_{xy} \end{bmatrix} \quad (A1)$$

Further, the bending stress resultants (M_x, M_y, M_{xy}) are related to the curvatures (k_x, k_y, k_{xy}) by

$$\begin{bmatrix} M_x \\ M_y \\ M_{xy} \end{bmatrix} = \begin{bmatrix} D_{11} & D_{12} & D_{16} \\ D_{12} & D_{22} & D_{26} \\ D_{16} & D_{26} & D_{66} \end{bmatrix} \begin{bmatrix} k_x \\ k_y \\ k_{xy} \end{bmatrix} \quad (A2)$$

In the above expressions, the extensional stiffness A_{ij} and the bending stiffness D_{ij} can be obtained from,

$$A_{ij} = \sum_{k=1}^N \bar{Q}_{ij}(k^{\text{th}} \text{ layer}) (Z_k - Z_{k-1}) \quad (A3)$$

$$3D_{ij} = \sum_{k=1}^N \bar{Q}_{ij}(k^{\text{th}} \text{ layer}) (Z_k^3 - Z_{k-1}^3) \quad (A4)$$

Each layer is assumed to be orthotropic and the angle between the fiber direction and the x axis is θ . Denoting $S = \sin \theta$ and $C = \cos \theta$, the stress strain relations are,

$$\begin{bmatrix} \sigma_x \\ \sigma_y \\ \sigma_{xy} \end{bmatrix} = \begin{bmatrix} \bar{Q}_{11} & \bar{Q}_{12} & \bar{Q}_{16} \\ \bar{Q}_{12} & \bar{Q}_{22} & \bar{Q}_{26} \\ \bar{Q}_{16} & \bar{Q}_{26} & \bar{Q}_{66} \end{bmatrix} \begin{bmatrix} \epsilon_x \\ \epsilon_y \\ \gamma_{xy} \end{bmatrix} \quad (A5)$$

where,

$$\begin{aligned} \bar{Q}_{11} &= Q_{11}c^4 + (2Q_{12} + 4Q_{66})s^2c^2 + Q_{22}s^4 \\ \bar{Q}_{22} &= Q_{11}s^4 + (2Q_{12} + 4Q_{66})s^2c^2 + Q_{22}c^4 \\ \bar{Q}_{12} &= (Q_{11} + Q_{22} - 4Q_{66})s^2c^2 + Q_{12}(s^4 + c^4) \\ \bar{Q}_{66} &= (Q_{11} + Q_{22} - 2Q_{12} - 2Q_{66})s^2c^2 + Q_{66}(s^4 + c^4) \\ \bar{Q}_{16} &= (Q_{11} - Q_{12} - 2Q_{66})sc^3 + (Q_{12} - Q_{22} + 2Q_{66})s^3c \\ \bar{Q}_{26} &= (Q_{11} - Q_{12} - 2Q_{66})s^3c + (Q_{12} - Q_{22} + 2Q_{66})sc^3 \end{aligned} \quad (A6)$$

Note that the stress strain relations in the material coordinate are,

$$\begin{bmatrix} \sigma_L \\ \sigma_T \\ \sigma_{LT} \end{bmatrix} = \begin{bmatrix} Q_{11} & Q_{12} & 0 \\ Q_{12} & Q_{22} & 0 \\ 0 & 0 & Q_{66} \end{bmatrix} \begin{bmatrix} \epsilon_L \\ \epsilon_T \\ \gamma_{LT} \end{bmatrix} \quad (A7)$$

The face sheet of the Advanced Launch System (ALS) structure is made of graphite/epoxy T300/934 material where the material parameters are,

$$\begin{aligned}
 E_L &= 20.1 \times 10^6 \text{ psi tension,} & E_L &= 19.4 \times 10^6 \text{ psi compression} \\
 E_T &= 1.5 \times 10^6 \text{ psi tension,} & E_T &= 2.4 \times 10^6 \text{ psi compression} \\
 G_{LT} &= 0.66 \times 10^6 \text{ psi} \\
 \nu_{LT} &= 0.294 , \\
 \text{density} &= \rho = 0.057 \text{ lb-mass/in}^3
 \end{aligned}
 \tag{A8}$$

In the present analysis, the tensile values of E_L and E_T are used so that,

$$\begin{aligned}
 E_L/E_T &= 13.400 \\
 G_{LT}/E_T &= 0.4400 \\
 \nu_{TL} &= (\nu_{LT}) (E_T/E_L) = 0.021940299
 \end{aligned}
 \tag{A9}$$

From Jones (1975), eqn. 2.61, one obtains,

$$\begin{aligned}
 (Q_{11}, Q_{22}, Q_{12}) &= (1/c_0) (E_L, E_T, \nu_{LT} E_T) \\
 Q_{66} &= G_{LT}, \quad c_0 = 1 - \nu_{LT} \nu_{TL}
 \end{aligned}
 \tag{A10}$$

Thus, in non-dimensional form,

$$\begin{aligned}
 (q_{11}, q_{22}, q_{12}, q_{66}) &= (1/E_T)(Q_{11}, Q_{22}, Q_{12}, Q_{66}) \\
 &= (13.48699717, 1.006492326, 0.295908744, 0.440000)
 \end{aligned}
 \tag{A11}$$

The ALS composite plate consists of 16 layers with a total thickness of 0.081 inch where the fiber angles are,

$$(0, 45^0, 90^0, -45^0, -45^0, 90^0, 45^0, 0^0)_s \quad (A12)$$

Since the laminate consists of 16 equal-thickness layers, the extensional stiffness can be written as (h = total thickness = 0.081 inch),

$$A_{ij} = (h/4) [\bar{Q}_{ij}(\theta=0^0) + \bar{Q}_{ij}(\theta=45^0) + \bar{Q}_{ij}(\theta=-45^0) + \bar{Q}_{ij}(\theta=90^0)] \quad (A13)$$

Note that,

$$\begin{aligned} \bar{Q}_{16}(\theta=0) &= 0, & \bar{Q}_{16}(\theta=90^0) &= 0, \\ \bar{Q}_{16}(\theta=45^0) &= -\bar{Q}_{16}(\theta=-45^0) \end{aligned} \quad (A14)$$

so that by inspection, $A_{16}=0$ and similarly, $A_{26}=0$. Further, $\bar{q}_{ij} = \bar{Q}_{ij}/E_T$

$$\begin{aligned} (a_{11}, a_{22}, a_{12}, a_{66}) &= (A_{11}, A_{22}, A_{12}, A_{66}) [1/(E_T h)] \\ &= (1/4) [\bar{q}_{ij}(\theta=0^0) + 2\bar{q}_{ij}(\theta=45^0) + \bar{q}_{ij}(\theta=90^0)] \end{aligned} \quad (A15)$$

Thus, we have,

$$\begin{aligned} a_{11} &= (1/4) [\bar{q}_{11}(\theta=0^0) + 2\bar{q}_{11}(\theta=45^0) + \bar{q}_{11}(\theta=90^0)] \\ a_{11} &= (1/4) [q_{11} + (2/4)(q_{11} + 2q_{12} + 4q_{66} + q_{22}) + q_{22}] = 5.729035748 \end{aligned}$$

$$a_{22} = (1/4) [\bar{q}_{22}(\theta=0^\circ) + 2 \bar{q}_{22}(\theta=45^\circ) + \bar{q}_{22}(\theta=90^\circ)]$$

$$a_{22} = (1/4) [q_{22} + (2/4) (q_{11} + 2q_{12} + 4q_{66} + q_{22}) + q_{11}] = a_{11}$$

$$a_{12} = (1/4) [\bar{q}_{12}(\theta=0^\circ) + 2\bar{q}_{12}(\theta=45^\circ) + \bar{q}_{12}(\theta=90^\circ)]$$

$$a_{12} = (1/4) [q_{12} + (2/4) (q_{11} + q_{22} - 4q_{66} + 2q_{12}) + q_{12}] = 1.813617745$$

$$a_{66} = (1/4) [q_{66} + (2/4) (q_{11} + q_{22} - 2q_{12} - 2q_{66} + 2q_{66}) + q_{66}] = 1.957709001$$

(A16a,b,c)

From Jones (1975), the extensional stiffness for an isotropic homogeneous plate is,

$$A_{ij} = \left(\frac{E_{av} h}{1 - \nu_{av}^2} \right) \begin{bmatrix} 1 & \nu_{av} & 0 \\ \nu_{av} & 1 & 0 \\ 0 & 0 & (1 - \nu_{av})/2 \end{bmatrix} \quad (A17)$$

Thus, the in-plane "average" Young's modulus and "average" Poisson's ratio can be obtained from,

$$5.729035784 \quad E_T = E_{av} / (1 - \nu_{av}^2)$$

$$1.813617745 \quad E_T = \nu_{av} E_{av} / (1 - \nu_{av}^2) \quad (A18)$$

$$1.957709001 \quad E_T = E_{av} / 2(1 + \nu_{av})$$

which implies,

$$\nu_{av} = 1.813617745/5.729035784 = 0.316565966 \quad (A19)$$

$$E_{av} = 7.732359197 \times 10^6 \text{ psi}$$

For a 16-layer laminate, the bending stiffness D_{ij} can be computed using the appropriate weighting factor for each layer (Tsai and Hahn 1980, Table 6.6, page 234),

$$3d_{ij} = 2(1/16)^3 \left\{ 169 \bar{q}_{ij}(\theta=0^\circ) + 127 \bar{q}_{ij}(\theta=45^\circ) + 91 \bar{q}_{ij}(\theta=90^\circ) + 61 \bar{q}_{ij}(\theta=-45^\circ) \right. \\ \left. + 37 \bar{q}_{ij}(\theta=-45^\circ) + 19 \bar{q}_{ij}(\theta=90^\circ) + 7 \bar{q}_{ij}(\theta=45^\circ) + \bar{q}_{ij}(\theta=0^\circ) \right\} \quad (A20)$$

$$d_{ij} = D_{ij}/(E_T h^3)$$

Since $\bar{q}_{16}(\theta=0^\circ)=0$, $\bar{q}_{16}(\theta=90^\circ)=0$, one obtains,

$$3d_{16} = 2(1/16)^3 [134 \bar{q}_{16}(\theta=45^\circ) + 108 \bar{q}_{16}(\theta=-45^\circ)] = 2(1/16)^3 26q_{16}(\theta=45^\circ)$$

$$d_{16} = (2/3)(1/16)^3 (26/4) (q_{11}-q_{22}) = 0.013203659 \quad (A21)$$

$$d_{26} = d_{16} = 0.013203659$$

The remaining bending stiffness coefficients (d_{11} , d_{22} , d_{12} , d_{66}) can be computed from,

$$d_{ij} = (2/3)(1/16)^3 \left\{ 170 \bar{q}_{ij}(\theta=0^\circ) + 232 \bar{q}_{ij}(\theta=45^\circ) + 110 \bar{q}_{ij}(\theta=90^\circ) \right\} \quad (A22)$$

so that, $(d_{22}/d_{11} = 0.778487408)$,

$$d_{11} = (2/3)(1/16)^3 [170q_{11} + (232/4)(q_{11}+2q_{12}+4q_{66}+q_{22}) + 110q_{22}]$$

$$d_{11} = 0.550216712 = D_{11}/(E_T h^3)$$

$$d_{22} = (2/3)(1/16)^3 [170q_{22} + (232/4)(q_{11}+2q_{12}+4q_{66}+q_{22}) + 110q_{11}]$$

$$d_{22} = 0.428336782 = D_{22}/(E_T h^3)$$

$$d_{12} = (2/3)(1/16)^3 [170q_{12} + (232/4)(q_{11}+q_{22}-4q_{66}+2q_{12}) + 110q_{12}]$$

$$d_{12} = 0.139277710 \quad (A23)$$

$$d_{66} = (2/3)(1/16)^3 [170q_{66} + (232/4)(q_{11}+q_{22}-2q_{12}) + 110q_{66}]$$

$$d_{66} = 0.151285315$$

From Jones (1975), the bending stiffness for an isotropic homogeneous laminate is,

$$D_{ij} = \left(\frac{\bar{E} h^3}{12(1-\bar{\nu}^2)} \right) \begin{bmatrix} 1 & \bar{\nu} & 0 \\ \bar{\nu} & 1 & 0 \\ 0 & 0 & (1-\bar{\nu})/2 \end{bmatrix} \quad (A24)$$

Therefore, by comparison,

$$0.550216712 E_T = \bar{E} / [12(1-\bar{\nu}^2)]$$

$$0.428336782 E_T = \bar{E} / [12(1-\bar{\nu}^2)]$$

(A25)

$$0.139277710 E_T = \bar{\nu} \bar{E} / [12(1-\bar{\nu}^2)]$$

$$0.151285315 E = \bar{E} / 24(1-\bar{\nu})$$

ORIGINAL PAGE IS
OF POOR QUALITY

Thus, by assuming that $\bar{\nu}=0.3$, one obtains,

$$\bar{E} = 9.0125497 \times 10^6 \text{ psi}$$

$$\bar{E} = 7.016156489 \times 10^6 \text{ psi}$$

(A26)

$$\bar{E} = 7.6045629 \times 10^6 \text{ psi}$$

$$\bar{E} = 7.08015274 \times 10^6 \text{ psi}$$

Since $D_{22}/D_{11} = 77.848\%$, it is obvious that the bending stiffness in the 1-direction is not the same as that in the 2-direction. This causes a non-axisymmetric behavior in the deflection of a circular plate under a lateral concentrated force at its center. For a conservative design, one should use the average Young's modulus of 7.01615×10^6 psi.

APPENDIX B Coefficients of Hertz Law

According to Hertz Law, the energy due to the contact between two elastic bodies is,

$$E_c = (2/5) P^{5/3} / n^{2/3} \quad (B1)$$

where P is the contact force and (see Shivakumar et al. 1985b)

$$n = 4 R_I^{1/2} / [3\pi (K_1 + K_2)] \quad (B2)$$

$$K_2 = \frac{(C_{22})^{1/2} \{ [(C_{11}C_{22})^{1/2} + G_{zr}]^2 - (C_{12} + G_{zr})^2 \}^{1/2}}{(2\pi)(G_{zr})^{1/2} (C_{11}C_{22} - C_{12}^2)}$$

In the above, R_I is the radius of the impactor, E_I and ν_I are the Young's modulus and Poisson's ratio of the impactor and

$$\begin{aligned} c_{11} &= C_{11}/E_{av} = (E_z/E_{av})(1 - \nu_{av})\beta \\ c_{22} &= C_{22}/E_{av} = (\delta)(1 - \nu_{zr}^2\delta)/(1 + \nu_{av}) \\ c_{12} &= C_{12}/E_{av} = \nu_{zr}\beta, \quad g_{zr} = G_{zr}/E_{av} \end{aligned} \quad (B3)$$

$$\beta = 1 / [1 - \nu_{av} - 2\nu_{zr}^2\delta]$$

$$\delta = E_{av}/E_z$$

ORIGINAL PAGE IS
OF POOR QUALITY

Thus, equations B2 can be written in the non-dimensional form,

$$n^* = n/(E_{av} h^{1/2}) = 4 (R_I/h)^{1/2} / [3\pi(E_{av} K_1 + E_{av} K_2)]$$

$$E_{av} K_1 = (1 - \nu_I^2)(E_{av}/E_I)/\pi$$

$$E_{av} K_2 = \frac{(c_{22})^{1/2} \{ [(c_{11}c_{22})^{1/2} + g_{zr}]^2 - (c_{12} + g_{zr})^2 \}^{1/2}}{(2\pi)(g_{zr})^{1/2} (c_{11}c_{22} - c_{12}^2)} \quad (B4)$$

In the present analysis, we have,

$$E_{av} = 7.0000 \times 10^6 \text{ psi}, \quad \nu_{av} = 0.30 \quad (B5)$$

From Shivakumar et al 1985b, one can estimate the following material parameters,

$$\nu_{zr} = 0.060, \quad G_{zr} = 0.59 \times 10^6 \text{ psi}, \quad E_z = 1.70 \times 10^6 \text{ psi} \quad (B6)$$

so that,

$$\delta = E_{av}/E_z = 4.117647059, \quad \beta = 1.491751492 \quad (B7)$$

$$(c_{11}, c_{22}, c_{12}, g_{zr}) = (0.253597754, 1.130491131, 0.089505090, 0.084285714)$$

Based on the computed values of c_{11} , c_{22} , c_{12} , g_{zr} , one obtains,

$$E_{av}K_2 = 1.244177058 \quad (B8)$$

For the impactor,

$$\nu_I = 0.30, \quad E_I = 29.0 \times 10^6 \text{ psi}, \quad R_I = 0.250 \text{ in}$$

$$E_{av}K_1 = 0.069918413 \quad (B9)$$

so that,

$$n^* = 0.567400142 \quad (B10)$$

APPENDIX C Design Guideline for Stacking Sequence of Quasi-Isotropic Laminated Plates

From Appendix A, it was demonstrated that the bending stiffness in the 2-direction is only 77.848% of the bending stiffness in the 1-direction. The material parameters of the ALS graphite-epoxy T300/934 laminate are,-

$$E_L/E_T = 13.400, \quad G_{LT}/E_T = 0.44, \quad \nu_{LT} = 0.294$$

and the stacking sequence is,

$$(0^0, 45^0, 90^0, -45^0, -45^0, 90^0, 45^0, 0^0)_s$$

There are sixteen layers and the total thickness is 0.081 in. From Tsai and Hahn (1980 table 5.4 and table 6.6) and Jones (1975), if the laminate consists of "equal-thickness" lamina, the extensional stiffnesses ($A_{11}, A_{22}, A_{12}, A_{66}, A_{16}, A_{26}$) are independent of the stacking sequence. That is, an interchange of say any two of the above layers would not change the "in-plane" A_{ij} stiffnesses and each layer carries the weighted factor of unity. On the other hand, the "out-of-plane" bending stiffnesses ($D_{11}, D_{22}, D_{12}, D_{66}, D_{16}, D_{26}$) depends on the stacking sequence such that outer layers carry a larger weighted factor than the layers near the middle surface (halfway between the top and bottom fibers). For example in the small deflection bending of a beam subjected to a three point bending load, the top half of the beam is under compression and the bottom half is under tension so that the middle surface has zero in-plane stress and the layers near the middle surface should carry a smaller weighted factor than those near the outer fibers. The weighted factors

for a 32 layers laminate is (Tsai and Hahn 1980),

$$(721, 631, 547, 469, 397, 331, 271, 217, 169, 127, 91, 61, 37, 19, 7, 1)_S$$

in the present ALS panel which consists of 16 layers, the weighted factors are (there are "four" sets of the 0, 90, 45, -45 layup),

$$(169, 127, 91, 61, 37, 19, 7, 1)_S$$

It was demonstrated from the Utah-laminate computer program that as one increases the number of "sets" to 16 for a 64 layer laminate, the bending stiffness D_{11} and D_{22} are essentially the same (within 1%). If the number of layers is only 16, one can interchange say two layers so that the ratio of D_{22} to D_{11} would be closer to unity. For example, in the above stacking sequence, one obtains,

for the 0° , the weighted factor is $169+1 = 170$

for the 45° , the weighted factor is $127+7 = 134$

for the 90° , the weighted factor is $91+19 = 110$

for the -45° , the weighted factor is $61+37 = 98$

Consider the following stacking sequence,

$$(45, -45, 0, 90, 90, -45, 0, 45)_S$$

one can easily show that D_{11} is identical to D_{22} since $91+7 = 61+37$.

However, such stacking sequence has the drawback that bending stiffness in the +45 or -45 directions are not the same ($169+1=170$ and $127+19=146$).

A compromise stacking sequence may be,

$$(A, B, C, D, B, D, A, C)_S$$

where the weighted factors of A, B, C, D are $(169+7=176, 127+37=164, 91+1=92, 61+19=80)$ and A, B, C and D refer to $0^\circ, 90^\circ, 45^\circ, -45^\circ$ respectively or A,B,C,D, may refer to $90^\circ, 0^\circ, 45^\circ, -45^\circ$, respectively, etc. This stacking sequence represents the "best" design since the composite plate behaves like an isotropic-homogeneous plate.

Halpin (1984, section 4.6.2) suggested that the interlaminar shear stresses σ_{zx} will be "significantly" lower if the $+45^\circ$ and -45° layers are separated by a 0° or 90° layer. for a quasi-isotropic layup involving $(45, -45, 90, 0)$. He showed that there are only 12 distinct stacking possibilities. Among these 12 possibilities, six of them involve adjacent $\pm 45^\circ$ layers and six with $\pm 45^\circ$ interspered between 0° or 90° layers. (see tables B1 and B2 from Halpin 1984).

Thus, there is no simple solution in order to satisfy the two criteria (i) the laminate behaves like an isotropic-homogeneous plate (ii) the interlaminar stresses are minimized. It appears that increasing the number of "sets" to say 6 for a total of 24 layers, making sure that the $+45^\circ$ and -45° layers are separated by 0° or 90° layers, would be the best stacking sequence design.

Strength Hierarchy	Laminate Stress σ_y (KSI)	Laminate	Interface Moment in./b in	Finite Element Maximum Stresses (KSI)
7	-26.5 \rightarrow -0.5 \rightarrow 13.5 \cdot 13.5 \leftarrow	90 0 45 45	-0.33 -1.00 1.50 -1.67	$\sigma_z = -8.2$ $\tau_{zx} = 9.0$
8	-26.5 \rightarrow 13.5 \leftarrow 13.5 \leftarrow -0.5 \rightarrow	90 45 -45 0	-0.33 0.82 0.98 -0.98	$\sigma_z = 7.4$ $\tau_{zx} = -9.2$
9	-0.5 \rightarrow -26.5 \rightarrow 13.5 \leftarrow 13.5 \leftarrow	0 90 45 -45	-0.01 0.34 -0.85 -1.02	$\sigma_z = -7.6$ $\tau_{zx} = -9.2$
10	0.5 \rightarrow 13.5 \cdot 13.5 \cdot 26.5 \cdot	0 45 45 90	-0.01 0.15 0.12 0.98	$\sigma_z = 10.0$ $\tau_{zx} = 8.3$
11	13.5 \leftarrow 13.5 \leftarrow -26.5 \rightarrow 0.5 \rightarrow	45 -45 90 0	0.17 0.67 1.02 1.02	$\sigma_z = 9.0$ $\tau_{zx} = -7.7$
12	13.5 \leftarrow 13.5 \cdot 0.5 \cdot 26.5 \rightarrow	45 45 0 90	0.17 0.67 1.34 1.67	$\sigma_z = 10.9$ $\tau_{zx} = 7.2$

○ maximum τ_{zx}
 □ maximum σ_z
 T/300 5208 Graphite Epoxy
 $\epsilon_x = 0.5\%$

Table C1 Normal Stress and Interlaminar Stress for adjacent $\pm 45^\circ$ Quasi-isotropic laminate

ORIGINAL PAGE IS
OF POOR QUALITY

Strength Hierarchy	Laminate Stress σ_y (KSI)	Laminate	Interface Moment in-/b in	Finite Element Maximum Stresses (KSI)
1	-26.5 \rightarrow 13.5 \leftarrow -0.5 \rightarrow 13.5 \leftarrow	90 45 0 45	-0.33 -0.83 -1.16 -1.33	$\sigma_z = -6.8$ $\tau_{zx} = -6.9$
2	-0.5 \rightarrow 13.5 \leftarrow 26.5 \rightarrow 13.5 \leftarrow	0 45 90 45	-0.01 0.15 0.15 0.02	$\sigma_z = 6.2$ $\tau_{zx} = 6.6$
3	13.5 \leftarrow -26.5 \rightarrow -0.5 \rightarrow 13.5 \leftarrow	45 90 0 45	0.17 0.17 -0.16 -0.33	$\sigma_z = 6.6$ $\tau_{zx} = 5.9$
4	13.5 \leftarrow -26.5 \rightarrow 13.5 \leftarrow 0.5 \rightarrow	45 90 45 0	0.17 0.17 0.02 0.02	$\sigma_z = 6.9$ $\tau_{zx} = 6.5$
5	13.5 \leftarrow 0.5 \rightarrow 13.5 \leftarrow -26.5 \rightarrow	45 0 90 45	0.17 0.50 0.99 1.33	$\sigma_z = 7.6$ $\tau_{zx} = 5.8$
6	13.5 \leftarrow -0.5 \rightarrow 13.5 \leftarrow -26.5 \rightarrow	45 0 90 45	0.17 0.50 0.99 1.33	$\sigma_z = 10.4$ $\tau_{zx} = 6.0$

○ maximum $|\tau_{zx}|$
 □ maximum $|\sigma_z|$
 T/300/5208 Graphite-Epoxy
 $\epsilon_x = 0.5\%$

Table C2 Normal Stress and Interlaminar Stress for Interspersed $\pm 45^\circ$ with either a 0° or 90° Quasi-isotropic Laminate

Appendix D Equilibrium and Compatibility equation for Circular Plates and Rectangular Plates

From Chia(1980,section 3.2), the nonlinear equilibrium and compatibility equations (written in terms of the out-of-plane displacement W and a stress function F) are, respectively, assuming axi-symmetric deflection,

$$(D)(R) \left[(1/R)(RW_{,R})_{,R} \right]_{,R} = \int_{s=0}^{s=R} sq \, ds + F_{,R}W_{,R} \quad (D1)$$

$$R \left[(1/R)(RF_{,R})_{,R} \right]_{,R} = (-Eh/2) (W_{,R})^2 \quad (D2)$$

where

$$N_r = (1/R)F_{,R}$$

$$N_\theta = F_{,RR} \quad (D3)$$

$$N_{r\theta} = 0$$

In the above expression, R is the radial coordinate, E is Young's modulus, h is the thickness, q is the applied stress, and N_r , N_θ are the membrane stress resultants. Assuming that the concentrated load can be represented by an applied stress over the contact area of radius a_{contact} , and dropping the nonlinear term $F_{,R}$ and $W_{,R}$ in the equilibrium equation for small deflection, one can show that the exact deflection is of the form,

$$W = W_1 (1 + c_1 r^2 + c_2 r^{2+\epsilon}) \quad (D4)$$

where ϵ is arbitrarily close to zero

The governing nonlinear equilibrium and compatibility equations for symmetrically laminated rectangular plates are, respectively, (Hui 1985a,b)

$$L_{D^*}(W) = F_{,YY}W_{,XX} + F_{,XX}W_{,YY} - 2F_{,XY}W_{,XY} \quad (D5)$$

$$L_{A^*}(F) = (W_{,XY})^2 - W_{,XX}W_{,YY} \quad (D6)$$

where W is the out-of-plane deflection, F is the stress function, X and Y are the in-plane coordinates and $L_{D^*}(\)$ and $L_{A^*}(\)$ are the differential operators defined by,

$$L_{A^*}(\) = A_{22}^*(\),_{XXXX} + (2A_{12}^* + A_{66}^*)(\),_{XXYY} + A_{11}^*(\),_{YYYY}$$

$$L_{D^*}(\) = D_{11}(\),_{XXXX} + (2D_{12} + 4D_{66})(\),_{XXYY} + D_{22}(\),_{YYYY}$$

The A_{ij}^* and D_{ij} are the material parameters defined by Jones (1975).

Finally, an extension of the work by Eringen(1953) to laminated plates was presented by Sun and Chattopadhyay (1975) based on the summation of the various deflection modes corresponding to different frequencies of an anisotropic rectangular plate. This method was used by Chou and Mortimer (1976) who presented a computer code to predict the contact force, deflection and bending strains of an anisotropic plate. Using this code, the predicted strains were in good agreement with the experimental data as reported by Dobyns and Porter (1981).

The present work deals with the prediction of the peak impact force due to low energy impact on graphite/epoxy circular and square plates and ALS honeycomb sandwich panels. Using the energy balance method, the initial kinetic energy is dissipated in terms of the bending energy of the plate, the membrane energy(due to the stretching of the mid-surface of the plate in finite deflection), the Hertzian contact energy (due to the imbedment of the impact in the plate) and the energy loss (due to the vibration of the impactor punching system). The "average" Young's modulus and "average" Poisson's ratio as well as the estimated out-of-plane material parameters (see Shivakumar and Crews 1982 and Kriz and Stinchcomb 1979) are reported based on the ALS 16-layer quasi-isotropic layup. The Hertzian parameters are then computed in Appendix B. The theoretical contact forces are in good agreement with the experiments. Some design guidelines for various stacking sequence are presented in Appendix C.

REFERENCES

- Agarwal, B.D. and Broutman, L.J., "Analysis and Performance of Fiber Composites", John Wiley and Sons, New York, 1980.
- Bass, M., Gottesman, T. and Fingerhut, U., "Criticality of Delaminations in Composite Materials Structure", 28th Israel Annual Conf. on Aviation and Astronautics, Feb 19-20, 1986, Haifa, Israel, pp. 186-190.
- Bernard, M.L. and Lagace, P.A., "Impact Resistance of Composite Sandwich Plates", Proc. of the American Society for Composites, Second Technical Conf., Sept. 23-25, Univ. of Delaware, 1987.
- Bernard, M.L., "Impact Resistance and Damage Tolerance of Composite Sandwich Plates", TELAC Report 87-11, May 1987.
- Bostaph, G.M. and Elber, W., "Static Indentation Tests on Composite Plates for Impact Susceptibility Evaluation", Proc. of the Army Symposium of Solid Mechanics 1982, Critical Mechanics Problems in Systems Design, AMMRC MS 82-4, US Army Sept 1982, pp. 288-317.
- Bostaph, Gretchen M., "The Effect of Matrix on Composite Impact Resistance for Various Toughened Matrix Materials", ASME Winter Annual Meeting, Dec. 9-13, 1984, New Orleans.
- Chia, C.Y., "Nonlinear Analysis of Plates", McGraw-Hill Book Co., 1980.
- Chou, P.C. and Mortimer, R.W., "Impact Behavior of Polymeric Matrix Composite Plates", AFML-TK-76-242, Dec. 1976, 94pp.
- Ciarns, D.S. and Lagace, P.A., "Transient Response of Graphite/Epoxy and Kevlar/Epoxy Laminates subjected to Impact", AIAA/ASME/ASCE/AHS 29th Structures, Structural Dynamics and Materials Conf., Williamsburg, Virginia, AIAA Paper No. 88-2328.
- Conway, H.D., "The Pressure Distribution Between Two Elastic Bodies in Contact", Zeitschrift fur Angewandte Mathematik und Physik, ZAMP, Vol. 7, 1956, pp.460-465.

- Dahan, M. and Zarka, J., "Elastic Contact Between a Sphere and a Semi Infinite Transversely Isotropic Body", Int. J. of Solids and Structures Vol. 13, 1977, pp. 229-238.
- Dobyns, A.L. and Porter, T.R., "A Study of the Structural Integrity of Graphite Composite Structure subjected to Low Velocity Impact", Polymer Engineering and Science, Vol. 21, No. 8, June 1981, pp.493-498.
- Eringen, A.C., "Transverse Impact on Beams and Plates", J. of Applied Mechanics, Transactions of ASME, Vol. 20, No. 4, 1953, pp.461-468.
- Gottesman, T., Bass, M. and Samuel, A., "Criticality of Impact Damage in Composite Sandwich Structures", Sixth Int Conf on Composite Materials, edited by Matthews, F.L. et al., July 1987, published by Elsevier, New York, pp. 3.27-3.35.
- Greszczuk, L.B., "Response of Isotropic and Composite Materials to Particle Impact", Foreign Object Impact Damage to Composites, edited by Greszczuk, L.B., AS TM Special Technical Publication 568, 1975, pp.183-211.
- Greszczuk, L.B. and Chao, H., "Impact Damage in Graphite-Fiber-Reinforced Composites", Composite Materials: Testing and Design (Fourth Conf.), edited by Davis, J.G., Jr., ASTM Special Tech Pub 617, 1977, pp.389-408.
- Greszczuk, L.B., "Application of Four-Point Ring-Twist Test for Determining Shear Modulus of Filamentary Composites", Test Methods and Design Allowables for Fibrous Composites, edited by C.C. Chamis, ASTM Special Technical Pub. 734, 1981, pp.21-33.
- Greszczuk, L.B., "Damage in Composite Materials due to Low Velocity Impact", Impact Dynamics, edited by Zukas, J.A. Nicholas, T., Swift, H.L., Greszczuk, L. and Curran, D.R. , John Wiley and Sons, New York, 1982, pp. 55-94.
- Halpin, J.C., "Primer on Composite Materials: Analysis", Technomic Pub. Co., 1984.
- Hui, D., "Viscoelastic Response of Floating Ice Plates under Distributed or Concentrated Loads", Journal of Strain Analysis, March 1986, pp.

- Hui, D., "Soft-Spring Nonlinear Vibrations of Antisymmetrically Laminated Rectangular Plates", Int. J. of Mechanical Sciences, Vol. 27, 1985, pp. 397-408.
- Hui, D., "Effects of Geometric Imperfections on Frequency-Load Interaction of Biaxially Compressed Antisymmetric Angle Ply Rectangular Plates", ASME J. of Applied Mechanics, Vol. 52, 1985, pp. 155-162.
- Jones, R.M., "Mechanics of Composite Materials", McGraw-Hill Book Co., 1975.
- Kriz, R.D. and Stinchcomb, W.W., "Elastic Moduli of Transversely Isotropic Graphite Fibers and Their Composites", Experimental Mechanics, Vol. 19, Feb. 1979, pp. 41-49.
- Labor, J.D. and Bhatia, N.M., "Impact Resistance of Graphite and Hybrid Configurations", Fibrous Composites in Structural Design, Army Materials and Mechanics Research Center, Plenum Press, New York, 1980.
- Lukasiewicz, S.A., "Introduction of Concentrated Loads in Plates and Shells", Progress in Aerospace Science, Vol. 17, No. 2, 1976, pp. 109-146.
- Lukasiewicz, S., "Local Loads in Plates and Shells", Sijthoff and Noordhoff, The Netherlands, 1979.
- Oplinger, D.W. and Slepetz, "Impact Damage Tolerance of Graphite/Epoxy Sandwich Panels", Foreign Object Impact Damage to Composites, ASTM Special Technical Pub. 568, edited by Greszczuk, L.B., Sept. 1973.
- Rhodes, M.D., Williams, J.G. and Starnes, J.H., Jr., "Low-Velocity Impact in Graphite-Fiber Reinforced Epoxy Laminates", 34th Annual Conference on Reinforced Plastics/Composite Institute, The Society of Plastic Industry, Inc., Jan 29-Feb 2, 1979, New Orleans.
- Rhodes, M.D., "Low Velocity Impact on Composite Sandwich Structures" Second Air Force Conf. on Fibrous Composites in Flight Vehicle Design", Dayton, Ohio, May 1974.
- Rhodes, M.D., "Impact Tests on Fibrous Composite Sandwich Structures", NASA Technical Mem. 78719, Oct. 1978

- Sharma, A.V., "Low-Velocity Impact Tests on Fibrous Composite Sandwich Structures", Test Methods and Design Allowables for Fibrous Composites, ASTM Special Tech Pub 734, edited by Chamis, C.C., 1981, pp. 54-70.
- Shih, W.K. and Jang, B.Z., "Instrumented Impact Testing of Composite Sandwich Panels", J. of Reinforced Plastics and Composites, Vol. 8, May 1989, pp. 270-298.
- Shivakumar, K.N. and Elber, W., "Delamination Growth Analysis in Quasi-Isotropic Laminates under Loads Simulating Low-Velocity Impact", NASA Tech Mem. 85819, June 1984.
- Shivakumar, K.N., Elber, W. and Illg, W., "Prediction of Low-Velocity Impact Damage in Thin Circular Laminates", AIAA Journal, Vol. 23, No. 3, March 1985, pp. 442-449.
- Shivakumar, K.N., Elber, W. and Illg, W., "Prediction of Impact Force and Duration Due to Low-Velocity Impact on Circular Composite Laminates", ASME J. of Applied Mechanics, Vol. 52, Sept 1985, pp. 674-680.
- Sjoblom, P.O., Hartness, J.T. and Cordell, T.M., "On Low-Velocity Impact Testing of Composite Materials", J. of Composite Materials, Vol. 22, January 1988, pp. 30-52.
- Sun, C.T., and Chattopadhyay, S., "Dynamic Response of Anisotropic Laminated Plates under Initial Stress to Impact of a Mass", ASME J. of Applied Mechanics, Vol. 42, Sept. 1975, pp. 693-698.; also AFML-TR-74-258, March 1976, 41pp.
- t'Hart, W.G.J., "The Effect of Impact Damage on the Tension-Compression Fatigue Properties of Sandwich Panels with Face Sheets of Carbon/Epoxy", National Aerospace Lab, Amsterdam, Dec. 1981.
- Timoshenko, S. and Woinowsky-Krieger, S., "Theory of Plates and Shells", McGraw-Hill Book Co., New York, 1959.
- Timoshenko, S. and Goodier, J.N., "Theory of Elasticity", McGraw-Hill Book Co., 1970.
- Ugural, A.C., "Stresses in Plates and Shells", McGraw-Hill Book Co., New York, 1981.

Vol'mir, A.S., "Flexible Plates and Shells", AFFDL-TR-66-216, April 1967, 489pp.

Willis, J.R., "Hertzian Contact of Anisotropic Bodies", J. of the Mechanics and Physics of Solids", Vol. 14, 1966, pp. 163-176.

1989

NASA/ASEE SUMMER FACULTY FELLOWSHIP PROGRAM

MARSHALL SPACE FLIGHT CENTER
THE UNIVERSITY OF ALABAMA IN HUNTSVILLE

INVESTIGATIONS INTO A NEW ALGORITHM FOR CALCULATING
H[∞] OPTIMAL CONTROLLERS

Prepared by:	R. Dennis Irwin
Academic Rank:	Assistant Professor
University and Department:	Ohio University Department of Electrical and Computer Engineering
NASA/MSFC:	
Laboratory:	Structures and Dynamics
Division:	Control Systems
Branch:	Pointing Control Systems
MSFC Colleague:	Henry Waites
Date:	August 31, 1989
Contract:	The University of Alabama in Huntsville NGT 01-008-021

INVESTIGATIONS INTO A NEW ALGORITHM FOR CALCULATING H^∞ OPTIMAL CONTROLLERS

by

R. Dennis Irwin
Assistant Professor of Electrical and Computer Engineering
Ohio University
Athens, Ohio

ABSTRACT

A new algorithm for calculating H^∞ optimal controllers is investigated. The new algorithm is significantly simpler than existing approaches and yields much simpler controllers. The design equations are first presented. Special system transformations required to apply the new algorithm are then presented. The use of the new algorithm with sampled-data systems is outlined in detail.

Several constraints on the characteristics of the problem formulation are required for the application of the design equations. The consequences of these constraints are investigated by applying the algorithm to a simplified design for a subsystem of a large space structure ground test facility. The investigation of these constraints is continued by application of the design equations and constraints to an extremely simple tracking problem. The result of these investigations is the development of a frequency dependent weighting strategy that allows realistic control problems to be cast in a form compatible with the new algorithm.

Further work is indicated in the area of developing strategies for choosing frequency-dependent weights to achieve specific design goals. The use of the freedom in problem formulation to achieve robustness/performance tradeoffs should also be investigated.

It is not clear that the new algorithm always leads to simpler controllers. The more restrictive formulation may dictate that frequency-dependent weighting adds to the controller order disproportionately. This effect must also be investigated.

NOMENCLATURE

$\sigma_{\min}(A)$	minimum singular value of a matrix A
$\sigma_{\max}(A)$	maximum singular value of a matrix A
$ F(s) _{\infty}$	infinity norm of a system transfer function matrix
IMC	image motion compensation
BET	base excitation table
LOS	line of sight
LQG	linear-quadratic Gaussian

INTRODUCTION

Until the recent work by Glover and Doyle^[1], the design of H^∞ controllers promised to be a long and arduous ordeal for the designer. Moreover, the resulting controllers tended to be extremely complex, sometimes exceeding the order of the control model by a factor of five. Their publication of design equations for controllers of the same order as the control model is thus a significant advance in the state of the art. However, the question of whether H^∞ control techniques can be successfully applied to large space structure (LSS) control design problems is by no means answered.

The foremost question in the mind of any LSS control designer is that of applicability of H^∞ techniques to the usual goals of LSS control. It is known that H^∞ optimization can achieve (at least mathematically) any of the goals of disturbance rejection, command tracking, and robustness. What is not known is whether H^∞ design methods can be used to design controllers which simultaneously give acceptable performance and do not suffer from the known shortcomings of LQG techniques, e.g., lack of robustness. The purpose of the work presented here is to address the issues of the applicability of the new algorithm for calculating H^∞ controllers for large space structures.

The organization of the report is as follows. Section 1.0 contains a brief discussion of the H^∞ performance criterion and the design equations which must be solved in order to find the optimal H^∞ controller.

Section 2.0 describes a transformation required to satisfy constraints on using the design equations. The result is a set of equations that can be readily used to transform a given state space realization to one of the required form.

Section 3.0 outlines modifications to the state space formulation that are required in order to apply H^∞ design formulas to sampled data systems. The result is a set of state space formulas for applying the well known w-plane transformation to multivariable control problems. The [2] equations, minus the derivation, can be found in Glover. An outline of the derivation is included here for completeness.

Section 4.0 documents the application of H^∞ techniques to a simplified model of the ACES IMC subsystem, including BET disturbance effects. Section 5.0 uses a simple tracking problem to discuss weighting schemes which allow the new algorithm to be applied to realistic control design problems.

Section 6.0 contains conclusions and recommendations for further work. In particular, it is suggested that strategies for developing frequency-dependent weights be investigated.

1.0 H^∞ PERFORMANCE CRITERION AND DESIGN EQUATIONS

The H^∞ control problem can be stated as follows. The system equations are

$$\dot{x} = Ax + B_1 w + B_2 u$$

$$z = C_1 x + D_{11} w + D_{12} u$$

$$y = C_2 x + D_{21} w + D_{22} u$$

where w is in R^{m_1} , u is in R^{m_2} , z is in R^{p_1} , and y is in R^{p_2} . The signal w is an exogenous input which may be either disturbances or command signals; u is the control input vector; z is actually the performance related vector; and y is the vector of measurements that is actually available for feedback.

Although most calculations with this technique are done in state space form, the performance criterion is most easily stated in the frequency domain in terms of the closed loop transfer function matrix. The open loop transfer function matrix can be expressed in terms of appropriate partitions as

$$G_{11}(s) = [A, B_1, C_1, D_{11}]$$

$$G_{12}(s) = [A, B_2, C_1, D_{12}]$$

$$G_{21}(s) = [A, B_1, C_2, D_{21}]$$

$$G_{22}(s) = [A, B_2, C_2, D_{22}].$$

If a controller with transfer function matrix $K(s)$ is connected from y to u , the closed loop transfer function matrix is given by

$$T(s) = G_{11} + G_{12}K(I - G_{22}K)^{-1}G_{21}.$$

The H^∞ control problem is to find a controller K which yields a stable closed loop system and for a prespecified real number Γ ,

$$\|T\|_\infty < \Gamma$$

where

$$\|T\|_\infty = \sup_w \sigma_{\max}(T(jw)).$$

In the special case of a scalar transfer function, the goal can be stated as simply insuring that the closed loop frequency response has a magnitude less than Γ . This is clearly important in disturbance rejection problems and can be used also for tracking type problems.

The H^∞ optimal control problem is that of finding the smallest such Γ such that a stabilizing controller exists. Note that once a method of satisfying a given Γ bound is identified, the job of obtaining an optimal solution is not difficult, although it is iterative. The significance of the recent work of Glover and Doyle is that their equations yield not only a controller that achieves the prespecified bound but is only the order of the original control model. The original factorization algorithms tended to yield controllers many times as large as the original plant.

Several constraints must be placed on the plant equations in order to apply the design equations. The first constraint is that the realization (A, B_2, C_2) be

stabilizable and detectable, as is usual.

The second constraint is actually two constraints that are artifacts of the derivation procedure and are required for well-posedness. They are

$$\text{rank } D_{12} = m_2$$

and

$$\text{rank } D_{21} = p_2.$$

One of the consequences of the above rank conditions is that the control input u must appear in the performance oriented regulated variable z . This condition is similar to a condition required for well posedness of the LQG problem. These conditions also insure the calculation of a realizable controller. It will also be seen in subsequent sections that these requirements cause some difficulty in calculating a low order controller.

An assumption which is not independent of the above rank conditions is that

$$D_{12} = [0 \ I]^T$$

and

$$D_{21} = [0 \ I].$$

Transformations to achieve the required forms for D_{12} and D_{21} will be derived later.

The final constraints are necessary for the design equations to yield a solution. They are not necessary in the strict sense. However, it is not known how to calculate controllers to achieve the bound when these conditions are violated. Sufficient conditions for the design equations to work are

The realizations of G_{12} and G_{21} are minimal.

$$\text{rank } G_{12}(j\omega) = m_2 \text{ for all } \omega$$

and

$$\text{rank } G_{21}(j\omega) = p_2 \text{ for all } \omega.$$

The design equations can be presented in an abbreviated form by denoting the solution to the Riccati equation

$$Q + XA + A^T X - XPX = 0$$

by its Hamiltonian matrix

$$X = \text{Ric} \begin{bmatrix} A & -P \\ -Q & -A^T \end{bmatrix}.$$

D_{11} is also partitioned as

$$D_{11} = \begin{bmatrix} D_{1111} & D_{1112} \\ D_{1121} & D_{1122} \end{bmatrix}.$$

Two intermediate variables are defined:

$$D_{1x} = [D_{11} \ D_{12}]$$

$$D_{x1} = [D_{11}^T \ D_{12}^T]^T.$$

Then define

$$R = D_{1x}^T D_{1x} - \begin{bmatrix} \Gamma^2 I_{m1} & 0 \\ 0 & 0 \end{bmatrix}$$

$$\bar{R} = D_{x1} D_{x1}^T - \begin{bmatrix} \Gamma^2 I_{p1} & 0 \\ 0 & 0 \end{bmatrix} .$$

$$X_\infty = \text{Ric} \begin{bmatrix} U & -P \\ -Q & -U^T \end{bmatrix}$$

where

$$P = BR^{-1}B^T, \quad U = A - BR^{-1}D_{1x}^T C_1, \quad \text{and} \quad Q = C_1^T C_1 - C_1^T D_{1x} R^{-1} D_{1x}^T C_1.$$

Similarly,

$$Y_\infty = \text{Ric} \begin{bmatrix} U & -P \\ -Q & -U^T \end{bmatrix}$$

where now

$$P = C^T \bar{R}^{-1} C, \quad U = A^T - C^T \bar{R}^{-1} D_{x1} B_1^T, \quad \text{and} \quad Q = B_1 B_1^T - B_1 D_{x1}^T \bar{R}^{-1} D_{x1} B_1^T.$$

Similarly to LQG design, matrices F and H are defined as

$$F = -R^{-1} [D_{1x}^T C_1 + B^T X_\infty] = [F_{11}^T \quad F_{12}^T \quad F_{22}^T]$$

$$H = -[B_1 D_{x1}^T + Y_\infty C^T] \tilde{R}^{-1} = [H_{11} \ H_{12} \ H_2].$$

At this point, it is necessary to perform tests to determine whether it is possible to achieve the specified Γ by designing a controller via the design equations. The first test has important practical consequences in terms of proper problem setup. It involves direct feed through of the disturbance input w in terms of D_{11} :

$$\Gamma > \max\{\sigma_{\max}[D_{1111} \ D_{1112}], \sigma_{\max}[D_{1111}^T \ D_{1121}^T]\}.$$

The last test involves the characteristics of the solutions to the two Riccati equations:

$$X_\infty > 0$$

$$Y_\infty > 0$$

and

$$\mu_{\max}(X_\infty Y_\infty) < \Gamma, \text{ where } \mu \text{ is an eigenvalue.}$$

Under the constraints listed and subject to passage of the tests an n^{th} order stabilizing controller which achieves the inequality $\|T\|_\infty < \Gamma$ is given by

$$D_{11} = -D_{1121} D_{1111}^T (\Gamma^2 I - D_{1111} D_{1111}^T)^{-1} D_{1112} - D_{1122}$$

D_{12} and D_{21} satisfy

$$D_{12} D_{12}^T = I - D_{1121} (\Gamma^2 I - D_{1111} D_{1111}^T)^{-1} D_{1121}^T \text{ and}$$

$$D_{21}^T D_{21} = I - D_{1112}^T (\Gamma^2 I - D_{1111} D_{1111}^T)^{-1} D_{1112}$$

from which

$$B_2 = (B_2 + H_{12})D_{12}$$

$$C_2 = -D_{21}(C_2 + F_{12})Z$$

$$B_1 = -H_2 + B_2D^{-1}_{12}D_{11}$$

$$C_1 = F_2Z + D_{11}D^{-1}_{21}C_2$$

$$A = A + HC + B_2D^{-1}_{12}C_1$$

and

$$Z = (I - \Gamma^{-2}Y_0X_0)^{-1}.$$

An n^{th} order controller which achieves the norm bound is then given by the realization (A, B_1, C_1) . There exist other controllers which satisfy the norm bound; however, they are not necessarily of n^{th} order. The controller design equations for this case are omitted. These more complex design equations may be found in Glover and Doyle^[1].

2.0 Transformation to the Standard Form

In Section 1.0, it was stated that the use of the design equations place constraints on the form of D_{12} and D_{21} . This section outlines in detail a method for achieving the required form for these matrices. The first step is to write them in terms of their singular value decompositions as is shown for D_{12} :

$$D_{12} = [U_{121} \ U_{122}][\Sigma_{12} \ 0]^T V_{12}^T$$

$$D_{12} = [U_{122} \ U_{121}][0 \ \Sigma_{12}]^T V_{12}^T$$

ORIGINAL PAGE IS
OF POOR QUALITY

$$D_{12} = [U_{122} \ U_{121}][0 \ I]^T \Sigma^{-1}_{12} V^T_{12}.$$

Similarly,

$$D_{21} = U_{21}[\Sigma_{21} \ 0][V_{211} \ V_{212}]$$

$$D_{21} = U_{21}[0 \ I][V_{212} \ V_{211}]^T.$$

Now let

$$X_{12} = \Sigma^{-1}_{12} V^T_{12}$$

$$X_{21} = U_{21} \Sigma^{-1}_{21}$$

$$U'_{12} = [U_{122} \ U_{121}]$$

$$V'_{21} = [V_{212} \ V_{211}].$$

Then

$$D_{12} = U'_{12}[0 \ I]^T X_{12}$$

$$D_{21} = X_{21}[0 \ I](V'_{21})^T.$$

The equations for z and y are

$$z = C_1 x + D_{11} w + D_{12} u$$

$$y = C_2 x + D_{21} w + D_{22} u$$

or

$$z = C_1 x + D_{11} w + U'_{12}[0 \ I] X_{12}$$

$$y = C_2x + X_{21}[0 \ I](V'_{21})^T w + D_{22}u$$

or

$$(U'_{12})^T z = (U'_{12})^T C_1 x + (U'_{12})^T D_{11} w + [0 \ I]^T X_{12} u$$

$$X^{-1}_{21} y = X^{-1}_{21} C_2 x + [0 \ I](V'_{21})^T w + X^{-1}_{21} D_{22} u.$$

Letting

$$z' = (U')^T z$$

$$u' = X_{12} u$$

$$y' = X^{-1}_{21} y$$

$$w' = (V'_{21})^T w$$

gives

$$A' = A$$

$$B'_1 = B_1 V'_{21}$$

$$B'_2 = B_2 X^{-1}_{12}$$

$$C'_1 = (U'_{12})^T$$

$$D'_{11} = (U'_{12})^T D_{11} V'_{21}$$

$$D'_{12} = [0 \ I]^T$$

$$C'_2 = X^{-1}_{21}C_2$$

$$D'_{21} = [0 \ I]$$

$$D'_{22} = X^{-1}_{21}D_{22}X^{-1}_{12}$$

The significance of the transformation is that the norms of z and w are preserved. This means that designing a controller to achieve a particular $\|T\|_\infty$ for the transformed system is equivalent to designing a controller to achieve the same goal for the untransformed system, once the reverse transformation is applied to the controller.

3.0 Modifications for Sampled-Data Systems

More traditional controller design techniques must be developed separately for sampled-data and continuous-time systems. Fortunately, this is not necessary for H^∞ designs due to the fact that the performance criterion has a relatively simple frequency domain representation. The approach is equivalent to "w-plane" design for single-input, single-output systems. The open loop system is assumed to have the form

$$x(k+1) = Ax(k) + B_1w(k) + B_2u(k)$$

$$z(k) = C_1x(k) + D_{11}w(k) + D_{12}u(k)$$

$$y(k) = C_2x(k) + D_{21}w(k) + D_{22}u(k).$$

This discrete time representation can be obtained using standard techniques such as those found in Kuo^[3]. The transfer function matrix is given by

$$G(z) = D + C(zI - A)^{-1}B$$

where for simplicity B , C , D are appropriate concatenations of the open loop system matrices. The bilinear transform

$$z = \frac{1 + w}{1 - w}$$

is applied to $G(z)$ to obtain

$$\begin{aligned} G(w) &= D + C[(I + wI)(I - wI)^{-1} - A]^{-1}B \\ &= D + C(I - wI)[w(I + A) - (A - I)]^{-1}B \\ &= D + C(I - wI)[wI - (I + A)^{-1}(A - I)]^{-1}(I + A)^{-1}B. \end{aligned}$$

Using the identity

$$[I - wI][wI - (I + A)^{-1}(A - I)]^{-1} = -I + \frac{[I - (I + A)^{-1}(A - I)]}{[wI - (I + A)^{-1}(A - I)]^{-1}}$$

$$G(w) = D - C(I + A)^{-1}B + C(I + A)^{-1}[wI - (I + A)^{-1}(A - I)]^{-1}(I + A)^{-1}B$$

so that the w -plane state space representation of $G(w)$ is

$$D_s = D - C(I + A)^{-1}B$$

$$C_s = 2C(I + A)^{-1}$$

$$B_s = (I + A)^{-1}$$

$$A_s = (I + A)^{-1}(A - I).$$

The controller is then designed using this representation to obtain $K(w)$, which is represented as a set of continuous time state equations with matrices A_k , B_k , C_k , D_k . The inverse transform

$$w = \frac{z - 1}{z + 1}$$

is applied to obtain $K(z)$. State space formulas for this transformation are

$$A_z = -(A_k + I) (A_k - I)^{-1}$$

$$B_z = (I + A_z) B_k$$

$$C_z = C_k (I + A_k)$$

$$D_z = D_k + C_k (I + A_k)^{-1} B_k.$$

4.0 Problem Setup for IMC Controller Design

The ACES configuration of the Marshall Space Flight Center Large Space Structure Ground Test Facility is shown in schematic form in Figure 1. The image motion compensation (IMC) subsystem is comprised of the line-of-sight (LOS) detectors and the IMC pointing gimbals. The base excitation table (BET) is the excitation device.

The natural setup for IMC controller design to minimize the effects of BET excitation is outlined here. The equations are obtained from a FEM model of the LSS ACES ground test facility. The first step in the problem setup is to define the z , w , y , and u . Since the actuators and sensors are limited to the IMC components, y and u are the x and y axis detector signals and pointing gimbal torques, respectively:

$$u = [IMC_x \ IMC_y]^T$$

$$y = [DET_x \ DET_y]^T.$$

The disturbance vector is most naturally chosen to be the x and y axis BET excitation table forces:

$$w = [BET_x \ BET_y].$$

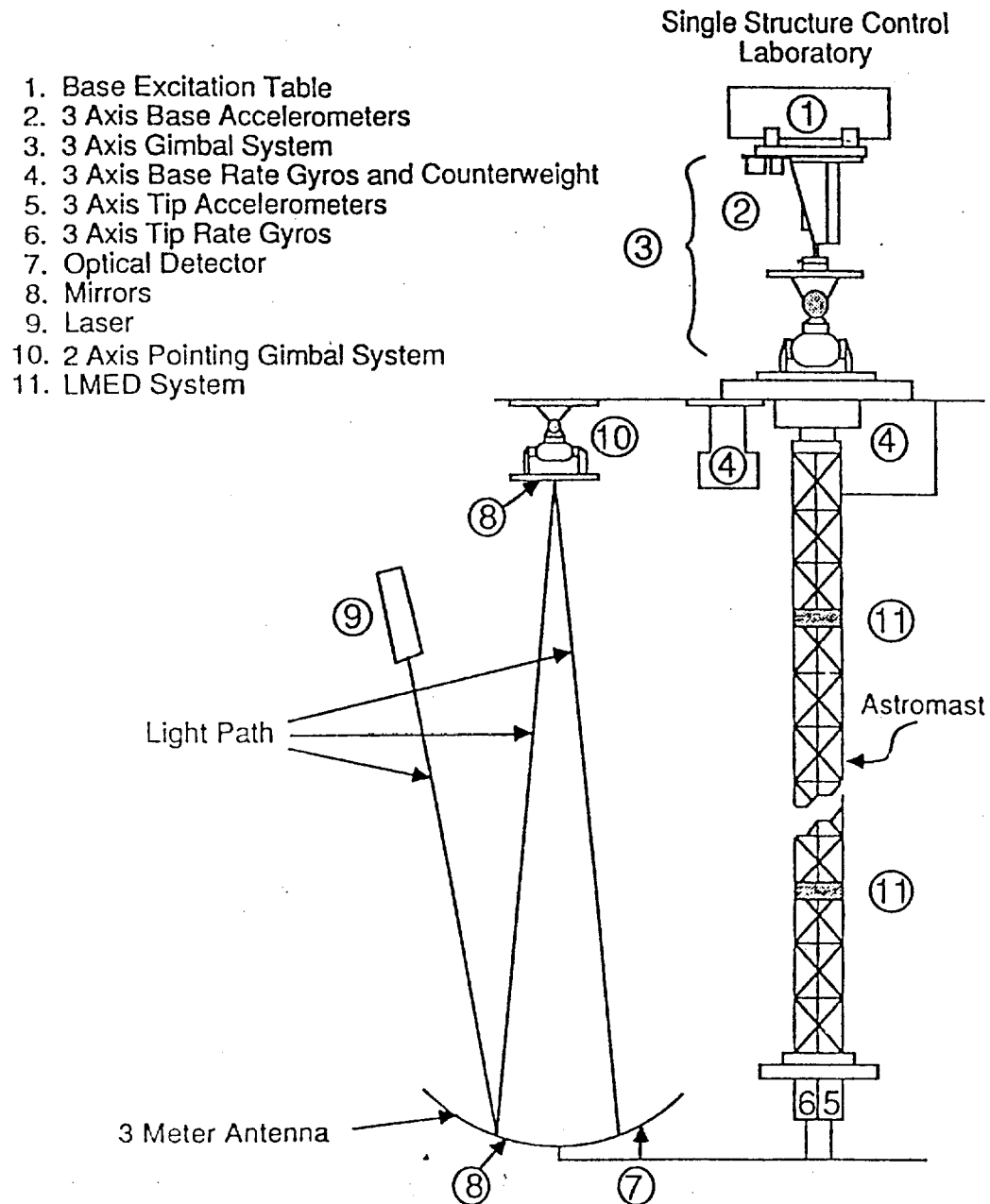


Figure 1. ACES Configuration of the Marshall Space Flight Center Large Space Structure Ground Test Facility

The first elements of the performance oriented controlled variable vector are

$$z_1 = [\text{DET}_x \text{ DET}_y]^T$$

since the goal of this system is to reduce the displacement of the line-of-sight of the laser beam from its equilibrium position on the detector. However, this is not sufficient to insure that the conditions of the design equations are met. The additional requirement of control input weighting is achieved by letting

$$z_2 = [\text{IMC}_x \text{ IMC}_y]^T.$$

This satisfies the rank condition on D_{12} . The remainder of the parameters of the problem can be chosen as follows.

B_1 is comprised of the appropriate modal gains at the BET actuators.

B_2 is comprised of the appropriate modal gains at the IMC actuators.

C_1 is comprised of the LOS gains at the detector

C_2 is also derived from the LOS gains at the detector.

Also,

A is in block 2×2 diagonal form and

$$D_{11} = [0 \ 0]^T, \quad D_{12} = [0 \ I]^T$$

$$D_{21} = 0, \quad D_{22} = 0.$$

The design equations still cannot be applied due to the rank

condition on D_{21} . This condition is equivalent to requiring that the same disturbance enters at two physically separated points in the system. The reason for the condition is a mathematical technicality. Unfortunately, it places actual constraints on the formulation of the problem.

A possible solution to this rank problem is to define D_{21} to be a very small constant with respect to the norm of the transfer function matrix G_{12} at all frequencies of interest.

However, it turns out that this is not the only theoretical problem with the above formulation. Another difficulty is the minimality condition on the G_{12} realization. The difficulty in the present setup is that the requirement is equivalent to the requirement that the disturbance (in this case the modes which can be excited by the BET) must be controllable at the IMC pointing gimbals. Unfortunately, this is not the case. In fact, the pointing gimbals have significant authority over only four or five modes. This is especially troublesome if the technique is used without regard to the minimality condition, as the design equations will yield a controller without regard to the satisfaction of the requirement. In this case, however, the controller will not satisfy the norm bound.

The minimality condition is an artifact of the particular procedure used to derive the design equations. In the usual factorization approach to H^∞ control, the minimality condition is not required since it is possible to carry along completely unrelated realizations for each of the four transfer functions matrices. It is interesting to note that an equivalent requirement for an LQG approach would be that the disturbance states be controllable as well as observable.

The consequences of violating the minimality condition are illustrated in Figures 2 and 3. Figure 2(a) is the magnitude of the open loop frequency response from the x-axis BET force input to the x-axis detector. The mode at .15 hertz is the AGS hinge point pendulum mode and is uncontrollable at the IMC gimbals. The other modes are controllable. Figure 2(b) is the magnitude of the closed loop frequency response from the x-axis BET force input to the x-axis detector. It is apparent that the modes which are controllable at the IMC gimbals have been effectively suppressed. However, the AGS hinge point pendulum mode continues to predominate, although the low frequency baseline has been reduced. Figure 3 illustrates the fact

that the closed loop norm is not improved. In Figure 3(a) the open loop frequency response from the y-axis BET force input to the y-axis detector has a maximum of roughly -3 decibels, as does the closed loop response of Figure 3(b). In each case, the values are reliable indicators of the infinity norm, since the the x and y axes are only slightly coupled. All frequency responses are in transformed input/output coordinates, as discussed in Section

As these problems were uncovered in the attempt to obtain an IMC controller design, it was decided to investigate the properties of the design equations using an extremely simple model. The next section documents the findings of this investigation.

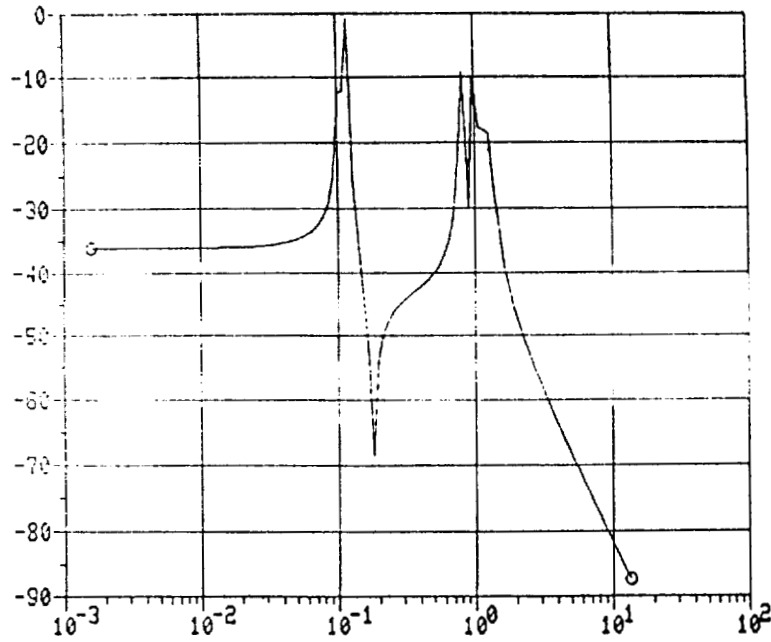


Figure 2(a). Open Loop Frequency Response Magnitude
(BET_x to LOS_x)

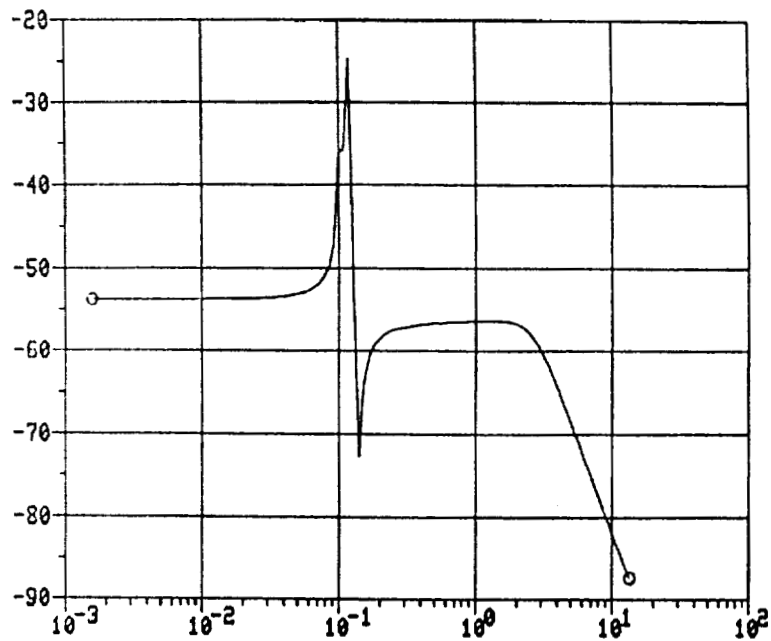


Figure 2(b). Closed Loop Frequency Response Magnitude
(BET_x to LOS_x)

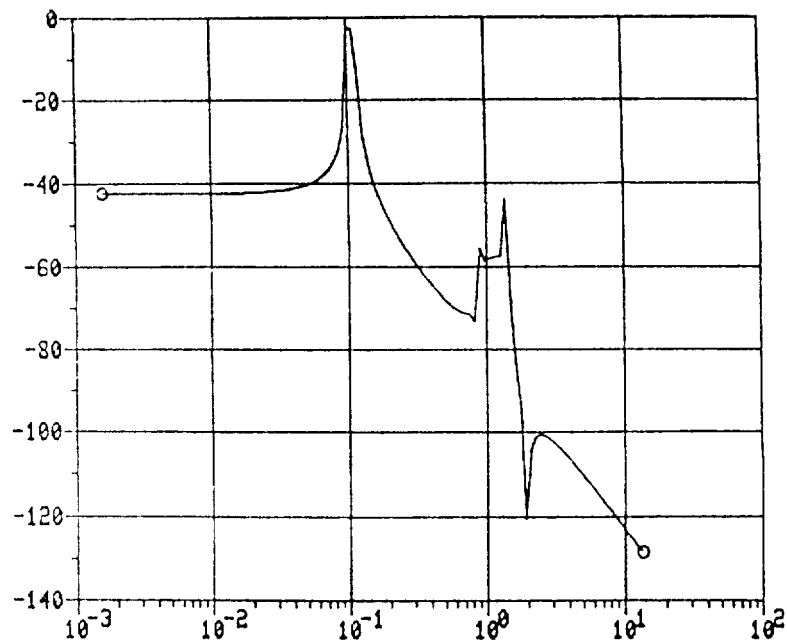


Figure 3(a). Open Loop Frequency Response Magnitude
(BET_y to LOS_y)

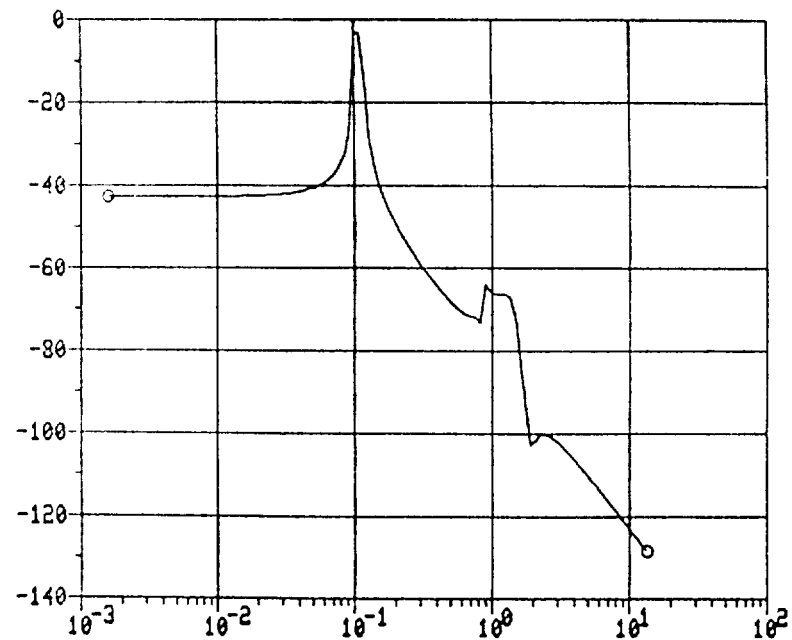


Figure 3(b). Closed Loop Frequency Response Magnitude
(BET_y to LOS_y)

5.0 SIMPLE TRACKING PROBLEM

The usual way to introduce design flexibility in the factorization approach to H^∞ optimal control is via frequency dependent weightings. To see the effect of frequency dependent weighting, the usual parametrization of the closed loop transfer function is useful. For a stable plant, the closed loop transfer function can be written as

$$T_1 = T_2 Q T_3$$

where

$$T_1 = G_{11}$$

$$T_2 = G_{12}$$

$$T_3 = G_{21}.$$

Any stable transfer function Q generates a stable closed loop transfer function and a controller which achieves that transfer function. In fact, every stable closed loop transfer function is generated by some stable Q .

The usual requirement for a solution to exist is that T_2 and T_3 have constant rank on the extended $j\omega$ axis. No minimality condition is required. Weighting is introduced by solving the modified problem of minimizing the infinity norm of

$$T_1 = T_2 W_2 Q W_3 T_3$$

where W_2 and W_3 are chosen to satisfy the constant rank condition and to define frequency ranges over which optimality is emphasized. The major difference in the general H^∞ problem and the problem solved by the new design equations in question is the presence of the two minimality conditions. The effects of the constraints are most easily seen by examining the block diagram of Figure 4.

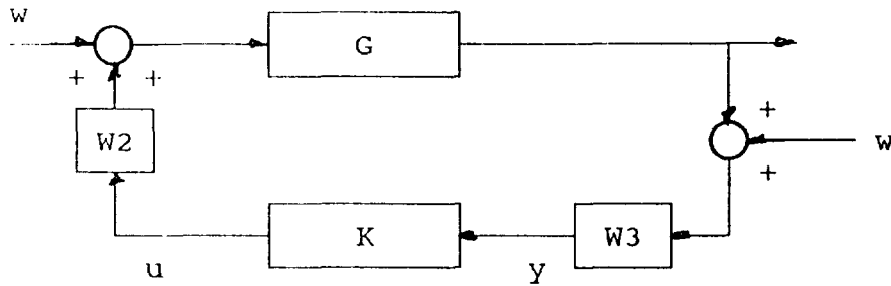


Figure 4. Block Diagram Used for Examining the Effects of Frequency Dependent Weighting.

The minimality constraints imply the following:

The system realization is simultaneously completely controllable by u and observable by z .

The system realization is simultaneously completely controllable by w and observable by y .

The first can be satisfied by including the signal y in the definition of z . A consequence of this is that T_1 is also weighted by W_3 . The second condition can only be satisfied if W_2 has zero dynamical order and is a fundamental limitation of the new algorithm. It should be pointed out that if W_2 is derivative in nature, an appropriate realization can be obtained, but it will generally increase the order of the plant, and hence the controller. Also, the appropriate modifications to account for nonzero D_{22} must be used. The actual details of combining the weightings into an appropriate realization remain to be worked out.

Although no results are available using the weighting scheme of Figure 4, the alternate weighting scheme of Figure 5 was used with an extremely simple plant to illustrate what is possible when all of the constraints of the new algorithm are satisfied.

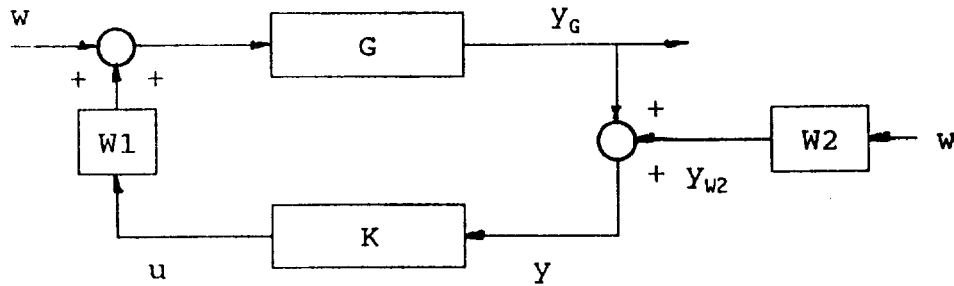


Figure 5. Alternate Weighting Scheme Used for a Simple Tracking Problem

The plant transfer function is

$$G(s) = 1/(s + 1).$$

The weights are given by

$$W_1 = .99(s/10 + 1)$$

$$W_2 = .001.$$

The z vector is defined by

$$z_1 = Y_G - Y_{W2}$$

$$z_2 = 10^{-5}u.$$

It is interesting to note that although the plant is scalar, the two-dimensional nature of the z vector means that H^∞ control is inherently a multivariable problem. The z_2 element is chosen small enough to simplify the process of obtaining an approximate solution. Another important point to note is that the .99 multiplier in W_1 is necessary to achieve a high gain controller.

Figure 7 is the closed loop frequency response when the

controller is implemented in the block diagram of Figure 6. The important point to be made here is that an H^∞ approach can be used to design a simple tracking system with specified closed loop bandwidth (by choosing the break frequency of W_1) and specified steady-state error constants (in this case less than .01 error to a unit step input).

CONCLUSIONS AND RECOMMENDATIONS

The design equations and appropriate constraints and assumptions for a new simplified algorithm for designing H^∞ optimal controllers have been reviewed. A transformation required to satisfy an important constraint has been derived. The use of the design equations with sampled-data systems is outlined in detail and the required state space transformations are summarized.

The requirement of using frequency-dependent weights is illustrated via two examples. One of the examples is a simplified but realistic design for a subsystem of a large space structure ground test verification facility. The other is used to illustrate the efficacy of a particular weighting scheme.

Further work is indicated in the area of developing strategies for finding weights to achieve particular design goals. It is also suggested that possible tradeoffs between performance and robustness be investigated by studying various problem formulations.

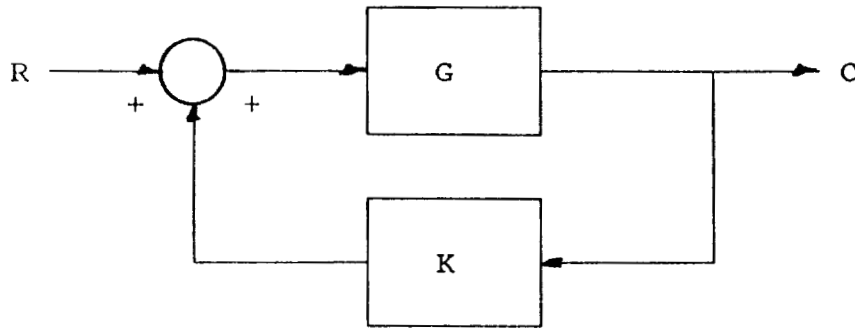


Figure 6. Block Diagram for Implementation of Controller for Simple Tracking Problem.

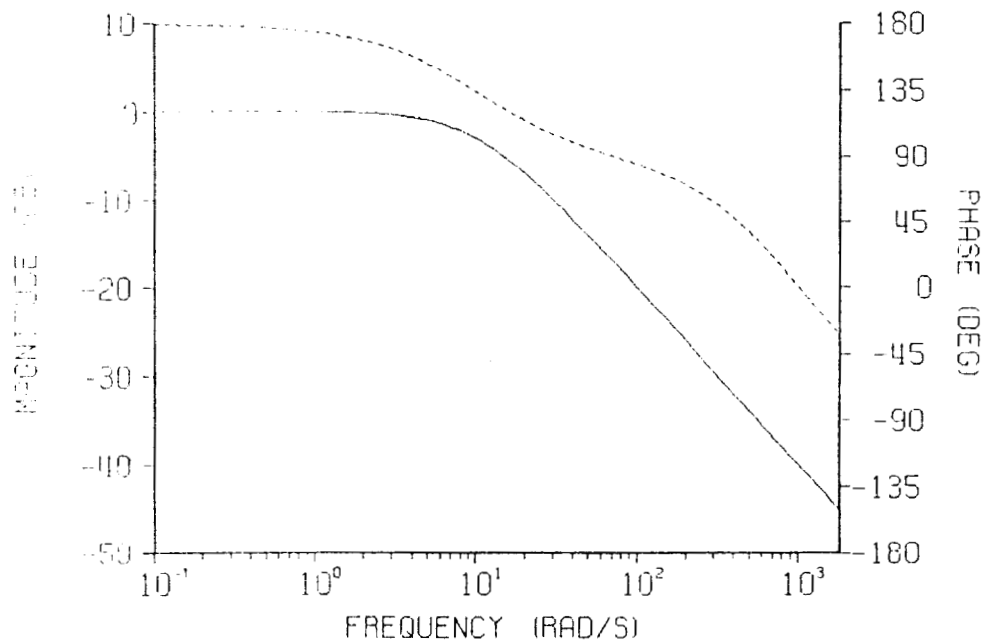


Figure 7. Closed Loop Frequency Response of Simple Tracking Problem of Figure 6.

REFERENCES

- [1] K. Glover and J. Doyle, "State-Space Formulae for All Stabilizing Controllers That Satisfy an H^∞ Norm Bound and Relations to Risk Sensitivity," System and Control Letters, vol. 11, pp. 167-172, 1988.
- [2] K. Glover, "All Optimal Hankel Norm Approximations of Linear Multivariable Systems and their L-Infinity Error Bounds," Int. J. Contr., vol. 39, pp. 1115-1193, 1984.
- [3] B.C. Kuo, Digital Control Systems, Holt, Rinehart, and Winston, New York, 1980.

1989

NASA/ASEE SUMMER FACULTY FELLOWSHIP PROGRAM

**MARSHALL SPACE FLIGHT CENTER
THE UNIVERSITY OF ALABAMA IN HUNTSVILLE**

**EVALUATION OF THE HEAT TRANSFER MODULE (FAHT) OF FAILURE
ANALYSIS NONLINEAR THERMAL AND STRUCTURAL INTEGRATED
CODE (FANTASTIC)**

Prepared by:	Majid Keyhani
Academic Rank:	Assistant Professor
University and : Department	University of Tennessee, Knoxville Mechanical & Aerospace Engineering

NASA/MSFC:

Laboratory:	Structures and Dynamics
Division:	Thermal Engineering & Life Support
Branch:	Thermal Analysis

MSFC Colleague:	Kenneth E. McCoy
-----------------	------------------

Date:	September 12, 1989
-------	--------------------

Contract No.:	The University of Alabama in Huntsville, NGT-01-008-021
---------------	---

11

Evaluation of the Heat Transfer Module (FAHT) of Failure Analysis Nonlinear
Thermal and Structural Integrated
Code (FANTASTIC)

Majid Keyhani

Assistant Professor of Mechanical and Aerospace Engineering
University of Tennessee
Knoxville, Tennessee

ABSTRACT

The heat transfer module of FANTASTIC Code (FAHT) is studied and evaluated to the extend possible during the ten weeks duration of this project. A brief background of the previous studies is given and the governing equations as modeled in FAHT are discussed. FAHT's capabilities and limitations based on these equations and its coding methodology are explained in detail. It is established that with improper choice of element size and time step FAHT's temperature field prediction at some nodes will be below the initial condition. The source of this unrealistic temperature prediction is identified and a procedure is proposed for avoiding this phenomenon. It is further shown that the proposed procedure will converge to an accurate prediction upon mesh refinement. Unfortunately due to lack of time, FAHT's ability to accurately account for pyrolysis and surface ablation has not been verified. Therefore, at the present time it can be stated with confidence that FAHT can accurately predict the temperature field for a transient multi-dimensional, orthotropic material with directional dependence, variable property, with nonlinear boundary condition. Such a prediction will provide an upper limit for the temperature field in an ablating decomposing nozzle liner. The pore pressure field, however, will not be known.

ACKNOWLEDGEMENT

It was a great pleasure for me to work as a NASA/ASEE Summer Faculty Fellow at Marshall Space Flight Center. Mr. Richard Brown was instrumental in providing this opportunity for my participation and I am grateful for it.

My NASA/MSFC Colleague, Dr. Kenneth E. McCoy "Doc" was a great help and a steadfast teacher. I would like to acknowledge the rest of staff of ED64 Branch, specifically the Branch Chief Jim Owen, for creating a helpful and a pleasant environment to work in. I would like to thank Glenn Jamison for providing his extensive literature collection to me. My discussions with Roy Sullivan were very helpful and is appreciated.

Finally, I like to express my thanks and appreciation to Dr. Gerald Karr and Dr. Frank Six for going beyond the call of duty to make sure that the Summer Faculty Fellows had an enjoyable and rewarding experience at MSFC.

TABLE OF CONTENTS

	Page
ABSTRACT	XVII-i
ACKNOWLEDGEMENT	- ii
NOMENCLATURE	- iv
I. INTRODUCTION	- 1
I.1 Overview	- 1
I.2 Objectives of the Present Work	- 1
II. BACKGROUND	- 2
II.1 Previous Work	- 3
II.2 Governing Equations	- 6
II.3 FAHT's Capabilities and Limitations	- 8
III. VERIFICATION OF FAHT'S CAPABILITIES	- 10
III.1 Transient Solution Routine	- 10
III.2 Nonlinear Boundary Condition Routine	- 19
III.3 Variable Property Routine	- 20
III.4 Application to MNASA Nozzle	- 21
IV. CONCLUSIONS AND RECOMMENDATIONS	- 25
IV.1 Conclusions	- 25
IV.2 Recommendations	- 26
REFERENCES	- 28

NOMENCLATURE

B	Permeability matrix
B_{ij}	Components of the Permeability matrix
C_m	Defined by Eq. (FAHT-5)
C_p	Specific heat
k	Thermal Conductivity
K	Thermal Conductivity matrix
K_{ij}	Components of the Thermal Conductivity matrix
P	Pore pressure
Q	Volumetric heat source/sink
Q_c	Heat convected by pyrolysis gas, defined by Eq. (FAHT-2)
R_g	Specific gas constant
\dot{S}	Rate of surface recession
t	Time
Δt	Time step size in an analysis
T	Temperature
T_g	Gas Temperature
T_i	Initial Temperature
T_s	Surface Temperature
V	Velocity vector
∇	Vector differential operator del
x	Coordinate in 3-D space
x_i	A generic cartesian coordinate
Δx	Element thickness in the direction of heat flow
α	Thermal diffusivity
δ	Penetration depth
γ	Defined by Eq. (FAHT-3)
ϵ	Emissivity
λ	Eigen value of the exact solution
μ	Dynamic viscosity
π	Pi
ρ	Density
ϕ	Porosity
Φ	Volumetric mass source/sink

I. INTRODUCTION

1.1 Overview

The FANTASTIC code is in its final stage of development by Failure Analysis Associates (FaAA) for Marshall Space Flight Center. The code is presently under review and evaluation for its capabilities. The intended use of the Code is to increase the capabilities and accuracy of the thermal and structural analysis of solid rocket motor nozzles. The code consists of three modules for thermochemical analysis, heat transfer and mass diffusion analysis, and structural analysis.

1.2 Objectives of the Present Work

The present work is limited to the evaluation of the heat transfer and mass diffusion module (FAHT) of the FANTASTIC Code. In order to proceed with the stated task within the rather short time period of the project, the following sub-tasks were chosen:

1. A brief review of previous efforts in the area of code development.
2. Verification of the various required capabilities of the FAHT module, such as transient, nonlinear boundary condition and variable property solution routines.
3. A limited attempt at use of FAHT for prediction of the temperature distribution in MNASA nozzle.

II. BACKGROUND

Charring ablators have proven to be one of the most successful thermal protection systems for applications with high thermal loading such as reentry and solid rocket nozzles. The materials used are a combination of plastics that decompose to a porous char zone and pyrolysis gases. The pyrolysis gases transport energy to the surface under thermal loading thereby reduce the rate of energy input into the virgin material. The decomposition process along with endothermic reactions of the pyrolysis gases with the carbon in the char zone are of further help in reducing the rate of energy input into the virgin material. A cross-sectional view of a charring and decomposing ablator of a nozzle is depicted in Fig. 1. The events taking place in the char and pyrolysis zones can be summarized as follows:

Char Zone

- a. Thickness of this zone is about 2 to 4 mm depending on the material used.
- b. Pyrolysis gases flowing through this porous zone have a cooling effect due to convective transport of energy to the surface.
- c. Pyrolysis gases are not frozen in this region and endothermic reactions with carbon of the char zone takes place, resulting in a "cooling" of the char zone.
- d. Chemical reactions between the char zone and the pyrolysis gases result in a constant change in the porosity and the permeability of the char layer.

Pyrolysis Zone

- a. Thickness of this zone in typical ablators is about 1 to 2 mm.
- b. Porosity and permeability in this region are changing rapidly.
- c. A volumetric energy source/sink is present due to decomposition of the virgin material.

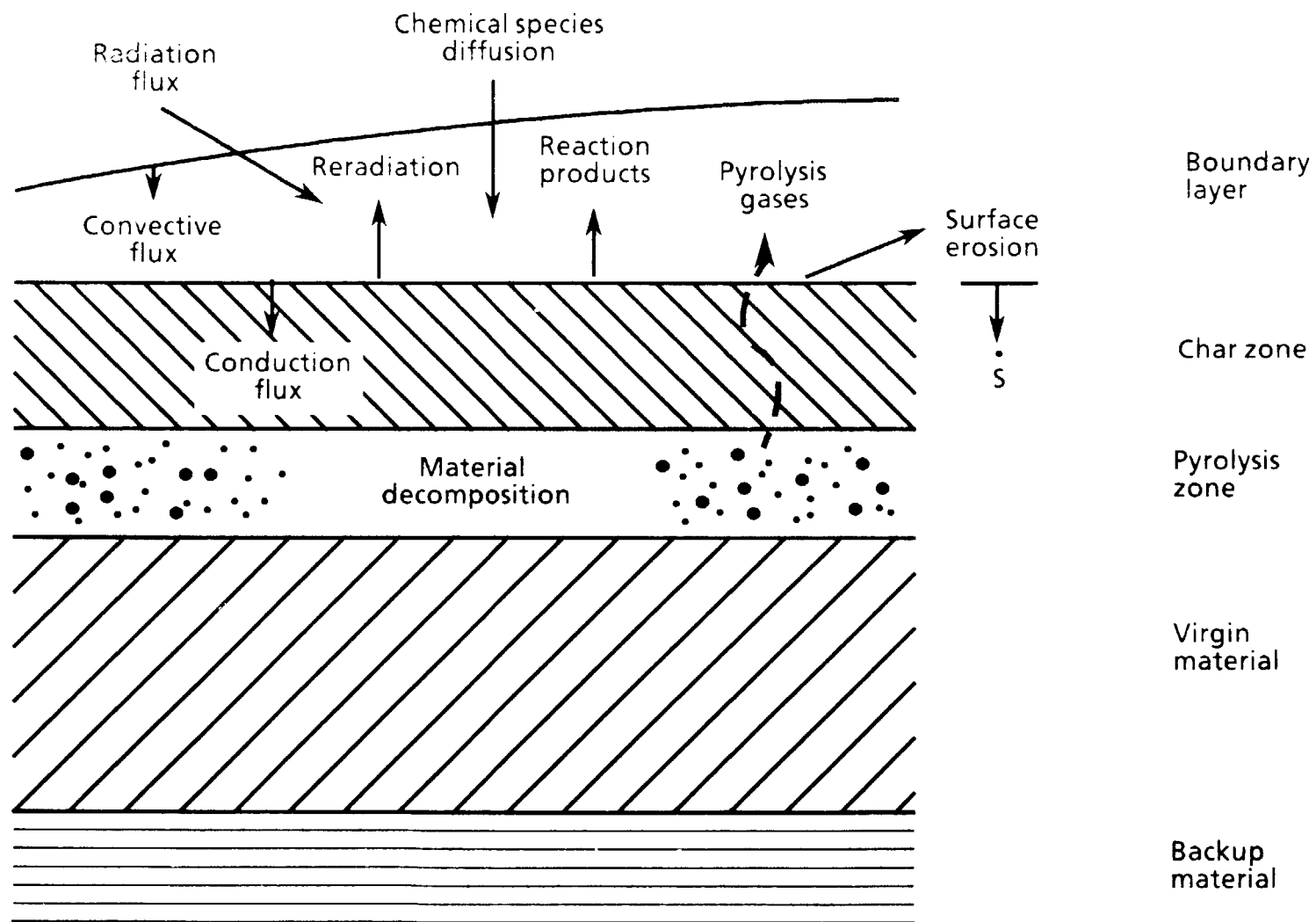


Figure 1. Cross-sectional view of a charring and decomposing ablator of a nozzle.

The above summary of the phenomena taking place in a charring ablator clearly shows the complexity of the problem. Other factors that add to the difficulty of accurate prediction of temperature and pore pressure values in a charring ablator are:

- a. Temperature variation in space and time is substantial, therefore the evaluation of the thermophysical properties at the proper temperature is very important.
- b. The material is orthotropic, therefore the conservation equations for energy and momentum are more difficult to model.
- c. As mentioned earlier porosity and permeability are changing with time. Therefore, they are variables in the momentum equation. The porosity variation can be accounted for via its relation to density variation governed by the rate equation of the Arrhenius form. The modeling of the variable permeability for an orthotropic material, however, is not trivial. It appears that no empirical relation for relating the permeability of this class of materials to its porosity is available at the present time.
- d. The nonequilibrium chemical reaction between the pyrolysis gases and the char zone has not been thoroughly investigated for all the candidate materials for nozzle liner.

II.1 Previous Work

A review of the literature indicates that research and code development effort in the area of thermal analysis of charring and decomposing ablators had a rather high priority for NASA during the decade of 1962-1972. It appears that the development of new candidate materials for a charring-decomposing ablator may require initiation of a rigorous research program in this important area. A brief summary of the previous work is given in this report.

- Aerotherm charring material thermal response and ablation program (CMA, Aerotherm report 75-148, 1975)
 - One-dimensional transient finite difference model
 - No resistance to flow of pyrolysis gases
 - Frozen flow of pyrolysis gases through the char zone
- NASA report NASA TN-D-6895 (1972)
 - Two-dimensional transient axisymmetric finite difference model
 - Resistance to flow of pyrolysis gases incorporated via Darcy's law
 - Frozen flow of pyrolysis gases through char zone
- NASA reports NASA TN D-1370 (1962) CHAP I and NASA TN D-2976 (1965) CHAP II
 - One-dimensional Transient finite difference program
 - No resistance to flow of pyrolysis gases
 - Frozen Flow of Pyrolysis gases through the char zone (CHAP I)
 - Chemical reaction between the pyrolysis gases and the char incorporated (CHAP II)
- NASA report NASA TN D-6085 (1970), COSMIC
 - One-dimensional transient finite difference model
 - No resistance to flow of pyrolysis gases
 - Frozen flow of pyrolysis gases through the char zone

- NASA report NASA CR-1903 (1971)
 - One-dimensional steady-state finite difference model
 - Modified form of Darcy's equation used to model resistance to flow of pyrolysis gases
 - Flow of pyrolysis gases through the char zone analyzed as
 1. Frozen
 2. Equilibrium
 3. Non-Equilibrium

II.2 Governing Equations

In this section the energy, momentum and mass conservation equations as they appear in the FANTASTIC/FAHT theoretical manual (version 1.0) will be reported and discussed.

Energy equation:

$$\rho C_p \frac{\partial T}{\partial t} = \frac{\partial}{\partial x_i} \left(K_{ij} \frac{\partial T}{\partial x_j} \right) + Q \quad (\text{FAHT-1})$$

The volumetric source/sink term (Q) in Eq. (FAHT-1) accounts for the energy associate with the decomposition process. It should be noted that the energy transport term due to convection of pyrolysis gases does not appear in Eq. (FAHT-1). FAHT theoretical manual states that the heat convected by pyrolysis gases is calculated by

$$Q_c = \rho C_p \mathbf{V} \cdot \nabla T, \quad (\text{FAHT-2})$$

and can be accounted for via: NONLINEARHEATBC, THERMALGAPCONTACT OR LUMPEDHEATCAPACITY Options.

Proper form of the energy equation is given by

$$\rho C_p \frac{\partial T}{\partial t} + \rho C_p \mathbf{V} \cdot \nabla T = \frac{\partial}{\partial x_i} \left(K_{ij} \frac{\partial T}{\partial x_j} \right) + Q \quad (1)$$

It is very important to note that the temperature pressure and velocity in a decomposing ablator are undergoing substantial changes with a rather small change in time. Literature contains a very large volume of papers dealing with various convection heat transfer problems. This author is not aware of a single case where the convection term is not explicitly treated in the energy equation as is the case with Eq. (FAHT-1).

In verbal communication with Dr. McCoy (NASA/MSFC-ED64) FaAA Personnel have stated that the heat convected by pyrolysis gases (Eq. FAHT-2) is accounted for as part of the load term Q. In that case the energy equation is not related accurately.

Momentum Equation:

$$\mathbf{V} = - \frac{\gamma}{\phi \mu} \mathbf{B} \nabla P^T \quad (\text{FAHT-3})$$

$$\gamma = R_g \text{ when ideal gas or } \gamma = \frac{dP}{d\rho}$$

The momentum equation as given by Eq. (FAHT-3) is dimensionally inconsistent. The proper form of the momentum equation based on the Darcy law is

$$\mathbf{V} = - \frac{1}{\phi \mu} \mathbf{B} \cdot (\nabla P) \quad (2)$$

Mass Conservation Equation:

$$\frac{d}{dt} [\phi \rho] + \nabla \cdot (\phi \rho \mathbf{V}) = \Phi \quad (\text{FAHT-4})$$

In order to obtain an explicit equation for pore pressure, FAHT theoritical manual states that Eqs. (FAHT-3) and (FAHT-4) are combined to get,

$$\frac{\partial}{\partial t} [C_m P] = \frac{\partial}{\partial x_i} \left(\frac{B_{ij}}{\mu} \frac{\partial P}{\partial x_j} \right) + \Phi \quad (\text{FAHT-5})$$

$$\text{where } C_m = \phi \frac{\partial \rho}{\partial P} \quad \text{or} = \quad \frac{\phi}{R_g T}$$

It should be noted that the pore pressure equation as given by Eq. (FAHT-5) is also dimensionally inconsistent. The proper form of the pore pressure equation is

$$\frac{d}{dt} (\phi \rho) = \frac{\partial}{\partial x_i} \left(\frac{\rho B_{ij}}{\mu} \frac{\partial P}{\partial x_j} \right) + \Phi \quad (3)$$

$$\text{where } \rho = \frac{P}{R_g T}$$

The problem with Eqs. (FAHT-3) and (FAHT-5) may be due to a typographical error, and they are correct in the program. If that is the case, then it is an indication of a poor editing job of various versions of manual up to version 1.0 which have been released by FaAA.

II.3 FAHT'S Capabilities and Limitations

In order to get an estimate of FAHT's potential capabilities it is necessary to come to a conclusion about the governing equations as described in FAHT's theoretical manual (version 1.0). The following assumptions are made with regards to modeling of the governing equations in the FAHT module.

- (a) The convected energy by the pyrolysis gases are accounted for as part of the load term (Q) in Eq. (FAHT-1)
- (b) The problem with Eqs. (FAHT-3) and (FAHT-5) is typographical, and these equations are indeed dimensionally consistent in the program.

Based on the above assumptions, FAHT's potential capabilities in analysis of a charring-decomposing ablator are as follows:

- (i) The temperature field solution will have some errors due to lack of explicit treatment of the convection term.
- (ii) The pore pressure equation, as given by Eq. (3) is nonlinear. This equation, however, is treated as a linear equation in FAHT. Therefore, the pore pressure solution will not be accurate, which will result in an inaccurate velocity solution. The inaccuracy associated with the velocity solution, in turn, will increase the error in the temperature solution.
- (iii) The flow of pyrolysis gases through the char zone are modeled as a non-reacting low (frozen). Therefore, the endothermic reactions which take place in this zone can not be accounted for. Furthermore, the changes in the porosity and permeability in this zone cannot be calculated and accounted for.
- (iv) The permeability of the material is assumed to have the same value in the virgin, decomposition and char zones. As mentioned earlier, the permeability is changing rapidly with time in the decomposition zone. Nonetheless, FAHT can not account for this variation.
- (v) There are no provisions for accounting for the initial porosity of the virgin material.
- (vi) The momentum equation is based on the Darcy law. However, it is known (NASA CR-1903, 1971) that the inertial effects play an important role due to relatively high mass fluxes of the degradation products. An accurate modeling of the momentum equation requires the inclusion of the Forchheimer term. Another motivation for the use of Forchheimer-extended Darcy equation of motion for flow through porous media is the following. One of the objectives of the exploratory test program of the Solid Propulsion Integrity Program (SPIP) is to provide empirical relations for permeability of various candidate materials. There may be cases where the permeability should be determined via the Forchheimer-extended Darcy equation. In that case we do not have any analysis tool that can properly use the permeability data.

III. VERIFICATION OF FAHTS' CAPABILITIES

III.1 Transient Solution Routine

In the process of assessment and verification of the heat transfer module of the FANTASTIC code, many attempts have been made at obtaining solutions for simple cases of transient conduction heat transfer. It appears that in many cases the predicted short-time temperatures at some nodes were below the initial input values. Thus, the code indicated that those nodes were cooling while the physics of the problem imposed a rather high heating rate for the material. A number of explanations along with corrective remedies have been forwarded by FaAA. It has been suggested by FaAA that for high heating rate cases (high thermal gradients) the input values of time step and element size should be such that the value of the element Fourier number is rather low. The element Fourier number is defined as $\alpha \Delta t / \Delta x^2$. The parameter α is the thermal diffusivity of the material and can not be arbitrary changed. The only alternative for reducing the element Fourier number is then using a smaller time step and/or larger elements. The choice of a smaller time step and/or larger element size does not resolved the problem and indeed results in even lower values. Therefore, we are in a situation where we cannot get realistic solutions to transient problems with high heating rates. It may be noted that our intended application is precisely what FAHT apparently cannot solve.

The source of the problem with the FAHT's inability for solving transient problems with high gradients is not a "bug." It is a rather fundamental problem related to the physics of the process. Before we proceed further, the terms "unrealistic" and "realistic" should be defined. First, note that in solving "real world" problems we do not know the exact answer. Thus, a realistic answer is one which makes physical sense to the analyst but may not be accurate. Realistic answers can be very dangerous. Shortly, I will explain why I consider them dangerous to an inexperienced analyst. The unrealistic answer is very easy to detect such as the case of cooling nodes predicted by FAHT where the model has specified a high heating rate.

Finite difference computer codes rarely give an unrealistic answer to a high heating rate transient problem. However, finite element codes, depending on the choice of

shape function, are prone to give unrealistic answers when the thermal gradients are high. As stated earlier, the problem with this class of finite element programs (including FAHT) is one of fundamental nature. A high thermal gradient results in a propagation of a thermal front into an isothermal domain (initial condition). For a given time step, this thermal front moves into the domain by a distance called penetration depth (δ). Figure 2 depicts the movement of penetration depth into a domain. If δ is smaller than the element length (Δx), then depending on the choice of the shape function, the nodal temperatures are determined with unrealistic values as depicted in Fig. 3. For further detail about this phenomena please refer to Hogge and Gerrekens (1982). The remedy for this problem is a choice of a larger time step and/or smaller elements. Obviously, if the solution routine is explicit, then the chosen time step should not violate the stability criterion.

To illustrate the fact that the suggested remedy does indeed result in a realistic answer by FAHT, let's consider a simple test problem as shown in Fig. 4.

Test Problem

Transient one-dimensional conduction heat transfer
in a plane wall with constant properties. The
parameters of the problem are:

width of the wall = 0.2m
density = 2600 kg/m³
specific heat = 808 J/kg·K
thermal conductivity = 3.98 W/m·K

Boundary Conditions:

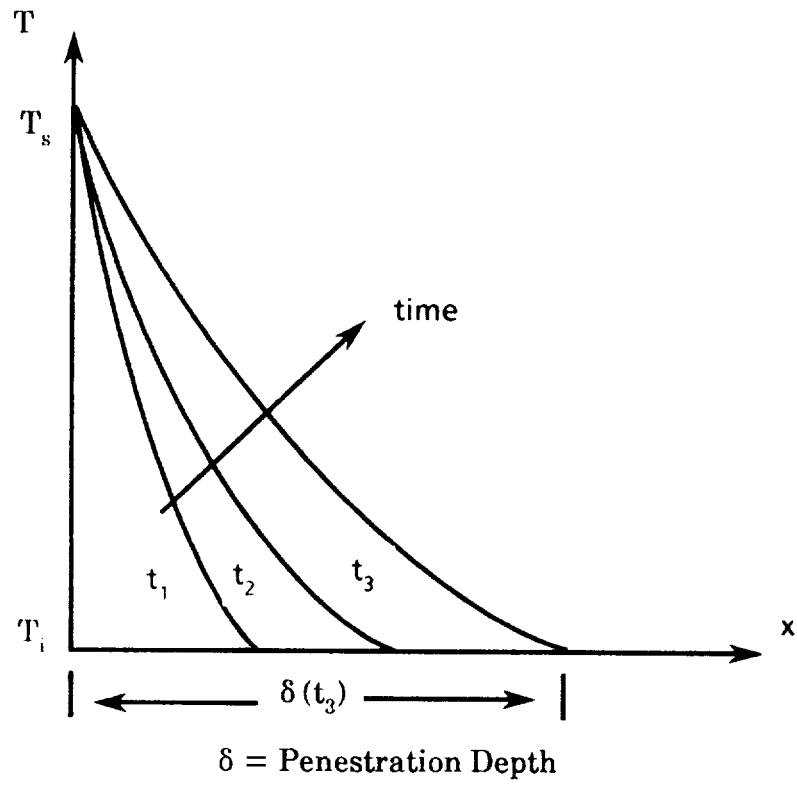
$$T(x = 0, t) = T_g = 3600 \text{ K}$$

$\partial T / \partial X (x = L, t)$, insulated backwall

Initial Condition:

$$T(x, t = 0) = T_i = 300 \text{ K}$$

The temperature distribution in the wall at time = 10 seconds will be presented in the following tables. All solutions are obtained via the implicit formulation.



$$T(0,t) = T_s; \quad \left. \frac{\partial T}{\partial x} \right|_{x=\infty} = 0;$$

$$T(x,0) = T_i$$

Figure 2. Short-time transient temperature profile in a domain.

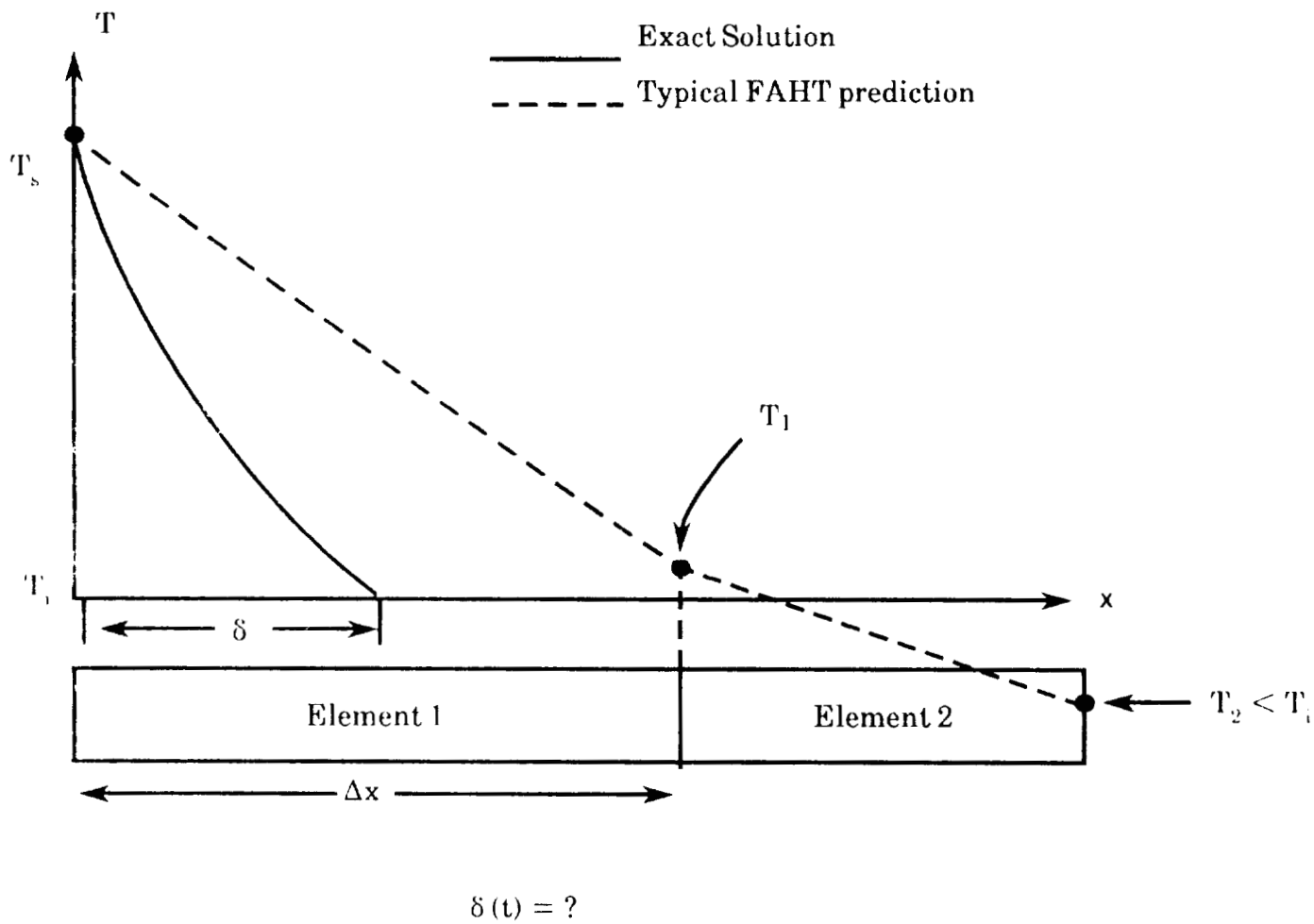
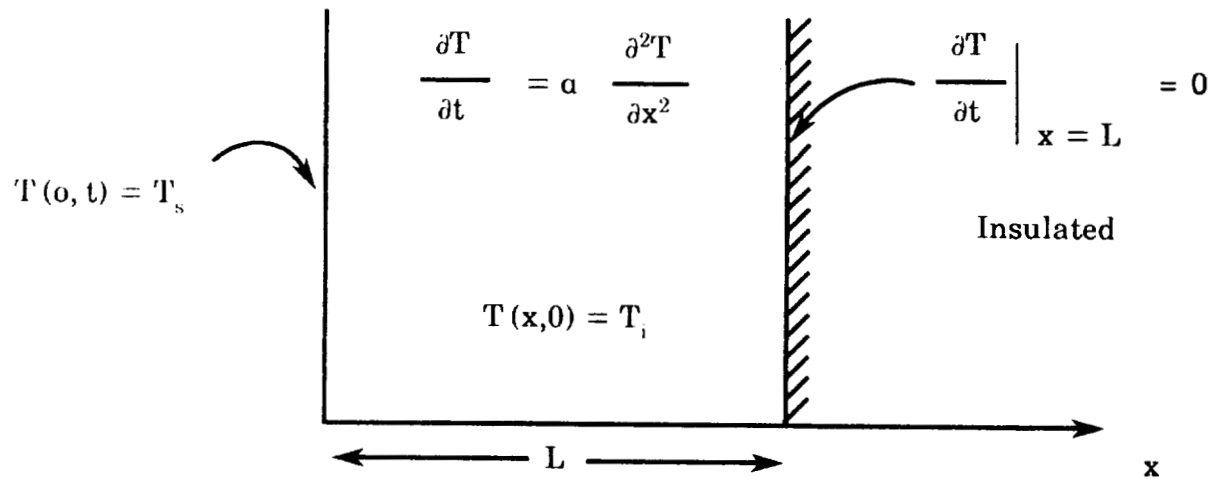


Figure 3. Element size (Δx) versus Penetration depth (δ).



Input Data:

$$T_s = 3600 \text{ K}, \quad T_i = 300 \text{ K}$$

$$K = 3.98 \text{ W/m}\cdot\text{K}$$

$$\rho = 2600 \text{ Kg/m}^3$$

$$C_p = 808 \text{ J/Kg}\cdot\text{K}$$

$$L = 0.2 \text{ m}$$

Exact Solution:

$$\frac{T(x, t) - T_i}{T_s - T_i} = 1 - \frac{4}{\pi} \sum_{n=0}^{\infty} \frac{\sin(\lambda_n x)}{(2n + 1)} e^{-(\lambda_n^2 \alpha t)}$$

$$\lambda_n = \frac{(2n + 1) \pi}{2L}$$

Figure 4. Description of the test problem and its exact solution.

Table 1: FAHT temperature predictions ($T(x,t) - T_i$) for various element sizes, and time steps at time = 10 seconds.

Run No.	X = 0.01 (m)	0.02	0.03	0.04	No. of Elements	Time Step (Seconds)
FE-1	189.4	-120.1	24.6	-2.4	20	2
FE-2	261.1	-124.3	20.3	-0.4	20	0.2
FE-3	233.0	-6.9	-0.1	0.03	40	2
FE-4	272	1.0	0	0	80	2

The following observations can be made with regards to the results in Table 1:

- A comparison of the results of runs FE-1 and FE-2 shows that when unrealistic (negative) nodal values are obtained, a decrease in time step does not help.
- A comparison of the results of runs FE-1, FE-3, and FE-4 indicates that when unrealistic nodal values are obtained, increasing the number of elements thereby decreasing Δx yields a realistic solution.
- Consider that the exact answer is unknown. Furthermore, consider that the first choice of an analyst was the input values of run FE-4. The results of this run are indeed realistic and make sense. A 20cm wall is divided into 80 elements ($\Delta x = 2.5$ mm). Moreover, a time step of 2 seconds for transition from zero time to 10 seconds is rather a reasonable choice.
- The above discussion indicates that the analyst may well choose to accept the results of run FE-4 as reasonable. However, the "realistic" answer of the run FE-4 is in substantial error. Indeed, the values at $x = 0.01$ and 0.02 are, respectively, 21% and 74% lower than the exact answer. This is a good example of the case where "realistic" answers should be treated with caution.

I hope that my earlier comment about the potential danger of a “realistic” answer is clarified. It is reasonable to ask then, how should an analyst ensure that the realistic answer is reasonably accurate when the accurate answer is unknown?

The penetration depth (δ) of a thermal front into an isothermal semi-infinite domain can be approximated as (Ozisik, 1980)

$$\delta \approx \sqrt{12 \alpha t} \quad (4)$$

In order to obtain a realistic answer, δ for the first time step should be large enough to cover a number of elements i.e.,

$$\delta(\Delta t) = \sqrt{12 \alpha \Delta t} > \Delta x \quad (5)$$

The stability criterion for the explicit solution scheme is given by,

$$\Delta x > \sqrt{2 \alpha \Delta t} \quad (6)$$

Equation (6) describes an inter-dependence between the time step and the element size. In implicit solution routines this equation is irrelevant in terms of the stability. However, any stable implicit solution is not necessarily an accurate solution. In order to ensure that an implicit solution is a fairly accurate one, gross violations of equation (6) should be avoided.

The following relation which satisfies equation (5) and does not result in a gross violation of equation (6) is proposed

$$\sqrt{\alpha \Delta t} < \Delta x < \sqrt{3 \alpha \Delta t} \quad (7)$$

The upper limit in the equation (7) ensures that δ for the first time step covers more than two elements. The lower limit on Δx as given by equation (6) is relaxed by a factor of $\sqrt{2}$.

A Suggested Procedure for Obtaining Accurate Transient Results from FAHT:

1. Start with a reasonable time step.
2. Select Δx by calculating the acceptable limits, and obtain the code prediction.

$$\sqrt{a \Delta t} < \Delta x < \sqrt{3 a \Delta t} \quad (8)$$

3. Reduce Δx by a factor of two and select Δt using the following relation, and obtain the solution for the new Δx and Δt .

$$\frac{\Delta x^2}{3a} < \Delta t < \frac{\Delta x^2}{a} \quad (9)$$

4. Compare the two results. If the changes in the temperature field are more than an "acceptable variation" then repeat step 3. Obviously, the degree of the accuracy depends on the selected criterion for the "acceptable variation."

It should be noted that the above procedure for selection of Δt violates the stability criterion for explicit scheme and should not be used for explicit solution.

Let's apply the above procedure to the example problem:

Step 1: $\Delta t = 2$ seconds (the same as run FE-1).

Step 2: $1.95\text{mm} < \Delta x < 3.37\text{mm}$. Select $\Delta x = 2.5\text{mm}$ (80 elements). This step clearly shows that for a time step of $\Delta t = 2$ seconds, 20 and 40 elements runs were inappropriate. Note that the results for $\Delta x = 2.5$ mm and $\Delta t = 2$ sec. are realistic (please see Table 2).

Step 3: Double the number of elements.
160 elements; $\Delta x = 1.25$ mm.
 $0.27 < \Delta t < 0.82$; choose $\Delta t = 0.4$ seconds.

Step 4: A substantial change in the temperature field is observed. Repeat step 3.
320 elements; $\Delta x = 0.625$ mm.
 $0.07 < \Delta t < 0.21$; choose $\Delta t = 0.1$ seconds.

The results of these numerical experiments are tabulated in Table 2. The exact solution is also given in this table. A finite difference code based on the implicit formulation was programmed and the above outline for a "search" for an "accurate" answer was followed. The results of this program are also included in Table 2.

TABLE 2. "Search" for Accurate Temperature Prediction, $(T(x,t) - T_i)$, at Time = 10 seconds.

Solution Method	$x = 0.01$ (m)	0.02	0.03	0.04	No. of Elements	Time Step (Seconds)
Exact	344.1	3.8	0.01	~ 0	-	-
FAHT						
FE-4	272	1.0	0	0	80	2
FE-5	329.2	2.75	0	0	160	0.4
FE-6	340.4	3.5	0	0	320	0.1
Finite Difference						
FD-1	352.6	14.2	2.0	0	80	2.0
FD-2	345.6	6.1	0.03	0	160	0.4
FD-3	344.4	4.4	0	0	320	0.1
SINDA-87	344.9	4.4	0	0	320	0.1

The FAHT results in Table 2 show that the above procedure in 3 iterations resulted in a fairly accurate answer (compare runs FE-6 and FD-3 with the exact solution). The exact solution is given in Fig. 4.

A reflection on the number of elements or nodes used to obtain the results given in Table 2, points to the gross inefficiency in the grid selection. For example, 320 elements are uniformly distributed in the domain of $x = 0$ to 0.2. However, the results at time = 10 seconds show that the heat transfer is taking place in the region of $x = 0$ to 0.03, which contains 48 elements. Therefore, the remainder of the elements (272) are practically irrelevant. Of course, a number of techniques, such as deforming grid formulation, are available for efficient solution of this class of problems (Hogge and Gerrekens, 1982).

III.2 Nonlinear Boundary Condition Routine

In order to verify the nonlinear boundary condition routine of FAHT, the boundary condition of the test problem at the $x = 0$ surface is changed. There are various ways to impose a nonlinear boundary condition at this surface. The most logical one, considering the intended usage of the FAHT program, is a radiation boundary condition. Thus, the boundary condition at this surface is changed to radiation heat transfer from a gas at a temperature of $T_g = 3600$ K. The surface emissivity ϵ is taken to be 0.8. In section III.1 it was determined that for the test problem the values of $\Delta x = 0.625$ mm and $\Delta t = 0.1$ sec will result in an accurate solution by FAHT. Therefore, the radiation boundary condition problem is solved by FAHT with the same values for Δx and Δt . The predicted temperatures, $T(x,t) - T_i$, at time = 2 sec for nodes from $x = 0$ to 2.5 mm are tabulated in Table 3. In order to verify the accuracy of FAHT's prediction, the predicted values obtained from SINDA-87 program (for the same parameters) are also given in Table 3.

The maximum variation between the results of FAHT and SINDA-87 is less than 0.1%. It should be noted that SINDA-87 is a widely used program and its accuracy in solving rather complex problems has been established over the years. Therefore, it can be stated with confidence that FAHT's nonlinear boundary condition routine is reliable and accurate.

Table 3. Comparison of FAHT and Sinda-87 Temperature Predictions, $T(x,t) - T_i$, at Time = 2 seconds (Radiation Boundary Condition Verification).

Code	$x = 0$ mm	0.625	1.25	1.875	2.5
FAHT	3002	2410	1887	1448	1098
SINDA-87	3001	2411	1888	1449	1099

- Test problem with $T_{gas} = 3600$ K, $\epsilon = 0.8$
- 320 elements, $\Delta t = 0.1$ sec
- Constant properties

III.3 Variable Property Routine

The radiation test case is extended to one with a variable thermal conductivity with $k = 3.98 + 0.002 T$, while density and specific heat are kept constant. The specified thermal conductivity function will result in an increase in k and thermal diffusivity by a factor 2.44 over the temperature range of 300 to 3600 K. It should be added that it is not necessary to have all the thermophysical properties as variables in order to verify the variable property routine. This is due to the fact that the same logic and routine is used to evaluate the new property values.

In section III.1 Eq. (9) was proposed for selection of a time step (for a given Δx) which would ensure a realistic answer, and upon further mesh refinement would lead to an accurate solution. Thermal diffusivity is a parameter in Eq. (9). For variable property problems, it is recommended to use the maximum and minimum values of α to obtain the corresponding limits on Δt . The maximum α value will result in a smaller allowable time step range. However, it should be noted that the thermal penetration front moves into the undisturbed domain at a temperature which is less than the maximum value. Once a region is penetrated with the thermal front, the finite element solution routine is not prone to result in unrealistic temperature values due to subsequent changes in α . Therefore, the value of α at the highest temperature of the region penetrated during a given Δt is the controlling parameter. Usually this controlling temperature is much lower than the maximum value.

Based on $k = 3.98 \text{ W/m}\cdot\text{K}$ and $\Delta x = 0.625\text{mm}$ Eq. (9) results in $0.07 < \Delta t < 0.21$ sec. The highest possible value of thermal conductivity (at $T = 3600 \text{ K}$) is $11.18 \text{ W/m}\cdot\text{K}$. The allowable Δt range corresponding to this k value is $0.025 < \Delta t < 0.075$ sec. As discussed earlier the controlling temperature is indeed much smaller than the maximum value (3600K). Therefore, $\Delta t < 0.075$ sec, is not an accurate estimation of the upper limit on Δt . Thus, the variable property test problem solution is obtained for $\Delta x = 0.625\text{mm}$ and $\Delta t = 0.1$ sec. (same as previous cases), and the results are tabulated in Table 4 along with SINDA-87 prediction.

The maximum variation between FAHT and SINDA-87 results is less than 0.8%. Thus, it can be stated with confidence that FAHT's variable property routine is reliable and accurate.

Table 4. Comparison of FAHT and SINDA - 87 Temperature predictions, $T(x,t) - T_i$, at Time = 2 seconds (Variable Property Verification).

Code	x = 0 mm	0.625	1.25	1.875	2.5
FAHT	2691	2341	1997	1667	1362
SINDA-87	2705	2357	2012	1371	1680

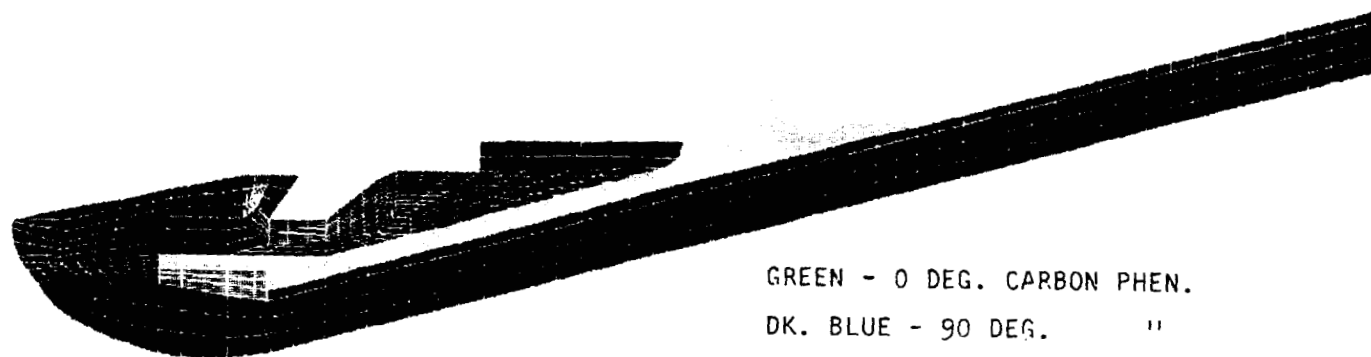
- Test problem with $T_{\text{gas}} = 3600 \text{ K}$, $\epsilon = 0.8$
- Thermal conductivity variable, $k = 3.98 + 0.002 T$
constant density and specific heat
- 320 elements, $\Delta t = 0.1 \text{ sec}$

III.4 Application to MNASA Nozzle

The variable property and nonlinear boundary condition routines of FAHT have been verified. Moreover, a procedure is proposed for obtaining a realistic transient solution from FAHT. It is further shown that with mesh refinement the procedure will converge to an accurate solution.

In this section, a course mesh model of MNASA nozzle will be used to obtain the temperature solution for variable property case with convection and radiation boundary condition. Since the results cannot be compared with any reliable solution, no attempts will be made at mesh refinement for obtaining an accurate solution. The course mesh model of MNASA nozzle along with the description of its various materials is depicted in Fig. 5.

The largest element size in the radial direction along the exposed surface to the thermal load is 0.547 in. Thermal diffusivity of all the materials (i.e., carbon phenolic, glass phenolic, silica phenolic, NBR rubber and steel) maybe relevant in the calculation of the allowable time step via Eq. (9). If the transient time is such that the thermal front reaches an interior material, then α of that region should be considered. Therefore, each material has its own restriction on the allowable time step. Moreover, the element size in the direction of heat flow may change from



GREEN - 0 DEG. CARBON PHEN.
 DK. BLUE - 90 DEG. "
 LT. BLUE - 60 DEG. "
 BLACK - 15 DEG. "
 YELLOW - 8 DEG. SILICA PHEN.
 LAVENDER - -15 DEG. GLASS PHEN.
 RED - NBR (RUBBER)
 PINK - STEEL

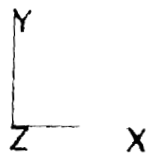


Figure 5. Coarse Mesh Model of MNASA Nozzle

material to material as well as within a given region. Variation of α with temperature is another factor which complicates the selection of proper time step. It is not in the scope of this study to calculate all the potential applicable ranges for the allowable time step. Therefore, the allowable time ranges for carbon phenolic and glass phenolic regions based on α values at about 1000°R and $\Delta x = 0.547$ in are calculated and presented. Δt range based on Eq. (9):

Carbon Phenolic: $90 < \Delta t < 270$ sec; Glass phenolic: $770 < \Delta t < 2300$ sec.

$$\alpha = 1.1 \times 10^{-3} \text{ in}^2/\text{sec};$$

$$\alpha = 1.3 \times 10^{-4} \text{ in}^2/\text{sec}$$

The criterion for carbon phenolic indicates that $\Delta t > 90$ sec. However, an estimate of location of the thermal front should be obtained to see if the glass phenolic region will be effected for time > 90 sec. The estimated penetration depth for $\alpha = 1.1 \times 10^{-3} \text{ in}^2/\text{sec}$ (carbon phenolic) and $\Delta t = 120$ sec is 1.26 in. It should be emphasized that $\delta = 1.26$ in is an estimate of the location of the thermal front. This calculation shows that the thermal front at time = 120 sec will be very close to the glass phenolic region. Therefore, the thermal diffusivity of this region may be relevant.

A FAHT run for the model with $\Delta t = 120$ sec resulted in a number of temperatures below the initial condition value. This indicates that the thermal front does indeed reach the glass phenolic region and the Δt restriction for this region should be considered ($770 < \Delta t < 2300$ sec). It should be added that the Δt restriction of this region is an estimate based on element thickness of 0.547 in and α at 1000°R. The actual element thickness in this region is less than 0.547 in, and a $\Delta t < 770$ sec will be acceptable. As stated earlier, the objective is to show the details of the procedure for Δt selection rather than tedious calculation.

FAHT's predicted temperature field for the coarse mesh model of MNASA nozzle with $\Delta t = 700$ sec after one time step is shown in Fig. 6. The predicted temperature field seems reasonable. In absence of a reliable solution to compare with no other conclusion can be drawn. The maximum predicted temperature at one node is 6007°F which is greater than $T_g = 6000^\circ\text{R}$. This is obviously an error. This error may be due to the input mesh geometry. Detail study of the mesh has revealed that in some regions the nodes of adjacent elements do not coincide. Moreover, there are elements which are triangular elements with four distinct nodes. FAHT can not account for triangular elements when the third and fourth nodes do not coincide. Unfortunately, the limited duration of this project did not allow for mesh correction and further investigation of the source of this error.

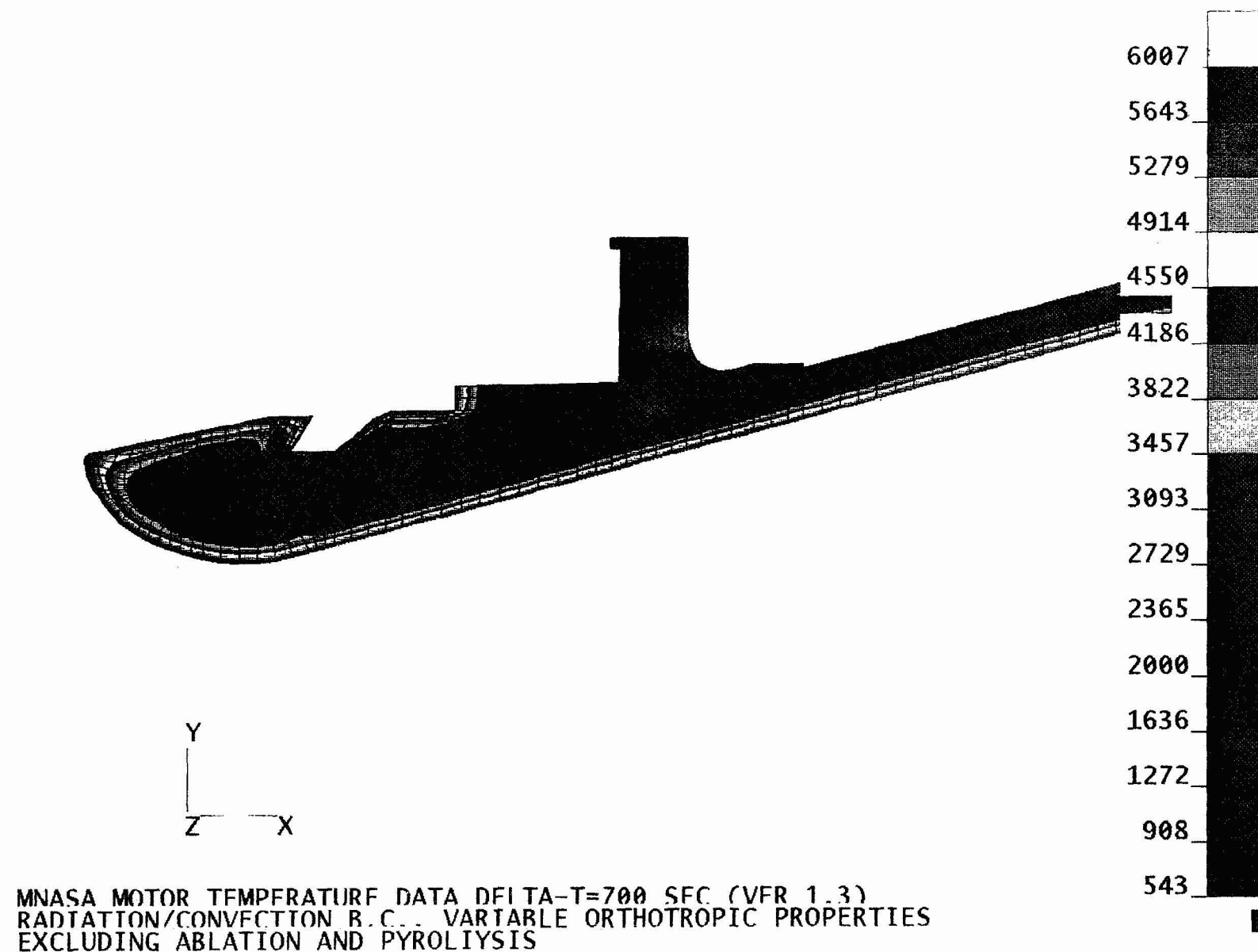


Figure 6. FAHT's Temperature Predictions at 700 sec with $T_i = 530^\circ\text{R}$, $T_{\text{gas}} = 6000^\circ\text{R}$.

IV. CONCLUSIONS AND RECOMMENDATIONS

IV.1 Conclusions

The heat transfer module of FANTASTIC code (FAHT) is studied and evaluated to the extend possible during the ten weeks duration of this project. The conclusions of this work are:

- It is established that with improper choice of element size and time step FAHT's temperature prediction at some nodes, will be below the initial condition value. The source of this unrealistic temperature prediction is identified and a procedure is proposed for avoiding this phenomenon. It is further shown that the proposed procedure will converge to an accurate prediction upon mesh refinement.
- Radiation boundary condition solution routine of FAHT is verified.
- Variable property solution routine of FAHT is verified.
- Verification of the ability of FAHT to model convection heat transfer in a porous domain, independent of pyrolysis process, is not possible.
- FAHT users are advised to bypass the transient logic of FAHT by specifying a fixed time step based on the proposed criteria.
- Experienced and dedicated personnel working as a team are required for successful usage of FANTASTIC Code.
- The temperature field solution will have some errors due to lack of explicit treatment of the convection term.
- The pore pressure equation, as given by Eq. (3) is nonlinear. This equation, however, is treated as a linear equation in FAHT. Therefore, the pore pressure solution will not be accurate, which will result in an inaccurate velocity solution. The inaccuracy associated with the velocity solution, in turn, will increase the error in the temperature solution.
- The flow of pyrolysis gases through the char zone are modeled as a non-reacting low (frozen). Therefore, the endothermic reactions which take place in this zone can not be accounted for. Furthermore, the changes in the porosity and permeability in this zone cannot be calculated and accounted for.
- The permeability of the material is assumed to have the same value in the virgin, decomposition and char zones. As mentioned earlier, the permeability is changing rapidly with time in the decomposition zone. Nonetheless, FAHT can not account for this variation.

- There are no provisions for accounting for the initial porosity of the virgin material.
- The momentum equation is based on the Darcy law. However, it is known (NASA CR-1903, 1971) that the inertial effects play an important role due to relatively high mass fluxes of the degradation products. An accurate modeling of the momentum equation requires the inclusion of the Forchheimer term. Another motivation for the use of Forchheimer-extended Darcy equation of motion for flow through porous media is the following. One of the objectives of the exploratory test program of the Solid Propulsion Integrity Program (SPIP) is to provide empirical relations for permeability of various candidate materials. There may be cases where the permeability should be determined via the Forchheimer-extended Darcy equation. In that case we do not have any analysis tool that can properly use the permeability data.

IV.2 Recommendations

The recommendations of this study have two objectives. First, the issues which should be worked in order to get FAHT in an operational status. The second objective has a long term view of the required capabilities for accurate analysis of charring-decomposing ablator materials including future candidate composites.

Immediate issues which should be addressed in order to get FAHT in an operational status are:

- Fixing of the identified bugs.
- Details of the modeling and programming of the convection heat transfer of the pyrolysis gas as well as the mass diffusion equation should be provided by FaAA for accuracy analysis.
- Verification of pyrolysis modeling (without ablation) through a comparison of a one-dimensional problem with CMA.
- Verification of FAHT's ability to model the moving ablating surface through a comparison of a one-dimensional problem with CMA.
- Test run of an MNASA motor model with a refined mesh.

The motivation for recommending a long-term plan of work is as follows. The problem of analysis of a charring-decomposing material with an ablating surface is very complex and difficult. Experimental verification of any code is difficult, expensive and at best will provide a very rough, within the range, comparison. At the present time we do not have a "research" tool which models the energy and pore pressure equations accurately without any expedient simplifications for ease of programming. Moreover, we do not have a tool which models a dynamic permeability and can account for reactions between the pyrolysis gases and the char zone. Additional concern is that we do not have a code whose momentum equation includes the inertial effects which can play an important role when the mass fluxes are relatively high. In short, we do not have a research tool that includes all the known effects. Therefore, the research, development, design and testing verification can not proceed in a systematic manner. A research code, not a user friendly code or necessarily computationally efficient code, is needed to approach the problem in a systematic fashion. In that case, we can establish and distinguish primary, secondary and tertiary effects. This research code should have provisions to accommodate the data about the behavior of new candidate materials as becomes available. Concurrent with development of this research code, experimental work must proceed to provide extensive data about thermophysical properties, permeability and the possible reactions that take place in the char zone.

REFERENCES

1. April, G.C., Pike, R.W., and del Valle, E.G., "On Chemical Reactions in the Char Zone During Ablation," NASA CR-1903, October 1971.
2. Failure Analysis Associates, FANTASTIC/FAHT Heat Transfer Analysis Module, Theoretical Manual Version 1.0, " Palo Alto, CA, June 1988.
3. Hogge, M., and Gerrekens, P., "One-Dimensional Finite Element Analysis of Thermal Ablation With Pyrolysis," Computer Methods in Applied Mechanics and Engineering, Vol. 33, pp. 609-634, 1982.
4. Matting, F.W., "Analysis of Charring Ablation with Description of Associated Computing Program," NASA TN D-6085, November 1970.
5. OZISIK, M., N., Heat Conduction, John Wiley & Sons, Inc., New York, NY, 1980.
6. Pittman, C.M., and Howser, L.M., "Numerical Analysis of the Transient Response of an Axisymmetric Ablative Char Layer Considering Internal Flow Effects," NASA TN D-6895, September 1972.
7. Suchsland, K.E., "Analytical Procedure for the Thermal Response of Solid Propellant Nozzles," Aerotherm Division/Acurex Corporation, Mountain View, California, Aerotherm Report No. 75-148, August 1975.
8. Swann, R.T., and Pittman, C.M., "Numerical Analysis of the Transient Response of Advanced Thermal Protection Systems for Atmospheric Entry," NASA TN D-1370, July 1962.
9. Swann, R.T., Pittman, C.M., and Smith, J.C., "One-Dimensional Numerical Analysis of the Transient Response of Thermal Protection Systems," NASA TN D-2976, September 1965.

1989

NASA/ASEE SUMMER FACULTY FELLOWSHIP PROGRAM

**MARSHALL SPACE FLIGHT CENTER
The University of Alabama in Huntsville**

**Radial Response of the
Burst And Transient Source Experiment**

Prepared by:	John Patrick Lestrade
Academic Rank:	Assistant Professor
University and Department:	Mississippi State University Department of Physics and Astronomy
NASA/MSFC:	
Laboratory:	Space Science
Division:	Astrophysics
Branch:	High-Energy Astrophysics
MSFC Colleague:	G. J. Fishman
Date:	July 21, 1989
Contract No.:	The University of Alabama in Huntsville NGT-01-008-021

Radial Response of the Burst And Transient Source Experiment

by

John Patrick Lestrade
Assistant Professor of Physics and Astronomy
Mississippi State University
Mississippi State, Mississippi, 39762

Abstract

The Gamma Ray Observatory includes four experiments designed to observe the gamma-ray universe. Jerry Fishman in the High Energy Astrophysics Branch at Marshall Space Flight Center is the principal investigator for one of these experiments, the Burst And Transient Source Experiment (BATSE).

During my first summer with the BATSE team in 1988, we completed laboratory measurements to test the response of the BATSE modules to gamma-ray sources that are non-axial. The results of these observations are necessary for the correct interpretation of BATSE data obtained after it is put in Earth orbit.

Subsequent analysis of the data revealed a shift in the centroids of the full-energy photopeaks for angles of incidence between about 70° and 110° . This effect was diagnosed as being due to a radial dependence of the light collecting efficiency of the large-area detector (LAD). Energy-depositing events that occur near the perimeter of the 10-inch radius NaI disc are not as efficiently collected as those events that occur near the disc's center.

In this report we analyze this radial response and in so doing we are able to explain the non-gaussian shape of the photopeaks seen in the spectra taken at all angles.

Acknowledgements:

The summer of 1989 has been another chapter in the exciting story of my association with the High Energy Astrophysics group at the Marshall Space Flight Center. My colleagues have given unselfishly of their time and expertise to make me an integral part of the group. I appreciate all that I have learned from them. I am sincerely grateful for their acceptance and friendship.

In particular I would like to thank Jerry Fishman for the opportunities that he has provided me. His patience with my naïve questions has been of immeasurable help.

I am also indebted to Dr. Edward West of the Solar Physics Branch of MSFC for his help in converting data from eight-inch floppy diskettes to a PC-compatible format. Several times during this past summer I have called upon him and each time he has unhesitatingly provided help.

The administrative aspects of a program this large are quite complex. It is a credit to Frank Six, Jerry Karr, and Mike Freeman that it appears to us, the visiting faculty, to run so effortlessly.

Finally, I would be remiss if I didn't also show appreciation for the support and friendship of Chip, Tom, John, Scott, Jeff, Philip, Bob, Bill, Bob, Billy Bob, and Ellen.

John Patrick Lestrade

July 21, 1989

List of Figures

	page
Figure 1 BATSE detector module	XVIII-9
Figure 2 Gamma-ray spectra (Cesium-137)	XVIII-10
Figure 3 The spectrum of a gamma-ray burster event (OSO-7 and IMP-6).	XVIII-11
Figure 4 Peak centroid shift for Cs-137 and Se-75.	XVIII-12
Figure 5 Cs-137 full-energy peak showing the inadequate fit of a single gaussian.	XVIII-13
Figure 6 Source holder for the radial response tests.	XVIII-14
Figure 7 Source positions for the radial response tests.	XVIII-15
Figure 8 Hg-203 279 keV peak at $r = 0, 6$, and 9.5 in. in TPS-119.	XVIII-16
Figure 9 Peak centroid position (channel number) for Hg-203 keV peak for modules 1-3.	XVIII-17
Figure 10 Three quadratic fits to the radial response for Hg-203 (72, 279 keV) and Am-241 (60 keV).	XVIII-18
Figure 11 Peak centroid position (channel number) for Hg-203 279 keV peak for modules 4-6.	XVIII-19
Figure 12 Peak centroid position (channel number) for Hg-203 279 keV peak for modules 7, 0/8, and P.	XVIII-20
Figure 13 Three theoretical radial response functions (solid lines) and measurements of the Hg-203 279 keV peak.	XVIII-21
Figure 14 Comparison of observed (solid) and calculated (dotted) photopeaks for Cs-137 662 keV for the case $r_0 = 5.5$ in., $\alpha = 0.020$, and edge deficiency = 10%, 12%, and 14%.	XVIII-22
Figure 15 Comparison of observed (solid) and calculated (dotted) photopeaks for Cs-137 662 keV for the case $\alpha = 0.020$, edge deficiency = 12%, and $r_0 = 5.0, 5.5$, and 6.0 in.	XVIII-23
Figure 16 Comparison of observed (solid) and calculated (dotted) photopeaks for Cs-137 662 keV for the case $r_0 = 5.5$ in., $\alpha = 0.015, 0.020$, and 0.025 , and edge deficiency = 12%.	XVIII-24
Figure 17 Comparison of Monte Carlo (dotted) and observed (solid) spectra for Hg-203	XVIII-25

—

—

—

1. Introduction:

1.1 The Gamma-Ray Observatory

Before the year 2000 NASA plans to launch more than 9 major space missions. These observatories will study the universe in the infrared, visible, ultraviolet, x-ray, and gamma-ray portions of the spectrum. The objects to be studied include the earth, the planets, the sun, and other more exotic, cosmological objects in which high-energy processes are taking place.

One of the more enigmatic objects that will be studied is the gamma ray burster (GRB). Since the discovery of the first in 1969 we have recorded hundreds of these peculiar objects. The frequency of discovery has reached approximately one GRB every two days.

The spectra of GRB's are confined almost totally to the gamma ray portion of the spectrum. This is quite strange for explosive astronomical bodies. Attempts to locate visual counterparts have been only partially successful. This inability to locate a companion means it is also difficult to assign distances to GRB's and therefore their absolute magnitudes remain unknown. Typical burst durations are on the order of tens of seconds with the shortest being measured in milliseconds and the longest several minutes. In general they show very short rise times and somewhat longer decays. Further, several GRB's display periodicities in brightness during the decay phase. Current GRB models adopt a neutron star as the primary source of energy. An excellent review of gamma-ray bursters has been given by Hurley (1989).

All agree that better data are needed. Higher resolution in time, space, and energy are necessary to eliminate the dozens of models which currently abound. Fortunately, this improvement in GRB data is imminent. One major, earth-orbiting platform for the study of GRB's is nearing completion. The Gamma Ray Observatory (GRO) is, at the time of this writing, undergoing final testing before its launch in the summer of 1990.

GRO is a 17-ton satellite carrying 4 experiments; the Oriented Scintillation Spectrometer Experiment (OSSE), the Imaging Compton Telescope (COMPTEL), the Energetic Gamma-Ray Experiment (EGRET), and the Burst And Transient Source Experiment (BATSE). Together, these instruments detect gamma radiation at energies from 30 keV to 30 GeV. GRO is scheduled to be launched to a nominal altitude of 250 miles (450 km). Its nominal lifetime is five years.

The High-Energy Astrophysics Branch in the Space Science Laboratory at Mar-

shall Space Flight Center has designed, built, and is now testing the BATSE detectors. As a NASA/ASEE Summer Faculty Fellow I have been involved in some of the laboratory testing of the BATSE modules and in the analysis of the acquired data.

1.2 Burst And Transient Source Experiment

BATSE is composed of eight detector modules (Figure 1). These modules will be situated at the eight "corners" of GRO. In this orientation it is able to monitor the complete sky except for that part temporarily blocked by the earth. As the name implies, BATSE is designed to observe and record gamma-ray events that are short-lived. Although its *raison d'être* is the study of gamma-ray bursters, it also has been designed to observe sources of gamma radiation that are long-lived – such as the sun, pulsars, and black holes.

The principal detector in each module is called the Large-Area detector (LAD). This is a sodium iodide crystal in the shape of a disc with a diameter of 20 inches and a thickness of 0.5 inches. The shape and size of the crystal were chosen to make BATSE more sensitive to the low-energy gamma ray spectrum (i.e., 30 keV~240 keV) and to permit the measurement of very weak sources.

1.2.1 BATSE Testing and Calibration

One of the problems inherent in an observational science is the effect that the observer's instrument has on the data. That is, given a uniquely-valued input, the output contains a finite spread in values reflecting the instrument's nature. In the case of a gamma-ray instrument, such as BATSE, there are contributions to this dispersion from inhomogeneities in the crystal, statistical fluctuations in the conversion of gamma-ray energy into an electrical signal, electronic noise, and other sources. Each of these contributions tends to spread the monoenergetic input into an approximate gaussian shape (Price, 1964). Examples of the resultant output spectra are shown in Figure 2. As seen here, a typical gamma-ray spectrum has additional complexity. Not only is the input energy spread into a wide peak (cf. 662 keV peak in Figure 2), but scattering events which result in only partial deposition in the crystal add other features to the spectrum.

When a monoenergetic beam of photons strikes the sodium iodide crystal in the detector, some of the photons are completely converted into an electrical response that becomes recorded as counts in one of the channels of the photopeak. However, some photons deposit only part of their energy and are scattered out of the detector. These become recorded as lower-energy events and show up as counts in the Compton continuum. Still other photons lose some energy outside of (often

behind) the crystal and are then scattered back into the crystal where they become recorded as counts in the backscatter peak. As seen in this figure, even when the input is monoenergetic, these effects distort the spectrum in a very complicated way. When the source is *not* monoenergetic, as in the case of gamma ray bursters, the situation is considerably more complicated.

Figure 3 presents an observation of a gamma-ray burster (Metzger *et. al.*, 1974). The exponentially decaying energy spectrum is typical of these events and is consistent with a model based on thermal bremsstrahlung. These are certainly more complicated than the monoenergetic case. Before we can determine the true spectrum that was *incident* on the detector, we must solve a complicated problem that depends on how the detector responds to incident photons. This response is a function of not only the incident energy but also of the angle of incidence. At MSFC part of our responsibility is to provide a response matrix that describes the detector's effects on an input spectrum. To this end we have spent the past year and a half measuring the spectra with several sources under various conditions. This report presents results of the radial response tests.

2. Radial Response: TPS-119

During a gamma-ray event for BATSE in earth orbit there are at least four detectors responding to the flux of radiation. Since these detectors are oriented in different directions, it is important to know how the detector response changes as a function of the angle of incidence.

The expected effect is the decrease in efficiency due to the smaller projected area as the crystal is turned relative to the flux. This decrease was observed. What was also observed, but not fully expected, was a shift in the peak centroids as the crystal was rotated. In other words the observed energy of the incident beam *decreased* as the angle of incidence changed from 70° to 90° . This decrease for Cs-137 and Se-75 photopeaks is shown in Figure 4. The total angular dependence of this decrease is complicated and is discussed in greater detail by Lestrade (1988). In this report we are primarily concerned with the implications of this secondary effect – the apparent decrease of the incident energy with increasing angle of incidence.

The discovery of the shift in the centroids of the full-energy photopeaks for angles of incidence between about 70° and 90° was diagnosed as being due to a radial dependence of the light collecting efficiency of the large-area detector (LAD). Measurements showed that for energy deposited near the perimeter, the detector has a light collection efficiency that is about 12% less than for that deposited near the center. This is not a property of the scintillator, but rather, a property of the light-collection process. As the crystal is turned the principal area of energy deposition moves from the whole disc at 0° to that local area of the perimeter facing the

source at 90°. Therefore, when the crystal is illuminated at any angle, the output is a superposition of many gaussians, not centered about the true centroid, but shaded to the left (i.e., lower energies).

At angles near 0° the resultant photopeak shows contributions from all areas of the disc. However, for angles of incidence near 90° (or 270°) the photopeak is representative of only the perimeter.

The former effect is seen in Figure 5. This figure presents the 662 keV peak of Cs-137 at an angle of 0°. Note that at normal incidence the peak is a superposition of gaussians. The theoretical gaussian shown in this figure has a centroid at 662 keV. Similar spectra taken at 266°, on the other hand, peak at a lower energy, are less dispersed, and show a purer gaussian shape because they arise from a more localized region of the crystal (cf. Lestrade, 1988).

2.1 Disc Integration

If we assume azimuthal symmetry, then the centroids of the individual gaussians that constitute the photopeak are functions of only the radius, r . In this case, the contribution from the annulus between r and $r + dr$ of the LAD is the simple gaussian given by

$$2\pi r dr e^{-\alpha(E-E_0(r))^2}, \quad (1)$$

where α is a constant yet to be determined, and the centroid position $E_0(r)$ is the radial response. The total photopeak, $P(E)$, in counts per channel is therefore given by the integration of these annuli from disc center to perimeter, viz.

$$P(E) = \int_0^{10} 2\pi r e^{-\alpha(E-E_0(r))^2} dr. \quad (2)$$

One might expect, given a measured spectrum $P(E)$, to be able to solve Equation (2) for $E_0(r)$. This is not an easy task. We decided to approach the problem in a more straight-forward way – we would directly measure $E_0(r)$.

2.1 Measurement of the Radial Response

The table below lists the radioactive sources used in this test. The Am-241 and Na-22 sources were used on only detector DM 1. Mercury-203 was used for all nine modules (eight flight and one protoflight). For the purposes of this report and historical reasons the modules are numbered 1-7, 0/8, and 'P'.

Radioactive Sources Used in Radial Response			
Isotope	$\frac{A}{Z}$ Symbol	Half-Life	Energies (MeV)*
Americium-241	$\frac{241}{95}$ Am	458 yr.	59.5
Mercury-203	$\frac{90}{203}$ Hg	47 d.	[72.9], 279.2
Sodium-22	$\frac{22}{11}$ Na	2.62 yr.	<u>511</u> , <u>1275</u>

* underscore indicates coincident gammas, square brackets indicate sum peaks.

With a source holder and collimator especially built for this test, we were able to restrict the gamma-ray flux to local regions of the disc (Figure 6). Fifteen radial positions as shown in Figure 7 were chosen. The illuminated spot size on the disc was calculated to be approximately 0.75 inches. By illuminating such a small region we were hoping to measure 1) the shift in peak centroid as the holder was moved across the face of the crystal and 2) the width of the gaussians that were a result of the electronic response of the instrument and not contaminated by the combination of gaussians from all portions of the disc.

2.2 Results

Figure 8 presents three Hg-203 spectra to show the shift in peak centroid with increasing radial position. There is minimal shift in the centroid for points as far out as 6 inches from the disc center. However, at 9.5 inches the shift is significant.

Figure 9 presents the centroid positions for modules 1 through 3 as a function of radius for Hg-203. (In this and following radial response figures, the data from the left and right sides of the disc are averaged.) Note the singular depression in the radial response for DM 1 near the disc center. At first we thought that this may have been caused by an error in measurement. However, as Figure 10 shows, the same deficiency is evident in the spectra of all nuclides when DM 1 is used. Further checking found the culprit – a small piece of tin purposely left in the center of this module after removal of an unneeded light sensor. Its presence will not affect other measurements. Included in this figure are the formulae for the energy of the centroid as a quadratic in radius for these three peaks.

For completeness Figure 11 and Figure 12 present the centroid positions vs. radius for the 279 keV peak for the remaining 6 modules.

With an idea of the width of the gaussians from the localized regions of the disc and the radial dependence of the centroids of these peaks, we thought it would be interesting to try to reconstruct the photopeaks measured in full-disc illumination by substituting for α and $E_0(r)$ and performing the integration in equation (2). In order to simplify the functional form of the radial response, $E_0(r)$, we assumed a

constant centroid position for gaussians formed within a distance r_0 of disc center and a linear decrease from that point to the perimeter. Three such functions along with the measurements of the 279 keV peak are shown in Figure 13. Remembering that the depression at $r = 0$ is not representative of what is actually going on near the center, this simple model fits the radial response quite well.

The radial response function in this case is given by

$$E_0(r) = \begin{cases} \mathcal{E}_0 & 0 \leq r < r_0; \\ \frac{(10-r(1-f)-fr_0)}{(10-r_0)} \mathcal{E}_0 & r_0 \leq r \leq 10. \end{cases} \quad (3)$$

where \mathcal{E}_0 is independent of r and equals the centroid position for gaussians that result from events where $r < r_0$ and f is the "edge deficiency" or fractional shift in centroid position for gaussians originating from the perimeter. For example, in figure 12 $f = 0.12$ and $r_0 = 5$ in.

With this function, equation (2) reduces to

$$P(E) = \int_0^{r_0} 2\pi r e^{-\alpha(E-\mathcal{E}_0)^2} dr + \int_{r_0}^{10} 2\pi r e^{-\alpha\{E-\mathcal{E}_0[10-r(1-f)-fr_0]/(10-r_0)\}^2} dr, \quad (4)$$

Performing the first integration gives

$$\pi r_0^2 e^{-\alpha(E-\mathcal{E}_0)^2} + \int_{r_0}^{10} 2\pi r e^{-\alpha\{E-\mathcal{E}_0[10-r(1-f)-fr_0]/(10-r_0)\}^2} dr. \quad (5)$$

3. Conclusions

The three variables in this model are thus f , r_0 , and α . However, these are not totally free variables. They are constrained by the radial response measurements as shown in Figures 8-10. Still, even with these restrictions the results are very good.

Figure 14 presents the Cs-137 662 keV peak (from Figure 5) along with $P(E)$ calculated from Equation 5 for the three cases of edge deficiencies of 10%, 12%, and 14%. The data are clearly much better fit by the 12% case.

The next figure (Figure 15) shows the same peak but with $P(E)$ calculated for an edge deficiency of 12% and center radii, r_0 , of 5, 5.5, and 6 in. Here an r_0 of 5.5 in. provides a better fit.

Finally Figure 16 shows that an α near 0.020 is correct.

It is reassuring that these parameters are independent and in rough agreement with the radial response test results. For example, Figures 8 and 11 indicate that an edge deficiency of 12% and an r_0 of 5.5 are reasonable values.

Pendleton (1989) recently used the quadratic fits to radial response in his Monte Carlo simulation of a mercury-203 spectrum in the Absolute Efficiency Tests (TPS-118). Figure 17 shows a comparison of the observations with his calculated spectrum.

There are still several questions that remain unanswered about the effect of the LAD radial response on the output photopeaks. For example, several Na-22 511 keV photopeaks measured during the science tests in 1988 (TPS-59) showed a double-peak structure. At that time we attributed this to cracks in the crystal structure. It would be interesting to see if a "simple" radial response function could explain at least part of this shape.

Bibliography

1. Hurley, K., 1989, Cosmic Gamma-Ray Bursts, Lectures given at the NATO Adv. Studies Inst., Erice, Italy, April, 1988.
2. Lestrade, J. P. (1988) Angular Response Calibration of the Burst And Transient Source Experiment. *NASA Technical Reports*, **CR-183553**, XIX:1-35.
3. Metzger, A. E., R. H. Parker, D. Gilman, L. E. Peterson, and J. I. Trombka, 1974, Observation of a Cosmic Gamma-Ray Burst on *Apollo 16*. I. Temporal Variability and Energy Spectrum, *Astrop. J.*, **194**, L19-L25.
4. Pendleton, G. E., 1989, Private communication.
5. Price, W. J., 1964, Nuclear Radiation Detection, Second Edition, McGraw-Hill Book Company, New York.

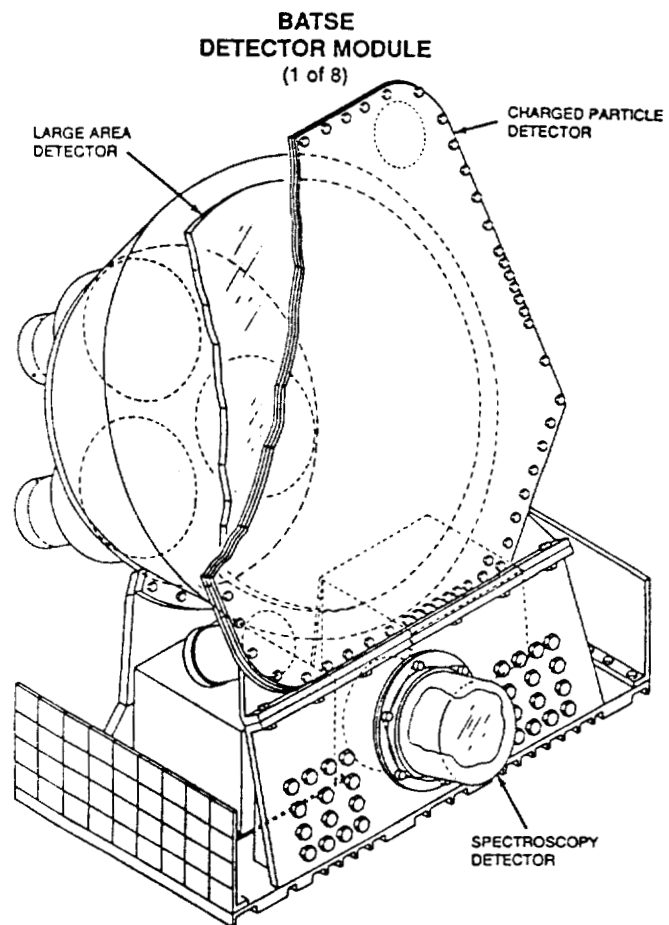


Figure 1

XVIII-9

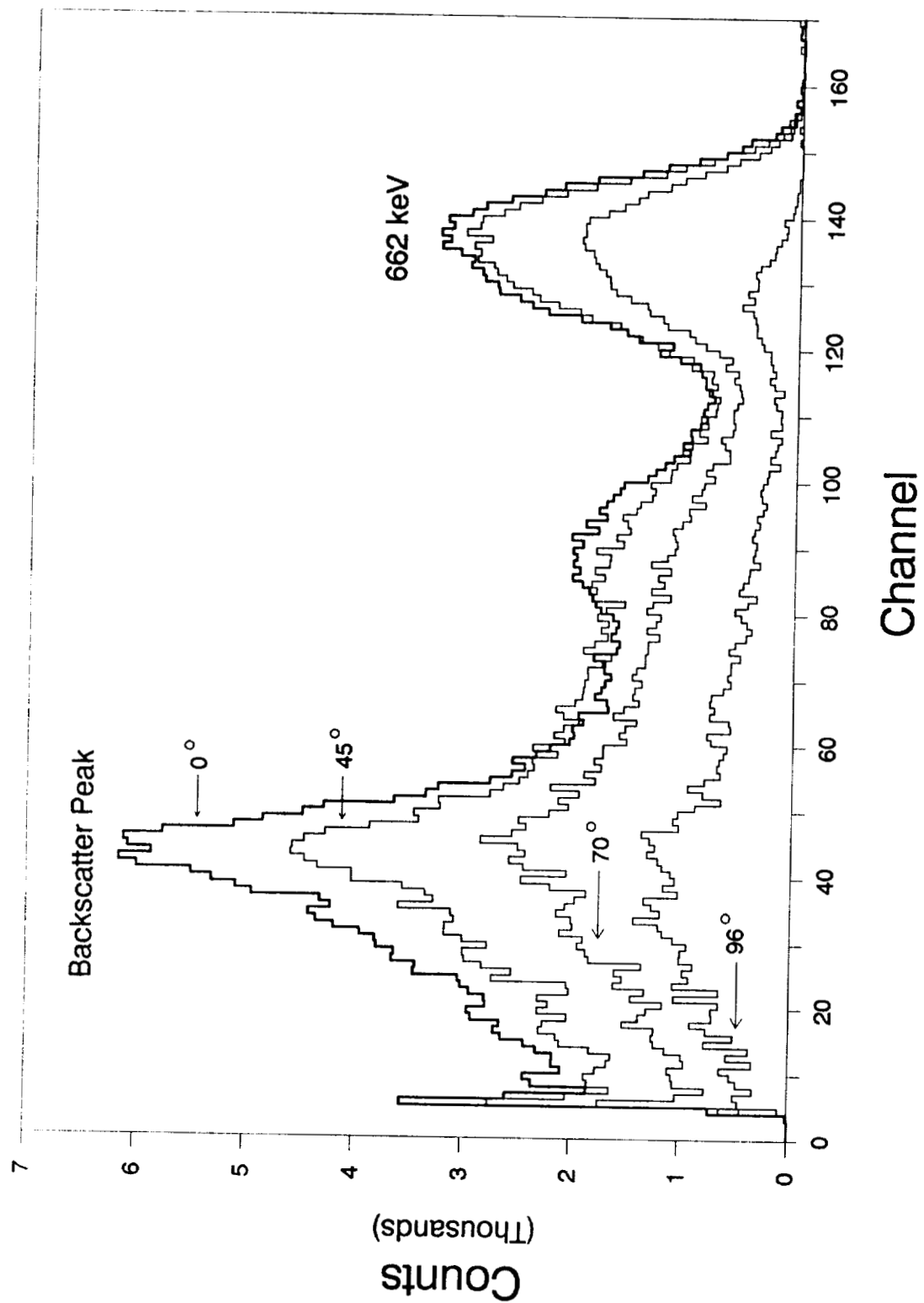


Figure 2

COSMIC GAMMA-RAY BURST

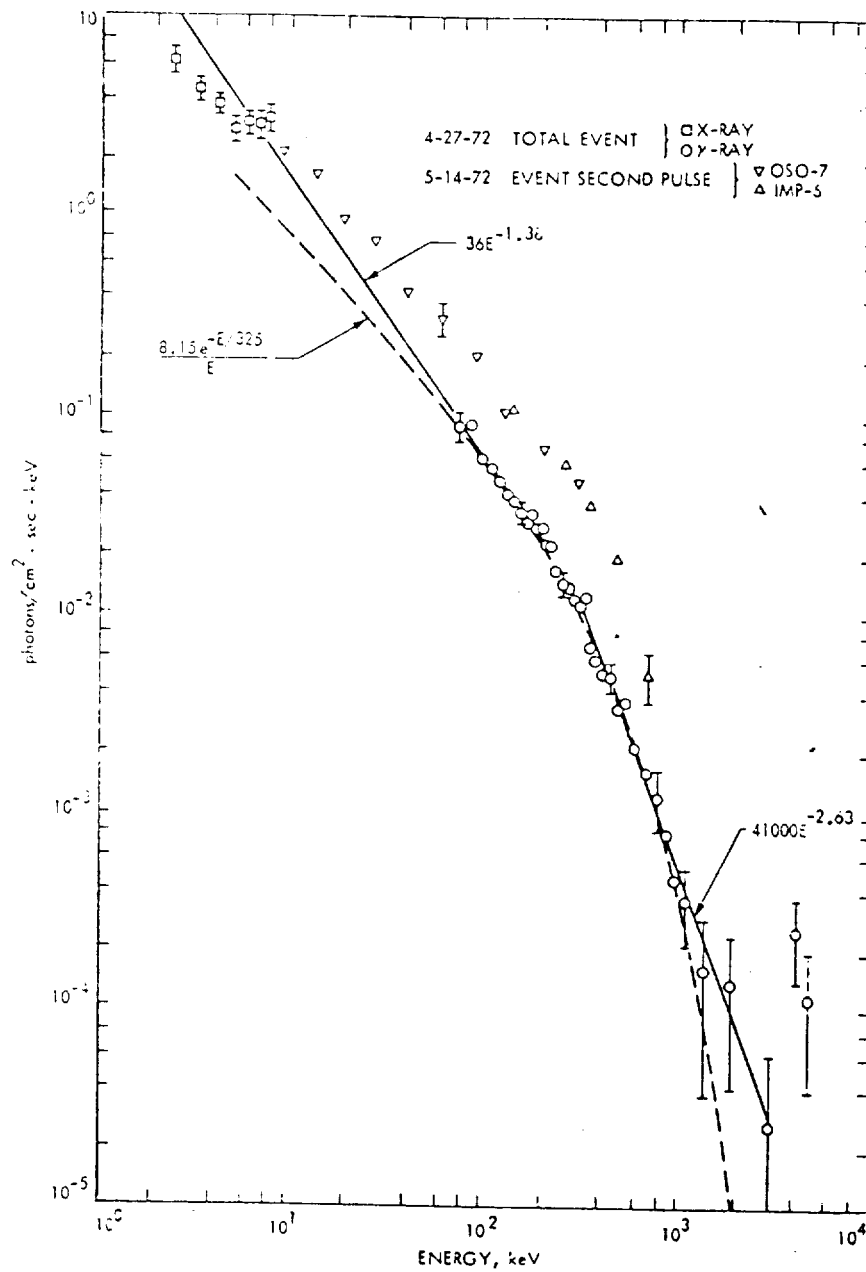


Figure 3

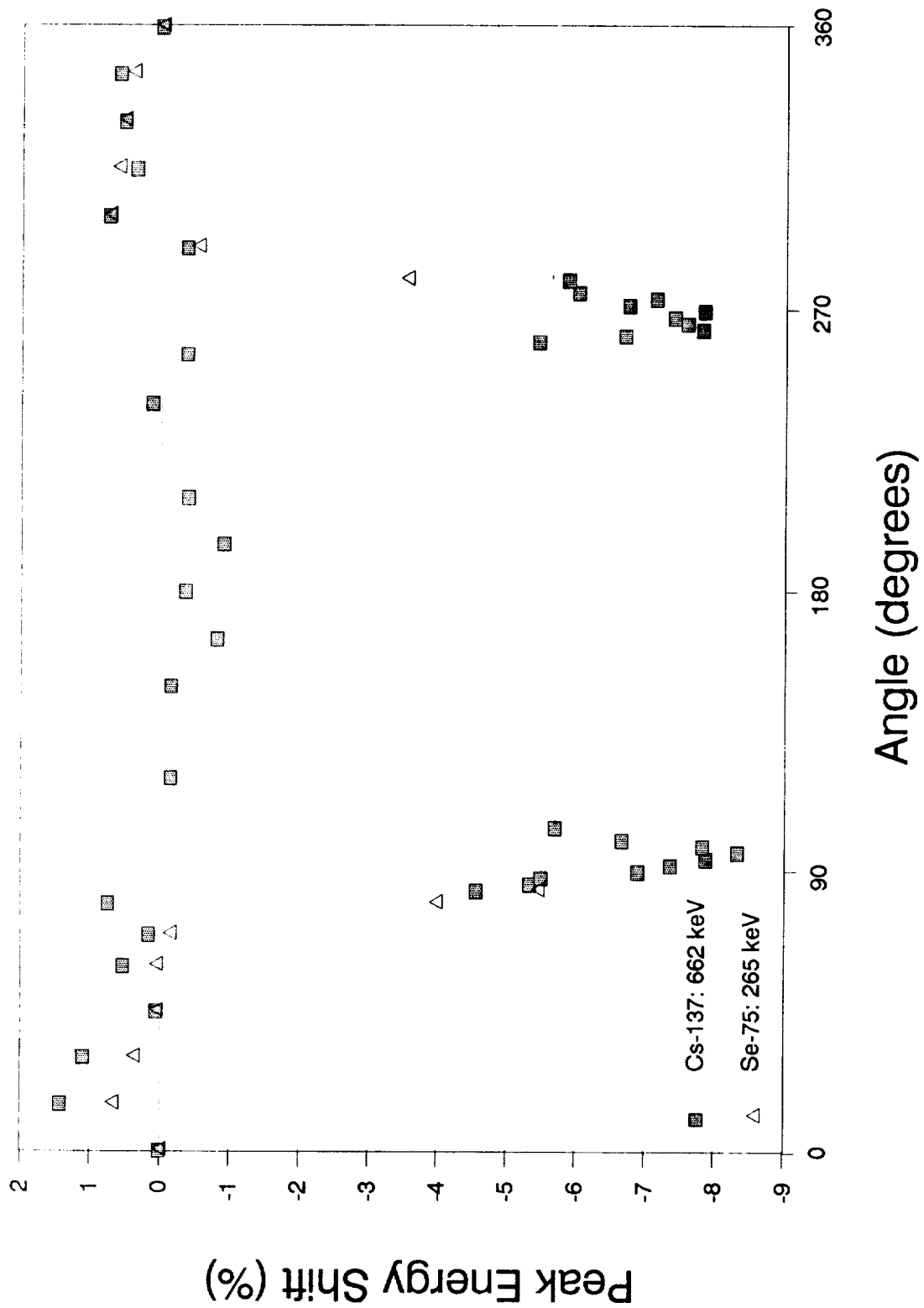
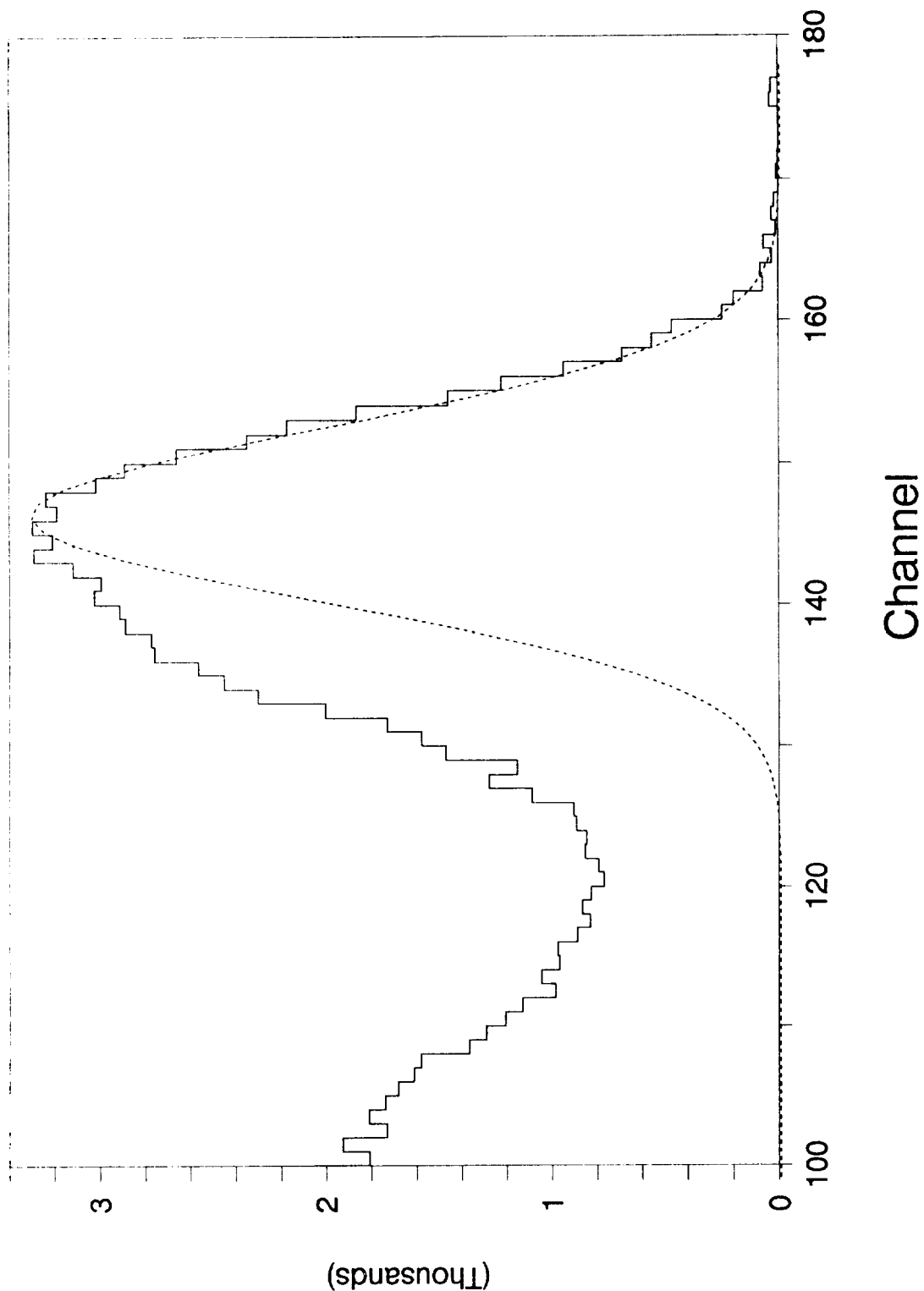


Figure 4

XVIII-12

Cesium-137 Full-Energy Peak

Cs-137: 662 keV
TPS-119: DM 1



Counts

Figure 5

XVIII-13

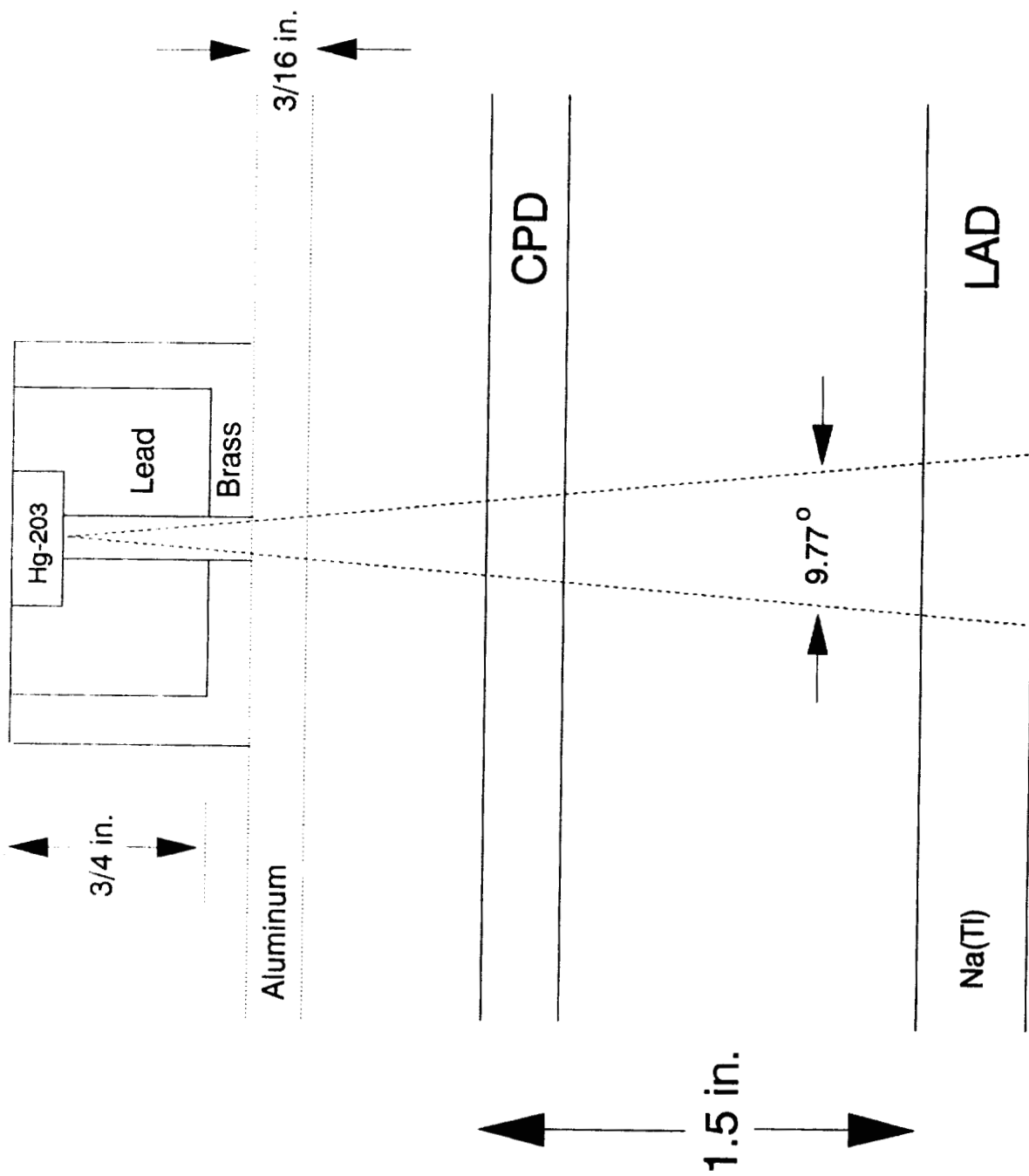


Figure 6
XVIII-14

Source Holder: TPS-119

Radial Positions for TPS-119

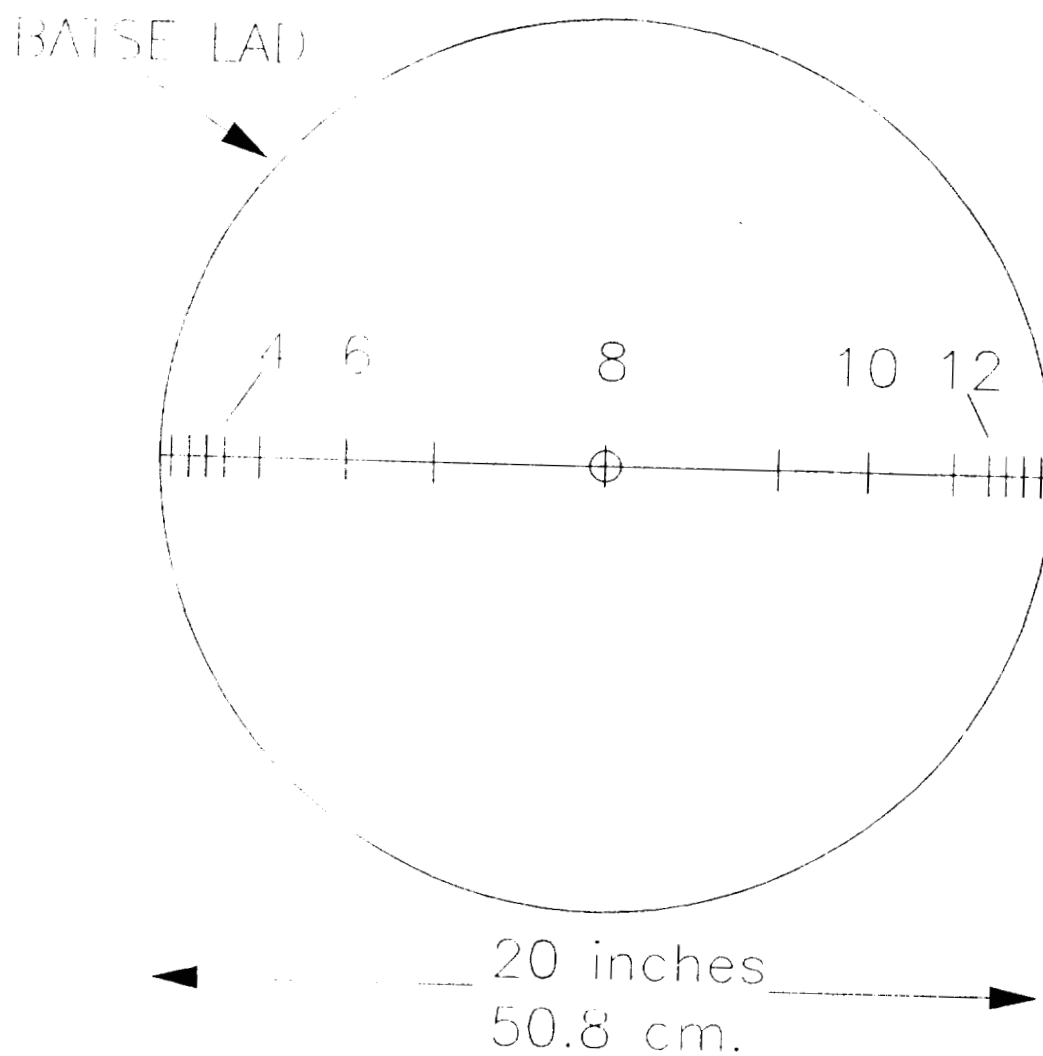


Figure 7

Radial Response

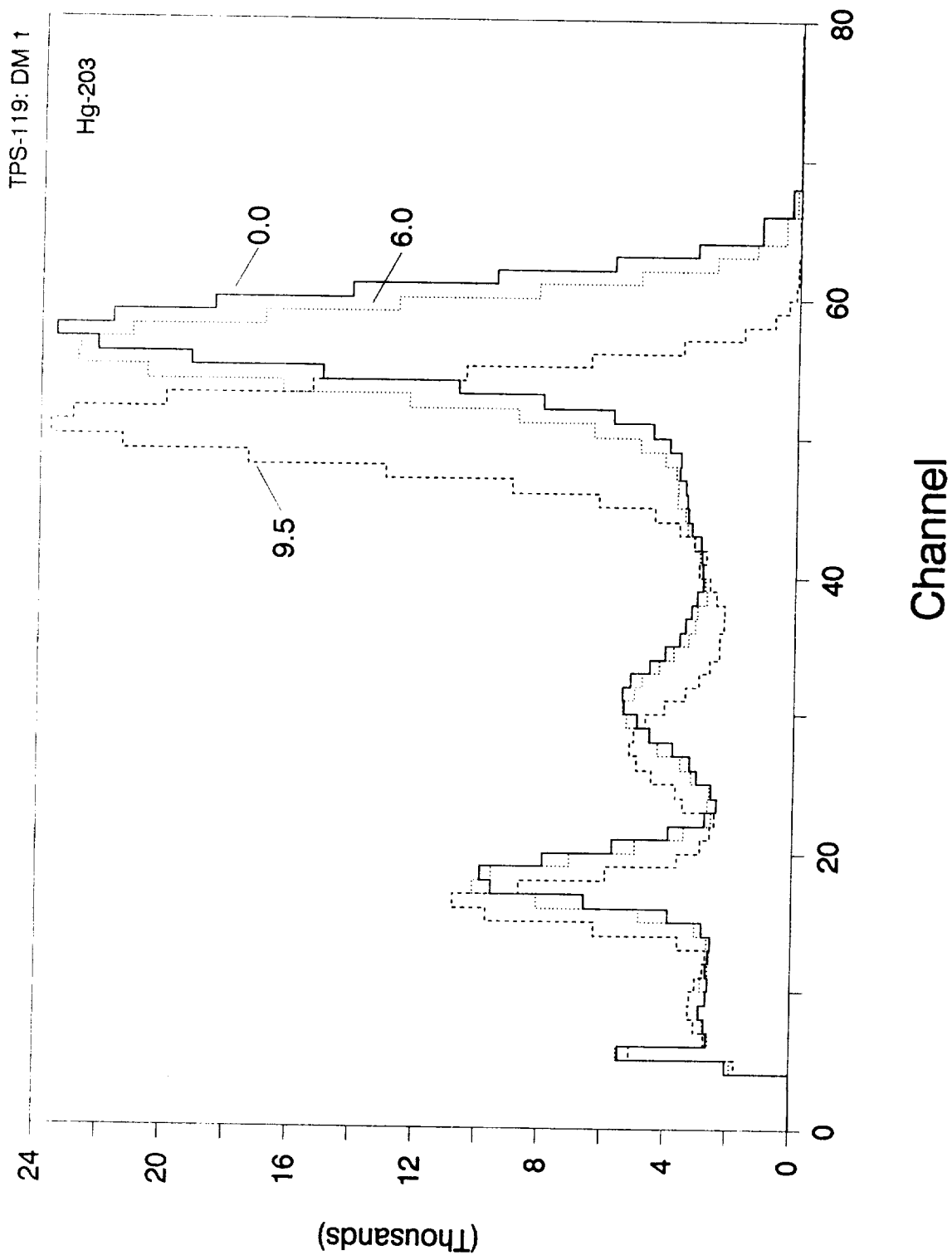


Figure 8

Radial Response

Centroid Position of Hg-203: 279 keV

TPS-119: DM's 1, 2, & 3

Centroid Channel

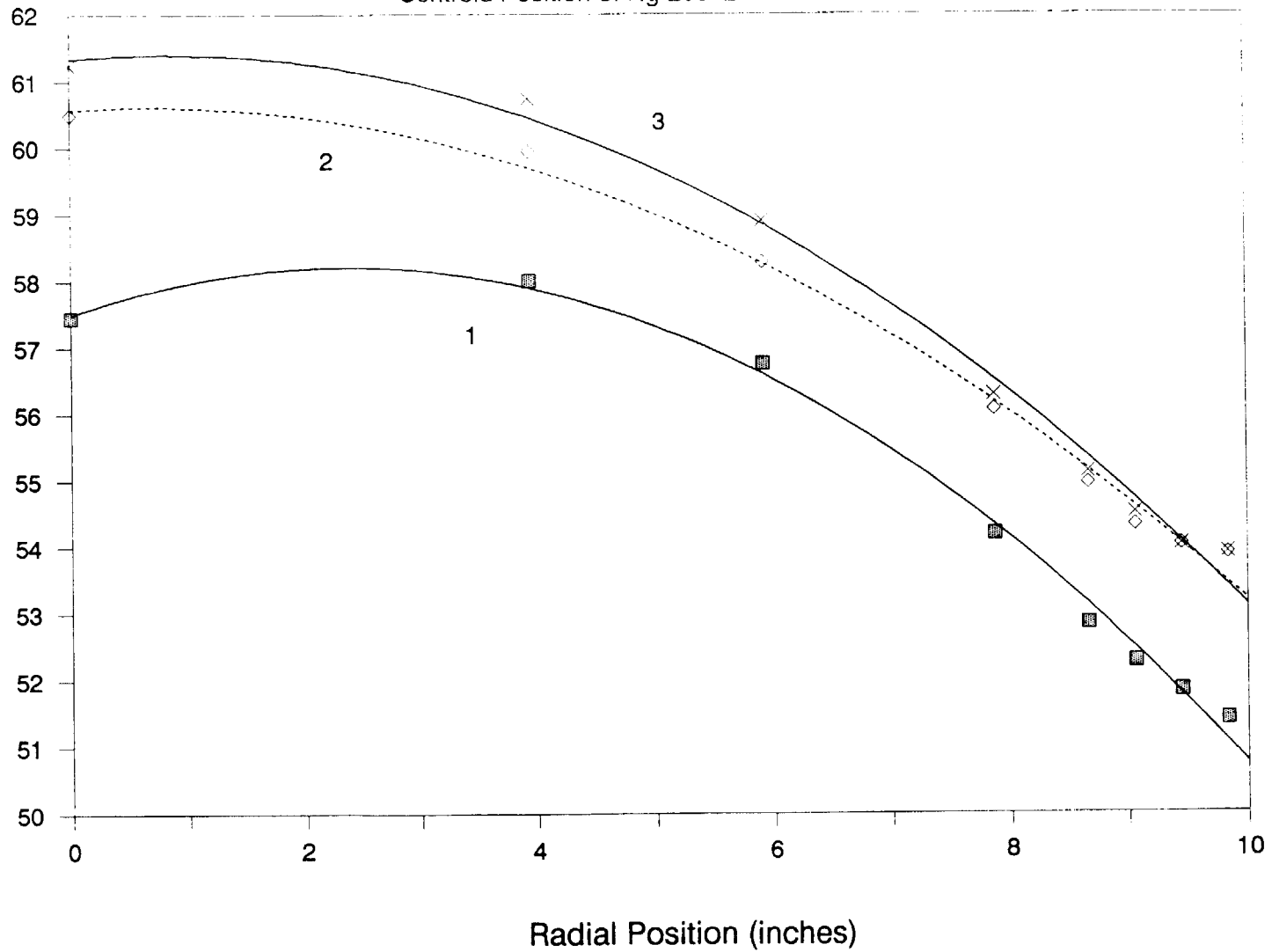


Figure 9

XVII-17

Radial Response

Normalized Centroid Energies

TPS-119: DM 1

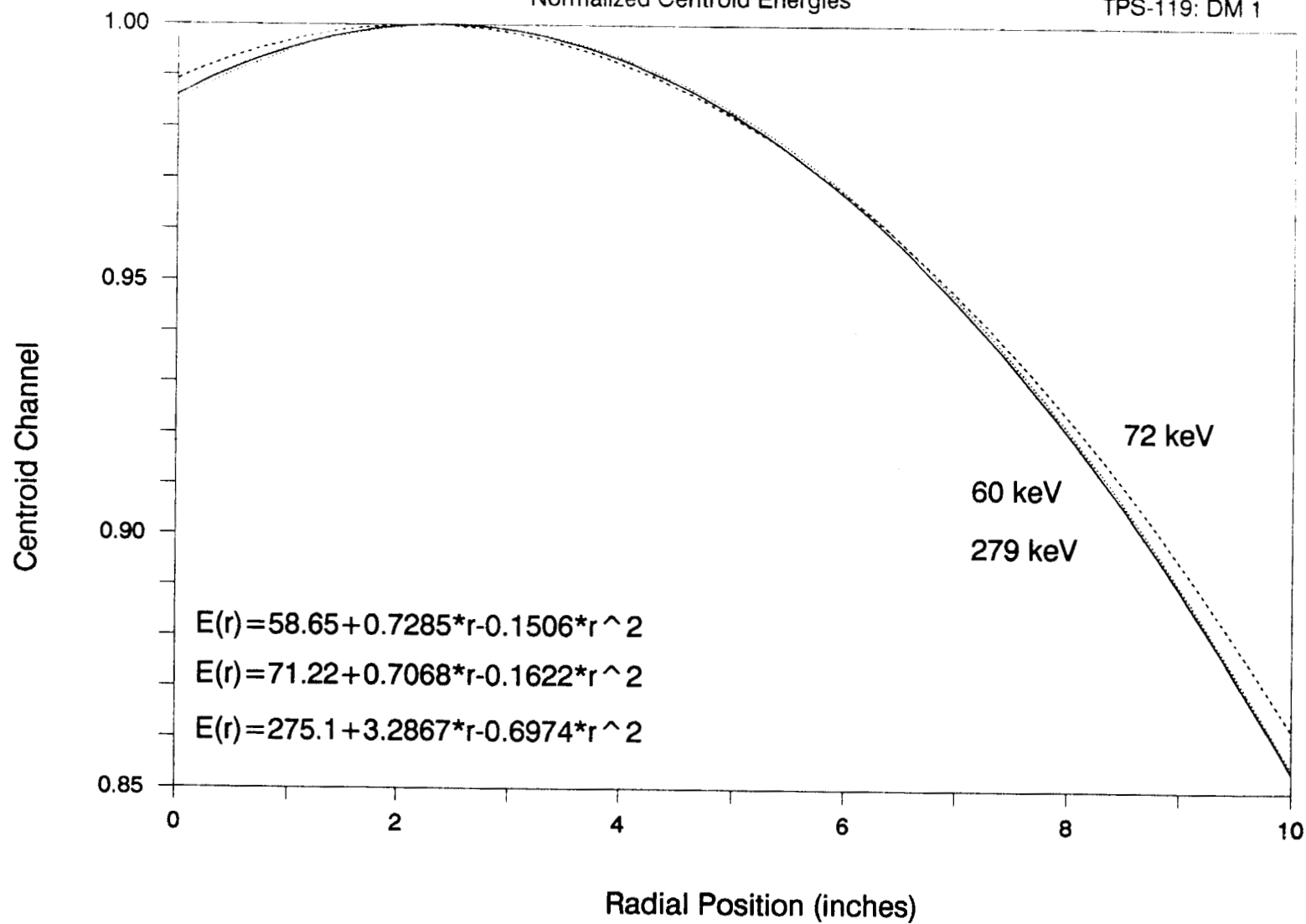


Figure 10

XVIII-18

Radial Response

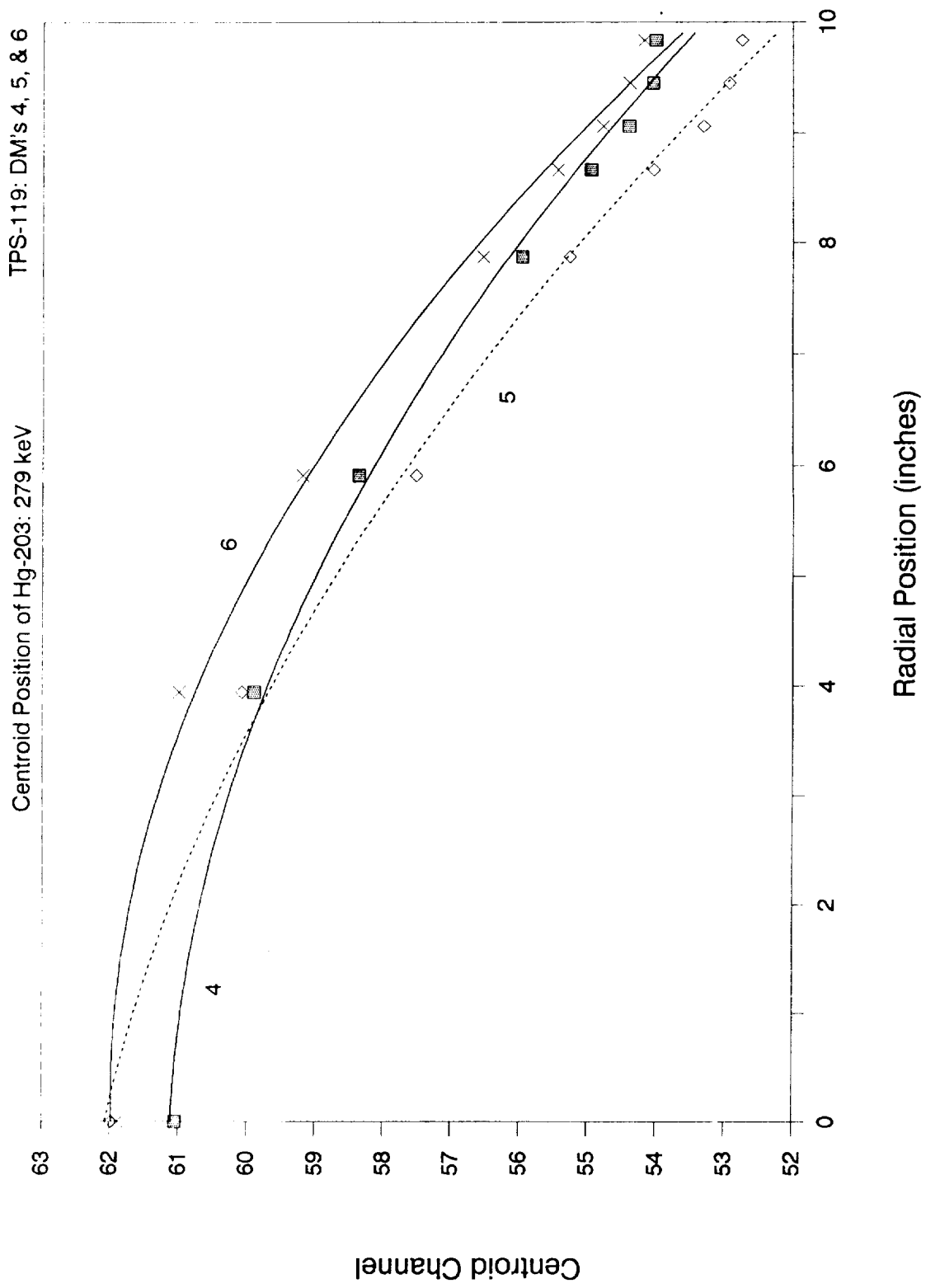


Figure 11

Radial Response

Centroid Position of Hg-203: 279 keV

TPS-119: DM's 7, 0/8, & P

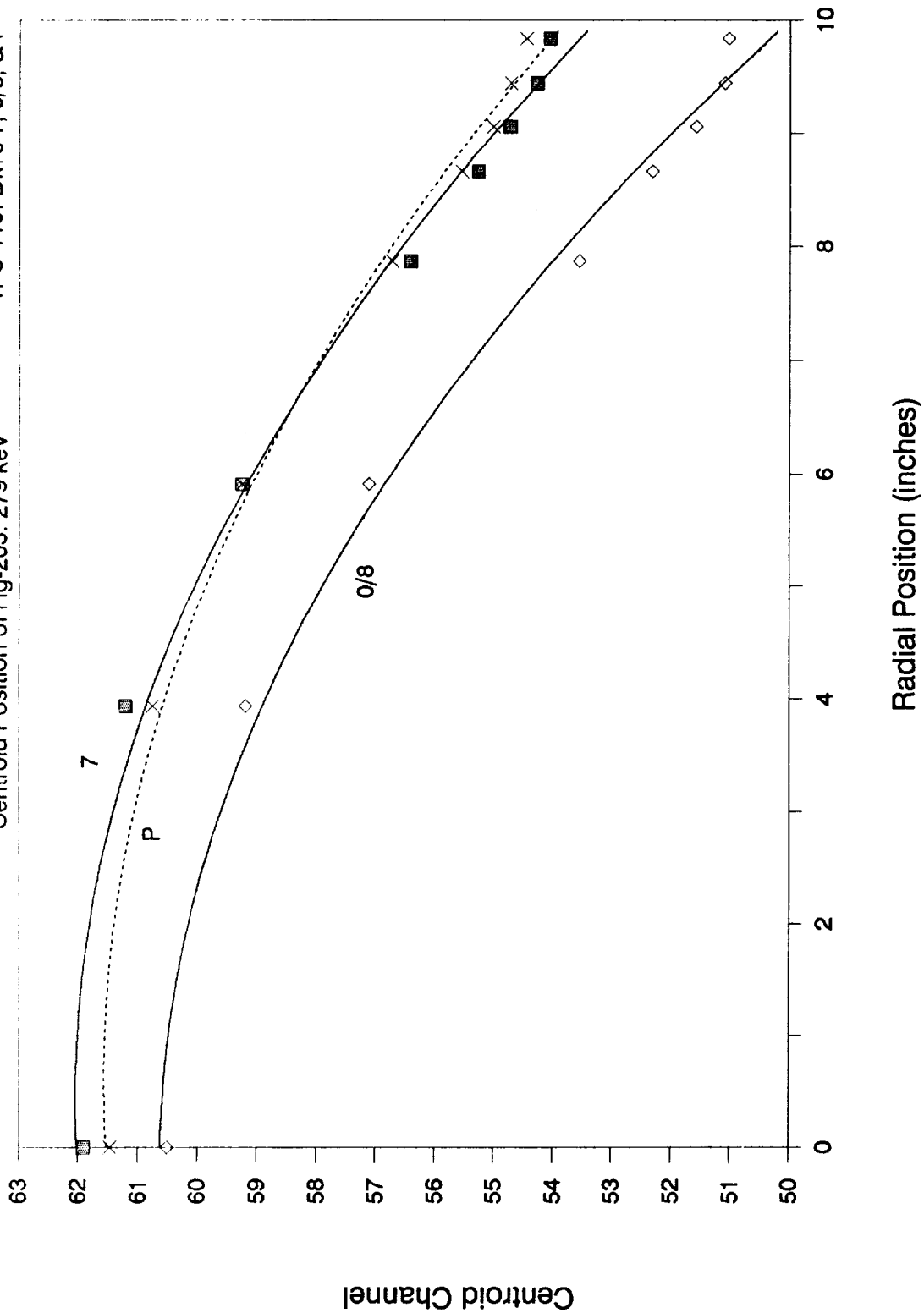


Figure 12

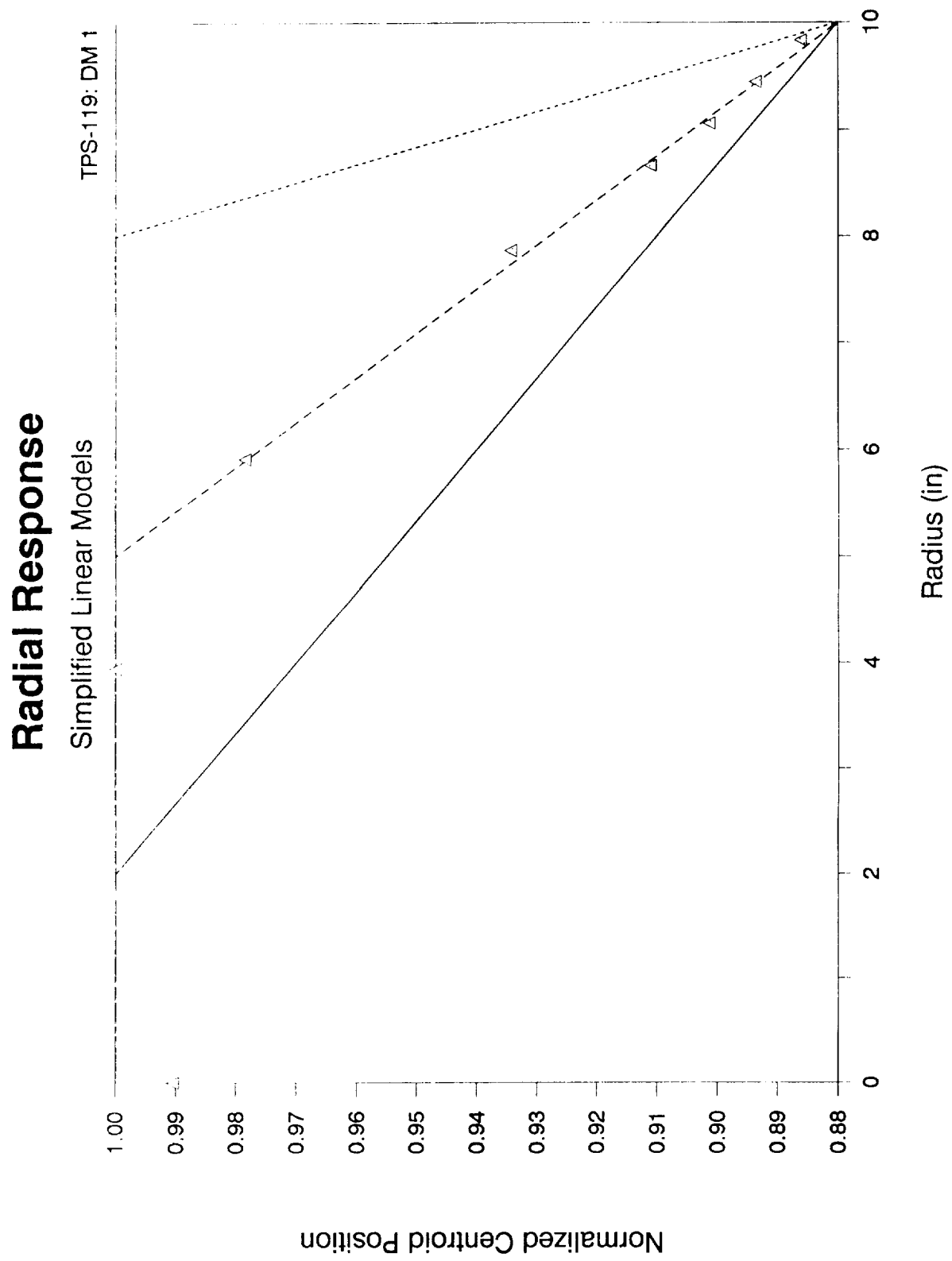


Figure 13

Radial Response

Cs-137: 662 keV
TPS-119: DM 1

Comparison of theory with data

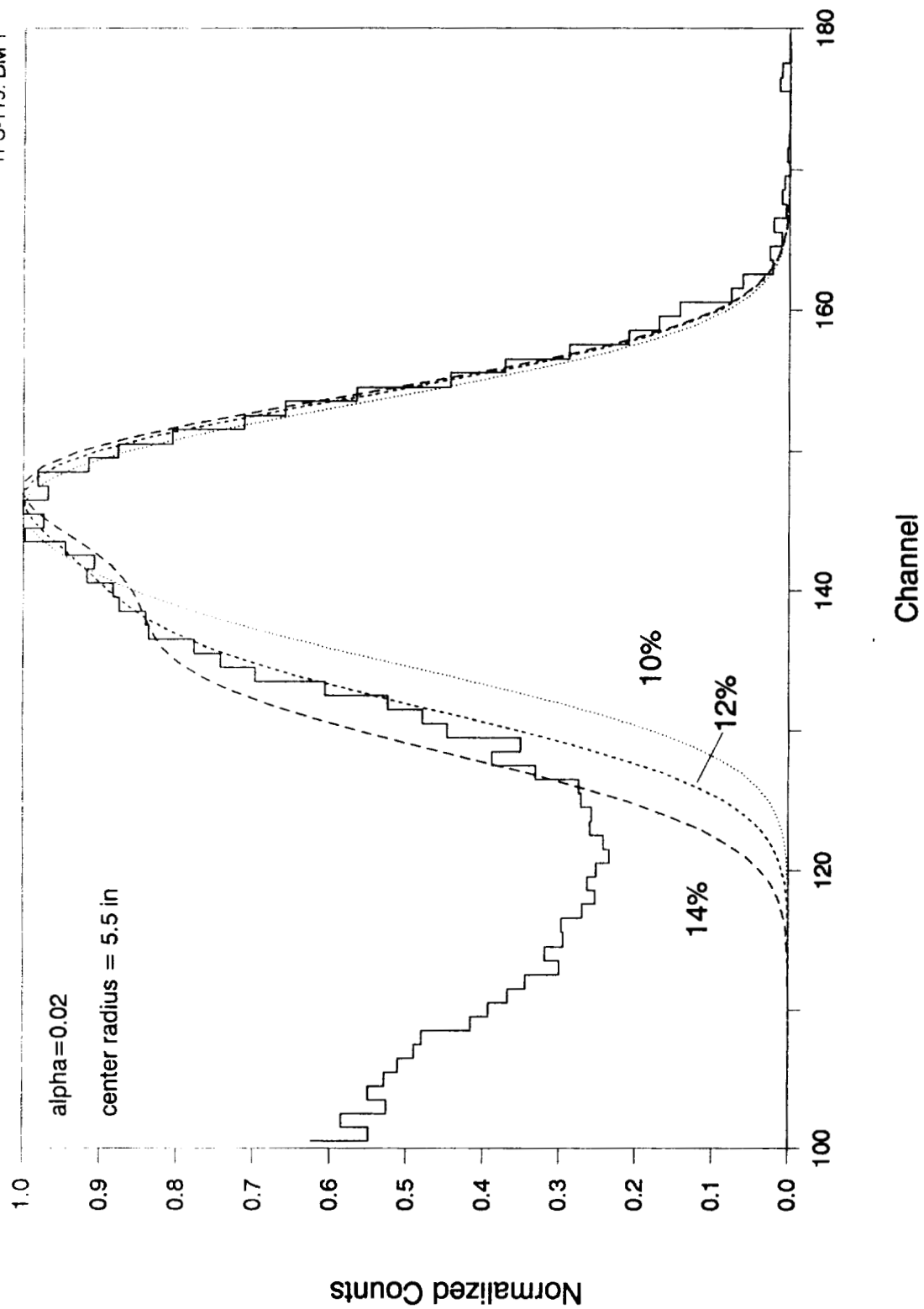


Figure 14

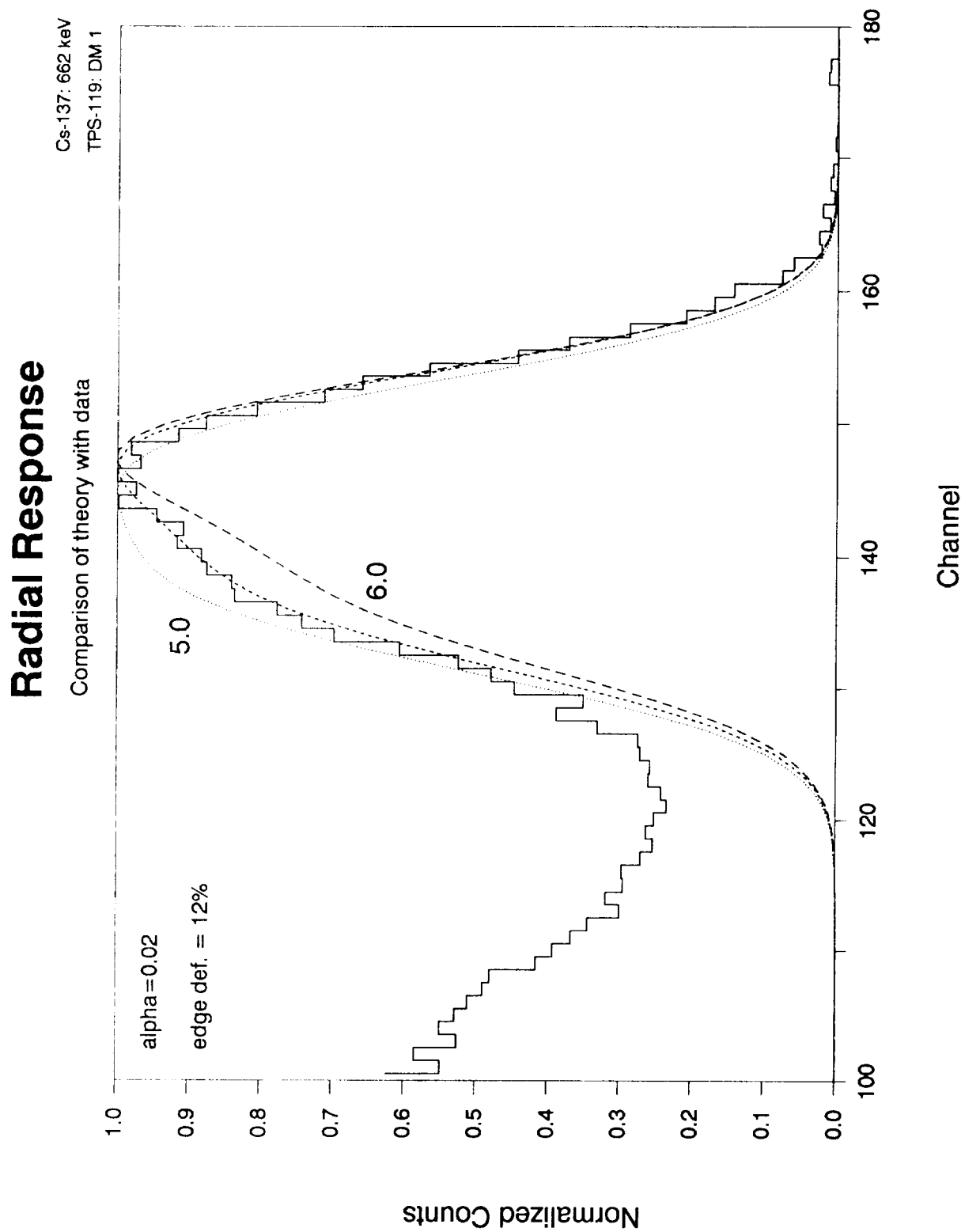


Figure 15

Radial Response

Comparison of theory with data

Cs-137: 662 keV
TPS-119: DM 1

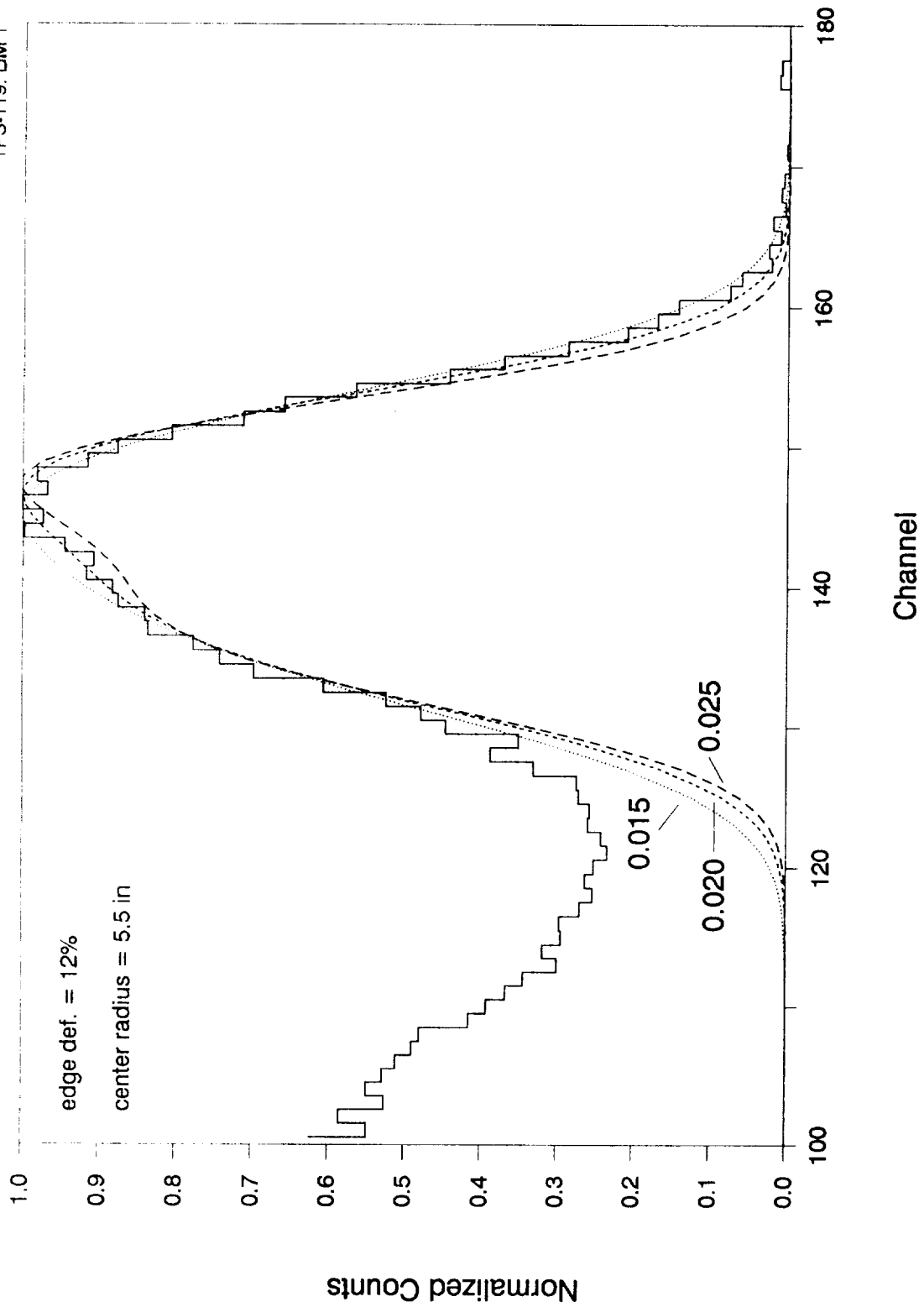
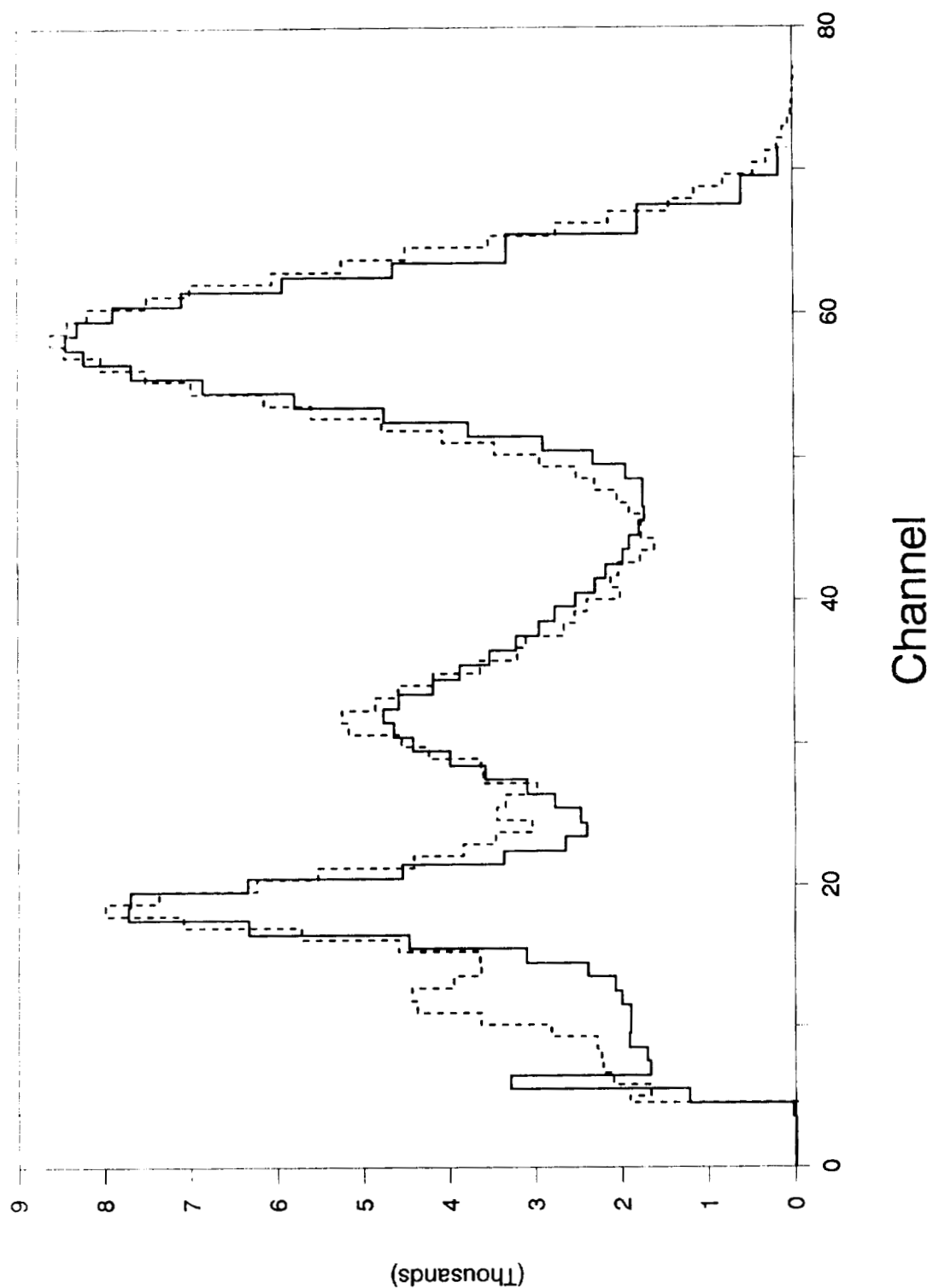


Figure 16



Counts

Figure 17

XVII-25

1989

NASA/ASEE SUMMER FACULTY FELLOWSHIP PROGRAM

**MARSHALL SPACE FLIGHT CENTER
THE UNIVERSITY OF ALABAMA IN HUNTSVILLE**

**DETERMINATION OF THE IMPLEMENTATION OF THE 3-AXIS
ATTITUDE MOTION SIMULATOR DIGITAL POSITION CONTROLLER**

Prepared by:	Mario E. Magaña
Academic Rank:	Assistant Professor
University and Department:	The University of Alabama Tuscaloosa Electrical Engineering
NASA/MSFC:	
Laboratory:	Information and Electronic Systems
Division:	Software and Data Management
Branch:	Data Management
MSFC Colleagues:	Tom Dollman and Ken Fernandez
Date:	August 11, 1989
Contract No.:	The University of Alabama in Huntsville NGT-01-008-021

DETERMINATION OF THE IMPLEMENTATION OF THE 3-AXIS ATTITUDE
MOTION SIMULATOR DIGITAL POSITION CONTROLLER

by

Mario E. Magaña
Assistant Professor of Electrical Engineering
The University of Alabama
Tuscaloosa, Alabama

ABSTRACT

In this work we mathematically reconstruct and document the digital position controller implemented in the control computer of the 3-axis attitude motion simulator, since the information supplied with the executable code of this controller was insufficient to make substantial modifications to it. We also develop methodologies to introduce changes in the controller which do not require rewriting the software. Finally, recommendations are made on possible improvement to the control system performance.

**ORIGINAL PAGE IS
OF POOR QUALITY**

ACKNOWLEDGMENTS

I would like to express my gratitude and appreciation to my NASA colleagues Tom Dollman and Ken Fernandez for giving me the opportunity to demonstrate my ability to solve engineering problems in the field of automatic control systems. Special thanks go to Jack Hemby from Boeing and to Ellen Howell for their valuable assistance in solving the assigned problem.

INTRODUCTION

The objective of this project is to investigate the nature and details of the implementation of the digital position controller of the three-axes attitude motion simulator in order to effect changes in its parameters without having to rewrite the software, since the source code is not available.

To get a good understanding of this digital position controller, several experiments were carried out on the simulator via the control computer, with the assistance of NASA/Boeing personnel. The goal of these experiments was to determine whether or not the position controller implemented in the control computer was the discrete-time equivalent of the position controller implemented for the analog mode operation of the simulator [1].

**ORIGINAL PAGE IS
OF POOR QUALITY**

DETERMINATION OF THE DIGITAL POSITION CONTROLLER

During the analog mode operation of the simulator, the position controller of any of the three axes has the form

$$G_c(s) \triangleq \frac{U(s)}{E(s)} = \frac{K(s/\omega_1+1)(s/\omega_2+1)}{s(s/\omega_3+1)}, \quad (1)$$

where $E(s)$ is the Laplace transform of the error signal $e(t)$ and $U(s)$ is the Laplace transform of the control signal $u(t)$. The error signal $e(t)$ is defined as the difference between the commanded angular position $\theta_c(t)$ and the actual system angular position $\theta(t)$.

To obtain a discrete-time equivalent of this analog controller, the industry-accepted way of doing it is by applying the bilinear transformation, since it preserves the stability properties of its continuous-time counterpart, i.e.,

$$\begin{aligned} G_c(z) &\triangleq \frac{U(z)}{E(z)} \triangleq G_c(s) \Big|_s = \frac{2}{T} \frac{1-z^{-1}}{1+z^{-1}}, \\ &= \frac{K \left(\frac{2}{T\omega_1} \frac{1-z^{-1}}{1+z^{-1}} + 1 \right) \left(\frac{2}{T\omega_2} \frac{1-z^{-1}}{1+z^{-1}} + 1 \right)}{\left(\frac{2}{T} \frac{1-z^{-1}}{1+z^{-1}} \right) \left(\frac{2}{T\omega_3} \frac{1-z^{-1}}{1+z^{-1}} + 1 \right)}, \\ &= K_0 \left(\frac{a_0 + a_1 z^{-1} + a_2 z^{-2}}{1 + b_1 z^{-1} + a_2 z^{-2}} \right), \end{aligned} \quad (2)$$

where

$E(z) \triangleq$ Z-transform of the discrete-time error signal $e(kT)$,

$U(z) \triangleq$ Z-transform of the discrete-time control signal $u(kT)$,

$$K_0 \triangleq \frac{K \omega_3}{\omega_1 \omega_2}, \quad (3)$$

$$a_0 \triangleq \frac{\left(\frac{2}{T}\right)^2 + \frac{2}{T} (\omega_1 + \omega_2) + \omega_1 \omega_2}{\left(\frac{2}{T}\right)^2 + \frac{2}{T} \omega_3} , \quad (4)$$

$$a_1 \triangleq - \frac{2 \left[\left(\frac{2}{T}\right)^2 - \omega_1 \omega_2 \right]}{\left(\frac{2}{T}\right)^2 + \frac{2}{T} \omega_3} , \quad (5)$$

$$a_2 \triangleq \frac{\left(\frac{2}{T}\right)^2 - \frac{2}{T} (\omega_1 + \omega_2) + \omega_1 \omega_2}{\left(\frac{2}{T}\right)^2 + \frac{2}{T} \omega_3} , \quad (6)$$

$$b_1 \triangleq \frac{\frac{4}{T} \omega_3}{\left(\frac{2}{T}\right)^2 + \frac{2}{T} \omega_3} , \quad (7)$$

$$b_2 \triangleq - \frac{\left(\frac{2}{T}\right)^2 - \frac{2}{T} \omega_3}{\left(\frac{2}{T}\right)^2 + \frac{2}{T} \omega_3} , \quad (8)$$

$T \triangleq$ sampling interval (in seconds).

From equation (2) we find that the output of the digital position controller at the sampling instant kT is given by

$$\begin{aligned} u(kT) = & - b_1 u(kT-T) - b_2 u(kT-2T) + K_0 a_0 e(kT) + K_0 a_1 e(kT-T) \\ & + K_0 a_2 e(kT-2T) . \end{aligned} \quad (9)$$

According to the information available on the implementation of the digital position control algorithm [1], the parameters of the controller can be changed from the keyboard when INIT (initialization) is selected from the control computer main menu screen. When this entry is selected, a total of nine constants (labeled "coefficients") per axis appear on the screen; however, it is known that only seven of them correspond to the digital position control algorithm, one to the digital rate command scaling, and one is set to zero.

As shown in equation (9), there is a total of five coefficients, which strongly suggests that the digital position controller implemented in the control computer is not the one obtained by applying the bilinear transform to the analog position controller transfer function given by equation (1).

It should be pointed out at this stage, nonetheless, that there are other realizations of the digital position controller given by equation (2) and that more constants could be generated for scaling purposes to avoid the usual problems encountered when fixed point arithmetic is used. However, the numerical values of the coefficients of these other realizations do not match those that appear on the INIT screen for any of the three axes.

To figure out the actual structure of the controller, several experiments were carried out to determine, for example, if integration of the error signal was taking place to make sure that the controller integrator had been implemented. Experimental results indicated that integration of the input signal did indeed occur, therefore, to generate the exact seven coefficients per axis, it became apparent that either a pole or a pole and a zero had been added to the original analog position controller.

Let us modify the analog position controller by adding a pole at $s = -\omega_4$, i.e.,

$$G'_c(s) = K \frac{(s/\omega_1 + 1)(s/\omega_2 + 1)}{s(s/\omega_3 + 1)(s/\omega_4 + 1)} \quad (10)$$

Then, application of the bilinear transform to this controller transfer function yields the following discrete-time equivalent controller

$$\begin{aligned} G'_c(z) &= G'_c(s) \Big|_{s = \frac{2}{T} \frac{1-z^{-1}}{1+z^{-1}}} , \\ &= K'_0 \left(\frac{c_0 + c_1 z^{-1} + c_2 z^{-2} + c_3 z^{-3}}{1 + d_1 z^{-1} + d_2 z^{-2} + d_3 z^{-3}} \right) , \end{aligned} \quad (11)$$

where

$$K'_0 = \frac{KT\omega_3\omega_4}{2\omega_1\omega_2} \quad (12)$$

$$c_0 = \frac{\left(\frac{2}{T}\right)^2 + \frac{2}{T} (\omega_1 + \omega_2) + \omega_1 \omega_2}{\left(\frac{2}{T}\right)^2 + \frac{2}{T} (\omega_3 + \omega_4) + \omega_3 \omega_4}, \quad (13)$$

$$c_1 = \frac{-\left(\frac{2}{T}\right)^2 + \frac{2}{T} (\omega_1 + \omega_2) + 3\omega_1 \omega_2}{\left(\frac{2}{T}\right)^2 + \frac{2}{T} (\omega_3 + \omega_4) + \omega_3 \omega_4}, \quad (14)$$

$$c_2 = \frac{-\left(\frac{2}{T}\right)^2 - \frac{2}{T} (\omega_1 + \omega_2) + 3\omega_1 \omega_2}{\left(\frac{2}{T}\right)^2 + \frac{2}{T} (\omega_3 + \omega_4) + \omega_3 \omega_4}, \quad (15)$$

$$c_3 = \frac{\left(\frac{2}{T}\right)^2 - \frac{2}{T} (\omega_1 + \omega_2) + \omega_1 \omega_2}{\left(\frac{2}{T}\right)^2 + \frac{2}{T} (\omega_3 + \omega_4) + \omega_3 \omega_4}, \quad (16)$$

$$d_1 = \frac{-3\left(\frac{2}{T}\right)^2 - \frac{2}{T} (\omega_3 + \omega_4) + \omega_3 \omega_4}{\left(\frac{2}{T}\right)^2 + \frac{2}{T} (\omega_3 + \omega_4) + \omega_3 \omega_4}, \quad (17)$$

$$d_2 = \frac{3\left(\frac{2}{T}\right)^2 - \frac{2}{T} (\omega_3 + \omega_4) - \omega_3 \omega_4}{\left(\frac{2}{T}\right)^2 + \frac{2}{T} (\omega_3 + \omega_4) + \omega_3 \omega_4}, \quad (18)$$

$$d_3 = \frac{-\left(\frac{2}{T}\right)^2 + \frac{2}{T} (\omega_3 + \omega_4) - \omega_3 \omega_4}{\left(\frac{2}{T}\right)^2 + \frac{2}{T} (\omega_3 + \omega_4) + \omega_3 \omega_4}. \quad (19)$$

A direct time domain realization of this digital controller is given by

$$u(kT) = -d_1 u(kT-T) - d_2 u(kT-2T) - d_3 u(kT-3T) + K'_0 c_0 e(kT) \\ + K'_0 c_1 e(kT-T) + K'_0 c_2 e(kT-2T) + K'_0 c_3 e(kT-3T) \quad . \quad (20)$$

This direct realization of the digital position controller is by no means the best realization as it is susceptible to round-off and quantization errors. However, the numerical values of its coefficients were found to be the same as those that appear on the INIT screen for each of the three axes once ω_4 was determined, thus leading to the conclusion that the controller given by equations (11) and (20) is the one that has been implemented in the control computer (PC). In fact, the extra pole ($-\omega_4$) is located at -20, -25, and -22.8 for the roll, yaw, and sidereal axis, respectively.

The following analog transfer functions were determined to have been the source of the discrete-time, equivalent position controllers implemented in the control computer.

Roll:

$$G'_c(s) = 0.0047 \frac{(s/0.056 + 1)(s/0.66 + 1)}{s(s/5.6 + 1)(s/20 + 1)} \quad , \quad (21)$$

Yaw:

$$G'_c(s) = 0.025 \frac{(s/0.095 + 1)(s/0.588 + 1)}{s(s/1.43 + 1)(s/25 + 1)} \quad , \quad (22)$$

Sidereal:

$$G'_c(s) = 0.03 \frac{(s/0.068 + 1)(s/12.5 + 1)}{s(s/20 + 1)(s/22.8 + 1)} \quad . \quad (23)$$

Comparing equations (21) to (23) with those found on page 3-13 of Reference 1, we can conclude that the analog position controllers were modified by adding a pole before they were discretized to obtain the digital position controllers.

Application of the bilinear transform (with $T = 0.01$ sec) to equations (21) to (23) yields the following discrete-time equivalent position controllers.

Roll:

$$G'_c(z) = \frac{6.32005 \times 10^{-2} - 6.274936 \times 10^{-2} z^{-1} - 6.320026 \times 10^{-2} z^{-2} + 6.274959 \times 10^{-2} z^{-3}}{1 - 2.763707 z^{-1} + 2.537319 z^{-2} - 7.736116 \times 10^{-1} z^{-3}} \quad , \quad (24)$$

Yaw:

$$G'_c(z) = \frac{7.08467 \times 10^{-2} - 7.036407 \times 10^{-2} z^{-1} - 7.084631 \times 10^{-2} z^{-2} + 7.036446 \times 10^{-2} z^{-3}}{1 - 2.763579 z^{-1} + 2.530314 z^{-2} - 7.667345 \times 10^{-1} z^{-3}}, \quad (25)$$

Sidereal:

$$G'_c(z) = \frac{6.979685 \times 10^{-2} - 6.153802 \times 10^{-2} z^{-1} - 6.979127 \times 10^{-2} z^{-2} + 6.154359 \times 10^{-2} z^{-3}}{1 - 2.613514 z^{-1} + 2.26424 z^{-2} - 6.507263 \times 10^{-1} z^{-3}}. \quad (26)$$

Let

$$K_1 \triangleq K'_0 c_0, \quad (27)$$

$$K_2 \triangleq K'_0 c_1, \quad (28)$$

$$K_3 \triangleq K'_0 c_2, \quad (29)$$

$$K_4 \triangleq K'_0 c_3, \quad (30)$$

$$K_5 \triangleq -d_1, \quad (31)$$

$$K_6 \triangleq -d_2, \quad (32)$$

$$K_7 \triangleq -d_3. \quad (33)$$

Then the digital position controller for any of the **three axes** is given by

$$G'_c(z) = \frac{K_1 + K_2 z^{-1} + K_3 z^{-2} + K_4 z^{-3}}{1 - K_5 z^{-1} - K_6 z^{-2} - K_7 z^{-3}}. \quad (34)$$

The reason for writing the digital position controller in the form of equation (34) is that when the INIT menu selection is made, the coefficients of the digital position controller appear on the control computer monitor screen as K_1 through K_7 . For example, the coefficients of the digital position controller for the roll axis are:

$$\begin{aligned}
K_1 &= 6.32005 \times 10^{-2} \quad , \\
K_2 &= -6.274936 \times 10^{-2} \quad , \\
K_3 &= -6.320026 \times 10^{-2} \quad , \\
K_4 &= 6.274959 \times 10^{-2} \quad , \\
K_5 &= 2.763707 \quad , \\
K_6 &= -2.537319 \quad , \\
K_7 &= 7.736116 \times 10^{-1} \quad .
\end{aligned}$$

The present implementation of the digital position controller is therefore given by

$$\begin{aligned}
u(kT) &= K_5 u(kT-T) + K_6 u(kT-2T) + K_7 u(kT-3T) + K_1 e(kT) + K_2 e(kT-T) \\
&\quad + K_3 e(kT-2T) + K_4 e(kT-3T) \quad .
\end{aligned} \tag{35}$$

Remark: The dc gains of the controllers given by equations (21) through (23) are smaller than those of the original analog position controllers (shown on page 3-13 of Reference 1) because of the fact that the position sensors used in the analog and digital modes are different. In the analog mode, a single turn potentiometer is used to sense the angular position. This potentiometer has a gain embedded in it, in fact, it is equal to 0.05 Volts/degree for the roll axis and 0.1 Volts/degree for the yaw and sidereal axis. In the digital mode, a resolver-inductosyn pair, along with two resolver to digital converters, are used to obtain the angular displacement. The resolver to digital converters have a third-order dynamic model with unity dc gain. Therefore, this change in the gain is reflected by the reduction of the gain of the modified analog equivalent position controllers of equations (21) through (23).

CONCLUSIONS AND RECOMMENDATIONS

The structure of the three-axes attitude motion simulator digital position controller implemented in the control computer has been determined through experimentation and educated guesses, since no documentation about (or computer program source code implementation of) such a controller is available.

Thus, given that only the executable code of the controller is available, its structure cannot be changed without rewriting the entire control software; however, it is possible to make some on-line changes which do not require new controller software. For instance, the original location of the analog equivalent position controller poles and zeros could be changed to new desired values $-\omega'_1$, $-\omega'_2$, $-\omega'_3$, and $-\omega'_4$ and then compute K_1 through K_7 off-line using equations (27) to (33). Also, another zero located at $s = -\omega_0$ could be added to improve global stability as well as the speed of response of the simulator.

If a zero is added to the modified analog equivalent position controller, i.e.,

$$G'_c(s) = K' \frac{(s/\omega_0 + 1)(s/\omega_1 + 1)(s/\omega_2 + 1)}{s(s/\omega_3 + 1)(s/\omega_4 + 1)}, \quad (36)$$

then the discrete-time equivalent position controller will still be given by equation (11), however, K'_0 , c_0 , c_1 , c_2 , and c_3 will change to

$$K'_0 = \frac{K' T \omega_3 \omega_4}{2 \omega_0 \omega_1 \omega_2}, \quad (37)$$

$$c_0 = \frac{\left(\omega_0 + \frac{2}{T}\right) \left[\left(\frac{2}{T}\right)^2 + \frac{2}{T} (\omega_1 + \omega_2) + \omega_1 \omega_2\right]}{\left(\frac{2}{T}\right)^2 + \frac{2}{T} (\omega_3 + \omega_4) + \omega_3 \omega_4}, \quad (38)$$

$$c_1 = \frac{\left(\omega_0 + \frac{2}{T}\right) \left[-2\left(\frac{2}{T}\right)^2 + 2\omega_1 \omega_2\right] + \left(\omega_0 - \frac{2}{T}\right) \left[\left(\frac{2}{T}\right)^2 + \frac{2}{T} (\omega_2 + \omega_2) + \omega_1 \omega_2\right]}{\left(\frac{2}{T}\right)^2 + \frac{2}{T} (\omega_3 + \omega_4) + \omega_3 \omega_4}, \quad (39)$$

$$c_2 = \frac{\left(\omega_0 + \frac{2}{T}\right) \left[\left(\frac{2}{T}\right)^2 - \frac{2}{T} (\omega_1 + \omega_2) + \omega_1 \omega_2\right] + \left(\omega_0 - \frac{2}{T}\right) \left[-2 \left(\frac{2}{T}\right)^2 + 2\omega_1 \omega_2\right]}{\left(\frac{2}{T}\right)^2 + \frac{2}{T} (\omega_3 + \omega_4) + \omega_3 \omega_4}, \quad (40)$$

$$c_3 = \frac{\left(\omega_0 - \frac{2}{T}\right) \left[\left(\frac{2}{T}\right)^2 - \frac{2}{T} (\omega_1 + \omega_2) + \omega_1 \omega_2\right]}{\left(\frac{2}{T}\right)^2 + \frac{2}{T} (\omega_3 + \omega_4) + \omega_3 \omega_4} \quad (41)$$

The new values of the coefficients K_1 to K_4 can again be computed off-line using equations (37) to (41) and (27) to (30). Notice that the values of the coefficients K_5 to K_7 will not change because they do not depend on the zeros. It should also be pointed out that when a zero is added to the modified analog equivalent position controller the value of the coefficients K_1 through K_4 may be larger than 1 and can cause some overflow problems [5] if provisions are not made to handle such numbers because the INTEL 8086 microprocessor utilizes 2's complement arithmetic. This problem can be alleviated by reducing the dc gain K' of the equivalent analog position controller of equation (36).

Another possible improvement in the performance of the simulator could be achieved by introducing frequency prewarping of the analog equivalent position controller corner frequencies; however, the improvement would be minute in this case because the sampling rate used in the control algorithm is unusually high (100 Hz).

Once the coefficients K_1 through K_7 have been recomputed off-line, the old values can be changed interactively in the control computer when INIT is selected from the main menu.

It should be apparent by now that the suggested changes only involve the recomputation of the coefficients K_1 through K_7 since they reflect any changes that may take place in the location of the poles and zeros of the modified analog equivalent position controller of equation (10) or the addition of another zero as in equation (36).

Although the performance requirements of the simulator are not terribly stringent, it is deemed by the author that a much more robust controller can be designed to operate at a substantially lower sampling rate (much lower than 100 Hz as it is presently implemented) and yet outperform the present digital position controller in every aspect, such as global stability, speed of response, and flexibility. This, however, would require rewriting the control software.

To begin with, an improved controller design would have to take into account the dynamics of the resolver to digital converter which is used to determine the angular position of each of the simulator axes, since this device is installed in the feedback path of the position loop. This type of converter is modeled as a type II tracking loop and possesses the closed-loop transfer function (ILC Data Devices Corp.)

$$G_{R/D}(s) = \frac{A(s/B + 1)}{\frac{1}{10B} s^3 + s^2 + \frac{A}{B} s + A}, \quad (42)$$

where

$$A = \begin{cases} 50176 & , \text{ XDC-19147-303} \\ 184800 & , \text{ XDC-19197-304} \end{cases},$$

$$B = \begin{cases} 100 & , \text{ XDC-19147-303} \\ 300 & , \text{ XDC-19197-304} \end{cases},$$

where the XDC-19147-303 and the XDC-19197-304 are the 14- and 16-bit resolution resolver to digital converters installed in the attitude simulator digital control cards, respectively. Furthermore, it would make use of the velocity signal which is also generated by the same resolver to digital converter since the noise content of this signal is much smaller than the one generated by a mechanical transducer such as a tachometer.

This new controller would also implement the rate compensation totally in the digital domain since the velocity signal generated by the resolver to digital converter can be digitized using an analog to digital converter without much difficulty. This approach would add a tremendous flexibility to the controller design.

Finally, this controller would be designed in such a way that its performance does not deteriorate with changes of simulator parameters such as inertia, i.e., it would have some level of adaptation that takes care of variations in the system parameters.

REFERENCES

- [1] UNISYS, "Operation and Maintenance Manual for NASA's Three-Axis Attitude Motion Simulator System," UNISYS Corporation, 15 June 1988.
- [2] Ogata, K., "Discrete-Time Control Systems," Prentice Hall, 1987.
- [3] Åström, K.J. and Wittenmark, B., "Computer Controlled Systems, Theory and Design," Prentice Hall, 1984.
- [4] Tompkins, W.J. and Webster, J.G., "Interfacing Sensors to the IBM PC," Prentice Hall, 1988.
- [5] Phillips, C.L. and Nagle, H.T., "Digital Control System Analysis and Design," Prentice Hall, 1984.

1989

NASA/ASEE SUMMER FACULTY FELLOWSHIP PROGRAM

MARSHALL SPACE FLIGHT CENTER
THE UNIVERSITY OF ALABAMA IN HUNTSVILLE

MECHANICS OF AEOLIAN PROCESSES-
SOIL EROSION AND DUST PRODUCTION

Prepared by:	M. M. Mehrabadi, Ph.D.
Academic Rank:	Associate Professor
University and Department:	Tulane University Department of Mechanical engineering
NASA/MSFC Laboratory:	Space Science Laboratory
Division:	Earth Science and Applications Division
Branch:	Fluid Dynamics
MSFC Colleague:	Nicholas C. Costes, Ph.D.
Date:	August 22, 1989
Contract No.:	The University of Alabama in Huntsville NGT-01-008-021

XX

MECHANICS OF AEOLIAN PROCESSES-
SOIL EROSION AND DUST PRODUCTION

by

M. M. Mehrabadi
Dept. of Mechanical Engineering
Tulane University
New Orleans, Louisiana 70118

ABSTRACT

Aeolian (wind) processes occur as a result of atmosphere / land-surface system interactions. A thorough understanding of these processes and their physical/mechanical characterization on a global scale is essential to monitoring global change and, hence, is imperative to the fundamental goal of the Earth Observing System (Eos) program.

Soil erosion and dust production by wind are of consequence mainly in arid and semi arid regions which cover 36% of the Earth's land surface. Some recent models of dust production due to wind erosion of agricultural soils and the mechanics of wind erosion in deserts are reviewed and the difficulties of modeling the aeolian transport are discussed in this report.

ACKNOWLEDGMENTS

The financial support of the NASA/ASEE Summer Faculty Program is gratefully acknowledged. The author is indebted to Drs. N. C. Costes (NASA/MSFC), Goudarz Ahmadi (Clarkson University), Bruce White (University of California, Davis), Robert S. Anderson (University of California, Santa Cruz), Dale A. Gillette (National Oceanic and Atmospheric Administration), Ayo Oyediran (NRC), and Yemo Fashiola (UAH) for stimulating discussions of their publications on this subject matter.

FIGURE CAPTIONS

FIG. 1 Major deserts of the world and directions and distances of dust transport (after Pewe, 1981)

FIG. 2 Major paths of airborne soil dust from West Africa and North Africa (from Rapp, 1977, after Pewe, 1981)

FIG. 3 Log-height vs. wind speed profiles for deriving the hypothetical wind speed $U(z_r)$ at reference height z_r (with reference roughness height z_{or}) from the wind speed $U(z_s)$ measured at station height z_s (with effective upwind roughness height z_{os}) (redrawn from Wieringa, 1976)

FIG. 4 Vertical flux of dust ($\text{g cm}^{-2} \text{s}^{-1}$) as a function of friction velocity (cm s^{-1}) (after Gillette and Passi, 1988)

FIG. 5 Schematic representation of modes of aeolian transport (from Kind, 1989)

FIG. 6 Differential intensity of bombardment on windward and lee slopes (after Bagnold, 1941)

FIG. 7 Coincidence of ripple wavelength and range of characteristic path of grain (after Bagnold, 1941)

FIG. 8 Coefficient A as a function of the threshold particle friction Reynolds number, B (after White, 1986)

FIG. 9 Schematic diagram showing the trajectory of a particle.

FIG. 10 Saltation trajectories (after White, 1986)

MECHANICS OF AEOLIAN PROCESSES - SOIL EROSION AND DUST PRODUCTION

1. INTRODUCTION

Aeolian (wind) processes occur as a result of atmosphere/land-surface system interaction. Study of this interaction is one of the broad geologic science issues identified by the Earth Observing System (Eos) Science and Mission Requirement Group (Butler et al., 1984) and the Eos Science Steering Committee (Butler et al., 1987). A fundamental goal of Eos is to develop an improved understanding of the processes that control the formation and evolution of the solid Earth. Aeolian processes are persistent sculptors of the face of the planet Earth (and Mars). Hence a thorough understanding of these processes and their physical/chemical characterization is essential to monitoring global change and, thus, is imperative to this goal.

Wind erosion and transport are active geologic processes that occur mainly in arid and semi-arid regions which cover 36% of the Earth's land surface. Arid and semi-arid areas suffering from "desertification" undergo destruction of native vegetation which is quickly followed by an excessive soil erosion. Examples of areas with severe soil erosion are northern China, including part of the Loess Plateau and Inner Mongolia, the Thar desert of eastern Pakistan and northwest India, and the U.S. Great Plains, including parts of Texas, Oklahoma, and New Mexico.

Although soil erosion by wind is of consequence mainly in arid and semi-arid regions, it may occur wherever soil, vegetation, and climatic conditions are conducive. Generally, wind erosion is effective when soil is loose, fine, and dry, and has little or no vegetation. The present rate of fertile soil loss in the United States may be as high as 100 tons per acre per year in half a dozen major agricultural regions, including the corn-belt states of Iowa, Missouri and Illinois. The Council on Environmental Quality (Sheridan, 1981) estimates that about 10 percent of the U.S. land mass is in a state of severe or very severe desertification.

Large dust storms originate in major deserts of the world (Fig. 1). In most of these deserts, dust is formed by in situ weathering of bedrock and from abrasion of the bedrock by the wind-blown sand (Goudie, 1978). Large,

frequent dust storms originate from normally semi-arid areas (e.g., the Great Plains of the United States; Central India; and the Russian steppes) that periodically become arid, undergo abnormally strong windy periods, or have their vegetation removed by man or nature (Pewe, 1981).

In terms of particle size, dust can be divided into two major groups depending on how far a distance they can be transported by the wind (Pewe, 1981). Dust particles that are carried between a few kilometers to less than 100 km, by dust devils and dust storms, are mostly between 0.005 mm to 0.05 mm. The other type of dust consists of particles between 0.002 mm and 0.01 mm in size. This fine-grained, sorted dust is carried to the troposphere as an aerosol (i.e., a dust that remains suspended in the air until brought down by rainfall onto water and land surfaces). Dust from the Sahara collected in the Caribbean (Fig.2) has been reported to be more than 98% smaller than 0.01 mm (Prospero, et al., 1970).

Aerosols affect the reflectance, transmittance and absorptance of the atmosphere (Verstraete, et al., 1988). They modify the amount of shortwave radiation absorbed and longwave radiation emitted by the climatic system. Their impact on the climate is further enhanced by their role as cloud condensation nuclei.

Aerosols impact on the transfer of radiation through the atmosphere also affects the interpretation of the satellite remote sensing data. While this creates a nuisance for data obtained using passive remote sensing techniques, aerosols provide excellent tracers when active instruments such as the Laser Atmospheric Wind Sounder (LAWS) are used for wind velocity measurements.

Dust has many other serious environmental consequences. These include its effect on crop growth, ocean sedimentation and its effect on the acid/base balance of atmospheric deposition. Dust storms cause disease, suffocation of cattle, development of static electricity, disruption of transportation, and destruction of property.

A model for the estimation of total dust production for the United States has been discussed recently by Gillette (1988). After reviewing this model in Sec. 3, the mechanics of aeolian transport of particulate materials is discussed in Sec. 4. The long and short term goals of this research effort are described in the next section.

2. OBJECTIVES

Some recent literature on mechanical modeling of aeolian processes are reviewed in this report. Specifically, two kinds of models are discussed. The first kind deals with the agricultural soil erosion and dust production by wind. The second kind deals with the more basic problem of wind erosion in deserts.

This effort is part of a comprehensive program of research focused on assessing the potential impact of desertification on climate changes and global habitability. The ultimate goal of this research is to develop a quantitative understanding of the mechanics of atmospheric coupling with land systems, as related to desert processes in arid and semi-arid regions. Existing data banks, data generated by laboratory experimentation and, later, data generated by Eos sensors will be used in the validation stage of the model.

The short term goal of this research is the formulation and validation of a model for the main mechanisms involved in the aeolian transport of particles based on principles of mechanics at the particle-scale. At present, no comprehensive quantitative analysis of such processes is available.

3. A MODEL FOR DUST EMISSION BY WIND EROSION

A model for the total dust production for the United States, recently proposed by Gillette and Passi (1988), is reviewed in this section. The primary use of the model is in the inventory of alkaline elements for use in acid/base balance studies of atmospheric precipitation by the National Acid Precipitation Assessment Program (NAPAP).

3.1 Wind Profile in the Lower Planetary Boundary Layer

In the atmospheric inertial sublayer, which is the lower part of the planetary boundary layer, the wind speed can be assumed to vary with height according to the logarithmic wind profile (see, e.g., Priestely, 1959, or Plate, 1971)

$$U(z) = \frac{V_*}{0.4} \ln \frac{z}{z_0} \quad (3.1)$$

if the stratification is nearly adiabatic (for winds above the velocity required for wind erosion of soils, Gillette, 1981, reported that the atmosphere was neutrally stratified). In (3.1), z_0 denotes atmospheric roughness height, taken to be 1 cm for smooth surfaces (e.g., airport surfaces), and V_* is the friction velocity defined in terms of the shearing stress (shearing force per unit area of ground surface parallel to the wind direction) as

$$V_* = \sqrt{\frac{\tau}{\rho}} \quad \text{or} \quad \tau = \rho V_*^2 \quad (3.2)$$

where ρ is the air density. Note that V_* is the velocity of the wind at a height approximately equal to $1.492 z_0$.

It is convenient sometimes to introduce a drag coefficient, C_d , defined by (Priestely, 1959)

$$C_d \equiv \frac{\tau}{\rho U^2} = \left(\frac{V_*}{U} \right)^2 \quad (3.3)$$

where (3.3)₂ has been written using (3.2)₂ to eliminate τ . Gillette and Passi (1988) use a method proposed by Wieringa (1976) to evaluate the drag coefficient C_d . This procedure is summarized in the next two paragraphs.

Wieringa (1976) takes the wind speed at a height of $z_b = 60$ m to be regionally constant. In other words, he assumes that the wind speed at that height, $U(z_b)$, does not show excessively the influence of the particular roughness element close to the wind station where an average wind speed $U(z_s)$ is measured at a height z_s . Suppose that at the same location we wish to know the average wind speed $U(z_r)$ over a hypothetical flat open reference terrain at a height z_r . Referring to Fig. 3, and calculating the slopes of the two wind profiles, will give

$$\frac{\ln z_b/z_s}{U(z_b) - U(z_s)} = \frac{\ln z_s/z_{os}}{U(z_s)} \quad (3.4)$$

and

$$\frac{\ln z_b/z_r}{U(z_b) - U(z_r)} = \frac{\ln z_r/z_{or}}{U(z_r)} \quad (3.5)$$

Eliminating $U(z_b)$ between (3.4) and (3.5), one finds

$$U(z_r) = U(z_s) \frac{\ln z_b/z_{os} \ln z_r/z_{or}}{\ln z_s/z_{os} \ln z_b/z_{or}} \quad (3.6)$$

This is the required relation between $U(z_r)$ and $U(z_s)$.

If z_r is taken to be $1.492 z_{or}$, so that $\ln z_r/z_{or} = 0.4$, then from (3.1) it follows that $U(z_r) = V_x$ and from (3.6) it follows that

$$V_x = U(z_s) \frac{0.4 \ln z_b/z_{os}}{\ln z_s/z_{os} \ln z_b/z_{or}} \quad (3.7)$$

Using (3.7), the drag coefficient can be calculated from (3.3) as

$$C_d = \left[\frac{0.4 \ln z_b/z_{os}}{\ln z_s/z_{os} \ln z_b/z_{or}} \right]^2 \quad (3.8)$$

Gillette and Passi (1988), use a value for $z_{os} = 1$ cm, typical of clipped grass at airports, and $z_{or} = 0.002$ cm, from an average measured aerodynamic roughness heights they obtained in many experiments. With these values they find that

$$C_d = \left(\frac{0.23}{\ln z_s} \right)^2 \quad (3.9)$$

where z_s is in cm. Substitution of (3.9) in (3.3) yields

$$V_* = \frac{0.23}{\ln z_s} U \quad (3.10)$$

which relates the friction velocity to the wind speed.

3.2 Threshold Friction Velocity

Threshold friction velocity for wind erosion corresponds to the minimum wind stress needed to overcome forces holding soil particles in place. Threshold friction velocity is denoted by V_{*t} and is defined in terms of surface shear stress at threshold (or "threshold wind stress"), τ_t , by the relations

$$V_{*t} = \sqrt{\frac{\tau_t}{\rho}} \quad \text{or} \quad \tau_t = \rho V_{*t}^2 \quad (3.11)$$

Although one must rely heavily on the values of the threshold friction velocity for estimation of dust production and wind erosion, there exists no theory for relating this quantity to the physical characteristics of the soil.

Threshold friction velocity has been determined experimentally for idealized surfaces by many investigators (see Gillette, 1988, for references) starting with the pioneering work of Bagnold (1941) who proposed a formula for V_{*t} in terms of the particle diameter and density (see section 4.1 of this report). The physical circumstances in agricultural soils is complicated, however, because of a wide variety of particle sizes and the effects of wetting/drying, freezing/thawing, vegetation, and aggregation of particles. Measurements of the threshold friction velocities for dust production for a wide class of agricultural soils has been reported only recently by Gil-

lette (1988). Gillette and Passi's estimation of dust production is based on the measurements of Gillette (1988) and the values of threshold friction velocity obtained for arid regions by Gillette et al. (1980, 1982).

3.3 Dust Flux as a Function of Wind Speed

Figure 4 shows the vertical flux of dust, G ($\text{g cm}^{-2} \text{s}^{-1}$) as a function friction velocity. The data were reported by Gillette (1974, 1981) who measured dust fluxes in outdoor eroding fields, Fairchild and Tillery (1982) and Borman and Jaenicke (1987), who measured fluxes with indoor wind tunnels.

Gillette and Passi (1988) express the flux of dust, G , by the relation

$$G = C_1 V_*^4 \left(1 - \frac{V_{*t}}{V_*} \right) \quad (3.12)$$

where C_1 is a constant. This is shown as curve A in the Figure. Gillette and Passi (1988), state that (3.12) is based on an unpublished theory of Owen (personal communication between Gillette and Owen, 1987).

Substituting from (3.10) into (3.12), gives

$$G(U) = C_1 \left(\frac{0.23}{\ln z_s} \right)^4 U^4 \left(1 - \frac{U_t}{U} \right) \quad (3.13)$$

where U_t is the threshold wind velocity obtained from (3.10), i.e.,

$$V_{*t} = \frac{0.23}{\ln z_s} U_t \quad (3.14)$$

Let $p(U)$ be the probability density function of the wind speed during the time period of interest. A widely used probability density function for natural winds is the two-parameter Weibull distribution (Gillette and Passi, 1988)

$$p(U) = \frac{k}{c} \left(\frac{U}{c} \right)^{k-1} e^{-(U/c)^k} \quad (3.15)$$

where the two parameters c and k are determined directly from the wind data. The data set used by Gillette and Passi (1988), "the Wind Energy Resource Information System (WERIS)", provided monthly values of the mean hourly wind speed and the "pattern factor" statistics

$$x = \frac{\overline{U^3}}{\bar{U}^3} \quad (3.16)$$

where a bar over a quantity indicates the mean of the quantity for each month. WERIS provided data for a 31-year period, 1948-1978, for 1432 wind measuring locations in the United States. It turns out that the pattern factor x is a unique function of Weibull shape parameter, k , so that

$$x = \frac{\Gamma(1+3/k)}{\Gamma^3(1+1/k)} \quad (3.17)$$

where Γ is the gamma function. Given x , (3.17) can be solved for k by trial and error.

With the probability density function of the wind speed $p(U)$, given by (3.15), $G(U)$ is integrated for all wind speeds above the threshold, U_t for each location (subarea) of the region of interest, i.e.,

$$\begin{aligned} \bar{G}(U_t) &= \int_{U_t}^{\infty} G(U) p(U) dU \\ &= C_1 \left(\frac{0.23}{\ln z_s} \right)^4 \frac{k}{c} \int_{U_t}^{\infty} U^3 \left(1 - \frac{U_t}{U} \right) \left(\frac{U}{c} \right)^{k-1} e^{-(U/c)^k} dU \end{aligned} \quad (3.18)$$

where $\bar{G}(U_t)$ is the average value of the flux estimates, $G(U)$, for one sub-area, and where (3.13) and (3.15) are used to write (3.18).

3.4 Estimation of Total Dust

The region of interest is divided into N sub-areas. Then the average value of the flux estimate for each sub-area $\bar{G}(U_{ti})$ (mass per unit area per unit time) is calculated from (3.18). This averaged estimates are then summed over all erosion areas within the region of interest, using various parameters as weighting function. Thus the mass of dust, E, emitted in the time period ΔT is written as (Gillette and Passi, 1988)

$$E = C \sum_{i=1}^N R_i g(L_i) A_i \bar{G}(U_{ti}) \Delta T \quad (3.19)$$

where C is a constant to be determined by calibration (the constant C, coming from G is lumped into C); i is the index of summation over N different erodible areas within the region of interest; R_i is the effect of soil roughness; $g(L_i)$ is the effect of field length, L_i ; A_i is the area of the land being considered.

Roughness of the soil has the effect of trapping soil particles, increasing the friction velocity of the wind and thus inhibiting erosion. For this reason the exact effect of soil roughness is complicated. Gillette and Passi (1988) examined data from the U.S. Department of Agriculture 1982 National Resource Inventory (NRI) for soil information, land use, and wind erosion parameters to evaluate a "ridge roughness function" proposed by Armbrust et al. (1964) which was based on wind tunnel tests. Since over 97% of these values examined in the data set were between 0.5 and 1 (for prominent erosion areas located largely in the panhandles of Texas and Oklahoma), they conclude that the maximum effect on dust production can not be more than a factor of 2.

The effect of field length on dust production is thought to be (Gillette and Passi, 1988) (i) an aerodynamic feedback mechanism whereby the airborne sand increase the aerodynamic roughness height by absorbing forward momentum from the wind and thus decreasing its speed, and (ii) an increase of soil flux with increasing field length due to sandblasting of the loosened downwind soils. Gillette and Passi (1988) assume $g(L_i)$ to be 1, ignoring the effect of change with distance downwind of the dust flux. It should be noted that mechanisms

similar to those described in (i) and (ii) are incorporated in a recent numerical model considered by Anderson and Haff (1988).

To evaluate C in equation (3.19), Gillette and Passi (1988) make use of data from total dust production for a large area including the panhandles of Texas and Oklahoma. They find a value of 1.4×10^{-15} for the constant C.

4. AEOLIAN TRANSPORT OF SAND IN DESERTS

A major contribution to the study of the physics of wind-blown sand in deserts was made by the classic work of Bagnold (1941) who combined extensive in-situ observations and wind-tunnel experiments to describe the motion of sand particles in the air.

Transport of dust, sand and other particulate materials by wind takes place mainly in the form of surface creep, saltation, and suspension (Bagnold, 1941). Surface creep, also known as "traction" is the movement of particles along the surface. Saltation refers to a leaping motion of particles where they lift off the surface and travel in ballistic-type trajectories in the air before returning to the surface. Suspension is the motion of (less massive) particles that are carried upwards by the wind to travel at indefinite heights within atmosphere (Fig. 5).

Bagnold (1941) states that of the total sand in motion in air about three-fourths move in saltation and a quarter in surface creep. The surface creep consists of slow jerky advance of the surface grains which are knocked along the surface by the impact of descending saltating grains. According to Bagnold, a saltation of fine grains can maintain a surface creep over a bed composed of grains far too large to be moved by the direct action of the wind.

Bagnold notes that a flat sand surface is inherently unstable. He argues that since the grains are of varying size, the surface is not perfectly even and tiny depressions can form such as the one shown, much magnified, in Fig. 6. The series of parallel lines shown in the figure are supposed to represent the descending saltating grains. On the lee side, along the line AB, the points of impact are far apart, but on the windward side many impacts occur. This means that the original depression will get bigger. Eventually, grains accumulate at C and a second lee slope CD is formed, and so on. Using this line of reasoning, Bagnold explains the formation of ripples and argues that the range of the characteristic path of grains is coincident with the ripple wavelength (Fig. 7).

Since saltation is the main mechanism of aeolian transport in sand, the remainder of this section is devoted to a review of some recent works on this topic (White, 1986, Anderson and Hallet, 1986).

4.1 Threshold Conditions

Bagnold (1941) has shown that at the initiation of saltation, the surface shear stress at threshold is

$$\tau_t = A^2 (\rho_p - \rho) g D_p \quad (4.1)$$

where A is a varying empirical coefficient, ρ_p is the particle density, g is the acceleration due to gravity, and D_p is the mean particle diameter. In terms of the friction speed at threshold, V_{*t} ,

$$V_{*t} = A \sqrt{\frac{(\rho_p - \rho) g D_p}{\rho}} \quad (4.2)$$

Since the particle density (2.64 g/cm³ for quartz) is much greater than the atmospheric air density (1.22 x 10⁻³) we have

$$\frac{\rho_p}{\rho} \approx 2164 \gg 1 \quad (4.3)$$

Thus (4.2) can be written as

$$V_{*t} = A \sqrt{\frac{\rho_p g D_p}{\rho}} \quad (4.4)$$

Bagnold and others have shown that $A = A(B)$, where

$$B = \frac{V_{*t} D_p}{\nu} \quad (4.5)$$

is the particle friction Reynolds number. In (4.5), ν is the kinetic viscosity of air. The variation of A with B obtained from wind tunnel data is shown in Fig. 8 (after White, 1979). Note that $A \approx 0.118$ for values of $B > 10$.

4.2 Forces acting on the Particle

Forces acting on the particle are (i) body force which results from gravity, \vec{F}_G , (ii) aerodynamic drag, \vec{F}_D , (iii) aerodynamic lift, \vec{F}_L , and (iv) Magnus lift which results from particle spin, \vec{F}_M . The trajectory of a typical saltating is schematically represented in Fig. 9. Note that a number of forces including the force due to buoyancy (since $\rho \ll \rho_p$) and the interparticle force have been neglected; see White (1986) for a detailed discussion of these and other forces.

Aerodynamic drag is a function of the velocity of the particle relative to the air, \vec{v}_{rel} ,

$$\vec{v}_{rel} = \vec{U} - \vec{U}_p \quad (4.6)$$

where \vec{U}_p (with components \dot{x} and \dot{z}) is the particle velocity. The drag force is expressed as

$$\vec{F}_D = \frac{1}{2} C_D \left(\frac{\pi D_p^2}{4} \right) \vec{v}_{rel} |\vec{v}_{rel}| \quad (4.7)$$

where C_D is the drag coefficient which is a function of the particle Reynolds number, $Re = v_{rel} D_p / \nu$, i.e.,

$$C_D = C_D(Re) \quad (4.8)$$

Aerodynamic lift is due to shear flow and its magnitude is given by (see Anderson and Hallet, 1986)

$$\vec{F}_L = \frac{1}{2} C_L \left(\frac{\pi D_p^2}{4} \right) (\vec{U}_{top} - \vec{U}_{bot}) \quad (4.9)$$

where U_{top} and U_{bot} are the air speeds, at heights corresponding to the top and bottom of the grain, and C_L is given by (Chepil, 1958)

$$C_L = 0.85 C_D \quad (4.10)$$

The Magnus lift is given by (see White, 1986, and Anderson and Hallet, 1986)

$$\vec{F}_M = f \left(\frac{\pi D_p^3}{8} \right) (\vec{\Omega} \times \vec{v}_{rel}) \quad (4.11)$$

where $\vec{\Omega}$ is the angular velocity of the particle.

Rubinow and Keller (1961) derived the following relations for the moment, M , on a particle due to its spin Ω ,

$$M = \mu (\pi D_p^3) \left(\frac{1}{2} \frac{\partial U}{\partial z} - \Omega \right) \quad (4.12)$$

where μ is the air viscosity. Given the forces and the moment acting on the particle, equations of motion for the particle can be written and a numerical solution for the particle trajectories can be obtained (see White, 1986, and Anderson and Hallet, 1986).

4.3 Saltation Trajectories

Given a liftoff angle, α , speed of liftoff U_{p0} , and initial particle spin, Ω_0 , the particle trajectory is numerically obtained using time iterations. At each time step, the Reynolds number is calculated, a drag coefficient is found, and the spin rate and local shear are calculated. Using these, accelerations, velocities, and displacements are updated for each increment. Results obtained by White (1986) are shown in Fig. 10.

5. CONCLUSIONS AND RECOMMENDATIONS

Some recent models of dust production due to wind erosion of agricultural soils (Gillette and Passi, 1988) and mechanics of wind erosion in deserts (Bagnold, 1941, and others) were reviewed in sections 3 and 4 of this report. It can be seen that in spite of the progress made so far, there are several issues that need more attention.

Within the framework of the models described two specific issues should be addressed as a next step (i) modeling of the threshold velocity particularly for agricultural soils, relating it to texture, moisture, etc., and (ii) the initiation of saltation which is still a source of controversy. The actual mechanism of particle liftoff and the forces operating at the initial stage are not well understood. The recent work of Anderson and Haff (1988) seem to be promising in this regard.

More generally, however, there are several viewpoints for modeling of particle-gas flows, namely, the "discrete particle" or "tracking" approach (see, for example, Durst, et al., 1981) and the "non-discrete" or continuum approach (see Ahmadi, 1986). The suitability of these approaches for modeling aeolian transport of soils must be examined in detail. The most significant aspect of the problem is modeling the interaction between the air-particle mixture and the boundaries of the flow. There is a continuous exchange of mass, momentum and energy between the bed and the air-particle system. Unless we take these exchanges into account, using basic principles, we have to rely on empirical formulas for dealing with wind erosion and dust production problems.

6. REFERENCES

- Ahmadi, G. (1982), "A Continuum Theory for Two Phase Media," *Acta Mechanica*, 44, 299.
- Anderson, R.S., and Hallet, B. (1986), "Sediment Transport by Wind: Toward a General Model," *Geol. Soc. America Bull.*, 97.
- Anderson, R.S., and Haff, P.K. (1988), "Simulation of Eolian Saltation," *Science*, 24, August.
- Armbrust, D.W., Chepil, W., and Siddoway, F. (1964), "Effects of Ridges on Erosion of Soil by Wind," *Soil Sci. Soc. Am. Proc.* 28.
- Bagnold, R. A. (1941), *The Physics of Blown Sand and Desert Dunes*, Methuen, London.
- Borrman, S., and Jaenicke, R. (1987), "Wind Tunnel Experiments on the Resuspension of Sub-micrometer Particle From a Sand Surface," *Atmos. Environ.*, 21, 1891-1898.
- Butler, D., et al. (1984), *Earth Observing System: Science and Mission Requirements Working Group Report, Vol I*, NASA TM 86129.
- Butler, D., et al. (1987), *From Pattern to Process: The Strategy of the Earth Observing System, Report of the Eos Science Steering Committee, Vol. II*.
- Chepil, W.S. (1958), "The Use of Evenly Spaced Hemispheres to Evaluate Aerodynamic Forces on a Soil Surface," *Trans., American Geophysical Union*, 39, 3.
- Durst, F., et al. (1984), "Eulerian and Lagrangian Predictions of Particulate Two-Phase Flows: A Numerical Study," *Appl. Math. Modelling*, 8.
- Fairchild, C.I., and Tillery, M.I. (1982), "Wind Tunnel Measurements of the Resuspension of Ideal Particles," *Atmos. Environ.*, 16.
- Gillette, D.A. (1974), "On the Production of Soil Wind Erosion Aerosols Having the Potential for Long Range Transport," *J. Rech. Atmos.*, 8.
- Gillette, D.A., et al. (1980), "Threshold Velocities for Input of Soil Particles Into the Air by Desert Soils," *J. Geophys. Res.*, 85.

Gillette, D.A. (1981), "Production of Dust That Can Be Carried Great Distances," Geol. Soc. Am., 186.

Gillette, D.A., et al. (1982), "Threshold Friction Velocities and Rupture Moduli for Crusted Desert Soils for the Input of Soil Particles into the Air," J. Geophys. Res. 87.

Gillette, D.A. (1988), "Threshold Friction velocities for Dust Production for agricultural Soils," J. Geophys. Res.

Gillette, D.A., and Passi, R. (1988), "Modeling Dust Emission by Wind Erosion," J. Geophys. Res., 93.

Goudi, A.S. (1978), "Dust Storms and Their Geomorphological Implications," J. of Arid Environ., 1.

Kind, R.J. (1989), "Mechanics of Aeolian Transport of Snow and Sand," Proc. 6th U.S. Nat. Conf. on Wind Eng., U. of Houston, Houston, Texas.

Pewe, T.L. (1981), Desert Dust: Origin, Characteristics, and Effect on Man, Geol. Soc. Am. 186.

Plate, E.J. (1971), Aerodynamic Characteristics of Atmospheric Boundary Layer, U.S. Atomic Energy Commission, Office of Information Services.

Priestley, C.H.B., Turbulent Transfer in the Lower Atmosphere, University of Chicago Press, Chicago.

Prospero, J.M., et al. (1970), "Dust in the Caribbean Atmosphere Traced to an African Dust Storm," Earth and Planetary Science Letters, 9.

Sheridan, D., Desertification of the United States, Council on Environmental Quality; Superintendent of Documents, U.S. Government Printing Office, Washington, D.C.

Verstraete, M.M., et al., (1988) "The NASA/EOS Aerosol Project," NCAR Ms. 8076/88-4.

White, B.R. (1979), "Soil Transport by Winds on Mars," J. Geophys. Res., 84.

White, B.R. (1986), "Particle Dynamics in Two-Phase Flows," Encyclopedia of fluid Mechanics, Gulf Publishing Co. Houston, Texas.

Wieringa, J. (1976), "An Objective Exposure Correction Method for Average Wind Speeds Measured at a Sheltered Location," Q. J. R. Meteorol. Soc., 102.

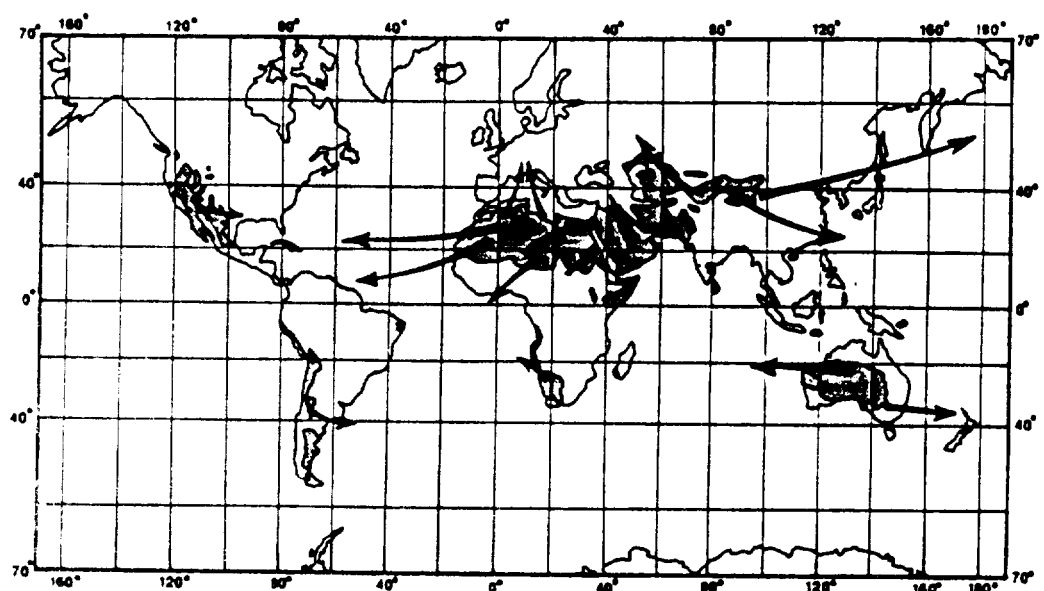


FIG. 1

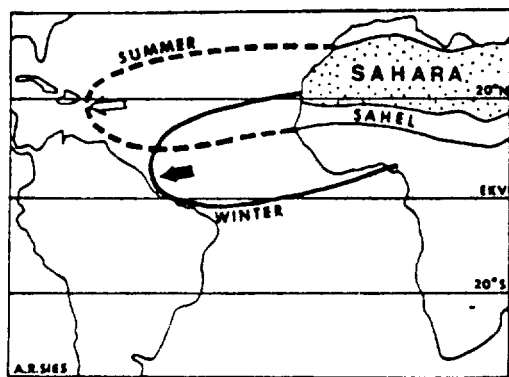


FIG. 2

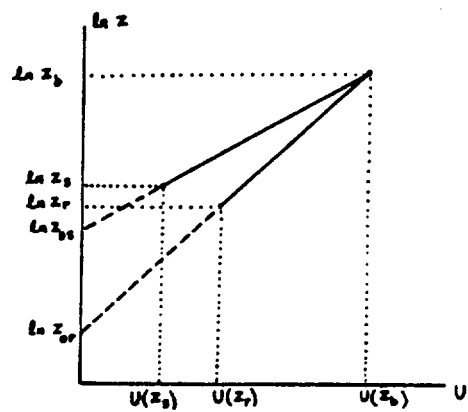


FIG. 3

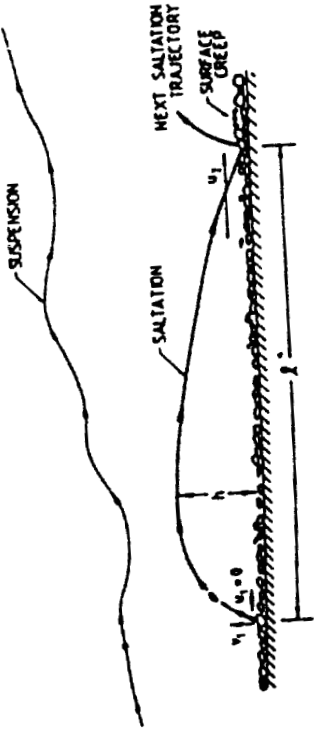


FIG. 5

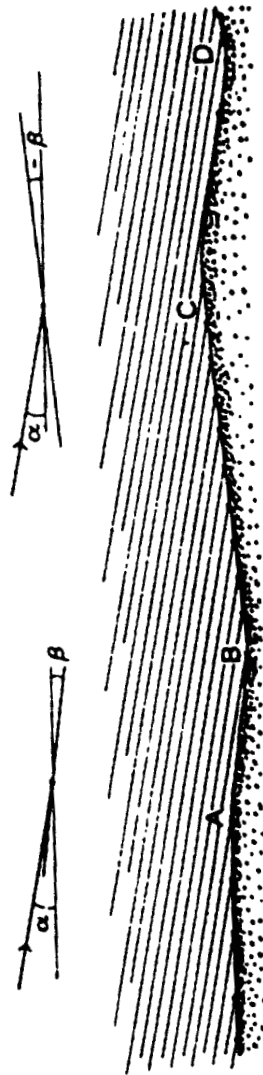


FIG. 6



FIG. 7

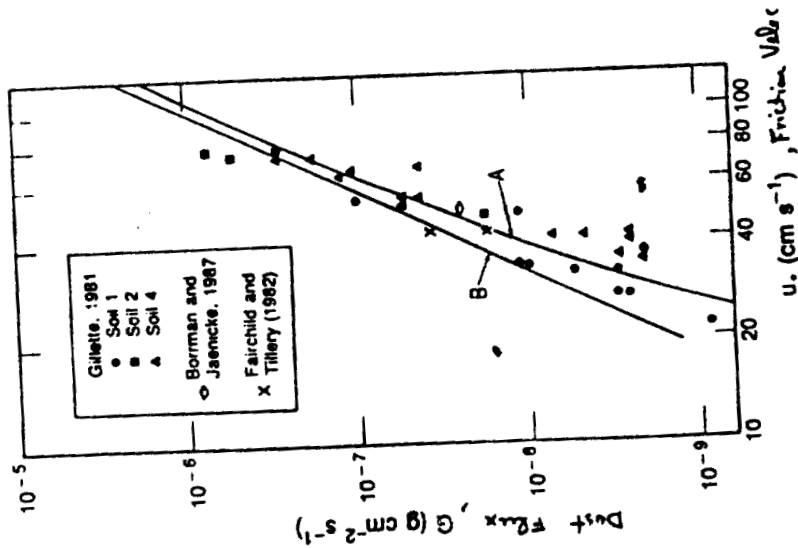


FIG. 4

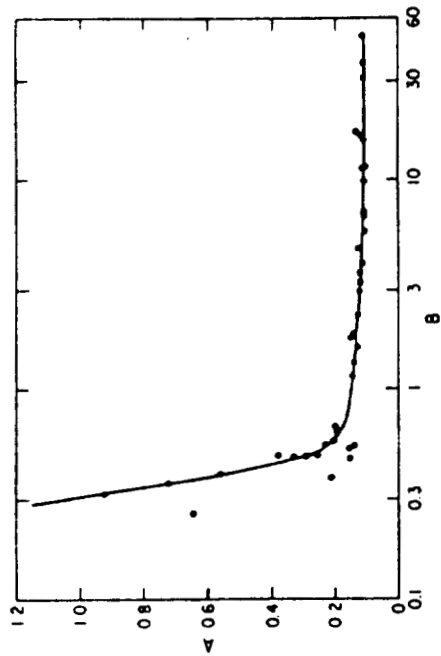


FIG. 8

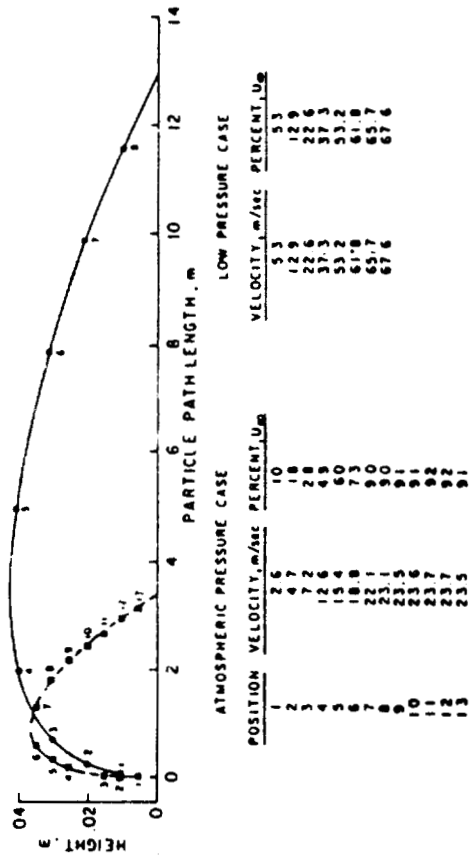


FIG. 10

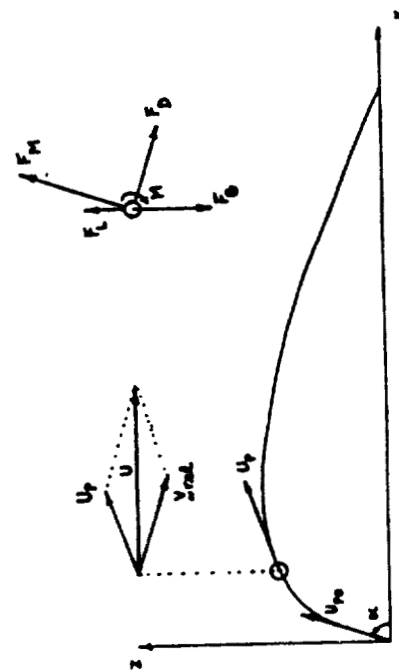


FIG. 9

1989

NASA/ASEE SUMMER FACULTY RESEARCH FELLOWSHIP PROGRAM

MARSHALL SPACE FLIGHT CENTER
THE UNIVERSITY OF ALABAMA IN HUNTSVILLE

EVALUATION AND ANALYSIS OF THE
ORBITAL MANEUVERING VEHICLE
VIDEO SYSTEM

Prepared By:	Robert J. Moorhead II
Academic Rank:	Assistant Professor
University and Department:	Mississippi State University Electrical Engr. Department
NASA/MSFC:	
Laboratory:	Information and Electronic Systems
Division:	Computers and Communications
Branch:	Communications Systems
NASA Colleagues	H. Leann Thomas G. Daryl Craig
Date:	August 18, 1989
Contract No.:	The University of Alabama in Huntsville NGT-01-008-021

ABSTRACT

This report contains a summary of work accomplished in the summer of 1989 in association with the NASA/ASEE Summer Faculty Research Fellowship Program at Marshall Space Flight Center. The task involved study of the Orbital Maneuvering Vehicle (OMV) Video Compression Scheme. This included such activities as reviewing the expected scenes to be compressed by the flight vehicle, learning the error characteristics of the communication channel, monitoring the CLASS tests, and assisting in development of test procedures and interface hardware for the bit error rate lab being developed at MSFC to test the VCU/VRU.

Numerous comments and suggestions to the appropriate people have been made during the course of the fellowship period regarding the design and testing of the OMV Video System. Unfortunately from a technical point of view, the program appears at this point in time to be trouble from an expense prospective and is in fact in danger of being scaled back, if not cancelled altogether. This makes technical improvements prohibitive and cost-reduction measures necessary. Fortunately some cost-reduction possibilities and some significant technical improvements that should cost very little were identified.

ACKNOWLEDGEMENTS

There are many people I should thank. H. Leann Thomas supervised and directed the work, besides being a general source of information on other important matters (like where to eat). G. Daryl Craig made himself available for consultation and discussions, as well as participating in most of the meetings in which I was involved. J. Porter Clark was invaluable in keeping the computers operating properly and establishing communications between various machines and the printer. Dr. Wayne Smith, a fellow Fellow, taught me how to use the word processor programs. Dr. Frank Ingels of Mississippi State University assisted in many logistic and technical matters, both before and during my tenure here this summer. Bernd Seiler, Branch Chief, and Jim Atherton, Division Chief, made themselves available for any matters with which they could assist. Their assistance and direction is gratefully acknowledged.

TABLE OF CONTENTS

NOMENCLATURE	iv
1. INTRODUCTION	1
2. TASK DESCRIPTION	2
3. VIDEO SYSTEM DESCRIPTION	3
3.1 Overview	3
3.2 Detailed Description	3
3.2.1 VCU.	4
3.2.1.1 Pixel Pairing	5
3.2.1.2 DPCM.	5
3.2.1.2.1 Subframe Edges	6
3.2.1.2.2 Image Edges.	6
3.2.1.3 Quantizer	7
3.2.1.4 Entropy Coding.	7
3.2.1.5 Subframe Format	8
3.2.1.6 Transmission Buffer/Bit Rate Controller	8
3.2.1.7 Reed Solomon Encoder.	8
3.2.2 VRU.	9
3.2.3 Cameras.	9
4. STATUS	10
5. ANALYSIS	12
5.1 Video Data Quality	12
5.2 NASCOM Induced Delay	12
5.3 Bitrate Controller	13
5.4 High Resolution.	13
5.5 Encryption/Decryption.	14
6. SUGGESTIONS.	15
7. AREAS NEEDING FURTHER STUDY.	17
7.1 Color.	17
7.2 Increased Resolution	17
8. CONCLUSIONS.	18
9. REFERENCES	19
FIGURE 1: Quantizer Bin Boundaries.	21
FIGURE 2: Quantization Bin Representative Values.	22

ORIGINAL PAGE IS
OF POOR QUALITY

NOMENCLATURE

CEI	Contract End Item
CLASS	Communications Link Analysis and Simulation System
CTF	Contrast Transfer Function
DPCM	Differential Pulse Code Modulation
dB	decibel
f/s	frames/sec
FOV	field of view
FWSI	Fairchild Weston Systems, Inc.
GCC	Ground Control Console
GSFC	Goddard Space Flight Center
JSC	Johnson Space Center
Kbps	Kilobits per second
MHz	Megahertz
OMV	Orbital Maneuvering Vehicle
PDA	Preliminary Design Audit
PDR	Preliminary Design Review
RS	Reed Solomon
RFI	Radio Frequency Interference
STel	Stanford Telecommunications, Inc.
TBD	to be decided
TDRS	Tracking and Data Relay Satellite
TDRSS	Tracking and Data Relay Satellite System
VCU	Video Compression Unit
VS	Video System
VRU	Video Reconstruction Unit
WSGT	White Sands Ground Terminal

1. INTRODUCTION

The Orbital Maneuvering Vehicle is an unmanned spacecraft which is scheduled to be launched in the early 1990's. Its purpose is to relocate satellites and other orbiting objects in space. One of its primary tasks is to reboost large observatories as their orbits gradually decay. The OMV Video System (VS) captures 5 frames of video data per second, compresses it by a factor of 5.5, and transmits it via TDRS to a GCC at JSC. The VS will be primarily used for remote-controlled docking with the orbiting object, since the final approach and rendezvous will be controlled by a ground-based pilot.

The OMV VS is crucial to a successful mission. However, it is highly constrained. The image quality must be sufficient for the pilot to precisely locate both the OMV and the target object. The data must be limited because of communication channel constraints. The hardware to compress the data is constrained by power and heat dissipation limitations on the OMV.

2. TASK DESCRIPTION

My task was described as follows:

1. Study OMV image processing technique using OMV documentation. List average bits/pixel at various points in the system, such as:

- a) after frame rate reduction from 30 frames/sec to 5 frames/sec.
- b) after 4 pixel:1 pixel averaging.
- c) after DPCM.
- d) after entropy encoding and Huffman runlength encoding.

2. Review scenes, digitized pixel histograms, etc. from scenes with Daryl Craig.

3. Review motion, spin, etc. of OMV and errors on channel.

4. Written report discussing the following points:

- a) expected attributes/disadvantages of OMV video compression technique.
- b) effects of the 5 frame/sec sampling rate versus motion of OMV.
- c) effects of 9.5445 MHz sampling of analog video voltage from CCD elements with bandwidth of 4.25 MHz.
- d) effects of elastic buffer/scalar feedback loop on picture quality and what feedback counts would optimize picture quality versus tendency for buffer to overflow.
- e) recommend other video compression techniques compatible with error channel characteristics and motion of OMV that could guarantee 486 Kbps data rate per camera. Compare these other techniques against OMV Video Compression Scheme relative to hardware complexity and to the factors a) through d) above.

5. Review CLASS test results/impact to OMV design.

6. Assist in development of test procedures for the bit error rate lab VCU/VRU based on channel characteristics from CLASS tests and OMV compression technique.

3. VIDEO SYSTEM DESCRIPTION

3.1 Overview

References [2-4] all have a system description to some extent. However, the system is constantly evolving. This description will emphasize the aspects that are presently under discussion or test.

The part of the video system that will be on the OMV consists of 2 redundant VCU's, 2 redundant zoom cameras, 2 redundant docking cameras, and 4 sets of docking lights. Although they are functionally not part of the video system, there are 6 sets of navigational lights which provide illumination. The ground-based portion of the video system consists of 2 redundant VRU's [2].

The primary function of the VCU's is the compression of television imagery to a bandwidth narrow enough for returning to the ground-based pilot via TDRSS at S-band [2]. The VCU's can accept video from one or two cameras simultaneously. The raw video data is compressed, RS error encoded, helically interleaved, and convolutionally encoded before being transmitted to the ground at 486 or 972 Kbps. The frame rate is fixed at 5 frames/sec. There are four compression modes from which the ground-based pilot can select (p. 1-67 of [2]):

Mode A: 2 cameras, each camera compresses 5 f/s to 486 Kbps for a total bit rate of 972 Kbps.

Mode B: 1 camera, compresses 5 f/s to 972 Kbps. The whole FOV is used.

Mode C: 1 camera, compresses 5 f/s to 486 Kbps.

Mode D: 1 camera, compresses 5 f/s to 972 Kbps. A constrained FOV is used.

In addition to the aforementioned 4 cameras, there are 2 camera interfaces designated for kit or payload cameras and 2 camera interfaces for cameras located on the Three Point Docking Mechanism. Thus the OMV had 8 camera locations and each of the 2 VCU's can read data from any of the 8 cameras.

3.2 Detailed Description

The nominal operating mode will be Mode A -- two compressed streams, each stream being 486 Kbps, interleaved for a total bit rate of 972 Kbps. In this mode, the 510x488

pixels obtained from each camera will be pixel-paired to give a 255(H) x 244(V) pixel array to be compressed. The cameras will normally be capturing 30 f/s of which 5 out of every 6 frames will simply be dropped. There is a camera mode in which 6 frames are averaged to provide a better video signal in low illumination situations. In Mode B vertical pixel pairing is performed. In Mode C, pixel pairing is performed in both dimensions, just like in Mode A. In fact, the only difference in Mode A and Mode C is that Mode A is two channel and Mode C is one channel. In Mode D only a 255x244 array of pixels -- centered in the FOV -- is used; no pixel pairing is performed. The ramifications that the nominal mode is a low resolution mode will be discussed in the ANALYSIS section below.

The video input from the cameras is standard RS-170A -- 525 lines/frame, 30 f/s, 2-to-1 interlaced. Since only 5 f/s are sent, in the nominal mode (Mode A) after pixel pairing, only a 5.5 to 1 compression ratio is needed. This is accomplished using DPCM and entropy coding techniques. The 5.5 to 1 compression yields on the order of 453,600 bits/sec, leaving room in the compressed stream for a (255,238) RS error correcting code scheme to be applied. In Modes C & D, the information for 255x244 pixels is also compacted into the same size code stream. In Mode B, there are twice as many pixels to compress per frame, but the average bits/pixel is the same. Mode B should be the easiest mode in which to achieve sufficient compression, since the compression rate scales with the square root of the area, not the area. In Mode A, the compressed video streams from each of the 2 channels are helically interleaved to depth 8 for error spreading. In the other 3 modes, 8 consecutive RS codewords are helically interleaved.

The VRU reconstructs the video and substitutes data from the previous frame for any current data that contains detectable, but uncorrectable, errors.

3.2.1 VCU

The VCU accepts analog RS-170A video from any 2 of the eight camera ports. The VCU provides a composite sync signal to the camera ports. The received signal is low-pass filtered. The latest specifications on the filter [15] indicate that the frequency response will be down 0 dB at 4.2 MHz, down 3 dB at 4.35 MHz, down 12 dB by 4.47 MHz, and eventually fall off by 45 dB. This information should be better documented. After the video signal is DC restored, it is normally routed to an 8-bit A/D converter. However, it may be routed to the bypass output if the VCU is in the bypass mode. The analog signal is sampled at 9.5445 MHz.

This a rather interesting value since it is not an integer multiple of the color subcarrier frequency or the cutoff frequency. It is sufficiently above the Nyquist rate so that sharp edges should not have ringing.

FWSI is still deciding on how they will handle the synchronization and buffering problem between the camera and the VCU. The two choices are one buffer, which is serially filled and emptied, or two buffers, one being filled while the other is being emptied. I think the two buffer approach makes more sense, but FWSI appears to be going with the one buffer approach. This means the actual compression process must occur faster which means more heat and power dissipation although it is a 75% duty cycle.

A compander circuit is used to push the coding error into the higher luminance ranges where it is not as easily detected by the eye (p. 309-310 of [9]).

3.2.1.1 Pixel Pairing

Pixel pairing (averaging two vertically adjacent pixels or averaging 4 adjacent pixels in a 2x2 area) is used to reduce the information input to the DPCM process. As previously indicated, 4 pixel pairing is used in Mode A and C, and 2 pixel pairing is used in Mode B. There is a better way to achieve this data reduction without having the negative effect on the DPCM process mentioned below [10]; this technique is discussed in the ANALYSIS section.

3.2.1.2 DPCM

DPCM is a good choice for a compression technique. Lossless coding using DPCM is generally able to achieve between 2:1 and 3:1 compression (p. 556 of [6]), so obtaining the 5.5:1 necessary for OMV should not be difficult since lossy coding is acceptable. The predictor that FWSI has chosen is consistent with what many others have determined to be the optimum 3 valued predictor ([7], [8], and p.322 of [9]). Namely, in the diagram below of 4 adjacent pixels,

C B
A X

if X is the pixel value to be predicted, the predictor X' is:

$$X' = 3A/4 + 3B/4 - C/2$$

Note that A, B, and C are previous and adjacent pixel values, and X is the predicted value. Since the video signal is interlaced, to obtain the best prediction (i.e., have the highest correlation), A, B, and C should be in the same field as X. Modes A, B, and C all have vertical pixel pairing so this point is not applicable; however, in mode D, pixels C and B appear to be in the other field in the FWSI algorithm. If there is very little interfield motion, the compression reduction will be negligible, but then very little motion makes an even better case for interframe coding. (See SUGGESTIONS section for a discussion on interframe coding.)

3.2.1.2.1 Subframe Edges

There are some special cases in the FWSI DPCM technique. The first 3 special cases are basically a result of the subframe structure and the necessity of handling the leading edges of the subframes. They are:

(1) the first pixel of each subframe is a reference pixel and is PCM 8-bit coded, i.e.,

$X=0$ (but normal correction mechanism is not used)

(2) the rest of the pixels on the first line of the subframe use only the pixel to the left as the predictor, i.e.,

$X=A$

(3) the first pixel on the rest of the lines in the subframe uses only the pel above as the predictor, i.e.,

$X=B$

3.2.1.2.2 Image Edges

The fourth caveat is an edge predictor circuit. Namely if $|C-A|$ is much greater than $|C-B|$, then a horizontal edge is assumed to occur between the two lines and $X = A$. Likewise, if $|C-B|$ is much greater than $|C-A|$, then a vertical edge is assumed to occur between the two columns and $X = B$. As seen by the results on the hex split screen test chart, this works great -- IF THE PICTURE CONTAINS NO NOISE. However, I question its value for a real scene. In fact, it appears NOT TO BE IN THE HARDWARE as documented 22 May 1989 for the timing audit conducted 14 April 1989 at FWSI.

3.2.1.3 Quantizer

The quantizer in the DPCM loop is used to control the rate at which compressed information is generated. A scalar, K , which establishes the bin width is determined by the bitrate controller. The K value is re-calculated every line pair. In the latest incarnation of the system [13], K can take on 16 different values ranging from 8 to 40. There are always 16 bins ranging in index from -8 to 7. The bin width, except for the 0 bin, is $2K$ wide. The 0 bin goes from $-K/2$ to $K/2$. For example, if $K=8$, any prediction error with a magnitude less than 4 falls into the 0 bin, any prediction error between 4 and 16 falls into the +1 bin, any prediction error between 16 and 32 falls into the +2 bin, and so forth. See Figure 1 (p. 2-35 of [2]). Representative values are indicated in Figure 2. Note that there is NOT a +8 bin, but there is a -8 bin. EVEN WITH $K=40$, THE SYSTEM IS NOT FAIL-SAFE. There are images -- antenna grid arrays and wire meshes -- that cannot be guaranteed to compress 5.5:1 with $K=40$. An obvious example, albeit slightly pedagogical, that is guaranteed to fail is a black and white checkerboard. Also, without the edge prediction circuit, the hex split screen test pattern would not compress sufficiently. THE SYSTEM NEEDS TO BE STRESSED. For the few test results that I have seen, the image content is so simplistic that the K value never moves into the higher values.

3.2.1.4 Entropy Coding

The quantized difference value is entropy coded (Huffman coded) in one of three forms. First, an attempt is made to send consecutive difference values via a runlength encoding of zero differences (i.e., succession of bin 0 values). The allowable runlengths are 10 to 74. Apparently FWSI found that little compression was gained by coding shorter or longer runlengths. If an appropriately long string of consecutive zero differences does not exist, then the case of 4 consecutive small differences (-1, 0, or 1 bin numbers) is tried. If that too fails, then the bin number is singly coded in a single Huffman code word.

The probability of getting runlengths of zero or four-datum groupings is enhanced by interleaving the pixel differences on adjacent video lines. For example, if X and Y are two consecutive lines of pixels,

```
... X(i-1)  X(i)  X(i+1) ...  
... Y(i-1)  Y(i)  Y(i+1) ...
```

then the differences are examined in the order

..., X(i-1), Y(i-1), X(i), Y(i), X(i+1), Y(i+1), ...

Note that there are 65 codewords associated with runlength encoding, 81 codewords associated with 4 datum groupings, and 16 associated with single difference encoding. Four different codebooks are used, each codebook being associated with a group of four consecutive K values. See pages 2-38 to 2-42 of [2] for more details.

An unexplained anomaly exists in that THE FREQUENCY OF OCCURRENCE OF rlc=64 IS TWO ORDERS OF MAGNITUDE GREATER THAN ITS NEIGHBORS (p. 2-40 of [2]). It appears that FWSI was using some type of look ahead mechanism at some point in their code; IS THAT MECHANISM STILL IN THE CODE BEING RUN AT CLASS, BUT NOT IN THE HARDWARE?

3.2.1.5 Subframe Format

For error truncation purposes, each frame is divided into subframes. Each frame is 244 lines. A subframe can be 4, 10, or 20 lines, with 20 lines being the default. Each subframe is handled on a line-pair basis. Every subframe starts with a syncword (whose uniqueness is questionable [14]), a subframe I.D., and the reference pixel mentioned before. Every line pair includes the 4-bit scalar index and 2 lines of compressed video data. The assignment of size and value to some of these parameters -- sync word, subframe I.D., and scalar index -- is somewhat arbitrary, but the sizes and values NEED TO BE CLEARLY STATED. The subframe syncword (size and value) and one of the scalar values appear to have changed since C&DM PDR [2], for example. Note that all frames end with a 4 line subframe. Also there are 3 sync words -- subframe, RS, and Viterbi -- to keep up with.

3.2.1.6 Transmission Buffer and Bit Rate Controller

This is the part of the VCU that is still changing and is untested. What the Bit Rate Controller is supposed to do is try to maintain a constant bitrate per line-pair. The actual implementation is still evolving. The size of the output buffer is also changing. The latest guess from FWSI is that it is 32 kbits or 64 kbits.

3.2.1.7 Reed Solomon Encoder

Since the TDRSS will be affected by bursty RFI, the compressed data is RS encoded and helically interleaved to depth 8 for error detection, correction, and spreading. The RS format is such that every 255 bytes has 238 bytes of

data, 16 bytes of error detection and correction code, and 1 sync byte.

3.2.2 VRU

Basically the VRU undoes what the VCU did. It de-interleaves the compressed data, performs error detection and correction, and decompresses the data. The one added complication is when an error is detected that cannot be corrected. This error may be detected as a result of an incorrect pixel count, an incorrect subframe I.D., or may come from the RS decoder. Independent of the source, the VRU simply retains the old data for that subframe rather than replace it with new, but known incorrect data. This is called subframe replacement.

3.2.3 Cameras

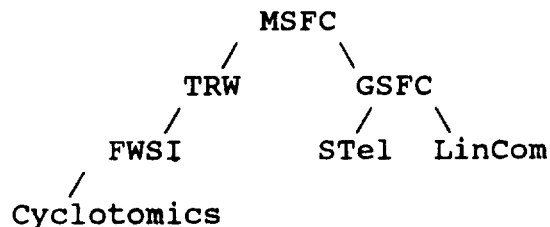
The cameras are a crucial part of the whole system. If they do not deliver a clear, clean, crisp, sharp video signal to the VCU, then the resulting image at the GCC will be degraded. The old computer paradigm holds true -- garbage in, garbage out. The key to obtaining a sharp, high resolution image is probably the CTF. Unfortunately, the only spec on the CTF is its value at the Nyquist frequency. It would be better if the roll-off was better specified, like the CTF at 90% and 110% of the Nyquist rate (see p. 2-62 of [2]).

4. STATUS

The original OMV proposal occurred in 1985; TRW is the prime contractor (p. 1-28 of [2]). TRW in turn subcontracted to FWSI to design and build the video system. FWSI in turn proposed that Cyclotomics be subcontracted to supply the RS coding/decoding once that function was added to the video system.

The other side of the organization chart is a result of the need to test the design and development activities. The present test activity is for the video return link. It was decided to do both static and dynamic tests at the CLASS facility at GSFC. GSFC has contracted with STel to integrate the test and model systems (e.g., to integrate the FWSI VCU/VRU code into CLASS), for setup and maintenance of the special configuration for the test, for system operation of the test, and to maintain the database. GSFC has contracted with LinCom to do model and analysis system development and to do special purpose analysis as required. LinCom generated the test plan and associated requirements and defined the special purpose models, analysis systems, and test points, i.e., the unique interfaces for OMV. Thus the organizational chart looks somewhat like this:

design/development <-----> test



A unit level PDR for the VCU/VRU was performed in 06/88 (Table 1.1-3, "Video Equipment Development Schedules" in [2].) Unfortunately, the cameras have yet to have even a PDR, although the C&DM PDR in 08/88 indicated that PDR for the cameras was scheduled for 02/89. The docking and navigational lights had their PDR in 12/88, with no further design reviews for the lights on the schedule in Table 1.1-3 of [2].

On June 20, 1989, GSFC reported good success with the tests of the RFI link using the FWSI VCU/VRU software.

On July 20, 1989, FWSI reported that they got the VCU/VRU hardware working. At this point all seemed well. However, soon after the GSFC presentation on June 20, I noticed that the bit rate was too low by about 6.4%. It turned out that the FWSI code had a bug in the bitrate controller section. Bytes were being reserved in the compressed data stream for the RS error correction bytes, but the bitrate was controlled as if the RS error correcting bytes would be appended. For example, the bit rate being obtained was 91,000 bits/frame instead of 97,200 bits/frame. 910 is 93.6% of 972. The RS code is a (255,238) code, i.e., for each 238 data bytes, 16 error correction bytes and 1 sync byte are added. 238 is 93.3% of 255. The amount of compressed data was being too heavily constrained; the FWSI compression code was forcing both the data and the check bytes into 91,000 bits instead of only the data into 91,000 bits. It is problems like this that make us leery of becoming too confident all is well.

The latest "schedule" for the video processing delay requires that the data from one frame of video be sent out every 200 msec. There is a long latency allowed (~100 msec) between when the first pel is camera-captured and the data corresponding to the last pixel is sent to TDRS, but this delay pales in comparison to the 3 second delay between the pilot sending a command from the GCC and the results being seen at the GCC.

The mechanism(s) for indicating subframe replacement rate and bit error rate at the GCC is still undecided. The need for 4 and 10 line subframes seems to be less obvious that it once was. With 20 line subframes, the knee in the margin curve (image quality vs. link margin) has been seen to be very sharp in the results from the CLASS tests [14].

Within the last few days there has been much discussion about cancelling or scaling back the OMV effort. As of 18 August 1989 OMV is still alive, but knowledgeable sources say it is likely it will be at least scaled back.

5. ANALYSIS

5.1 Video Data Quality

On page 1-41 and 1-42 of [2] is a specification of the Video Data Quality Requirement (CEI Paragraph 3.2.1.11.7.5). It is broken down into 4 parts: a) pixels/frame, b) FOV, c) frames/sec, and d) Video-Peak-Signal to RMS-Error Ratio. The paucity the requirements of parts a) and c) have been discussed above and will be discussed some more below, but they ARE specified. Part b) is probably best argued from a "we have to see the object" perspective. I have no problems with it. HOWEVER, part d) was left as a TBD. It was pulled out and discussed on page 1-74 and 1-75 of [2] as an issue which needed further study. The discussion there is generally to the point, but I take issue with the position that RMS error measures are meaningless -- they are less than perfect but much better than anything else. They are, in fact, least meaningful for noisy source images, which will occur on the OMV unless there are good lighting and cameras.

MSFC needs to make sure that the sequences being used by TRW, FWSI, and CLASS are as good an example of what OMV will see as possible. This means the noise content, the spatial sampling, and the dynamic range should match what the flight VCU will compress. A good test image would be obtained by adding 0.01 variance white noise to the present hex split screen test pattern. Rough calculations indicate it will NOT be sufficiently compressed since the white noise will defeat the edge predictor scheme. This, I claim, is a better approximation to scenes that will be encountered in space than the test pattern without noise.

5.2 NASCOM Induced Delay

Both a NASA report [1] and a TRW Quarterly Report (pp. 158-165 of [5]) address this concern: the 3 second delay between the time a pilot initiates a command and the result is displayed on a video monitor at the GCC. It is my understanding that this implies a 1.5 second delay in the forward link. I am told that this delay would be cut by 33% if the pilot was at WSGT or if the link between WSGT and JSC were terrestrial. Although the simulations indicate that this added delay would only reduce the probability of a successful first docking by 7% percent -- from 97% with a 2 second delay to 90% with a 3 second delay (p. 9 of [1]) -- that is a significant problem. Facets of the mission that

will be negatively impacted include fuel consumption, mission time planning, and accuracy of actual docking attempt. This appears to be AN ADMINISTRATIVE PROBLEM that upper management NEEDS to address.

5.3 Bitrate Controller

The bitrate controller being used in the CLASS tests is one which FWSI had in their software simulator up to the end of last year. In January, 1989, FWSI proposed a new bitrate controller, which is supposedly the one they are implementing in the hardware they are building. The two controllers do differ; how much and is it significant are the questions. A timing audit [11] was performed on the FWSI VCU by TRW in April 1989. The bitrate controller board had a number of "possible problems". Few details were given about its operation (one block diagram at the level of PROMs, latches, and counters). More information must be forthcoming. Since the bitrate controller assures a fixed bit rate and makes sure the transmission buffer does not overflow, its correct operation is rather crucial.

I have a lot of questions about this board/scheme, primarily because I question the validity of the image test data being feed the VCU code at CLASS. The system simply has not been forced to do some real compression. It appears nobody has determined what will happen if the transmission buffer overflows. The way the FWSI VCU is designed, underflow should be preventable, but overflow is another issue; the scalar values simply do not go high enough. What will happen if the transmission buffer overflows?

The bitrate controller does seem to give a steady image quality over the whole picture. Unfortunately I was never cleared to look at the details of the FWSI code or certain documents. I suspect, however, they have methods to prevent the scalar value from oscillating or changing values wildly, since such methods and the needs for such methods have been well documented in the literature [8,12].

5.4 High Resolution

The preliminary specs I have seen on the cameras do indicate they are capable of capturing a good video signal. However, the VCU modes limit the resolution. The pixel pairing in Modes A, B, & C immediately half the spatial frequency in at least one, if not both, dimensions. I think it would have been better to have kept the input resolution into the VCU high and compressed more when necessary. Pixel pairing is like giving up before you start. There are better ways to get the same effect -- less input pixels.

One example is to compress the first field and use a smart interpolation/replication scheme for the second [7,10]. Note this reduces the input bit rate by a factor of 2, but keeps as high a spatial resolution as can be had with only one field. If a higher resolution picture of a stationary object is needed, both fields can be processed. Once the second field is processed, the data for it remains valid as long as the pixel values on the two adjacent lines, which are in the first field, do not change. However, once the object starts moving -- either from the camera moving or the object moving -- the motion is tracked by interpolating lines from the first field to produce the second field. Motion can be detected simply by examining the prediction error of the first field pixels.

Mode D is the only mode presently in which the pilot will be able to distinguish fine details; unfortunately the FOV is limited.

The present temporal resolution of 5 f/s seems sufficient for almost all possible OMV operations since NASA takes great pains to assure that everything happens in space at as deliberate a pace as possible.

5.5 Encryption/Decryption

Since the bits in the compressed data cannot be easily picked out and associated with a particular pixel, some encryption is being performed simply by the compression process. Changing the sync signals on every occurrence would add to the encryption process, otherwise the repetition could be picked out and the "code" begin to be broken. A compression technique that would even better encryption and has been shown to give 5-15% more compression on photographic quality images is arithmetic coding [7,10].

6. SUGGESTIONS

The first suggestion I was going to make was to have a system test of all the units. However, I understand that that idea has been already proposed and subsequently denied. I am especially concerned about the VCU box FWSI is building. The block diagrams from the April 1989 Timing Audit have MANY mistakes -- symbols/sec rates off by factors of 2, rounding and not rounding 9.5445 MHz to 10 MHz in the same figure (figure 5), D flip-flops that have input/output lines unlabelled, mislabelled, and multiply labelled, etc.. The document is so badly composed and so full of errors, I gave up trying to figure out what they were doing, much less whether it was good.

Once the Bit Error Rate Lab get setup, one of the first things that needs to be done is to simply run MANY, MANY (maybe 200) pictures through to check the bit rate controller and the transmission buffer parameters. Unfortunately the VCU/VRU scheme in the FWSI code differs appreciably -- the question is is it significantly -- from the VCU/VRU scheme being implemented in the hardware. This will taint anything that is discovered, but that may be the best that can be done.

There are some (minor) suggestions I have regarding the FWSI video compression scheme:

1) Quantizer Bin Representative Values: Rather than using the centroid of the distribution of values within the bin, a savings in hardware and pipeline delay can be had by using the smallest magnitude value in each quantization bin as the representative value [7,10]. This eliminates the need to clip the reconstructed pel values -- a PROM delay -- and also reduces the width of the adder output from 9 to 8 bits. Experimentally, the image degradation is usually unnoticeable. Note this is COST REDUCTION suggestion.

2) Gap Bridging: There is a technique known as gap bridging which should increase the length of the zero bin runs [7,12]. It has been shown to give 15-20% rate reduction, with little if any degradation in image quality. In fact it tends to eliminate noise spikes, thereby improving the image quality. Note this does indeed mean the SNR will go down since noise is being eliminated but measured as if it were added. I.e., the noise reduction will increase the difference between the original and the reconstructed image, thereby increasing the SNR. Gap

bridging does not, however, appear to be a necessary function since no test picture has really stressed the VCU yet.

3) Scalar Values (K): Although the bigger problem with the compression scheme lately has been underflow, there is a rather easy way to guarantee the VCU will never overflow. If the maximum value of K was increased from 40 to 64, the VCU would essentially have a Delta modulation mode, since all differences would fall into one of 3 bins: -1, 0, or 1. This would mean all the entropy encoding would be run length encoding or 4-datum encoding. The highest bits/pel average then would be 2.5, since some 4-datum groups require 10 bits. The easiest way to absolutely guarantee that all images could be compressed to 97,200 bits would be to have another codebook for K=64 in which the maximum bits/pel never exceeds 1.5. This is another of those "granularity vs. range" problems analogous to those encountered in designing floating point number formats.

My biggest suggestion is a big one -- use an interframe compression technique. The compression ratio should almost double [6]. The extra computation may be zero [10] and the extra memory will be one framebuffer. There are techniques to truncate the error propagation [10]. In short, it is almost a no-loss improvement. This is work I think should be done regardless of the planned missions for OMV; there is simply no reason to be using that much bandwidth to get that little video information to earth. Since I have already presented this suggestion elsewhere, I'll not expound too much on it here.

7. AREAS NEEDING FURTHER STUDY

7.1 Color

Processing full color images would do two things: 1) make the video "sexier", and 2) assist in object discrimination. Full color is tri-stimulus; therefore from capture to some point in the system three times the data will have to be handled. Ultimately, at the output buffer, the amount of compressed data should only increase by 10-30% over the compressed data from processing just the luminance information. The amount of additional computation depends on the scheme.

It is worth noting where the workstation and PC markets are going. Most PC companies have emphasized obtaining 256 colors, whereas most producers of scientific workstations have put more emphasis on spatial resolution. The pictures I am seeing from the OMV video test data appear not to have reached the limit of spatial resolution. That, I think, is a more important goal for space-based imaging. Color would increase the perceived resolution, but why not increase the real resolution first? The NEXT computer is an example of just how good images that have 2-bit (no pun intended) pixels, but lots of them, can look.

7.2 Increased Resolution

Just how much spatial resolution is needed is obviously mission dependent. If all OMV has to do is dock with the Hubble Space Telescope, the OMV Video System may have spatial resolution to spare. If, on the other hand, OMV will be used for remote inspection of antenna grid arrays or wire meshes, then the ultimate in image quality will be needed.

8. CONCLUSIONS

For what it is intended to do (dock with, transport, and reboost the Hubble Space Telescope), the OMV Video System appears adequate. I personally think a more aggressive compression technique should have been used -- which would have increased the signal power -- but it wasn't. I think the present scheme could have been made more flexible for minimum cost if that had been deemed important earlier. Probably the biggest deficiency in the whole video system is a Goddard problem -- the 3 second roundtrip from GCC to OMV and back.

Some of my concerns are a fear of the unknown. I never got clearance to look at certain documents that would have indicated whether or not certain requirements and specifications were being met. Other concerns are due to incomplete specifications. There are, however, some real potential problems.

Personally, I hope OMV flies. It would be nice to see on commercial TV (note the visual medium) something about which I know this much.

9. REFERENCES

- [1] Richard Dabney & Gena Crook, "Results of POLY-2000 OMV Video Downlink Study," NASA MSFC, March 10, 1988.
- [2] TRW, OMV PM12-PDR, Volume 4 - Avionics, Part 3 - Communications & Data Management, August 22, 1988.
- [3] Frank Ingels, Glenn Parker, and Leann Thomas, "Simulated Performance Results of the OMV Video Compression Telemetry System," International Telemetry Conference, Oct. 30 - Nov. 2, 1989, San Diego, CA.
- [4] Frank Ingels, Glenn Parker, and Leann Thomas, "OMV Video Compression Error Correction Coding System," Southeastcon 89, April 1989, Columbia, SC.
- [5] TRW, OMV Quarterly Review, 18 April 1989.
- [6] A.K. Jain, Fundamentals of Digital Image Processing, Prentice-Hall, 1989.
- [7] D. Anatassiou, W.B. Pennebaker, J.L. Mitchell, "Gray Scale Image Coding for Freeze Frame Videoconferencing," IEEE Trans. on Comm., Vol. COM-34, No. 4, pp. 382-394, April 1986.
- [8] H.G. Mussman, "Predictive Coding" chapter in the book Image Transmission Techniques, edited by W.K. Pratt, Academic Press, 1979.
- [9] A.N. Netravali and B.G. Haskell, Digital Pictures: Representation and Compression, Plenum Press, 1988.
- [10] R.J. Moorhead, J.S. Ma, and C.A. Gonzales, "Realtime Video Transmission over a Fast Packet-Switched Network," Digital Image Processing Applications, Ying-wei Lin, Ram Srinivasan, Editors, Proc. SPIE 1075, 118-123 (1989).
- [11] TRW FWSI VCU Timing Audit Results, 22 May 1989.
- [12] B.G. Haskell, P.L. Gordon, R.L. Schmidt, and J.V. Scattaglia, "Interframe Coding of 525-Line, Monochrome Television at 1.5 Mbits/s," IEEE Trans. on Comm., Vol. COM-25, No. 11, pp. 1339-1348, Nov. 1978.
- [13] "The C.L.A.S.S. OMV DATACOMP Test System," Demonstration: March 27-30, 1989, NASA/GSFC.

[14] CLASS Results Meeting, June 20, 1989, NASA/MSFC.

[15] Frank Ingels, private conversation.

BIN	BIN BOUNDARY VALUES				
	GENERAL	K = 1	K = 8	K = 16	K = 32
0	-K/2 K/2	-0.5 0.5	-4 4	-8 8	-16 16
1	2 K K/2	2 0.5	16 4	32 8	64 16
-1	-2 K -K/2	-2 -0.5	-16 -4	-32 -8	-64 -16
2	4 K 2 K	4 2	32 16	64 32	128 64
-2	-4 K -2 K	-4 -2	-32 -16	-64 -32	-128 -64
3	6 K 4 K	6 4	48 32	96 64	192 128
-3	-6 K -4 K	-6 -4	-48 -32	-96 -64	-192 -128
•	• •	• •	• •	• •	• •
•	• •	• •	• •	• •	• •
•	• •	• •	• •	• •	• •
7	14 K 12 K	14 12	112 96	224 192	448 384
-7	-14 K -12 K	-14 -12	-112 -96	-224 -192	-448 -384
8	-16 K -14 K	-16 -14	-128 -112	-256 -224	-512 -448

FIGURE 1: Quantizer Bin Boundaries

FIGURE 2: Quantization Bin Representative Values

SCALAR	BIN NUMBER								
K	0	1	2	3	4	5	6	7	8
1	0	1	2	3	4	5	6	7	8
8	0	6	19	35	53	68	85	102	119
9	0	6	22	41	60	77	95	114	133
10	0	6	25	45	67	86	107	128	149
11	0	8	27	49	73	94	117	140	163
12	0	9	29	54	80	103	128	153	178
13	0	10	32	58	86	111	138	165	192
14	0	10	34	63	93	120	148	178	206
15	0	11	37	67	100	128	159	191	221
16	0	12	39	72	106	137	169	203	235
17	0	13	42	77	113	146	179	216	246
18	0	14	44	81	120	154	190	228	253
19	0	14	46	86	126	163	200	241	255
20	0	15	49	90	133	171	211	247	255
24	0	18	59	108	159	206	247	255	255
32	0	23	78	144	211	255	255	255	255

1989

NASA/ASEE SUMMER FACULTY FELLOWSHIP PROGRAM

MARSHALL SPACE FLIGHT CENTER
THE UNIVERSITY OF ALABAMA IN HUNTSVILLE

TRANSMISSION AND REFLECTION STUDIES
OF THIN FILMS IN THE VACUUM ULTRAVIOLET

Prepared by:	Lennart R. Peterson
Academic Rank:	Professor
University and Department:	University of Florida Department of Physics

NASA/MSFC:	
Laboratory:	Space Science Laboratory
Division:	Solar-Terrestrial Physics
Branch:	Atomic Physics

MSFC Colleague:	James F. Spann
-----------------	----------------

Date:	August 3, 1987
-------	----------------

Contract Nnumber:	The University of Alabama in Huntsville NGT-01-008-021
-------------------	--

TRANSMISSION AND REFLECTION STUDIES OF
THIN FILMS IN THE VACUUM ULTRAVIOLET

by

Lennart R. Peterson

Department of Physics
University of Florida
Gainesville, Florida

ABSTRACT

Both the transmittance and reflectance of 2 mm thick MgF_2 substrates and of thin films of BaF_2 , CaF_2 , LaF_3 , MgF_2 , Al_2O_3 , HfO_2 , and SiO_2 deposited on these substrates have been measured for the wavelength range 120 nm to 230 nm. Results for BaF_2 , LaF_3 , and MgF_2 show promise as being good materials from which interference filters can be made. The software and related hardware needed to take large amounts of data automatically in future measurements of the transmittance and reflectance has been developed.

ACKNOWLEDGEMENTS

The author wishes to express his warm thanks to the leadership of the Summer Faculty Fellowship Program for their splendid hospitality and also wishes to acknowledge the smoothness and quality with which the program was run. Secondly, the author wishes to thank his MSFC colleague, Jim Spann, for his helpful, friendly and very professional support during the 10 week visit.

LIST OF FIGURES

Figure 1 - The Vacuum Ultraviolet Calibration Facility

Figure 2 - Transmittance and Reflectance Measurements of
2 mm Thick Parallel (for T) and Wedged (for R)
Substrates of MgF_2

Figure 3 - Transmittance and Reflectance Measurements of
a 53 nm Film of BaF_2 on an MgF_2 substrate

Figure 4 - Transmittance and Reflectance Measurements of
a 51 nm Film of LaF_3 on an MgF_2 substrate

Figure 5 - Transmittance and Reflectance Measurements of
a 68 nm Film of MgF_2 on an MgF_2 substrate

INTRODUCTION

The theory and understanding of thin-film optics has a long and honored history^{1,2}. In addition, the use of thin-film interference effects to design high reflectivity mirrors and narrow band-pass filters is a well established technology, especially at the visible wavelengths. Not so well established at present, however, is the extension of this technology down to the vacuum ultraviolet (120 nm - 230 nm). Because of the shorter wavelengths of UV compared to visible light (by factors of 1/3 or 1/4), the required film thicknesses must not only be thinner but also must be more carefully controlled. Furthermore, values of the refractive indices n and the extinction coefficients k are poorly known at these wavelengths for materials likely to be useful as film materials.

In the face of the extensive work that needs to be done in the vacuum UV, there is also a natural and growing need to improve optical instrumentation designed for use in the UV. For example, satellite UV imaging of auroral and other emissions from Earth has distinct advantages over visible and IR imaging. Since the earth's atmosphere does not backscatter solar UV efficiently and is also highly absorptive of UV, satellite UV images of Earth allow for a reasonably direct viewing of auroral and airglow emissions, day or night, uncontaminated by the earth's albedo.

Determination of the wavelength-dependent optical constants n and k in the range 120 nm to 230 nm for a variety of materials is crucial. In particular, these values are necessary to the design of narrow band-pass filters needed for the UV Imager to be flown on the POLAR satellite of the ISTP Program. This satellite, scheduled for launch in 1993, will be in an eccentric polar orbit at heights ranging from about 2 R_E to 9 R_E and will provide an ideal platform for imaging the aurora. The emissions of interest are the strong H-Lyman alpha line at 1216 Angstroms, the 1304 and 1356 atomic oxygen lines, the weaker LBH N_2 bands between 1400-1700 and 1700-2300, and the atomic nitrogen lines at 1493 and 1744.

OBJECTIVES

The focus of this research study then is to determine the transmittance and reflectance of films having known thicknesses and composition. The materials are 2mm thick high quality commercially made MgF_2 substrates and thin films of BaF_2 , CaF_2 , LaF_3 , MgF_2 , Al_2O_3 , HfO_2 , and SiO_2 deposited on these substrates by the Optical Aeronomy Laboratory at the University of Alabama in Huntsville. The measured values of transmittance (T) and reflectance (R) are sufficient for calculation of the more fundamental quantities n and k as functions of wavelength. The actual process of obtaining n and k from the reported T and R data is to be carried out by Zukic, et. al.^{3,4}. These results are part of the program to design and construct five narrow band-pass filters for the UV Imager on satellite POLAR, including band-pass windows centered on the wavelengths 1216, 1304, 1356, 1500 and 1800 Angstroms.

Because of the time-consuming nature of taking large quantities of data under high-vacuum conditions, there is also a need for as much automation of data acquisition as is practical. Thus, a useful task is to interface the existing hardware and software with upgraded versions. An existing computer program will be modified and enhanced to accomplish these tasks.

DESCRIPTION OF FILM SAMPLES

The film depositions are carried out by the Optical Aeronomy Laboratory at the University of Alabama in Huntsville. The film materials, BaF_2 , CaF_2 , LaF_3 , MgF_2 , Al_2O_3 , HfO_2 , and SiO_2 are deposited in vacuum on MgF_2 substrates 12.7 mm in diameter by 2 mm thick. When needed, a 3 degree wedged substrate is used to eliminate background contributions to reflectance coming from reflection off the backside surface of the substrate. Film thicknesses for samples measured vary from about 50 nm to 100 nm. The substrates have a surface roughness of about 2.5 nm, marginally smooth for the film thickness deposited. All handling, deposition and transportation of substrates is done under standard clean-room procedures to ensure a minimum of contamination.

DESCRIPTION OF THE VACUUM ULTRAVIOLET CALIBRATION FACILITY

The vacuum ultraviolet calibration facility is a 1000 liter hydrocarbon-free system currently being used to measure reflectance and transmittance. The configuration at present is shown in Figure 1. Briefly stated, the facility consists of a main chamber containing an instrument platform on which filter samples can be mounted. Mated to the main chamber is the smaller source chamber containing a .2 meter monochromator and an optical system capable of delivering a collimated UV beam having a 1 nm bandwidth and dimensions of approximately 2 cm square. The main chamber is a cylinder having diameter 1 m and length 1.25 m; the source chamber is also a cylinder but having a diameter .3 m and length 1 m. The light source is a sealed deuterium lamp with a MgF_2 window and provides continuous useful spectra from about 115 nm to 230 nm.

Samples are mounted on an 8-slot wheel in the main chamber, operated by with a small stepping motor controlled by means of electrical feedthroughs. Behind the filter wheel is a photometer fixed in a position to measure transmitted intensity. A second photometer is positioned to view reflected light under the condition that the filter wheel is oriented to a 4 degree incident angle with respect to the beam. The vacuum system provides a hydrocarbon-free environment at a pressure of order 10^{-5} Torr, maintained by a pair of cryo pumps.

In order to enable a means of monitoring the beam signal strength as well as of checking background at each wavelength, three of the eight filter-wheel positions are occupied. One of the three positions contains a calibrated UV enhanced aluminum mirror for use in determining the reference beam intensity for reflectance measurements. The other two positions are used to monitor the reference beam and background intensities for transmittance measurements. Thus, in any single run, 5 or fewer samples can be measured for both T and R at all wavelengths from 120nm to 230nm, consistent with the range of usefulness of the deuterium lamp. Measurements are made by setting the monochromator at a particular wavelength and then successively rotating the filter wheel to each of the required positions. When all positions for a given wavelength are complete, the computer, which has accumulated the photometer current data directly on-line, calculates the value of T (or R) along with statistical uncertainties.

Software has been developed which gives the user several levels of automatic operation. At the lowest level of automation, the monochromator is set by hand, the filter wheel is positioned manually by means of a vacuum rated stepping motor, and on command, the photometer current is sampled repeatedly by the computer. At the highest level of automation, the filter wheel and monochromator are set manually to the starting value, after which the computer guides the system through a complete set of specified input wavelengths and filter-wheel positions, both taking and processing data as obtained. Upon completion of a run, graphs and tables are produced of T and R as a function of wavelength.

The monochromator stepping motor (model PH296-01B, Vextra) has been interfaced with the parallel input/output port of the computer by means of a motor driver circuit (model 2D3128, Anaheim Automation). Two bit-positions of the eight-bit port are used for motor control. The in-vacuum filter wheel stepper motor (model C, Princeton Research Instruments) has similarly been interfaced using a motor driver circuit board (model ESH081/R2D23, CyberResearch). An optoisolator (model ESH 085, CyberResearch) protects the computer system from electrical noise and potentially damaging voltages. Four additional bit-positions are used for the vacuum stepping motor operation.

RESULTS AND CONCLUSIONS

Examples of transmittance and reflectance measurements are shown in Figures 2, 3, 4 and 5. As a result of the measurements, optical constants for these and other film materials have been determined and will be used in the design of UV narrowband filters⁴. Indications from these calculations are that high values of the refractive index make LaF_3 and BaF_2 good for use with MgF_2 , having lower refractive index, in making narrowband transmission filters. Because the measurement process is now automated, more accurate and consistent measurements are able to be obtained than previously, without the stress and tedium imposed on the operator.

REFERENCES

1. O. S. Heavens, *Physics of Thin Films*, G. Hass and R. Thun, Eds. Vol. 2 (Academic Press, New York, 1964)
2. M. Born and E. Wolf, *Principles of Optics*, (Pergamon Press, 1980)
3. M. Zukic, *Damped Least Squares Technique for the Design of Optical Multilayer Filters*, MS thesis, (unpublished) Imperial College, London (1984)
4. M. Zukic, D. G. Torr and J. F. Spann, *Optical constants of BaF_2 , CaF_2 , LaF_3 , MgF_2 , Al_2O_3 , HfO_2 , and SiO_2 thin films in the VUV*, (to be published)

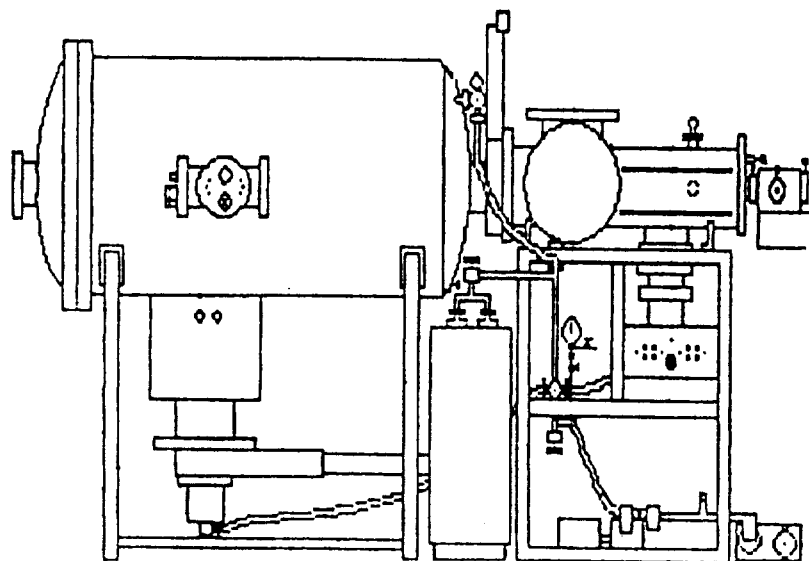


FIGURE 1

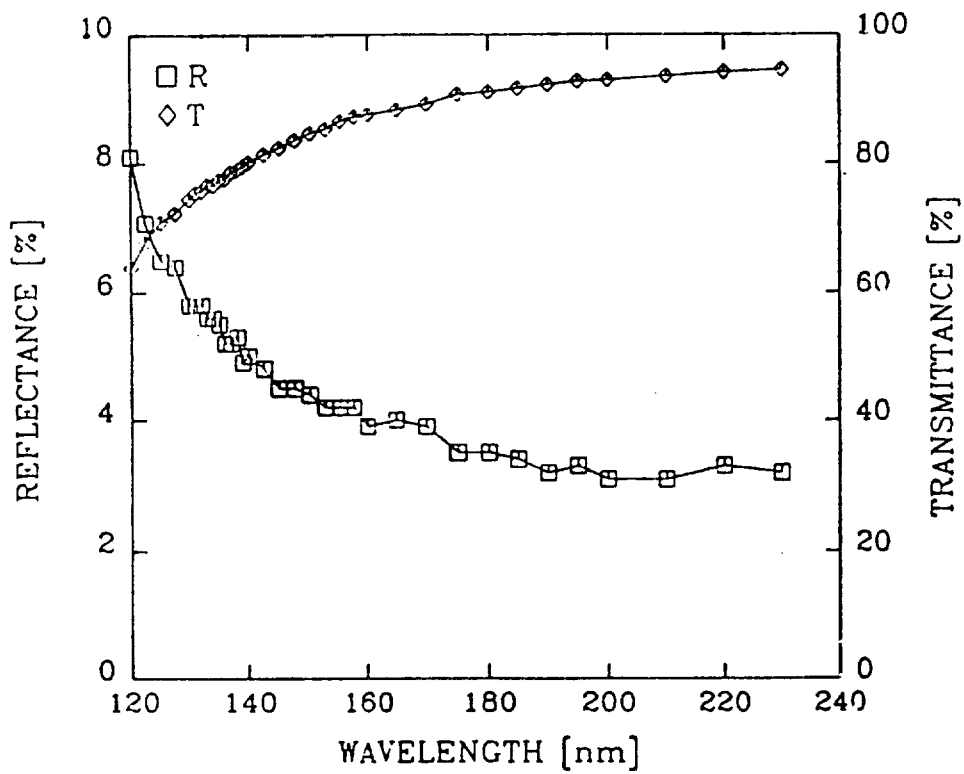


FIGURE 2

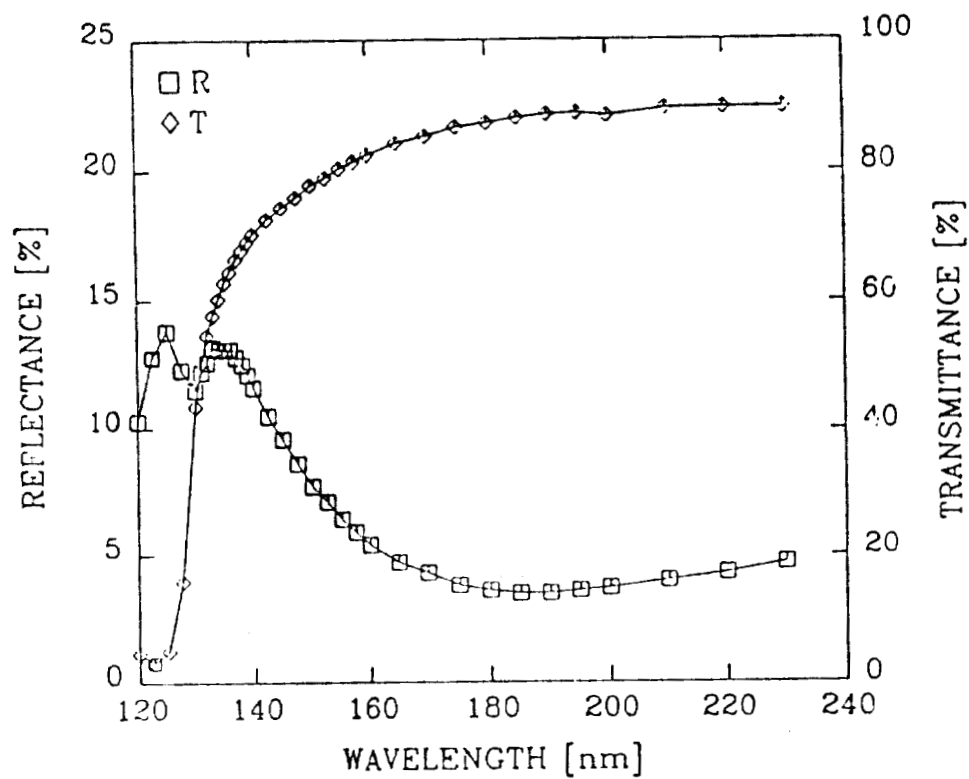


FIGURE 3

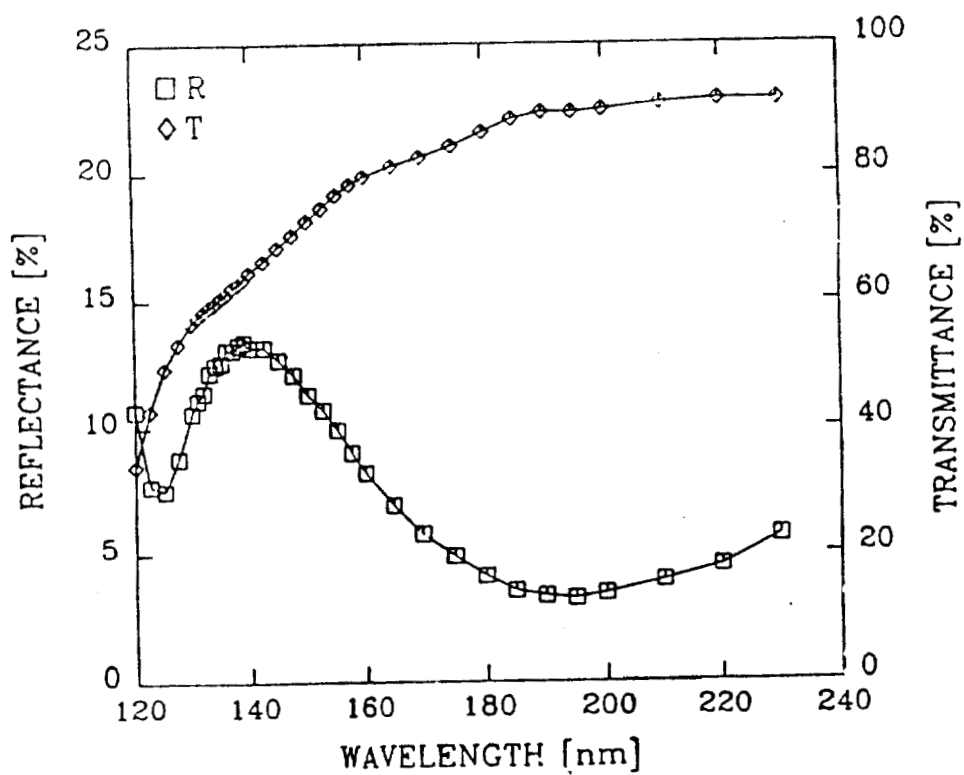


FIGURE 4

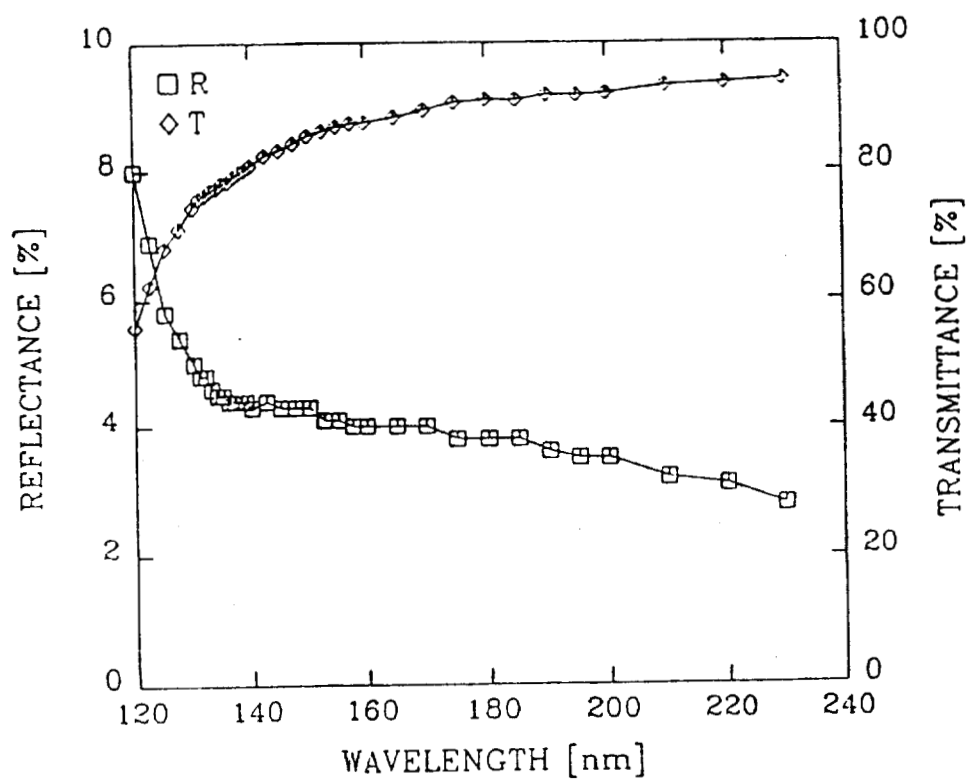


FIGURE 5

1989

NASA / ASEE SUMMER FACULTY FELLOWSHIP PROGRAM

**MARSHALL SPACE FLIGHT CENTER
THE UNIVERSITY OF ALABAMA IN HUNTSVILLE**

**ANALYTICAL OPTICAL
SCATTERING IN CLOUDS**

Prepared by:	Dieudonne D. Phanord
Academic Rank:	Assistant Professor
University and Department:	University of Alabama In Huntsville Department of Mathematical Sciences
NASA / NSFC:	
Laboratory:	Space Science
Division:	Earth Sciences / Applications
Branch:	Remote Sensing
MSFC Colleagues:	Richard J. Blakeslee Douglas Mach Huge Christian
Date:	August 24, 1989
Contract No .:	The University of Alabama In Huntsville NGT-01-008-021

TABLE OF CONTENTS

ABSTRACT	ii
ACKNOWLEDGEMENTS	iii
LIST OF FIGURES	iv
I. INTRODUCTION	1
II. OBJECTIVES	2
III. SOLUTION INSIDE THE CLOUD	3
IV. THE EQUIVALENT MEDIUM	8
V. CONCLUSIONS AND RECOMMENDATIONS	9
VI. REFERENCES	10

ABSTRACT

We report on the development of an analytical optical model for scattering of light due to lightning by clouds of different geometry. We use the self-consistent approach and the equivalent medium concept of Twersky to treat the case corresponding to outside illumination. Thus, the resulting multiple scattering problem is transformed with the knowledge of the bulk parameters, into scattering by a single obstacle in isolation. Based on the size parameter of a typical water droplet as compared to the incident wave length, the problem for the single scatterer equivalent to the distribution of cloud particles can be solved either by Mie or Rayleigh scattering theory. The super computing code of Wiscombe can be used immediately to produce results that can be compared to the Monte Carlo computer simulation for outside incidence.

A fairly reasonable inverse approach using the solution of the outside illumination case has been proposed to model analytically the situation for point sources located inside the thick optical cloud. Its mathematical details are still being investigated. When finished, it will provide scientists an enhanced capability to study more realistic clouds.

For testing purposes, the direct approach to the inside illumination of clouds by lightning is under consideration. Presently, we are on the verge of obtaining an analytical solution for the cubic cloud. For cylindrical or spherical clouds, we need preliminary results of scattering by bounded obstacles above or below a penetrable surface interface.

ACKNOWLEDGEMENT

The author expresses his appreciation to Richard J. Blakeslee, Douglas Mach, and Hugu Christian for their time, help, and ideas during his appointment as a NASA / ASEE Summer Faculty Fellow. Thanks also go to Nathaniel D. Reynolds for helpful discussions regarding testing and improving the Bohren computer code for Mie scattering. Lastly, the financial support of the NASA / ASEE Summer Faculty Fellowship Program, Gerald F. Karr, Director and Frank Six, Administrator, is gratefully acknowledged.

LIST OF FIGURES

Figure 1. Geometry for Points Sources Inside the Cloud	2
Figure 2. Single Scatterer in Isolation	3
Figure 3. Multiple Scatterers (only 3 scatterers)	5
Figure 4. The Equivalent Medium Approach	9

I. INTRODUCTION

We consider the scattering of light (visible or infrared) due to lightning by cubic, cylindrical, and spherical clouds. In this report, a typical cloud is represented by a statistically homogeneous ensemble of configurations of N identical and aligned spherical water droplets whose centers are uniformly distributed in its volume V . The radius of a droplet varies from 5 to 15 microns. The incident light is from outside the penetrable cloud.

The optical effects of clouds on the light produced by lightning have received great interest for many years. Different techniques have been used in trying to explain the complicated nature of these effects. In particular, we mention the Monte Carlo method which is a computer simulated technique. In a Monte Carlo program, we follow the path of the photons emitted into the cloud by lightning. A photon is said to be scattered if it escapes from the cloud after colliding with the spherical droplets. Otherwise, it is considered as being absorbed by the cloud [1 to 8].

The two main limitations of the Monte Carlo method [9] are the limited number of photons which can be traced through an optically thick cloud with finite computer time, and the fact that a Monte Carlo program cannot be formally proven to be mathematically correct for a finite number of photons. Also, it is very difficult to obtain reliable statistics with the Monte Carlo program.

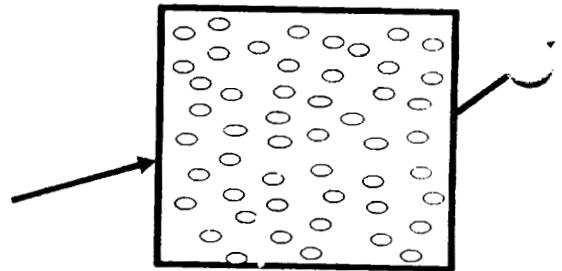
In this paper, we extend to cloud physics the work done by Twersky [10 to 12] for single and multiple scattering of electromagnetic waves. We solve the interior problem separately to obtain the bulk parameters for the scatterer equivalent to the ensemble of spherical droplets. With the interior solution or the equivalent medium approach, the multiple scattering problem is reduced to that of a single scatterer in isolation. Hence, the computing methods of Wiscombe [13] specialized to Mie scattering can be used to generate numerical results to compare with those given by different literatures.

II. OBJECTIVES

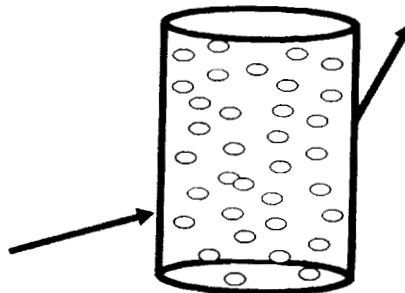
The primary objective of this project is to obtain an analytical optical model for the scattering of light due to lightning from different point sources located inside the cloud. We seek acceptable results in short computer time which will take into account the cloud physics and its boundary effects. To accomplish this objective, it was necessary to solve the multiple scattering problem with outside incidence. By varying the outside angle of incidence, we will obtain for a fixed point inside the cloud an orthogonal set of radiative solutions. From the same point source inside the cloud, we impose a uniformly radiative answer and expand it in terms of the orthogonal set of radiative solutions. The expansion coefficients will determine the outside incidence corresponding to the uniformly radiative imposed inside solution (see figure #1).

Geometry For Points Sources Inside The Cloud

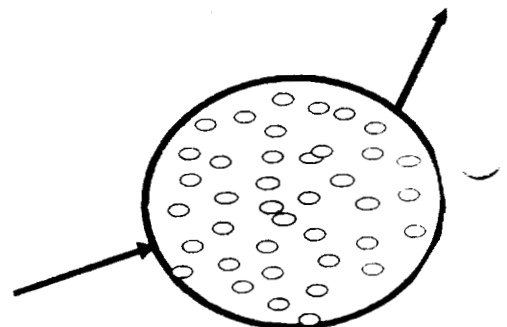
(i). The Cubic Cloud



(ii). The Cylindrical Cloud



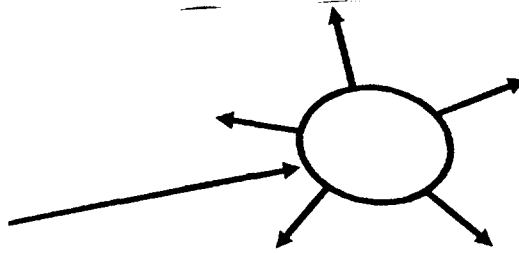
(iii). The Spherical Cloud



III. SOLUTION INSIDE THE CLOUD FOR OUTSIDE INCIDENCE

The solution inside the cloud for outside illumination corresponds to the multiple scattering of a plane electromagnetic wave by an ensemble of configurations of N identical and aligned spherical water droplets. To obtain the solution inside the cloud, we first consider (see figure #2):

(i). The Single Scatterer In Isolation



For an incidence plane electromagnetic wave $\vec{\phi} = \hat{\mathbf{a}} e^{i\vec{\kappa}_1 \cdot \mathbf{r}}$, $\kappa_1 = k\eta'$, and η' being the complex relative index of refraction for the host medium inside the cloud, the total outside solution

$$\vec{\psi} = \vec{\phi} + \mathbf{u}_o \quad (1)$$

satisfied the following differential equation obtained from Maxwell's equations after suppressing the harmonic time dependence factor $e^{-i\omega t}$

$$\left[\vec{\nabla} \times \vec{\nabla} \times + \kappa_1^2 \right] \vec{\psi} = 0, \vec{\nabla} \cdot \vec{\psi} = 0. \quad (2)$$

The solution inside the single spherical water droplet in isolation $\vec{\psi}_{in}$ satisfied

$$\left[\vec{\nabla} \times \vec{\nabla} \times + \kappa_2^2 \right] \vec{\psi}_{in} = 0, \vec{\nabla} \cdot \vec{\psi}_{in} = 0. \quad (3)$$

Here,

$$\kappa_2 = \kappa_1 \eta'' = k\eta' \eta'', \quad (4)$$

with η'' being the complex relative index of refraction for the medium inside the spherical water droplet.

Similar to Twersky [11], we have from (1)

$$\begin{aligned}\vec{\psi} &= \hat{\mathbf{a}} e^{i\vec{\kappa}_1 \cdot \mathbf{r}} + \left\{ \tilde{h}(\kappa_1 |\mathbf{r} - \mathbf{r}'|), \mathbf{u}_0(\mathbf{r}') \right\} \\ &\quad \text{with} \\ \mathbf{u}_0(\mathbf{r}') &= \left\{ \tilde{h}, \mathbf{u}_0 \right\} \\ &\equiv -\frac{\kappa_1}{i4\pi} \int \left[(\tilde{h} \times \hat{\mathbf{n}}) \cdot (\vec{\nabla} \times \mathbf{u}_0) - (\vec{\nabla} \times \tilde{h}) \cdot (\hat{\mathbf{n}} \times \mathbf{u}_0) \right] dS(\mathbf{r}').\end{aligned}\tag{5}$$

Here,

$$\begin{aligned}\tilde{h} &= \left(\tilde{\mathbf{I}} + \frac{\vec{\nabla} \vec{\nabla}}{\kappa_1^2} \right) h(\kappa_1 |\mathbf{r} - \mathbf{r}'|), \\ &\quad \text{and} \\ h(x) &= \frac{e^{ix}}{ix},\end{aligned}\tag{6}$$

and $\tilde{\mathbf{I}}$ being the identity dyadic.

Asymptotically, for $\kappa_1 r \gg 1$, we can write

$$\begin{aligned}\mathbf{u}_0(\mathbf{r}) &= \mathbf{h}(\kappa_1 r) \mathbf{g}(\hat{\mathbf{r}}, \hat{\kappa}_1 : \hat{\mathbf{a}}), \hat{\mathbf{r}} \cdot \mathbf{g} = 0 \\ &\quad \text{and} \\ \mathbf{g}(\mathbf{r}) &= \tilde{\mathbf{I}}_t \cdot \mathbf{g}(\mathbf{r}), \\ \tilde{\mathbf{I}}_t &= (\tilde{\mathbf{I}} - \hat{\mathbf{r}} \hat{\mathbf{r}}).\end{aligned}\tag{7}$$

The scattering amplitude

$$\mathbf{g}(\hat{\mathbf{r}}, \hat{\kappa}_1 : \hat{\mathbf{a}}) = \left\{ \tilde{\mathbf{I}}_t e^{-i\vec{\kappa}_1 \cdot \mathbf{r}'}, \mathbf{u}_0(\mathbf{r}') \right\}\tag{8}$$

can also be evaluated from Mie scattering theory.

The spectral representation of the scattered wave for a single spherical water droplet is

$$\begin{aligned}\mathbf{u}_0(\mathbf{r}) &= \frac{1}{2\pi} \int_c e^{i\vec{\kappa}_{1c} \cdot \mathbf{r}'} \mathbf{g}(\hat{\mathbf{r}}) d\Omega(\theta_c, \varphi_c) \\ &\quad \text{with} \\ r &> (\hat{\mathbf{r}} \cdot \mathbf{r}'), \vec{\kappa}_{1c} = \kappa_{1c} \hat{\mathbf{r}}_c(\theta_c, \varphi_c).\end{aligned}\tag{9}$$

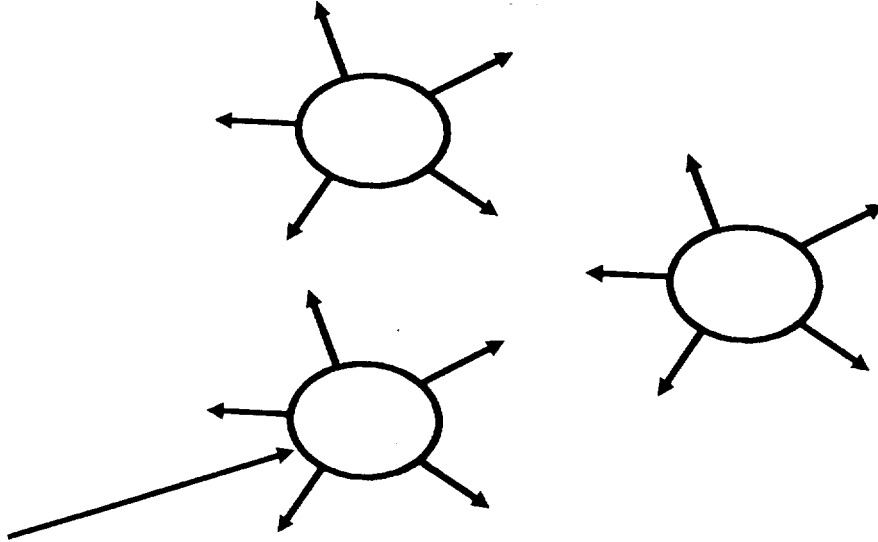
From general reciprocity relations, we have Twersky [11]

$$\begin{aligned}
 -\Re [\hat{\mathbf{a}} \cdot \mathbf{g}(\hat{\kappa}_1, \hat{\kappa}_1 : \hat{\mathbf{a}})] &= \frac{\sigma_a + \sigma_s}{\sigma_o} \\
 &\text{with} \\
 \sigma_o &= \frac{4\pi}{\kappa_1^2}, \frac{\sigma_a}{\sigma_o} = \frac{1}{2} \left\{ \vec{\psi}^*, \vec{\psi} \right\} \\
 &\text{and} \\
 \frac{\sigma_s}{\sigma_o} &= \frac{1}{2} \{ \mathbf{u}_o^*, \mathbf{u}_o \} = \frac{1}{4\pi} \int \mathbf{g}^* \cdot \mathbf{g} d\Omega(\hat{\mathbf{r}}) \\
 &\equiv \mathbf{M} |\mathbf{g}(\hat{\mathbf{r}}, \hat{\kappa} : \hat{\mathbf{a}})|^2.
 \end{aligned} \tag{10}$$

Here, σ_a and σ_s are the absorption and scattering cross sections. The operator \mathbf{M} is the mean over all directions of observation.

Equations (1) to (10) solve the single scattering problem.

(ii). A Fixed Configuration N Identical Scatterers (see figure #3)



We consider a fixed configuration of N identical scatterers with centers located by $\mathbf{r}_m (m=1,2,3,\dots,N)$.

The total outside field $\Psi(\mathbf{r})$ for an incoming wave $\vec{\phi}$ is

$$\Psi(\mathbf{r}) = \vec{\phi}(\mathbf{r}) + \sum_{m=1}^N U_m(\mathbf{r} - \mathbf{r}_m) \quad (11)$$

$$U_m(\mathbf{r} - \mathbf{r}_m) = U_m(\mathbf{r} - \mathbf{r}_m; \mathbf{r}_1, \mathbf{r}_2, \dots, \mathbf{r}_N),$$

with

$$U_m(\mathbf{r} - \mathbf{r}_m) \sim h(\kappa_1 |\mathbf{r} - \mathbf{r}_m|) \mathbf{G}_m \quad (12)$$

for $|\mathbf{r} - \mathbf{r}_m| \rightarrow \infty$. The multiple configurational scattering amplitude is given by

$$\mathbf{G}_m(\hat{\mathbf{r}}) = \left\{ \vec{\mathbf{I}}_t e^{-i\vec{\kappa}_1 \cdot \mathbf{r}'} U_m \right\}. \quad (13)$$

Equivalently, for the scatterer located at t , we use the self-consistent approach of Twersky [10] to obtain the total outside configurational field

$$\Psi_t(\mathbf{r}) = \vec{\phi}(\mathbf{r}) + \sum'_m U_m(\mathbf{r} - \mathbf{r}_m) + U_t(\mathbf{r} - \mathbf{r}_t), \quad (14)$$

with

$$\sum'_m = \sum_{m \neq t}.$$

Using (14) and the general reciprocity relation

$$\left\{ \Psi, \vec{\psi}_a \right\}_t = 0 \quad (15)$$

for any arbitrary direction of incidence, we derive as in [11] the self-consistent integral equation for the multiple configurational scattering amplitude

$$\mathbf{G}_t(\hat{\mathbf{r}}) = \tilde{\mathbf{g}}_t(\hat{\mathbf{r}}, \hat{\kappa}_1) \cdot \hat{\mathbf{a}} e^{i\vec{\kappa}_1 \cdot \mathbf{r}_t} + \sum'_m \int_c \tilde{\mathbf{g}}_t(\hat{\mathbf{r}}, \hat{\mathbf{r}}_c) \cdot \mathbf{G}_m(\hat{\mathbf{r}}_c) e^{i\vec{\kappa}_{1c} \cdot \mathbf{R}_{tm}}, \quad (16)$$

with

$$\mathbf{R}_{tm} = \mathbf{r}_t - \mathbf{r}_m, \text{ and } \int_c = \frac{1}{2\pi} \int d\Omega_c.$$

(iii). Ensemble of Configurations

We take the average of (16) over a statistically homogeneous ensemble of configurations of N identical and aligned scatterers whose centers are uniformly distributed in the volume of the thick cloud. Using the equivalent medium approach and Green's theorems, we obtain [11] the dispersion relation determining the coherent parameters

$$\begin{aligned} \mathcal{G}(\vec{\kappa}_1|\vec{K}) = & -\frac{\rho}{c_o(K^2 - \kappa_1^2)} \left\{ \left[e^{-i\vec{K}\cdot\mathbf{R}}, \mathbf{U} \right] \right\} \\ & + \rho \int_{V_\infty - v} [f(\mathbf{R}) - 1] e^{-i\vec{K}\cdot\mathbf{R}} \mathbf{U} d(\mathbf{R}). \end{aligned} \quad (17)$$

Here, \mathcal{G} is the equivalent scattering amplitude and \mathbf{U} is the radiative function defined by

$$\begin{aligned} & \left[\vec{\Delta}_{|\mathbf{R}|} + \kappa_1^2 \right] \mathbf{U} = 0, \\ \mathbf{U} = & \int_c \tilde{\mathbf{g}}(\hat{\mathbf{r}}, \hat{\mathbf{r}}_c) \cdot \mathcal{G}(\vec{\kappa}_{1c}|\vec{K}) e^{i\vec{\kappa}_{1c}\cdot\mathbf{R}}, \\ & \rho = \frac{N}{V} \end{aligned} \quad (18)$$

and the bulk propagation parameter is

$$K = \kappa_1 \eta \quad (19)$$

with η being the bulk index of refraction.

In equation (17), $[f(\mathbf{R}) - 1]$ is the total correlation function, and $(V_\infty - v)$ represents the depleted volume (the volume of all space less that of the exclusion region). The operator

$$\{[f, g]\} = \int_S [f \partial_n g - g \partial_n f] dS \quad (20)$$

is the Green exclusion surface operator with outward unit normal from v .

Equation (17) solves formally the interior problem for the cloud. To obtain numerical results, one can apply stationary phase method [12] on

(18) and reduce (17) to

$$\begin{aligned}
 K - \kappa_1 &\sim -\frac{ig\sigma_o}{2\eta} \mathfrak{L}^{-1} \\
 &\text{and} \\
 \mathfrak{L} &= \left\{ 1 - \rho \frac{g\sigma_o}{2\eta} \int_0^\infty [f(\mathbf{R}) - 1] e^{i(\kappa_1 - K)\mathbf{R}} d(\mathbf{R}) \right\}.
 \end{aligned} \tag{21}$$

To obtain equation (21), we neglect back scattering in the forward direction since the spherical droplets are large tenuous scatterers and the magnitude of the single scattering amplitude is evaluated in the forward direction. Equation (21) can be solved numerically, iteratively or directly subject to explicit restriction on

$$g = \hat{\mathbf{e}} \cdot \mathbf{g}(\hat{\mathbf{K}}, \hat{\mathbf{K}}). \tag{22}$$

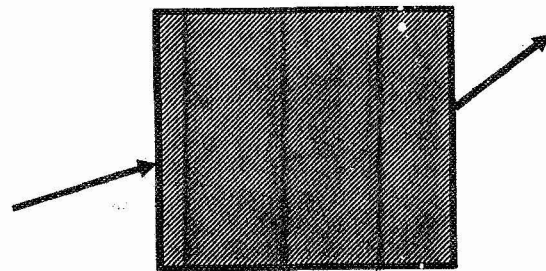
It is important to stress that equation (21) can be subjected to different approximations procedures [14] depending on the cloud composition and the nature of its boundary. In particular, we mention the asymptotic leading term approximation, the generalized Rayleigh's approximation, and the two-space scatterer formalism leading term approximation [11].

The two-space scatterer formalism can be used directly in cloud with a slab geometry, and it will preserve the self-consistency of the solution. The scatterers in the slab geometry will be excited by a coherent wave traveling in the equivalent medium but will radiate into free space.

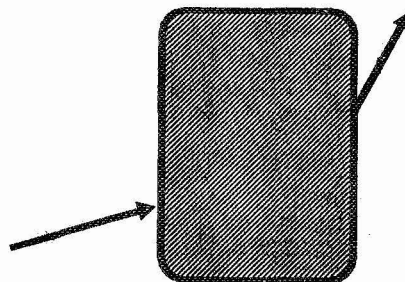
IV. THE EQUIVALENT MEDIUM APPROACH

Now, we can use the results of part (III) to solve the outside illumination for clouds with different geometry since the net behavior of the interior is known. The multiple scattering problem becomes the scattering by a single obstacle (see figure #4). To produce numerical results, we can apply Wiscombe's advanced super computer code specialized to Mie scattering Geometry of The Equivalent Medium Approach

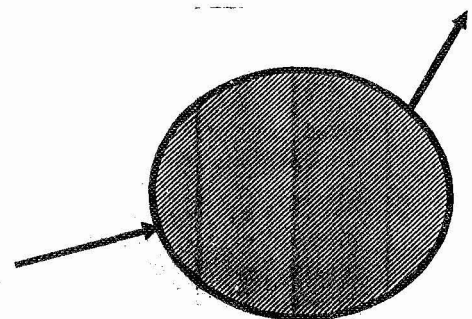
(i). The Cubic Cloud (front view)



(ii). The Cylindrical Cloud



(iii). The Spherical Cloud



V. CONCLUSIONS AND RECOMMENDATIONS

The analytical solution for the outside illumination of clouds by lightning using the equivalent medium approach has been completed. The multiple scattering problem has been reduced to that of a single scatterer in isolation. Depending on the size parameter of the cloud particles as compared to the wave length of the incident light, either Rayleigh or Mie scattering technique can be used to determine Q_{ext} , Q_{scat} , and Q_{bacs} .

With the bulk parameters, we can use Wiscombe's computer code to obtain in short computer time, acceptable numerical results for a medium with a complex relative index of refraction which is an improvement of Bohren [15]. The equivalent medium approach gives naturally the polarizations and the angular distributions of photons which escape the cloud surface.

Due to the complexity of the problem and the time constraint, the mathematical details for point sources inside the cloud are still being worked out. They will be the subject of more studies in the future. To the best of my knowledge, no analytical solution of the problem has yet been published. Even partial results will play a major role in describing the transport of radiation produced by lightning from point sources located inside the cloud.

To test the analytical solution, we intend to solve the cubic case directly since we know the results of scattering by a penetrable plane interface. For cylindrical and spherical clouds however, one has to establish preliminary results for the scattering of light by an obstacle above or below a penetrable surface interface.

With the completion of the analytical model, we will have the ability and the capability to study the transfer of radiation through realistic clouds. That is to say, we will be able to consider clouds made up of water and ice particles, of inhomogeneous distribution of diversified constituents; we will be able to study the fluctuational changes of polarization of light through the cloud due to sudden geometrical deformations of its boundary and the frequent realignment of its particles (e.g, needle shape ice particles aligned in a strong electric field).

VI. REFERENCES

1. Aida, M., 1977: Scattering of solar radiation as a function of cloud dimensions and orientation. *J. Quant. Spectrosc. Radiat. Transfer*, 17, 303-310.
2. Bucher, E. A., 1973: Computer simulation of light pulse propagation for communication through thick clouds. *Appl. Opt.*, 12, 2391-2400.
3. Danielson, R. E., D. R. Moore and H. C. van de Hulst, 1969: The transfer of visible radiation through clouds. *J. Atmos. Sci.*, 26, 10778-1087.
4. Davies, R., 1978: The effect of finite geometry on the three dimensional transfer of solar irradiance in clouds. *J. Atmos. Sci.*, 35, 1712-1725.
5. Davis, J. M., S. K. Cox and T. B. McKee, 1979: Vertical and horizontal distributions of solar absorption in finite clouds. *J. Atmos. Sci.*, 36, 1976-1984.
6. McKee, T. B., and S. K. Cox, 1974: Scattering of visible radiation by finite clouds. *J. Atmos. Sci.*, 31, 1885-1892.
7. Plass, G. N., and G. W. Kattawar, 1968: Monte Carlo calculations of light scattering from clouds. *Appl. Opt.*, 1, 126-130.
8. Van Blerkom, D., 1969: Diffuse reflection from clouds with horizontal inhomogeneities. *Astrophys. J.*, 166, 235-242.
9. Thomason, L. W., and E. P. Krider, 1982: The effects of clouds on the light produced by lightning. *J. Atmos. Sci.*, 39, 2051-2065.
10. Twersky, V., 1977: Coherent scalar field in pair-correlated random distributions of aligned scatterers. *J. Math. Phys.*, 18, 2468-2486.
11. Twersky, V., 1978: Coherent electromagnetic waves in pair-correlated random distributions of aligned scatterers. *J. Math. Phys.*, 19, 215-230.
12. Twersky, V., 1983: Propagation in correlated distributions of large-spaced scatterers. *J. Opt. Soc. Am.*, 73, 313-320.
13. Wiscombe, W. J., 1979. Mie scattering calculations: Advances in technique and fast, vector-speed computer codes, NCAR/TN-140 +STR, National Center for Atmospheric Research, Boulder, Colo.
14. Twersky, V., 1983: Wavelength-dependent refractive and absorptive terms for propagation in small-spaced correlated distributions. *J. Opt. Soc. Am.*, 73, 1562-1567.
15. Twomey, S., and C. F. Bohren, 1980: Simple approximations for calculations of absorption in clouds. *J. Atmos. Sci.*, 37, 2086-2094.

1989

NASA/ASEE SUMMER FACULTY RESEARCH PROGRAM

**Marshall Space Flight Center
The University of Alabama in Huntsville**

**RADAR TRANSPONDER ANTENNA PATTERN
ANALYSIS FOR THE SPACE SHUTTLE**

Prepared by:	Roger Radcliff
Academic Rank:	Associate Professor
Affiliation:	Dept. of Electrical and Computer Engineering Ohio University Athens, Ohio
NASA/MSFC:	
Laboratory:	Information and Electronics Systems
Division:	Computers and Communications
Branch:	Communications Systems
NASA Colleague:	Lee Malone
Date:	August 25, 1989

RADAR TRANSPONDER ANTENNA PATTERN ANALYSIS FOR THE SPACE SHUTTLE

**Roger Radcliff
Associate Professor of Electrical
and Computer Engineering
Ohio University
Athens, Ohio**

ABSTRACT

In order to improve tracking capability, radar transponder antennas will soon be mounted on the shuttle solid rocket boosters (SRB). These four antennas, each being identical cavity-backed helices operating at 5.765 GHz, will be mounted near the top of the SRB's, adjacent to the intertank portion of the external tank. The purpose of this study is to calculate the roll-plane pattern (the plane perpendicular to the SRB axes and containing the antennas) in the presence of this complex electromagnetic environment.

The large electrical size of this problem mandates an optical (asymptotic) approach. Development of a specific code for this application is beyond the scope of a summer fellowship; thus a general purpose code, the Numerical Electromagnetics Code - Basic Scattering Code, was chosen as the computational tool. This code is based on the modern Geometrical Theory of Diffraction, and allows computation of scattering of bodies composed of canonical problems such as plates and elliptic cylinders.

Apertures mounted on a curved surface (the SRB) cannot be accommodated by the code, so an antenna model consisting of wires excited by a method of moments current input was devised that approximated the actual performance of the antennas. The improvised antenna model matched well with measurements taken at the MSFC range. The SRB's, the external tank, and the shuttle nose were modeled as circular cylinders, and the code was able to produce what is thought to be a reasonable roll-plane pattern.

ACKNOWLEDGEMENTS

The author would like to thank Mr. Lee Malone, EB33, for arranging this summer fellowship. Thanks also go out to Mr. J.A. Dunkin and his staff at the antenna range for all their assistance and for creating a pleasant work atmosphere. The efforts of Drs. Karr and Six are also appreciated.

I would like to gratefully acknowledge Dean T.R. Robe, Dr. J.R. Mitchell and the Stocker Endowment for making it possible for me to accept this fellowship.

INTRODUCTION

In order to improve tracking of the shuttle's solid rocket boosters (SRB) after normal separation from the external tank (or in the event of abnormal separation), four radar transponder antennas will be mounted on the SRB's. The antennas are cavity-backed helices operating at a frequency of 5.765 GHz, and a pair them will be mounted on opposite sides of each SRB cylinder.

The patterns of two of these antennas mounted on a metallic cylinder having the same diameter as an SRB but only 4.5 feet tall have been measured at the MSFC antenna range and they appear to yield acceptable coverage. An attempt to measure the three-dimensional pattern of the antennas in the presence of both SRB's, the external tank (ET), and the orbiter is not practical, since the frequency of operation needed for a usable shuttle scale model is in the neighborhood of 90 GHz.

The purpose of this effort is to gain more information on the pattern of these antennas in the presence of the entire shuttle cluster. Since experimental means are not practical, classical electromagnetic theory along with modern computational methods will be used. Given the time restraints of a ten-week fellowship, the pattern is calculated in only one plane (the plane containing the antennas and which is perpendicular to the SRB axes).

OBJECTIVES

The objective of this effort is to calculate the two-dimensional pattern of the four radar transponder antennas in the presence of both SRB's, the ET, and the orbiter. The plane of interest is the plane containing the four antennas, which happens to be perpendicular to the SRB cylinder axis (and will henceforth be referred to as the "roll-plane" pattern). Specific attention will be given to accurate modeling of the antennas performance and matching model results to actual measurements.

The following assumptions are made throughout the report:

1. Portions of the shuttle cluster that do not penetrate the roll-plane are not included in the computations. This implies that the effects, if any, of the rounded ends of the SRB's, ET, and orbiter are ignored.
2. Polarization measurements were not made, but it is assumed that the radiation is circularly polarized.
3. The antennas will be placed at points on the SRB's that are adjacent to the intertank portion of the ET. This intertank section contains strengthening corrugations which are on the order of a wavelength high. In this analysis, the ET is assumed to be a smooth cylinder.

PATTERN CALCULATION

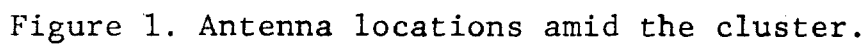
The locations for the radar transponder antennas on the shuttle cluster are shown in Fig. 1. The antennas are assumed to be operating at a frequency of 5.765 GHz and that the radiation is circularly polarized. Due to the symmetry of the problem and the fact that objects not in the roll-plane are being ignored, it is irrelevant whether the cluster is looked upon from the front or rear (this is why the direction of flight is not identified on cluster drawings in Figs. 7-10).

Previous to this effort, an estimate of the shadowing due to the cluster was made using a line-of-sight shadowing code [1]-[2]. In addition, some preliminary work was done to model the antennas in the presence of two cylinders [3], and the effects of corrugations of the external tank were partially examined [4]. The roll-plane pattern of all antennas in the presence of the entire cluster was not obtained, however.

Due to the large electrical size of the problem, we are forced to use an optics approach. The integral equation and differential equation methods require far too much computer memory and time for a problem of this size [5]. Physical optics could be applied, but there is no general purpose physical optics code in the public domain, and writing one for this specific purpose is beyond the scope of a summer fellowship. Thus, the only technique within our grasp is geometrical optics and the associated Geometrical Theory of Diffraction (GTD).

The modern GTD is an extension of Keller's diffraction theory. It modifies the geometrical optics field (direct, reflected, and refracted fields) to yield a field distribution which is continuous across spatial boundaries at which geometrical optics alone would predict discontinuities. It is a high-frequency asymptotic technique, however, and becomes more accurate as the frequency of operation becomes higher. Given the radar antenna wavelength and the size of the shuttle cluster, GTD can be expected to give good results for this problem.

Invoking GTD requires development of "diffraction coefficients" associated with the given problem [6]. Diffraction coefficients have been found for several



canonical problems, including plates, wedges, cones, and elliptic cylinders. Many practical antenna and scattering problems have been solved with GTD by approximating the antenna or scatterer by one or more canonical geometries. Since the scattered field is obtained by summing many rays that can exist from source to observation point, building a model of a structure from canonical problems is easy, since induced current interactions between different parts of the structure do not have to be explicitly computed.

This GTD ray tracing process lends itself well to the creation of a general purpose code; this was done by Prof. Ron Marhefka and his associates at the Ohio State University [7]. The code is named the Numerical Electromagnetics Code - Basic Scattering Code (NEC-BSC) and is implemented on the MSFC antenna range Compaq 386/20 personal computer.

The aspect of NEC-BSC that applies to this problem is its ability to calculate the far field pattern of an antenna array in the presence of complex structures, provided the structure can be modeled as a combination of canonical geometries. In reality, it is possible that many ray paths exist between the source and observation point; the code handles only the lower-order paths. For example, the code will compute direct, singly-reflected, singly-diffracted, doubly reflected, reflected-diffracted, and diffracted-reflected rays, but not doubly-diffracted ones.

These limitations in ray tracing can be significant, but the code does have limited warning capability which warns the user when a particular mode which is not calculated may be significant. This was not encountered during the course of this investigation. We will see that it does, however, introduce small discontinuities in the final pattern. This is not important; the theory of GTD tells us that the ignored modes would simply smooth out the discontinuity.

It should be stressed that NEC-BSC is, like many other general purpose electromagnetic codes, sensitive to the user's understanding of the underlying theory of the code and of electromagnetic theory in general. This was evident during this investigation when it was discovered that compiling NEC-BSC with an optimizing compiler causes

errors in output when a linear source is placed parallel to the axis of a cylinder. A person without proper training using the code would not have noticed the problem and, most likely, would have generated erroneous results. Further comment on this can be found in the Results and Recommendations section.

Much of this effort was devoted to modeling the helix antennas, and is along the lines of that in [3]. Fig. 2a. represents the two antennas mounted on an SRB, with the aperture flush with the cylinder surface. NEC-BSC allows the user to specify an aperture as a source, but it cannot be mounted on a curved surface (Fig. 2b.). This is because the problem of a source mounted on a curved surface is a completely different type of diffraction problem (the "radiation" problem), and the code does not incorporate this diffraction theory.

Apertures are permitted to be mounted on flat plates, however. It seems logical, then, to mount an aperture on a small flat plate placed a small distance above the circular cylinder representing the SRB (the circular cylinder is another canonical problem which the code handles). Unfortunately, this will not work because doubly-diffracted fields are not computed, and thus the cylinder would not be illuminated by the antenna.

Since the actual helix antennas are circularly polarized, our model must be also. Circular polarization can also be obtained by crossed dipoles or crossed slots. It is known that a half-loop and its associated image can produce a field similar to that of a slot mounted on the cylinder surface [3]. Two of these half-loops are shown in Fig. 2d.; to create the other slot would require two more perpendicular to those drawn.

This cannot be trusted, however, because this would place the sources too close to the cylinder. This is because NEC-BSC is based on a high-frequency asymptotic theory and no two objects should ever be closer than one-quarter wavelength apart. This problem could be alleviated by raising the loops one-quarter wavelength off the cylinder surface, as shown in Fig. 2e.

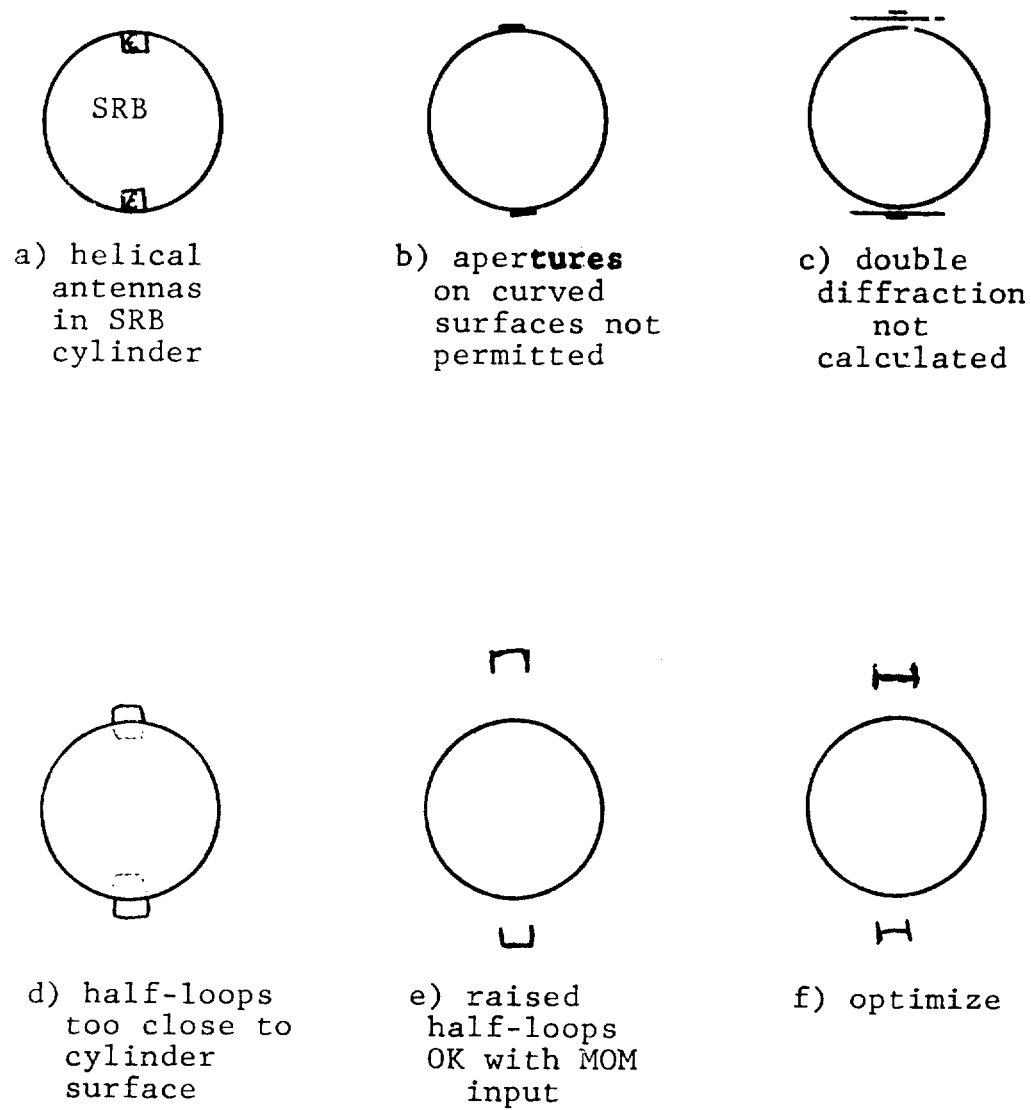


Figure 2. Antenna model development.

This is obviously not a physically viable situation. That is irrelevant though, since the code allows wire segments to be placed anywhere with any current magnitude and phase desired. In reality, the currents would interact and redistribute themselves to satisfy boundary conditions, but this input option is intended to allow the results from a method of moments analysis to be used as a source. In other words, any wire segment interaction would have already been included in the method of moments calculation (NEC-BSC cannot perform the current interaction calculation since it is not based on an integral equation approach). So, even though the currents used on the half-loop model are not derived from a method of moments procedure, we can still take advantage of this input option to create our antenna model.

The next step was to adjust the relative phasing, magnitude, and distance from the cylinder of the wire segments in an attempt to obtain a model that matched well with measured data taken at the antenna range. This was somewhat time-consuming, and was done on what was essentially a trial-and-error basis (Fig. 2f.).

To make the measurements at the antenna range, two of the cavity-backed helix antennas were mounted on a 4.5 foot high cylinder having the same diameter as the SRB. Thus, when developing the antenna model, a 4.5 foot high cylinder was assumed. When only one antenna was modeled, some discontinuities were evident on the side opposite the antenna. This is because of the fact that the code has some difficulty dealing with caustics (places where an infinite number of rays intersect). It so happens that the location of the caustic is at the maximum of the second antenna's pattern; fortunately this drowns out the discontinuity and yields an essentially continuous pattern. The final modeled pattern of two antennas mounted on a 4.5 foot high SRB section is given in Fig. 3. The radiation is very close to being circularly polarized.

The measured pattern for the same situation is given in Fig. 4, and both patterns are plotted for comparison purposes in Fig. 5. The calculated and measured patterns agree very well almost everywhere.

ORIGINAL PAGE IS
OF POOR QUALITY

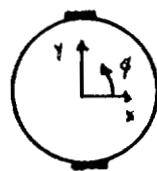
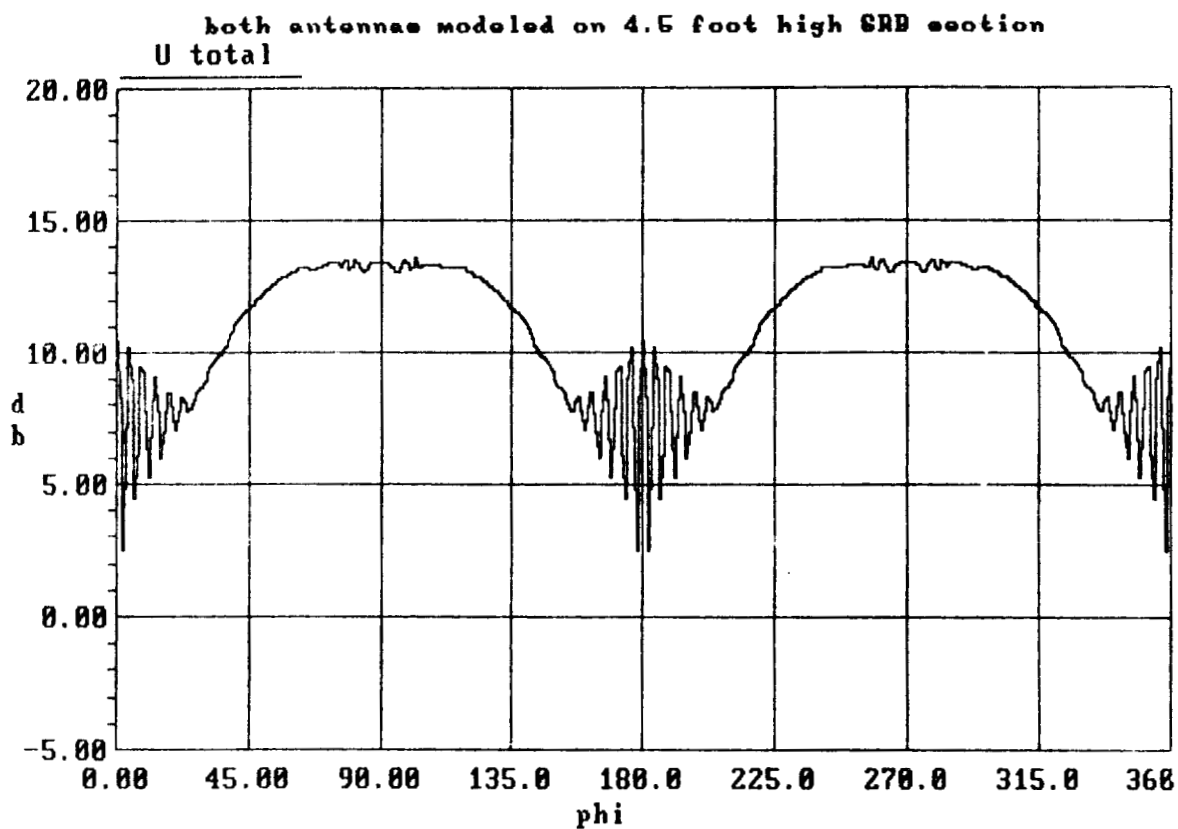


Figure 3. Pattern of two antenna models on
one 4.5 foot high SRB section.

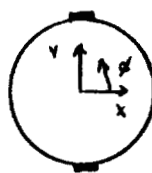
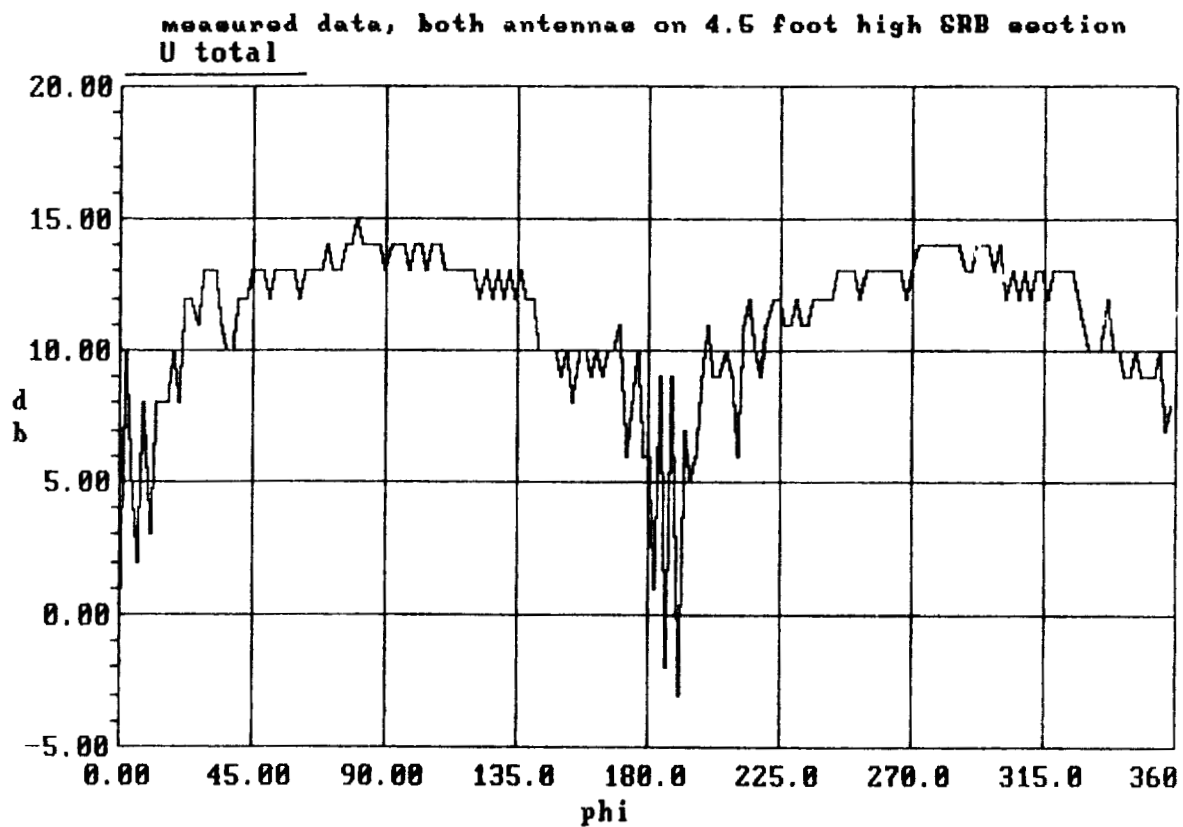


Figure 4. Measurement of roll-plane pattern of two antennas on 4.5 foot high SRB section.

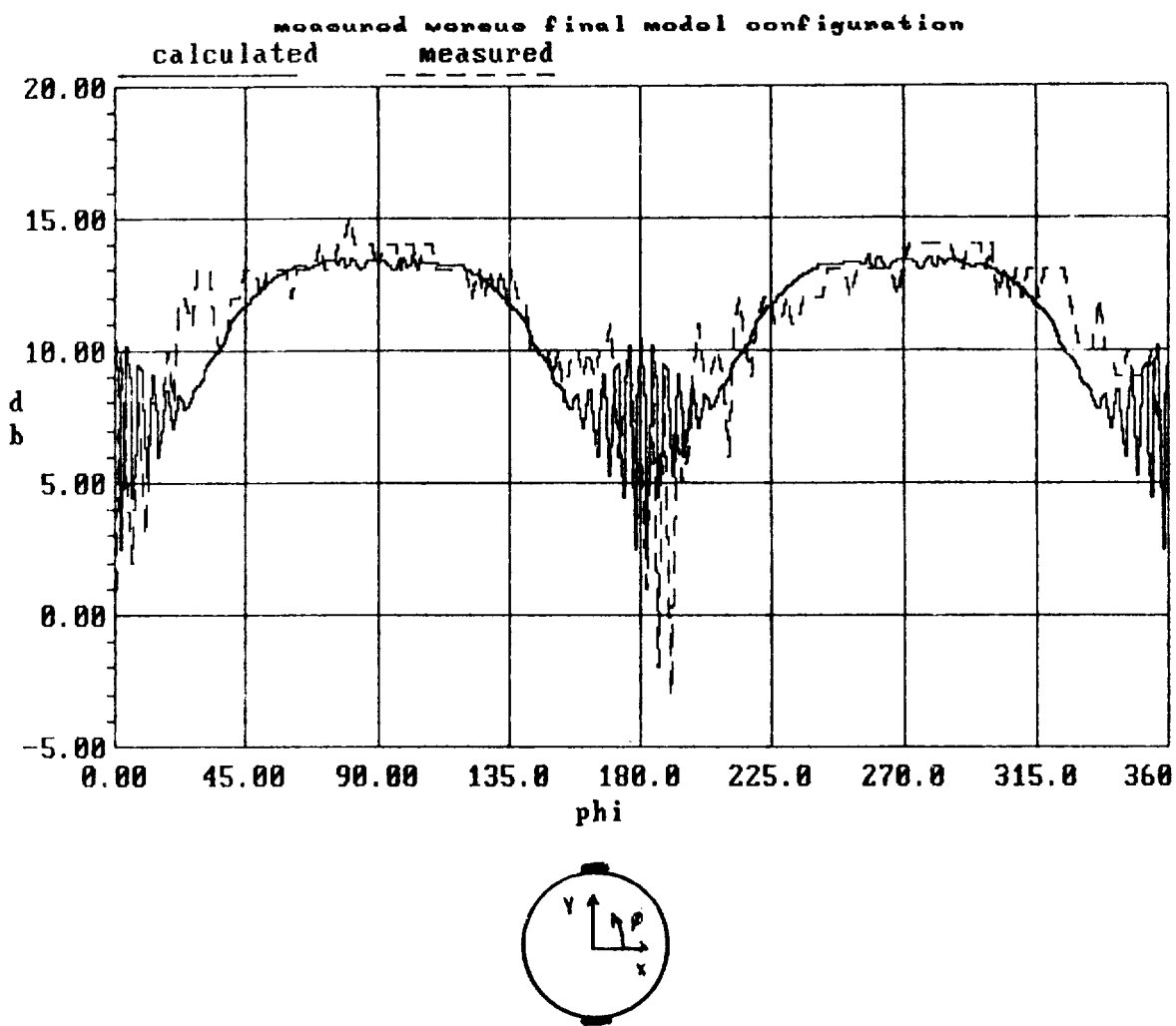


Figure 5. Comparison of measured pattern with calculated pattern.

Now that the two antenna/SRB model is developed, it is a straightforward matter complete the analysis. Fig. 6 gives the pattern of both SRB's, with the cylinders rotated by 35 degrees, to coincide with Fig. 1. The pattern is quite complicated, with very short distances between adjacent maxima and minima. This is to be expected, since the scattering centers are very far apart electrically. To gain more confidence in the pattern at this point in the development, the pattern of two dipoles tilted at 35 degrees from the x-axis operating at the same frequency was calculated and is plotted in Fig. 7. The periodicity between adjacent maxima and minima is similar to that of Fig. 6. Dipoles were chosen since they have a similar pattern to that of the two antenna/SRB model. The more complicated nature of the pattern of Fig. 6 can be attributed to multiple cylinder interactions.

Fig. 8 gives the final roll-plane pattern calculation, obtained by using the input file which created Fig. 6 and adding cylinders to represent the ET and the cross section of the orbiter's nose in the roll-plane. Figs. 9 and 10 present the same data in expanded form. Shuttle dimensions used in creating the input file are taken from [8].

There are some small discontinuities evident in Figs. 9 and 10. These may be due to the basic limitations in the code's ray tracing procedure or to the fact that computations can only be done at a minimum of 1 degree increments. But this pattern is believed to be reasonable and accurate to within the code's limitations and the simplifying assumptions.

Due to the 25 page limit on this report, there is no room for discussion of the details of the input data file. It is listed as an appendix at the end of this report, and may be interpreted with the use of [7].

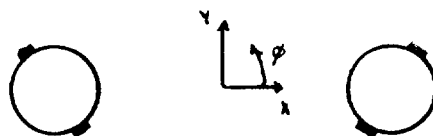
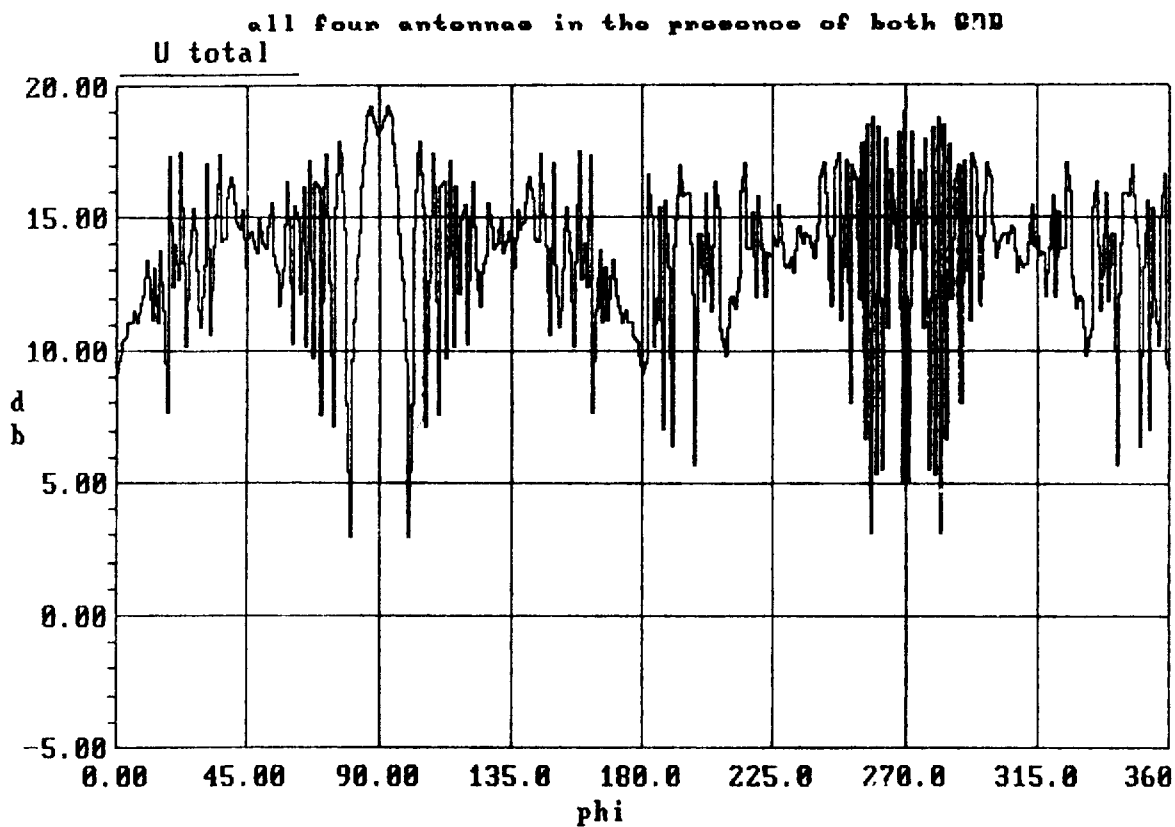


Figure 6: Pattern of all four antennas in the presence of both SRB's.

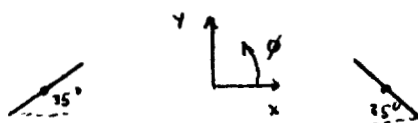
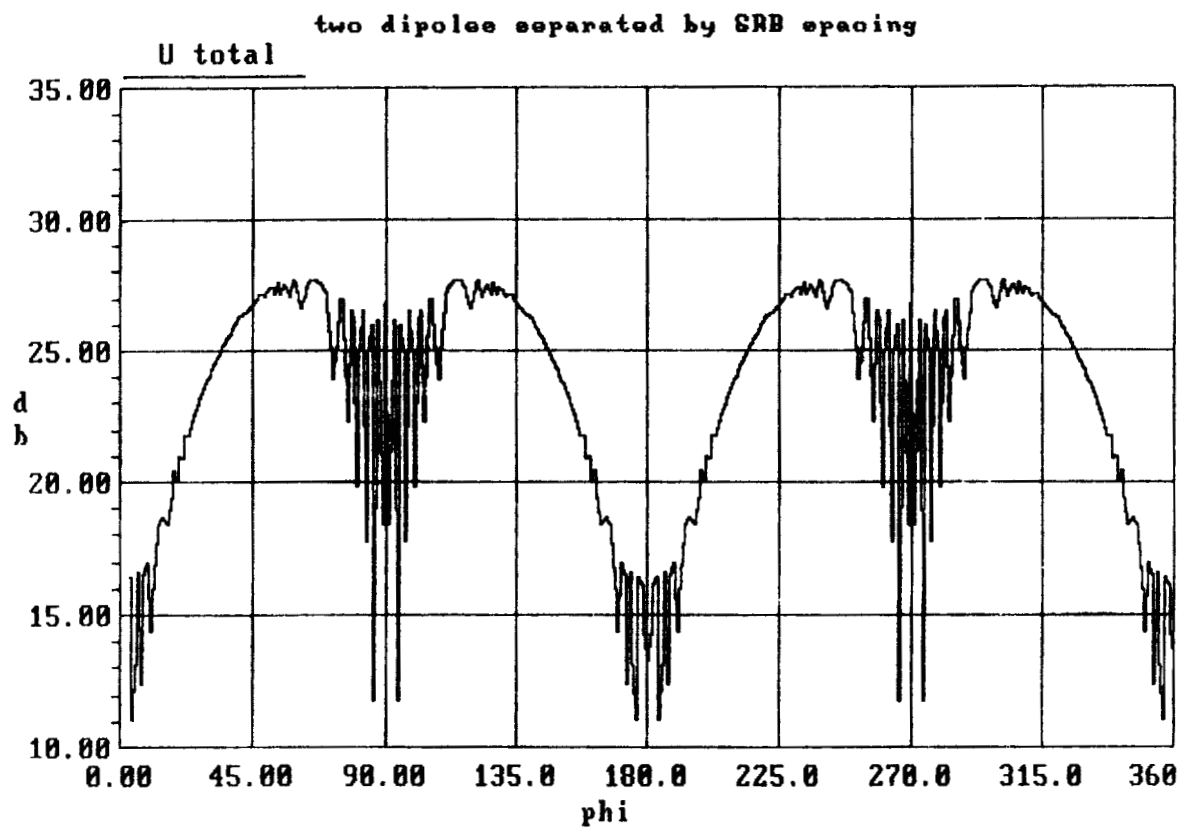


Figure 7. Pattern of two dipoles separated by the distance between the SRB's.

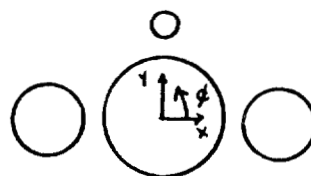
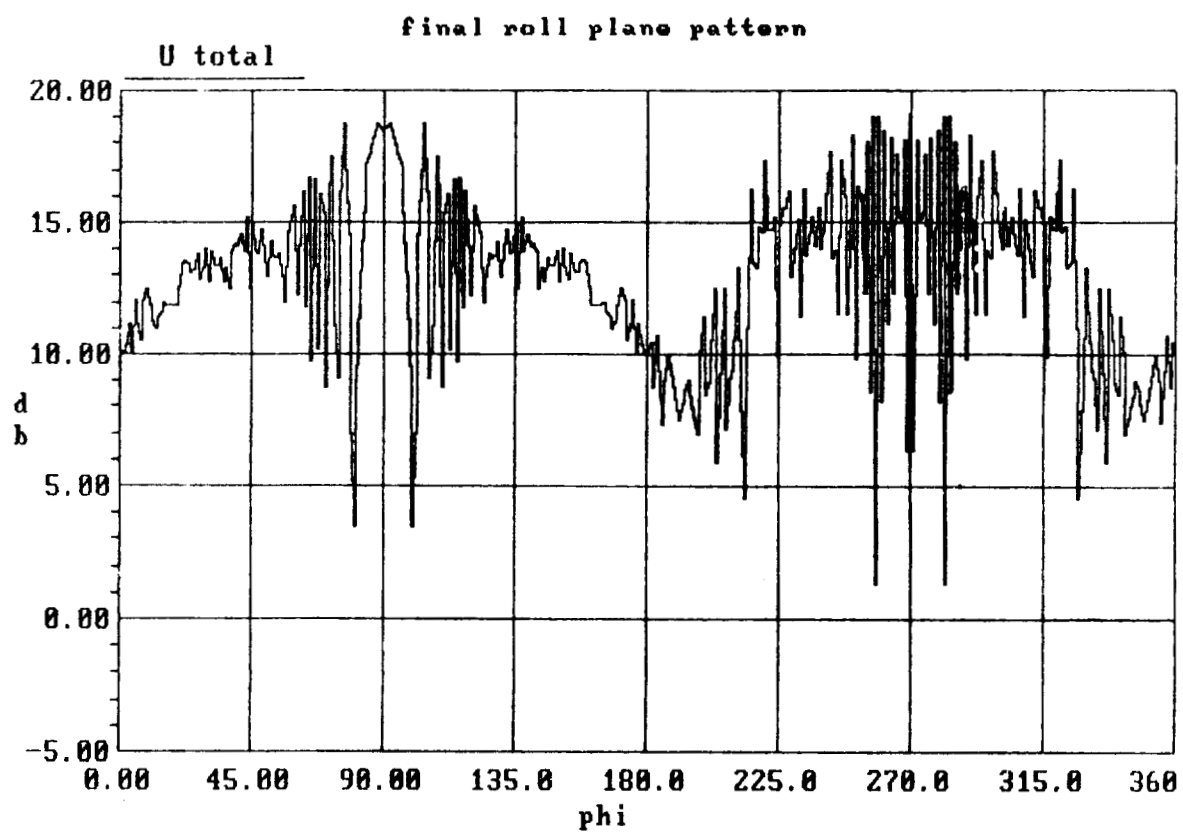


Figure 8. Final result.

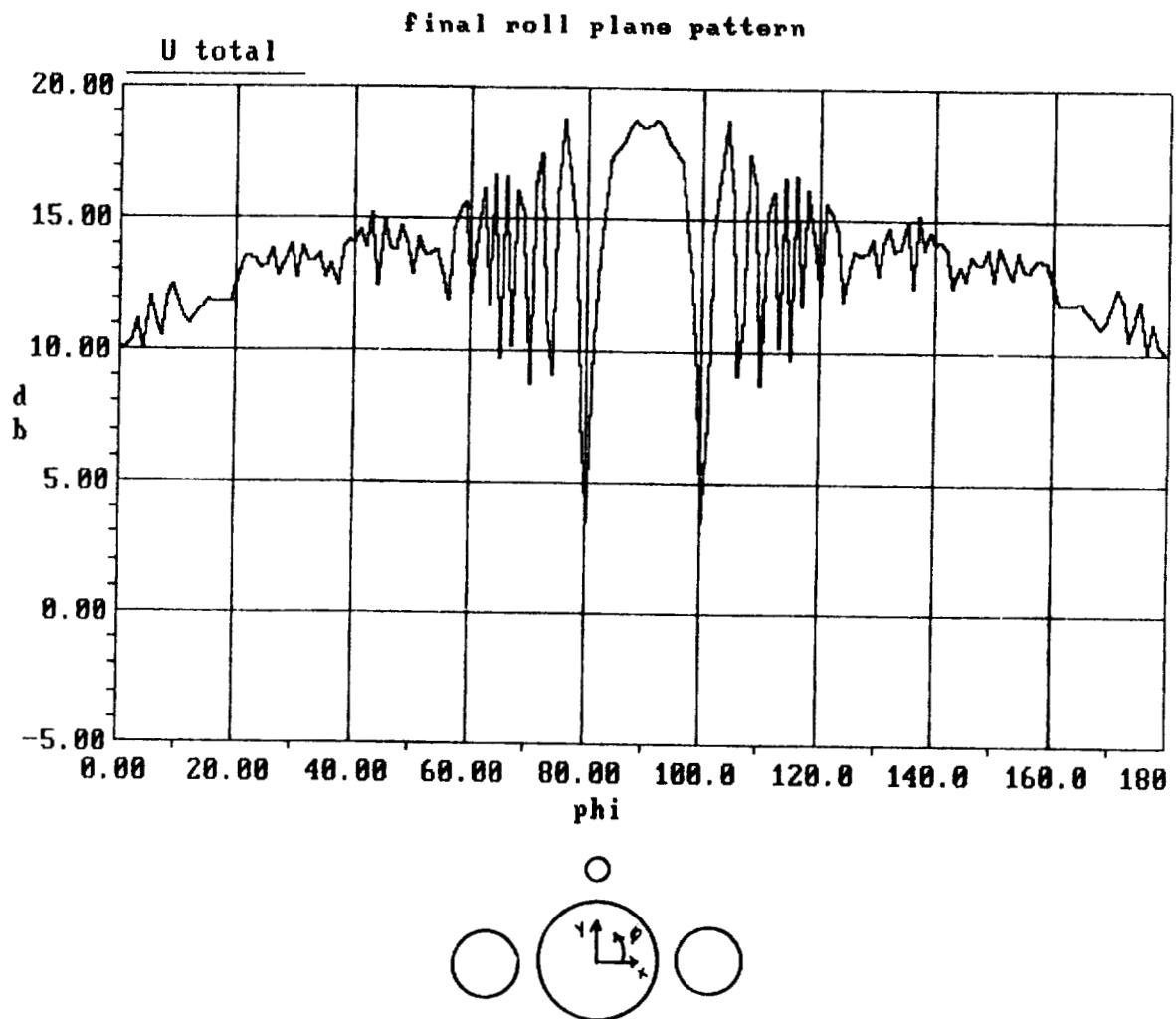


Figure 9. Final result - 0° through 180°.

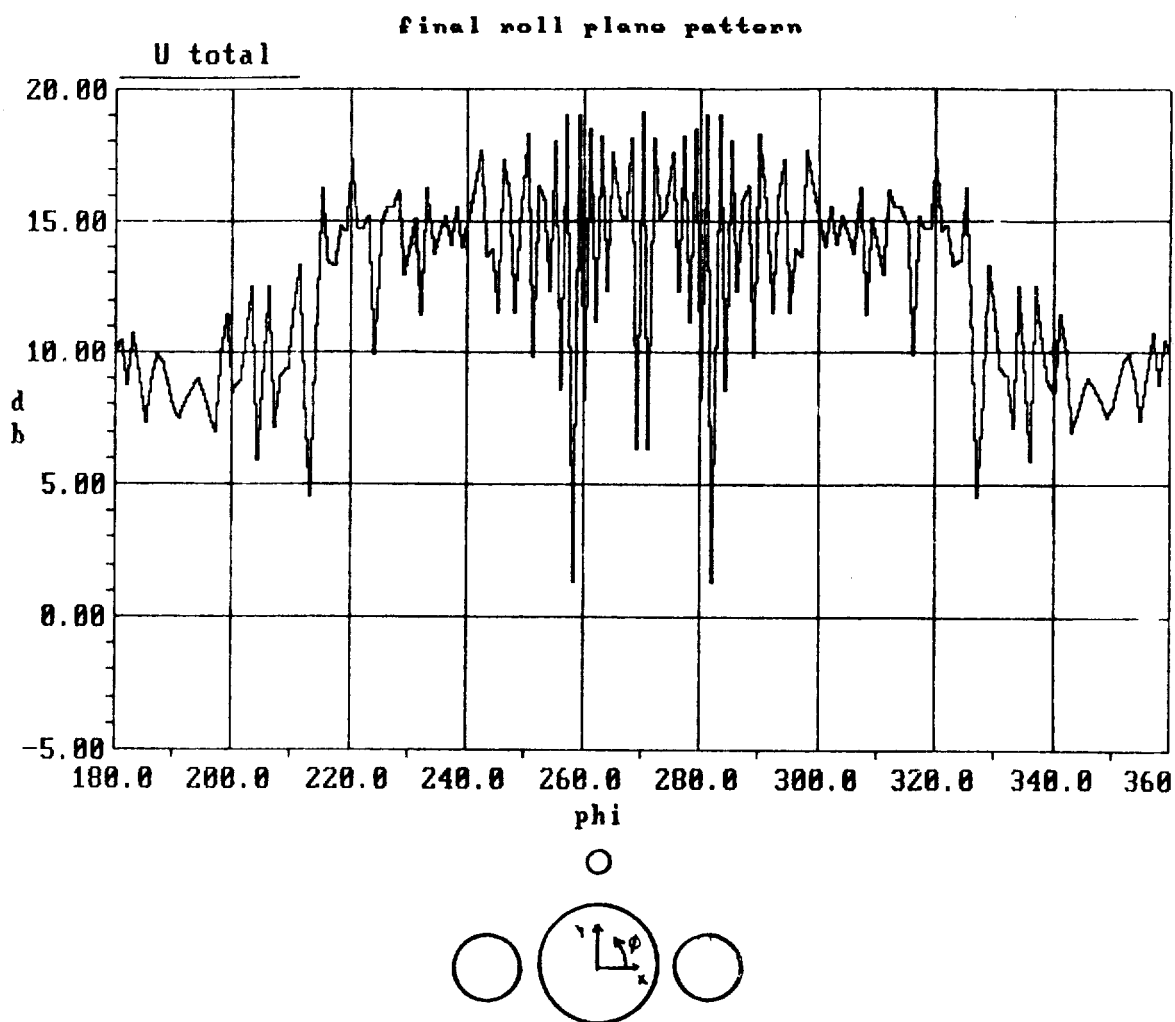


Figure 10. Final result - 180° through 360°.

CONCLUSIONS AND RECOMMENDATIONS

The roll-plane pattern of the radar transponder antennas given in Figs. 8-10 is believed to be reasonable, given the assumptions listed in the Objectives section. The absence of contributions to the roll-plane pattern due to portions of the cluster not in the roll-plane would modify it somewhat, but they are not expected to be significant.

However, if a better estimate of the roll-plane pattern is desired, it is necessary to investigate the effects of the corrugations on the external tank. This problem was examined to some degree [4], but the author stresses that the extent of his investigation was not sufficient to come to a hard conclusion. It appears that the main reason for this was the modeled corrugations were placed on a flat plate, rather than a circular cylinder. This is understandable, since the code used in the study could not handle a problem of this magnitude.

This problem of scattering from electrically large corrugations on a circular cylinder could possibly be solved by a combination of theories used in the examination of frequency selective surfaces (Floquet harmonics [9]) along with the method of moments to solve for induced currents in a periodic cell (one corrugation adjacent to its flat neighbor). This approach was successful in calculation of scattering from a flat array of conducting plates; extension to a cylindrical surface is straightforward but tedious.

Of course, the roll-plane pattern alone is not sufficient to completely describe the performance of the antenna system mounted on the shuttle cluster; a three-dimensional pattern would be necessary. This would not be an easy problem, but is clear that a geometrical optics approach is necessary, and some simplifying approximations would have to be made.

It is also recommended that steps be taken to educate the personnel at the MSFC antenna range on modern techniques to perform analyses such as the one described in this report. There are some very powerful tools available today to aid the electromagnetic engineer perform calculations that he/she could not possibly do

by hand and would otherwise have to rely on crude rule-of-thumb methods. It must be stressed that purchasing codes and reading the associated manuals is not enough; proper understanding of the underlying theory is crucial. The computing power that already resides at the antenna range is sufficient; it is recommended that arrangements be made to have the author present several hands-on seminars to MSFC personnel to increase what is now a very small electromagnetic computational capability. This could be done for a small cost (several thousand dollars).

REFERENCES

- [1] Harper, W., "Transmission Path Obscuration for Radar Transponder Antennas on Shuttle SRB", report ARI/R-89-575, Applied Research, Inc., March 24, 1989.
- [2] R.J. Marhefka and L. Takacs, "Manual for Obscuration Code with Space Station Applications", NASA Contractor Report 178099 on Grant NSG-1498, The Ohio State University, May 1986.
- [3] Harper, W., "Antenna Pattern Study Final Report", report ARI/R-88-510Z, Applied Research, Inc., July 15, 1988.
- [4] Harper, W., "Electromagnetic Scattering by Shuttle External Tank Surface", report ARI/R-89-573, Applied Research, Inc., February 27, 1989.
- [5] E.H. Newman, "A User's Manual for the Electromagnetic Surface Patch Code: ESP Version IV", The Ohio State University, August 1988.
- [6] C.A. Balanis, "Advanced Engineering Electromagnetics", Wiley, 1989.
- [7] R.J. Marhefka and W.D. Burnside, "Numerical Electromagnetic Code - Basic Scattering Code", Technical Report 712242-14, The Ohio State University, December 1982.
- [8] NASA Interface Control Document ICD-2-00001, "Shuttle Vehicle Mold Lines and Protuberances"
- [9] C.H. Tsao and R. Mittra, "Spectral-Domain Analysis of Frequency Selective Surfaces Comprised of Periodic Arrays of Cross Dipoles and Jerusalem Crosses", IEEE Transactions on Antennas and Propagation, vol. AP-32, no. 5, pp.478-486, May 1984.

APPENDIX
DATA INPUT TO BSC FOR FINAL MODEL

CM: OUSIM29
CM: ALL CYLINDERS, WITH MULTIPLE INTERACTIONS
CE: LONG CYLINDERS, ROLL PLANE
UN:
1
US:
1
FR:
5.765
CG:
6.36433, 0, 0
0, 0, 90, 0
1.8293, 1.8293
-500, 90, 500, 90
CG:
-6.36433, 0, 0
0, 0, 90, 0
1.8293, 1.8293
-500, 90, 500, 90
CG:
0, 0, 0
0, 0, 90, 0
4.2304, 4.2304
-500, 90, 500, 90
0, 6.184, 0
0, 0, 90, 0
1.1725, 1.1725
-500, 90, 500, 90
SM:
12.5
24
5.3007536, -1.507604, 0, .00130095, 0, 235
5.31141, -1.515068, 0, .00130095, 0, 55
5.306082, -1.511335, 0, .0130095, 0, 145
5.306082, -1.511335, .00650475, .00130095, 0, 235
5.306082, -1.511335, -.00650475, .00130095, 0, 55
5.306082, -1.511335, 0, .0130095, 90, 0
7.417254, 1.515068, 0, .00130095, 0, 235
7.4279064, 1.507604, 0, .00130095, 0, 55
7.422578, 1.511335, 0, .0130095, 0, 325
7.422578, 1.511335, .00650475, .00130095, 0, 235
7.422578, 1.511335, -.00650475, .00130095, 0, 55
7.422578, 1.511335, 0, .0130095, 90, 0
-5.311406, -1.515068, 0, .00130095, 0, 305
-5.3007536, -1.507604, 0, .00130095, 0, 125

-5.306082, -1.511335, 0, .0130095, 0, 215
-5.306082, -1.511335, .00650475, .00130095, 0, 305
-5.306082, -1.511335, -.00650475, .00130095, 0, 125
-5.306082, -1.511335, 0, .0130095, 90, 0
-7.4279064, 1.507604, 0, .00130095, 0, 305
-7.417254, 1.515068, 0, .00130095, 0, 125
-7.422578, 1.511335, 0, .0130095, 0, 35
-7.422578, 1.511335, .00650475, .00130095, 0, 305
-7.422578, 1.511335, -.00650475, .00130095, 0, 125
-7.422578, 1.511335, 0, .0130095, 90, 0

5, 0

5, 0

1, 0

0, 5

0, 5

0, -1

5, 0

5, 0

1, 0

0, 5

0, 5

0, 1

5, 0

5, 0

1, 0

0, 5

0, 5

0, -1

5, 0

5, 0

1, 0

0, 5

0, 5

0, 1

PD:

0, 0, 90, 0

T, 90

0, 360, 1

TO:

F, F, F, F

T, T, F

T

T, T, T, T, T, T

T, T, T, T, T

F, F, F, F

XQ:

EN:

1989

NASA/ASEE SUMMER FACULTY FELLOWSHIP PROGRAM

MARSHALL SPACE FLIGHT CENTER
THE UNIVERSITY OF ALABAMA IN HUNTSVILLE

ROCOPT - A USER FRIENDLY INTERACTIVE CODE
TO OPTIMIZE ROCKET STRUCTURAL COMPONENTS

PREPARED BY:	WILLIAM K. RULE
ACADEMIC RANK:	ASSISTANT PROFESSOR
UNIVERSITY AND DEPARTMENT:	THE UNIVERSITY OF ALABAMA IN TUSCALOOSA DEPT. OF ENGINEERING MECH.
NASA/MSFC:	
LABORATORY:	STRUCTURES AND DYNAMICS
DIVISION:	STRUCTURES
BRANCH:	STRUCTURAL DEVELOPMENT
MSFC COLLEAGUE:	PEDRO I. RODRIGUEZ
DATE:	AUGUST 11, 1989
CONTRACT No.:	THE UNIVERSITY OF ALABAMA IN HUNTSVILLE NGT-01-008-021

ABSTRACT

ROCOPT is a user-friendly, graphically-interfaced, microcomputer-based computer program (IBM compatible) that optimizes rocket components by minimizing the structural weight. The rocket components considered are ring stiffened truncated cones and cylinders. The applied loading is static, and can consist of any combination of internal or external pressure, axial force, bending moment and torque. Stress margins are calculated by means of simple closed form strength of material type equations. Stability margins are determined by approximate, orthotropic-shell, closed-form equations. A modified form of Powell's method, in conjunction with a modified form of the external penalty method, is used to determine the minimum weight of the structure subject to stress and stability margin constraints, as well as user input constraints on the structural dimensions. The graphical interface guides the user through the required data prompts, explains program options and graphically displays results for easy interpretation.

ACKNOWLEDGEMENTS

The author would like to thank Pete Rodriguez for initially suggesting this project and helping to carry it out. The author would also like to thank Clyde Nevins for his support during the course of this effort, and Stan Jones for the encouragement to apply for this fellowship. Thanks are also due to Jerry Karr, Frank Six, and Mike Freeman for running a very enjoyable and productive summer faculty program. Finally, the author would like to thank his wife Audrey and daughter Amethyst for enduring the separation from our home and friends in Tuscaloosa this summer.

TABLE OF CONTENTS	PAGE
Abstract	XXV-1
Acknowledgements	XXV-ii
Introduction	XXV-1
Objectives	XXV-4
Conclusions and Recommendations	XXV-5
1. Description of ROCOPT Programs	
1.1 Getting ROCOPT Running	XXV-7
1.2 ROCOPT Batch Program	XXV-7
1.3 HEADER Program	XXV-8
1.4 MATINPUT (Material Type Input) Program	XXV-8
1.5 STRINPUT (Structure Type Input) Program	XXV-8
1.6 LODINPUT (Load Input) Program	XXV-9
1.7 CONE and CYLINDER Optimization Programs	XXV-9
1.8 OUTPUT Program	XXV-10
1.9 HELP and MANUAL Programs	XXV-10
2. Stress Margin Calculation	
2.1 Cylinder Stress Margin	XXV-12
2.2 Cone Stress Margin	XXV-14
3. Stability Margin Calculation	
3.1 Cylinder Stability Margin	XXV-15
3.2 Cone Stability Margin	XXV-16
4. Optimization Technique	XXV-17
References	XXV-23
Appendix - Program Listings	XXV-24

INTRODUCTION

The goal of this project was to develop a user-friendly, graphically-interfaced, microcomputer-based computer program (IBM compatible) to optimize rocket structural components by minimizing the total structural weight. The resulting program is called ROCOPT. It consists of a number of separate executable programs written in Microsoft QuickBASIC that are linked together by means of a DOS batch file. The program is designed to allow the user to rapidly determine a reasonable preliminary design for ring stiffened conical and cylindrical rocket structural components subjected to any static combination of internal or external pressure, axial force, bending moment, and torque. User input constraints on structural dimensions are also applied. Stress margins are calculated by means of simple closed form strength of materials type equations. Stability margins are determined by approximate, orthotropic-shell, closed-form equations. Thus, the preliminary design will require checking by means of a detailed finite element model.

QuickBASIC was chosen because of its excellent programming environment and built-in graphics capabilities. QuickBASIC can run in an interpretive mode which greatly facilitates debugging, and it can also run in an compile mode to generate executables that do not have to be run from within the BASIC environment. Many members of the Structural Design Branch are already familiar with BASIC. Thus, in-house maintenance and enhancement of ROCOPT should be feasible.

ROCOPT consists of a number of stand-alone executable programs (each of which has a separate function) rather than a single large program. This was done for three main reasons:

1. Each program has a separate function. This made the programming task easier by breaking a large program into a number of smaller ones that could be developed and debugged separately. This technique should also simplify program maintenance and enhancement.
2. Any of the ROCOPT programs can be replaced by another program written in a different programming language. Thus, personnel in charge of enhancement are not necessarily required to know BASIC.
3. ROCOPT can be made arbitrarily large since only one of

the ROCOPT programs is loaded into the memory at any time. A single program doing all the functions of ROCOPT would have to all be loaded in the computer memory at the same time. This could cause memory shortage problems if ROCOPT should grow.

The programs of ROCOPT are conveniently linked together by a DOS batch file. The batch file controls the sequence of program execution, allows for rerunning all the programs without restarting, and permits a graceful halting of the program sequence should an error occur. The batch file also allows for the user to quit the program at any time.

A modified form of Powell's method (a zero order method) is used for the optimization algorithm. Instead of using the identity matrix as the initial matrix of search vectors as Powell suggested, a matrix of random vectors (each normalized such that the maximum magnitude of any vector component is unity) is used instead. This modification appears to improve performance, on the average, for any given run. It has the added advantage that if multiple runs are made then entirely new search paths are followed. This is useful for verifying that the minimum structural weight obtained is indeed the global minimum. This is so if several runs end up selecting the same point in the design space as the optimum.

A modified form of the exterior penalty method is used to constrain the solution to having nonpositive stress and stability margins of safety. The method is modified as follows. The traditional penalty factor is replaced by a penalty factor multiplied by the weight of the structure. The constraint functions (stress and stability margins) are always of order unity and thus some scheme is required to scale the constraints up to the magnitude of the structural weight. This scheme avoids the problem of how to reliably select a suitable scaling factor for the penalty part of the pseudo-objective function. Also, the constraint functions are typically squared. This is not done here.

A standard strength of materials approach is used to calculate the stress margin. Here the stress margin is defined as the maximum von Mises (also called "effective") stress divided by the allowable stress, minus unity. Thus, a component with a stress margin greater than zero is over stressed. Stress margins are calculated for both the shell and the ribs. Similarly, a stability margin is calculated based on allowable stresses (both circumferential and longitudinal) calculated from approximate orthotropic thin shell buckling equations. A relatively thin shell with

relatively small closely spaced ribs is the assumed structural type for all margin calculations. The exact definition of what is meant by small and the effects of deviations from these requirements are difficult to assess without going to a detailed finite element model of the proposed structure.

A "strip-chart" of change in structural weight versus iteration number is shown on the screen as the optimization proceeds to allow the user to monitor the process. The optimization process can be stopped at any time by simply pressing the F1 function key. A cross section of the optimized structure is drawn approximately to scale on the screen for the user to visually assess the suitability of the optimum structure. Also, all the user inputs and the calculated results are echoed to a file for later inspection.

OBJECTIVE

The objective of this project was to develop a user-friendly, graphically-interfaced, microcomputer program (IBM compatible) to determine the minimum feasible structural weight of statically loaded, ring-stiffened, conical and cylindrical rocket components using approximate closed form stress and stability equations.

CONCLUSIONS AND RECOMMENDATIONS

The following conclusions were reached during the course of this project:

1. Microsoft QuickBASIC is an ideal language for PC-based interactive engineering analysis codes.
2. Using a DOS batch file is a convenient way to link together a series of executable programs. Large programs can be developed because only one of possibly many executable programs is loaded into the memory at a time. The executable programs can be written in any computer language capable of producing an executable code. This allows code developers to use any computer language they wish for their part of the total package.
3. There is a large amount of uncertainty with respect to predicting buckling of ring stiffened cones and cylinders subjected multiple loads using closed form analytical equations.
4. The optimization scheme developed during the course of this project appears to be relatively easy to program, robust, and efficient.
5. ROCOPT appears to be capable of successfully optimizing ring stiffened cone and cylinder structures within a reasonable amount of run time. A typical ROCOPT run takes less than five minutes. However, multiple runs should be made to ensure that the global optimum (lowest feasible weight) has been located.

The recommendations are as follows:

1. Further development work on the stability equations should be performed.
2. Additional rib cross section type options should be added to ROCOPT. Currently, rectangular and I-beam cross sections are treated.
3. The capability to handle stringers should be added to ROCOPT.
4. The capability of treating composite materials should be incorporated into ROCOPT.

5. An option to automatically create an MSC/PAL input deck of the optimized structure should be provided. This would facilitate the checking of the optimized structure by means of a detailed finite element model.

6. Detailed finite element models of ROCOPT optimized structures should be built and analyzed to confirm that stress and stability constraints are not violated.

1. DESCRIPTION OF ROCOPT PROGRAMS

1.1 Getting ROCOPT Running

The following procedure should be followed to run ROCOPT. First, create a subdirectory on your hard disk. Then, copy all the files contained on the ROCOPT floppy disk(s), which are in the envelope at the back of the manual, into your subdirectory. Get into the subdirectory and start the program by typing ROCOPT. The program will automatically prompt you for inputs by making selections from menus. Menu selections are made by using the up and down arrows until the desired choice is highlighted and then pressing RETURN. A brief description of each highlighted menu choice is given across the bottom of the screen. The purpose of the current program module of ROCOPT is displayed across the top of the screen. Your computer should have a math coprocessor and EGA or VGA color graphics capability.

1.2 ROCOPT Batch Program

ROCOPT consists of a DOS batch program (ROCOPT.BAT) that runs a series of other programs written in Microsoft QuickBASIC. These programs and their associated data files are illustrated in Figure 1. An overview of these programs will now be given. Listings of all ROCOPT programs are given in the Appendix.

The batch program ROCOPT.BAT sequentially runs the other programs of ROCOPT. The batch program checks for the existence of a program before attempting to run it. If the program is not present on the directory, an error message is printed and execution is stopped. The inputs and outputs of the previous run are stored (by program OUTPUT) in a file called OLDINPUT.DAT. The batch program checks if this file exists. If not, it creates one by copying the file NOOLDINP.DAT which contains the statement "NO PREVIOUS RUN DATA AVAILABLE!".

The user always has the option to quit running ROCOPT while running any of the ROCOPT programs. If the user elects to do so, a file called QUIT.DAT is created. The batch program checks for the presence of this file after every program is run. If detected, the batch program will stop itself. If an error is detected while running a program then a file named ERROR.DAT is created on the directory. If this file is detected, then the batch program will output an error

message and then the batch program will stop itself.

If the user elects to optimize a cone or a cylinder then the empty files CONE.DAT and CYLINDER.DAT are created (by program STRINPUT), respectively. The batch program will execute the appropriate program (CONE or CYLINDER) depending on which of these files is present.

If the user decides to rerun the analysis without exiting the batch program then the empty file RERUN.DAT is created (by program OUTPUT). When the batch file detects the presence of RERUN.DAT, it loops back to the start of itself to begin again (without rerunning program HEADER).

1.3 HEADER Program

The first program run by the batch program is called HEADER. This program simply displays the name and version of the program as well as a brief description of the purpose of the program. No calculations are performed, and no data is input here.

1.4 MATINPUT (Material Type Input) Program

The next program executed is MATINPUT. This program inputs the following characteristics of both the shell and rib materials: material name (15 characters maximum), the elastic modulus, the shear modulus, the allowable stress, and the density. Any consistent set of units can be used. The user has the option of using values from a previous run, selecting values from a database file (MATERIAL.DAT), or entering data directly through the keyboard. The user has the option of writing the directly entered data into MATERIAL.DAT. MATERIAL.DAT is a simple ASCII file that can be modified by most word processing programs. MATINPUT also prompts the user for a title for the current run and samples the computer's clock for date and time. All input data is written to file INPUT.DAT for later use.

1.5 STRINPUT (Structure Type Input) Program

STRINPUT is the next program executed. This program prompts the user for the type of shell (cone or cylinder) and the type of rib (rectangular cross section or I-beam). Minimum and maximum dimensions are also prompted for. Zero minimum dimensions are not allowed. If the input maximum dimension is less than the minimum dimension then the program assumes that there is no restriction on the maximum magnitude of that dimension. The user has the option of selecting previous shell types, rib types, and dimensions, which are

contained in file OLDINPUT.DAT. A graphical interface is provided to help the user with the input. All input data is written to file INPUT.DAT for later use.

1.6 LODINPUT (Load Input) Program

LODINPUT is run next to input information on the static loads. The loads include: uniform pressure, axial force, bending moment, and a torque. The uniform pressure is assumed to be applied in such a manner as to produce both circumferential and longitudinal stress. The user has the option of using the loads of the previous run, which are contained in file OLDINPUT.DAT. All input data is written to file INPUT.DAT for later use.

1.7 CONE and CYLINDER Optimization Programs

Next ROCOPT will run program CONE if a cone is to be optimized, otherwise program CYLINDER is run. Both programs are very similar in nature. They read the user supplied data in file INPUT.DAT and then prompt the user for parameters relating to the optimization process. Then CONE or CYLINDER perform stress margin, stability margin, and optimization calculations. Detailed descriptions of how these calculations are performed are given in sections 2, 3, and 4 of this report, respectively. The goal of these programs is the find the structural configuration with the lowest possible weight that is stable (no buckling) and not over stressed. User input constraints on minimum and maximum structural dimensions must also be satisfied. The change in the total structural weight as a function of iteration number is graphically shown on the screen, in a continuously updated bar chart format, to show the user how the optimization is proceeding. Also, the total structural weight, the stress margin, and the stability margin are shown on the screen above the bar chart periodically to further indicate the health of the optimization process.

The user can safely halt the iteration process at any time by simply pressing the F1 function key. This may be desirable if the bar chart of change in weight versus iteration number shows that there has been no change in the structural weight after many iterations. A typical optimization run takes less than 5 minutes to execute on a 80286 class of machine. Details of the final optimized structure are written to file INPUT.DAT for later output.

As discussed in section 4, CONE and CYLINDER use random numbers in their optimization algorithm. The random number generator is programmed to use the number of seconds from

midnight on the computer's clock (suitably scaled) as a seed. Each time CONE or CYLINDER is run, entirely different numbers will be used in the optimization algorithm. Thus, it is desirable to make several runs of ROCOPT with the same structural configuration to ensure that the lightest feasible structure has been found. It is not uncommon for any optimization process to get trapped in a local minimum. Making several runs from different points in the design space is a way to defeat this problem.

1.8 OUTPUT Program

The last program the batch program runs is called OUTPUT. This program performs the following functions:

1. Reads the user input data and calculated results contained in data file INPUT.DAT and writes them in ASCII format to a new file that program OUTPUT creates that is named by the user. The file can be in a different directory from that of the ROCOPT PROGRAM by specifying a path before the file name. For instance, specifying the file name A:\RESULTS\SHUTTLEC.OUT will cause the results to be written to file SHUTTLEC.OUT located in directory A:\RESULTS. If the file already exists, then it will be overwritten. OUTPUT also offers the user the option of printing the file out. The file is formatted reasonably nicely and could perhaps be included directly in some reports. Alternatively, most word processors could read the file into a report document, where the layout of the file could be refined as required.

2. Displays the optimum structural dimensions, margins, and weight on the screen. Also, OUTPUT displays a cross section of the optimized structure on the screen approximately to scale. The purpose of these options is to allow the user to quickly assess if the optimum structure appears to be reasonable when compared with past experience.

3. OUTPUT also allows the user to restart the analysis. The built in capability of all the ROCOPT programs to use the user inputs of the previous run, allows for rapid reruns when there are no modifications or slight modifications to the input data.

1.9 HELP and MANUAL Programs

Finally, there are two additional auxiliary programs in the ROCOPT family of programs that work outside of ROCOPT and are purely for helping the user run ROCOPT more successfully. One is called HELP. This program simply allows the user to select topics of interest from a menu and then

to access the ASCII text file containing that information. HELP allows the user to page through the text file by means of the PAGE UP and PAGE DOWN keys as well as go to the start and end of the text file by pressing the HOME and END keys. The text files are currently empty - the user must use a text editor to add information to these files as pertinent information becomes available. Thus, HELP simply provides an organized way of storing data related to ROCOPT. For instance, the HELP menu selection SHELL could be tied to a text file containing information such as the shell thicknesses and shell materials used previously for the Saturn V, Titan, Shuttle SRM, and so forth. The topics displayed by the HELP menu and their associated text file names are stored in a file called HELP.MNU. This ASCII file can be easily modified by the ROCOPT user to add more topics or remove some of the topics currently in place. The format of this file consists of groups of three records relating to each topic. A typical entry would be as follows:

```

      .
      .
      .
SHELL
This file contains previously used shell thicknesses.
c:\HELPPFILES\SHELL.HLP
      .
      .
      .

```

For this case, SHELL (15 characters max.) will be the menu prompt, the second record (78 characters max.) will appear at the bottom of the screen when SHELL is the highlighted menu selection, and the associated text file (could be any legal DOS name) is named SHELL.HLP and is located in subdirectory (could be any legal subdirectory) c:\HELPPFILES.

This help utility can be accessed by simply typing HELP.

The second auxiliary program is called MANUAL. This program allows the user to page through an unformatted ASCII version of this document called (ROCOPT.DOC) interactively on the computer screen. This will conveniently avoid the problem of locating a hard copy of the manual if a question about ROCOPT should arise. Also, the user is free to customize ROCOPT.DOC with additional information. Any word processor or editor capable of working with ASCII files could be used for this purpose. This auxiliary program may be accessed by typing MANUAL.

2. STRESS MARGIN CALCULATION

2.1 Cylinder Stress Margin

The stress margin is defined here as the largest von Mises stress (also called effective stress) divided by the allowable stress for the material, minus one. Thus, a positive stress margin implies that the component is overstressed. The von Mises failure theory is only applicable to isotropic metallic materials that are behaving in a ductile manner [1]. Typically the allowable stress is determined by dividing the yield stress by an appropriate factor of safety. Program CYLINDER calculates the stress margin for the shell material and the rib material and then uses the largest of these two in the optimization calculations.

The circumferential (hoop) stress in the shell wall, $\sigma_{y,shell}$, was determined as follows. The traditional (no ribs) stress formula is [1]:

$$\sigma_{y,shell} = \frac{PD}{2t} \quad (1)$$

where P is the pressure (positive if internal), D is the mean diameter, and t is the shell thickness. Tensile stresses are positive. Here, this equation must be modified to account for the ribs. It is assumed that the ribs will sustain the same strain level as that of the shell throughout their entire depth (no flexure). For this assumption to be accurate the diameter of the cylinder must be much larger than the depth of rib and the ribs must be fairly closely spaced (so shear lag will not occur). Also, since the ribs could be fabricated from a different material, the rib cross sectional area, A_R , must be multiplied by the modular ratio, M, to convert the rib area to an effective area of rib (as if it was made from the shell material). The modular ratio is E_R/E_S , where E_R and E_S are the elastic moduli of the rib and the shell, respectively. Let the number of ribs per unit length of shell be N. Modifying (1) to account for the ribs gives:

$$\sigma_{y,shell} = \frac{PD}{2t + 2A_R MN} \quad (2)$$

It is assumed that P is the only applied load causing stress in the ribs. The rib stress in the circumferential direction

may be calculated by multiplying the strain in the shell, which is assumed to be equal to the strain in the rib, by the elastic modulus of the rib:

$$\sigma_{y,rib} = E_R (\epsilon_{y,shell} / E_S) \quad (3)$$

Stress in the shell in the longitudinal direction is generated by the applied pressure P, the axial force F, and the bending moment B. Here the sign convention is such that a positive P will generate tensile stress, as will a positive F. B will generate both tensile and compressive stress, regardless of sign, and thus both cases must be considered in the calculations. P, F, and B are assumed to generate no stress in the ribs in the longitudinal direction. The stress due to P is simply the pressure times the total longitudinal cross sectional area of the cylinder divided by the longitudinal cross sectional area of cylinder wall material. The axial force creates a stress equal to F divided by the longitudinal cross sectional area of shell material. The bending stress can be calculated from the flexure formula. Thus the shell stress in the longitudinal direction, $\sigma_{x,shell}$, is given by:

$$\sigma_{x,shell} = \frac{PD}{4t} + \frac{F}{\pi D t} + \frac{4B}{\pi D^2 t} \quad (4)$$

The longitudinal rib stress is assumed to be equal to zero.

The applied torque T, is assumed to generate a shear stress in the shell material (uniform through the thickness), $\tau_{xy,shell}$, but to have no effect on the ribs. The classical strength of materials formula was used to calculate the shear stress:

$$\tau_{xy,shell} = \frac{2T}{\pi D^2 t} \quad (5)$$

The sign of the shear stress does not matter as it is squared in the von Mises stress formula.

After, the stress components have been calculated, the von Mises (effective) stress, $\sigma_{E,shell}$, is calculated for the shell material [1]:

$$\sigma_{E,shell} = (\sigma_{x,shell}^2 + \sigma_{y,shell}^2 - \sigma_{x,shell}\sigma_{y,shell} + 3\tau_{xy,shell}^2)^{1/2} \quad (6)$$

In general, $\sigma_{E,shell}$ will have to be calculated twice since B generates both tensile and compressive stress. The largest of these two is used to calculate the stress margin for the shell material. The von Mises stress for the rib is simply the absolute value of $\sigma_{y,rib}$.

2.2 Cone Stress Margin

Precisely the same assumptions that are applied to the calculating the stress margins in the cylinder are applied to calculating the stress margins in the cone. Stress equations applicable to the cone can be obtained from the cylinder equations by replacing t with $t/\cos(\text{cone angle})$. Here, the cone angle is the angle the side of the cone makes with the longitudinal axis (a cylinder has a cone angle of zero). Also, all stresses must be checked at both ends of the cone as there are now two diameters to consider.

3. STABILITY MARGIN CALCULATION

3.1 Cylinder Stability Margin

The stability margin is defined as the applied compressive load divided by the calculated critical buckling load minus one. Thus, a stability margin greater than zero implies that buckling could occur.

The stress levels that could cause instability (buckling) of the cylinder are calculated from an approximate orthotropic cylinder theory exactly as presented in Ref.[2] except that a factor of safety of 2 against buckling was incorporated. This safety factor is to allow for the approximations inherent in the theory and also to account for small imperfections in the structural geometry. The theory assumes that the ribs are sufficiently closely spaced so that the shell can be modeled as an orthotropic continuum. The equations employed by ROCOPT can be obtained from [2].

There are many approximations associated with these calculations. Thus, the resulting final optimum structure should be checked with a detailed finite element model.

The stability calculations involve the positive integer parameters m and n , which are the number of longitudinal, and circumferential buckles (pop outs or pop ins), respectively, in the buckled shell wall. From physical considerations (no kinks in the shell wall) n must consist of even integers. Also, [2] recommends that $n=2$ not be used. The standard procedure is to vary these parameters until a minimum theoretical buckling load is determined.

The computer program does this in an iterative manner. During each optimization iteration, the program tries nine combinations of three adjacent, feasible m -values and n -values, and stores the m, n combination that produces the the lowest calculated buckling load. During the next optimization iteration, the procedure is repeated with previously stored m and n values at the middle of the sets of m and n trial values. For instance, if the previously stored m and n values were 5 and 8, respectively, then during the next optimization iteration the following values would be tried: $m=[4,5,6]$ and $n=[6,8,10]$. Three trial values were selected to give m and n the freedom to either increase or decrease with each iteration with a minimum number of m, n trial combinations.

The smallest dimension of a buckle is prevented from being smaller than twenty times the shell thickness. The computer program sets limits on the maximum values of m and n to apply this limit. The author developed this constraint to ensure that the calculated buckled configuration is physically reasonable. Experimental results of testing full scale shell structures do not indicate the formation of very fine buckles.

3.2 Cone Stability Margin

As suggested by [3], cone buckling loads are evaluated by first "converting" the cone into an "equivalent" cylinder and then using cylinder stability equations. The equivalent cylinder has a diameter equal to the mean diameter of the cone and a length equal to the side wall length (axial dimension/cos[cone angle]) of the cone. This approximation reflects the desire for simple design equations and the lack of a wide spectrum of experimental data to verify more sophisticated cone stability equations. However, this approach should be sufficient for preliminary design calculations, which is the intended purpose of ROCOPT.

4. OPTIMIZATION TECHNIQUE

Many optimization techniques have been reported in the literature. These iterative schemes vary from the simple to the very complex. The simple schemes are typically easy to program, are very simple and reliable in the sense that they nearly always work, and require little or no specialized help from the user. Unfortunately, simple schemes are usually the most computationally expensive. Complex optimization techniques are difficult to program, do not always work, and in many cases require careful monitoring by an experienced optimization expert. However, complex optimization schemes can be orders of magnitude less computationally expensive than the simple schemes, as well as produce more accurate results.

It is anticipated that the average ROCOPT user will not be acquainted with optimization theory. Also, most ROCOPT users will probably be willing to wait a few minutes longer for assured results, rather than run the risk of obtaining incorrect results or no results at all very quickly. These considerations led to the choice of a relatively simple optimization technique.

ROCOPT uses Powell's method combined with the exterior penalty method [4]. The author modified both these methods for this application to increase reliability and efficiency. The optimization technique used will now be discussed.

The purpose of ROCOPT is to find the structure with the lowest weight that does not violate any of the constraints. The weight of the structure is called the objective function. The purpose of any optimization technique is to minimize the objective function subject to the constraints.

There are two different types of constraints that must be treated by ROCOPT. The design variables (shell thickness, rib depth and so forth) must be made to stay within their user defined minimum and maximum ranges. This type of constraint is called a side constraint. Also, the stress and stability margins of the final design must be less than or equal to zero. These are termed inequality constraints.

Side constraints are most efficiently handled directly. If any design variable is found to be outside of its allowable range, the design variable is simply increased or decreased as appropriate, until it is back within its allowable

range. This is done before additional optimization calculations are performed. Thus, throughout the optimization iterations, the design variables are explicitly forced to remain within their allowable ranges. This approach is feasible because each side constraint is a function of a single design variable.

Inequality constraints are usually functions of many design variables and thus there is no direct way to treat a constraint violation. One approach is to add violated (greater than zero) inequality constraints to the objective function in some fashion. The objective function so modified is typically called the pseudo-objective function (POF). This converts the problem from one of minimizing an objective function subject to inequality constraints, to one of minimizing an unconstrained pseudo-objective function. The form of the pseudo-objective function developed by the author is:

$$POF = (\text{weight})[1 + r_p \left(\frac{\text{stress}}{\text{margin}} + \frac{\text{stability}}{\text{margin}} \right)] \quad (7)$$

Note, the margins are only allowed to enter the above equation if they are greater than zero (constraint violated). r_p is a positive parameter called the penalty parameter. Notice that a large value for the penalty parameter will provide a big incentive to the optimizer to adjust the design variables to alleviate the constraint violations, at the expense of increasing the structural weight. However, since the margins are actually multiplied by the weight times the penalty factor, the constraint violations tend to be removed in a manner that increases the weight the least.

The magnitude of the penalty parameter is a user controlled input. A value of 10 is suggested. A relatively small penalty factor is used in the initial phase of the optimization process so that the optimizer will effectively be working on reducing both the structural weight and the constraint violations. If the penalty parameter is too large initially, then too much emphasis will be placed on eliminating the constraints at the expense of greatly increasing the structural weight. This will result in an inefficient optimization process because many iterations will be required to find the lowest possible structural weight, after the constraint violations (and thus the penalty factor effect) have been removed. The recommended procedure is to start with a relatively small penalty factor

and then increase it as the optimization process continues [4]. ROCOPT increases the user input penalty factor by a factor of 100 by the end of the iterations. A high penalty factor is used at the end to ensure that the final design will be feasible (no constraints violated). The user is free to try various initial values for the penalty parameter to try improving the optimization efficiency.

Having set up the POF, the problem now becomes one of finding the unconstrained minimum of this function.

The design variables associated with this optimization problem vary greatly in magnitude. For instance, the shell thickness could be 0.1 inches and the shell length could be 1000 inches, a difference of four orders of magnitude. Because of this, using these design variables directly is inconvenient and can lead to numerical problems. Thus, it is advisable to work with nondimensionalized design variables that have been scaled to a magnitude of unity. This is similar to the rationale for using isoparametric elements in finite element analysis.

To achieve this nondimensionality, ROCOPT works with percentage changes in design variables. This conveniently provides a uniform treatment for all the design variables, regardless of magnitude. It also provides a simple way of controlling the amount of change in the design variables from one optimization iteration to the next. If the maximum allowable percentage change is too large, the optimizer could thrash back and forth around the optimum design point without ever converging to it. Alternatively, if the maximum allowable percentage change is too small then it could take an infeasible number of iterations to get to the minimum, or the optimizer could get "stuck" in a local minimum of the pseudo-objective function before getting to the global minimum.

ROCOPT calls the maximum allowable change in the nondimensionalized design variable magnitudes the "search magnitude parameter". This is a user controlled input parameter. A value of 0.4 (equivalent to a 40% change) is recommended. ROCOPT is designed to reduce the magnitude of the search magnitude parameter as the optimization process proceeds. The final value will be 1/100 of the initial value. The idea here is to allow large changes in the design variables initially, to quickly get into the vicinity of the global minimum in the design space, and then use finer steps to precisely locate the global minimum. The user is free to change this parameter to try to improve optimization efficiency.

The initial values for the design variables are randomly selected between their minimum and maximum values. If no maximum value is provided for a design variable, then a random value between the minimum value and four times that value is used. The number of seconds from midnight on the computer's clock is used as the seed for the random number. Thus, a series of ROCOPT runs will all start from different points in the design space. A global minimum is indicated if essentially same the optimum solution is obtained from a series of ROCOPT runs.

Finally, there is the problem of determining the search vectors. A search vector is a vector of changes to be made in the design variables to seek minimization. A common approach is to use the negative of the gradient vector. However, this method is somewhat computationally expensive and may not be reliable in cases where there are many constraints (discontinuous gradients) or where the gradient function changes rapidly throughout the design space. The literature contains many variations of the gradient search method as well as a vast array of simpler and more complex methods.

The method chosen here for search vector selection is based on Powell's method [4]. This is a first order method that does not require the calculation of the gradient vector. The author modified this method in an attempt to increase efficiency. Initially, a number of search vectors equal to the number of design variables are created. The components of these vectors are random numbers between -1 and +1. The components of each random search vector are then scaled, such that the largest component has a magnitude of unity. These vectors are stored as columns of a "search matrix". Next, the POF is evaluated at the current point in the design space and at design points given by \pm the search magnitude parameter times the first column of the search matrix. If either of the $+$ or $-$ design points has a POF less than the POF of the current design point, then the design point corresponding to the lowest POF will become the new design point. Otherwise, the design point does not change. The search vector multiplier (\pm search magnitude parameter or zero) used with the search vector is stored for later use. This procedure is then repeated with the remaining columns of the search matrix.

A new search vector is created after using all of the search vectors in the search matrix. This new vector is created by vectorially adding together all of the search vectors times their search vector multipliers. The new search vector is a

vector sum of previous successful search vectors since unsuccessful search vectors have search vector multipliers of zero. Thus, the new search vector represents (stores) the trend of the optimization process. The new search vector is scaled such that the magnitude of it's largest component is unity and then is used to replace the first column of the search matrix. The procedure is repeated, a new search vector is determined, and then used to replace the second column of the search matrix, and so forth until only the last column of the original search matrix remains untouched. Then an entirely new search matrix is created using the random number generator, and the process continues.

If at any time in the iterative process, a new search vector has a magnitude of zero (implying all current search directions are not beneficial), then a new random search matrix is created immediately. The random number generator uses a seed based on the number of seconds from midnight on the computer's clock. Each successive run of ROCOPT will use a different set of search vectors. Thus, it is advisable to make several successive runs of ROCOPT with identical inputs to ensure that the lowest possible structural weight has been found.

The number of search matrices generated is governed by a user input parameter called the "iteration parameter". The number of random search matrices generated is equal to the number of design variables times the iteration parameter. The suggested value for the iteration parameter is 20. However, the user has the option of shutting off the optimization process at any time by pressing the F1 function key. Changes in the structural weight and the margins are displayed on the screen (as the iterations progress) to help the user decide on an appropriate time to shut off the iterations.

Each time a new random search matrix is created, the penalty parameter is multiplied by a factor such that, by the time the optimization process is completed, the penalty factor will be 100 times its initial value. The same is true for the search magnitude parameter except that it's magnitude is reduced by a factor of 100. In both cases, this assumes that the user did not stop the iterations by pressing the F1 key.

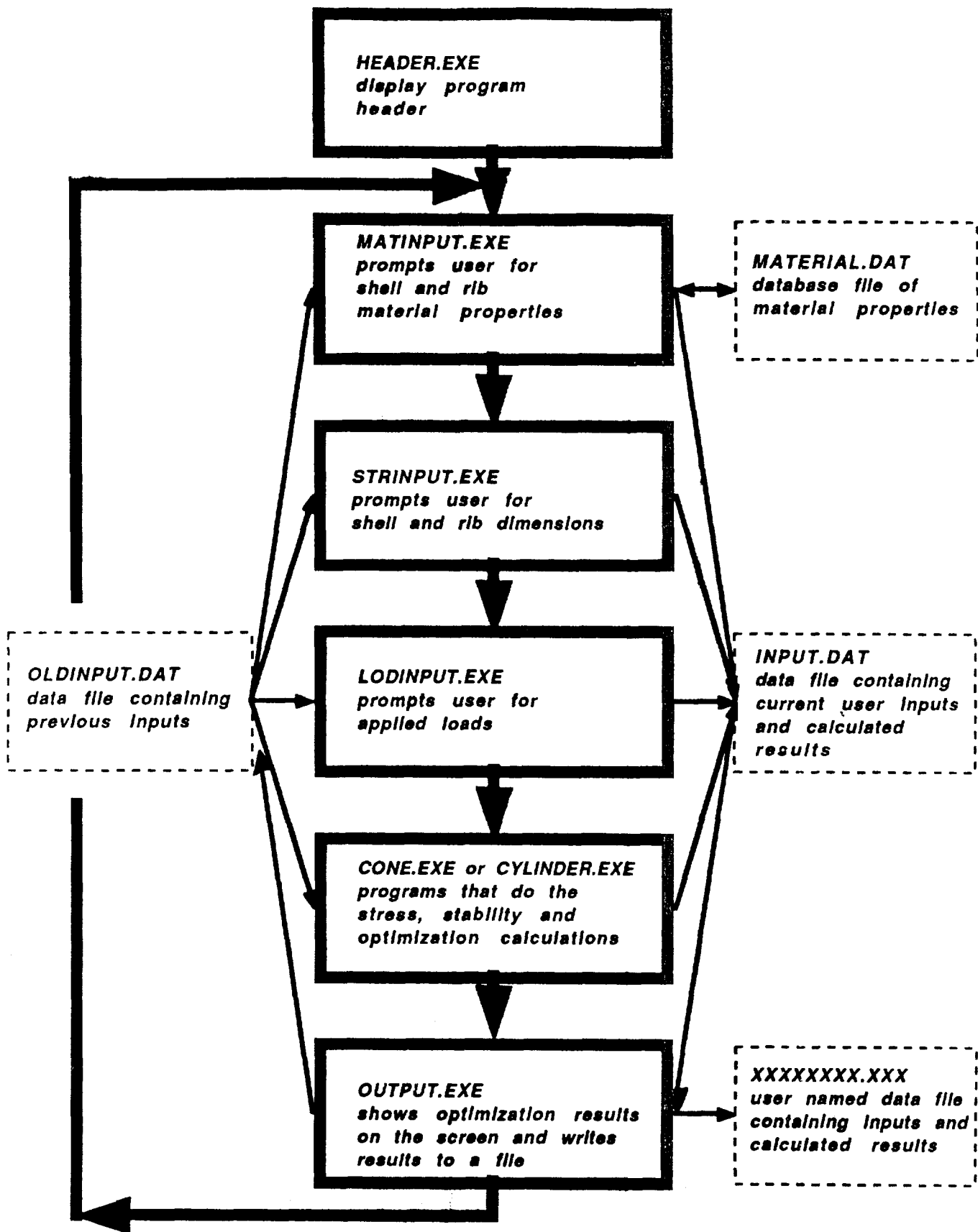


Figure 1 ROCOPT Data Flow Diagram

REFERENCES

1. Cook, R.D., and Young, W.C., "Advanced Strength of Materials," Macmillan Publishing Company, New York, 1985.
2. Weingarten, V.I., Seide, P. and Peterson, J.P., "Buckling of Thin-Walled Circular Cylinders," NASA SP-8007, 1968.
3. Weingarten, V.I. and Seide, P., "Buckling of Thin-Walled Truncated Cones," NASA SP-8019, 1968.
4. Vanderplaats, G.N., "Numerical Optimization Techniques for Engineering Design: With Applications," McGraw-Hill Book Company, New York, 1984.

APPENDIX - PROGRAM LISTINGS

1989

NASA/ASEE SUMMER FACULTY FELLOWSHIP PROGRAM

MARSHALL SPACE FLIGHT CENTER
THE UNIVERSITY OF ALABAMA IN HUNTSVILLE

ITERATIVE PROCEDURES FOR
SPACE SHUTTLE MAIN ENGINE PERFORMANCE MODELS

Prepared by:	L. Michael Santi
Academic Rank:	Associate Professor
University and Department:	Memphis State University Mechanical Engineering Department
NASA/MSEC:	
Laboratory:	Propulsion
Division:	Propulsion Systems
Branch:	Performance Analysis
MSEC Colleague:	Charles F. Schafer
Date:	August 8, 1989
Contract Number:	The University of Alabama in Huntsville NGT-01-008-021

ABSTRACT

Performance models of the Space Shuttle Main Engine (SSME) contain iterative strategies for determining approximate solutions to nonlinear equations reflecting fundamental mass, energy, and pressure balances within engine flow systems. Both univariate and multivariate Newton-Raphson algorithms are employed in the current version of the engine Test Information Program (TIP). Computational efficiency and reliability of these procedures is examined. A modified trust region form of the multivariate Newton-Raphson method is implemented and shown to be superior for off nominal engine performance predictions. A heuristic form of Broyden's Rank One method is also tested and favorable results based on this algorithm are presented.

ACKNOWLEDGEMENTS

I would like to express my sincere appreciation to all those individuals who have contributed to this work by their advice, assistance, and encouragement. Gratitude is expressed to Dr. Charles Schafer for his organized approach to defining this effort, suggestions, and periodic review of results. I also wish to acknowledge the efforts Mr. Brian Piekarski of Martin Marietta Corporation for his assistance in preparing and organizing documentation associated with the TIP code. Special thanks are extended to Mr. John Butas for his valuable advice and assistance during the course of this investigation.

INTRODUCTION

Predictions of the steady-state operational characteristics of the Rocketdyne Space Shuttle Main Engine (SSME) are provided by computer programs which model and analyze engine system performance. The Test Information Program (TIP) is a FORTRAN based engine analysis software package which performs the following functions.

1. Power Balance - Simulates engine performance by balancing mass and energy flows for assumed nominal operation of SSME components.
2. Data Reduction - Uses actual test data to define operating characteristics of a specific SSME by adjusting component performance parameters.
3. Base Balance - Refines operating predictions of the Data Reduction portion by adjusting nine performance variables.
4. Rated Portion - Extends refined performance model to simulate actual engine operation over a range of conditions.

TIP balances mass and energy flows during engine performance prediction, and balances theoretical results with test information to refine these predictions. Figure 1 displays the SSME flow system network that is balanced by TIP to ensure satisfaction of the conservation of mass and conservation of energy principles as well as adherence to limitations imposed by the Second Law of Thermodynamics.

Since flow processes within the SSME are governed by a set of nonlinear equations, iterative techniques are required to computationally predict a balanced steady-state flow condition. Two subroutines within the TIP code perform iterative nonlinear equation solving functions. These routines are described below.

TIP Iteration Subroutines

1. NLEST - a single nonlinear equation root finding routine
CALL statement accessed as subroutine NLEST
ENTRY statement accessed as subroutine NLEST

NLEST - Find z such that $(x-y) = F(z) = 0$.
NLEST - Find x such that $(x-y) = F(x) = 0$.

ORIGINAL PAGE IS
OF POOR QUALITY

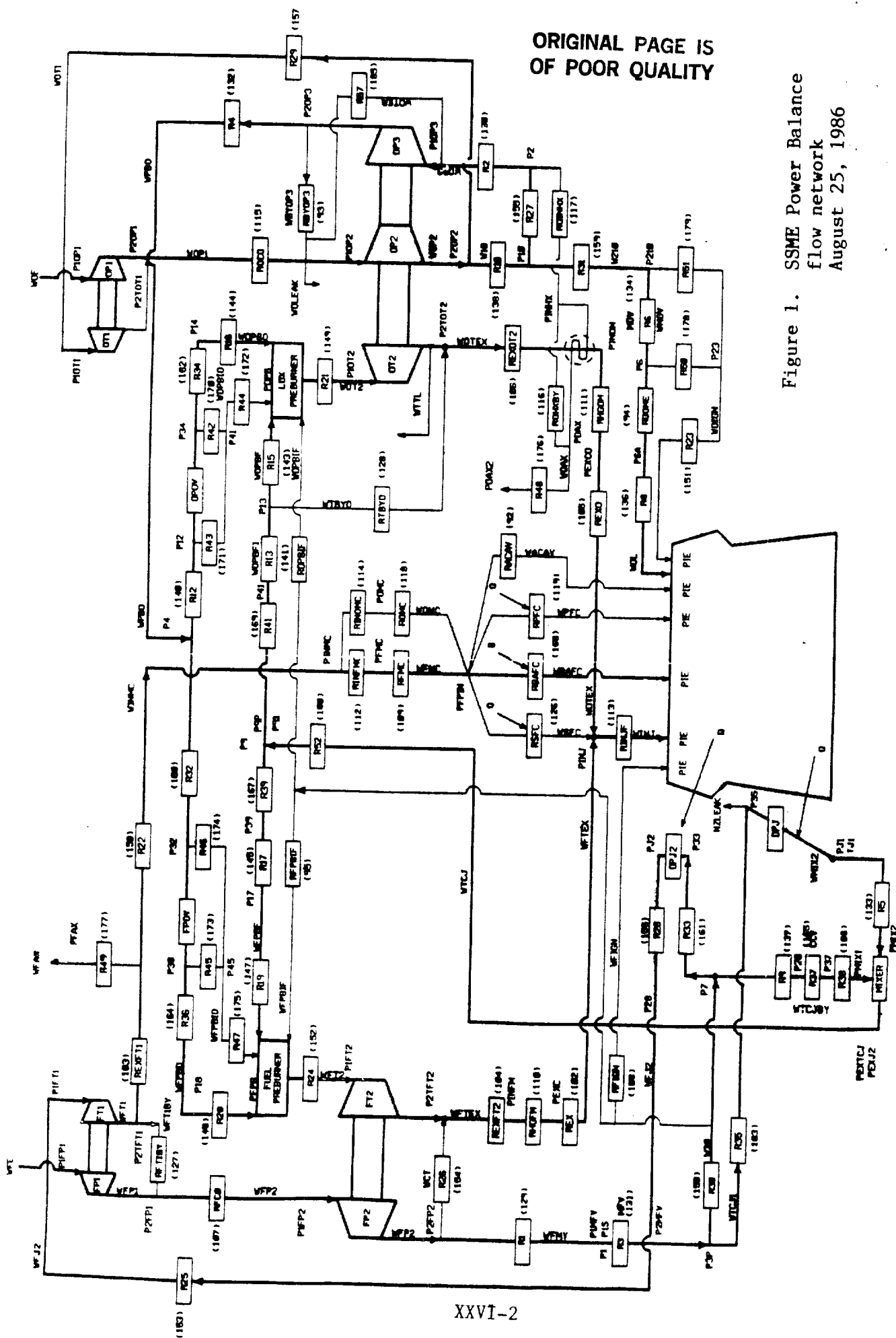


Figure 1. SSME Power Balance
flow network
August 25, 1986

2. NLESTN - a simultaneous nonlinear equation solver
CALL statement accessed as subroutine NLESTN

NLESTN - Find $\mathbf{x} = (x_1, x_2 \dots x_N)$ such that

$$y_1 = F_1(\mathbf{x}) = 0$$

$$y_2 = F_2(\mathbf{x}) = 0$$

$$\vdots$$

$$y_N = F_N(\mathbf{x}) = 0$$

The basic function of TIP is to provide steady-state operation and performance predictions. Engine flow conditions are established by solving systems of nonlinear balance equations arising from fundamental flow mechanics. Hence, use of the above described solver routines is fundamental to and pervasive within TIP as evidenced by the ninety-four calls to NLEST (or NLREST) and NLESTN which occur in the current version of this performance analysis package.

In addition to being pervasive, the iteration loops initiated by calls to subroutines NLEST and NLESTN are programmed in a complex sequence with considerable nesting and crossover. As an example of this complexity, consider the iteration loop sequencing of subroutine BAL exhibited in Appendix 1. Subroutine BAL is the routing routine for the Power Balance component of TIP. Significant iteration loop nesting, as many as seven loops deep, and loop crossover are apparent upon examination of this listing.

OBJECTIVES

Because of the intrinsic importance of the iterative nonlinear equation solvers in the TIP code, it is important that these procedures be both reliable and efficient. The objectives of this research effort are

1. To evaluate the iterative schemes employed within the TIP performance model
2. To modify and test these schemes as suitable to achieve greater reliability and efficiency
3. To perform a cursory review of fundamental TIP code logic and procedure

NONLINEAR EQUATION SOLVERS

The nonlinear equation root finding scheme currently employed in the TIP subroutine NLEST is a heuristic procedure which combines a secant method search with a false positions method (see e.g. Burden and Faires [1]). Initially the secant method is used to update the root approximation. Whenever successive applications of the secant method establish a bracket about the root, NLEST switches to a false positions technique. It is possible to lose the established root bracket due to loop nesting and the accompanying effects of shifting due to inner loop convergence tolerances. Because of this an ad hoc strategy for switching between secant and false positions searches is employed.

Within the context of the TIP code, the existing root finding scheme in NLEST was tested against several other well known procedures. The procedures implemented and tested by this author are listed below.

1. Finite difference Newton-Raphson
2. Secant (only)
3. False positions with step bracketing
4. Quadratic interpolation polynomial

In few instances were results superior to those obtained using the current NLEST algorithm, and in many cases the overall performance and convergence of the TIP code were adversely affected. Hence, the heuristic root finding strategy implemented within subroutine NLEST appears to be a robust and effective method within the TIP performance analysis model.

The simultaneous nonlinear equation solver currently implemented within subroutine NLESTN is a finite difference multivariate Newton-Raphson method (often referred to as simply Newton's method, see e.g. reference [1], page 486) with a direction skewing trust region boundary. To evaluate the effectiveness of this algorithm it is necessary to refer to the theoretical basis of the Newton-Raphson method. This basis will be outlined below.

The fundamental problem addressed by simultaneous nonlinear equation solvers can be expressed mathematically as follows.

$$\begin{aligned} \text{Find} \quad & \mathbf{x} = (x_1, x_2, \dots, x_N)^T \quad \text{in } \mathbb{R}^N \\ \text{such that} \quad & \mathbf{F} = (F_1(\mathbf{x}), F_2(\mathbf{x}), \dots, F_N(\mathbf{x}))^T = \mathbf{0} \\ \text{or equivalently} \quad & \begin{aligned} F_1(\mathbf{x}) &= 0 \\ F_2(\mathbf{x}) &= 0 \\ &\vdots \\ F_N(\mathbf{x}) &= 0 \end{aligned} \end{aligned} \quad (1)$$

$$\text{where} \quad \mathbf{F} : \mathbb{R}^N \longrightarrow \mathbb{R}^N$$

At stage k the fundamental iteration of the Newton-Raphson method for solving problems of this type can be written

$$\mathbf{x}_{k+1} = \mathbf{x}_k - \mathbf{J}_k^{-1} * \mathbf{F}_k \quad (2)$$

where

$$\mathbf{F}_k = \mathbf{F}(\mathbf{x}_k)$$

and

\mathbf{J}_k = the Jacobian of \mathbf{F} evaluated at \mathbf{x}_k

Rapid convergence of the Newton-Raphson method to the solution of (1) can be established rigorously if, for some k , \mathbf{x}_k is

sufficiently close to the solution vector designated \mathbf{x}^* .

Formal conditions for convergence are stated in the following theorem (see e.g. Rheinboldt [2]).

Theorem.

If \mathbf{F} has continuous first partial derivatives in some neighborhood of the solution \mathbf{x}^* , if the Jacobian of \mathbf{F} is nonsingular at \mathbf{x}^* and its elements satisfy a Lipschitz condition, and if \mathbf{x}_k is sufficiently close to \mathbf{x}^* for some k , then the Newton-Raphson method is well defined for all k and converges at second order, i.e. there exists a positive integer m and a positive real number b such that

$$\|\mathbf{F}_{k+1}\| / \|\mathbf{F}_k\|^2 < b \quad \text{whenever} \quad k > m$$

Despite the second order (or quadratic) convergence indicated in the above theorem, the Newton-Raphson method suffers from two serious disadvantages from the point of view of practical calculation. First, computation of the Jacobian matrix at each stage of the iteration is extremely costly in terms of computer resources. Often analytical partial derivatives are not available and finite difference approximations lack the precision necessary for ultimate convergence. The second disadvantage of the Newton-Raphson method arises from the need to have a

sufficiently accurate initial estimate of the solution in order to guarantee convergence. Satisfaction of this requirement is impossible to measure before initiation of the iteration sequence and often difficult to obtain in practice.

Extension of the basic Newton-Raphson procedure to include a subiteration or line search have been somewhat successful in removing the accurate initial estimate requirement. These methods include a strategy to select a positive real number lambda such that the iteration scheme

$$\mathbf{x}_{k+1} = \mathbf{x}_k + \text{lambda} * \mathbf{J}_k^{-1} * \mathbf{F}_k \quad (3)$$

reduces some measure of error, typically

$$\|\mathbf{F}_{k+1}\| < \|\mathbf{F}_k\| \quad (4)$$

at each stage. Although Newton-Raphson methods incorporating line searches extend the domain of convergence, they do so with significant computational overhead.

Trust region or restricted step methods are a compromise between convergence limited self-scaling iteration procedures and computationally intense methods incorporating line searches. These methods simply provide an upper bound on the distance between iteration steps. This bound may be absolute or scaled by position within the domain of \mathbf{x} .

The current version of subroutine NLESTN provides a multivariate Newton-Raphson method with a trust region approach. Unfortunately, the trust region bound is applied componentwise on \mathbf{x} which has the effect of skewing the correct Newton-Raphson method search direction. This skewing process removes any theoretical convergence characteristics and indicates the possibility of convergence difficulties when the iteration procedure is initiated at a point remote from the immediate vicinity of the solution. Difficulties of this type are currently experienced as will be discussed in the next section.

In an effort to correct the skewing problem inherent in the current version of NLESTN, a modified trust region form of the multivariate Newton-Raphson method was implemented within TIP. The basic iteration sequence of this method is given by

$$\mathbf{x}_{k+1} = \mathbf{x}_k - \text{lambda} * \mathbf{J}_k^{-1} * \mathbf{F}_k \quad (5)$$

where

$$\text{lambda} = \min \left[1, \frac{\|\text{PCTMAX} * \mathbf{x}_k\|}{\|\mathbf{J}_k^{-1} * \mathbf{F}_k\|} \right] \quad (6)$$

PCTMAX is a user defined parameter which serves to scale the size of the trust region. A comparison of search steps obtained using the skewed direction trust region approach and the corrected strategy are displayed in Figure 2. A complete listing of the modified trust region form of NLESTN implemented within TIP is given in Appendix 2. Results using this implementation are presented in the next section.

A trust region form of the Broyden Rank One [3] nonlinear system solver was also implemented and tested in an effort to

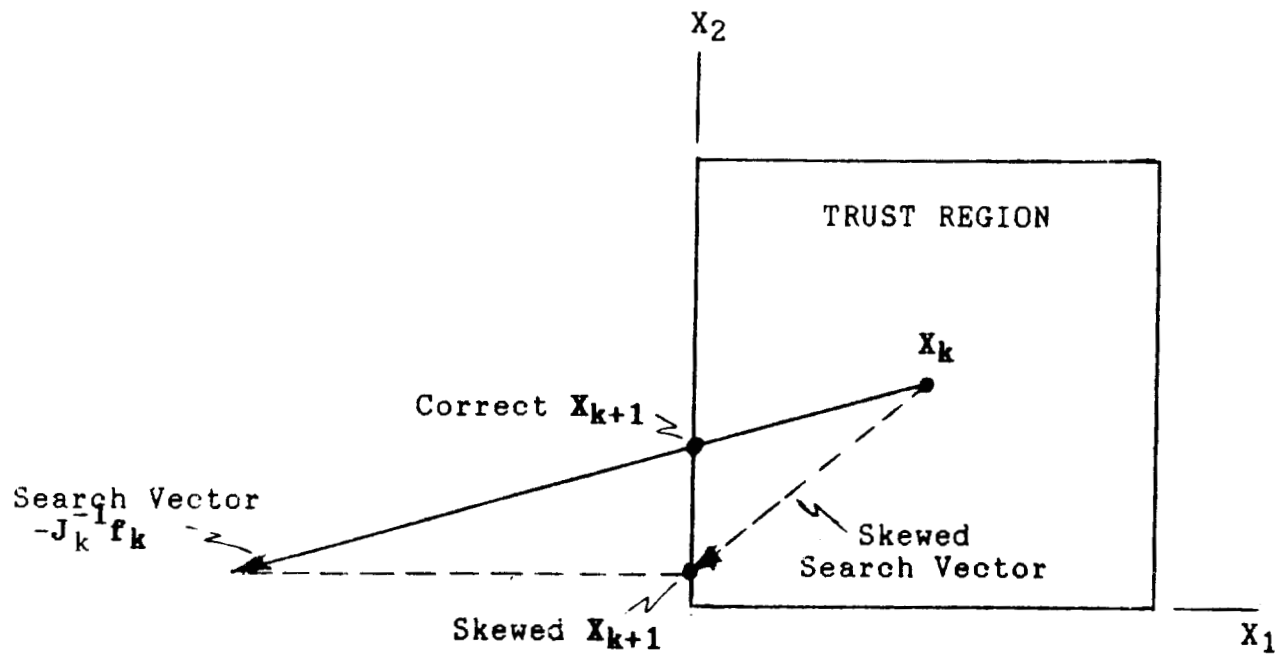


Figure 2. Comparison of skewed trust region search vector and correct trust region search vector.

reduce the computational overhead associated with Jacobian calculations and linear system solvers in the Newton-Raphson algorithm. The Broyden Rank One method is a modified Newton-Raphson iteration in which the Jacobian matrix is replaced by an approximation B which is updated at each iteration by using current information about F . In the Broyden strategy, a rank one modification of B is made at each iteration. The basic method is described below.

Basic Broyden Rank One Method

0. Select x_0 the iteration starting point and
 B_0 an $N \times N$ matrix approximation to the inverse
Jacobian of F at x_0 .

For $k = 0, 1, 2, \dots$

1. Evaluate F_k
2. Set $s_k = -B_k * F_k$
3. Set $x_{k+1} = x_k + s_k$
4. Evaluate F_{k+1}
5. Set $y_k = F_{k+1} - F_k$
6. If $y_k = 0$ Set $B_{k+1} = B_k$
Otherwise set $B_{k+1} = B_k + (s_k - B_k y_k) * v^T$
where $v^T = s^T * B_k / (s^T * B_k * y_k)$

Theoretical convergence properties of the basic Broyden Rank One algorithm have been clarified by Gay [4,5]. Although not as rapidly convergent theoretically as the Newton-Raphson method, testing has often shown the Broyden technique to be superior [3].

A complete listing of the Broyden Rank One trust region form of NLESTN implemented within TIP is given in Appendix 3. Results using this implementation are presented in the next section.

Function minimization strategies have often been used to solve nonlinear systems. A class of specialized minimization techniques (see e.g. [6]) been developed which address least squares problems of the type

$$\text{minimize } F(x)^T * F(x) \quad \text{by selection of } x \quad (7)$$

General nonlinear minimization algorithms can also be employed to solve problems such as (7) which arise naturally from nonlinear equation systems. These methods are typically computer intensive although potentially effective and robust.

Although no testing of TIP performance using sophisticated minimization methods was conducted, such techniques hold promise for future application within engine performance models.

COMPUTATIONAL RESULTS

Computations involving the TIP performance model were conducted on the EADS network at Marshall Space Flight Center. An IBM 3084 was the host processor. Within TIP, only Power Balance model prediction analyses were run. Initializing input data was fixed for all computations with the exception of LOX-fuel ratio and power level expressed as a percentage of engine rated power. Values for these flow characteristics were specified within and outside of the nominal operating ranges defined below.

Nominal SSME Operating Range

LOX-Fuel ratio	6.0 - 6.5
Power Level (%)	65 - 109

Variation of these operating control parameters permitted an evaluation of the function of the nonlinear equation solving algorithms over a range of practical problems.

Output from a typical Power Balance model analysis is extensive and includes many operating and performance characteristics of the SSME subsystems. These physical data will not be presented. Since the object of this investigation was to test and evaluate performance model iteration methods, computational performance data involving subroutines NLEST and NLESTN were collected. These data were organized and presented for each convergent Power Balance analysis as shown in Table 1. The prescribed values of mixture ratio and power level for the specific analysis are displayed at the top of this table. In addition, the univariate and multivariate iteration procedures used in the particular analysis are presented. Performance evaluation data for each iterative procedure are presented as described below.

NLEST Loop Summary Information

Loop	- iteration loop identification number
Entered	- number of times specific iteration loop was entered
Closed	- number of times specific iteration loop successfully converged and closed
Max	- maximum number of iterations required for convergence of specific iteration loop
Average	- average number of iterations required for convergence of specific iteration loop

Table 1. Iteration loop performance data for a typical Power Balance model analysis.

MIXTURE RATIO - 6.5 POWER LEVEL - 109 %

NLEST - ORIGINAL

NLESTN - BROYDEN RANK ONE

NLEST LOOP SUMMARY	LOOP	ENTERED	CLOSED	MAX	AVERAGE
	1	71	67	3	1.060
	2	67	59	3	1.136
	3	589	294	3	2.003
	5	6	3	2	2.000
	6	10	5	2	2.000
	7	434	428	3	1.014
	8	315	174	3	1.810
	9	87	69	2	1.261
	11	149	67	7	2.224
	12	788	428	2	1.841
	14	1002	550	4	1.822
	15	550	294	3	1.871
	16	1029	510	5	2.018
	17	119	69	3	1.725
	18	1100	428	4	2.570
	19	657	290	5	2.266
	20	679	290	4	2.341
	21	13	5	3	2.600
	23	1113	428	4	2.600
	24	2108	720	3	2.928
	25	861	428	3	2.012
	26	1698	788	3	2.155
	27	1737	856	3	2.029
	28	977	428	4	2.263
	30	117	69	3	1.696
	31	5528	2517	3	2.196
	32	191	69	8	2.768
	35	442	69	8	6.406
	36	3	1	3	3.000
	37	5	1	5	5.000
	38	429	428	2	1.002
	39	191	191	1	1.000
	40	5	1	5	5.000
	42	856	428	2	2.000
	43	69	19	6	3.632
	45	69	69	1	1.000
	46	769	408	4	1.885
	48	388	294	2	1.320
	49	431	294	2	1.466
	50	174	87	2	2.000
	60	594	360	2	1.650
	61	177	122	3	1.451
	62	122	67	3	1.821
	67	3	1	3	3.000
	70	4	1	4	4.000

NLESTN SUMMARY	LOOP	ENTER	JACOB	CLOSE	MAX	JE/C	LP/C
	1	510	157	149	5	1.054	3.423
	2	19	8	1	8	8.000	19.000
	3	769	361	136	3	2.654	5.654
	4	294	65	69	3	0.942	4.261
	5	286	79	69	3	1.145	4.145
	6	3375	675	675	1	1.000	5.000

NLESTN Loop Summary Information

Loop	-	same as above
Enter	-	same as above for entered
Jacob	-	total number of Jacobian or Jacobian approximation evaluations
Close	-	same as above for closed
Max	-	same as above
JE/C	-	average number of Jacobian evaluations per convergent iteration
LP/C	-	average number of iteration loop passes per convergent iteration

The amount of effort expended in iteration processes is evident from Table 1, with over 15,000 univariate loop entries and over 5,000 multivariate loop entries documented for this specific Power Balance analysis in order to achieve convergence. This effort level is typical of convergent analyses performed in this study.

In order to compare the efficiency and reliability of various NLESTN implemented multivariate nonlinear equation solving methods, the total number of NLESTN loop entries was tabulated for each of several analyses using different multivariate iteration strategies. These data are presented in Table 2. Examination of the information in Table 2 suggests the following

Conclusions Based on Table 2 Data

1. The current (N-R Orig) Newton-Raphson implementation often fails to converge for mixture ratios or power levels outside the nominal region. This result was expected since the direction skewing trust region method forces the iteration sequence to take less appropriate steps for conditions that cause the solution to be further removed from the initiation data. It is notable that within the nominal region for mixture ratio and power level, the current Newton-Raphson implementation performs almost the same as the modified method (N-R Mod). This occurs because within the nominal operating range, the trust region boundary is not reached during the search process since the initiation data is close to the converged solution.
2. The modified Newton-Raphson method (N-R Mod) with corrected trust region is more efficient, requiring fewer total NLESTN loop passes, for conditions outside and on the boundary of the nominal regions for mixture ratio and power level. This is due to the corrected search direction method employed at the trust region boundary. In addition, the modified Newton-Raphson method is more reliable than the original method, converging for several cases with outside nominal mixture ratios or power levels.

3. The Broyden Rank One method implementation is extremely reliable, having converged for all cases considered. The efficiency of this method is somewhat erratic, often requiring substantially fewer loop passes for convergence than the Newton-Raphson methods and yet occasionally requiring substantially more effort to arrive at a converged solution. This erratic behavior was not wholly unexpected due to the approximate nature of the Jacobian estimate employed and updated by the algorithm.

Further comparisons of the modified Newton-Raphson and Broyden Rank One methods with the current NLESTN implementation are presented in Table 3. Results are presented only for analyses in which the current multivariate iteration strategy achieved convergence. The improved efficiency gained by use of the modified Newton-Raphson method outside the nominal operating range is again evident. The erratic efficiency of the Broyden method is clearly displayed.

Table 2. Loop passes through multivariate subroutine NLESTN.

MR	PL(%)	N-R Orig	N-R Mod	Broyden
6.0	65	9,077	9,077	2,527
6.0	100	10,586	10,586	6,099
6.011	104	4,993	4,993	14,711
6.5	104	9,152	9,152	6,515
6.5	109	13,308	7,209	5,253
6.6	109	F	11,491	6,009
6.7	109	F	11,514	13,434*
6.8	109	F	24,935*	10,303*
6.5	112	11,757	11,723	13,309
6.5	115	15,118	12,213	21,829
6.5	120	F	F	7,809

F - Failure to converge to specified tolerance in allowed number of iterations

* - Trust region interval reduced to $\pm 5\%$ of current independent variable value

Table 3. Change (%) in number of loop passes through subroutine NLESTN using the original Newton-Raphson method results as standard.

MR	PL(%)	% Change	
		N-R Mod	Broyden
6.0	65	0	- 72.2
6.0	100	0	- 42.4
6.011	104	0	+194.6
6.5	104	0	- 28.8
6.5	109	- 45.8	- 60.5
6.5	112	- 0.3	+ 13.2
6.5	115	- 19.2	+ 44.4

RECOMMENDATIONS

The following recommendations for improvement of the iterative procedures within the Test Information Program are motivated by the computational results described in the previous section of this report and by investigation of TIP logic.

Recommendations for Improvement of Iterative Procedures

1. Immediately implement modified multivariate Newton-Raphson method with corrected trust region approach in subroutine NLESTN. The subroutine described in Appendix 2 is one implementation of this method.
2. Continue to test and refine the potentially effective Broyden Rank One method for the iterative solution of simultaneous nonlinear equations. The subroutine described in Appendix 3 is one implementation of this method.
3. Perform computational experimentation using flexible loop tolerances and flexible trust region bounds in the iterative routines. These modifications could substantially improve the efficiency of the TIP iteration sequence.
4. Incorporate and test a formal line search algorithm within the multivariate iteration scheme to enhance convergence and reliability for strongly off nominal engine operation.
5. Perform a detailed sensitivity analysis of all iteration loop independent variables to determine uncertainty limits associated with loop tolerances.
6. Review iteration loop logic sequencing. Modify and test sequencing to achieve improved computational efficiency.

In addition to the recommendations involving computational procedure listed above, a limited review of the TIP code motivates the structuring recommendations provided below.

Code Structuring Recommendations

1. Clearly identify and separate TIP program components.
 - Theoretical base (flow physics)
 - Computational base (formal numerical algorithms)
 - Experimental base (engineering performance parameters and other approximations)

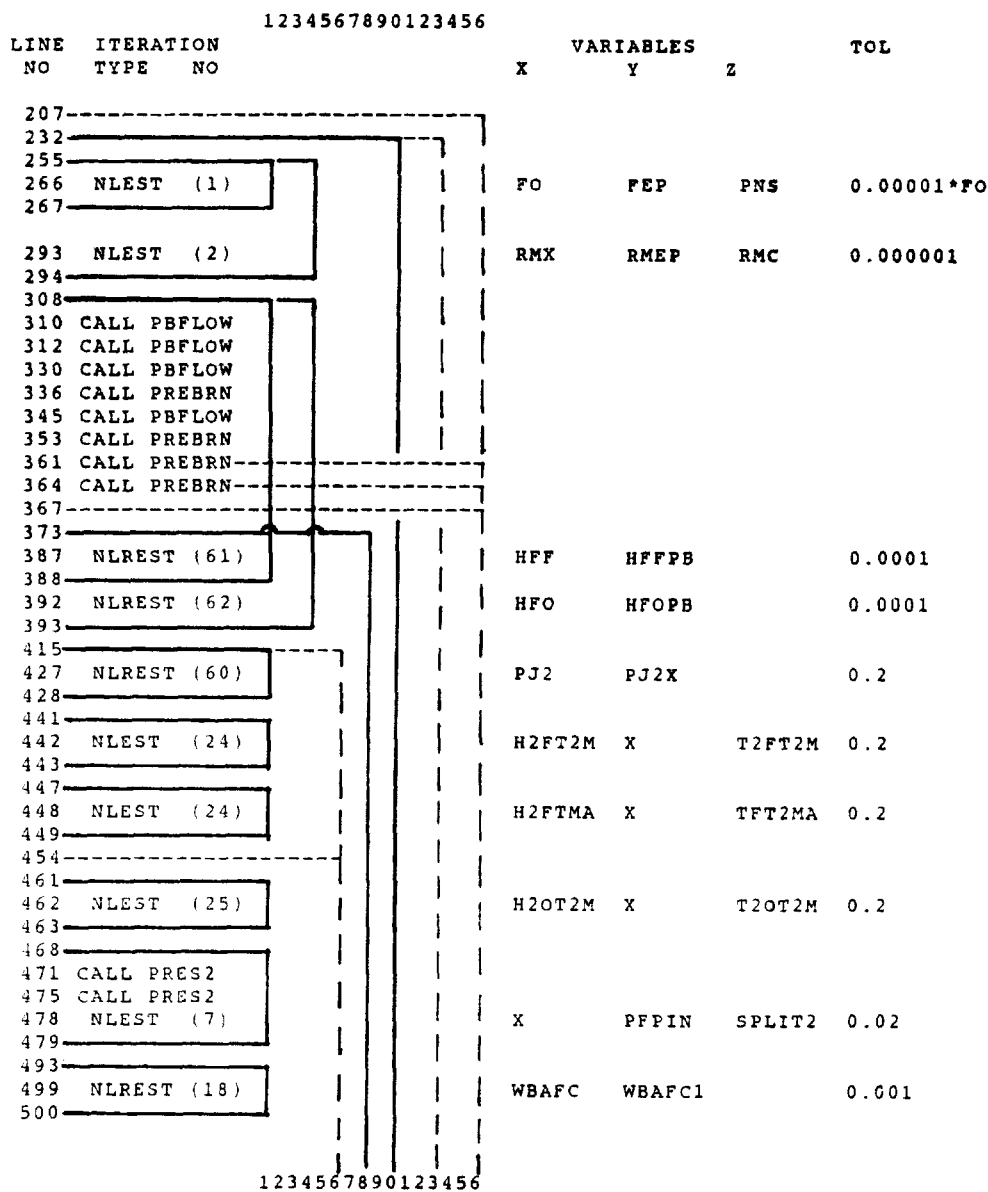
2. Clearly identify the following.
 - Independent variables of model analysis (user defined and controlled physical inputs)
 - Arbitrarily prescribed and constant parameters of model analysis (code designer defined and restricted input)
 - Dependent variables of model analysis (solution variables requiring initial approximation)
3. Review prescribed flow and performance variable dependencies in model for accuracy and completeness.
4. Formalize an organized data input structure descriptive of SSME flow systems, i.e. number nodes, branches, and devices and formally identify connectivity within the data structure.
5. Fully document TIP program physical logic sequence.
6. Construct postprocessors that clearly exhibit physical balances for appropriate engine subsystems as a means of verification.

These recommendations are very basic and if implemented will improve confidence in and reliability of TIP analysis results.

Appendix 1. Iteration loop sequencing in subroutine BAL

TIP88MMC 22 JUN 89

SUBROUTINE BAL - ITERATION LOOP SEQUENCING



ORIGINAL PAGE IS
OF POOR QUALITY

1234567890123456									
504									
506	NLREST	(23)					TPFC	TPFC1	0.01
507									
532									
533	NLEST	(26)					X	H2FHGM	TEXC 0.02
534									
535	CALL PRES2								
536	NLREST	(12)					PEXC	PEXCP	0.02
537									
544									
545	NLEST	(27)					X	H2OHGM	TEXCO 0.005
546									
547	CALL PRES2								
548	NLREST	(42)					PEXCO	PEXCOP	0.02
549									
557									
558	NLEST	(28)					X	HINJ	TINJ 0.005
559									
563									
568	NLREST	(38)					RO1FP1	ROFP1	0.0001
569									
573									
574									
580	NLEST	(16)					P1FT1	P1FT1P	PRFT1 0.1
581									
584	NLESTN	(1)					P2TFT1	(PINJ-PINJP)	0.2
							P2TOT2	(PINJP-PINJP1)	0.1
							P2TFT2	(PIE-PIEP)	0.2
590									
591									
629	NLEST	(11)					HPFT1	HPFP1	ENFT1 0.0001*HPFP1
630									
635	CALL H2PUMP								
668	CALL OT2								
671	CALL FT2								
687									
692	NLREST	(45)					P2MFVP	P2MFV	0.1
693									
701									
709									
720	NLREST	(39)					P37P	P37	2.0
722									
733									
737	NLREST	(46)					PJ1	PJ1X	0.2
738									
745	NLEST	(32)					X (PMIX2-PMIX1)	SPLIT1	0.05
746									
751	NLREST	(47)					WAUG	WAUX	0.001
752									
1234567890123456									

Appendix 2. Subroutine NLESTN implementation with corrected trust region Newton-Raphson method.

```

C ***** CODE DESIGNATION TRUST *****
C
C      SUBROUTINE NLESTN (ID,N,A,KK,X1,Y1,T1,F1,X2,Y2,T2,F2,X3,Y3,T3,F3,
+ X4,Y4,T4,F4,X5,Y5,T5,F5,X6,Y6,T6,F6)
C
C      IMPLICIT REAL*8(A-H,O-Z)
C
C -NLESTN- 2- TO 6-DIMENSIONAL MULTIVARIATE NEWTON-RAPHSON METHOD FOR
C THE ITERATIVE SOLUTION OF SIMULTANEOUS NONLINEAR ALGEBRAIC
C EQUATIONS.
C
C CALL STATEMENT...
C CALL NLESTN (ID,N,A,KK,X1,Y1,T1,F1,X2,Y2,T2,F2,...,XN,YN,TN,FN)
C ...WHERE N IS )=6.
C
C      ID IS THE ITERATION LOOP NUMBER (MINIMUM VALUE = 1, MAXIMUM
C VALUE = 10). EACH NUMBER OF A NEST OF LOOPS MUST HAVE A DIFFERENT
C LOOP NUMBER, BUT OTHERWISE LOOP NUMBERS ARE ARBITRARY WITHIN THE
C ABOVE LIMITS.
C
C      N IS THE NUMBER OF INDEPENDENT VARIABLES TO BE ITERATED UPON
C (X1,X2,...,XN) IN ORDER TO DIMINISH THE DEPENDENT VARIABLE ERROR
C VALUES (Y1,Y2,...,YN) TO WITHIN SPECIFIED TOLERANCES (T1,T2,...,TN).
C NOTE- 2 <= N <= 6.
C      (F1,F2,...,FN) ARE INDEPENDENT VARIABLE INCREMENT MULTIPLIERS
C USED IN THE FINITE DIFFERENCE APPROXIMATIONS FOR THE JACOBIAN
C MATRIX PARTIAL DERIVATIVES.
C
C      A IS AN N-BY-N MATRIX DIMENSIONED IN THE CALLING PROGRAM.
C      KK IS A FLAG AS FOLLOWS...
C      KK=-3 SINGULAR MATRIX.
C      KK=-1 ALLOWABLE NUMBER OF ITERATIONS HAS BEEN EXCEEDED.
C      KK= 0 ALL Y'S ARE LESS THAN TOLERANCE, ITERATION COMPLETE.
C      KK= 1 ONE OR MORE Y'S ARE GREATER THAN TOLERANCE, REITERATE.
C
C
C      INCLUDE (INSAVE)
C      INCLUDE (DPSAVE)
C
C      DIMENSION B(36),SX(6),SY(6),ST(6),SF(6),SDF(6)
C      DIMENSION D(6,6),A(N,N),C(36)
C      DATA LIMIT,PCTMAX/20,0.2/
C
C ***** ARRAY INITIALIZE SUBROUTINE INPUT ARGUMENTS
C
C      SX(1)=X1
C      SX(2)=X2
C      SX(3)=X3
C      SX(4)=X4
C      SX(5)=X5
C      SX(6)=X6
C
C
C      SY(1)=Y1
C      SY(2)=Y2
C      SY(3)=Y3
C      SY(4)=Y4
C      SY(5)=Y5
C      SY(6)=Y6

```

ORIGINAL PAGE IS
OF POOR QUALITY


```

C      ST(1)=T1
      ST(2)=T2
      ST(3)=T3
      ST(4)=T4
      ST(5)=T5
      ST(6)=T6

C      SF(1)=F1
      SF(2)=F2
      SF(3)=F3
      SF(4)=F4
      SF(5)=F5
      SF(6)=F6

C ***** STEP 1. CHECK FOR CONVERGENCE
C      L=LOOPN(ID)
      NUMN(ID,1)=NUMN(ID,1)+1
      ICONV=0
      DO 10 I=1,N
      IF (ICONV.GT.0) GO TO 10
      IF (DABS(SY(I)).GT.DABS(ST(I))) ICONV=1
10     CONTINUE
      IF (ICONV.GT.0) GO TO 20
      NUMN(ID,3)=NUMN(ID,3)+1
      NUMN(ID,4)=MAX0(NUMN(ID,4),KOUNL(ID))
      KOUNL(ID)=0
      KK=0
      GO TO 200

C ***** STEP 2. CHECK FOR EXCESSIVE ITERATIONS
C      20 IF (KOUNL(ID).LT.LIMIT) GO TO 30
      WRITE (4,901) LIMIT,ID,(SY(I),ST(I),SX(I),I=1,N)
901  FORMAT (
+    1H , 'ERROR IN NLESTN, NO SOLUTION WITHIN',I3,' ITERATIONS',/,
+    1H , 'FIRST ARGUMENT IN THE CALL STATEMENT IS',I5,/,
+    1H , 'ERROR VALUES      TOLERANCES INDEPENDENT VARIABLES',/,
+    3(G15.6))
      K=1
      GO TO 130

C ***** STEP 3. INITIALIZE ITERATION SEQUENCE
C      30 DO 40 I=1,N
      40 SDF(I)=SF(I)-1.0
      IF (L.GT.0) GO TO 60
      L=0
      DO 50 I=1,N
      A(I,N)=SY(I)
50   A(I,N-1)=SX(I)
      KOUNL(ID)=KOUNL(ID)+1
      NUMN(ID,2)=NUMN(ID,2)+1
      GO TO 180

C ***** STEP 4. ESTIMATE JACOBIAN PARTIALS
C      60 IF (L.LT.N) GO TO 80

```


ORIGINAL PAGE IS
OF POOR QUALITY

```

      DO 70 I=1,N
70    B(I)=A(I,N)
80    SX(L)=SX(L)/SF(L)
      DP=SX(L)*SDF(L)
      DO 100 I=1,N
100   A(I,L)=(SX(I)-A(I,N))/DP
      IF (L.LT.N) GO TO 180
C
C ***** STEP 5. DETERMINE NEWTON-RAPHSON STEP INCREMENT
C      COLUMN 1 OF ARRAY D AS RETURNED FROM
C      FUNCTION ROUTINE ISIMDD IS THE DOT
C      PRODUCT OF THE INVERSE JACOBIAN WITH
C      THE DEPENDENT VARIABLE VECTOR
C      (Y1,Y2...YN)
      DO 110 I=1,N
      DO 110 J=1,N
110   D(I,J)=A(I,J)
      SCALE=0.
      K=ISIMDD (6,N,1,D,B,SCALE,C)
C
C ***** STEP 6. CHECK FOR SINGULAR JACOBIAN
      IF (K.EQ.1) GO TO 150
      WRITE (4,902) K,ID,KOUNL(ID)
902   FORMAT(1H0,'ERROR IN NLESTN, MATRIX FAILURE USING ','ISIMDD,',
+         ' ERROR INDICATOR IS',I3,/,
+         1H , 'FIRST ARGUMENT IN THE CALL STATEMENT IS',I5,
+         ' LOOP COUNTER IS',I3,
+         ' THE COLUMN AND SQUARE MATRICES FOLLOW')
      DO 120 I=1,N
120   WRITE (4,903) B(I),(A(I,J),J=1,N)
903   FORMAT(1H ,G14.6,SX,6(G14.6))
130   DO 140 I=1,10
      KOUNL(I)=0
140   LOOPN(I)=0
      KK=-K
      GO TO 210
C
C ***** STEP 7. INCREMENT INDEPENDENT VARIABLES WITHIN TRUST REGION
150   FACT=1.0
      DO 160 I=1,N
      TFACT=DABS(D(I,1))/(PCTMAX*DABS(SX(I)))
160   IF (TFACT.GT.FACT) FACT=TFACT
      DO 170 I=1,N
170   SX(I)=SX(I)-D(I,1)/FACT
      L=0
      GO TO 190
C
C ***** STEP 8. RESET ARGUMENT LIST INDEPENDENT VARIABLES AND COUNTERS
180   L=L+1
      SX(L)=SX(L)*SF(L)
190   KK=L+1
C
      X1=SX(1)
      X2=SX(2)
      X3=SX(3)
      X4=SX(4)
      X5=SX(5)
      X6=SX(6)
C
200   LOOPN(ID)=L
C
210   RETURN
      END

```


Appendix 3. Subroutine NLESTN implementation with trust
region Broyden Rank One method.

```

C ***** CODE DESIGNATION BROYDEN *****
C
C      SUBROUTINE NLESTN (ID,N,A,KK,X1,Y1,T1,F1,X2,Y2,T2,F2,X3,Y3,T3,F3,
C      + X4,Y4,T4,F4,X5,Y5,T5,F5,X6,Y6,T6,F6)
C
C      IMPLICIT REAL*8(A-H,O-Z)
C
C      -NLESTN- 2- TO 6-DIMENSIONAL BROYDEN'S (GOOD) RANK ONE METHOD FOR
C      THE ITERATIVE SOLUTION OF SIMULTANEOUS NONLINEAR ALGEBRAIC
C      EQUATIONS.
C
C      CALL STATEMENT...
C      CALL NLESTN (ID,N,A,KK,X1,Y1,T1,F1,X2,Y2,T2,F2,...,XN,YN,TN,FN)
C      ...WHERE N IS >=6.
C
C      ID IS THE ITERATION LOOP NUMBER (MINIMUM VALUE = 1, MAXIMUM
C      VALUE = 10). EACH NUMBER OF A NEST OF LOOPS MUST HAVE A DIFFERENT
C      LOOP NUMBER, BUT OTHERWISE LOOP NUMBERS ARE ARBITRARY WITHIN THE
C      ABOVE LIMITS.
C      N IS THE NUMBER OF INDEPENDENT VARIABLES TO BE ITERATED UPON
C      (X1,X2...XN) IN ORDER TO DIMINISH THE DEPENDENT VARAIBLE ERROR
C      VALUES (Y1,Y2...YN) TO WITHIN SPECIFIED TOLERANCES (T1,T2...TN).
C      NOTE- 2 <= N <= 6
C      (F1,F2...FN) ARE INDEPENDENT VARIABLE INCREMENT MULTIPLIERS
C      USED IN THE FINITE DIFFERENCE APPROXIMATION TO THE JACOBIAN
C      MATRIX AT SELECTED STAGES.
C      A IS AN N-BY-N MATRIX DIMENSIONED IN THE CALLING PROGRAM.
C      KK IS A FLAG AS FOLLOWS...
C      KK=-3 SINGULAR MATRIX.
C      KK=-1 ALLOWABLE NUMBER OF ITERATIONS HAS BEEN EXCEEDED.
C      KK= 0 ALL Y'S ARE LESS THAN TOLERANCE, ITERATION COMPLETE.
C      KK= 1 ONE OR MORE Y'S ARE GREATER THAN TOLERANCE, REITERATE.
C
C      INCLUDE (INSAVE)
C      INCLUDE (DPSAVE)
C
C      DIMENSION NBROY(10),SX(6),SY0(10,6),SY(6),ST(6),SF(6),SDF(6)
C      DIMENSION A(N,N),C(36),SK(10,6),SID(6,6)
C      DATA LIMIT,PCTMAX,SMNUM/50,0.2,1.0D-8/
C
C      ***** ARRAY INITIALIZE SUBROUTINE INPUT ARGUMENTS
C      SX(1)=X1
C      SX(2)=X2
C      SX(3)=X3
C      SX(4)=X4
C      SX(5)=X5
C      SX(6)=X6
C
C      SY(1)=Y1
C      SY(2)=Y2
C      SY(3)=Y3
C      SY(4)=Y4
C      SY(5)=Y5
C      SY(6)=Y6

```

ORIGINAL PAGE IS
OF POOR QUALITY

ORIGINAL PAGE IS
OF POOR QUALITY

```

C      ST(1)=T1
      ST(2)=T2
      ST(3)=T3
      ST(4)=T4
      ST(5)=T5
      ST(6)=T6

C      SF(1)=F1
      SF(2)=F2
      SF(3)=F3
      SF(4)=F4
      SF(5)=F5
      SF(6)=F6

C
C ***** STEP 1. CHECK FOR CONVERGENCE
      L=LOOPN(ID)
      NUMN(ID,1)=NUMN(ID,1)+1
      ICONV=0
      DO 10 I=1,N
      IF (ICONV.GT.0) GO TO 10
      IF (DABS(SY(I)).GT.DABS(ST(I))) ICONV=1
10    CONTINUE
      IF (ICONV.GT.0) GO TO 20
      NUMN(ID,3)=NUMN(ID,3)+1
      NUMN(ID,4)=MAX0(NUMN(ID,4),KOUNL(ID))
      KOUNL(ID)=0
      KK=0
      GO TO 200

C
C ***** STEP 2. CHECK FOR EXCESSIVE ITERATIONS
20    IF (KOUNL(ID).LT.LIMIT) GO TO 30
      WRITE (4,901) LIMIT,ID,(SY(I),ST(I),SX(I),I=1,N)
- 901  FORMAT (
+    1H , 'ERROR IN NLESTN, NO SOLUTION WITHIN',I3,'ITERATIONS',/,
+    1H , 'FIRST ARGUMENT IN THE CALL STATEMENT IS',I5,/,
+    1H , 'ERROR VALUES      TOLERANCES INDEPENDENT VARIABLES',/,
+      3(G15.6))
      K=1
      GO TO 130

C
C ***** STEP 3. DECIDE ON ITERATION PROCEDURE FOR
C                      CURRENT PHASE
C                      NBROY(ID)=0    NEWTON-RAPHSON STEP
C                      NBROY(ID)>0    BROYDEN RANK 1 STEP
30    IF (KOUNL(ID).LE.0) NBROY(ID)=0
      IF (NBROY(ID).GT.0) GO TO 300

C
C ***** STEP 4. INITIALIZE ITERATION SEQUENCE FOR
C                      MULTIVARIATE NEWTON-RAPHSON STAGE
      DO 40 I=1,N
40    SDF(I)=SF(I)-1.0
      IF (L.GT.0) GO TO 60
      L=0
      DO 50 I=1,N

```



```

50 SY0(ID,I)=SY(I)
   KOUNL(ID)=KOUNL(ID)+1
   NUMN(ID,2)=NUMN(ID,2)+1
   GO TO 180
C
C ***** STEP 5. ESTIMATE JACOBIAN PARTIALS
60 SX(L)=SX(L)/SF(L)
   DP=SX(L)*SDF(L)
   DO 100 I=1,N
100 A(I,L)=(SY(I)-SY0(ID,I))/DP
   IF (L.LT.N) GO TO 180
C
C ***** STEP 6. DETERMINE INVERSE JACOBIAN MATRIX
C          MATRIX [A] AS RETURNED FROM
C          FUNCTION ROUTINE ISIMDD IS THE
C          INVERSE JACOBIAN APPROXIMATION
   SCALE=0.
   K=ISIMDD (N,N,-N,A,SID,SCALE,C)
C
C ***** STEP 7. CHECK FOR SINGULAR JACOBIAN
   IF (K.EQ.1) GO TO 150
   WRITE (4,902) K,ID,KOUNL(ID)
902 FORMAT(1H0,'ERROR IN NLESTN, MATRIX FAILURE USING ','ISIMDD,',
+        ' ERROR INDICATOR IS',I3,/,
+        1H , 'FIRST ARGUMENT IN THE CALL STATEMENT IS',I5,
+        ' LOOP COUNTER IS',I3,
+        ' THE COLUMN AND SQUARE MATRICES FOLLOW')
   DO 120 I=1,N
120 WRITE (4,903) SY0(ID,I),(A(I,J),J=1,N)
903 FORMAT(1H ,G14.6,5X,6(G14.6))
130 DO 140 I=1,10
   KOUNL(I)=0
140 LOOPN(I)=0
   KK=-K
   GO TO 210
C
C ***** STEP 8. INCREMENT INDEPENDENT VARIABLES WITHIN TRUST REGION
150 DO 155 I=1,N
   SK(ID,I)=0.0
   DO 155 J=1,N
155 SK(ID,I)=SK(ID,I)-A(I,J)*SY0(ID,J)
   FACT=1.0
   DO 160 I=1,N
   TFACT=DABS(SK(ID,I))/(PCTMAX*SX(I))
160 IF (TFACT.GT.FACT) FACT=TFACT
   DO 170 I=1,N
   SK(ID,I)=SK(ID,I)/FACT
170 SX(I)=SX(I)+SK(ID,I)
   L=0
   NBROY(ID)=1
   GO TO 190
C
C ***** STEP 9. PROVIDE BROYDEN RANK ONE UPDATE FOR
C          INVERSE JACOBIAN APPROXIMATION
300 KOUNL(ID)=KOUNL(ID)+1

```


ORIGINAL PAGE IS
OF POOR QUALITY

```

      NUMN(ID,2)=NUMN(ID,2)+1
      SBY=0.
      DO 320 I=1,N
      SB=0.
      DO 310 J=1,N
310    SB=SB+SK(ID,J)*A(J,I)
320    SBY=SBY+SB*(SY(I)-SY0(ID,I))
      IF (DABS(SBY).LT.SMNUM) GO TO 355
      DO 350 I=1,N
      BY=0.
      DO 330 II=1,N
330    BY=BY+A(I,II)*(SY(II)-SY0(ID,II))
      DO 350 J=1,N
      SB=0.
      DO 340 JJ=1,N
340    SB=SB+SK(ID,JJ)*A(JJ,J)
350    A(I,J)=A(I,J)+(SK(ID,I)-BY)*SB/SBY
355    DO 360 I=1,N
      SK(ID,I)=0.
      DO 360 J=1,N
360    SK(ID,I)=SK(ID,I)-A(I,J)*SY(J)
      FACT=1.0
      DO 370 I=1,N
      TFACT=DABS(SK(ID,I))/(PCTMAX*SX(I))
370    IF (TFACT.GT.FACT) FACT=TFACT
      DO 380 I=1,N
      SK(ID,I)=SK(ID,I)/FACT
      SX(I)=SX(I)+SK(ID,I)
380    SY0(ID,I)=SY(I)
      NBROY(ID)=NBROY(ID)+1
      IF (NBROY(ID).GT.N) NBROY(ID)=0
      L=0
      GO TO 190
C
C ***** STEP 10. RESET ARGUMENT LIST INDEPENDENT VARIABLES AND COUNTERS
180    L=L+1
      SX(L)=SX(L)*SF(L)
190    KK=L+1
C
      X1=SX(1)
      X2=SX(2)
      X3=SX(3)
      X4=SX(4)
      X5=SX(5)
      X6=SX(6)
C
200    LOOPN(ID)=L
C
210    RETURN
      END

```


REFERENCES

1. Burden, R. L. and Faires, J. D., Numerical Analysis. 3rd Edn., PWS, Boston, 1985.
2. Rheinboldt, W. C., Methods for Solving Systems of Nonlinear Equations. SIAM, Philadelphia, 1974.
3. Broyden, C. G., "A Class of Methods for Solving Nonlinear Simultaneous Equations," Math. Comp., Vol. 19, 1965, pp 577-593.
4. Gay, D. M. and Schnabel, R. B., "Solving Systems of Nonlinear Equations by Broyden's Method with Projected Updates," Nonlinear Programming 3, O.L. Mangasarian, R.R. Meyer, and S.M. Robinson, eds., Academic Press, New York, 1978, pp 245-281.
5. Gay, D. M., "Some Convergence Properties of Broyden's Method," SIAM J. Num. Anal., Vol. 16, No. 4, 1979, pp 623-630.
6. Fletcher, R., Practical Methods of Optimization. 2nd Edn., Wiley, New York, 1987.

1989

NASA/ASEE SUMMER FACULTY RESEARCH FELLOWSHIP PROGRAM

MARSHALL SPACE FLIGHT CENTER
THE UNIVERSITY OF ALABAMA IN HUNTSVILLE

MARSHALL AVIONICS
TESTBED SYSTEM (MAST)

Prepared By:	Wayne D. Smith
Academic Rank:	Associate Professor
University and Department:	Mississippi State University Computer Science Department
NASA/MSFC:	
Laboratory:	Information and Electronic Systems
Division:	Computers and Communications
Branch:	Communications Systems
NASA Colleagues	Frank H. Emens Delisa Young
Date:	August 11, 1989
Contract No.:	The University of Alabama in Huntsville NGT-01-008-021

ABSTRACT

This report contains a summary of the work accomplished in the summer of 1989 in association with the NASA/ASEE Summer Faculty Research Fellowship Program at Marshall Space Flight Center. The project was aimed at developing detailed specifications for the Marshall Avionics System Testbed (MAST). This activity was to include the definition of the testbed requirements and the development of specifications for a set of standard network nodes for connecting the testbed to a variety of networks. The project was also to include developing a timetable for the design, implementation, programming and testing of the testbed. Specifications of both hardware and software components for the system were to be included.

ACKNOWLEDGEMENTS

I would like to thank my NASA colleagues on the MAST project, Frank Emens and Delisa Young, who did so much to make my summer research effort at NASA productive. They have consistently offered information, direction and encouragement during my stay at Marshall Space Flight Center. Without their help, little would have been accomplished.

I also need to thank Porter Clark and David Trice who, while not directly connected with the MAST project, nevertheless offered invaluable assistance during the summer. They generously provided me with lots of much needed assistance throughout the project. Leann Thomas also provided much needed encouragement and support. Thanks also to Leslie Murphy for help with the VME bus.

Finally, many thanks go to Charlene Breazeale for her assistance with the Xerox machine and related office equipment devices and procedures. Without her help, the paperwork would never have gotten finished.

TABLE OF CONTENTS

1 Introduction	2
2 MAST System Overview	2
2.1 Network Test System	2
2.2 Provisions for Hardware and Software Testing	3
2.3 Future Expansion Capabilities	4
3 MAST System Hardware Components	4
3.1 Network Capabilities	4
3.1.1 Control Network	5
3.1.2 Test Network	6
3.2 System Computers	7
3.2.1 The Mast Control Node	8
3.2.2 Node Interface Controllers	9
3.2.3 Hardware Component Interface	10
3.2.4 Network Monitors	10
3.2.5 Gateways, Bridges and Routers	11
4 MAST System Software Components	12
4.1 Software Development System	12
4.2 MAST Network Operating System	12
4.2.1 Test Configuration and Initiation	12
4.2.2 Test Monitoring	13
4.2.3 Test Analysis	14
5 System Operation	14
5.1 Network Test Overview	14
5.2 A Hypothetical Example	16
5.2.3 Network Test Summary	18
6 Development Plan	18
6.1 System Operating Specifications Development and System Hardware Specification and Procurement	18
6.2 System Software Specification and Procurement	19
6.2.1 Networking Capability	19
6.2.2 Software Development System (SDS)	20
6.2.3 MAST Network Operating System (MNOS)	20
6.3 System assembly and testing	22
6.4 System operation and maintenance	23
6.5 Development Time Table	23
7 Conclusions and Recommendations	23

LIST OF FIGURES

Figure 1: The Marshall Avionics System Testbed.....	27
Figure 2: Node Interface Controller Hardware.....	28
Figure 3: Mast Network Operating System Software Overview.	29
Figure 4: Test Configuration Software.....	30
Figure 5: Test Initiation Software.....	31
Figure 6: Network Operation Software.....	32
Figure 7: Network Test Report Generation.....	33
Figure 8: Tentative MAST Development Timetable.....	34

1 Introduction

This report deals with the design and structure of the proposed Marshall Avionics System Testbed. This system is intended to provide a universal testbed for testing data communications networks of any type. This will include ground based networks as well as networks placed aboard space vehicles.

The testbed will provide facilities for network simulation experiments, as well as actual hardware interfaces for various types of flight and ground based hardware. NASA engineers and/or contractors can utilize the MAST facility to test proposed hardware or software components of a network. The MAST facility will provide the capacity to passively monitor network activity or to actively participate in network data transfer activities in order to stress the network to any desired level.

2 MAST System Overview

The MAST system consists of a network within a network that uses the facilities of one network to test the performance of the other network. Figure 1 indicates the general concept of the MAST facility. In addition to the two networks, there are a series of nodes that interconnect the networks in various ways.

2.1 Network Test System

The inner network is the network that is undergoing testing (TN). Due to the design of the MAST facility, only data pertaining to the network that is being tested is ever routed over the TN. Because of the generalized nature of MAST, there are few restrictions as to the topology or configuration of the TN. Bus, tree, token ring and even star type networks can be monitored and tested with MAST. The system can be reconfigured rapidly so that different types of networks can be tested in succession with minimum reconfiguration time.

The outer network is the control network (CN), and is associated with the testing and monitoring of the TN. This network is a 80 Mbps fibre optic network, and is used for all traffic pertaining to the initialization and monitoring

of tests on the TN. Because the outer network must monitor and control the TN that is transporting data at rates up to 10 Mbps, it is designed to be significantly faster ($\approx X10$) than the network that is being tested.

2.2 Provisions for Hardware and Software Testing

The nodes that connect the two networks are of several types. The most significant node is the MAST Controller Node (MCN). This node provides facilities for MAST system software development, as well as providing the capabilities to initiate and monitor network tests for purposes of system software development. This node can be accessed through the system console, ten RS-232 ports or through an IEEE 802.3 (Ethernet) interface. In order to preserve the integrity of test results, system test operations must be initiated and controlled from the system console. Whenever a system network test is not in progress, the software development facilities are available.

A number of network interface controllers (NIC) comprise the remainder of the nodes that connect the network. These NIC nodes fall into three general classes which are:

- Hardware Interface Nodes
- Node Emulation Units
- Network Monitor Nodes

The hardware interface nodes are used to interconnect various types of non-network hardware to both the TN and the CN. There are nodes with provisions for both digital and analog input signals. These NIC's are programmable, and can format the input data into the appropriate protocol for the network under test.

The node emulation units provide the capability for emulating any type of unit that might be connected to the TN. By using appropriate emulation units, the equivalent of a full network system can be provided in order to establish a test environment for a new node without the expense of providing a full hardware mock-up of the TN. In addition the node emulators can be used to run tests on network parameters without any actual network hardware in place.

The network monitor modes provide the capability to monitor the TN. These can be operated in an entirely passive (spy) mode that will induce no traffic on the TN,

since all the monitor traffic will be routed over the CN. One monitor can also be operated in the active (probe) mode. In this mode, the monitor is used to induce traffic onto the network so that the performance of the network in response to this traffic can be monitored. The active monitor node can also be used to generate traffic volumes that will stress the network toward its upper limit capabilities. The active monitor can generate intentional errors and emulate a malfunctioning node by losing tokens, generating collisions, etc.

2.3 Future Expansion Capabilities

All the components of the mast system are designed so as to permit easy and quick modification of the system. Different types of TN interfaces can be configured from the MCN by down-loading software from the MCN to the appropriate NIC's. The NIC's can also be added to or removed from the TN under software control. Additional hardware interfaces can be connected to the TN by attaching these units to hardware interface nodes that are in place on the network and by loading these NIC's with appropriate software from the MCN via the CN.

It is, in fact, possible to have several hardware networks physically present in the MAST system at one time and to operate these separate networks under completely independent test conditions. Of course, only one network can be tested at a time without affecting the traffic flow, but since the system can be reconfigured by simply down-loading different software, this restriction should not constitute a major problem.

Due to the modularity of the MAST design, any of the components of the system can be replaced without having an adverse effect on the system. Nodes can be added or deleted as desired. The network under test can be changed as needed. If future needs dictate, the CN could be replaced with a faster model, such as FDDI. Even the MCN can be replaced if that were to be considered desirable.

3 MAST System Hardware Components

The MAST system hardware consists of several microcomputers that are connected between two or more physical networks. One of the networks is the TN, while the other is the CN. The microcomputers serve as nodes interfaces and node emulators on the TN.

3.1 Network Capabilities

As already mentioned, the network capabilities of the MAST system are considerable. The CN is used to initialize and monitor test experiments on any of a number of TNs. The dual network capability relieves the TN from the responsibility for transporting test configuration and metrics information, and avoids inducing monitoring artifacts onto the TN.

3.1.1 Control Network

The CN is the basis of the MAST system. It is currently configured as a 80 Mbps, bi-directional, counter-rotating, fiberoptic Proteon ProNet 80 network. The speed of this network is roughly an order of magnitude faster than any network likely to be tested by MAST in the near future. This high speed allows for the collection and transmission of network metrics from the TN in real time.

The CN consists of a hardwired configuration that is likely to remain static over relatively long periods of time. Nodes may be added to or deleted from the CN as needed, but this type of modification is relatively uncritical with respect to time. Such modifications are not likely to take place while tests on the TN are in progress.

The CN provides the medium that permits the performance of four essential functions of the MAST system:

- Initiate the system from a cold start
- Configure the network prior to testing
- Monitor the network during testing
- Reconfigure the test network during testing

System initialization from a cold start is a mundane but necessary function. Power failures and system maintenance will require an occasional cold start. When the MCN is initially powered-up, the MAST system will have to be initialized. This will require configuring the MCN itself, and also configuring the individual NIC's. The software to configure the NIC's will be transmitted from the MCN to the NIC's via the CN.

Configuration of the TN prior to testing consists essentially of down-loading selected software modules to the NIC's, over the CN. The software modules that are down-loaded will determine the configuration of the network under

test. For this operation, the high speed of the CN is not essential, but does contribute to the capability to reconfigure the system after one test in preparation for another test. With the appropriate test hardware already in place, reconfiguration of the system for other tests should require minimal time.

During the test phase, the CN can be used to pass TN performance metrics to the MCN. This capability permits a less expensive network monitor than would otherwise be possible, because the monitor node does not require data storage capabilities. Depending on the test, the monitor node can distill the data and forward only descriptive statistics to the MCN. The speed of the CN makes it possible for the NIC to forward raw data directly to the MCN if desired, however.

During an active test run, the MCN can transmit control data to the passive monitor NIC as needed. The MCN can, for example, wait for certain events to happen before instructing the monitor NIC to begin observing the network traffic. The MCN can also discontinue monitoring at any desired point during the test.

In the case of the active (probe) monitor, the MCN can initiate a number of node malfunction operations by downloading software and/or instructions to the probe monitor NIC. These malfunctions could include a simulated dead node, continuous or an unusually high frequency of transmissions from a node, loss of token, duplicate tokens, intentional collisions, etc. Software to control these operations would be down-loaded to the probe monitor NIC via the CN, and be activated and disabled by the MCN via the CN.

During a test, the CN can also be used to permit the MCN to reconfigure the TN on-the-fly while a test is in progress. This would permit the simulation of stations dropping off the network or being added to the network in real time. This capability would be especially useful for simulating the operation of the network of a multi-stage space vehicle, where stage separation results in a planned, but nonetheless radical changes in the topology of the TN.

3.1.2 Test Network

While the CN is relatively fixed in topology and structure, the system is designed so that the TN can be varied at will. Each NIC serves as a connection between the

CN and one other network. The CN will remain more or less permanently connected to a number of NIC's. Each NIC is then in turn connected to one or more other networks that are to serve as a TN.

The operation of each NIC is controlled by the MCN by means of the software that is down-loaded from the MCN to the NIC. Each NIC can be loaded with software that will activate that node onto the TN as needed. Alternatively, any NIC can be loaded with software that will cause that node to remain inactive during any specific test. By enabling or disabling various NIC's, the operation of the test node can be controlled directly from the MCN.

With this software reconfiguration capability, it is possible for there to be several TNs physically in place at one time. By selectively activating the appropriate nodes, the TN can be changed very rapidly. This not only allows changing the structure of a particular type of network, but even permits changing the TN from Mil-Std-1553 to MAP to Ethernet, etc.

MAST hardware is currently provided to configure the TN into any of several standard networks. These include MIL-STD-1553, MAP and Ethernet. NIC's for other networks can be added to MAST as needed.

The Mil-Std-1553 network is a popular network for use in avionics systems. This network was developed by the UASF, and is a primary/secondary type bus network. The primary station polls secondary units that then have the opportunity to transmit data to the primary or another secondary unit.

The MAST hardware currently supports 15 NIC's that will each connect to two separate Mil-Std-1553 busses. Since there is some common circuitry in the two circuits, both 1553 networks cannot be operational at the same time.

The Manufactures Automation Protocol (MAP or IEEE 802.4) network was developed for use in manufacturing environments. This is a token bus network that has the advantage of insuring that a node with data to transmit will eventually have an opportunity to do so. The network operates in a fashion similar to a token ring network except that the physical interconnection between nodes is a bus topology. The token is passed in a ring fashion, but the

ring exists only in the order of token passing determined by software.

The MAST hardware currently has two NIC's that can be configured as MAP network nodes. Additional units can be added as needed.

The Ethernet (IEEE 802.3) is a Carrier Sense Multiple Access/Collision Detection (CSMA/CD) network. It has a bus or tree topology, and is probably the most widely used network in the world today. The network provides each node with an equal opportunity to access the bus. When a unit wants to transmit a message, it waits for an idle bus and then transmits. If two units attempt to transmit at the same time, a collision occurs. In this case, both nodes stop transmitting and try again later.

The MAST system has provisions for two NIC's with an interface to Ethernet. These nodes provide an interface for network testing. There is an additional 802.3 interface on the MCN, but this interface is intended primarily for use during software system development. It could, however, be used to interface to the TN (802.3) if desired.

The generic NIC unit is easily interfaced to any other potential TN. As will be explained below, the cpu and CN interface are standard to all NIC's. To provide an interface to any other network, only the interface from a VME bus to that specific network would have to be added. This would include token ring networks and all types of proprietary vendor specific networks.

There are currently no NIC units configured for networks other than the three discussed above.

3.2 System Computers

The basis of the MAST system is the MAST Control Node (MCN) and a number of Node Interface controllers (NIC). Each of these components consists of a microcomputer system dedicated to the specific task assigned to each node. Each microcomputer is independent and self-contained, including rack, card cage and power supply. In the interest of standardization for software development, all microcomputers are based on Motorola 680xx microprocessors.

3.2.1 The Mast Control Node

The MCN is the heart of the MAST system. The MCN provides the facilities for two essential tasks associated with the MAST system. It serves as a software development environment for producing the software needed for the operation of MAST during system tests. It also provides the software needed to initiate, monitor, terminate and report the results of all network system tests. The software development facilities are provided through the operating system of the MCN computer itself. The test facilities are provided through the a MAST Network Operating System (MNOS).

The MCN is a Heurikon model # HSE/17 digital computer with a Motorola 68030 processor, 4 MBytes of main memory in a VMEBus cage. The computer has a 80 MB hard disk, a 1.2 MB floppy disk drive and a cartridge tape system. There are interfaces for a system console, an Ethernet connection and ten RS-232 connections. Users may interface to the software development system either via the ten RS-232 ports or via the Ethernet interface.

3.2.2 Node Interface Controllers

The Node Interface Controllers (see Figure 2) consist of a several separate interface controllers that are interconnected to the MCN through the CN. All MAST NIC nodes contain some common hardware, with variations only in the interface to the TN associated with that node. The common hardware includes a VMEBus card cage with power supply, a Heurikon Model HK68D/V2F 68020 based microcomputer printed circuit card with a separate system controller board. Limited system software is provided in EPROM for each node to facilitate assembly of the system.

Each node is also equipped with a ProNET interface to the CN. This interface consists of a Proteon 1580 control card, a Host Specific VME interface and the Proteon 3280 fiberoptic interface controller. This results in a total of four VME cards in each NIC card cage.

In addition, each node contains appropriate interface cards for the network to which the node in question is to be

interfaced. These network specific cards are one of the following:

For Mil-Std-1553: BUS 65502 card
For MAP : MVME 272 and MVME 371FA cards
For Ethernet : Excellan LC-302 card

It would be possible for a single node to contain an interface to more than one TN, but such a configuration would probably not be cost effective. The interaction between the traffic on two different networks would make the analysis of network performance very difficult.

3.2.3 Hardware Component Interface

For a node that is to function in a node emulation mode, only the modules outlined above will be used, depending on the network under test. When a hardware component is to be interfaced to the network, additional translator cards will be utilized.

For a digital network interface, Data Translation DT 1417 card can be used to interface up to four eight-bit ports onto the VME bus and thence to the network. For analog signals, a similar DT 1414 board provides 16 analog to digital (A/D) channels, and also has 16 programmable digital inputs. In either case, the NIC computer reads the input data as required and packages the data for transmission on the TN.

3.2.4 Network Monitors

A critical function of the MAST system is the capability to monitor network traffic while the network test is in progress. This function is accomplished through special network monitors. A network monitor is a node that has been modified so as to respond to all traffic on the network, not just the traffic addressed to a particular node. Such monitors will observe traffic on the network, and keep records relating to the performance of the network.

A standard NIC node will require hardware modification in order to perform as a monitor. Specialized software will also be required for the monitor nodes. There will have to be one modified network interface monitor for each TN that is to be monitored. Since only one network test will be active at any one time, all these interfaces can be

installed in a single NIC that is dedicated to the network monitor function.

The passive monitor will simply observe the TN without itself actively participating in the traffic on the TN. That is, it observes and records traffic, but is neither the source or destination for any network traffic. The monitor function may be started, suspended or stopped by messages sent to the monitor from the MCN over the CN. Data collected by the monitor may be transmitted directly to the MCN as raw data, or the monitor may be programmed to forward only statistical data to the MCN. The monitor can observe all traffic, or only a selected subset of traffic as determined by the needs of the user.

A probe monitor can also be configured from the NIC hardware discussed above. In this case, the monitor is active in the traffic on the network. The probe monitor will introduce traffic onto the network and then observe the effects of this traffic. Some types of data cannot be collected by a passive monitor, and must be collected by a probe monitor. For example, only a probe monitor can determine the average time delay in acquiring network facilities for the transmission of data.

The probe monitor can also be used to stress the network to any desired level. By generating a high volume of spurious traffic, the effects of this traffic on the throughput of traffic from other nodes can be observed. Probe monitors can also generate intentional errors and interference on the network if desired.

3.2.5 Gateways, Bridges and Routers

Since each node in the MAST system has a hardware interface to two networks, the capability is present to program any node to perform as a bridge, gateway or router. By adding the appropriate software, any node could perform any of these functions. This means that a bridge between ProNET 80 and either Mil-Std-1553, MAP, or Ethernet represents would be relatively easy to implement. Such utilization of a node would, however, dedicate that particular node to the bridge, gateway or router function, and would prohibit its use during MAST tests.

A more interesting possibility would be to utilize a node with two different network interfaces along with a ProNET interface. This configuration would provide a bridge

between the two networks in question, and permit monitoring the traffic on two different networks simultaneously. With proper programming it would also permit the collection of performance metrics of internet traffic between the two networks.

4 MAST System Software Components

There are two major components of the MAST system software. These components are the Software Development System and the MAST Network Operating System.

4.1 Software Development System

The software development system is a relatively standard UNIX operating system environment that provides the software tools for developing the modules required for the MAST Network Operating System (MNOS) as described below. Facilities provided include a compiler for C that generates code that can be down-loaded to the NIC's. There is also a 68030 assembler, a linker, a debugger and various device drivers. FORTRAN and Pascal compilers can be added later.

All the system development software is accessible through the ten RS-232 ports or the Ethernet interface on the MCN. The development system is available at any time that a network test is not in progress. The advisability of using the software development system while a network test is in progress requires further investigation.

4.2 MAST Network Operating System

The MNOS is the heart of the system testbed. The MNOS will permit the configuration of a network prior to a test by down-loading appropriate software to the NIC's. MNOS will initiate the test by activating the software within the appropriate NIC's. During the test, performance metrics will be collected. After the test, MNOS will make the data relating to network performance available for analysis.

An overall chart of the structure of the MNOS is included in Figure 3. This figure depicts the general interrelationship between the components of the system. To the maximum extent possible, MNOS is a menu driven system with graphical displays of TN configuration, operation and performance.

4.2.1 Test Configuration and Initiation

The test configuration section (Figure 4) of the MNOS allows the user to establish the software environment to configure the network on which the test is to be conducted. Prior to this stage, all hardware components must be in place. Note that all NIC's are permanently attached to both the CN and TN. Only hardware units that are to undergo testing would have to be added to the basic testbed.

The test configuration section permits the user to specify the type of network (Mil-Std-1552, MAP or Ethernet) to be tested. The NIC's that are configured for interface to the TN will then be marked as available for test use. All other NIC's will be disabled by software.

From the available nodes, the user may then choose any combination of hardware interface nodes and software emulation nodes. Appropriate software is down-loaded to insure that the selected nodes perform in the desired manner. Any unneeded nodes are disabled by software.

The user can select the number and types of network monitors that are to be used during the test. The user also specifies the type of metric information that is to be collected during the test, and when the information is to be collected. Probe monitor parameters may also be set during configuration of the network.

When the network is fully configured, the test is initiated (Figure 5). During the initiation, parameters relating to the test, such a length of test, abnormal termination criteria, etc. are established. The MCN then signals all NIC's to begin the test operation.

4.2.2 Test Monitoring

While the network test is in progress, the MCN will present the user with selected real time system operation statistics (Figure 6). The user will be able to select from several graphical displays that contain the network operating characteristics. The user can monitor the overall operation of the TN and terminate or modify the test if that appears desirable.

The user will also be given the opportunity to interact with the network nodes in real time. For example, the user can disconnect nodes from the network or add new nodes to

the network. The user can also modify the monitor data collection instructions or command the probe monitor to change operating modes.

4.2.3 Test Analysis

After the test is completed, the user can review the statistics that were collected by the MCN during the test (Figure 7). The user has the choice of access directly to the raw data, or may choose from several levels of distilled data. In order that data from one network test can be analyzed while another test is in progress, the test results will be available in hard copy and also from the test data base via the software development system facilities. Adequate statistical routines will be available to permit analysis of the results.

5 System Operation

The basic purpose of MAST is to provide a generalized testbed that will permit the testing of network components. The most common test would probably consist of testing a single hardware unit that is to be added to an existing network in order to evaluate the effectiveness of the unit and its effect on network performance. In many cases, however, it may be desirable to run a test on the characteristics of the proposed hardware device through the use of a software emulation module that will mimic the predicted performance of the hardware prior to testing the hardware interface itself.

It is also possible to test a completely new network design using either emulation nodes or actual hardware interfaces for all the nodes on the proposed network. MAST provides the capability to take an existing network configuration and modify the network protocols to determine the effects that different protocols would have on network performance. Being completely general, MAST also permits varying the number of elements in a network as well as evaluating different priority schemes for the elements.

5.1 Network Test Overview

The user begins a test from the MCN console. From the initial menu, the user chooses to enter the test configuration section of the software. At this point, the user may define the hardware and software emulation

components that will constitute the elements of the network that is to be tested.

When the user enters the network configuration section, the TN defaults to a null network with no nodes. Through a series of questions and responses, the user can configure any type of network (Mil-Std-1553, MAP or Ethernet) that is desired. From all the NIC's available, The MCN configuration software will then select only those nodes that interface to the network type selected. All other NIC's are disabled.

If the user has one or more nodes that contain a network interface to external hardware, these nodes are specified next. When the user dedicates a node to a hardware interface node, an absolute NIC address must be provided for that node so that the MCN can match the downloaded software to the hardware attached to that NIC. As nodes are added to the configuration, the network configuration data will be updated to indicate the presence of all such nodes connected to the TN.

After hardware interface nodes (if any) are selected, the software emulation nodes (if any) can then be specified. With software emulation nodes, the user needs only to specify the type of node that is to be emulated, and the appropriate software for this node will be down-loaded to any available NIC.

After all operating network nodes have been specified, the monitor requirements for the test in question are specified. Monitor specification includes both passive (spy) nodes and active (probe) monitors. The amount and type of data that is to be collected from the network is indicated as the monitor nodes are specified.

Once the configuration of the TN has been established, the user can enter the test initiation section of the MNOS. At this point the user will be given options as to the start time of the test operation, the length of the test and other parameters. When all the parameters are set, the test can begin.

When the test operation begins, the user can view performance statistics on the MCN console. This will include graphical displays of network performance. The user will be given the option of selecting any of several different screen displays that present various network

performance statistics. The user can also interact with the TN to dynamically alter the topology and configuration of the network while the test progresses. The user can also terminate the test or extend the test duration from the MCN.

When the test terminates, the user will have access to the data that was collected by the monitor nodes during the test operation. This data can be analyzed to determine system performance during the test. The data analysis phase will be conducted through the software development system facilities rather than through the MCN.

5.2 A Hypothetical Example

Perhaps the easiest way to get a general understanding of the operation of MAST is to consider a simple example that will reflect most of the options available for a MAST test. In this example, we assume that a new hardware device is to be tested for inclusion on an already existing Mil-Std-1553 network.

For our example, we assume that the existing network contains an engine health monitor (EHM), several transducers, several sensors and a flight controller. This network has been tested previously, and there are existing software emulators and hardware interface modules stored in the MAST module library. Network configuration information is also already stored in the library. The purpose of the test is to evaluate the effectiveness of an new improved EHM that is to replace the old EHM.

In most cases, it will be desirable to model the predicted behavior of the new EHM through a software emulation module before the actual hardware for the EHM is begun. In this situation, the initial step would be to develop a software module to model the expected behavior of the new EHM. This module could be fairly realistic with respect to the volume and type of traffic that would be generated by the new EHM.

In performing the emulation test, the test conductor would first load the old network configuration from the MAST library. This configuration would then be modified by deleting the old EHM emulator and replacing it with the new EHM. A complete test would be run using emulation modules for the entire network or by using a mixture of emulation modules and previously tested hardware interface controllers.

After the emulation module tests indicate that the new unit is operating satisfactorily, the experiment would proceed to test the proposed hardware itself. In some cases, the emulation test might be skipped and the test would begin directly with the hardware interface.

For a hardware interface test, the first step would be is to develop the software to interface the new EHM to the network. This software is designed to read the digital and/or analog inputs from the EHM hardware and format the input data into the appropriate protocol for the network being used. This data is placed onto the network in accordance with the contention algorithms used by the network in question.

When any component is replaced in a test configuration, it is also likely that the monitor parameters will need to be modified. In the example in question, all the system components except the new EHM have already been tested, and can be assumed to be operational. Collecting data on these units would probably be unnecessary. The performance characteristics of the new EHM are unknown, however, and the monitor might need to be instructed to observe and record all traffic to and from the new EHM node. At the same time, general network data such as number of messages carried, number of collisions, average message length, etc., might also be collected in order to assess the effects that the new EHM may have on the network as a whole.

After the network is configured, the user enters the test initiation phase. Here the start and stop time for the test is established. These time can be clock time, or network events. For example, if the new EHM was in the first stage of a flight vehicle, the test could begin at the initiation of the countdown sequence and end with separation of the first stage. Both these events could be identified from network traffic.

During the test, the user would monitor the operation of the new EHM by selecting to display on the console a summary of messages to and from the EHM. Alternatively other displays of network traffic could be viewed as desired.

After the test is completed, the user can leave the MCN and examine the test statistics from one of the terminals in the software development system. Modifications can be made to the emulation module and/or the hardware interface module

if desired, and the test can be repeated with different parameters.

5.2.3 Network Test Summary

In performing network tests, the MAST system can perform two basic operations on any of three (or more with new hardware) networks. These experiments consist of testing a node emulation module or a node hardware interface. With any number of nodes possible, and with three different network interfaces permanently connected, there is an almost unlimited number of test configurations that can be established on the MAST system.

In addition, the network parameters, such as packet length, token hold time, backoff algorithms, etc., can also be tested. Hence, the MAST system provides the capability to perform almost any conceivable network test or experiment. Further, the experiments can be configured and executed with minimum set-up time between different experiments.

6 Development Plan

The development of the MAST system can be divided into roughly five phases. These phases are somewhat interdependent, and overlap to some extent. The major phases are:

- System operating specifications development
- System hardware specification and procurement
- System software specification and procurement
- System assembly and testing
- System operation and maintenance

The development of the MAST system is already in progress. The system operating specifications have been developed, and most of the hardware specifications have been completed. Much of the hardware for MAST has been procured and is already in place in EB33.

There are two major tasks remaining before the MAST system can enter the operational phase. These tasks are: software specification and procurement, and system assembly and testing.

6.1 System Operating Specifications Development and System Hardware Specification and Procurement

As noted above, the majority of the operating specifications for the MAST system have been completed. Minor revisions to accommodate omissions and corrections will still be necessary, but the major work is completed.

In addition, the system hardware specifications are complete. The MCN and NIC device specifications have been determined, and the equipment procured. The ProNET 80 hardware is also in house, as well as a number of interface components for the three initial TNs. Minor components remain to be fabricated or procured, but, in general, the hardware for MAST is in place.

6.2 System Software Specification and Procurement

By far the largest task remaining in the MAST program is the development of the specifications for and the procurement of all the software required for the testbed. This includes the development of the MNOS as well as the emulation and hardware interface modules, the monitor software and the statistical routines for the test result analysis.

6.2.1 Networking Capability

The networking capabilities required for the MAST system are extensive. Each NIC will have to interface to two different networks. A survey of current literature reveals little or no information on this type of dual ported network nodes. Of course, there are bridge and gateway systems that interface to two networks, but these are an order of magnitude less complex than the MAST NIC's will be. The development of software to control access to two heterogeneous networks will present an interesting challenge.

The software will have to interact with both networks simultaneously. During major portions of the test, the operation of the CN will be invisible to the NIC, but under special circumstances, the NIC will have to recognize and respond to commands from the CN while maintaining full operation on the TN. This implies the extensive use of interrupt facilities on the NIC hardware.

During test configuration there will have to be extensive down-load capability built into the CN. It will be essential for the MCN to be able to control the operation of each NIC. This includes up-loading and down-loading of software, initiation of test runs, network reconfiguration in real time and premature termination of tests.

The equipment on hand for MAST varies greatly in the type and amount of software provided by the vendor. MAP interface boards come with the full seven level OSI protocol, at least according to the supplier. The ProNET 80 boards, on the other hand, require software interfacing at the register and buffer manipulation level. Software for other boards lies somewhere between these levels. It will be a significant undertaking just to get all the interfaces to all these different networks operational at some common user- acceptable level.

6.2.2 Software Development System (SDS)

Most of the software for the SDS is already in place. This software was purchased as an option with the UNIX operating system for the MCN. The software contain a C compiler, an assemblers, linkers, debuggers, device drivers, etc. Unless a more user-friendly environment than UNIX is desired, this software should suffice for most software development operations.

Since it is desirable to have the data analysis software available from any SDS terminal rather than just from the MCN, some sort of interface to the test data storage will have to be made available from the SDS. This could be anything from a locally written system to a statistical package such as SPSS or a simple data base program. The requirements for this program are currently unspecified.

6.2.3 MAST Network Operating System (MNOS)

Developing the software for the MNOS offers an interesting challenge. The software required ranges all the way from a very high level operating system user interface (MNOS) itself all the way down to some rather primitive register manipulation procedures in the hardware interface modules. Not only does the development of the software present an interesting challenge, but the prospect of having up to 18 network nodes, two monitor nodes and the MCN

operate in harmony over two different networks simultaneously adds to the complexity of the task.

MAST will require all the features and facilities normally associated with computer network operations, but will require everything four times over for the four different networks used on the system (the CN and three TNs). Even utilizing Internet Protocols (IP), the task will be formidable. At some point, NIC's will be used as bridges and gateways, and MAST will evaluate the effectiveness of internet communications operations. Monitoring these bridges and gateways will present another opportunity for exciting software development.

6.2.3.1 Test Configuration Section

The test configuration section is software that is unique to the MAST system, and will have to be written specifically for the MAST system. The driver portion of the software will be the user interface to the set-up of a network experiment. The program will be utilized by users that are generally unfamiliar with the overall MAST system, and will therefore have to be robust and easy to use.

The configuration software will have to be menu driven, and if possible should have graphics capabilities. The user should be able to select options from various menu lists in order to configure the network to be tested. The graphics capability would be beneficial in displaying the configured network for inspection and modification.

As a part of the configuration section, the various modules associated with the NIC nodes must be available. This includes the hardware interface modules and the software emulation modules. Development of the software emulation modules will represent a sizable software engineering task. There will have to be software modules to emulate the performance of any component that might be placed on the network. This includes engine health monitors, transducers, sensors, flight controllers, RF data links, etc. Such simulation modules will have to be developed for many different kinds of the same devices, since the performance will vary from one contractor to another.

Hardware interface modules will have to be developed for any hardware that is to be interfaced to a TN. A few of these may need to be developed initially as generic

interfaces, but in general, these will be one of a kind interfaces that will have to be developed as they are needed. Since each interface is specific to the hardware involved, it is likely that the MAST user will develop these interfaces as they are needed for a specific test.

6.2.3.2 Test Parameter Initialization

The parameter initialization section of MNOS permits the user to specify the specifics of a single network experiment after the configuration of the network has been established. Software will have to be written that will interact with the user as the experiment parameters are entered. This software should also be developed as menu driven software.

There should be provisions for setting abnormal test conditions that will halt the test, and also for setting network "breakpoints" that will permit stopping the test at certain points for observation of the status of the network.

6.2.3.3 Test Operation and Monitoring

During the actual test, the MNOS software will be required to monitor the operation of the network and display summary data to the user. This software must also provide interactive capability to modify the test parameters while the test is in progress. The software will receive data from the monitor nodes and dispatch commands to all nodes via the CN.

6.2.3.4 Metric Collection and Statistical Analysis

While the test is in progress, the software in the monitor nodes will collect and store network performance data. As necessary this data will be transferred to the MCN over the CN for storage on disk. Parameters to control the data collection are specified as the test is initiated, but can be changed as necessary during the test operation. Data is stored for analysis later under facilities provided in the software development system.

6.3 System assembly and testing

The MAST system hardware is to be assembled and initial software development initiated in the very near future. Since the building that will eventually house the MAST system will not be completed until 1991, the assembly

process will be in two or three phases. The initial phase will assemble the MCN and two or three NIC's in room B-240 of building 4487. The final phase will occur when the MAST system is moved to its permanent location in a new building proposed for that purpose.

Depending on the completion date of the new building and progress made in developing software during the first phase, a second phase may be necessary. In this case, a secondary location in building 4487 will be used to set up a more complex MAST development system consisting of about ten nodes plus the MCN. A location in A wing of 4487 has been tentatively identified for this purpose.

6.4 System operation and maintenance

Once the system is developed, operation and maintenance will begin. Operation of the testbed will normally be under the direction of the organization that wishes to test a network of a specific network node or interface. Development of specialized software for the interfacing of specific hardware devices will probably remain the responsibility of the organization proposing the hardware.

Software emulation modules will have to be developed for a wide variety of devices that will need to be emulated on the network. Development of these modules will probably remain the responsibility of the organization operating the MAST facility. It is reasonable to assume, however, that users of the MAST system who develop emulation modules in the normal process of testing their own designs will make such modules available to other MAST users through the NOS library.

6.5 Development Time Table

A very tentative time table for the development of the MAST system is included in Figure 8. Tentative completion time is December 1991. The software development and system testing will occupy the majority of the project time.

7 Conclusions and Recommendations

The preliminary specifications for the MAST system are essentially complete, and the majority of the hardware is in place. Some preliminary hardware tests have been conducted this summer. The hardware chosen appears to be appropriate

for the task specified, and seems to operate at the specified levels.

Software development has not yet been initiated. Due to the complexity of the undertaking, and due to the fact that there is little current literature relating to a testbed as complex as MAST will be, there is a significant software development task ahead. System programming should not begin until such time as system software specifications have been completed.

The design of the software component of the MAST system needs to be addressed in the very near future in order to insure a timely development of the entire system.

REFERENCES

- Frank Ingles, John Owens, Stephen Daniel, F. Ahmad, and W. Courrellion, "A Study of the Marshall Avionics System Testbed, Final Report, Phase 1", Electrical Engineering Department, Mississippi State University, Sept 30, 1989.
- D. Jakobson, S. Gaitonde, J. Kim, J. Lee, D. Rover, M. Sarwar, M. Shafiq, "A Master/Slave Monitor Measurement Technique for an Operating Ethernet Network", IEEE Network, Vol. 1, No. 3, pp 40-48, July, 1987.
- David C. Wolfe, Jr., "Baseband Emulators for the Protocol Testing of Multimedia Communications Networks", IEEE Network, pp 8-13, November, 1988.
- Lillian N. Cassel and Paul D. Amer, "Management of Distributed Measurement Over Interconnected Networks", IEEE Network, Vol. 2, No. 2, pp 50-55, March, 1988.
- Howard Salwen, "How to Get Ready for FDDI", Proc. 1987 IEEE 12th Conference on Local Computer Networks, pp 12-13, 1987.
- Ilan Kolnik and Joseph Garodnick, "First FDDI Local Area Network", Proc. 1987 IEEE 12th Conference on Local Computer Networks, pp 7-11, 1987.
- Larry Green, "Planning for FDDI", Proc. 1987 IEEE 12th Conference on Local Computer Networks, pp 4-6, 1987.
- William M. Seifert, "Bridges or Routers", Proc. 1987 IEEE 12th Conference on Local Computer Networks, pp 118-129, 1987.
- John Hart, "Extending the IEEE 802.1 MAC Bridge Standard to Remote Bridges", IEEE Network, Vol. 2, No. 1, pp 10-15, January, 1988.
- Floyd Backes, "Transparent Bridges for Interconnection of IEEE 802 LANs", IEEE Network, Vol. 2, No. 1, pp 5-9, January, 1988.
- Michael Soha, "A Distributed Approach to LAN monitoring using Intelligent High Performance Monitors", IEEE Network, Vol. 1, No. 3, pp 13-20, July, 1987.

- Dick C. A. Bulterman and Eva Manolis, "Application Level Performance Prediction Tools for Network-Based Systems", IEEE Network, Vol. 1, No. 3, pp 6-12, July, 1987.
- R. Aronoff, K. Mills, M. Wheatley, "Transport Layer Performance Tools and Measurement", IEEE Network, Vol. 1, No. 3, pp 21-31, July, 1987.
- Donna Ritter and Marilyn Seale, "A Multi-Purpose, Distributed LAN Traffic Monitoring Tool", IEEE Network, Vol. 1, No. 3, pp 32-39, July, 1987.
- B. Lewis Barnett, III, Kanishka Abeynayake, Mirosław Malek, "LANCET: Local Area Network Comprehensive Evaluation Tool", Proc. 1988 Computer Networking Symposium, IEEE Press, pp 340-347, 1988.
- B. Lewis Barnett, III and Michael K. Molloy, "The Local Area Network Testbed", Technical Report TR-85-25, Department of Computer Sciences, University of Texas at Austin, May 1985.
- John McConnell, "Internetworking Computer Systems", Prentice Hall, New Jersey, 1988
- William Stallings, "Data and Computer Communications", second edition, Macmillan Publishing Company, New York, 1988.
- Andrew S. Tannenbaum, "Computer Networks", second edition, Prentice Hall, New Jersey, 1988.
- Excellan Inc., "EXOS 302 Intelligent Ethernet Controller for VMEBus Systems Reference Manual", Publication Number 4200090-00, Excellan, Inc. 1988.
- Motorola, Inc. and VMEBus International Trade Association (VITA), "VMEBus Specification Manual, Revision C1", Motorola, Inc. and VMEBus International Association, Oct 1985.
- Proteon, Inc., "ProNET Model p1580 VME Local Network System Installation and Programming Guide", Proteon, Inc., Westborough, MA, April 1986.
- Proteon, Inc., "ProNET Model p3280 ProNET-80 Counter-Rotating Ring Fiberoptic Interface Installation and Operation Guide", Revision A, Proteon, Inc., Westborough, MA, June 1988.

Heurikon Corporation, "Heurikon HK68/V20 (Including HK68/V2F and HK68V2FA) User's Manual", Heurikon Corporation, Madison, WI, May, 1988.

Heurikon Corporation, "Heurikon Hbug Monitor User's Manual", Revision D, Heurikon Corporation, Madison, WI, Oct., 1987.

IEEE Standards Board, "An American National Standard IEEE Standards for Local Area Networks: Token Ring Access Method and Physical Layer Specifications", 1985.

IEEE Standards Board, "An American National Standard IEEE Standards for Local Area Networks: Carrier Sense Multiple Access with Collision Detection (CSMA/CD) Access Method and Physical Layer Specifications", 1985.

IEEE Standards Board, "An American National Standard IEEE Standards for Local Area Networks: Logical Link Control", 1984.

IEEE Standards Board, "An American National Standard IEEE Standards for Local Area Networks: Token Passing Bus Access Method and Physical Layer Specifications", 1984

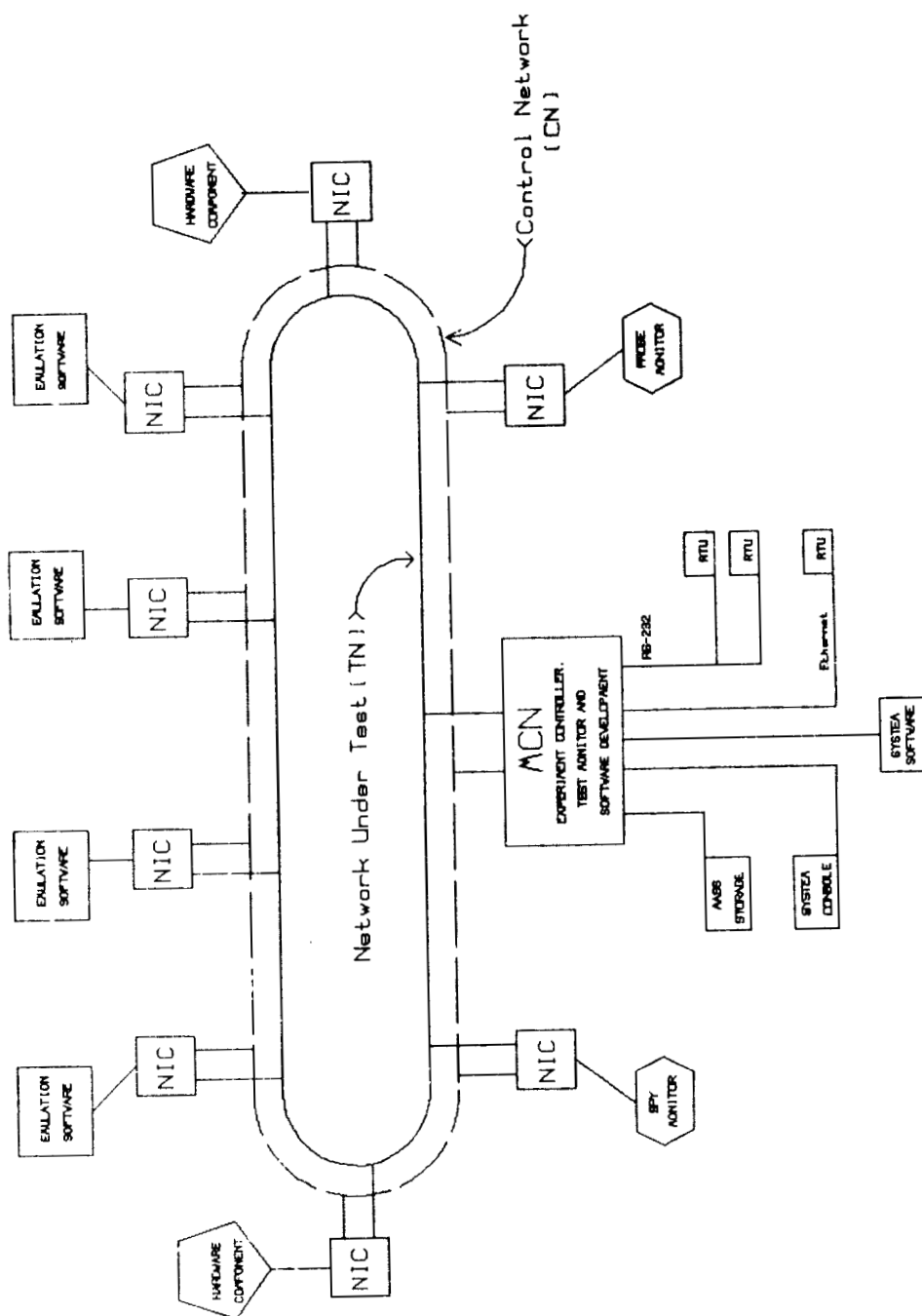


Figure 1: The Marshall Avionics System Testbed

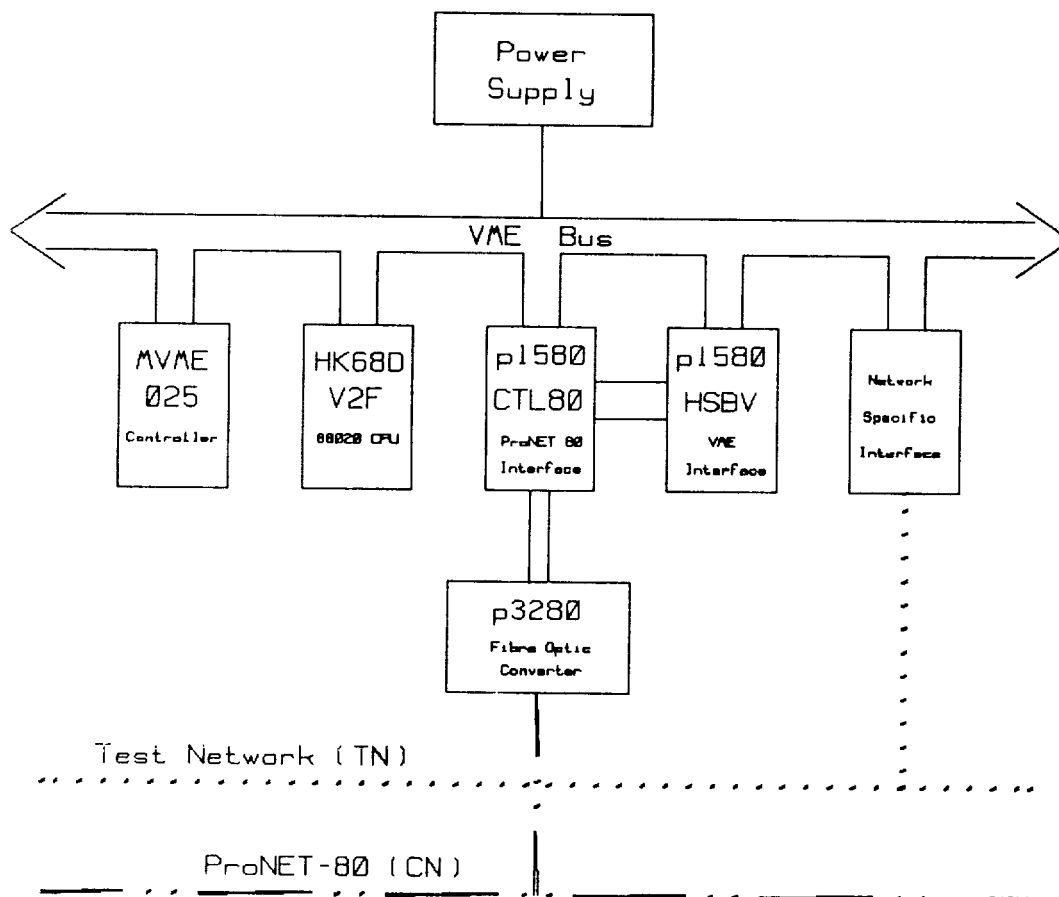


Figure 2: Node Interface Controller Hardware

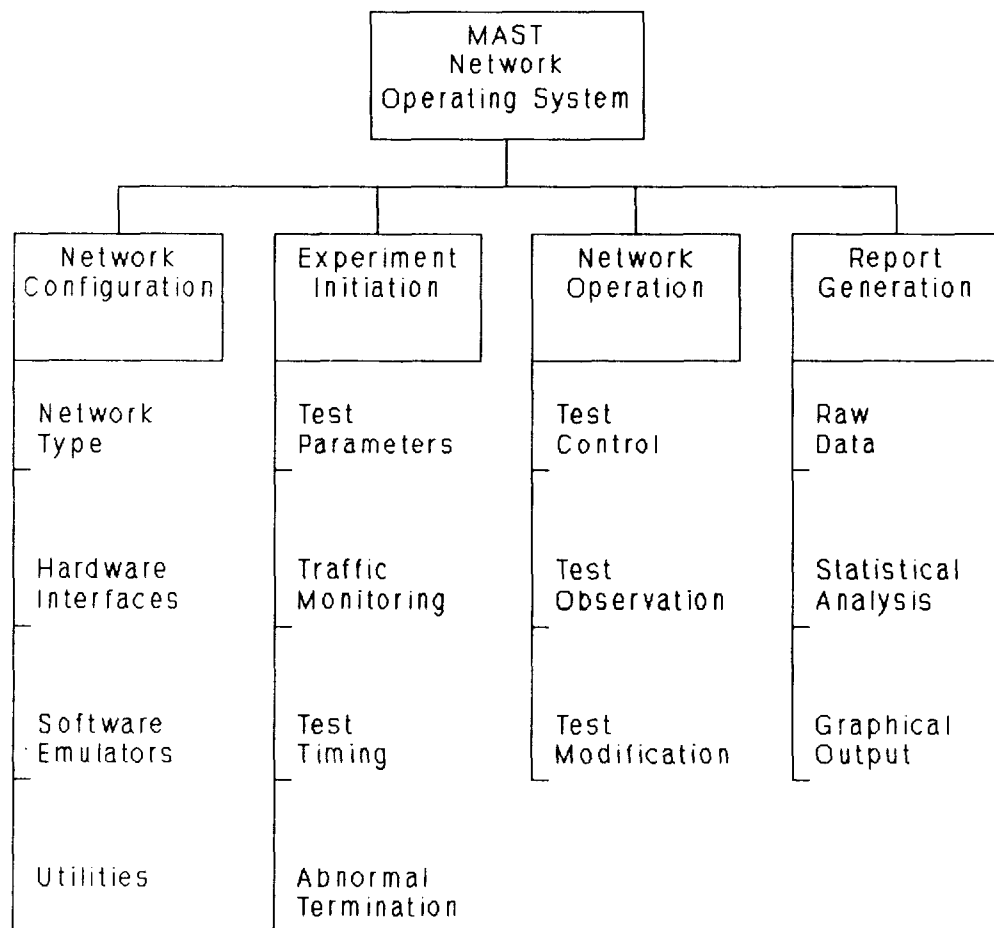


Figure 3: Mast Network Operating System Software Overview

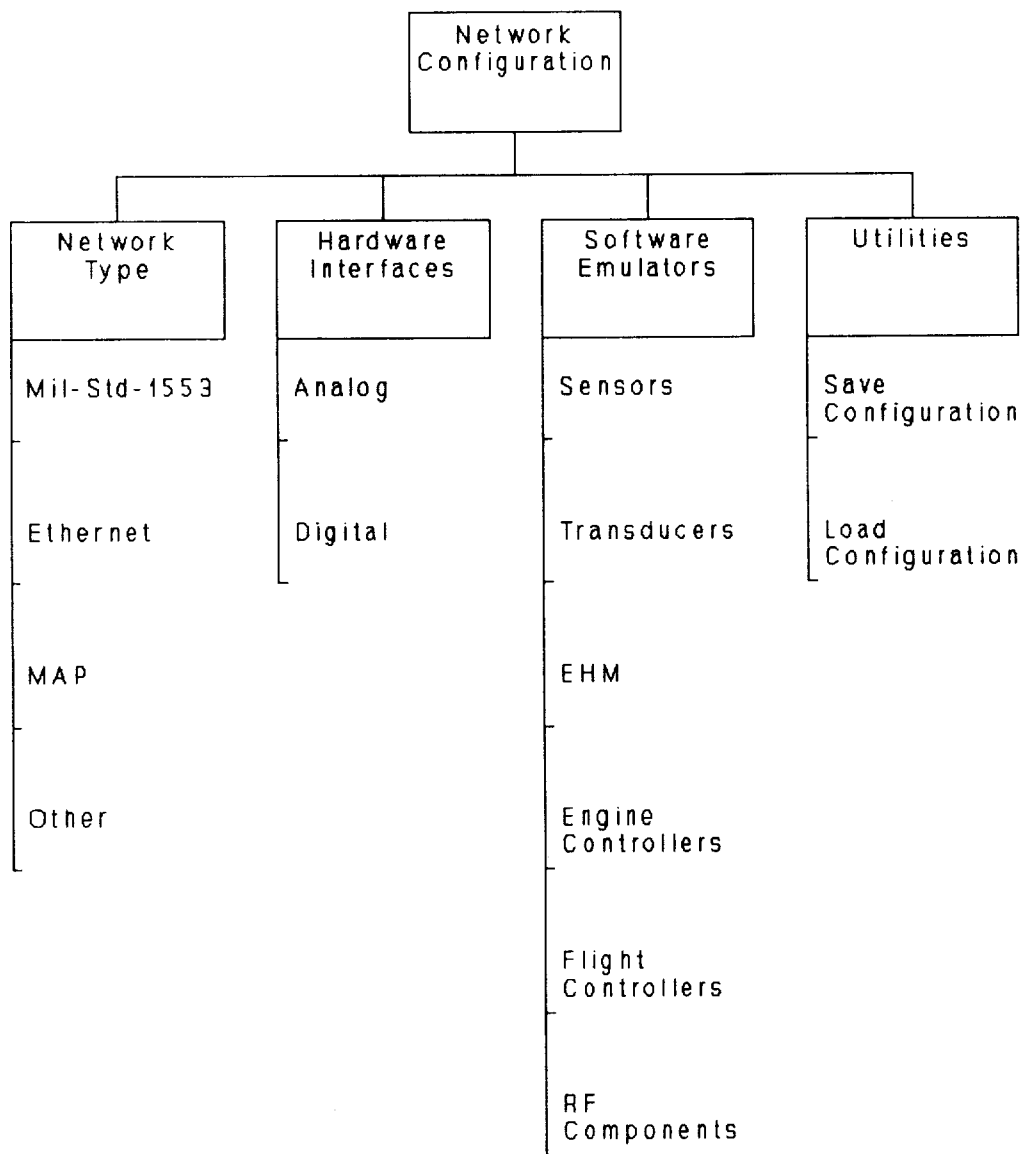


Figure 4: Test Configuration Software

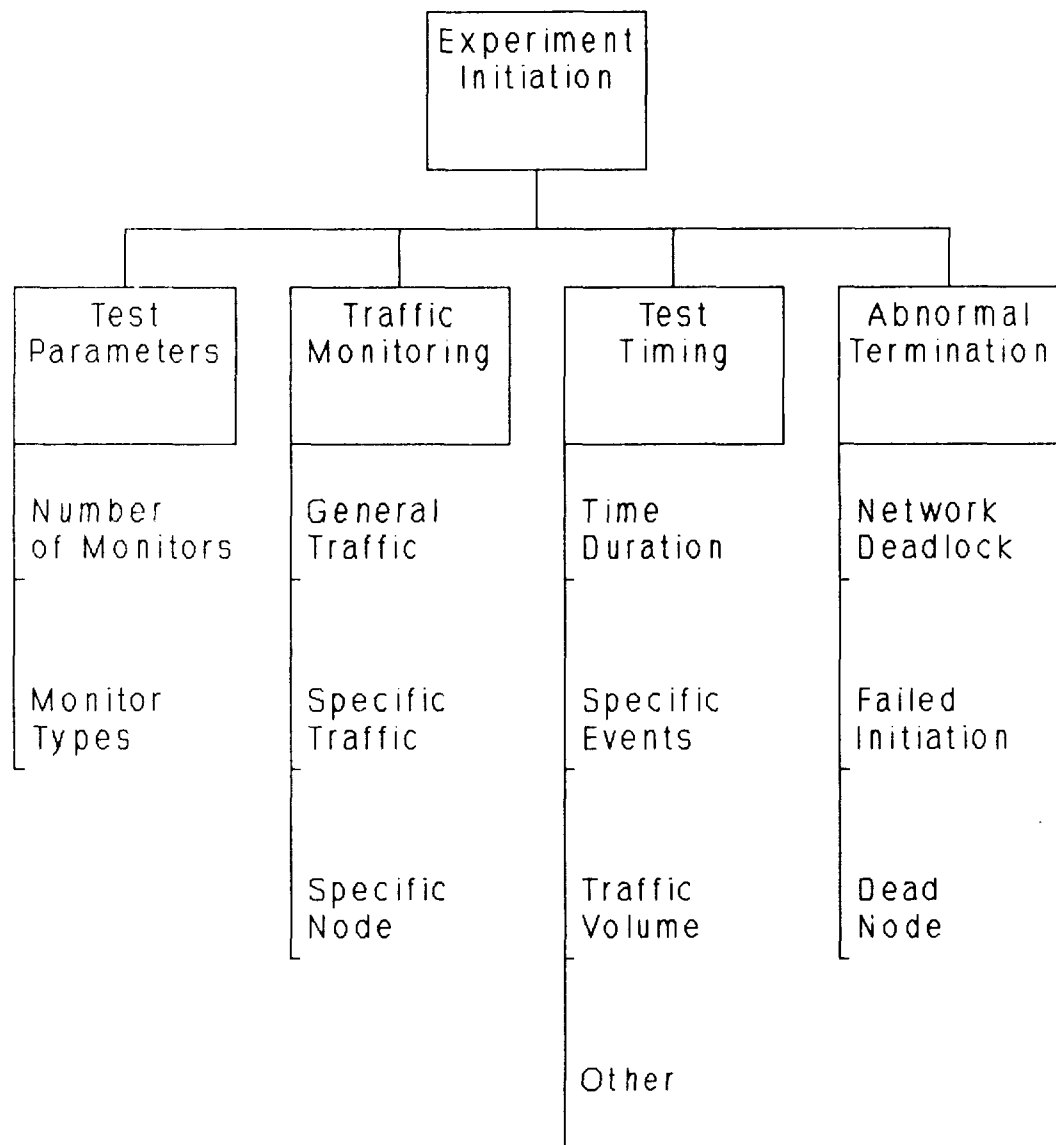


Figure 5: Test Initiation Software

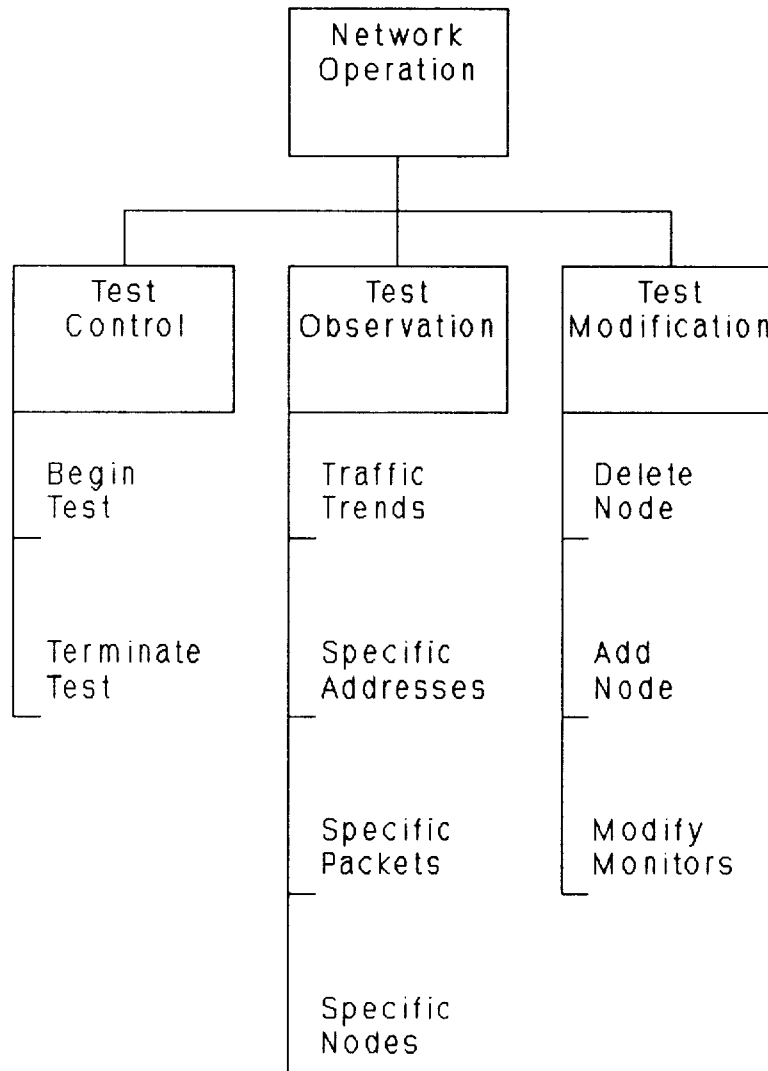


Figure 6: Network Operation Software

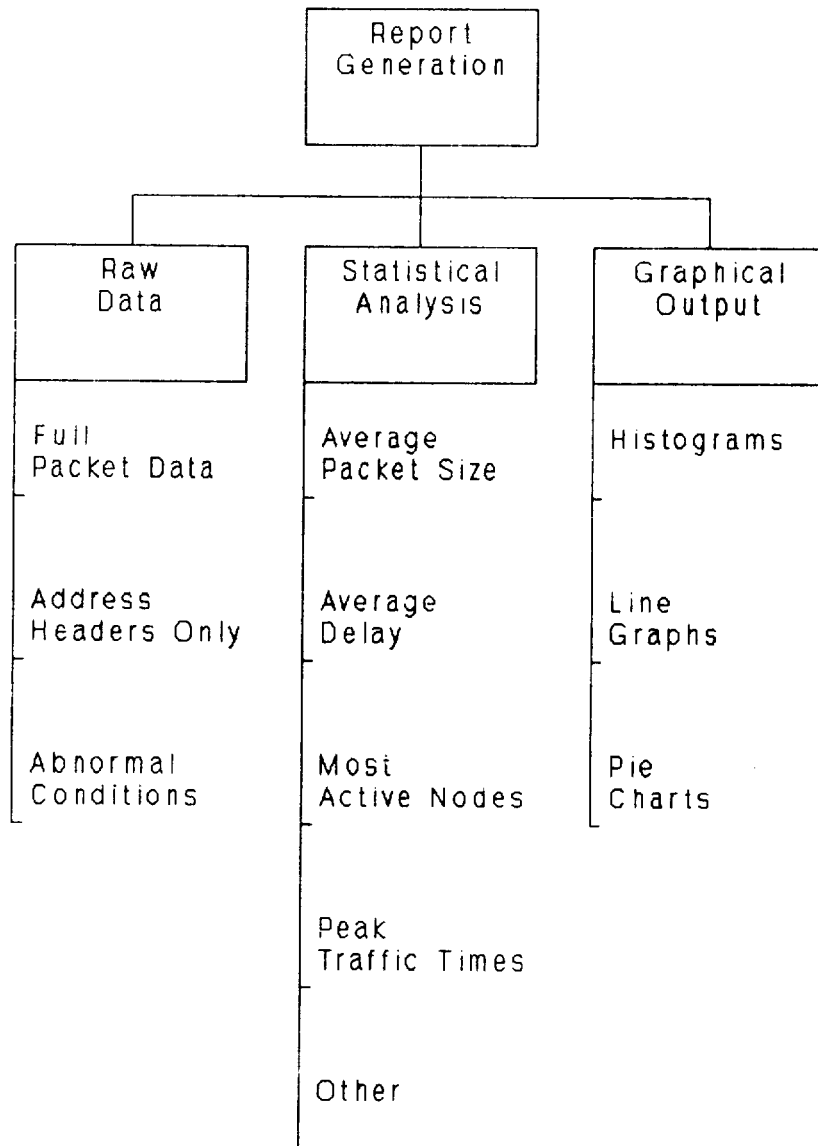


Figure 7: Network Test Report Generation

	1989			1990					1991																		
	O	N	D	J	F	M	A	M	J	J	A	S	O	N	D	J	F	M	A	M	J	J	A	S	O	N	D
1																											
2																											
3																											
4																											
5																											
6																											
7																											

Task Definitions:

1. Write specifications for MNOS software
2. Procure¹, install and test ProNET software
3. Procure, install and test other network software
4. Procure, install and test MNOS software
5. Assemble three node system hardware
6. Assemble ten node system
7. Assemble full system in permanent location

Figure 8: Tentative MAST Development Timetable

¹Commercial software may not be available that meets specifications. Software may need to be written in-house or obtained through contract.

1989

NASA/ASEE SUMMER FACULTY FELLOWSHIP PROGRAM

MARSHALL SPACE FLIGHT CENTER
THE UNIVERSITY OF ALABAMA IN HUNTSVILLE

HEAT SINK EFFECTS ON WELD BEAD - VPPA PROCESS

Prepared by:	Paul O. Steranka, Jr.
Academic Rank:	Assistant Professor
University and Department:	Wichita State University Department of Mechanical Engineering
NASA/MSFC:	
Laboratory:	Materials and Processes
Division:	Process Engineering
Branch:	Metals Processes
MSFC Colleague:	Arthur C. Nunes
Date:	July 28, 1989
Contract No.:	The University of Alabama in Huntsville NGT-01-008-021

HEAT SINK EFFECTS ON WELD BEAD - VPPA PROCESS

by

Paul O. Steranka, Jr.

Assistant Professor of Mechanical Engineering

Wichita State University

Wichita, Kansas

ABSTRACT

An investigation into the heat sink effects due to weldment irregularities and fixtures used in the variable polarity plasma arc (VPPA) process has been conducted. A basic two-dimensional model was created to represent the net heat sink effect of surplus material using Duhamel's theorem to superpose the effects of an infinite number of line heat sinks of variable strength. Parameters were identified that influence the importance of heat sink effects. A characteristic length, proportional to the thermal diffusivity of the weldment material divided by the weld torch travel rate, correlated with heat sinking observations. Four tests were performed on 2219-T87 aluminum plates to which blocks of excess material were mounted in order to demonstrate heat sink effects. Although the basic model overpredicted these effects, it correctly indicated the trends shown in the experimental study and is judged worth further refinement.

INTRODUCTION

The purpose of this study was to identify the important parameters that determine the "heat sink" effects due to fixtures used in the variable polarity plasma arc (VPPA) welding process and to develop a model for the prediction of these effects. This study is one contribution to an ongoing project to develop a comprehensive weld model to be used for automatic control of the welding process.

Arc welding is a complex process that involves such diverse fields as arc physics, metallurgy, heat transfer, and fluid mechanics. Understanding of the interactions among various constituent processes is necessary for the accurate modeling required for the automatic control of welding. The complexity of the task of developing automatic control of welding processes is indicated in a report prepared by the Committee on Welding Controls of the National Materials Advisory Board of the National Research Council [1]. In this report discussion of various types of welding is provided and gas-tungsten-arc (GTA) welding is identified as "probably the most amenable to control of the various arc welding processes." In assessing the state of the art in control of the GTA process, the Committee on Welding Controls identifies 14 "main inputs (controllable at time and point of welding)" and 47 "disturbing inputs (not at present controllable and subject to variation at time and point of welding)." Five of the 47 "disturbing inputs" are tied to the fixturing and tooling used in the welding process. A similar list of inputs could be made for the VPPA process that would include the thermal effects of fixtures studied in the current project.

Plasma arc welding is classified by the International Institute of Welding as a "high power density" welding process along with such processes as electron beam welding and laser welding [2]. In plasma arc welding, as in GTA welding, an arc is established through an inert gas (typically argon) between a non-consumable tungsten electrode and the workpiece. In the plasma arc process the pressure created by the impinging jet of gas together creates a depression in the weld pool and in some cases the jet may completely penetrate the the object being welded. Under these circumstances metal being melted in advance of the moving welding torch moves around the "keyhole" formed by the beam and solidifies behind the torch. VPPA welding is a form of plasma arc welding frequently (although not always) performed in this "keyhole mode" in

which the polarity of the electrode relative to the workpiece is periodically reversed from direct current electrode negative (DCEN) to direct current electrode positive (DCEP). This periodic reversal of polarity (DCEP for approximately 4 milliseconds out of a 23 millisecond cycle) provides a "cleansing" of oxide films that readily form on the surface of a metal. This process has been described in the literature [3,4] and has been used successfully to weld aluminum in such applications as the welding of the Space Shuttle External Tank.

In VPPA welding, as in any welding process, heat transfer from the weld zone to the surroundings, including fixtures used in the process, plays an important role in determining the characteristics of the weld. The fixtures used in welding vary greatly in form, mass, placement in relation to the weld zone, and the like. In perhaps the simplest case, a fixture may consist of a simple metal frame to which a workpiece is connected using C-clamps as shown in Figure 1. In this case the fixture contact points may be far from the weld zone. In other cases, fixtures may consist of a series of "fingers" or solid jaws that may clamp down on the workpiece close to the weld zone over the whole length of the weld as shown in Figure 2. In the case of the welding of an object such as the Space Shuttle External Tank, a fixture may have to be a major structure in itself as seen in Figure 3. Although it is not possible to simply characterize all the fixtures used in practice, it is possible to identify certain characteristics of fixtures that may lead to significant heat absorption during a welding process.

Different authors have presented results of calculations or measurements of the temperature distributions created in welding. In the 1940's, Rosenthal [5] published analytical solutions for temperature distributions created by moving sources of heat such as those used in welding. A number of authors, including Christensen, Davies, and Gjermundsen [6] and Nunes [7], have used the Rosenthal solutions as starting points for their analyses. Other investigators, for example Zacharia, Eraslan, and Aidun [8] and Okada, Kasugai and Hiraoka [9], have proposed numerical solutions for temperatures in and around the weld pool. In the references cited, the attention of the authors was generally directed to the phenomena taking place in the weld pool which is obviously of importance. As a consequence, the assumptions made about conditions outside the weld zone were kept simple, for example, negligible heat transfer from the surface of the workpiece to the surroundings and constant temperature at large distances from weld or a well-behaved convective boundary condition from the surface to a constant temperature.

It appears that no general studies to assess the importance of heat absorption due to fixtures have been performed to date. The current project is an attempt to provide a first step in that direction.

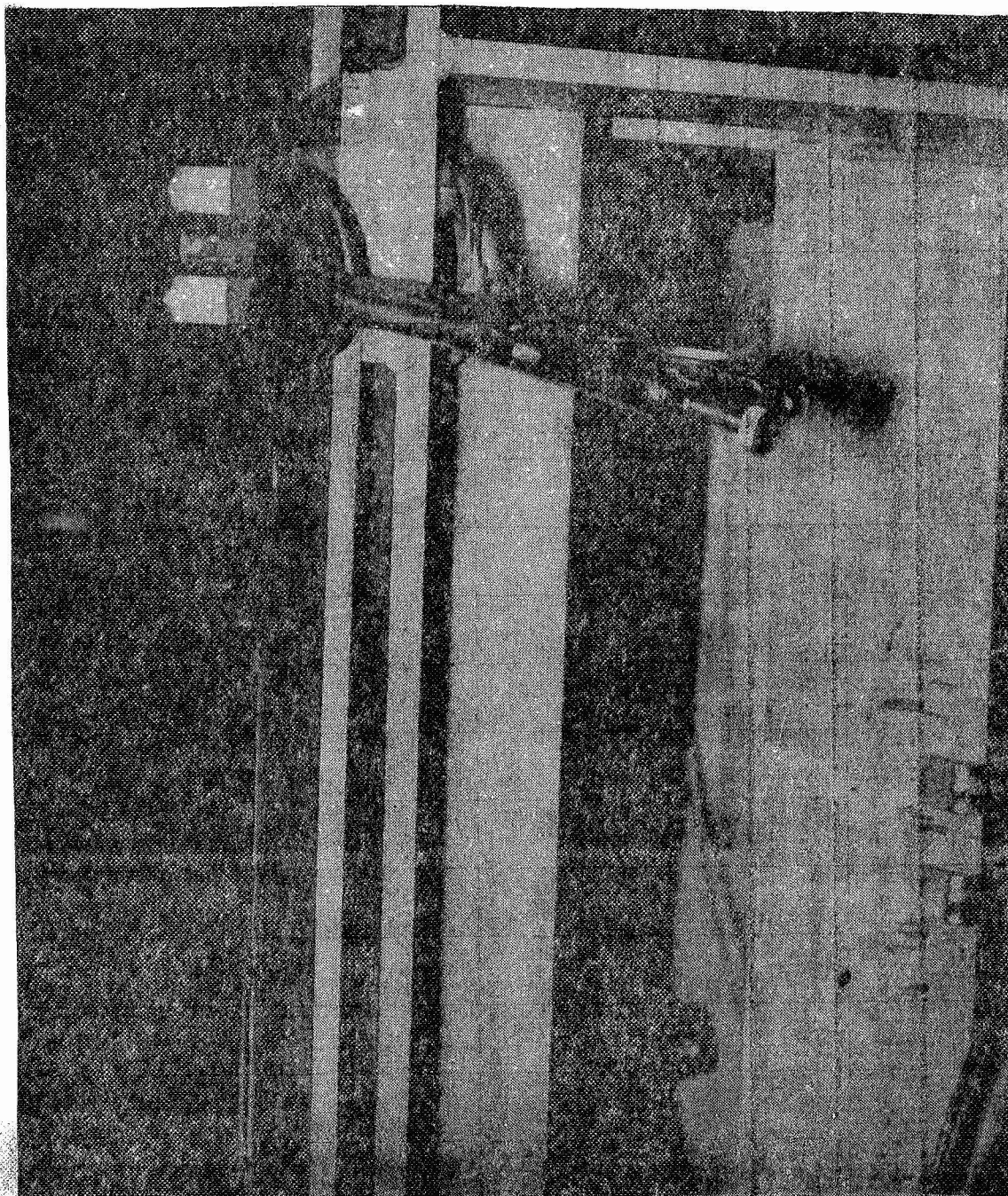


Figure 1. Simple welding fixture.

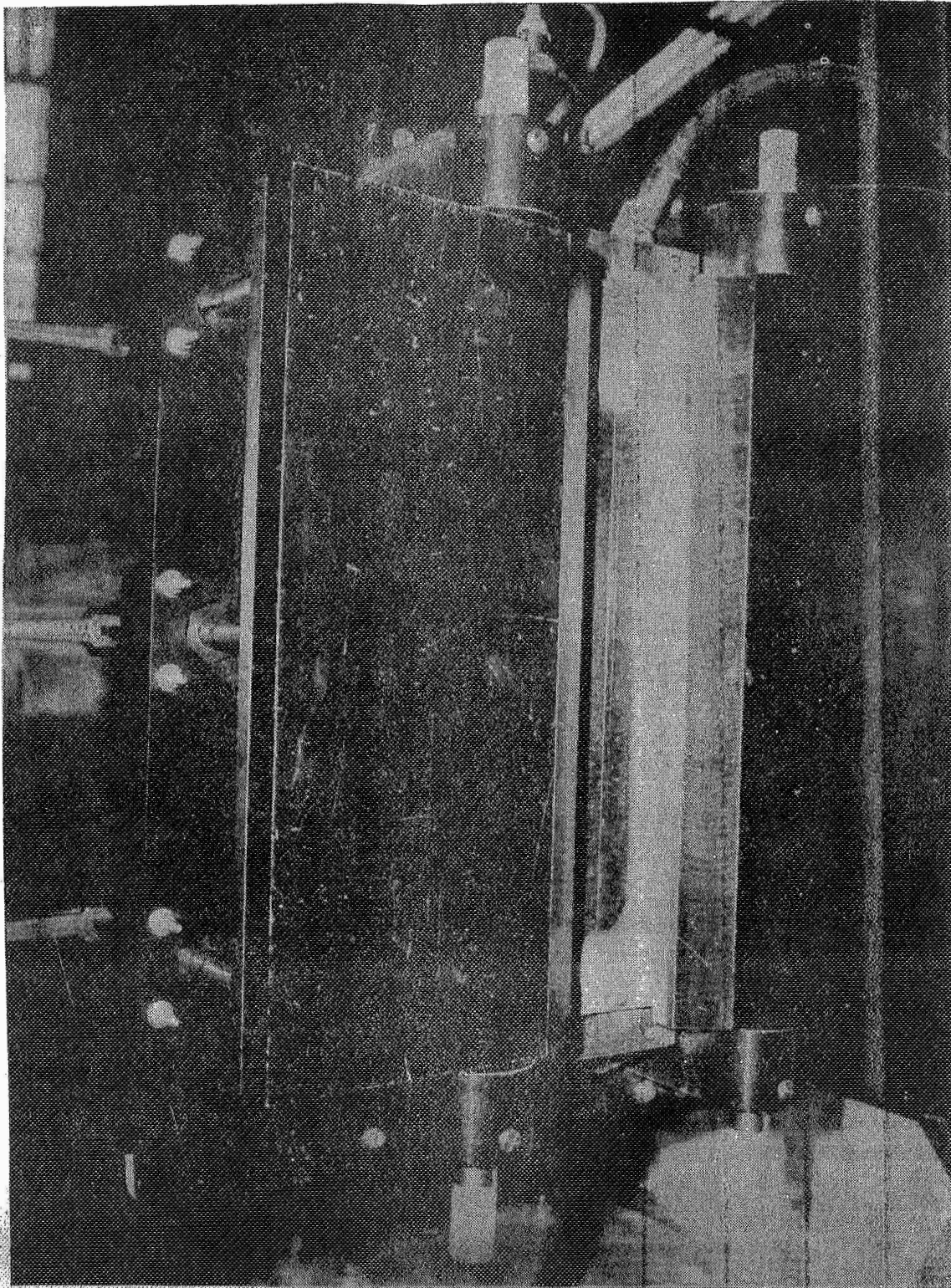


Figure 2. Welding fixture with contact along length of weld.

XXVIII-4

ORIGINAL PAGE
BLACK AND WHITE PHOTOGRAPH

ORIGINAL PAGE IS
OF POOR QUALITY

ORIGINAL PAGE
BLACK AND WHITE PHOTOGRAPH

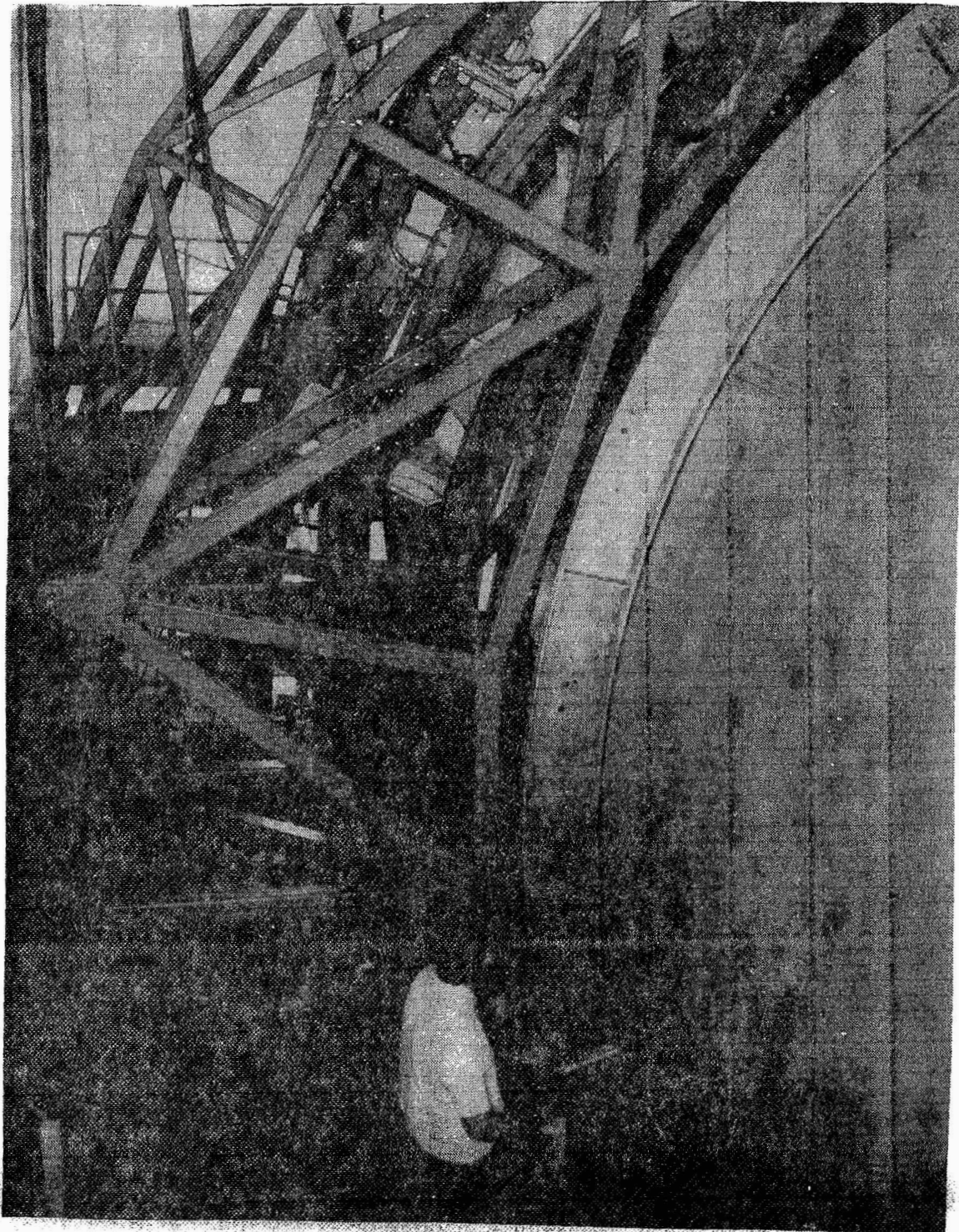


Figure 3. Fixture for welding of Space Shuttle External Tank.

XXVIII-5

ORIGINAL PAGE IS
OF POOR QUALITY

OBJECTIVES

The primary objectives of this project were to investigate the importance of the effects of heat transfer to fixtures or to irregularities in the structure of the weldment itself on the VPPA welding process and to develop a basic model to estimate these effects. Experimental demonstration of the "heat sinking" effect due to material in contact with a plate being welded was also planned in order to evaluate the model.

Progress was made toward identifying the circumstances under which fixtures used in the welding of plates play a significant role in the heat transfer of the process. A basic model was developed to estimate the magnitude of these "heat sink" effects. The experimental demonstration indicated that although the current model correctly predicts the trends in the importance of heat sinking with variation of heat sink parameters, it overpredicts the magnitude of these effects.

MODEL DEVELOPMENT

The present study involved identification of the parameters that determine the importance of the absorption of heat in surplus material near the weld zone and development of a simple two-dimensional model to indicate the magnitude of the heat sinking effect under different conditions. In the development of such an model, a method for computing the temperature field created by the welding process is required. For a fixture to have a thermal effect on the weld zone, the temperature distribution created by the welding process itself must first reach the fixture location. Then through approximation of the interaction of the temperature field with the fixture material, the heat sink effect of the fixture may be estimated.

For the present model a simple expression that reflects the important characteristics of the temperature distribution created by the welding process was sought. Rosenthal's closed form solution [5] for the two-dimensional temperature distribution created by a moving line source was selected for this purpose. This solution is based on the assumptions of constant thermal properties, negligible natural convection losses from the front and back of the plate, even heat input per unit length along the line source through the plate, and a fixed temperature at large distances from the source. The resulting steady temperature distribution for a moving coordinate system attached to the source is given by

$$T_R(x, y) - T_0 = \frac{Q'}{2\pi k} e^{-(Vx/2\alpha)} K_0(Vr/2\alpha)$$

where the motion of the source is parallel to the x-direction with velocity V; Q' is the source strength per unit length; k and α are the thermal conductivity and thermal diffusivity of the plate, respectively; K_0 is the modified Bessel function of the second kind of order 0; and $r = (x^2 + y^2)^{1/2}$.

If the Rosenthal solution is examined in detail, it is seen that the exponential factor accounts for the "skewing" of the temperature distribution to create steep temperature gradients ahead of the source (when $x > 0$) compared to the shallow gradients behind the source. The Bessel function factor is symmetric about the source with a singularity at the origin and its values drop off rapidly with increasing values of its

argument. The product of these factors generates a typical form for contours of constant temperature about the source that is shown schematically in Figure 4. In both factors the characteristic length $L = 2\alpha/V$ appears. It is interesting to note the range of values that L may have for different materials. Representative values of L for 2219-T87 aluminum, type 304 stainless steel, and Inconel 718 for a torch travel speed of 8 inches/min. (20.3 cm/min) are shown in Table 1. The values vary greatly due to the different values of thermal diffusivity of these materials. The implication of these values is that for a given disturbance (such as the heat sink effect due to contact with a fixture) to have a similar effect on the welding of two different materials, the fixture would have to be located at different distances from the weld zone. For example, to have a similar effect on the welding of an aluminum plate as on a stainless steel plate, a fixture would have to be placed closer to the weld zone by a factor of 11 on the stainless steel plate. For an aluminum plate and an Inconel 718 plate the characteristic lengths differ by a factor of more than 80! The values of this characteristic length thus have great importance in estimation of the significance of potential heat sink effects. A fixture located at a distance of several of these characteristic lengths should have no significant effect on the heat transfer in the vicinity of the welding torch.

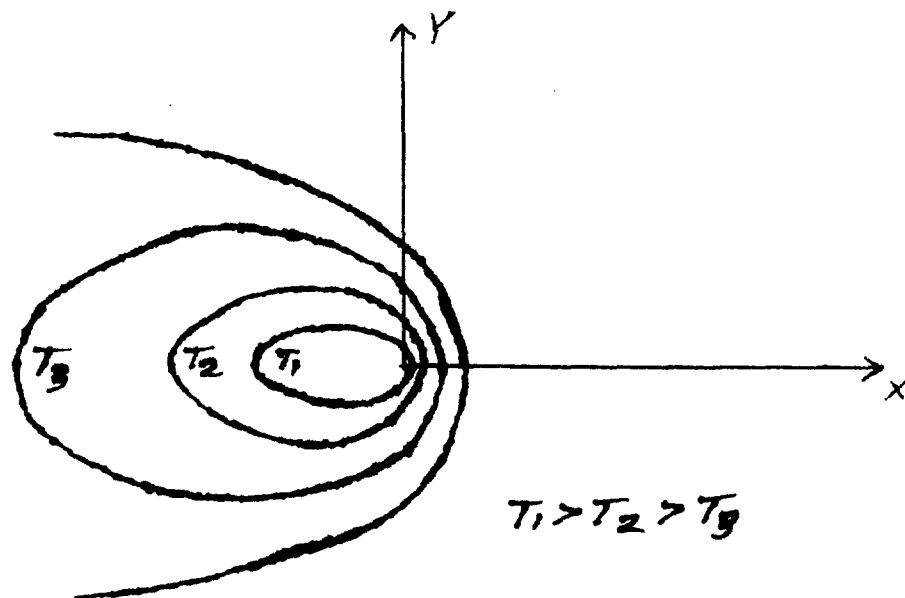


Figure 4. Typical form of constant temperature contours from the Rosenthal line source solution.

Table 1. Typical values of characteristic length L for different materials for a torch travel rate of 8 in./min (20.3 cm/min).

<u>MATERIAL</u>	<u>CHARACTERISTIC LENGTH L</u>
2219-T87 Aluminum	1.2 in (3.0 cm)
Type 304 Stainless Steel	0.11 in (0.28 cm)
Inconel 718	0.014 in (0.036 cm)

After selection of the Rosenthal model to represent the temperature distribution in a plate created by the welding process, a method was developed for estimation of the heat sinking effect due to interaction of this temperature field with a mass in contact with the plate at a fixed location. From the Rosenthal moving line source solution it is possible to generate the temperature history at a point on the plate. If a small mass on the plate were to interact with the moving temperature distribution, a simple estimate of the heat it would draw from the plate would be equal to the quantity of heat required for the temperature of the small mass to attain the temperatures prescribed for its location by the Rosenthal solution. This premise forms the basis of the model created for estimation of the heat sink effect.

With the frame of reference for the calculations moving with the welding torch fixed at the origin, as in the Rosenthal solution, the heat sink effect caused by a mass fixed to the plate is equivalent to that of a moving heat sink of variable strength. Carslaw and Jaeger [10] provide the solution for the two-dimensional temperature distribution created by an instantaneous line source of strength per unit length Q' occurring at time τ located at (x_0, y_0) as

$$T(x, y, t) - T_0 = \frac{Q'}{4\pi\alpha(t-\tau)} \exp[-\{(x-x_0)^2 + (y-y_0)^2\} / \{4\alpha(t-\tau)\}]$$

For a moving source (or sink) of variable strength, Duhamel's theorem may be used to superpose the effects of an infinite number of instantaneous heat sources to determine an equivalent effect at a desired time and location. In the current model the instantaneous strength S of the heat sink at time τ is given by

$$S(z) = - \frac{mC_p}{d} (dT_R/dz)_{x',y',z}$$

where x' and y' are the instantaneous coordinates of the heat sink, m and C_p are the mass and specific heat of the sink material, d is the thickness of the plate, and dT_R/dz is the rate of change of the temperature from the Rosenthal solution at the location of the sink. Substitution of this expression into the Carslaw and Jaeger solution for an instantaneous source and applying Duhamel's theorem yields the following expression for determining the effect on the temperature at a point (x,y) at time t due to a sum of instantaneous sources occurring between time t_0 and time t :

$$T - T_0 = \int_{t_0}^t \frac{S(z)}{4\pi k(t-z)} \exp[-\{(x-x')^2 + (y-y')^2\} / \{4\alpha(t-z)\}] dz$$

Numerical integration of this expression is performed by the computer program HTSINK.BAS described in the Appendix in order to determine the approximate maximum temperature depression at the weld zone due to the heat sink effect of a mass in contact with a plate being welded. Once this temperature depression is identified, the program goes on to shift the temperature distribution from the Rosenthal solution by the amount of the depression and to estimate the reduced weld bead width based on the melting isotherm shift for comparison with the bead width without the heat sink effect.

EXPERIMENTAL DEMONSTRATION OF HEAT SINK EFFECT

As part of the project it was desired to demonstrate heat sink effects in the welding of plates and correlate the results with the predictions of the computer model. To set up the first experiment, the computer model was used to estimate the effects of placing small blocks of aluminum near the weld zone prior to performing a bead-on-plate weld. A 1/4-inch 2219-T87 plate was selected for the test and 12 aluminum blocks measuring 2 in. X 1 in. X 0.5 in. (5.1 cm X 2.5 cm X 1.3 cm) were bolted in sets of four at distances of 1 in. (2.5 cm), 1.5 in. (3.8 cm), and 2 in. (5.1 cm) from the weld centerline on the front and back of the plate as shown in Figure 5. The computer model predicted a reduction of 22 % near the closest blocks, 10 % for the intermediate blocks, and less than 5 % for those furthest from the weld zone. The weld was performed using weld parameter settings of arc current: 155 amps, arc voltage: 28 volts, and torch travel rate: 11 in./min (28 cm/min). As may be observed in the photograph of Figure 6, no measurable effect occurred due to any of the blocks. Thus, the model had overpredicted the heat sinking effect.

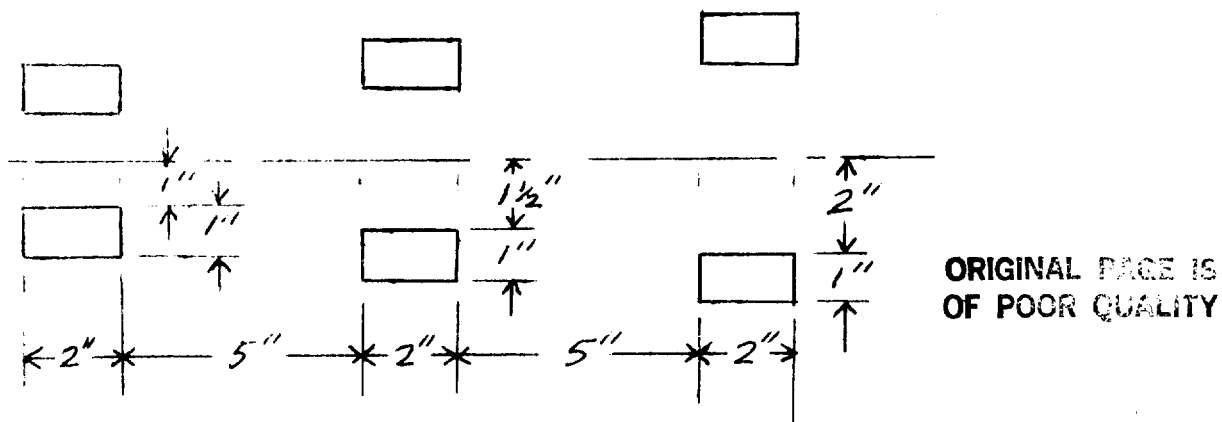


Figure 5. Heat sink block locations on plate 1.

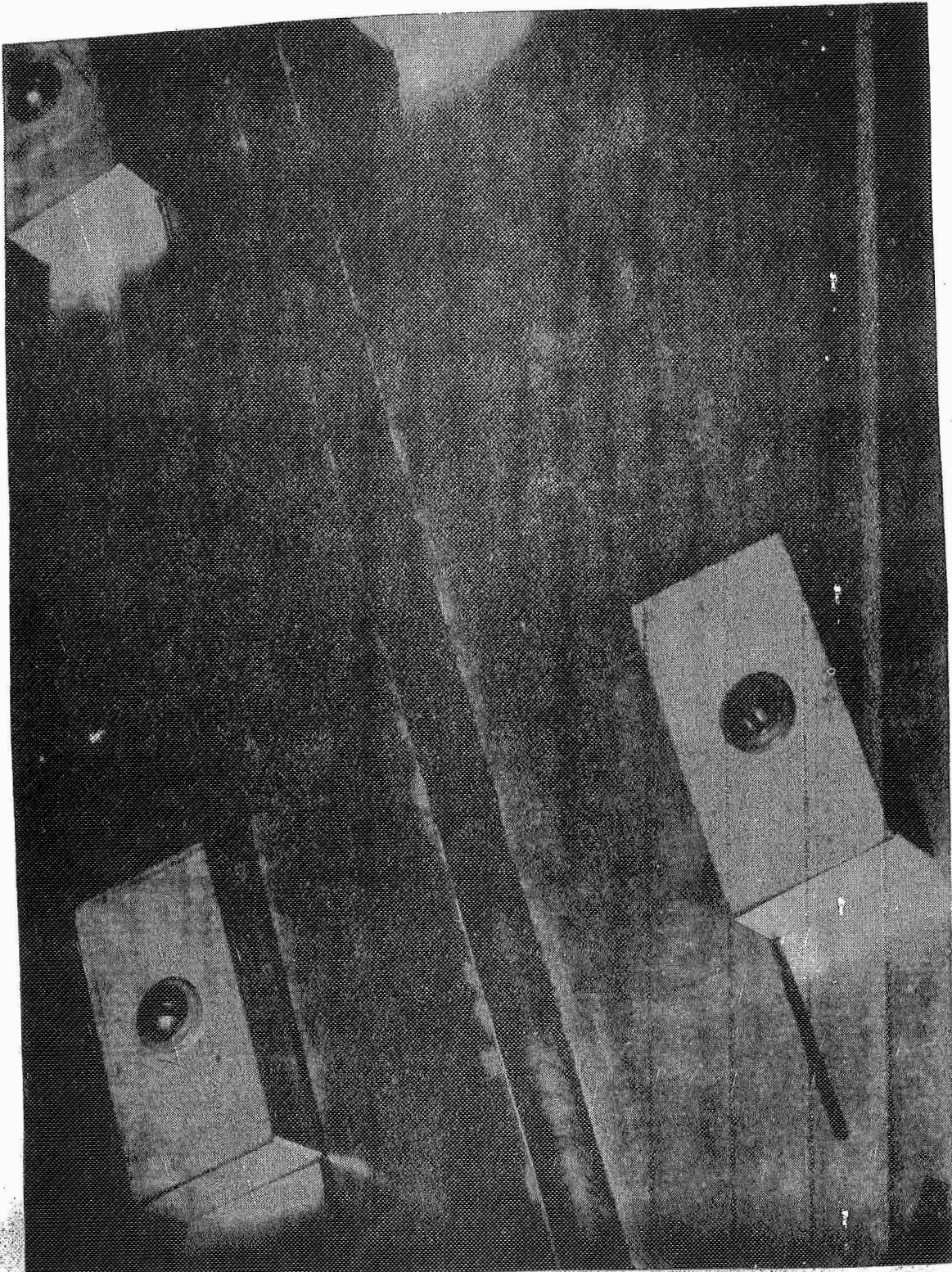


Figure 6. Weld bead on plate 1 near heat sink blocks.

XXVIII-12

ORIGINAL PAGE
BLACK AND WHITE PHOTOGRAPH

ORIGINAL PAGE IS
OF POOR QUALITY

In order to increase the heat sink effect, the model indicates that the torch velocity or the distance from the weld zone could be decreased or the mass of the sink material increased. Due to clearance requirements for the VPPA torch, it was not possible to place blocks closer to the weld zone on the front of the plate. Since this limitation did not exist on the back of the plate, it was decided to mount larger blocks on the back of the plate closer to the weld zone. For this second experiment four 4 in. X 2 in. X 1 in. (10.2 cm X 5.1 cm X 2.5 cm) were bolted to the back of a 1/4-inch aluminum plate. Two of the blocks were placed 0.75 in. (1.9 cm) on either side of the weld centerline and the other two were 1.25 in. (3.2 cm) from the centerline as shown in Figure 7. The weld parameters used were the same as those for the first plate. In this case the model predicted reductions of 27 % and 13 % for the two sets of blocks. Once again, however, no noticeable reduction occurred during the experiment.

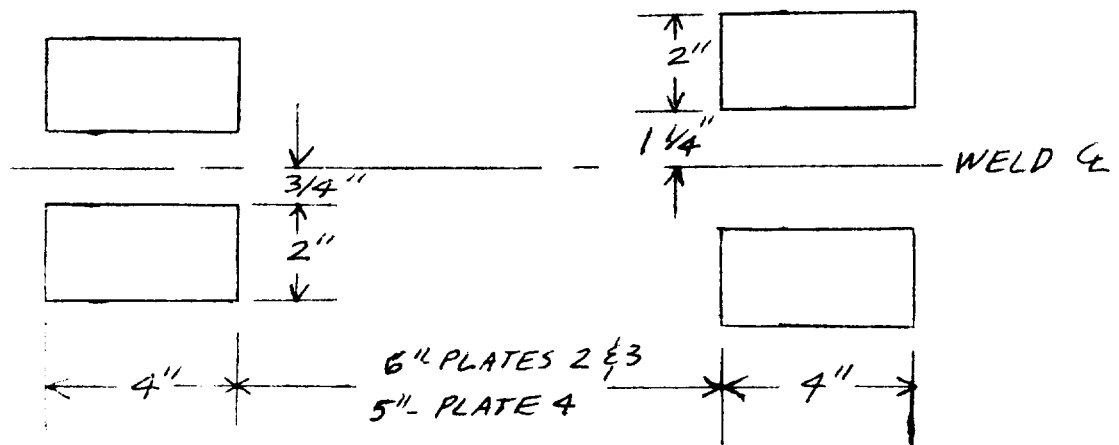


Figure 7. Heat sink block locations of plates 2, 3. and 4.

A third experiment was conducted using the same blocks and spacing relative to the weld centerline as in the second experiment, but using a 1/2-inch 2219-T87 aluminum plate. For this weld the welding parameters were changed to arc current: 218 amps, arc voltage: 29.6 volts, and torch travel rate: 5.5 in./min (14 cm/min). Thus, the third factor for increasing the heat sink effect indicated by the model, torch velocity decrease, was added in this experiment. For these conditions the model predicted reductions of 40 % and 23 % for the two sets of blocks. On the back of the plate (where the blocks were mounted) maximum reductions of 18 % and 6 % were observed in the width of the root of the weld. The crown of the weld, on the other hand, showed no evidence of the heat sinking effect.

One factor that is suspected to play a significant role in determining heat sinking effects is contact resistance. In order to obtain an idea of the importance of contact resistance, a last experiment was conducted using the same blocks with the same spacing from the weld zone as in the second and third plates. For this fourth plate, the thickness of 1/2-inch was used again and the schedule of weld parameters was changed slightly to arc current: 215 amps, arc voltage: 28.5 volts, and torch travel rate: 5.5 in./min (14 cm/min). This time, however, the four blocks were coated with heat-conducting grease prior to being bolted to the plate. Under these circumstances the reductions in the width of the weld root were determined to be 13 % and 8 %. These reductions may be observed in Figure 8. It therefore appears that the addition of the heat conducting grease created no significant increase in the heat sink effect. In fact, in the experiment conducted the reduction in weld bead width due to the closest blocks actually decreased.

In addition to comparison with predictions from the current model, the crown and root weld bead widths from the experimental study were used as inputs to the existing MSFC Weld Model [7] in order to estimate the power absorbed by the heat sink blocks. According to the model, for plate 3, the root bead reductions of 18 % and 6 % correspond to absorption of 2.7 % and 1.0 % of the power transmitted to the plate, respectively. For plate 4, the 13 % and 8 % reductions correspond to absorption of 1.6 % and 1.1 % of the transmitted power. It is interesting to note that it appears that a power increase on the order of a few per cent would be sufficient to compensate for the heat sink effect of the blocks used in the experiment.

ORIGINAL PAGE
BLACK AND WHITE PHOTOGRAPH

ORIGINAL PAGE IS
OF POOR QUALITY

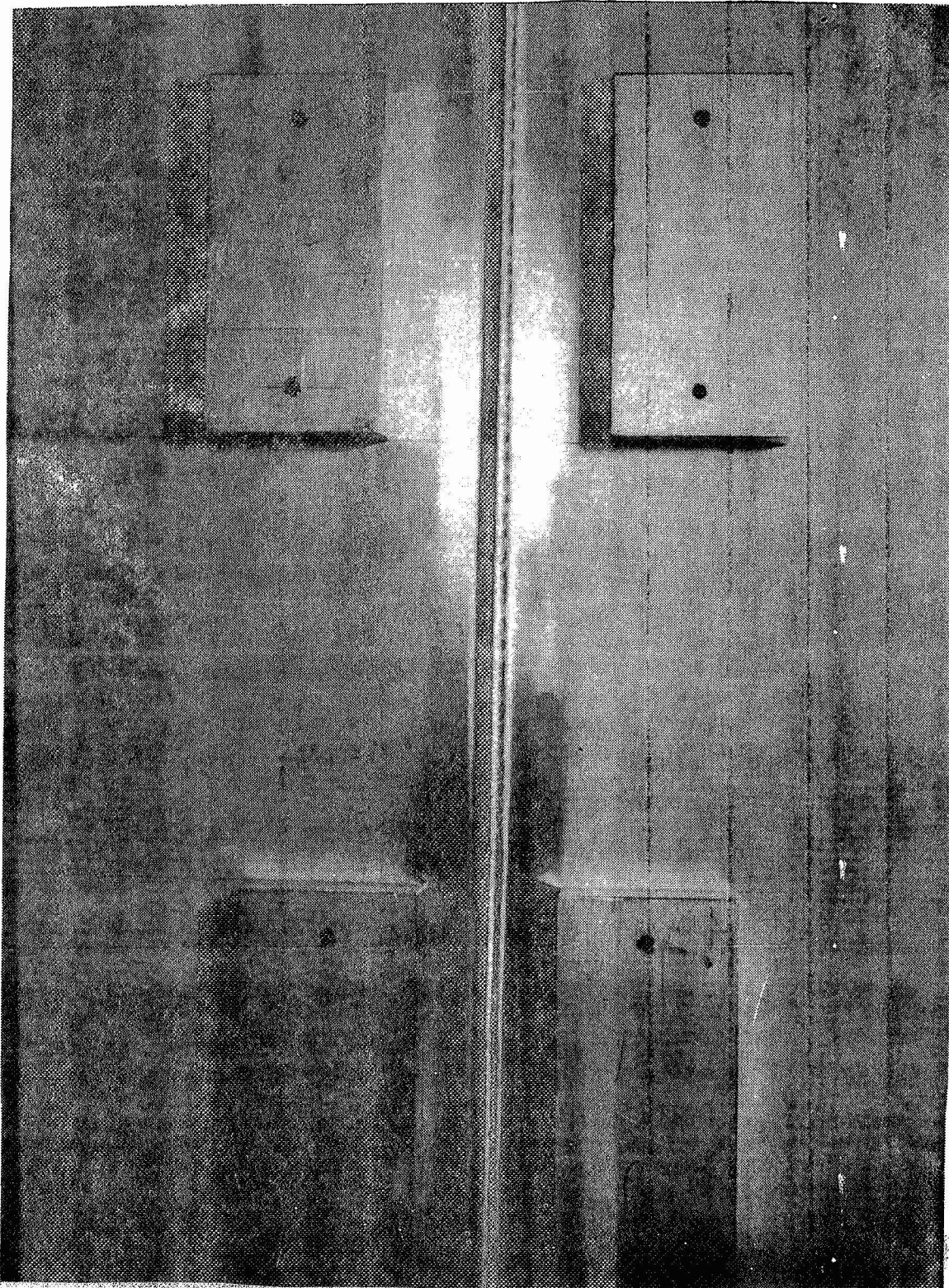


Figure 8. View of weld bead on plate 4.

CONCLUSIONS AND RECOMMENDATIONS

The objectives of this project were to identify parameters important to the heat sink effects due to weldment irregularities and to fixtures used in the VPPA welding process, to develop a basic model for prediction of these effects, and to demonstrate these effects in the laboratory. All these objectives were satisfied.

Two important heat sink parameters that were identified were the distance from the weld zone and the thermal capacity of the sink material. The distance of the fixture from the weld zone may be expressed in terms of a characteristic length equal to the $2\alpha/V$, where α is the thermal diffusivity of the plate being welded and V is the torch travel velocity. Any sink more than a few of these characteristic lengths from the weld zone has little effect on the weld. The thermal capacity (mass times specific heat) of the heat sink material in contact with the workpiece also plays an obvious role in determining the amount of energy that may be absorbed in the heat sink.

A simple two-dimensional model was developed for predicting the heat sink effect of a small mass in contact with a plate being welded. Although the model consistently overpredicted the magnitude of the heat sink effects, it appears to reflect the trends observed in the experimental demonstration. The current version of the model lacks the accuracy that would be required for its use for control of the welding process, but it presents a beginning susceptible to considerable improvement.

Continued work is recommended in the study of heat sink effects. A more sophisticated model appears to be necessary to accurately predict the importance of these effects in different situations. In particular, a model that would represent the three-dimensional features of heat sink phenomena would provide greater flexibility to analyze configurations found in practical welding applications. Another area to be examined in the model development is the ability to handle different boundary conditions. Generally, studies of welding heat transfer effects to date have been based on simple boundary conditions, such as constant temperature at large distances from the weld or well behaved convective heat transfer over the entire weldment outside the weld zone itself. More complex conditions exist in any

practical situation and examination is needed of the effects of these conditions. One phenomenon that requires further work is contact resistance. Although the experiment conducted during the current project indicated contact resistance was not important in the case considered, further study is needed to assess the importance of this factor under different circumstances.

Finally, it should be noted that the importance of the study of heat sink effects is not confined to the VPPA process. Similar problems are present in other welding processes, in the heat treatment of metals, in dealing with hot spots in engines, and in many other processes. One interesting application is that of welding in space where both the heat transfer to the weldment from the welding apparatus and the heat transfer from the weldment to the surroundings would differ significantly from the processes that occur on earth. Another difficulty related to heat sink effects that is encountered in practice involves the welding of objects that have significantly different thermal masses such as joining a thin sheet of metal to a large block of metal. The situations cited are only a few of instances where heat sink effects play an important role. Further understanding of these effects will thus be of benefit in many applications.

REFERENCES

1. "Control of Welding Processes", Report of the Committee on Welding Controls, National Materials Advisory Board, National Academy Press, 1987.
2. The Physics of Welding, 2nd edition, J. F. Lancaster, editor, International Institute of Welding, Pergamon Press, 1986, pp. 306-328.
3. Tomsic, M. and Barhost, S., "Keyhole Arc Welding of Aluminum with Variable Polarity Power", Welding Journal, Vol. 63, No. 2, 1984, pp. 25-32.
4. Nunes, Jr., A.C., Bayless, Jr., E.O., Jones, III, C.S., Munafo, P.M., Biddle, A.P., and Wilson, W.A., "Variable Polarity Plasma Arc Welding on the Space Shuttle External Tank", Welding Journal, Vol. 63, No. 9, 1984, pp. 27-35.
5. Rosenthal, D., "The Theory of Moving Sources of Heat and Its Application to Metal Treatments", Transactions of the A.S.M.E., Vol. 68, 1946, pp. 849-866.
6. Christensen, N., Davies, V. de L., and Gjermundsen, K., "Distribution of Temperatures in Arc Welding", British Welding Journal, February 1965, pp. 54-75.
7. Nunes, Jr., A.C., "An Extended Rosenthal Weld Model", Welding Journal, Vol. 62, No. 6, 1983, pp. 165s-170s.
8. Zacharia, T., Eraslan, A.H., and Aidun, D.K., "Modeling of Non-Autogenous Welding", Welding Journal, Vol. 67, No. 1, 1988, pp. 18s-27s.
9. Okada, A., Kasugai, T., and Hiraoka, K., "Heat Source Model in Arc Welding and Evaluation of Weld Heat-affected Zone", Transactions of the Iron and Steel Institute of Japan, Vol. 28, No. 10, 1988, pp. 876-882.
10. Conduction of Heat in Solids, Carslaw, H.S. and Jaeger, J.C., 2nd edition, Oxford University Press, 1959, p. 258.

APPENDIX

This appendix contains a description and a listing of the computer program HTSINK.BAS that was created to estimate the effects of heat sinking due to surplus material, such as a welding fixture, in contact with a plate to be welded. HTSINK.BAS is an interactive program and begins with input of parameters concerning the weld: plate material, plate thickness, arc current, arc voltage, weld energy transfer efficiency, and torch travel speed. Then the mass, specific heat, and initial position of the sink with respect to the torch are entered. Finally, the ambient temperature and the total length of time to be analyzed are supplied.

With the information about the weld and heat sink supplied by the user, the program calculations begin. The undisturbed (by the heat sink) weld bead width is first determined. The width is determined by identification of the point where the distance from the weld centerline to the melt isotherm (based on the Rosenthal temperature solution) is greatest. This point is determined by applying the dichotomous search strategy to the region between the torch position and the puddle length along the weld axis. (Note: The Newton-Raphson technique is employed for solution of the nonlinear equations involved in the puddle length and width calculations.) With the bead width determined, the program proceeds to analyze the heat sink effects. The program numerically integrates the expression for net heat sink effect for various lengths of time and identifies the maximum sink effect and the position of the sink at the time it occurs. Finally this heat sink effect is superimposed on the Rosenthal temperature solution and a new bead width is determined and compared with the undisturbed bead width.

Listing of HTSINK.BAS

```
110 CLEAR
112 DIM TE(40)
115 PRINT "SELECT PLATE MATERIAL"
116 PRINT " "
120 PRINT "1 = 2219 ALUMINUM"
121 PRINT "2 = 304 STAINLESS STEEL"
122 PRINT "3 = INCONEL 718"
123 PRINT "4 = OTHER MATERIAL WITH USER SUPPLIED PROPERTIES"
124 PRINT " "
```



```

130 INPUT "SELECTION"; A1
131 IF A1 = 1 THEN GOSUB 2100
132 IF A1 = 2 THEN GOSUB 2200
133 IF A1 = 3 THEN GOSUB 2300
134 IF A1 < 1 OR A1 > 3 THEN GOSUB 3000
140 INPUT "PLATE THICKNESS (IN.) "; TH
145 TH = TH/12
150 REM *** INPUT WELDING PARAMETERS ***
151 INPUT "WELDING CURRENT (AMPS)"; IO
152 INPUT "WELDING VOLTAGE (VOLTS)"; VO
153 INPUT "WELDING EFFICIENCY (%)"; EF
155  $P = 3.412 * VO * IO * EF / 100$ 
157 INPUT "TORCH VELOCITY (IN/MIN)"; V
158  $V = V / 720$ 
160 REM ** SINK CHARACTERISTICS **
163 PRINT " "
164 PRINT "SINK CHARACTERISTICS"
166 INPUT "SINK MASS (LB)"; M
168 INPUT "SINK SPECIFIC HEAT (BTU/LB-F)"; CP
169 PRINT " "
170 PRINT "INITIAL POSITION OF SINK (IN) RELATIVE TO TORCH"
171 PRINT "(TORCH MOTION IN X-DIRECTION; Y-DIRECTION
PERPENDICULAR"
172 PRINT " TO WELD PATH) "
173 PRINT " "
175 INPUT "X0,Y0"; X0,Y0
176  $X0 = X0 / 12$ 
177  $Y0 = Y0 / 12$ 
180 REM ** TORCH AT ORIGIN **
181 X=0
182 Y=0
189 PRINT " "
190 INPUT "AMBIENT TEMPERATURE (F) "; TR
191 PRINT " "
193 PRINT "*** DETERMINING WELD WIDTH ***"
194 REM ** FIND STEADY WELD BEAD HALF WIDTH **
195 GOSUB 6000
196  $BO = BW * (2 * A / V)$ 
197 PRINT " "
198 PRINT "INITIAL WELD BEAD WIDTH: ";  $BO * 24$ ; " INCHES"
199 PRINT " "
200 INPUT "LENGTH OF PERIOD TO BE STUDIED (SEC)"; TX
201 REM ** SET UP PARAMETERS AND BEGIN INTEGRATION **
202 PRINT " "
203 PRINT "*** NUMERICAL INTEGRATION BEGUN ***"
204 T0=0
206  $JJ = INT((TX - T0) / 10)$ 
208 FOR J=1 TO JJ
210  $TF = 10 * J$ 
212  $N = 4 * INT(TF / (2 * A / V^2)) + 4$ 

```



```

214 D = (TF-T0)/N
216 L=0
218 R=0
220 FOR I = 0 TO N
230 T1 = T0 + I*D
240 IF I = N THEN F = 0
250 IF I = N THEN GOTO 270
260 GOSUB 1000
270 Z = L/2 - INT(L/2)
280 IF Z>0 AND L<N THEN LET T=4*F
290 IF Z=0 AND L<N-1 THEN LET T=2*F
300 IF L=0 OR L=N THEN LET T=F
310 L=L+1
320 R=R+T
330 NEXT I
340 Q= D*R/3
350 TE(J) = - 45.5945*P*Q*M*CP/(K*TH)^2
:REM CONST=3600/(8*PI)^2
355 REM PRINT "TIME = "; TF; " TEMP. DEPRESSION = "; TE(J)
360 IF J=1 THEN GOTO 380
365 IF TE(J)>TE(J-1) THEN GOTO 400
380 NEXT J
400 TD=TE(J-1)
410 TI=TF-D
420 PRINT " "
430 PRINT "MAXIMUM TEMPERATURE DEPRESSION AT ORIGIN IS: "; TD
440 PRINT "AND OCCURS WHEN TORCH IS "; 12*(V*(TI-T0)-X0);
" INCHES"
450 PRINT "PAST SINK"
460 TR=TR+TD
470 REM ** FIND NEW WELD HALF WIDTH **
480 GOSUB 6000
490 BN=BW*(2*A/V)
500 PRINT "REDUCED WELD BEAD WIDTH: "; BN*24; " INCHES"
510 PRINT " "
520 PRINT "REDUCTION OF "; 100*(BO-BN)/BO; " %"
530 STOP

1000 REM SUBROUTINE FOR INTEGRAND
1010 X1=X0-V*(T1-T0)
1020 X2= X-X1
1030 Y2=Y-Y0
1035 FOR J4 = 1 TO 2
1040 BA=V*SQR((X1-(-1)^J4*V*D/2)^2+Y0^2)/(2*A)
1050 EX = (X2^2+Y2^2)/(4*A*(TF-T1)) +
(X1-(-1)^J4*V*D/2)*V/(2*A)
1055 IF (-EX-BA)<-80 THEN F=0 :GOTO 1120
1056 IF (-EX-BA)>-80 AND (BA>80) THEN FL=1
1060 GOSUB 1500
1065 IF FL=1 THEN F=K0*EXP(-EX-BA)/(TF-T1) : GOTO 1075

```



```

1070 F = K0 * EXP (-EX) / (TF-T1)
1075 FL=0
1080 IF J4=1 THEN LET FO=F
1090 IF J4=2 THEN LET FP=F
1100 NEXT J4
1110 F=(FP-FO)/D
1120 RETURN

1500 REM *** MODIFIED BESSEL FUNCTION, SECOND KIND OF ORDER
0 ***
1510 REM *** POLYNOMIAL APPROXIMATION ***
1520 IF BA<> 0 THEN 1550
1530 K0=100000!
1540 RETURN
1550 IF BA > 2 THEN 1650
1560 GOSUB 1700
1570 LET G2 = BA*BA/4
1580 LET K0 = ((.0000074*G2+.0001075)*G2 +2.62698E-03)*G2
1590 LET K0 = ((K0+.0348859)*G2+.2306976)*G2
1600 LET K0 = ((K0+.4227842)*G2-.5772157)-.5*LOG(G2)*I0
1610 GOTO 1690
1650 LET G2 = 2/BA
1660 LET K0=((5.3208E-04*G2-.0025154)*G2 +5.87872E-03)*G2
1670 LET K0=((K0-1.062446E-02)*G2 + 2.189568E-02)*G2
1675 IF FL=1 THEN LET
K0=((K0-7.832358E-02)*G2+1.253314)/SQR(BA)
1676 IF FL=1 GOTO 1690
1680 LET K0=((K0-7.832358E-02)*G2+1.253314)/SQR(BA)/EXP(BA)
1690 RETURN

1700 REM *** MODIFIED BESSEL FUNCTION, FIRST KIND OF ORDER 0
***
1710 REM *** POLYNOMIAL APPROXIMATION ***
1720 IF BA>3.75 THEN 1780
1730 LET G1 = BA*BA
1740 LET I0=((5.923979E-10*G1+6.56017E-08)*G1+6.80123E-06)*G1
1750 LET I0=((I0+4.3394E-04)*G1+.0156252)*G1
1760 LET I0=(I0+.25)*G1+1
1770 GOTO 1820
1780 LET I0=((153.445/BA-171.822)/BA+73.2919)/BA
1790 LET I0=((I0-15.2595)/BA+1.81198)/BA
1800 LET I0=((I0-.0830909)/BA+.0316855)/BA
1810 LET I0=((I0+.0498222)/BA+.3989423)*EXP(BA)/SQR(BA)
1820 RETURN

2000 REM PROPERTY VALUE SUBROUTINES
2100 REM 2219 ALUMINUM PROPERTIES
2110 REM THERMAL DIFFUSIVITY IN FT^2/S AND
2111 REM CONDUCTIVITY IN BTU/HR/FT/F
2120 MT$="2219 ALUMINUM"

```



```

2130 A=.000503
2140 K=72
2150 TM=1190
2160 RETURN
2200 REM 304 STAINLESS STEEL PROPERTIES
2210 REM THERMAL DIFFUSIVITY IN FT^2/S AND
2211 REM CONDUCTIVITY IN BTU/HR/FT/F
2220 MT$="304 STAINLESS STEEL"
2230 A=.0000524
2240 K=14
2250 TM=2800
2260 RETURN
2300 REM INCONEL 718 PROPERTIES
2310 REM THERMAL DIFFUSIVITY IN FT^2/S AND
2311 REM CONDUCTIVITY IN BTU/HR/FT/F
2320 MT$="INCONEL 718"
2330 A=.0000063
2340 K=12
2350 TM=2437
2360 RETURN
3000 REM USER SUPPLIED MATERIAL PROPERTIES
3010 INPUT "MATERIAL DESIGNATION"; MT$
3020 INPUT "THERMAL DIFFUSIVITY IN FT^2/S"; A
3030 INPUT "THERMAL CONDUCTIVITY IN BTU/HR/FT/F"; K
3040 RETURN

4100 REM *** MODIFIED BESSEL FUNCTION, FIRST KIND OF ORDER 1
***
4110 REM *** POLYNOMIAL APPROXIMATION ***
4120 IF BA>3.75 THEN 4180
4130 LET G1 = (BA/3.75)^2
4140 LET I1=((3.2411E-04*G1+3.01532E-03)*G1+2.658733E-02)*G1
4150 LET I1=((I1+.15084934#)*G1+.51498869#)*G1
4160 LET I1=((I1+.87890594#)*G1+.5)*BA
4170 GOTO 4230
4180 LET G1=BA/3.75
4190 LET
I1=(-4.20059E-03/G1+1.787654E-02)/G1-2.895312E-02)/G1
4200 LET
I1=((I1+2.282967E-02)/G1-1.031555E-02)/G1+1.63801E-03)/G1
4210 LET I1=(I1-3.62018E-03/G1-3.988024E-02)/G1+.39894228#
4220 LET I1=I1*EXP(BA)/SQR(BA)
4230 RETURN

5100 REM *** MODIFIED BESSEL FUNCTION, SECOND KIND OF ORDER
1 ***
5110 REM *** POLYNOMIAL APPROXIMATION ***
5120 IF BA<> 0 THEN 5150
5130 K1=100000!
5140 RETURN

```



```

5150 IF BA > 2 THEN 5220
5160 GOSUB 4100
5170 LET G2 = BA*BA/4
5180 LET K1 = ((-4.686E-05*G2-1.10404E-03)*G2-1.919402E-02)*G2
5190 LET K1 = ((K1-.18156897#)*G2-.67278579#)*G2
5200 LET K1 = ((K1+.15443144#)*G2+1)/BA+LOG(BA/2)*I1
5210 GOTO 5260
5220 LET G2 = 2/BA
5230 LET K1 = ((-6.8245E-04*G2+3.25614E-03)*G2-7.80353E-03)*G2
5240 LET K1 = ((K1+1.504268E-02)*G2-.0365562)*G2
5250 LET K1 = ((K1+.23498619#)*G2+1.25331414#)/SQR(BA)/EXP(BA)
5260 RETURN

```

```

6000 REM *** SUBROUTINE FOR FINDING WELD BEAD WIDTH ***
6005 REM *** BASED ON DICHOTOMOUS SEARCH STRATEGY ***
6010 C1=TM-TR
6015 C2=P/(2*3.14159265#*K*TH)
6100 C0 = C1/C2
6110 LU=0
6120 GOSUB 7000
6130 LL=-PL
6140 ER=ABS(LL)/10000
6150 FOR J1=1 TO 100
6160 L1=(LL+LU)/2 - ER
6170 L2=(LL+LU)/2 + ER
6175 LA=L1
6176 GOSUB 6300
6180 W1=WI
6181 REM PRINT "W1=";W1
6185 LA=L2
6186 GOSUB 6300
6190 W2=WI
6191 REM PRINT "W2=";W2
6200 IF W1>=W2 THEN LET LU=L2
6210 IF W2>W1 THEN LET LL=L1
6211 REM PRINT "LL=";LL;"LU=";LU
6220 IF ((LU-LL)/ABS(LL)) < .05 THEN GOTO 6250
6230 NEXT J1
6240 PRINT "FAILURE TO FIND WELD BEAD WIDTH AFTER 100
ITERATIONS"
6250 BW = (W1+W2)/2 :REM ** (NONDIMENSIONAL) **
6260 RETURN
6300 REM *** SUBROUTINE FOR FINDING PUDDLE WIDTH FOR GIVEN
6305 REM LONGITUDINAL POSITION USING NEWTON-RAPHSON
TECHNIQUE ***
6310 REM ** ENTER INITIAL ESTIMATE **
6320 WI=EXP(-C0)
6330 FOR J3 = 1 TO 100
6340 BA=SQR(LA^2+WI^2)
6350 GOSUB 1500

```



```

6360 GOSUB 5100
6370 F = C0*EXP(LA) - K0
6380 DF = 2*K1*WI/BA
6390 WN = WI-F/DF
6400 IF WN <= 0 THEN LET WI=WI/2
6410 IF WN > 0 THEN LET WI=WN
6420 IF ABS(F/DF/WI) < .01 THEN GOTO 6450
6430 NEXT J3
6440 PRINT "FAILURE TO FIND PUDDLE WIDTH AFTER 100 ITERATIONS"
6450 RETURN

7000 REM *** SUBROUTINE TO FIND TIP OF MELT ISOTHERM TAIL ***
7050 REM *** BASED ON NEWTON-RAPHSON SEARCH TECHNIQUE ***
7110 BA = 1
7120 FOR J2=1 TO 100
7130 GOSUB 1500
7140 F1 = EXP(BA) * K0 - C0
7150 GOSUB 5100
7160 DF = EXP(BA) * (K0-K1)
7170 B1 = BA - F1/DF
7180 IF B1 < 80 AND B1 > 0 THEN LET BA = B1
7190 IF B1 > 80 THEN LET BA = (BA+80)/2
7200 IF B1 <= 0 THEN LET BA = BA/2
7210 IF (ABS(F1/DF)/BA) < .001 THEN GOTO 7240
7220 NEXT J2
7230 PRINT "FAILURE TO FIND MAX. DISTANCE FROM SOURCE TO MELT
ISOTHERM"
7240 PL=BA
7250 RETURN

```


1989

NASA/ASEE SUMMER FACULTY FELLOWSHIP PROGRAM

MARSHALL SPACE FLIGHT CENTER
THE UNIVERSITY OF ALABAMA IN HUNTSVILLE

FREQUENCY RESPONSE OF ELECTROCHEMICAL CELLS

Prepared by:	Daniel L. Thomas
Academic Rank:	Assistant Professor
University and Department:	The University of Alabama in Huntsville Chemical Engineering Program Mechanical Engineering Department
NASA/MSFC:	
Laboratory:	Electronics and Information Systems
Division:	Electrical
Branch:	Electrical/Electronics Parts
MSFC Colleague:	Teddy M. Edge
Date:	August 11, 1989
Contract No.:	The University of Alabama in Huntsville NGT-01-008-021

ACKNOWLEDGEMENTS

I wish to acknowledge the staff of the Electronics Division of the Electronics and Information Systems Laboratory led by Mr. Jim Miller. In particular, I wish to thank Mr. Al Norton, Jr., for helping to round up equipment and fabrication the test cell and reference electrode, Mr. Ted Edge and Mr. Mike Martin for sponsoring me, and Mr. Roy Lanier for supplying some of the equipment used.

FREQUENCY RESPONSE OF POROUS BATTERY ELECTRODES

Daniel L. Thomas
Assistant Professor of Chemical Engineering
The University of Alabama in Huntsville
Huntsville, AL 35899

ABSTRACT

Impedance concepts can be applied to the analysis of battery electrodes, yielding information about the structure of the electrode and the processes occurring in the electrode. Structural parameters such as the specific area (surface area per gram of electrode) can be estimated. Electrode variables such as surface overpotential, ohmic losses and diffusion limitations may be studied.

Nickel and cadmium electrodes were studied by measuring the A.C. impedance as a function of frequency, and the specific areas that were determined were well within the range of specific areas determined from BET measurements by other workers. Impedance spectra were measured for the nickel and cadmium electrodes, and for a 20 A-hr NiCd battery as functions of the state of charge. More work is needed to determine the feasibility of using frequency response as a non-destructive testing technique for batteries.

INTRODUCTION

Electrochemical processes may and have been studied using frequency response techniques and modeled using impedance concepts. Processes that occur at electrodes may be modeled as resistance, capacitance or complex impedance. More information may be gained using dynamic techniques than by using steady-state D.C. techniques. For example, one could study an electrode by measuring steady D.C. current and potential, or the same system could be studied using A.C. over a range of frequencies with an increase in the amount of information learned. Dynamic techniques have been used to estimate the specific area of porous lead-acid battery electrodes (Newman and Tiedemann, 1976), the kinetics and mechanisms of electrode reactions and the rate of mass-transport processes such as diffusion (Bard and Faulkner, 1980). Attempts have been made to correlate cell state of charge with A.C. impedance spectra (Brodd and DeWane, 1963; Sathyanarayana et al., 1979). Zimmerman et al. (1982) studied the very low frequency impedance (as low as 0.1 Hz) of NiCd cells.

OBJECTIVES

The objective of this work was to examine the feasibility of using frequency response techniques 1) as a tool in destructive physical analysis of batteries, particularly for estimating electrode structural parameters such as specific area, porosity and tortuosity and 2) as a non-destructive testing technique for obtaining information such as state of charge and acceptability for space flight. It would be desirable to have a non-destructive battery test that can be run rapidly and as close to launch of spacecraft as possible. The battery frequency response may be such a test.

THEORY

This section will briefly review the physical phenomena that contribute to the frequency response of an electrode.

Electric Double Layer

The double layer is a thin (about 20 Angstrom) layer of electric charge that exists at the boundary between two phases, such as an electrode/solution interface, and can form for several reasons. One of the poles in a polar solvent molecule may be preferentially oriented toward the surface. Figure 1 shows how the negative pole of a water molecule may be oriented toward a surface and create a separation of charge. Double layers also occur because positive or negative ions may be preferentially adsorbed by a surface. For example, chloride ions in a solution of potassium chloride are adsorbed onto mercury in preference to potassium ions as shown in Figure 2, resulting in a separation of charge.

Finally, double layers are formed when electrodes are charged. Consider the situation in Figure 3, where two inert metal surfaces such as gold are immersed in NaF solution. These ions are not preferentially adsorbed by the metal. If a potential difference less than the 1.2 V required to decompose water is placed across the cell no steady state current can flow, yet there must be a potential drop. The potential drop occurs at the double layers that exist at each electrode surface. Electrodes which behave in this way are called ideally polarizable electrodes (IPE).

The double layer can be considered as an electric capacitor since it acts to store charge. The concept of the double layer was experimentally verified with mercury which has the advantage of a reproducible liquid surface and of inhibiting hydrogen evolution and hence approaching IPE

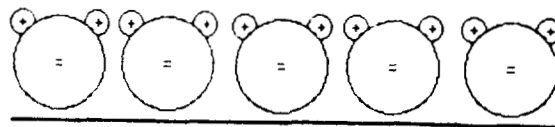


Figure 1. Double layer formation by solvent molecule orientation.

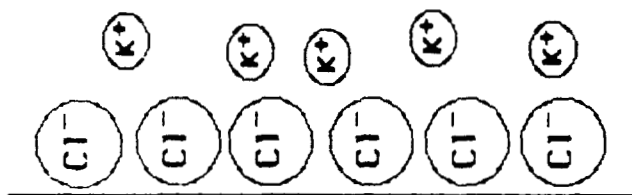


Figure 2. Double layer formation by ion adsorption.

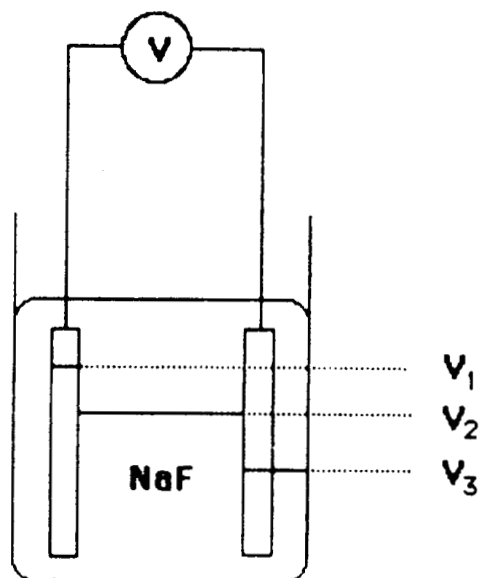


Figure 3. Voltage profile in cell with ideal polarizable electrodes.

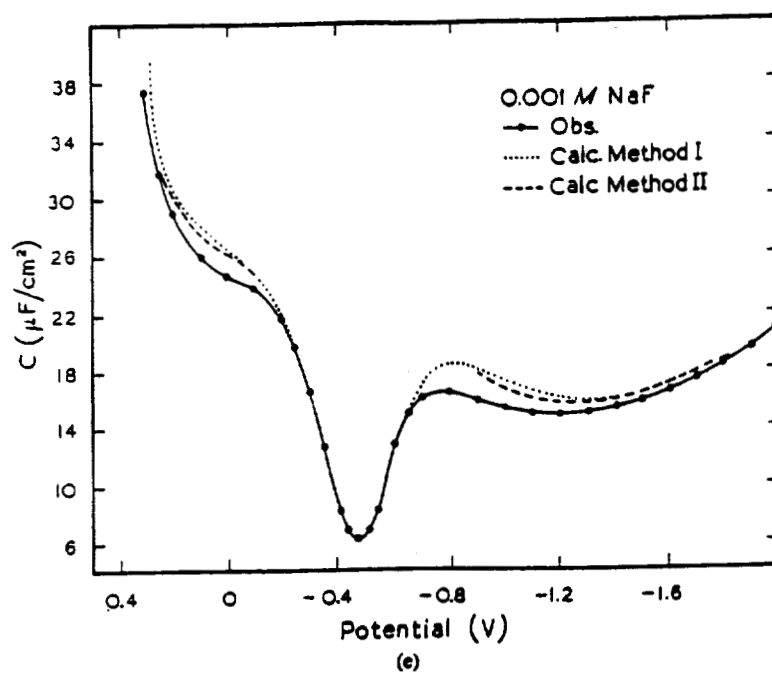


Figure 4. Double layer capacity of 0.001 M NaF/Hg electrode.

behavior over a wide potential range (Newman, 1973). Figure 4 shows how the double layer capacitance of mercury in 0.001 M NaF varies with applied potential. The capacitance was also calculated from the mercury surface tension (which varies with potential and charge) and from direct measurement of charge, both of which require liquid metal electrodes. The double layer capacitance is on the order of $10 \mu\text{F}/\text{cm}^2$, which corresponds to a parallel plate capacitor with a plate separation of about 20 Å, the double layer thickness. The double layer capacitance is potential dependent, but can be treated as constant over small (7 mV) potential range.

Electrochemical Reaction

The rate of electrochemical reaction is an exponential function of the potential drop across the double layer

$$i_f = i_0 \left\{ \exp\left(\frac{\alpha_a F (V_m - V_s)}{RT}\right) - \exp\left(-\frac{\alpha_c F (V_m - V_s)}{RT}\right) \right\} \quad (1)$$

where i_0 is the exchange current density, α is a kinetic symmetry parameter usually taken to be 0.5, F is Faraday's constant, R is the gas constant, T is the absolute temperature and $V_m - V_s$ is the potential drop across the double layer. The first term in brackets is the rate of the forward or anodic reaction while the second term is the rate of the reverse or cathodic reaction. When $V_m = V_s$ then these two rates are equal (to the exchange current density) and there is no net current.

Equation 1 is highly non-linear and must be linearized before using in an impedance analysis:

$$R_f = \frac{d(V_m - V_s)}{di_f} \bigg|_{(V_m - V_s)^0}$$

Linear expressions are valid for potential variations of 7 mV or less.

Combined Reaction and Double Layer Charging

Most electrodes, particularly those used in batteries, have combined reaction and double layer charging. For a bare metal electrode in contact with solution this can be modeled as a resistor (R_f) and capacitor (C_d) in parallel as shown in Figure 5. The solution resistance R_s also must be considered. At very high frequencies the phase angle is 0 and the modulus of the impedance is R_s , while at sufficiently low frequencies the phase angle is 0 and the modulus is $R_s + R_f$. Hence R_f and R_s can be separately determined, which could not be done readily using a steady D.C. experiment.

Diffusion Effects

Slow diffusion of reactants to the electrode surface or of reaction products away from the surface also causes the potential to lag the current. The Nernst equation, and its linearized form, gives the potential drop due to concentration differences:

$$V_b - V_s = \frac{nF}{RT} \ln \frac{C_s}{C_b} \approx \frac{nF}{RTC_b} (C_b - C_s) \quad (4)$$

where C_b is the bulk solution concentration and C_s is the concentration adjacent to the electrode. Again, the linearization is valid for a potential range of 5-7 mV. Hence, as the reaction proceeds and the reactant near the surface is consumed this potential drop increases.

The Warburg impedance is the impedance due to slow diffusion. For a planar electrode in a large excess of electrolyte solution

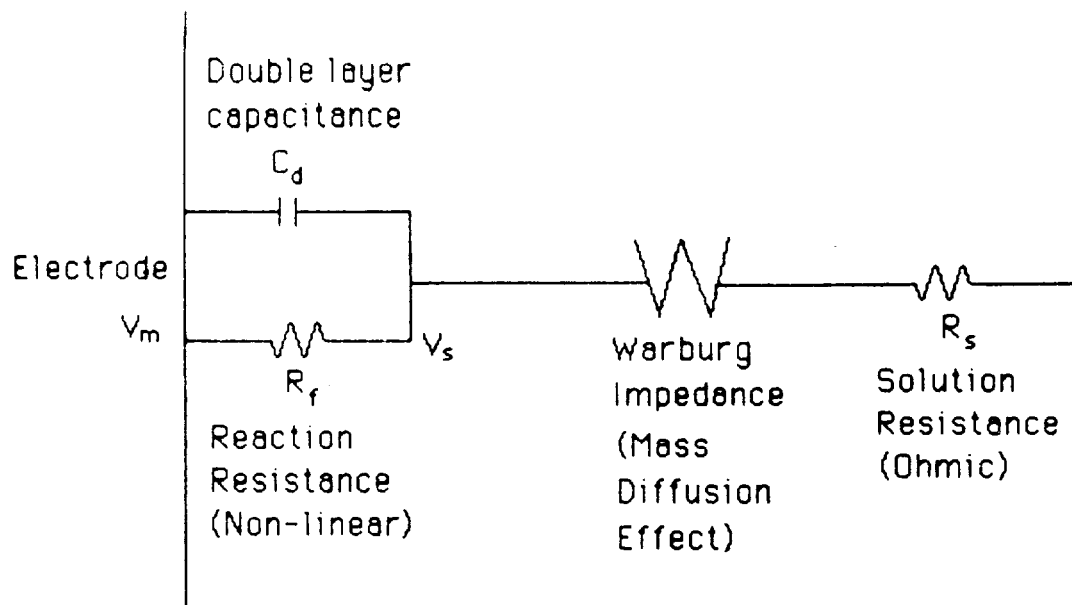


Figure 5. Equivalent circuit for electrode with capacitance, reaction, Warburg impedance and ohmic resistance.

$$Z_w \propto (j\omega D)^{-0.5} \quad (5)$$

The real and imaginary Warburg impedances are equal for this case. The Warburg impedance is usually manifested at frequencies less than 1 Hz. Measurements at frequencies as low as 0.0001 Hz have been reported. The period of such a measurement is about as long as a battery cycle, hence higher frequencies would be needed for state of charge determinations without substantially changing the state of charge.

Porous Electrodes

Most actual battery electrodes are high surface area porous electrodes. The electrode processes are distributed throughout the electrode volume instead of at a single surface. One porous electrode model is the idealized cylindrical pore shown in Figure 6. The pore walls are the solid surface where the electrode reaction and double layer charging occurs. At the electrode grid ($x=0$) all of the current is in the solid phase while at the electrode/separator boundary ($x=L$) all of the current is in the liquid phase. The current is transferred from the liquid to the solid along the pore wall.

Figure 7 shows the model circuit for the pore, which is often called a transmission line model. The impedance Z can include reaction, double layer capacitance and Warburg impedance. The impedance of the electrode, assuming a very large solid conductivity and no Warburg impedance is

$$Z_{\text{pore}} = \frac{\cosh(mL)}{km \sinh(mL)} \quad (7)$$

$$m^2 = \frac{a}{k} (R_f^{-1} + j\omega C_d)$$

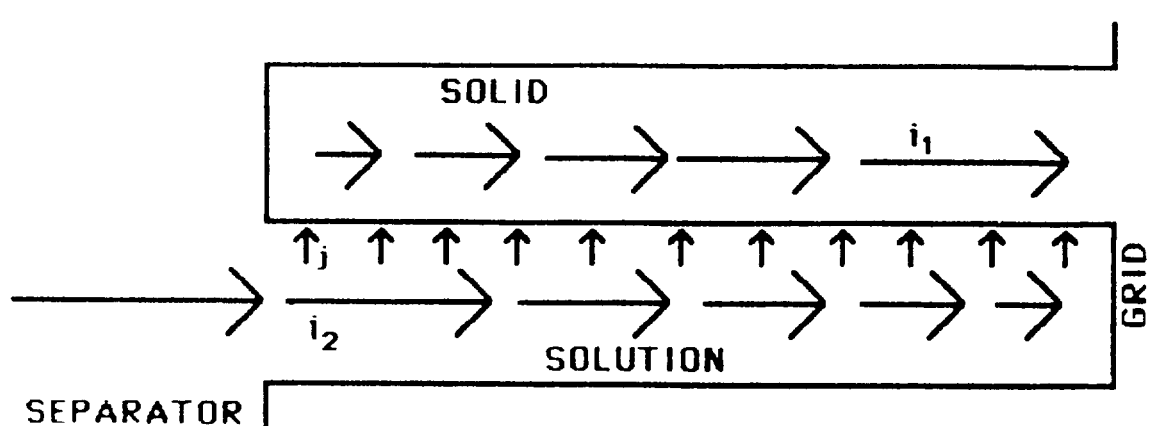


Figure 6. Idealized model of a cylindrical pore.

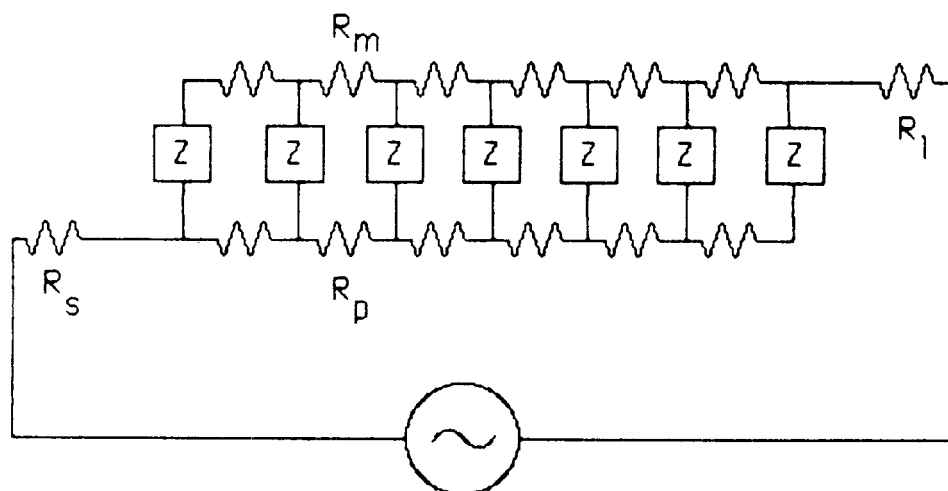


Figure 7. Equivalent circuit for the model in Figure 6.

This is a complicated expression to interpret, especially since m is a complex number, but it can be linearized for small values of mL , and the resulting expression is useful for estimating specific surface area. The important result is

$$\text{Im}(Z_{\text{pore}}) = \frac{awC_d L^3}{45 k^2}$$

Equation 8 is an approximation of Equation 7 that is valid at low frequencies, providing that the frequency is high enough that Warburg impedance is not a factor. A plot of $\text{Im}(Z)$ vs. frequency is linear in this range, and the specific area can be determined from the slope of the line.

EXPERIMENTAL

A three electrode cell was made by sandwiching a Cd electrode between two Ni electrodes. The electrodes were from an Eagle-Picher 50 A-Hr cell that had undergone destructive physical analysis. Separator material from the cell was used as separator in this cell. The cell was immersed in 31% KOH solution. A Ag/AgO reference electrode was placed in a separate compartment with 31% KOH. The two compartments were connected by a 1 mm Teflon tube filled with electrolyte, and the tube was placed near the Cd electrode at the center of the cell.

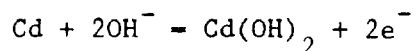
A EG&G/PAR model 363 potentiostat was used to control the potential between the Cd and reference electrode. A Wavetek signal generator supplied the voltage perturbations that were added to the D.C. offset voltage of the potentiostat. The potential and current monitors of the potentiostat were connected to a Tektronics storage oscilloscope, from which the peak current,

peak voltage and phase angles were obtained. Impedance spectra were obtained for GE 20 A-Hr cells using similar instrumentation. The reference electrode lead from the potentiostat was connected directly to the counter electrode terminal.

RESULTS

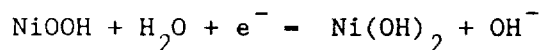
Eagle-Picher Electrodes

Figure 8 shows the experimental Nyquist plot for a charged and discharged Eagle Picher Cd electrode in a frequency range of 0.001 Hz on the right hand side to 1 Hz on the left hand side. The Warburg impedance dominated this part of the diagram, and it is much larger for the discharged electrode than the charged electrode. This can be explained by considering the electrode reaction



which produces $\text{Cd}(\text{OH})_2$ upon discharge. A solid film of reaction product would be a mass transfer barrier that would increase the electrode impedance.

Figure 9 shows the Nyquist diagram for the Ni electrode in the same frequency range as Figure 8. $\text{Re}(Z)$ is an order of magnitude smaller than for the Cd, while $\text{Im}(Z)$ is two orders of magnitude smaller. The primary mass transport process in the Ni electrode is thought to be proton (H) diffusion in the solid as the electrode reaction occurs:



Proton diffusion occurs rapidly since the hydrogen atom is small and easily moves between larger atoms in the solid lattice, hence the Warburg impedance of the Ni electrode is smaller. The curves for the charged and discharged electrodes are the same, indicating that a film does not grow during a cycle

Eagle-Picher Cd Electrode

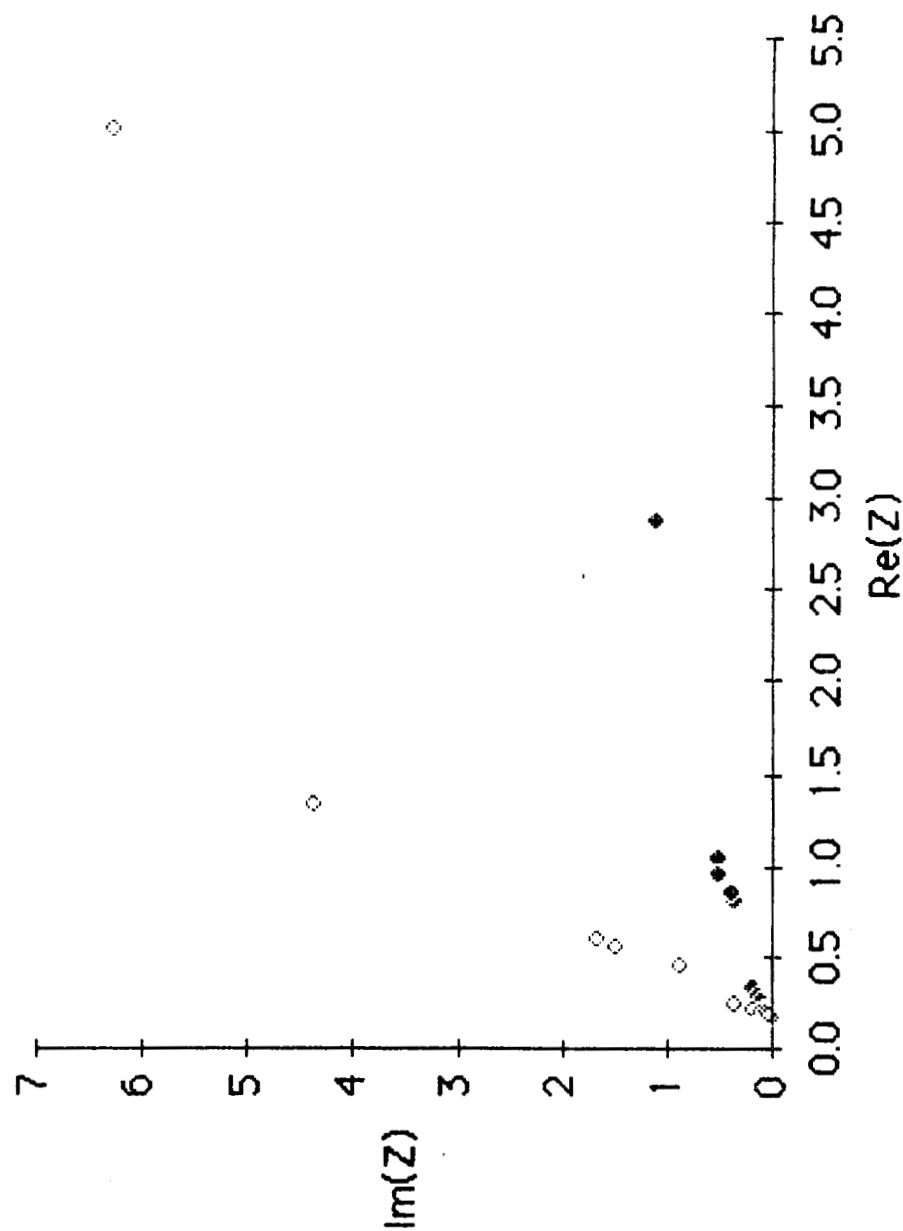


Figure 8. Nyquist plot for Eagle-Picher Cd electrode.

Eagle-Picher Ni Electrode

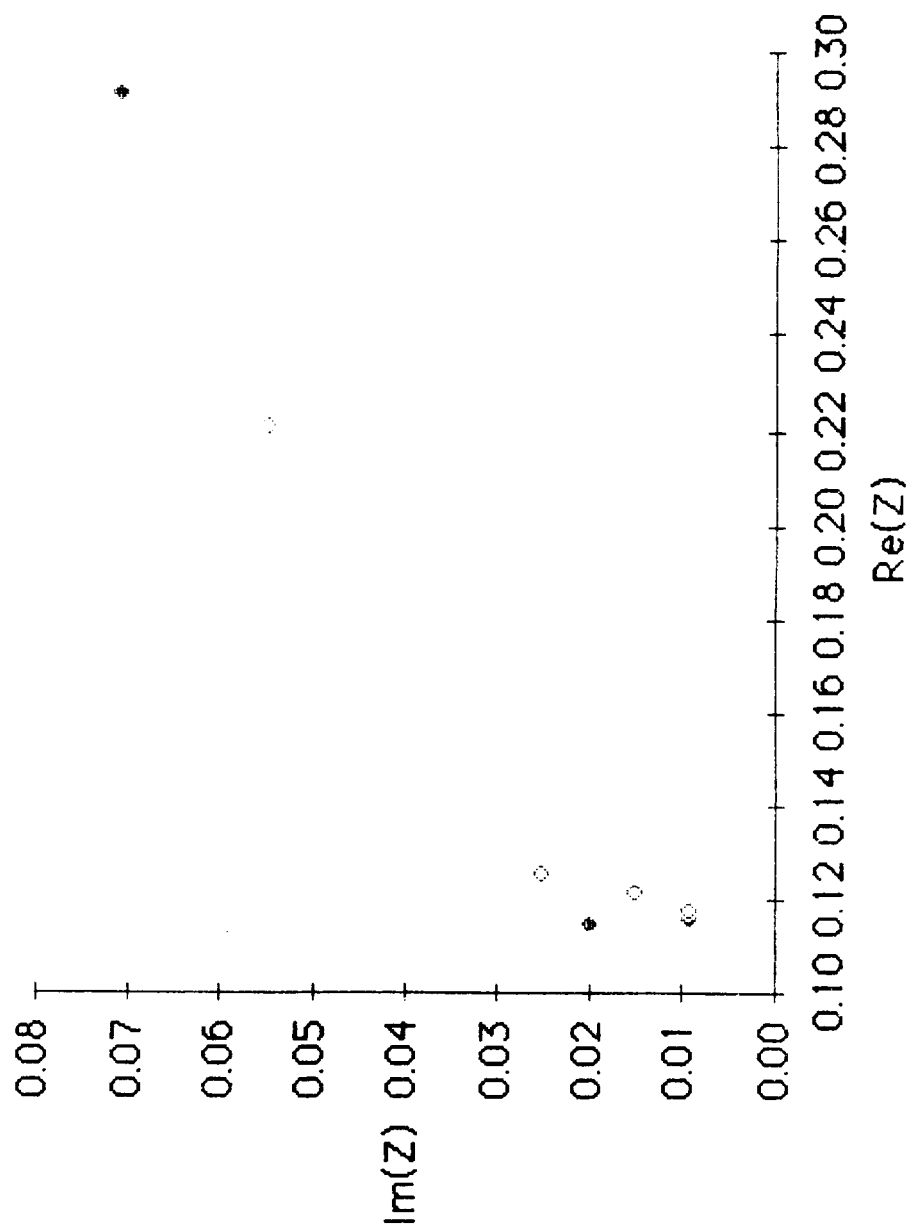


Figure 9. Nyquist plot for Eagle-Picher Ni electrode.

ORIGINAL PAGE IS
OF POOR QUALITY

Figure 10 shows a plot of $\text{Im}(Z)$ vs. frequency in a range from 100 - 3000 Hz for the Cd electrode. The plot is linear and the interfacial area can be estimated from the slope of the line. The double layer capacitance was assumed to be $80 \mu\text{F}/\text{cm}$ (Latham and Hampson, 1973), the electrode thickness was 0.04 cm, the solution conductivity $0.5 \text{ ohm}^{-1} \text{ cm}^{-1}$ and the effective conductivity in the porous electrode was estimated using the Bruggemann equation

$$k_{\text{eff}} = k(\text{porosity})^{1.5}$$

with a porosity of 0.25 to 0.3. The interfacial area was estimated to be 8 to $15 \text{ m}^2/\text{g}$, which compares with results of 2 to $50 \text{ m}^2/\text{g}$ determined by Pickett (1975) from BET (hydrogen adsorption) measurements. The BET technique determines total area, while the present technique measures only the electrochemically active area.

G.E. Cell

Some impedance spectra were measured for a G.E. 20 A-Hr cell. The cell had been on the shelf for about 14 years with the terminals shorted. It was cycled several times and a capacity of 21 A-Hr was obtained, however, the cell did not retain charge- it lost about half its capacity during overnight stand. The impedance spectra was measured in the low frequency range (0.001 to 1 Hz) in the following conditions: 1) discharged and overnight stand, 2) fresh charge, 3) fresh discharge, and 4) recharged and overnight stand. At 1 Hz the phase angle was zero, while at frequencies of about 100 Hz and larger the potential led rather than lagged the current, indicating that induction effects, which do not have an electrochemical explanation, dominated the capacitance effects.

Figure 11 compares the spectra of conditions 1 and 2. The impedance of the discharged cell is larger than the charged cell due to the $\text{Cd}(\text{OH})_2$ film

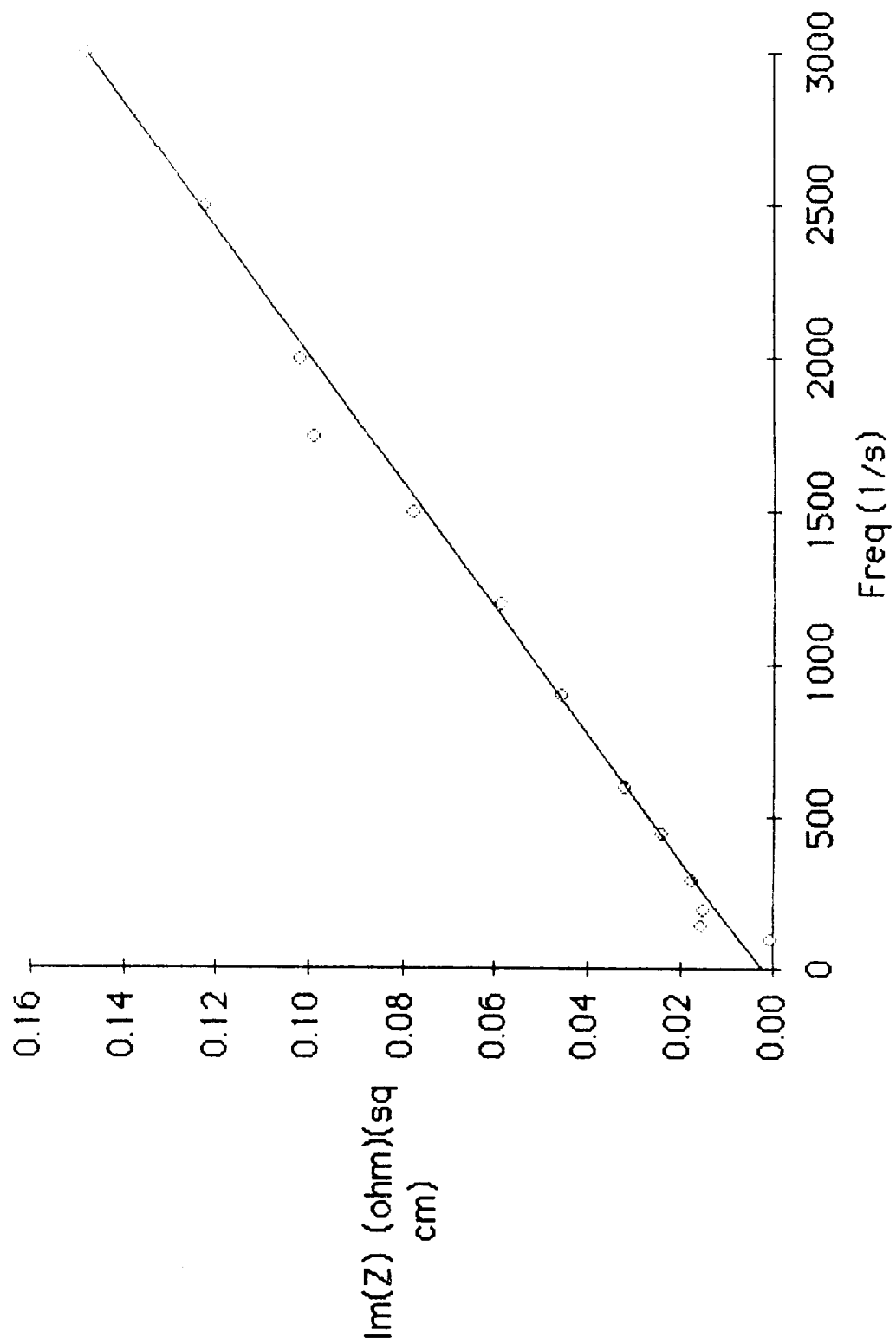


Figure 10. Imaginary impedance component vs. frequency for Eagle-Picher Cd electrode.

GE 20 A-Hr Cell

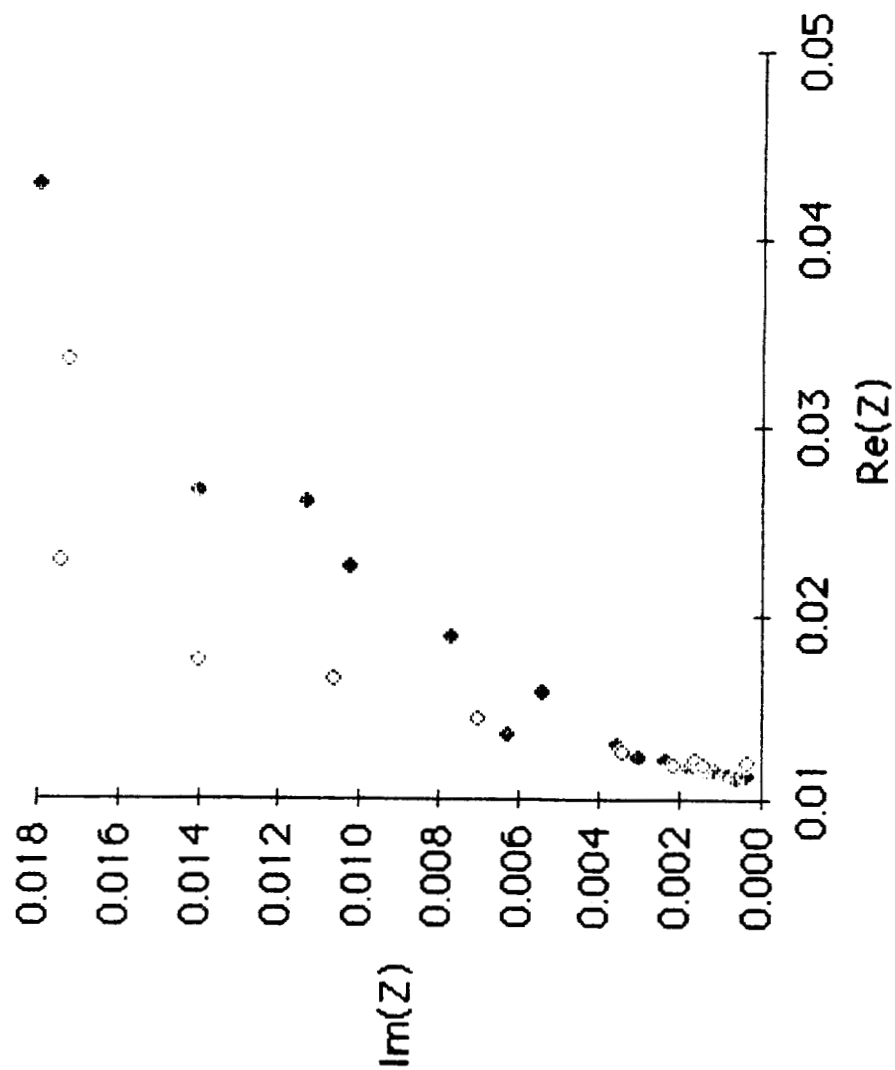


Figure 11. Nyquist plot for GE 20 A-Hr Cell.

that hinders diffusion. Figure 12 compares conditions 1 and 3, both of which are discharged conditions and yield similar spectra. Figure 13 compares the two recharged conditions, and there is a clear difference between the two results. The spectra for condition 4 are unlike the others observed. More data are needed to conclusively determine whether it is a bad set of measurements or if it represents reality. The dotted line shows how two humps, representing two time constants (one for each electrode) may be important. This would indicate that the recharged nickel electrode degrades upon stand.

CONCLUSIONS AND RECOMMENDATIONS

The following conclusions are made concerning this study: 1) the specific area of battery electrodes can be estimated using frequency response techniques during DPA. The results are consistent with those obtained by other workers. 2) Attempts to correlate cell state of charge are inconclusive. It seemed to work better for individual electrodes during DPA than for cells.

It is recommended that 1) methods for evaluating other electrode structural parameters such as porosity and tortuosity be developed, 2) a long term study of frequency response as a non-destructive battery test be undertaken. Ten weeks is insufficient time for such a study. The results of such a study would be a correlation of state of charge and of battery acceptability for space flight. 3) Develop quantitative data analysis of impedance in the low frequency (mass-transfer dominated) range. 4) Apply frequency response techniques outlined in this report to Ni/H₂ and Ag/Zn cells.

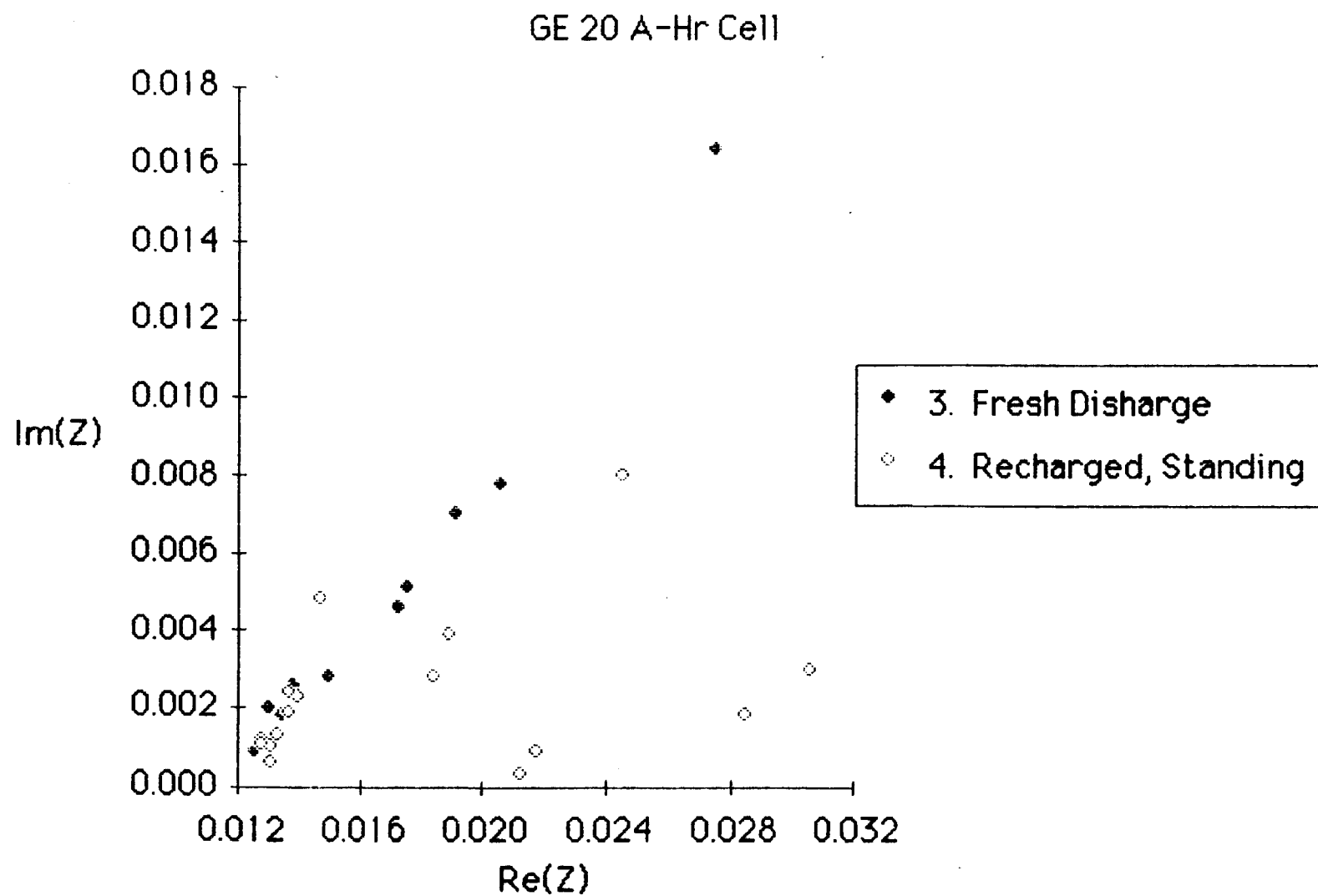


Figure 12. Nyquist Plot for G.E. 20 A-Hr cell (continued).

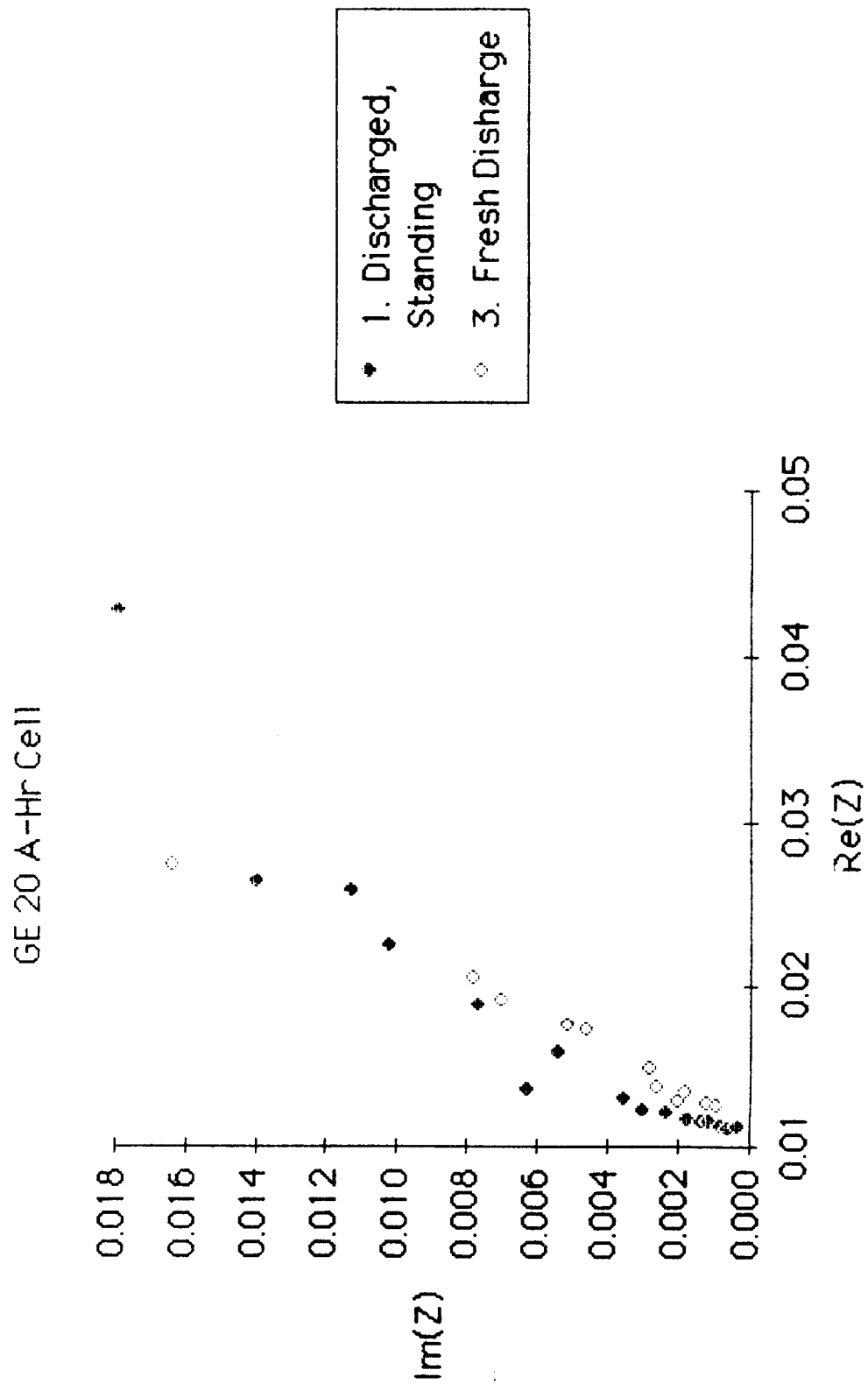


Figure 13. Nyquist plot of G.E. 20 A-Hr cell (continued).

REFERENCES

- R.D. Armstrong and K. Edmondson, Electroanal. Chem. and Interfac. Electrochem, vol 53, pp 371-387, 1974.
- R.D. Armstrong, K. Edmondson and J.A. Lee, J. Electroanal. Chem., vol 63, pp. 287-302, 1975.
- A.J. Bard and L.R. Faulkner, Electrochemical Methods, J. Wiley and Sons, New York, 1980.
- R.J. Brodd and H.J. DeWane, J. Electrochem. Soc., vol 110, p. 1091, 1963.
- R. Haak, C. Ogden and D. Tench, J. Power Sources, vol 12, pp 289-303, 1984.
- R.J. Latham and N.A. Hampson, in Encyclopedia of Electrochemistry of the Elements, vol 1, A.J. Bard, ed., Marcel Dekker, New York, 1973.
- J. Newman, Electrochemical Systems, Prentice Hall, Englewood Cliffs, NJ, 1973.
- D.F. Pickett, Air Force Aero. Propulsion Lab., Report No. AFL-TR-75-34, 1975.
- S. Sathyanarayana, S. Venugopalan and M.L. Gopikanth, J. Appl. Electrochem., vol 9, pp. 125-139, 1979.
- W. Tiedemann and J. Newman, J. Electrochem. Soc., vol 122, pp 70-74 1975.
- A.H. Zimmerman, M.R. Martinelli, M.C. Janecki and C.C. Badcock, ibid, pp. 289-298, 1982.

**1989
NASA/ASEE SUMMER FACULTY RESEARCH FELLOWSHIP PROGRAM**

**MARSHALL SPACE FLIGHT CENTER
THE UNIVERSITY OF ALABAMA IN HUNTSVILLE**

YAW RATE CONTROL OF AN AIR BEARING VEHICLE

Prepared by:	Bruce L. Walcott, Ph.D
Academic Rank:	Assistant Professor
University and Department:	University of Kentucky Department of Electrical Engineering
NASA/MSFC:	
Laboratory:	Flat Floor Facility
Division:	Information and Electronic Systems
Branch:	Control Electronics
MSFC Colleagues:	E.C. Smith and Frank Nola
Date:	August 11, 1989
Contract No.	The University of Alabama in Huntsville NGT-01-008-021

YAW RATE CONTROL OF AN AIR BEARING VEHICLE

by

*Bruce L. Walcott
Assistant Professor of Electrical Engineering
University of Kentucky
Lexington, KY 40506-0046*

ABSTRACT

This report summarizes the results of a 6 week project which focused on the problem of controlling the yaw (rotational) rate the air bearing vehicle used on NASA's flat floor facility. Contained within is a listing of the equipment available for task completion and an evaluation of the suitability of this equipment. This report also details the identification (modeling) process of the air bearing vehicle as well as the subsequent closed-loop control strategy. The effectiveness of the solution is discussed and further recommendations are included.

ACKNOWLEDGEMENTS

The author expresses his deepest appreciation and gratitude for the warmth and hospitality extended by his adopted family, the friendly people of EB24. In particular, he wishes to thank his principal colleagues, E.C. Smith Frank Nola for their advice, supervision, encouragement and mentoring. The author also wishes to acknowledge Bill Jacobs for his assistance and expertise concerning the air bearing vehicle and Tom Bryan for his advice and midnight-oil-burning chats. A special thanks is extended to Cindy Coker and Harry Reid for their discussions and advice on the two projects the author worked on during the four weeks following the completion of the project outlined in this report. The author is grateful to Riczy Howard, Mike Book, Charles Oliver and Tom Sutherland for the use of their equipment (and for challenging homework problems!). Of course, Andy Gamble, Zack Barnett, Jon McInroy and Kirk Smith are to be awarded the highest commendations for making exiled life in 4619 bearable. Lastly, Dr. Gerald Karr and Dr. Frank Six are to be congratulated on their outstanding seminars and superb supervision of the 1989 ASEE/NASA MSFC Summer Faculty Fellowship Program. Great job guys!

1 INTRODUCTION

The Marshall Space Flight Center in Huntsville, Alabama is home to the largest precision flat floor facility in the world. This 4200 square foot floor is constructed of self-leveling black epoxy and is flat to within 1/1000 of an inch over any given square yard and to within 3/1000 of an inch from corner to corner. The featured player on this ebony stage is a 4400 pound cubicle vehicle built from NASA's own design. This vehicle rides 6/1000 of an inch above the flat floor on a cushion of air supplied by three air bearings. Satellite and Orbital Maneuvering Vehicle mock-ups are mounted to the front of the vehicle in order to perform docking and rendezvous simulations. Lighting conditions can be completely controlled on the floor plus the vehicle can transmit video and telemetry via an RF link. Unstable satellites can be simulated using the eight degree of freedom dynamic overhead target simulator (DOTS). Thus, even the most difficult OMV docking problems can be simulated using the vehicle and the DOTS. A total of 24 air thrusters are mounted on the lower four corners of the vehicle to enable the vehicle to move in X, Y and Yaw directions while servo motors on the front of the vehicle give mock-ups the added capabilities of Z, Roll, and Pitch. Thus, a mock-up on the vehicle has a total of six degrees of freedom.

In the past, prestigious high-tech corporations such as General Electric, TRW, and Martin Marietta have utilized the flat floor and the air bearing vehicle to develop and validate docking and rendezvous strategies as well as to investigate contact dynamic problems. These companies have future commitments to the flat floor facility thereby making continual operation and functionality enhancement high priorities of NASA.

2 OBJECTIVES

The following is a list of objectives which must be attained in order to complete the project:

1. Develop an assembly language driver for the data acquisition board. This driver should be capable of interfacing with a C language program.

2. Mount a static inverter on the air bearing vehicle
3. Become familiar with Microsoft 5.1 C.
4. Mount CMGs and rate gyros on the vehicle.
5. Connect torquer motor servo input to D/A output of data acquisition board and rate gyro output to A/D input.
6. Model the open loop system consisting of the input to the torquer servo and the output of the rate gyros. Initially, this identification will be performed off-line. If an adaptive control is required, this identification will be done on-line as part of the control loop.
7. Develop a control law based on the results of the identification scheme. Initially, this control law will be developed off-line but should have the capability of being developed on-line should an adaptive control scheme be required.
8. Implement and test the control law.
9. Devise and implement a scheme for desaturating the CMGs.

3 PROBLEM STATEMENT

3.1 Motivation

The results of earlier research and experimentation demonstrated that the use of the air thrusters to control translational (X and Y) and rotational (Yaw) motion on the vehicle is inefficient. This is due to the high degree of coupling which exists between the thrusters dedicated to translational movement and the thrusters responsible for rotational motion. That is, a translational motion from the thrusters introduced a rotational component and vice-versa. Thus, the thrusters act opposedly rather than separately in controlling the vehicle. Consequently, finding a decoupled control law or suitable alternative source of motion for the vehicle is of urgency to NASA.

3.1.1 Control Moment Gyros

One possible solution to the coupled control problem detailed above is to replace the Yaw thrusters by control moment gyros (CMGs). The theory behind the use of CMGs to control Yaw can be summarized by Newton's second law of motion as applied to rotational systems. Newton's second law states that the rate of change of momentum of a body is equal to the sum of the external torques acting upon it. That is,

$$\sum T_{\text{external}} = \frac{dH}{dt}$$

where H is the angular momentum of the gyro and T_{external} are the external torques. A CMG operates in the exact opposite manner as an inertial guidance gyro. In an inertial guidance gyro, a torque is applied to the gyro when the body changes direction. This torque produces a rate perpendicular to the gyro's spin axis, which is measured. Conversely, in a CMG a rate is produced perpendicular to the gyro's spin axis by a torquer motor. This rate causes a change in the angular momentum which produces a torque perpendicular to the gyro's spin axis.

To illustrate, consider Figure 1. Figure 1 shows a one degree of freedom

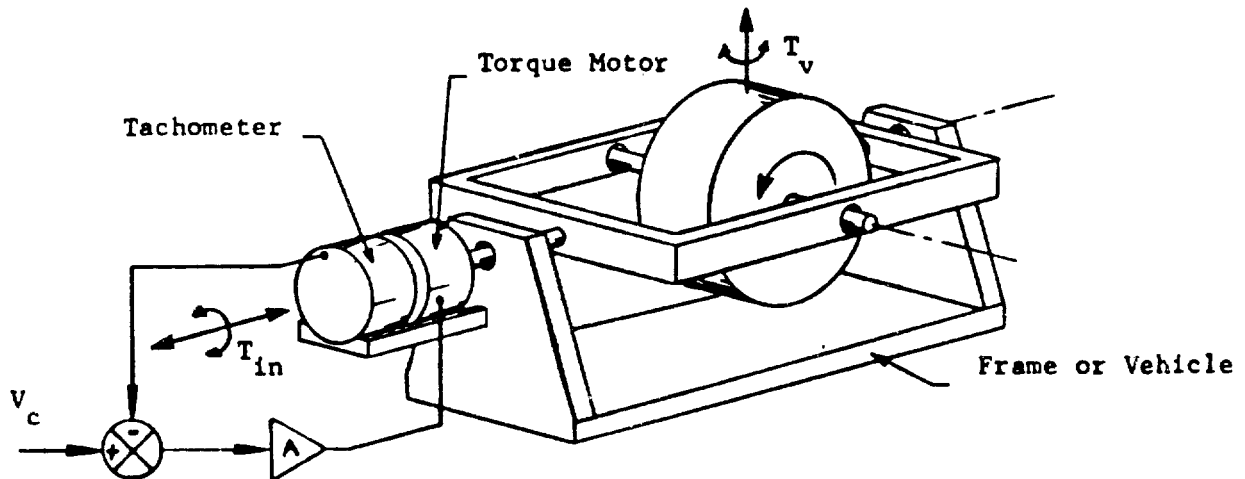


Figure 1 - Single Degree of Freedom CMG

CMG [1]. The servo torquer motor produces a rate ω as shown. This rate yields a torque, T , given by

$$T = \omega \times H$$

If we assume that the magnitude of the angular momentum is constant (i.e., the gyro is spinning at a constant rate), then the component of torque produced in the horizontal plane is

$$T_{yaw} = H\omega \cos\theta \quad (1)$$

where θ is the angle formed between the spin axis of the gyro and the horizontal plane in which the vehicle travels.

Therefore, as a solution to the coupling control problem, a single degree of freedom CMG could replace the yaw thrusters.

4 PROPOSED SOLUTION

4.1 Available Equipment and Specifications

Hardware which can be dedicated to the project includes:

- Two Sperry reaction wheels and brushless DC torquer motor.
- One Apollo Telescope Mount (ATM) rate gyro rated at 1 deg/sec
- Two Spring-driven rate gyros rated at 60 deg/sec
- One TELEX 1280 PC-AT clone operating at 12 MHz
- One IBM PC Data Acquisition and Control Adapter
- One Avionics Instruments Static Inverter

Software which is available for the project includes:

- Microsoft C 5.1
- Microsoft Assembler 5.0

• Matlab 3.13 and the Control and System Identification Toolbox

To determine if the hardware available is sufficient to solve the problem, let us consider the yaw specifications of the OMV mock-up which is the most popular mock-up on the vehicle. The proposed OMV will be able to achieve a maximum yaw rate of 2.3 deg/sec. If we consider the vehicle as a uniform rectangular solid with a mass of 2000 kg and the dimensions 1.5 meters wide by 2 meters long by 2 meters tall, then we may calculate the moment of inertia by

$$I_{vehicle} = \frac{2000[(1.5)^2 + (2.0)^2]}{12} = 1041 kgm^2 \quad (2)$$

Next, let us note that the maximum rate of the available DC brushless torquer motor is approximately 1.0 rad/sec. Recall from equation (1) that the torque supplied by the CMG varies with $\cos \theta$ where θ is the angle formed between the gyro's spin axis and horizontal. To estimate the torque required to meet the OMV specifications, let us assume that the torquer motor turns the gyro at a constant rate equal to the motor's maximum rate (i.e., 1.0 rad/sec). We will further assume that θ is allowed to vary from 0 radians to $\frac{\pi}{2}$ radians. Neglecting the dynamics of the torquer, the time necessary to turn the gyro from 0 to $\frac{\pi}{2}$ radians is $\frac{\pi}{2}$ seconds. Therefore, the maximum torque required to achieve the OMV specification is estimated at

$$T_v = \frac{1041 \times 2.3 \times \left(\frac{\pi}{180}\right)}{\frac{\pi}{2}} = 26.6 Nm$$

Thus, the angular momentum required of the gyro is

$$H = \frac{T_v}{\omega(\cos \theta)_{ave}} = \frac{26.6}{1.0 \times \frac{2}{\pi}} = 41.8 kgm^2/s$$

where $\cos \theta_{ave}$ is the average value of the $\cos \theta$ as the torquer turns the gyro from 0 to $\pi/2$ radians. The reaction wheels are rated at an angular momentum of 11.4 kgm^2/s at a speed of 1500 rpm. Recall that the angular momentum of a rotating cylinder is $mr^2\omega$. Thus, to satisfy the rate demanded by the OMV specification plus a safety margin, two Sperry reaction wheels running at 3000 rpm must be used in the CMG design. This configuration yields a total angular momentum of 45.6 kgm^2/s , more than

the required $41.8 \text{ kgm}^2/\text{s}$. The reaction wheels were mounted at opposite ends of the torquer motor shaft with the two spin axes parallel to each other and perpendicular to the motor shaft. Thus, each reaction wheel behaves as a single degree of freedom gyro. Although the gyros can be coupled at any point on the vehicle and still transmit their maximum torque to the vehicle, they were mounted as close to the center of mass as possible to minimize any unbalance the gyros might introduce.

Since a variety of mock-ups and payloads will be used on the air bearing vehicle, an adaptive control strategy may be required to adequately replace the yaw control. In addition, the CMGs supplying the torque to the vehicle will have to be desaturated intermittently. That is, when θ nears 90 deg, the amount of torque which the CMG's can supply is nearly zero and if θ exceeds 90 deg, the horizontal component of the torque will switch directions. Consequently, the problem solution should include a scheme whereby the CMGs can be returned to $\theta = 0$ without affecting the rate of the vehicle.

4.2 Restatement of Objectives

The following is a restatement of the objectives (tasks) which must be attained in order to complete the project:

1. Develop an assembly language driver for the data acquisition board. This driver should be capable of interfacing with a C language program.
2. Mount a static inverter on the air bearing vehicle.
3. Become familiar with Microsoft 5.1 C.
4. Mount CMGs and rate gyros on the vehicle.
5. Connect torquer motor servo input to D/A output of data acquisition board and rate gyro output to A/D input.
6. Model the open loop system consisting of the input to the torquer servo and the output of the rate gyros. Initially, this identification will be performed off-line. If an adaptive control is required, this identification will be done on-line as part of the control loop.

7. Develop a control law based on the results of the identification scheme. Initially, this control law will be developed off-line but should have the capability of being developed on-line should an adaptive control scheme be required.
8. Implement and test the control law.
9. Devise and implement a scheme for desaturating the CMGs.

Both of the above remarks indicate that the control solution should be completed on a microprocessor or micro-computer. Since a Telex PC-AT clone and data acquisition board are available for this project, the decision was made to design the control law around a micro-computer.

5 PROJECT SUMMARY

The first two weeks of the project were devoted to developing an assembly language driver for the IBM data acquisition board which could be interfaced with a C language control program. This time was also used to learn the peculiarities of Microsoft C 5.1 which differs significantly from Turbo C 2.0 used at the University of Kentucky.

Fortunately, NASA engineer Charles Oliver had already developed an assembly language driver for the IBM data acquisition board which had been modified by NASA engineer Bill Jacobs to interface to Microsoft Quick BASIC programs. However, as was painfully discovered during the initial two weeks of the project, calling and return conventions are entirely different in C programs than in BASIC programs. BASIC programs pass the long address (segment and offset) of pointers to the arguments of the subroutine on the stack while C programs pass the actual pointers themselves on the stack. Furthermore, BASIC programs expect the return values to be passed on the stack while C programs expect the return values of functions to be stored in the AX register.

The source listing for the assembly language driver is contained in Appendix A.

After the completion of the assembly language driver, the ensuing two weeks were dedicated to the installation of the static inverter and to obtaining a model for the vehicle with the input being the voltage to the torquer

servo loop and the output being the voltage out of the rate gyros measuring the yaw of the vehicle. The static inverter was installed with the invaluable aid of Bill Jacobs. The inverter, which is of aircraft quality, converts the 28 volt DC power present on the vehicle to 115 volts 60 Hz AC signal thereby enabling the PC-AT clone with the data acquisition board to be mounted on the vehicle.

In the initial stages of modeling the system, it was discovered that the spring driven gyros rated at 60 deg/sec worked reasonably well in lieu of a tachometer in the torquer servo loop. Here, rates of up to 1 rad/sec (57 deg/sec) are being measured. The maximum yaw rate of the vehicle is 2.3 deg/sec, however, which is still within the noise level of the spring-driven gyros. Consequently, the decision was made to use the ATM rate gyro to measure the yaw of the vehicle. This gyro saturated at 1 deg/sec which corresponded to an output of 6.6 volts (after a voltage division circuit), but gave an extremely clean and linear signal up to that point. Yet, the relatively low saturation level inhibited testing of the vehicle at yaw rates above 1 deg/sec. The decision was made to continue with the modeling procedure using the ATM gyro's output, but also to devote some thought to how one might increase the saturation level on the ATM.

Since an adaptive control strategy may be required to control the yaw rate of the vehicle, the identification (modeling) scheme must possess the capability of being implemented on-line. Consequently, the identification procedure purported by Ljung [2], Eykhoff [3], Astrom [4], Soderstrom and Stoica [5] and others was selected. In brief, this identification scheme consists of three parts: selection, application, and recording of data; selection of possible candidate models; and determination of the best-suited model. Once the structure of the model is known, model parameters can be estimated using a criterion such as least-squares.

5.1 Data Collection

In sampling data using our PC-AT clone data acquisition system, we must select a sampling interval which will avoid the effects of aliasing. Furthermore, since our application involves not just identification but control as well, we do not want to sample too fast which might lead to a non-minimum phase model and/or a model with a delay of many sampling periods. Thus,

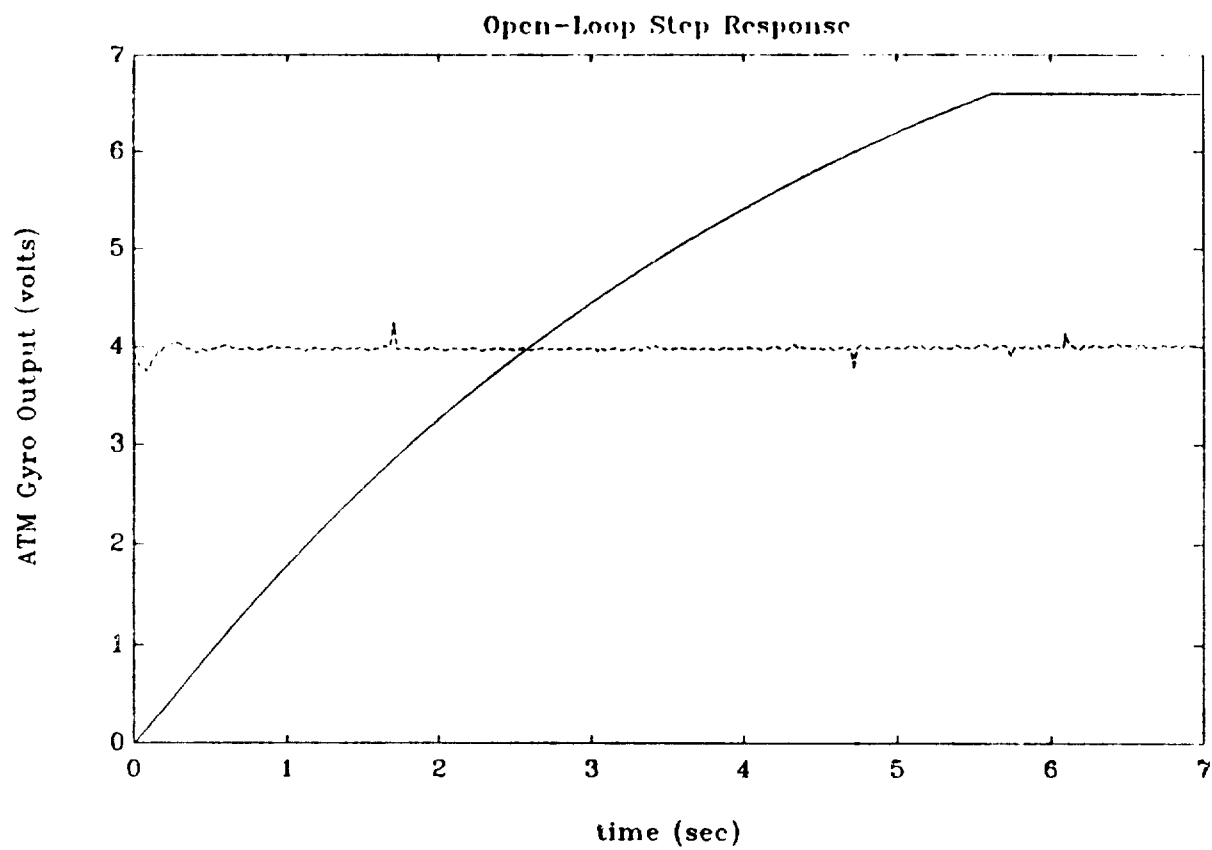


Figure 2 - Open-Loop Step Response of the Vehicle

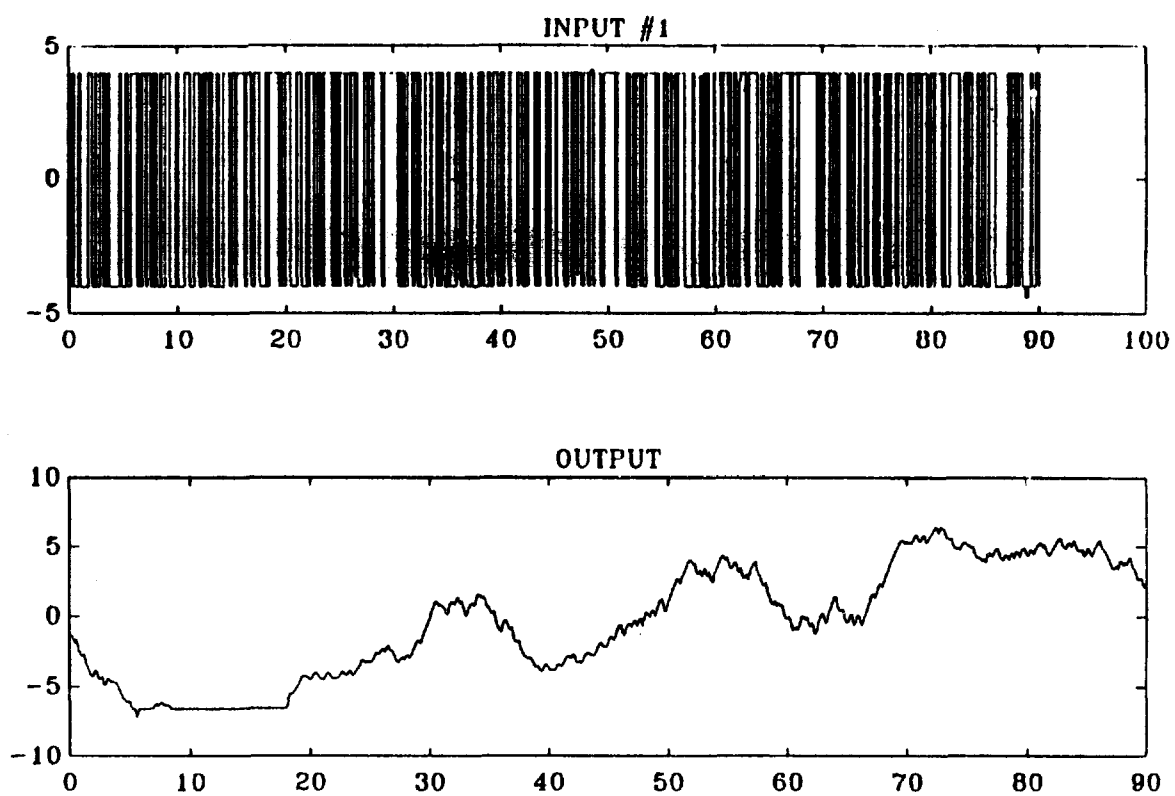


Figure 3 - Random Binary Input and Corresponding Output of ATM Rate Gyro

the choice of the sampling time, T , should be less than the dominant time constants of the system, but not significantly.

To obtain an estimate of a reasonable sampling time, the open-loop step response was found with the input being the voltage into the torquer-servo loop and the output being the voltage from the ATM gyro which is proportional to the rate of the vehicle until saturation. If the input were a step torque supplied from the gyro (i.e., if T_g were a step), we would expect the step response to produce some sort of ramp (assuming the vehicle is riding on a frictionless surface). However, since the input is a step voltage to the torquer servo, we would expect such an input to produce a constant precession rate, ω , in the gyros (neglecting the dynamics of the servo loop). The torque applied to the vehicle will not be constant, since equation (1) shows us that this torque varies with the cosine of θ . The results of the step response are displayed in Figure 2. All experiments on the vehicle were conducted at a setting of 50 psi on the air bearings. As can be seen from Figure 2, the step response is a cross between a type 0 step response and a type 1 step response. Although no actual dominant time constant can be measured, from the overall slow response depicted in Figure 2, a sampling time of about 150 milliseconds should suffice.

Upon selection of a reasonable sampling time, the system must be excited by a random signal which excites all of the modes of the system. Such an input is white noise. Since we are using a discrete magnitude-limited input, we cannot generate a true white noise signal. However, a binary input which switches values with a probability of 0.5 has the same effect as white noise (see Ljung (1987)). A magnitude of 4 volts was selected for the random binary signal. The results of the application of the random binary input as well as the input itself can be seen in Figure 3. A total of 600 data points were taken at a sampling interval of 0.15 sec.

Following the data collection, the next step in the identification process is to develop a list of possible model structure candidates and to pose a criterion for selecting the best-fitting structure. From the step response shown in Figure 2 and from the equations of motion used to estimate the torque required of the CMG, a linear model would be a reasonable choice to represent the vehicle. The particular linear model structure candidate was chosen to be an Auto-Regressive Exogeneous structure (ARX) with unknown parameters. The notation $ARX(m,n,p)$ represents the following

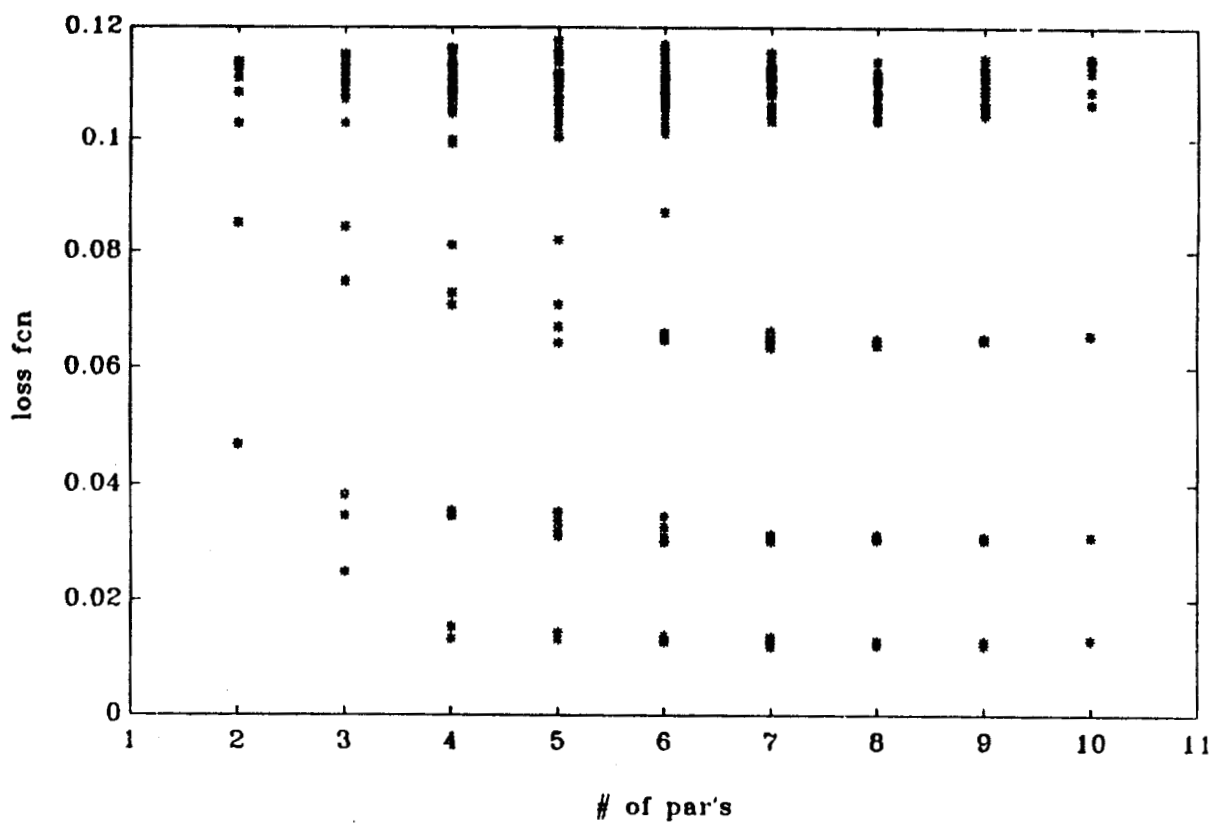


Figure 4 - Loss Function V for 250 ARX Candidates

input-output relationship:

$$y(t) + a_1 y(t - T_s) + \dots + a_n y(t - nT_s) = b_1 x(t - pT_s) + \dots + b_m x(t - (p + m - 1)T_s) \quad (3)$$

where T_s is the sampling time. That is, the transfer function $\frac{Y(q)}{X(q)}$ has n poles, $m-1$ zeros and a time delay of pT_s . The parameters a_i and b_i are the parameters to be estimated. The ARX structure was chosen over a ARMAX (auto-regressive with a moving average and exogenous term) because the disturbances on the system are not prominent. Furthermore, calculating the control law is simpler with an ARX model than an ARMAX model.

Once the model structure has been decided upon, a criterion for determining the best fitting ARX structure is needed. That is, the best combination of number of delays, the order of the numerator, and the order of the denominator needs to be evaluated. Also, the data must be divided into two categories: data for identification and data for validation. In other words, a portion of the data must be used to identify the best fitting ARX structure and then the remainder of the data should be used for cross verification purposes. To this end, the data was divided into two equal portions: the first three hundred points were used for estimation purposes while the final three hundred data points were employed for verification purposes.

In trying to identify a criterion for selecting the best-fitting ARX structure, two closely-related strategies predominate. The first is the Akaike Final Prediction Error (FPE) criterion where the following entity is desired to be minimized:

$$FPE = \frac{1 + n/N}{1 - n/N} V$$

where n is the total number of parameters to be estimated, N is the number of data points, and V is the quadratic loss function for the particular structure under scrutiny (see Ljung (1987)). The second criterion, called Akaike's Information Theoretic Criterion (AIC), is closely related to the FPE criterion. In the AIC, the following quantity is minimized:

$$AIC \approx \log[(1 + 2n/N)V]$$

The FPE criterion is selected for our identification problem.

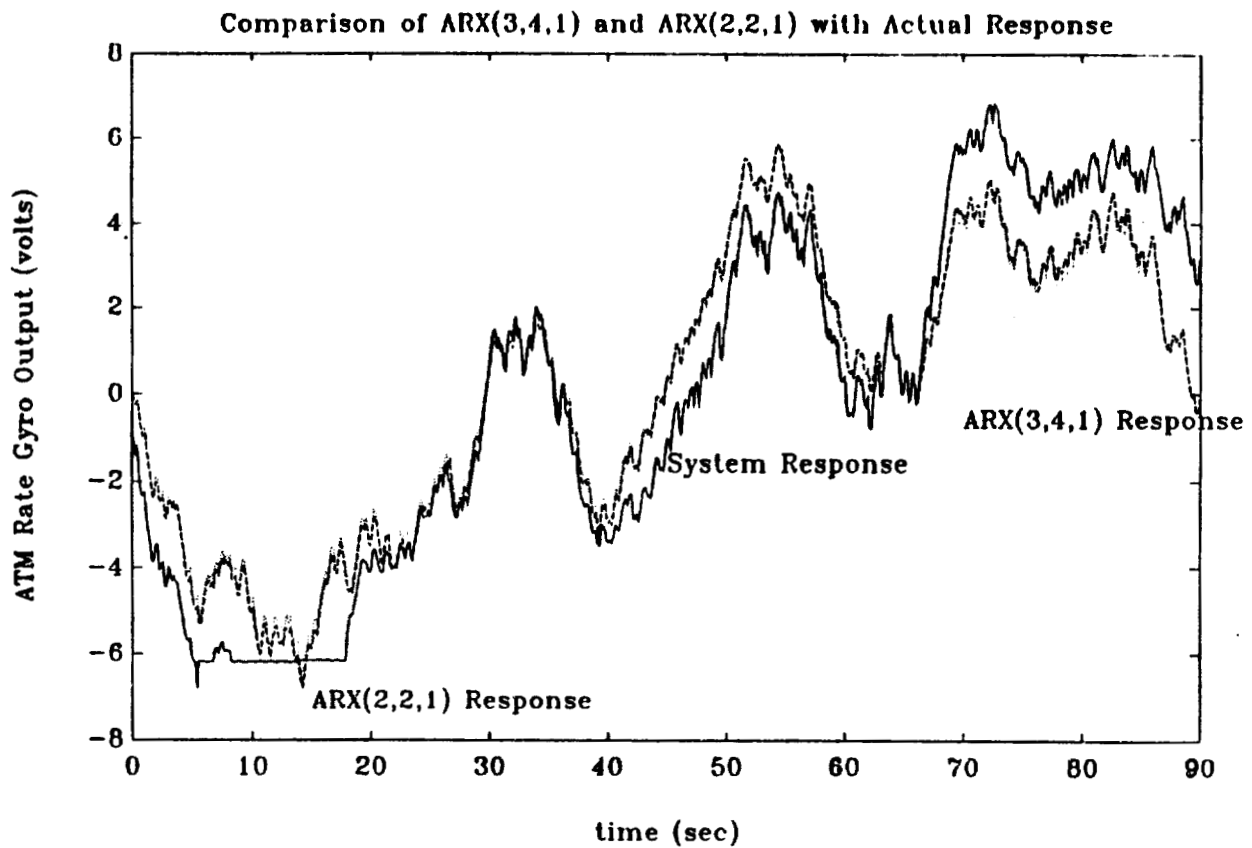


Figure 5 - Comparison of Response of the Two ARX Models to the Actual Response

Figure 3 depicts the binary input which was applied to the vehicle's torquer servo and the corresponding response. In the structure selection ARX(m,n,p) candidates were considered where m was varied from 1 to 5, n was varied from 1 to 5, and p was varied from 1 to 10. That is, a total of 250 structures were considered by calculating the FPE for each structure. The results of this examination are shown in Figure 4. The structure candidate which achieved the lowest overall FPE was an ARX(3,4,1) model with an FPE = 0.0242 and a loss function of V = 0.0231. This implies that the best model for the system (out of the 250 models considered) is

$$y(t) + a_1y(t - T_s) + \dots + a_5y(t - 5T_s) = b_1x(t - T_s) + b_2x(t - 2T_s) + b_3x(t - 3T_s)$$

Using a least-squares criterion, the 7 unknown parameters were estimated to be

$$a_1 = -1.0280, a_2 = 0.1515, a_3 = -0.2828, a_4 = 0.1633$$

and

$$b_1 = 0.0319, b_2 = 0.0548, b_3 = -0.0167$$

If we were concerned solely with identification, we would stop our search with the ARX(3,4,1) model. However, we are concerned with control as well as identification and a fourth-order model does not readily lend itself to control design, especially on-line computation. Thus, we should look for a lower order model which has an FPE comparable to the minimum of 0.0242. To this end we found that an ARX(2,2,1) structure has an FPE of 0.029 and a loss function of V = 0.0283 (compare to 0.0231). This second-order ARX structure is far preferable to the best-fitting ARX(3,4,1) model from a control perspective. An ARX(2,2,1) model has the input-output relationship:

$$y(t) + a_1y(t - T_s) + a_2y(t - 2T_s) = b_1x(t - T_s) + b_2x(t - 2T_s)$$

Using a least-squares criterion, the 4 unknown parameters were estimated to be

$$a_1 = -0.8025, a_2 = -0.1925, b_1 = 0.0320, b_2 = 0.0617 \quad (4)$$

To further illustrate that the ARX(2,2,1) model adequately represents the response of the vehicle, consider Figure 5 which depicts the actual response of the system to the binary input as well the responses of the

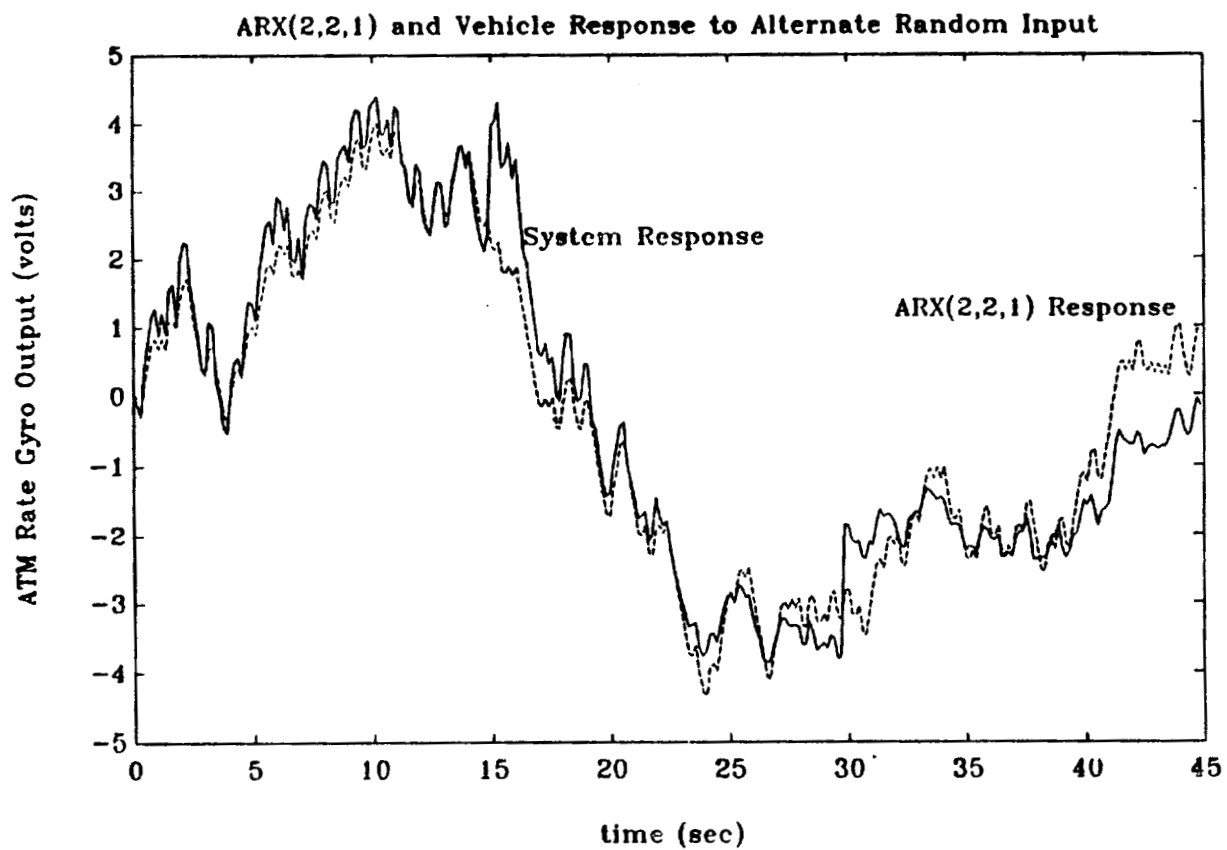


Figure 6 - Response of ARX(2,2,1) Model and Vehicle to Alternate Binary Input

best-fitting ARX(3,4,1) model and the ARX(2,2,1). As can be seen from Figure 5, there is very little difference between the two ARX responses and both closely follow the actual response of the vehicle. Hence, by selecting the ARX(2,2,1) model over the ARX(3,4,1) structure, we do not sacrifice much fidelity, yet gain a reduction in model order of one-half.

Figure 6 contains a final testament to the accuracy of the ARX(2,2,1) representation of the vehicle. Figure 6 shows the response of the vehicle to a random binary input different from that which was used to identify the ARX model. Also contained in Figure 6 is the response of the ARX(2,2,1) model to the same input. Note how closely the model response follows the vehicle response. Not only do the results displayed in Figure 6 indicate that the ARX(2,2,1) model adequately represents the system, but since these results were recorded on a date different from the data used to identify the system, they also suggest that an on-line identification scheme may not be necessary. That is, the dynamics of the system appear not to vary greatly with time (although no payload was attached), consequently the ARX parameters given in equation (3) accurately represent the system for all time t . This hypothesis will be true especially if our control law is sufficiently robust.

5.2 Control Design Considerations

Once the proper model for the vehicle has been selected, a closed-loop control law must be designed. The specifications for such a control are

1. Near zero steady-state error due to a step command
2. Settling time of less than 3 seconds
3. No overshoot
4. To be sufficiently robust so that an adaptive scheme is not necessary or to have the ability to be computed on-line

The settling time criterion stems from the 3 second time delay which is inherent in the OMV communication link when the OMV is piloted from the ground.

ORIGINAL PAGE IS
OF POOR QUALITY

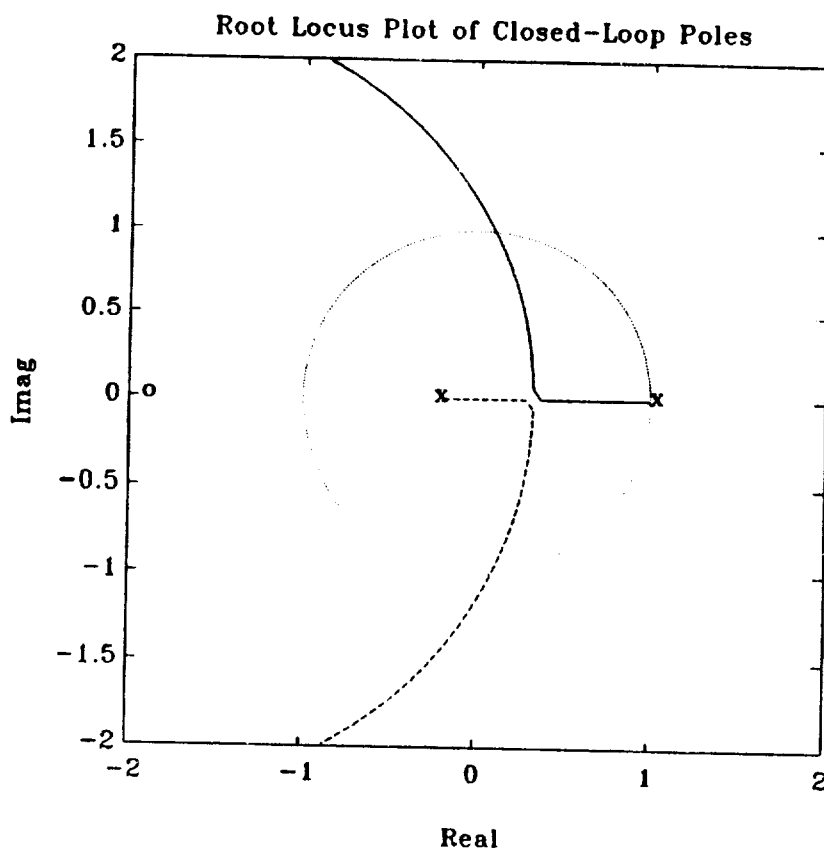


Figure 7 - Root Locus Plot of the Closed-Loop Poles

To address the first design specification, let us return our attention to Figure 2 which shows the open-loop step response of the vehicle. Note that the response does not attain a steady-state value and appears to ramp at a constant rate as t becomes large. This information suggests that the system type is greater than zero and that the closed-loop uncompensated step response would result in zero steady-state error. Therefore, no integrator is necessary in the feedback loop to satisfy the steady-state error specification.

To meet the settling time criterion, the poles in the s -plane must be to the left of $\sigma = -3/4$. Therefore, in the Z -plane the magnitude of the closed-loop poles must obey

$$|poles| \leq |e^{-3/4T_s}| = 0.8936$$

A root locus plot of the ARX(2,2,1) model is contained in Figure 7. To make the control design sufficiently robust without adding overshoot to the response, the value of the feedback gain is chosen such that the system is critically damped. That is, both poles are located at $\sigma = 0.3229$, $j\omega = 0$ which is well within the magnitude limit of 0.8936 imposed by the settling time specification. These closed-loop poles yield a theoretical settling time of

$$t_s = T_s \frac{\ln(0.3229)}{\ln(0.02)} = 0.5191 \text{ sec}$$

Such a large margin may appear at first to be overly conservative but if we drive our D/A output into saturation (± 10 volts), the settling time will probably be longer than this theoretical value.

The value of the feedback gain which yields a critically-damped system can be computed on-line from the values of the ARX parameters, a_1, a_2, b_1, b_2 . One can readily show that

$$k = - \left[\frac{(2a_1b_1 - 4b_2)^2 + [(2a_1b_1 - 4b_2)^2 - 4b_1^2(a_1 - 4a_2)]^{1/2}}{2b_1^2} \right] \quad (5)$$

For the values given in equation (4), equation (5) evaluates to

$$k = -4.9642$$

Although the above feedback gain causes our ARX off-line system model to become critically damped, if we choose to use an on-line parameter identification scheme, then equation (5) can easily be used on-line to calculate the necessary feedback gain.

5.3 Control Validation

To solve the problem of the ATM saturating at 1 deg/sec NASA engineers Hugo Berry and Bill Jacobs suggested that we use equation (1) to our advantage. That is, if the spin axis of the ATM gyro is tilted by an angle ϕ then the amount of yaw rate measured by the gyro in the plane of the vehicle will decrease by the $\cos\phi$. Thus, letting $\phi = 75^\circ$, the ATM gyro saturates at a value of $1 \times \frac{1}{\cos 75^\circ} = 3.864$ deg/sec rather than 1 deg/sec and the OMV maximum rate of 2.3 deg/sec can be easily realized. However, we have effectively decreased the forward loop gain by a factor of 3.864. Therefore, the critically-damped feedback gain listed in equation (5) must be multiplied by 3.864 to compensate which yields

$$k = -19.1802$$

Furthermore, spin axis of the ATM rate gyro is no longer parallel to the Earth's spin axis which implies that some variable rate disturbance will be introduced into the system depending upon the alignment of the vehicle on the flat floor. Although tilting the spin axis of the ATM gyro offers an inexpensive short-term remedy to the problem of low rate saturation, it is recommended that a more permanent solution be found either in the form of a different rate gyro, or in the form of a more effective modification of the current ATM rate gyro.

Appendix B contains two programs developed by Dr. Walcott during his 1989 tenure as an ASEE/NASA Summer Faculty Fellow. The first program closes the loop on the vehicle using the feedback control given in equation (5) and the computer control configuration shown in Figure 8. The desired output of the ATM gyro in volts (which is directly proportional to the yaw rate of the vehicle) is entered by the user via keyboard. This serves as the demand signal and is combined with the inverted ATM gyro output to form the error signal which is the input to the proportional control block. The output of the proportional control block is the actuating signal to the vehicle. The second program utilizes the same control strategy but the input demand can be varied via the user by typing a '1' to increase the demand signal by 1/8th of a volt and '2' to decrease the demand signal by the same amount.

The results of the first program are shown in Figure 9. For purposes

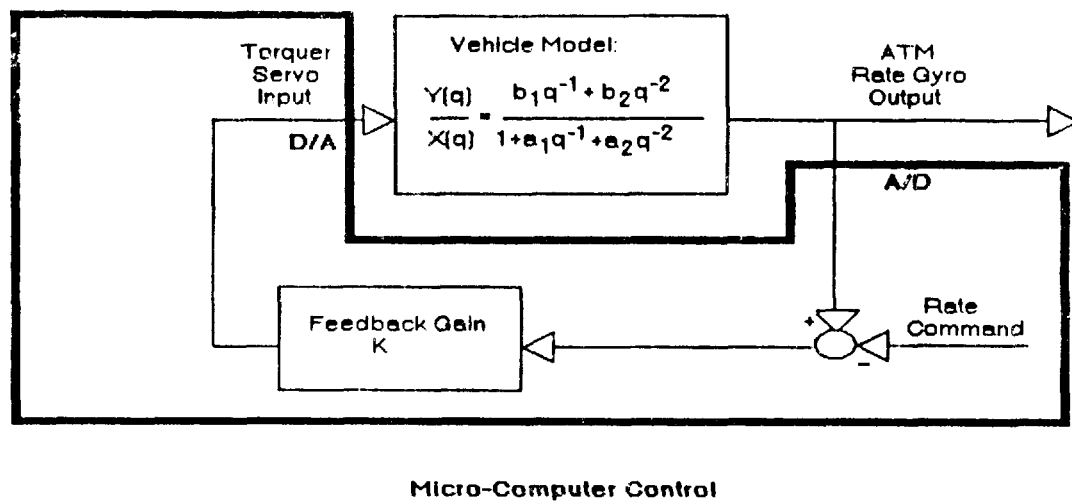


Figure 8 - Micro-Computer Control Block Diagram

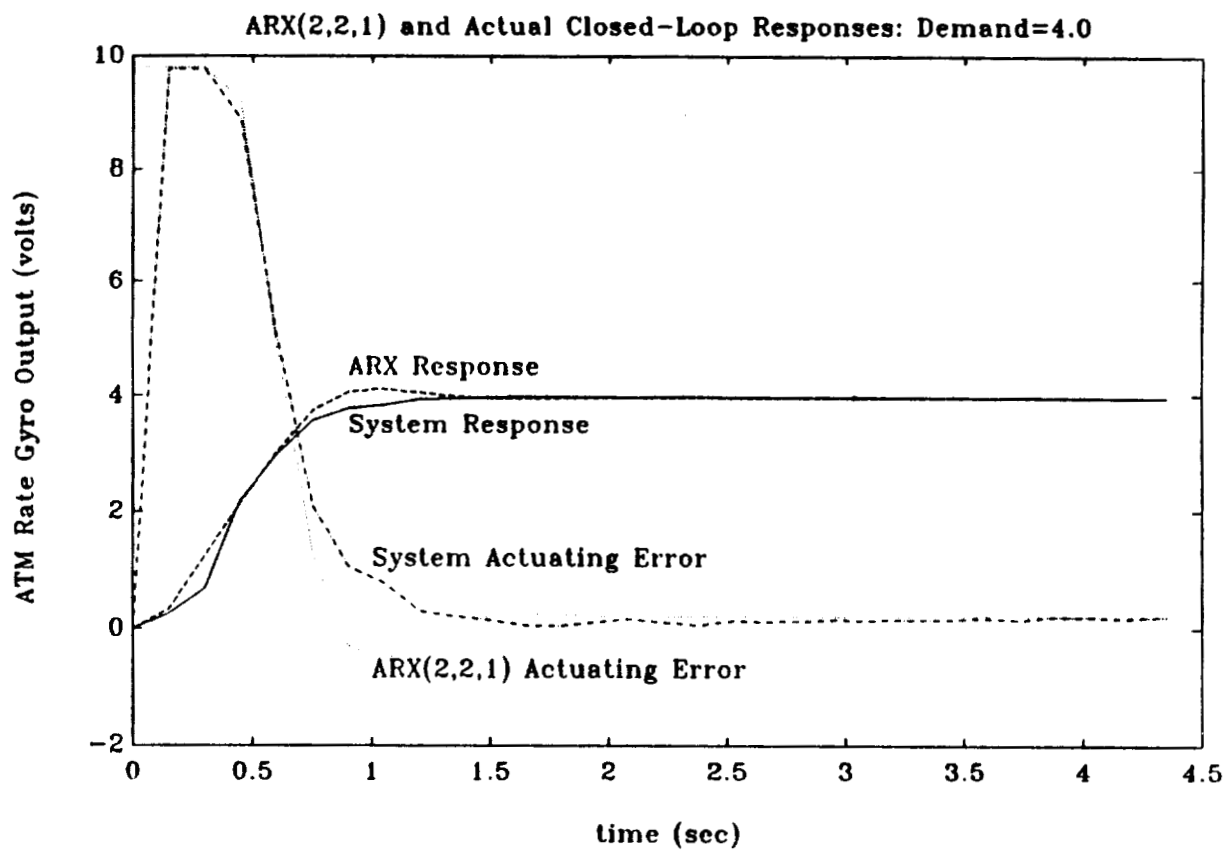


Figure 9 - Closed-Loop Response to a Rate Command of 4 Volts

of comparison, the ideal ARX(2,2,1) closed-loop response was generated by limiting the actuating error signal to ± 10 volts (which is the maximum available output of the D/A converter). Recall that a limiter acts as a low pass filter which causes the settling time to be much larger than the anticipated value of 0.5191 sec. The settling time of both the ideal and actual responses in Figure 9 is about twice this value, yet still well within the design specification of less than 3 seconds. In Figure 9 we also see that the ideal response overshoots ever so slightly while the actual response does not. The slight overshoot of the ideal response is caused by the presence of a closed-loop zero at $q = -1.9313$. Apparently, this zero is not as prominent in the actual system.

Figure 9 also reveals that the steady-state error for both the ideal and actual response is negligible and that the two responses are virtually identical except for the small difference in overshoot. This indicates that our off-line identification scheme has resulted in a high-fidelity model of the system and that on-line parameter identification is not necessary. Thus, we have met the first three control design specifications and the last specification, robustness, will be tested in the final phase of the project - solving the CMG desaturation problem.

5.4 CMG Desaturation

The benefits for utilizing the CMGs rather than the thrusters to control the yaw rate of the vehicle are that the CMGs deliver a pure torque which produces a rotational motion completely decoupled from translational motion. However, a disadvantage of the CMGs is that when the θ - the angle formed between the spin axis of the CMGs and horizontal - nears 90 degrees, very little torque is available in the plane of the vehicle. Moreover, if θ exceeds 90 degrees, the torque produced in the plane of the vehicle is in the opposite direction of the torque that was produced for θ less than 90 degrees. Therefore, we have a positive feedback situation and the system will go unstable. The identical problem occurs when θ nears -90 degrees so for purposes of discussion we will restrict our attention to the situation of θ increasing positively towards 90 degrees. These aforementioned problems illustrate the necessity of periodically desaturating the CMGs (that is, returning θ to 0 degrees).

The most obvious method for desaturating the CMGs is to sense the angle θ and fire the yaw thrusters in harmony with the torque produced by the CMGs as θ nears 90 degrees. That is, use the yaw thrusters to produce more torque than is demanded of the CMGs. This will act as a torque disturbance to the closed-loop control system and thereby produce an actuating error signal which will cause the torquer motor to turn the CMGs back towards decreasing values of θ . If the yaw thrusters continue to fire in harmony with the CMGs, the torquer will continue to desaturate the CMGs until $\theta = 0$ at which time the thrusters would cease fire.

This method may initially appear to re-introduce the problem of coupling between the translational thrusters and the yaw thruster but closer scrutiny bears that this is not the case. The yaw thrusters are no longer part of the closed-loop control and function merely as a bang-bang torque disturbance. Of course firing the yaw thrusters introduces a translational force disturbance in addition to the torque disturbance. This translational force disturbance can be compensated for by the translational thrusters and any additional torque disturbance produced by this compensation can be lumped with the original torque disturbance and eliminated by the CMGs, not the yaw thrusters. In other words, by virtue of the CMGs producing a pure torque, the torque disturbances produced by the translational thrusters are not coupled back to translational disturbances when counteracted by the CMGs.

This desaturation method assumes that the implemented control law is sufficiently robust to compensate for external torque disturbances without a significant deterioration in the error between the demand rate and the actual rate of the vehicle. Experiments with the control indicated that small disturbances such as convection currents and imperfections in the flat floor could easily be compensated. Whether the control was tight enough to counteract a large torque disturbance, remained to be seen.

Prior to testing the desaturation scheme, a few hardware modifications were necessary. First, the angle θ needed to be measured. Initially, this information was obtained by integrating the command to the torquer rate gyro. This solution worked amazingly well and would have sufficed if the torquer servo loop had been tighter. But the torquer rate gyro used spring driven operation which had a tendency to drift thus making accurate integration impossible for long periods of time. One solution would be to

replace the torquer rate gyro with a tachometer but a more inexpensive solution would be to mount a position sensor on the torquer axis. NASA engineer Bill Jacobs and NASA technician Zack Barnett came to the rescue by mounting a rotational potentiometer to the outside casing of one of the CMGs along the torquer spin axis. The output from the wiper arm of the pot was connected to an A/D channel of the adapter board with 0 volts corresponding to $\theta = 0$ and ± 8.3 volts corresponding to $\theta = \pm 90$ degrees.

Another hardware modification is to interface the yaw thrusters to the PC. The vehicle has two sets of yaw thrusters (clockwise and counterclockwise) and each set requires a 5 volt, low-current input to fire and an open circuit to cease fire. The IBM control adapter board has two D/A outputs and one of these has been consumed by the actuating signal output to the torquer servo. This implies that we must use a single D/A output to control both sets of thrusters.

The following circuit enables both sets of thrusters to be controlled from a single D/A output:

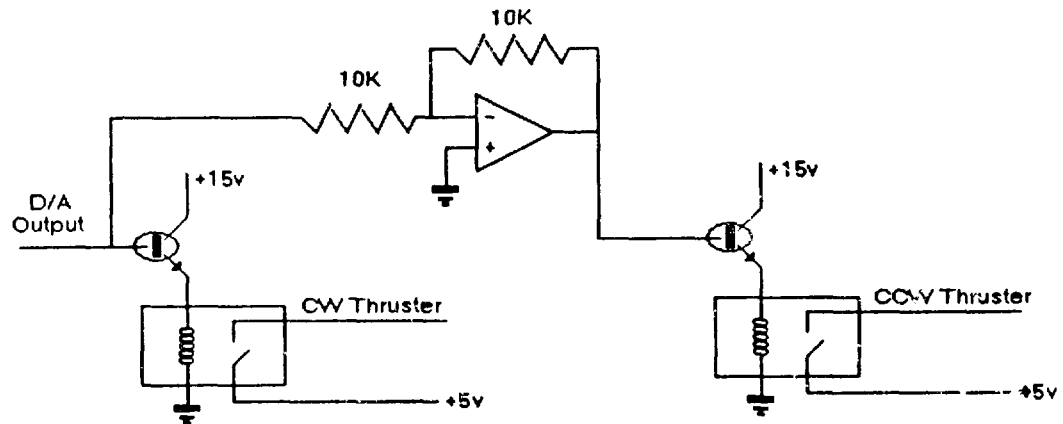


Figure 10 - Circuit to Control Yaw Thrusters

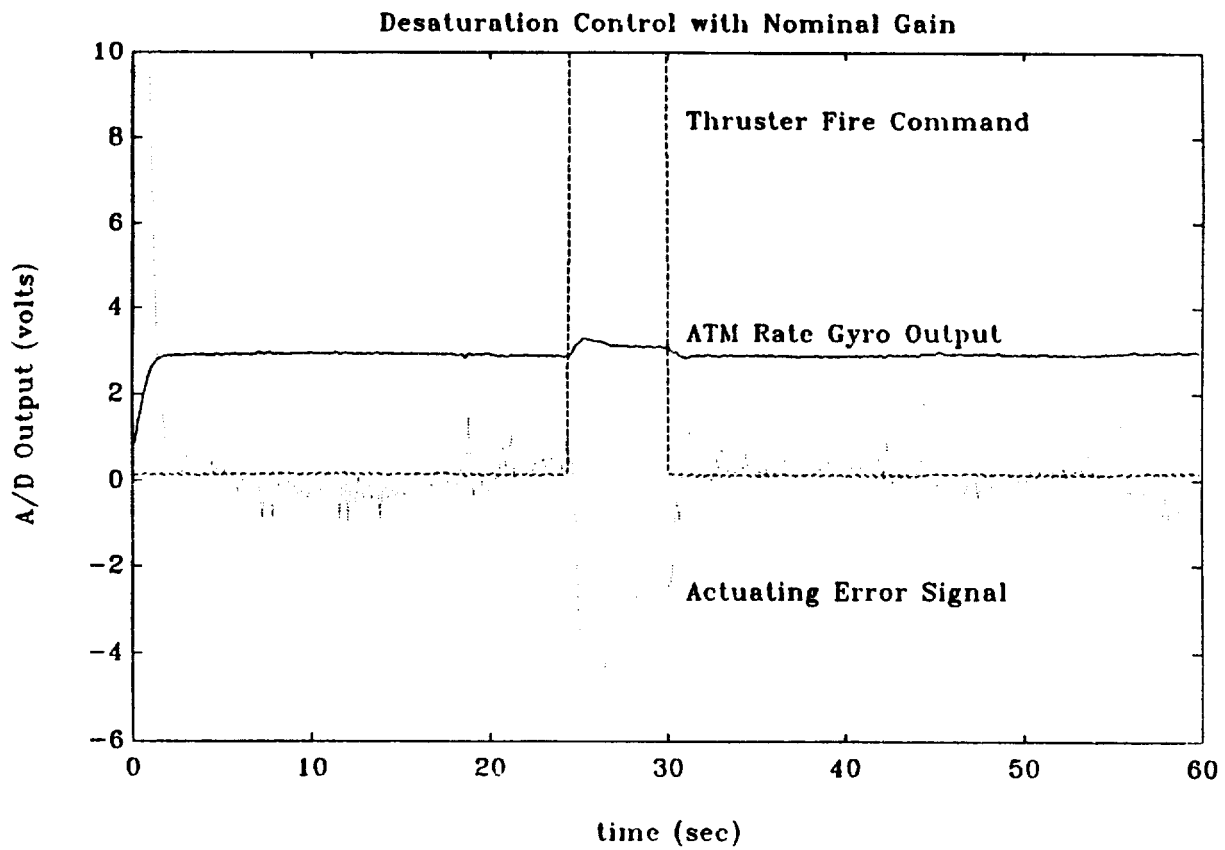


Figure 11 - Response of Desaturation Process with Nominal K

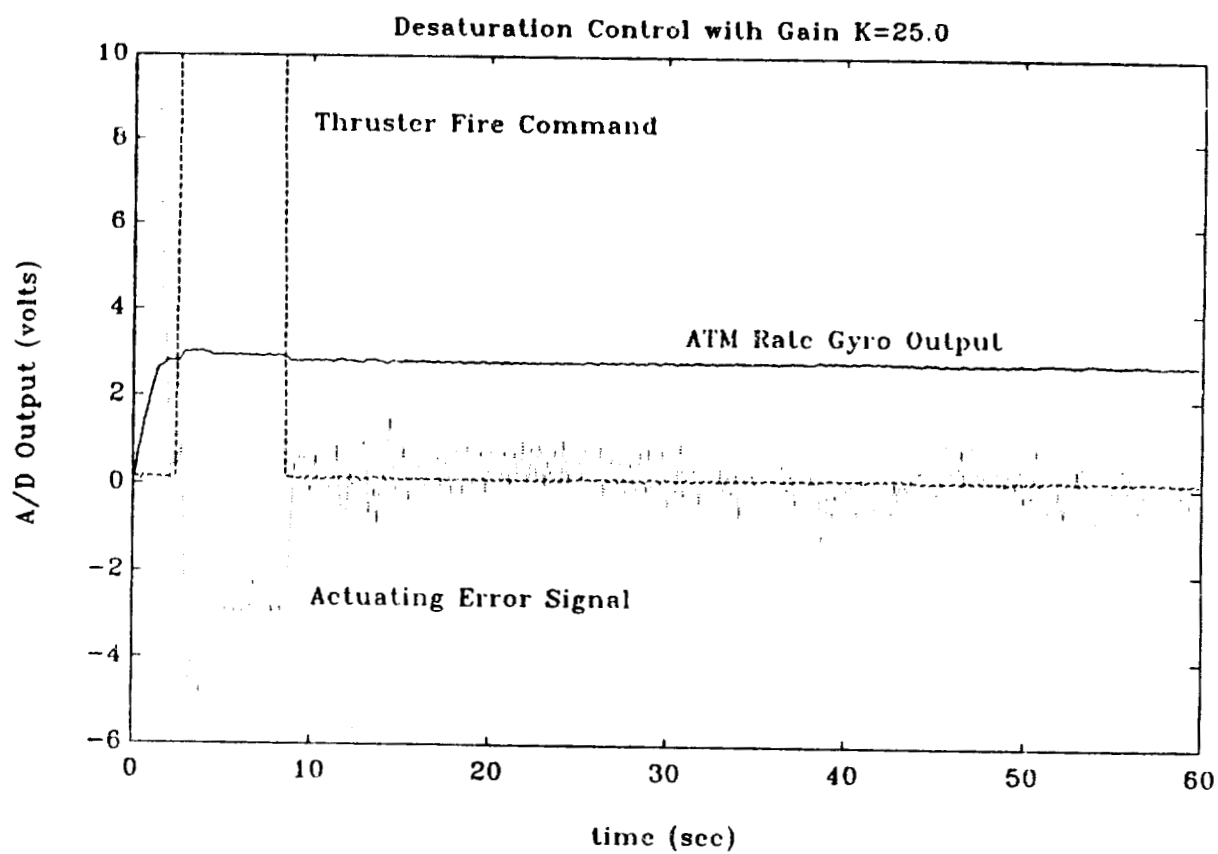


Figure 12 - Response of Desaturation Process with $K = 25$

Note that an output of 0 from the D/A does not affect a change in the relays while an output of +10 (-10) will turn on the left (right) transistor which in turn will close the left (right) relay thereby transmitting the necessary +5 volts to the clockwise (counter clockwise) thrusters.

After some experimentation, a value of $|\theta| = 65$ degrees was selected to trigger the desaturation process, at which point the available torque is still 42.3% of the maximum available torque. A value of $|\theta|$ closer to 90 degrees resulted in an insufficient amount of torque to counteract the disturbance while a value of $|\theta|$ closer to 0 resulted in desaturation occurring too frequently.

The results of the desaturation process are shown in Figures 11 and 12. Both trials were run with a setting of 50 psi on the air thrusters and on the air bearings. Figure 11 depicts the desaturation process for the nominal value of the feedback gain K. Here, a small increase in rate can be detected when the thrusters fire to desaturate the CMGs. If the application were teleoperation of the vehicle, this error could be tolerated since a pilot is in the loop making adjustments according to his display screen. If the application is autonomous, this disturbance may be outside of tolerance. The amount of rate error could be decreased, however, by increasing the value of the feedback gain. Recall that increasing the feedback gain increases the robustness of the system. Yet theoretically, our system is critically damped and any increase in the feedback gain will manifest itself in terms of overshoot. However, our ARX(2,2,1) model does not accurately represent the effects of limiting our input to ± 10 volts. Limiting our input acts much like a low pass filter in cascade with our control block. Therefore, we may be able to increase the gain without the response acquiring overshoot. Figure 12 shows the desaturation process when K is increased to 25. Notice that there is no overshoot and that the change in the rate of the vehicle during desaturation is imperceptible. Conclusion: if maintaining a constant rate is critical, then a value of 25 should be employed in the feedback gain.

6 Conclusions and Recommendation

This report has presented a summary of a six week project concerning the yaw rate control of NASA's air bearing vehicle using CMGs. From

the information presented, the following conclusions/recommendations are drawn:

- Two of the Sperry reaction wheels spinning at 3000 rpm are required to meet the the torque stipulations derived from the maximum yaw rate of the OMV.
- Of the 250 possible structures considered, an ARX(3,4,1) was the best fit according to the Akaike Final Prediction Error Criterion (FPE). However, an ARX(2,2,1) structure had a similar FPE and was chosen over the ARX(3,4,1) model for ease of control law design.
- A least squares estimation was employed off-line to compute the best parameter values for the ARX(2,2,1) structure. Although this estimation could be performed on-line, experimental data indicated that the parameters did not vary significantly. Thus, no adaptive estimation is necessary
- The open-loop step response and the results of the parameter estimation indicated that the vehicle behaved as a type 1 system. This implies that no integration is necessary in the feedback control loop to meet the steady-state error. A proportional feedback control (given by equation (5)) was designed so that the closed-loop was critically damped. This control can be computed on-line in a self-tuning scheme if necessary. Furthermore, due to the saturation effect of the D/A outputs, this feedback gain may be increased above this nominal value if more robustness is required during desaturation.
- Although tilting the ATM rate gyro's spin axis provided an excellent temporary solution to the problem of insufficient dynamic range, the vehicle is now sensitive to the Earth's rotation. A more permanent solution would be to rescale the electronics of the ATM or find an alternate rate gyro to devote to the project which has a dynamic range of approximately 3 degrees per second.
- The end product of this project is a control system - both hardware and software. Plans are currently underway to install an AT-bus 80386 computer on the vehicle. If and when this event transpires,

the control adapter can be installed in and the software ported to the new 80386 box.

- Using the thrusters to desaturate the CMGs did introduce some translational disturbance, but because the thrusters were not part of the closed-loop yaw control, this translational disturbance will not be coupled back into a rotational disturbance.

7 References

1. Clyde Jones, "Simplified Description of Control Moment Gyros," **NASA Technical Report R-ASTR-G-WP-12-67**, MSFC, July 11, 1967.
2. Lenart Ljung, **System Identification: Theory for the User**. Prentice-Hall, New Jersey, 1987.
3. P. Eykhoff, **Trends and Progress in System Identification**. Pergamon Press, Helmsford, New York, 1981.
4. K.J. Astrom, "Theory and applications of adaptive control -A survey", *Automatica*, vol. 19, pp. 471-486, 1983.
5. T. Soderstrom and P. Stoica, **Instrumental Variable Methods for System Identification**. Lecture Notes in Control and Information Sciences, Springer-Verlag, New York, 1983.

APPENDIX A


```

page      ,132
title     CONTROL MOMENT GYRO ASSEMBLY LANGUAGE DRIVER
subttl    SUPPORT DRIVER FOR IBM DATA ACQUISITION AND CONTROL ADAPTER

```

```

;source code filename:  ADAPTDRV.ASM

```

```

;programmer: Charles Oliver , EB24, NASA MSFC      APR 1, 1987

```

```

;   modified by Bruce L. Walcott, EB24, NASA MSFC  JUNE 5, 1989

```

```

; This program contains functions which are intended to be
; used by C programs compiled under MICROSOFT C 5.1 or higher
;
;

```

```

; analog_input function:
; MICROSOFT C STATEMENT:
;

```

```

; extern int far analog_input(int,int);
; int voltin, int channel, int adapter;
;
;

```

```

;voltin= analog_input(channel,adapter);
;

```

```

;returns an integer representation of the voltage on "channel"
;where channel is either 0, 1, 2, or 3 and adapter is 0 or 1 depending
;upon which board is desired.  If only one board is present, then
;adapter must be set to 0.
; The ADC's have 12 bit resolution and have been set to a -10 to 10 volt range.
; For an input voltage of -10 volts, voltin will equal 0.  For an input volt:
; of +10 volts, voltin will equal 4095.

```

```

; analog_output function
; MICROSOFT C STATEMENT:
;

```

```

; extern void far analog_output(int, int, int);
; int adapter, channel, voltout;
;
;

```

```

;analog_output(voltout,channel,adapter)

```

```

; The subroutine sets an analog output channel.  The three arguments must be
; integer variables.  adapter must be 0 or 1.  channel must be 0 or 1.
; The DAC's have 12 bit resolution and have been set to a -10 to +10 volt
; range.  voltout equals 0 produces a -10 volt output and voltout equals 4095
; produces a +10 volt output.
;

```

```

;equates for accessing IBM data acquisition and control adapter
;

```

```

.MODEL MEDIUM                      ;tells MS to use medium model
.CODE
device_number_reg0 equ 0c2e2h      ;< adapter 0 device number register >
device_number_reg1 equ 0c6e2h      ;< adapter 1 device number register >

analog_device      equ 9            ;code to select analog device
binary_device      equ 8            ;code to select binary device

```



```

AI_control_reg0    equ    02e2h    ;< adapter 0 analog input control register >
AI_status_reg0     equ    02e2h    ;< adapter 0 analog input status register >
AI_data_reg0       equ    22e2h    ;< adapter 0 analog input data register >
AI_control_reg1    equ    06e2h    ;< adapter 1 analog input control register >
AI_status_reg1     equ    06e2h    ;< adapter 1 analog input status register >
AI_data_reg1       equ    26e2h    ;< adapter 1 analog input data register >

```

```

ad0_channel        equ    0000h    ;code to select A/D channel 0
ad1_channel        equ    0100h    ;code to select A/D channel 1
ad2_channel        equ    0200h    ;code to select A/D channel 2
ad3_channel        equ    0300h    ;code to select A/D channel 3

```

```

convert_start      equ    0001h    ;convert start bit in AI_control
busy_state         equ    0001h    ;busy state bit in AI_status
count4_multiplexer_settling equ    0010h    ;count for delay while analog
                                           ;multiplexer settles

```

```

AO_control_reg0    equ    12e2h    ;< adapter 0 analog output control reg >
AO_data_reg0       equ    32e2h    ;< adapter 0 analog output data register >
AO_control_reg1    equ    16e2h    ;< adapter 1 analog output control reg >
AO_data_reg1       equ    36e2h    ;< adapter 1 analog output data register >

```

```

da0_channel        equ    0000h    ;code to select D/A channel 0
da1_channel        equ    0100h    ;code to select D/A channel 1

```

```

BI_status_reg0     equ    02e2h    ;< adapter 0 binary status register >
BI_control_reg0    equ    02e2h    ;< adapter 0 binary control register >
BI_input_reg0      equ    22e2h    ;< adapter 0 binary input register >
BI_output_reg0     equ    22e2h    ;< adapter 0 binary output register >
BI_status_reg1     equ    06e2h    ;< adapter 1 binary status register >
BI_control_reg1    equ    06e2h    ;< adapter 1 binary control register >
BI_input_reg1      equ    26e2h    ;< adapter 1 binary input register >
BI_output_reg1     equ    26e2h    ;< adapter 1 binary output register >

```

```

cntr_control_reg0  equ    0b2e2h    ;< adapter 0 counter control register >
cntr_control_reg1  equ    0b6e2h    ;< adapter 1 counter control register >
counter0_reg0      equ    82e2h    ;< adapter 0 counter 0 read/write register >
counter0_reg1      equ    86e2h    ;< adapter 1 counter 0 read/write register >
counter1_reg0      equ    92e2h    ;< adapter 0 counter 1 read/write register >
counter1_reg1      equ    96e2h    ;< adapter 1 counter 1 read/write register >
counter2_reg0      equ    0a2e2h    ;< adapter 0 counter 2 read/write register >
counter2_reg1      equ    0a6e2h    ;< adapter 1 counter 2 read/write register >

```

```

set_counter0_mode3 equ    36h      ;code to set counter 0 to mode 3
set_counter1_mode3 equ    76h      ;code to set counter 1 to mode 3
set_counter2_mode3 equ    0b6h     ;code to set counter 2 to mode 3
latch_counter2     equ    80h      ;code to latch counter 2

```

```

int_control_reg0   equ    0d2e2h    ;< adapter 0 interrupt control register >
int_status_reg0    equ    0d2e2h    ;< adapter 0 interrupt status register >
int_control_reg1   equ    0d6e2h    ;< adapter 1 interrupt control register >
int_status_reg1    equ    0d6e2h    ;< adapter 1 interrupt status register >

```

```

irq_stat           equ    01000000b    ;external interrupt status,  $\overline{\text{IRQ}}$ 

```

```

out_ax             macro    io_port, value
                    mov     dx,io_port
                    mov     ax,value
                    out     dx,ax
                    jmp     $+2
                    xxx-33

```



```

        jmp      $+2
    endm

out_al    macro    io_port, value
    mov     dx,io_port
    mov     al,value
    out     dx,al
    jmp     $+2
    jmp     $+2
    endm

;
;
;main program
;

prog      SEGMENT    para public 'CODE'
          ASSUME      cs:prog

;device driver header
          DD          -1                ;pointer to another driver
          DW          8000h            ;character device attribute
          DB          "stxdriv "
;end of header

device_number dw 0 ;locations used by binary and analog
BI_input      dw 0 ;input/output subroutines
BI_output     dw 0
channel       dw 0
AI_control    dw 0
AI_status     dw 0
AI_data       dw 0
AO_control    dw 0
AO_data       dw 0

bit15_flag   dw 0 ;used for triggering adscan with data bit 15
bit15_tlow   dw 0 ;timeout counter low word
bit15_thigh  dw 0 ;timeout counter high word

;
;
;analog_input function (called from C)
;

    PUBLIC _analog_input
_analog_input    proc      far

    push bp
    mov     bp,sp
    mov     bx,[bp+8]
    cmp     bx,0 ;compare ADAPTER argument with 0
    jne     l7 ;if not zero, setup for adapter
    mov     device_number,device_number_reg0 ;else, setup for
    mov     AI_control,AI_control_reg0 ;adapter 0
    mov     AI_status,AI_status_reg0
    mov     AI_data,AI_data_reg0
    jmp     l8

```



```

17:      mov     device_number,device_number_reg1
      mov     AI_control,AI_control_reg1
      mov     AI_status,AI_status_reg1
      mov     AI_data,AI_data_reg1

18:      mov     bx,[bp+6]
      cmp     bx,0           ;compare CHANNEL arg with 0
      jne     19
      mov     channel,ad0_channel      ;set for channel 0
      jmp     112
19:      cmp     bx,1           ;compare CHANNEL arg with 1
      jne     110
      mov     channel,ad1_channel      ;set for channel 1
      jmp     112
110:     cmp     bx,2           ;compare CHANNEL arg with 2
      jne     111
      mov     channel,ad2_channel      ;set for channel 2
      jmp     112
111:     mov     channel,ad3_channel      ;set for channel 3

112:     out_al   device_number,analog_device      ;select adapter
      out_ax   AI_control,channel      ;select channel

wait4:   mov     cx,count4_multiplexer_settling      ;wait for analog
      loop    wait4                      ;multiplexer to settle

      mov     ax,channel      ;start analog conversion
      or     ax,convert_start
      out_ax   AI_control,ax

wait5:   mov     dx,AI_status      ;wait for A/D conversion to finish
      in      ax,dx
      and     ax,busy_state
      jnz     wait5

      out_ax   AI_control,channel

      mov     dx,AI_data      ;input analog value
      in      ax,dx

      pop     bp
      ret                                ;return to BASIC

```

_analog_input endp

```

;
;
;analog_output function (called from C)
;

```

```

      PUBLIC _analog_output
_analog_output proc      far

```

```

      push     bp
      mov     bp,sp
      mov     bx,[bp+10]
      cmp     bx,0      ;compare ADAPTER argument with 0
      jne     113      ;if not zero, setup for adapter 1
      mov     device_number,device_number_reg0      ;else, setup for
      mov     AO_control,AO_control_reg0      ;adapter 0

```



```

        mov     AO_data,AO_data_reg0
        jmp     114
113:    mov     device_number,device_number_reg1
        mov     AO_control,AO_control_reg1
        mov     AO_data,AO_data_reg1

114:    mov     bx,[bp+8]
        cmp     bx,0      ;compare CHANNEL arg with 0
        jne     115      ;if not zero, setup for channel 1
        mov     channel,ad0_channel ;else, setup for channel 0
        jmp     116
115:    mov     channel,ad1_channel

116:    out_al   device_number, analog_device ;select analog device

        out_ax  AO_control,channel          ;select channel

        mov     bx,[bp+6]      ;send word from BASIC to analog
        out_ax  AO_data,bx     ;output channel

        pop     bp
        ret                ;return to basic

_analog_output endp

;
;

stack:   DB      64 dup ('s','t','a','c','k',' ',' ',' ',' ')
        DW      0

;
;
;end of program
;

lastword: DW      0

prog     ENDS

        END

```


APPENDIX B


```

/*****
*  stepdata.c
*
*  Programmer: Bruce L. Walcott
*
*  Written: June 19, 1989
*
*  This program collects data points from the airbearing vehicle in closed-loop
*  given a setpoint
*
*****/

/*
*  External connections are:  D/A channel 0 to torquer input
*                             D/A channel 1 to thruster circuit input
*                             A/D channel 0 to D/A channel 1
*                             A/D channel 1 to D/A channel 0
*                             A/D channel 2 to wiper arm of pot
*                             A/D channel 3 to ATM rate gyro output
*/

/* Includes and external declarations */

#include <graph.h>
#include <math.h>
#include <stdio.h>
#include <stdlib.h>
extern void far analog_output ( int, int, int);
extern int far analog_input ( int, int);

/*****
* Main Program
*****/

main()
{

/* Internal declarations */

FILE *f;
int analout,i, x, j, samptime, k, flag,number;
long color;
static float voltin[8000];
float voltout, offset, diff, posit1, posit2, epsilon, k0, u, y[3], saturate;

/* Initialize variables */

color=9;                /* 9 = blue */
number=0.;
k0 = 19.1802;           /* Feedback gain for critical damping */
epsilon=.005;           /* Tolerance for eliminating drift */
offset=0;                /* Initial value of DC offset to eliminate drift */

_settextwindow(1,1,25,80);
_setbkcolor(color);      /* Set-up graphics and clear screen */
_clearscreen(_GCLEARSCREEN);

_settextposition(6,20);  /* Print messages for gyro drift elimination */
_settextcolor(7);
_outtext("Eliminating rate gyro offset.");

```



```

_settextposition(6,20);
_outtext("      Please wait.      ");

while(1){
    posit1=(analog_input(2,0)/2048.)*10.-10.;    /* Take one pot reading */
    for(k=0 ; k < 500; k++){
        for(j=0; j < 300; j++) continue;    /* Wait */
    }
    posit2=(analog_input(2,0)/2048.)*10.-10.;    /* Take another */

    diff=posit2 - posit1;    /* If difference not within
    if( fabs(diff) > epsilon){    /* tolerance, change offset
        offset = offset - .05* fabs(diff)/diff;
        analog_output(2048+(int)((offset)*204.8),0,0);    /* Output offset
    }
    else break;    /* If difference is within toleranc
}

epsilon=0.01;    /* Now move gyros back to zero position */

while(1){
    posit1=(analog_input(2,0)/2048.)*10.-10.;
    if( fabs(posit1) > epsilon){
        analog_output(2048+(int)((offset-.5*fabs(posit1)/posit1)*204.8),
    }
    else {
        analog_output(2048+(int)((offset)*204.8),0,0);
        break;
    }
}

_settextposition(7,20);    /* Put sampling time in samptime */
_outtext("Enter the desired sampling time in milliseconds: ");
scanf("%d",&samptime);

_settextposition(8,20);    /* Put number of points in number */
_outtext("Enter the number of data points to capture: ");
scanf("%d",&number);

_settextposition(9,20);    /* Put setpoint in voltout */
_outtext("Enter the value for step on D/A output on channel 0: ");
scanf("%f",&voltout);

f = fopen("data\\stepdata.dat","w+");    /* Open data file */
if (f == NULL)
{
    printf("      Cannot open stepdata.dat");
    return;
}

/* Write header information */

fprintf(f,"samptime=%d, amplitude=%2.3f, offset=%2.3f, number=%d\n",samptime

saturate=6.;    /* Desaturate at +- 6 volts */
flag=0;    /* flag = 1 when desaturating CW, 2 when desaturating
x=2048;    /* x is command for thrusters */

```



```

/* Main control loop */

for (i=0;i < (4*number);i += 4)
{
    analog_output(x,1,0); /* Command thrusters */

    voltin[0+i]=(analog_input(0,0)/2048.)*10.-10.; /* Get inputs */
    voltin[1+i]=(analog_input(1,0)/2048.)*10.-10.;
    voltin[2+i]=(analog_input(2,0)/2048.)*10.-10.;
    voltin[3+i]=(analog_input(3,0)/2048.)*10.-10.;

    y[0]=voltin[3+i]-(voltout+offset); /* Calculate control */
    u=-k0*y[0];

    if(fabs(u) > 10) u=10*u/fabs(u); /* Limit value to +-10 volt */
    analog_output((int)((u+10)*4095/20),0,0); /* Output control */

    if( voltin[2+i] > saturate ) { /* Check for CW desaturatio */
        flag=1; /* Set flag */
        x=4095; /* Command CW thrusters off */
    }

    if(voltin[2+i] < -saturate ) { /* Check for CCW desaturati */
        flag=2; /* Set flag */
        x= 0; /* Command CCW thrusters on */
    }

    if (flag == 1 && voltin[2+i] < 0) { /* Check if back to zero */
        x=2048; /* Command CW thrusters off */
        flag=0; /* Reset flag */
    }

    if (flag == 2 && voltin[2+i] > 0) { /* Check if back to zero */
        x=2048; /* Command CCW thrusters off */
        flag=0; /* Reset flag */
    }

    for(k=0; k < 58; k++) continue; /* Wait sampling time */
    for(k=0; k < sampletime -1; k++)
    for(j=0; j < 300; j++) continue;
}

analog_output(2048+(int)((offset)*204.8),0,0); /* Exit loop and turn off */
analog_output(2048,1,0);

for(i=0;i < (4*number);i += 4) /* Write data */
{
    fprintf(f,"%2.3f %2.3f %2.3f %2.3f\n",voltin[i],voltin[i+1],voltin[i+2]-offs
}

```



```

/*****
* Posit.c
*
* Programmer: Bruce L. Walcott
*
* written: July 14, 1989
*
* This program closes the loop on the vehicle and desaturates the gyros
* using a potentiometer connected to the torquer motor spin axis. The
* user can command desired rate from the keyboard.
*
*****/

/*
* External connections are: D/A channel 0 to torquer input
*                           D/A channel 1 to thruster circuit input
*                           A/D channel 0 to D/A channel 1
*                           A/D channel 1 to D/A channel 0
*                           A/D channel 2 to wiper arm of pot
*                           A/D channel 3 to ATM rate gyro output
*/

/* Includes and external declarations */

#include <graph.h>
#include <conio.h>
#include <math.h>
#include <stdio.h>
#include <stdlib.h>
extern void far analog_output ( int, int, int);
extern int far analog_input ( int, int);

/*****
* Main Program
*****/

main()
{
/* Internal declarations */

FILE *f;
int analgout,i, x, j, samptime, k, flag;
long color;
static float voltin[8000];
float voltout, offset, zero1, zero2, diff, posit1, posit2, epsilon, k0, u, y[3],
char chr;

/* Initialize variables */

color=9;                /* 9 = blue */
chr = '0';
k0 = 19.1802;           /* Feedback gain for critical damping */
epsilon=.005;           /* Tolerance for eliminating drift */
offset=0;               /* Initial value of DC offset to eliminate drift */

_settextwindow(1,1,25,80);
_setbkcolor(color);      /* Set-up graphics and clear screen */
_clearscreen(_GCLEARSCREEN);

```



```

_settextposition(6,20);          /* Print messages for gyro drift elimination */
_settextcolor(7);
_outtext("Eliminating rate gyro offset.");
_settextposition(6,20);
_outtext("      Please wait.      ");

```

```

while(1){
    posit1=(analog_input(2,0)/2048.)*10.-10.;    /* Take one pot reading */
    for(k=0 ; k < 500; k++){
        for(j=0; j < 300; j++) continue;    /* Wait */
    }
    posit2=(analog_input(2,0)/2048.)*10.-10.;    /* Take another */
    diff=posit2 - posit1;                        /* If difference not within
    if( fabs(diff) > epsilon){                  /* tolerance, change offset
        offset = offset - .05* fabs(diff)/diff;
        analog_output(2048+(int)((offset)*204.8),0,0); /* Output offset
    }
    else break;                                /* If difference is within toleranc
}

```

```

epsilon=0.01;                                /* Now move gyros back to zero position *

```

```

while(1){
    posit1=(analog_input(2,0)/2048.)*10.-10.;
    if( fabs(posit1) > epsilon){
        analog_output(2048+(int)((offset-.5*fabs(posit1)/posit1)*204.8),
    }
    else {
        analog_output(2048+(int)((offset)*204.8),0,0);
        break;
    }
}

```

```

_settextposition(7,20);
_outtext("Type 0 to stop, 1 to go cw, 2 to go ccw, b to break ");

```

```

voltout=0.;    /* Initialize setpoint to 0 */
sampletime=150; /* Sampling time is 150 msec */
saturate=6.;   /* Desaturate at +- 6 volts */
flag=0;        /* flag = 1 when desaturating CW, 2 when desaturating
x=2048;        /* x is command for thrusters */

```

```

while(chr != 'b') {    /* Break when 'b' is entered */
    while(!kbhit())    /* Loop until key is struck */
    {
        analog_output(x,1,0);    /* Command thrusters */

        voltin[0]=(analog_input(0,0)/2048.)*10.-10.; /* Get inputs */
        voltin[1]=(analog_input(1,0)/2048.)*10.-10.;
        voltin[2]=(analog_input(2,0)/2048.)*10.-10.;
        voltin[3]=(analog_input(3,0)/2048.)*10.-10.;

        y[0]=voltin[3]-(voltout+offset);    /* Calculate control */
        u=-k0*y[0];

        if(fabs(u) > 10) u=10*u/fabs(u);    /* Limit value to +-10 volt
        analog_output((int)((u+10)*4095/20),0,0); /* Output control */
    }
}

```



```

if( voltin[2] > saturate ) {
flag=1;
x=4095;
}

if(voltin[2] < -saturate ) {
flag=2;
x= 0;
}

if (flag == 1 && voltin[2] < 0) {
x=2048;
flag=0;
}

if (flag == 2 && voltin[2] > 0) {
x=2048;
flag=0;
}

for(k=0; k < 58; k++) continue;
for(k=0; k < sampletime -1; k++)
for(j=0; j < 300; j++) continue;
}

chr=getch();
if(chr == '1') voltout = voltout+.125;
if(chr == '2') voltout = voltout - .125;
if(chr == '0') voltout = 0.;
}

analog_output(2048+(int)((offset)*204.8),0,0);
analog_output(2048,1,0);
}

```

```

/* Check for CW desaturation
/* Set flag */
/* Command CW thrusters off

/* Check for CCW desaturation
/* Set flag */
/* Command CCW thrusters on

/* Check if back to zero */
/* Command CW thrusters off *
/* Reset flag */

/* Check if back to zero */
/* Command CCW thrusters off
/* Reset flag */

/* Wait sampling time */

/* If is struck, get characte
/* If '1', increase setpoint
/* If '2', decrease setpoint
/* If '0', reset setpoint to

/* Exit loop and turn off */

```


1989

NASA/ASEE SUMMER FACULTY FELLOWSHIP PROGRAM

MARSHALL SPACE FLIGHT CENTER
THE UNIVERSITY OF ALABAMA IN HUNTSVILLE

THE INFLUENCE OF A WALL FUNCTION ON
TURBINE BLADE HEAT TRANSFER PREDICTION

Prepared by:	Kevin W. Whitaker
Academic Rank:	Assistant Professor
University and Department:	The University of Alabama Aerospace Engineering

NASA/MSFC:	
Laboratory:	Structures and Dynamics
Division:	Aerophysics
Branch:	Computational Fluid Dynamics
MSFC Colleague:	Helen V. McConnaughey
Date:	August 1, 1989
Contract No.:	NGT 01-008-021 The University of Alabama in Huntsville

THE INFLUENCE OF A WALL FUNCTION ON
TURBINE BLADE HEAT TRANSFER PREDICTION

by

Kevin W. Whitaker
Assistant Professor of Aerospace Engineering
The University of Alabama
Tuscaloosa, Alabama

ABSTRACT

The second phase of an continuing investigation to improve the prediction of turbine blade heat transfer coefficients has been completed. The present study specifically investigated how a numeric wall function in the turbulence model of a two-dimensional boundary layer code, STAN5, affected heat transfer prediction capabilities. Several sources of inaccuracy in the wall function were identified and then corrected or improved. Heat transfer coefficient predictions were then obtained using each one of the modifications to determine its effect. Results indicated that the modifications made to the wall function can significantly affect the prediction of heat transfer coefficients on turbine blades. The improvement in accuracy due the modifications is still inconclusive and is still being investigated.

ACKNOWLEDGEMENTS

For the second straight year I would like to thank the National Aeronautics and Space Administration along with the American Society for Engineering Education for sponsoring this fabulous opportunity. I have found the Summer Faculty Fellowship Program to be extremely beneficial and enjoyable. Without question, the program has played an important role in my professional development.

Sincere appreciation is due Helen V. McConnaughey whose interest in the Summer Faculty Fellowship Program provided me with what turned out to be a very interesting and timely project. I also appreciate the valuable assistance provided by Gerald Karr and Frank Six throughout the course of the program.

INTRODUCTION

The thermal aspect of blade design is one of the more difficult engineering tasks facing a designer of any modern gas turbine engine. Thermal (and many times aerodynamic) analysis procedures currently available to designers have deficiencies that do not permit achievement of design goals without expensive experimental development programs. For example, the external (gas-to-blade) heat transfer coefficient still eludes satisfactory prediction using computational fluid dynamic codes. Even if consideration is restricted to the nominally two-dimensional midspan region of a turbine blade, prediction is still unsatisfactory. The reasons for the unsatisfactory prediction capability of the codes are complex but ultimately lie in the fundamental concepts and models used to define the fluid dynamic and heat transfer behavior. Without question, the complex gas turbine engine environment pushes current models to their limit. Thus, there exists a need for an improved design approach making use of codes with sufficiently improved turbulence modeling.

The work presented here is part of a continuing effort to improve the prediction of turbine blade heat transfer coefficients. Specifically, it investigates the influence a wall function has on the predictive capabilities of a typical design code. Although a wall function is only a small part of a total turbulence model, its influence was identified as being important during a previous study.

OBJECTIVE

The overall objective of this study was to improve the computational prediction of the external (gas-to-blade) heat transfer coefficient for gas turbine engine applications. Such an improvement would reduce and perhaps eliminate the expensive experimental iterations that current engine designers must endure. Accurate prediction of heat transfer within a gas turbine engine environment is necessary to assist designers in the selection of blade materials, blade cooling requirements, etc. The result is that improved prediction capabilities would impact engine design in a very positive way.

PROCEDURE

CODE SELECTION

Current gas turbine engine design practice is to use a two-dimensional boundary layer analysis to calculate the gas-to-blade heat transfer coefficients. Certainly any computational method which does not solve the full time-dependent Navier-Stokes and energy equations cannot be expected to be universally valid over the entire range of circumstances governed by these equations. However, there are solutions from reduced sets of these equations that are valid for a subset of problems. Such is the case here where it is implied that the flow field immediately adjacent to the surface of an airfoil in typical gas turbine geometries can be analytically modeled using boundary layer equations.

Perhaps the most familiar and widely used boundary layer method is a finite difference technique which relies on algebraic relations for defining turbulence quantities. A very common design tool of this type is STAN5, a code developed by Crawford and Kays [1] and later modified by NASA Lewis Research Center [2]. For boundary layer flow with heat transfer, STAN5 involves the solution of two governing partial differential equations using the numerical scheme of Patankar and Spalding [3]. Turbulence closure is obtained using eddy diffusivity concepts. The STAN5 code has received wide attention because of its careful development, flexibility, and adequate documentation. For those very reasons, STAN5 was selected to be used for this study.

The STAN5 code allows many parameters to be adjusted and it was felt that one set of parameters should be selected and held constant throughout the test so that the influence of the wall function could be determined. Of course it was desirable to have the parameters describe a true gas turbine engine flow field as closely as possible.

Reviewing published data for flow over turbine blades, it was decided that a fully turbulent boundary layer on both the suction and pressure surfaces of the blade would be assumed. This is perhaps a point of contention but it was adopted for a couple of reasons. First, many transition models have been tried in the past with limited success [4]. Second, a typical gas turbine engine

environment flow field has a high free stream turbulence level. Also, any boundary layer character change (such as relaminarization) that might occur would be modeled through the pressure gradient implicitly contained in the input data.

STAN5 has two eddy diffusivity models, the Prandtl mixing length hypothesis (MLH) and the higher order turbulent kinetic energy (TKE) concept. For this study, the MLH method was selected based on the past attention given to it - especially in gas turbine engine studies. Also the choice of the MLH model can be considered a practical selection. The detailed experimental data required to realistically tune higher order turbulence models for gas turbine engine applications are quite scarce. On the other hand, the global-type boundary layer data normally used to develop lower order turbulence models (such as the MLH) are more common.

Another consideration was whether to assume the blade surface was a flat plate or to include the blade curvature into the analysis. A curvature model was available in STAN5 but previous studies [4] have revealed that using the curvature model did not significantly affect the heat transfer results. Also, as pointed out earlier, current design practice is to assume the flat plate. Therefore a flat plate model of the blade was assumed in this study.

Finally, all specifiable constants in STAN5 were set equal to values suggested by Crawford and Kays.

EXPERIMENTAL DATA

In order to evaluate the predictive capabilities of any computational method, it needs to be compared to experimental data. Many well documented heat transfer studies have been performed and there is a fair amount of reliable data available. This study used the work performed at Detroit Diesel Allison by Hylton et al. [4]. The main reason for selecting this data was that in addition to presenting their experimental results, the authors also provided the necessary STAN5 input data for their experimental configuration. This eliminated the need to develop the required input data thus allowing more time to be devoted to the task at hand.

The experimental program of Hylton et al. studied flow through a turbine cascade. The cascade contained three blades that were characteristic of a first-stage turbine. The blades were designated as "C3X" airfoils and the

profile of one is shown in Figure 1. The center blade in the cascade was instrumented and provided the aerodynamic and heat transfer data. The operating conditions for the data set used for comparison in this study are given below.

Inlet Total Temperature:	1460°F
Inlet Mach Number:	0.16
Inlet Reynolds Number:	640,000
Free-stream Turbulence Level:	6.55%
Blade Surface Temperature:	1182°F

THE WALL FUNCTION

A recent study [5] investigated the role turbulent Prandtl number models played in the prediction of heat transfer coefficients. It was found that the turbulent Prandtl number models did not appear to significantly improve the prediction of heat transfer coefficient. However, it was observed that the viscous sublayer model was very significant.

Within STAN5, the viscous sublayer is modeled via a wall function - a very common technique in computational fluid dynamics. Wall functions exist because boundary layers are regions of high gradients and, perhaps more important, very high gradients exist near a wall. Thus, a large number of grid points are needed to fully resolve the boundary layer region. Wall functions provide analytical expressions which can be used to "solve" the flow field in the near wall region. This solution can then be "patched" into the finite difference solution at some distance away from the wall.

Typically what is desired of the wall function is a distribution of nondimensional velocity (U^+) and enthalpy (I^+) with respect to a normalized distance from the wall (Y^+). The wall function in STAN5 assumes that the flow near a wall can be approximated by a Couette flow analysis. Thus the near-wall flow field is solved in STAN5 by using the following equations:

$$\frac{dU^+}{dY^+} = \frac{2\tau^+}{1 + [1 + 4\ell^{+2}\tau^+]^{1/2}} \quad (1)$$

$$\frac{dI^+}{dY^+} = \frac{Pr_{eff}}{\mu^+} + (Pr_{eff} - 1)W \frac{d}{dY^+}(U^{+2}/2) \quad (2)$$

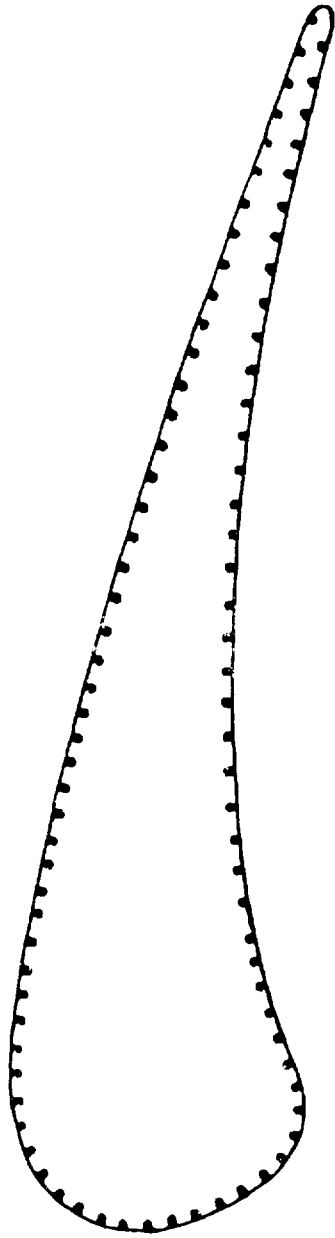


Figure 1. Profile of C3X Turbine Blade

Solution of these equations is very easy if shear stress (τ^+) and Prandtl mixing length (ℓ^+) are known as functions of Y^+ . The distributions of U^+ and I^+ can be determined by simply integrating the Couette flow equations from the wall out to some user defined distance (Y^+_{max}) into the flow field.

An expression for τ^+ as a function of Y^+ can be obtained by normalizing and rearranging the momentum equation:

$$\tau^+ = 1 + P^+Y^+ + [\text{acceleration terms}] \quad (3)$$

P^+ is a normalized pressure gradient term and the term designated "acceleration terms" represents the convective terms in the momentum equation.

An expression for ℓ^+ as a function of Y^+ can be found in Prandtl's mixing length theory:

$$\ell^+ = KY^+D \quad \text{where } D = 1 - \exp(Y^+/A^+) \quad (4)$$

The parameter "D" is the Van Driest damping function which essentially suppresses the linear dependence of ℓ^+ near the wall. The effective thickness of the viscous sublayer is represented by A^+ . The Von Karman constant is represented by K.

Equations (1)-(4) thus constitute the wall function utilized by STAN5. With a turbine blade flow field in mind, looking closely at how these equations are implemented in STAN5 reveals sources of inaccuracy. Five possible sources of error were identified. They are described below along with a brief explanation of how modifications were implemented to correct the deficiency.

- The acceleration terms in the definition of τ^+ (Eqn (3)) are neglected. A correction factor is applied in STAN5 to account for these missing terms but, for the most part, the correction is only for very mild accelerations. Flow around a turbine blade experiences very high accelerations and thus is not modeled correctly in STAN5. The code was modified by including the acceleration terms in their entirety when calculating τ^+ .
- The Van Driest damping function is normalized using the value of shear stress at the wall (τ_{wall}). This could cause problems in regions where the flow is very close to separating from the wall. Near separation the value of τ_{wall} is very small and can

cause divergence of the numerical scheme or an arithmetic overflow. To avoid this, the Van Driest damping function was redefined using the local value of shear stress (τ_{local}) to normalize.

- The Von Karman constant used in the definition of the mixing length is assumed to be a constant in STAN5 - a very common practice. However, recent studies of flows with strong accelerations suggest that the Von Karman constant is not constant and in fact varies with streamwise pressure gradient. An expression amenable to numerical implementation was suggested by Glowacki and Chi [6] and was included added to STAN5.
- A user defined value of Y^*_{max} dictates where the wall function is "patched" into the finite difference solution. Suggested values of Y^*_{max} range from 1 to 500 but all of these suggestions are based on flat plate studies. To determine the influence of Y^*_{max} on heat transfer coefficient predictions for a turbine blade flow field, a set of test cases having different values of Y^*_{max} was run.
- The thickness of the viscous sublayer depends on the stability of the boundary layer. Streamwise pressure gradients directly influence the stability of the boundary layer - favorable pressure gradients tend to stabilize and adverse pressure tend to destabilize. Therefore there is a direct relationship between streamwise pressure gradient and viscous sublayer thickness. An empirical correlation is included in STAN5 to correct the viscous sublayer thickness (represented by A^*) for the streamwise pressure gradient experienced by the flow. The correlation was based on numerous flat plate studies [1]. It was felt that the correlation should be modified to account for the actual relationship between sublayer thickness and pressure gradient on a turbine blade.

RESULTS

The heat transfer coefficient predictions produced by STAN5 with each one of the wall function modifications can be seen in Figures 2 through 6. For presentation, the heat transfer coefficient (H) has been normalized by a reference value (H_0) of 200 BTU/Hr/ft²/°F and the distance along the blade surface (S) is normalized by the total surface arc length (ARC). Also shown with the predictions is the experimental data of Hylton et al. Only distributions on the suction surface were investigated. The reason for this is that very good predictions on the pressure surface of the C3X blade were obtained in a previous study [5] by simply eliminating the viscous sublayer correction and using the wall function with no further modifications.

Figure 2 shows the heat transfer coefficient distributions using a shear stress definition with and without the acceleration terms. It can be seen that by including the acceleration terms in the wall function, the laminar-to-turbulent transition at 20% of the blade surface is no longer predicted. The coefficients are predicted reasonably well in the region from 25% to about 70% but are then over-predicted beyond that.

The effects of changing the normalized definition of the Van Driest damping function are shown in Figure 3. By using the local value of shear stress (τ_{local}) the previous over-prediction at the laminar-to-turbulent transition area is reduced. Beyond about the first 25% of the blade surface, the two curves exhibit similar trends. However, both of the predicted distributions are different from the distribution suggested by the experimental data.

Figure 4 shows predictions obtained by letting the Von Karman "constant" vary with streamwise pressure gradient. The distribution of heat transfer coefficients is predicted very well up to about 40% of the blade surface and then the coefficients are severely under predicted. It is perhaps important to note that although the predicted values are low beyond 40%, the shape of the distribution is generally correct.

The effect of where the wall function is patched into the finite difference grid is seen in Figure 5. Cases were run varying Y^*_{max} from 200 down to 5. Out to a surface distance of 20% the predictions were identical for all values of Y^*_{max} . After that the larger values of Y^*_{max}

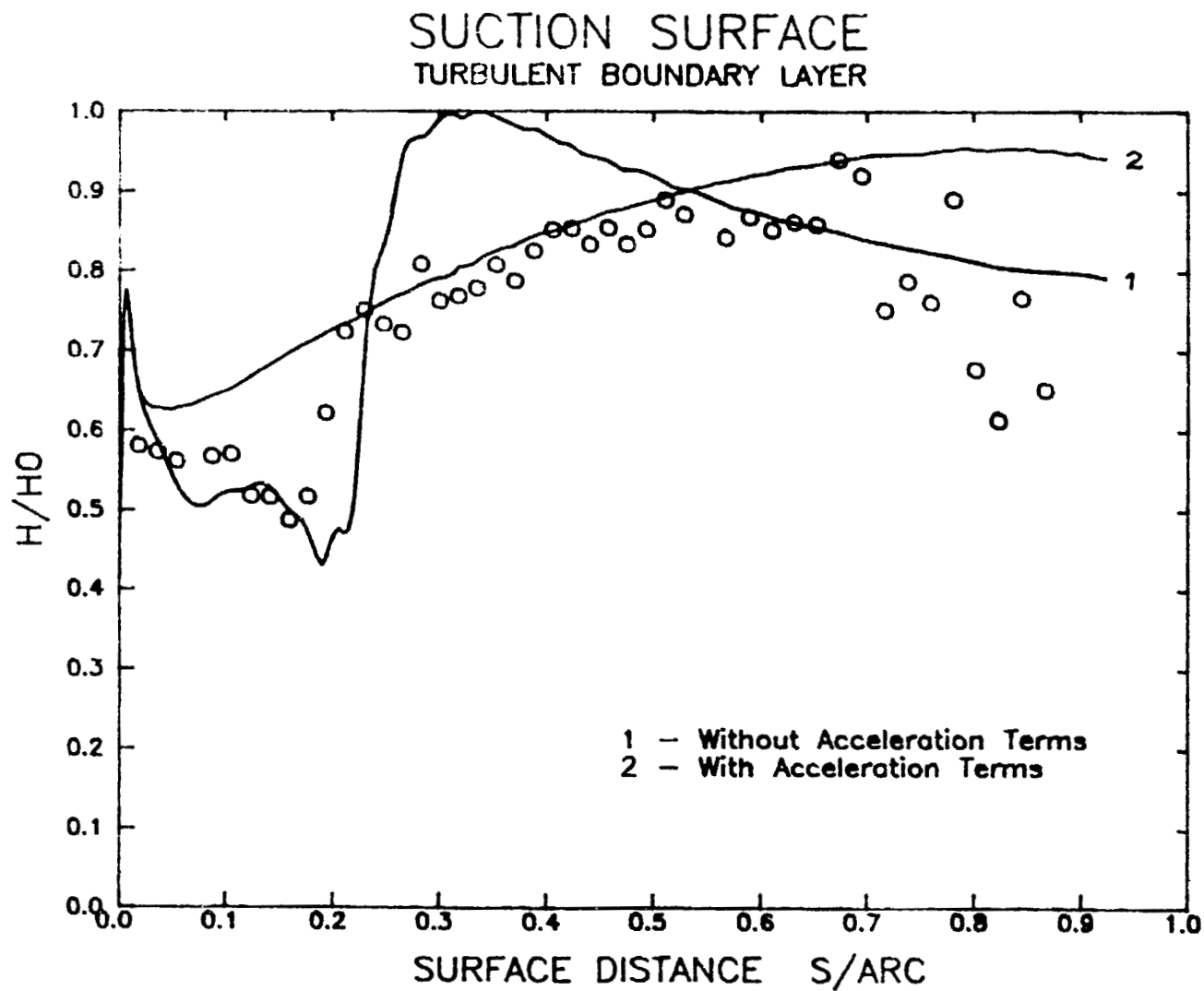


Figure 2. Effect of Acceleration Terms

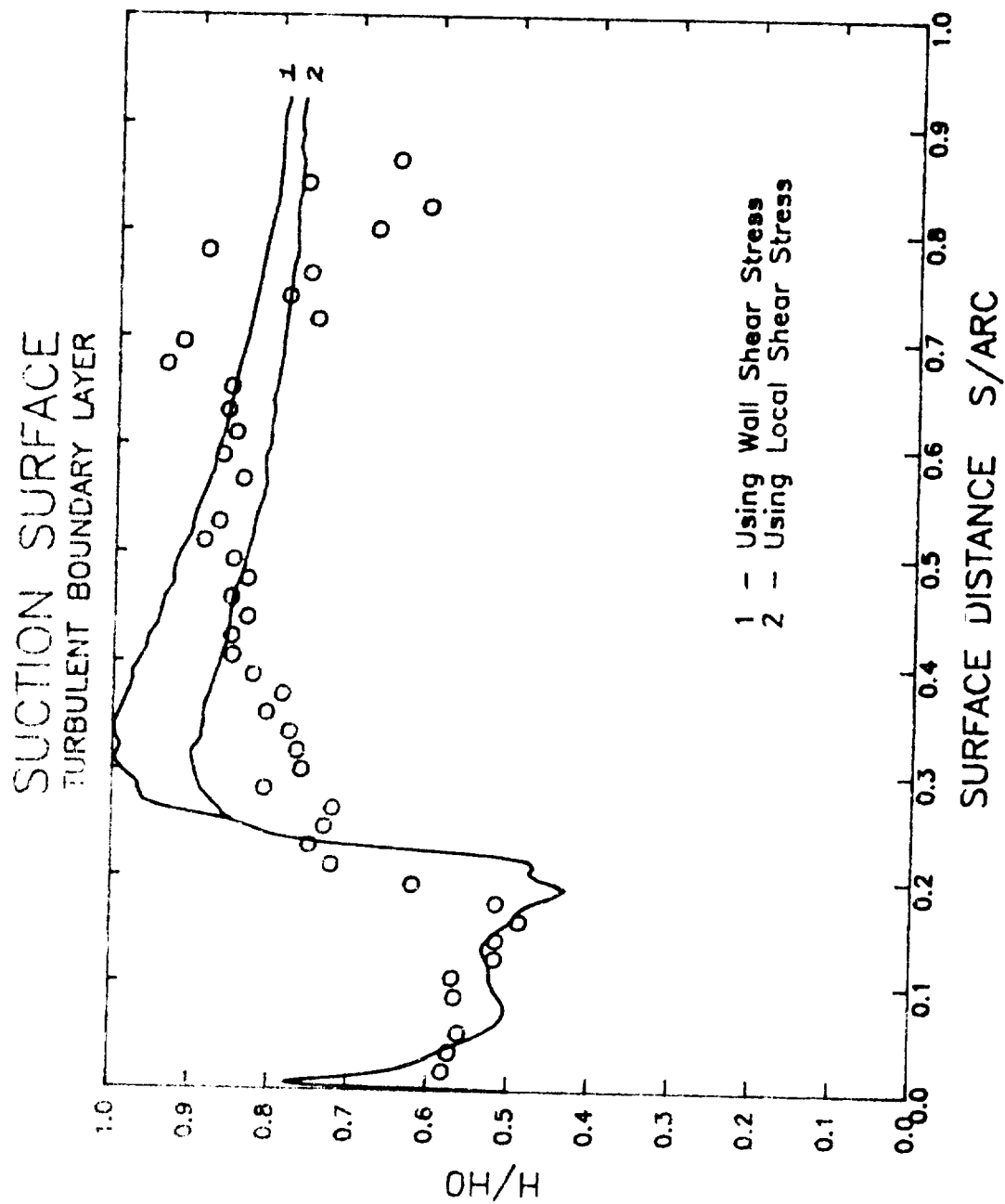


Figure 3. Effect of Van Driest Damping Function Normalization Technique

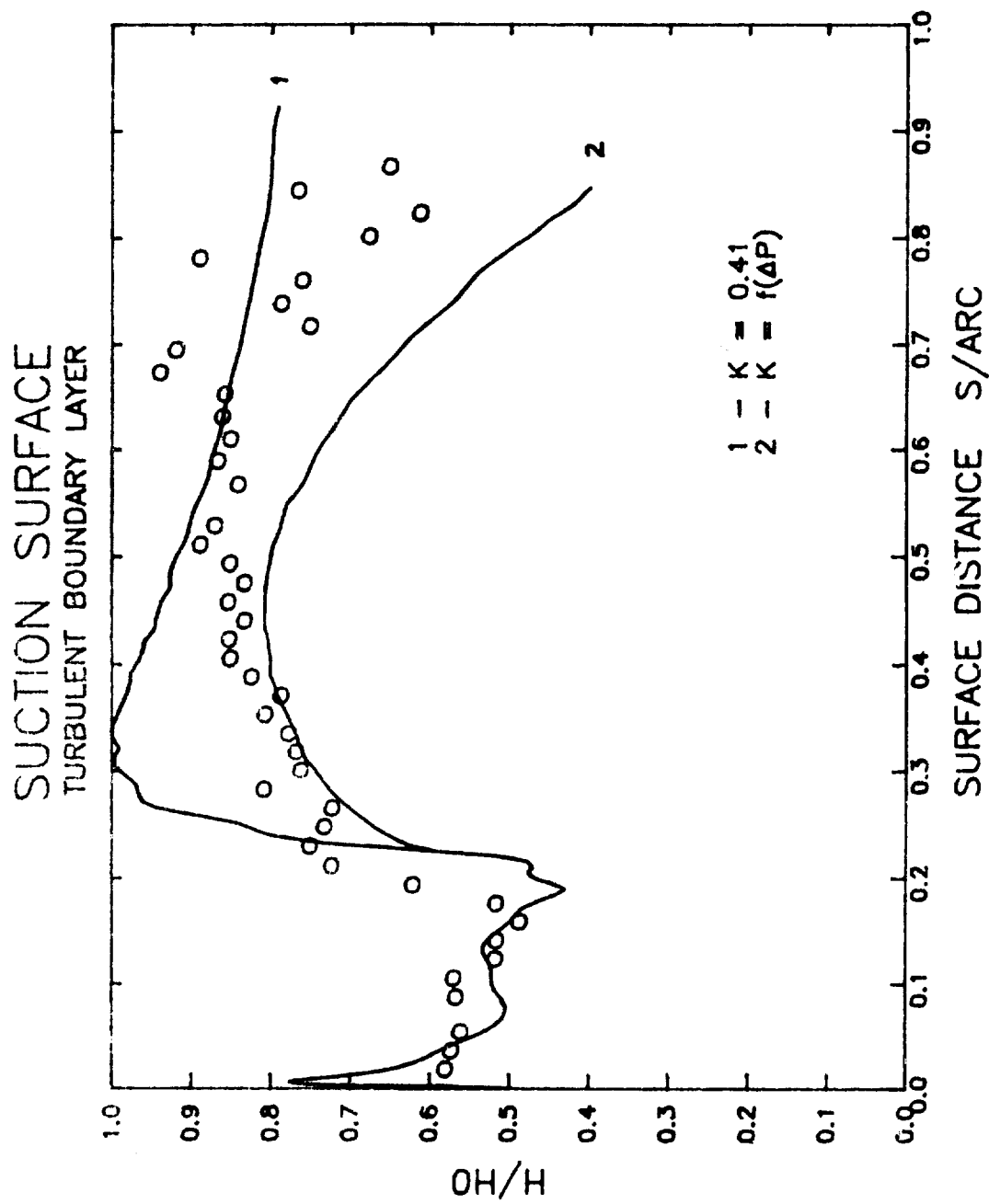


Figure 4. Effect of Von Karman "Constant" Definition

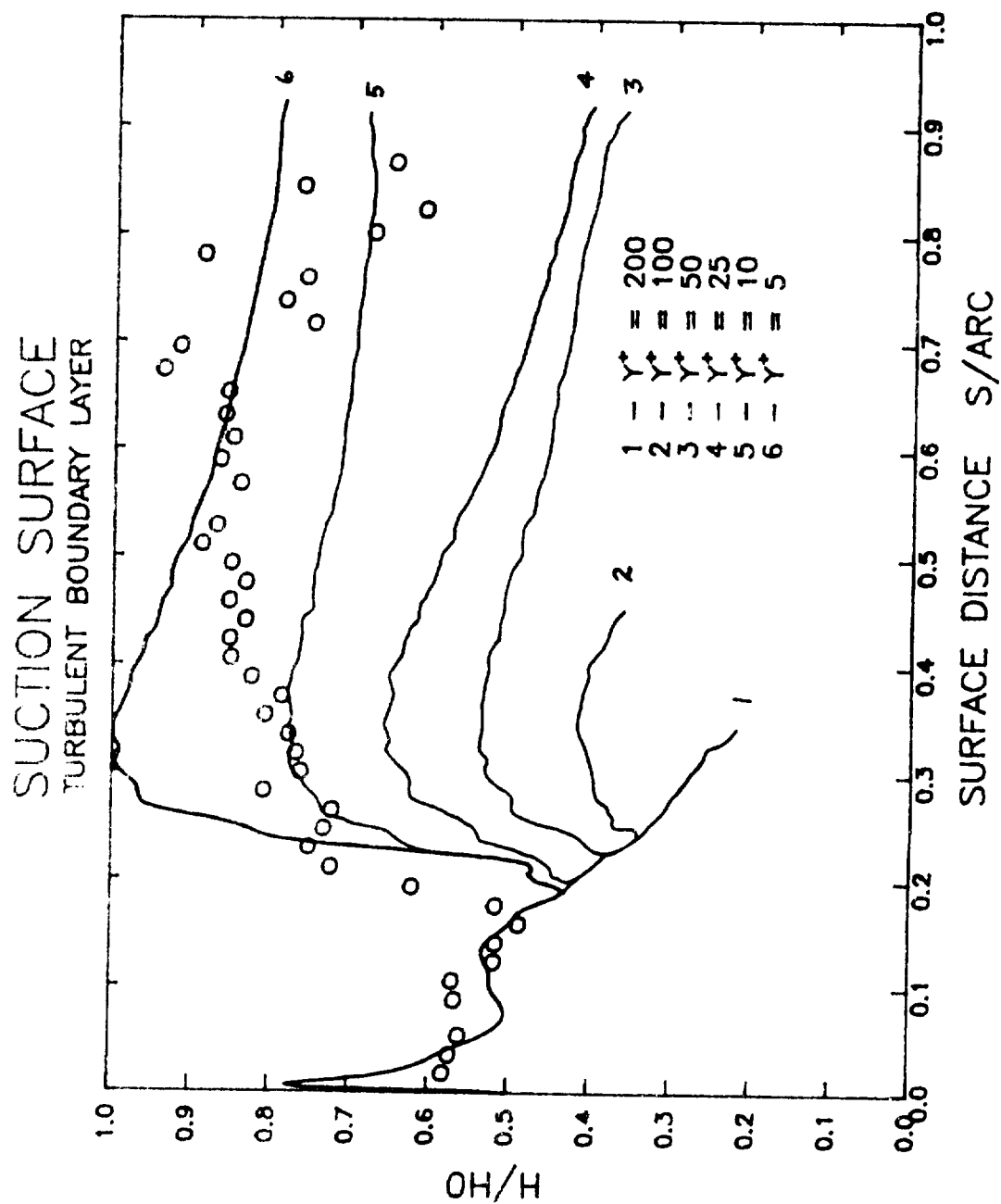


Figure 5. Effect of Wall Function "Thickness"

produced very erroneous results. As would be expected however, as the finite difference grid is brought closer to the wall (i.e. lower Y^*_{max} values) the predictions are improved. It appears that the best prediction for a turbine blade suction surface occurs with $Y^*_{max}=10$. This is questionable since $Y^*_{max}=5$ should be more accurate. Although the better agreement with $Y^*_{max}=10$ is most likely a coincidence, this observation merits further investigation.

Shown in Figure 6 is the correlation contained in STAN5 to correct the viscous sublayer thickness (A^+) for a streamwise pressure gradient. As discussed above, it was felt that this correlation needed to be modified for a turbine blade flow field. Qualitatively however, the curve is correct. Favorable pressure gradients stabilize the boundary layer promoting relaminarization and hence a thick viscous sublayer. Adverse pressure gradients destabilize the boundary layer thus reducing the thickness of the viscous sublayer. The curve as shown was generated from experiments on a flat plate [1]. It is highly probable that this curve does not represent a turbine blade but an experimental data base is necessary before any modifications can be made.

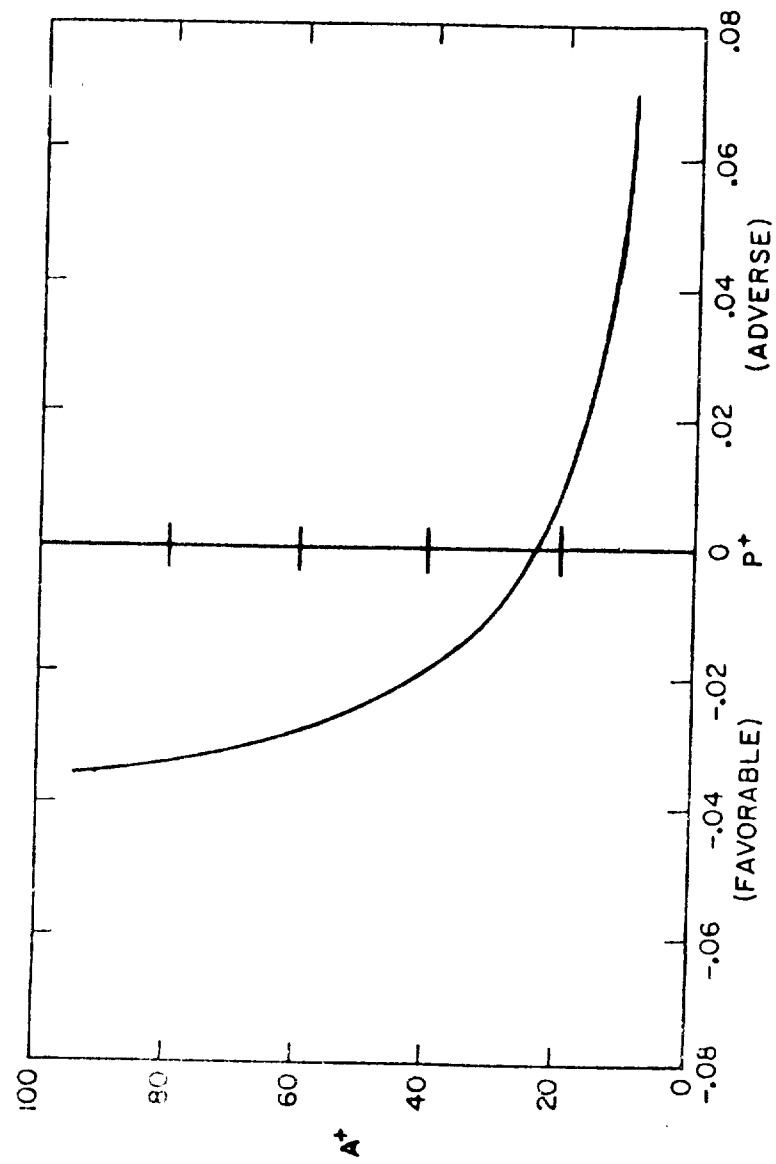


Figure 6. Correlation for Viscous Sublayer Correction

CONCLUSIONS AND RECOMMENDATIONS

Based on this investigation it was concluded that the wall function in STAN5 can be altered to improve the prediction of heat transfer coefficients. It should be realized that these statements are based on the code's performance compared with one data set. Further comparison is necessary to increase the confidence in the conclusions made. With that in mind the following statements summarize the findings of the study.

- With a favorable streamwise pressure gradient Y^+_{\max} should be kept as small as possible. Suggested values are $Y^+_{\max}=5$ or 10.
- Using the local value of shear stress (τ_{local}) to normalize the Van Driest damping function improves the heat transfer coefficient predictions.
- Use of the acceleration terms in the Couette flow equations did not accurately predict the transition region. However it is felt that use of the modification is still important and perhaps significant effects will be observed when this modification is coupled with a transition model.
- The use of a Von Karman "constant" which varies with streamwise pressure gradient gave good results on the first 40% of the blade surface. Beyond that the predictions are under-predicted. However, the trend of the curve was correct and thus further investigation is warranted.
- The viscous sublayer thickness correction in STAN5 is suspect. Qualitative enhancements were not possible due to the lack of experimental data on turbine blade boundary layers.

The following recommendations are also suggested by this study:

- The wall function enhancements need to be incorporated with other improvements like turbulent Prandtl number models, transition models, etc. It is very likely that each modification made does not improve the prediction capabilities significantly but modifications used in unison will produce improvement.

- The useful range of the wall function still needs to be identified for turbine blades. Comparisons with many sets of experimental data will be necessary to identify when the wall function must be patched into the finite difference grid.
- A correlation for correcting the viscous sublayer thickness must be developed for turbine blades. Development of such a correlation dictates a need for detailed boundary layer measurements on various turbine blades.

REFERENCES

1. Crawford, M.E. and Kays, W.M., "STAN5 - A Program for Numerical Computation of Two-Dimensional Internal and External Boundary Layer Flow", NASA CR-2742, 1976.
2. Gaugler, R.E., "Some Modifications to, and Operational Experiences with, the Two-Dimensional, Finite-Difference, Boundary Layer Code STAN5", ASME Paper No. 81-GT-89, 1984.
3. Patankar, S.V. and Spalding, D.B., "A Finite-Difference Procedure for Solving the Equations of the Two-Dimensional Boundary Layer", International Journal of Heat and Mass Transfer, Vol. 10, 1967, p. 1389.
4. Hylton, L.D., Mihelc, M.S., Turner, E.R., Nealy, D.A., and York, R.E., "Analytical and Experimental Evaluation of the Heat Transfer Distribution Over the Surfaces of Turbine Vanes", NASA CR-168015, 1983.
5. Whitaker, K. W., "The Role of the Turbulent Prandtl Number in Turbine Blade Heat Transfer Prediction", Research Reports - 1988 NASA/ASEE Summer Faculty Fellowship Program, NASA CR-183553, 1988, p. XXX.
6. Glowacki, W. J. and Chi, S. W., "A Study of the Effect of Pressure Gradient on the Eddy Viscosity and Mixing Length for Incompressible Equilibrium Turbulent Boundary Layers", AIAA Paper No. 72-213, 1972.

1989

NASA/ASEE SUMMER FACULTY FELLOWSHIP PROGRAM

MARSHALL SPACE FLIGHT CENTER
THE UNIVERSITY OF ALABAMA IN HUNTSVILLE

MULTIBODY MODELING AND VERIFICATION

Prepared by:	Gloria J. Wiens
Academic Rank:	Assistant Professor
University and Department:	Auburn University Mechanical Engr. Dept.

NASA/MSFC:	
Laboratory:	Structures and Dynamics
Division:	Control Systems Division
Branch:	Pointing Control Systems

MSFC Colleague:	Henry B. Waites
-----------------	-----------------

Date:	August 31, 1989
-------	-----------------

Contract No.:	The University of Alabama in Huntsville NGT-01-008-021
---------------	--

MULTIBODY MODELING AND VERIFICATION

Gloria J. Wiens
Assistant Professor
Mechanical Engineering Dept.
Auburn University
Auburn, Alabama

ABSTRACT

A summary of a ten week project on flexible multibody modeling, verification and control is presented. Emphasis was on the need for experimental verification. A literature survey was conducted for gathering information on the existence of experimental work related to flexible multibody systems. The first portion of the assigned task encompassed the modeling aspects of flexible multibodies that can undergo large angular displacements. Research in the area of modeling aspects were also surveyed, with special attention given to the component mode approach. Resulting from this is a research plan on various modeling aspects to be investigated over the next year. The relationship between the large angular displacements, boundary conditions, mode selection, and system modes is of particular interest.

The other portion of the assigned task was the generation of a test plan for experimental verification of analytical and/or computer analysis techniques used for flexible multibody systems. Based on current and expected frequency ranges of flexible multibody systems to be used in space applications, an initial test article was selected and designed. A preliminary TREETOPS computer analysis was run to ensure frequency content in the low frequency range, 0.1 to 50 Hz. The initial specifications of experimental measurement and instrumentation components were also generated. Resulting from this effort is the initial multi-phase plan for a Ground Test Facility of Flexible Multibody Systems for Modeling Verification and Control. The plan focusses on the Multibody Modeling and Verification (MMV) Laboratory. General requirements of the Unobtrusive Sensor and Effector (USE) and the Robot Enhancement (RE) laboratories were considered during the laboratory development.

ACKNOWLEDGEMENTS

I would like to express my deep appreciation to John Sharkey and Alan Patterson for assisting me on the technical details of the summer project. Without their help, this project could not have been done within the time frame allotted.

Neil Tyson, Michelle Bailey and Mark Whorton are also deeply appreciated for allowing me use of their computers and software. Thanks to John Rakoczy, Bill Walker and Dennis Irwin for sharing office space and reference materials. In addition, I would like to thank George Meyers, Mark West, and Shirley McKelvy for their provision of miscellaneous items and assistance.

My thanks go also to Dr. Gerald Karr, University Program Co-Director, and Dr. Frank Six, NASA/MSFC Program Co-Director, for providing meaningful diversions during the program.

And last but not least, many thanks to my colleague, Dr. Henry B. Waites, for giving me this rare opportunity to be involved in a new significant GTF program which will, without doubt, contribute advancements in research.

TABLE OF CONTENTS

List of Figuresiv
List of Tablesiv
Nomenclature	v
INTRODUCTION	1
Project Overview and Objectives	1
Research by Others.	2
Need for Multibody Modeling, Verification and Control GTF.	3
MODELING	5
EXPERIMENTAL VERIFICATION (Ground Test Facility).	8
Experimental Procedure.	9
Laboratory Facility and Layout.10
Measurement and Instrumentation Specifications.11
Partial Estimated Budget.14
CONCLUSIONS.15
RECOMMENDATIONS.15
REFERENCES32

List of Figures

Figure 1.	Planar Multibody with Three Flexible (Euler-Bernoulli) Links and Three Pinned Joints.16
Figure 2.	Proposed Flexible Multibody Test Article. . .	.17
Figure 3.	Normalized Mode Shapes for Link One18
Figure 4.	Normalized Mode Shapes for Link Two19
Figure 5.	Normalized Mode Shapes for Link Three20
Figure 6.	TREETOPS Configuration of Test Article.21
Figure 7.	Sample Open and Closed Tree Topologies [1]. . .	.22
Figure 8.	Lens Antenna Deployment Demonstration (LADD) Hardware23
Figure 9.	General Facility Layout for MMV, USE and RE . .	.24
Figure 10.	Current Major Structural Layout25
Figure 11.	Existing Facility Floor Plan with Unused Air-Handling Units Removed26
Figure 12.	Proposed Facility Layout, Top View.27
Figure 13.	Proposed Facility Layout, West View Facing East.28

List of Tables

Table 1.	MMV Test Article Material and Physical Properties.29
Table 2.	Component Mode Shapes and Frequencies.30
Table 3.	System Modal Frequencies31

Nomenclature

ACES	<i>Active Control Evaluation for Spacecraft</i>
AGS	Augmented Advanced Gimbal System
BET	Base Excitation Table
CASES	Control, Astrophysics and Structures Experiment for Space
FEM	Finite-Element Modeling
GTF	Ground Test Facility
JPL	Jet Propulsion Laboratory
LADD	Lens Antenna Deployment Demonstration
LSS	Large Space Structure
MACE	Middeck Active Control Experiment
MMV	Multibody Modeling Verification Laboratory
RE	Robot Enhancement Laboratory
RMS	Remote Manipulator System
TREETOPS	Control System Simulation for Structures with a Tree Topology Computer Software Package
USE	Unobtrusive Sensor and Effector Laboratory

INTRODUCTION

The NASA's LSS GTF (Large Space Structure Ground Test Facility) at MSFC (Marshall Space Flight Center) was developed for meeting the desired objectives of complex space projects and to become a national test bed for investigations in dynamics and controls [1]. The topics of this facility can be grouped into control development and synthesis, dynamics verification, dynamic modeling, and hardware flight systems for space structures. Due to the increase in complexity and more stringent requirements on spacecraft structures, investigations of multibody dynamics modeling and control have become essential. Many of the future space missions (such as extremely accurate pointing and tracking systems and the attainment of vibration-free observation image planes) require high performance from the LSS. The required state-of-the-art systems to be or currently under development consist of complex arrangements of interconnected rigid and flexible bodies. Presently, the LSS GTF provides ground test capabilities for many experiments involving large structures with flexible components. Therefore, a natural extension of the laboratory's activities would be to investigate the dynamics and controls of flexible multibody systems. Hence, presented in this report is a plan for addressing these needs and bringing into realization the Multibody Modeling and Verification (MMV) Program at the MSFC/LSS GTF.

Project Overview and Objectives

Since the 1960's, a significant amount of theoretical work has been undertaken in the area of modeling and simulation of multibody systems. However, for systems having flexible components, there still seems to be no well defined method for selecting component modes for systems, in which due to large displacements, the boundary conditions of the original assumed modes varies. Furthermore, there has been very limited experimental verification of the existing modeling and simulation techniques. In view of the last two statements, the summer task definition encompassed the following. First: The modeling aspects of flexible multibodies that can undergo large angular displacements are to be studied. The thrust of the study is for determining the sufficiency of component mode synthesis based on individual flexible component data for ascertaining the system modes. The systems subject of this study are those that exhibit configurations other than the initial one used for determining the component data. Second: A test plan is to be generated so that analytical and/or computer analysis can be verified experimentally. Third: If time permits, control methods for multibody systems are to be surveyed and an

experimental test plan generated for multibody control verification. The project's ten week procedure set forth was to achieve as much of the first two tasks' objectives as stated above. The third task was set aside and only taken into account throughout the project execution when it was appropriate.

Research by Others

In an attempt to complete a good portion of the tasks set forth, much time was spent in collecting background information and technical articles on flexible multibody systems. The literature search indicated a recently strong and growing interest emerging for developing experimental verification facilities [1, 2, 3, 4 and 5]. Much of the work in the field of multibody systems was largely motivated by the spacecraft problem [2]. This problem required analysis of systems experiencing large rotations while components (such as antennas and solar panels) were undergoing large relative motions. Another area in which independent developments of the same problems were simultaneously being addressed was in kinematics and machine design [6]. With today's technical advances and demands, researchers in both areas have been brought together by their common interests.

Due to the combination of both rigid body large displacements and small elastic deformations occurring in flexible multibody systems, the dynamic models have complex nonlinearity and model reduction problems. The conventional model reduction (modal coordinate truncation) methods still have not been securely established [7]. Other questions also arise in the representation of energy dissipation characteristics, selection of modes and boundary conditions, just to name a few. Hence, with varying degrees of generality and model complexity, a variety of ways have been developed for deriving the equations of motion for multibody systems [8-39]. These range from employing the Newton-Euler formulations, Hamilton's equations, Kane's method, Lagrange's form of D'Alembert's Principle approach to Component Mode Synthesis techniques directly or with special model variations. The methods and their variations can also be grouped as either an assumed mode approach or a finite-element approach. The modeling variations have been in terms of generalized coordinate selection, joint interfacing and flexibility modeling, representation of model uncertainties, computational bottleneck reduction, control system development, etc. To some degree the basic modeling choice is a matter of preference since the different strategies often produce the same results. Using ones preferred modeling scheme and computational methods, various computer simulation codes have been developed and made available to the research and commercial community. The list of computer codes is endless; MBODY, MFLEXBODY, DISCOS, AFBDAF,

TREETOPS, ADAMS, SADACS, CONTOPS, GRASP, MIDAS
New versions are continuously being generated as advances in research require updates and corrections to the codes when various problems are encountered. As of yet, no systematic comparison of these codes for accuracy or efficiency has been generated [2, 40]. Presently, JPL (Jet Propulsion Laboratory) is conducting a simulation technical verification survey with plans to develop an experimental verification facility [3].

The experimental research on flexible multibody systems can be found arising out of basically two areas: flexible structures with multiple components [19, 41, 42] and the robotics area. In the robotics area, there is numerous amounts of experimental work focussing on the rigid system. Only in recent years have researchers begun pursuing the issues of flexibility in the arms and joints [4, 20, 43-48]. This has been due to the increase in importance of high-speed operation, high accuracy requirements and lightweight designs for manufacturing and new space missions. Furthermore, with the advent of high speed computers, simulation analyses have become feasible. Also, in the field of flexible multibody systems are problems such as those studying the vibrations effects in high-speed machines and mechanisms which have had some experimental verification [49].

Need for Multibody Modeling, Verification and Control GTF

Although numerous theoretical and numerical research has been undertaken, very little experimental work has been carried out in the multibody dynamics and controls field. With the advantages of low power consumption, high load to weight ratios, large workspaces, and potential for high speed operation because of lower inertia, the currently proposed designs for lightweight high-performance multibody and/or robotic systems for space applications make it essential to analyze the fundamental modeling issues in greater detail. To enhance the understanding of multibody dynamic modeling and control, experimental verification is a key element. Issues which need to be addressed are the dynamic effects such as the interactions between the rigid and flexible dynamics, the sensor and actuator dynamics, and the model and controller dynamics. All these need to be analyzed and correlated with reference simulation models; hence, experimental verification of existing modeling and simulation methods. For future space missions which involve many multibody applications, ground testing is necessary to ensure their in-flight success and the safety of the crew. Furthermore, it is far less expensive to do the major research, analysis, and development of flight experiments in ground tests, readying them and the crew for the mission. Ground testing prior to flight has been the universally insisted upon approach for most aerospace structural systems

[50]. Current and proposed experimental research is now summarized.

The experimental approaches taken by researchers have been to work either in the horizontal plane, in an attempt to avoid gravitational effects in modeling [4, 48]; or the vertical plane, in which gravity must be included in the model and compensated for numerically, or offloading techniques must be used such as bungy suspension cables [5, 20, 44, 45]. A third approach is to perform the flexible multibody experiments in space. Presently, space missions are under development or proposed which involve experiments using the RMS arm on the orbiter [46, 47] and scaled multibody experiments to be conducted in the shuttle's middeck area (MACE), [5]. The orbiter-based experiments have their merits and will eventually need to be executed as future space missions warrant them. However, these in-flight experiments also have associated supporting ground testing laboratory development [5]. Even after orbiter-based testing techniques are fully devised and implemented, ground testing will be required and will usually constitute the highest loading environment [50]. Hence, the need for GTFs is considered essential for the successful execution of the expensive in-flight multibody experiments and future space missions.

Currently, the actual experimental research performed thus far has been limited to single link flexible arms and two links with only one being flexible [4, 20, 44, 48]. An exception to this, Book et al [45] has done extensive investigations using a planar arm with two flexible links. Cannon et al is currently extending his work to include two flexible links.

In spite of these efforts, there still needs to be more experimental research. Book et al [45] has shown by experimental verification that using strictly simulation methods can result in one missing some of the system modes in their analysis. He has also shown that experimental results assist in the determination of proper boundary conditions for analytical modeling. That is, boundary condition selection affects the accuracy of the analysis significantly; further, substantiating the need for experimental verification of existing modeling and simulation techniques. The maximum reliability and accuracy achieved by the correlation and modeling of dynamic parameters based on experimental and analytical results are also considered important aspects in aerospace engineering [51]. What follows is the 1989 Summer Faculty project's results in modeling aspects of flexible multibody systems and the initial plan for addressing the above foreseen needs of future space missions involving multibody systems (e.g. assembly of the space station, etc.)

MODELING

After surveying the various techniques and focussing on the question at hand (component mode selection versus system modes and large angular displacements), the Lagrangian formulation of the equations of motion using assumed modes [8] was selected. This to a large degree was a matter of personal preference and familiarity with the formulation technique. In addition, this approach for deriving the dynamic equations was selected because the resulting analytical form facilitates the exploration of the coupling relationship between the flexible and rigid body motions of the individual links and that of the total system. Also, this approach is less computationally intensive compared to the FEM approaches. The coupling appears in the off-diagonal matrix terms in the following compact symbolic representation of the system's equations of motion.

$$\begin{bmatrix} \mathbf{m}_{RR}' & \mathbf{m}_{R\theta}' & \mathbf{m}_{Rf}' \\ \text{symmetric} & \mathbf{m}_{\theta\theta}' & \mathbf{m}_{\theta f}' \\ & & \mathbf{m}_{ff}' \end{bmatrix} \begin{bmatrix} \ddot{\mathbf{R}}' \\ \ddot{\boldsymbol{\theta}}' \\ \ddot{\mathbf{q}}_f' \end{bmatrix} + \begin{bmatrix} \mathbf{0} & \mathbf{0} & \mathbf{0} \\ \mathbf{0} & \mathbf{0} & \mathbf{0} \\ \mathbf{0} & \mathbf{0} & \mathbf{K}_{ff}' \end{bmatrix} \begin{bmatrix} \mathbf{R}' \\ \boldsymbol{\theta}' \\ \mathbf{q}_f' \end{bmatrix} + \begin{bmatrix} \mathbf{C}_{R'}^T \\ \mathbf{C}_{\theta'}^T \\ \mathbf{C}_{q_f'}^T \end{bmatrix} \lambda \quad (1)$$

$$= \begin{bmatrix} (\mathbf{Q}_e')_R \\ (\mathbf{Q}_e')_\theta \\ (\mathbf{Q}_e')_f \end{bmatrix} + \begin{bmatrix} (\mathbf{Q}_v')_R \\ (\mathbf{Q}_v')_\theta \\ (\mathbf{Q}_v')_f \end{bmatrix}, \quad i = 1, 2, \dots, n_b$$

Using the component mode synthesis, the component equation of motion for each body in the system is as follows.

$$\begin{bmatrix} \mathbf{m}_{rr}' & \mathbf{m}_{rf}' \\ \mathbf{m}_{fr}' & \mathbf{m}_{ff}' \end{bmatrix} \begin{bmatrix} \ddot{\mathbf{q}}_r' \\ \ddot{\mathbf{q}}_f' \end{bmatrix} + \begin{bmatrix} \mathbf{0} & \mathbf{0} \\ \mathbf{0} & \mathbf{K}_{ff}' \end{bmatrix} \begin{bmatrix} \mathbf{q}_r' \\ \mathbf{q}_f' \end{bmatrix} = \begin{bmatrix} (\mathbf{Q}_e')_r \\ (\mathbf{Q}_e')_f \end{bmatrix} + \begin{bmatrix} (\mathbf{Q}_v')_r \\ (\mathbf{Q}_v')_f \end{bmatrix} - \begin{bmatrix} \mathbf{C}_{q_r'}^T \\ \mathbf{C}_{q_f'}^T \end{bmatrix} \lambda \quad (2)$$

Both forms have their corresponding constraints represented by the C matrices. Analyzing and understanding equations (1) and (2) are important for achieving the main objective of the MMV laboratory; that is, model verification. Being able to relate quantities in the equations of motion in terms of component mode synthesis and system modes with experimental results is critical. One should recall that model verification is a process of experimentally verifying an analytical (or numerical) model to gain confidence in its use for predicting system behavior [52]. If there exists any system misrepresentation, the model must be revised based on the new physical evidence. Note, caution must

always be taken to avoid the risk of changing the model to match data which are in error.

Applying the above symbolic formulations, the equations of motion of a planar multibody with three flexible links are derived. The links are assumed to be Euler-Bernoulli beams, in bending only, and attached by pin (revolute) joints. Gravity is included in the modeling since the MMV laboratory test articles are to be tested in the vertical plane. See figure 1. The next steps involve detailed analysis of component mode and boundary condition selection as a function of rigid-body motions. These steps have been left for execution during a proposed continuation project over the next twelve months. The project will be a study on the highly nonlinear functional relationship between rigid body and flexible body motions. The analysis will also include numerical techniques (TREETOPS and NASTRAN) in searching for an explicit and useful form of this relationship.

Next, an initial description of a MMV test article and its physical properties is given. The article is defined to exhibit low frequency content (0.1 Hz to 50 Hz), coupling between rigid and flexible body motions, and multiple configurations (open and closed tree topologies) due to large angular displacements, and to be of a large size to mimic those to be used in space applications. The three link flexible multibody of figure 1 possesses these characteristics. However, in selecting the physical dimensions, sensors, and actuators (torquers), the maximum torque versus weight characteristics of torquer motors significantly limited the feasibility of this multibody in open tree topology. To overcome the limitations, there are two options to choose: gravitational offloading via bungee suspensions or counter-balancing, or to redesign the test article. Since the dynamic interactions of bungee suspensions with test articles is not clearly defined and the use of counter-balancing results in greater system masses, the second approach is selected while keeping the other options still open.

The new test article currently under investigation is one in which the third link is made of S-Glass, an extremely lightweight and highly flexible material. It consists of a double branch formation to enhance the modal density, see figure 2. The other two links are made of a carbon/carbon composite material (lightweight and high strength). To meet the flexibility requirements, link one is selected to have a rectangular tubular cross-section with a wall thickness of $t=0.34\text{cm}$. Link two has a solid rectangular cross-section. The cross-sections are selected to exhibit a large degree of flexibility in only one plane. The objective is to restrict the first experimental testing to a planar flexible multibody system. However, out-of-the-plane motions will be

measured during the experimental testing to ensure planar motion is maintained. Future experiments will be conducted for spatial motion systems. The current multibody material and physical properties are listed in Table 1, [53].

To ensure desired frequency content before fabrication, a TREETOPS analysis was performed for the new test article. The component modes selected were:

Link One Clamped-free with a concentrated mass at the free end equal to the mass of motors two and three, and links two and three. See figure 3.

Link Two Clamped-free with a concentrated mass at the free end equal to the mass of motor three and link three. See figure 4.

Link Three Clamped-free. See figure 5.

The resulting component mode shapes and frequencies are given in Table 2. Table 3 shows the corresponding system modal frequencies and definitions of the terms used in Table 2. The lowest system mode was found to be 1.26 Hz. Comparing the system modes and the component modes shown in the tables, there appears to be very little modal coupling between the links. This is indicated by very little changes in the values between the component mode and system mode frequencies. Presently, there is still some uncertainty in whether the actual frequency content found from the TREETOPS analysis contains enough modal density in the low frequency range and if the values are correct. Since only one multibody static configuration (see figure 6) and set of boundary conditions has been analyzed, and the effects of gravity and sensor/actuator weights were not included, further TREETOPS and NASTRAN analyses are planned before finalizing the test article description for fabrication. This will be carried out in the proposed continuation project.

EXPERIMENTAL VERIFICATION (Ground Test Facility)

Moving into the next summer task, the following is a general plan for the Multibody Modeling Verification (MMV), Unobstrusive Sensors and Effectors (USE), and Robot Enhancement (RE) laboratories. The main focus is on the MMV laboratory with USE and RE space and general objectives specified. In defining the specifications for the data acquisition and analysis system, the test article described in figure 2 and Table 1 (or one similar) is assumed. Hence, measurement of the frequency range, 0.1 Hz to 50 Hz, is a specified requirement of the facility. The vertical plane (1-g) testing environment selection is heavily driven by the available space. However, this choice is considered viable based on past success by NASA/MSFC LSS GTF and Book et al [45] in conducting flexible body experiments in the same environment, and that many other experts in the flexible multibody for space applications field have vertical plane testing built into their overall projected laboratory plans [5]. In addition, designing the facility for vertical testing allows easy extension of the experiments to include large spatial motions. The general overall outline of the new multi-laboratory GTF is now given.

Phase I. (MMV) Main objectives are to improve multibody modeling and simulation and to experimentally verify component mode synthesis methods [1]. The test articles are to be planar and spatial in their motion characteristics.

A. Static

The first experiments to be conducted in MMV are to be of static multibody configurations. The results are to be used for static verification of the component mode selection process and to determine if a purely kinematic relationship exists between mode selection and large displacements. Open and closed tree topologies are to be tested, see figure 7.

B. Dynamic

Following static tests, the test articles are to be slewed through large angular displacements. The objective is to verify the dynamic relationship between component mode selection and large angular motions and rates. Plus, the laboratory is to be used for verifying existing dynamic modeling and simulation techniques.

C. Control

After exhaustive testing and analysis of parts A and B, the laboratory activities will involve the development, implementation and experimental verification of control techniques for flexible multibody systems.

Phase II. (USE) Laboratory is to investigate the use of sensors and actuators which are lightweight and have unobtrusive geometries. (The piezoelectric materials currently being tested will be used in the MMV laboratory) [1]. NASA/MSFC LSS Laboratory currently has a bid out for the acquisition of the LADD hardware to be used as a test article, see figure 8 [54].

Phase III. (RE) Laboratory is to involve a combination of (MMV) and (USE) results and to investigate the concept of a robot arm manipulating its highly flexible payload with assistance of the payload's own actuators and sensors by controlling them through electrical contacts in the endeffector. Hence, to prevent the TAIL Wagging the DOG phenomenon. An experiment involving the LADD suspended from a flexible boom is also being considered.

Experimental Procedure

In this project, only the experimental procedures, instrumentation and hardware for the MMV laboratory are specified. The following experimental procedures will describe only the initial planar flexible multibody experiments. The results of these experiments will provide vital information for the future spatial motion tests definitions.

Component Modal Experiment. This first experiment is to determine and verify the component modal selections for each link of the test article, individually. Each link will be suspended from the test stand in its desired orientation with the same boundary conditions as assumed for the analytical model (e.g. clamped-free at a 30 degree angle from the vertical and with a lumped mass at the free end). Using standard experimental modal analysis techniques, the component modal properties will be determined under various excitations. The sensors will be accelerometers, strain-gauges, and/or piezoelectric films.

Assembled Multibody System (Static). This experiment is to determine the system modal properties of the multibody in various static configurations. These will be used to verify the analytical model. If discrepancies are found between the analytical (and/or numerical) and the experimental results, steps will be taken to eliminate them or to formulate an explanation for delineating the nonconvergence. The assembled test article will be suspended from the test stand in various selected static configurations (open to closed tree topology when possible). In each configuration, standard modal testing techniques will again be used to determine the system modal properties. The same sensors as before will be used. The results will be compared with those obtained theoretically. Model and/or experimental adjustments and retesting will be done accordingly.

Assembled Multibody System (Dynamic). Following the above experiments, dynamic tests will be performed to determine the existence of a dynamic relationship between component modal selections and large angular motions and rates. Dynamic modeling and simulation techniques will also be verified. This experiment will involve equipping the static experiment's flexible multibody test article with any additional necessary joint actuators and sensors. The test article will then be commanded (open-loop control) to move through prescribed large angular motions. Simultaneously, sensor readings will be taken to determine the system's total response. Again, a theoretical and experimental correlation will be made followed with any model or experimental adjustments and generated explanations of nonconvergences.

Assembled Multibody System (Control). Utilizing the knowledge gained from the previous experiments, control techniques will be derived and implemented experimentally. Again, the sensors and instrumentation will essentially be the same with only special control features added.

The above experiments will be extended to include other test articles, both planar and spatial motion types.

Laboratory Facility and Layout

Figure 9 illustrates the general facility layout of the three laboratories, MMV, USE and RE. The physical space, already allocated for these laboratories, is located at NASA/MSFC, Huntsville, Alabama in the west high bay area of Building 4619. It consists of a 53.5'x29.0' floor space with approximately a 90' ceiling. The location is just east of the Flight Robotics Laboratory (EB-24) and west of the ACES and CASES control room. There is an existing platform at 42.5' with this control room as its only access. The present major structural layout of this space is shown in figure 10 (showing platform only) and 11 (top view after the removal of unused air-handling units along east wall and below the platform, verbal approval has already been given).

After surveying the facility, it was decided that using the existing platform with its access from the ACES and CASES control room would provide the most expeditious and cost effective approach for implementing the MMV and USE laboratories. The platform allows enough vertical height for suspending both the LADD structure and MMV test article, see figure 9. In addition, the control room has room for setting up the data acquisition and control equipment and is conveniently located. The only initial requirements will be the removal of the unused air-handling units and a few structural extrusions, and cutting a 5'x5' hole in the platform for suspending the MMV test article. And last but

not least, the leaks in the roof will need to be fixed in order to maintain the quality of the experimentation. The structural rigidity of the platform appears to be adequate for the initial implementation before final renovations (no tests were done to verify this). If these facility changes can be accomplished within the year, necessary instrumentation purchased, test article fabricated, and installation completed, the MMV and USE laboratories could start testing as early as Summer 1990.

The next stage of renovations will be to extend the platform as indicated in figure 12 and 13. This will provide ample volume for planned spatial flexible multibody experiments. Structural beams and bracing will need to be added or removed to ensure that the experiments' supporting structure's frequency content will not interfere with the experimental testing. These details will be determined in collaboration with the Facilities group. In order to provide alternate access to the platform, stairs are to be located on the north side of the platform. These stairs will also continue up another 40' to a second platform for the RE laboratory (not shown in the figures). The estimated cost for the stairs and MMV platform extension is \$150,000 (1989 dollars) and another \$250,000 for the second platform. The projected completion of renovation for this stage is sometime during 1990 to 1992, depending if it can be scheduled with the Facilities group. It is anticipated that the platform extension could be completed in 1991. The second platform probably would not be finished before 1992.

In the renovation plans, there are certain restrictions placed on the use of this space. One, the bay area doors must remain accessible and fully operational. Second, general passage for NASA employees and guests to and from the Flight Robotics Laboratory and Vibration Testing Facility must be provided (indicated in figure 13).

Measurement and Instrumentation Specifications

The following is a list of the major components of the measurement and instrumentation equipment and their specifications needed for the MMV laboratory. This covers the static, dynamic and most of the control experiments requirements. It should be noted that this is only an initial list and is subject to change as required. The specific selections of the following items is based on the desired characteristics of low noise-to-signal ratio, high resolution, small physical weight additions to test article, and capability with existing ACES and CASES equipment.

Frequency range of test specimen: 0.1 Hz to 50 Hz

The measurement equipment must be able to detect position, velocity and accelerations within this frequency range, in addition to large displacements.

Base Excitation Table (BET): The BET is to produce excitations via disturbance inputs to the multibody system for determining its dynamic characteristics and the effectiveness of control algorithms. Disturbance types to be included are programmable deterministic, random, sine dwell and sine sweep motions. It must be able to excite frequencies within the 0.1 Hz to 50 Hz range. The directions of excitation are to be along the horizontal x,y axes. The load carrying capacity required is 2.3 kN. (Should be able to support test article, sensors, actuators, and gimbal system.) It is anticipated that the BET will be similar to the one currently used for ACES which has a bandwidth of 10 Hz and a dynamic range of ± 15 cm. It is driven by a hydraulic servo-loop position controller.

Augmented Advanced Gimbal System (AGS): Should provide articulation and control about three rotational axes. Bandwidths should be in excess of 50 Hz. The dynamic range in the pitch/yaw axes should be 200 N-m and ± 45 degrees. For the roll axes, the dynamic range should be 50 N-m and ± 90 degrees. These requirements will allow large angular motions in three dimensions.

Joints and Actuators: For the static testing, frictionless joints which give no relative motion are required. For the dynamic and control testing, torquer motors of various sizes, depending on the outer links' weights, are to be selected to provide large angular displacements (± 45 degrees). They should have minimum cogging and friction characteristics (e.g. direct-drive brushless torquers).

Joint Sensors: The joint sensors are to measure positions and rates. They should have a resolution down into the arcminute and arcsecond ranges. Their dynamic range should be ± 45 degrees and 70 degrees per second. They should have minimum friction. Plus, the sensors must be lightweight since they are part of the test article. At this time, it appears that the incremental optical encoders may be able to meet these requirements.

Rate Gyroscopes: The gyroscopes are to measure x,y,z rates and positions of the ends of the links. They are to provide information for calculating the absolute angular motions of the following attached link due to rigid body motion and flexible bending of the previous link. In addition, three will be mounted to the underside of the AGS payload mounting plate to measure its input motion. The gyros are to be analog, capable

of measuring $25e-3$ degrees per second, have a dynamic range of 70 degrees per second, and bandwidth above 50 Hz.

Accelerometers: These sensors are to measure the multibody's response due to flexible modal content. They will be located in triax formations at discrete locations along each link for measuring traverse deflections in-the-plane and out-of-the-plane. Measurement capabilities should be within the 0.1 Hz to 50 Hz frequency range. Resolution should be at least 0.001g with a dynamic range of 5 to 10g. Again, they must be lightweight so as to not alter the system characteristics to a great degree. Two accelerometers will be used to measure x,y acceleration of the BET.

Unobtrusive Sensor: Since weight is a major factor in designing a flexible multibody used in a gravitational field, link three has been selected to be made of a very lightweight material. This requires use of unobtrusive sensors. It is intended to implement a piezoelectric type sensor developed in the USE program. It is capable of measuring traverse deflections in- and out-of-the-plane directions by reading voltage levels which are a function of the piezoelectric film deformations. The USE program is also investigating its use as a sensor/actuator pair.

Data Acquisition and Analysis System: This system has the following preliminary component selections which provide the sampling rates, data storage and analysis capabilities, signal conditioning and compatibility with existing ACES system. The recommended system is a HP9000 Series 300 workstation (32 bit); LMS (Fourier Monitor) data acquisition, University of Cincinnati modal analysis package or Test Data Analysis Software (TDAS) by Structural Dynamics Research Corporation (SDRC); a DIFA Measuring System front end signal conditioning (65 channels); and STRUCTCEL PCB 330A accelerometers. In addition to the BET, it is recommended to purchase a 30 lb, long stroke shaker excitation system to allow excitations at locations other than the base.

Other Data Storage Devices: These include analog strip chart recorders, analog magnetic tape recorders, HP-5423 and GenRad 2515 dynamic analyzers which are available for use in the LSS laboratory.

Vision Systems were considered. But do to the large test article(s) undergoing large displacements, they are not recommended at this time.

Partial Estimated Budget

HP9000, Series 300 workstation (32 bit)	\$ 60,000
Software - LMS (Fourier Monitor) data acquisition,	\$ 12,000
- University of Cincinnati	\$ 0
modal analysis package	
or	
- Test Data Analysis Software (TDAS)	\$ 20,000
by Structural Dynamics Research	
Corporation (SDRC)	
DIFA Measuring System, Front end signal	\$100,000
conditioning (~ 65 channels),	
A/D, D/A; amplifiers; filters	
STRUCTCEL accelerometers & instrumentation	\$ 11,000
60 PCB Structcel; 20 triax	(initial)
mounting blocks; 20 triax cables;	
4 patch panels; 4 extension cables	
Each additional 20 triax ~ \$5,000	
Excitation System	\$ 14,900
30 lb, long stroke shaker; amplifier;	
filter; load cell; conditioning	
Piezoelectric film, shielding and instrumentation	\$ 3,800
for link three's sensor (\$1,150) and	
actuator (additional \$2,650)	
Precision Products Group, FG 313 series gyroscopes	\$ 60,000
6 gyroscopes and instrumentation	
(Note, weight may be too large.)	
Base excitation table system	\$ 50,000
Augmented advanced gimbal system	\$100,000
Stairs and MMV platform extension	\$150,000
Second platform	<u>\$250,000</u>
Partial List Total	<u>\$831,700</u>

CONCLUSIONS

An attempt was made to complete a good portion of the tasks set forth. Much time was spent in collecting background information and technical articles on flexible multibody systems. It was found from the literature search a recently strong and growing interest has emerged for developing experimental verification facilities. In parallel with gathering background material, a general dynamic model analytical formulation of a multibody system, comprising of three flexible bodies connected with revolute joints, was derived symbolically. This was followed up with selecting physical properties and component modes of a three body system for defining a possible test article for the experimental verification plan. An initial TREETOPS analysis was performed to estimate the frequency content of the system. This modeling and analysis completed during the summer project has laid the foundation for a continuation project to be executed during the coming year. The project will involve further analysis and design of the test article via TREETOPS and NASTRAN and analytical techniques. Following the modeling and TREETOPS analysis, an initial laboratory plan for experimental model verification was generated. The first Phase's testing is expected to begin as early as summer 1990. The controls verification was taken into consideration during the plan development of the model verification laboratory. However, time did not permit a thorough search of existing control methods and test plan generation.

RECOMMENDATIONS

Based on the growing interest and significant need of understanding flexible multibody systems, it is recommended that the development of the MMV, USE, and RE laboratories and their associated research be continued. Due to the complexities and the dependence on existing numerical code, advances in the area of flexible multibody systems modeling and experimental verification have become essential for the success of future space missions. Hence, with the currently available space, the feasibility is there for beginning work on the MMV and USE laboratories as soon as possible. In addition, there still needs to be more work performed on modeling, analyzing and defining the fabrication specifications for the MMV test article(s).

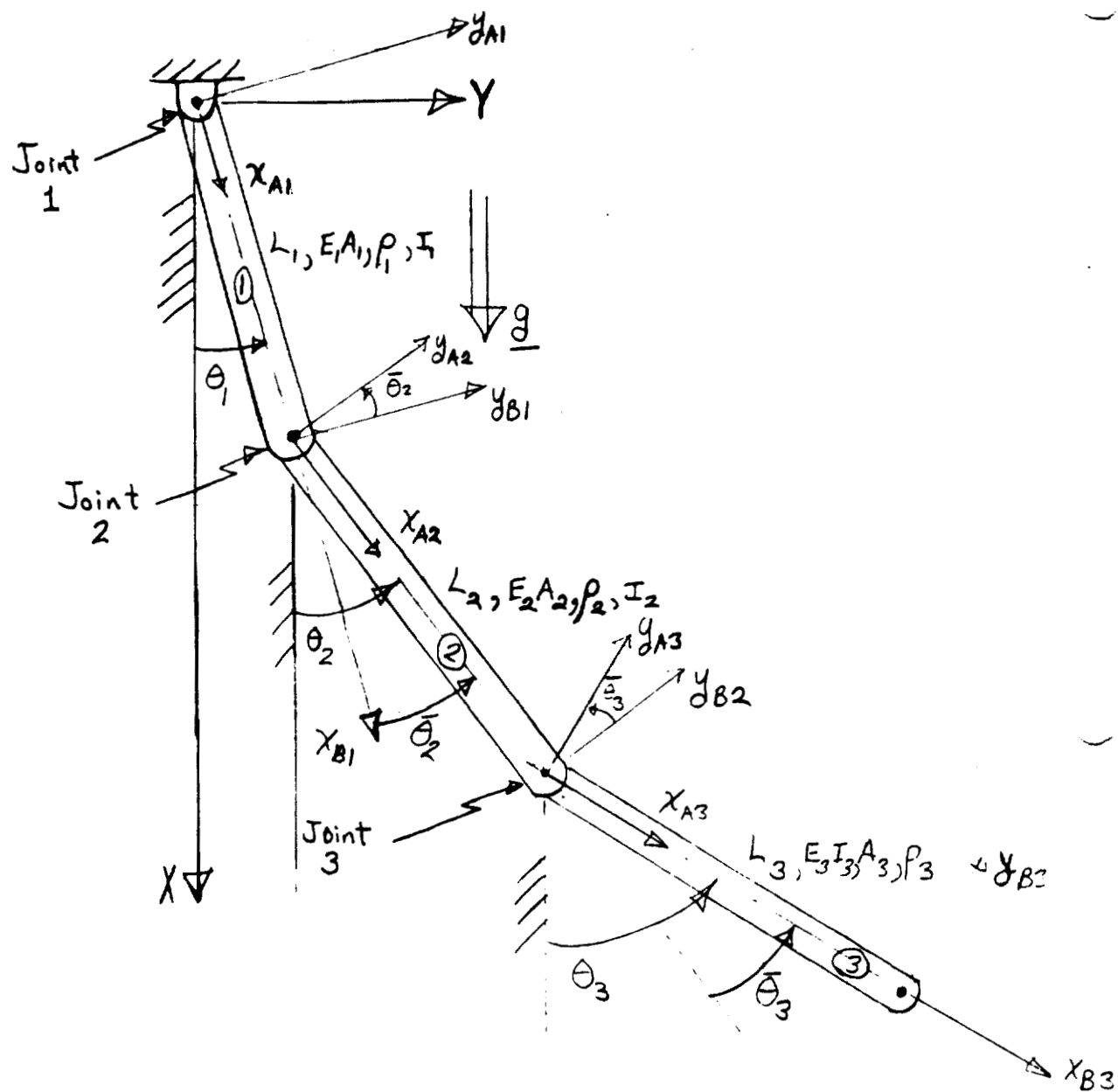


Figure 1. Planar Multibody with Three Flexible (Euler-Bernoulli) Links and Three Pinned Joints

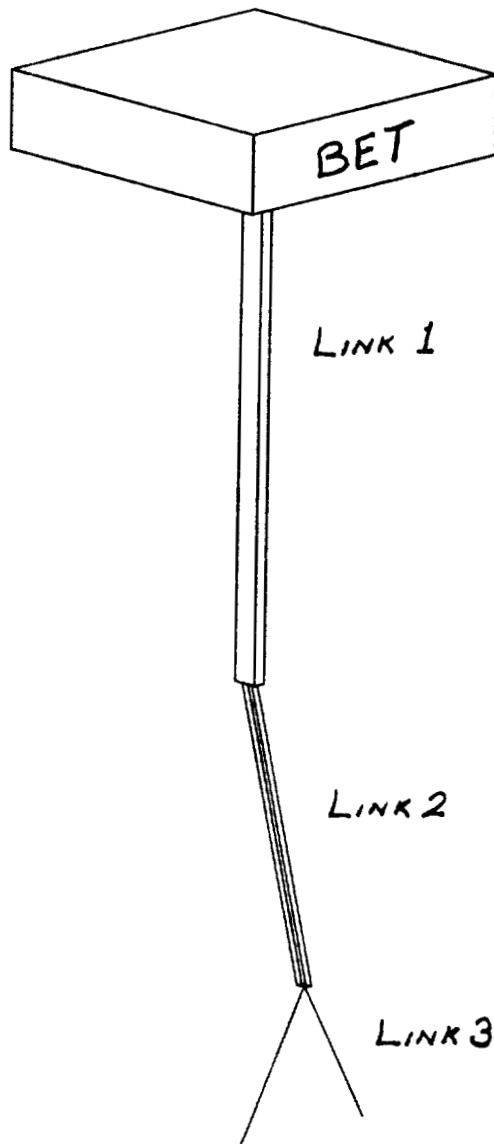


Figure 2. Proposed Flexible Multibody Test Article

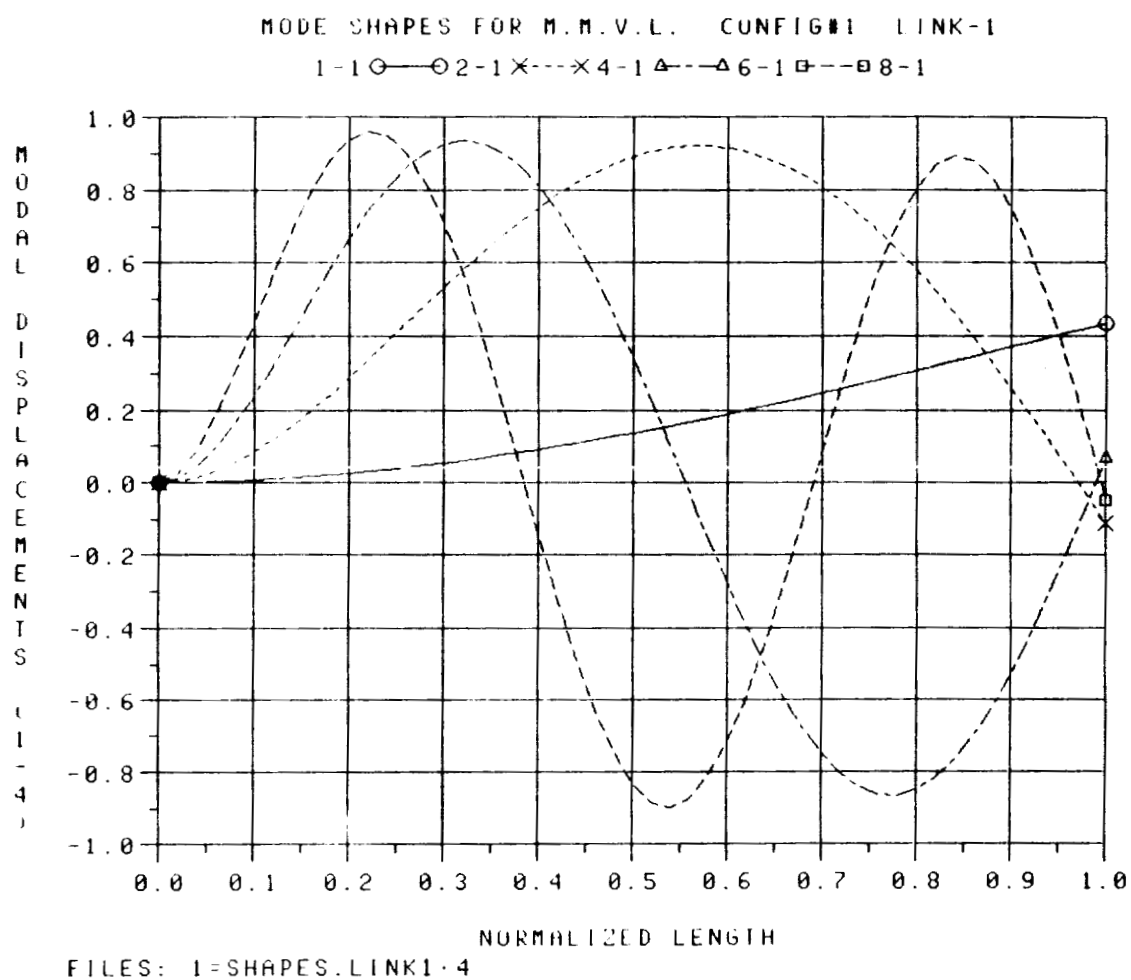


Figure 3. Normalized Mode Shapes for Link One

ORIGINAL PAGE IS
OF POOR QUALITY

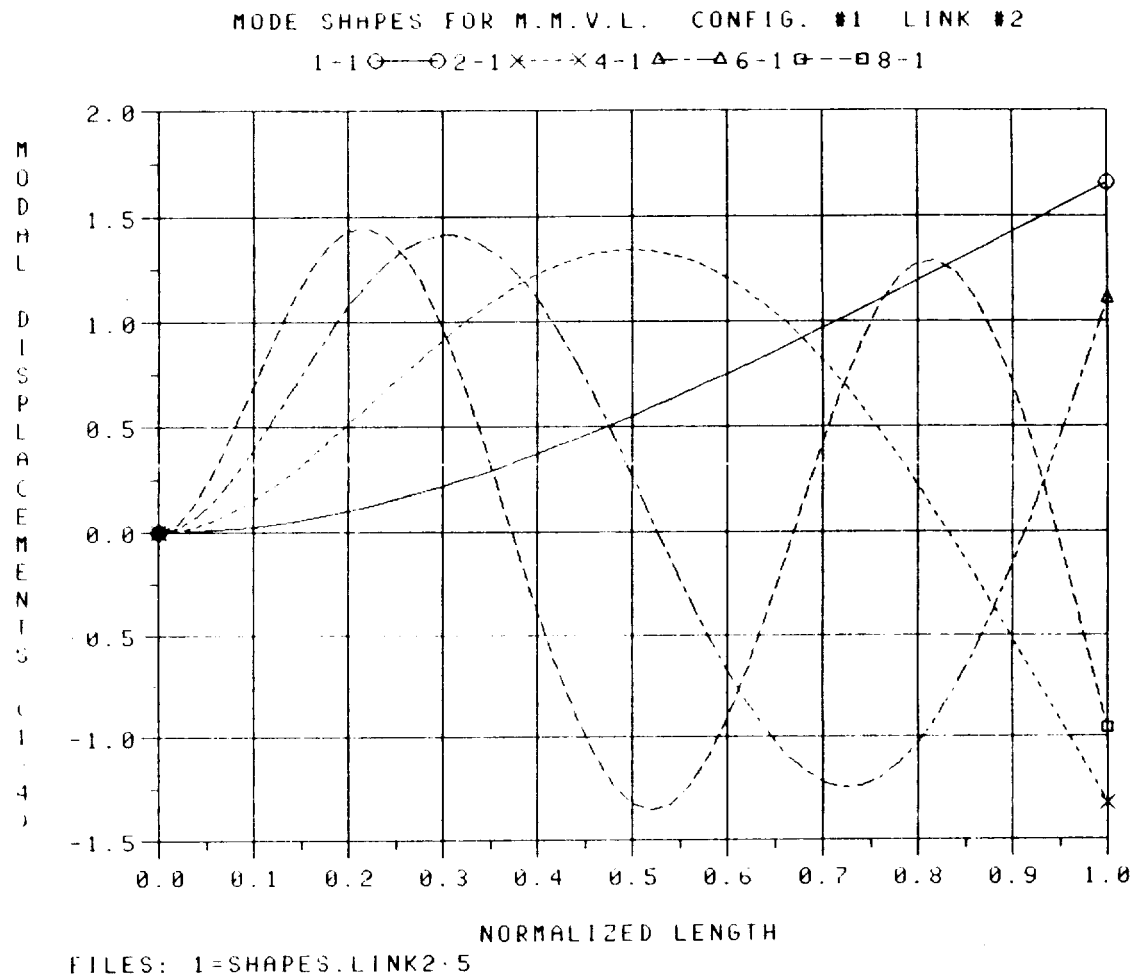


Figure 4. Normalized Mode Shapes for Link Two

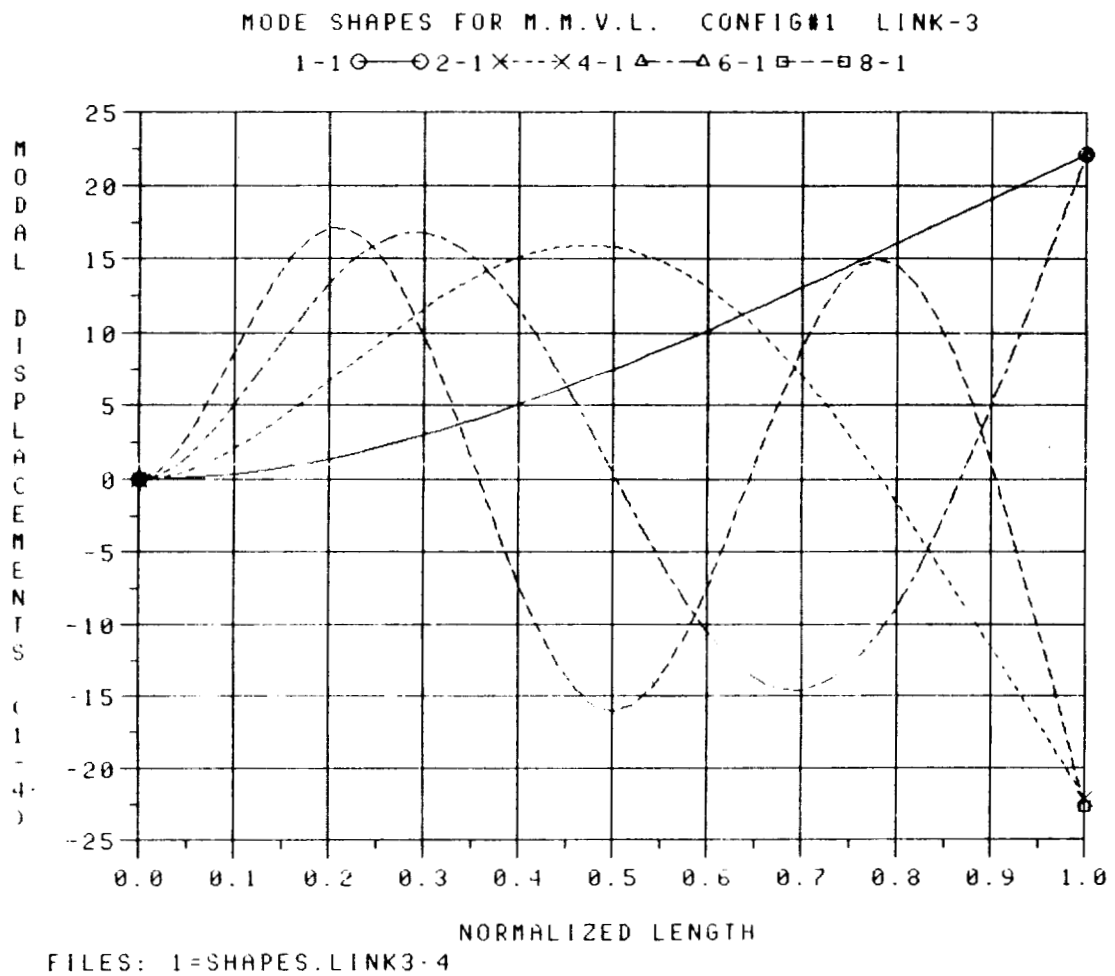


Figure 5. Normalized Mode Shapes for Link Three

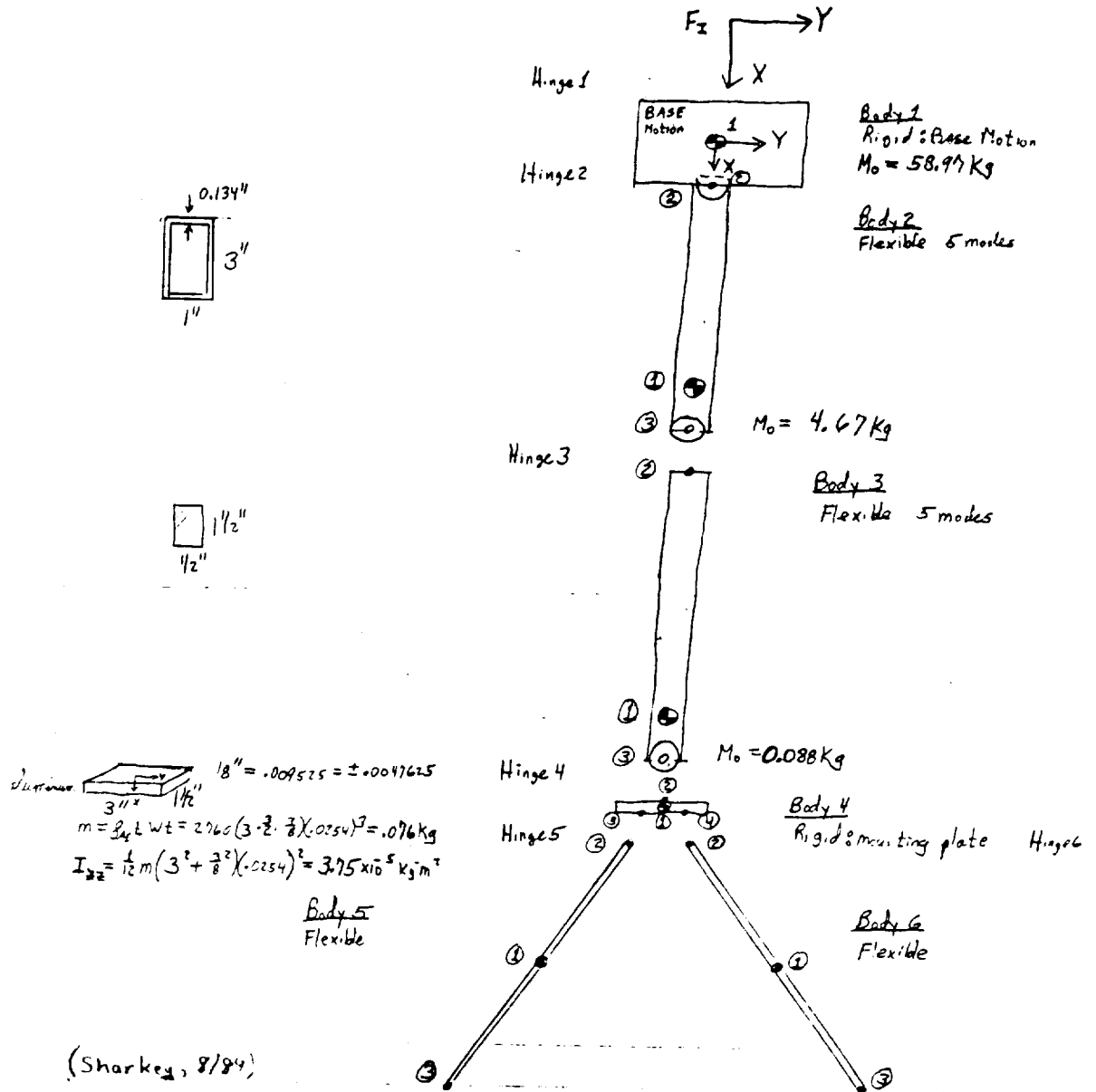


Figure 6. TREETOPS Configuration of Test Article

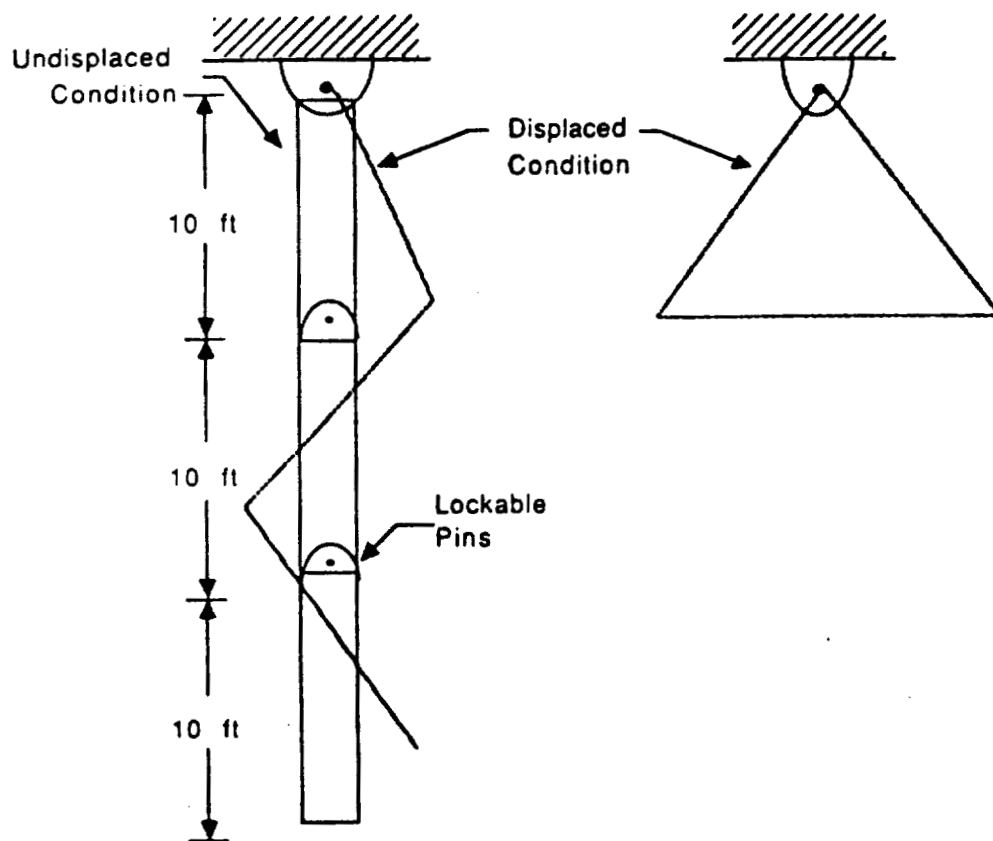


Figure 7. Sample Open and Closed Tree Topologies [1]

ORIGINAL PAGE
BLACK AND WHITE PHOTOGRAPH

ORIGINAL PAGE IS
OF POOR QUALITY

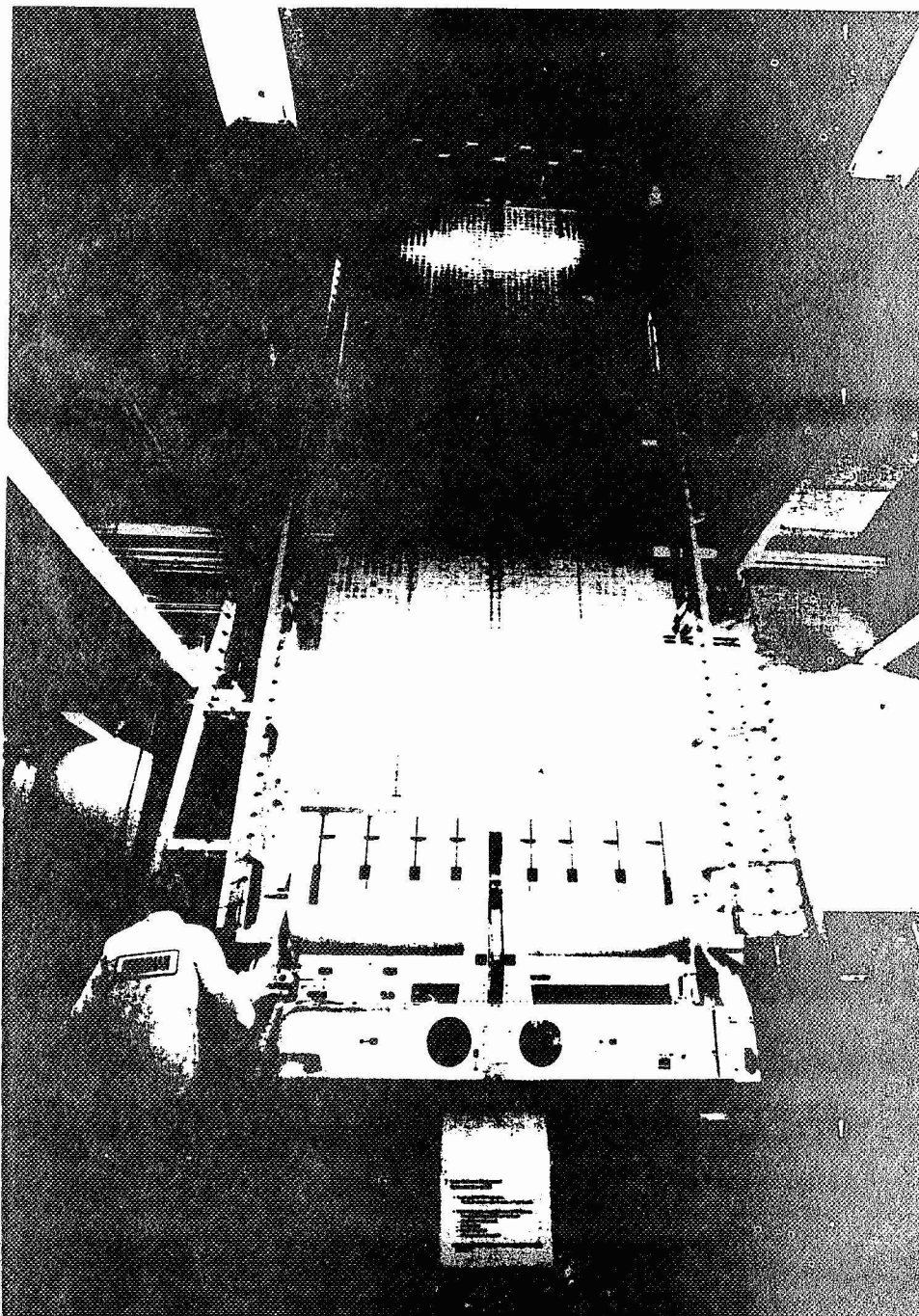


Figure 8. Lens Antenna Deployment Demonstration
(LADD) Hardware

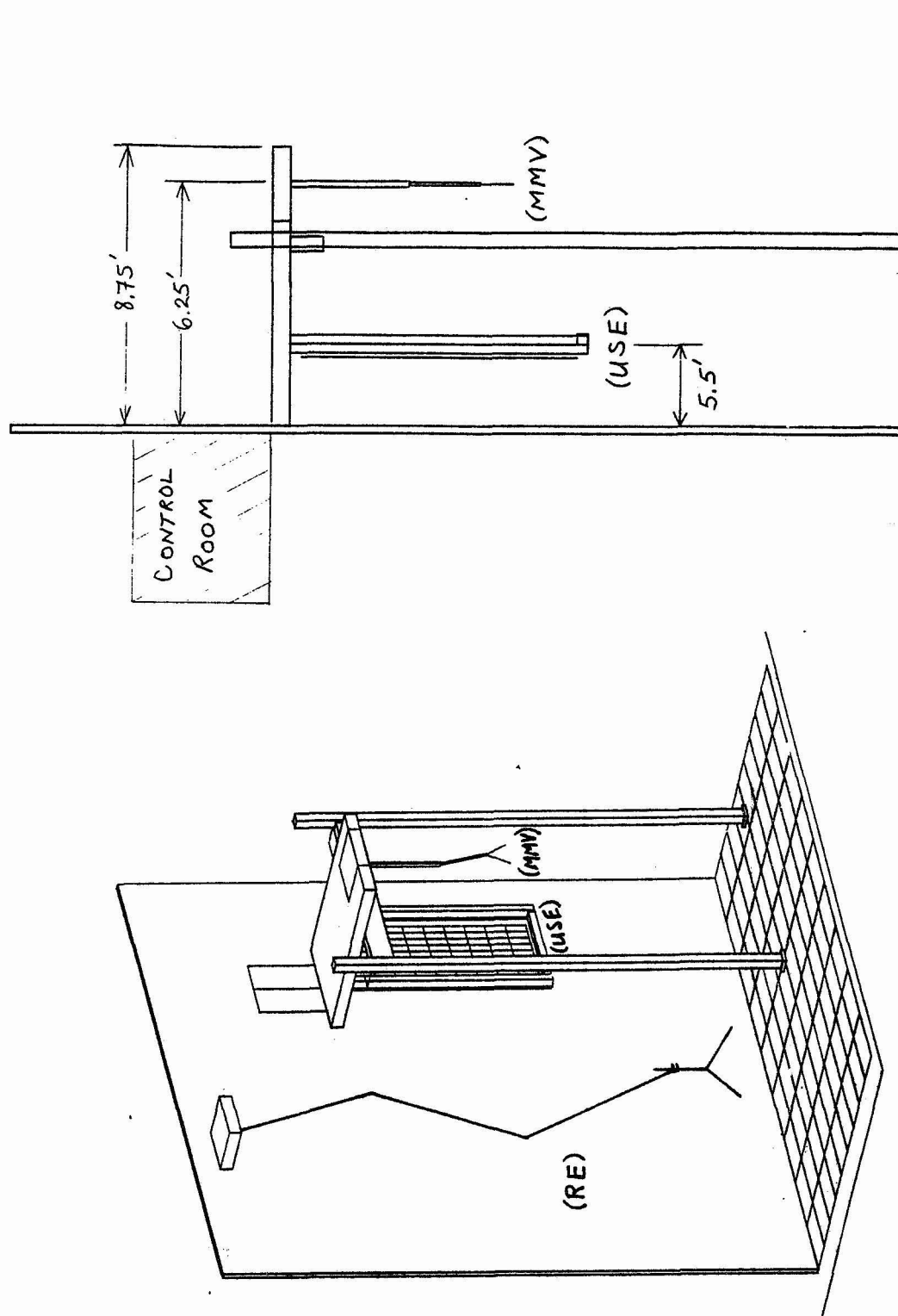


Figure 9. General Facility Layout for MMV, USE and RE

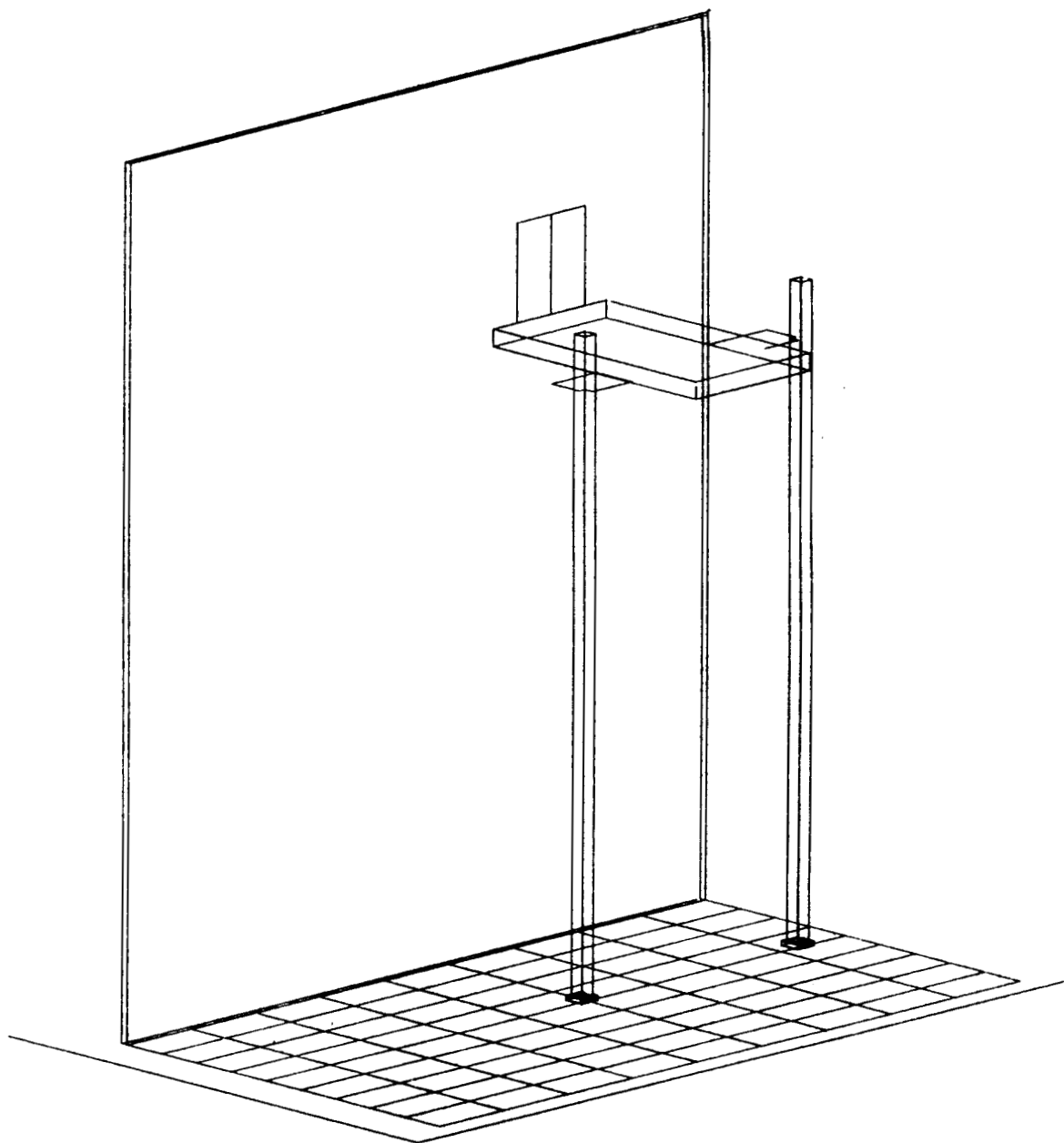


Figure 10. Current Major Structural Layout

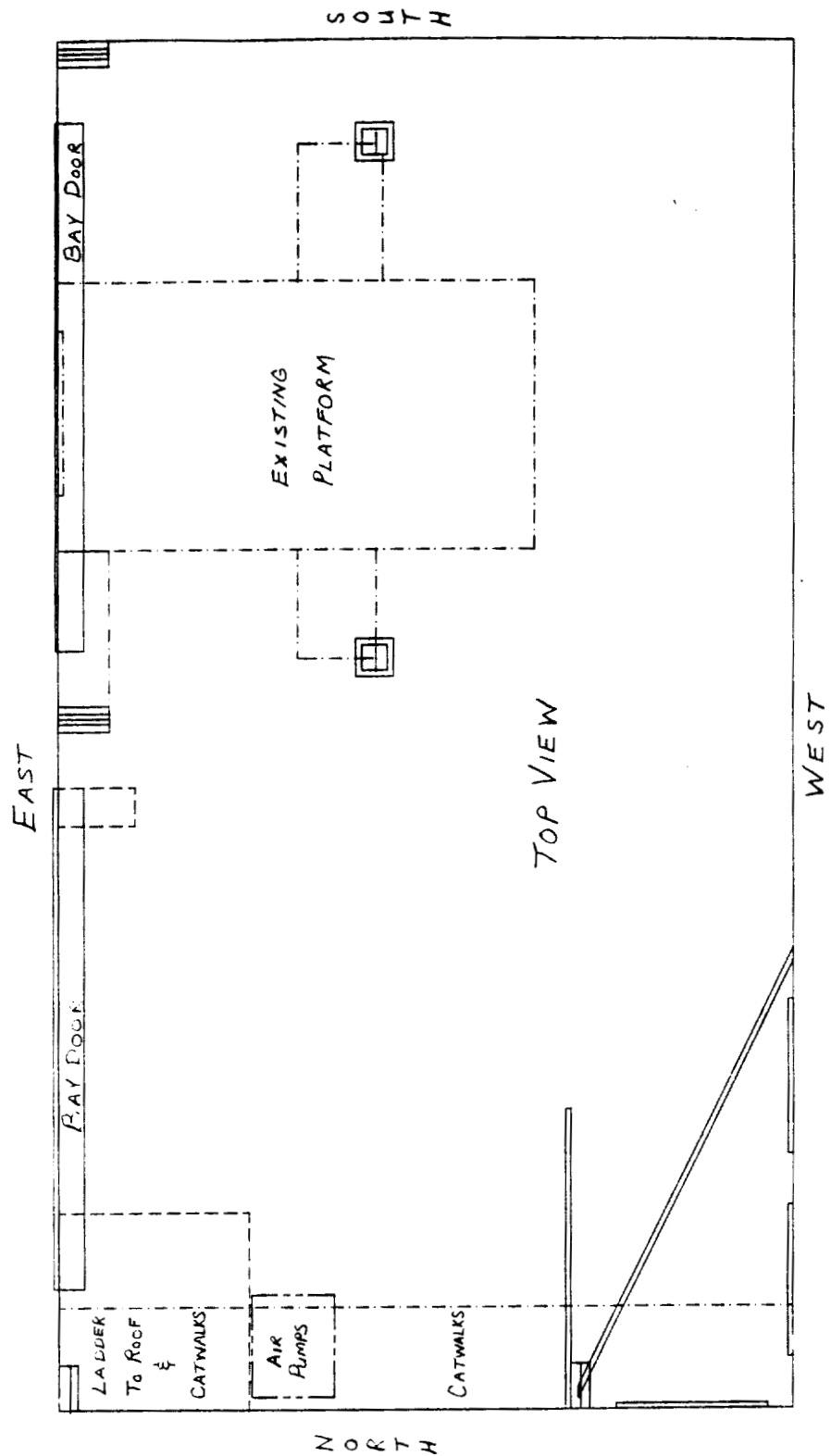


Figure 11. Existing Facility Floor Plan with Unused Air-Handling Units Removed

Architectural floor plan of the RE Laboratory. The plan shows a large rectangular room with various internal divisions and structural features. Key elements include:

- Rooms and Areas:** CONTROL ROOM, USE (10.9' x 2'), EXISTING PLATFORM (10.5' x 18.75'), OPENING FOR BET 5' x 5' CENTERED BY I-BEAM, EXTENSION OF EXISTING PLATFORM FOR MMV, RE LABORATORY, LADDER TO ROOF, CATWALKS (7.75' x 7.5') AREA, AIR PUMPS (REMOVE), CATWALKS (4' x 29') AREA.
- Structural Elements:** I-BEAM 21" x 9", I-BEAM 1' x 1', HAND RAIL, FLAT FLOOR CURTAIN BRACE.
- Dimensions:** 26.5', 10.5', 20.6', 19.6', 11', 10.5', 9.4', 10.5', 10', 6.5', 4', 19.9', 5.1', 3', 10', 3', 4.15', 4', 1.8', 7.5', 3.3', 9', 27', 29'.
- Other Features:** BAY DOOR, DOOR, STAIRS, I-BEAM 21" x 9" (bottom left), I-BEAM 21" x 9" (bottom right).

XXXII-27

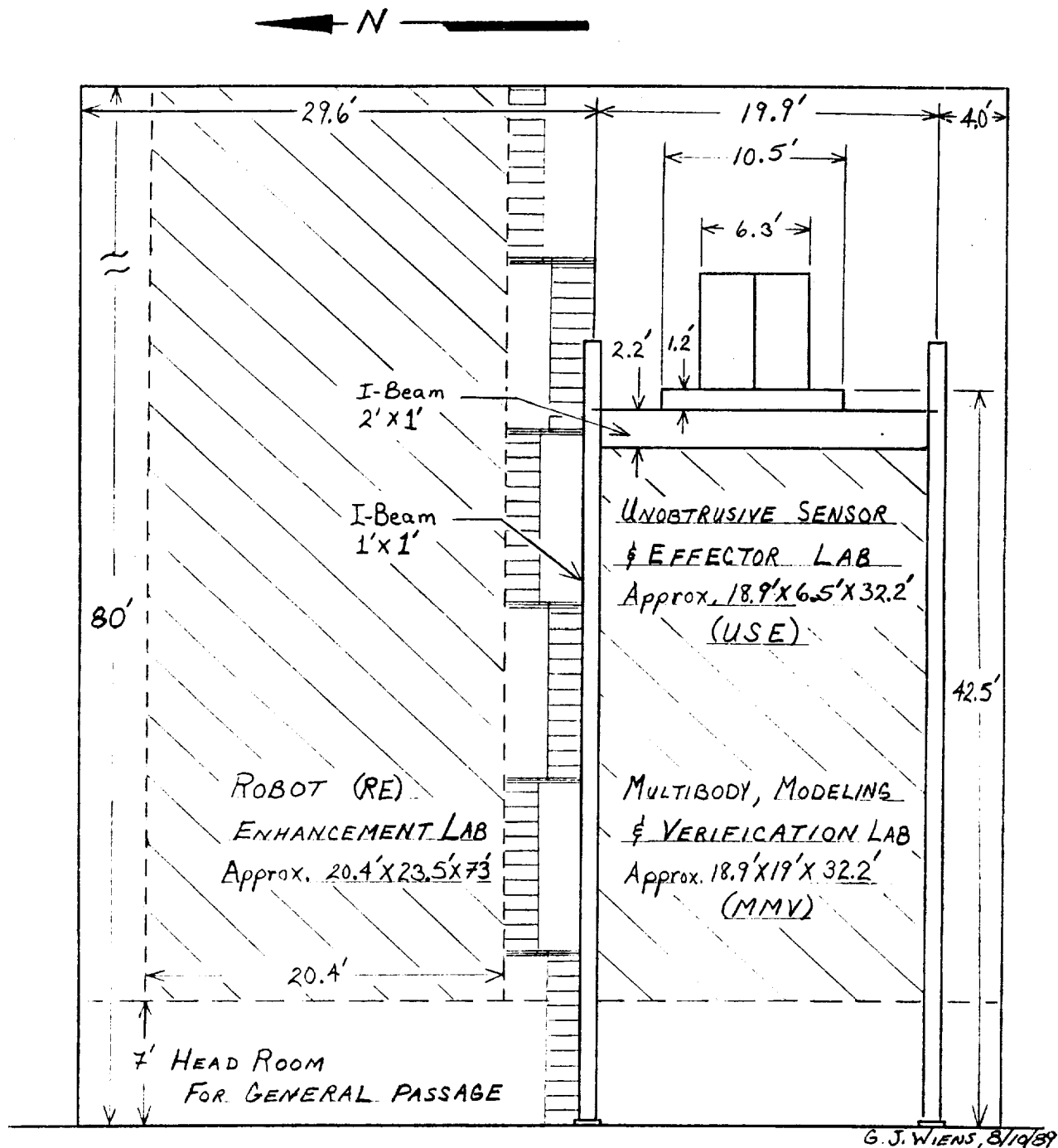


Figure 13. Proposed Facility Layout, West View Facing East

Table 1.

MMV Test Article Material and Physical Properties.

Link	R(cm)	b(cm)	h(cm)	t(cm)	A(m2)	I(m4)
1	-----	7.62	2.54	0.340	6.45e-4	6.69e-8
2	-----	3.81	1.27	-----	4.84e-4	6.50e-9
3	0.127 (each branch)	-----	-----	-----	5.07e-6	2.04e-12

Link	(kg/m3)	E(N/m2)	L(m)	mg(N)	Torquer wt.(N)
1	1.65e3	41.4e9	2.44	25.5	578
2	1.65e3	41.4e9	1.52	11.9	45.8
3	2.11e3 (each branch)	61.0e9	0.762	0.0799	0.862

Material: Link 1 -- Carbon/Carbon Composite
 Link 2 -- Carbon/Carbon Composite
 Link 3 -- Epoxy 70% S-Glass

$$A = b \cdot h \quad \text{or} \quad A = 2 \cdot t \cdot (b + h) - 4 \cdot t \cdot t$$

$$I = b \cdot h \cdot h \cdot h / 12 \quad \text{or} \quad I = [b \cdot h \cdot h \cdot h - (b - 2 \cdot t) \cdot ((h - 2 \cdot t) \cdot (h - 2 \cdot t) \cdot (h - 2 \cdot t))] / 12$$

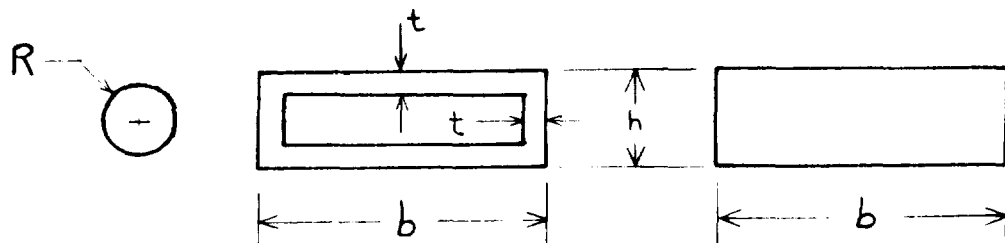


Table 2.

Component Mode Shapes and Frequencies

* LINK 01 NS= 1.7984 KS= 0.00000E+00 IS= 0.00000E+00 TS= 0.00000E+00												
B2FREQ= 1.3637		TMASS= 7.2668										
	MODE FREQ (Hz)	BETA	An	Bn	Cn	Dn	KA	KB	KC	KD	ALPHA	WNODE
1	1.656	1.102	0.5213	-.5478	-.5213	0.5478	0.9516	-1.000	-1.9516	1.000	0.3301	5.717
2	21.69	3.900	0.6186	-.6161	-.6186	0.6161	1.004	-1.000	-1.004	1.000	0.1100	0.4900
3	68.87	7.106	0.6185	-.6186	-.6185	0.6186	0.9999	-1.000	-1.9999	1.000	0.6221E-010	1.553
4	142.9	10.24	0.6355	-.6355	-.6355	0.6355	1.000	-1.000	-1.000	1.000	0.4435E-010	7.660E-01
* LINK02 NS= 0.78321E-01 KS= 0.00000E+00 IS= 0.00000E+00 TS= 0.00000E+00												
B2FREQ= 1.3143		TMASS= 1.2116										
	MODE FREQ (Hz)	BETA	An	Bn	Cn	Dn	KA	KB	KC	KD	ALPHA	WNODE
1	4.829	1.751	0.6750	-.9145	-.6750	0.9145	0.7301	-1.000	-.7301	1.000	0.7150	1.019
2	25.94	4.443	0.9409	-.9251	-.9409	0.9251	1.017	-1.000	-1.017	1.000	0.3928	0.1601
3	73.94	7.500	0.9309	-.9315	-.9309	0.9315	0.9993	-1.000	-1.9993	1.000	0.2302	0.5656E-01
4	146.9	10.57	0.9568	-.9568	-.9568	0.9568	1.000	-1.000	-1.000	1.000	0.1679	0.2925E-01
* LINK03 NS= 0.00000E+00 KS= 0.00000E+00 IS= 0.00000E+00 TS= 0.00000E+00												
B2FREQ= 0.93406		TMASS= 0.81516E-02										
	MODE FREQ (Hz)	BETA	An	Bn	Cn	Dn	KA	KB	KC	KD	ALPHA	WNODE
1	3.287	1.075	0.131	-11.00	-0.131	11.00	0.7341	-1.000	-.7341	1.000	0.672	0.3913E-01
2	20.60	4.694	11.28	-11.00	-11.28	11.00	1.010	-1.000	-1.010	1.000	4.806	0.6244E-02
3	57.60	7.055	11.07	-11.00	-11.07	11.00	0.9992	-1.000	-1.9992	1.000	2.019	0.2231E-02
4	113.0	11.00	11.34	-11.34	-11.34	11.34	1.000	-1.000	-1.000	1.000	2.062	0.1165E-02

[E00]

ORIGINAL PAGE IS
OF POOR QUALITY

Table 3

Displacement Functions

0.000000000000	0.205935594491
0.000000000000	0.000000000000
0.079167004522224	0.01260314320102
0.270024212611220	0.042975688191573
0.202093293470986	0.032164146621629
1.382382799500687	0.207267927942948
0.206526434400293	0.032869702913951
1.294278973489974	0.205990896370834

← 1 → Link 2
← 2 → Link 3
← 3 → Link 3

$$h_{mode} = \int_0^L \rho A x \phi(x) dx + L \phi(L) M_{TIP} ; M_{TIP} = \frac{m_{TIP} \dot{\phi}(L)}{2}$$

$$\phi(x) = A_n \sin \beta_n x + B_n \cos \beta_n x + C_n \sinh \beta_n x + D_n \cosh \beta_n x$$

$$1 = \int_0^L \rho A \phi_n^2(x) dx = \rho A \int_0^L (K_A \sin^2 \beta_n x + K_B \cos^2 \beta_n x + K_C \sinh^2 \beta_n x + K_D \cosh^2 \beta_n x) dx$$

$$A_n = PK_A ; B_n = PK_B ; C_n = PK_C ; D_n = PK_D$$

$$\alpha = \left[\left(\int_0^L \rho A \phi(x) dx + M_{TIP} \phi(L) \right) / \left(\int_0^L \rho A dx + M_{TIP} \right) \right]$$

REFERENCES

1. Waites, H. B., Jones, V. L., and Seltzer, S. M., "Cost Effective Development of a National Test Bed", NASA TM-100321, February 1988.
2. Likins, P. W., "Multibody Dynamics-An Historical Perspective", JPL D-5190, Vol. I, Proc. of the Workshop on Multibody Simulation, April 1988, pp. 10-24.
3. Man, G., Laskin, R. A., and Tolivar, A. F., "Computational Controls for Aerospace Systems", NASA TM-101578, Part One, "Workshop on Computational Aspects in the Control of Flexible Systems", Williamsburg, Virginia, July 1988, pp. 33-48.
4. Oakley, C. M., and Cannon, Jr., R. H., "Initial Experiments on the Control of a Two-Link Manipulator with a Very Flexible Forearm", Proc. of the American Control Conference, June 1988, pp. 996-1002.
5. Crawley, E. F., de Luis, J., and Miller, D. W., "Middeck Active Control Experiment (MACE)", SSL # 7-89, Final Report for NASA Grant NAG-1-915, June 1989.
6. Chace, M. A., and Smith, D. A., "DAMN-A Digital Computer Program for the Dynamic Analysis of Generalized Mechanical Systems", SAE paper 710244, January 1971.
7. Gregory, C. Z. "Reduction of Large Flexible Spacecraft Models Using Internal Balancing Theory", AIAA Paper 83-2292, G&C Conference, Gatlinburg, TN, August 1983.
8. Shabana, A. A., Dynamics of Multibody Systems, John Wiley & Sons, 1989.
9. Craig, Jr., R. R., Structural Dynamics, An Introduction to Computer Methods, John Wiley & Sons, 1981.
10. Craig, R. R., and Bampton, M. C., "Coupling of Substructures for Dynamic Analyses", AIAA Journal, Vol. 6, No. 7, July 1968, pp. 1313-1319.
11. Ho, J. Y., "Direct Path Method for Flexible Multibody Spacecraft Dynamics", Jr. Spacecraft, Vol. 14, No. 2, Feb. 1977, pp. 102-110.
12. Jerkovsky, W., "The Structure of Multibody Dynamics Equations", Jr. Guidance and Control, Vol. 1, No. 3, May/June 1978, pp. 173-182.

13. Singh, R. P., VanderVoort, R. J., and Likins, P. W., "Dynamics of Flexible Bodies in Tree Topology-A Computer Oriented Approach", Proc. of the AIAA Dynamics Specialist Conference, Palm Springs, CA, May 1984, pp. 327-385.
14. Shabana, A. A., "Substructure Synthesis Methods for Dynamic Analysis of Multi-Body Systems", Computers and Structures, Vol. 20, No. 4, 1985, pp. 737-744.
15. Khulief, Y. A., Shabana, A. A., "Dynamics of Multibody Systems with Variable Kinematic Structure", ASME Jr. of Mechanisms, Transmissions, and Automation in Design, Vol. 108, June 1986, pp. 167-175.
16. Fang, L. Y., Shabana, A. A., Agrawal, D. P., "Application of Perturbation Techniques to Flexible Multibody System Dynamics", Computers and Structures, Vol. 27, No. 5, 1987, pp. 631-637.
17. Benfield, W. A., and Hruda, R. F., "Vibration Analysis of Structures by Component Mode Substitution" AIAA Journal, Vol. 9, No. 7, July 1971, pp. 1255-1261.
18. Yoo, W. S., and Haug, E. J., "Dynamics of Flexible Mechanical Systems Using Vibration and Static Correction Modes", ASME Jr. of Mechanisms, Transmissions, and Automation in Design, Vol. 108, Sept. 1986, pp. 315-322.
19. Huckelbridge, A. A., and Lawrence, C., "Identification of Structural Interface Characteristics Using Component Mode Synthesis", ASME Jr. of Vibration, Acoustics, Stress, and Reliability in Design, Vol. 111, April 1989, pp. 140-147.
20. Chang, L.-W., and Gannon, K. K., "A Dynamic Model on a Single-Link Flexible Manipulator", ASME Modal Testing and Analysis, DE-Vol. 3, 1987, pp. 23-28.
21. Padovan, J., and Kazempour, A., "Multibody Instantly Centered Moving Lagrangian Observer Schemes-Part I. Formulation", Computers and Structures, Vol. 32, No. 1, 1989, pp. 93-100.
22. Lee, J. D., and Wang, B.-L., "Dynamic Equations for a Two-Link Flexible Robot Arm", Computers and Structures, Vol. 29, No. 3, 1988, pp. 469-477.
23. Bucher, C. U., "A Modal Synthesis Method Employing Physical Coordinates, Free Component Modes, and Residual Flexibilities", Computers and Structures, Vol. 22, No. 4, 1986, pp. 559-564.

24. Rauh, J., and Schiehlen, W., "Various Approaches for the Modeling of Flexible Robot Arms", Lecture Notes in Engineering: Refined Dynamics Theories of Beams, Plates and Shells and Their Applications, No. 28, Springer-Verlag, 1986, pp. 420-429.
25. Panossian, H. V., "Uncertainty Management in Modeling and Control of Large Flexible Structures", Structural Dynamics Testing and Analysis, SP-596, Aerospace Congress & Exposition, Long Beach, CA, Oct. 1984, pp. 55-58.
26. Kim, S. S., and Vanderploeg, M. J., "A General and Efficient Method for Dynamic Analysis of Mechanical Systems Using Velocity Transformations", ASME Jr. of Mechanisms, Transmissions, and Automation in Design, Vol. 108, June 1986, pp. 176-182.
27. Wittenburg, J., "Dynamics of Multibody Systems - A Brief Review", Acta Astronautica, Vol. 20, 1989, pp. 89-92.
28. Simo, J. C., and Vu-Quoc, L., "On the Dynamics of Flexible Beams Under Large Overall Motions--The Plane Case: Part I & II", ASME Jr. of Applied Mechanics, Vol. 53, Dec. 1986, pp. 849-863.
29. Simo, J. C., and Vu-Quoc, L., "Dynamics of Earth-Orbiting Flexible Satellites with Multibody Components", Jr. Guidance, Vol. 10, No. 6, 1987, pp. 549-558.
30. Li, D., and Likins, P. W., "Dynamics of a Multibody System with Relative Translation on Curved, Flexible Tracks", Jr. Guidance, Vol. 10, No. 3, 1987, pp. 299-306.
31. Thomas, M., and Tesar, D., "Dynamic Modeling of Serial Manipulator Arms", ASME Jr. of Dynamic Systems, Measurement, and Control, Vol. 104, Sept. 1982, pp. 218-228.
32. Engels, R. C., "A Solution to the Craig/Bampton Eigenvalue Problem for Multi-Component Structures", IMAC Proc. of the 3rd International Modal Analysis Conference, Orlando, FL, 1985, Vol. I, pp. 299-304.
33. Amirouche, F. M., and Jia, T., "Modelling of Clearances and Joint Flexibility Effects in Multibody Systems Dynamics", Computers and Structures, Vol. 29, No. 6, 1988, pp. 983-991.
34. Amirouche, F. M., and Jia, T., "Pseudouptriangular Decomposition Method for Constrained Multibody Systems

Using Kane's Equations", Jr. Guidance, Vol. 11, No. 1, 1988, pp. 39-46.

35. Ryan, R. R., "Flexible Multibody Dynamics: Problems and Solutions", JPL D-5190, Vol. I, Proc. of the Workshop on Multibody Simulation, April 1988, pp. 103-190.
36. Banerjee, A. K., and Lemak, M. E., "Large Motion Dynamics of Systems of Rigid Bodies, Beams and Plates", JPL D-5190, Vol. I, Proc. of the Workshop on Multibody Simulation, April 1988, pp. 219-234.
37. Jones, R. E., "Multi Flexbody Dynamics for Control Design", JPL D-5190, Vol. I, Proc. of the Workshop on Multibody Simulation, April 1988, pp. 354-382.
38. Ho, J. Y., "The Direct Path Method for Flexible Multibody Dynamics", JPL D-5190, Vol. I, Proc. of the Workshop on Multibody Simulation, April 1988, pp. 383-417.
39. Huston, R. L., "Redundant and Constrained Multibody Systems: Modelling and Computational Methods", JPL D-5190, Vol. I, Proc. of the Workshop on Multibody Simulation, April 1988, pp. 443-454.
40. Taylor, Jr., L. W., "A Comparison of Software for the Modeling and Control of Flexible Systems", NASA TM-101578, Part One, "Workshop on Computational Aspects in the Control of Flexible Systems", Williamsburg, Virginia, July 1988, pp. 33-48.
41. Steiber, M. E., "Flexible Structure Control Experiments Using a Real-Time Workstation for Computer-Aided Control Engineering", NASA TM-101578, Part One, "Workshop on Computational Aspects in the Control of Flexible Systems", Williamsburg, Virginia, July 1988, pp. 67-88.
42. Shabana, A., "Dynamics of Inertia-Variant Flexible Systems Using Experimentally Identified Parameters", ASME Jr. of Mechanisms, Transmissions, and Automation in Design, Vol. 108, Sept. 1986, pp. 358-366.
43. Oppenheim, I. J., and Shimoyama, I., "Flexible Robot Control: Modeling and Experiments", NASA TM-101578, Part Two, "Workshop on Computational Aspects in the Control of Flexible Systems", Williamsburg, Virginia, July 1988, pp. 549-579.
44. Ulsoy, A. G., "Experimental Validation of Flexible Robot Arm Modeling and Control", NASA TM-101578, Part Two, "Workshop on Computational Aspects in the Control

of Flexible Systems", Williamsburg, Virginia, July 1988, pp. 745-777.

45. Huggins, J. D., Kwon, D.-S., Lee, J. W., and Book, W. J., "Alternative Modeling and Verification Techniques for a Large Flexible Arm", 1987.
46. LaRC CSI Office and Draper Lab, "RMS-Based Controls-Structures Interaction (CSI) Flight Experiment", JSC Briefing, April 1989.
47. Demeo, M., and Turnbull, J., "Remote Manipulator System (RMS)-Based Controls Structures Interaction (CSI) Flight Experiment Feasibility Study", NASA Headquarters Briefing, July 1989.
48. Wang, W.-J., Lu, S.-S., and Hsu, C.-F., "Experiments on the Position Control of a One-Link Flexible Robot Arm", IEEE Trans. on Robotics and Automation, Vol. 5, No. 3, June 1989.
49. Turcic, D. A., Midha, A., and Bosnik, J. R. "Dynamic Analysis of Elastic Mechanism Systems. Part II: Experimental Results", ASME Jr. of Dynamic Systems, Measurement, and Control, Vol. 106, pp. 255-260.
50. Chen, J.-C., Garba, J. A., and Demsetz, L. A., "Verification of Large Space Structures using Scale Modelling Laws", Proc. of the 3rd International Modal Analysis Conference, Orlando, Florida, 1985, Vol. I, pp. 31-36.
51. Niedbal, N., "Experimental System Identification for Experimental/Analytical Correlation and Modelling", ASME AMD-Vol. 67, 1985, pp. 195-204.
52. Hasselman, T. K., and Chrostowski, J. D., "Dynamic Model Verification of a Multi-Component System", "Aerospace Congress & Exposition", Long Beach, CA, Oct. 1984, SP-596, pp. 89-96.
53. Popov, E. P., Mechanics of Materials, Prentice-Hall, 1976.
54. Hill, H., Johnston, D., and Frauenberger, H., "Development of the Lens Antenna Deployment Demonstration (LADD) Shuttle-Attached Flight Experiment", "First NASA/DOD CSI Technology Conference, Nov. 1986, pp. 125-144.

1989

NASA/ASEE SUMMER FACULTY FELLOWSHIP PROGRAM

**MARSHALL SPACE FLIGHT CENTER
THE UNIVERSITY OF ALABAMA IN HUNTSVILLE**

**A VECTORIZED ALGORITHM FOR 3D DYNAMICS OF A TETHERED
SATELLITE**

Prepared by:	Howard B. Wilson
Academic Rank:	Professor
University and Department:	The University of Alabama Department of Engineering Mechanics Tuscaloosa, Alabama
NASA/MSFC Laboratory:	Structures and Dynamics
Division:	Structural Analysis
MSFC Colleague:	Mario Rheinfurth
Date:	August 18, 1989
Contract No.:	The University of Alabama in Huntsville NGT 01-008-021

A VECTORIZED ALGORITHM FOR 3D DYNAMICS OF A TETHERED SATELLITE

by
Howard Wilson
Professor of Engineering Mechanics
The University of Alabama
Tuscaloosa, Alabama

ABSTRACT

Equations of motion characterizing the three dimensional motion of a tethered satellite during the retrieval phase are studied. The mathematical model involves an arbitrary number of point masses connected by weightless cords. Motion occurs in a gravity gradient field. The formulation presented accounts for general functions describing support point motion, rate of tether retrieval, and arbitrary forces applied to the point masses. The matrix oriented program language MATLAB is used to produce an efficient vectorized formulation for a) computing natural frequencies and mode shapes for small oscillations about the static equilibrium configuration; b) for integrating the nonlinear differential equations governing large amplitude motions. An example of time response pertaining to the skip rope effect is investigated.

ACKNOWLEDGEMENTS

I wish to express sincere appreciation to members of the Structures and Dynamics Laboratory Center for allowing me to have the opportunity during the current summer of working in the exciting and intellectually stimulating environment which prevails at Marshall Space Flight Center. I am particularly grateful to Bob Ryan, Mario Rheinfurth and John Admire. The technical guidance, interesting discussions and friendships I have enjoyed with these gentlemen is especially rewarding. Much credit is also deserved by Frank Six, Gerald Karr, and Mike Freeman for so successfully informing participants in the summer fellowship program about the pioneering leadership which NASA continues to foster and about the opportunities existing for involvement in their interesting research activities.

INTRODUCTION AND OBJECTIVES

Tethered satellites employed in space vehicles have many important practical applications. The time response occurring during the retrieval phase is of special interest since this motion can sometimes become unstable as the tether length is reduced to zero. One type of motion currently being studied is known as the skiprope mode. In this configuration a satellite is initially positioned on the line from the orbiter to the earth center (z-axis) and the tether is spinning about this axis in a sinusoidal curve resembling the deflection pattern of a skyrope. Some disagreement currently exists among analysts regarding the dynamics which occurs during retrieval. The author's efforts were directed toward developing a concise computer formulation to facilitate a response analysis in this problem.

NONLINEAR EQUATIONS FOR LARGE AMPLITUDE MOTIONS

Consider a tether model described as a series of point masses connected by weightless cords assumed to remain in tension throughout the motion. The geometry is shown in Figure 1. The vector from mass m_{j+1} to m_j is denoted by r_j . Thus

$$r_j = l_j \hat{e}_j(\theta_j, \varphi_j) \quad (1)$$

where l_j denotes the vector length and (θ_j, φ_j) are spherical coordinate angles for unit vectors \hat{e}_j which specify the member directions. We will assume that l_j are known functions of time. This allows for treatment of the tether retrieval problem during an interval over which l_n is reduced to zero at a specified rate. Once a particular link has been completely retrieved, the problem dimensionality can be reduced by one and the retrieval process can be continued.

The equations of motion can be integrated numerically when $\ddot{\theta}$ and $\ddot{\varphi}$ values are known for each link. The numerical procedure below is as follows.

1. For known $\theta, \varphi, \dot{\theta}$ and $\dot{\varphi}$ values, link tensions are computed and these are used to compute global accelerations
2. The global accelerations are used to compute \ddot{r} for each link.
3. The \ddot{r} values are used to compute $\ddot{\theta}$ and $\ddot{\varphi}$ values.

For convenient reference let us call the tether section between m_{i+1} and m_i as link i . The tension force in link i is representable as

$$T_i = \alpha_i r_i \quad (2)$$

where α_i is a scalar multiplier. A free body diagram of m_i is shown in Figure 2. The force F_i describes the effects of external loads such as gravity, aerodynamic drag, and electromagnetic phenomena. The position of mass i in a rotating reference frame tangent to the circular orbit is

$$R_i = \sum_{j=i}^n r_j + R_{n+1}, \quad i \leq n \quad (3)$$

The length of link i can be computed from

$$l_i^2 = r_i \cdot r_i = (R_{i+1} - R_i) \cdot (R_{i+1} - R_i) \quad (4)$$

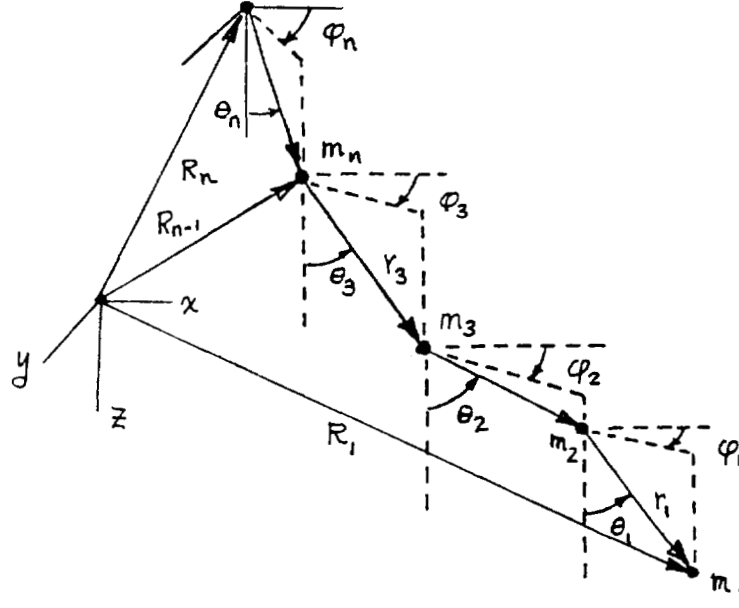


Figure 1: General Tether Configuration

Differentiation of this constraint gives

$$l_i \dot{l}_i = (R_{i+1} - R_i) \cdot (\dot{R}_{i+1} - \dot{R}_i) \quad (5)$$

and

$$\dot{l}_i^2 + l_i \ddot{l}_i = (R_{i+1} - R_i) \cdot (\ddot{R}_{i+1} - \ddot{R}_i) + (\dot{R}_{i+1} - \dot{R}_i) \cdot (\dot{R}_{i+1} - \dot{R}_i) \quad (6)$$

which is equivalent to

$$\dot{l}_i^2 + l_i \ddot{l}_i = -r_i \cdot (\ddot{R}_{i+1} - \ddot{R}_i) + \dot{r}_i \cdot \dot{r}_i \quad (7)$$

When a link has constant length then the constraint simplifies to

$$r_i \cdot (\ddot{R}_{i+1} - \ddot{R}_i) = \dot{r}_i \cdot \dot{r}_i \quad (8)$$

We write

$$r_i = l_i \hat{e}_i(\theta_i, \varphi_i) \quad (9)$$

so

$$\dot{r}_i = \dot{l}_i \hat{e}_i + l_i \left(\frac{\partial \hat{e}_i}{\partial \theta_i} \dot{\theta}_i + \frac{\partial \hat{e}_i}{\partial \varphi_i} \dot{\varphi}_i \right) = \dot{l}_i \hat{e}_i + l_i (\hat{e}_{i\theta} \dot{\theta}_i + \hat{e}_{i\varphi} \dot{\varphi}_i) \quad (10)$$

For the coordinate system of interest $\hat{e}_i, \hat{e}_{i\varphi}$ and $\hat{e}_{i\theta}$ form an orthogonal (but not orthonormal triad). Then

$$\dot{r}_i \cdot \dot{r}_i = |\dot{l}_i \hat{e}_i + l_i(\dot{\hat{e}}_{i\theta} \dot{\theta}_i + \dot{\hat{e}}_{i\varphi} \dot{\varphi}_i)|^2 \quad (11)$$

$$= \dot{l}_i^2 + l_i^2(|\dot{\hat{e}}_{i\theta}|^2 \dot{\theta}_i^2 + |\dot{\hat{e}}_{i\varphi}|^2 \dot{\varphi}_i^2) \quad (12)$$

So

$$l_i \ddot{l}_i = l_i^2 (|\dot{\hat{e}}_{i\theta}|^2 \ddot{\theta}_i^2 + |\dot{\hat{e}}_{i\varphi}|^2 \ddot{\varphi}_i^2) - r_i \cdot (\ddot{R}_{i+1} - \ddot{R}_i) \quad (13)$$

$$- r_i \cdot (\ddot{R}_{i+1} - \ddot{R}_i) = l_i \ddot{l}_i - l_i^2 (|\dot{\hat{e}}_{i\theta}|^2 \ddot{\theta}_i^2 + |\dot{\hat{e}}_{i\varphi}|^2 \ddot{\varphi}_i^2) = p_i \quad (14)$$

The Newtonian equation of motion for a typical mass implies

$$\ddot{R}_i = \frac{1}{m_i} [F_i + \alpha_{i-1} r_{i-1} - \alpha_i r_i] \quad (15)$$

so the constraint equation leads to the following relation among link tensions

$$r_i \cdot \left(\frac{1}{m_{i+1}} [F_{i+1} + \alpha_i r_i - \alpha_{i+1} r_{i+1}] - \frac{1}{m_i} [F_i + \alpha_{i-1} r_{i-1} - \alpha_i r_i] \right) = -p_i \quad (16)$$

$$\begin{aligned} -\frac{1}{m_i} (r_{i-1} \cdot r_i) \alpha_{i-1} + \left(\frac{1}{m_i} + \frac{1}{m_{i+1}} \right) l_i^2 \alpha_i - \frac{1}{m_{i+1}} (r_i \cdot r_{i+1}) \alpha_{i+1} = p_i \\ + r_i \cdot [F_i/m_i - F_{i+1}/m_{i+1}] \end{aligned} \quad (17)$$

Solution of this tridiagonal system determines the member tensions which can be used to compute global accelerations \ddot{R}_i . These global accelerations allow computation of

$$\ddot{r}_i = -(\ddot{R}_{i+1} - \ddot{R}_i) \quad (18)$$

Since $r_i = l_i \hat{e}_i$, we have

$$\dot{r}_i = \dot{l}_i \hat{e}_i + l_i(\dot{\hat{e}}_{i\theta} \dot{\theta}_i + \dot{\hat{e}}_{i\varphi} \dot{\varphi}_i) \quad (19)$$

$$\begin{aligned} \ddot{r}_i = \ddot{l}_i \hat{e}_i + 2\dot{l}_i(\dot{\hat{e}}_{i\theta} \dot{\theta}_i + \dot{\hat{e}}_{i\varphi} \dot{\varphi}_i) \\ + l_i(\ddot{\hat{e}}_{i\theta} \dot{\theta}_i + \dot{\hat{e}}_{i\varphi} \ddot{\varphi}_i + \ddot{\hat{e}}_{i\theta\theta} \dot{\theta}_i^2 + \ddot{\hat{e}}_{i\varphi\varphi} \dot{\varphi}_i^2 + 2\ddot{\hat{e}}_{i\theta\varphi} \dot{\varphi}_i \dot{\theta}_i) \end{aligned} \quad (20)$$

The last equation can be rearranged as

$$\ddot{r}_i = \ddot{l}_i \hat{e}_i + l_i \ddot{\hat{e}}_{i\theta} \dot{\theta}_i + l_i \ddot{\hat{e}}_{i\varphi} \dot{\varphi}_i + q_i \quad (21)$$

Since the coordinate system of interest satisfies the orthogonality condition

$$\hat{e}_i \cdot \hat{e}_{i\theta} = \hat{e}_i \cdot \hat{e}_{i\varphi} = \hat{e}_{i\theta} \cdot \hat{e}_{i\varphi} = 0 \quad (22)$$

then

$$(\ddot{r}_i - q_i) \cdot \hat{e}_{i\theta} = \ddot{\theta}_i l_i |\hat{e}_{i\theta}|^2 \quad (23)$$

implies

$$\ddot{\theta}_i = (\ddot{r}_i - q_i) \cdot \hat{e}_{i\theta} / (l_i |\hat{e}_{i\theta}|^2). \quad (24)$$

Similarly

$$(\ddot{r}_i - q_i) \cdot \hat{e}_{i\varphi} = \ddot{\varphi}_i l_i |\hat{e}_{i\varphi}|^2 \quad (25)$$

implies

$$\ddot{\varphi}_i = (\ddot{r}_i - q_i) \cdot \hat{e}_{i\varphi} / (l_i |\hat{e}_{i\varphi}|^2). \quad (26)$$

These relations form the basis for assembling the equations of motion. The coordinate reference frame used in the present study assumes a coordinate transformation of the form

$$r = (x, y, z) = l (\sin(\theta) \cos(\varphi), \sin(\theta) \sin(\varphi), \cos(\theta))$$

which leads to $|\hat{e}_{i\theta}| = 1$ and $|\hat{e}_{i\varphi}| = \sin(\theta)$. A set of $(l_i, \theta_i, \varphi_i)$ values defines the configuration of link i . The values of l_i are constant except for $i = n$, in which case, the time dependence of l_n , \dot{l}_n and \ddot{l}_n are specified by the chosen retrieval rate equation.

FORCE EFFECTS IN THE GRAVITY GRADIENT FIELD

We are interested in the dynamics of a tether attached to an orbiter moving about the earth with constant angular speed ω_0 in a circular orbit of radius ρ_0 . A balance of gravitational and centrifugal force requires an orbital speed $\omega_0 = \sqrt{g\rho_E^2/\rho_0^3}$ where ρ_E denotes the radius of the earth. The motion of objects moving relative to the satellite are appropriately referred to a frame which rotates with constant angular velocity about the earth center. The coordinate frame is positioned such that \hat{i} is pointed tangent to the orbit in the direction of motion, \hat{k} is directed toward the center of the earth, and \hat{j} is defined as $\hat{k} \times \hat{i}$ to give a right-handed system. Then the angular velocity of the satellite frame is $-\hat{k}\omega_0$ and the position of a generic point on the tether is

$$r = \hat{i} x_0 + \hat{j} y_0 + \hat{k} z_0 \quad (27)$$

The total acceleration of a point referred to the rotating axes is

$$a = \ddot{R}_0 + \dot{\omega} \times r + \omega \times (\omega \times r) + 2\omega \times \dot{r} + \ddot{r} \quad (28)$$

where R_0 is a vector from the earth center to the origin of the rotating frame, and \dot{r} and \ddot{r} are velocity and acceleration vectors measured in the rotating frame. The total acceleration of point (x_0, y_0, z) is therefore

$$a = (\hat{i} \ddot{x}_0 + \hat{j} \ddot{y}_0 + \hat{k} \ddot{z}_0) + \hat{i}(\omega_0^2 x_0 - 2\omega_0 \dot{z}_0) + \hat{k}(\omega_0^2(\rho_0 - z_0) + 2\omega_0 \dot{x}_0) \quad (29)$$

The gravitational force on a particle of mass m is $F_g = mg \rho_E^2 R/|R|^3$ where $R = -\hat{i} x_0 - \hat{j} y_0 + \hat{k} (\rho_0 - z_0)$. It is helpful to express F_g in a power series and neglect terms of order ρ_0^{-2} . The binomial theorem gives

$$F_g = m\omega_0^2 \left[-\hat{i} x_0 - \hat{j} y_0 + \hat{k}(\rho_0 - z_0) \right] \left[\left(1 + \frac{3z_0}{\rho_0}\right) + 0 (\rho_0^{-2}) \right] \quad (30)$$

When $0(\rho_0^{-2})$ is neglected in the last equation, it is found that a particle subjected to gravity loading and an additional force $\hat{i} F_x + \hat{j} F_y + \hat{k} F_z$ satisfies

$$\begin{aligned} m \left[\hat{i} \ddot{x}_0 + \hat{j} \ddot{y}_0 + \hat{k} \ddot{z}_0 \right] &= \hat{i} F_x + \hat{j} F_y + \hat{k} F_z + m \hat{i} (2\omega_0 \dot{z}_0) \\ &+ m \hat{j} (-\omega_0^2 y_0) + m \hat{k} (3\omega_0^2 z_0 - 2\omega_0 \dot{x}_0) \end{aligned} \quad (31)$$

This equation provides useful information regarding feasible two-dimensional states of motion in either the orbit plane (\hat{i}, \hat{k}) or the plane transverse to the orbit plane (\hat{j}, \hat{k}) . It is possible to have $y_0 = 0$, $F_y = 0$, and all other quantities dependent only on the x_0 and z_0 coordinates. However, if we assume that $F_x = 0$ and $x_0 = 0$,

then the gyroscopic term $\dot{\omega}_0 z_0$ produces an acceleration in the x_0 direction. Consequently, pure motion in the y, z plane is not possible unless \dot{z}_0 is negligible. This circumstance can occur when a tether, initially in static equilibrium along the z axis, is given a small perturbation in the yz plane. Then the motion component for the axial direction is of second order magnitude in comparison to the transverse components. The linearized problem for small transverse motions from static equilibrium is worth further discussion.

TETHER MOTION FOR SMALL PERTURBATION ABOUT THE Z-AXIS

The problem for motion of a tether experiencing small oscillations about the z-direction in the orbital plane were previously investigated by M. Rheinfurth and Z. Galaboff [2]. This paper showed that the static tension for extension along the z-axis is

$$T = \frac{3}{2} M_T \omega_0^2 \ell (\alpha + 1 - (\frac{z}{\ell})^2) \quad (32)$$

where M_T is the mass of a tether having length ℓ and a mass M_s attached at the free end. The parameter α equals $2M_s/M_T$. For small transverse oscillations, the static tension will not change substantially and motion in the z-direction will be negligible. It is useful to employ dimensionless coordinates according to $\xi = z/\ell$ and $\tau = \omega_0 t$. Following the analysis of Rheinfurth and Galaboff, the linearized equations of motion accounting for both in-plane and out-of-plane motion are

$$1.5 \frac{\partial}{\partial \xi} \left[(\alpha + 1 - \xi^2) \frac{\partial x}{\partial \xi} \right] = \frac{\partial^2 x}{\partial \tau^2} \quad (33)$$

$$1.5 \frac{\partial}{\partial \xi} \left[(\alpha + 1 - \xi^2) \frac{\partial y}{\partial \xi} \right] - y = \frac{\partial^2 y}{\partial \tau^2} \quad (34)$$

The boundary conditions at $\xi = 0$ are $x = y = 0$. Force balance conditions on the end mass M_s gives

$$-3 \frac{\partial x}{\partial \xi} = \frac{\partial^2 x}{\partial \tau^2} \quad (35)$$

$$-3 \frac{\partial y}{\partial \xi} - y = \frac{\partial^2 y}{\partial \tau^2} \quad (36)$$

Assuming modal forms $X = X(\xi) \sin(\omega \tau)$ and $y = Y(\xi) \sin(\omega \tau)$ leads to

$$1.5 \frac{d}{d\xi} \left[(\alpha + 1 - \xi^2) \frac{dX}{d\xi} \right] + \omega^2 X = 0 \quad (37)$$

$$1.5 \frac{d}{d\xi} \left[(\alpha + 1 - \xi^2) \frac{dY}{d\xi} \right] + (\omega^2 - 1)Y = 0 \quad (38)$$

with corresponding boundary conditions of

$$X(0) = 0, \quad 3X'(1) + \omega^2 X(1) = 0 \quad (39)$$

$$Y(0) = 0, \quad 3Y'(1) + (\omega^2 - 1)Y(1) = 0 \quad (40)$$

It shows from the above equations that the modal functions for in-plane and out-of-plane motion are identical and a frequency ω_x for the in-plane motion also corresponds to an out-of-plane frequency

$$\omega_y = \sqrt{\omega_x^2 + 1} \quad (41)$$

Reference [2] treated the problem of in-plane motion in considerable detail and gave an exact solution for the case where $M_s = 0$, ($\alpha = 0$). In that case, the exact dimensionless frequencies and modal functions are

$$\omega_{kx} = \sqrt{6k(k-1)}, \quad k = 1, 2, 3, \dots \quad (42)$$

$$X_k(\xi) = P_{2k-1}(\xi), \quad 0 \leq \xi \leq 1 \quad (43)$$

where ω_{kx} means the k 'th in-plane frequency and P_{2k-1} is the Legendre polynomial of degree $2k-1$. Rheinfurth and Galaboff showed that the first frequency equals $\sqrt{3}$ and this modal function is a straight line even for the case of a variable mass distribution. The general Rayleigh quotient formula from [2] expressed in dimensionless form is

$$\omega_{kx}^2 = \left[3 \int_0^1 (\alpha + 1 - \xi^2) [X'_k(\xi)]^2 d\xi \right] / \left[\alpha X_k^2(1) + 2 \int_0^1 X_k^2(\xi) d\xi \right] \quad (44)$$

when $M_s/M_T > 1$ and $n \geq 3$, the mode shapes are closely approximated by

$$X_n(\xi) \approx \sin [\pi(n-1)\xi] \quad (45)$$

so the Rayleigh quotient gives

$$\omega_{kx} \approx \pi(n-1) \sqrt{1 + 3M_s/M_T} \quad (46)$$

This formula is accurate within about 4% for $n \geq 3$ and $M_s/M_T > 1$.

A concise algorithm to compute frequencies and mode shapes for the general case can be obtained by employing PC-MATLAB [3] and finite differences as a formulation equivalent to that used in [1]. We want to solve

$$\frac{d}{d\xi} [(1 + \alpha - \xi^2) X'(\xi)] = -\lambda X(\xi) \quad \text{for } \alpha = 2M_s/M_T \text{ and } 0 \leq \xi \leq 1 \quad (47)$$

The boundary conditions are

$$X(0) = 0 \quad \text{and} \quad 2X'(1) = \lambda X(1) \quad (48)$$

This corresponds to a modal solution of the form

$$X(\xi, t) = X(\xi) \sin (\omega_0 \sqrt{1.5\lambda} t) \quad (49)$$

To express this problem in difference form we take

$$D = 1/N, \quad z_j = j D, \quad 0 \leq j \leq N \quad (50)$$

The boundary conditions are specified as

$$X_0 = 0, \quad (X_{N-2} - 4X_{N-1} + 3X_N)D^{-1} = \lambda X_N \quad (51)$$

and the differential equation becomes

$$\left[j^2 - (1 + \alpha)D^{-2} \right] [X_{j-1} - 2X_j + X_{j+1}] + j[X_{j+1} - X_j] = \lambda X_j, \quad 2 \leq j \leq N-1. \quad (52)$$

This gives an eigenvalue problem $AX = \lambda X$ which is solvable using linear algebra operators in MATLAB. Figure 2 shows a function *tetfrg* which determines frequencies and mode shapes. The figure also lists dimensionless in-plane frequencies for several combinations of mass ratio. Computations were made using $npts = 50$. The first four modal vectors for $M_s/M_T = 0.5$ are also shown in Figure 3.

MATLAB FUNCTION TO COMPUTE TETHER INPLANE FREQUENCIES

```
function [frqs,modevecs] = tetfrq(npts,msatovmtet)
% [frqs,modevecs] = tetfrq(npts,msatovmtet)
% Frequencies and modal vectors for a tether with an
% end mass attached in a gravity gradient field.
%   npts           number of segments into which the tether
%                   length is divided for finite difference
%                   approximation
%   msatomtet       sub-satellite mass divided by the
%                   tether mass
%   frqs            frequencies for transverse planar motion
%                   divided by the circular orbit frequency
%
% Technical reference: Mario H. Rheinfurth and Zachary
% J. Galaboff "Modal Analysis of a Nonuniform String
% With End Mass and Variable Tension", NASA Technical
% Paper 2198, August 1983
%
%   written by Howard Wilson, July 1989
%
a = zeros(npts,npts); d = 1/npts; b = (2*msatovmtet+1)/d^2;
a(1,1) = 2*(b-1); a(1,2) = -b; a(npts,npts-2) = 1/d;
a(npts,npts-1) = -4/d; a(npts,npts) = 3/d;
for j = 2:npts-1, a(j,j-1) = j*(j-1)-b;
    a(j,j) = 2*(b-j*j); a(j,j+1) = j*(j+1)-b;
end
[modevecs,frqs] = eig(a);
[frqs,id] = sort(sqrt(1.5*diag(frqs)));
modevecs = modevecs(:,id);
modevecs = [zeros(1,npts);modevecs];
```

TETHER INPLANE CIRCULAR FREQUENCY DIVIDED BY ORBIT ANGULAR SPEED

	Ratio of (Subsatellite Mass)/(Tether Mass)						
freq nmbr	0	0.5000	1.0000	1.5000	2.0000	2.5000	3.0000
1	1.7320	1.7320	1.7320	1.7320	1.7320	1.7320	1.7320
2	4.2425	5.5159	6.7081	7.7274	8.6294	9.4466	10.1990
3	6.7066	10.1300	12.7360	14.8847	16.7576	18.4400	19.9807
4	9.1551	14.9072	18.8904	22.1464	24.9748	27.5111	29.8311
5	11.5785	19.7213	25.0646	29.4180	33.1951	36.5799	39.6749
6	13.9503	24.5373	31.2296	36.6735	41.3939	45.6228	49.4888
7	16.2319	29.3394	37.3715	43.8992	49.5574	54.6256	59.2585
8	18.4152	34.1181	43.4807	51.0851	57.6751	63.5773	68.9722
9	20.5863	38.8659	49.5493	58.2226	65.7377	72.4680	78.6194
10	22.8428	43.5767	55.5703	65.3038	73.7366	81.2882	88.1900

Figure 2: Natural Frequency Analysis

ORIGINAL PAGE IS
OF POOR QUALITY

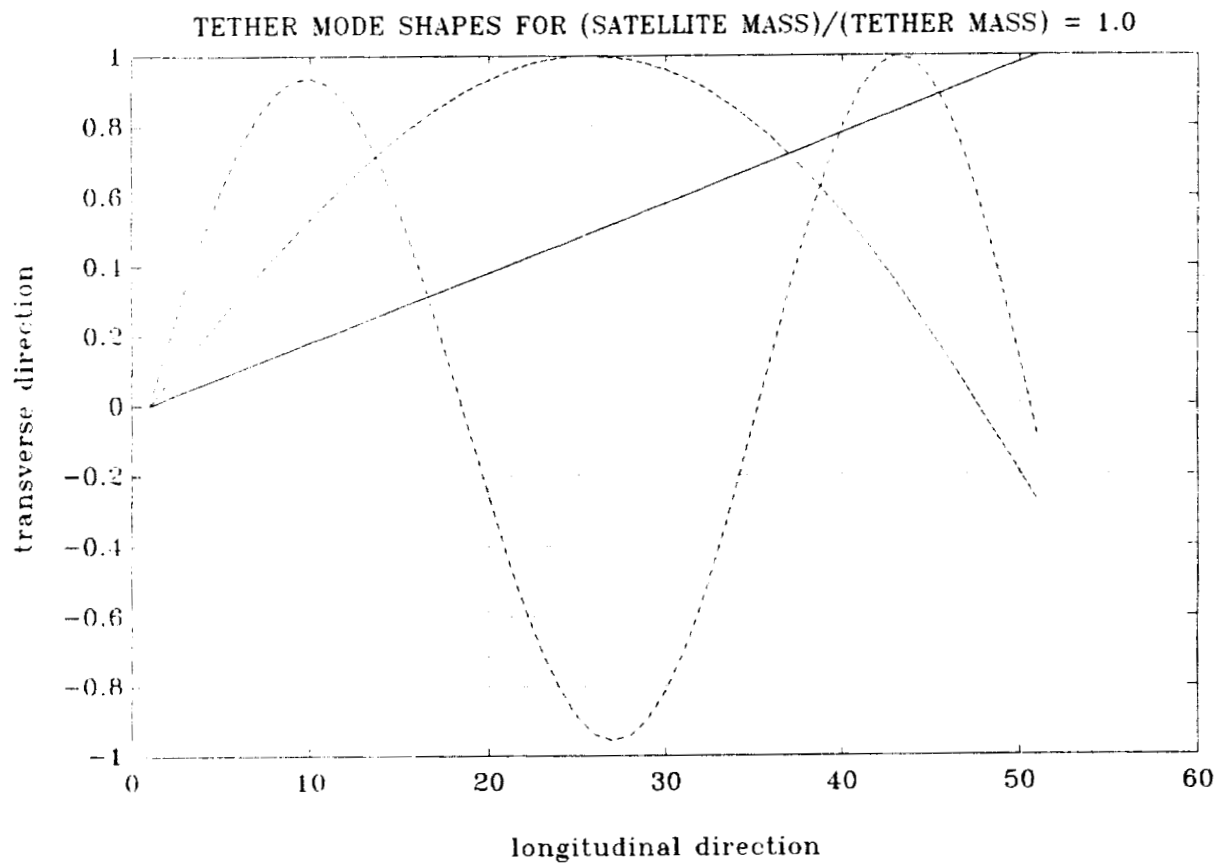


Figure 3: Tether Modal Shapes

COMPUTER IMPLEMENTATION

The 3D tether dynamics algorithm developed above was implemented in a MATLAB program having the following modules.

<u>module</u>	<u>function</u>
tetrun	Create data, call the integrator and print results
tetdat	Generate data for a tether moving in skip rope mode
tettim	Compute time when various lumped masses have been retrieved to the orbiter
tetlen	Compute the time dependent tether length and corresponding derivatives
tetforce	Compute gravity and Coriolis forces on the tether
tettop	Compute position, velocity and acceleration of the point to which the tether is retrieved
tetdef	Form the nonlinear equations of motion of the tether
odeven	Routine to compute solutions at even time increments
ode78	Seventh and eighth order Runge Kutta integrator based on Fehlberg formulas

At present, the program has not been checked fully although initial tension values computed for the skip rope are reasonable, angular values obtained are large. This is apparently caused by the necessity of dividing linear acceleration quantities by $\rho \sin \theta$ to get angular accelerations. Figures [4] and [5] show the angular displacements

obtained for θ and φ . The motion rapidly becomes confined to the orbital plane and amplitudes of θ angles become large. The validity of these results seem questionable.

ORIGINAL PAGE IS
OF POOR QUALITY

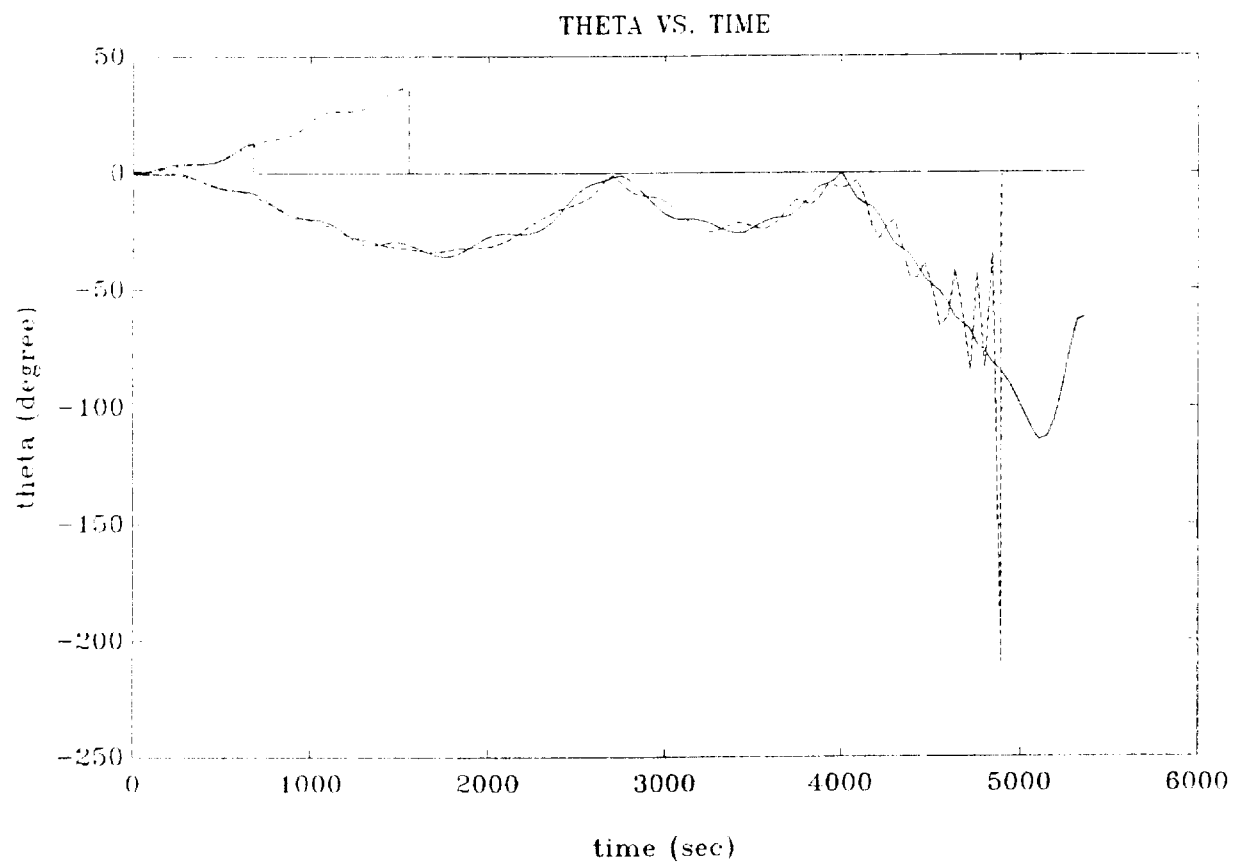


Figure 4

ORIGINAL PAGE IS
OF POOR QUALITY

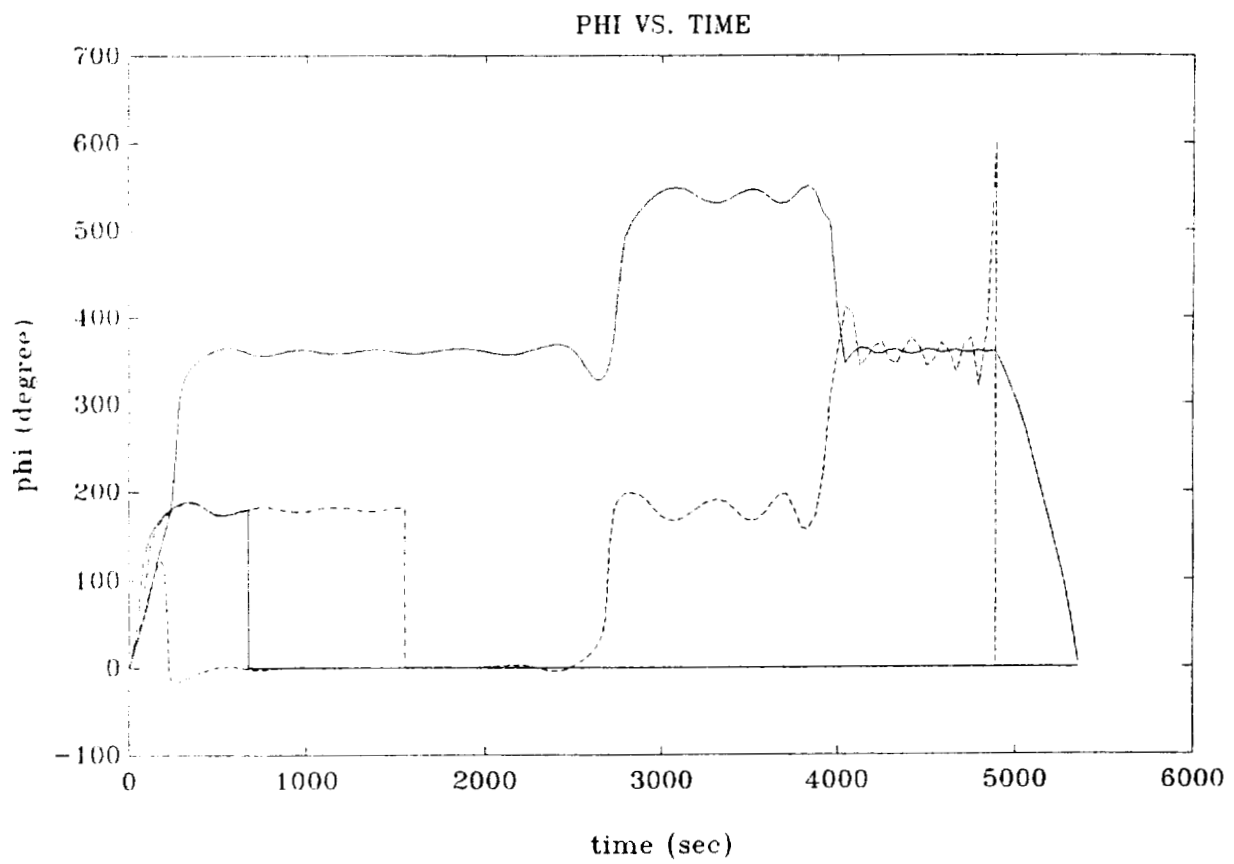


Figure 5


```

%      Program for 3D Dynamic Simulation of a Tether in a
%      Gravity Gradient Field.
%      by
%      Howard B. Wilson, Summer 1989

% The chosen data corresponds to a system which was analyzed by
% David B. Weaver in "Analysis of Transverse Wire Oscillations
% During The Tethered Satellite System Electromagnetic Mission",
% November 24,1987

% global variables for the tether analysis program

global nlink0_ lvec0_ lsum0_ cofexp_ gravity_
global omegac_ masvec0_ tretrv0_
global nlknow_ lvecnow_ masvcnow_

omegac_=1.1847e-3; % orbit angular speed in rad/sec
% The orbit period is 1.473 hours
gravity_=32.2; % gravity constant in ft/sec^2
omegaskip=.01134; % skip rope spin rate (rad/sec). This value
% is 11.31 times the orbit angular speed.
nlink0_=5; % number of links used in the model
mtet=11.43; % total tether mass in slugs
msat=37.7; % satellite mass
z1=65617; % satellite initial z coordinate in feet.
% This equals 20 kilometers
x1=10; % Satellite is initially on the z axis
xsin=286.315; % Amplitude of initial deflection curve
% which is half of a sine curve
omeg=1; % Parameter defining the spatial period
% length of the initial defelction curve
ph0=0; % Start initial motion in the x-z plane
phd0=omegaskip; % Initial spin about z axis
thd1=0; % Initial time derivatives of theta are zero.
thdn=0;
tfrac=7000; % Time at which frac*(total_tether_length)
% has been retrieved
frac=.9; % The solution is generated until
% frac*(total_tether_length) has been
% been retrieved

% Generate starting data

mt=mtet/nlink0_; masvec0_=[mt+msat;mt*ones(nlink0_-1,1)];

[lvec0_,thvec0_,phvec0_,thdvec0_,phdvec0_,z0,x0]=...
tetdat(nlink0_,thd1,thdn,ph0,phd0,z1,x1,xsin,omeg);
% Compute times when successive tether masses reach the
% orbiter

[tretrv0_,lsum0_,cofexp_]=tettim(frac,lvec0_,tfrac);

yinit=[thvec0(:);phvec0(:);thdvec0(:);phdvec0(:)];

for k=1:nlink0_,
    nlknow_=nlink0_-k+1;

```



```

% tmin=tretrv0_(k); tmax=.98*tretrv0_(k+1); h=(tmax-tmin)/50;
tmin=tretrv0_(k); tmax=tretrv0_(k+1)-10; h=(tmax-tmin)/50;
tol=1.e-12; trace=1;
[tout,yout]=odeven('tetdif',tmin,tmax,h,yinit,tol,trace);

ntp=2; nt=length(tout);
yinit=lagtrp(tretrv0_(k+1),tout(nt-ntp+1:nt),yout(nt-ntp+1:nt,:))';
tim=[tim;tout;tretrv0_(k+1)]; yout=[yout;yinit'];
ytep=[];
for j=4:-1:1,
    yinit(j*nlknow_)=[];
    yyy=[yout(:,(j-1)*nlknow_+1:j*nlknow_),zeros(nt+1,k-1)];
    ytep=[yyy,ytep];
end
zout=[zout;ytep];
end
save tet2

```

=====

```

function [lng,th,ph,thd,phd,z,x]=tetdat(n,thd1,thdn,ph0,phd0,zn,...
                                         x0,xsin,omeg)
% [lng,th,ph,thd,phd,z,x]=tetdat(n,thd1,thdn,ph0,phd0,zn,...
%                                x0,xsin,omeg)

```

% Compute data to define an initial planar tether configuration

```

% n          Number of links
% thd1,thdn  Initial values of the time derivative of theta.
%            Theta_dot varies linearly from thd1 at the first
%            link to thdn at the last link.
% ph0,phd0   Initial values of phi and the time derivative of
%            phi. All links have the same initial values for
%            these variable.
% zn         The projection of the tether length on the z axis
% xsin       Amplitude of a sine wave which is added to a
%            linear taper to create the initial radial deflection
%            in the x direction. This deflection has the
%            form  $x = x0*(1 - z/zn) + xsin*\sin(\pi*\omega*z/zn)$ .
% x0         Transverse deflection value at the free end of the
%            tether.

% lng        Vector of lengths of the individual tether links.
%            These lengths are defined by cords on the chosen
%            deflection curve.
% th,ph      Initial theta and phi values.
% thd,phd    Initial time derivatives of theta and phi.
% z,x        Initial z and x coordinates viewed normal to the
%            plane of the system.

```

```

nn=(0:n)'/n;
z=zn*nn;
x=x0*(1-nn)+xsin*sin(pi*omeg*nn);
zdif=z(2:n+1)-z(1:n);
xdif=x(2:n+1)-x(1:n);
ph=ph0*ones(n,1);
phd=phd0*ones(n,1);
th=-atan2(xdif,zdif);
thd=thd1+(thdn-thd1)*nn(2:n+1);
lng=sqrt(xdif.*xdif+zdif.*zdif);

```



```

=====
function [tvtrv,ltotl,cof]=tettim(frac,leng,tfinl)
% [tvtrv,ltotl,cof]=tettim(frac,leng,tfinl)

% This function computes the vector of times at which
% successive links in the tether reach the orbiter during
% retrieval according to an exponential length reduction rate.
% leng      The vector of link lengths. The links are
%            indexed with the bottom link as the first
%            and the base link as the last.
% frac      The fraction of the total length to be
%            retrieved by time tfinl.
% tfinl     The time at which frac*(total tether length)
%            has been taken into the orbiter according to
%            the exponential rate law.
% tvtrv     The vector of times at which link(n),...,
%            link(1) reach the orbiter.
% ltotl     The total tether length leng(1)+...+leng(1)
% cof       The exponent in the tether equation
%            Tether_length = ltotl*exp(cof*t)
n=length(leng); lngsum=flipx(cumsum(flipx(leng(:))));
ltotl=sum(leng); cof=log(1-frac)/tfinl;
lngsum=[lngsum;(1-frac)*ltotl];
tvtrv=log(lngsum/ltotl)/cof;

```

```

=====
function [lvec,lvecd,lvecdd]=tetlen(t)
% [len,lend,lendd]=tetlen(t)
% Compute the vector of lengths and their time derivatives.
% Only the last link changes during the current time interval.

% global variables for the tether analysis program

% global nlink0_ lvec0_ lsum0_ cofexp_
% global omegac_ masvec0_ tretrv0_
% global nlknow_ lvecnow_ masvcnow_

%lvec=lvec0_; lvecd=zeros(lvec); lvecdd=zeros(lvec);
%break

% remaining statements are presently inactive. the tether
% has constant length

len=lsum0_*exp(cofexp_*t);
lend=cofexp_*len;
lendd=cofexp_*lend;
len=len-sum(lvec0_(1:nlknow_-1));
lvec=len; lvecd=lend; lvecdd=lendd;
if nlknow_ > 1
    lvec=[lvec0_(1:nlknow_-1);lvec];
    lvecd=[zeros(nlknow_-1,1);lvecd];
    lvecdd=[zeros(nlknow_-1,1);lvecdd];
end

```

```

=====
function forc=tetforce(t,r,v)

```



```

% Force effects due to gavitational attraction and
% rotation in a gravity gradient field

% global variables for the tether analysis program

% global nlink0_ lvec0_ lsum0_ cofexp_ gravity_
% global omegac_ masvec0_ tretrv0_
% global nlknow_ lvecnow_ masvcnow_

wsq=omegac_*omegac_; w2=2*omegac_;
fx=w2*v(:,3).*masvec0_(1:nlknow_);
fy=-wsq*r(:,2).*masvec0_(1:nlknow_);
fz=( (3*wsq)*r(:,3)-w2*v(:,1) ).*masvec0_(1:nlknow_);
forc=[fx,fy,fz];
% 'in tetforce, (omegac_,masvec_,forc)'
% omegac_,masvec_,forc
% pause
%forc=[zeros(nlknow_,2),(gravity_*masvec0_(1:nlknow_)).*ones(nlknow_,1)];

=====

function [rtop,rtopd,rtopdd]=tetttop(t)
% [rtop,rtopd,rtopdd]=tetttop(t)
% Coordinates of the tether top and related derivatives.
% The top is fixed at present.
rtop =[0; 0; 0];
rtopd =[0; 0; 0];
rtopdd=[0; 0; 0];

=====

function yt=lagtrp(t,tdat,ydat)
% yt=lagtrp(t,tdat,ydat)
% Lagrange interpolation of a vector function yt which
% is a function of scalar time. Interpolation is
% performed such that at tdat(i) the value of yt is
% ydat(i,:). Thus, yt is a polynomial of degree n-1
% where n is the number of components in tdat
[mrow,mcol]=size(ydat);
yt=zeros(1,mcol);
for k=1:mrow
    yt=yt+ydat(k,:)*plag(k,tdat,t);
end

=====

function y=plag(j,tdat,t)
% y=plag(j,tdat,t)
% generates a Lagrange interpolating polynomial
td=tdat(:)'; td(j)=[ ];
y=prod(t-td)./prod(tdat(j)-td);

=====

function zp = tetdif(t,z)
% zp = tetdif(t,z)
% Dynamical equations for a lumped mass 3D tether model

%    written by Howard B. Wilson, Summer 1989

```



```

% global variables for the tether analysis program

% global nlink0_ lvec0_ lsum0_ cofexp_
% global omegac_ masvec0_ ttrrv0_
% global nlknow_ lvecnow_ masvcnow_

% t, z
% nlnow_=5;

n4 = length(z); n = round(n4/4); w3 = ones(1,3);
n1 = n+1; n2 = n1+n; n3 = n2+n; zn = zeros(n,1);

% Obtain local angular coordinates and their derivatives

th = z(1:n); ph = z(n1:n2-1); thd = z(n2:n3-1); phd = z(n3:n4);
ct = cos(th); st = sin(th); cp = cos(ph); sp = sin(ph);
zp = zeros(z); zp(1:n2-1) = z(n2:n4);

% Lengths of tether links and corresponding derivatives defined
% by an external function

[len,lend,lendd] = tetlen(t);

% Reciprocals of mass elements needed later

masinv = 1 ./masvec0_; miv3 = masinv*w3;

% Compute unit base vectors in spherical coordinates
% along with spatial derivatives of those vectors

ur = [st.*cp,st.*sp,ct];
ut = [ct.*cp,ct.*sp,-st];
% size(ur)
% size(zn)
up = [-ur(:,2),ur(:,1),zn];
utt = -ur;
utp = [-ut(:,2),ut(:,1),zn];
upp = [-ur(:,1:2),zn];
len3 = len*w3;
thd3 = thd*w3;
phd3 = phd*w3;

% Local Cartesian components of position vectors and
% velocity components

r = len3.*ur;
% [size(len3);size(ut);size(thd3);size(up);size(phd3)]

v = len3.*(ut.*thd3+up.*phd3)+lend*w3.*ur;

% Compute base point motion defined by an external function

[RT,RTD,RTDD] = tettetop(t);
RT = RT(:)'; RTD = RTD(:)'; RTDD = RTDD(:)';

% global coordinates and velocity vectors

R = ones(n,1)*RT+flipx(cumsum(flipx(r)));
V = ones(n,1)*RTD+flipx(cumsum(flipx(v)));

```



```

% Nodal forces defined by an external function depending on
% time, position and velocity

FRC = tetforce(t,R,V);

% Form the tridiagonal equations to solve for member tensions
if nlknow_ > 1,

    lsq = len.*len;
    b = lsq.*([masinv(2:n);0]+masinv(1:n));
    c = r(1:n-1,:).*r(2:n,:);
    c = -masinv(2:n).*sum(c')';
    fovm = [FRC.*miv3(1:n,:);RTDD];

    e = sum( (r.*( fovm(1:n,:)-fovm(2:n+1,:) ) )' )';
    e = e+sum((v.*v)')'-lend.*lend-len.*lendd;

% Solve for tension multipliers

    alp = trisol([0;c],b,c,e);

% Compute member forces

    tenfrc = [[0 0 0];(alp*w3).*r];

% Compute global accelerations of point masses

    RDD = (FRC+tenfrc(1:n,:)-tenfrc(2:n+1,:)).*miv3(1:n,:);
    RDD = [RDD;RTDD];

% Second derivatives of link radii

    rdd = RDD(1:n,:)-RDD(2:n+1,:);

else

    lsq = len.*len;
    b=lsq*masinv(1);
    fovm=FRC.*miv3(1,:)-RTDD;
    e=sum( (r.*fovm)')';
    e=e+sum( (v.*v)')'-lend.*lend-len.*lendd;
    alp=e/b;
    tenfrc=(alp*w3).*r;
    RDD=(FRC-tenfrc).*miv3(1,:);
    rdd=RDD-RTDD;

end

% Compute local velocity dependent acceleration terms

a = (utt.*thd3+utp.*phd3).*thd3+(upp.*phd3+utp.*thd3).*phd3;
a = a.*len3;

% Compute the second derivatives of the spherical coordinate
% angles to complete formation of the equations of motion.

rdda = rdd-a;
thdd = sum((rdda.*ut)')'-2*lend.*thd;

```



```

thdd = thdd./len;
phdd = sum((rdda.*up)')'./(st.*st)-2*lend.*phd;
phdd = phdd./len;
zp(n2:n4) = [thdd;phdd];

```

```

% End

```

```

=====
function [tout, yout] = odeven(F, t0, tfinal, h, y0, tol, trace)
%
% INPUT:
% F      - String containing name of user-supplied problem description.
%          Call: yprime = fun(t,y) where F = 'fun'.
%          t      - Time (scalar).
%          y      - Solution column-vector.
%          yprime - Returned derivative column-vector; yprime(i) = dy(i)/dt
% t0     - Initial value of t.
% tfinal - Final value of t.
% y0     - Initial value column-vector.
% h      - Time increment between which solution values are output
% tol    - The desired accuracy. (Default: tol = 1.e-3).
% trace  - If nonzero, each step is printed. (Default: trace = 0).
%
% OUTPUT:
% tout   - Returned integration time points in increments of h
%          (kolumn-vector).
% yout   - Returned solution, one solution column-vector per tout-value.
%
tout=(t0:h:tfinal)'; ntims=length(tout); ncols=length(y0);
yout=zeros(ntims,ncols); yout(1,:)=y0(:)';
for j=1:ntims-1
    [ttemp,ytemp]=ode78(F, tout(j), tout(j+1), yout(j,:) , tol, trace);
    [nr,nc]=size(ytemp);
    yout(j+1,:)=ytemp(nr,:);
end

```

```

=====
function [tout, yout] = ode78(F, t0, tfinal, y0, tol, trace)
% ODE78 Integrates a system of ordinary differential equations using
% 7th order formulas.
%
% [tout, yout] = ode78(F, t0, tfinal, y0, tol, trace)
%
% INPUT:
% F      - String containing name of user-supplied problem description.
%          Call: yprime = fun(t,y) where F = 'fun'.
%          t      - Time (scalar).
%          y      - Solution column-vector.
%          yprime - Returned derivative column-vector; yprime(i) = dy(i)/dt
% t0     - Initial value of t.
% tfinal - Final value of t.
% y0     - Initial value column-vector.
% tol    - The desired accuracy. (Default: tol = 1.e-6).
% trace  - If nonzero, each step is printed. (Default: trace = 0).
%
% OUTPUT:

```



```

% tout - Returned integration time points (row-vector).
% yout - Returned solution, one solution column-vector per tout-value.
%
% The result can be displayed by: plot(tout, yout).

% Daljeet Singh
% Dept. Of Electrical Engg., The University of Alabama.
% 11-24-1988.

% The Fehlberg coefficients:
alpha = [ 2./27. 1/9 1/6 5/12 .5 5/6 1/6 2/3 1/3 1 0 1 ]';
beta = [ [ 2/27 0 0 0 0 0 0 0 0 0 0 0 ]
[ 1/36 1/12 0 0 0 0 0 0 0 0 0 0 ]
[ 1/24 0 1/8 0 0 0 0 0 0 0 0 0 ]
[ 5/12 0 -25/16 25/16 0 0 0 0 0 0 0 0 ]
[ .05 0 0 .25 .2 0 0 0 0 0 0 0 ]
[ -25/108 0 0 125/108 -65/27 125/54 0 0 0 0 0 0 ]
[ 31/300 0 0 0 61/225 -2/9 13/900 0 0 0 0 0 ]
[ 2 0 0 -53/6 704/45 -107/9 67/90 3 0 0 0 0 ]
[ -91/108 0 0 23/108 -976/135 311/54 -19/60 17/6 -1/12 0 0 0 ]
[ 2383/4100 0 0 -341/164 4496/1025 -301/82 2133/4100 45/82 45/164 18/41 0 0 ]
[ 3/205 0 0 0 0 -6/41 -3/205 -3/41 3/41 6/41 0 0 ]
[ -1777/4100 0 0 -341/164 4496/1025 -289/82 2193/4100 51/82 33/164 12/41 0 0 ]
chi = [ 0 0 0 0 0 34/105 9/35 9/35 9/280 9/280 0 41/840 41/840 ]';
psi = [ 1 0 0 0 0 0 0 0 0 0 1 -1 -1 ]';
pow = 1/8;
if nargin < 6, trace = 0; end
if nargin < 5, tol = 1.e-6; end

% Initialization
t = t0;
% the following step parameters are used in ODE45
% hmax = (tfinal - t)/5;
% hmin = (tfinal - t)/20000;
% h = (tfinal - t)/100;
% The following parameters were taken because the integrator has
% higher order than ODE45. This choice is somewhat subjective.
hmax = (tfinal - t)/2.5;
hmin = (tfinal - t)/10000;
h = (tfinal - t)/50;
y = y0(:);
f = y*zeros(1,13);
tout = t;
yout = y.';
tau = tol * max(norm(y, 'inf'), 1);

if trace
% clc, t, h, y
clc, t, h
end
% The main loop
while (t < tfinal) & (h >= hmin)
if t + h > tfinal, h = tfinal - t; end

% Compute the slopes
f(:,1) = feval(F,t,y);
for j = 1: 12
f(:,j+1) = feval(F, t+alpha(j)*h, y+h*f*beta(:,j));
end

```



```

% Truncation error term
gammal = h*41/840*f*psi;

% Estimate the error and the acceptable error
delta = norm(gammal,'inf');
tau = tol*max(norm(y,'inf'),1.0);

% Update the solution only if the error is acceptable
if delta <= tau
    t = t + h;
    y = y + h*f*chi;
    tout = [tout; t];
    yout = [yout; y.'];
end
if trace
    % home, t, h, y
    home, t, h
end

% Update the step size
if delta ~= 0.0
    h = min(hmax, 0.8*h*(tau/delta)^pow);
end
end;

if (t < tfinal)
    disp('SINGULARITY LIKELY.')
    t
end

```


CONCLUSIONS AND RECOMMENDATIONS

The computer implementation of the 3D version tether dynamics program should be studied further to resolve numerical difficulties encountered when one or more of the θ -angles are small. An alternative formulation which may be appropriate for this case is to develop the equations of motion based on a different set of Euler angles than those presently used in the program. This work will be performed during the coming months.

REFERENCES

1. Baker, W. P. et al., "Tethered Satellite Study," NASA Technical Memorandum TM X-73314, Marshall Space Flight Center, Huntsville, Alabama, March 1976.
2. Rheinfurth, M. H. and Galaboff, Z. J. "Modal Analysis of a Nonuniform String With End Mass and Variable Tension, NASA Technical Paper 2198, Marshall Space Flight Center, Huntsville, Alabama, 1983.
3. MATLAB for MS-DOS Personal Computers, User's Guide, The MathWorks, Inc., 21 Eliot Street, South Natick, MA 01760.
4. Greenwood, D. T., Principles of Dynamics, 2nd Ed., Prentice-Hall, Englewood Cliffs, 1988.

1989

NASA/ASEE SUMMER FACULTY FELLOWSHIP PROGRAM

MARSHALL SPACE FLIGHT CENTER

THE UNIVERSITY OF ALABAMA IN HUNTSVILLE

TECHNIQUES FOR STUDYING THE EFFECTS OF MICROGRAVITY

ON MODEL PARTICLE/CELL SYSTEMS

Prepared by:	Ronald B. Young
Academic Rank:	Professor
University and Department:	Univ. of Alabama Huntsville Department of Biological Sciences

NASA/MSFC	
Laboratory:	Space Science
Division:	Low Gravity Science
Branch:	Biophysics
MSFC Colleague:	Robert Snyder
Date:	August 9, 1989
Contract No:	NGT-01-008-021 University of Alabama in Huntsville

TECHNIQUES FOR STUDYING THE EFFECTS OF MICROGRAVITY
ON MODEL PARTICLE/CELL SYSTEMS

by

Ronald B. Young
Professor of Biological Sciences
University of Alabama in Huntsville
Huntsville, Alabama 35899

ABSTRACT

In an effort to learn more about the effects of a simulated low gravity environment on skeletal muscle, skeletal muscle cell cultures were grown within the lumen of XM-80 hollow fibers (i.d. = 0.5 mm) in a Clinostat rotating at 100 rpm. Cells were isolated from the thigh muscle tissue of 12 day embryos and were cultured for up to 14 days in the hollow fiber environment. Cells proliferated to confluency within several days, and fusion into multinucleated myotubes was then apparent. Fibers were stretched by a built-in spring mechanism to hold the fiber tightly at the center of rotation, and sections of the fiber were removed at 3, 7 and 14 days for electron microscopic analysis. When the Clinostat is rotated in the horizontal position, the gravity vector approaches zero and the cells are in an environment that simulates microgravity. Control experiments consist of one fiber rotated in the vertical position in the clinostat and another fiber that is held in a horizontal configuration in a comparable sized tube that is not rotated at all. Examination of skeletal muscle cells by electron microscopy revealed that myoblast fusion and myofibril accumulation were extensive. Two general conclusions were apparent from this investigation. First, muscle cells undergo the normal progression of proliferation, fusion and myofibril assembly in the presence of simulated microgravity for the first week in culture. After 14 days, however, many muscle fibers undergo degeneration such that myofibrillar structures are not extensive or well organized. Second, although no major abnormalities in myofibril assembly were detected in Clinostat-rotated cultures in comparison to controls that were not rotated in a Clinostat, the myofibrils in non-rotated controls tend to be more highly organized than those in either horizontally or vertically rotated Clinostat samples.

ACKNOWLEDGEMENTS

I would like to acknowledge Dr. Robert S. Snyder for providing the opportunity for the Summer Faculty Fellowship and Ms. Teresa Miller for assistance with all aspects of the research. This work could not have been possible without the generous contributions of their time and space.

I also thank my coworkers in the Department of Biological Sciences at the University of Alabama in Huntsville for contributing to the development of this project. Special thanks go to Debbie Windham for her hard work and skill with the Clinostat and the electron microscopy portion of the work.

Finally, I am indebted to the National Aeronautics and Space Administration for providing this unique and scientifically beneficial program.

BACKGROUND

The primary reasons for our initial interest in this research emanate from our experience in studying protein synthesis, degradation and gene expression in skeletal muscle cells, and from the extensive physical problems resulting from atrophy and weakness of skeletal and cardiac muscles following prolonged exposure to a low gravity environment (c.f., Morey-Holton and Wronski, 1981; Oganov et al., 1982; Grigor'yeva and Kozlovskaya, 1983; Leonard et al., 1983). Clearly, dramatic alterations in the balance between the rate of protein synthesis and the rate of protein degradation must accompany major changes in the quantity of muscle tissue, and it also seems exceedingly unlikely that loss of up to 25% of skeletal muscle mass could take place in the absence of switches in myofibrillar protein gene expression. The extent of skeletal muscle loss in humans and experimental animals after space flight is rather dramatic. To cite two specific examples, crew members of the first two Skylab missions maintained a negative nitrogen balance of approximately 4.5 g/day at the same time that total body potassium was also decreasing (Whedon et al., 1977). Much of this increased protein catabolism was due specifically to muscle protein degradation as evidenced by elevated rates of 3-methylhistidine excretion (Leach et al., 1979). Also, a pronounced decrease in mass and in myofibrillar cross sectional area of the soleus muscle in rats after exposure to a low gravity environment for 7 days has been reported (Goldspink et al., 1980; Riley et al., 1987).

An interesting and intriguing explanation for the effect of prolonged space flight on muscle atrophy is that a secretory defect for growth hormone (GH) may be occurring in pituitary cells (Grindeland et al., 1987a; Motter et al., 1987). Specifically, anterior pituitary cells isolated from rats flown for 7 days on the SL-3 mission secreted approximately half as much of a biologically active form of GH into culture media as ground-based controls. This observation has been qualitatively confirmed and extended by several independent approaches, including the finding that the serum concentration of GH is reduced by 50% in rats exposed to simulations of microgravity by hindlimb suspension (Motter et al., 1987).

Additionally, Grindeland et al. (1987b) have concluded that muscles of rats exposed to microgravity are significantly more resistant to exogenous and circulating GH than the skeletal muscles of control rats, since administration of GH did not alleviate muscle atrophy in animals in which it was known that GH secretion rate and serum levels of GH were also decreased by 50%. These results imply that the defect in GH utilization may extend to skeletal muscles as well.

Thus, it seems clear that exogenous factors are responsible for at least a portion of muscle atrophy; however, it also seems possible that microgravity has direct intrinsic effects on the cytoskeletal and myofibrillar contractile systems. Examples of direct effects of microgravity on cells are rather limited, but available circumstantial data are consistent with the explanation that the cytoskeletal system is involved. For example, secretory processes in general, and by definition the secretion of hormones from the pituitary, are microfilament-dependent, and it is plausible that the reduced secretion of GH described above results from a direct effect on the cytoskeletal system. Moreover, if the defect in GH utilization extends to skeletal muscle cells, and if the Insulin-like Growth Factors (IGF's, which are regulated by GH and act directly on skeletal muscle) and their receptors are internalized by cytoskeletal-dependent processes into the cytoplasm of muscle cells, then this process may also be directly affected by microgravity. Since some of the contractile proteins in the highly organized myofibrillar protein arrays in sarcomeres are nothing more than different isoforms of some of the cytoskeletal contractile proteins, an effect on expression of one class of these proteins could logically be expected to have an effect on expression of the other. Further substantiation of this possibility results from the fact that the myosin heavy chain genes are members of a rather large multigene family that may have up to twenty members in some species such as chickens, and which is known to exhibit a significant level of plasticity in its ability to have different isoforms expressed under different tissue, developmental and environmental conditions. Most crucial, however, is the fact that neither the effect of actual microgravity nor the effect of simulated microgravity on the organization, synthesis/degradation or gene expression of the contractile proteins has ever been evaluated under critically controlled conditions. One of the only possible ways to evaluate this possibility in the absence of prolonged space flights is with cultured muscle cells grown within the fibers of a rotating Clinostat. As discussed below, this instrument has the effect of mimicing a low gravity environment, and therefore allows some of the above processes to be evaluated.

OBJECTIVES

The general objective of this research was to assess the effects of exposure to simulated microgravity on ultrastructural aspects of the contractile system in chicken skeletal muscle cells using a rotating Clinostat . This general objective had two specific experimental components: (1) The progression of changes in cell morphology, fusion, and patterns of contractile filament organization in muscle cell cultures grown in hollow fibers in the Clinostat were evaluated, with appropriate controls. (2) Since it was determined that muscle cells in culture obtain their maximum amount of myofibrillar proteins after approximately one week in culture, a more extensive comparison of the myofibrillar organization in horizontally and vertically rotated cultures was carried out on the 7-day muscle cells in the hollow fibers. The primary technique for this work was electron microscopy.

METHODS AND PROCEDURES

1. Chick skeletal muscle cell cultures

Thigh muscle from 12 day broiler chick embryos was removed and disaggregated into individual cells by vortexing the muscle in growth medium on a vortex mixer at maximum speed for 20-30 seconds (Young et al., 1981). The suspension was then filtered through nylon mesh to remove connective tissue and bone, and the cells were recovered by centrifugation. Following resuspension in an appropriate amount of growth medium (Eagle's Minimum Essential Medium containing 5% chick embryo extract, 10% horse serum, 50 units/ml penicillin, 50 ug/ml streptomycin, 2.5 ug/ml fungizone) to give a concentration of 1.5×10^{10} cells/ml, the cell suspension was injected into a 70 mm long piece of 0.5 mm (inner diameter) XM-80 hollow fiber using a 1cc syringe and a 26 3/8 gauge needle. Both ends of the fiber were sealed with hot wax, and the fiber was loaded into a glass tube containing 5 ml of complete media. The fiber was held taut by a spring so that it would always be at the center of rotation of the Clinostat, and the glass tube was then sealed and the entire assembly loaded into the Clinostat.

Muscle cell cultures prepared as described above proliferate, fuse and begin to synthesize myofibrillar protein within 2-3 days in culture, and under most experimental conditions we have employed so far, they attain a maximum and constant quantity of myofibrillar proteins by approximately 7 days. Because the synthesis rate and the degradation rate must be exactly equal to each other in order to maintain a constant quantity of protein at steady-state, and because perturbations in either synthesis or degradation rates will result in a net change in the quantity and/or organization pattern of myofibrillar proteins, these cells will provide an excellent model for studying the dynamics of muscle protein accumulation and loss.

2. Microscopic Evaluation of Cells Grown in the Clinostat

A. Light Microscopy

Fibers were removed from Clinostat cultures and fixed in a 5% neutral buffered formalin solution for a minimum of 24 hours. The fibers were dehydrated through a graded ethanol series of 70%, 95%

and absolute ethanol, followed by a final treatment in xylene. The fibers were soaked in hot paraffin for 4-8 hours, embedded in the paraffin in plastic molds and sectioned with a microtome. The thin sections were rehydrated through a reverse graded alcohol series (100%, 95%, 70%) and deionized water, and subsequently stained with a hematoxylin/eosin or PAS myofibril stain using standard staining procedures. Slides were viewed and photomicrographs made at 45X and 100X. These light micrographs were useful for routine monitoring of the rate of cell growth and differentiation under the different experimental treatments.

B. Transmission Electron Microscopy

Fibers containing the cell cultures from the Clinostat were fixed in 4% buffered glutaraldehyde, followed by 1% osmium tetroxide fixation. The fibers were partially dehydrated in ethanol (25% and 50%) and stained with 1% uranyl acetate. After complete dehydration through a graded ethanol series (85%, 95% and absolute) the fibers were embedded in Spurr embedding medium and thin sectioned using a microtome. Sections were viewed and photographed with a Philips Model 201C transmission electron microscope. These electron micrographs were analyzed to determine if simulated microgravity had direct ultrastructural effects on the sarcomeric and/or cytoskeletal system in muscle cells.

To facilitate unbiased comparison of electron micrographs, samples were analyzed in a double blind fashion. That is, the samples were coded in the cell culture laboratory by someone other than the investigator doing the microscopy. Thus, the microscopist had no knowledge about the identity of the samples being sectioned and photographed. The microscopist was given instructions only to study each sample and then to take four electron micrographs from each sample that best represented that sample. Particular attention was directed to photographing representative areas containing myofibrillar structures or any unusual intracellular components. The electron micrographs shown in Figures 1-10 in this report were selected from several hundred photographs to represent consensus patterns that were observed. It should be emphasized that enormous variations in muscle samples always are present, and it is not possible to quantitate or to statistically evaluate most data that are obtained by electron microscopy.

RESULTS

Theory of simulating microgravity using a Clinostat. The fast rotating Clinostat used for these experiments was designed at MSFC and generously loaned to us by Dr. Robert Snyder. Briefly, the Clinostat is made up of a culture chamber which rotates about a horizontal axis, and an XM-80 hollow fiber containing cells is mounted in the center of rotation. Depending on the density difference between the particles and the liquid in which they are suspended, the particles may settle within circular trails. At high enough speed of rotation, cells become motionless with respect to the gravity vector and microgravity can be simulated (Briegleb, 1983). The simulation approaches 100% for particles in suspension where centrifugal forces and Brownian motion offset each other. In the hollow fibers containing muscle cells, however, the diameter of the fiber is small enough that the centrifugal force is only approximately $0.006 \times g$ at 100 rpm of rotation. Operation of the Clinostat in the horizontal position simulates microgravity, and operation in the vertical position serves as a control since the gravity vector is always constant in the vertical position. Additional control experiments consisting of cells in hollow fibers lying horizontally in a sealed tube of the same approximate dimensions as the chamber of the Clinostat are also conducted to ensure that a horizontal, non-rotating control is always available. The cells are placed inside the small hollow fiber inside the rotating chamber, the ends are sealed with wax, and the fiber is held taut by the spring loaded mount. This ensures that the fiber is always held at precisely the center of rotation. A tachometer for monitoring the speed of rotation is outside the incubator.

Developmental changes in muscle cells. The first series of micrographs in this report were taken from control fibers (i.e., fibers that were held in the horizontal position and which were not rotated). After three days in hollow fibers, muscle cells have initiated the process of fusion and myofibrillogenesis. As shown in the electron micrographs in Figures 1 and 2, fusion has been initiated as indicated by the presence of adjacent nuclei in multinucleated myotubes. Additionally, the fact that myofibril assembly has been initiated is suggested by the filamentous material in the general vicinity of the nuclei in Figures 1 and 2. In some instances at this stage of differentiation, rudimentary banding patterns are being formed; however, they lack the highly organized pattern that is observed later in muscle development or in adult skeletal muscle (c.f., Figures 3 and 4).

By seven days in culture intact, functional, well-aligned myofibrils are present in large quantities (Figures 3 and 4). In many cases, the myotubes contain more myofibrils than shown in these two figures, and the side-to-side alignment of the myofibrils is sometimes not as well organized. The appearance of the muscle cells in these two figures is also representative of that which would be observed in muscle cells in culture on polystyrene culture dishes at approximately the same age.

By fourteen days in culture (Figures 5 and 6), several additional changes have occurred in the cells in hollow fibers that are also consistent with those observed in conventional cell cultures. One of the unfortunate consequences of growing skeletal muscle cells in culture in the absence of anchoring connective tissue is that the cells will sometimes contract so vigorously that they detach themselves from the surface and die (Once the cell membrane has been ruptured, the high concentration of calcium ions in the culture medium causes the fractured myotubes to contract to the point of complete disruption of the cell). Thus, after two weeks in culture many of the remaining cells are those in which no myofibrillar structures are present. Moreover, the percentage of nonmuscle cells will obviously be higher if some of the myotubes have become lost in the medium. These observations are borne out by the electron micrographs of fourteen-day cultures shown in Figures 5 and 6. Thus, for the purposes of this project, the optimum period of time to examine myofibrillar assembly is approximately one week after establishment of the cultures in the hollow fiber, and all subsequent comparisons were made at this time.

The experiment from which the electron micrographs in Figures 1 through 6 were taken was a control experiment in which the cells were held in a horizontal position and were not rotated. This is emphasized for two reasons. First, all subsequent electron micrographs of clinostat-treated samples after seven days in culture should be compared to the seven-day control samples in Figure 3 and Figure 4. Second, the developmental changes in myogenesis in the clinostat were comparable to those observed in the non-rotated control samples, with exceptions noted later in this section. In general, cells grew at the same rate, fused at the same general time and accumulated myofibrils to the same extent in both horizontally rotated samples and vertically rotated muscle samples.

Electron micrographs from muscle cells grown for seven days under conditions of horizontal rotation in the clinostat are shown in Figures 7 and 8, and micrographs from muscle grown for seven days

under conditions of vertical rotation in the clinostat are shown in Figures 9 and 10. Two general conclusions are apparent from these photographs. First, the intracellular organization in horizontally and vertically rotated samples is similar. Cross-striations of various degrees of organization are apparent in both horizontal and vertical samples, ranging from barely distinguishable banding patterns (Figure 7) to quite highly organized patterns in other cells (Figure 10). The second conclusion from this study is that the myofibrils seem generally to be more highly organized and in tighter register in the control cultures (i.e., horizontal, non-rotated) than in any of the Clinostat samples. Comparison of Figures 3 and 4 with Figures 7-10 illustrate this point. Thus, it appears that rotation of muscle samples alone has more effect on myofibrillar organization than whether the samples are rotated in the horizontal position (i.e., simulating microgravity) or in the vertical position (i.e., with the gravity vector constant on the cells).

LITERATURE CITED

- Brieglieb, W. 1983. Proceedings of Workshop on Space Biology. Cologne, Germany, March 9-11, 1983. 97-101.
- Goldspink, D.F., A.J. Morton, P. Loughna and G. Goldspink. Pflugers Archiv. 407: 333-340.
- Grindeland, R. et al., 1987a. Am. J. Physiol. 252: R209-R215.
- Grindeland, R.E., T.N. Fast, M. Vasques, T. Satyanaranyane and M. Ruder. 1987. Space Life Sciences Symposium: Three Decades of Life Science Research in Space. June 21-26, 1987. Washington, D.C., pp. 82-83.
- Grigor'yeva, L.S. and I.B. Kozlovskaya. 1983. Kosmicheskaya Biologiya i Aviakosmicheskaya Meditsina, 17: 29-35.
- Leach, C.S., S.I. Altchuler and N.M. Cintron-Trevino. 1983. Medicine and Science in Sports and Exercise. 15: 432-440.
- Leonard, J.I., C.S. Leach, P.C. Rambaut. 1983. Am. J. Clin. Nutr. 38: 667-669.
- Motter, K., M. Vasques, C. Hayes, M. Kendall, G. Tietjen, W.C. Hymer and R. Grindeland. 1987. Space Life Sciences Symposium: Three Decades of Life Science Research in Space. June 21-26, 1987. Washington, D.C., pp. 52-53.
- Morey-Holton, E. and T.J. Wronski. 1981. Animal models for simulating weightlessness. The Physiologist. 24 (6): S/45-S/48.
- Oganov, V.S., S.A. Skuratove, L.M. Murashko, M.A. Shirvinskaya, T. Szilagyi, A. Szoor, M. Rapcsak, O. Takacs, S.S. Oganessian, and Z.S. Davtyan. 1982. Biofizika, 27: 41-46.
- Riley, D.A., S. Ellis, G.R. Slocum and F.R. Sedlak. 1987. Space Life Sciences Symposium: Three Decades of Life Science Research in Space. June 21-26, 1987. Washington, D.C., pp. 106-107.
- Whedon, G.D., L. Lutwak, P. Rambaut et al. 1977. In: Biomedical Results from Skylab, NASA SP-377. R.S. Johnston and L.F. Dietlein (Eds.). Washington, DC: National Aeronautics and

Space Administration.

Young, R.B., D.G. McConnell, C.H. Suelter, T.A. Philips. 1981.
Muscle and Nerve 4, 117-124.

ORIGINAL PAGE
BLACK AND WHITE PHOTOGRAPH

ORIGINAL PAGE IS
OF POOR QUALITY



Figure 1. Control Muscle Cells After 3 Days of Incubation. x5,000

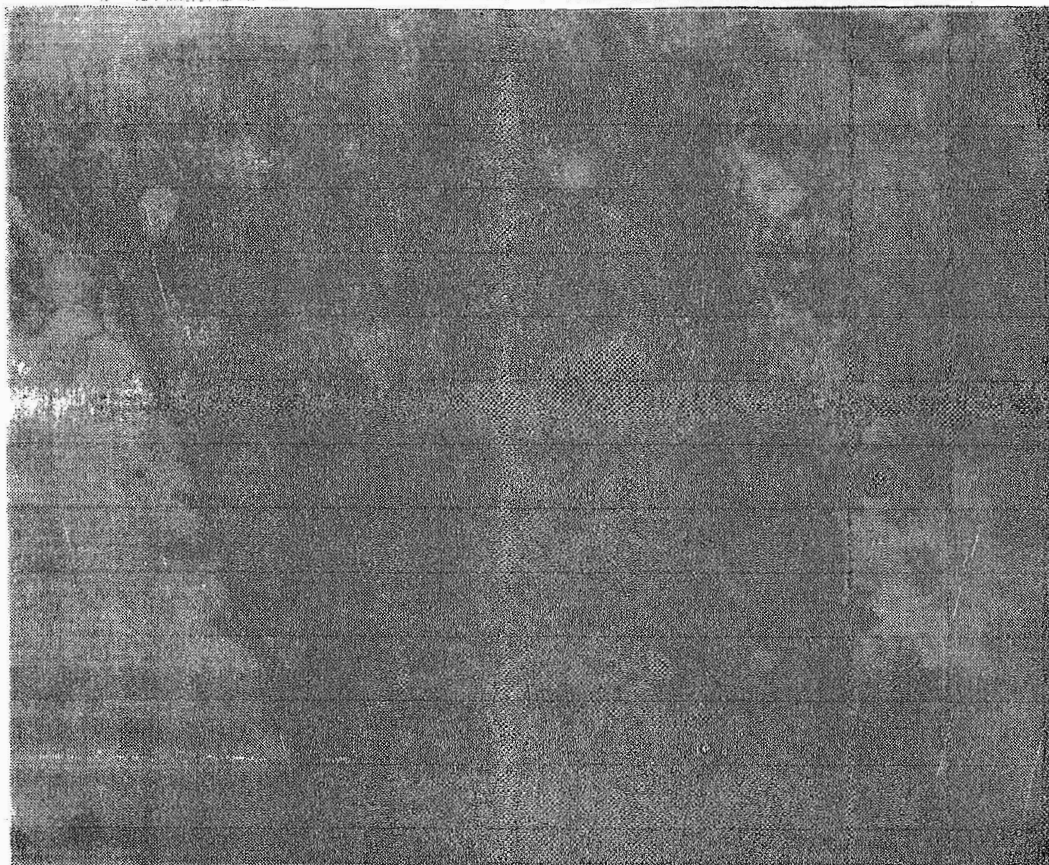


Figure 2. Control Muscle Cells After 3 Days of Incubation. x5,000

ORIGINAL PAGE
BLACK AND WHITE PHOTOGRAPH

ORIGINAL PAGE IS
OF POOR QUALITY



Figure 3. Control Muscle Cell After 7 Days of Incubation. x5,000



Figure 4. Control Muscle Cells After 7 Days of Incubation. x5,000

ORIGINAL PAGE
BLACK AND WHITE PHOTOGRAPH

ORIGINAL PAGE IS
OF POOR QUALITY

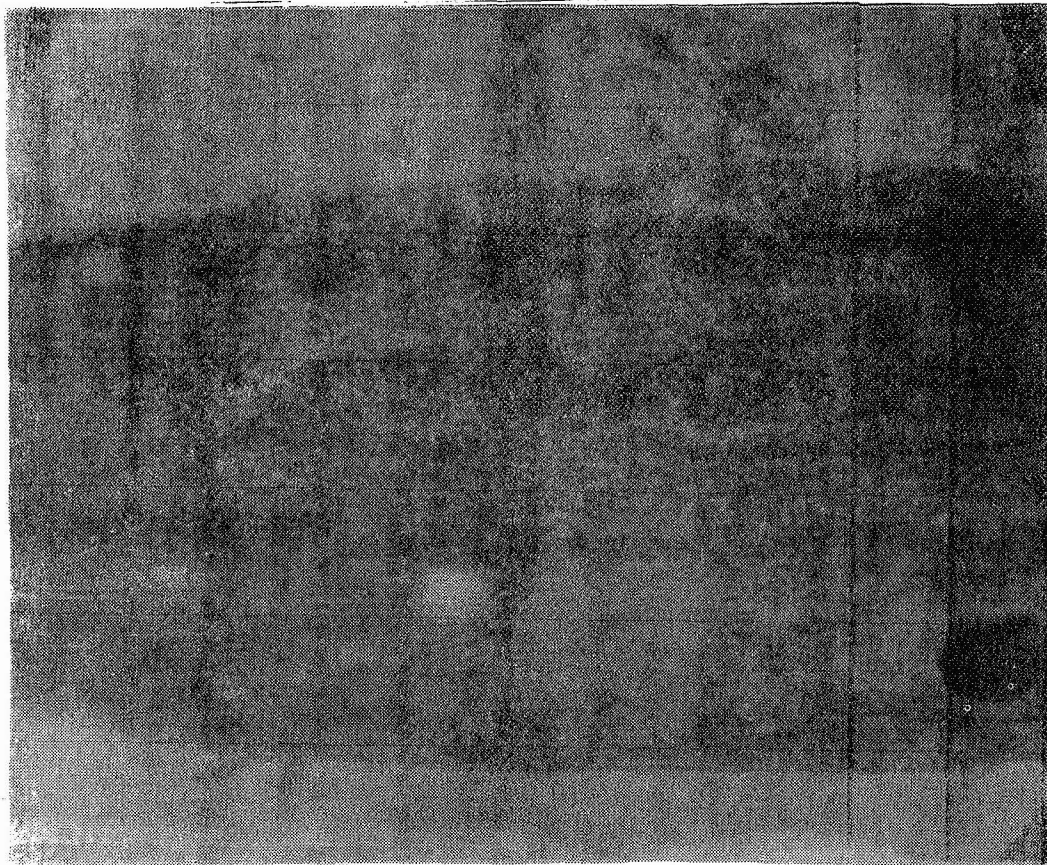


Figure 5. Control Muscle Cell After 14 Days of Incubation. x5,000

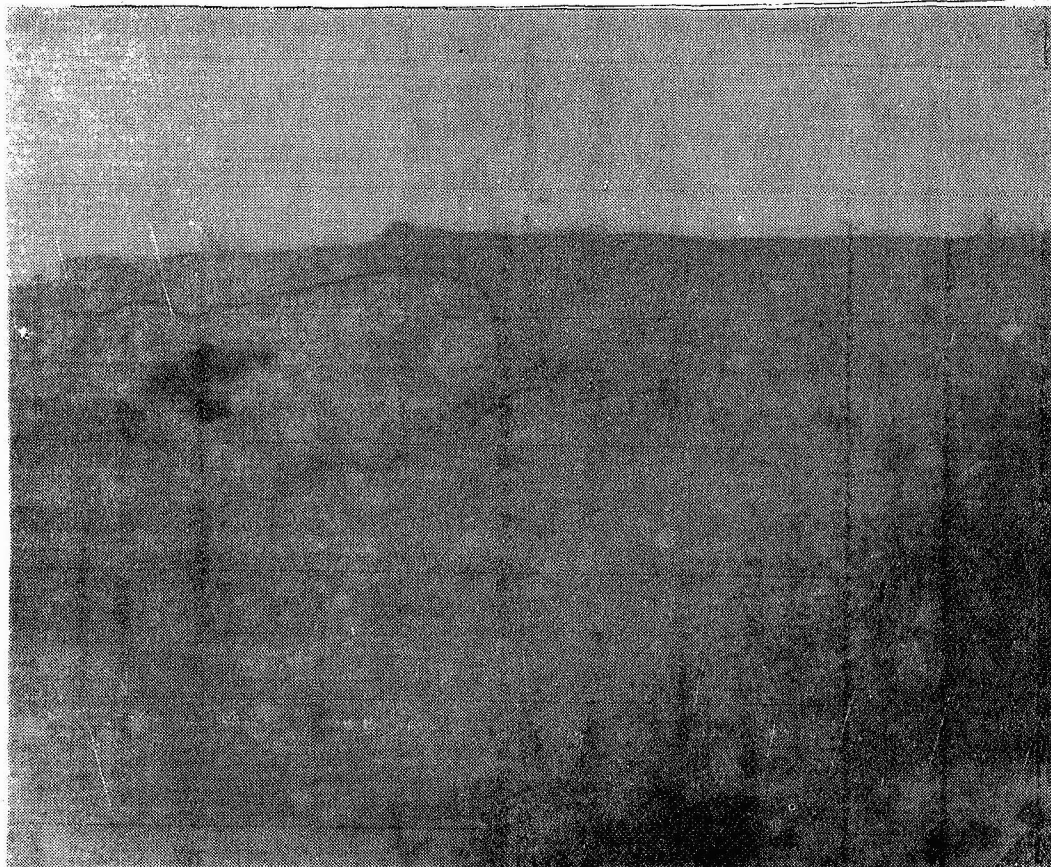
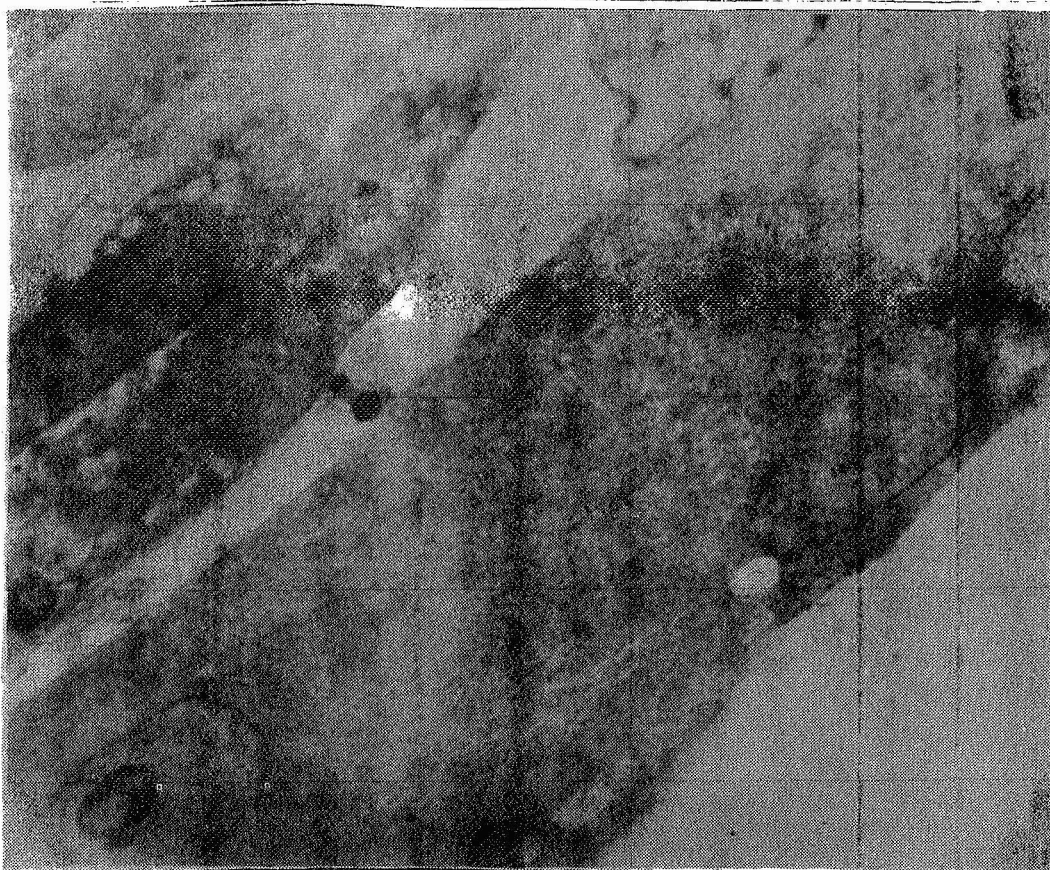


Figure 6. Control Muscle Cell After 14 Days of Incubation. x5,000



ORIGINAL PAGE IS
OF POOR QUALITY

Figure 7. Muscle Cell After 7 Days of Rotation in the Horizontal Position in the Clinostat at 100 rpm. x5,000

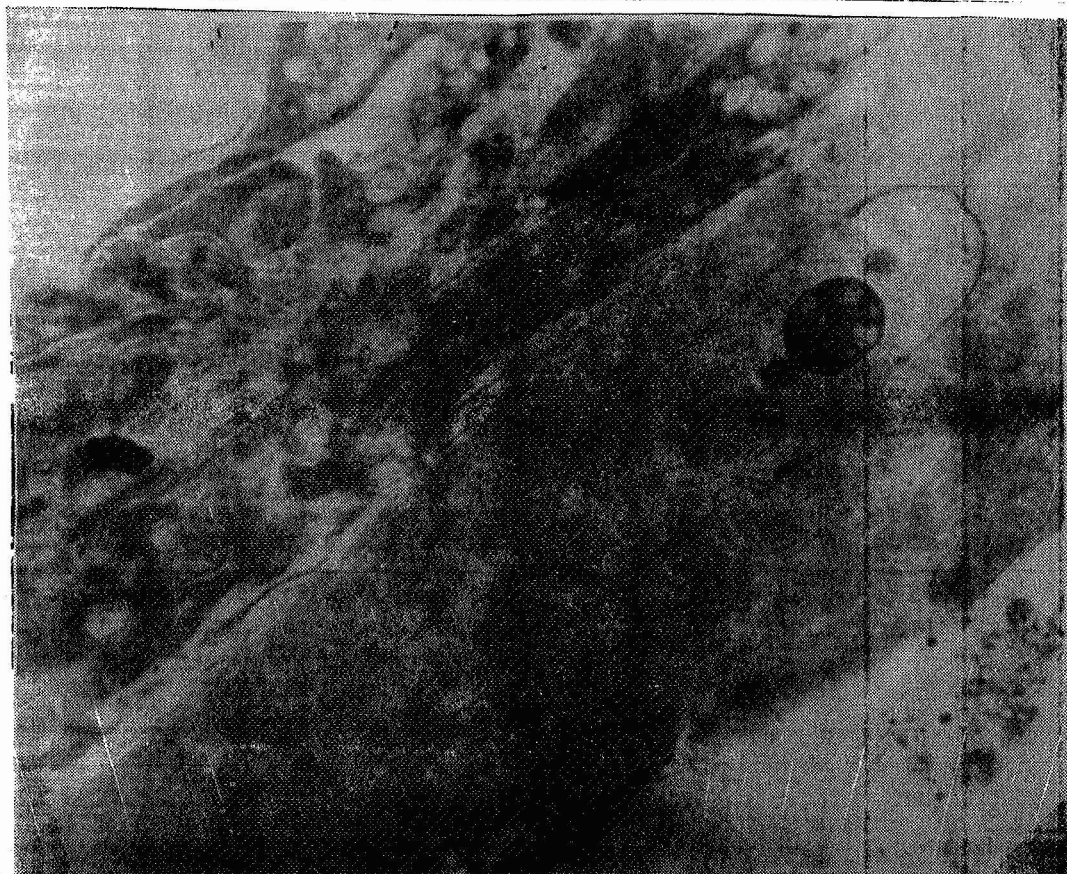


Figure 8. Muscle Cell After 7 Days of Rotation in the Horizontal Position in the Clinostat at 100 rpm. x5,000

ORIGINAL PAGE
BLACK AND WHITE PHOTOGRAPH

ORIGINAL PAGE IS
OF POOR QUALITY



Figure 9. Muscle Cell After 7 Days of Rotation in the Vertical Position in the Clinostat at 100 rpm. x5,000



Figure 10. Muscle Cell After 7 Days of Rotation in the Vertical Position in the Clinostat at 100 rpm. x5,000

